

Lecture Notes in Civil Engineering

M. S. Ranadive
Bibhuti Bhusan Das
Yusuf A. Mehta
Rishi Gupta *Editors*

Recent Trends in Construction Technology and Management

Select Proceedings of ACTM 2021

 Springer

Lecture Notes in Civil Engineering

Volume 260

Series Editors

Marco di Prisco, Politecnico di Milano, Milano, Italy

Sheng-Hong Chen, School of Water Resources and Hydropower Engineering,
Wuhan University, Wuhan, China

Ioannis Vayas, Institute of Steel Structures, National Technical University of
Athens, Athens, Greece

Sanjay Kumar Shukla, School of Engineering, Edith Cowan University, Joondalup,
WA, Australia

Anuj Sharma, Iowa State University, Ames, IA, USA

Nagesh Kumar, Department of Civil Engineering, Indian Institute of Science
Bangalore, Bengaluru, Karnataka, India

Chien Ming Wang, School of Civil Engineering, The University of Queensland,
Brisbane, QLD, Australia

Lecture Notes in Civil Engineering (LNCE) publishes the latest developments in Civil Engineering—quickly, informally and in top quality. Though original research reported in proceedings and post-proceedings represents the core of LNCE, edited volumes of exceptionally high quality and interest may also be considered for publication. Volumes published in LNCE embrace all aspects and subfields of, as well as new challenges in, Civil Engineering. Topics in the series include:

- Construction and Structural Mechanics
- Building Materials
- Concrete, Steel and Timber Structures
- Geotechnical Engineering
- Earthquake Engineering
- Coastal Engineering
- Ocean and Offshore Engineering; Ships and Floating Structures
- Hydraulics, Hydrology and Water Resources Engineering
- Environmental Engineering and Sustainability
- Structural Health and Monitoring
- Surveying and Geographical Information Systems
- Indoor Environments
- Transportation and Traffic
- Risk Analysis
- Safety and Security

To submit a proposal or request further information, please contact the appropriate Springer Editor:

- Pierpaolo Riva at pierpaolo.riva@springer.com (Europe and Americas);
- Swati Meherishi at swati.meherishi@springer.com (Asia—except China, and Australia, New Zealand);
- Wayne Hu at wayne.hu@springer.com (China).

All books in the series now indexed by Scopus and EI Compendex database!

M. S. Ranadive · Bibhuti Bhusan Das ·
Yusuf A. Mehta · Rishi Gupta
Editors

Recent Trends in Construction Technology and Management

Select Proceedings of ACTM 2021

 Springer

Editors

M. S. Ranadive
Department of Civil Engineering
College of Engineering Pune
Pune, Maharashtra, India

Bibhuti Bhusan Das 
Department of Civil Engineering
National Institute of Technology Karnataka
Mangalore, Karnataka, India

Yusuf A. Mehta
Department of Civil and Environmental
Engineering
Rowan University
Glassboro, NJ, USA

Rishi Gupta
Department of Civil Engineering
University of Victoria
Victoria, BC, Canada

ISSN 2366-2557

ISSN 2366-2565 (electronic)

Lecture Notes in Civil Engineering

ISBN 978-981-19-2144-5

ISBN 978-981-19-2145-2 (eBook)

<https://doi.org/10.1007/978-981-19-2145-2>

© The Editor(s) (if applicable) and The Author(s), under exclusive license to Springer Nature Singapore Pte Ltd. 2023

This work is subject to copyright. All rights are solely and exclusively licensed by the Publisher, whether the whole or part of the material is concerned, specifically the rights of translation, reprinting, reuse of illustrations, recitation, broadcasting, reproduction on microfilms or in any other physical way, and transmission or information storage and retrieval, electronic adaptation, computer software, or by similar or dissimilar methodology now known or hereafter developed.

The use of general descriptive names, registered names, trademarks, service marks, etc. in this publication does not imply, even in the absence of a specific statement, that such names are exempt from the relevant protective laws and regulations and therefore free for general use.

The publisher, the authors, and the editors are safe to assume that the advice and information in this book are believed to be true and accurate at the date of publication. Neither the publisher nor the authors or the editors give a warranty, expressed or implied, with respect to the material contained herein or for any errors or omissions that may have been made. The publisher remains neutral with regard to jurisdictional claims in published maps and institutional affiliations.

This Springer imprint is published by the registered company Springer Nature Singapore Pte Ltd.

The registered company address is: 152 Beach Road, #21-01/04 Gateway East, Singapore 189721, Singapore

Contents

Recent Trends in Concrete Technology	
Self-healing Behavior of Microcapsule-Based Concrete	3
B. S. Shashank and P. S. Nagaraj	
Durability Properties of Fibre-Reinforced Reactive Powder Concrete	15
Abbas Ali Dhundasi, R. B. Khadiranaikar, and Kashinath Motagi	
Performance of Geopolymer Concrete Developed Using Waste Tire Rubber and Other Industrial Wastes: A Critical Review	29
Dhiraj Agrawal, U. P. Waghe, M. D. Goel, S. P. Raut, and Ruchika Patil	
Thermal Behaviour of Mortar Specimens Embedded with Steel and Glass Fibres Using <i>KD2 Pro</i> Thermal Analyser	43
P. Harsha Praneeth	
Modulus of Elasticity of High-Performance Concrete Beams Under Flexure-Experimental Approach	57
Asif Iqbal A. Momin, R. B. Khadiranaikar, and Aijaz Ahmad Zende	
Impact of Phase Change Materials on the Durability Properties of Cementitious Composites—A Review	71
K. Vismaya, K. Snehal, and Bibhuti Bhusan Das	
Comparative Study of Performance of Curing Methods for High-Performance Concrete (HPC)	83
Sandesh S. Barbole, Bantiraj D. Madane, and Sariput M. Nawghare	

Development of a Mathematical Relationship Between Compressive Strength of Different Grades of PPC Concrete with Stone Dust as Fine Aggregate by Accelerated Curing and Normal Curing	101
N A G K Manikanta Kopuri, S. Anitha Priyadarshani, and P. Ravi Prakash	
Using Recycled Aggregate from Demolished Concrete to Produce Lightweight Concrete	111
Abd Alrahman Ghali, Bahaa Eddin Ghrewati, and Moteb Marei	
Recent Trends in Construction Materials	
A Study in Design, Analysis and Prediction of Behaviour of a Footbridge Manufactured Using Laminate Composites—Static Load Testing and Analysis of a Glass Fibre Laminate Composite Truss Footbridge	125
Col Amit R. Goray and C. H. Vinaykumar	
State-of-the-Art of Grouting in Semi-flexible Pavement: Materials and Design	135
Hemanth Kumar Doma and A. U. Ravi Shankar	
Utilization of Agro-Industrial Waste in Production of Sustainable Building Blocks	149
S. S. Meshram, S. P. Raut, and M. V. Madurwar	
Effect of Exposure Condition, Free Water–cement Ratio on Quantities, Rheological and Mechanical Properties of Concrete	161
Mahesh Navnath Patil and Shailendra Kumar Damodar Dubey	
Development of Sustainable Brick Using Textile Effluent Treatment Plant Sludge	185
Uday Singh Patil, S. P. Raut, and Mangesh V. Madurwar	
Utilization of Pozzolanic Material and Waste Glass Powder in Concrete	201
Lomesh S. Mahajan and Sariputt R. Bhagat	
Recent Trends in Construction Technology and Management	
Integrating BIM with ERP Systems Towards an Integrated Multi-user Interactive Database: Reverse-BIM Approach	209
M. Arsalan Khan	
Application of Game Theory to Manage Project Risks Resulting from Weather Conditions	221
Abd Alrahman Ghali and Vaishali M. Patankar	

Environmental Impact Analysis of Building Material Using Building Information Modelling and Life Cycle Assessment Tool	233
Kunal S. Bonde and Gayatri S. Vyas	
Enhancing the Building’s Energy Performance through Building Information Modelling—A Review	247
Dhruvi Shah, Helly Kathiriya, Hima Suthar, Prakhar Pandya, and Jaykumar Soni	
Analysis of Clashes and Their Impact on Construction Project Using Building Information Modelling	255
Samkit V. Gandhi and Namdeo A. Hedao	
Predicting the Performance of Highway Project Using Gray Numbers	271
Supriya Jha, Manas Bhoi, and Uma Chaduvula	
COVID-19—Assessment of Economic and Schedule Delay Impact in Indian Construction Industry Using Regression Method	283
Soniya D. Mahind and Dipali Patil	
Comparison of Afghanistan’s Construction and Engineering Contract with International Contracts of FIDIC RED BOOK (2017) and NEC4—ECC	299
Mohammad Ajmal and C. Rajasekaran	
Comparative Analysis of Various Walling Materials for Finding Sustainable Solutions Using Building Information Modeling	315
Amey A. Bagul and Vasudha D. Katare	
Studies on Energy Efficient Design of Buildings for Warm and Humid Climate Zones in India	327
Santhosh M. Malkapur, Sudarshan D. Shetty, Kishor S. Kulkarni, and Arun Gaji	
Recent Trends in Environmental and Water Resources Engineering	
Spatial Variability of Organic Carbon and Soil pH by Geostatistical Approach in Deccan Plateau of India	351
N. T. Vinod, Amba Shetty, and S. Shrihari	
Hydro-geo Chemical Analysis of Groundwater and Surface Water Near Bhima River Basin Jewargi Taluka Kalburgi, Karnataka	361
Prema and Shivasharanappa Patil	

Conjunctive Use Modeling Using SWAT and GMS for Sustainable Irrigation in Khatav, India	373
Ranjeet Sabale and Mathew K. Jose	
Modelling and Simulation of Pollutant Transport in Porous Media—A Simulation and Validation Study	387
M. R. Dhanraj and A. Ganेशa	
Adsorptive Removal of Malachite Green Using Water Hyacinth from Aqueous Solution	401
Sayali S. Udakwar, Moni U. Khobragade, and Chirag Y. Chaware	
Sediment Yield Assessment of a Watershed Area Using SWAT	415
Prachi A. Bagul and Nitin M. Mohite	
“NDVI: Vegetation Performance Evaluation Using RS and GIS”	425
A. Khillare and K. A. Patil	
Comparison of Suspended Growth and IFAS Process for Textile Wastewater Treatment	437
Sharon Sudhakar, Nandini Moondra, and R. A. Christian	
Innovative Arch Type Bridge Cum Bandhara for Economical and Quick Implementation of Jal Jeevan Mission	449
P. L. Bongirwar and Sanjay Dahasahasra	
Green Synthesis of Zinc Oxide Nanoparticles and Study of Its Adsorptive Property in Azo Dye Removal	467
C. Anupama and S. Shrihari	
Anthropogenic Impacts on Forest Ecosystems Using Remotely Sensed Data	481
Gaurav G. Gandhi and Kailas A. Patil	
Seasonal and Lockdown Effects on Air Quality in Metro Cities in India	497
K. Krishna Raj and S. Shrihari	
Inter-Basin Pipeline Water Grid for Maharashtra	511
Raibhann Sarnobbat, Pritam Bhadane, Vaibhav Markad, and R. K. Suryawanshi	
Removal of Heavy Metals from Water Using Low-cost Bioadsorbent: A Review	527
Praveda Paranjape and Parag Sadgir	
Adsorptive Removal of Acridine Orange Dye from Industrial Wastewater Using the Hybrid Material	547
Vibha Agrawal and M. U. Khobragade	

Basin Delineation and Land Use Classification for a Storm Water Drainage Network Model Using GIS 561
 Kunal Chandale and K. A. Patil

Prediction of BOD from Wastewater Characteristics and Their Interactions Using Regression Neural Network: A Case Study of Naidu Wastewater Treatment Plant, Pune, India 571
 Sanket Gunjal, Moni Khobragade, and Chirag Chaware

Floodplain Mapping of Pawana River Using HEC-RAS 579
 Tejas R. Bhagwat and Aruna D. Thube

Performance Evaluation of Varying OLR and HRT on Two Stage Anaerobic Digestion Process of Hybrid Reactor (HUASB) for Blended Industrial Wastewater as Substrate 597
 Rajani Saranadagoudar, Shashikant R. Mise, and B. B. Kori

Analysis of Morphometric Parameters of Watershed Using GIS 603
 Bhairavi Pawar and K. A. Patil

Mapping Ground Water Potential Zone of Fractured Layers by Integrating Electric Resistivity Method and GIS Techniques 613
 R. Chandramohan and B. Kesava Rao

Sustainable Development in Circular Economy: A Review 629
 Mohnish Waikar and Parag Sadgir

Biogas Generation Through Anaerobic Digestion of Organic Waste: A Review 641
 Vaishali D. Jaysingpure and Moni U. Khobragade

Recent Trends in Geotechnical Engineering

A Cost Comparison Study of Use of Cased and Uncased Stone Column in Marshy Soil 653
 Starina J. Dias and Wilma Fernandes

Review on Field Direct Shear Test Methodologies 665
 Kakasaheb D. Waghmare and K. K. Tripathi

Numerical Prediction of Tunneling Induced Surface Settlement of a Pile Group 673
 B. Swetha, S. Sangeetha, and P. Hari Krishna

Numerical Study of Pile Supported Embankment Resting on Layered Soft Soil 685
 Uzma Azim and Siddhartha Sengupta

A Review on Application of NATM to Design of Underground Stations of Indian Metro Rail 715
 Sandesh S. Barbole, M. S. Ranadive, and Apurva R. Kharat

Slope Stability Analysis of Artificial Embankment of Fly Ash and Plastic Recycled Polymer Using Midas GTS-NX	729
Prajakta S. Chavan, Kalyani G. Patil, and Sariput M. Nawghare	
Lateral Capacity of Step-Tapered Piles in Sand Deposits	739
K. V. S. B. Raju, K. S. Rajesh, L. Dhanraj, and H. C. Muddaraju	
Strength and Dilatancy Behaviour of Granular Slag Sand	753
K. V. S. B. Raju and Chidanand G. Naik	
Parametric Study of the Slope Stability by Limit Equilibrium Finite Element Analysis	767
Prashant Sudani, K. A. Patil, and Y. A. Kolekar	
Model Testing on PET Bottle Mattress with Aggregate Infill as Reinforcement Overlaying on Fly Ash Under Circular Loading	779
Shahbaz Dandin, Mrudula Kulkarni, and Maheboobsab Nadaf	
Recent Trends in Structural Engineering	
Sustainable Project Planning of Road Infrastructure in India: A Review	799
Appa M. Kale and Sunil S. Pimplikar	
Behaviour of Space Frame with Innovative Connector	805
Pravin S. Patil and I. P. Sonar	
Seismic Analysis of Base Isolated Building Frames with Experimentation Using Shake Table	819
Mahesh Kalyanshetti, Ramankumar Bolli, and Shashikant Halkude	
Critical Study of Wind Effect on RC Structure with Different Permeability	839
Ankush Asati and Uday Singh Patil	
Performance Assessment of SMA-LRB Isolated Building Structure Due to Underground Blast-Induced Ground Motion	861
Sonali Upadhyaya, Narendranath Gogineni, and Sourav Gur	
Research Progress on the Torsion Behavior of Externally Bonded RC Beams: Review	875
Rajesh S. Rajguru and Manish Patkar	
Study on Static Analysis and Design of Reinforced Concrete Exterior Beam-Column Joint	887
Yogesh Narayan Sonawane and Shailendrakumar Damodar Dubey	
Refined Methodology in Design of Reinforced Concrete Shore Pile: A Design Aid	897
Mahesh Navnath Patil and Shailendra Kumar Damodar Dubey	

Investigating the Efficacy of the Hybrid Damping System for Two-Dimensional Multistory Building Frame Using Time History Analysis 919
 A. P. Kote and R. R. Joshi

Thermal Buckling Analysis of Stiffened Composite Cutout Panels 935
 K. S. Subash Chandra, T. Rajanna, and K. Venkata Rao

Effect of Isolated Wind Incidence on Local Peak Pressure 949
 Supriya Pal, Ritu Raj, and S. Anbukumar

Investigation of Performance of Perforated Core Steel Buckling Restrained Brace 961
 Prajakta Shete, Suhasini Madhekar, and Ahmad Fayeeg Ghowsi

A Method for Evaluating Maximum Response in Multi-storied Buildings Due to Bi-directional Ground Motion 973
 P. B. Kote, S. N. Madhekar, and I. D. Gupta

Finite Element Analysis of Piled Raft Foundation Using Plaxis 3D 991
 Anupam Verma and Sunil K. Ahirwar

FRP Strengthened Reinforced Concrete Beams Under Impact Loading: A State of Art 1001
 Swapnil B. Gorade, Deepa A. Joshi, and Radhika Menon

Effect of Lateral Stiffness on Structural Framing Systems of Tall Buildings with Different Heights 1015
 A. U. Rao, Sradha Remakanth, and Aditya Karve

Free Vibration Response of Functionally Graded Cylindrical Shells Using a Four-Node Flat Shell Element 1031
 R. B. Dahale, S. D. Kulkarni, and V. A. Dagade

The Behaviour of Transmission Towers Subjected to Different Combinations of Loads Due to Natural Phenomenon 1047
 Devashri N. Varhade and R. R. Joshi

Fragility Assessment of Mid-Rise Flat Slab Structures 1061
 B. P. Dhumal and V. B. Dawari

Seismic Response of RC Elevated Liquid Storage Tanks Using Semi-active Magneto-rheological Dampers 1073
 Manisha V. Waghmare, Suhasini N. Madhekar, and Vasant A. Matsagar

Virtual Testing of Prototypes Using Test Frame Designed for Lateral Load 1089
 Suyog Nikam and I. P. Sonar

Crack Simulation and Monitoring of Beam-Column Joint by EMI Technique Using ANSYS	1101
Tejas Shelgaonkar and Suraj Khante	
The Impact of Perforation Orientation on Buckling Behaviour of Storage Rack Uprights	1115
Kadeeja Sensy, Ashish Gupta, K. Swaminathan, and J. Vijaya Vengadesh Kumar	
Modelling Interfacial Behaviour of Cement Stabilized Rammed Earth Using Cohesive Contact Approach	1127
T. Pavan Kumar Reddy and G. S. Pavan	
Four Node Flat Shell Quadrilateral Finite Element for Analysis of Composite Cylindrical Shells	1135
V. A. Dagade and S. D. Kulkarni	
Exact Elasticity Analysis of Sandwich Beam with Orthotropic Core	1149
Ganesh B. Irkar and Y. T. LomtePatil	
Flexural Fatigue Analysis of Cross Ply and Angle Ply Laminates	1171
Sammed Patil and Y. T. LomtePatil	
Recent Trends in Transportation and Traffic Engineering	
Review on Mechanisms of Bitumen Modification: Process and Variables	1185
N. T. Bhagat and M. S. Ranadive	
Alkali Activated Black Cotton Soil with Partial Replacement of Class F Fly Ash and Areca Nut Fiber Reinforcement	1193
B. A. Chethan, A. U. Ravi Shankar, Raghuram K. Chinnabhandar, and Doma Hemanth Kumar	
Development of Road Safety Models by Using Linear and Logistic Regression Modeling Techniques	1205
Krantikumar V. Mhetre and Aruna D. Thube	
Finite Element Analysis for Parametric Study of Mega Tunnels	1227
Shilpa Kulkarni and M. S. Ranadive	
Development of Financial Model for Hybrid Annuity Model Road Project	1245
Pratiksha B. Gilbile and Gayatri S. Vyas	
Analysis of Perpetual Pavement Design Considering Subgrade CBR, Life-Cycle Cost, and CO₂ Emissions	1257
Saurabh Kulkarni and M. S. Ranadive	

Laboratory Investigation of Lateritic Soil Stabilized with Arcanut Coir Along with Cement and Its Suitability as a Modified Subgrade 1273
B. A. Chethan, B. M. Lekha, and A. U. Ravi Shankar

Pavement Analysis and Measurement of Distress on Concrete and Bituminous Roads Using Mobile LiDAR Technology 1287
Prashant S. Alatgi and Sunil S. Pimplikar

Laboratory Study on New Type of Self-consolidating Concrete Using Fly Ash as a Pavement Material 1295
Bhupati Kannur and Hemant Chore

FTIR Analysis for Ageing of HDPE Pyro-oil Modified Bitumen 1311
H. P. Hadole and M. S. Ranadive

Utilization of Aluminium Refinery Residue (ARR), GGBS and Alkali Solution Mixes in Road Construction 1329
Nityanand S. Kudachimath, Raviraj H. Mulangi, and Bhibuti Bhusan Das

About the Editors

Prof. M. S. Ranadive is currently working as Professor and Head, Department of Civil Engineering, College of Engineering Pune (COEP), Pune, Maharashtra. He obtained his B.E. (Civil) from the University of Pune, Maharashtra; M.E. (Civil) From Shivaji University, Kolhapur and Ph.D. from the University of Pune. His major areas of research interests include quality monitoring of pavements, use of anti-stripping agents in bituminous concrete, effective use of bio-oil obtained by pyrolysis of municipal solid waste in flexible pavement, continuous pavement monitoring through dynamic responses by instrumentation. He has published 22 papers in leading international journals, 20 papers in national journals and in all there are more than 100 papers on his account. Professor M. S. Ranadive was a Guest Editor for the Journal of Performance of Constructed Facilities, ASCE. He is a member of American Society of Civil Engineers, Member of Indian Roads Congress, the Life Member of the Indian Geotechnical Society, Member of Indian Concrete Institute, and many more. He is a reviewer for various journals like *Journal of Materials in Civil Engineering*, ASCE, *International Journal of Construction Management and Economics*, Germany; *Journal of Transportation Engineering*; *International Journal of Pavement Engineering*, Taylor and Francis; *Journal of Building Engineering*, Elsevier Publication; *International Journal of Innovative Infrastructure Solutions*, Springer and many more.

Dr. Bibhuti Bhusan Das is currently working as an Associate Professor at the Department of Civil Engineering, National Institute of Technology Karnataka (NITK), Surathkal, Mangalore, India. He obtained his B.Tech. (Civil) from Orissa University of Agriculture and Technology, Orissa; M.Tech. from Indian Institute of Technology (IIT) Delhi in Construction Engineering and Management; Ph.D. from Indian Institute of Technology (IIT) Bombay and Post-doctoral from Lawrence Technological University, Southfield, Michigan, USA. His major areas of research interests include concrete technology, sustainable construction, building materials. He has published more than 40 research papers in and SCI Scopus indexed journals. Dr. Bibhuti Bhusan Das has edited four books namely *Sustainable Construction and*

Building Materials, Recent Developments in Sustainable Infrastructure, Smart Techniques for Sustainable Development, and Recent Trends in Civil Engineering which were published by Springer Nature Singapore. Dr. Bibhuti Bhusan Das is a member of the Indian Concrete Institute, Chennai, India; American Society for Testing and Materials; Prestressed Concrete Institute, Chicago; American Society of Civil Engineers and various other reputed Societies. He is also a reviewer for reputed journals such as *Journal of Materials in Civil Engineering*, ASCE, *Canadian Journal of Civil Engineering, Construction and Building Materials*, Elsevier Publications, and many others.

Prof. Yusuf A. Mehta is currently a Professor at the Department of Civil and Environmental Engineering, Rowan University, USA; and Director, Centre of Research and Education in Advanced Transportation Engineering Systems. He obtained his B.S. from the University of Bombay, India; M.S. from the University of Oklahoma, Norman; and Ph.D. from Pennsylvania State University. Since coming to Rowan, Dr. Mehta, has received approximately \$25 million dollars of external funding in pavements and materials. He has extensive experience working on several research projects with New Jersey, Florida, Wisconsin and Rhode Island departments of transportations, Federal Highway Administration and Federal Aviation Administration, and Department of Defense. He has also led the effort to acquire the Heavy Vehicle Simulator (HVS) that can simulate 10-20 years of traffic in a few years. Dr. Mehta has received several teaching awards, such as ASCE-NJ Educator of the Year Award, May 2014 and the 2012 Louis J. Pignataro Memorial Transportation Engineering Education Award. The award was for outstanding record of achievement in transportation engineering research, and undergraduate and graduate engineering education. He has received the Mid-Atlantic American Society of Engineering Education Section Distinguished Teaching Award, West Point, 2008. He has also received the faculty research achievement award in 2014. Under the direction of Dr. Mehta, CREATEs has expanded its capabilities to integrate research in Intelligent Transportation Systems, transportation safety, geotechnical engineering, cementitious materials, and Structural engineering by collaborating with faculty members at Rowan University. These collaborations will allow CREATEs to seek research funding in the above mentioned areas. The CREATEs award is approximately \$37 M since its inception. CREATEs provides hands-on experience to sixty undergraduate and graduate students in various fields of transportation. This expansion has allowed CREATEs to conduct research, education, and outreach in all the above mentioned fields.

Dr. Rishi Gupta is a professor at the Department of Civil Engineering, University of Victoria, Canada where he also leads the Facility for Innovative Materials and Infrastructure Monitoring (FIMIM). He obtained his Diploma from Bombay Technical Board (India); B.E. (Civil) from Pune University (India); M.A.Sc. in Civil Engineering from University of British Columbia and Ph.D. in Civil Engineering (Materials) from University of British Columbia. His major areas of research interests include shrinkage and self-sealing characteristics of concrete and development

of ‘crack-free’ cement composites, structural health monitoring (SHM) of infrastructure, durability and corrosion studies of reinforced concrete, sustainable construction technologies, and advanced materials for structures. Dr. Rishi Gupta holds several patents to his name. He has published more than 70 papers in refereed international journal publications and more than 50 refereed conference publications. Dr. Rishi Gupta has been awarded UVic’s REACH award for excellence in Undergraduate Research Enriched teaching, June 2020; Drishti award for Innovation in Science and Technology, 2020; Nominated for Medal for distinction in Engineering Education, Engineers Canada award, 2020; Recipient of EGBC’s President’s Awards for Teaching Excellence in Engineering and Geoscience Education, 2019; Awarded fellowship with Engineers Canada or Geoscientists Canada, February 2017. Dr. Rishi Gupta is a Member of the Board of Examiners at Engineers and Geoscientists of British Columbia (since July 2018); Editorial board member (2010–2017), EGBC Burnaby/NW Chair (2011-2012); Vice-Chair (2009–2011), Volunteer (2007–to date), EGBC-Burnaby/New Westminster Branch; UVic faculty liaison for EGBC’s Victoria Branch (Since May 2015); Member of The Centre for Advanced Materials and Related Technology (CAMTEC); University of Victoria, (Since October 2013) and Board member of Habitat for Humanity Victoria and many other respected boards. He is a reviewer for *Construction and Building Materials*, Elsevier Publications, *ASCE Journal of Materials in Civil Engineering*, *Journal of American Society of Testing and Materials*, *Canadian Journal of Civil Engineering*, *Construction Materials*, Institute of Civil Engineers, UK, and many more.

Recent Trends in Concrete Technology

Self-healing Behavior of Microcapsule-Based Concrete



B. S. Shashank and P. S. Nagaraj

Abstract In general, it is a well-known fact that it is very difficult to detect the cracks at the very initial stage of concrete, and the same cracks later create problems for structure. Further adding to this always the physical intervention is essential for periodic inspection and repair of these cracks. To increase the durability of concrete structures, many self-healing mechanisms are used, out of which microcapsule-based healing mechanisms appear to be feasible. The microcapsule-based self-curative process is an effective process for sealing the cracks in the concrete. Microcapsule-based self-curative starts with the crack occurrence and progresses once it gets in contact with the microcapsule, then self-healing agents are released into cracks, which are contained in capsules. In this study, an effort has been made to synthesize self-healing materials that are synthetic or artificially produced polymer-based substances that have the incorporated ability to naturally repair damage to themselves without any physical contact or human interference. The sodium silicate agent is used as a self-healing material and in situ polymerization method is used for the manufacturing of capsules. It is found that adding 2 and 3% amount of these capsules will heal the concrete after cracking and better the durability.

Keywords Self-healing · In situ polymerization · Microcapsule · Strength

1 Introduction

In the current scenario, concrete is the most widely consumed material other than water. Due to its wonderful behavior of showing defects, durability is a big concern; hence different modern tools are being experimented with to meet the standards of the construction industry to new heights [1–4]. Different types of processes, methods,

B. S. Shashank (✉)

School of Construction Management, NICMAR University, Pune, India

e-mail: shashankbsbhat.bs@gmail.com

P. S. Nagaraj

Department of Civil, UVCE Bangalore University, Bengaluru, India

© The Author(s), under exclusive license to Springer Nature Singapore Pte Ltd. 2023

M. S. Ranadive et al. (eds.), *Recent Trends in Construction Technology*

and Management, Lecture Notes in Civil Engineering 260,

https://doi.org/10.1007/978-981-19-2145-2_1

and raw materials are used to attain sustainable, very good, and more economic concrete. But due to human errors, unskilled labor, and incorrect handling [5], an efficient building is difficult to sustain life for a longer duration. Many issues like weathering, micro-cracks, leakages, excessive bending, etc., arise after the construction. To solve these types of problems, many remedial methods are used before and after the construction. One of the remedial techniques is microcapsule-based self-healing concrete [6].

The concept of microcapsules healing is carried out by the healing agent which is coated by a shell material when it is placed in concrete. After the crack appears in concrete and reaches the microcapsule, the microcapsule breaks and the healing material is circulated into the crack to heal by sodium silicate [7]. The microcapsule consists of a healing agent as sodium silicate and the encapsulating material as urea-formaldehyde. And an additional material is added along with this, i.e., polypropylene fiber to advance the strength and property of the concrete at a certain percentage of the cement content [8].

1.1 Objectives

- Manufacturing of microcapsule with suitable process
- To heal the cracks and to increase the durability of the structures using microcapsules.

2 Microcapsule

Microcapsule is a polymer-based compound that fulfills the criteria that it can incorporate the core material with an encapsulation material. The strength of the microcapsules mainly depends on the shell material and its thickness.

2.1 Morphology of Microcapsules

The structure of the microcapsule is mainly dependent on the healing agent called core material and coating material called encapsulation material. The core material is evenly distributed within the shell material to form a microcapsule as shown in Fig. 1 [9].



Fig. 1 Microcapsule with core healing agent

2.2 Core Material

The core material is a polymer matrix to be encapsulated by coating material and it may be in a solid or liquid state depending on the functional requirements. In the present study, sodium silicate is used as a core material that will act as a healing agent in concrete [10].

2.3 Coating Material

The physical and chemical properties of microcapsule are mainly dependent on the encapsulation material which protects the core material from external pressure and extend the sustainability of core material [9].

2.4 Release Mechanisms

The main purpose of microencapsulation is to release the core material which is coated by encapsulation material at the time of usage of the microcapsule. The shell material should break at the time of usage and react with the surroundings. Whenever a crack appears in concrete and that gets into contact with a microcapsule, it will break and the healing agent will be released into the crack to heal the concrete [10, 11]. The same can be observed in Fig. 2.

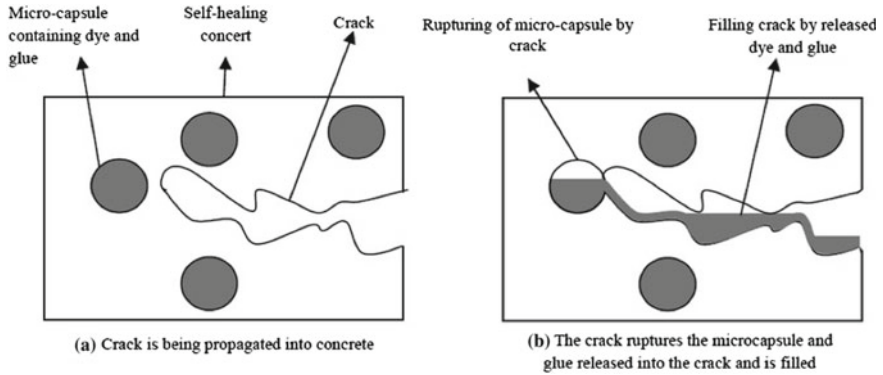


Fig. 2 Healing agent release mechanisms

Table 1 List of chemicals required for the synthesis process

Chemical	Quantity
Sodium silicate	60 ml
Urea	5.00 g
Formaldehyde	12.7 g
Ammonium chloride	0.50 g
Resorcinol	0.50 g
Sodium hydroxide	20 ml (dropwise)
Hydrochloric acid	20 ml (dropwise)

3 Materials and Methods

3.1 Synthesis of Microcapsules

The production process of sodium silicate microcapsule was based on the in situ polymerization method and the process is mainly based on some of the parameters such as agitation, temperature, and pH range [12, 13]. Table 1 and Fig. 3 show the materials for the preparation of microcapsule and prepared sample, respectively.

3.2 Concrete Mix Design

Mix design of concrete was made according to IS 10262-2019 and two different grades of concrete were designed M20 and M40 with testing all basic materials required for the test as cement sand and aggregate, and the mix design for M20 and M40 is shown in Table 2.



Fig. 3 Preparation of microcapsule and prepared sample

Table 2 Mix design

Grade of concrete	Cement kg/m ³	Fine aggregate kg/m ³	Coarse aggregate kg/m ³	Polypropylene fibre kg/m ³	Water l/m ³
M20	394	750	1037	0.25%	197
M40	420	625	1085	0.25%	180

Table 3 Mix design designation

S. No.	Grade designation				Grade of concrete
	CC	0.25% fibers	2% microcapsule	3% microcapsule	
1	CC-1	CCF-1	CCFM-1	CCFM-3	M20
2	CC-2	CCF-2	CCFM-2	CCFM-4	M40

3.3 Mix Design Designation

As there are many mixes to understand better grade designation mentioned, it is shown in Table 3.

4 Results and Discussion

4.1 SEM Analysis

The microcapsules were scanned using scanning electron microscopy (SEM) in the range of 400–6000 cm⁻¹ to get a clear picture of the microcapsules which have

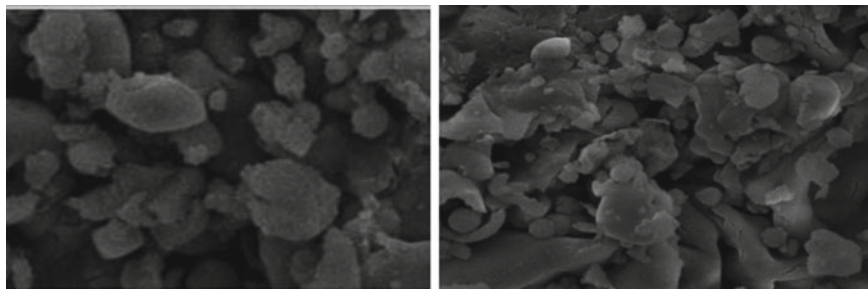


Fig. 4 SEM images of the microcapsule

been synthesized, by focusing on the particular range that can say that the prepared microcapsules as a diameter of 5–10 μm , as shown in Fig. 4. Some of the capsules are irregular in shape, so average diameter has been taken to predict the size of the capsules.

4.2 FTIR Analysis

Fourier-transform infrared spectroscopy (FTIR) examines the peak range of urea–formaldehyde and sodium silicate which was used and the results showed that they were almost matched with the standard range of peak value. So, by this test, we can confirm the presence of the core and encapsulate, and the same can be noted from the graph shown in Fig. 5 and Table 4.

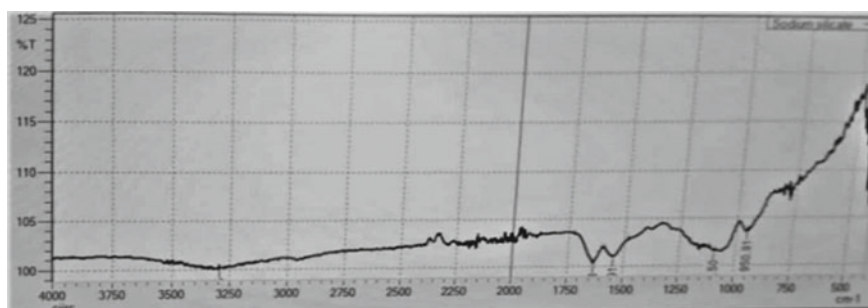


Fig. 5 FTIR analysis graph

Table 4 Chemicals present in the core material

S. No.	Peak	Content	Standard peak range
1	3296.35	Sodium silicate	3000–3500
2	1097.50	Urea–formaldehyde	1000–1250

Table 5 Variation in a slump across the different mix

Mix	Conventional concrete	0.25% fibers	2% microcapsule	3% microcapsule	Grade of concrete
Slump in mm	CC-1	CCF-1	CCFM-1	CCFM-3	M20
	95	89	85	83	
Slump in mm	CC-2	CCF-2	CCFM-2	CCFM-4	M40
	92	82	79	79	

4.3 Slump Flow Test

The workability of concrete was tested according to IS 7320:1974 and it was found that workability will reduce as the percentage of microcapsule increases in both M20 and M40 grade concrete as shown in Table 5. Further with the addition of fibers also contributed to the reduction in the slump of concrete. The effect of both can be solved by proper admixture usage.

4.4 Compressive Strength

A compressive strength test was performed based on the IS 516:1959. Concrete with microcapsule is initially tested by applying 50% of the load for inducing minor cracks, then sufficient time was provided to heal. After healing the concrete was once again tested for its compressive strength. It was observed that for M20 grade concrete it took 22 days and for M40 it took 26 days to heal up to a considerable extent. Testing samples revealed that after healing of concrete the compressive strength decreased by 14% and 12% for 2% and 3% microcapsule, respectively, compared to conventional concrete and original samples for M20 grade concrete, and the compressive strength decreased by 11% and 8% for 2% and 3% microcapsule, respectively, for M40 grade concrete compared to conventional concrete. The same has been shown in Fig. 6. But the decrease in the compressive strength of concrete has not affected the grade of concrete.

4.5 Split Tensile Strength

A split tensile strength test was performed according to IS 5816:1999. Similar to the compressive strength of concrete, samples with microcapsule are showing a decrease in split tensile strength as the percentage of microcapsule are increased compared to original concrete but the strength of these concretes is better than that of conventional concrete. Further, the healing was observed in the specimens after 22 and 26 days

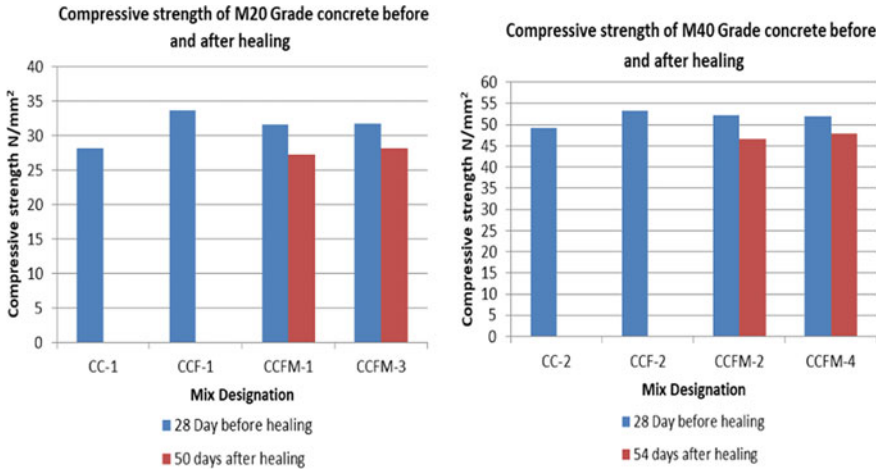


Fig. 6 Variation in compressive strength of M20 and M40 grade concrete

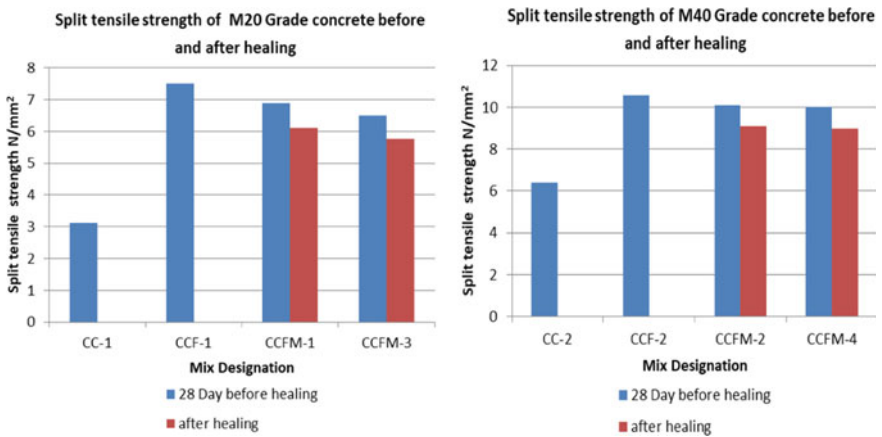


Fig. 7 Variation in split tensile strength

for M20 and M40 grade concrete, respectively. The same has been shown in Fig. 7, and also Fig. 8 shows the healing of the concrete cylinder.

4.6 Flexural Strength

A flexural strength test was performed according to IS 516:1959 with a beam size of 150 × 150 × 500 mm. By observing variation in flexural strength, it was found that as the percentage of microcapsule increases, the flexural strength of concrete was



Fig. 8 Healing of concrete cylinder due to microcapsule

decreased for both M20 and M40 grade concrete compared to conventional concrete. But after healing the flexural strength reduced by 15 and 29% for M20 grade concrete and 11 and 16% for M40 grade concrete for 2% and 3% microcapsule, respectively, compared to its original samples. Variation in flexural strength is shown in Fig. 9.

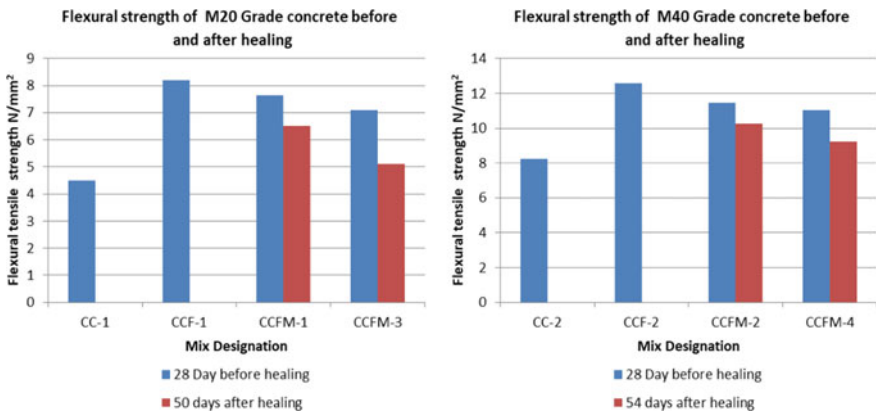


Fig. 9 Variation in flexural strength

4.7 Cost Analysis

The amount of microcapsules required for 2% and 3% for 1 cum meter of concrete is 8.82 kg and 13.23 kg, respectively. And the cost for the preparation of the microcapsules of 2% and 3% is Rs 4410 and Rs 6615, respectively. The cost of microcapsules-based concrete is more compared to conventional concrete, but taking into consideration the maintenance and the life of the self-healing concrete the cost can be justified.

5 Conclusion

1. By using the in situ polymerization process microcapsules are prepared and these are having a size of less than 1 micron which is vital for any material to blend with cement and also FTIR analysis and FEM analysis are validating the presence of a healing agent in the microcapsule which helps to self-heal the concrete during the crisis.
2. Incorporation of the microcapsule showed excellent healing of concrete within 22–28 days, which is a significant development.
3. The compressive strength before and after cracking showed that sodium silicate can be used as a healing agent, which contributes to the strength development of concrete.
4. Although there is a decrease in compressive, split tensile, and flexural strength of concrete and an increase in microcapsule percentage before healing, but as the percentage of microcapsule increases, the healing ability also increases. Further, the strength of concrete is more compared to conventional concrete but less compared to its original value, which is acceptable as there is no change in the grade of concrete.
5. Cost analysis concludes that self-healing concrete cost is slightly more than conventional concrete, but compared to its durability and maintenance aspects, it is a worthy investment in the end.

References

1. Bonilla L et al (2018) Dual self-healing mechanisms with microcapsules and shape memory alloys in reinforced concrete. *J Mater Civ Eng* 30(2):04017277
2. Sahoo S, Das BB, Mustakim S (2017) Acid, alkali, and chloride resistance of concrete composed of low-carbonated fly ash. *J Mater Civ Eng* 29(3):4016242
3. Snehal K, Das BB, Akanksha M (2020) Early age, hydration, mechanical and microstructure properties of nano-silica blended cementitious composites. *Constr Build Mater* 233:117212
4. Snehal K, Das BB (2021) Acid, alkali and chloride resistance of binary, ternary and quaternary blended cementitious mortar integrated with nano-silica particles. *Cement Concr Compos* 123:104214

5. Sangadji S (2017) Can self-healing mechanism helps concrete structures sustainable? *Procedia Eng* 171:238–249
6. Beglarigale A et al (2018) Sodium silicate/polyurethane microcapsules used for self-healing in cementitious materials: monomer optimization, characterization, and fracture behavior. *Constr Build Mater* 162:57–64
7. Restuccia L et al (2017) New self-healing techniques for cement-based materials. *Procedia Struct Integr* 3:253–260
8. Bashir J et al (2016) Bio concrete-the self-healing concrete. *Indian J Sci Technol* 9(47)
9. Li W et al (2016) Preparation and properties of melamine urea-formaldehyde microcapsules for self-healing of cementitious materials. *Materials* 9(3):152
10. Kanellopoulos A et al (2017) Polymeric microcapsules with switchable mechanical properties for self-healing concrete: synthesis, characterisation and proof of concept. *Smart Mater Struct* 26(4):045025
11. Ahn E et al (2017) Principles and applications of ultrasonic-based nondestructive methods for self-healing in cementitious materials. *Materials* 10(3):278
12. Gruyaert E et al (2016) Capsules with evolving brittleness to resist the preparation of self-healing concrete. *Mater Constr* 66(323):e092
13. Šavija B et al (2017) Simulation-aided design of tubular polymeric capsules for self-healing concrete. *Materials* 10(1):10

Durability Properties of Fibre-Reinforced Reactive Powder Concrete



Abbas Ali Dhundasi, R. B. Khadiranaikar, and Kashinath Motagi

Abstract Concrete used for sewer lines, piers and deck slabs of bridges, highways and nuclear power plants are prone to acid attacks. Hence it is required to study the mechanical properties along with durability aspects to assign its service life. In the present study, fibre-reinforced reactive powder concrete (FRPC) with varying silica fume content, superplasticizer and dosages of steel fibres are produced. Strengths under compression, flexure and tension have been obtained. Durability studies have been carried out by acid tests, salt crystallization test and permeability tests. Strengths of 140, 150 and 160 MPa have been achieved. To study the resistance against acid attacks, concrete is subjected to H_2SO_4 solution with 0.5, 1, 1.5 and 2% concentrations. Crystallization of salts is studied by immersing specimens in Na_2SO_4 solutions for 10–50 cycles. The concrete shows greater resistance towards the permeability of chloride ions. A considerable amount of loss in strength and mass is observed when subjected to a higher dosage of acid environment. An optimum dosage of 2.5% of fibres is suggested. Addition of fibres improved the strength and durability properties.

Keywords Reactive powder concrete · Steel fibres · Acid test · Salt crystallization test · Rapid chloride ion penetration test

1 Introduction

The performance of any concrete is governed by its mechanical properties and durability aspects under adverse environmental conditions throughout its service life. Based on strength parameters concrete is categorized as normal strength (20–40 MPa), high strength (40–60 MPa) and ultrahigh-strength (>80 MPa) concretes [1]. Reactive powder concrete is a new-generation ultrahigh-strength concrete with strengths in the range of 100–800 MPa. Its applications include the construction of storage bunkers for nuclear waste, sea harbour structures, bridge piers and pathways, highways, airways, sewage canals etc.

A. A. Dhundasi (✉) · R. B. Khadiranaikar · K. Motagi
Department of Civil Engineering, Basaveshwara Engineering College, Bagalkot, Karnataka, India
e-mail: abbasdhandasi@gmail.com

© The Author(s), under exclusive license to Springer Nature Singapore Pte Ltd. 2023
M. S. Ranadive et al. (eds.), *Recent Trends in Construction Technology and Management*, Lecture Notes in Civil Engineering 260,
https://doi.org/10.1007/978-981-19-2145-2_2

15

P. Richard and M. Cheyrezy from France are the pioneers who produced reactive powder concrete in the early 1990s. Coarse aggregates were eliminated to enhance the homogeneity. Silica fume was added as pozzolanic material. W/B ratio was reduced to 0.15–0.19 and a workable mix was obtained by adding superplasticizers. The microstructure was enhanced by the application of pressure and post heat treatment at 20 and 90 °C. The ductility was improved by the addition of steel fibres. RPC with strengths of 200–800 MPa were produced [2]. A study on various types of superplasticizers and their effect on workability at a low w/c ratio was carried out by Collepardi et al. [3]. RPC with 285 MPa strength was produced with low-pressure steam curing and 90°C hot water curing [4]. Applying 50 MPa presetting pressure and a very high dosage of 1900 kg/m³ of cement yielded RPC with 500 MPa compressive strength [5]. RPC with strengths 120–300 MPa is produced with autoclave curing, hot water, hot air and steam curing [6–10]. The researchers concluded that heat curing has a profound influence on strength development and hence higher strength RPCs can be produced.

The ductility and tensile strengths of concrete can be improved by the addition of fibres [11–14]. Various types of fibres that can be incorporated in concrete are steel, polypropylene, nylon, glass, basalt fibres etc. The fibre-reinforced concretes (FRC) can be used for the construction of bridge deck slabs, highway slabs as well as in runways of airports. A study on the dosage of polypropylene fibres with different lengths was carried out on self-compacting concrete. Mechanical properties and spalling tendency were evaluated. The concrete was cured under elevated temperatures [15]. A model using ANSYS was proposed to determine the tensile strength of concrete with fibres varying in aspect ratio (length/depth) [16].

An extensive study on the mechanical properties of FRC was done by Zuzana et al. The fibres were made of steel, nylon, polypropylene and glass materials with cross-sections of round, rectangular and irregular in nature. Shapes considered were (a) straight, (b) hooked, (c) wave and (d) deformed. The ends of fibres were (a) hooked, (b) button and (c) deformed. The results concluded that straight fibres with hooked ends improved density, tensile strength, fracture energy and shear resistance [17]. RPC with strength 200–315 MPa was produced with a w/c ratio of 0.2 and 20% silica fume. Steel fibres with 16 mm dia. and length 6 mm were added in 0.5–4% by volume. Properties and microstructure were evaluated. It was concluded that the addition of fibres increases both compressive and flexural strengths. It was also suggested that the volume fraction of fibres should not exceed 3% to get optimum results [18].

The concrete is susceptible to chemical attacks from an acidic environment and dissolved acid which precipitate in the form of acidic rain. Many researchers have shown that the durability of concrete can be expressed in terms of loss in weight/mass and compressive strength. Amongst the acids, sulphuric acid (H₂SO₄), hydrochloric acid (HCl), nitric acids (HNO₃) etc. cause massive deterioration of concrete. The concrete used in sewer pipes is severely exposed to sulphuric acid attacks. These cause corrosion in concrete. The chemical reactions by several bacterial activities under low pH values and anaerobic conditions result in the generation of sulphuric acid around concrete. Commonly found bacteria are desulphovibrio, *Thiobacillus*

plumbophilus, *Halothiobacillus neapolitanus*, and *Acidithiobacillus thiooxidans*. An investigation on corrosion of concrete caused by such bacteria has been carried out [19]. Acid resistance of normal strength blended concrete (20–40 MPa) was carried out by immersing specimens in 5% H₂SO₄ and 5% HCl solution for 28 and 90 days. It was observed that 40% weight loss had taken place [16]. Effect of sulphuric acid on fly ash-based geopolymer concrete was done for 7, 28 and 56 days. The strengths were 53 and 62 MPa. The specimens were immersed in 10% solution. The results indicated that GPC shows higher resistance to sulphuric acid attack [20]. Sulphuric acid has a significant effect on the weight loss and the compressive strength of concrete [21–27]. Durability tests on RPC with 180 MPa strength were done. Acid tests, accelerated corrosion and RCPT tests were performed. Mass was reduced up to 20% and compressive strength up to 60% [28]. In chemical industries producing medicines, artificial manure etc., nitric acid is formed in the presence of water by the reaction of compounds and radicals of nitrates. It is then released into the atmosphere. The product of cement hydration (Ca(OH)₂) reacts with such acid and transforms into highly soluble nitro aluminate calcium hydrates and salts of calcium nitrate. This leads to the deterioration of concrete [29]. A comparative study on various ageing tests to evaluate salt crystallization damage was also done to assess the durability characteristics of concrete [30].

Many researches have been carried out on assessing the mechanical properties and durability studies on normal, high strength, reinforced, self-compacting and geopolymer concrete etc. Many studies have been carried out only on the production of RPC by varying constituent materials and curing conditions. However, very few investigations are done on durability properties. Hence the present research focuses on producing steel fibre-reinforced reactive powder concrete with constituent materials available in the southern part of India and studying its mechanical properties and durability properties. The optimum dosage of fibres along with the variation of silica fume is determined. The durability properties of fibre-reinforced RPC are assigned by performing various tests which will help the constructure engineers to utilize the material efficiently for many applications.

2 Materials and Mix Proportions

The reactive powder concrete mix proportions are prepared with OPC 53 Grade cement complying with IS:12269(1987). Superfine silica fume 920D is added as pozzolanic material procured from Elkem India Pvt. Ltd. Quartz powder (QP) of 300–600 μm size is used to improve microstructure. It has high silica content and acts as filler material unless the curing temperature exceeds 200 °C, at which it produces silicates and contributes to an increase in strength. Potable water, free from any impurities, is used with variable ratios. A BASF product Glanium-8233 is added as a superplasticizer. The aggregates constitute high-purity silica sand. The details of mix proportions are shown in Table 1.

Table 1 Design mix proportions for RPC

Mix	Cement	Sand	W/B ratio	Silica fume		QP	Superplasticizer		Fibre
	kg/m ³	kg/m ³		kg/m ³	%		kg/m ³	kg/m ³	
R1-A	1000	959.51	0.21	50	5	100	15	1.5	1.5
R1-B	1000	947.69		50			15		2.0
R1-C	1000	935.88		50			15		2.5
R2-A	1000	924.06	0.20	100	10	100	20	2.0	1.5
R2-B	1000	912.24		100			20		2.0
R2-C	1000	900.42		100			20		2.5
R3-A	1000	897.67	0.19	150	15	100	25	2.5	1.5
R3-B	1000	885.88		150			25		2.0
R3-C	1000	874.06		150			25		2.5

3 Experimental Programme

3.1 RPC Production

Three grades of fibre-reinforced ultrahigh-strength concrete, i.e. R1, R2 and R3, with compressive strengths of 140, 150 and 160 MPa are produced with a varying dosage of silica fume and fibre content. The silica fume is varied in 5, 10 and 15% and fibres are added in 1.5, 2.0 and 2.5% of the dosage. Dry mix and wet mix are done in a 200 l capacity pan mixer. The mixer rotates at a speed of 140–280 RPM [7]. To get a workable mix superplasticizer dosage is varied w.r.t. w/c ratio. Care is taken to disperse the steel fibres evenly throughout the mix to avoid flocculation. It takes 18 ± 2 min to get a workable mix. Wet mix is then compacted in three layers on a vibrating table to remove air voids. The demoulded specimens are kept for hot water steam curing at 90°C for 48 h and then for normal water curing for up to 28 days. Cube specimens of 100 × 100 × 100 mm, cylinder specimens of 100 mm dia. and 150 mm height and beams of 100 × 100 × 500 mm are cast and the mechanical properties are noted down for uniaxial monotonic loads.

3.2 Durability Tests

RPC samples are immersed in acid-resistant trays of 100 × 150 × 150 cm, with a calculated amount of predetermined concentration of acid solutions. Separate specimens are used for each durability study.

a. Acid Test

The concentration of H₂SO₄ solution is varied in the range of 0.5, 1.0, 1.5 and 2%. The observations were taken at intervals of 7, 28, 60 and 90 days. At the end of each

period, samples are taken out of solutions and washed thoroughly with clean water. To remove absorbed water, samples are oven-dried. The samples exposed to different solutions of H_2SO_4 show deterioration. Due to the chemical reactions leading to the degradation of concrete, the pH of the solution is observed to change. Hence at each 24-h interval, a constant pH is maintained carefully. The deterioration of concrete is measured in terms of weight loss and compressive strength loss. The percentage loss is calculated from the following equations:

Reduction in compressive strength (%):

$$\frac{f'_i - f'_f}{f'_i} \times 100 \quad (1)$$

where f'_i , f'_f are initial and final compressive strengths at 28 days and after degradation, respectively.

Percentage weight/mass loss is calculated as follows:

$$\frac{W_1 - W_2}{W_1} \times 100 \quad (2)$$

where W_1 and W_2 are initial and final weights after deterioration.

b. Salt Crystallization Test

The 28 days cured, clean and oven-dried samples are immersed in 14% Na_2SO_4 solution. The steps for the salt crystallization test of each cycle are as follows: (1) Samples are immersed in an acidic solution for 18 h at room temperature. (2) The removed samples are drained for 30 min. (3) The drained samples are oven-dried for 4 h at 105 ± 5 °C and later cooled down to room temperature. This completes one cycle of 24 h. For the present study, the number of cycles is varied from 0, 10, 20, 30, 40 to 50 cycles.

c. Rapid Chloride Penetration Test

Cylindrical specimens are cut using a diamond saw cutter to get samples of 50 mm thickness and 100 mm dia. RCPT tests were performed on these samples [22]. A DC voltage of 60 V is applied between two cells of 0.3 N NaOH and 3% NaCl solutions. The chloride ion penetration is governed by the measure of the total amount of charges passed after 360 min in each specimen. The resistance towards chloride ion penetration is calculated for the grades of FRPC (Figs. 1 and 2).

Fig. 1 Specimens in H₂SO₄ solution



Fig. 2 Specimens in Na₂SO₄ solution



4 Results and Discussion

4.1 Production of Fibre-Reinforced RPC

The steel fibres are added to improve the mechanical properties of all grades of RPC designed for 1.5, 2 and 2.5% dosage. The fibres are of round shape with hooked ends. The aspect ratio (l/d) is 60, with a length of 12 mm and a diameter of 0.2 mm. The 28 days strengths obtained for each mix are shown in Table 2.

It is observed that a higher dosage of fibres contributes to an increase in strength. An optimum of 2.5% dosage is suggested. The flexural strength of FRPC is observed to be 20–25 MPa, i.e., 15% of compressive strength. An average of 15–20 MPa tensile strength was achieved. These strengths are much greater than normal strength and high strength reinforced concretes [6–10]. Thus, in fibre-reinforced ultrahigh strength

Table 2 Mechanical proportions of UHSC

Mix	Compressive strength (MPa)		Flexural strength (MPa)	Tensile strength (MPa)
	Designed	Achieved		
R1-A	140	138.84	14.12	8.89
R1-B		141.21	16.94	12.11
R1-C		142.85	20.89	15.31
R2-A	150	147.95	16.34	11.33
R2-B		150.19	18.67	14.02
R2-C		154.54	22.28	16.94
R3-A	160	156.71	18.45	13.86
R3-B		161.08	21.72	16.74
R3-C		165.47	24.88	20.16

concrete, steel bars as reinforcement to resist tensile stresses can be omitted, which helps in the conservation of natural resources for future generations.

4.2 Durability Tests

4.2.1 Acid Tests

The effect of different concentrations of H_2SO_4 is discussed as follows:

- a. **0.5% H_2SO_4** : The visual observations show that there is no change in shape or structure of the specimen exposed for up to 7 days. However, a small amount (2%) of weight loss is observed in R1 samples. R2 and R3 samples show better resistance at the initial stage and up to 28 days exposure period. Samples show white deposits as a result of surface erosion for 60 days of exposure. A noticeable amount of weight loss and compressive strength loss is observed. Scaling of the top surface layer is observed for samples kept for 90 days, shown in Fig. 3a. The weight loss is 10.49%, 9.63% and 7.23% for R1, R2 and R3, respectively. The strength loss is 26.95%, 20.59% and 19.24%, respectively. These are shown in Figs. 4a and 5a.
- b. **1.0% H_2SO_4** : Surface erosion is initiated even at 7 days of exposure. Discolouration of samples from greenish-grey to whitish-grey is observed at 28 days of exposure. No signs of corrosion are observed. Scaling of the concrete takes place at a higher exposure period, which increases progressively and peeling of the surface takes place at 90 days of exposure as shown in Fig. 3b. The weight is reduced by 13.63%, 12.82% and 10.60% and correspondingly compressive strength reduction is 38.45%, 29.27% and 24.55% for R1, R2 and R3, respectively. These are shown in Figs. 4b and 5b.

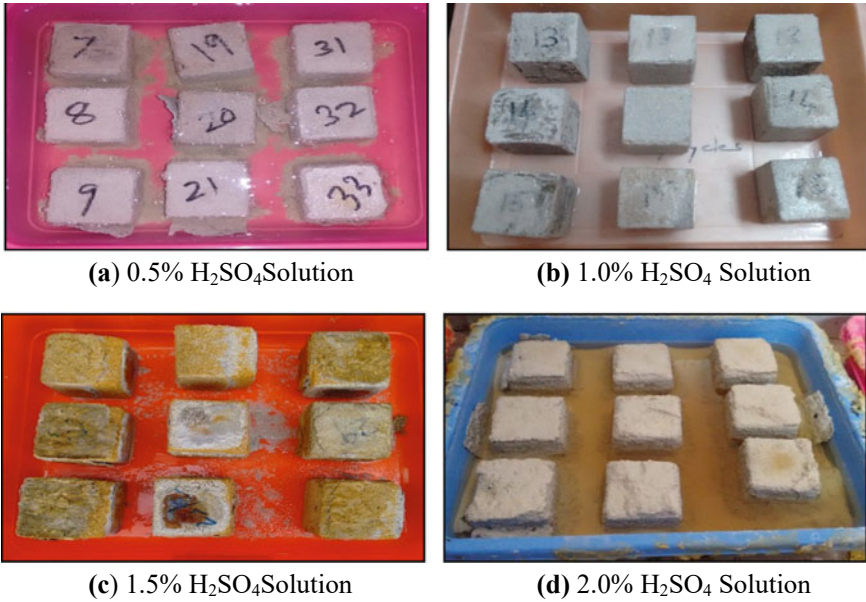


Fig. 3 FRPC samples exposed to H_2SO_4 solutions

- c. **1.5% H_2SO_4** : It is observed that the scaling of concrete is predominant even on lower days of exposure. Capillary pores are formed. Corrosion of steel is initiated. Reddish-brown deposits are seen on the surface as shown in Fig. 3c. These are the results of steel fibre corrosion. However, concrete shows resistance towards spalling. As shown in Figs. 4c and 5c, 16.91%, 15.82% and 14.01% of mass reduction and 56.07%, 46.78% and 40.22% of loss in compressive strength are observed for R1, R2 and R3.
- d. **2.0% H_2SO_4** : This acidic solution induces severe damage to all the specimens. Corrosion of steel fibres is predominant. The solution percolates through capillary pores and oxidation of Fe^{2+} ions results in the formation of ferric oxides and ferric hydroxides in the form of rust. The volume of this layer reaches up to seven times its original value inducing bursting pressure. Thus, spalling of concrete is observed as shown in Fig. 3d. The embedded fibres are exposed and the rate of corrosion increases with an increase in the exposure period. Samples are disintegrated to a greater extent. A huge amount of weight loss is observed, i.e. 23.98%, 20.09% and 18.38% with strength loss of 76.05%, 67.63% and 59.72% for all the grades of concrete. It is shown in Figs. 4d and 5d.

4.2.2 Salt Crystallization Test

Ordinary portland cement is susceptible to damage caused by various acids. This can be overcome by adding superfine pozzolanic material which improves microstructure

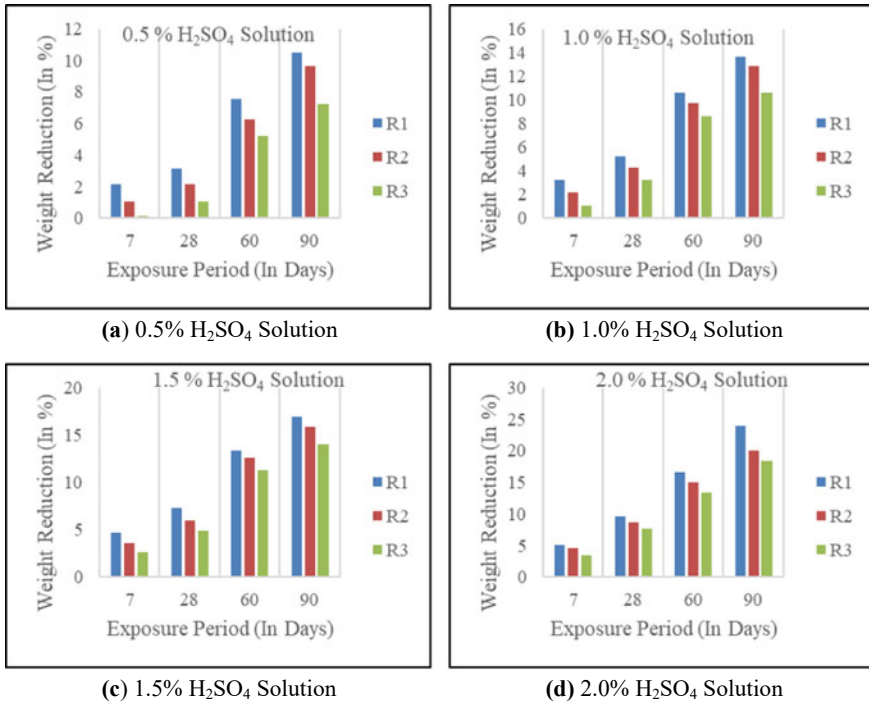


Fig. 4 Reduction in weight for FRPC samples

and density by reducing porosity and permeability. The addition of fibres improves bond strength between aggregate phase and paste which further improves density. The 5% of silica fume in R1 and w/c ratio of 0.21 produced a homogeneous mix and design strength is achieved. However, it is observed that more air voids and pores are generated compared to R2 and R3 when subjected to the salt crystallization test. Thus, from Figs. 8 and 9, it is noted that the percentage of weight loss and reduction in compressive strength in R1 is relatively more than other mixes of FRPC. From Fig. 9 it is seen that all the mixes of FRPC show better resistance towards salt crystallization up to 20 cycles. Thereafter significant damage is induced with an increase in the number of cycles. The damage increases progressively with an increase in each cycle ultimately leading to the failure of the specimen. The results are tabulated in Table 3. The maximum weight loss is up to 6–10% of its original weight corresponding to a 50% loss of strength in compression at 50 cycles. It can be stated that the higher the grade of concrete, the higher the resistance towards salt crystallization (Figs. 6 and 7).

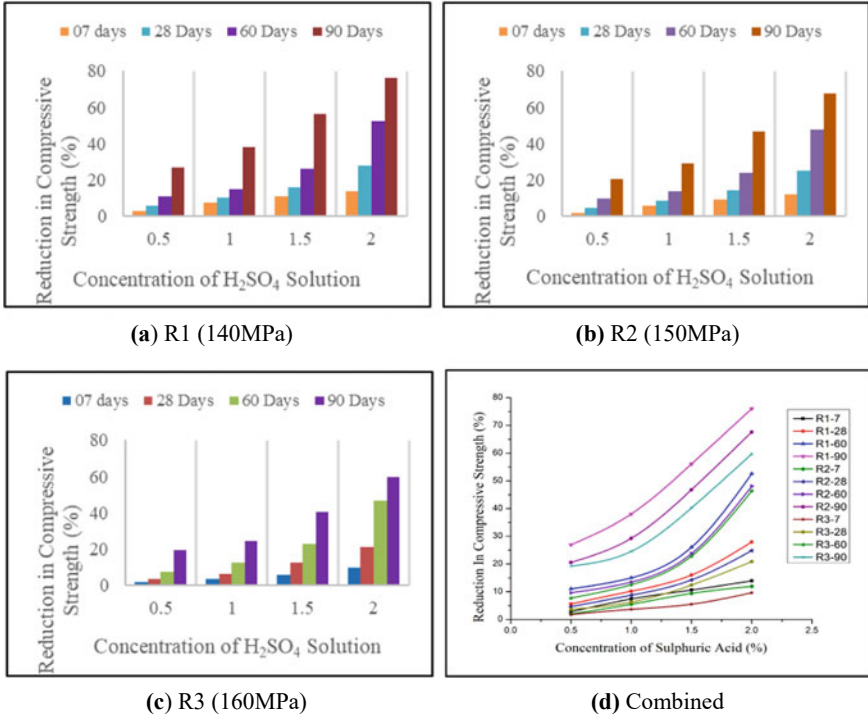


Fig. 5 Reduction in compressive strength for FRPC samples

Table 3 Variation of weight loss and compressive strength with durability cycles

Cycles	Weight reduction (%)			Compressive strength (MPa)		
	M1	M2	M3	M1	M2	M3
0	0.00	0.00	0	140	150	160
10	1.75	1.24	0.89	134.36	143.26	152.62
20	2.67	2.03	1.76	128.49	135.42	144.17
30	6.23	5.09	4.01	116.92	121.65	130.82
40	7.92	6.48	5.24	103.14	108.62	117.54
50	10.92	8.21	6.45	87.92	97.05	108.36

4.2.3 Rapid Chloride Ion Penetration Test (RCPT)

Three samples of each grade of concrete were cast with a w/c ratio varying between 0.19, 0.20 and 0.21. The purpose of this test is to determine the impact of the w/c on chloride permeability. Re-recorded values of average charges passed through each specimen are shown in Table 4. It is observed that higher charges are passed through

Fig. 6 Salt crystals in FRPC samples



Fig. 7 Delamination of surfaces in R1, R2 and R3



Fig. 8 Weight loss in FRPC samples

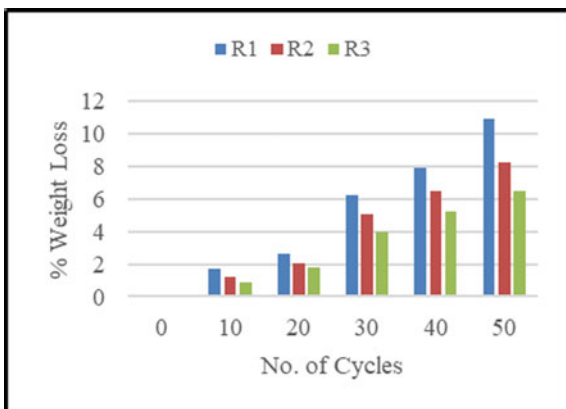


Fig. 9 Strength loss in FRPC samples

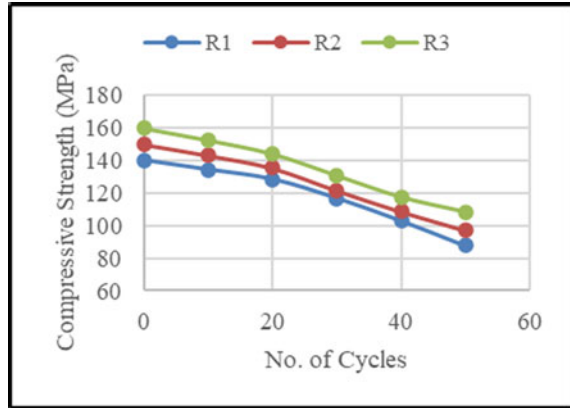


Table 4 RCPT test results

FRPC	W/C ratio	Charges passed (in Coulomb)	Average charges (in Coulombs)	Chloride ion permeability
R1-A	0.21	153	158	Very low
R1-B		157		
R1-C		163		
R2-A	2.0	119	125	Very low
R2-B		125		
R2-C		131		
R3-A	0.19	103	109	Very low
R3-B		109		
R3-C		115		

R1 samples compared to R2 and R3; however, these are very low. Hence it is stated that FRPC shows greater resistance to chloride ion penetration.

5 Conclusions

Based on the laboratory tests conducted on the RPC specimen, the following conclusions are drawn:

1. Fibre-reinforced reactive powder concretes of 140, 150 and 160 MPa are produced. An increase in the dosage of silica fume and steel fibres improves the strengths of concrete under compression, flexure and tension, and an optimum of 2.5% is obtained for the dosage of fibres.

2. Concrete properties can be assessed with visual observations of discolouration, scaling, peeling, corrosion of fibres and spalling of concrete.
3. The highest form of deterioration is observed for samples exposed to acid solutions of H_2SO_4 . The higher concentration of solutions resulted in weight loss of 20–25% and strength loss of 60–75%.
4. FRPC with high density shows better resistance towards the crystallization of soluble salts with an average weight loss of 6–10% at 50% strength reduction.
5. Higher grade FRPC (R3) shows better resistance to acid attacks compared with other grades of concrete (R1 and R2).
6. A very low amount of charges is passed through all FRPC specimens, which indicates that it has high resistance towards the permeability of chloride ions.

References

1. Hiremath PN, Yaragal SC (2017) Effect of different curing regimes and durations on early strength development of reactive powder concrete. *Constr Build Mater* 154:72–87. <https://doi.org/10.1016/j.conbuildmat.2017.07.181>
2. Richard P, Cheyrezy M (1994) Reactive powder concretes with high ductility and 200–800 MPa compressive strength. *ACI SP 144(4)*:507–518
3. Coppola L, Cerulli T, Troli R, Collepardi M (1996) The influence of raw materials on performance of reactive powder concrete. In: International conference on high-performance concrete and performance and quality of concrete structures, Florianopolis, pp 502–513
4. Bonneau O, Lachemi M, Dallaire E, Dugat J, Aitcin P-C (1997) Mechanical properties and durability of two industrial reactive powder concretes. *ACI Mater J* 94:286–290
5. Teichmann T, Schmidt M (2004) Influence of the packing density of fine particles on structure, strength and durability of UHPC. In: First international symposium on ultra high performance concrete, Die Duetsche Bibliothek, Kassel, 2004, pp 313–325
6. Dhundasi AA, Khadiranaikar RB (2019) Effect of curing conditions on mechanical properties of reactive powder concrete with different dosage of quartz powder. In: Das B, Neithalath N (eds) Sustainable construction and building materials. Lecture notes in civil engineering, vol 25. Springer, Singapore. https://doi.org/10.1007/978-981-13-3317-0_33
7. Hiremath PN, Yaragal SC (2018) Performance evaluation of reactive powder concrete with polypropylene fibers at elevated temperatures. *Constr Build Mater* 169:499–512. ISSN 0950-0618. <https://doi.org/10.1016/j.conbuildmat.2018.03.020>
8. Hiremath P, Yaragal SC (2017) Investigation on mechanical properties of reactive powder concrete under different curing regimes. *Mater Today: Proc* 4(9):9758–9762. <https://doi.org/10.1016/j.matpr.2017.06.262>
9. Ipek M, Yilmaz K, Sümer M, Saribiyik M (2011) Effect of pre-setting pressure applied to mechanical behaviours of reactive powder concrete during setting phase. *Constr Build Mater* 25:61–68. <https://doi.org/10.1016/j.conbuildmat.2010.06.056>
10. Courtial M, De Noirfontaine MN, Dunstetter F, Signes-Frehel M, Mounanga P, Cherkaoui K, Khelidj A (2013) Effect of polycarboxylate and crushed quartz in UHPC: microstructural investigation. *Constr Build Mater* 44:699–705. <https://doi.org/10.1016/j.conbuildmat.2013.03.077>
11. George RM, Das BB, Goudar SK (2019) Durability studies on glass fiber reinforced concrete. *Sustain Constr Build Mater:ials*, 2019, 747–756
12. Yadav S, Das BB, Goudar SK (2019) Durability studies of steel fibre reinforced concrete. *Sustain Constr Build Mater* 737–745

13. Srikumar R, Das BB, Goudar SK (2019) Durability studies of poly propylene fiber reinforced concrete. *Sustain Constr Build Mater* 727–736
14. Snehal K, Das BB (2018) Mechanical and permeability properties of hybrid fibre reinforced porous concrete. *Indian Concr J* 98:54–59
15. Influence of length and dosage of polypropylene fibres on the spalling tendency and the residual properties of self-compacting concrete after heated at elevated temperatures
16. Sideris KK, Manita P (2013) Influence of length and dosage of polypropylene fibres on the spalling tendency and the residual properties of self-compacting concrete after heated at elevated temperatures. *MATEC Web of Conferences* 6.<https://doi.org/10.1051/mateconf/20130602004>
17. Vasily R, Belyakov V, Moskovsky S (2016) Properties and design characteristics of the fiber concrete. *Procedia Eng* 150:1536–1540. <https://doi.org/10.1016/j.proeng.2016.07.107>
18. deb T, Jacek Ś (2011) The influence of selected material and technological factors on mechanical properties and microstructure of reactive powder concrete (RPC). *Arch Civ Eng* 57:227–246. <https://doi.org/10.2478/v.10169-011-0017-1>
19. Okabe S, Odagiri M, Ito T, Satoh H (2007) Succession of sulfur-oxidizing bacteria in the microbial community on corroding concrete in sewer systems. *Appl Environ Microbiol* 73(3):971–980. <https://doi.org/10.1128/AEM.02054-06>
20. Murthi P, Venkatachalam S (2008). Studies on acid resistance of ternary blended concrete. *Asian J Civ Eng* 9
21. Song XJ, Marosszekya M, Brungs M, Munn R (2005) Durability of fly ash based geopolymer concrete against sulphuric acid attack. In: International conference on durability of building materials and components, Lyon, France, 17–20 Apr 2005
22. Rendell F, Jauberthie R (1999) The deterioration of mortar in sulphate environments. *Constr Build Mater* 13(6):321–327
23. Aydin S, Yazici Yigiter H, Baradan B (2007) Sulfuric acid resistance of high-volume fly ash concrete. *Build Environ* 42(2):717–721
24. Ariffin MAM, Bhutta MAR, Hussin MW, Tahir MM, Aziah N (2013) Sulphuric acid resistance to blended ash geopolymer concrete. *Constr Build Mater* 43:80–86
25. Khatri RP, Sirivivatnnon V, Yang JL (1997) Role of permeability in sulphate attack. *Cem Concr Res* 27:1179e1189
26. Snehal K, Das BB (2021) Acid, alkali and chloride resistance of binary, ternary and quaternary blended cementitious mortar integrated with nano-silica particles. *Cem Concr Compos* 128:104214
27. Sahoo S, Das BB, Mustakim S (2017) Acid, alkali, and chloride resistance of concrete composed of low-carbonated fly ash. *J Mater Civ Eng* 29(3):04016242
28. Muralan SM, Khadiranaikar RB (2014) Study on the durability characteristics of reactive powder concrete. *Int J Struct Civ Eng Res* 3(2):45–56
29. Olusola KO, Joshua O (2012) Effect of nitric acid concentration on the compressive strength of laterized concrete. *Civ Environ Res* 2(10):48–57. <http://www.iiste.org/Journals/index.php/CER/article/view/3539/3587>
30. Lubelli B, Van Hees RPJ, Nijland TG (2014) Salt crystallization damage: how realistic are existing ageing tests? In: AMS'14 proceedings of the international conference on aging of materials and structures, 2014, pp 103–111. <http://resolver.tudelft.nl/uuid:363f94aa-21c6-40ca-933e-93271b29497b>

Performance of Geopolymer Concrete Developed Using Waste Tire Rubber and Other Industrial Wastes: A Critical Review



Dhiraj Agrawal, U. P. Waghe, M. D. Goel, S. P. Raut, and Ruchika Patil

Abstract The use of concrete as a construction material is one of the highest among other materials used throughout the world. Due to this, enormous demand for concrete exists and its constituents became very vital economically and technologically with respect to the growth of any nation. The primary binder material used in the concrete is cement, and the process of making cement plays a vital role in infrastructural growth. Cement production releases a vast amount of carbon dioxide into the atmosphere, causing severe environmental health hazards like global warming and other issues allied to it. To control the cost of cement and to keep a tab on problems arising from its manufacturing, there is a need to find a substitute of cement so that this substitute can be used as a partial/complete replacement of cement in the manufacturing of concrete. Geopolymer concrete is one way to tackle this problem. Further, industrialization is established very rapidly in the last three decades, particularly in developing countries. Distinct industrial wastes are being generated from these industries leading to the problem of their disposal and various health and environmental concerns. The proper utilization of such wastes is the need of the present time. Extensive research has been carried out on developing the geopolymer concrete along with the use of different industrial wastes. Most of the studies on geopolymer concrete have given promising results for strengths and durability in comparison to conventional concrete. This work presents a detailed review of the studies based on the use of various industrial wastes, like fly ash, ground granulated blast furnace slag, metakaolin etc. along with the various alkaline activators for developing the geopolymer concrete to reduce cement footprint. A detailed review is reported considering the performance of the geopolymer concrete for different mechanical properties, its strengths and durability in comparison with the conventional concrete. It has been found that the enhancement in the strengths is observed for the geopolymer concrete as compared to the

D. Agrawal (✉) · U. P. Waghe · S. P. Raut · R. Patil
Department of Civil Engineering, Yeshwantrao Chavan College of Engineering (YCCE), Nagpur
441110, India
e-mail: dgagrawal@ycce.edu

M. D. Goel
Department of Applied Mechanics, Visvesvaraya National Institute of Technology (VNIT),
Nagpur 440010, India

concrete prepared using cement. Furthermore, limitations in the manufacturing of the geopolymer concrete using these wastes are also discussed.

Keywords Industrial wastes · Geopolymer concrete · Cement · Alkaline activators

1 Introduction

The rapid growth of industrialization is observed in the last three decades in all developing countries of the world. Infrastructural development is considered to be the most important part of the growth of a nation. Instant infrastructural expansion is being carried out using concrete structures in several nations. The use of concrete leads to the demand for cement as a binder material, hence the manufacturing of cement increased very rapidly during this tenure. The production of cement releases almost an equal amount of carbon dioxide (CO₂) into the atmosphere [1–4]. Owing to this, cement consumption has become a foremost challenge for sustainable progression. 5–8% of anthropogenic CO₂ emission was caused by concrete and 95% of it was due to cement manufacturing [5–7]. The worldwide cement production from 2015 to 2019 in various fastest-growing countries is displayed in Fig. 1, which can be considered as the base for the amount of CO₂ emissions and its effect on the environment [8]. From Fig. 1 it can be observed that China, India and other Southeast Asian kingdoms produce almost 65–68% of the total production of cement, and ultimately they also

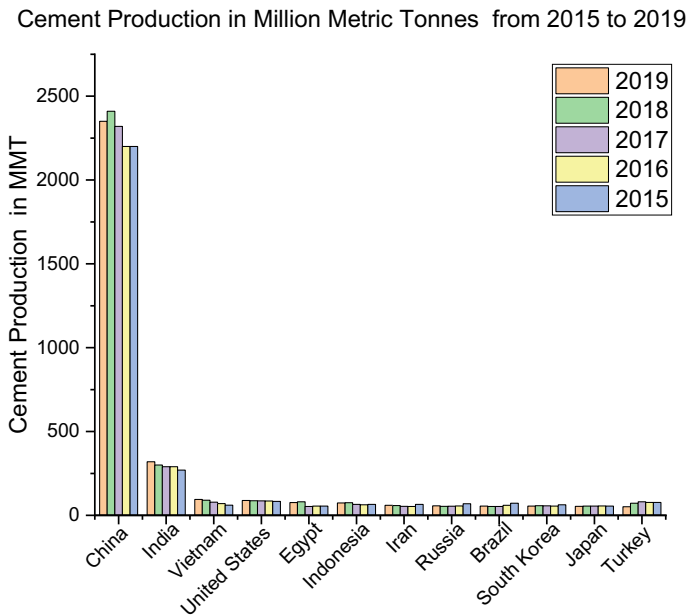


Fig. 1 Major cement production nations in the world

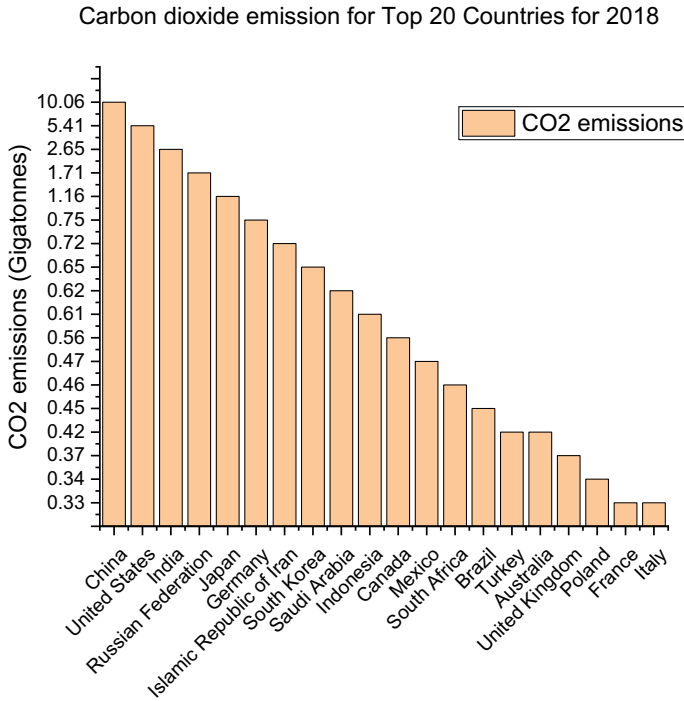


Fig. 2 Carbon dioxide emission for top 20 countries for 2018

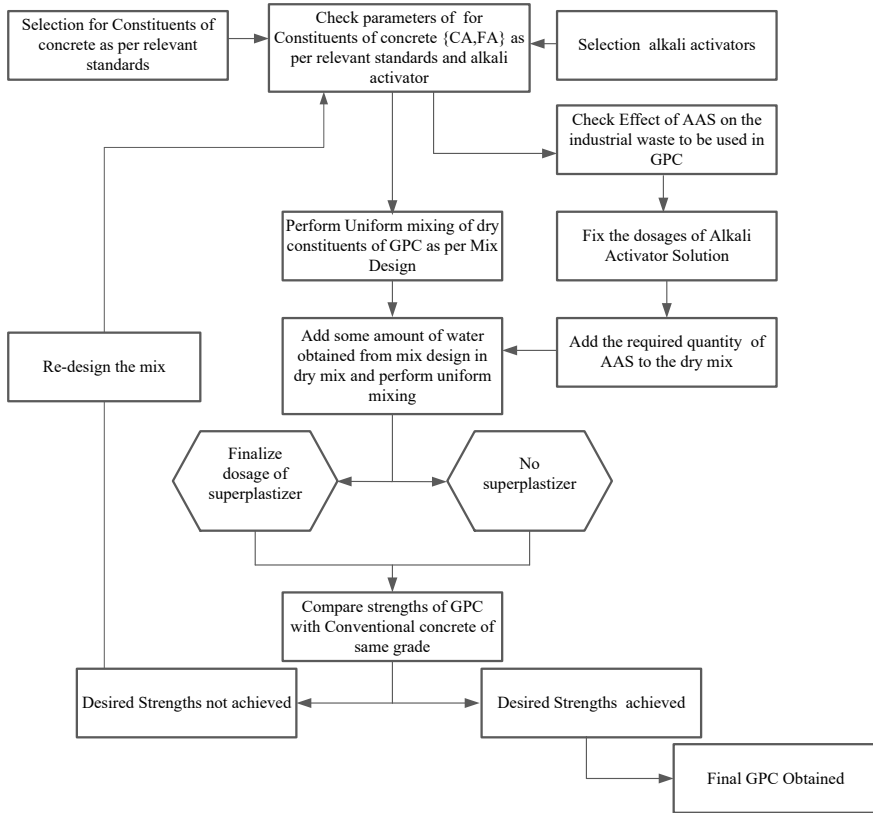
contribute to the same amount of CO₂ emissions. Figure 2 presents the scenario of CO₂ emission in the world by the top 20 CO₂ emitting countries in 2018 [9]. Almost 7% of total greenhouse gas emission is caused due to production of cement [10]. So for developing countries like India, it becomes a serious concern in aspects of a good and healthy environment and sustainable development to develop an alternative to the current conventional construction culture. At the same time, while considering the infrastructural growth around the globe, production of cement, its acute shortage due to gigantic demand and the effect of cement production on the environment, industrial evolution is also at its peak in the entire biosphere with the production of enormous industrial wastes, creating the problem of disposal, land, water and air pollution. This thing also needs strong attention. Extended research was carried out around the world for finding an alternative for binding material in concrete using numerous agro-industrial wastes [11–13]. These investigations have concluded the possible use of some industrial wastes like fly ash (FA), rice husk ash (RHA), ground granulated blast furnace slag (GGBS), metakaolin as a partial replacement for cement but it has some technical precincts and it also does not provide the widespread solution on the concern. Along with this, these wastes also contributed to the generation of CO₂ during electricity generation or in iron industries.

The concept of geopolymer was first announced by Joseph Davidovits in which the reaction of silica and aluminum with various alkaline activators was pronounced [14]. Geopolymers are an inorganic, non-combustible, heat-resistant, three-dimensional network of alumino-silicate materials [15]. The geopolymer fusion is established on the basis of alkali activation in which alumino-silicate material reacts with alkali activators like sodium hydroxide (NaOH) or sodium silicate (Na_2SiO_3) etc. to develop the alumino-silicate gel [16, 17], which can perform as a binder in concrete. Geopolymer binders can be used as products as a complete replacement of cement in concrete production [18], hence it can be a viable solution for sustainable development as it can overcome the problems of scarcity of cement in constructional development of the state, CO_2 emissions and its adverse effects on the ecosystem. Based on the earlier research studies it has been found that some industrial wastes have shown very promising results when utilized for making geopolymers. The wastes like fly ash (FA), ground granulated blast furnace slag (GGBS), crumb rubber, metakaolin etc. were used in distinct studies. The industrial wastes with rich silica or aluminum contents can play a vital part in alumino-silicate alkaline gel formation and are able to impart comprehensive properties of concrete/mortar. This paper describes the detailed study of the researches carried out in the past on the performance of geopolymer concrete (GPC) with industrial wastes. This technique of using industrial wastes in geopolymer concrete can not only solve the problem of environmental contamination but also signifies the prospect of enhancement in mechanical properties of geopolymer concrete over the conventional concrete prepared using cement. The use of geopolymer concrete may also become a cost-effective elucidation in the infrastructure industry.

2 Development of Geopolymer Concrete Using Industrial Wastes

2.1 Methodology to Prepare Geopolymer Concrete

The key constituent of geopolymer concrete is the alkaline activator solution (AAS), and its dosages are fixed in the mix. As the focus of this study is on the use of industrial wastes in geopolymer concrete, the response of these industrial wastes with AAS must be studied well in advance before testing the other parameters of concrete. Sodium or potassium-based alkaline activators are generally used in the preparation of geopolymers in the concrete [19]. NaOH and Na_2SiO_3 are mainly used. The simplified reaction mechanism of geopolymerization consists of the procedure as solid alumino-silicates are dissolved due to alkaline hydrolysis by the inclusion of water. At high pH values dissolution of alumino-silicates is rapid. Due to condensation, gel formation is quicker [20]. In the process of preparing GPC, the mix design should be calculated using relevant standards. Later on, proper mixing of dry constituents of concrete should be carried out before adding some amount of



FA: Fine Aggregate, CA: Coarse Aggregate, GPC: Geopolymer Concrete, AAS: Alkali Activator Solution

Fig. 3 Methodology to prepare the mix of geopolymer concrete

water out of the total quantity of water obtained from the mix design. Polymer activator and catalyst activator are to be added subsequently and uniform mixing should be performed. After the preparation of geopolymer concrete (GPC) the mechanical properties of newly prepared GPC should be compared with conventional concrete for the desired grade. Figure 3 illustrates the methodology to prepare the mix of geopolymer concrete using industrial wastes.

2.2 Use of Various Industrial Wastes in Geopolymer Concrete

2.2.1 Use of Crumb Rubber in Geopolymer Concrete

As per past studies, the use of crumb rubber as a partial substitution of coarse aggregates and fine aggregates in concrete and geopolymer concrete has shown promising

results. Many experimental studies have shown the enhancement of strength in concrete using crumb rubber [21]. The 10% replacement of coarse and fine aggregate improved the compressive strength of slag-based geopolymer concrete with alkaline activators such as NaOH and Na₂SiO₃ due to pre-treatment of rubber with NaOH [22]. Due to improved impact resistance, the rubberized GPC has a low stiffness with higher flexibility as compared to the GPC without crumb rubber and hence the enhanced energy absorption is observed in rubberized GPC [22]. The density of concrete is observed as the same for convention ordinary portland cement (OPC) concrete and geopolymer control concrete with a decline in density is observed with the inclusion of crumb rubber as fractional substitution of aggregates in GPC [23]. As per the research study [24], the tensile strengths were increased. GPC has shown enhancing results in the pull-off strength test of concrete than OPC concrete. The reduction in the compressive strength for OPC concrete is observed at 52% in comparison to the normal OPC concrete, wherein there was a 41% reduction for the GPC with a 30% replacement of aggregates by crumb rubber when compared to the normal GPC [24]. The dynamic properties of geopolymer concrete after a partial switch of coarse and fine aggregates are found to be improved when compared to the normal GPC [25]. The slowdown of crack propagation was observed with the inclusion of crumb rubber in GPC with an enhancement in the impact resistance of GPC [25]. From the various studies, it is observed that the partial replacement of coarse aggregate in GPC by crumb rubber reduces the mechanical properties like compressive strength rapidly, even at less percentage of replacement whereas the fractional replacement of fine aggregates by rubber offers required strengths to both GPC and OPC concrete. According to the journal article [26], the lightweight GPC can be prepared with the use of crumb rubber as a partial replacement for coarse aggregates. Non-structural applications of lightweight geopolymer concrete can be promising using rubber waste. Reduction of the slump was noted with the replacement of more than 30% of aggregates by rubber [27]. The size of aggregates has shown its effect on the compressive strengths. The activator solution provides the pre-treatment to the rubber, so the bonding of rubber with other constituents of concrete is enriched. The clear zones of phenolphthalein indicators were not seen for assessing the carbonation depth [27]. The modulus of elasticity is found to be greatly reduced by implementing the partial replacement of aggregates using crumb rubber while the difference between the densities of normal GPC to rubberized GPC is found to be reduced [28]. Due to the weak bonding between rubber crumbs and other ingredients of GPC, the porosity is found to be increased, which in turn resulted in the reduction of compressive strengths. Along with this, the density of normal GPC and rubberized GPC is found to be increased due to the immersion of specimens in seawater [29]. The maximum decrease in compressive strength is detected up to 60% as related to the normal GPC and rubberized GPC with 15% replacement of aggregates by crumb rubber [30]. Table 1 indicates the compressive strengths obtained for distinct grades of GPC with varying replacement ratios of coarse and fine aggregates by crumb rubber.

Table 1 Compressive strengths for geopolymer concrete in MPa for research papers studied

% replacement of fine/coarse aggregates by crumb rubber	Source of information							
	[23]	[24]	[25]	[26]	[27]	[28]	[29]	[30]
0	37.40	56.23	54.00	42.10	57.90	46.04	50.00	65.00
5	–	–	–	–	–	41.55	40.00	48.00
10	40.00	49.67	–	29.10	–	37.01	35.00	30.00
15	–	–	26.20	–	19.20	34.06	24.00	20.60
20	28.30	42.11	–	28.90	–	–	20.00	15.80
25	–	–	–	–	–	–	–	–
30	24.80	33.00	11.70	–	6.20	–	–	–

2.2.2 Use of Siliceous Material in Geopolymer Concrete

Rashad [31] used the combination of GGBS and quartz powder in GPC. The addition of quartz powder has shown the enhancement of compressive strengths and other mechanical properties of GPC. According to the detailed study by Rashad [32], the setting time and workability were found to be increased with the inclusion of fly ash. In further research, he concluded that the use of silica fume showed positive results as the production of hydrates of calcium and silicates intensified with densifying the pore structure. With the use of quartz powder, the flowability of concrete is increased with a reduction in porosity. At the same time, the quartz powder also showed resistance to the cyclic thermal loadings [31]. Rendering to the studies by Pasupathy et al., it is observed that carbonation is increased with maximum use of fly ash, whereas the proper mixing of FA and GGBS gives similar trends of carbonation of OPC concrete [33]. The effect of palm oil fuel ash as a replacement of GGBS in GPC has been studied, and it is concluded that there is a noteworthy decrement in the setting time with an increment in the replacement of GGBS by palm oil fuel ash. In continuation with this, it is also noted that the 100 palm oil fuel ash-based GPC has 35% reduced strength as compared to the GPC with 100% GGBS [34]. In comparison of the alkali-activated concrete FA and GGBS with Portland cement concrete, it is detected that the tensile strength for alkali-activated concrete is more than Portland cement concrete. On the other hand, the comparison of alkali-activated concrete made using FA with the alkali-activated concrete prepared using GGBS has shown similar mechanical properties [35]. The use of metakaolin in GPC has displayed upgrading for the reduction in shrinkage of exposed specimens. The fire resistance of GPC is also improved due to the inclusion of metakaolin [36]. In continuation to the use of metakaolin, it is concluded that the enhancement of compressive strength by 18% is seen when 20% aluminum oxide is mixed with 80% metakaolin in GPC and matched to the GPC with 100% metakaolin [35]. As per the study conducted by Lee et al. [36], on alkali-activated controlled low-strength materials (CLSMs) with the use of fly ash, slag and bottom ash, it is observed that the increase in the amount of bottom ash has shown a lessening in flowability of

alkali-activated CLSM. In addition, they also commented that the bleeding rate is reduced with an increase in the quantity of slag. At the same instant, the compressive strength is also increased due to the inclusion of slag as it imparts later strength to CLSM. Chemical analysis of alkali-activated mortars is carried out by Winnefeld et al. [37] with high and low calcium fly ashes obtained from the combustion of hard coal. They commented that the low calcium fly ash is more reactive than the high calcium lignite coal fly ashes in alkali-activated systems. The specimens with low calcium fly ashes also showed sufficient compressive strengths [37]. According to the study on porous concrete [38], it is seen that the compressive strength of porous concrete made up of coal-bottom ash using geopolymeric binder was less than that of porous concrete with gravel and cement, whereas the porous concrete with coal bottom ash has provided immobility to the heavy metals leached from bottom ash. A research on the Australian brown coal fly ash collected from three different sources was carried out, and it is observed that the brown coal fly ash is insufficient to achieve satisfactory results. Blending these brown coal ashes with class F fly ash and blast furnace slag is required to get promising outcomes [39]. An experimental study on pervious concrete is completed by Zaetang [40], the ordinary portland cement is replaced with FA and bottom ash was used as coarse aggregate in this study. Limited substitution of cement by FA is carried out and the obtained results show that sodium hydroxide plays a vital role in augmenting strengths. It is recommended that 15% replacement of cement by FA gives encouraging results in aspect of strengths. The study on the combined utilization of crumb rubber as a partial replacement for sand and FA as a binder [42] was conceded and it is concluded that there is a reduction in compressive strength of GPC due to the inclusion of rubber irrespective of the type of fly ash used. The fineness of fly ash reduces the rate of reduction of compressive strength. The use of FA and GGBS is done in the study [41, 42], and it is found that the replacement of FA with GGBS boosts the modulus of elasticity and compressive strength of GPC. The compressive strength is amplified by 1.48 times when the strengths of GPC with 100% FA are harmonized with the GPC with 30% FA and 70% GGBS on the 28th day of testing of specimens. For the same comparison, the modulus of elasticity is increased by 42.85%. As per an experiment by Olivia and Nikraz [43], it was concluded that the GPC was made with the use of FA as a binder material and a total of nine distinct specimens were cast with one OPC sample with 55 MPa strength. The almost same or high strength is achieved by the samples of GPC. The higher tensile and flexural strengths were observed for GPC as compared to OPC concrete. Tawatchai Tho-in presented experimental results on the pervious GPC using FA as the binder material, the ratio of coarse aggregate to FA was 1:8. The compressive strength and splitting tensile strengths were determined, and it is found that these strengths for pervious alkali-activated GPC are slightly higher than that of normal pervious concrete prepared using cement as a binder. The density of pervious GPC is 30% less than the orthodox pervious concrete [43]. A combined study was conceded on the use of cement and FA as a binder material in concrete. The conventional concrete was compared to fractional and integral replacement of cement by FA and it is perceived that the mechanical properties like compressive, flexural and split tensile strengths were improved by 43.6%, 36.07% and 51.13%,

respectively, at 50% replacement of cement by FA and compared with the specimens having 100% cement as binder material [44]. Table 2 presents the chemical oxide composition of distinct industrial wastes used in the formation of GPC in referred papers. Figure 4 presents the amount of oxides of silica, aluminum and iron present in different industrial wastes, which are the main components of cement.

3 Discussion

The widespread literature revisions were accomplished concerning the development of sustainable concrete without using cement and other conventional constituents of concrete like sand. Figures 1 and 2 depict how harmful activity cement production is. The generation of greenhouse gases and CO₂ emissions will be the long-lasting glitches as the development of nations cannot be compromised. So it is the need and duty of each nation to think about sustainable development. As reviewed from the studies cement is the main matter to emit CO₂, so GPC became the most viable elucidation as an alternative to cement that can be generated using alkaline activators and other siliceous by-products disposed of by industries as binder material. It is marked in Table 1 that the researchers have used crumb rubber as a replacement for fine aggregate in concrete and in GPC by overcoming the environmental intimidations generated by the production of cement due to stockpiled tires. The generation of discarded tires is a never-ending problem for our ecosystem as the automobile industry grows rapidly day by day. It is observed from [20–22] that the crumb rubber gives promising results in view of the strengths of GPC while comparing them with orthodox concrete, and the dynamic behavior of rubberized GPC is improved to that of normal concrete. At the same time, it is also seen that the molarity ratio, blending of NaOH and Na₂SiO₃ also affects the performance of crumb rubber in GPC and in normal concrete. From Table 2 it is realized that many siliceous materials recycled from industrial wastes can be used as binder materials in GPC as a replacement for cement. The use of quartz powder [31] has shown enhancement in the strengths of concrete. Figure 4 proves the efficiency of industrial wastes in the replacement of cement in concrete. GGBS and FA are the most used binders in GPC. More focus is needed on experimental studies on GPC as more encouraging results are predictable for practical implementation of GPC over conventional concrete. The source/collection of industrial wastes should be studied as it affects the properties of concrete.

4 Conclusion

The use of divergent industrial wastes concerning to prepare geopolymer concrete has been reviewed. In accordance with the studied literature on experimental lessons, the following conclusions have been drawn:

Table 2 Chemical oxide composition for siliceous material used in GPC

Source	IW	SiO ₂	Al ₂ O ₃	Fe ₂ O ₃	CaO	MgO	Na ₂ O	K ₂ O	SO ₃	TiO ₂	P ₂ O ₅	MnO ₂	Cl	L.O.I
[19]	GGBS	36.95	10.01	1.48	33.07	6.43	1.39	0.74	3.52	0.52	0.10	0.52	0.05	0.00
	QP	98.81	0.14	0.05	0.51	0.02	0.04	0.03	0.03	0.02	0.32	0.00	0.00	0.32
[21]	GGBS	36.95	10.01	1.48	33.07	6.43	1.39	0.74	3.52	0.52	0.10	0.52	0.05	0.00
	QP	98.81	0.14	0.05	0.51	0.02	0.04	0.03	0.03	0.02	0.32	0.00	0.00	0.32
[22]	FA	80.40	14.00	0.04	0.31	3.57	0.10	0.09	0.85	0.04	0.08	0.49	-	0.54
	GGBS	34.20	13.80	43.10	5.40	0.40	0.10	-	0.40	-	0.80	-	-	1.80
[23]	POFA	47.37	3.53	6.19	11.83	4.19	-	-	-	0.24	-	-	0.88	1.84
	GGBS	34.10	13.50	0.36	42.70	4.50	-	-	-	-	-	0.20	0.01	1.40
[24]	GGBS	36.00	10.50	0.70	39.80	7.90	0.30	0.20	2.10	-	-	-	-	-
	FC	37.70	20.00	5.60	23.40	4.30	1.70	0.60	2.40	-	-	-	-	-
[26]	FA	42.10	28.60	14.40	6.26	2.60	-	2.40	0.61	-	-	-	-	-
	BFS	35.17	13.93	0.58	42.50	4.12	-	0.46	2.03	-	-	-	-	-
[27]	LCFA	56.00	25.00	8.70	1.90	3.10	0.20	3.30	0.45	1.00	0.29	-	0.05	2.19
	HCFA	44.00	7.30	3.80	29.00	4.10	1.10	0.70	10.00	0.46	0.02	-	8.90	2.24
[28]	FA	42.10	28.60	14.40	6.26	2.60	-	2.40	0.61	-	-	-	-	-
	BFS	35.17	13.93	0.58	42.47	4.12	0.15	0.46	2.03	-	-	-	-	-
[29]	LYDP	48.90	15.16	9.68	2.44	5.38	4.86	0.41	7.48	1.58	-	0.05	-	4.04
	GGBS	32.38	12.24	0.49	44.04	5.13	0.22	0.33	4.21	0.51	-	0.37	-	0.08
	FC	51.88	25.92	12.66	4.35	1.54	0.78	0.71	0.24	1.3	-	0.15	-	0.55
[30]	OPC	14.40	2.70	3.40	70.40	0.90	0.20	0.60	4.30	0.30	-	-	-	2.40
	FA	35.90	15.10	17.30	17.20	2.30	0.90	3.20	5.90	0.90	-	-	-	1.10

(continued)

Table 2 (continued)

Source	IW	SiO ₂	Al ₂ O ₃	Fe ₂ O ₃	CaO	MgO	N ₂ O	K ₂ O	SO ₃	TiO ₂	P ₂ O ₅	MnO ₂	Cl	L.O.I
[31]	BA	31.80	12.10	18.00	25.30	2.40	0.90	2.50	3.70	0.50	-	-	-	2.60
	T-1 FC	50.67	18.96	6.35	14.14	3.12	-	0.69	-	0.74	-	-	-	-
	T-2 FC	58.05	21.59	5.10	9.42	1.86	-	0.92	-	0.39	-	-	-	-
	T-3 FC	54.70	29.00	6.74	1.29	0.80	-	1.88	-	0.10	-	-	-	-
[32]	FA	58.27	26.10	3.60	2.89	1.31	0.51	0.90	1.06	0.56	0.30	2.90	-	1.60
	GGBS	33.20	13.20	1.05	45.77	3.25	0.88	-	0.82	-	-	1.97	-	1.95
[34]	FA	50.50	26.57	13.77	2.13	1.54	0.45	0.77	0.41	-	1.00	-	-	0.60
	Cement	21.10	4.70	2.80	63.80	2.00	0.50	-	2.50	-	-	-	0.01	2.10
	FA	57.90	31.11	5.07	1.29	0.97	0.09	1.00	0.05	-	-	-	0.04	0.80

IW Industrial waste, GGBS Ground granulated blast furnace slag, FA Fly ash, QP Quartz powder, POFA Palm oil fuel ash, FC Class F fly ash, BFS Blast furnace slag, LCFA Low calcium fly ash, HCFA High calcium fly ash, LYDP Loy young dry precipitator ash, OPC Ordinary portland cement, BA Bottom ash, T-1 FC Type 1 class C fly ash, T-2 FC Type 2 ultra-fine class C fly ash, T-3 FC Type 3 class f fly ash

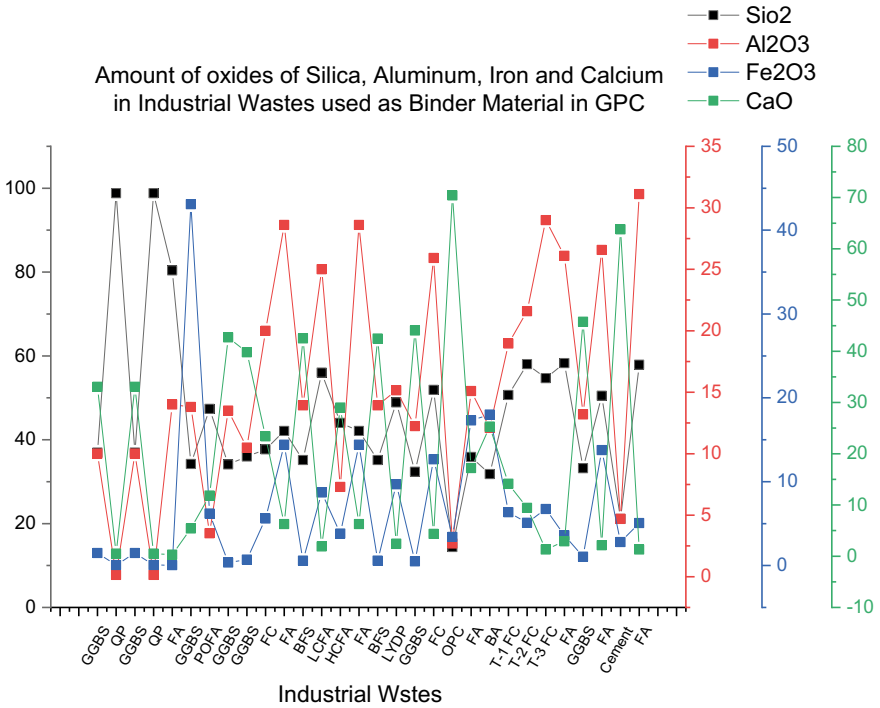


Fig. 4 Amount of oxides of silica, aluminum, iron, and calcium available in industrial wastes used as binder materials in GPC

- The alkali-based geopolymers are the finest alternative to the cement as sufficient strength can be achieved.
- Limited use of crumb rubber as partial substitution of fine aggregate can be acceptable as it gives desired strengths in both normal concrete and GPC. 30% optimum replacement of fine aggregate by crumb rubber is possible, beyond this the compressive strengths of specimens may be reduced.
- Dynamic properties of concrete have been improved in some studies after the incorporation of crumb rubber. The effect of the size of rubber particles on the strengths of GPC should be studied.
- GGBS and FA have shown very interesting results when reacted with an alkali-activator solution and achieved higher strengths than conservative concrete.
- GPC can be used as an environment-friendly and economical solution for infra-structural development as it involves the use of recycled industrial by-products and minimizes environmental pollution.

References

1. Mehta A, Siddique R (2016) An overview of geopolymers derived from industrial by-products. *Constr Build Mater* 127:183–198
2. Snehal K, Das BB (2021) Acid, alkali and chloride resistance of binary, ternary and quaternary blended cementitious mortar integrated with nano-silica particles. *Cem Concr Compos* 128:104214
3. Sahoo S, Das BB, Mustakim S (2017) Acid, alkali, and chloride resistance of concrete composed of low-carbonated fly ash. *J Mater Civ Eng* 29(3):04016242
4. Snehal K, Das BB, Akanksha M (2020) Early age, hydration, mechanical and microstructure properties of nano-silica blended cementitious composites. *Constr Build Mater* 233:117212
5. Shivaprasad KN, Das BB (2018) Determination of optimized geopolymerization factors on the properties of pelletized fly ash aggregates. *Constr Build Mater* 163:428–437
6. Farsana C, Das BB, Snehal K (2021) Influence of fineness of mineral admixtures on the degree of atmospheric mineral carbonation. *Smart Technol Sustain Dev* 117–136
7. Ouellet-Plamondon C, Habert G (2015) Life cycle assessment (LCA) of alkali-activated cements and concretes. *Handbook of alkali-activated cements, mortars and concretes*, pp 663–686
8. Datis Export Group (2019) Worldwide cement production from 2015 to 2019, 12 July 2020 [online]. Available at: <https://datis-inc.com/blog/worldwide-cement-production-from-2015-to-2019/>. Accessed 15 Dec 2020
9. Union of Concerned Scientists (2020) "<https://www.ucsusa.org/>" Union of Concerned Scientists, 12 Aug 2020 [Online]. Available at: <https://www.ucsusa.org/resources/each-countrys-share-co2-emissions>. Accessed 20 Dec 2020
10. Oyeibisi S, Ede A, Olutoge F, Omole D (2020) Geopolymer concrete incorporating agro-industrial wastes: effects on mechanical properties, microstructural behaviour and mineralogical phases. *Constr Build Mater* 256
11. Agrawal D, Hinge P, Waghe UP, Raut SP (2014) Utilization of industrial waste in construction material—a review. *Int J Innov Res Sci Eng Technol (IJIRSET)* 3(1):8390–8397
12. Dalinaidu A, Das BB, Singh DN (2007) Methodology for rapid determination of pozzolanic activity of materials. *J ASTM Int* 4(6):1–11
13. Shivaprasad KN, Das BB (2018) Effect of duration of heat curing on the artificially produced fly ash aggregates. *IOP Conf Ser: Mater Sci Eng* 431(9):092013
14. Grant Norton M, Provis JL (2020) 1000 at 1000: geopolymer technology—the current. Springer
15. Abbas Mohajerani A, Suter D, Jeffrey-Bailey T, Song T, Arulrajah A, Horpibulsuk S, Law D (2018) Recycling waste materials in geopolymer concrete. *Clean Technol Environ Policy*
16. Nuruddin MF, Malkawi AB, Fauzi A, Mohammed BS, Almattarneh HM (2016) Geopolymer concrete for structural use: recent findings and limitations. In: *International conference on innovative research 2016—ICIR Euroinvent*. IOP Publishing
17. Sharath BP, Shivaprasad KN, Athikkal MM, Das BB (2018) Some studies on sustainable utilization of iron ore tailing (IOT) as fine aggregates in fly ash based geopolymer mortar. *IOP Conf Ser: Mater Sci Eng* 431(9):092010
18. Pavithra P, Srinivasula Reddy M, Dinakar P, Hanumantha Rao B, Satpathy BK, Mohanty AN (2016) A mix design procedure for geopolymer concrete with fly ash. *J Clean Prod* 117–125
19. McKenzie W (2020) Geopolymer concrete—playing in the laboratory, 25 June 2014. [Online] Available at: <https://www.youtube.com/watch?v=-86Grly1E-c&feature=youtu.be>. Accessed 12 Dec 2020
20. Agrawal D, Waghe UP, Raut SP (2021) Performance evaluation of rubberized concrete with the use of steel fibers. In: *Advances in civil engineering and infrastructural development*. Springer, Singapore, pp 709–717
21. Aly AM, El-Feky MS, Kohail M, Nasr E-SAR (2019) Performance of geopolymer concrete containing recycled rubber. *Constr Build Mater* 207:136–144
22. Luhar S, Chaudhary S, Luhar I (2019) Development of rubberized geopolymer concrete: Strength and durability studies. *Constr Build Mater* 204:740–753

23. Pham TM, Liu J, Tran P, Pang V-L, Shi F, Chen W, Hao H, Tran TM (2020) Dynamic compressive properties of lightweight rubberized geopolymer concrete. *Constr Build Mater*
24. Aslani F, Deghani A, Asif Z (2020) Development of lightweight rubberized geopolymer concrete by using polystyrene and recycled crumb-rubber aggregates. *J Mater Civ Eng*
25. Dong M, Elchalakani M, Karrech A, Yang B (2020) Strength and durability of geopolymer concrete with high volume rubber replacement. *Constr Build Mater*
26. Taylor SJ (2018) Mechanical properties of crumb rubber geopolymer concrete. UNSW Canberra at ADFA, Canberra
27. Yahya Z, Abdullah MMAB, Ramli SNH, Minciuna MG, Abd Razak R (2018) Durability of fly ash based geopolymer concrete infilled with rubber crumb in seawater exposure. In: IOP conference series: materials science and engineering, Euroinvent ICIR 2018
28. Azmi AA, Al Bakri Abdullah MM, Ghazali CMR, Sandu AV, Hussin K (2016) Effect of crumb rubber on compressive strength of fly ash based geopolymer concrete. In: MATEC web of conferences IConGDM 2016
29. Rashad AM, Zeedan SR, Hassan HA (2012) A preliminary study of autoclaved alkali-activated slag blended with quartz powder. *Constr Build Mater* 70:77
30. Rashad AM (2013) A comprehensive overview about the influence of different additives on the properties of alkali-activated slag—a guide for civil engineer. *Constr Build Mater* 47:29–55
31. Rashad AM (2014) An exploratory study on alkali-activated slag blended with quartz powder under the effect of thermal cyclic loads and thermal shock cycles. *Constr Build Mater* 70:165–174
32. Rashad AM (2013) Alkali-activated metakaolin: a short guide for civil engineer—an overview. *Constr Build Mater* 41:751–765
33. Pasupathy K, Berndt M, Castel A, Sanjayan J, Pathmanathan R (2016) Carbonation of a blended slag-fly ash geopolymer concrete in field conditions after 8 years. *Constr Build Mater* 125:661–669
34. Salih MA, Farzadnia N, Ali AAA, Demirboga R (2015) Development of high strength alkali activated binder using palm oil fuel ash and GGBS at ambient temperature. *Constr Build Mater* 93:289–300
35. Thomas RJ, Peethamparan S (2015) Alkali-activated concrete: engineering properties and stress–strain behavior. *Constr Build Mater* 93:49–56
36. Lee NK, Kim HK, Park IS, Lee HK (2013) Alkali-activated, cementless, controlled low-strength materials (CLSM) utilizing industrial by-products. *Constr Build Mater* 49:738–746
37. Winnefeld F, Leemann A, Lucuk M, Svoboda P, Neuroth M (2010) Assessment of phase formation in alkali activated low and high calcium fly ashes in building materials. *Constr Build Mater* 24:1086–1093
38. Jang JG, Ahn YB, Souri H, Lee HK (2015) A novel eco-friendly porous concrete fabricated with coal ash and geopolymeric binder: heavy metal leaching characteristics and compressive strength. *Constr Build Mater* 79:173–181
39. Tennakoon C, Sagoe-Crentsil K, San Nicolas R, Sanjayan JG (2015) Characteristics of Australian brown coal fly ash blended geopolymers. *Constr Build Mater* 101:396–409
40. Zaetang Y, Wongsa A, Sata V, Chindaprasirt P (2015) Use of coal ash as geopolymer binder and coarse aggregate in pervious concrete. *Constr Build Mater* 96:289–295
41. Park Y, Abolmaali A, Kim YH, Ghahremannejad M (2016) Compressive strength of fly ash-based geopolymer concrete with crumb rubber partially replacing sand. *Constr Build Mater* 118:43–51
42. Olivia M, Nikraz H (2012) Properties of fly ash geopolymer concrete designed by Taguchi method. *Mater Des* 36:191–198
43. Tho-in T, Sata V, Chindaprasirt P, Jaturapitakkul C (2012) Pervious high-calcium fly ash geopolymer concrete. *Constr Build Mater* 30:366–371
44. Shehab HK, Eisa AS, Wahba AM (2016) Mechanical properties of fly ash based geopolymer concrete with full and partial cement replacement. *Constr Build Mater* 126:560–565

Thermal Behaviour of Mortar Specimens Embedded with Steel and Glass Fibres Using *KD2 Pro* Thermal Analyser



P. Harsha Praneeth

Abstract Understanding the thermal behaviour aspects of cement mortar has a significant role in the applications of sustainable buildings, chimneys, cooling towers, bridges, etc. as mortar is the main constituent in all concrete structures and masonry walls. It is often desirable to have lower thermal conductivity (K) values for the sake of thermal insulation; higher values are needed to optimize the thermal stresses in the structure. Hence, a need exists in understanding these behaviours, so that the desired material can be tailored and used in the places of need. The current study aims at investigating the thermal properties of mortar specimens, i.e. thermal conductivity, specific heat capacity (C), thermal diffusivity (D), and thermal resistivity (ρ) of reinforced mortar specimens embedded with steel and glass fibres. Thermal properties are determined using a *KD2 pro* thermal property analyser on five mortar specimens at temperature ranges of room temperatures (27) 50, and 100 °C and hydration periods of 3, 14, and 28 days. The results indicated that in specimens reinforced with 1% glass fibres, thermal conductivity decreased significantly with the increase in the hydration period and temperatures, while the effect of the hydration period of 1% steel fibre specimens on thermal conductivity is relatively low. It is concluded that mortar specimens reinforced with steel fibres have higher K ; relatively glass fibres have K on the lower side. Mortar specimens with 0.5 and 1% of glass fibre have shown the highest resistance to heat flow. While the inclusion of 1% steel fibre is most favourable for effective heat transfer across the mortar specimens.

Keywords Thermal conductivity · Thermal behaviour · Thermal diffusivity · Mortar

P. Harsha Praneeth (✉)
Department of Civil Engineering, Geethanjali College of Engineering and Technology,
Hyderabad, India
e-mail: iharshaent@gmail.com

© The Author(s), under exclusive license to Springer Nature Singapore Pte Ltd. 2023
M. S. Ranadive et al. (eds.), *Recent Trends in Construction Technology and Management*, Lecture Notes in Civil Engineering 260,
https://doi.org/10.1007/978-981-19-2145-2_4

43

1 Introduction

The energy efficiency of buildings, nuclear power plants, rocket launching facilities, large furnaces, gravity dams, etc. can be improved, by engineering a material, which can mimic the properties of an insulating material, where the ability of a material to conduct heat is at its optimum. In order to achieve this, the inclusion of minerals, chemicals, and fibres in the concrete or mortar mix has been the trend of the day. By incorporating such supplements in the preparation of concrete mixes, the mechanical and thermal properties of concrete will be significantly affected [7, 16, 22, 21]. The inclusion of various fibre dosages and their dispersion, during the concrete manufacturing process, can affect the thermal properties of concrete enormously [8, 20, 27] (Arikumar et al., 2019). Especially the effects of fibres on the values of thermal conductivity (K) can be very significant. As K is not the only critical aspect in thermal behaviour studies, the applications focusing on this aspect are of significance in the design of certain aspects of construction material deployed in buildings.

Studies pertaining to the changes taking place in mechanical properties and thermal properties with the inclusion of limestone [1], conductive fibres [5], rubber particles [10], mineral admixtures [6], etc. were extensively examined. Keeping such material in mind, numerous studies carried out by the researchers indicated variations of moisture content in the mortar specimens were not observed up to 50 °C, while declination is linear and steep until 100 °C [26]. The inclusion of sand has decreased the specific heat (C) while K has increased, a complete opposite phenomenon was observed due to the inclusion of silica fumes C [26]. K is usually determined by three methods: two linear parallel probe methods (TLPP), lane heat source (PHS), and hot guarded plate (HGP). PHS and HGP methods are similar to the TLPP method (Kim et al.). Mortar specimens were prepared with partial replacement of mineral admixtures, such as Fly ash (FA), Silica fume (SF), and Blast furnace slag (BFS) in Portland cement (PC). Compressive strength, K values are compared with plane mortar specimens, in relation to the specimens replaced partially with 10, 20, and 30% of FA, SF, and BF. Comparing all the results, lower K values are reported for specimens prepared with SF, with respect to other mineral admixtures [6]. Mortar specimens with Palm oil fuel ash (POFA) as a mineral admixture and partially replaced with Ordinary Portland cement (OPC), along with Acrylic and Polypropylene (PP) fibre. The casted specimens were exposed to thermal loads of 300 and 600 °C, and compressive strength, water adsorption, and K are investigated. A drop of 50% in K was achieved in the mixes replaced with 50% POFA, due to the presence of higher internal air voids, and similar behaviour was observed with the specimens incorporated with acrylic fibres [11]. Cork fibre and paper waste are embedded into the gypsum matrix during the manufacturing of composite panels. The composite panels are investigated for water adsorption, compression, flexural strength, sound propagation, and K . Inclusion of 60% of cork fibre into the composites has decreased the K by 300% [17]. Mendes et al. [9] proved the relation between variations in the K is dependent on the porosity of the specimens, a relation was stated between the testing methods of Ultrasonic pulse velocity and heat flow meter. Contrafatto et al. [4] indicated that a

significant correlation does not exist between K and open porosity of the specimens prepared using pyroclasts that are porous in nature and that are embedded into the mortar mix. Hot wire parallel technique was adopted to determine the effects of moisture content and porosity on K , D , and C of the aluminium refractory concrete specimens in the temperature ranges of ambient temperature – 1000 °C [18]. K , D , and density decrease with the increase in temperature. While moisture content will directly affect the K [19], conductivity and D are determined for hempcrete at higher temperatures using a hot box test [15]. Methods such as the guarded hot plate method, hot wire method, heat flow method, and probe method are adopted in common. For the current experimental investigations, probe methods were adopted. Studies indicated that with the increasing temperatures, the thermal diffusivity decreases; as a result of increasing temperatures, moisture content tends to reduce [28]. Thermal analysers such as Thermogravimetric Analysis, Differential Thermal Analysis, and Differential Scanning Calorimetry are used to understand the mass loss and heat flow of cement specimens at elevated temperatures [14–14, 23, 24].

The primary focus of this research article is to determine the effects of steel and glass fibre concentration on the thermal properties of mortar specimens. Thermal properties such as K , C , D , and ρ are determined using $KD2$ Pro thermal analyser for the first time. The variations in the thermal properties are determined for the mortar specimen prepared with 0.5 and 1% of steel and glass fibre concentrations, and the results are compared to plane mortar specimens subjected to 50 and 100 °C. The suitability of $KD2$ Pro thermal analyser in determining the thermal properties was investigated and discussed.

2 Experimental Groundwork

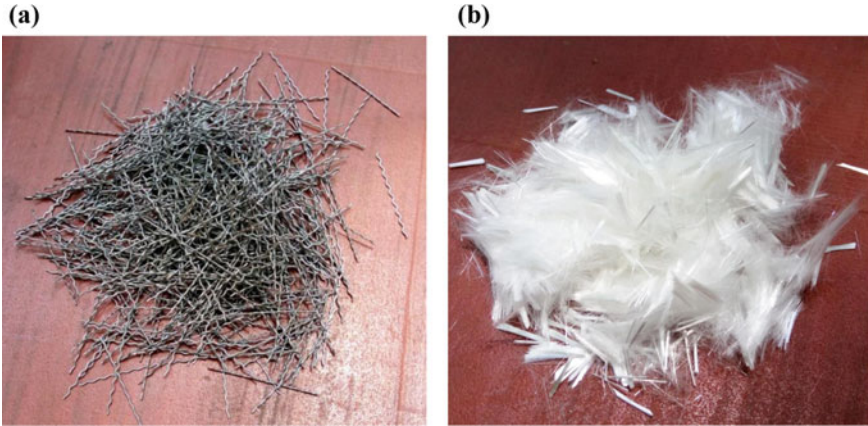
2.1 Materials

Cement binder of OPC, i.e. OPC-53 grade of cement (GoC) was chosen for the current experimental study, due to the ease in availability and its frequent use. The standard consistency of the cement paste is 30%, determined using IS:4031 (Part-4)-1988. While specific gravity of cement is 3.15, determined using IS:2720(Part-3). The fine aggregate (FA) used for the present investigation is Ennore sand, confining to the code specifications of IS: 650-1991. FA confined to three groups of particle size distribution, i.e. <2 mm and >1 mm, <1 mm and >50 μm , and <500 μm and >90 μm ; while the ratios of each grade of FA are 33.33%. Two types of commercially available fibres are incorporated in to the mortar mix.

For the mortar mix, corrugated crimped stainless steel fibres that are cold drawn from mild steel wire are used. The mechanical properties of crimped fibres and their samples are shown in Table 1 and Fig. 1a. Along with steel fibre, Alkali resistance (Ar) glass fibre, where the integral part of the glass fibre is zirconium, constitutes 19%

Table 1 Mechanical properties of steel fibres

Type of fibre	Steel	Glass
Diameter (\emptyset)	0.55 mm	13.5-14 μ m
Length (L)	50 mm	6 mm
Tensile strength	1168 MPa	3500 MPa
L/\emptyset	90.90	444.44
K (W/m K)	16	1.05
Specific gravity	7.85	2.6

**Fig. 1** Appearance of **a** corrugated crimped steel fibre and **b** Ar glass fibre

of the total fibre content. Ar glass fibres are highly abrasive resistant and noncombustible. The mechanical properties and the fibre samples are shown in Table 1 and Fig. 1b.

2.2 Mix Proportions

To determine the compressive strength of mortar specimens, i.e. plane mortar specimens are cast using *OPC-53* (200 g), and Ennore sand (Zone-I, II, and III—200 g each), a total of 600 g, is mixed with a water content of $(P/4) + 3\%$ (P —water percentage required for producing a paste of standard consistency as per *IS:4031*(Part-1)-1988), i.e. 84 g. The mortar specimens are cast, as per the code specifications of *IS: 4031*(Part-6)–1988. Five types of specimens are cast for the current investigation, i.e. specimens with Plane mortar, 0.5%, 1% concentrations of corrugated crimped steel fibres, and Ar fibres incorporated into the plane mortar mix.

2.3 Testing

Mortar mix specimens are placed in $70.7 \times 70.7 \times 70.7 \text{ mm}^3$ molds. While thermal properties are determined on cylindrical specimens, for which a set of three cylindrical specimens were cast into the molds 50 mm in diameter (\varnothing) and length (L). The mortar mix was poured into the desired mold, as three layers, while each layer was compacted by means of a mechanical vibrator. In order to place the sensors in Fig. 2b into the mortar specimens, two grooves are provided on top of the specimen, before the hardening of the mortar mix Fig. 2a, and placed in the curing tank for the desired curing periods. Once the desired curing periods are achieved, the specimens are taken out of the curing tank and subjected to desired temperature loading using an oven, since the heating temperatures are very low.

In order to acquire the parameters under investigation, from KD2 Pro thermal analyser, the following procedure was adopted for all the specimens. K , C , D , and ρ of the cast mortar specimens are determined using *Decagon KD2 Pro* setup. The setup uses a method of transient line heat source for determining the thermal properties, while the dual needle *SH-1* sensor is used to obtain the parameters under investigation. A read time of 2 min was adopted, from which the data is acquired to predict the thermal properties. Out of the considered 2 min of read time taken for the SH-1 sensor, half of the time is spent for temperature equilibrium prior to initiation of heat. While the rest is the time utilized for heating; however, the measurements are taken for the entire duration. Depending on the type of material used for the study, different sensors can be used, and the read time to be adopted will be altered, as per the manufacturer's specifications.

Care is taken while inserting the dual needle sensor setup, and needles should remain parallel during the process of insertion into the specimens. To achieve this, a red tab with sample holes was inserted into the specimens at the time of cast, mortar specimens with dual needle holes Fig. 2a. Since the sensor releases a heat pulse, a

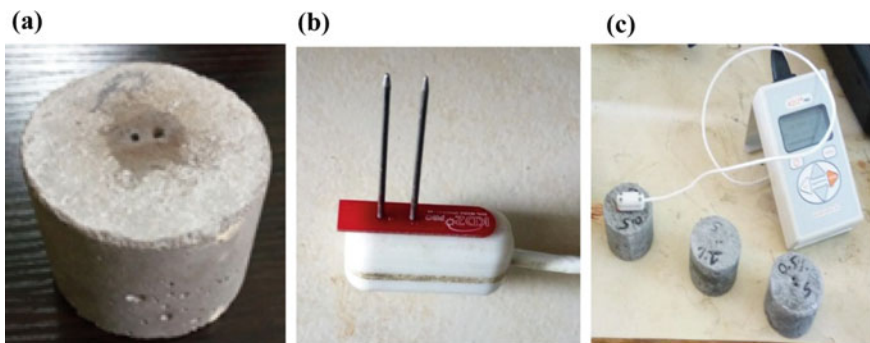


Fig. 2 a Specimen with pre-inserted whole, b dual needle SH1 sensor, and c thermal properties test setup

minimum extra spacing of 1.5 cm is left parallel to the sensor in all the directions, to avoid errors while the collection of the readings.

In order for the *KD2 Pro* analyser to predict the results accurately, a good thermal contact between sensor and mortar specimens needs to be achieved, for which the thermal grease has been applied to the sensors, before placing the needles into the provided slots.

K is the ability of a material to conduct heat, the unit being $\frac{W}{m-K}$. The quantity of heat flow through a material is directly proportional to the cross-sectional area and the varying temperature gradient, along the surface through which the heat flows, while inversely proportional to the material thickness. It is calculated by Eq. 1:

$$Q = \left(\frac{k * A * (t_2 - t_1)}{L} \right) \quad (1)$$

where Q = Quantity of heat; A = Area of the cross section; $(t_2 - t_1)$ = Temperature difference; L = Distance of flow (Thickness).

D is the rate at which the temperature can be spread across the material. Higher diffusivity indicates the rate of heat transfer will be high. D is dependent on K , C , and density of the material. D is measured using SH-1 dual needle sensor, derived by Eq. 2:

$$D = \frac{K}{(d * C)} \quad (2)$$

where K = Thermal conductivity; d = Density; C = Specific heat capacity.

In solid members, the C is determined by low heat exchange. C is the amount of heat required per unit mass to raise the temperature by a °C. C is very much influenced by the type of aggregates, and the effects of embedded steel fibre reinforcement are negligible, in the high-strength concrete (HSC) at elevated temperatures [25]. C values increase up to a temperature of 500 °C, then decrease from 700 to -900 °C and later increases [19]. ' C ' is calculated by Eq. 3:

$$C = \frac{Q}{m(t_2 - t_1)} \quad (3)$$

where Q = Amount of heat transfer (J); m = Mass of the substance (kg).

ρ is the ability of a material to resist the heat flow; it is the reciprocal of ' K '. It is calculated by Eq. 4:

$$\rho = \frac{1}{k} \quad (4)$$

3 Results and Discussions

To understand the effects of hydration periods on the values of K , for specimens prepared with plane mortar, 0.5% steel and glass fibre, 1% steel and glass fibre at curing periods of 3, 14, and 28 days are plotted and discussed. These fibre concentrations are selected, as an increase in steel fibre concentrations causes the balling effect, which resulted in an improper compaction of mortar specimens. Along with these results, K , C , D , and ρ effects of temperature, i.e. at 27, 50, and 100 °C on all the five mixes were determined. The values plotted in the table are the average of three readings of KD2 pro thermal analyser for each specimen, and the averages of the three specimen's values are plotted. Such a method was adopted to achieve consistency in the readings, and the discussion for the achieved results is as follows:

3.1 Thermal Conductivity (K)

The final values showing the variations in K values of all the specimens at 3, 14, and 28 days of hydration, for all the five mortar mixes, are shown in Fig. 3. The mortar specimens of 0.5% glass fibre, 1% steel, and glass fibre have shown a reasonable drop in the K values, with the increase in hydration, while in the plane mortar and

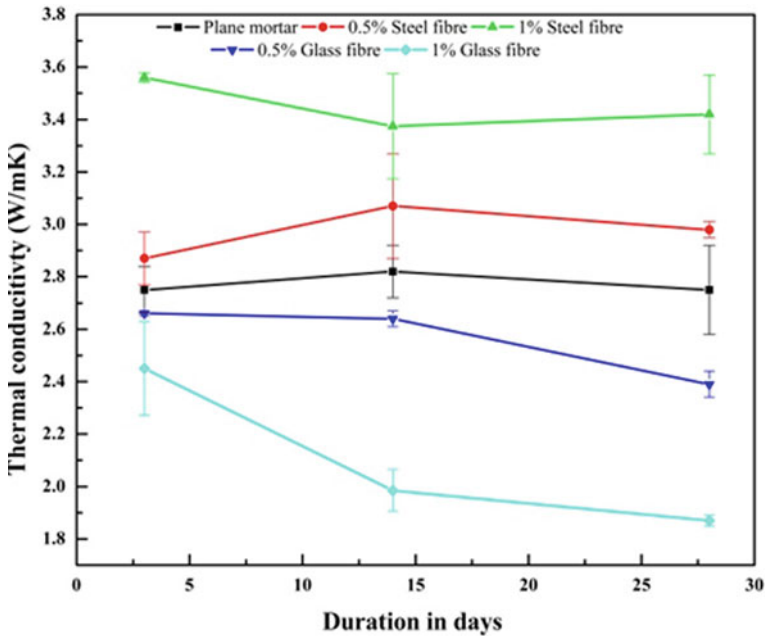


Fig. 3 Thermal conductivity of various specimens at several stages of hydration

0.5% steel fibre specimens, variations in the K are negligible. From the data obtained in the current investigation and mentioned by the other researchers, the effects of K , with varying hydration periods, are not observed in the specimens of plane mortar and 0.5% steel fibre.

The specimens with 1% glass fibre replacement in the mortar have the lowest K values, while 1% steel fibre has the highest. Among the specimens under investigation, for specimens replaced with 1% glass fibre, the drop in K values was 23.67% from the day of the cast to 28 days of hydration. This indicates a dispersion of 1% glass fibre is well spread across the specimen, with respect to 1% steel fibre. From Table 1, one can observe the lower values of K for glass fibre, i.e. 1.05, while for steel fibre is 16, which has a significant effect on the overall K values when embedded in the specimens. An average K value of 0.5% steel fibre is 2.87 and 2.98 at 3 and 28 days of hydration, while 3.56 and 3.42 for 1% steel fibre. This indicates with the increasing steel fibre dosages, the K values increases, thereby making the material highly conductive. While 0.5% glass fibre has K value 2.66 and 2.39, for 1% glass fibre, it is 2.45 and 1.87 at 3 and 28 days of hydration. This phenomenon can be attributed due to the inclusion of fibres in the mortar specimens with different dosages of weight percentages, increasing the water adsorption capacity of the specimens. The higher the percentage inclusion of fibre content into the specimens, the greater will be the distribution of pores across the specimens. This behaviour was observed during the preparation of the fibre-reinforced mixes, which affected the consistency of the mix. As the clustering of fibres in the specimens leads to entrapment of air during the hydration of the mix, the pastes with standard consistency couldn't penetrate the fibres. This results in a lot of interconnected pores in the fibre specimens, due to the clustering of fibres. As specific gravity of glass fibres is three times lower than that of steel fibres. In the case of glass fibre, the distribution of fibre content is higher with respect to steel fibre, which increases the entrapped air content. From Fig. 3, we can say that 1% steel fibre specimens will have lesser pore content, since the density of specimens with fibre reinforcement is greater, and specimens with higher densities result in larger K values [5]. However, due to the higher aspect ratios of glass fibre, K values are fifteen times lower than that of steel fibres, while the density of the specimens is low in relation to steel fibre. This resulted in the lower conductivity of the mortar mixes embedded with glass fibres. One can infer from the available data that the higher the concentration of glass fibre dosages in the mix, the lower K values can be achieved, and in doing so, the materials can act as insulators.

Temperature effects on the ' K ' at 27, 50, and 100 °C are shown in Fig. 4b, and the effects on the K due to changes in temperature are significant. The optimum K values of concrete specimens should be greater than 1.74 (W/m K), else the flux that can be attenuated will be restricted [15]. The porosity present in the concrete specimens plays a crucial role in governing the values of K . Types of pores, i.e. filled with air or moisture, will also affect the K [5]. Figure 4b indicates that the effects of the types of fibre and their ratios have a significant role in governing the thermal efficiency of the concrete as a whole. The average K values determined for the plane mortar specimens at 27, 50, and 100 °C are 2.75, 2.67, and 2.35. The K value at 27 and 100 °C has dropped by 15%, while in 0.5 and 1% of steel fibre

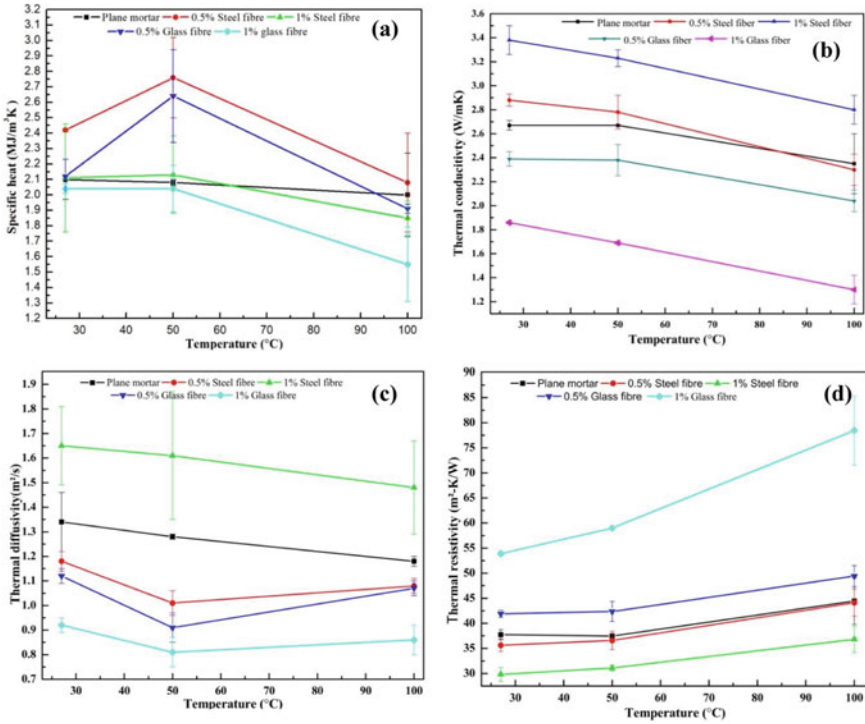


Fig. 4 Relation between **a** specific heat and temperature, **b** thermal conductivity and temperature, **c** thermal diffusivity and temperature, and **d** thermal resistivity and temperature

specimens, it is 22.82 and 18.12%. The effects of 0.5% steel fibre incorporation into plane mortar specimens are negligible, as the values are very much similar, i.e. 2.35 and 2.30 at 50 and 100 °C. The inclusion of the steel fibre into the specimens has increased the *K* values, in comparison to the rest of the specimens. As *K* values are higher for steel fibre concentration, among the specimens with different fibre concentrations, in order for the concrete to conduct temperature effectively across the concrete members, during thermal loading, higher steel fibre concentrations are desirable. As the maximum permitted steel reinforcement is 6% (Column) and 4% (slab and beam) in concrete members provided with steel reinforcement. Hence, *K* transfer during fire accidents will be more in the column, with respect to other structural members. The reported *K* for the mortar specimens embedded with 0.5 and 1% glass fibre at 100 °C is 2.40 and 1.30. While the loss in *K* values due to 0.5 and 1% glass fibre incorporation into the mortar is 14.65 and 30.48%. In specimens with 1% glass and steel fibre, the *K* values at 100 °C are 1.30 and 2.80, indicating that the steel fibre specimens can conduct heat two times more effectively than the specimens with 1% glass fibre. The 1% glass fibres specimens at 100 °C has lower *K* values, which indicates the glass fibre replacement can restrict the attenuation heat flux more effectively, with respect to any other specimens in the current study.

3.2 Specific Heat Capacity (C)

Temperature effects on the fluctuations in C at different temperatures and fibre concentrations are shown in Fig. 4a. Negligible variations in values of C were observed in plane mortar specimens at all temperatures. The initial values of C reported for plane mortar specimens are 1.18 kJ/kg [25] and the current values are 2.1 kJ/kg (Kodur et al.). When comparing the previous results with the current, the obtained variations in C are within the limits, at specimens subjected to 100 °C is 2 kJ/kg. Higher losses in C values are obtained for the specimens cast with 0.5% steel fibre, i.e. 2.42, and the loss in C is 14%. As the specimens' temperature increased, a significant drop in C values was observed in all the fibre-reinforced specimens. Drop in C values is significant for specimens embedded with 1% glass fibre, after the specimens were exposed to 100 °C. However, in the specimens with 0.5% steel fibre and glass fibre content, the ability to conduct heat has increased from room temperature to 50 °C. As temperature effects are too low on the mortar specimens at 50 °C, it does not cause any moisture loss in the specimens. The reason for the rise in the C values needs to be investigated. From the results of C , it is observed that with the increase in temperature during thermal loadings, effects on concrete can be optimized by substituting with glass fibre, as heat can spread less effectively in the event of fire in 1% glass fibre specimens than other specimens, observed from the plots.

3.3 Thermal Diffusivity (D)

Temperature effects on D are shown in Fig. 4c, plotted for all plane and fibre-reinforced specimens. As D values are dependent on the mass of the specimen, fluctuations in the density of the specimen are evident from the results. The specimens with higher glass and steel fibre content, i.e. 1% have set the upper and lower threshold values of ' D '. As diffusivity is derived from K divided by the product of specific heat and density of the material [2], the D values obtained for the plane mortar specimens are 1.34, 1.28, and 1.18 m²/s at 27, 50, and 100 °C. The drop in the values of D is very less under the temperatures of 100 °C, as the effects of changes taking place in moisture content and density are very optimum [3, 15]. The D values for 1% glass fibre are 0.92, 0.81, and 0.86 m²/s, while for 1% steel fibre, the values are 1.65, 1.61, and 1.48 m²/s at the above-mentioned temperatures.

3.4 Thermal Resistivity (ρ)

Variations in the values of ρ with different types of fibre concentrations at three temperatures are shown in Fig. 4d. ρ is the ability of a material to resist the ability

to conduct heat, i.e. higher values of ρ indicate greater will be the ability to resist heat. One can observe from Fig. 4d that the specimens with 1% glass fibre have the highest resistance to heat, i.e. 53.89, and as the temperature increased to 100 °C, the resistance increased by 45%. Among all the specimens, the mortar specimens with 0.5 and 1% of glass fibre have shown the highest resistance to heat flow. As the concentration of steel fibre is 1%, the least ρ is shown by the mortar specimens. The specimens with plane mortar and 0.5% steel fibre are very much similar at 100 °C, i.e. 44.45 and 44.13. Hence, the inclusion of 0.5% steel fibre is insignificant in controlling the ability of the heat to flow across the specimens. The inclusion of 1% steel fibre is most favourable for effective heat transfer across the mortar specimens, while 1% inclusion of glass fibre optimizes the heat flow.

4 Conclusion

An experimental investigation is conducted to understand the thermal properties such as thermal conductivity, thermal diffusivity, thermal resistivity, and specific heat of mortar specimens embedded with 0.5 and 1% of glass and steel fibre into the plane mortar specimens. While variations in the thermal properties were observed with respect to the fibre embedded and plane mortar specimens, the following research findings are made from the study.

- The higher the concentration of glass fibre dosages in the mix, the lower K values can be achieved, and in doing so, the mortar insulation properties can be enhanced.
- Higher doses of steel fibre are effective in conducting the temperature across the mortar during thermal loading.
- An increase in temperature effects on mortars during thermal loadings can be optimized by substituting with glass fibre, as heat can spread less effectively in the event of fire in 1% glass fibre specimens, rather than plane and steel fibre specimens, observed from the plots of C .
- Mortar specimens with 0.5 and 1% of glass fibre have shown the highest resistance to heat flow. While the inclusion of 1% steel fibre is most favourable for effective heat transfer across the mortar specimens.
- Kd2 Pro thermal analyser is a suitable test method for determining the thermal properties of mortar specimens at elevated temperatures; however, the determination of thermal properties is limited to 150 °C.

References

1. Bosiljkov VB (2003) SCC mixes with poorly graded aggregate and high volume of limestone filler. *Cem Concr Res* 33(9):1279–1286. [https://doi.org/10.1016/S0008-8846\(03\)00013-9](https://doi.org/10.1016/S0008-8846(03)00013-9)
2. Carman AP, Nelson RA (2007) The thermal conductivity and diffusivity of concrete. *Univ Illinois Bull* 18(34):1–46
3. Choktaweekarn P et al (2009) A model for predicting thermal conductivity of concrete. *Mag Concr Res* 61(4):271–280. <https://doi.org/10.1680/macrc.2008.00049>
4. Contrafatto L et al (2020) Physical, mechanical and thermal properties of lightweight insulating mortar with recycled etna volcanic aggregates. *Constr Build Mater* 240:117917. <https://doi.org/10.1016/j.conbuildmat.2019.117917>
5. Cook DJ (1974) The thermal conductivity of fibre-reinforced concrete. *Cem Concr Res* 4:497–509
6. Demirboğa R (2003) Influence of mineral admixtures on thermal conductivity and compressive strength of mortar. *Energy Build* 35(2):189–192. [https://doi.org/10.1016/S0378-7788\(02\)00052-X](https://doi.org/10.1016/S0378-7788(02)00052-X)
7. Farsana C, Snehal K, Das BB (2020) Influence of fineness of mineral admixtures on the degree of atmospheric mineral carbonation. *Smart technologies for sustainable development. Lecture notes in civil engineering*, vol 78, pp 117–136
8. George RM, Das BB, Goudar SK (2019) Durability studies on glass fiber reinforced concrete. *Sustain Constr Build Mater* 747–756
9. Mendes JC et al (2020) Correlation between ultrasonic pulse velocity and thermal conductivity of cement-based composites. *J Nondestruct Eval* 39(2). <https://doi.org/10.1007/s10921-020-00680-7>
10. Meshgin P et al (2012) Utilization of phase change materials and rubber particles to improve thermal and mechanical properties of mortar. *Constr Build Mater* 28(1):713–721. <https://doi.org/10.1016/j.conbuildmat.2011.10.039>
11. Mo KH et al (2017) Thermal conductivity, compressive and residual strength evaluation of polymer fibre-reinforced high volume palm oil fuel ash blended mortar. *Constr Build Mater* 130:113–121. <https://doi.org/10.1016/j.conbuildmat.2016.11.005>
12. Nari V et al (2020) A comparative study on the thermal behaviour of PPC and OPC cement. *Mater Today: Proc* 2–7. <https://doi.org/10.1016/j.matpr.2020.05.708>
13. Pavani HP et al (2020) Thermal behaviour of PPC and OPC-53 when exposed to extreme temperatures. *Adv Cem Res* 32(8):358–370. <https://doi.org/10.1680/jadcr.18.00066>
14. Praneeth H et al (2020) Characterisation of micro- and mesoporosity in portland cement at elevated temperatures. *Mag Concr Res* 72(6):304–313. <https://doi.org/10.1680/jmacr.18.00321>
15. Reilly A et al (2019) The thermal diffusivity of hemplime, and a method of direct measurement. *Constr Build Mater* 212:707–715. <https://doi.org/10.1016/j.conbuildmat.2019.03.264>
16. Sahoo S, Das BB, Mustakim S (2017) Acid, alkali, and chloride resistance of concrete composed of low-carbonated fly ash. *J Mater Civ Eng* 29(3):4016242
17. Sair S et al (2019) Development of a new eco-friendly composite material based on gypsum reinforced with a mixture of cork fibre and cardboard waste for building thermal insulation. *Compos Commun* 16:20–24. <https://doi.org/10.1016/j.coco.2019.08.010>
18. dos Santos WN (2003) Effect of moisture and porosity on the thermal properties of a conventional refractory concrete. *J Eur Ceram Soc* 23(5):745–755. [https://doi.org/10.1016/S0955-2219\(02\)00158-9](https://doi.org/10.1016/S0955-2219(02)00158-9)
19. Shin K-Y, Kim S-B (1999) Thermophysical properties and transient heat transfer of concrete at elevated temperature, pp 233–241
20. Snehal K, Das BB (2018) Mechanical and permeability properties of hybrid fibre reinforced porous concrete. *Indian Concr J* 98:54–59
21. Snehal K, Das BB (2021) Acid, alkali and chloride resistance of binary, ternary and quaternary blended cementitious mortar integrated with nano-silica particles. *Cem Concr Compos* 123:104214

22. Snehal K, Das BB, Akanksha M (2020) Early age, hydration, mechanical and microstructure properties of nano-silica blended cementitious composites. *Constr Build Mater* 233:117212
23. Snehal K, Das BB (2020) Effect of phase-change materials on the hydration and mineralogy of cement mortar. *Proc Inst Civ Eng-Constr Mater*. ISSN 1747*650X. <https://doi.org/10.1680/jcoma.20.00045>
24. Snehal K, Das BB, Sumit K (2020) Influence of integration of phase change materials on hydration and microstructure properties of nanosilica admixed cementitious mortar. *J Mater Civ Eng* 32(6):04020108. [https://doi.org/10.1061/\(ASCE\)MT.1943-5533.0003178](https://doi.org/10.1061/(ASCE)MT.1943-5533.0003178)
25. Taerwe L, De Schutter G (1995) Specific heat and thermal diffusivity of hardening concrete. *Mag Concr Res* 47(172):203–208
26. Xu Y, Chung DDL (2000) Effect of sand addition on the specific heat and thermal conductivity of cement. *Cem Concr Res* 30(1):59–61. [https://doi.org/10.1016/S0008-8846\(99\)00206-9](https://doi.org/10.1016/S0008-8846(99)00206-9)
27. Yadav S, Das BB, Goudar SK (2019) Durability studies of steel fibre reinforced concrete. *Sustain Constr Build Mater* 737–745
28. Zhang Z-X (2016) Effect of temperature on rock fracture. *Rock Fract Blast* 111–133. <https://doi.org/10.1016/b978-0-12-802688-5.00005-1>

Modulus of Elasticity of High-Performance Concrete Beams Under Flexure-Experimental Approach



Asif Iqbal A. Momin, R. B. Khadiranaikar, and Aijaz Ahmad Zende

Abstract The modulus of elasticity of High-Performance Concrete (HPC) is one of the characteristics found to be greater than conventional concrete. This enhanced elastic property of HPC makes it suitable for most of the structures with heavy loads and long spans. Also, the elastic property of reinforced HPC differs as compared to pure HPC. This research work aims at determining the modulus of elasticity of reinforced HPC beam under flexure using an experimental approach. The beam models of size 150 mm × 300 mm × 2000 mm with varying percentages of tension reinforcement for M_{60} , M_{80} and M_{100} grade HPC beams are studied experimentally. The modulus of elasticity of reinforced HPC beam under flexure is determined using experimental stress–strain curves and bending equations from the experimental data. The equation for modulus of elasticity is proposed in terms of longitudinal tension reinforcement ratio and grade of HPC. The modulus of elasticity of reinforced HPC beam under flexure increased with the increase in longitudinal tension reinforcement ratio of the concrete section.

Keywords High-performance concrete · Modulus of elasticity · Conventional concrete · Longitudinal tension reinforcement ratio

1 Introduction

The elastic property of concrete, i.e. the modulus of elasticity measures its rigidity. This property of concrete is defined as the ratio between the stress applied and the strain obtained within the defined limit of proportionality. The limit of proportionality

A. I. A. Momin (✉) · A. A. Zende

Department of Civil Engineering, BLDEA's Vachana Pitamaha Dr. P.G Halakatti College of Engineering and Technology Vijayapur, Affiliated to VTU, Belagavi, Karnataka, India
e-mail: asifarzanmomin@gmail.com

R. B. Khadiranaikar

Department of Civil Engineering, Basaveshwar Engineering College, Bagalkot, Affiliated to VTU, Belagavi, Karnataka, India

is “the maximum stress the material tolerates without deviating from the stress–strain proportionality (Hooke’s law).” The applied stress may be static or dynamic; however, this study is limited to static stress. It is generally related to the compressive strength of concrete; it increases with an increase in compressive strength. Hence, the modulus of elasticity of concrete may be articulated as a function of the compressive strength of concrete [1]. But the increase in the rate of modulus of elasticity is comparatively less than that of the compressive strength of concrete [2]. Modulus of elasticity generally depends upon many parameters like aggregate type, the mix proportions, curing conditions, rate of loading, etc. The larger the amount of coarse aggregate with a high elastic modulus, the higher would be the modulus of elasticity of concrete. Researchers have also studied that the addition of mineral admixtures enhances the strength, modulus of elasticity and durability of concrete [2–9]. The concrete specimens tested in wet conditions show about 15% higher elastic modulus than those tested in dry conditions [10]. This property is evaluated by drawing the slope for the stress–strain curve. As most of the part of the stress–strain curve is non-linear, different methods for computing the modulus of elasticity are shown in Fig. 1. The secant modulus is the commonly used method for evaluating this property by different codes and researchers [11–14]. Now the modulus of elasticity of reinforced concrete members is very indifferent to the modulus of elasticity of concrete alone [15, 16]; hence, the use of the modulus of elasticity of concrete overestimates the design values in the design of structural members. Also, in the design of structural members, the total cross-sectional area of the section is considered neglecting the effect of confining steel reinforcements. The high-strength concrete and the high-performance concrete differ largely from the conventional cement concrete because of use of the cementitious material like silica fume, fly ash, etc. and hence because of which the mechanical properties of HSC/ HPC also differs [17–19] and the proposed equation for modulus of elasticity of concrete or reinforced concrete may not be applied either for HPC or reinforced HPC.

Fig. 1 Stress–strain curve for concrete

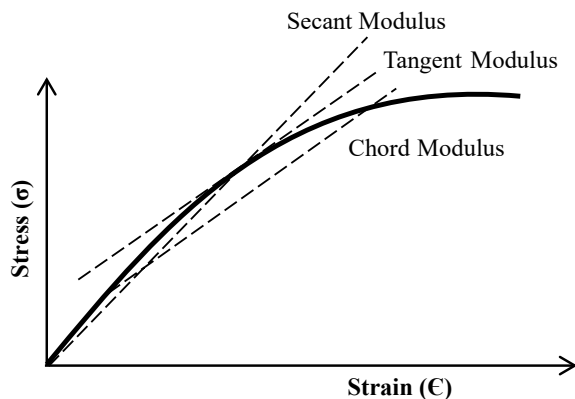


Table 1 Modulus of elasticity of concrete

Sl. No.	Code/researcher(s)	Equation for modulus of elasticity of concrete (MPa)
1	IS-456:2000	$E_c = 5000\sqrt{f_{ck}}$, applicable for concrete grades < M ₅₅
2	ACI-318-14	$E_c = 4730\sqrt{f'_c}$, applicable for $f'_c < 41.4$ MPa
3	ACI-363-10 [20]	$E_c = 3320\sqrt{f'_c} + 6900$, applicable for $f'_c < 83$ MPa
4	NS 3473 [21]	$E_c = 9500(f'_c)^{0.3}$, applicable for $25 \leq f'_c \leq 85$ MPa
5	CSA A23.3-M84 [22]	$E_c = 5000\sqrt{f'_c}$
6	EN 1992-1-1:2004	$E_c = 22000 \left[\frac{(f_{ck}+8)}{10} \right]^{0.3}$
7	CSA A23.3	$E_c = 4500\sqrt{f'_c}$

Table 2 Modulus of elasticity of reinforced concrete

Sl. No.	Code/researcher(s)	Equation for modulus of elasticity of reinforced concrete (MPa)
1	Kulkarni et al., 2014	$E_c = 3774.23p_t^2 + 2789.67p_t + 5000\sqrt{f_{ck}}$

The database for modulus of elasticity of concrete, reinforced concrete and high-strength concrete/high-performance concrete as proposed by different codes and researchers is presented in Tables 1, 2 and 3.

Table 3 Modulus of elasticity of HSC/ HPC

Sl. No.	Code/researcher(s)	Equation for modulus of elasticity of HSC/HPC (MPa)
1	D. Mostofinejad and M. Nozhati [23]	$E_c = 10.25(f'_c)^{0.316}$, ($R^2 = 0.87$) for limestone aggregate $E_c = 8(f'_c)^{0.352}$, ($R^2 = 0.85$) for andesite aggregate $E_c = 10.75(f'_c)^{0.312}$, ($R^2 = 0.88$) for quartzite aggregate
2	M. A. Rashid, M. A. Mansur and Paramasivam [24]	$E_c = 8900\beta(f'_c)^{0.33}$, β = coarse aggregate coefficient, applicable for $20 \leq f'_c \leq 130$ MPa
3	Hani H. Nassif et al.	$E_c = 0.036(w_c)^{1.5}(f'_c)^{0.5}$, w_c = unit weight of concrete in kg/m ³
4	Andrew Logan et al. [25]	$E_c = 0.000035k_1(w_c)^{2.5}(f'_c)^{0.33}$, applicable up to 124 MPa k_1 is the correction factor to account for the source of aggregates

2 Research Objectives

The main objective of this research study is to predict the equation for modulus of elasticity for reinforced HPC beam and is stated as follows:

- i. To analyse and evaluate Stress–Strain parameters for varying percentages of longitudinal reinforcement experimentally.
- ii. To evaluate the secant modulus of elasticity of reinforced HPC beam for 60, 80 and 100 MPa strength from experimental results through bending equation and Stress–Strain curve.
- iii. Prediction of the equation for secant modulus of elasticity of reinforced HPC beam by regression investigation.

3 Methodology

In this study, four beam models of each 60, 80 and 100 MPa reinforced HPC are studied for different longitudinal reinforcement ratios (0.132–0.407) experimentally, and the secant modulus of elasticity is evaluated. The secant modulus of elasticity is evaluated using the experimental stress–strain curves and using bending equation (1). The beam is subjected to two-point loads.

$$E = \frac{23WL^3}{648\delta I} \quad (1)$$

where E = Modulus of Elasticity,
 W = Load,
 L = Effective Span of the beam,
 δ = deflection and
 I = Moment of Inertia of the section.

3.1 Experimental Setup

The reinforced HPC beam is tested as a simply supported beam with 2.0 m effective span, 150 mm in width and 300 mm in depth as shown in Figs. 2 and 3 for beam 60SB2. Steel plates of size 90 mm × 150 mm × 12.5 mm were used as cushions at loading and support points [20, 21]. The details of longitudinal reinforcement, area of steel and reinforcement ratio for HPC beams studied are shown in Table 4.

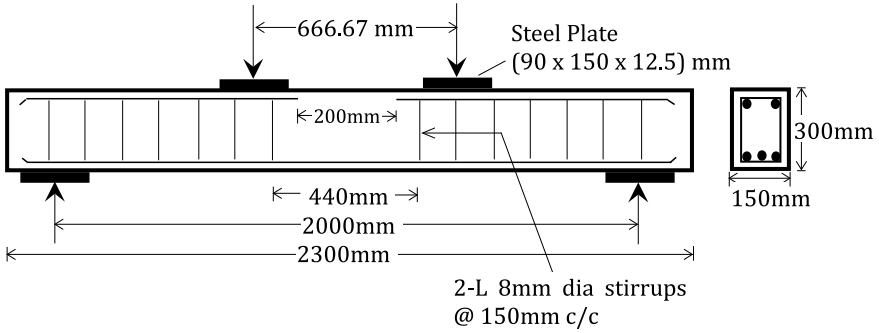


Fig. 2 Experimental setup



Fig. 3 Experimental setup for HPC beam 60SB2

4 Evaluation of Stress–Strain Parameters

4.1 Using Experimental Data

Under pure flexure test for single-span HPC beams subjected to monotonic two-point loading, the load and the corresponding deformations were recorded by using LVDTs at extreme tensile and compression fibre at the centre of the span. The LVDT at the tensile fibre was kept closed so that it was allowed to open during expansion, while the LVDT at the extreme compression fibre was opened and allowed to close during compression. Later, the tensile and the compressive strains were calculated from the deformations. The stresses are calculated using the bending equation (2).

Table 4 Details of beam models

Beam designation	Longitudinal reinforcement	% of reinforcement		ρ_b	ρ/ρ_b
		Ast (mm ²)	ρ		
60SB1	2 # 12 mm	226.19	0.789	4.762	0.166
60SB2	2 # 10 + 1# 12 mm	270.16	0.938	4.850	0.193
60SB3	2 # 16 + 1# 10 mm	480.66	1.695	4.800	0.353
60SB4	2 # 16 + 2# 10 mm	559.20	1.972	4.849	0.407
80SB1	2–12 mm and 1–10 mm	304.73	0.778	5.104	0.152
80SB2	3–12 mm	339.29	0.866	4.981	0.174
80SB3	2–10 mm and 1–16 mm	358.13	0.911	5.069	0.180
80SB4	2–12 mm and 1–16 mm	427.25	1.091	5.052	0.216
100SB1	2 # 12 mm	226.19	0.789	5.997	0.132
100SB2	2 # 10 + 1# 12 mm	270.16	0.938	6.087	0.154
100SB3	2 # 16 + 1# 10 mm	480.66	1.695	6.137	0.276
100SB4	2 # 16 + 2# 10 mm	559.20	1.972	5.922	0.333

The applied Moment ‘ M ’ under two-point loading is determined using Eq. (3).

$$f_c = \frac{M y_t}{I} \quad (2)$$

$$M = \frac{wl}{6} \quad (3)$$

The stresses-strain curves obtained for varying longitudinal reinforcement ratios and HPC grades for single-span HPC beams are shown in Figs. 4, 5 and 6.

5 Evaluation of Modulus of Elasticity of HPC Beam

(a) Using experimental stress–strain curves

The commonly used method of secant modulus is employed for evaluating the modulus of elasticity of the HPC beam from the stress–strain curves. The modulus of elasticity is determined from the slope of the line joining origin and a point on the curve representing 40% stress at failure. Thus, the modulus of elasticity obtained using experimental stress–strain curves is shown in Table 5.

(b) Using bending equation from the experimental data

Experimental evaluation of the secant modulus of elasticity is also done for the same beam specimens by using the bending equation. The single-span HPC beam being subjected to two-point loads, and the maximum deflection due to

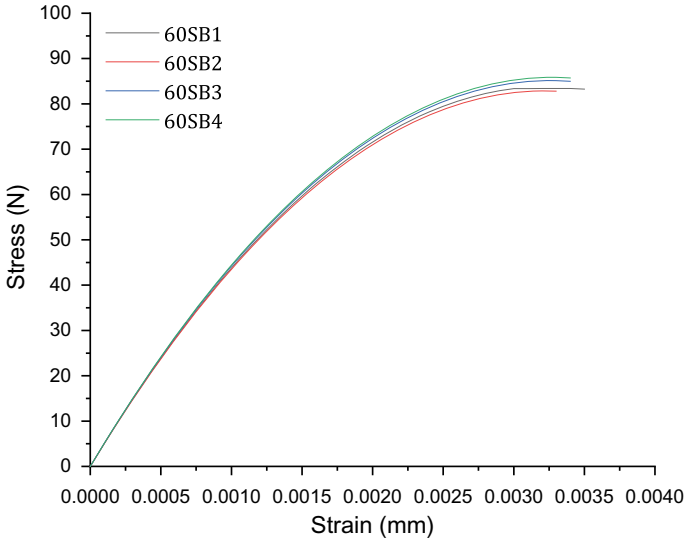


Fig. 4 Experimental stress–strain curves for 60 MPa single-span HPC beam specimens

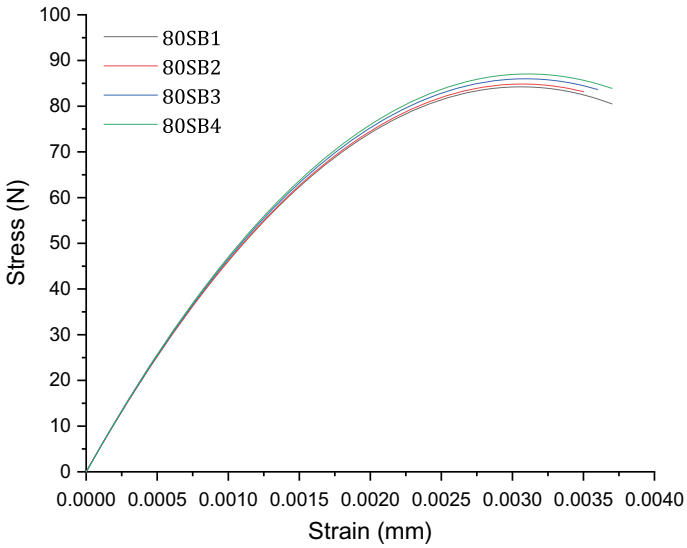


Fig. 5 Experimental stress–strain curves for 80 MPa Single-span HPC beam specimens

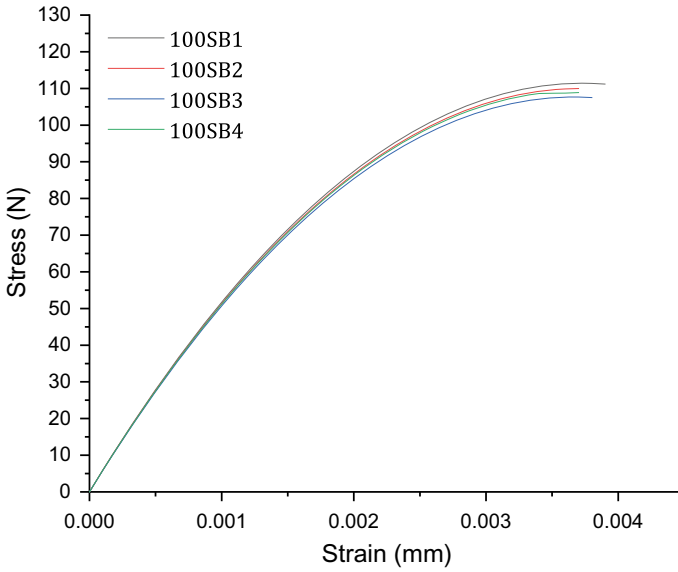


Fig. 6 Experimental stress–strain curves for 100 MPa single-span HPC beam specimens

Table 5 Modulus of elasticity from experimental stress–strain parameters

Beam designation	Longitudinal reinforcement ratio ρ/ρ_b	Modulus of elasticity (MPa) from experimental stress–strain curves
60SB1	0.166	46,188.00
60SB2	0.193	45,662.60
60SB3	0.353	46,296.70
60SB4	0.407	46,486.88
80SB1	0.152	48,849.50
80SB2	0.174	49,031.82
80SB3	0.180	49,366.58
80SB4	0.216	49,672.86
100SB1	0.132	52,959.17
100SB2	0.154	52,612.30
100SB3	0.276	52,061.04
100SB4	0.333	52,496.29

the applied load ‘ W ’ is given by Eq. 4.

$$\delta_l = \frac{23 Wl^3}{648 E_c I} \quad (4)$$

The deflection due to the self-weight of the HPC beam is given by Eq. 5 and the total deflection considering the self-weight of the HPC beam is given by Eq. 6.

$$\delta_s = \frac{5wl^4}{384E_c I} \tag{5}$$

$$\delta = \delta_s + \delta_l \tag{6}$$

The applied load ‘W’ is taken as half the load at the first visible crack and the corresponding deflection as ‘δ’. The values of load at the first visible crack and its corresponding deflection for different beam specimens tested with varying strength of the HPC and longitudinal reinforcement ratio are shown in Table 6. By substituting these values, the static modulus of elasticity is determined using Eq. 7 for HPC beam specimens.

$$E_c = \frac{1}{\delta I} \left[\frac{5wl^4}{384} + \frac{23 Wl^3}{648} \right] \tag{7}$$

Table 6 Modulus of elasticity from experimental data using bending equation

Beam designation	Longitudinal reinforcement ratio ρ/ρ_b	Load corresponding to first visible crack (kN)	Deflection corresponding to first visible crack (mm)	Modulus of elasticity (MPa)
60SB1	0.166	66.75	5.00	50,160.65
60SB2	0.193	71.45	4.75	53,090.57
60SB3	0.353	109.05	5.70	51,739.64
60SB4	0.407	117.52	5.60	52,546.43
80SB1	0.152	105.00	3.16	51,867.06
80SB2	0.174	117.00	3.30	53,461.88
80SB3	0.180	95.32	2.50	53,781.80
80SB4	0.216	122.30	3.10	54,236.83
100SB1	0.132	70.35	5.00	57,748.24
100SB2	0.154	94.05	6.22	58,875.64
100SB3	0.276	124.00	6.60	59,289.27
100SB4	0.333	128.32	6.23	59,326.57

6 Results and Discussion

The static modulus of elasticity of HPC beam specimens determined using experimental stress–strain curves and bending equation from experimental data are compared in Table 7. The average static modulus of elasticity is also presented in Table 7 for different longitudinal reinforcement ratios.

The stiffness of the HPC beam increases with an increase in longitudinal reinforcement ratio as such, and the trend line of the average variation of modulus of elasticity from different methods shows that it increases with an increase in the grade of HPC and longitudinal reinforcement ratio (Fig. 7). The values obtained from different methods are almost the same for the same longitudinal reinforcement ratio with a variation of 9.61%. However, from Fig. 7, the variation for M₈₀ grade HPC beams was found to be lesser compared to M₆₀ and M₁₀₀ grade because the variation of percentage of tension reinforcement within the beams was kept smaller in the range of 0.778–1.091, while the range for M₆₀ and M₁₀₀ grade was higher and of same ratios (0.789–1.972). It is also observed that the variation of modulus of elasticity within the same grade does not have higher variation as compared to variation within the different grades of HPC.

Taking the data of Modulus of Elasticity from bending equation, a regression test is performed, and following generalized Eq. 8 is derived, for reinforced single-span HPC beams.

$$E_{\text{Ref,HPC}} = 5000\sqrt{1.075 f_{ck}} + \left(300\sqrt{1.36 f_{ck}}\right) \rho \quad (8)$$

Table 7 Comparison of modulus of elasticity from different methods

Beam designation	Modulus of elasticity (MPa)		Average modulus of elasticity (MPa)
	Using experimental stress–strain curves	Using bending equation from the experimental data	
60SB1	46,188.00	50,160.65	47,465.27
60SB2	45,662.60	53,090.57	48,193.54
60SB3	46,296.70	51,739.64	48,161.48
60SB4	46,486.88	52,546.43	48,602.50
80SB1	48,849.50	51,867.06	49,762.66
80SB2	49,031.82	53,461.88	50,782.92
80SB3	49,366.58	53,781.80	50,931.92
80SB4	49,672.86	54,236.83	51,280.11
100SB1	52,959.17	57,748.24	54,618.09
100SB2	52,612.30	58,875.64	54,760.74
100SB3	52,061.04	59,289.27	54,529.10
100SB4	52,496.29	59,326.57	54,831.22

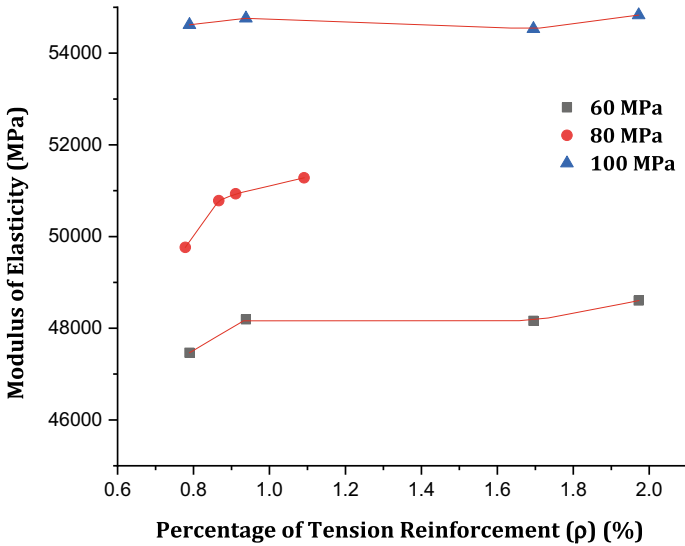


Fig. 7 Average variation of modulus of elasticity with longitudinal tension reinforcement

Equation 8 predicts the value of Modulus of Elasticity for varying grades of HPC and percentage of tension reinforcement. The first part of the equation represents stiffness due to the HPC element, while the second part represents stiffness due to reinforcement. The second part of the equation is itself the additional stiffness because of the reinforcement (Fig. 7).

7 Conclusions

The present work evaluates the modulus of elasticity of HPC beam under flexure for 60–80 MPa strength of concrete. The following are the conclusions drawn based on the present experimental and analytical study.

1. The modulus of elasticity of reinforced HPC beam under flexure increases with the increase in longitudinal reinforcement ratio of the concrete section.
2. The modulus of elasticity of reinforced HPC beam for 60–80 MPa can be determined for different longitudinal reinforcement ratios by the proposed Eq. (2).
3. The maximum variation obtained was 11% from the different methods of evaluation of modulus of elasticity of HPC beam (Table 7).

References

1. Baalbaki W, Aitcin PC, Ballivy G (1992) On predicting modulus of elasticity in high-strength concrete. *ACI Mater J* 89(5):517–520
2. Nassif HH, Najm H, Suksawang N (2005) Effect of pozzolanic materials and curing methods on the elastic modulus of HPC. *Cem Concr Compos* 27(6):661–670. ISSN 0958–9465
3. Bilodeau A, Malhotra VM (1992) High-volume fly ash system: concrete solutions for sustainable development. *ACI Mater J* 97(1):41–48
4. Bouzoubaa N, Fournier B, Malhotra VM, Golden D (2002) Mechanical properties and durability of concrete made with high volume fly ash blended cement produced in cement plant. *ACI Mater J* 99(6):560–567
5. Graciela M, Giaccio GM, Malhotra VM (1988) Concretes incorporating high volume fractions of ASTM class F fly ash. *Cem Concr Aggr* 10(12):88–95
6. Nassif H, Suksawang N (2002) Effect of curing methods on durability of high-performance concrete. *Transp Res Rec: J Transp Res Board* (1798):31–38. TRB, National Research Council, Washington, DC
7. Farsana C, Snehal K, Das BB (2020) Influence of fineness of mineral admixtures on the degree of atmospheric mineral carbonation. In: *Smart technologies for sustainable development. Lecture notes in civil engineering*, vol 78, pp 117–136
8. Snehal K, Das BB, Akanksha M (2020) Early age, hydration, mechanical and microstructure properties of nano-silica blended cementitious composites. *Constr Build Mater* 233:117212
9. Snehal K, Das BB (2021) Acid, alkali and chloride resistance of binary, ternary and quaternary blended cementitious mortar integrated with nano-silica particles. *Cem Concr Compos* 233:104214
10. Zia P, Ahmad S, Leming M (1989–1994) High-performance concretes a state-of-art report. Federal Highway Administration Research and Technology, FHWA Publications
11. Building Code Requirements for Structural Concrete (ACI 318–14) Commentary on Building Code Requirements for Structural Concrete (ACI 318R-14). Farmington Hills, MI, 317 p
12. Kankam CK, Meisuh BK, Sossou G, Buabin TK (2017) Stress-strain characteristics of concrete containing quarry rock dust as partial replacement of sand. *Case Stud Constr Mater* 7(2017):66–72. <https://doi.org/10.1016/j.cscm.2017.06.004>
13. Eurocode 2: Design of concrete structures - Part 1–1: General rules and rules for buildings, Dec-2004
14. Domagała L (2017) A study on the influence of concrete type and strength on the relationship between initial and stabilized secant moduli of elasticity. *Solid State Phenom* 258:566–569
15. Kulkarni S, Shiyekar MR, Shiyekar SM (2017) Confinement effect on material properties of RC beams under flexure. *J Inst Eng India Ser A* 98:413. <https://doi.org/10.1007/s40030-017-0221-3>
16. Kulkarni SK, Shiyekar MR, Shiyekar SM et al (2014) Elastic properties of RCC under flexural loading-experimental and analytical approach. *Sadhana* (39):677–697. Indian Academy of Sciences. <https://doi.org/10.1007/s12046-014-0245-6>
17. Iravani S (1996) Mechanical properties of high-performance concrete. *ACI Mater J* 93(5):416–426
18. Das BB, Pandey SP (2011) Influence of fineness of fly ash on the carbonation and electrical conductivity of concrete. *J Mater Civ Eng* 23(9):1365–1368
19. Goudar SK, Das BB, Arya SB (2019) Microstructural study of steel-concrete interface and its influence on bond strength of reinforced concrete. *Adv Civ Eng Mater* 8(1):171–189
20. ACI Committee 363, Report on High-Strength Concrete (ACI 363R – 10), ACI, Farmington Hills, MI, p 27
21. Norwegian Code NS 3473, Design of Concrete Structures, Norwegian Council for Standardization, Oslo, Norway, 1992
22. CSA A23.3-94 (1995) Design of concrete structures. Canadian Standard Association, Rexdale, Ontario, Canada

23. Mostoufinezhad D, Nozhati M (2005) Prediction of the modulus of elasticity of high strength concrete. *Iranian J Sci Tech Trans B Eng* 29(B3)
24. Rashid MA, Mansur MA, Paramasivam P (2002) Correlations between mechanical properties of high-strength concrete. *J Mater Civ Eng* 203–238
25. Logan A, Choi W, Mirmiran A, Rizkalla S, Zia P (2009) Short-term mechanical properties of high-strength concrete. *ACI Mater J* 106(5)
26. Momin AA, Khadiraikar RB (2019) Experimental and finite element analysis of 80 MPa two-span high-performance concrete beam under flexure. In: *Sustainable construction and building materials*, vol 25, Chapter 35, pp 381–396
27. Kumar PS, Mannan MA, Kurian VJ, Achuytha H (2007) Investigation on the flexural behaviour of high-performance reinforced concrete beams using sandstone aggregates. *Build Environ* 42(7):2622–2629

Impact of Phase Change Materials on the Durability Properties of Cementitious Composites—A Review



K. Vismaya, K. Snehal, and Bibhuti Bhusan Das

Abstract Phase change materials (PCMs) are the novel thermal storage materials which have an ability to engross and dispel heat during the process of phase transition from solid to liquid and vice versa. Utilization of PCMs in cementitious composites has gained a lot of attention from the research fraternity to minimize the energy loadings used for space conditioning and heating in building. Impact of PCM's presence in cementitious composites on the durability parameters is the need for its better usage. This paper gives the state of review on the influence of inclusion of phase change materials in the cementitious system on its various durability aspects. Durability properties such as porosity, water absorption, shrinkage, chloride ingress, and chemical attacks are compiled in this article. It is stated that the integration of PCM in cement composites enhances the porosity of cementitious system. Major hindrance described by the researchers is the interruption of hydration activity of cementitious system by the addition of PCM. Literature also signified that the micro/nano encapsulates PCMs and the use of highly reactive Pozzolans such as silica fume or nano-silica in conjunction with PCMs has the ability to lock up the limitations of PCMs.

Keywords Phase change material · Durability · Shrinkage · Porosity

1 Introduction

Rapid growth of industrialization and urbanization has imposed many environmental threats including the rise in global temperature, increase in the emission of greenhouse gases, and over exploitation of natural resources. The present scenario forces us to significantly target sustainability when dealing with innovations. The construction industry is one of the main consumers of material resources and energy. As the energy sources are of diminishing and expensive in nature, submissive methods of controlling the temperature inside the building become more significant. Mostly in the absence of heating and cooling systems the thermal conditions inside the

K. Vismaya · K. Snehal · B. B. Das (✉)
N. I. T. K., Mangalore, India
e-mail: bibhutibhusan@gmail.com

© The Author(s), under exclusive license to Springer Nature Singapore Pte Ltd. 2023
M. S. Ranadive et al. (eds.), *Recent Trends in Construction Technology and Management*, Lecture Notes in Civil Engineering 260,
https://doi.org/10.1007/978-981-19-2145-2_6

building will be often outside the acceptable range of human comfort [21]. Hence the development of energy efficient buildings should be our priority to contribute toward increased energy security. Many researchers engrossed to improve the heat storing ability of structures by incorporating phase change materials (PCMs) [4]. PCMs have received substantial attention due to the ability to store latent heat in building envelopes. Various studies report the extensive application of PCMs in plasters and wall boards to create more effectiveness in HVAC systems [1, 16]. The studies also reported that PCMs are helpful in mitigating thermal cracking in cementitious composites by controlling thermal variations [24]. The principle of PCMs in optimizing the thermal variations is quite simple. When the marginal temperature increases the material changes from solid phase to liquid by absorbing heat. Correspondingly, the moment when temperature drops to certain level material changes its state from liquid to solid by desorbing stored heat through an exothermic reaction [15].

Based on the chemical composition phase change materials are categorized into three groups (i) Organic compounds (ii) Inorganic compounds (iii) Eutectic mixtures [3, 12, 18]. The group of organic PCMs can be divided into paraffins and non-paraffins. Paraffins are advantageous by the fact that their melting point matches the human coziness temperature ranges and additionally they have high heating ability, compatible melting without segregation, and hardly show the tendency to supercool during phase change [5]. But Paraffins exhibit low thermal conductivity and high-volume changes [18]. Fatty acids, esters, alcohols, and glycols can be classified as non-paraffins. They have eminent melting and freezing properties, low flammability and renewable nature but they are expensive than paraffins [4]. Inorganic PCMs include hydrated salts. They are cheap and non-flammable. These PCMs have high heat of fusion and good thermal conductivity but they have a corrosive effect on metals and undergo supercooling [1]. Based on the composition material Eutectics are divided into three groups (i) organic-organic, (ii) inorganic-inorganic, and (iii) inorganic-organic. They have sharp melting points and relatively high storage density than that of organic compounds [3]. PCMs can be incorporated into a number of building materials including gypsum boards, masonry wall with bricks, concrete or natural stone, asphalt, etc. Since cement-based concrete/mortar is a porous and widely used construction material, it acts as an ideal media for PCMs. Mainly they can be incorporated by three methods (i) direct incorporation, (ii) immersion, and (iii) encapsulation [8, 22, 31]. As the name signifies in direct incorporation PCM is directly added into the mortar mix. In immersion technique PCM is immersed into a porous construction material like gypsum, brick, or concrete blocks. PCM gets easily adsorbed into the pores of the material due to the capillary forces [30]. In the encapsulation technique PCM is encapsulated by a polymeric shell in the form of a capsule [25].

Previous studies reported that the method of incorporation of PCMs influences the properties of cement composites [1, 4, 7, 26–29]. Cunha et al. studied the effect of direct incorporation of PCM and stated that it is the most economical and promising method as compared to microencapsulation technique. Sharma et al. reported that direct incorporation method altered the micropore structure of the cement matrix

by increasing the intruded pore volume due to lesser hydration. It was found that the unhydrated cement particles were coated with PCM which made it unable to hydrate further. The microstructural studies of Snehal and Das [26, 27] described that direct addition of PCM resulted in a porous media with pronounced traces of calcium hydroxide and lesser formation of Calcium silicate hydrate (CSH). Jayalath et al. studied the influence of microencapsulated PCMs in cement composites and reported that the fineness of PCM imparted a filler effect and thereby increased the hydration of cement. Studies reported that microencapsulated PCMs are vulnerable to damage or rupture of the shell during the mixing stage and the leaked PCM interferes with the hydration products causing strength reduction. Microencapsulated PCMs tend to reduce the density of the concrete as it replaces aggregates which possess comparatively a higher density [9, 13]. Paksoy et al. reported that the addition of PCM in bulk and microencapsulated forms reduces the compressive strength of the concrete. PCMs can be impregnated in concrete products for latent heat storage but the stability of PCM is the primary factor of consideration for this method. It is reported that the use of modified concrete can successfully incorporate PCMs through immersion method especially those which are unstable in alkaline media [12, 25]. Hence it can be understood that different methods of PCM incorporation have both benefits and drawbacks which can influence the strength and durability parameters of the composite.

This paper discusses the comprehensive findings of various researches on the influence of phase change materials (PCMs) on the durability parameters such as porosity, water absorption, density, and shrinkage characteristics of cementitious composites.

2 Durability Properties of PCM—Cementitious Composites

The durability properties of concrete influence the overall performance as it stipulates the resistance of the structures to the severe environmental conditions to which it may get exposed to. Various researchers made attempts to assess the effect of incorporation of PCMs on the durability parameters of cementitious composites.

2.1 Porosity

Various studies conducted by researchers [8, 9, 13] reported that the integration of PCM in cement composites increased the percentage of porosity matrix which is collated and represented in Fig. 2. The influence of PCM content on the critical pore diameter which is one of the controlling factors of durability of concrete is investigated by various researchers [2, 8] which is represented in Fig. 3 (Fig. 1).

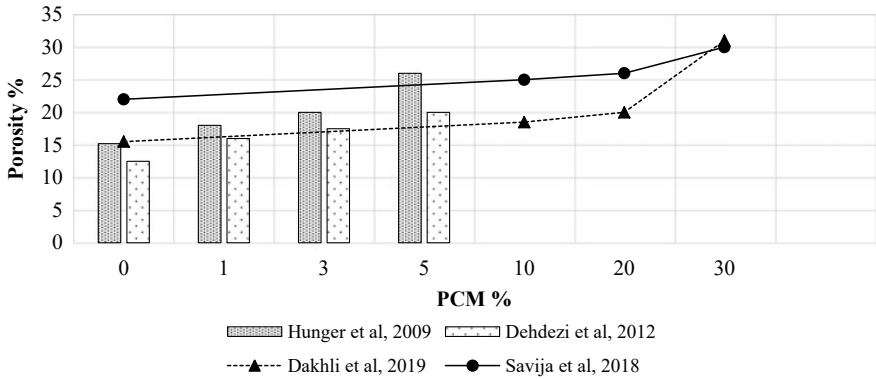


Fig. 1 Variation of porosity with percentage of PCM

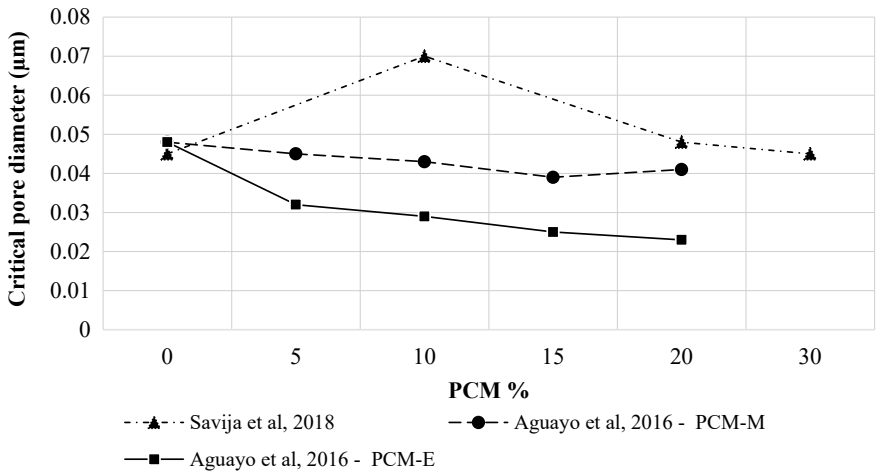


Fig. 2 Representation of critical pore diameter with different percentages of phase change materials

Hunger et al. studied the porosity of self-compacting concrete with different PCM contents directly mixed in microencapsulated form into the concrete. A mixture of paraffins commercially named as Micronal DS 5008 X having melting point at 23 °C was used for the study. The results obtained showed that porosity increased with increase in PCM content which is due to the structural change of packing density of concrete and lower density of PCM than the other ingredients of concrete.

Dakhli et al. studied the porosity of cement passively integrated with microencapsulated PCM composed of vegetal wax in a powder form. The PCM used for the study is industrially referred as INERTEK 23 P. It was observed that porosity increased with the percentage of PCM which could be attributed to the presence of vegetable waxes. From the graph plotted, the sample with 30% PCM was found to

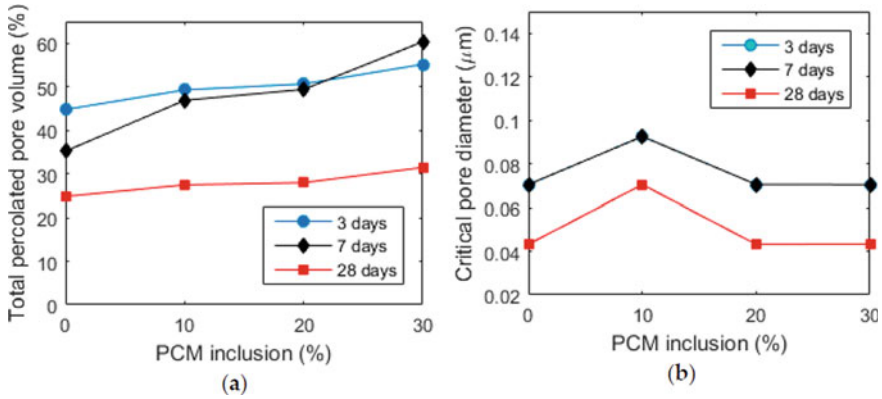


Fig. 3 Plot representing **a** total pore volume **b** critical pore size for cement paste with different PCM dosages at varied ages [24]

be more porous than that of 0, 10, and 20% PCM. Additionally, it can be also noticed that the relationship between porosity and percentage of PCM is non-linear.

Dehdezi et al. studied the porosity of PCM incorporated cementitious system and stated that Porosity increased with PCM content due to its lower particle density (0.9 kg/m^3) as compared to that of the sand replaced (2.64 kg/m^3). The PCM used for the study was a microencapsulated paraffin wax in powdered form with an acrylic outer shell having a melting point at around 26°C .

Savija et al. studied the critical pore diameter and porosity of PCM incorporated cement paste. Microencapsulated PCM composed of paraffin core with melamine formaldehyde (MF) shell was used for the study. It was found that the critical pore volume remained constant for different PCM dosages except for 10% PCM mix which showed comparatively a large pore volume. The study reported that the critical pore size was non-dependent on PCM content but dependent on the hydration degree of the composite. The study also reported that the percentage of percolated porosity increased with increase in percentage of PCM.

Aguayo et al. investigated the critical pore diameter of a cementitious system incorporating microencapsulated, paraffinic PCMs of size $10 \mu\text{m}$ and $7 \mu\text{m}$, respectively. A significant reduction was obtained in the parameter owing to the enhanced reactivity of the PCMs due to their smaller particle size. Due to the smaller particle size, the PCM act as nucleation sites for the increased formation of hydrated calcium hydroxide.

2.2 Water Absorption

Data presented by Cunha et al. on the water absorption by capillarity and immersion by the inclusion of non-encapsulated PCM in a developed mortar and a fiber-based mortar at varied temperatures is plotted in Fig. 4 (Fig. 5).

It can be noted that water absorption by capillarity and immersion decreased with the addition of non-encapsulated PCM. It can be verified that the water absorption is not varying much under varied temperatures which indicates that PCM remains within the mortar matrix in its different phases (solid and liquid). With reference to the obtained data researchers have observed that mortar mixes with no PCM proliferated the water absorption rate. This was due to the availability of larger pores in the cementitious matrix. The mortars exposed to 10 °C temperatures exhibited low water absorption and found that it was attributed to the solid state of PCM. The mortars submitted to higher temperatures (25 and 40 °C) exhibited a higher rate of

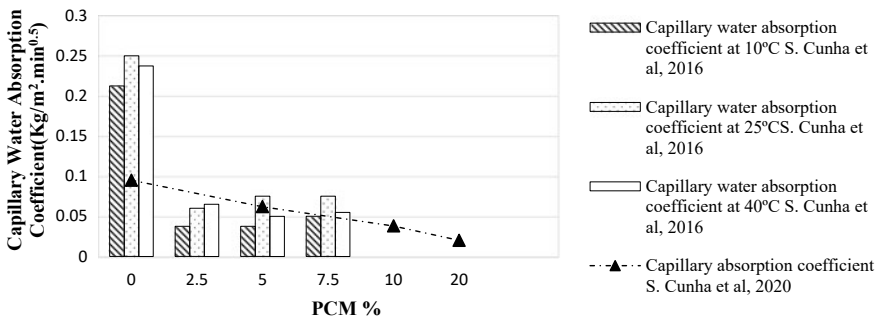


Fig. 4 Representation of capillary water absorption coefficient with different percentages of PCMs

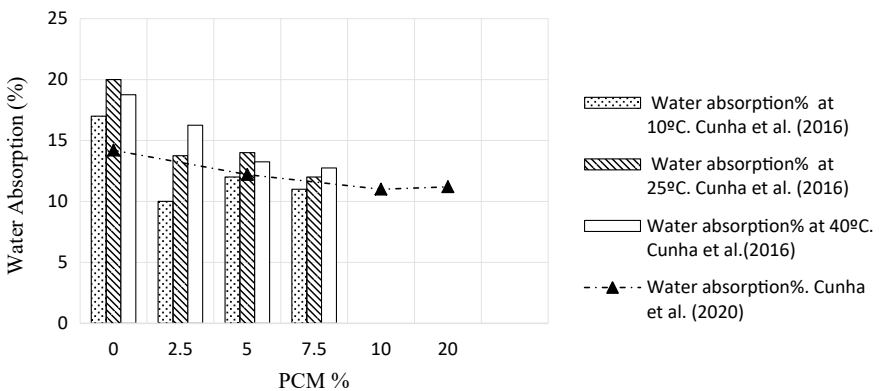


Fig. 5 Plot representing percentage of water absorption with different percentages of PCM inclusion

capillary water absorption, due to the phase transition (solid to liquid) of PCM as it occupies in a relatively smaller volume of the pores.

2.3 Density

The influence of PCM incorporation on the density of cementitious matrix investigated by various researchers [9, 11, 13, 15] is represented in Fig. 6. From the results of the study it can be observed that the integration of PCM tends to lower the density of the matrix as the PCM normally substitutes the materials with greater density. It was also reported that the reduction in density can be owed to the increased in porosity of the mixes with the incorporation of PCMs.

Hunger et al. studied the influence of direct mixing of microencapsulated PCM in self-compacting concrete on its material properties. The PCM used was a mixture of paraffin waxes in powder form, encapsulated in polymethyl methacrylate microcapsules named Micronal DS 5008 X with a melting point of 23 °C. Dehdezi et al. investigated the thermal, mechanical, and microstructural properties of concrete incorporating different amounts of microencapsulated phase change materials (PCMs). Paraffin wax core in the form of dry powder encapsulated with acrylic outer shell having a melting temperature of 26 °C was used for the study. Both the studies reported that the concrete density decreased with increase in PCM content which can be attributed to the low density of the PCM (0.90–0.915 g/cm³) and a physical change of concrete filling density which can be shown from the increased porosity of the matrix.

Kheradmand et al. experimentally investigated the thermal and physical properties of mortar integrated with phase change materials (PCMs) having peak melting point of 34 °C. The PCM was dispersed in grated pristine form into mixtures as macro capsule core. It was reported that density reduced by 87 and 83% of the reference mortar with the addition of 10 and 20% of PCM in grated pristine form. The reduction

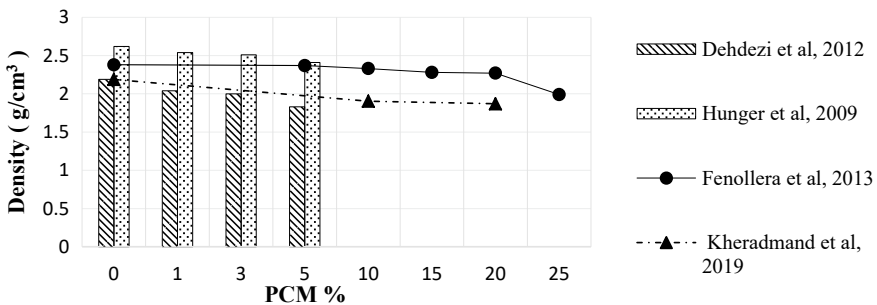


Fig. 6 Plot representing the variation of density with different percentages of PCM

of density for PCM mixtures can be ascribed to the lesser density of the PCM than the sand particles.

Fenollera et al. analyzed the mechanical behavior of a self-compacting concrete incorporated with microencapsulated phase change material. Microencapsulated PCM of Micronal DS 5007 X in aqueous dispersion having a melting point at 23 °C was used for the study. The density and the difference of average densities of the samples were tested for the fresh state as well as after 24 h for the same volume. It was reported that density reduced proportionately with the increase in PCM content. This decrease was more than for the 25% mix due to the total replacement of the filler by PCM, which leads to an increase in water/(cement + filler) ratio. Density in the fresh state decreased by 1.1% for each 5% of PCM inclusion.

Niall et al. studied the thermal behavior and properties of PCM—concrete composite incorporated with microencapsulated and impregnated forms of PCM. Microencapsulated paraffin was added to the fresh concrete during the mixing process and the light weight aggregate used in the concrete mix was impregnated with butyl stearate. The study also investigated the influence of 50% GGBS cement replacement in the mixes. The density of both composites was lesser than control concrete due to the lesser density of PCM material. The panels containing GGBS showed a insignificant rise in density which may be attributed to the lowering of porosity due to its filler effect.

2.4 Shrinkage

Yang et al. investigated the mechanical properties of PCM admixed concrete by adopting mixes with PCM addition as well as replacement of total volume under two temperature state of, i.e., at 23 °C (PCM is in solid state) and 40 °C (PCM is in liquid state). It was reported that in PCM—modified concrete the drying shrinkage was found to be amplified PCM content regardless of temperature conditions. The lack of strength/stiffness for the PCM and its replacement with materials possessing comparatively high strength/stiffness minimized the ability to act against volumetric changes which attributed to higher drying shrinkage of the composite. In the mixes with total replacement increase in PCM content increased the w/c ratio and decreased the cement which caused a rise in drying shrinkage characteristics. The study also evaluated the change in drying shrinkage value during sat 23 and 40 °C. Drying shrinkage at 40 °C was found to be lesser than that at 23 °C for mixes without PCM. But for the mix with 10% and 20% replacement of fine aggregates with PCM the drying shrinkage at 40 °C was reported as higher than that at 23 °C by 6.3% and 4.7%, respectively.

N. P. Sharifi et al. investigated the enhancement in thermal performance of buildings and pavements by incorporating Phase Change materials. Three different PCMs of paraffin blend with melting points of -10, 6, and 28 °C with a specific gravity less than one were used for the study. The applicability of Light weight aggregate and Rice husk ash as a PCM carrier was examined. It was reported that the mix with light

weight aggregate pre-soaked in PCM underwent autogenous expansion. The observations of the study suggested that a portion of the pre-soaked PCM was released to the media by light weight aggregate (LWA) or some amount of PCM from the surface of the light weight aggregate entered the mix. Similarly, an autogenous expansion was reported for the mixes with pre-soaked Rice Husk Ash (RHA) which can be implied to the leakage or adhering on the surface of RHA which may further enter the bulk cement paste. However, it was reported that the total shrinkage increased in the mixes with incorporation of LWA and RHA pre-soaked with PCM regardless of the amount of PCM pre-soaked (Fig. 7).

Wei et al. examined the influence of PCM addition on drying shrinkage in cementitious composites containing microencapsulated PCMs which is represented in Fig. 8. The study was conducted in mortars prepared at different proportions of microencapsulated PCM and/or quartz inclusions. It was reported that for the mixes containing both PCM and quartz, the shrinkage reduced with increasing quartz inclusion as the stiff inclusion impeded the shrinkage of the paste. Furthermore, it was also reported that the dosage of PCM inclusion did not influence the drying shrinkage of the composites as the soft inclusion does not have the ability to resist the shrinkage upon drying.

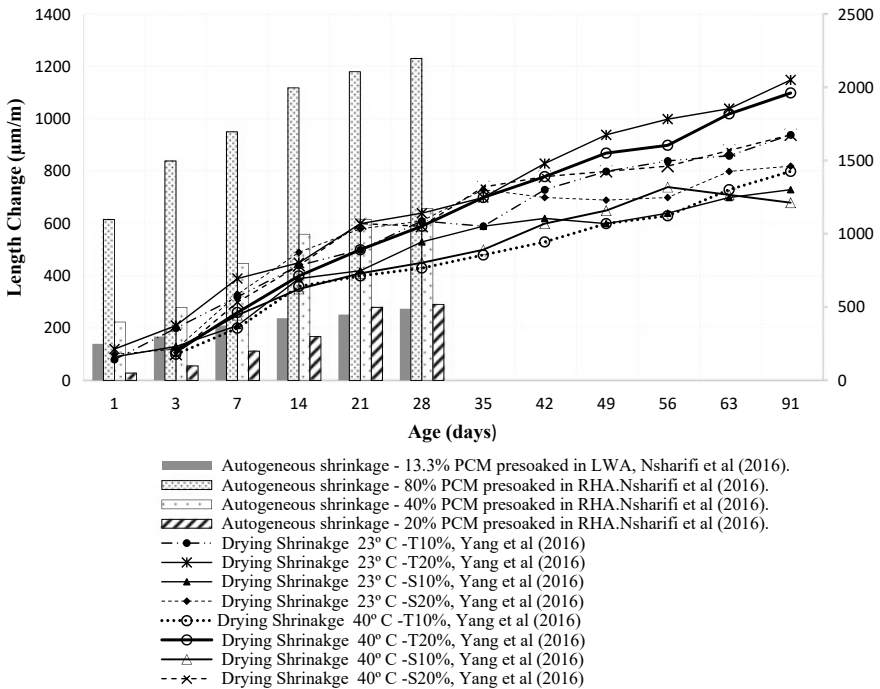


Fig. 7 Representation of autogenous shrinkage and drying shrinkage at different ages (days)

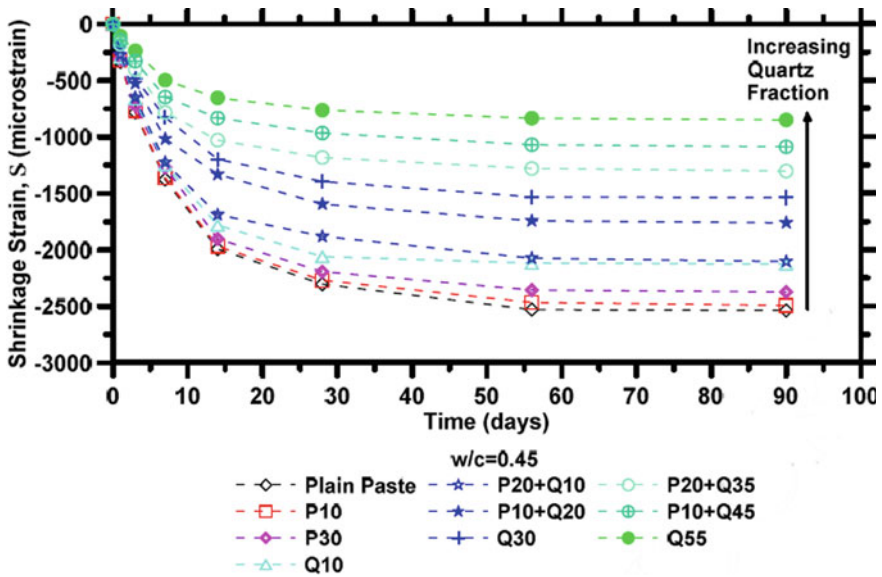


Fig. 8 Plot representing the rate of drying shrinkage for PCM and/or quartz admixed cementitious composites with respect to time

3 Conclusion

The review paper gives an understanding on the influence of PCMs on the durability properties of cementitious system. The following conclusions can be made from the referred literatures.

1. The porosity of cementitious composite increased with PCM content which can be attributed to structural change of packing density of concrete and lower density of PCM than the other ingredients of concrete.
2. The critical pore diameter is not dependent of the PCM content but depended on the hydration rate of the composite. A significant reduction in the parameter can be owed to the enhanced reactivity of the PCMs due to their smaller particle size.
3. Water absorption caused due to the facts of capillarity and immersion for the composites decreased with the addition of PCM without polymeric capsulation which can be attributed to the reduction in the volume of free pores in the microstructure.
4. Higher ambient temperature conditions enhanced the capacity of capillary water absorption which can be attributed to the transformation of PCM from solid to liquid phase as it occupies relatively a smaller volume in the mortar pores.
5. The density of the matrix decreased with the incorporation of PCMs as it replaces filler materials having relatively higher density. It can be also attributed to the increased porosity of the matrix.

6. Drying shrinkage in PCM—modified concrete increased with PCM inclusion. This can be owed to the reduced capacity of the matrix to resist volume changes due to the replacement of the materials with higher stiffness or strength.
7. The composites with PCM impregnated into light weight aggregate and rice husk ash as carriers underwent autogenous expansion which implies the release of PCM into the media by leakage or adhering to the surface of the carrier.

References

1. Adesina A (2019) Use of phase change materials in concrete: current challenges. *Renew Energy Environ Sustain* 4:9
2. Aguayo M, Das S, Maroli A, Kabay N, Mertens JC, Rajan SD, Sant G, Chawla N, Neithalath N (2016) The influence of microencapsulated phase change material (PCM) characteristics on the microstructure and strength of cementitious composites: experiments and finite element simulations. *Cem Concr Compos* 73:29–41
3. Baetens R, Jelle BP, Gustavsen A (2010) Phase change materials for building applications: a state-of-the-art review. *Energy Build* 42:1361–1368
4. Berardi U, Gallardo A (2019) Properties of concretes enhanced with phase change materials for building applications. *Energy Build* 199:402–414
5. Cedeño FO, Prieto MM, Espina A, García JR (2001) Measurements of temperature and melting heat of some pure fatty acids and their binary and ternary mixtures by differential scanning calorimetry. *Thermochim Acta* 369(1–2):39–50
6. Cunha S, Leite P, Aguiar J (2020) Characterization of innovative mortars with direct incorporation of phase change materials. *J Energy Stor* 30:101439
7. Cunha S, Aguiar J, Ferreira V, Tadeu A (2013) Influence of adding encapsulated phase change materials in aerial lime-based mortars. *Adv Mater Res* 687:255–261
8. Dakhli Z, Chaffar K, Lafhaj Z (2019) The effect of phase change materials on the physical, thermal and mechanical properties of cement. *Sci* 1(2019):27
9. Dehdezi PK, Hall MR, Dawson AR, Casey SP (2012) Thermal, mechanical and microstructural analysis of concrete containing microencapsulated phase change materials. *Int J Pav Eng* 1–14
10. Fabiani C, Anna Laura P, D' Alessandro A, Ubertini F, Luisa FC, Franco C (2018) Effect of PCM on the hydration process of cement-based mixtures: a novel thermo-mechanical investigation. *Materials* 11(6):871
11. Fenollera M, Míguez JL, Goicoechea I, Lorenzo J, Ángel Álvarez A (2013) The influence of phase change materials on the properties of self-compacting concrete. *Materials* 6:3530–3546
12. Hawes DW, Banu D, Feldman D (1991) The stability of phase change materials in concrete. *Sol Energy Mater Sol Cells* 27:103–118
13. Hunger M, Entrop AG, Mandilaras I, Brouwers HJH, Founti M (2009) The behavior of self-compacting concrete containing micro-encapsulated Phase Change Materials. *Cem Concr Compos* 31:731–743
14. Jayalath A, Nicolas RS, Sofi M, Shanks R, Ngo T, Ayea L, Mendis P (2016) Properties of cementitious mortar and concrete containing micro-encapsulated phase change materials. *Constr Build Mater* 120:408–417
15. Kheradmand M, Vicente R, Azenha M, Aguiar JL (2019) Influence of the incorporation of phase change materials on temperature development in mortar at early ages: experiments and numerical simulation. *Constr Build Mater* 225:1036–1051
16. Kuznik F, David D, Johannes K, Roux JJ (2011) A review on phase change materials integrated in building walls. *Renew Sustain Energy Rev* 15(1):379–391

17. Lecompte T, Le Bideau P, Glouanec P, Nortershauser D, Le Masson S (2015) Mechanical and thermo-physical behaviour of concretes and mortars containing Phase Change Material. *Energy Build* 94(2015):52–60
18. Ling TC, Poon CS (2013) Use of phase change materials for thermal energy storage in concrete: an overview. *Constr Build Mater* 46:55–62
19. Sharifi NP (2016) Application of phase change materials to improve the thermal performance of buildings and pavements. Doctoral Thesis, Worcester Polytechnic Institute
20. Niall D, West R, McCormack S, Kinnane O (2017) Mechanical and thermal evaluation of different types of PCM–concrete composite panels. *J Struct Integr Maint* 2(2017):100–108
21. Norvell C, Sailor DJ, Dusicka P (2013) The effect of microencapsulated phase-change material on the compressive strength of structural concrete. *J Green Build* 8(3):16–24
22. Paksoy H, Kardas G, Konuklu Y, Cellat K, Tezcan F (2017) Characterization of concrete mixes containing phase change materials. *IOP Conf Ser: Mater Sci Eng* 251:012118
23. Cunha S, Lima M, Aguiar JB (2016) Influence of adding phase change materials on the physical and mechanical properties of cement mortars. *Constr Build Mater* 127:1–10
24. Savija B (2018) Smart crack control in concrete through use of phase change materials (PCMs): a review. *Materials* 11:654
25. Sharma B (2013) Incorporation of phase change materials into cementitious systems. Thesis, Arizona State University, USA
26. Snehal K, Das BB, Kumar S (2020) Influence of integration of phase change materials on hydration and microstructure properties of nanosilica admixed cementitious mortar. *J Mater Civ Eng* 32(6)
27. Snehal K, Das BB (2020) Effect of phase-change materials on the hydration and mineralogy of cement mortar. *Proc Inst Civ Eng—Constr Mater*. ISSN: 1747-650X
28. Snehal K, Das BB (2020) Influence of incorporating phase change materials on cementitious system—a review. *Recent trends in civil engineering. Lecture notes in civil engineering*, vol 105, pp 33–63
29. Snehal K, Das BB (2020) Experimental set-up for thermal performance study of phase change material admixed cement composites—a review. *Smart technologies for Sustainable development. Lecture notes in civil engineering*, vol 78
30. Snehal K, Archana Dinesh T, Das BB Experimental investigation on the influence of phase change material (PCM) on the properties of cement mortar. In: 4th UKIERI concrete congress—concrete: the global builder, 5–8 March 2019, Dr B R Ambedkar National Institute of Technology Jalandhar, India
31. Souayfane F, Fardoun F, Biwolle PH (2016) Phase Change Materials (PCM) for cooling applications in buildings: a review. *Energy Build* 129:396–431
32. Wei Z, Falzone G, Wang B, Thiele A, Puerta-Falla G, Pilon L, Neithalath N, Sant G (2017) The durability of cementitious composites containing microencapsulated phase change materials. *Cem Concr Compos* 81:66–76
33. Yang HB, Liu TC, Chern JC, Lee MH (2016) Mechanical properties of concrete containing phase-change material. *J Chin Inst Eng* 39(5):521–530

Comparative Study of Performance of Curing Methods for High-Performance Concrete (HPC)



Sandesh S. Barbole, Bantiraj D. Madane, and Sariput M. Nawghare

Abstract In this paper, the results statistical and graphical analysis of a comparative study of curing methods for high-performance concrete is discussed. The results are obtained from an experimental investigation carried out on concrete cubes. Mainly, two experiments were conducted: concrete cube strength test using a Compressive Testing Machine (CTM) and a permeability test. Concrete cubes of M35, M45, M50, M60, and M70 were cast and they were cured for 8 h, 3 days, 7 days, 14 days, 28 days, 56 days, and 128 days by three curing methods, namely, steam curing, water curing and sealing compound curing. By using results obtained from this experimental investigation is compared to find out the strength of concrete at the age of all curing periods mentioned above for individual grades of concrete. In addition, a comparison of the compressive strength of concrete with the early strength of concrete across all grades is investigated. Furthermore, a study on the percentage change in strength w. r. t. water is also conducted.

Keywords Steam curing · Water curing · Compound curing · Compressive testing machine (CTM) · Permeability test

1 Introduction

The quality, strength, and durability of concrete completely depend on the efficient continuous curing method. The method of curing depends on the nature of concrete,

S. S. Barbole (✉)

P.G. Diploma in Rail & Metro Technology (PGDRMT), College of Engineering Pune (COEP), Pune, India

e-mail: barboless19.pgdrmt@coep.ac.in

B. D. Madane

Maharashtra Metro Rail Corporation Limited (Maha-Metro), Pune, India

e-mail: bantiraj.madane@mahametro.org

S. M. Nawghare

College of Engineering Pune (COEP), Pune, India

e-mail: smn.civil@coep.ac.in

properties of concrete, application of concrete, the surrounding temperature, and relative humidity. It is essential to keep concrete moist and stop the loss of moisture from it, while it is gaining strength through the hydration process. There are many methods of curing, which are depending on site conditions and the requirement of construction. There are many arguments on which method of curing concrete gives good strength, therefore this topic has gained wide scope for research and application in the construction industry. There was much research conducted to find effective curing and the effect of type of curing on curing properties. Common properties of concrete, which are measures, are strength and permeability. Very few studies had been conducted on curing of High-Performance Concrete (HPC). Site constraints restrict the curing by a conventional method, hence there is a need to explore and establish modern curing for high strength and performance of concrete.

The application of steam curing at atmospheric pressure to the curing chamber is one of the oldest and most widely used methods of accelerated curing of concrete. Under ideal conditions, the curing of concrete by steam at atmospheric pressure (low-pressure accelerated) has the advantage over other methods of accelerated curing in that the curing environment of the concrete is near saturation in regards to moisture. Evaporation of water from the products is minimized, which is especially important where products like block, pipe, etc. are involved. Although the steam curing of masonry units, pipe, and precast or prestressed concrete products follows the same basic rules, curing procedures are different for each. Heat transfer and evaporation will be fast. Pipe and precast products may be cured in a form where evaporation is minimum or may be of such large mass that heat transfer is slow, and large temperature gradients and resultant stresses may exist between the centre and the outside of the mass [1]. Steam curing has been used for many years. It is used to speed up the strength development of concrete products. With an increase in curing temperature, the rate of hydration of cement also increases. Therefore, the speed of strength gain of concrete can be increase with the help of steam curing [2]. The curing temperature has a huge influence on the strength development rate of concrete.

One of the major challenges is the lack of availability of Indian standard codes suitable for Indian climatic conditions for steam curing and compound curing. In order to study across all three methods, i.e., water curing, steam curing, compound curing we have referred IS 456(2000) for water curing, ASTM C 309 for compound curing, and ACI SP-32 for steam curing. Synchronization and simulation of practical conditions was the biggest challenge faced by us. This research will help in the standardization of Indian codes for steam and compound curing.

2 Literature Review

The following are the previous research reviews based on the effect of various curing methods on concrete properties.

Tan and Zhu [3] have studied the influence of curing methods and mineral admixtures on the strength and chloride permeability of concrete is discussed. Analysis was

conducted by using results obtained from the experimental analysis. The chloride permeability of concrete was measured using rapid chloride ion penetration tests (ASTM C 1202). The results obtained by tests show that the compressive strength of plain concrete is decreased by 11% by steam curing. The reason for this decreased in strength was the use of slag, fly ash, and silica fume. However, after using autoclave, the strength of concrete surpasses 80 MPa. Compared with normal curing methods, steam and autoclave curing increases the electric charge passed through plain cement concrete by 110 and 224%, respectively.

Yazıcı and Arel [4] have investigated the effect of steam curing on mortar. Mortar includes mineral admixtures with 3, 1, and 0.5 of aggregate, binders, and water ratios are adopted. In mortars 0, 10, 20, and 30% of fly ash or 0, 5, 10, and 15% of silica fumes were used. 24, 48, and 72 h strength of concrete cubes were measured. This discussed accelerated curing temperature and early strength time is discussed according to compressive strength test results.

Mahmet Gesog Lu has discussed the influence of steam curing on the compressive strength, ultrasonic pulse velocity, water sorptivity, chloride ion permeability, and electrical resistivity of metakaolin and silica fume blended concrete. Various combinations of Portland cement, silica fumes, and metakaolin are studied with constant water or binder ration. The use of silica fumes and metakaolin shows a decrease in water sorptivity and chloride ion permeability of concrete.

3 Methods of Curing

3.1 Water Curing

Water curing is the oldest and most common method of curing. In this method, concrete cubes are submerged in water for a designed period. We have done water curing has been done as per IS 456:2000. This method is commonly used in a laboratory. The main purpose of water curing is to continuously keep concrete in a moist environment. Another purpose of water curing is to maintain water temperature. Water curing plays a key role in the promotion of hydration, elimination of shrinkage, and absorption of heat of hydration. The temperature of the water should not decrease by 5 °C than the temperature of concrete. In water curing, cold water should not be used as it may give a thermal shock, which might lead to cracking. On-site, water curing is done by various methods like ponding, immersion, water spraying, wet covering, etc. Precast concrete structures are commonly immersed in water is adopted. The curing of vertical structures is usually conducted by spread curing. Wet curing is done by using gunny bags, hessian bags, jute matting, etc.

3.2 Compound Curing

Compound curing involves the application of the liquid sealing compound to the hardened concrete. It restricts penetration of liquids and gases, which might cause reinforcement corrosion, acid attack, and damages to concrete. There is a variety of curing compounds available on market. With the curing compound, conventional curing is also important. It forms a protective layer of moisture-retentive film over the concrete. Curing cannot be avoided with curing compounds. Curing compounds increase the durability of concrete. This curing compound must not be used over paint, additional concrete layer, or tiles. This method of curing is used at the site where there is a shortage of water. As Indian standards for compound curing are not yet been thoroughly defined, we have done compound curing as per ASTM C 309.

3.3 Steam Curing

Currently, the use of steam curing in the construction industry is increasing with the demand for rapid and speedy construction. The need for early and high-strength concrete is completed by this method of curing. It is mostly adopted for precast members where early high strength is required. It is executed by using water vapor at atmospheric or high pressure. Pressure is approximately between 40 and 70 °C (100–160 °F). In the steam curing procedure, it is suggested that to start the curing procedure a few hours after casting. This period is called as pre-steaming period, which can be from 2 to 6 h. Initial steam curing temperature starts with 10–20 °C and the maximum curing temperature permitted is 85–90 °C. Steam curing is very advantageous in a cold-weather environment. It is done with help of canvas covering or sheets to cover the structure and inside the covering, steam curing is taken place. As Indian standards for compound curing are not yet been thoroughly defined, we have done compound curing as per ACI SP 32 (Figs. 1 and 2).

4 Material Used for High-Performance Concrete (HPC)

The details of concrete mix design are given in Table 1.

Table 2 represents the properties of Fine Aggregates.

Table 3 represents the properties of Fine Aggregates.

Table 4 represents the properties of Cement.

Fig. 1 Water curing by ponding



Fig. 2 Compound curing



5 Methodology for Concrete Mix of HPC

1. Identification of site for raw materials—various sites in the vicinity of the Pune area of Maharashtra, India are visited for suitable raw materials. While deciding on the suitability of raw materials following points are mainly considered.
 - i. Availability of enough requirement of quantity required for research.
 - ii. Materials having required properties as per IS2386.

Table 1 Material used for high-performance concrete (HPC)

Ingredients	Grades of concrete (N/mm ²)				
	M35	M45	M50	M60	M70
Cement OPC53	215	250	430	440	465
GGBS	215	230	70	35	NA
Microsilica	NA	NA	NA	25	35
20 mm down aggregate	814	758	782	788	778
10 mm down aggregate	349	357	368	371	366
Crusher sand	1006	832	832	832	827
Admixture dosage (%)	1.2	1.2	0.8	1.1	1.1
W/C ratio	0.40	0.36	0.29	0.28	0.29

Note Ingredient’s weights are in kilogram (kg/m³)

Table 2 Properties of fine aggregates

Sr. No.	Properties	Values
1	Bulk density (loose) (kg/m ³)	1650
2	Bulk density (compacted) (kg/m ³)	1770
3	Specific gravity	2.87
4	Water absorption (percentage)	3.12

Table 3 Properties of course aggregates

Sr. No.	Properties	Values
1	Bulk density (loose)	1678
2	Bulk density (compacted) (kg/m ³)	1800
3	Specific gravity	2.98
4	Water absorption	1.06

Table 4 Properties of cement (PPC)

Sr. No.	Properties	Values
1	Consistency (percentage)	28
2	Initial setting time (min)	135
3	Final setting time (min)	195
4	Compressive strength (MPa)	33
5	Fineness (m ² /kg)	290
6	Soundness (mm)	0.8
7	Density (g/cc)	3.14

- iii. Materials and water are free from impurities as well as located close to each other in order to reduce transportation costs to a lab
2. Based on the above factors site at Talegaon, Pune, Maharashtra India has been selected.
3. Raw materials, i.e., coarse aggregate, fine aggregate collected and tested as per IS 2386 for properties such as flakiness index, elongation index, sieve analysis for gradation of aggregates similarly cement is tested for soundness, Initial setting time, final setting time, etc.
4. Proportioning of aggregates on maximum density approach as per IS 2386. Admixtures and other materials are tested for the properties at the time of procurement from the vendor.
5. Now, for finalization of design mix, design is done according to IS10262 for grades M35, M45, M50, M60, and M70 at the same time relevant international codes such as ACI are referred for design. Trial mixes are carried out at the lab according to the design accordingly, mix design is finalized as per getting satisfactory results.
6. Both W/C ratio and Plasticizer dosage are finalized on the basis of mix design and trial mixes carried out consequently to get desired strength, i.e., M35, M45, M50, M60, and M70. Also, the study has been done on industrial practice which is currently being used for W/C ratio and Plasticizer dosage in the heavy civil industry to make the study practically viable.
7. Standard sized cubes are casted, i.e., $1\text{ M} \times 1\text{ M} \times 1\text{ M}$. 80 no's of cubes are cast for each grade i.e., a total of 500 cubes are cast for grades M35, M45, M50, M60, and M70. The intention behind huge sampling was to reduce possible errors due to site handling and bring uniformity to the data.
8. Casting of samples is done at three different curing conditions, i.e., Steam curing, curing by using curing compound, and water curing.
9. Calibration of testing apparatus, i.e., Compression Testing Machine (CTM) is done before going for cube tests.
10. Testing of samples at age of 8 h, 3 days, 14 days, 28 days, 56 days, 90 days, and 180 days is performed as shown in the figure on CTM. Strengths got across different concrete grades and different curing conditions are will be discussed and interpreted further in this paper.
11. It is to be noted here that weather conditions are jot down at the time of casting of the cube, testing of cube whenever felt necessary to eliminate variations on the readings.

Fig. 3 Cube casting



6 Statistically and Graphical Analysis

6.1 Methodology

1. Compressive strength after 7, 28 days is plotted against M50, M60 design mix, respectively.
2. Results are compared with the target strength equation given by IS 10262:2019.

$$f''_{ck} = f'_{ck} + 1.65 \times S$$

where f'_{ck} = target mean compressive strength at 28 days, in N/mm^2 ;
 f_{ck} = characteristic compressive strength at 28 days, in N/mm^2 ;
 S = standard deviation ($5 N/mm^2$).

3. Finally, the graphical analysis is done (Figs. 3 and 4).

6.2 Results and Interpretations

6.2.1 Compressive Strength of Steam Curing, Water Curing, and Compound Curing

The compressive strength of M35, M45, M50, M60, and M70 of steam curing, water curing, and compound curing are given in Table 5.

Fig. 4 Cube testing

Comparative Interpretation Across the Different Grades

Table 5 and Graphs 1, 2, 3, 4, and 5 demonstrate strengths of concrete subjected to different methods of curings, i.e., water curing, steam curing, and curing using curing compound.

Horizontal Interpretation for All Grades for Early Strength

Early Strength (i.e., 8 h) achieved by steam curing varies between 32.12 and 19.61% (grades M35–M70). As grade of concrete is increased from M35 to M70 variation in the achievement of the early strength achievement decreases, i.e., difference between hydration of concrete decreases as the grade increases. When same conditions and grades are repeated for comparison of compound curing with water curing is found that early strength (8 h) found in the experimental test varies between 12.25 and 10.59% between grades M35 and M70. Here it can be deduced that early strength achieved by using steam curing is higher for all grades (Table 6) after which compound curing is found effective and water curing at last. This might be due to tricalcium aluminate (it has potential capacity to yield a high early strength.) formation reaction speeds up by steam curing due to steam temperature and ability to penetrate the concrete pores and carry out early hydration. In case of curing compound, reasons might be attributed to chemical properties of curing compound penetrate the concrete and speed up hydration of reaction forming tricalcium aluminate which in turn ends up adding to early strength of concrete [1–5].

Table 5 Compressive strength of concrete

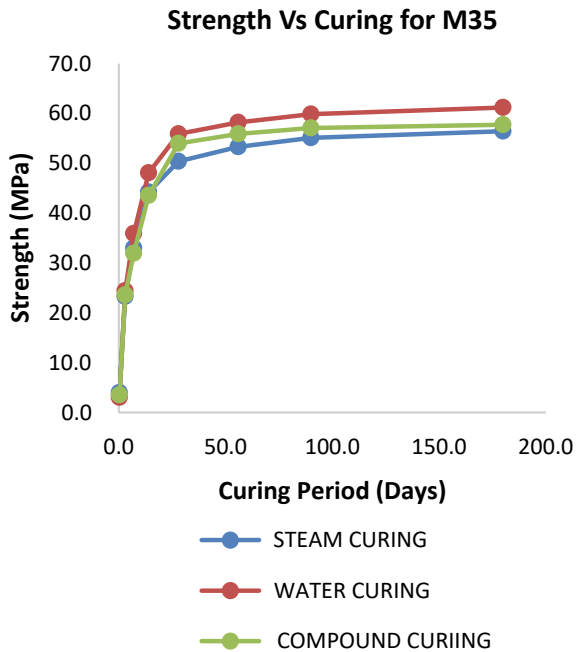
Grade of concrete	Curing in days	Compressive strength (MPa)		
		Steam curing	Water curing	Compound curing
M35	0.33 (8 h)	03.50	03.02	03.06
	3	23.27	24.40	23.58
	7	33.00	30.89	31.94
	14	44.25	40.10	43.53
	28	50.37	53.89	53.97
	56	53.30	58.20	55.89
	90	55.11	59.85	57.09
	180	56.46	61.20	57.74
M45	0.33 (8 h)	03.77	03.27	03.59
	3	31.88	33.30	20.77
	7	45.20	49.91	28.13
	14	60.61	59.60	38.33
	28	69.00	72.67	47.53
	56	73.01	80.22	49.23
	90	75.48	81.99	50.28
	180	77.34	83.91	50.85
M50	0.33 (8 h)	04.47	03.90	04.21
	3	33.15	38.5	33.10
	7	47.01	52.88	44.84
	14	63.03	69.35	61.10
	28	71.76	79.80	75.77
	56	75.93	83.90	78.46
	90	78.50	85.57	80.14
	180	80.43	87.19	81.05
M60	0.33 (8 h)	05.25	04.30	04.89
	3	34.13	42.81	36.77
	7	55.13	59.16	49.81
	14	76.13	78.16	67.87
	28	81.67	86.28	84.16
	56	83.87	93.40	87.15
	90	87.16	95.04	89.02
	180	88.88	96.43	90.03
M70	0.33 (8 h)	06.10	05.10	05.64
	3	42.70	45.14	44.60

(continued)

Table 5 (continued)

Grade of concrete	Curing in days	Compressive strength (MPa)		
		Steam curing	Water curing	Compound curing
	7	61.01	70.36	60.42
	14	81.80	84.93	82.33
	28	96.13	99.10	102.10
	56	103.70	114.40	105.70
	90	105.20	116.10	108.00
	180	107.61	117.40	109.20

Graph 1 Strength versus curing for M35

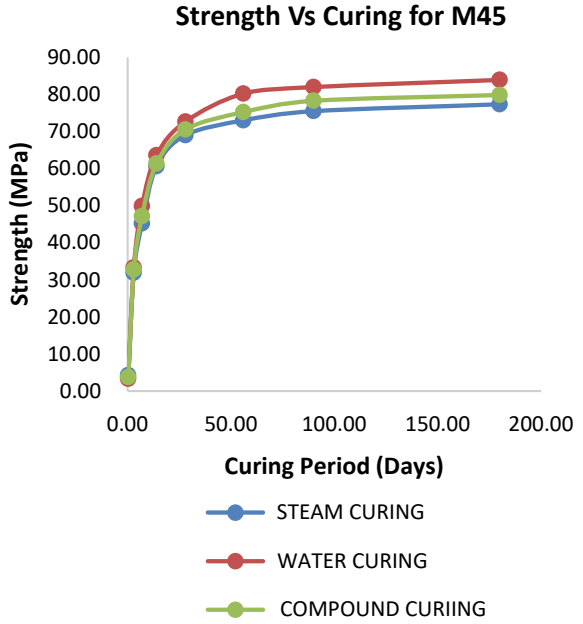


Hence, from above it can be deduced that early strength of concrete varies mentioned in the following order: **Steam curing > Compound curing > Water curing.**

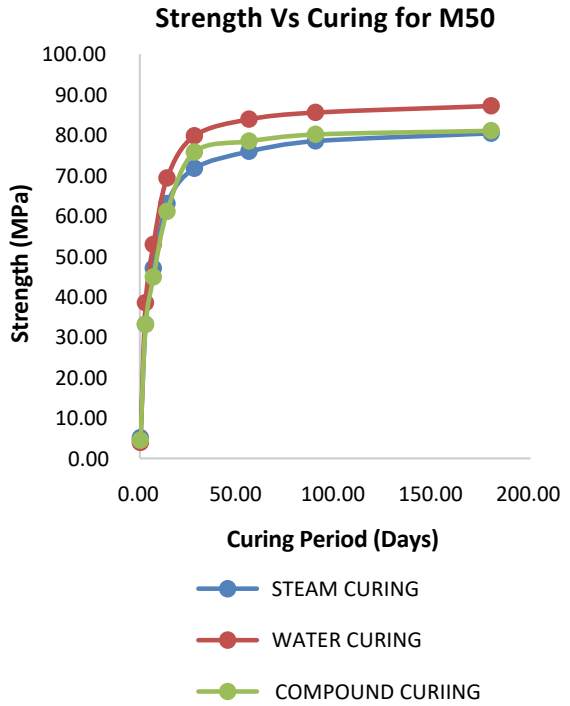
Horizontal Interpretation for All Grades for 28 and 180 days Strength

Cubes casted as mentioned in methodology, tested in parts according to requirement. 28 days strength of concrete by method of steam curing varies from -9.87 to -3% (-ve sign indicates % strength lower than water) lower than strength achieved by

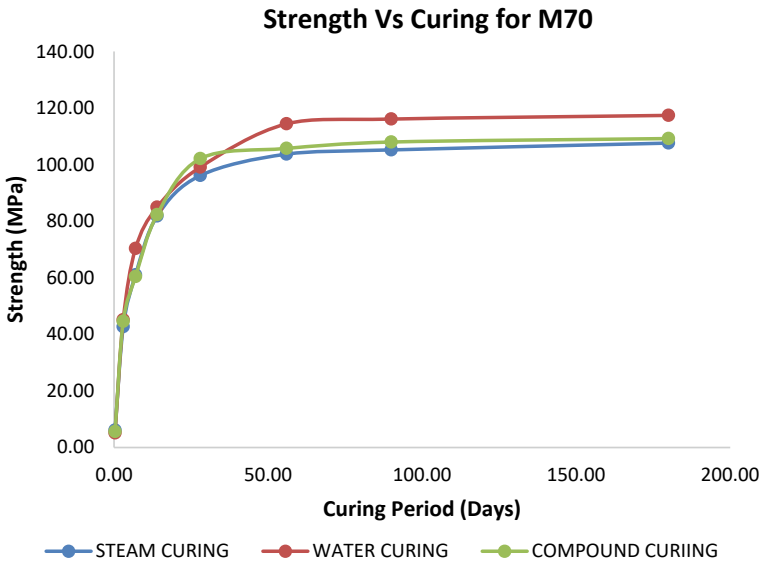
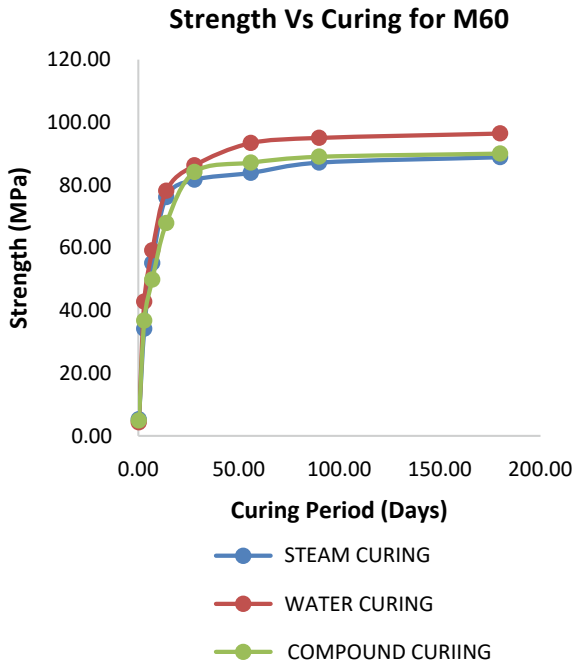
Graph 2 Strength versus curing for M45



Graph 3 Strength versus curing for M50



Graph 4 Strength versus curing for M60



Graph 5 Strength versus curing for M70

Table 6 Percentage change in strength with water

Curing period	Percentage change in strength with water									
	Water curing versus steam curing					Water curing versus compound curing				
	M35	M45	M50	M60	M70	M35	M45	M50	M60	M70
0.33 (8 h)	32.12	30.28	30.77	22.09	19.61	16.56	15.29	14.54	13.72	10.59
3	-4.63	-4.27	-13.90	-20.29	-5.41	-3.36	-1.60	-14.03	-14.12	-1.20
7	-8.05	-9.43	-11.10	-6.81	-13.29	-10.99	-5.57	-15.20	-15.81	-14.13
14	-8.01	-4.70	-9.11	-2.60	-3.69	-9.51	-3.56	-11.90	-13.17	-3.06
28	-9.87	-5.04	-10.08	-5.34	-3.00	-3.43	-2.93	-5.06	-2.46	3.02
56	-8.42	-8.98	-9.50	-10.20	-9.35	-3.96	-6.23	-6.48	-6.69	-7.59
90	-7.93	-7.93	-8.26	-8.29	-9.39	-4.61	-4.52	-6.35	-6.34	-6.99
180	-7.75	-7.83	-7.75	-7.83	-8.34	-5.65	-4.84	-7.04	-6.64	-6.98

Note –ve sign indicate that strength is lower than strength achieved by water curing

water curing between grades M35 and M70. The reasons can be attributed to the rate of reaction of hydration of compound tricalcium alumina ferrite C3AF is higher in presence of water instead of steam, which in turn adds to later strength of the concrete.

From the above it can be deduced that long-term strength, i.e., 28 days is always greater for water curing than the other two methods of the curing, i.e., steam curing and curing by using curing compound. Strength of concrete 28 days varies in the following sequence:

Water curing > compound curing > steam curing

Experimental result at 180 days age of concrete, it is found that strength by using steam curing varies from -7.75 to -8.34% (-ve sign indicates percentage strength lower than water) lower than strength achieved by water curing between grades M35 and M70. In addition, at same conditions strength of concrete by using compound curing varies in the range of -5.65 to -6.98 (-ve sign indicates % strength lower than water) lower than strength achieved by using water curing [6–8].

In case of steam of curing reason for getting 28 days and 180 days strength lower than water curing can be attributed to rate of hydration reaction which forms **tricalcium alumino ferrite C4AF** which intern is responsible for development of later strength in concrete. In case of compound curing 28 days and 180 days strength is lower than strength achieved by water curing under same conditions can be deduced that compound contributing to latest strength of concrete, i.e., tricalcium alumino ferrite is formed at faster rate by water curing than compound curing [9, 10]. The reason might be attributed to continuous contact with water accelerates hydration reaction of formation of all 4 compounds C3S C2S C4A C4AF but steam curing and compound curing affect these rates differently. Compound responsible for early strength of concrete is formed at a faster rate in case steam curing, compound curing, and water curing respectively but as strength achieved over longer period

is cumulative of all 4 compounds, which are better formed by water curing (Table 5).

Another notable observation is that strength achieved through experiment for same curing period, i.e., 180 days but across different grades of concrete, i.e., M35, M45, M50, M60, M60, and M70 variation from later strength (180 days) achieved by water curing later strength (180 days) of concrete increases as compared with respective grades of concrete in water curing (Table 5). As exact reason behind this behavior cannot be deduced from available research, it could be a potential gray area of the research.

Summary of Interpretation of All the Results

Water curing always beats the other two methods of curing when it comes to the later strength of the concrete (Tables 5 and 6). Compound contributing to early strength of concrete (**tricalcium alumino ferrite C4AF**) (8 h strength) is hydrated faster in the sequence of steam curing, compound curing, and water curing, respectively. But it is found that trend reverses in case of strength achieved in case of later strength (28, 180 days) in which sequence found to be water curing, compound curing, and steam curing, respectively. Hence, condition where water curing is feasible then the method should be preferred over the other two, i.e., steam curing and compound curing.

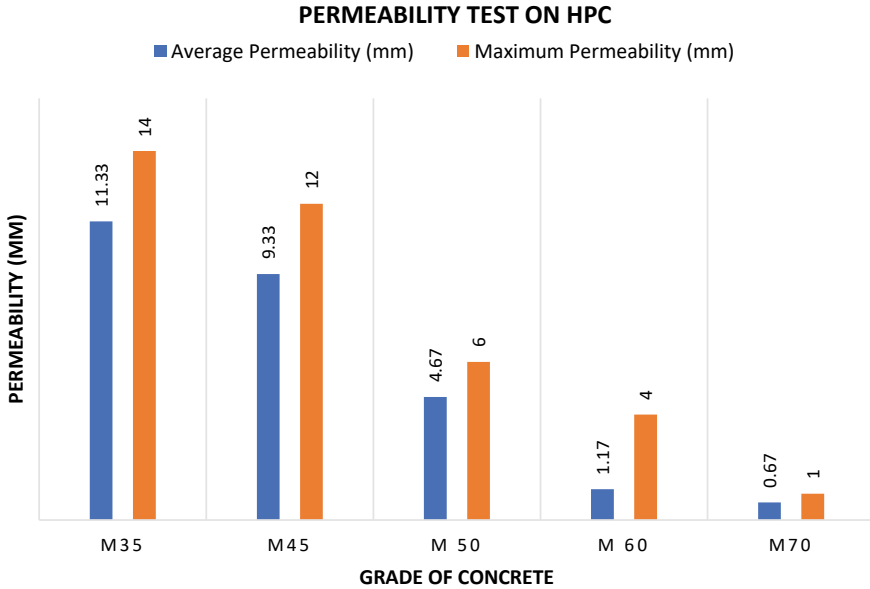
6.2.2 Permeability Test or Water Penetration Test

See Table 7 and Graph 6.

Permeability is directly proportional to the durability of concrete. For low-grade concrete, more water penetration results were obtained and for higher grades almost negligible water penetration shows. This shows that higher grade HPC has more resistance against hydrostatic pressure [11].

Table 7 Permeability test/water penetration test

Sr. No.	Grade of concrete	Penetration in mm	
		Average	Maximum
5	M35	11.33	14
6	M45	9.33	12
7	M50	4.67	6
8	M60	1.17	4
9	M70	0.67	1



Graph 6 Permeability test/water penetration text

7 Conclusion

It is found that early strength (8 h) by steam curing is in the range of 32–19% higher than water curing and early strength (8 h) achieved by curing compound is in the range of 17–11% higher than water curing also. Further, it is observed that 3, 28, and 180 days strength trend said above reverses, i.e., here strengths decrease in the range of 7.75–8.34% for steam curing and –5.65 to –6.98% for compound curing which implies that water curing is best as compared to other two in long term.

Horizontal comparison, i.e., across the grades for same age (M35, M45, M50, M60, M70) showed that achievement of strength varies inversely with the grades, i.e., strength achieved decreases w.r.t water curing as grade of concrete increases irrespective of age of concrete.

It is found that there is a direct correlation between permeability and grade of concrete, i.e., as grade of concrete increases permeability decreases which can be interpreted as concrete which is cured by different methods of curing will have permeability lower for higher grade of concrete which is achieved as per sequence mentioned in results point this paper.

7.1 Potential Applications of the Research Outcomes

1. The industries where achievement of the early lifting strength is important steam curing of the concrete could be done but concrete of higher grade than mentioned should be used in order to avoid effect on ultimate strength or if same grade is being used then it should be made sure that minimum required grade is being achieved for long term according to relevant standard codes at that place.
2. The situations where curing by using steam is not possible compound curing could be done by taking care of things said above.

References

1. Reported by ACI Committee 5 17. Accelerated curing of concrete at atmospheric pressure-state of the art. Revised 1992
2. Gesoğlu M (2010) Influence of steam curing on the properties of concretes incorporating metakaolin and silica fume. *Mater Struct*
3. Tan K, Zhu J (2016) Influences of steam and autoclave curing on the strength and chloride permeability of high strength concrete. Springer
4. Yazıcı S, Arel HS (2016) The influence of steam curing on early-age compressive strength of pozzolanic mortars. *Arab J Sci Eng*
5. ACI Committee 305R-99 “Hot Weather Concreting” Reported by ACI Committee 305. ACI Manual of Concrete Practice (2009)
6. Goel A, Narwal J, Verma V, Sharma D, Singh B (2013) A comparative study on the effect of curing on the strength of concrete. *Int J Eng Adv Technol (IJEAT)*
7. Lee MG. Effect of steam-curing on the strength of precast concrete. In: Proceedings of the seventh international conference on composites engineering, ICCE, Denver, USA, pp 513–514
8. Singh DN, Pandey SP, Das BB (2014) Influence of initial curing humidity on compressive strength and ultrasonic properties of concrete. *Indian Concr J* 88(2):48–56
9. Williams RP, Van Riessen A (2010) Determination of the reactive component of fly ashes for geopolymer production using XRF and XRD. *Fuel* 89(12):3683–3692
10. Olivia M, Nikraz H (2012) Properties of fly ash geopolymer concrete designed by Taguchi method. *Mater Des* (1980–2015) 36:191–198
11. Lü J, Guan H, Zhao W, and Ba H (2011) Compressive strength and permeability of high-performance concrete. *J Wuhan Univ Technol Mater Sci Ed* 26

Development of a Mathematical Relationship Between Compressive Strength of Different Grades of PPC Concrete with Stone Dust as Fine Aggregate by Accelerated Curing and Normal Curing



N A G K Manikanta Kopuri, S. Anitha Priyadharshani, and P. Ravi Prakash

Abstract Concrete is a composite material made from cement, water, fine and coarse aggregates. In recent times, a lot of studies are conducted to find a new fine aggregate material from industrial wastes. In this study, full replacement of fine aggregate with stone dust is carried out. Concrete specimens are cast by replacing fine aggregate with stone dust. The quality of concrete is an important factor in assimilating the strength of a structure. Curing is a significant factor that influences the quality of concrete. In this study, normal water curing and accelerated curing by boiling water method are considered. The important aspect of construction is the time constraint that leads to a high impact on the economy. The strength and the curing of concrete can be expedited by rising the temperature and thereby increasing the rate of hydration. This study aims at investigating the behavior of the strength of M_{20} , M_{25} , M_{30} , M_{35} , and M_{40} grades of concrete with **PPC** when cured under both conditions. The mix design is prepared with reference to IS10262:2019. The specimens are prepared and tested according to IS: 516-1959. From the study, it is concluded that the strength of specimens with normal and accelerated curing is more than the target mean strengths of all grades of concrete.

Keywords Portland Pozzolana cement · Stone dust · Normal curing · Accelerated curing

N A G K Manikanta Kopuri (✉) · S. Anitha Priyadharshani · P. Ravi Prakash
Department of Civil Engineering, NIT Warangal, Warangal, India
e-mail: na720012@student.nitw.ac.in

S. Anitha Priyadharshani
e-mail: priyadharshanianitha@nitw.ac.in

P. Ravi Prakash
e-mail: rprakash@nitw.ac.in

1 Introduction

Concrete is a versatile material used as a principal element in the construction industry. The use of industrial waste materials as fine aggregates in concrete is a good alternative to conventionally used fine aggregates. Stone dust is one of the best alternative materials for fine aggregate. Accelerated curing method is used to get early high compressive strength in concrete [7]. This method is also used to find out 28 days' compressive strength of concrete in 28 h. (As per IS: 9013-1978-Method of making, curing, and determining compressive strength of accelerated cured concrete test specimens.)

2 Literature Review

The review of literature on the replacement of fine aggregate with different materials and the comparison of normal and accelerated curing is presented below.

Pooravshah and Bhavanashah [1] developed a mathematical model to predict early age strength for blended cement through accelerated curing. They proposed the mathematical model of 28 and 56 days compressive strength of cubes for OPC cement and blended cement individually which gives the confidence level of around 95%. This mathematical model was also helpful for precast manufacturers.

Gholap [2] studied the behavior of concrete made of blended cement with accelerated curing. They also studied the formation of the mathematical model. It is concluded that the compressive strength of concrete with accelerated curing is increased significantly and higher than the target strength of concrete.

Pawar et al. [3] compared the 28 days' compressive strength of concrete under accelerated curing and normal moist curing. It is noticed that the warm water method gives quite comparable results and is hence acceptable for obtaining early strength.

Patel et al. [4] studied the effect of traditional and accelerated curing methods on the compressive strength of concrete prepared with industrial waste. The compressive strength of concrete subjected to the accelerated curing method was found to be higher than membrane curing and saturated wet covering.

Das and Gattu [5] conducted studies to understand the performance of quarry dust as fine aggregate in concrete. The results showed that with the increased proportion of quarry dust, maximum strength was observed at 40% proportion, followed by a subsequent drop in strength and decreased workability.

Jyothi and Rao [6] investigated the compressive strength of high-strength concrete made with fly ash by accelerated curing. A slight increase in compressive strength was observed from the accelerated curing test.

3 Experimental Procedure

In this study, five sets of (M_{20} , M_{25} , M_{30} , M_{35} , and M_{40}) specimens are cast and tested. Each set comprises 3 cubes for determining the compressive strength of concrete at 28 days of ordinary curing and accelerated curing, respectively.

4 Materials Used

PPC (Portland Pozzolana cement), fine aggregates (Zone II stone dust), coarse aggregates, and water are used in this study.

The properties of cement, quarry dust, and coarse aggregate obtained from the tests are shown in Tables 1, 2 and 3. The quantity of materials required by weight

Table 1 Cement properties

S. No.	Parameter	Result	Limits as per IS 1489 (Part 1): 1991
1	Consistency	31%	31%
2	(a) IST	35 min	Not less than 30 min
	(b) FST	7 h	Not more than 600 min
3	Fineness	3.1%	Not more than 10%
4	Specific gravity	2.68	Not more than 3

Table 2 Quarry dust properties

S. No.	Parameter	Result	Limits as per IS:383-1970
1	Specific gravity	2.79	Should be between 2.4 and 2.8
2	pH	8	Should be between 6 and 8
3	Fineness modulus	2.44	Should be between 2.2 and 3.2
4	Zone	II	–

Table 3 Coarse aggregate properties

S. No.	Parameter	Result	Limits as per IS:2386(PART IV)-1963
1	Aggregate abrasion value	25%	Not more than 30%
2	Specific gravity	2.85	Should be between 2.5 and 2.9
3	Fineness modulus	6.70	Should be between 6 and 10
4	Aggregate crushing value	21.25%	Not more than 30%
5	Aggregate impact value	21.58%	Not more than 30%

Table 4 Materials required by weight for concrete of grade M 20

Cement	Fine aggregate	Coarse aggregate	W/C ratio
357.7	710.89	1188.98	186
1	1.99	3.32	0.52

Table 5 Materials required by weight for concrete of grade M 25

Cement	Fine aggregate	Coarse aggregate	W/C ratio
395.74	695.85	1163.81	186
1	1.76	2.94	0.47

Table 6 Materials required by weight for concrete of grade M 30

Cement	Fine aggregate	Coarse aggregate	W/C ratio
432.55	681.28	1139.46	186
1	1.58	2.63	0.43

Table 7 Materials required by weight for concrete of grade M 35

Cement	Fine aggregate	Coarse aggregate	W/C ratio
442.86	677.21	1132.64	186
1	1.53	2.56	0.42

Table 8 Materials required by weight for concrete of grade M 40

Cement	Fine aggregate	Coarse aggregate	W/C ratio
450	683.07	1146.59	180
1	1.517	2.55	0.4

for various grades of concrete (M_{20} , M_{25} , M_{30} , M_{35} , and M_{40}) is shown in Tables 4, 5, 6, 7 and 8.

5 Preparation of Testing Specimens

- **Mixing**

Mixing of ingredients is done by the method of hand mixing.

- Casting of specimens;
- Curing of the specimens (normal curing and accelerated curing).

6 Test Results

Compressive Strength values PPC M₂₀ at 28 days of Normal curing and Accelerated curing

Table 9 presents compressive strength values and their mathematical relationship to M₂₀ concrete mix at 28 days of normal curing and accelerated curing.

Compressive Strength values PPC M₂₅ at 28 days of Normal curing and Accelerated curing

Table 10 presents compressive strength values and their mathematical relationship to M₂₅ concrete mix at 28 days of normal curing and accelerated curing.

Table 9 Compressive strength values and mathematical relationship for normal and accelerated curing of M₂₀ concrete

S. No.	Normal curing compressive strength (MPa)	Accelerated curing compressive strength (MPa)
1	31.95	41.69
2	31.51	44.89
3	30.71	41.18

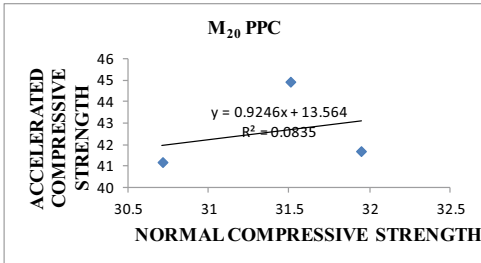
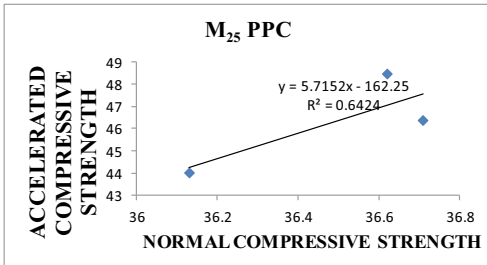


Table 10 Compressive strength values and mathematical relationship for normal and accelerated curing of M₂₅ concrete

S. No.	Normal curing compressive strength (MPa)	Accelerated curing compressive strength (MPa)
1	36.62	48.47
2	36.13	44.02
3	36.71	46.35



Compressive Strength values PPC M₃₀ at 28 days of Normal curing and Accelerated curing

Table 11 presents compressive strength values and their mathematical relationship to M₃₀ concrete mix at 28 days of normal curing and accelerated curing.

Compressive Strength values PPC M₃₅ at 28 days Normal curing and Accelerated curing

Table 12 presents compressive strength values and their mathematical relationship to M₃₅ concrete mix at 28 days of normal curing and accelerated curing.

Table 11 Compressive strength values and mathematical relationship for normal and accelerated curing of M₃₀ concrete

S. No.	Normal curing compressive strength (MPa)	Accelerated curing compressive strength (MPa)
1	40.84	50.00
2	40.17	49.13
3	41.06	50.43

M₃₀ PPC

$y = 1.3502x - 5.0648$
 $R^2 = 0.9882$

Table 12 Compressive strength values and mathematical relationship for normal and accelerated curing of M₃₅ concrete

S. No.	Normal curing compressive strength (MPa)	Accelerated curing compressive strength (MPa)
1	42.66	52.04
2	42.35	53.57
3	44.57	52.84

M₃₅ PPC

$y = -0.0654x + 55.64$
 $R^2 = 0.0105$

Table 13 Compressive strength values and mathematical relationship for normal and accelerated curing of M₄₀ concrete

S. No.	Normal curing compressive strength (MPa)	Accelerated curing compressive strength (MPa)
1	46.26	56.48
2	45.46	58.31
3	45.02	55.75

M₄₀ PPC

$y = 0.2394x + 45.936$
 $R^2 = 0.013$

Compressive Strength values PPC M₄₀ at 28 days of Normal curing and Accelerated curing

Table 13 presents compressive strength values and their mathematical relationship to M₄₀ concrete mix at 28 days of normal curing and accelerated curing.

Table 14 gives regression equation for different grades of concrete.

Table 14 Regression equation for normal curing and accelerated curing

Grade of concrete	Regression equation
M20 (PPC)	$Y = 0.9246x + 13.564$
M25 (PPC)	$Y = 5.7152x - 162.25$
M30 (PPC)	$Y = 1.3502x - 5.0648$
M35 (PPC)	$Y = 0.0654x + 55.64$
M40 (PPC)	$Y = 0.2394x + 45.936$

7 Reason for Enhanced Compressive Strength Under Accelerated Curing

Accelerated curing uses heat or a combination of heat and moisture, in the early stages of the curing process to increase the rate of cement hydration. Heat causes cement hydration reactions to occur at an expedited rate, which causes concrete to develop strength at a faster rate. The increase in strength with increased curing temperature is due to the speeding up of chemical reactions of hydration. This increase affects only the early strengths without any harmful effects on the ultimate strength and cracking of the concrete due to thermal shock. Hence, the curing of concrete and its gain of

strength can be speeded up by raising the temperature of curing in which the curing period is reduced.

8 Conclusions

1. Based on the study, it is concluded that accelerated curing values are more than normal curing values for all grades of concrete.
2. Based on the study, it is concluded that the average strength of accelerated curing specimens is 35.64% more than the average strength of normal curing specimens for M20 grade of concrete.
3. Based on the study, it is concluded that the average strength of accelerated curing specimens is 26.86% more than the average strength of normal curing specimens for M25 grade of concrete.
4. Based on the study, it is concluded that the average strength of accelerated curing specimens is 22.51% more than the average strength of normal curing specimens for M30 grade of concrete.
5. Based on the study, it is concluded that the average strength of accelerated curing specimens is 22.27% more than the average strength of normal curing specimens for M35 grade of concrete.
6. Based on the study, it is concluded that the average strength of accelerated curing specimens is 24.70% more than the average strength of normal curing specimens for M40 grade of concrete.
7. Based on the study, it is recommended that accelerated curing can be adopted as a time-consuming method than normal curing.
8. The replacement of fine aggregate with stone dust is more economical.

References

1. Pooravshah, Bhavanashah (2011) Development of mathematical model to predict early age strength for blended cement through accelerated curing. In: National conference on recent trends in engineering & technology
2. Gholap MS(2014) Experimental study of concrete with blended cement with accelerated curing and formation of mathematical model. *IOSR J Mech Civ Eng (ISOR-JMCE)* 11(2):42–51. e-ISSN: 2278-1684, p-ISSN: 2320-334x
3. Pawar AJ, Nikam JS, Dhake PD (2015) Comparison of 28 days concrete compressive strength by accelerated curing and normal moist curing. *Int J Res Eng Technol (IJRET)* 04(13):219–222. CISSN: 2319-1169, PISSN:2321:7308
4. Patel K, Pitrada J, Raval AK (2017) Effect of traditional and accelerated curing method on compressive strength of concrete incorporating with industrial waste. *IJCRT* 5(4):2336–2339. ISSN: 2320-2882
5. Das B, Gattu M (2018) Study on performance of quarry dust as fine aggregate in concrete. In: International conference advances in construction materials and structures (ACMS-2018) IIT Roorkee, Uttarakhand, India

6. Jyothi RN, Rao K (2019) Effect of accelerated curing on compressive strength of high strength concrete with fly ash. *Int J Recent Technol Eng (IJRTE)* 7(6c2):193–198. ISSN:2277–3878
7. Shivaprasad KN, Das BB (2018) Effect of duration of heat curing on the artificially produced fly ash aggregates. *IOP Conf Ser: Mater Sci Eng* 431(9):092013

List of Codes

1. IS:9013-1978 Indian Standard Method of making, curing and determining compressive strength of accelerated-cured concrete test specimens
2. IS:10262-2019 Guidelines for Concrete Mix Design
3. IS 383-1970 Indian Standard Specification Coarse and Fine Aggregates from Natural Sources for Concrete
4. IS: 516-1959 Indian Standard Methods of Tests for Strength of Concrete
5. IS 2386(PART IV)-1963 Indian Standard Methods for Aggregates for Concrete

Using Recycled Aggregate from Demolished Concrete to Produce Lightweight Concrete



Abd Alrahman Ghali, Bahaa Eddin Ghrewati, and Moteb Marei

Abstract The need for urbanization continues all over the world, greatly increasing the need for concrete. On the other hand, concrete debris from building demolitions causes a major environmental obstacle to storage, and it is a big challenge to use it appropriately. The research aims to study the possibility of using an aggregate of recycled concrete from demolished buildings to produce no-fines lightweight concrete. After studying the properties of recycled aggregate and comparing it with natural aggregate, it was found that the specific gravity of the recycled aggregate was lower, but its wear and water absorption were greater than natural aggregate. We conducted laboratory experiments on five different mixtures of no-fines lightweight concrete from natural aggregate using different sizes of aggregate. In addition to conducting laboratory experiments on three different mixtures of no-fines lightweight concrete from recycled aggregate, using different sizes of aggregate, we found that the density of no-fines lightweight concrete which was produced by demolished concrete is 5% less than that of lightweight concrete produced by the natural aggregate, and the compression resistance is close to each other. The best sample of lightweight concrete free of soft materials (no-fines) from demolished concrete had a compression resistance of 130 kg/cm² and the density was 1704 kg/m³ where W/C = 0.37 and aggregate size was between 12.5 and 19 mm.

Keywords Lightweight concrete · Lightweight aggregate · Recycled aggregate

A. A. Ghali (✉) · B. E. Ghrewati
Department of Civil Engineering, Siksha 'O' Anusandhan University, Bhubaneswar, India
e-mail: abboudghali@gmail.com

M. Marei
Department of Civil Engineering, Aleppo University, Aleppo, Syria

1 Introduction

Cities expand and urban development leads to facing debris ridding matter, every building that is designed has a certain period of service years. After that, we have to demolish and rebuild again, leading to the accumulation of large quantities of concrete debris and facing a new challenge to the community and environment. Therefore, scientists think about a specific methodology for disposing of this waste and converting it to valid materials, using it again in a different way to save the environment [1] (Fig. 1).

This process involves collecting demolition and construction waste, treating it and reusing it again. And it is returned to the life cycle and be a usable material for the same or other purposes, instead of being the cause of many problems on various levels. Lightweight concrete is known to have a density of less than 1800 kg/m^3 compared to normal concrete It has a density of $2240\text{--}2480 \text{ kg/m}^3$, and it has gathered the economic and practical benefits available in lightweight concrete in recent years, having an important place in the construction of facilities and the demand for manufacturing them continues to increase [2].



Fig. 1 Demolished concrete structures

2 Research Objective

The research was conducted to study the possibility of using the aggregate of demolished concrete structures in the production of lightweight concrete with a density of not more than 1800 kg/m^3 , by making a comparison between natural and recycled aggregate and determining the appropriate method for producing lightweight concrete, and the study of appropriate diameters for recycled aggregate and using additives to improve lightweight concrete specifications.

3 Literature Review

Cracking the concrete to produce coarse aggregate in order to produce new concrete is a universally popular feature for more environmentally friendly concrete, which in turn reduces the consumption of natural resources, as well as the requirements for waste dump. In order to study this possibility, it was necessary to get acquainted with some international experiences in this field and to identify the properties of materials resulting from the crushing of demolished structures.

It is important to recognize the difference between recycled aggregate and natural aggregate; in this way, the differences may be taken into account when using recycled aggregate in concrete.

For example, Tamadur [3] made a comparison between the natural aggregate and recycled aggregate from the automatic grinding of concrete cubes, and it was found that the largest nominal size for natural and recycled aggregates is 44 mm and it reached the following results (Table 1).

Another research for Athanas [4] used two types of coarse aggregate, namely natural aggregate (solid granite fracture) and recycled aggregate (crushing debris).

Table 2 shows the characteristics of the two types.

Table 1 Comparison between natural and recycled aggregate according to Tamadur's study

Specifications	Natural aggregate	Recycled aggregate
Saturated surface dry	2.67	2.51
Absorption	1.17%	5.15%
Bulk density, kg/m^3	1335	1270
Wear rate	19%	32.4%

Table 2 Comparison between natural and recycled aggregates according to Athanas' study

Aggregate type	Size (mm)	Density (g/cm^3)	Water absorption (%)	Los Angeles factor %
Natural	5–15	2.7	1.46	16.2
Natural	15–25	2.7	1.46	16
Recycled	8–25	2.61	6.39	26

Table 3 Comparison between natural and recycled aggregates according to Akbari's study

Specifications	Natural aggregate	Recycled aggregate
Bulk density (kg/m^3)	1470	1451
Specific gravity	2.87	2.68
Absorption	1.7%	7%

Also, Akbari et al. [5] used two types of coarse aggregate, namely natural aggregate (solid granite fracture with a maximum groud of 20 mm) and recycled aggregate (breaking the cubes at the materials lab, where the maximum size was 20 mm and the minimum size was 4.75 mm.) Table 3 shows the characteristics of the two types.

4 Lightweight Concrete

Lightweight concrete has an expansion factor that increases the size of the mixture, leading to decrease in the dead load. Using lightweight concrete is increasing widely in countries such as the USA, the United Kingdom and Sweden. Lightweight concrete maintains large blanks and has a density between 300 and 1840 kg/m^3 , which is 8–23% lighter than traditional concrete [6–11].

Lightweight concrete can be classified according to the obtaining method into three types:

- Concrete free of soft materials,
- Concrete of lightweight aggregate, and
- Foam concrete (Fig. 2).

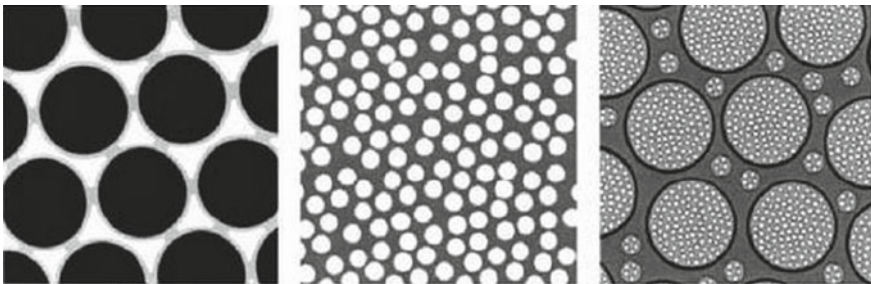


Fig. 2 Kinds of lightweight concrete

5 Experimental Study

Lightweight concrete free of soft materials was produced using Portland cement, water and aggregate. Two types of aggregate were used in this paper; natural aggregate and aggregate from destroyed facilities.

The natural aggregate was the crushed type of dolomitic origin (Fig. 3; Table 4).

The recycled aggregate which has used was of two different types.

- **The first type:** the aggregate produced by crushing previous samples in the construction laboratory (Table 5).
- **The second type:** the aggregate produced by demolished concrete structures, and sorted into three types—soft, medium, and coarse.

Particle-size distribution was performed for the three types as shown in Fig. 4 (Table 6; Figs. 5 and 6).

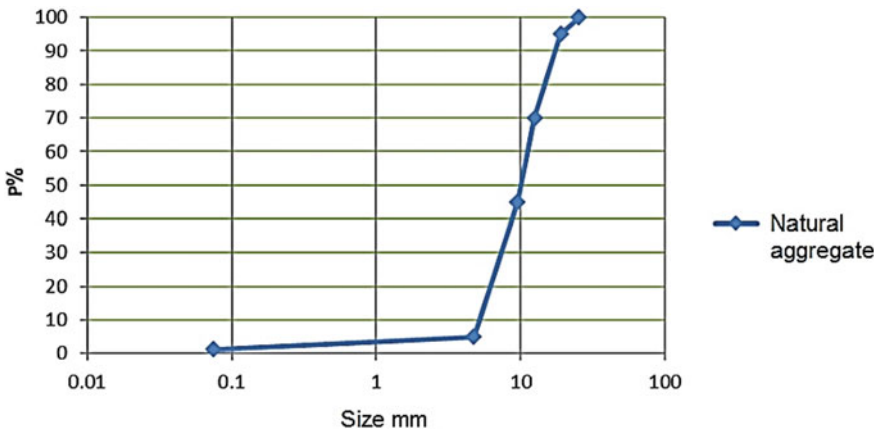


Fig. 3 Particle-size distribution for natural aggregate

Table 4 Physical and mechanical properties of natural aggregate

Specific gravity	Density (kg/m ³)	Water absorption	Wear ratio
2.825	1410	1.3%	18.7%

Table 5 Properties of recycled aggregate from crushed samples

Specific gravity	Density (kg/m ³)	Water absorption	Wear ratio
2.6	1290	7.2%	37%

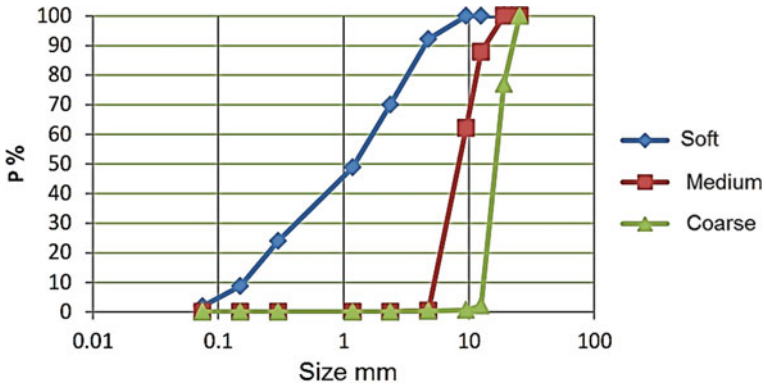


Fig. 4 Particle-size distribution for recycled aggregate

Table 6 Density of recycled aggregate

Recycled aggregate	Density (kg/m ³)
Soft	1340
Medium	1280
Coarse	1370



Fig. 5 Mixing machine

5.1 Experiments of Lightweight Concrete Produced by Natural Aggregate

- **First mixture:** the aggregate size was between 8 and 25 mm and the cement to aggregate ratio was 1/6. W/C = 0.45 and cement calibre was 340 kg/m³.

Fig. 6 Breaking samples of the first mixture



Compression resistance was up to 147.6 kg/cm^2 after 28 days and the density was 1963 kg/m^3 , and this density was deemed high for lightweight concrete free of soft materials.

- **Second mixture:** the aggregate size was between 12.5 and 25 mm and the same proportions of aggregates, cement and water as in the first mixture was used.

Compression resistance was up to 108.5 kg/cm^2 after 28 days and the density was 1789 kg/m^3 , and this density is acceptable for lightweight concrete free of soft materials.

- **Third mixture:** the aggregate size was between 12.5 and 19 mm and the same proportions of aggregates, cement and water as in the first mixture was used.

Compression resistance was up to 108.6 kg/cm^2 after 28 days and the density was 1771 kg/m^3 , and this density is acceptable for lightweight concrete free of soft materials.

- **Fourth mixture:** the aggregate size was between 12.5 and 19 mm and the same proportions of aggregates and cement as in the first mixture was used. But we added a high active plasticizer of 1.5% to the cement weight and added 35% of water to the cement weight with the same operability $W/C = 0.35$.

Compression resistance was up to 188.2 kg/cm^2 after 28 days and the density was 1901 kg/m^3 , and this density is acceptable for lightweight concrete free of soft materials.

Table 7 Experimental results of lightweight concrete produced by natural aggregate

Mixture	Size (mm)	W/C	Density (kg/m ³)	Compression resistance (kg/cm ²)
First	8–25	0.45	1963	147.6
Second	12.5–25	0.45	1789	108.5
Third	12.5–19	0.45	1771	108.6
Fourth	12.5–19	0.35	1901	188.2
Fifth	19–25	0.35	1833	103.2

- **Fifth mixture:** the aggregate size was between 19 and 25 mm and the same proportions of plasticizer, aggregates, cement and water as in the fourth mixture was used.

Compression resistance was up to 103.2 kg/cm² after 28 days and the density was 1833 kg/m³. Both density and compression resistance decreased compared to the fourth mixture because of the big size of aggregate (Table 7).

The results show that increasing the size range of aggregate leads to an increase in both compression resistance and density.

5.2 Experiments of Lightweight Concrete Produced by Recycled Aggregate

The recycled aggregate which has used was of two different types.

5.2.1 The First Type

The aggregate is produced by crushing previous samples in the construction laboratory. The aggregate size was between 9.5 and 25 mm and the cement to aggregate ratio was 1/6 and W/C = 0.47.

Compression resistance was up to 98.5 kg/cm² after 28 days and the density was 1778 kg/m³ (Fig. 7).

5.2.2 The Second Type

The aggregate is produced by demolished concrete structures.

- **First mixture:** the aggregate size was between (12.5 and 19 mm) and the same proportions of aggregates, cement and water as in the first-type experiment was used.



Fig. 7 Broken samples in construction labs

Compression resistance was up to 95 kg/cm^2 after 28 days and the density was 1686 kg/m^3 . The density decrease was caused the decrease of recycled aggregate density.

- **Second mixture:** the aggregate size was between 9.5 and 12.5 mm) and the same proportions of aggregates, cement and water as in the first mixture was used.

Compression resistance was up to 96 kg/cm^2 after 28 days and the density was 1699 kg/m^3 .

- **Third mixture:** the aggregate size was between 12.5 and 19 mm and the same proportions of aggregates and cement as in the first mixture was used. But we added a high active plasticizer of 1.5% to the cement weight and added 37% of water to the cement weight $W/C = 0.37$.

Compression resistance was up to 130 kg/cm^2 after 28 days and the density was 1704 kg/m^3 , and this density is acceptable for lightweight concrete free of soft materials (Fig. 8).

For recycled aggregate without adding plasticizer, the best density was 1686 kg/m^3 and the compression resistance was 95 kg/cm^2 , where the size was between 12.5 and 19 mm, $W/C = 0.47$ and the cement to aggregate ratio was 1/6. However, after adding the plasticizer with $W/C = 0.37$, the density was 1704 kg/m^3 and the compression resistance was 130 kg/cm^2 (third mixture.) The plasticizer led to an increase in both density and compression resistance (Table 8; Fig. 9).

6 Conclusions

- The aggregate produced by demolished concrete structures has a lower density but has a greater rate of wear and absorption than natural aggregate.
- The compression resistance for lightweight concrete free of soft materials from natural aggregate was 108.6 kg/cm^2 and the density was 1771 kg/m^3 , where $W/C = 0.45$, the size was between 12.5 and 19 mm, the cement to aggregate ratio was 1/6 and cement calibre was 340 kg/m^3 . After adding the plasticizer, the compression



Fig. 8 Breaking samples of the third mixture

Table 8 Experimental results of lightweight concrete produced by recycled aggregate

Aggregate type	Mixture	Size (mm)	W/C	Density (kg/m ³)	Compression resistance (kg/cm ²)
Laboratory samples		9.5–25	0.47	1778	98.5
Demolished concrete	First	12.5–19	0.47	1686	95
	Second	9.5–12.5	0.47	1699	96
	Third	12.5–19	0.37	1704	130

resistance increased to 188.2 kg/cm² and the density increased to 1901 kg/m³, where W/C = 0.35 and the size between was 12.5 and 19 mm.

- The compression resistance for lightweight concrete free of soft materials from demolished concrete was 95 kg/cm² and the density was 1686 kg/m³, where W/C = 0.47, the size was between 12.5 and 19 mm, the cement to aggregate ratio was 1/6 and cement calibre was 340 kg/m³. After adding the plasticizer, the compression resistance increased to 130 kg/cm² and the density increased 1704 kg/m³ where W/C = 0.37 and the size was between 12.5 and 19 mm. It was the best sample in this research because it had low density and good compression resistance.
- The compression resistance for lightweight concrete free of soft materials from demolished concrete was close to which is from the natural aggregate.
- The density for lightweight concrete free of soft materials from demolished concrete was less of 5% than which is from natural aggregate, because the recycled aggregate has less specific gravity.
- The plasticizer increased the compression resistance effectively.

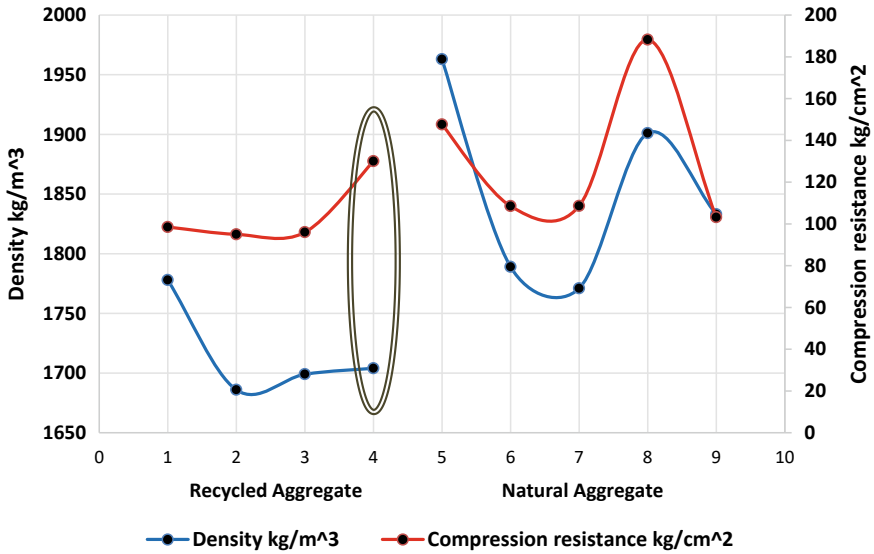


Fig. 9 Comparing results between recycled and natural aggregate

- We can use the lightweight concrete produced by the recycled aggregate in parking and pavement, and also we can use it in wooded pavement and drainage layers because it has good permeability (Fig. 10).

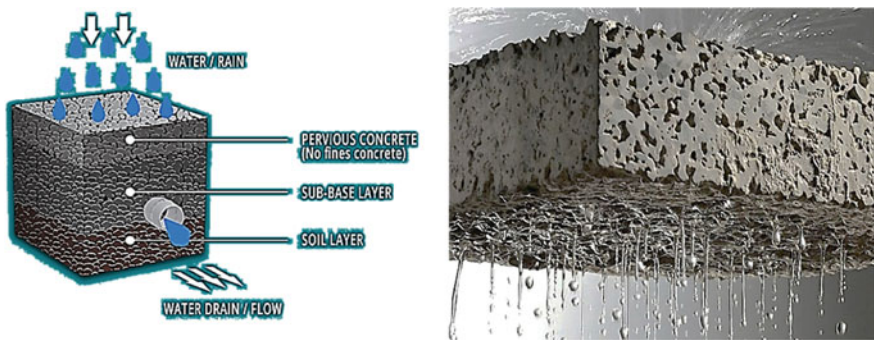


Fig. 10 Uses of lightweight concrete in pavement and drainage layers

References

1. Rajamony Laila L, Gurupatham BGA, Roy K, Lim JBP (2021) Effect of super absorbent polymer on microstructural and mechanical properties of concrete blends using granite pulver. *Struct Concr* 22:E898–E915
2. Rajamony Laila L, Gurupatham BGA, Roy K, Lim JB (2021) Influence of super absorbent polymer on mechanical, rheological, durability, and microstructural properties of self-compacting concrete using non-biodegradable granite pulver. *Struct Concr* 22:E1093–E1116
3. Muqbil T (2014) Experimental study on the concrete produced from recycled aggregate. *Tishreen Univ J Res Sci Stud* 36(4):2 (in Arabic)
4. Konin A, Kouadio DM (2011) Influence of cement content on recycled aggregates concrete properties. *Mod Appl Sci* 5(1):23
5. Akbari YV, Arora NK, Vakil MD (2011) Effect on recycled aggregate on concrete properties. *Int J Earth Sci Eng* 4(6):924–928
6. IS 4031:1988. Methods of physical test for cement. Bureau of Indian Standards, New Delhi
7. IS 383:1970. Specification for coarse and fine aggregates from natural sourced for concrete. Bureau of Indian Standards, New Delhi
8. IS 2386:1963. Methods of test for aggregates for concrete. Bureau of Indian Standards, New Delhi
9. IS 10262:2009. Guidelines for concrete mix design. Bureau of Indian Standards, New Delhi
10. ASTM, C. (2017). 150 standard specification for portland cement, ASTM International
11. Snehal K, Das BB (2019) Mechanical and permeability properties of hybrid fibre reinforced porous concrete. *Indian Concr J* 93(1):54–59

Recent Trends in Construction Materials

A Study in Design, Analysis and Prediction of Behaviour of a Footbridge Manufactured Using Laminate Composites—Static Load Testing and Analysis of a Glass Fibre Laminate Composite Truss Footbridge



Col Amit R. Goray and C. H. Vinaykumar

Abstract Structural steel has been used extensively in civil engineering since time immemorial. However, despite being a material of choice, it suffers from being susceptible to the vagaries of nature in the form of corrosion. The high unit weight of steel has resulted in researchers trying and succeeding in developing materials that are stronger and lighter than steel. The present attempt is to study and utilise a very well-known material used in aerospace for civil engineering purposes. GFRP is known for its high specific strength and specific modulus, and these properties are studied and exploited in the present case to develop a footbridge. A bridge span of 4 m is manufactured using Glass Fibre-Reinforced Plastics. This footbridge has been designed to carry pedestrian traffic while at the same time being lightweight and modular. The bridge being lightweight and robust can be used in mountainous regions and jungle trails. The modular nature enables the bridge to be easily dismantled and each module is carried out by one man. The bridge was tested for static loading condition and the results are validated using FEM software. The close match between the results of numerical simulations matches the values obtained through in situ experimental testing. This study has proven that it is possible to design structural members for civil engineering by deriving the strength of a GFRP laminate using Equivalent Single-Layer (ESL) method. This study opens up the use of composite laminates for other related applications in civil engineering besides bridging, thus making it an exciting material for civil engineers in the future.

Keywords Footbridge · GFRP · Laminate · Deflection

C. A. R. Goray (✉) · C. H. Vinaykumar
Department of Civil Engineering, CME Research Center (Savitribai Phule Pune University),
Dapodi, Pune 411031, India
e-mail: amitgoray@gmail.com

© The Author(s), under exclusive license to Springer Nature Singapore Pte Ltd. 2023
M. S. Ranadive et al. (eds.), *Recent Trends in Construction Technology and Management*, Lecture Notes in Civil Engineering 260,
https://doi.org/10.1007/978-981-19-2145-2_10

125

1 Introduction

Glass Fibre-Reinforced Plastics (GFRP) has been very commonly used in the aerospace industry since the early 1970s by NASA. They are lightweight and strong with a high specific modulus and strength. The manufacture of advanced composites using glass fibres involves embedding the fibres in a resin matrix. The glass fibre provides the strength while the epoxy resin provides a limited amount of flexibility as desired. Due to the method of manufacture of the composite and also the fact that glass 'fibres' display a property to resist only unidirectional tensile force, the method of construction/manufacture of a composite laminate attains great importance. Each application utilising an advanced composite material will require a unique process of manufacture, construction and layout of the lamina. This definitely leads to a comparatively higher cost for fabrication and also the fact that advanced composites are non-isotropic materials, becomes a major drawback. The advantage of advanced composites, however, lies in the fact that they provide a high value of specific modulus and also specific strength.

$$\text{Specific modulus} = E/\rho$$

$$\text{Specific Strength} = \sigma_{\text{ult}}/\rho$$

where

E —Modulus of elasticity,

ρ —Density of material,

σ_{ult} —Ultimate Tensile strength.

In the present instance, a need was felt to exploit the properties of advanced composites to design, construct and study the behaviour and utility of bridges using GFRP composites. These could be utilised for providing quick connectivity during emergencies in rural, mountainous regions and also for military use.

The reports and studies related to human-induced vibrations, namely JRC report on EUR 23984 EN [1], HIVOSS Studies [2], Sétra Norms [3] and also various papers have been referred to in order to analyse this new material. Pedestrian loading has been considered to be a periodic function in the form of a Fourier series. The static loading has been taken to reach a maximum of 4.071 kN/m² of the loading area.

2 Description of the Bridge

This footbridge is a simply supported truss structure. It is modular and can be dismantled into parts for easy carriage. Each bay can be broken up into three components to enable ease of carriage. A view of the bridge laid out prior to testing is shown in Fig. 1.



Fig. 1 04m bridge laid out for testing at CoE, Pune. The location of the deflection sensors can also be seen

The GFRP bridge has been designed and developed by utilising Glass Fibre-Reinforced Plastic pultruded sections and also purposely designed laminates. The aim of the design was to produce a bridge with the abilities as follows:

- Light in weight: Ease of handling and carriage of a single by two individuals only.
- Modular Design: Each bay should have be capable of being used independently while also being able to be stacked, unloaded and joined with other bays. The basic unit was hence designed as a single bay acting as a module.
- Ease of transport: The bay dimensions should enable ease of loading on the roof of an SUV and also interlocking.
- Simple to assemble at site.
- Ease of assembly: Minimal number of parts for assembling and launching the bridge.
- Easy to launch and de-launch.
- Easily transportable to desired places using helicopters.
- Can be reused after de-launch.
- No repair is needed during the lifecycle of bridge.
- If needed, parts and components can be replaced in situ.

Excellent dynamic response properties.

3 Materials

In the manufacture of this bridge, GFRP was used in two forms, pultruded section of the GFRP was used to form the truss and a purposely designed laminate for the joints.

The footbridge has been constructed using pultruded sections and joints manufactured through a unique process. The bridge was tested at the Government College of Engineering, Pune. The prototype bridge was subjected to a series of load tests and the static loading was as per norms listed out by the RDSO, Lucknow [4].

Each pipe is constructed through pultrusion. The density of the pultrusion is **21.57 kN/m³**. The properties of the pultruded pipe are shown in Table 1.

The joints are constructed using various layers of fabric constructed using E-glass with varying orientations (+45/−45, +90/−90) with a thickness of 5 mm. The resin used is flame-retardant vinyl ester. Further treatment has been carried out to cater for damage due to UV radiation. The mechanical property of the joints was calculated by the method given in RDSO [4] and presented in Table 1.

The joint has been constructed using E-glass fabrics. E-glass fabric of Unidirectional (U), Biaxial (B) and Triaxial (T) orientation was used. CSM was also incorporated within the joint. To prevent damage due to pedestrian movement and environmental effects (UV radiation), gelcoat, PU coat were given. An anti-skid layer was provided to prevent any accidents. Quality control of the components was ensured and joints with voids were rejected. The inspection was carried out visually and also by measuring and comparing the weight of each component manufactured.

The composite was analysed and an ABD matrix was derived. The properties of this laminate were calculated and substituted into a software model for the individual components of the truss bridge.

The results of FEA analysis using this software model were thereafter compared with actual testing for the various components in order to confirm the properties and behaviour of each individual component of the Truss bridge.

Table 1 Properties of GFRP pipes and laminate joints

Title	Properties of GFRP	
	Pultruded pipe	Laminate joints
E1 (MPa)	28,044.50	14,110.40
E2 (MPa)	13,611.20	10,923.80
G12 (MPa)	8524.42	5860.00
G23 (MPa)	3520.81	2466.13
μ_{12}	0.48	0.42
Density (kN/m ³)	21.57	20.10

4 Load Tests

Load testing and deflection for pultruded pipe were carried out with a 3-point loading in laboratory and on the software FEA model. A photograph of the experimental 3-point setup is in Fig. 2. A comparative table of load versus deflections is given in Table 2. The comparative results between the experimental values and those obtained by FEA modelling are shown in Fig. 3.

As observed, the software model for loading matches the experimental results for the deflection of the pultruded pipe. These results were used to verify the software model. Thereafter, an experimental test for a fully rigged footbridge was carried out. This was for a 4 m span bridge loaded as per the norms of the Indian railways. The



Fig. 2 3-point load testing of pultruded pipe

Table 2 Comparison of loading on pultruded pipe experimental versus FEA

S. No.	Load (N)	Deflection (mm)		Remarks
		Actual	FEA	
1	0	0	0	
2	135	6.875	10.042	
3	270	13.125	13.549	
4	405	20.000	23.592	
5	540	26.563	27.099	
6	675	40.625	40.648	
7	810	47.375	50.690	
8	945	54.313	54.198	
9	1080	61.563	64.240	
10	1215	68.750	67.747	
11	1349.46	76.250	77.789	

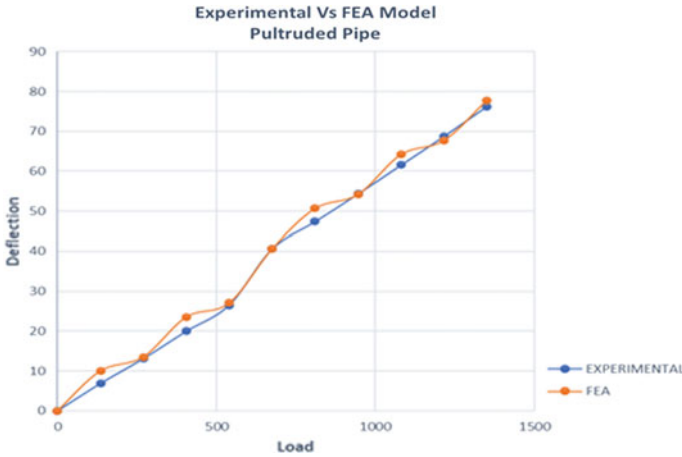


Fig. 3 Graph experimental versus FEA results (pultruded pipe)

Table 3 Comparative deflection values of the 04 m footbridge experimental versus FEA model

S. No.	Result	Deflection (mm)			Remarks
		Location 1	Location 2	Location 3	
1	Experimental	2.25	1.48	2.3	6.92 N load
2	FEA	2.012	1.854	2.103	6.92 N load

value of deflection after 24 h was also obtained to check for any residual deflection if any.

The bridge was tested for static loads [5] as well as pedestrian loads [6]. The deflection values obtained by experiment for the static loading and using the FEA model are mentioned in Table 3.

The deflection values are noted for the static loading. The loading on the bridge was also carried out by people jumping on the bridge simultaneously to simulate dynamic loading. However, the present paper only looks at static loading. The details of deflection due to static loading on the 4 m bridge are shown in Table 3 and Fig. 3.

5 Software Simulation and Analysis

While a number of methods exist to model the behaviour of composite laminates, only the equivalent single layer was used to calculate the properties of the material. Additionally, certain factors of safety were also incorporated to further refine the results of the analysis. This has been done in order to make the process of analysis and design simple and easier to understand for practising engineers. For constructing any civil structure, the next stage would be to set up ideal factors of safety.

This is because the aim is to establish norms for establishing thumb rules based on actual testing and failure.

The computer model of the bridge has been created using AutoCAD, thereafter meshing is carried out using Netgen. The model was then imported into Mecway FEA. The FEA analysis of the geometry of the bridge was analysed considering the components of the bridge as a Shell lamina. The properties of the various layers were input into the FEA model for the joints and the pipes based on validated theoretical values had been tested and the results were validated.

The mesh used for the analysis was a 2D mesh of an approximate size of edge as 25 mm, 182,808 nodes and 150,035 elements.

The supports were assigned by setting boundary conditions on elements at the bottom of the bridge where actual support was placed as simply supported.

After the mesh and the model were imported into the Mecway software, properties and boundary conditions were assigned, and the results of the static deflection as obtained in the FEA analysis are shown in Fig. 4 and closely matched the actual values obtained through the experiment. A comparison of the values of deflection for static loading obtained experimentally versus FEA is shown in Table 3.

There is a very close co-relation between the experimental and observed results. Thus, the same model can now be extrapolated to larger spans and exploited to arrive at a solution.

6 Results and Discussions

The aim of the study was to create an accurate FEA model for the static and dynamic testing of a bridge manufactured using GFRP. The model has been found to satisfactorily predict the behaviour of the GFRP footbridge in both static and dynamic loadings. The results of the static loading on the footbridge are being shared and have also formed the basis for accurately modelling the dynamic response and carrying out a modal analysis of the footbridge.

The in situ results obtained have been plotted against the results obtained from the FEM modelling of the bridge. Vertical displacement was measured and averaged out over the two sides of the bridge. The results of numerical simulation and actual test are close and indicate that the bridge was correctly modelled in the FEA software.

The FEA model is also accurate enough after incorporating the various factors of safety to predict the behaviour for loading over a 24-h cycle.

Deflection as predicted by the model varies within limits of 10–25% over the full span. This needs further refinement. But it can be seen to enable derivation of a ‘**Safety Factor**’ for a similar design in the future. The results are encouraging and have been found to fairly predict the behaviour of a footbridge constructed using composites. The same can be considered while preparing a design table at a later date. However, considering the overall values of deflection as ranging between 2 and 4 mm, they are well within the permissible limits of bridge codes.

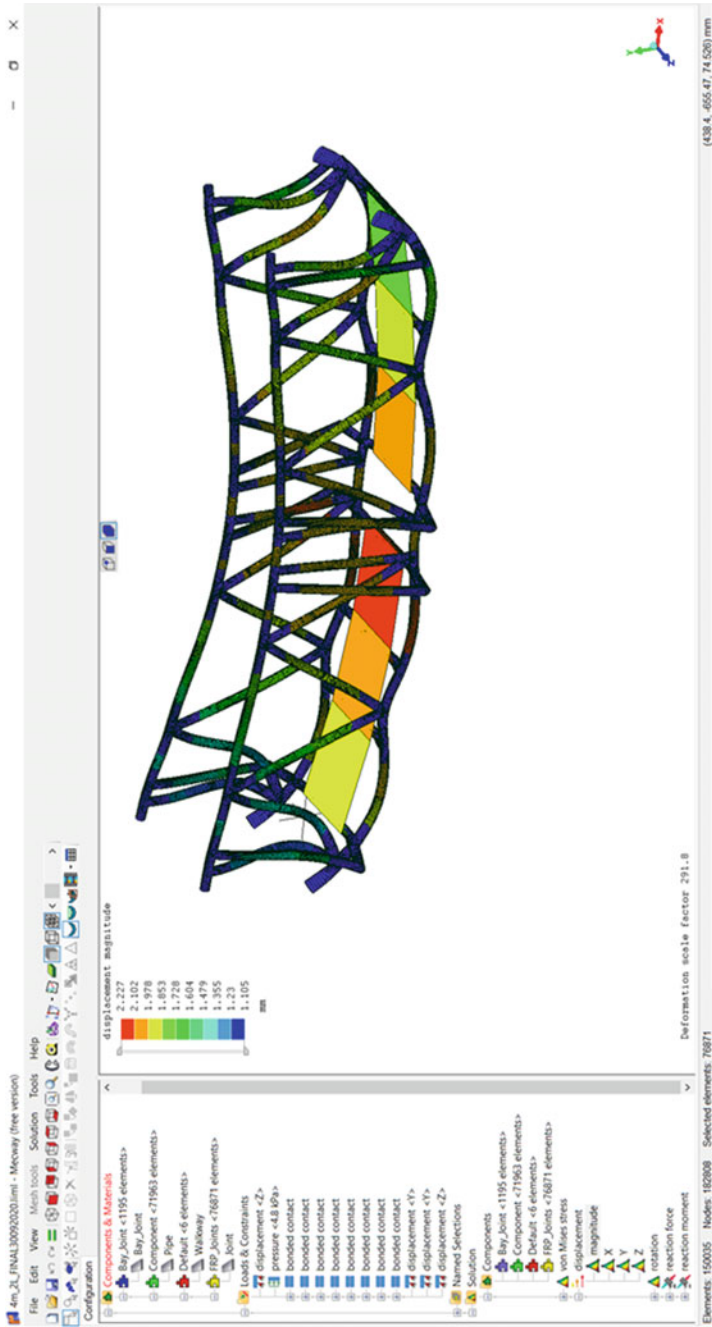


Fig. 4 Results of FEA analysis of the 04 m footbridge

7 Conclusions

The study shows that Equivalent Single-layer (ESL) modelling can be used safely in estimating the strength and properties of the GFRP material. The findings of the study can be summarised as follows:

- The ESL model has an in-built factor of safety and values of deflection obtained theoretically are slightly larger than those obtained in the experimental study. This implies that the ESL model can be used along with derived factors of safety to enable the design of structures utilising GFRP.
- The ESL model provided a very accurate prediction of the deflection between experimental and theoretical values for the bridge. The variation in measured deflection was between 10 and 25%.
- The deflection pattern due to the presence of stiffer joints was well reflected in the FEA model. The software model has mimicked the actual behaviour observed during in situ testing.
- Long-term effects of creep need to be further studied in greater detail.
- The success in being able to predict the material behaviour of GFRP indicates the possibility of developing design tables for the footbridge.

References

1. Design of lightweight footbridges for human induced vibrations—JRC first edition, May 2009 (EUR 23984 EN)
2. Murray TM, Allen DE, Ungar EE (1997) Steel design guide series 11: floor vibrations due to human activity. American Institute of Steel Construction
3. Sétra, Footbridges, Assessment of vibrational behaviour of footbridges under pedestrian
4. Loading TG (2006) Service d'Etudes Techniques des Routes et Autoroutes. France, Paris
5. Mechanics of composite materials: Autar K. Kaw. ISBN-13: 978-0849313431/ISBN-10: 0849313430
6. Rules specifying the loads for design of super-structure and sub-structure of bridges and for assessment of the strength of existing bridges issued by the Research Designs and Standards Organisation, Lucknow
7. IRC:6, para 209 for Pedestrian loads
8. Indian Standard Code for Steel. IS: 800-2000

State-of-the-Art of Grouting in Semi-flexible Pavement: Materials and Design



Hemanth Kumar Doma and A. U. Ravi Shankar

Abstract Semi-flexible Pavement (SFP) is a composite pavement that consists of an open-graded friction course (OGFC) or porous asphalt mixture (PAM) having an air void content of 20–35%, grouted with cement paste/mortar with a fluidity of 10–16 s. The OGFC or PAM provides flexibility, skid resistance, and the grouting provides rigidity, capacity to carry heavy traffic without rutting, together to achieve a joint-free, rut-resistant pavement. The interconnected voids in the asphalt mixture filled with grout will be the secondary skeleton and help in load transfer, being the stone-on-stone contact with the primary skeleton. The review of supplementary cementitious materials (SCM), the formulation of the materials to meet the grouting design requirements, and the parameters to measure the efficiency are necessary to provide a more durable and fatigue-resistant pavement. The first part of the study discusses the mechanical properties of the materials, the design and preparation of the grouting. The grouting parameters and the contribution of grouting to SFP's performance are discussed in the later part. The review indicated that the marginal aggregates can also be used, and with the use of SCM, durability, and strength can be increased. Concerning the benefits of grouting in SFP, scope exists for further research to design and understand the grouting better, which helps SFP perform better.

Keywords Grouting · Semi-Flexible pavement · Supplementary cementitious materials · Mechanical properties

1 Introduction

Flexible pavement provides good riding quality, high skidding resistance, easy maintenance, but with rapidly increasing traffic, the occurrence of rutting and cracking has become obvious [14]. The rigid pavement has high fatigue life but needs more time to allow the traffic and poor driving comfort due to the joints [4]. There is a

H. K. Doma (✉) · A. U. Ravi Shankar

Department of Civil Engineering, National Institute of Technology Karnataka, Mangaluru, India
e-mail: dhemanthgukt@gmail.com

© The Author(s), under exclusive license to Springer Nature Singapore Pte Ltd. 2023
M. S. Ranadive et al. (eds.), *Recent Trends in Construction Technology and Management*, Lecture Notes in Civil Engineering 260,
https://doi.org/10.1007/978-981-19-2145-2_12

135

need for a new type of pavement, such as SFP, to overcome the drawbacks and to enhance the performance of both flexible and rigid pavement [13]. The SFP or Grouted Macadam is a pavement that consists of the OGFC or PAM having an air void content of 20–35%, grouted with cement paste/mortar [15]. The OGFC or PAM provides flexibility, skid resistance, and the grouting provides rigidity, the capacity to carry heavy traffic without rutting, together to achieve a joint free, rut-resistant pavement [13, 17]. The OGFA or PAM possesses a large porous structure, ensuring the stone-on-stone contact to bear the traffic load and to provide the voids for grout to easily permeate.

2 Grouting

2.1 Materials

The grouting of SFP should have good flowability to fill the voids and be required to provide good compressive and flexural strength to sustain the loads and to resist the drying shrinkage. In other words, it should have high workability, permeating ability, and strength. Researchers investigated the grouts with various types of cement with different proportions of SCM such as fly ash (FA), silica fume (SF), and various dosages of superplasticizers (SP), which are used to achieve this goal. The two types of grouting materials were used such as the cement paste (CP) and cement mortar (CM), mainly consisted of cement, mineral powder, coal ash, and water [20]. Flexible admixtures such as neutral ethylene–vinyl acetate (EVA), SBR latex, asphalt emulsions were used to improve the flexibility of the grout [6]. The penetrants such as naphthalene-based superplasticizer (NS), air-entraining superplasticizer (AS), and polycarboxylene-based superplasticizer (PS) were used to improve the flowability of cement paste (CP). The high-performance cement paste (HPCP) was prepared with the expansion admixture of UEA (UEA), air-entraining agent of ZY-99 triterpenoid saponins (AEA), and polycarboxylate-based TH-928 superplasticizer (PSP) [16]. The chemical admixtures were necessary to produce the high-performance cement slurry [6].

The sand finer than the 600 μm IS sieve size should be used in the preparation of grout (IRC). The fine sand passing through a 45 μm IS sieve can also be used so that the grout fills the voids in the asphalt mixture easily. The sand passing through a 300 μm sieve was used to prepare grout [8]. The sand content decreases, in general, the flowability of grout. However, the flowability was affected most with mineral powder (MP), water/cement (W/C) ratio, and the content of fly ash (FA), in comparison with the sand content [20]. The grout flowability can be increased with the addition of fly ash (FA) and silica fumes (SF) [10]. The FA should conform to IS:3812 with minimum of 65% passing the 45 μm IS sieve. These SCMs produce additional hydration products through pozzolanic reaction, leading to better strength and lower shrinkage than ordinary Portland cement (OPC) [8]. The drying shrinkage

and the fluidity were improved with the increase in FA content, however, the flexural and compressive strengths were decreased [20]. The SF reduces the segregation and bleeding of grouting material and the shrinkage can be reduced with the use of aluminite powder [19]. The MP content improved the fluidity, the drying shrinkage, and reduced the strength of CP. The MP eliminates the bleeding during the preparation of the grout [20]. To obtain the asphalt's flexibility and cement's high strength, the cement asphalt emulsion paste (CAEP) prepared with asphalt emulsion, cement, finer sand, and chemical admixtures was used widely and has the great potential to be grout material in SFP.

2.2 Mechanical Properties

2.2.1 Fluidity

To determine the fluidity of grout mixtures, the flow cone test confirming to ASTM C939 can be used. The efflux time required for the grout volume of 1725 ml is noted as the fluidity. The Leeds flow cone test: The cone has a funnel of 200 mm upper diameter with an orifice of 18 mm that narrows down to 15 mm diameter over a length of 100 mm. The time required for the slurry volume of 1725 ml to flow through the cone was used to assess the fluidity. The fluidity of 9–11 s was recommended to penetrate a porous asphalt specimen of a depth of 100 mm [8]. Koting et al. [11] used 11–16 s flow time for 1 lt of grout as measured by the Malaysian mortar flow cone test to evaluate the different SPs. Fang et al. [6] limited the fluidity of the initial grouts, while formulating, to 15 s maximum based on testing the slurry formulations with the maximum allowable amount of admixtures and high W/C, but, accepted the fluidity range of 9–13 s. To evaluate the effect of the dosages and type of penetrant on the fluidity, three penetrants, i.e., NS, PS, and AS, at 1, 3, 5, 7, and 10% by mass of cement to the cement slurry, at the constant 0.6 W/C ratio, were used [6]. Figure 1 depicts the fluidity of cement slurry with NS was relatively stable, though couldn't meet the requirement. However, the dosages of PS had an insignificant effect on

Fig. 1 The effects of different dosages of penetrant on the fluidity of cement slurry [6]

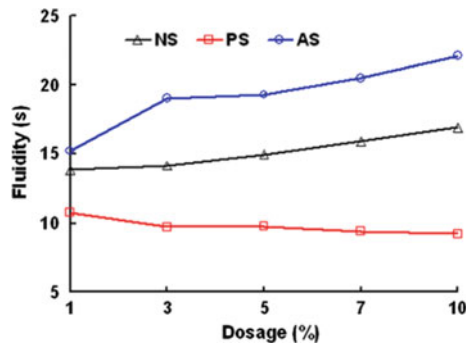
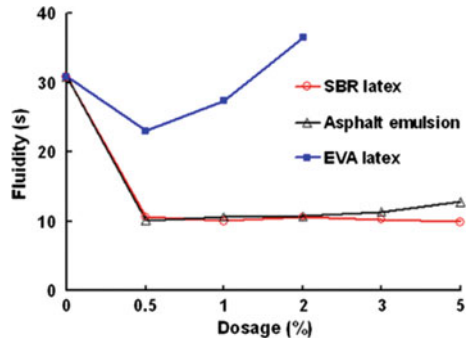


Fig. 2 The effects of flexible admixture on the fluidity of selected cement slurry [6]



the fluidity and the grout with AS had high fluidity. The dosage of 1% penetrant for both PS and NS was considered as optimal dosage and concluded that the PS had a significant effect on the fluidity than the AS and NS penetrants. Figure 2 depicted the effect of flexible admixtures at optimal W/C of 0.6 and PS of 1% and the fluidity was beyond the required value, hence, not recommended to prepare the grouts. The asphalt emulsion and SBR latex had met the fluidity requirement and had a similar effect on fluidity and concluded that the SBR latex could be used as a flexible admixture to prepare the fresh cement slurry.

Zarei et al. [19] added the CAEP in 20%, 40%, and 60% proportions of CAEP/C produced the grouts with good fluidity of 10–20 s while the cement paste exhibited the high fluidity due to the lower W/C ratio. Three additives such as PSP, UEA, and AEA were used and found that the PSP has a significant influence on fluidity followed by W/C ratio, AEA content, and UEA [16].

2.2.2 Compressive Strength

The prism samples, prepared using the rectangular steel molds with dimensions of 40 × 40 × 160 mm, were cast to determine the compressive strength. Hassan et al. [8] replaced the OPC with 5% of SF and achieved the compressive strength of 56 MPa on 1-day curing and increased to 115 MPa on 28 days. The FA/SF (used together) grout resulted in lower compressive strength of 28 MPa on 1-day curing, as expected because the FA has an adverse effect at early ages, but achieved higher strength upon 28 days of curing. The SBR affected the early strength development similar to FA but achieved lesser compressive strength than FA grout. The addition of either SBR or sand or both together reduced compressive strength significantly. Fang et al. [6] concluded that the compressive strength of hardened cement paste for 3, 7, and 28 days of curing, at the W/C of 0.6, decreased by 72%, 45%, and 8.7%, respectively, with the increase in dosage of SBR latex from 1%, 2%, and 3%. The flexural strength of hardened cement paste for 3 and 28 days of curing decreased by 4.5% and 24%, respectively, but for 7 days of curing, flexural strength was increased by 54%. The compressive strength of AE included grout at 7 and 28 days of curing

were decreased in the range of 50–53% and 34–38%, respectively, in comparison with CP grout, with the increase in AE content [19]. There was no significant decrease observed in compressive strength with an increase in CAEP content, indicating that the dosage of CAEP had no significant influence on the strength. The increment rate of compressive strength from 7 to 28 days was about 38% for CAEP grout while the cement paste had very less increment. Pei et al. [16] concluded that the SP content and W/C ratio had the greatest influence on strength of the HPCP.

2.2.3 Flexural Strength

The specimens, prepared using the steel rectangular prism molds with the dimension of $40 \times 40 \times 160$ mm, were cast to determine the flexural strength. Zarei et al. [19] observed that the flexural strength at 28 days was increased around 5–15% in comparison with CP grout, with the addition of CAEP. However, 7-day flexural strength decreased by about 40%. It was mentioned that the ratio of the flexural strength and the compressive strength of grouting paste increased with CAEP content. The ratio was the indication of the toughness of the grout material. The flexural strength was significantly affected by the W/C ratio and PSP content [16].

2.2.4 Bond Strength

The pull-off test was conducted on a Positest AT-A device to determine the bond strength between the asphalt-coated aggregate and the grout [2]. A homogenous uniform thin asphalt film of maximum 0.2 mm thickness was poured onto the preheated aggregate plate and a square glassy plastic mould having dimensions of 2 mm thickness, diameter of 21 mm and was positioned on the preheated aggregate plate. The bond between the grout material and asphalt was formed by pouring the grout into the circular holes. Eventually, after curing time, the hardened grouting was pasted with the metal pull-off stubs and then tested for the failure load to determine the bond strength or pull-off strength. The pull-off test was used to determine the bond strength between the asphalt and CAEP and observed that the bond strength increased with the increasing CAEP content, while the bond strength of CP was very less [16]. It is concluded that the interface between the hardened cement paste and asphalt coated aggregate was most critical to failure and can be reduced with the addition of CAEP.

2.2.5 Drying Shrinkage

The SFP specimens were immersed for 24 h in water for measuring the drying shrinkage. The length of the SFP specimen after wiping and further on 14 days of storage at room temperature was measured. The percentage reduction of the length

will give the drying shrinkage. The drying shrinkage will be significantly influenced by the type of expansion admixture [16].

2.3 *Composition and Formulation*

2.3.1 *Composition*

The long molecules in the superplasticizer enclose the cement particles to make them repel each other by providing a negative charge, thereby attaining the higher flowability with a lesser W/C ratio. The one sulfonated naphthalene formaldehyde-based SP and two polycarboxylic ether polymer-based SPs were used to determine the effect of superplasticizer dosage and type on the flowability and the strength of the grout [11]. The dosage of the first type of polycarboxylic ether polymer-based SP and W/C ratio were varied from 0.5 to 2.0% by weight of grout and 0.24–0.50, respectively, to attain a fluidity of 11–16 s and observed that the higher dosages of SP increased the flowability irrespective of W/C ratio. The sulfonated naphthalene formaldehyde-based SP produced the grout mixtures of 136 s flow time and also observed as expected that the compressive strength was decreased with the increase in W/C. The W/C ratio was the important factor affecting the mechanical properties of the grout. The higher W/C causes the cracks due to the temperature shrinkage and the decrease in strength. Zachariah et al. [18] investigated the effect of the W/C ratio (0.5, 0.6, and 0.7) on the performance of the SFP and concluded that the residual porosity was decreased with the increase in W/C, which in turn increases the performance of SFP. However, the grout with a W/C ratio of 0.7 showed lesser compressive strength than grout with 0.5 irrespective of grout volume. Therefore, the W/C ratio should be selected based on fluidity without compromising the strength. Fang et al. [6] determined the optimum W/C of cement slurry as 0.6.

Pei et al. [16] determined the optimal W/C ratio for the grout having the additives, PSP, UEA, and AEA, based on the required range of fluidity, drying shrinkage, flexural and compressive strengths. When the W/C ratio varied from 0.51 to 0.54, the fluidity decreased from 25 to 16 s. A decrease of 5% and 5.7% was observed in the 7-day flexural and compressive strengths, respectively, with an increase in the W/C ratio to 0.57 from 0.51. Similarly, a decrease of 9% and 10.7% was observed in the 28 days' flexural and compressive strengths, respectively, with an increase in W/C ratio to 0.57 from 0.51. The drying shrinkage increased about 33% first with the increase of the W/C ratio from 0.51 to 0.54, then, reduced with a further increase in the W/C ratio. Based on the above mentioned analysis, the optimal range of W/C ratio was recommended as 0.55–0.57. The PSP content of 1% improved the flexural strength at 7 days and 28 days by about 12% with the corresponding strength of CP, but a significant improvement in the compressive strength and the drying shrinkage was not observed. The recommended amount of PSP was 1%. Up to the expansion admixture content of 10%, the admixture had no significant influence on the fluidity, flexural, and compressive strengths; however, the drying shrinkage

was reduced by around 18% significantly. Therefore, the expansion admixture of 10% was recommended. The AEA content had a significant effect on the fluidity and increased the 7-day flexural strength with the increase in AEA content but had no influence on the compressive strength. However, 0.008% content was recommended due to the workability provided during the mixing process.

The grouted specimens should be cured for sufficient time to attain strength. The SFP samples were concealed with plastic sheets and then cured for 7 days at 20 ± 2 °C, relative humidity of 95%, and then cured at the same temperature with a relative humidity of $65 \pm 5\%$ for 28 days curing period [16]. After demolding, the SFP specimens were cured at room temperature indoors [16]. Hassan et al. [8] cured the specimens at 25 °C in a temperature-controlled chamber with 65% relative humidity until testing. Gong et al. [7] cured the SFP samples for 14 days curing period at 20 ± 2 °C and relative humidity of 95%.

2.3.2 Formulation

The composition of the grout materials affects the performance of SFP and the effect of each material should be carefully understood. The composition was done mostly, in general, on trial and error, which is a hectic laboratory work [6, 9]. The formulation of grout should be done in a scientific way to understand the effect of composition, ultimately the required grout can be achieved. Zhang et al. [20] analyzed the effects of grout composition with the preparation of two grouts, CP and CM, and determined the flowability, shrinkage, flexural, and compressive strengths. The influence factor levels of CP and CM were determined based on the literature. Tables 1 and 2 present the factor level of CP and CM. The approximate orthogonal arrays ($12, 3^4 4^1$) and orthogonal Table L9 (3^4) were adopted for CP and CM respectively. The grout should have fluidity ranging from 10 to 14 s, a compressive strength of 10 to 30 MPa, and a flexural strength of a minimum of 3.0 MPa.

To achieve the fluidity of 10–14 s, the W/C ratio of 0.63, FA content of 20%, and MP of 20% were the best proportions for CP grout based on the analysis. The

Table 1 Factor level of CP

Factor level	W/C ratio	FA content (%)	MP content (%)
1	0.48	0	0
2	0.53	10	10
3	0.58	20	20
4	0.63	–	–

Table 2 Factor level of CM

Factor level	W/C ratio	FA content (%)	MP content (%)	Sand content (%)
1	0.55	0	0	10
2	0.60	10	10	15
3	0.65	20	20	20

fluidity was affected by the W/C ratio most and followed by FA content and MP content. Similarly, the W/C ratio of 0.65, FA content of 20%, MP content of 20%, and sand content of 10% were proportions for CM grout and the factors affecting the fluidity were of the same order as CP's factors except the sand content being the last. The W/C ratio was the most influential factor and the MP was the least factor of all. To achieve the flexural strength of more than 3 MPa at 7 days curing period and the compressive strength of 10–30 MPa at 7 days curing period for the CP, the W/C ratio of 0.48 should be used without FA content and MP content. It was concluded that the FA content had a great impact on the flexural strength while the W/C ratio had the most effect on the compressive strength. For 7 days flexural and compressive strengths of CM, the best proportion was W/C of 0.55, the sand content of 20%, with no FA content and MP content, and the FA and MP contents being the most influencing factors, respectively. To achieve the 28-day compressive strength of CM, the W/C of 0.55 and the sand content of 15% with no FA, MP contents were the best mix proportion and the MP was the great influence. The mixture prepared with a W/C ratio of 0.53, the FA of 20%, and the 0% MP content was the best mixture to reduce the drying shrinkage of CP. The W/C ratio of 0.60, the FA content of 10%, and the sand content of 20% were the best proportion to reduce the drying shrinkage of CM. The W/C ratio had a great influence on the drying shrinkage of the CP and the CM. To achieve the targeted values of fluidity, drying shrinkage, compressive, and flexural strengths of CP or CM, considering any one of the properties, the optimal proportions and combinations of W/C ratio, the content of MP, the content of FA, and the sand content were determined. The fluidity of grout was the main criteria and followed by the lesser drying shrinkage and higher strength, respectively, to select the optimal composition of grout. To determine the optimal W/C ratio, the plots of fluidity, ductility, shrinkage, and strengths of cement pastes (CP) for 7, 28 days against the W/C ratio were drawn and the optimal ranges of W/C ratio to meet the relevant standard requirement were determined. The recommended range of W/C ratio for CP is about 0.56 to 0.58. Similarly, the graphs of FA content against the ductility, shrinkage, ductility, and strengths of CP were drawn and the optimal FA content was determined as 10%. In the same way, the optimal mineral powder content of 10% was determined. In a similar way, recommended the composition of CM as a W/C ratio of 0.61–0.63, sand content of 15%, and 10% FA content as grouting material. It was concluded that the CP was more suitable as grouting materials than the CM. The CP grout was more stable than the CM when W/C was varied.

Pei et al. [16] used the three additives such as PSP, UAE, and AEA, to prepare the HPCP and the contents of the additive were set as shown in Table 3 based

Table 3 Factor level of HPCP

Factor level	W/C ratio	PCP content (%)	UEA content (%)	AEA content (%)
1	0.57	0	0	0
2	0.54	0.5	10	0.008
3	0.51	1	12	0.012

Table 4 The recommended range/ratio and selected ratios of HPCP

Factor level Recommended value range	Sample Name	W/C ratio: 0.55–0.57	PCP content: 0.5–1.0%	UEA content: 10%	AEA content: 0.008%
The recommended ratios of HPCP	HP1	0.56	0.5%	10%	0.008%
	HP2	0.56	0.5%	10%	0.0%
	HP3	0.56	1.0%	10%	0.008%

on recommended dosages and relevant research. For each factor-level analysis, the orthogonal table L9 (3^4) was adopted. The three HPCP grouts, HP1, HP2, and HP3, were prepared with the obtained optimal ratios/ranges through an orthogonal test to evaluate the performance through the fluidity, drying shrinkage, and strength. The composition of HP1, HP2, and HP3 grouts were given in Table 4. HP2 and HP3 grouts performed well and were recommended as grouting materials while HP1 was omitted as flowability decreased significantly with time.

3 Evaluation and Contribution of Grouting

3.1 Evaluation of Grouting

Hou et al. [9] investigated the engineering properties of grouted macadam composite materials and recommended the fluidity of 9–11 s based on trial and error to have the void volume of 30% filled with the grout. Pei et al. [16] and Zhang et al. [20] evaluated the various grouts based on the fluidity, the drying shrinkage, and the strength to choose the best suitable grout. Zachariah et al. [18] prepared the porous asphalt mixtures (PAM) with 18%, 21%, and 24% air voids and observed the increment of 4–10% in Marshall stability of grouted mixtures with the increase in percentage air void from 18 to 24% and [5] reported the same. However, higher initial void content of asphalt mixtures was not always resulted in higher grouting because of poor interconnectivity of the voids in the asphalt mixtures. Therefore, the initial air void content was not a good parameter to evaluate the grouting. The interconnectivity of voids can be assessed through the permeability of the asphalt mixture. The higher permeability indicates that the grout can easily fill the voids. Setyawan [17] observed that the increase in binder content reduced the porosity, and so did the permeability. Generally, the water permeability of porous asphalt mixtures was about 1.44×10^{-3} – 1.61×10^{-3} m/s. The PAM gradations were used to increase the porosity and permeability of asphalt mixtures, which makes grouts fill the voids easily. Though the permeability was not dependent on the porosity itself, the pore size also had a significant impact on the grouting. Ding et al. [5] studied the asphalt mixtures with different pore structures of the same air void content and observed that the mixture with homogenous grade had a good pore size and distribution, which reflected in

better performance of asphalt mixtures. It was concluded that the large air void with homogenous grade should be adopted for SFP. Pei et al. [16] evaluated grouting flowability based on the three parameters; the volume of grout/unit area, grouting depth, and residual porosity of grouting composites.

1. Volume of grout/unit area

The maximum volume of the grout was measured per unit area by preparing the asphalt mixture rutting samples to achieve targeted porosity.

2. Depth of grout

The grouting depth represents the fluidity of grout and can be observed in both field and laboratory conditions. The rutting slabs were prepared and then grouted with the maximum volume of grout determined using a volume of grout/unit area. After the curing period, the samples were cored and observed for the grouting depth of grouts.

3. Residual porosity of SFP [12, 16];

The residual porosity of SFP was determined based on the volumetric properties.

4. Grouting saturation degree [12]

The grouting saturation degree represents the grouted material quantity in the asphalt mixtures and is determined using Eq. (1).

$$s_g = \frac{(w_2 - w_1)}{\rho \times V \times V_a} \times 100\% \quad (1)$$

where S_g = Grouting saturation degree (%); w_2 = sample weight before grouting (g); w_1 = sample weight after grouting (g); ρ = cement mortar's density (g/cm^3); V = specimen's volume (cm^3); V_a = porosity of asphalt mixture (%).

A generalized increasing trend of the grouting volume with an increase in air void content was observed indicating that the grouting parameters were representing the grouting conditions well (Figs. 3, 4 and 5). The grouting volume and the grouting depth showed the variation at 18% air void of the asphalt mixture. The variation was reduced and attributed to the effective void content increment, which allowed the grout to permeate easily. The grout intensity was determined using image analysis on the sectioned cylindrical sample [18].

Fig. 3 Variation of grouting volume

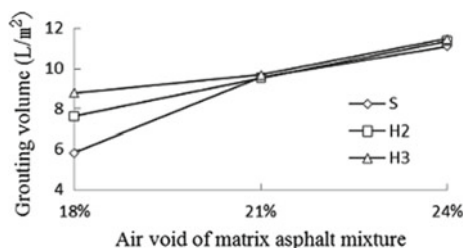


Fig. 4 Variation of the depth of grout

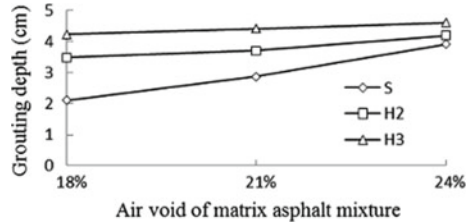
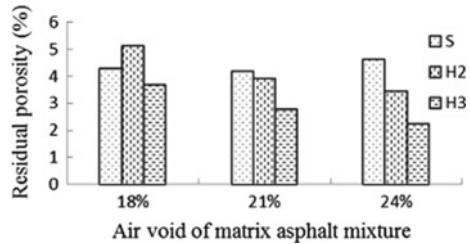


Fig. 5 Variation of volume of residual porosity



3.2 Contribution of Grouting

The aggregate skeleton in the asphalt mixture transfers the load through the contact points. The high internal friction among the aggregates increases with the number of contact points leads to the high rutting resistance. The internal friction contribution to rutting resistance is about 70%, which stated the significance of the aggregate skeleton of asphalt mixture in load transfer [1]. The internal friction decreases with the use of weaker aggregates and excessive bitumen content, leading to rutting [9]. Zachariah et al. [18] investigated the potential usage of the nonconventional aggregates in the CGBM, the crushed first-class brick aggregates (CFCBA), and the crushed over-burnt brick aggregates (COBBA). The grouted brick aggregate mixtures exhibited a higher tensile strength ratio (TSR) of more than 100%, i.e., 101.85%, reduced rut depth by about 35%, and increased the fatigue lives by about 144% in comparison with hot mix asphalt mixtures (HMA) samples. The rut reduction and fatigue life increment of grouted over burnt brick aggregate mixtures were 24.04% and 132.91%, respectively, while grouted first brick aggregate mixture exhibited the rut depth reduction of 3.4% and increment of 118.87% in fatigue lives. It was concluded that the marginal aggregates could be used and the over burnt brick aggregates could perform well. However, to avoid the negative influence on the hydration process in SFP samples, the investigation of brick aggregates' porous surface and the high water absorption was needed. Zachariah et al. [19] investigated the relationship between bitumen to cement grout mass ratio (B/CG) and the performance of grouted samples, i.e., rutting depth and fatigue lives and a good relationship with R^2 of 0.81 existed with fatigue life than the rutting depth. It was concluded that the strength and the amount of grout in CGBM affected the fatigue behavior while the quality of grout influenced the rutting behavior more. Hassan et al. [8] investigated the effect of cementitious grouts

on the performance of grouted macadam and the five grouting mixes were prepared with different proportions of SF, FA/SF (both were used), Styrene-butadiene rubber (SBR), sand. The compressive strengths of SF and FA/SF grouted macadams were almost the same, i.e., 13.7 MPa and 13.8 MPa, even though the SF grouted macadam showed higher early strength. The compressive strengths of SF and FA/SF grouted macadam was increased by 16% and 13%, respectively, compared to the compressive strength of OPC-grouted macadam. Similarly, the 4–7% increment in indirect tensile stiffness modulus was observed and shrinkage strains were reduced by 22% and 18%, respectively, when compared with OPC-grouted macadam. The dynamic creep test was used to assess the permanent deformation resistance of grouted specimens at 40 °C, 60 °C and it was observed that the creep stiffness of grouted macadam were 170–200 MPa at 40 °C and 130–180 at MPa 60 °C where the asphalt mixture had 15 MPa at 40 °C, 8 MPa at 60 °C.

Zarei et al. [19] investigated the effect of CAEP on the cracking resistance of grouted samples at low temperature and compared SFP with CP. The CAEP was added to cement in proportions of 20%, 40%, and 60% by weight. The rutting depth was increased up to 2 mm with an increase in the CAEP content while SFP with CP was no rut material. Though the Marshall stability, retained Marshall stability, indirect tensile strength (ITS), and TSR were decreased with the increase in CAEP content, the flexural strength of SFP with CAEP 20% was increased to 6.43 MPa in comparison with SFP with CP. With increasing CAEP content, the flexural strength of SFP was reduced to 6.02 MPa. The pull-off strength of CAEP with asphalt mixture was increased to 42.55 kPa from 19.66 kPa of SFP with CP, which benefited the flexural strength of grouted samples. The 14% increment in flexural strain in comparison to SFP with CP was observed with the addition of 20% CAEP, but, the further increment in CAEP reduced the flexural strains by 20%. It was concluded that the grouting with a suitable modulus should be used to obtain the low-temperature resistant SFP. Cai et al. [3] studied the effect of the grouting and the fiber on the mechanical behavior of SFP and porous asphalt (PA) samples through the Acoustic Emission signal and dynamic modulus test. Figure 6. depicted that the SFP had a larger modulus than the PA mixture. The SFP and PA samples had higher storage modulus than the loss modulus demonstrating the lower cracking resistance. The storage modulus was decreased and the loss modulus was increased with the addition of fiber. Figure 7 depicted the failure strains of PA mixtures, with and without fibers, which were reduced by 34.7% and 44.7%, respectively. The 40% and 15% of the failure strains of SFP-30 mixture, with and without fibers, respectively, were reduced after grouting. The strength of SFP was not improved significantly with the addition of the fiber.

4 Conclusions

This study conducted a brief review on the performance and formulation of grouting materials and the following findings were observed.

Fig. 6 Typical master curves of SFP and PA at 15 °C

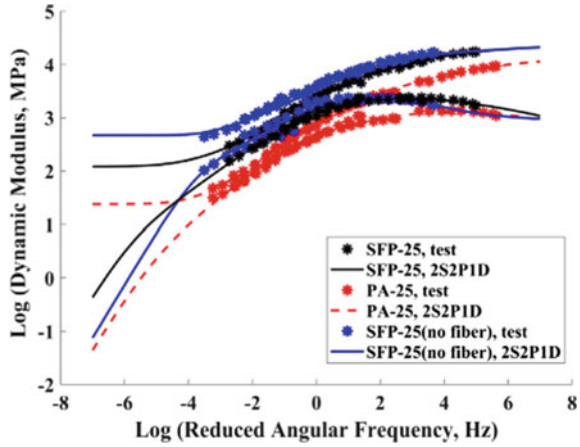
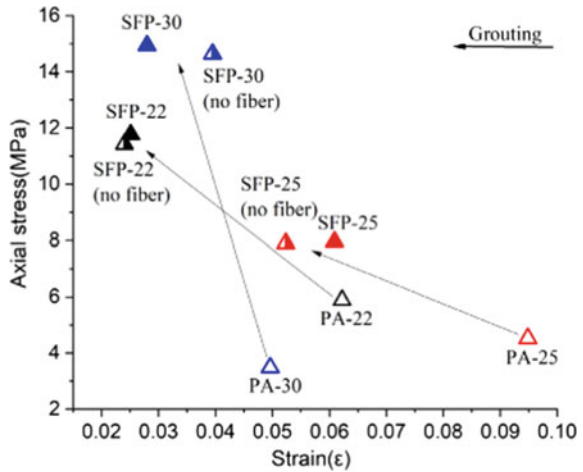


Fig. 7 Peak stress and corresponding strain of SFP and PA



1. The nonconventional aggregates or the marginal aggregates can be used in SFP
2. The SCM and the additives improve the performance of grout when used at certain proportions/dosages.
3. The formulation of grouting materials should be used to obtain the required grout properties
4. The grouting parameters should be used to evaluate the grouting efficiency.

References

1. Anderson DA, Kennedy TW (1993) Development of SHRP binder specification (with discussion). *J Assoc Asphalt Paving Technol* 62
2. ASTM (2014) D4541-09: standard test method for pull-off strength of coatings using portable adhesion. ASTM Int. <https://doi.org/10.1520/D4541-17.2>
3. Cai X et al (2020) Damage analysis of semi-flexible pavement material under axial compression test based on acoustic emission technique. *Constr Build Mater* 239:117773. <https://doi.org/10.1016/j.conbuildmat.2019.117773>
4. Deep P et al (2020) Evaluation of load transfer in rigid pavements by rolling wheel deflectometer and falling weight deflectometer. *Transp Res Procedia* 45(2019):376–83. <https://doi.org/10.1016/j.trpro.2020.03.029>
5. Ding Q et al (2011) The performance analysis of semi-flexible pavement by the volume parameter of matrix asphalt mixture mix design and test scheme. *Adv Mater Res* 168:351–356. <https://doi.org/10.4028/www.scientific.net/AMR.168-170.351>
6. Fang B et al (2016) Laboratory study on cement slurry formulation and its strength mechanism for semi-flexible pavement. *J Test Eval* 44(2). 907–913. <https://doi.org/10.1520/JTE20150230>
7. Gong M et al (2019) Evaluation on the cracking resistance of semi-flexible pavement mixture by laboratory research and field validation. *Constr Build Mater* 207:387–395. <https://doi.org/10.1016/j.conbuildmat.2019.02.064>
8. Hassan KE et al (2002) Effect of cementitious grouts on the properties of semi-flexible bituminous pavements. In: *Proceedings of the fourth european symposium on performance of bituminous and hydraulic materials in pavement*, pp 113–20
9. Hou S et al (2016) Investigation into engineering properties and strength mechanism of grouted macadam composite materials. *Int J Pavement Eng* 17(10):878–886. <https://doi.org/10.1080/10298436.2015.1024467>
10. IRC (2018) cement grouted bituminous mix surfacing for urban roads IRC SP 125 2019. E-Conversion—proposal for a cluster of excellence
11. Koting S et al (2007) Influence of superplasticizer type and dosage on the workability and strength of cementitious grout for semi-flexible pavement application. In: *Proceedings of the eastern asia society for transportation studies*, vol 6, pp 280–280
12. Luo S et al (2020) Open-Graded asphalt concrete grouted by latex modified cement mortar. *Road Mater Pavement Des* 21(1):61–77. <https://doi.org/10.1080/14680629.2018.1479290>
13. Mayer J, Mikael T (2001) Jointless pavements for heavy-duty airport application: the semi-flexible approach. In: *Proceedings—international air transportation conference*, pp 87–100. [https://doi.org/10.1061/40579\(271\)7](https://doi.org/10.1061/40579(271)7)
14. Moghaddam TB et al (2011) A review on fatigue and rutting performance of asphalt mixes. *Sci Res Essays* 6(4): 670–82. *Acad J*
15. Oliveira JRM (2006) Grouted macadam-material characterisation for pavement design. no. May, The University of Nottingham
16. Pei J et al (2016) Design and performance validation of high-performance cement paste as a grouting material for semi-flexible pavement. *Constr Build Mater* 126:206–217. <https://doi.org/10.1016/j.conbuildmat.2016.09.036>
17. Setyawan A (2009) Design and properties of hot mixture porous asphalt for semi-flexible pavement applications. *Media Teknik Sipil* 5(2):41–46
18. Zachariah JP et al (2020) A study on the properties of cement grouted open-graded bituminous concrete with brick as aggregates. *Constr Build Mater* 256:119436. <https://doi.org/10.1016/j.conbuildmat.2020.119436>
19. Zarei S et al (2020) Experimental analysis of semi-flexible pavement by using an appropriate cement asphalt emulsion paste. *Constr Build Mater* 230:116994. <https://doi.org/10.1016/j.conbuildmat.2019.116994>
20. Zhang J et al (2016) Formulation and performance comparison of grouting materials for semi-flexible pavement. *Constr Build Mater* 115:582–592. <https://doi.org/10.1016/j.conbuildmat.2016.04.062>

Utilization of Agro-Industrial Waste in Production of Sustainable Building Blocks



S. S. Meshram, S. P. Raut, and M. V. Madurwar

Abstract Increase in industrial waste has led to an environmental concern. Such types of waste are directly dumped on land, which can cause pollution. This waste should be used in the construction of building materials such as building blocks, which not only helps in reducing pollution but is also a cost-effective choice to design sustainable buildings. Brick is usually one of the essential construction materials, generally prepared from clay, shale, soft slate, calcium silicate, stones, etc. In view of utilizing agro-industrial waste, this study focused on the consumption of cupola slag and rice husk ash to develop sustainable building blocks. Cupola slag and rice husk ash were used in various proportions and cement is used as a binder with a constant ratio. The physicochemical properties of developed sustainable building blocks were carried out and it meets the requirements of Indian standards. The results shows that the cupola slag–cement–rice husk ash mixture can be probably used in the manufacturing of economical bricks.

Keywords Rice Husk Ash · Cupola Slag · Sustainable building blocks · Physicochemical properties

1 Introduction

Brick is a commonly used construction material across the globe. Because of its extraordinary properties such as low cost, high strength, and great durability, brick plays an important role in the construction industry [1]. Due to the continuously growing population, infrastructural needs are also increasing, which in turn increases the demand for construction materials. The application of various waste materials to develop building blocks reduces the exploitation of conventional construction

S. S. Meshram (✉) · S. P. Raut
Department of Civil Engineering, YCCE, Nagpur, India
e-mail: sangitameshram3@gmail.com

M. V. Madurwar
Department of Civil Engineering, VNIT, Nagpur, India

materials and provides a sustainable solution to the construction industry [2–9]. In India, about 960 million tons of solid wastes are currently produced annually as by-products during industrial, mining, and mining operations [10–15]. Nowadays, various industrial and agricultural wastes have been used to develop building blocks, which give sustainable solutions to the construction industry [16]. Cupola slag is a waste product manufactured by the cast iron industry, generated during the separation of the molten steel in cupola furnaces from the impurities [17]. In cupola furnaces, about 5–7% of the waste is produced during cast iron production. The industry is producing 50–3000 tons of C.I. Based on the size and specifications of the furnace [18], Cupola slag has been used as a partial replacement for cement with cupola slag in concrete [19]. Also, the behaviour of concrete was investigated using cupola slag as a partial replacement of both fine and coarse aggregate combinations in concrete [20]. Many researchers have utilized cupola slag as a replacement for cement, fine and coarse aggregates in concrete, pavement, and mortar. In addition, no research on cupola slag used in bricks is available. This can be utilized efficiently in building block manufacturing.

In this study, cupola slag as an industrial waste and a main raw material along with rice husk ash as an agricultural waste with a constant cement proportion were used. Cupola slag and rice husk ash were characterized physically and chemically to check their feasibility to be used as a raw material to develop sustainable building blocks. These developed bricks were subjected to various physicomaterial properties. This study is mainly focused on the efficient use of cupola slag to develop economical, sustainable, and high-performance building blocks which gives another solution for the management of industrial waste and pollution control.

2 Materials and Test Methods

2.1 Raw Materials and Preparation of the Brick Specimen

In this paper, cupola slag is used as industrial waste and rice husk ash as agricultural waste. Cement is used as a binding material. Though the cement percentage were kept constant while rice husk ash and cupola slag were used in different proportions to get a wide range of result. Rice husk ash is obtained when the rice husk is burned for a long time. Rice husk is a waste product obtained from rice farms. This husk can only be used for burning purposes and to generate heat. The ash obtained can only be used for ground filling purposes. Rice husk was collected from Bhandara, Maharashtra. The rice husk was dried under sunlight for 24 h. Rice husk burns slowly and hence needs time. Burning of rice husk requires 48–72 h. Out of all ash, only 30% of it was usable because ashes need to be sieved from a 300- μm sieve shown in Fig. 1. The sieved ash is used in the preparation of brick mix. Cupola slag is an industrial waste obtained from the steel industry, Kapilanshu Dhatu Udyog Pvt. Ltd., it is a pipe manufacturing factory situated in Kamthee, Nagpur. This can be only used

Fig. 1 Rice husk ash sample

for landfilling purpose. Cupola slag is a thick material containing large iron filling in it. Slag needs to be sieved before using it in bricks. It was sieved from a 1.18 mm IS sieve as given in Fig. 2. Cement was of OPC grade 53 used as a binding material. It was used in minimum percentage and constant for all proportions.

The quantity required for raw materials was first calculated for different combinations of cupola slag, rice husk ash, and cement as per the dimension of the mold as $190 \times 90 \times 90$ mm and densities of all the raw materials. As per the proportions given in Table 1, cupola slag was first dry-mixed with rice husk ash and cement. Then the water was incorporated into the dry mixture using hand mixing and resumed blending until it achieved homogeneous consistency. While casting brick, frog of dimension $140 \times 60 \times 10$ mm was cast using the same dimensioned wooden piece. Bricks (Fig. 3) were prepared using appropriate molds. Then, the bricks were set aside for sun drying for 7 days under rain protected shed.

Fig. 2 Cupola slag sample

Table 1 Mix proportions of raw materials for bricks

Mix	Cupola Slag (%)	Rice Husk Ash (%)	Cement (%)
M1	80	10	10
M2	75	15	10
M3	70	20	10
M4	65	25	10
M5	60	30	10

Fig. 3 Brick specimen

2.2 Test Methodology

The chemical constituent of raw materials has been determined using X-ray fluorescence (XRF). The elemental composition of cupola slag and rice husk ash was investigated using an XRF spectrometer (Indian Bureau of Mines, Nagpur). The specific gravity of raw materials was determined as per IS 2386 (Part III):1963 [21]. The particle size distribution of the cupola was also determined. Densities of blocks are determined as per IS 2185 (Part 1): 2005 [22]. The compressive strength test for cupola slag brick specimens (Fig. 3) was carried out according to IS 3495 (Part 1): 1992 [23]. At a uniform rate of 14 N/mm² per minute, all developed bricks were subjected to compressive load until failure occurred. Water absorption for bricks was carried out based on the weight of bricks submerged in water for 24 h and oven-dried brick specimen.

3 Results and Discussion

3.1 Properties of Raw Materials

3.1.1 Chemical Composition

Table 2 shows the chemical composition of cupola slag and rice husk ash. Cupola slag consists of a significant amount of silica and alumina, which are suitable for

Table 2 Chemical properties of the raw materials

Chemical composition	Cupola slag (CS)	Rice husk ash (RHA)
Lime, CaO (%)	15.91	1.31
Silica, SiO ₂	31.57	81.93
Alumina, AL ₂ O ₃	9.03	0.39
Iron oxide, Fe ₂ O ₃	18.58	0.35
Magnesia, MgO	1.52	0.44
Sulphur trioxide, SO ₃	0.88	0.59
Sodium Oxide, Na ₂ O	0.42	0.09
Potassium oxide, K ₂ O	0.64	0.57
Titanium Oxide, TiO ₂	1.58	0.05
Pentium Oxide, P ₂ O ₅	0.22	1.17
Fluoride ion, F	0.42	0.19
Sodium Oxide, NaO	0.42	0.09
Chloride, CL	0.06	0.57
Strontium Oxide, SrO	0.02	–
Barium Oxide, BaO	0.04	–
Magnesium dioxide, MnO ₂	0.51	0.22
Chromium trioxide, CrO ₃	0.04	–
Nickel oxide, NiO	0.01	–
Cupric oxide, CuO	0.02	–
Rubidium Oxide, Rb ₂ O	0.02	–
Loss of ignition, LOI	18.42	8.86

Table 3 Physical Properties of the cement, rice husk ash, and cupola slag

S. No.	Tests performed	Cement	Test results	
			Rice husk ash	Cupola slag
1	Specific gravity	3.15	2.19	1.36
2	Density	1440 kg/m ³	414 kg/m ³	1414.86 kg/m ³
3	Standard consistency	31%	–	–
4	Fineness	6%	15.03	–
5	Water absorption	–	9%	11.5%
6	Initial setting time	70 min	–	–
7	Final setting time	135 min	–	–

brick manufacturing. Slight amounts of calcium oxide, magnesium oxide, and iron oxides were also present in the cupola slag. A large amount of silica present in the cupola slag gives a better binding property to the brick specimen. Also, the quantity of silica present in rice husk ash is more. Calcium oxide present in cupola slag is higher as compared to rice husk ash which can contribute to pozzolanic activity. Cupola slag shows a higher loss of ignition as compared to rice husk ash which can increase the porosity of brick specimen. Rice husk ash showed fewer amounts of aluminum, calcium, and magnesium oxide.

3.1.2 Specific Gravity and Unit Weight

The specific gravities of CS and RHA were 1.36 and 2.19, respectively. CS has a comparatively lower specific gravity than RHA. The densities of CS and RHA were 1414.86 kg/m³ and 414 kg/m³, respectively, which would be able to assist in minimizing the weight of a single brick, resulting in a lighter and more economical structure. The physical properties of cement are given in Table 3.

3.1.3 Particle Size Distribution

Figure 4 shows the particle size distribution of cupola slag. It is observed that 95% of cupola slag particles were under the category of sand (Table 4). This indicates that the cupola slag particles can be used in making bricks. Only 5% of particles were comes under the category of silt. Table 4 shows there are zero particles under the category of gravel and clay.

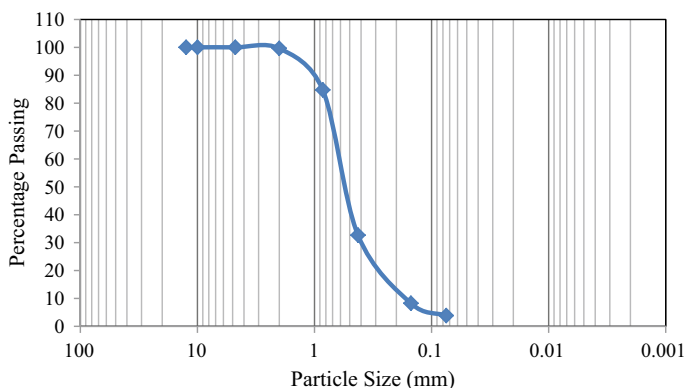


Fig. 4 Particle size distribution for cupola slag

Table 4 Cupola slag particle size distribution

Percentage distribution	Size specifications (in mm)	Cupola slag
Clay	<0.002	0
Silt	0.002–0.075	5
Sand	0.075–2	95
Gravel	>2	0

3.2 Mechanical Properties

3.2.1 Density

As per IS 2185 (Part 1):2005 [22], hollow (open and closed cavity) concrete blocks bearing units shall have a minimum block density of 1500 kg/m^3 . These can be manufactured for minimum average compressive strengths of 3.5, 4.5, 5.5, 7.0, 8.5, 10.0, 12.5, and 15.0 N/mm^2 , respectively, at 28 days. The increase in the percentage of CS in the mix resulted in a decrease in the density of bricks. The dry density decreased, that is, from 1689.9 to 1340.57 kg/m^3 by 20% as shown in Table 5 when the percentage of CS varied from 80 to 60% as per Fig. 5. This trend was observed in

Table 5 Density for brick specimens

Mix proportion	Density (kg/m^3)
M1	1689.9
M2	1646.1
M3	1540.57
M4	1450.57
M5	1340.57

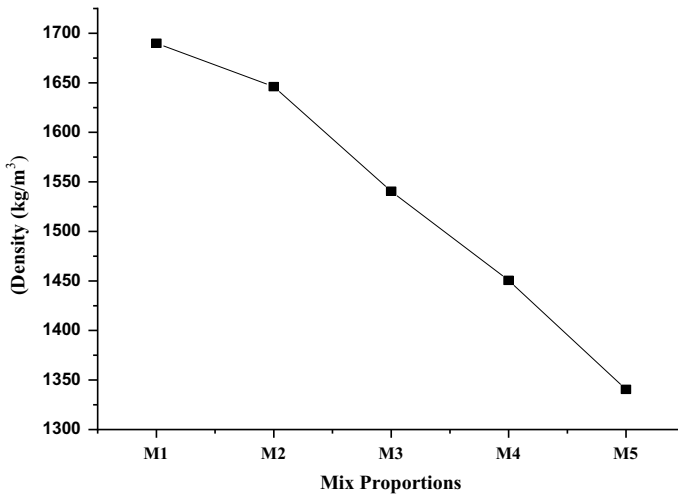


Fig. 5 Density for brick specimens

density because of the lesser density of rice husk ash and cupola slag content present in the brick mix. This was useful in producing lightweight bricks. Therefore lighter bricks were more cost-efficient, more economical, and easy for transport.

3.2.2 Water Absorption

The quality and strength of bricks are significantly impacted by the water absorption. From Fig. 6, it can be observed that after incorporating cupola slag in the brick mix, the water absorption decreases from 12 to 6% as the percentage of cupola slag decreases as per Table 6. For all combinations water absorption is less than 15% as recommended by the IS 1077:1992 [24]. This can be used for higher brick classes and values less than 20% could be used for brick classes up to 12.5. The addition of CS can, therefore, be helpful in generating masonry bricks that are more durable, economical, and eco-friendly.

3.2.3 Compressive Strength

Compressive strength is an important parameter as it gives an idea about the strength and quality of the brick. The results for all the tested bricks are shown in Fig. 7. Table 7 indicates that the compressive strength decreases from M1 to M5 mixes, which is 4.4–3.8 N/mm² with a reduction of 12.5% (Fig. 8). Maximum strength was obtained for M1 (80 CS: 10 RHA: 10 cement) proportion mix. This is due to the chemical composition of raw materials. A lesser amount of CaO present in the chemical composition leads to the higher compressive strength of brick mixes integrating cupola slag.

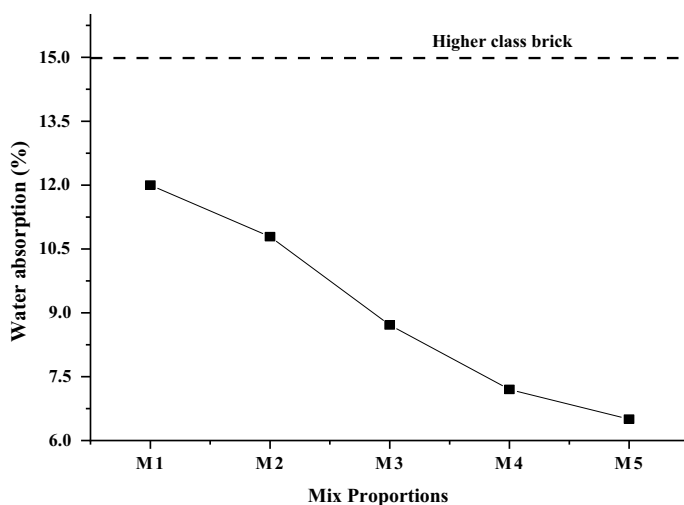


Fig. 6 Effect of CS on water absorption

Table 6 Water absorption for brick specimens

Mix proportion	Water absorption (%)
M1	12
M2	10.789
M3	8.713
M4	7.2
M5	6.5

The minimum compressive strength requirements according to the Indian standard code 1077:1992 [24] are 3.5 N/mm^2 . All brick specimens composed of cupola slag attained a compressive strength as per the IS recommendations. Also, it meets the requirements of I Class brick 4 N/mm^2 . Hence, the developed blocks can be used for eco-friendly construction.

4 Conclusion

Dumping on land and disposal of cupola slag causes land-related contamination issues that directly impact the ecosystem. Therefore, its productive use to a certain degree in the manufacture of bricks provides an alternative treatment for such problems. Cupola slag, a by-product of the cast iron manufacturing industry was used in the production of brick along with rice husk ash as agro-waste with a constant cement ratio. The presence of silica and alumina in the cupola slag shows its potential to be used in the production of sustainable building blocks. From the 5 different

Fig. 7 Compression test on brick specimen



Table 7 Compressive strength of brick specimens incorporating CS

Mix proportion	Compressive strength (N/mm ²)
M1	4.4
M2	4.2
M3	4.1
M4	3.9
M5	3.8

mixes with varying CS percentages such as 80–60%, M1 mix with 80% CS, 10% RHA, 10% cement was found to have a higher compressive strength of 4.4 N/mm². Minimum water absorption and density were obtained for brick mix M1 (60 CS: 30 RHA: 10 cement) as 6.5% and 1340.57 kg/m³, respectively. Water absorption value for all the mixes was found to be less than 20%, hence satisfying the requirements as per standards. Therefore, cupola slag can be utilized in the preparation of sustainable building blocks. Cupola slag is a waste product obtained from the iron industry that can be potentially used in making bricks. Also, it reduces its disposal and landfilling problem which ultimately helps in minimizing land pollution. Based on experimental findings, it can be recommended that CS can be used in the manufacture of large-scale building blocks with the possibility of to improve the physicommechanical properties of bricks, contributing to economical, environmentally safe, and sustainable building construction.

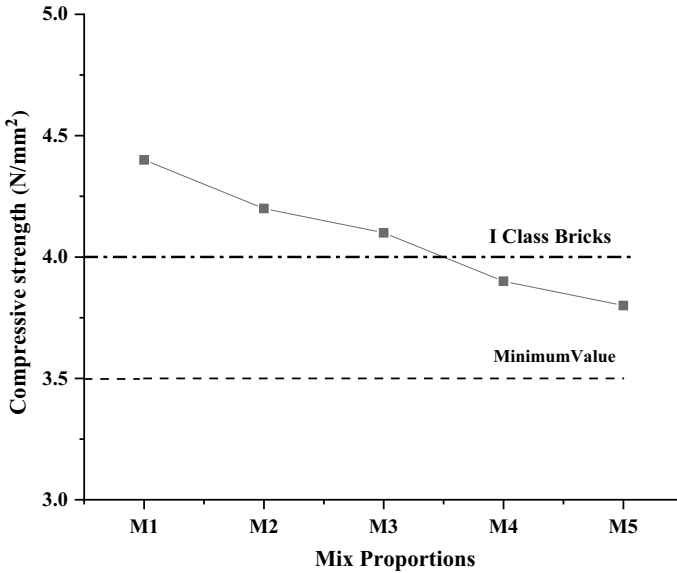


Fig. 8 Compressive strength of brick specimens incorporating CS

References

1. Zhang Z, Wong YC, Arulrajah A, Horpibulsuk S (2018) Review of studies on bricks using alternative materials and approaches. *Constr Build Mater* 188:1101–1118
2. Raut SP, Ralegaonkar RV, Mandavgane SA (2011) Development of sustainable construction material using industrial and agricultural solid waste: a review of waste-crete bricks. *Constr Build Mater* 25:4037–4042
3. Shivaprasad KN, Das BB (2018) Determination of optimized geopolymerization factors on the properties of pelletized fly ash aggregates. *Constr Build Mater* 163:428–437
4. Goudar SK, Shivaprasad KN, Das BB (2019) Mechanical properties of fiber-reinforced concrete using coal-bottom ash as replacement of fine aggregate. *Sustain Constr Build Mater Lect Notes Civil Eng* 25
5. Sharath BP, Shivaprasad KN, Athikkal MM, Das BB (2018) Some studies on sustainable utilization of iron ore tailing (IOT) as fine aggregates in fly ash based geopolymer mortar. In: *IOP conference: series, material science an engineering*, vol 431, p 092010
6. Prasanna KM et al (2021) Fast setting steel fibre geopolymer mortar cured under ambient temperature. In: *Recent developments in sustainable infrastructure*. Springer, Singapore, 769–787
7. Prasanna KM, Tamboli S, Das BB (2021) Characterization of mechanical and microstructural properties of FA and GGBS-Based geopolymer mortar cured in ambient condition. In: *Recent developments in sustainable infrastructure*. Springer, Singapore, pp 751–768
8. Goudar SK, Das BB, Arya SB (2019) Microstructural study of steel-concrete interface and its influence on bond strength of reinforced concrete. *Adv Civil Eng Mater* 8(1):171–189
9. Goudar SK et al (2020) Influence of sample preparation techniques on microstructure and nano-mechanical properties of steel-concrete interface. *Constr Build Mater* 256:119242
10. Shivaprasad KN, Das BB (2017) Influence of alkali binder dosage on the efficiency of pelletization of aggregates from iron ore tailing and fly ash. *Int J Eng Res Mechan Civil Eng* 2(3):388–392

11. Shivaprasad KN, Das BB, Sharath SP (2020) Pelletisation factors on the production of fly-ash aggregates and its performance in concrete. In: Proceedings of the institution of civil engineers, construction materials, pp 1–20
12. Sharath BP, Das BB (2021) Production of artificial aggregates using industrial by-products admixed with mine tailings—a sustainable solution. In: Recent trends in civil engineering. Lecture Notes in Civil Engineering, vol 105, pp 383–397
13. Sumukh EP, Goudar SK, Das BB (2021) A review on the properties of steel-concrete interface and characterization methods. *Smart Technol Sustain Dev* 167–203
14. Sumukh EP, Goudar SK, Das BB (2021) Predicting the service life of reinforced concrete by incorporating the experimentally determined properties of steel–concrete interface and corrosion. *Recent Trends Civil Eng* 399–417
15. Pappu A, Saxena M, Asolekar (2007) Solid wastes generation in India and their recycling potential in building materials. *J Build Environ* 42:2311–232
16. Bories C, Borredon M, Vedrenne E, Vilarem G (2014) Development of eco-friendly porous fired clay bricks using pore-forming agents: a review. *J Environ Manage* 143:186–196
17. Balaraman R, Anne Ligoria S (2015) Utilization of cupola slag in concrete as fine and coarse aggregate. *Int J Civil Eng Technol (IJCIET)* 6(8):06–14
18. Mistry VK, Patel BR, Varia DJ (2016) Suitability of concrete using cupola slag as replacement of coarse aggregate. *Int J Sci Eng Res* 7(2)
19. Afolayan JO, Alabi SA (2013) Investigation on the potentials of cupola furnace slag in concrete. *Int J Integr Eng* 5:59–62
20. Balaraman R, NS Elangovan (2018) Behaviour of cupola slag in concrete as partial replacement with a combination of fine and coarse aggregates
21. IS 2386 (Part III): 1963—Methods of tests for aggregate of concrete
22. IS 2185(Part 1): 2005—Concrete Masonry Units- Specification
23. IS 3495 (Part 1): 1992—Methods of tests of Burnt Clay Building bricks
24. IS 1077: 1992—Common Burnt Clay Building Bricks—Specification

Effect of Exposure Condition, Free Water–cement Ratio on Quantities, Rheological and Mechanical Properties of Concrete



Mahesh Navnath Patil and Shailendra Kumar Damodar Dubey

Abstract This research paper explores the effects of environmental exposure conditions, water/cement ratio and cement content on the rheological and mechanical properties of concrete. Even though the grade of concrete is identical, environmental exposure conditions with respect to water–cement ratio significantly controls the quantities of ingredients of concrete. Properties of fresh concrete such as slump value and compaction factor are changing with respect to cement content. It is possible to determine relations between them. Experimentation had been carried out under different water–cement ratios (0.3, 0.36, 0.4, 0.45 and 0.5) with and without the use of chemical admixture to establish graphical relationships. Mechanical properties are determined with respect to age and the effect of admixture. Suggested fresh concrete relations are quite suitable for concretes with and without utilization of chemical admixtures. Workability of concrete depends upon the dose of chemical admixtures such as superplasticizer and time-period after mixing of all ingredients of concrete. Sincere effort had been made to establish the relationship among slump loss, time-period after mixing and dosage of ingredients for different water–cement ratios through graphical representation. Relationship among water–cement ratio, quantity of cement per cubic meter, slump in mm and compaction factor are determined. The quantity of ingredients with respect to various environmental exposure conditions with and without chemical admixture is presented graphically. It was observed that slump values versus cement content and compaction factor show linear variation. Experiments show desired compressive strength couldn't be achieved without superplasticizer in case of higher grade concrete.

Keywords Environmental exposure condition · Water/cement ratio · Rheological and mechanical properties of concrete · Slump · Compacting factor

M. N. Patil (✉)

Research Scholar, Kavyitri Bahinabai Chaudhari North Maharashtra University, Jalgaon, India
e-mail: m.patil123@gmail.com

S. K. D. Dubey

Professor and Head of the Civil Engineering Department SSVPS BSD COE, Dhule, India
e-mail: dubey.dhule@gmail.com

1 Introduction

Workability defines the properties and behaviour of freshly mixed concrete. Consistency plays a vital role and defines the criteria in the concrete mix design. It affects the behaviour of concrete starting from placing to the hardened stage concrete.

The properties of concrete workability, consistency and finishing ability of concrete are difficult to measure, as they do not have any quantitative measurement. The slump cone test and compact factor test give a general idea of workability of concrete. The slump cone test is most widely used on site. The compaction factor test defines the compacting ability and finishing ability of fresh concrete [1]. Consistency and cohesiveness measure the finishing and compacting ability of concrete. Consistency represents the flowing ability of freshly mixed concrete. It is a measure of the wetness of the fresh concrete. The requirement of workability depends on the type of construction, method of placement, moulding shape of formwork and structural design [2].

Setting of concrete defines the transition between a fluid and a solid state of concrete. Period of setting starts when concrete loses its plasticity and is complete when concrete gain enough strength to withstand with self-weight and superimposed load [3]. The process of gaining strength is a continuous process later leading to a hardening stage [4]. Rheological properties of concrete change with respect to the initial and final setting time of concrete. Workability decreases with respect to time continuously. Energy consumption increases continuously in subsequent stages.

This study focuses on the effect of environmental exposure conditions; water–cement ratio on the quantity and properties of fresh concrete, which is still a topic of research. Mild, moderate, severe, very severe, extreme exposure are five environmental exposure conditions given in the guidelines of IS 456:2000. The water–cement ratios considered in this study are 0.3, 0.36, 0.4, 0.45, 0.5, 0.55 and 0.6. The slump test and compaction factor test are the indicators of workability. The workability of concrete very much depends upon the dose of superplasticizer and the time-period after mixing of all ingredients of concrete [5]. In this study, polycarboxylic ether polymer-based FOSROCK plasticizer is used. Efforts had been taken to establish the relationship between slump loss, time period after mixing and dosage of ingredients for different water–cement ratios through graphical representation. Workability of concrete decreases with a decrease in compaction factor. Relation between water–cement ratios, quantity of cement per cubic meter, slump in mm and compaction factor established through graphical representation with various environmental exposure conditions with and without the addition of superplasticizer.

Compressive strength is a performance indicator of concrete. In this study, experimental work was carried out to notice the optimum water–cement ratio for M40 grade concrete through crushing strength. Extreme environmental exposure condition is considered for mix design. Five different water–cement ratios of 0.3, 0.36, 0.4, 0.45, and 0.5 are used. Experimentation is carried out with and without a superplasticizer. The variation of compressive strength and failure load with and without plasticizer is shown graphically [6, 7].

2 Material Properties

The cement used is the Portland Pozzolana Cement (PPC) manufactured by Ambuja Cement Ltd. (Unit: Maratha Cement Works) confirming requirements as per IS: 1489 (Part1):2015 [8]. PPC cement used is blended with 32% of fly ash. The specific gravity of cement and bulk density of cement was determined experimentally and it was 2.76 and 1493.3 kg/m³, respectively. The fine aggregate used is natural sand which passes over a 4.75 mm IS sieve, confirming to zone-I as per IS 383: 2016. It is clean and free from impurities with specific gravity of 2.52 and bulk density of 1900 kg/m³. Coarse aggregate used is a natural stone retaining on 4.75 mm IS sieve and passing from 20 mm IS sieve as per IS 383: 2016 with specific gravity 2.88 and bulk density 1710 kg/m³. Laboratory pan mixer of capacity 40 L was used to make the mixture. Technical specification of cement, superplasticizer, standard deviation, water content per cubic metre of concrete, proportionate volume of coarse aggregates tabulated below are essential for mix design as per IS 10262:2019 [9]. Potable water free from impurities as per the Indian Standard Code of practice used for mixing and curing of concrete specimens [7]. Superplasticizer is used to increase workability without affecting the strength of the concrete and without the use of additional water. High-range water reducing admixture under the brand name Auramix 200 manufactured by Fosroc was used. The vibrating table is used for compacting fresh concrete mix for a time-period of 1 min (Tables 1, 2, 3, 4, 5 and 6).

Table 1 Standard deviation (IS 10262:2019)

S. No	Grade	Assumed Standard Deviation
1	M10	3.5
2	M15	3.5
3	M20	4
4	M25	4
5	M30	5
6	M35	5
7	M40	5
8	M45	5
9	M50	5
10	M55	5
11	M60	5
12	M65	6
13	M70	6
14	M75	6
15	M80	6

Table 2 Water content per cubic metre of concrete (IS 10262:2019)

S. No	Size of aggregates	Water content
1	10	208
2	20	186
3	40	165

Table 3 Cement content per cubic metre of concrete (IS 10262:2019)

Exposure	W/C ratio		Cement Content R.C.C.(kg)
	PCC	RCC	
Extreme	0.4	0.4	360
Mild	0.6	0.55	300
Moderate	0.6	0.5	300
Severe	0.5	0.45	320
Very Severe	0.45	0.45	340

3 Environmental Exposure Conditions

In this study, the quantities of ingredients of concrete were calculated according to the norms given in IS 10262:2019. Environmental exposure conditions, water–cement ratio, and use of chemical admixtures such as superplasticizer affect the quantity of ingredients in concrete. Five different environmental exposure conditions are tabulated in Table 15 with reference to IS 456:2000 (Table 7).

Seven different water–cement ratios 0.3, 0.36, 0.4, 0.45, 0.5, 0.55, 0.6 were tried. The quantity of material (cubic metre) in different environmental exposure conditions along with the effect of admixture is represented graphically as below (Figs. 1, 2, 3, 4, 5, 6, 7, 8, 9, 10, 11, 12, 13 and 14).

4 Workability of Concrete

Workability describes the ease with which a fresh concrete can be assorted, placed, consolidated, and finished with the least loss in the consistency of concrete. Workability is one of the crucial properties of concrete, which has a direct impact on the quality of concrete in terms of compressive strength, placement and finishing operation.

4.1 Factors Affecting Workability

Properties, characteristics, proportion of raw material, admixture used in concrete and environmental exposure made an impact on workability and other properties of

Table 4 Technical specification of cement used (as provided by the manufacturer) [8, 10, 11]

S. No.	Characteristic	Requirement as per IS: 1489 (Part-I):2015	Test results
<i>1.0 Chemical requirements (Clause 6)</i>			
1.1	Insoluble residue (%)		28.90
	a.Maximum	$X + \frac{4.0(100-X)}{100}$	
	b.Minimum	0.6 X (where X is the declared percentage of fly ash in the given PPC)	
1.2	Magnesia (%)	6.0 (Max)	1.19
1.3	Total sulphur as SO ₃ %	3.5 (Max)	2.02
1.4	Loss on ignition %	5.0 (Max)	1.47
1.5	Chloride content	0.1 (Max)	0.010
		0.05 (Max.) for prestressed Structure	
<i>2.0 Physical requirements (Clause 7)</i>			
2.1	Fineness (m ² /kg)	300 Min	367
2.2	Soundness		
2.2.1	By Le Chatelier method (mm)	10 (Max)	1
2.2.2	By auto calve test method (%)	0.8 (Max)	0.02
2.3	Setting time		
2.3.1	Initial (Minutes)	30 (Min)	190
2.3.2	Final (Minutes)	600 (Max)	260
2.4	Compressive strength in Mpa		
2.4.1	72 + - 1 h (3 Days)	16 (Min)	29.8
2.4.2	168 + - 2 h (7 Days)	22 (Min)	40.0
2.4.3	672 + - 4 h (28 Days)	33 (Min)	60.0
2.5	Drying Shrinkage (%)	0.15 (Max)	0.06

Table 5 Technical specification of superplasticizer used

Base	Appearance	Density	pH value	Chloride content	Air entrainment	Compatibility
Polycarboxylic ether polymer	Light brown liquid	1.07 + -0.02 kg/lit	6	Nil	Nil	All types of Portland cement

concrete. Some of the factors affecting the workability of concrete are enlisted and described below.

Table 6 Proportionate volume of coarse aggregates (IS 10262:2019)

S. No.	Size of aggregate	Volume of coarse aggregates/total volume for Different Zones of Fine Aggregates			
		Zone-I	Zone-II	Zone-III	Zone-IV
1	10	0.48	0.50	0.52	0.54
2	20	0.60	0.62	0.64	0.66
3	40	0.69	0.71	0.72	0.73

Table 7 Environmental exposure conditions given in IS456:2000 [12]

S. No.	Environment	Exposure condition
1	Mild	Concrete surfaces are protected against weather or aggressive conditions, except for those situated in the coastal area
2	Moderate	Concrete surfaces sheltered from severe rain or freezing whilst wet. Concrete exposed to condensation and rain Concrete continuously under water. Concrete in contact or buried under non-aggressive soil/groundwater. Concrete surfaces sheltered from saturated salt air in the coastal area
3	Severe	Concrete surfaces exposed to severe rain, alternate wetting and drying or occasional freezing whilst wet or severe condensation. Concrete completely immersed in seawater. Concrete exposed to the coastal environment
4	Very severe	Concrete surfaces exposed to seawater spray, corrosive fumes or severe freezing conditions whilst wet. Concrete in contact with or buried under aggressive sub-soil/groundwater
5	Extreme	Surface of members in the tidal zone. Members in direct contact with liquid/solid aggressive chemicals

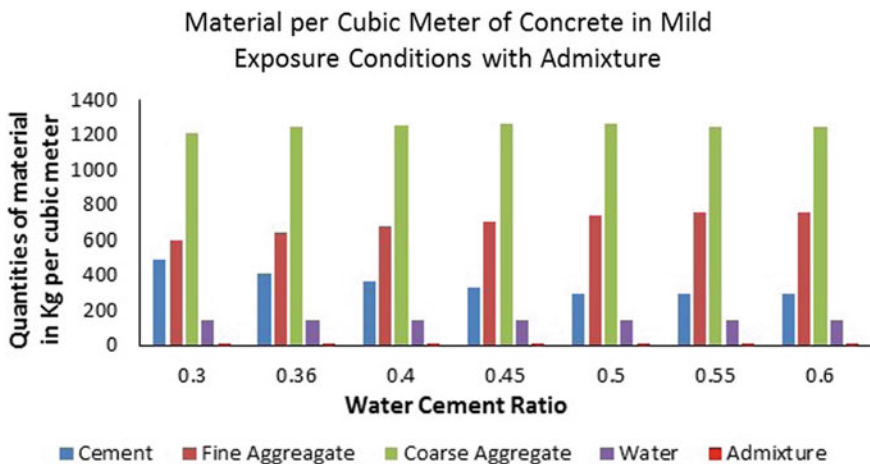


Fig. 1 Quantities of material per cubic material in mild exposure condition with admixture

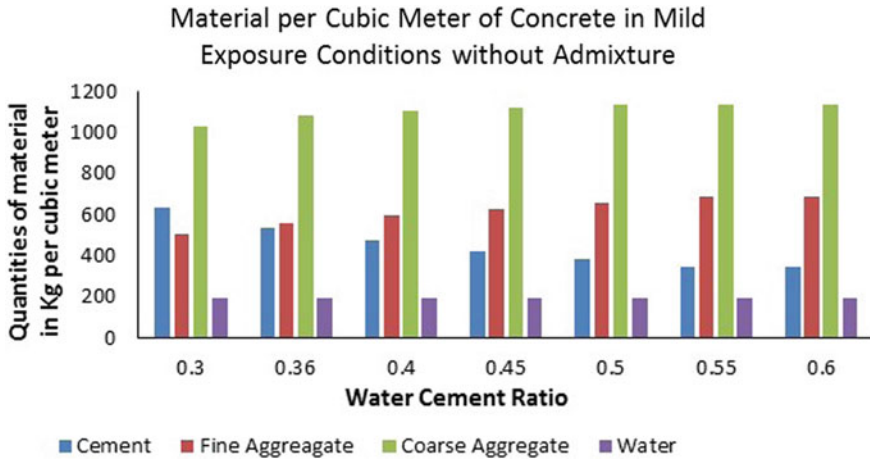


Fig. 2 Quantities of material per cubic material in mild exposure condition without admixture

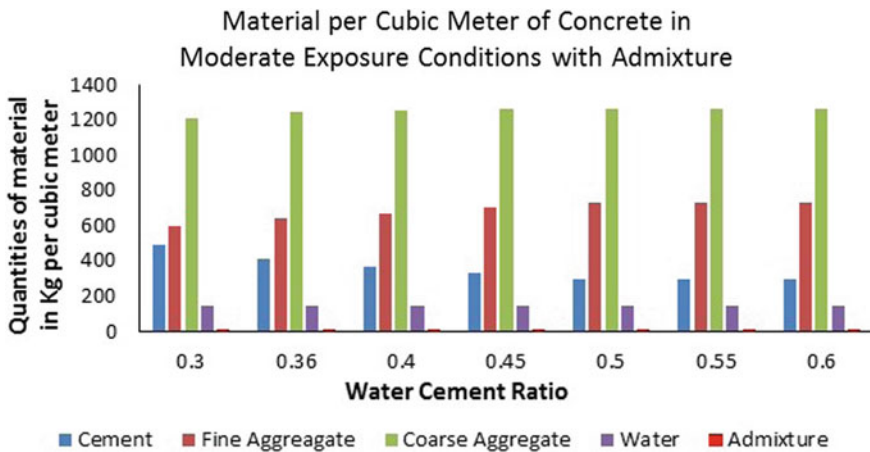


Fig. 3 Quantities of material per cubic material in moderate exposure condition with admixture

4.1.1 Water–Cement Ratio

Water–cement ratio has an impact on the compressive strength and durability of the concrete. A higher quantity of cement with a judicious amount of water during mix design reflects the desirable strength. Paste of cement and water forms coating over the surface of aggregate results in appropriate consolidated finishing. Insufficient quantity of water in concrete cannot fulfil the requirement of cement for the hydration process.

It may result in poor compressive strength. Lesser quantity of water also resists workability due to which, placement and finishing of concrete are affected. Vice

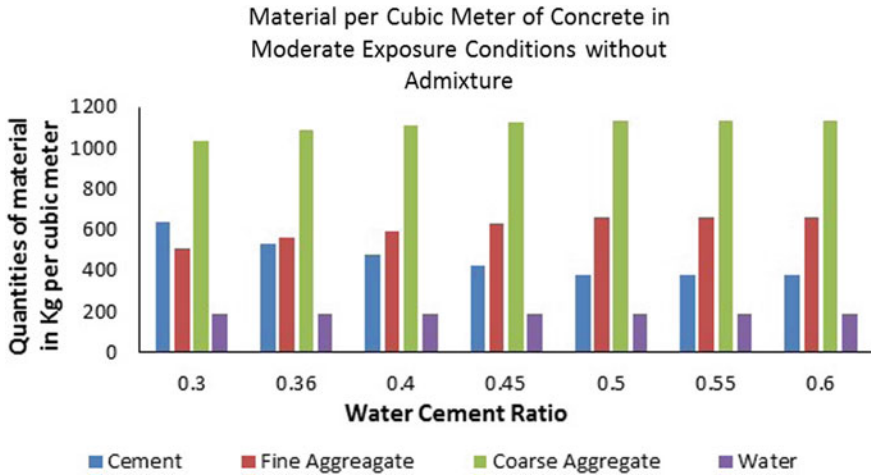


Fig. 4 Quantities of material per cubic material in moderate exposure condition without admixture

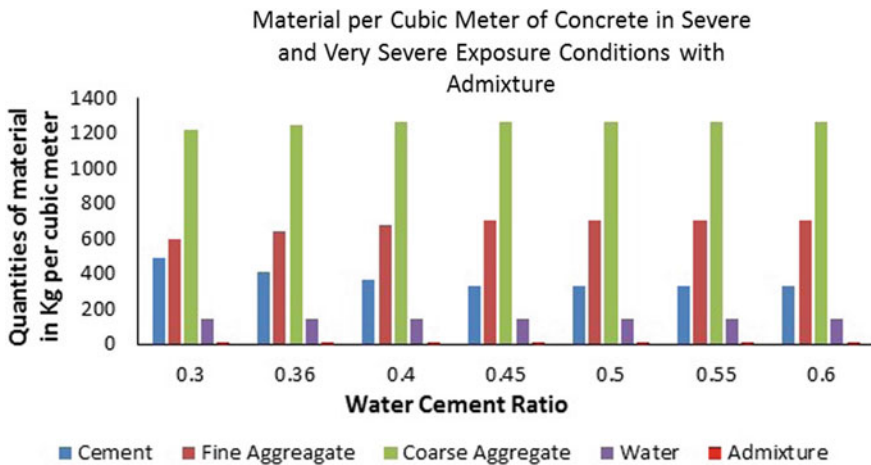


Fig. 5 Quantities of material per cubic material in severe/very severe exposure with admixture

versa due to the excessive amount of water, workability increases but it may result in segregation and weaker concrete. The water–cement ratio should be selected as per the guidelines given in IS 456:2000 and IS 10262:2019 considering the desired strength and environmental exposure conditions.

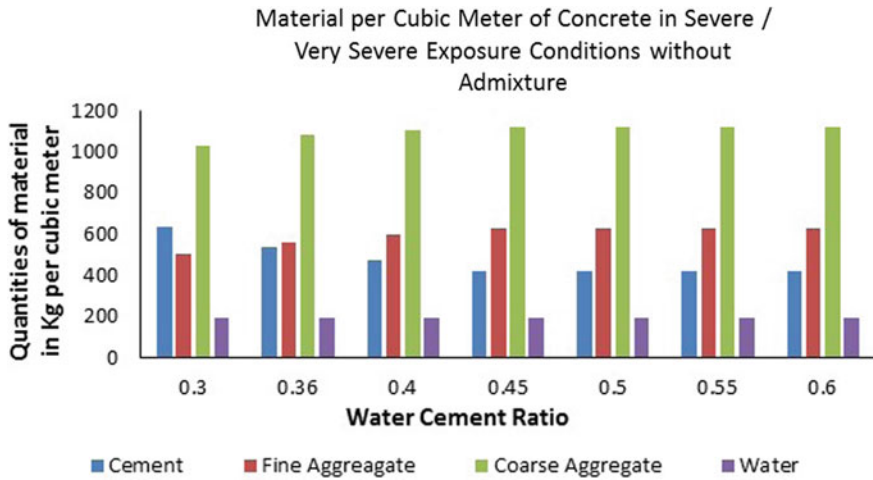


Fig. 6 Quantities of material per cubic material in extreme exposure condition without admixture

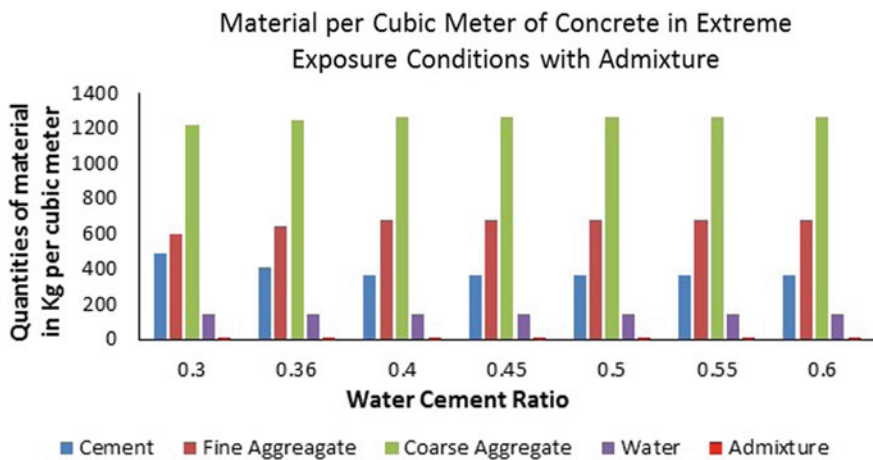


Fig. 7 Quantities of material per cubic material in extreme exposure condition with admixture

4.1.2 Size and Shape of Aggregate

IS 383:2016 provides guidelines for coarse and fine aggregate of concrete. Larger size aggregates need more cement paste to cover the whole surface as compared to smaller size aggregates. According to IS 383:2016 and IS 456:2000, elongated, flaky and angular aggregates should be avoided due to larger surface area. Circular and rounded particles are also avoided. Though rounded aggregate has a smaller surface area, due to shape, aggregate interlocking cannot be attained. It invariably affects the

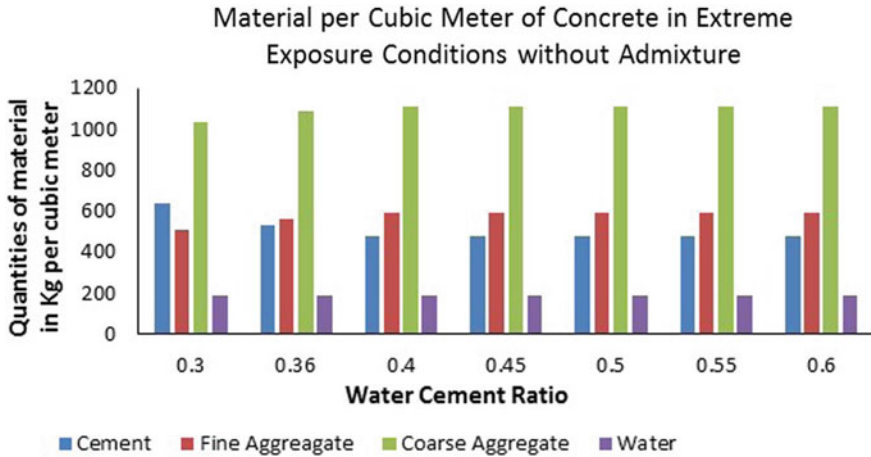


Fig. 8 Quantities of material per cubic material in severe/very severe exposure without admixture

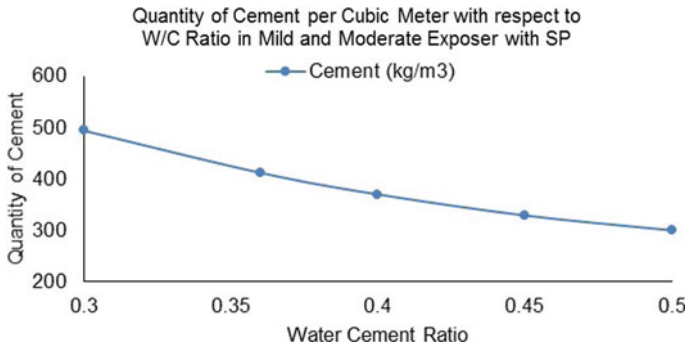


Fig. 9 Quantification of cement per cubic meter for different w/c ratio at mild and moderate exposer condition with use of SP

strength parameters. Crushed stone aggregates with proper size proportion provide better bond as well as workable concrete [12, 13].

4.1.3 Admixtures

Admixtures like superplasticizers make concrete workable by reducing adhesion between cement and aggregate particles. Plasticizers make the concrete flowable without affecting the strength characteristics of concrete [14].

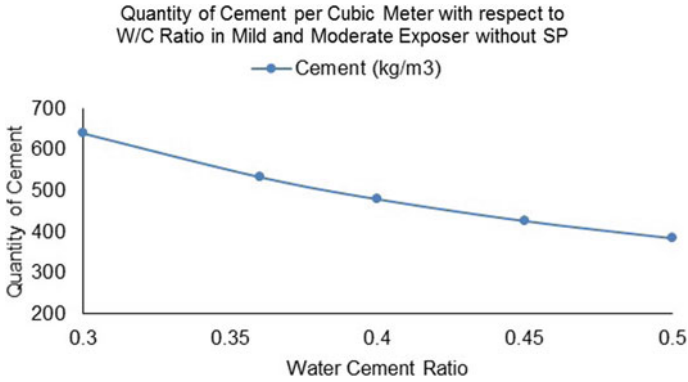


Fig. 10 Quantification of cement per cubic metre for different water/cement ratios at mild and moderate exposure condition without use of SP

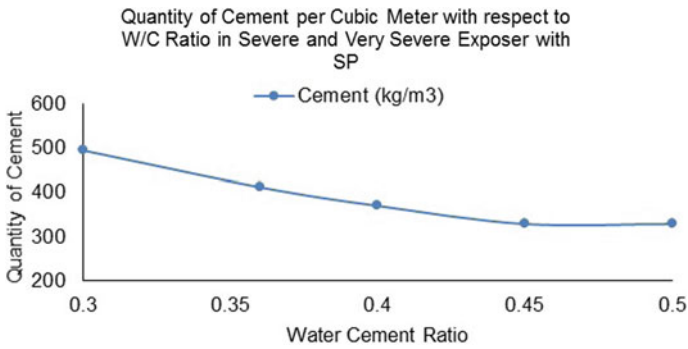


Fig. 11 Quantification of cement per cubic metre for different water/cement ratios at severe and very severe exposure condition with SP

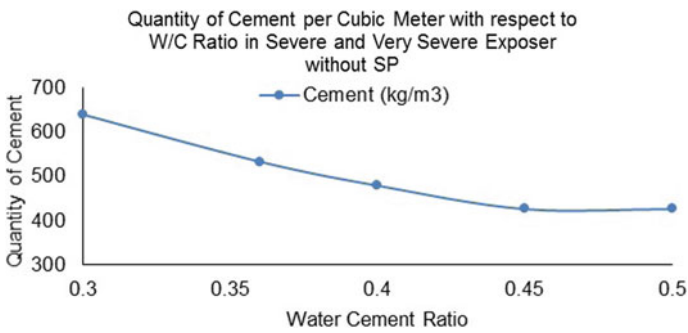


Fig. 12 Quantification of cement per cubic metre for different water/cement ratios at severe and very severe exposure condition without SP

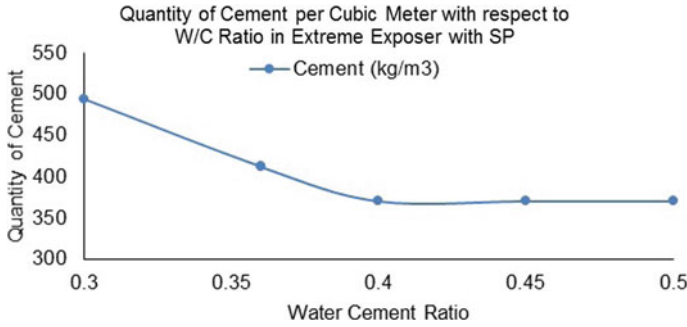


Fig. 13 Quantification of cement per cubic metre for different water/cement ratios at extreme exposure condition with SP

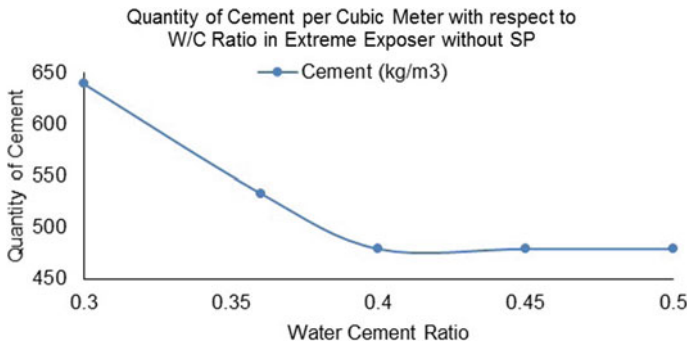


Fig. 14 Quantification of cement per cubic metre for different weight/cement ratios at extreme exposure condition with SP

4.2 Slump Cone Test

Slump cone test is a popular measure of workability. The consistency of fresh concrete can be measured before it sets. It is carried out as per the guidelines given in IS 1199-1959 (Fig. 15).

Slump cone test can be performed with the help of a slump cone (Abrams cone). Based on the profile of concrete, the slump is classified into the following three types.

1	Collapse Slump	Concrete gets collapsed completely. It indicates that the concrete is too wet and highly workable
2	Shear Slump	Concrete gets slipped off from the sides. It indicates a lack of cohesion in concrete, possibility of bleeding, and segregation of concrete. So not desirable for the strength and durability of concrete
3	True Slump	The whole mass of concrete slipped off evenly without any collapse or shear off. It is the desirable slump

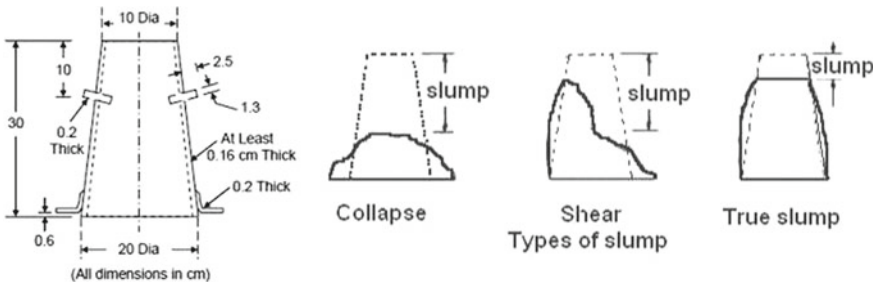


Fig. 15 Dimensions of slump cone and types of slump (35)

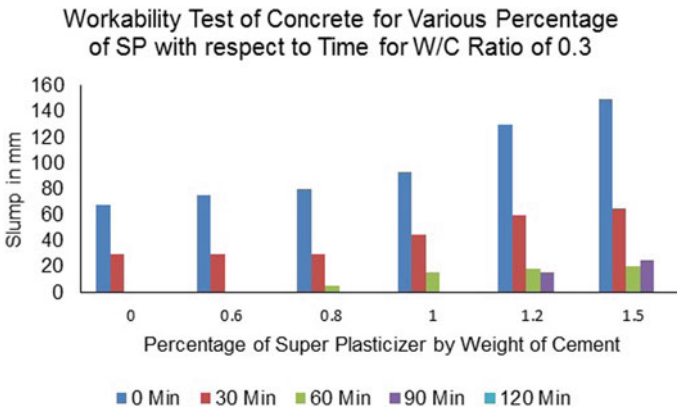


Fig. 16 Workability test of concrete for various % of SP with respect to time for water/cement ratio of 0.3

4.2.1 Slump Loss Variation According to Time

Polycarboxylic ether polymer-based FOSROCK plasticizer was used in this study. Technical specifications are given in Table 5. The workability of concrete depends upon the dose of superplasticizer and time period after mixing of all ingredients of concrete. Sincere effort had been made to establish a relationship among slump loss, time period after mixing, and dosage of ingredients for different water–cement ratios through graphical representation (Figs. 16, 17, 18, 19 and 20).

4.3 Compaction Factor Test

It is a laboratory/field test used to check the workability of concrete. This test is preferred for medium to low workable concrete. It is carried out as per the guidelines of IS 1199-1959. It is more precise and accurate than the slump cone test. Compaction

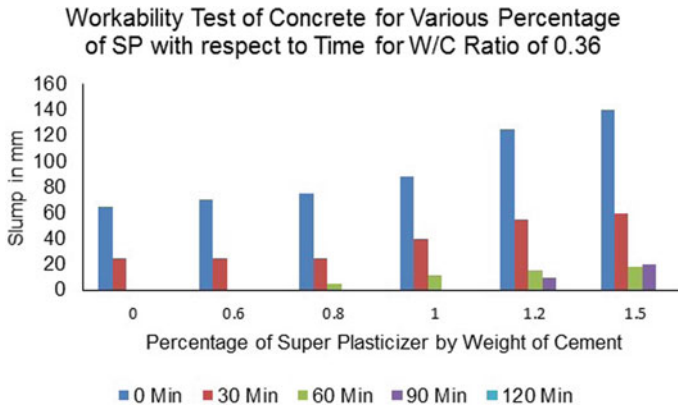


Fig. 17 Workability test of concrete for various % of SP with respect to time for water/cement ratio of 0.36

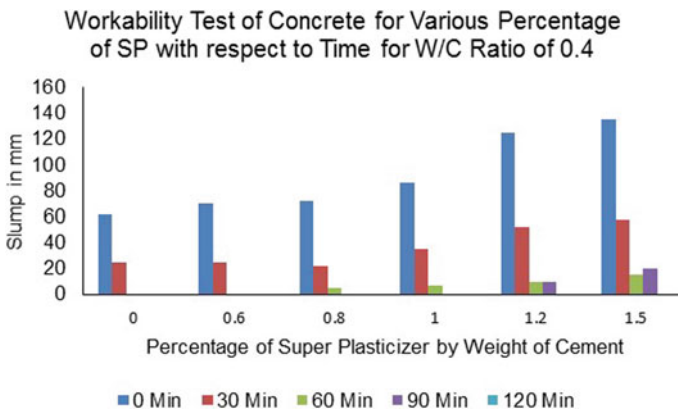


Fig. 18 Workability test of concrete for various % of SP with respect to time for water/cement ratio of 0.4

factor is the ratio of the weight of semi-compacted concrete to fully compacted concrete. Workability of concrete decreases with a decrease in compaction factor. This study represents the relationship among water–cement ratio, quantity of cement per cubic meter, slump in mm and compaction factor through graphical representation with various environmental exposure conditions with and without the addition of superplasticizer (Figs. 21, 22, 23, 24, 25, 26, 27, 28, 29, 30, 31, 32 and 33).

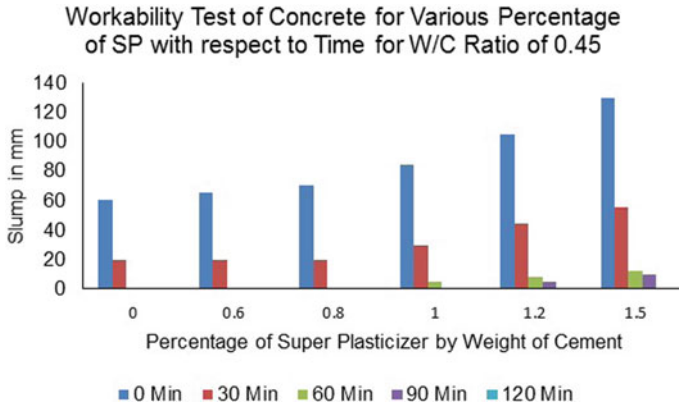


Fig. 19 Workability test of concrete for various % of SP with respect to time for water/cement ratio of 0.45

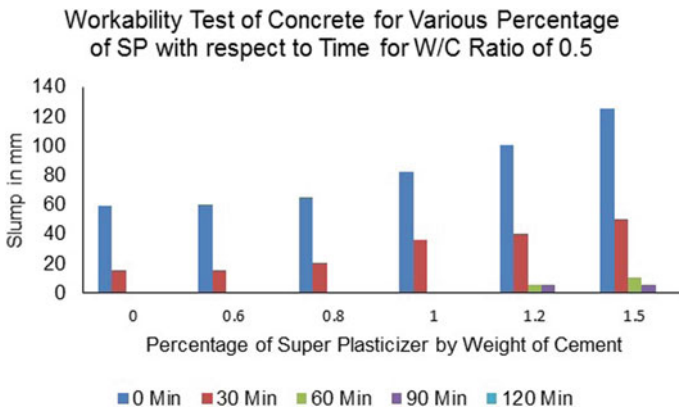


Fig. 20 Workability test of concrete for various % of SP with respect to time for water/cement ratio of 0.5

5 Compressive Strength of Concrete

Compressive strength is a performance indicator of concrete. The test was performed as per the guidelines of IS 516:1959. Depending upon environmental exposure conditions, mechanical properties and durability requirements, concrete mix design are carried out to achieve the desired compressive strength. Compressive strength of concrete is the characteristic strength of a concrete cube of 15 cm size measured after 28 days.

Fig. 21 Compaction factor test on concrete (36)

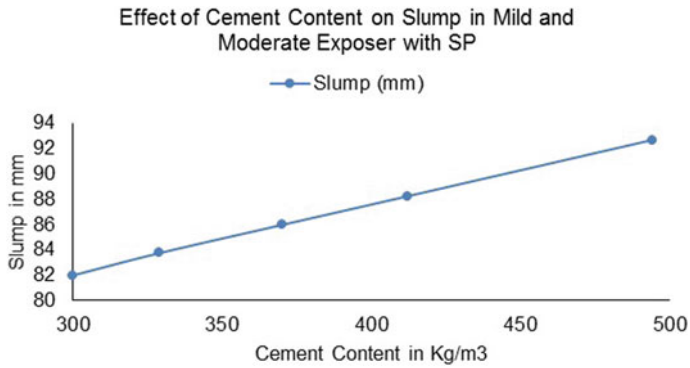
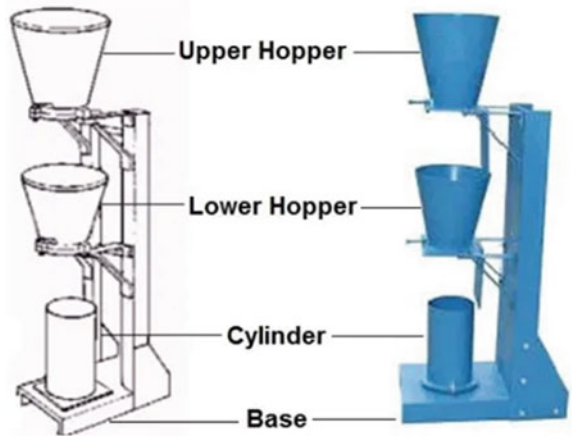


Fig. 22 Effect of cement content on slump in mild and moderate exposure condition with Super Plasticizer

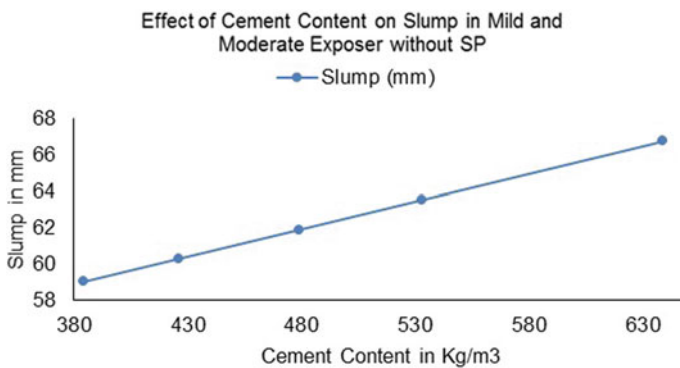


Fig. 23 Effect of cement content on slump in mild and moderate exposure condition without Super Plasticizer

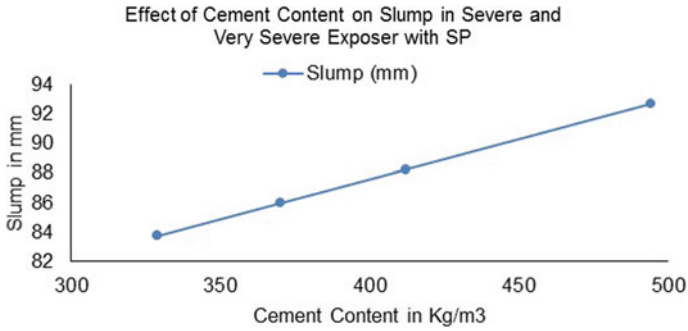


Fig. 24 Effect of cement content on slump severe and very severe exposure condition with Super Plasticizer

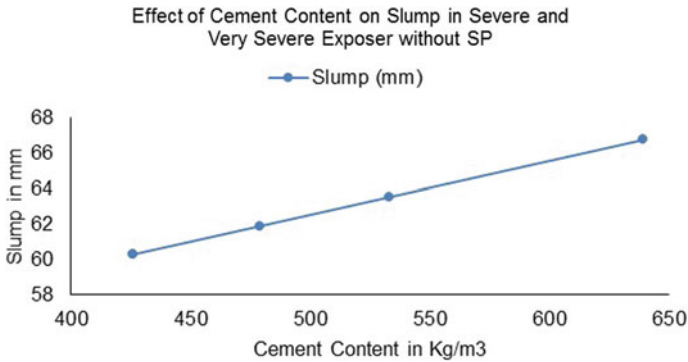


Fig. 25 Variation of failure load with respect to age of concrete at different water/cement ratios without Super Plasticizer

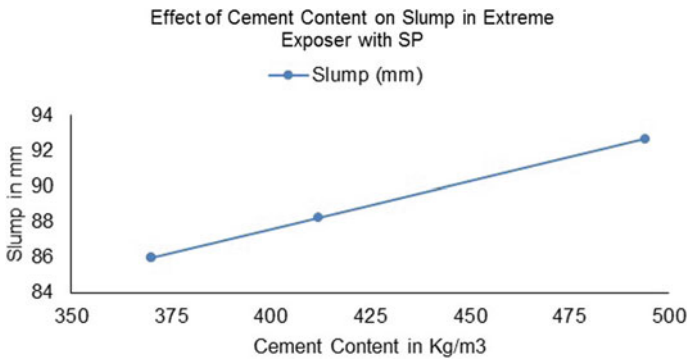


Fig. 26 Effect of cement content on slump in extreme exposure condition with Super Plasticizer

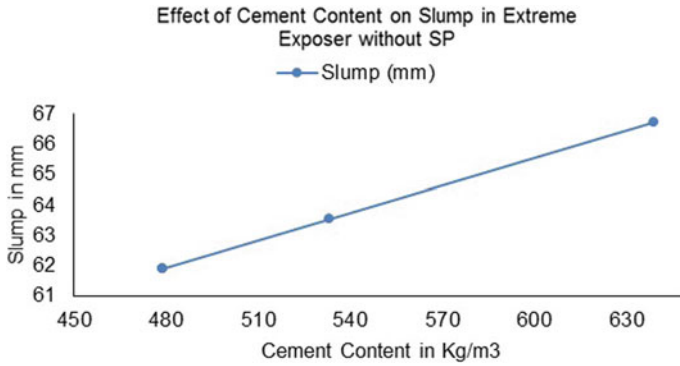


Fig. 27 Effect of cement content on compaction factor in extreme exposure condition without Super Plasticizer

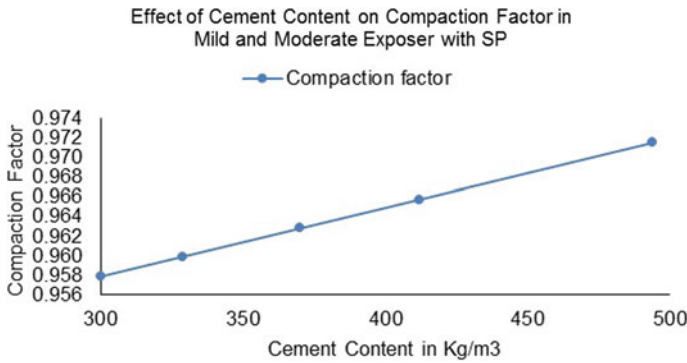


Fig. 28 Effect of cement content on compaction factor in mild and moderate exposure condition with Super Plasticizer

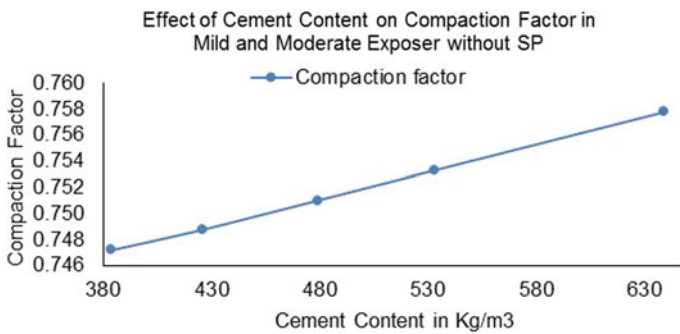


Fig. 29 Effect of cement content on compaction factor in mild and moderate exposure condition without Super Plasticizer

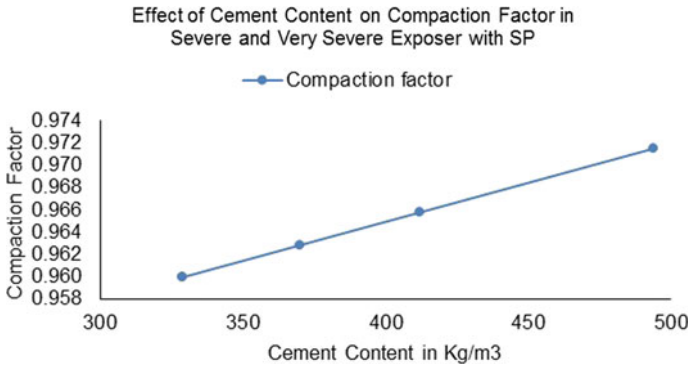


Fig. 30 Effect of cement content on compaction factor in severe and very severe exposure condition with Super Plasticizer

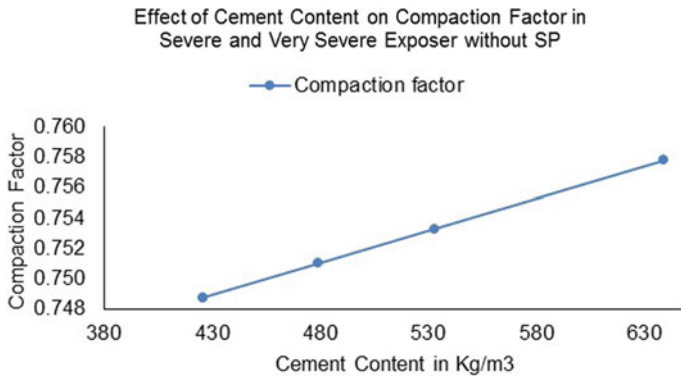


Fig. 31 Effect of cement content on compaction factor in severe and very severe exposure condition without Super Plasticizer

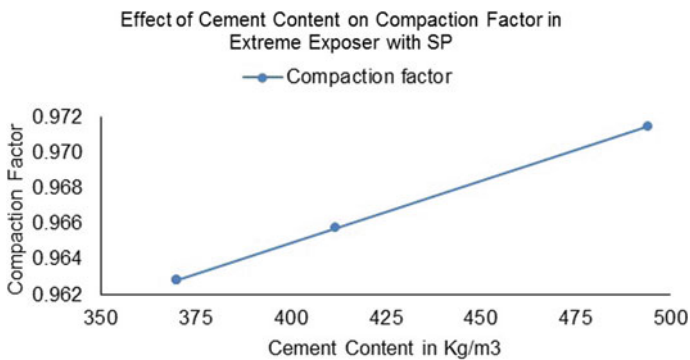


Fig. 32 Effect of cement content on compaction factor in extreme exposure condition with Super Plasticizer

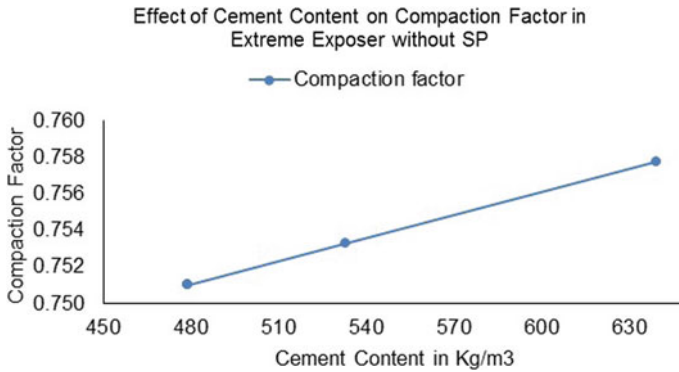


Fig. 33 Effect of cement content on compaction factor in extreme exposure condition with Super Plasticizer

In this study, experimental work was carried out to notice the optimum water-cement ratio for M40 grade concrete through crushing strength. Extreme environmental exposure condition was considered for mix design. Five different water-cement ratios of 0.3, 0.36, 0.4, 0.45, and 0.5 were used. Experimentation was carried out with and without a superplasticizer. The variation of compressive strength and failure load with and without plasticizer was shown through graphical representation (Figs. 34, 35, 36 and 37).

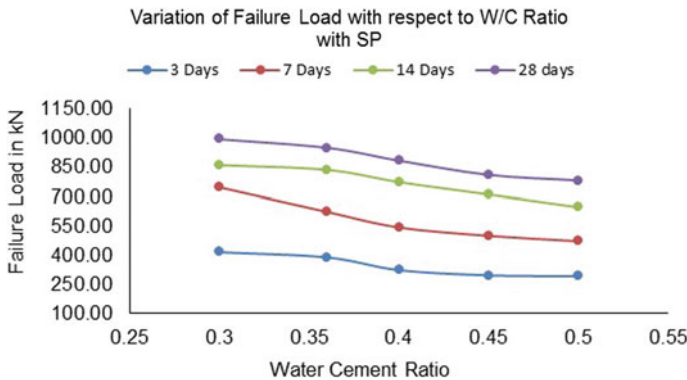


Fig. 34 Variation of failure load with respect to age of concrete at different w/c ratio with use of Super Plasticizer

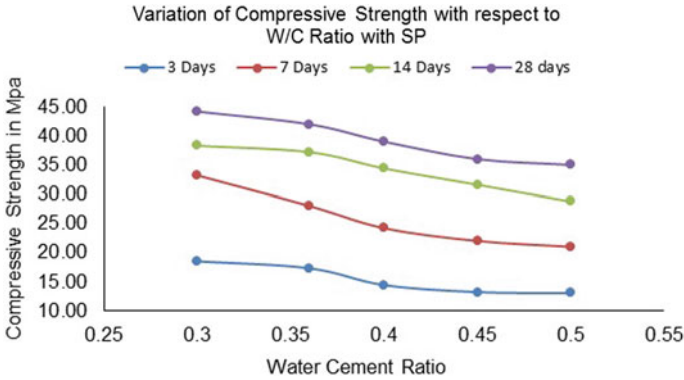


Fig. 35 Variation of compressive strength with respect to age of concrete at different w/c ratio with Super Plasticizer

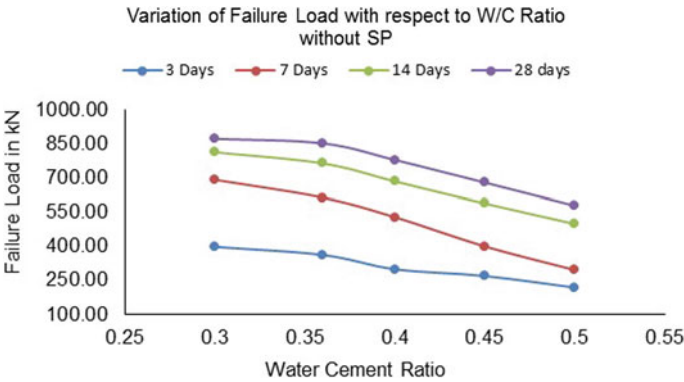


Fig. 36 Effect of cement content on slump severe and very severe exposure condition without Super Plasticizer

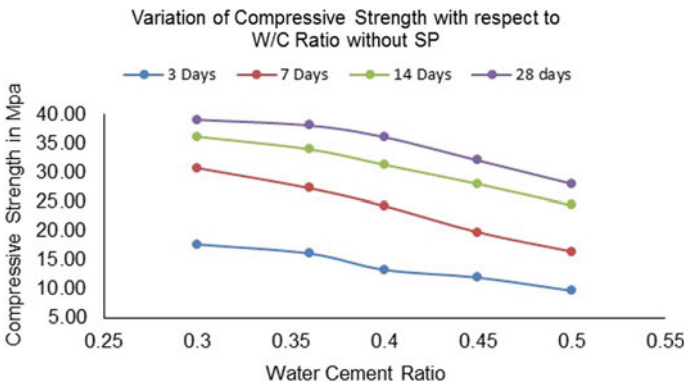


Fig. 37 Variation of failure load with respect to age of concrete at different w/c ratio without using Super Plasticizer

6 Result and Discussion

In the present study, a series of testing had been carried out to investigate the rheological and mechanical properties of M40 grade concrete. As per IS 456:2000, the minimum grade of concrete for extreme exposure is M40. M40 grade standard concrete was considered for experimentation. The following conclusions are drawn based on the experimental results and guidelines of IS code [12].

1. Maximum free water–cement ratio for reinforced concrete structures with mild, moderate, severe, very severe and extreme environmental exposure condition are 0.55, 0.50, 0.45, 0.45 and 0.40, respectively.
2. Improvement in the workability of concrete is observed with the addition of superplasticizer. However, the cohesiveness of concrete is prejudiced with higher dosages of superplasticizer.
3. Superplasticizer can be used to reduce slump loss.
4. Slump cone test is performed on different water–cement ratios of 0.3, 0.36, 0.4, 0.45 and 0.5. By experimentation, the optimum dose of superplasticizer is found to be 1 percent by the weight of cement.
5. Slump and compaction factor increase with an increase in cement content per cubic metre.
6. A linear relationship between slump and cement content was obtained.
7. A linear relationship between compaction factor and cement content was obtained.
8. Desired compressive strength cannot be achieved without a superplasticizer.
9. Optimum values of compressive strength, i.e., M40 grade concrete can be achieved with water–cement ratios of 0.3 and 0.36 at extreme environmental exposure.
10. Water–cement ratio of 0.36 is the most appropriate. Though water–cement ratio of 0.3 gives desired compressive strength, workability of concrete is affected.

References

1. Mehta PK, Monteiro PJ (2014) Concrete: structure, properties, and materials. McGraw-Hill, third edition. ISBN: 978-0-07-179787-0
2. Khayat KH (1999) Workability, testing, and performance of self-consolidating concrete. *ACI Mater J* 96(3):346–353
3. Pinto RC, Hover KC (1999) Application of maturity approach to setting times. *ACI Mater J* 96(6):686–691
4. Reinhardt HW, Grosse CU (2004) Continuous monitoring of setting and hardening of mortar and concrete. *Constr Build Mater* 18(3):145–154
5. Aruntas HY, Cemalgil S, Simşek O, Durmus G, Erdal M (2008) Effects of super plasticizer and curing conditions on properties of concrete with and without fiber. *Mater Lett* 62(19):3441–3443
6. IS:9013-1978, Indian Standard, Method of making, curing and determining compressive strength of accelerated-cured concrete test specimens

7. De la Verga I., Spragg RP, Di Bella C, Castro J, Bentz DP, Weiss J (2014) Fluid transport in high volume fly ash mixtures with and without internal curing. *Cem Concr Compos* 45:102–110
8. IS 1489 (Part-1): 1991, Portland-Pozzolana cement- specification
9. IS10262:2019, Concrete Mix Proportioning-Guidelines (Second revision).
10. IS 269:2013, Ordinary portland cement , 33 Grade-specification
11. IS 1489 (Part-1):2015, Portland pozolona cement fly ash based
12. IS 456:2000, Plain and Reinforced Concrete- Code of Practice.
13. IS 383:2016, Coarse and fine aggregates for concrete-specification (Third revision)
14. IS 9103: 1999, Concrete admixtures spcification

Development of Sustainable Brick Using Textile Effluent Treatment Plant Sludge



Uday Singh Patil, S. P. Raut, and Mangesh V. Madurwar

Abstract A huge quantity of textile effluent treatment plant (TETP) sludge is generated from 21,076 units in India. Significant environmental impacts occur due to the landfilling of TETP sludge, such as land and water pollution. Thus, effective management of this sludge is important, which otherwise adds to the ever-escalating cost of disposal. With the rapid industrialization and urbanization, there is also an increased demand for construction materials to fulfill the shortage of housing in India (i.e., 18.78 million in urban and 43.9 million in rural). Brick is one of those significant construction materials, whose production is found to increase by 30% from 2000 to 2020 which consequently leads to an increase in carbon footprints. The present study, therefore, focuses on the effective utilization of TETP sludge to develop cost-effective, environmentally friendly bricks, which serve as an alternate solution for solid waste management, conservation of natural resources, and earning carbon credits. Sludge incorporated bricks were prepared with varying compositions of cement (6–24%), sludge (50–70%), and quarry dust (25%). Bricks are tested as per the Bureau of Indian Standards (BIS). The TETP sludge is characterized using X-ray fluorescence (XRF) and the properties of bricks were evaluated by conducting various tests such as compressive strength, water absorption, and density. Obtained results were also compared with commercially available fly ash bricks and clay bricks. The maximum strength of 4.2 N/mm² was observed for the combination of 24% cement, 51% sludge, and 25% quarry dust, which exceeds the value of 4 N/mm² for grade D, load-bearing units of IS: 2185(part1)—1979 and found to be greater than 3.5 N/mm² that meets the criteria of IS: 1077–1979 for bricks in load-bearing units. When textile sludge is used in the range of 50–57%, the water absorption value of bricks was found to be less than 20%, thus meeting the requirement of BIS. The resultant unit weight of the brick is also found to be lesser than the conventional bricks. Thus, it can be said that TETP sludge has the potential to develop sustainable

U. S. Patil (✉) · S. P. Raut
Department of Civil Engineering, Yeshwantrao Chavan College of Engineering, Nagpur, India
e-mail: patil.udaysingh4@gmail.com

M. V. Madurwar
Department of Civil Engineering, Visvesvaraya National Institute of Technology, Nagpur, India

bricks that meet the requirements of BIS, similar to the other sustainable materials, viz., concrete, mortar, etc., developed using other industrial wastes.

Keywords Sustainable brick · Material characterization · Physicomechanical properties · Sustainable construction material · Textile effluent treatment plant sludge

1 Introduction

In India, due to rapid growth, a huge amount of industrial waste is produced annually and gets accumulated, which is difficult to handle without proper management [1–10].

A substantial portion of the land is utilized for dumping these industrial wastes, thus causing soil and water pollution [11]. Therefore, effective management of this sludge is important which otherwise adds to the ever-escalating cost of disposal. Rapid urbanization has also increased the demand for building materials in urban and rural areas thereby exponentially rising the demand for new, economically viable building materials. As per the report on development alternatives [12] and technical group on an estimation of the urban /rural housing shortage [13], there will be a large demand for building materials to minimize housing shortages, i.e., 18.78 million housing shortages in urban areas with an approximate rural housing shortage of 43.9 million. It is seen that 90% of this scarcity applies to society's economically weaker and lower income classes, which is a cause of concern. The high construction costs cannot be afforded by an economically weaker segment, thus there is a need to increase the production of sustainable materials to satisfy these requirements. Consequently, an increase in output contributes to an increase in CO₂ emissions. It is observed that in India, about 22% of total CO₂ emissions are produced annually by the construction industry, of which 80% are mainly from industrial processes, involving the manufacture of steel, cement, bricks, and lime. One of the world's leading textile industries is the Indian textile industry. Approximately 21,076 textile units are distributed in India [14]. During the processing of textiles, a significant amount of water is used by the textile industry. As a result, an enormous amount of wastewater is produced, which needs to be properly handled before it is disposed of safely. In the effluent treatment plant units, this industrial wastewater is treated and a large amount of sludge is produced during the treatment process. This sludge is then disposed of for landfilling, resulting in pollution of the environment. The present study, therefore, focuses on the effective utilization of TETP sludge to develop cost-effective, environmentally friendly bricks that serve as an alternate solution for solid waste management, conservation of natural resources, and earning carbon credits.

2 Methodology for the Development of Sustainable Construction Material

2.1 Collection of Raw Materials

2.1.1 Collection and Preparation of Sludge Sample

Dewatered and open-air dried textile sludge sample was collected from the Morarjee textile industry located in MIDC Butibori, Nagpur (Figs. 1 and 2). The sludge obtained from the industry was in semi-solid form, therefore it was sun-dried until



Fig. 1 Image of dry textile effluent sludge

Fig. 2 TETP sludge before pulverization



the sludge is completely dried. The dried samples were then ground and pulverized to convert them into fine powder. This material was then sieved through 300 μ for the proper bonding between cement and sludge. The percentage of various size particles in the textile effluent sludge sample is determined using sieve analysis. The coefficient of curvature and uniformity coefficient is also calculated.

2.1.2 Collection of Cement and Quarry Dust

Similarly, other raw materials such as cement and quarry dust are collected. The cement used is the Ordinary Portland Cement (OPC) of Grade 53 conforming to BIS, IS:12269 [15]. The consistency limit of cement and cement with different percentages of sludge is determined using standard Vicat apparatus IS: 4031-4 [16]. Initial and final setting time tests were also performed using the Vicats apparatus. A density bottle test is performed to measure the specific gravity of the cement and sludge IS: 4031-11 [16]. Quarry dust is a by-product, released from the cutting and crushing process of stone and was collected from Gupta Industries located at MIDC Buti Bori, Nagpur.

2.2 Chemical Characterization of Textile Effluent Treatment Plant Sludge

The sludge is characterized (Tables 2 and 3) for various physicochemical parameters using an X-ray fluorescence test (Fig. 3). The USEPA and toxicity characteristic leaching procedure (TCLP) (Table 4) tests were performed on developed bricks. The leaching test was carried out at ANACON Laboratories Pvt. Ltd., Butibori MIDC, to check the feasibility of textile sludge for the development of sustainable bricks.

2.3 Manufacture of Brick Specimens

Sludge integrated bricks with different cement and sludge compositions (6–30 % wt.) were prepared (Fig. 4) with a constant proportion of quarry dust (Table 1) in a mould of 230 \times 150 \times 1000 mm. The required quantities of raw materials were calculated for various combinations of cement, sludge with quarry dust, and then hand-mixed with a required quantity of water until a homogenous mixture is obtained. The material is then poured into the mould in three layers and immediately after the casting, each layer is tamped 25 times to expel the entrapped air present in it. (Fig. 5) After forming, the bricks were sun-dried for about 15 days. The compressive strength of bricks is evaluated as per IS 3495- 1, Cl.4.1.4. Three [17] samples were subjected to a compressive strength test in the Universal Testing Machine after 28 days of curing.

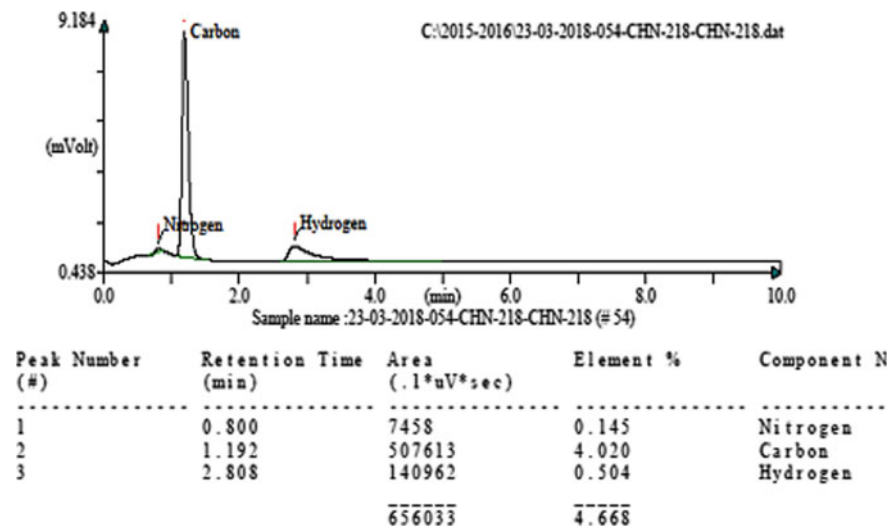


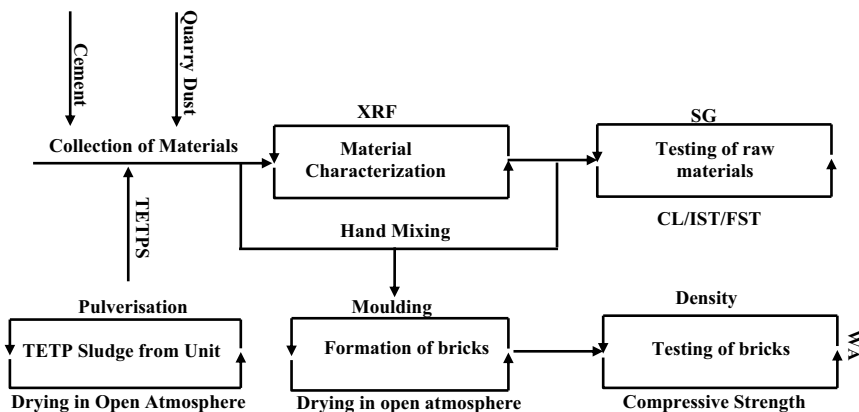
Fig. 3 Chemical characterization of TETP Sludge



Fig. 4 Formation of brick specimens

Table 1 Specimen ID with proportions

S. No.	Proportions	ID
1	6% cement+69% sludge+25% quarry dust	6C94S25Q
2	9% cement+66% sludge+25% quarry dust	9C66S25Q
3	12% cement+63% sludge+25% quarry dust	12C63S25Q
4	15% cement + 60% sludge+25% quarry dust	15C60S25Q
5	18% cement+57% sludge+25% quarry dust	18C57S25Q
6	21% cement + 54% sludge + 25% quarry dust	21C54S25Q
7	24% cement+51% sludge+25% quarry dust	24C51S25Q



XRF: X-ray fluorescence, CS: Compressive Strength, WA: Water Absorption, SG: Specific Gravity, CL: Consistency limit, IST: Initial Setting Time, FST: Final Setting Time

Fig. 5 Flowchart for development of sustainable bricks [19]

The average result of these specimens is taken as the brick’s compressive strength. For the comparison of strength, different samples of commercially available bricks such as clay brick and fly ash brick have been taken. To obtain water absorption values, three samples of bricks were selected. The bricks are weighed in dry condition and immersed in water for 24 h. After 24 h, the brick is properly wiped and the weight is taken in wet condition. For the calculation of the percentage of water absorption, IS 3495- 2, Cl.4.1.4 [18] is referred.

3 Results and Discussion

3.1 Chemical Characterization of Textile Effluent Treatment Plant Sludge

From Table 2, the specific gravity of sludge obtained is 2.4. Total volatile solids of about 31.85% are found, which will result in an increase in ash content during incineration, hence it is not recommended as a technique for sludge disposal. During the treatment process of textile wastewater, the addition of excess lime makes the concentration of calcium oxide as 108.22 mg/l, which is considered one of the chief components of the sludge and affects the pH content. The pH of sludge is found to be 9.13, which shows its alkaline nature. The presence of various oxides (Table 3) shows its potential to develop a sustainable construction material. The present study is also focused on the concentration of heavy metals such as Cu, Ni, Cd, Pb, Zn, Co, and Cr in TETP sludge, which is commonly found in the textile effluent due to the usage of dyes and other chemicals. The presence of metals in TETP sludge is of concern

Table 2 Characterization of textile effluent treatment plant sludge waste

S. No.	Property	Values
1	Water content (%)	28.72
2	Specific gravity	2.4
3	pH	9.13
4	Average particle size	–
5	Cadmium(mg/kg)	3.96
6	Copper (mg/kg)	57.48
7	Total chromium(mg/kg)	2.98
8	Zinc (mg/kg)	91.6
9	Nickel (mg/kg)	0.68
10	Lead (mg/kg)	12.1
11	Ferrous (mg/kg)	180.5
12	Sulphates (mg/l)	116
13	Sulphides (mg/l)	BDLa
14	Calcium (mg/l)	108.22
15	Magnesium (mg/l)	154.30
16	Chlorides (mg/l)	5445
17	Total hardness as CaCO ₃ (mg/l)	905
18	Total volatile solids	31.85%

Table 3 Chemical composition of textile effluent treatment plant sludge waste (% By Mass)

S. No	Composition	Sludge (%)
1	SiO ₂	14.85
2	Al ₂ O ₃	2.87
3	Fe ₂ O ₃	–
4	CaO	21.04
5	MgO	9.53
6	K ₂ O	–
7	Na ₂ O	–
8	SO ₃	–
9	SO ₄	1.55
10	TiO ₄	1.12
11	LOI	–

because of its toxicity to aquatic and mammalian species. The possible sources of metals are incoming fibre, water, dyes, and chemical impurities. Some dyes include metals as an integral part of the dye molecule. The concentrations of heavy metals are compared with the CPCB guideline (Table 4) and found that the concentrations of all heavy metals, including chromium species, are within the regulatory limits

Table 4 TCLP test result on TETP sludge

S. No.	Composition	Test method	Limits as per CPCB guideline	Test result (mg/l)
1	Arsenic	USEPA test method	Max. 5	absent
2	Barium		Max.100	0.13
3	Cadmium		Max.1	absent
4	Chromium		Max.5	absent
5	Lead		Max.5	absent
6	Manganese		Max.10	0.07
7	Mercury		Max.0.2	absent
8	Selenium		Max.1	absent
9	Silver		Max.5	absent
10	Ammonia	TCLP	Max.50	10.15
11	Cyanide		Max.20	0.02
12	Nitrate		Max.1000	8.51

indicating that the sludge is non-hazardous. Hence, this sludge can be explored for the possibility of reuse and recycling using some suitable technology rather than disposing of it in a landfill. It is also observed that the results of the characterization of TETP sludge vary from industry to industry and depend on the type of chemical used during the processing of textiles.

3.2 Physical Tests on Raw Materials

The physical properties of the cement and quarry dust are shown in Table 5. The specific gravity of cement obtained is 3.15 and that of quarry dust is 2.64. Results

Table 5 Physical test results of cement and quarry dust

S. No.	Tests conducted	Test results	
		Cement	Quarry dust
1	Specific gravity	3.15	2.64
2	Density	1440 kg/m ³	1650 kg/m ³
3	Water absorption	–	10.6
4	Standard consistency	30%	–
5	Initial setting time	80 min	Not less than 30 min
6	Final Setting time	125 min	Not more than 600 min

Fig. 6 Sieve analysis of TETP sludge



of grain size analysis of dried textile sludge are shown in Figs. 7 and 8. The particle size distribution of the sludge sample (Fig. 6) shows that the maximum percentage of sludge particles was retained on a 0.075 mm sieve. The curve shows that the sample of textile sludge consists of materials of all sizes. Effective sizes of the textile sludge before pulverization were obtained as $D_{10} = 0.019$ mm, $D_{30} = 0.14$ mm and $D_{60} = 0.4$ mm. Whereas, after pulverization, it is $D_{10} = 0.014$ mm, $D_{30} = 0.13$ mm and $D_{60} = 0.3$ mm. The values of uniformity coefficient C_u and coefficient of curvature C_c were 21.045 and 2.57, respectively. Whereas, after pulverization, the values of C_u and C_c obtained are 21.42 and 4.02, respectively.

3.3 Physico-Mechanical Tests on Brick

3.3.1 Density of Sustainable Bricks

The clay bricks normally have a bulk density of 1.8–2.0 g/cm³. It is found that the dry density of the TETP sludge is lower, so the resulting unit weight of the material would get reduced when used as building materials. In the current research, similar findings have been found. From Fig. 9, it can be seen that with the increase in the cement and corresponding decrease in the textile sludge, the density of bricks increases.

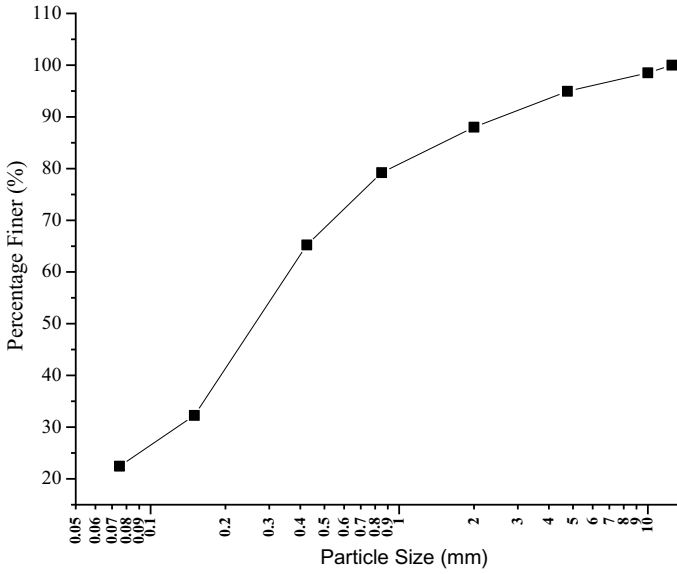


Fig. 7 Grain size analysis before pulverizing

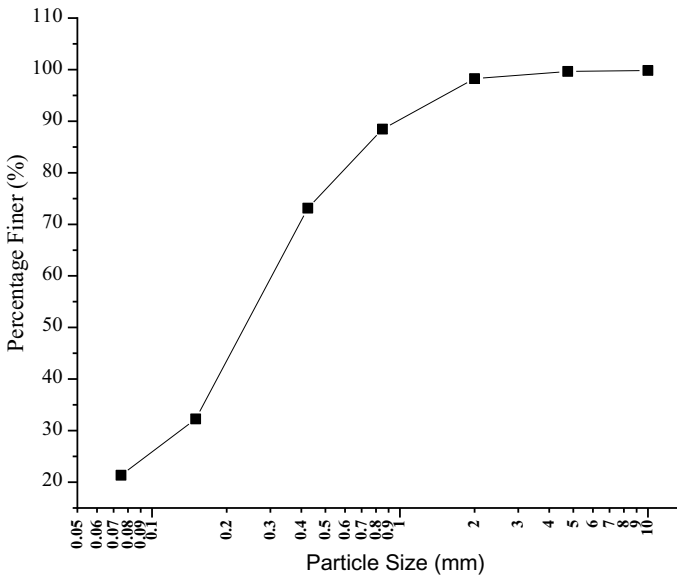


Fig. 8 Grain size analysis after pulverizing

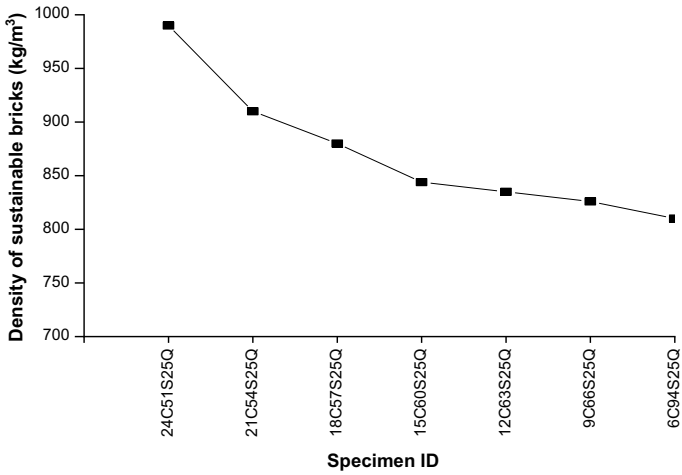


Fig. 9 Density of sustainable bricks

3.3.2 Compressive Strength of Sustainable Bricks

Figures 10 and 11 demonstrate the results of the average compressive strength of bricks. It is observed from Fig. 10 that, when TETP sludge is used as a partial substitute for cement, the compressive strength of the bricks decreases as the percentage

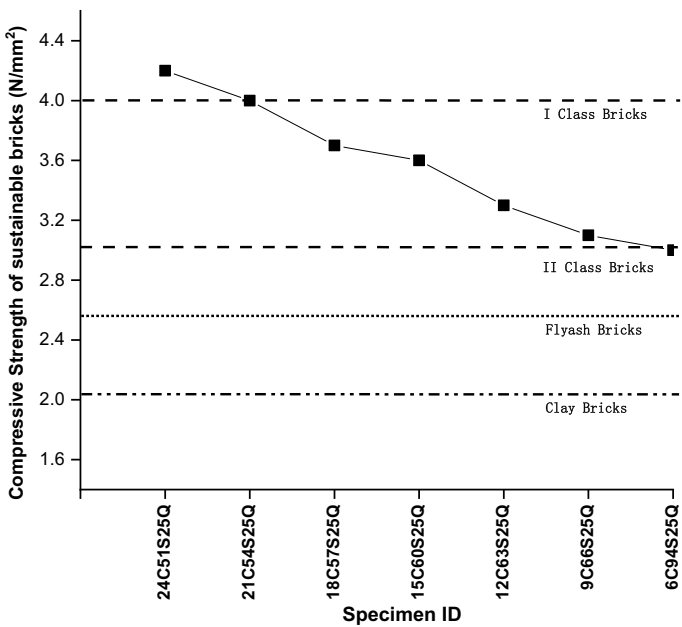


Fig. 10 Compressive strength of sustainable bricks

Fig. 11 Compressive strength test on third sample of the brick



of textile sludge increases. There is a maximum decrease of 29%, this reduction in strength might be due to fineness in particles of textile sludge compared to cement particles. The sludge is hygroscopic in nature [20], which increases the volume of the sample, so the demand for the water increases to preserve workability during mixing, thereby affecting the water–cement ratio. This may cause a reduction in the strength of bricks. The existence of chloride (Table 2) in the TETP sludge often reduces the quality of construction materials [21]. The obtained strength was found to meet the specifications of non-structural materials or components [22], as stated in various standards. The maximum strength of 4.2 N/mm^2 was observed for the combination of 24% cement, 51% sludge, and 25% quarry dust, which is greater than 4 N/mm^2 for grade D, load-bearing units of IS: 2185-1 [23], hence meets the criteria of required minimum strength, and found to be greater than 3.5 N/mm^2 as specified in IS: 1077 [24] for bricks in load-bearing units. The results also indicate that the compressive strength for the sludge incorporated brick is higher than that of the commercially available fly ash brick (2.5 N/mm^2) and clay brick (2.02 N/mm^2).

3.3.3 Water Absorption of Sustainable Bricks

From Fig. 12, it is observed that with the increase in the quantity of TETP sludge the value of water absorption increases. A maximum increase of 93% is observed. With an increase in the content of TETP sludge in the bricks, the porosity increases consequently the water absorption value increases [22]. Also, the presence of higher voids in the microstructure of sludge bricks subsequently increases the consumption of water [14]. With an optimum usage of TETP sludge of around 50%, the sustainable bricks showed promising results, i.e., compressive strength of 4.2 N/mm^2 with a corresponding water absorption value of 16%. This value is found to be less than the water absorption value of commercially available fly ash bricks, i.e., 18.43% and clay bricks, i.e., 27.11%.

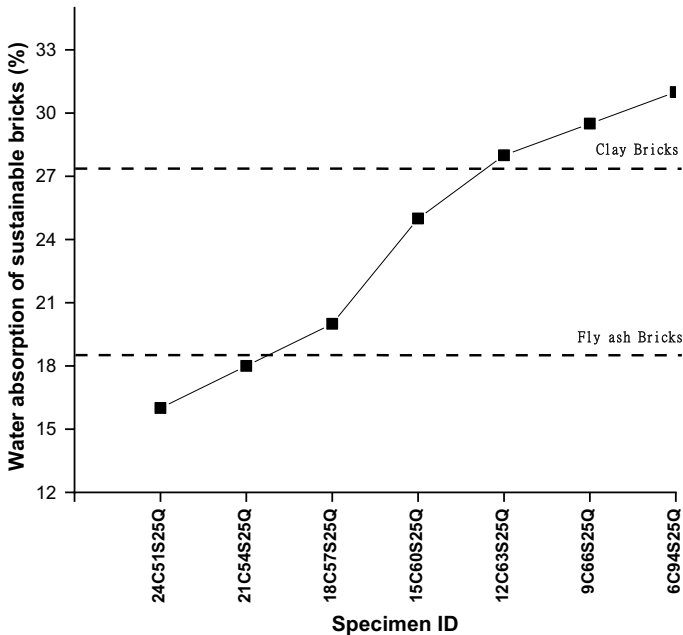


Fig. 12 Water absorption value of the brick

4 Conclusions

The disposal of textile effluent treatment plant sludge has a detrimental effect on the environment. Thus, its effective utilization in the production of the bricks is carried out, which proves to be a good alternative solution to such problems. Thus following conclusions have been drawn based on the detailed experimental investigation:

1. The presence of calcium and magnesium in sludge suggests its potential as a partial substitute for the development of sustainable building materials.
2. The heavy metals are found to be within regulatory limits and can therefore be used directly as a raw material without producing any harmful effects.
3. Developed bricks showed the maximum strength of 4.2 N/mm^2 for the combination of 24% cement, 51% sludge, and 25% quarry dust, which exceed the value of 4 N/mm^2 for grade D, load-bearing units of IS: 2185(part1)–1979 [23] and found to be greater than 3.5 N/mm^2 that meets the criteria of IS: 1077–1979 [24] for bricks in load-bearing units.
4. The textile sludge incorporated bricks were found to have strength greater than conventional fly ash and clay bricks.
5. When textile sludge is used in the range of 50–57%, the water absorption value of bricks was found to be less than 20%, thus meeting the requirement according to standards.

6. The bricks made with textile effluent sludge showed a lesser density compared to the other conventional bricks thus the resultant unit weight of the brick is lesser.
7. The optimum range of 51% of sludge for the manufacture of sustainable bricks in combination with quarry dust and cement is recommended.
8. The present study concludes that the utilization of TETP sludge for the production of sustainable bricks provides promising results of physico-mechanical properties when compared with commercially available bricks.

References

1. Goudar SK, Shivaprasad KN, Das BB (2019) Mechanical properties of fiber-reinforced concrete using coal-bottom ash as replacement of fine aggregate. *Sustain Constr Build Mater Lect Notes Civil Eng* 25
2. Sharath BP, Shivaprasad KN, Athikkal MM, Das BB (2018) Some studies on sustainable utilization of iron ore tailing (IOT) as fine aggregates in fly ash based geopolymer mortar. In: IOP conference: series, material science an engineering, vol 431, p 092010
3. Shivaprasad KN, Das BB (2017) Influence of alkali binder dosage on the efficiency of pelletization of aggregates from iron ore tailing and fly ash. *Int J Eng Res Mechan Civil Eng* 2(3):388–392
4. Shivaprasad KN, Das BB, Sharath PS (2020) Pelletisation factors on the production of fly-ash aggregates and its performance in concrete. *Proc Inst Civil Eng Constr Mater* 1–20
5. Sharath BP, Das BB (2021) Production of artificial aggregates using industrial by-products admixed with mine tailings—a sustainable solution, recent trends in civil engineering. *Lect Notes Civil Eng* 105:383–397
6. Snehal K, Das BB, Kumar S (2020) Influence of integration of phase change materials on hydration and microstructure properties of nanosilica admixed cementitious mortar. *J Mater Civil Eng* 32(6):04020108
7. Goudar SK, Das BB, Arya SB (2019) Microstructural study of steel-concrete interface and its influence on bond strength of reinforced concrete. *Adv Civil Eng Mater* 8(1):171–189
8. Goudar SK et al (2020) Influence of sample preparation techniques on microstructure and nano-mechanical properties of steel-concrete interface. *Constr Build Mater* 256:119242
9. Sumukh EP, Sharan KG, Das BB (2021) Predicting the service life of reinforced concrete by incorporating the experimentally determined properties of steel–concrete interface and corrosion. In: *Recent trends in civil engineering*. Springer, Singapore, pp 399–417
10. Sumukh EP, Sharan KG, Das BB (2021) A review on the properties of steel-concrete interface and characterization methods. In: *Smart technologies for sustainable development*. Springer, Singapore, pp 167–203
11. Balasubramanian J et al (2006) Reuse of textile effluent treatment plant sludge in building materials. *Waste Manage* 26(1):22–28. <https://doi.org/10.1016/j.wasman.2005.01.011>
12. Ministry of Rural Development (2011) Working group on rural housing for the 12th five-year plan. New Delhi, India
13. Ministry of Housing and Urban Poverty Alleviation. “Report of the technical group (TG-12) on urban housing shortage”. 2011, NBO, India
14. Shathika Sulthana Begum B et al (2013) Utilization of textile effluent wastewater treatment plant sludge as brick material. *J Mater Cycles Waste Manage* 15(4) 564–570. <https://doi.org/10.1007/s10163-013-0139-4>
15. BIS (Bureau of Indian Standard) IS: 12269:1987. Specification for 53 Grade Ordinary Portland Cement. BIS, New Delhi, India

16. BIS (Bureau of Indian Standard) IS: 4031(part 4):1980. Methods of Physical Tests for Hydraulic Cement. BIS, New Delhi, India
17. BIS (Bureau of Indian Standard) IS 3495–1992 (Part 1). Methods of Tests of Burnt Clay Building Bricks: Determination of Compressive Strength. BIS, New Delhi, India
18. BIS (Bureau of Indian Standard) IS 3495–1992 (Part 2). Methods of Tests of Burnt Clay Building Bricks: Determination of Water Absorption. BIS, New Delhi, India
19. Patil U, Raut SP, Ralegaonkar RV, Madurwar MV (2021) Sustainable building materials using textile effluent treatment plant sludge: a review. *Green Mater* 1–15. <https://doi.org/10.1680/jgrma.21.00027>
20. Kaur H (2019) Utilization of textile mill sludge waste in concrete—an experimental study. *Int J Pure Appl Biosci* 7(5):179–85. <https://doi.org/10.18782/2320-7051.7615>
21. Raghunathan T, Gopalsamy P, Elangovan R (2010) Study on strength of concrete with ETP sludge from dyeing industry. *Int J Civ Struct Eng* 1(3):379–389
22. Rahman, Md. Mostafizur, et al (2017) Textile effluent treatment plant sludge: characterization and utilization in building materials. *Arab J Sci Eng* 42(4):1435–42. <https://doi.org/10.1007/s13369-016-2298-9>
23. BIS (Bureau of Indian Standard) (1979) IS: 2185(1):1979. Specification for concrete masonry units - hollow and solid concrete blocks. BIS, New Delhi, India
24. BIS (Bureau of Indian Standard) IS: 1077–1979. Common Burnt Clay Building Bricks-Specification. BIS, New Delhi, India

Utilization of Pozzolanic Material and Waste Glass Powder in Concrete



Lomesh S. Mahajan  and Sariputt R. Bhagat

Abstract The material of glass has been used in various forms for versatile applications but it has a low life span compared to other materials. After the utilization of glass products, it has been either used as landfills or stored with stack piled. The landfills with broken glass products could not be the right choice, as it is a nonbiodegradable substance. Due to the strong need for alternative solution to landfills, the glass has been used in the concrete industry on a trial basis. For the concrete industry, mainly three places of waste glass is tried to suit, i.e. replacement to coarse aggregate, fine aggregate, and cement. However, the replacement of coarse aggregate has found lower results in compressive strength perspective. The similar phase of pozzolanic materials has seen in construction applications. The present work introduces the use of glass powder as a replacement for cement to assess the pozzolanic activity of fine glass powder in concrete. The experimentally evaluates its performance with other pozzolanic materials like silica fume and fly ash. The compressive strength study is conducted by considering specimens 15% and 30% replacement of cement by silica fume, fly ash, and glass powder. In addition, the particle size effect is evaluated using glass powder of size 150–100 μm . After tests, the results concludes that waste glass power has pozzolanic behavior. It reacts with lime at the early stage of hydration forming extra C-S-H gel and easily forming denser cement matrix and increases the durability property of concrete. When compared with fly ash mix concrete, fine glass powder concrete found slightly more strength.

Keywords Pozzolanic material · Cement · Fly ash · Silica fume · Glass

L. S. Mahajan (✉)

Research Scholar, Dr. Babasaheb Ambedkar Technological University, Lonere 402103, India

e-mail: loms786@gmail.com

S. R. Bhagat

Head, Department of Civil Engineering, Dr. Babasaheb Ambedkar Technological University, Lonere 402103, India

e-mail: srbhagat@dbatu.ac.in

1 Introduction

In India, about 960 million tons/year quantity of solid waste is thrown into the environment and out of this, about 21 million shares are of glass waste materials. Nowadays, these unutilized wasted glass materials are suitably addressed in the construction materials. Concrete is the indispensable complex material in the construction arena. The concrete industry depends on raw materials such as cement, sand, and aggregate. The mixture of concrete is generally prepared with Portland or pozzolana cement, sand, aggregate, and water content. All the civil engineering works are designed with concrete element to withstand the harsh environment. The use of pozzolanic substances is to minimize the reliability of cement and similarly, the waste material of glass is creditable to minimize the aggregate share in concrete. The global warning scenario becomes harmful due to huge cement production.

In the general case, glass does not create a nuisance in the environment because it is a non-polluted substance, but it causes harm to human beings. Pollution is created due to the dumping of glass on the land. The waste can be minimize the environmental hazards by using concrete as binding material. Glass material is categorized into nonbiodegradable substances. Thus, to sustain the environmental needs, we have to alter technology developed. Concrete could be the good place for accomplish such waste piece of glasses. The term “glass” contains several chemical uniformities including soda–lime silicate, alkali-silicate, and borosilicate glass. In few places, the powder has been used as concrete for cement and aggregate due to pozzolan property. The alkali content of cement is improved by adding the waste glass substance. Waste glass is also helpful in the ceramic and brick manufacturing industry. It benefits are decrease in the raw material requirement and protects landfill areas. The glass provides a way to recycle with recycling ratio near to 100% and can be safely used in concrete without scaring quality. de Moura et al. [7] stated that the fine glass powder improves the previous concrete’s property. Waste glass powder associated with the type and size ratio provided a positive effect on concrete durability [11]. The long-term durability enhancement was seen due to pozzolanic reactivity. Mineral additives mass and types of additives are also equally responsible for the strength of concrete.

Enough work is carried out to explore the pozzolanic benefits in the concrete for enhancing their properties ([12–16]). Ternary blends of fly ash, silica fume, and ordinary Portland cement offers good properties over binary cementitious blends [10]. Hyeongi [5] were investigated silica-based industrial additives for cement substituent. Partial replacement upto 20% of cement weight was used for assessing mechanical property and found that glass powered mix concrete exhibited more compressive strength. The amorphous nature of glass compounds possesses reduction in porosity. Ali [1] found pozzolanic characteristics, but irrelevant effect on setting time and expansion test of blended material. The range for incorporation of glass powder was suggested up to 20% for getting an improvement in the strength of concrete. The glass causes the difficulties of damaging alkali-silica reaction. If the glass is superbly ground, powder achieves the pozzolanic belongings of cement

which is essential for hydration. The cement is replaced by 5–20% of glass by dropping the cost of the binding material. Fly ash and bottom ash are useful for mortar strength [9]. The combination of cement, fly ash, and silica fume is also effective in the mortar for opting for beneficial workability and strength. The slag and fly ash benefits in concrete have been studied by Bijen [2], and alkali silica reaction was found beneficial in their investigation. Lam et al. [8] investigated the fracture behavioral effect of fly ash and silica fume and reported that enhancement in strength possible is due to silica fume–fly ash concrete.

This study focused on the pozzolanic use of waste glass powdered for a partial amount of cement in concrete. In addition, the effect of fly ash and silica use is evaluated. Various strategies have been adopted to improve the strength of fly ash concrete. Different approaches have been used to improve the early age strength of fly ash concrete. These consist of the addition of silica fume, high fineness fly ash use, and addition of hydrated lime [3, 4, 6].

2 Experimental Program

The mix of concrete M20 grade was chosen for the experimental program. OPC cement: 53 grade, Fly ash: F grade, and Silica fume: ASTM-C (1240) materials were used for the experimentation as cementations materials. The engineering properties of materials are presented in Table 1 and related consistency is presented in Table 2.

Table 1 Chemical properties of binder mixes

Mineral additives	SiO ₂	Al ₂ O ₃	Fe ₂ O ₃	MgO	CaO	K ₂ O	Na ₂ O	SO ₃
Glass	70.88	2.18	0.52	1.41	10.80	0.26	12.99	0.1
Cement	20.62	5.22	3.11	0.79	65.69	0.59	0.15	3.2
Silica Fume	96.21	0.28	0.48	0.45	0.35	0.49	0.28	0.18
Fly ash	33.44	19.55	5.28	6.54	26.27	0.1	1.44	2.39

Table 2 Normal consistency of binder mixes

Mix designation	Description	Cement (g)	Silica fume (gm)	Fly ash (gm)	Glass powder (gm)	Consistency in (%)
C	Cement	300	0	0	0	31.6
C-S	C with 15% SF	255	45	0	0	38.67
C-F	C with 15% F	255	0	45	0	39.3
C-G	C with 15% G	255	0	0	45	37.3

C Cement; SF Silica fume; F Fly ash; G Glass powder

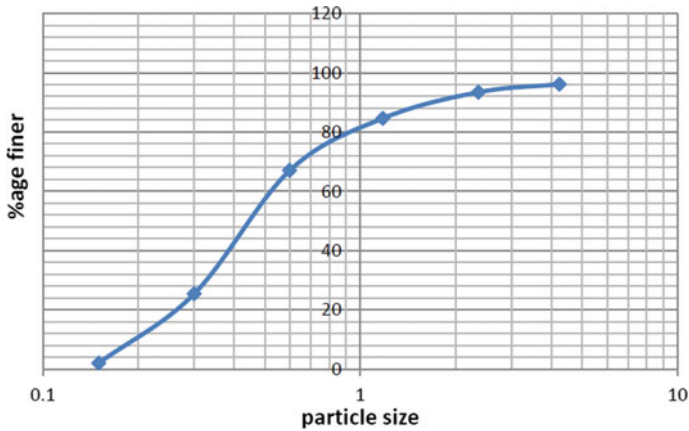


Fig. 1 Particle size analysis of locally available river sand

Locally available Tapi river sand is used as fine aggregate in the present work. The details of particle size are shown in Fig. 1. Fifteen percent and 30% cement replacement concrete specimens are cast and tested in the compressive testing machine after 28 days and 56 days curing period. The particle size (150–100) μ effect of glass powder is investigated. Capillary absorption test is also performed to check the alkali aggregate reaction. IS: 4031 Part4 (1988) is used for normal consistency testing. The compressive strength of various mix condition cubes is reported in Table 3.

A compression examination typically provides an overall interpretation of the property of concrete because strength linked directly to hydrated cement paste. The strength enhancement in the concrete is significantly tested by the compression test. As the results obtained, compressive strength for 28 days seen medium range as compared to the combination of C-S and C-F. For the 30% partial replacement specimens, the C-S combination was found in the same range, while C-F was found to have 24.19% reduction. C-G combinations were found to have much lesser values

Table 3 Compressive Strength Results

Silica fume content (%)	Designation of samples	Compressive strength N/mm ² (28 Days)	Compressive strength N/mm ² (56 Days)
30	C(1)	25.03	30.21
30	C-S(1)	25.48	29.59
30	C-F(1)	20.97	22.49
30	C-G(1)	17.89	22.68
15	C(2)	26.09	31.35
15	C-S(2)	27.87	29.98
15	C-F(2)	20.55	23.83
15	C-G(2)	21.01	24.53

for higher replacement, i.e., for 30%. This depletion goes 25.18% lesser at 15% replacement, while 28.52% reduced results obtained at 30% SF content. All obtained results of M20 designed concrete suitably addressed utility for a combination of 15% SF with cement and glass.

3 Conclusion

- Cement can be substituted by waste glass powder possessing pozzolanic behavior.
- Glass powdered concrete results are more committable with fly ash concrete due to fineness property.
- Silica fume is the better pozzolanic material and provides higher strength due to their smaller grain shape.
- The glass powdered, silica fume, and fly ash can easily replace cement in concrete up to 15% without failing original results.
- All obtained results of M20 designed concrete suitably addressed utility for a combination of 15% SF with cement and glass. The mechanical strength found in silica fume, fly ash, glass are adaptable materials as cement replacement by 15%. If considering the observed reading of 56 days curing period, the adaptive range of pozzolanic materials modified up to 30%.

References

1. Aliabdo AA, Abd Elmoaty M, Abd Elmoaty, Aboshama AY (2016) Utilization of waste glass powder in the production of cement and concrete. *Constr Build Mater* 124:866–877
2. Bijen J (1996) Benefits of slag and fly ash. *Constr Build Mater* 10(5):309–314
3. Barbhuiya SA, Gbagbo JK, Russell MI, Basheer PAM (2009) Properties of fly ash concrete modified with hydrated lime and silica fume. *Int J Constr Build Mater* 23:3233–3239
4. Chindaprasirt P, Chai J, Sinsri T (2005) Effect of fly ash fineness on compressive strength and pore size of blended cement paste. *Cem Concr Res* 27:425–428
5. Lee H, Hanif A, Usman M, Sim J, Oh H (2018) Performance evaluation of concrete incorporating glass powder and glass sludge wastes as supplementary cementing material. *J Cleaner Prod* 170:683–693
6. Jeyakumar M, Salman AM (2011) Experimental study on sustainable concrete with the mixture of low calcium fly ash and lime as partial replacement of cement. *Adv Mater Res* 250–253
7. de Moura JMBM, Pinheiro IG, Aguado A, Rohden AB (2021) Sustainable pervious concrete containing glass powder waste: performance and modelling. *J Cleaner Prod* 316:128213
8. Lam L, Wong YL, Poon CS (1998) Effects of fly ash and silica fume on compressive and fracture behavior of concrete. *J Cem Concrete Res* 28:271–283
9. Mahajan LS, Bhagat SR (2020) The contribution of bottom ash toward filler effect with respect to mortar. *Lect Notes Civil Eng* 72:145–154
10. Thomas MDA, Shehata MH (1999) Use of ternary cementitious systems containing silica fume and fly ash in concrete. *Cem Concrete Res* 29:487–495
11. Dong W, Li W, Tao Z (2021) A comprehensive review on performance of cementitious and geopolymeric concretes with recycled waste glass as powder, sand or cullet. *Resour Conserv Recycl* 172:105664

12. Sahoo S, Das BB (2019) Mineralogical study of concretes prepared using carbonated flyash as part replacement of cement. *Sustain Constr Build Mater* 519–529. Springer, Singapore
13. Shetti AP, Das BB (2015) Acid, alkali and chloride resistance of early age cured silica fume concrete. *Adv Struct Eng* 1849–1862. Springer, New Delhi
14. Sahoo S, Das BB, Mustakim S (2017) Acid, alkali, and chloride resistance of concrete composed of low-carbonated fly ash. *J Mater Civil Eng* 29(3):04016242
15. Sahoo S et al (2015) Acid, alkali and chloride resistance of high volume fly ash concrete. *Indian J Sci Technol* 8(19):1
16. Das BB, Pandey SP (2011) Influence of fineness of fly ash on the carbonation and electrical conductivity of concrete. *J Mater Civ Eng* 23(9):1365–1368

Recent Trends in Construction Technology and Management

Integrating BIM with ERP Systems Towards an Integrated Multi-user Interactive Database: Reverse-BIM Approach



M. Arsalan Khan

Abstract In the context of rapid technological advancements, the Architectural, Engineering and Construction sectors (AEC) are preparing themselves towards the enhanced level of co-ordination. This requires integration at every phase of the construction process, including design, processes, engineering services, fabrication, construction and maintenance phases—all together to help implement Level-3 Building Information Modeling (BIM). In this regard, the current understanding of BIM models is largely restricted to the graphical representation of the services, such as architectural model, structural model, plumbing model, etc. However, such decisions are confined to their respective departments before a ‘blueprint’ is released; for example, a design office may require changes to be incorporated into an architectural drawing or vice-versa. Such conflict of interests or process repetitions, particularly during planning, design and implementation stages, are identified as the main sources of significant delays in the overall project. For an integrated project delivery to overcome the fragmentation or loss of information, this paper proposes an architecture and demonstrates the feasibility of the implementation of Enterprise Resource Planning (ERP) system as a method to integrate the BIM processes among different departments that are using a heterogeneous environment of software packages. It is identified that the concept of ERP can be utilized not only to generate a read-only information database, but also rather reversibility in processes can be achieved by developing an interactive (read and write) database format to reach a consensus-based decision between seemingly scattered departments. A wide range of tasks is identified to be integrated during the planning, design, construction and operation phases. This will eliminate unnecessary time delays, for example, by minimizing or eliminating rotation of ‘blueprints’, enhancing the transfer of knowledge and overcoming the information-fragmentation. With a worked-out example, it is established that the available products on BIM-ERP integration can be expanded to directly

M. A. Khan (✉)

Department of Civil Engineering, Z.H. College of Engineering and Technology, Aligarh Muslim University, Aligarh, Uttar Pradesh 202001, India
e-mail: mohd.arsalan.khan@hotmail.co.uk

School of Architecture, Building and Civil Engineering, Loughborough University,
Loughborough LE11 3TU, UK

integrate structural or other heterogeneous software, but this requires realignment of processes.

Keywords Building information modelling · Enterprise resource planning · Collaborative working · SMEs · Systems integration

1 Introduction

Utilising the strength of computers in recent years, after the introduction of CAD software as a major breakthrough to generate graphical representation, researchers are introducing multiple dimensions to a drafting tool to call it Levels of BIM, moving from BIM Level 1 (models, objects, collaboration) to Level 3 (transactable, interoperable data), which is seen as an object-intelligent architectural CAD tool [1, 2]. The work of [3–5] identifies key literature and examples to contribute towards the current significance of the BIM model explaining consistent efforts that are being made to incorporate up to seven dimensions. That is, a 3D model (BIM Level 1) is evolved through the incorporation of virtual construction and space-conflict identification method(s), time and cost estimation, sustainability and maintenance aspect in BIM Level 2 that can provide point solutions. Mark Bew and Mervyn Richards model [6] suggests that BIM Level 3 maturity requires building lifecycle management through Integrated Web Services (BIM Hub development); now the progress is resulting in the launch of standard BS EN ISO 19650 [7].

With the progress of research work into BIM technologies, Hosseini et al. [8] asserted that the BIM and collaboration on BIM-assisted construction projects are subsets of ICT (Information and Communication Technology). In order to foster collaboration, Sackey et al. [9] maintained that the members of BIM-assisted construction projects are to become constant leaders. For example, Merschbrock [10] attempted to enhance collaboration through advanced collaboration technologies. Although, Dassault Systems [11] are seemingly the first to suggest BIM Level 3 integration; however, the initiation and adoption of such methodologies require additional expertise, there are no official leaders in the building industry to take a decisive first step; meanwhile, the architects and engineers find themselves caught within the nitty-gritty of the procurement logic on a project-by-project basis that does not support long-term development and sustainable drives. Thus, an ERP platform needs to be project and asset centric, and support functions specific to the industry. Meanwhile, such solutions should also be flexible as per their deployment needs so as to cater to the needs of users to achieve the desired solution at their own pace.

For example, the communication gaps and delays particularly at designer's, owner's and contractor's end in case of small building projects [12]. Although within the AEC market, these require extensive data-driven processes, however, the adoption of integration systems (ERP/EAM/project management) may still be widely feasible within micro, small and medium-sized enterprises (SMEs).

Putting concisely the focus of this paper, it is proposed that ERP integration techniques may be extended to handle the core tasks of AEC sectors. This can be integrated with BIM; for this, a re-engineering process is also proposed. It is suggested that this may be a cost-effective approach, particularly for SMEs, whose structure is relatively easier to revamp and implement ERP-BIM integration. Through a worked-out example, it is demonstrated that this would allow to-and-fro coordination between previously isolated departments before reaching a final decision which would now be binding from the initial stage of the project, achieved through the involvement of all the parties from the beginning of the project life cycle.

1.1 ERP System and Integration

ERP referred to as ‘Enterprise-wide Information Systems’ [13] or ‘Enterprise Systems’ [14, 15] is defined as ‘configurable information systems packages’ that integrate information and information-based processes within and across functional areas in an organization [16]. ERP systems are also defined as ‘computer-based systems designed to process an organization’s transactions and facilitate integrated and real-time planning, production and customer response’ [17]. According to Davenport [15], ‘ERP comprises of a commercial software package that promises the seamless integration of all the information flowing through the company– financial, accounting, human resources, supply chain and customer information’.

Integrated ERP systems have been widely assisting industries, such as manufacturing, to manage demand and supply-chain processes through recording of orders, procurements, controlling production and inventory, maintaining financial records and managing distribution as demonstrated through a block diagram by Zeng [18] shown in Fig. 1. Enterprise application integration (EAI) can be used to link applications that are at the disposal of the end-user with the main database of the system end; example package: SAP ERP. Gartner Group explains that EAI is the ‘unrestricted

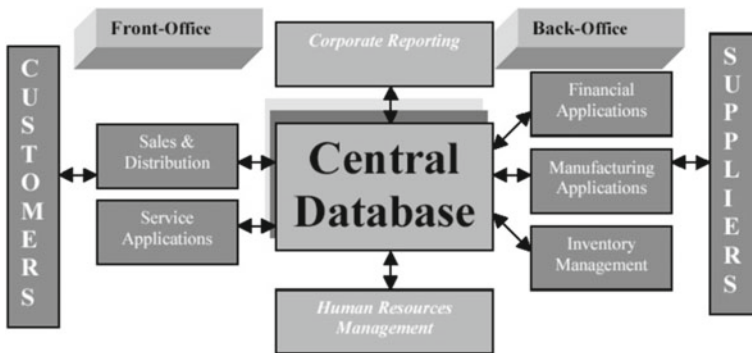


Fig. 1 ERP system concept. Source [18]

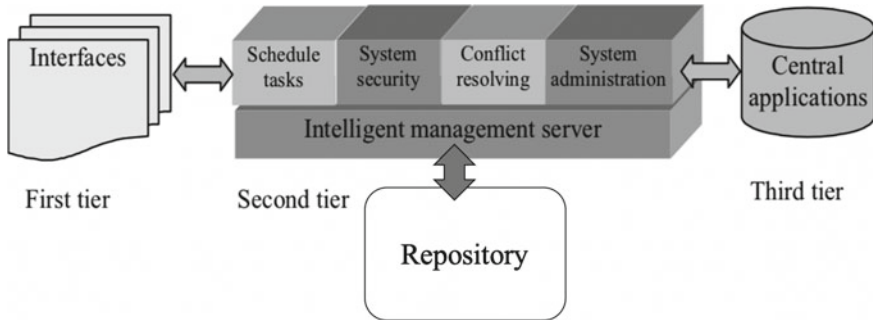


Fig. 2 A 3-tier architecture to construct-ERP. *Source* Edited after [20]

sharing of data and business processes among any connected application or data sources in the enterprise'. In the words of the research firm Gartner, EAI is the 'unrestricted sharing of data and business processes among any connected application or data sources in the enterprise' [19].

Projects in the AEC sector require wide expertise due to which often a number of clients are attached to a project using different digital platforms. As presented in Fig. 2, Shi and Halpin [20] presented a 3-tier architecture for ERP to be implemented in construction firms.

Whereas, using case studies, Ahmed et al. [21] established that 'A standard, best methodology for implementation does not exist. It is up to each company to approach ERP in the way that best fits its business needs'. With this in effect, this paper proposes that integration of BIM platforms within AEC sectors is also feasible that could be linked with estimating scopes of work, timescales, risks, quality, cost control and managing subcontracts. This means that the implementation of an ERP system as a truly integrated platform needs to address the following:

- Engineering, procurement and construction companies (EPCs) should be able to meet the needs of operator/owner typically engaged in creating digital assets through 3D CAD tools. The associated data with the CAD model can be modified with the progress of the project. This model serves as the basis for BIM processes.
- Specifications are preferably extracted from the BIM environment for tendering purposes to prospectus EPCs and contractors responsible for building an asset. Bidding out of the project is down in parts as per the scope of work.
- Companies often use BoQs as the basis for estimation of quantities which are based on various historical approaches centred on the scopes of work. A move or trend towards considering the BIM model for estimation is changing traditional estimation approaches. Using the BIM model for the purpose is proving efficient as many factors go into developing a successful bid, these include: subcontract work, plant and equipment rental, material and labour resources.
- Managing subcontract is essential to the construction industry, the need of which is required when the main contractor starts sub-bidding out the parts of the

project to subcontractors. In relation to the discrete manufacturer, this is similar to component sourcing.

- As the project progresses, emphasis is given to coordination that is done through available tools, costs that need to be checked, and managing project milestones and timelines. This requires the need to track the old data and update with the new one that can be cycled through and into the BIM environment.
- On the completion of construction and commissioning of the asset, it is handed over to the operator/owner. Enterprise asset management (EAM) system's role is to facilitate in this process and ensure smoothness of the data transfer. Through 'data drops', in contrary to final document 'handover', this is helping to build asset data repositories and thus leveraging BIM processes.

To avoid data loss due to the use of different software tools within the architecture sector, Oh et al. [22] developed a BIM checker and BIM modeller to help integrate many people with a common BIM server. Whereas, the objective of our proposal or hypothesis extends to associate itself to remind or to signify the fact that the main aim of BIM is not to be confined within any specific AEC office(s) to create an information/decision-making database that is disconnected, it is rather to interlink the flow of data within all sectors of AEC to the satisfaction of customers. Subsequently, with the use of new digital information systems within AEC, BIM can be a key approach towards adopting a truly integrated database, one such concept is proposed in this article.

2 Method

As mentioned by AIA [23], process re-engineering may be required to eliminate the trade-off among cost, time and quality to suit the main purpose of BIM tools to maximize lean construction by reducing wastage and maximizing value at the project delivery level. Therefore, for an integrated project delivery (IPD), a heterogeneous environment created by the use of software tool systems requires an establishment of the common database in a format easily apprehensible by all parties. Shen et al.[24] have identified that to enable data integration in heterogeneous environments, a common neutral model acts as the most feasible solution. This technique roots out errors and inconsistencies during the data recreation process and enables the enrichment and re-use of data throughout the building lifecycle. Recently, BIM has demonstrated large potential to become a platform for design and construction integration [25]; however, it is argued by Howard and Bjork [26] maintaining that BIM solutions are too complex in nature and their application has a limited scope initially. In addition, the observations suggest that although their application has evolved from a focussed toolset, however, it is evidently restricted to the idea of data models organizing the data of certain domains of interest for clients. To address this, the author suggests that in making use of the available resources or common software, there has to be an approach for systems (and AEC sectors) integration that

can be adopted depending upon a case-to-case basis such that maximum tasks of integration are understood (and achieved) at the beginning of any project.

As reported by Sun et al. [27], over 30% of completed projects suffer from bad quality and around 30% of construction is simply reworked, while the client is largely dissatisfied due to overspending and delays of over 50% of construction projects. Therefore, to target this gap and to overcome the one-way project execution approach of [28], a procedure in our study suggests both-way communication to encourage swift reversibility in decision-making. That is, for example, an architectural drawing or/and an engineering drawing would only be finalized through the mutual consent of all the offices/sectors involved that now can have a facility to instantaneously review the drawings (a traditional BIM approach) as well as to simultaneously record the desired changes onto the drawings (a proposed approach) before finalizing a blueprint (reaching decision) by either office. The author assumes that this approach is likely to resolve areas of conflict of interest between different sectors at the early stages of the construction lifecycle. Figure 3 identifies some possible changes (process re-engineering) between a proposed model and the model of Anumba et al. [28] used by primary BIM users (decision-makers) in areas of control and decision-making.

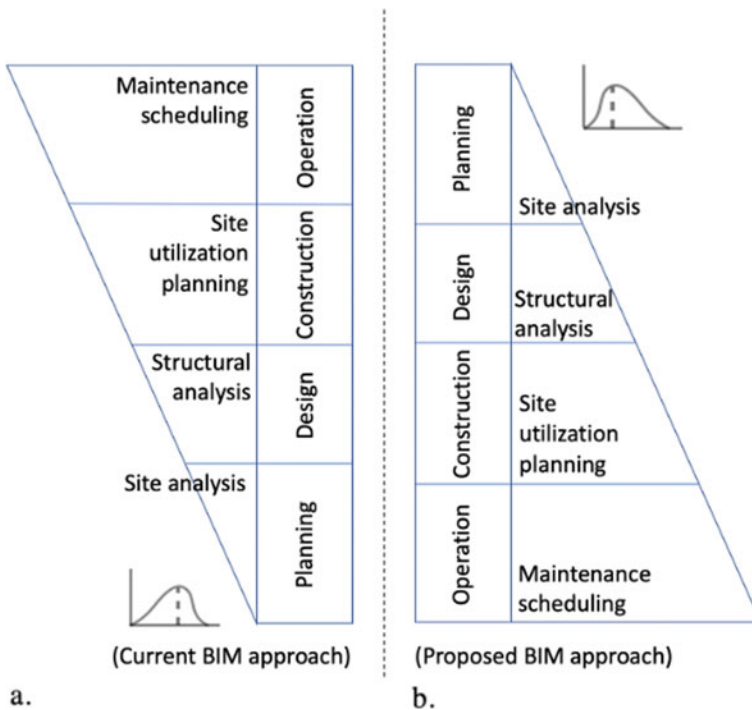


Fig. 3 Pyramid of BIM Uses throughout a Building Lifecycle: **a** Current approach (inverted pyramid), **b** proposed approach (reverse-BIM, balanced pyramid), noting changes in MacLeamy’s curve

Reshuffling the order of processes, Fig. 3b looks like a pyramid of co-ordination from the side and would look more like a pizza chart if seen from the top. The planning and site analysis stage lies at the ground level to indicate that maximum work needs to be done at this stage (indicates the foundation work at the base), it is then followed by Design and Construction stages on the next higher level, and the Operation stage forms the top to indicate the reduced amount of hassle (in management and control) left in co-ordination all the ongoing activities during a life span of a project. Such activities include 3D coordination, Design reviews, Site work. This could easily be compared when the ongoing practice of BIM activities, as indicated by Anumba et al. [28], are put into this form as shown in Fig. 3a, showing an inverted pyramid (hence, less balanced), where planning and site analysis are given least emphasis at the start of the project (foundation); thereby, shifting the stress of workload from Planning to Operation, leading to wastage and proving costly once a need of reconstruction arises that could otherwise have been resolved beforehand using process re-engineering of Fig. 3b through enhanced (two way) co-operation. Noteworthy is also the fact that, for a generic project consisting of Pre-design, Schematic design, Design development, Construction documentation, Procurement, Construction Administration, and Operation, the cost–time graph would be reversed with the choice of BIM practice; an example of how this works is demonstrated by Patrick MacLeamy [29] through Patrick MacLeamy curve. The applicability of MacLeamy’s curve to support automation in industries is also demonstrated by Delavar [30] through BIM models. And, with the adoption of our proposed model (of Fig. 3b), an architectural drawing or/and an engineering drawing would now be finalized through the mutual consent of all the office bearers involved that can now have a facility to review the drawings (a conventional BIM approach), to record the desired changes onto the drawings (a current approach) and to simultaneously over-write changes using a heterogeneous system of software (a proposed approach) before finalizing a blueprint (reaching decision) by either office from early stages of the construction lifecycle. This allows the peak of the MacLeamy’s curve to shift further towards the early stages of the project. However, the development or selection of a suitable system integration methodology is needed to implement the suggested BIM approach. Addressing this, Fig. 4 proposes an outlook on ERP-BIM integration plan towards systems integration. Different software in AEC offices are now connected through common database using ERP integration.

3 Working Example and Technical Details

To establish an understanding of the hypothesis for developing an ERP system linking the two key offices of architecture and designing, the author of this study has picked two legacy software packages (being widely adopted), that is, AutoCAD (2006) by

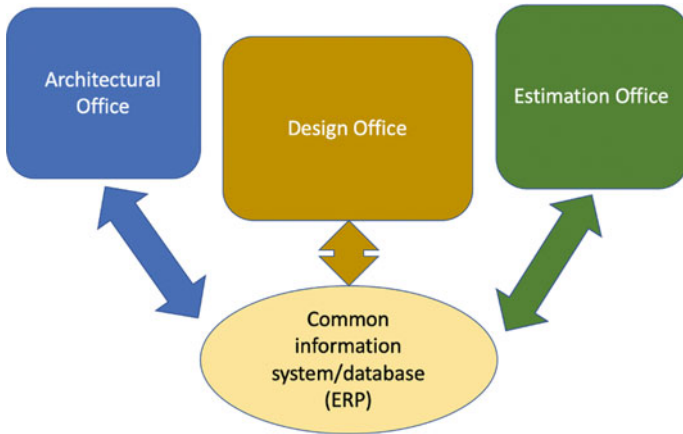


Fig. 4 Construct on the integration of ERP—BIM technologies

architects and STAAD Pro (v8i) by designers; that are integrated here for collaboration with the help of the most widely used open-source agent system development tool JADE (Java Agent Development Framework (version 7u11-windows-i586); compiled through Eclipse open-source compiler software. Following the outlook shown in Figs. 4 and 5, this required developing three adaptor codes linking: AutoCAD, STAAD Pro and file for cost estimation and commissioning purposes into a common data pool format so that the output information is not just read-only but is also writable on input file formats adopted by both the architecture and design software hereby selected. In this aspect, the flowchart of Fig. 5 identifies areas of data flow and interlinking of tasks from the start of the project through to completion.

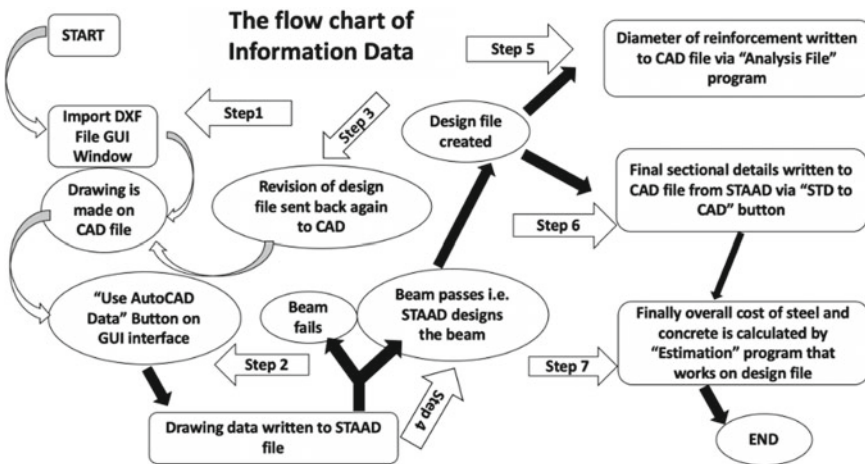


Fig. 5 Process flow diagram of new BIM approach using example

For example, once a design is not satisfactorily reached, it can be sent back to the architectural office for reconsideration before a final agreement is made. Thereby, in a multidisciplinary context, BIM-ERP integration will further be able to bridge the information loss in real time by allowing all the stakeholders to pro-actively make changes to, add to and refer back to all the information and share concerns required to make informed decision(s) during the lifecycle of the project. Therefore, the conflicts can be well addressed beforehand through the integration of ERP system into BIM technologies.

In order to integrate architectural and design stages, the system is divided into six classes; out of these, three are main classes (Beam, AnalysisFile and EstimationGUI) and objects of the other three (File class, File2 class and File3 class) are called from among one of the main class. Java code programs for these classes are written. The class inherits the JFrame class of Java swing and makes use of objects of JPanel, JTextField, JLabel and JButton, etc., to represent a desirable GUI window. On pushing 'OK' button (working example follows later below), the object of 'File' class is called which reads coordinates of length and width in both STAAS and CAD files along with other necessary information. The object of 'File2' class is called on clicking 'Use AUTOCAD DATA' button, this writes the coordinates of length and width extracted from AutoCAD file onto Staad file format along with necessary information. While pushing 'STAAD to CAD' button made available on the GUI interface, the object of 'File3' class is called upon to acquire the coordinates from Staad file and be re-written over AutoCAD file format. Therefore, here the sub-classes of Beam class are meant for mainly architectural drawing (without design elements). 'EstimationGUI', a main class, also extends the JFrame class to create a GUI interface to show the required information necessary for cost estimation after the final drawing/blueprint for site execution (after design analysis) is agreed upon by architecture and design offices.

A trial beam Sect. (450 mm × 100 mm × 100 mm having 4 numbers 8 mm diameter bars to start with) under 10 kN load (4-point bending problem) for lab experiment is taken (refer to Fig. 6) to be tested on our common information system. To facilitate the understanding of the procedure, Fig. 6 is linked with the steps mentioned previously in Fig. 5. First of all the plan and cross-section is drawn on AutoCAD software. Once an agreement on design is reached, the sectional details are passed onto the STAAD software, which then designs a final section (now changed to 750 mm × 150 mm × 150 mm, 10 mm diameter bars) ready for blueprint. Once the final drawing is submitted by the design office, the estimate of the entities, namely concrete and steel, will be calculated automatically by the estimation interface. The same methodology is applied to produce tests on beams [31–33].

4 Conclusion

An integrated and scalable solution was needed to deliver functionalities for any project, the lifecycle issues lacked in-depth understanding that needed to be addressed

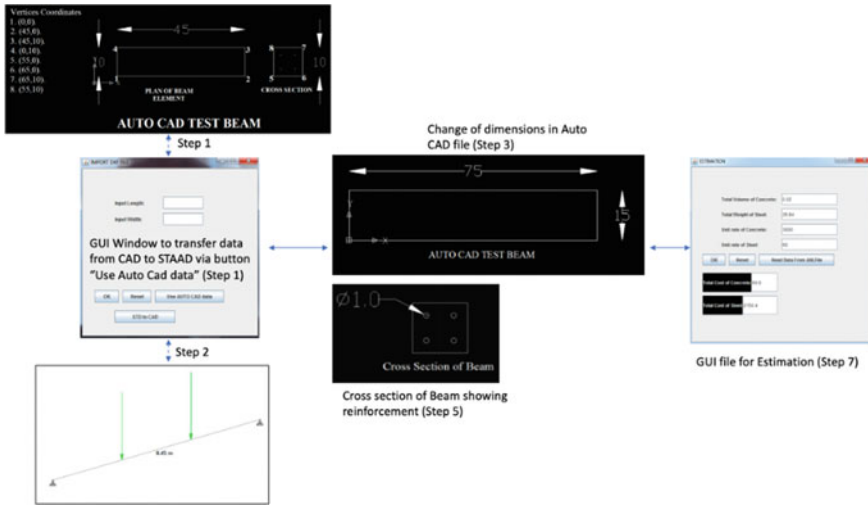


Fig. 6 Reverse-BIM-ERP verification through RC beam design

during modelling and planning, and the ability to assess the impact and uncertainties of risks and failures was not mature due to a lack of evaluation knowledge and availability of limited tools. After years of R&D, the willingness of AEC sectors and policymakers to embrace software systems to promote the concepts of integration and collaboration using data-driven platforms such as the adoption of Building Information Modelling (BIM) tools to better manage the entire asset lifecycle (towards BIM Level 3), an exceeding need is felt to integrate enterprise-class systems to further the adoption of 3D design and tools of product life-cycle management. To this end, this work presented a process re-engineering methodology (reverse BIM approach) to integrate BIM with ERP system to allow the creation of interdisciplinary consortia with to-and-fro coordination within AEC sectors for SMEs. The idea is demonstrated with the help of an example of designing a reinforced concrete (RC) beam.

Additionally, the drawbacks and lessons learned can be expanded to develop the presented concept at practical scale:

- The study is conducted using only two software packages used in the AEC industry namely AutoCAD and STAAD Pro.
- Although, the methodology proposed herewith considered the practicality of the problem by adopting two popular software (AutoCAD and STAAD Pro) for lab testing; however, no practical exercise of sizable scale is conducted to verify the approach mainly due to two reasons: (1) lack of funds, (2) leaves scope for further study.
- The beam element we considered in developing the common information system is not an actual element that is being used in the construction industry.

- Also, there can be a slight difference between the design data provided by STAAD for the beam and between manual calculations; however, this falls under software-specific limitations. This would affect the connected steps, such as the estimation of quantities of concrete and steel.

Therefore, when it comes to a system of heterogenous software, data pooling and integration can be a tedious task; however, ERP integration across AEC offices is a way forward and can be achieved within SMEs.

Acknowledgements Part of the software work was analyzed by Mr. S. Zameer under the guidance of the author of this paper M. Arsalan Khan [PhD, MSc Engg. ACI (Faculty member, USA), IStructE (Graduate, UK), MIES (Chartered with Institution of Engineers Singapore), IACM (Spain), IET (UK)]. The author is extremely thankful for the invaluable support from his late mother.

References

1. Murphy M, McGovern E, Pavia S (2013) Historic Building Information Modelling – Adding intelligence to laser and image based surveys of European classical architecture. *ISPRS J Photogrammetry Remote Sens* 76:89–102
2. Thomsen C, Darrington J, Dunne D (2010) *Managing integrated project delivery*. Virginia, USA
3. Altun M, Akcamete A (2019) A method for facilitating 4D modeling by automating task information generation and mapping. In: *Advances in informatics and computing in civil and construction engineering*. Springer International Publishing, Cham, pp 479–486
4. Antwi-Afari MF, Li H, Pärn EA, Edwards DJ (2018) Critical success factors for implementing building information modelling (BIM): a longitudinal review. *Autom Constr* 91:100–110
5. Koo B, Fischer M (2000) Feasibility study of 4D CAD in commercial construction. *J Constr Eng Manag* 126(4):251–260
6. BIM Industry Working Group (2011) A report for the government construction client group—building information modelling (BIM) working party strategy paper. *Communications (March)*:107
7. Cdbb (n.d.) *GSL 1 Intro—Centre for digital built britain*
8. Hosseini MR, Chileshe N, Zuo J, Baroudi B (2015) Adopting global virtual engineering teams in AEC projects. *Constr Innovation* 15(2):151–179
9. Sackey E, Tuuli M, Dainty A (2015) Sociotechnical systems approach to BIM implementation in a multidisciplinary construction context. *J Manag Eng* 31(1):A4014005
10. Merschbrock C (2012) Unorchestrated symphony: The case of inter-organizational collaboration in digital construction design. *Electron J Inf Technol Constr Royal Inst Technol* 17:333–350
11. Marvy R (2014) What Is BIM Level 3? 3D perspectives. <https://blogs.3ds.com/perspectives/what-is-bim-level-3/>. 24 Feb 2019
12. Shalwani A, Lines BC (2020) An empirical analysis of issue management in small building construction projects. *Int J Constr Educ Res*
13. Milford M, Stewart G (2000) Are ERP implemenations qualitatively different from other large systems implementations? In: *AMCIS 2000 proceedings*
14. Chen IJ (2001) Planning for ERP systems: analysis and future trend. *Bus Process Manage J* 7(5):374–386
15. Davenport TH (1998) Putting the enterprise into the enterprise system. *Harvard Bus Rev* 76(4):121–131. Harvard University Graduate School of Business Administration, Boulder, CO, USA

16. Kumar K, Van Hillebergersberg J (2000) ERP experiences and evolution. *Commun ACM* 43(4):22–26
17. O’Leary DE (2000) *Enterprise resource planning systems : systems, life cycle, electronic commerce, and risk*. Cambridge University Press
18. Zeng Y (2010) PPT—risk management for enterprise resource planning system implementations in project-based firms. Digital Repository at the University of Maryland, University of Maryland, College Park, MD 20742-7011
19. Gartner (2001) Enterprise applications- adoption of e-business and document technologies: 2000–2001 Europe
20. Shi JJ, Halpin DW (2003) Enterprise resource planning for construction business management. *J Constr Eng Manag* 129(2):214–221
21. Ahmed SM, Ahmad I, Azhar S, Mallikarjuna S (2003) Implementation of enterprise resource planning (ERP) systems in the construction industry. American Society of Civil Engineers, Reston, VA, Construction Research Congress, pp 1–8
22. Oh M, Lee J, Hong SW, Jeong Y (2015) Integrated system for BIM-based collaborative design. *Autom Constr* 58:196–206
23. AIA (2007) *Integrated project delivery: a guide California Council National*. The American Institute of Architects
24. Shen W, Hao Q, Mak H, Neelamkavil J, Xie H, Dickinson J, Thomas R, Pardasani A, Xue H (2010) Systems integration and collaboration in architecture, engineering, construction, and facilities management: a review. *Adv Eng Inf* 24(2):196–207
25. Young WN, Jones SA, Bernstein HM (2007) *SmartMarket report on building information modeling: transforming design and construction to achieve greater industry productivity*. McGraw-Hill Construction
26. Howard R, Björk B-C (2008) Building information modelling—experts’ views on standardisation and industry deployment. *Adv Eng Inf* 22(2):271–280
27. Sun M, Sexton M, Senaratne S, Chung P, El-Hamalawi A, Motawa DI, Lin Yeoh M, Plc B, Atkins W (2004) Managing changes in construction projects
28. Anumba C, Dubler C, Goodman S, Kasprzak C, Kreider R, Messner J, Saluja C, Zikic N (2010) *BIM project execution planning guide—version 2.0*. Computer Integrated Construction Research Program, The Computer Integrated Construction Research Group, Pennsylvania
29. CURT (2004) Collaboration, integrated information and the project lifecycle in building design. *Constr Oper WP-1202*
30. Delavar M (2017) *BIM assisted design process automation for pre-engineered buildings (PEB)*. Electronic Thesis and Dissertation Repository, The University of Western Ontario
31. Khan MA (2021) Towards key research gaps in design recommendations on flexurally plated RC beams susceptible to premature failures. *J Bridge Eng*
32. Khan MA (2022) Bond parameters for peeling and debonding in thin plated RC beams subjected to mixed mode loading—Framework. *Adv Struct Eng* 25(3): 662–682. <https://doi.org/10.1177/13694332211065184>
33. Khan MA (2021). Towards progressive debonding in composite RC beams subjected to thermo-mechanical bending with boundary constraints—a new analytical solution. *Compos Struct* 274114334. <https://doi.org/10.1016/j.compstruct.2021.114334>

Application of Game Theory to Manage Project Risks Resulting from Weather Conditions



Abd Alrahman Ghali and Vaishali M. Patankar

Abstract Construction projects are distinguished from other projects, and in that, they are greatly affected by emergencies such as inclement weather conditions, drilling and backfilling surprises and supply delays. These incidents are known as risks, which usually have negative consequences and constitute an obstacle to the completion of the project as they may cause delays and increase in cost, efficiency loss and quality deterioration. In this research, we have gathered information on the most important risks that could hinder the completion of the project, in general, through previous studies and conducted a questionnaire survey among the engineers to collect the largest number of risks faced by the construction projects in Bhubaneswar, India. After collecting the information, it is analysed and modelled according to the game theory for probabilistic decision-making which helps in choosing the best strategy to address risks and reduce their negative impact on the engineering project. The focus of the research will be on the risks arising from weather conditions in Bhubaneswar, India as a case study.

Keywords Game Theory · Risks management · Risk evaluation · Weather risks

1 Introduction

Risk management is the way to identify all future challenges that may negatively or positively affect the progress of the project. Negative risks that may stop or delay the project for various reasons are the most dangerous and must be identified. The possibility of occurrence of these risks and the degree of its impact on the project will determine the mechanism of dealing with it when it occurs, either by accepting it, or mitigating its effects. As for the positive risks, it is an assisting factor for the project manager. For example, the decrease in the prices of some materials, as measured by the market performance for a period of time or during the period similar to previous

A. A. Ghali (✉) · V. M. Patankar
Department of Civil Engineering, Siksha 'O' Anusandhan (Deemed to be University),
Bhubaneswar, India
e-mail: abboudghali@gmail.com

© The Author(s), under exclusive license to Springer Nature Singapore Pte Ltd. 2023
M. S. Ranadive et al. (eds.), *Recent Trends in Construction Technology
and Management*, Lecture Notes in Civil Engineering 260,
https://doi.org/10.1007/978-981-19-2145-2_18

221

years may help the project manager to save some sums and expenses and use them elsewhere in the project. At the beginning of any project, any risks that may affect the project must be identified, arranged in terms of impact on the project from the top to the bottom, and plans are drawn up to avoid these risks, especially to those of the highest rank because they affect the time and cost of the project. The engineer must study the risks, study their impact on the project and provide solutions and proposals that help address these challenges and reduce their impact on the project as much as possible. This is known as a risk management plan [1]. ‘Most project risks are common concern to project participants; the industry has shifted from risk transfer to risk reduction’ [2]. ‘Currently the Government of India has proposed a risk rating system that will help the developers to develop projects at a faster pace by taking quick decisions. Each rating agency will have its own methodology to rate projects’ [3]. Jayasudha and Vidivelli [3] provided a study ‘that should assist management in identifying activities where there is a risk of Financial, Time and Construction aspects and hence provide a basis for management to take objective decisions on the reduction of risk to an agreed level’ [3].

There are many practical methods that help in analysing the risks that could affect the engineering project, and they also help in choosing the most appropriate strategy that ensures the success of the project and its completion with the least possible losses. We will present in this paper one of these methods, which is game theory. This research aims to review the most important steps involved in risk management, and then model these steps according to the methodology of game theory, which helps in choosing the best strategy to address risks and reduce their negative impact as much as possible on the engineering project. The focus of the research will be on the risks resulting from weather conditions and weather.

2 Research Methodology

- Information gathering: through a reference study of the most important risks that may hinder the completion of the project according to the drawn plan, as well as strengthening the information obtained by conducting a questionnaire among the engineers, in order to collect the largest number of proposals and solutions that can be used to address risks and reduce their negative impact on the project, information gathering is done.
- Modelling: after collecting the information, it is analysed and modelled according to game theory methodology in probabilistic decision-making.

3 Literature Review

After we know that risk is one of the most vital problems that affect projects and that all vital projects are exposed to risks, it is possible, through a review of the

literature, to determine the types of these risks more accurately. Some of them are simple and fade and do not affect the progress of projects. Some of them develop and turn into a problem with dimensions, and a plan must be drawn up to fix it quickly. A small percentage may damage the entire project. The aim of studying the risks is to ensure that the third type can completely disappear when well planned by the risk management. Through previous studies, in general, we can classify the risks facing construction projects into these categories:

1. **Physical risks:** represented by workers who are not technically qualified, or an accident due to lack of safety measures or the supply of materials that are not valid, or do not comply with specifications
2. **Environmental risks:** they occur as a result of very bad and harsh weather conditions, or as a result of the difficulty in complying with the laws and prevailing environmental legislation, or as a result of environmental disasters (flood or earthquake) or unexpected pollution, or as a result of the difficulty in accessing the site.
3. **Design Risks:** Errors in design, inconsistencies between bill of quantities and specifications, or as a result of architectural design mismatch with structural.
4. **Logistical risk:** a result of high competition occurs during bidding, inaccurate project scheduling, insufficient labour availability, poor communication with the contractor and using new devices for the first time without training
5. **Financial risk:** it occurs as a result of late payment of payments according to the contract, and lack of cash flow control
6. **Legal risks:** legal disputes during the construction phase between the project parties, difficulty in obtaining licenses and starting work and lack of clarity in work legislation.
7. **Risks related directly to implementation:** difference in actual and contractual quantities, changes in design, reducing work quality versus time commitment, delays and technical problems with contractors, the difference between implementation and specifications as a result of misunderstanding the plans and specifications and the lack of documentation of change orders resulting during work.
8. **Political risks:** insecurity during project implementation, unexpected wars, political pressures and changes in prevailing laws.
9. **Administrative risks:** change in management methods, problems in managing resources, lack of information, poor communication between parties and planning incomprehensible due to project complexity [4–17].

4 The questionnaire

The questionnaire was conducted among a group of civil engineers and architects in public and private sector companies, and the response was made by 33 engineers. In the first phase, the most important risks that may be exposed to engineering projects in Bhubaneswar were identified. Table 1 shows these dangers in order of importance.

Table 1 Risks ranked according to the importance

Risks	Sorted by importance
Harsh weather conditions	1
Accident due to lack of safety measures	2
Supply of non-conforming materials	3
Technically unqualified labour	4
Land pollution due to work	5
Difficulty accessing the site	6
The mismatch between quantities, plans and specifications	7
The fluctuation of productivity rates for workers and equipment	8
Design errors	9
Inaccuracy in calculating quantities	10
Assigning the design to an inept office	11
Design mismatch (structural, architectural)	12
Difficulty and cost of adhering to environmental legislation	13
Environmental disasters	14

Knowing that the engineer’s answer was weighted according to the number of years he worked in the construction field.

In the second phase of the questionnaire, the focus was on the risk (harsh weather conditions). Where the cases shown in Table 2 related to weather conditions affecting the project were proposed. And depending on the results recorded in weather stations for the year 2020, which we obtained from the University of (Siksha ‘O’ Anusandhan), and by asking the engineers to determine the number of days in each month that pertains to each weather condition, and by adopting the weighted average, we obtained the results as shown in Table 3.

In addition, the questionnaire showed the duration of stoppage for each of the main project operations, depending on the weather situation, Table 4. Where the following classification was adopted: total stop, large-stop, partial stop and non-stop.

Table 2 Weather conditions

The description	Status	code
Strong winds, hurricanes, rain and thunderstorms	Bad weather	A ₁
Very hot weather	Moderately bad weather	A ₂
Stable or semi-stable weather	Good weather	A ₃

Table 3 Weather conditions by month

	Status					
	A ₁		A ₂		A ₃	
	days	P(A _i) %	days	P(A _i) %	days	P(A _i) %
January	6	0.194	2	0.064	23	0.742
February	6	0.207	–	–	23	0.793
March	6	0.193	3	0.096	22	0.709
April	6	0.2	11	0.366	13	0.433
May	7	0.225	4	0.129	20	0.645
June	14	0.466	1	0.033	15	0.5
July	14	0.451	–	–	17	0.584
August	19	0.612	–	–	12	0.387
September	15	0.5	–	–	15	0.5
October	15	0.5	–	–	16	0.516
November	3	0.1	–	–	27	0.9
December	10	0.323	–	–	21	0.677

Table 4 The duration of the project work stoppage depending on the weather condition

	Downtime depending on weather conditions		
	Bad weather (A ₁)	Moderately bad weather (A ₂)	Good weather (A ₃)
Soil work	Total stop	Total stop	Non-stop
Structural work	Total stop	Large-stop	Non-stop
Outer brick	Total stop	Non-stop	Non-stop
Inner brick	Partial stop	Non-stop	Non-stop
Outer finishing	Total stop	Non-stop	Non-stop
Inner finishing	Partial stop	Non-stop	Non-stop

5 Responding to Risk Using Game Theory

I. Principles of Game Theory

Game theory is concerned with studying the issues of duelin and competition between two or more parties, and these two parties have different goals, and each party acts consciously, thoughtfully and opposes the actions of the other party in order to achieve its goal optimally. The set of options available to the player to act and confront the other party is called a set of strategies, and it changes from one step to another. If the number of these strategies is finished, the game is finished, otherwise, it is called

an endless game. The game is called zero-sum if the sum of what one side wins is equal to what the other loses in the considered step. If the strategy makes the largest possible profit (or the least possible loss) when the game is repeated as many times as possible, it is called a perfect strategy. The player can choose a single strategy and he can also choose several strategies together, which is then called a composite strategy, in this case, each individual strategy constituting the composite strategy is associated with a probability frequency distribution.

II. Payoff Matrix

Assuming we have a double-ended game:

- (A) has the following strategies: $A_1, A_2 \dots A_m$
- (B) has the following strategies: $B_1, B_2 \dots B_n$.

If player A chooses strategy A_i and player B chooses strategy B_j , then the outcome of the game for A is a specific number a_{ij} . The a_{ij} values make up the payoff matrix—Table 5. The minimum price for the game is calculated according to the principle of (MaxMin). A chooses the largest possible profit and B what makes A's profit the lowest i.e., $\alpha_i = \text{Max} (\text{Min } a_{ij})$. The maximum price of the game is calculated according to the principle of (MinMax). B chooses the smallest winnings for player A, and player A matches him by choosing the largest that player B has set for him. i.e., $\beta_i = \text{Min} (\text{Max } a_{ij})$. The game is stable if the lower price of the game equals its higher price and the corresponding strategy for both is the best appropriate reaction to the game being studied ($V = \alpha_i = \beta_j$). if the lower and higher prices are not equal, then we resort to determining the probability distribution for each proposed work strategy, and the final solution will determine the percentage that should be used with each proposed strategy (Table 5).

Game theory is usually used within the focus of responding to risk, specifically in planning to avoid and reduce risk. We will study the application of game theory to hazards arising from weather and weather conditions, as the fluctuations of weather and weather conditions (such as snowfall, heavy rain, frost, strong winds, extreme heat) usually delay the project and increase its cost, and it may also cause a decrease in quality, especially during specific times of the year. Here, nature is the opponent for project management in planning the risk response.

Strategies (alternatives) available for player 1 (nature) can be proposed for weather conditions affecting the project as shown in Table 2. Strategies available to the second

Table 5 Payoff Matrix (a risk aversion matrix)

$A \setminus B$	B_1	B_2	B_n	α_i
A_1	a_{11}	a_{12}	...	a_{1n}	α_1
A_2	a_{21}	a_{22}	...	a_{2n}	α_2
....
A_m	a_{m1}	a_{m2}	a_{mn}	α_m
β_j	β_1	β_2	β_n	

player (project manager) represent the probable month to start the project as shown in Table 6.

III. Probability of occurrence (P_i)

Using the questionnaire results shown in Table 3, the probability of occurrence of each of the three previous cases (A_1, A_2, A_3) was calculated and it was coded $P(A_i)$ as it appears as a percentage.

IV. Impact probability (F_j)

The project usually consists of a set of tasks and activities, some of which are affected by very bad weather only, and some of them are affected by the weather, even if it is moderately bad, and some of them are not affected by the weather, whatever its condition, in other words, it is not necessary for the mission (A_1) to be affected by the weather even if it is bad. Total stoppage means that the effect will be 100%, and if the stoppage is partial, it will be matched by a partial percentage of the damage according to the studied mission. Based on the results of the questionnaire shown in Table 4, the probability of an impact was determined for each mission, as shown in Table 7, as a percentage.

V. Project damage (game price a_{ij})

The elements of the a_{ij} payoff matrix in Table 5 represent the percentage of delay in the project according to the studied weather condition, i.e., equal to the total amount of damage to the tasks located on the critical path (Project Damage = Total Damage to the missions on the Critical Path). The damage size for mission i in weather condition A_j = probability of occurrence of weather condition A_j , which is $P(A_i) * \text{probability of impact } F_{jk}$. [18, 19].

6 Practical Application

Figure 1 shows a brief bar chart for the critical path of an apartment building project in addition to the duration of each task per day according to the months of the year and considering 26 working days in every month.

Payoff matrix: the game price for each A_i state according to strategy j is $a_{ij} = \sum P_{ik} * F_{kj}$

$$\begin{aligned}
 A_{11} &= (15*1 + 11*1)*0.194 + 26*1*0.207 \\
 &+ 26*1*0.193 + 26*1*0.2 + 26*1*0.225 \\
 &+ 26*1*0.466 + (20*1 + 6*1)*0.451 \\
 &+ (24*1 + 2*0.2)*0.612 + (18*0.2 + 8*1)*0.5 \\
 &+ (10*1 + 16*0.2)*0.5 = 77.6688
 \end{aligned}$$

Table 6 Strategies of the project manager

January	February	March	April	May	June	July	August	September	October	November	December
B ₁	B ₂	B ₃	B ₄	B ₅	B ₆	B ₇	B ₈	B ₉	B ₁₀	B ₁₁	B ₁₂

Table 7 Impact potential

F_{jk}^*	Downtime depending on weather conditions		
	Bad weather (A ₁)	Moderately bad weather (A ₂)	Good weather (A ₃)
Soil work	total stop 100%	total stop 100%	non-stop 0%
Structural work	total stop 100%	large-stop 70%	non-stop 0%
Outer brick	total stop 100%	non-stop 0%	non-stop 0%
Inner brick	partial stop 20%	non-stop 0%	non-stop 0%
Outer finishing	total stop 100%	non-stop 0%	non-stop 0%
Inner finishing	partial stop 20%	non-stop 0%	non-stop 0%

* F_{jk} The probability of affecting mission J when K occurs



Fig. 1 Gantt chart for the considered project

By applying the principle of equalizing the lowest and highest price of the game, we note that the least delay in the project corresponds to that the starting month is October (Table 8).

7 Conclusions

Using the previous methodology and by adopting two main variables which are the expected total project duration and the method of its spread, the following rules were concluded:

Table 8 The payoff matrix for each of the three cases (A_1 , A_2 and A_3) depending on the proposed start-up month over an entire year

	A1	A2	A3	β
January	77.6688	12.8096	0	77.6688
February	80.524	11.3568	0	80.524
March	86.4456	11.7888	0	86.4456
April	85.5516	11.2566	0	85.5516
May	87.068	3.5289	0	87.068
June	86.4344	0.7491	0	86.4344
July	79.6096	0.896	0	79.6096
August	73.3352	1.1648	0	73.3352
September	66.0832	2.5088	0	66.0832
October	61.4908	8.036	0	61.4908
November	62.1724	11.3792	0	62.1724
December	71.7116	12.383	0	71.7116
α	61.4908	0.7491	0	61.4908

- If the project is a floor building and its duration does not exceed 1 year, in order for the project to be affected by weather factors as little as possible, it is preferable not to start its implementation in the winter season and start the implementation in the last quarter of the year.
- If the project is a floor building and its duration is more than 2 years and is spread vertically (i.e., the number of floors is not less than 3), and in order for the project to be affected by weather factors as little as possible, it is preferable to start its implementation in the spring months, and if it is spread horizontally, it is preferable to start it in the summer period.

The use of game theory greatly supports the project manager in making the best decision regarding the preferred project start time. Reducing the risk of weather factors during the project implementation period was studied based on game theory, but the rest of the risks over the project period, such as financing risks, soil surprises risks and also risks of disruption of renewable and non-renewable resources have not been studied, and this could be the focus of future research in this field.

References

1. Project Management Institute (2017) A guide to the project management body of knowledge. Sixth edn
2. Tang W, Qiang M, Duffield CF, Young DM, Lu Y (2007) Risk management in the Chinese construction industry. *J Constr Eng Manag* 133(12):944–956
3. Jayasudha K, Vidiyelli B (2016) Analysis of major risks in construction projects. *ARNP J Eng Appl Sci* 11(11):6943–6950

4. Miller MB (2018) Quantitative financial risk management. Wiley
5. Hopkin P (2018) Fundamentals of risk management: understanding, evaluating and implementing effective risk management. Kogan Page Publishers
6. Damnjanovic I, Reinschmidt K (2020) Data analytics for engineering and construction project risk management. Springer, Cham, Switzerland
7. Baloi D, Price AD (2003) Modelling global risk factors affecting construction cost performance. *Int J Project Manage* 21(4):261–269
8. Belassi W, Tukel OI (1996) A new framework for determining critical success/failure factors in projects. *Int J Project Manage* 14(3):141–151
9. Bunni NG (2003) Risk and insurance in construction. Routledge
10. Dikmen I, Birgonul MT, Han S (2007) Using fuzzy risk assessment to rate cost overrun risk in international construction projects. *Int J Project Manage* 25(5):494–505
11. Iyer KC, Jha KN (2005) Factors affecting cost performance: evidence from Indian construction projects. *Int J Project Manage* 23(4):283–295
12. Saqib M, Farooqui RU, Lodi SH (2008) Assessment of critical success factors for construction projects in Pakistan. In: First international conference on construction in developing countries, pp 392–404
13. Tah JH, Carr V (2000) A proposal for construction project risk assessment using fuzzy logic. *Constr Manag Econ* 18(4):491–500
14. Wang J, Yuan H (2011) Factors affecting contractors' risk attitudes in construction projects: Case study from China. *Int J Project Manage* 29(2):209–219
15. Zavadskas EK, Turskis Z, Tamošaitiene J (2010) Risk assessment of construction projects. *J Civ Eng Manag* 16(1):33–46
16. Zayed T, Amer M, Pan J (2008) Assessing risk and uncertainty inherent in Chinese highway projects using AHP. *Int J Project Manage* 26(4):408–419
17. Zeng J, An M, Smith NJ (2007) Application of a fuzzy based decision making methodology to construction project risk assessment. *Int J Project Manage* 25(6):589–600
18. Cox LA Jr (2009) Game theory and risk analysis. *Risk Anal Int J* 29(8):1062–1068
19. Neogy SK, Bapat RB, Dubey D (2018) Mathematical programming and game theory. Springer Singapore

Environmental Impact Analysis of Building Material Using Building Information Modelling and Life Cycle Assessment Tool



Kunal S. Bonde and Gayatri S. Vyas

Abstract The construction industry consumes a large number of resources and energy, producing a negative impact on the environment. Nowadays, the world is facing problems of climate change, ozone layer depletion, temperature rises, etc. with an increase in greenhouse gas emissions. In India to get an environment clearance certificate for any project, environmental impact assessment is most important, which is measured by means of life cycle impact assessment. The aim of this research work is to measure the impact of various building materials by evaluating energy consumption at different stages throughout the life span of the building. This work follows a life cycle assessment framework based on the ISO 14040 and ISO 14044 guidelines within the available databases using Autodesk Revit (building information modelling tool) and One-Click LCA (life cycle assessment tool) integration. The main objectives of the research work are: (1) to compare concrete frame structure and steel frame structure; (2) to compare conventional and modern building materials, on the basis of their environmental impact. To achieve the objectives of the work, a real-life case study of the residential apartment building is selected and analysis of energy consumption is done. The results from the energy consumption calculation indicate that steel frame with modern building materials produces a less negative impact on the environment as compared to concrete frame and conventional building material. This research work is limited to the environmental impact of building frame type and material selection during the early design phase of the building. It encourages the application of steel frames as well as modern building materials to protect the natural environment and climate change.

Keywords Building information modelling · Concrete frame · Environmental impact assessment · Life cycle assessment · Steel frame

K. S. Bonde (✉)
College of Engineering, Pune, India
e-mail: bondeks19.civil@coep.ac.in

G. S. Vyas
Department of Civil Engineering, College of Engineering, Pune, India

1 Introduction

In recent years, the usage of energy in buildings has been on the rise, due to the population increase, economic growth, and extremely luxurious life. The construction industry consumes a large number of natural resources and hence contributes to increasing greenhouse gas emissions and climate change. Due to this, the world is witnessing the depletion of natural resources as well as non-renewable energy resources. According to Tusher et al. [13], globally 27% of overall energy consumption and 17% of CO₂ production were due to the housing sector. Jin et al. [2] stated that, globally, 20–40% of total energy usage is due to the building sector. Sandberg et al. [12] suggested that new sustainability requirements have been progressed by the environmental impact from the built environment regarding the building's performance throughout life cycle cost and energy. According to the World Green Council, buildings are using 40% of energy, 32% of natural resources, and are responsible for 36% of greenhouse gas emissions. India ranks 3rd in electricity consumption as of 2018 with 1181 kwh/ capita/ year use. In India, 80% of electricity is produced from fossil fuel. This burning of fossil fuels produces harmful emissions that affect the environment. Through these activities, GHG emissions such as CO₂, CH₄, N₂O, etc. develop at the higher layer and result in global warming.

1.1 Building Information Modelling

Building information modelling (BIM) tools help architects, designers, and construction engineers to create 3D, 4D (time schedule), 5D (cost estimation), 6D (sustainable design) model for a better understanding of the building construction process. As per the National BIM Standard Project Committee in the United States of America (2017), BIM is defined as “it is a digital representation of physical and functional characteristics of a facility. A BIM is a shared knowledge resource for information about a facility forming a reliable basis for decisions during its life-cycle; defined as existing from earliest conception to demolition”.

3D model of the building is developed with great precision and optimum level of detailing using Autodesk Revit. It is the platform where architecture, MEP (mechanical, electrical, plumbing), and structural engineers work together. It is a BIM tool that is capable of making detailed plans using the material library available in its database. The building model is developed in Revit and transferred to life cycle assessment (LCA) software for energy analysis. In this study, an apartment building model is developed and LCA is done throughout the construction stages. The different stages of construction are shown in Fig. 1.



Fig. 1 Building construction phase [9]

1.2 Life Cycle Assessment

Life cycle assessment is used to measure the environmental impact of various types of projects. It helps in the decision-making process prior to the construction stage. There are various software for life cycle assessment. In this research work, One-Click LCA software, which is a plugin to Autodesk Revit is used for energy analysis. Life cycle assessment methodologies follow ISO 14040 (principle and formwork) and ISO 14044 (defining goal and scope). It considers the life cycle right from the extraction of raw material to the demolition stage for environmental impact calculation. The life cycle stages and energy involved in a particular stage are shown in Table 1. Pre-building phase consists of activities right from the extraction of raw material to transportation at the site and the energy involved in this phase is embodied energy.

2 Literature Review

Nowadays, LCA is one of the most popular tools for supporting environmental decision-making for products, services, and technologies [2]. LCA aims to determine the environmental impact of the product right from raw material extraction to the demolition stage [3]. LCA research methodology is divided into four phases according to ISO 14040 and ISO 14041 [4]: (1) Aim and scope definition: specifying the goal, scope, and limit of LCA research [1]; (2) Inventory analysis (life cycle inventory): energy and material data is collected and established the inventory

Table 1 LCA phase, activities, and energy involve

Life cycle phase	Activities	Energy involves
Pre-building phase	Extraction of raw materials, manufacturing, packaging, and transporting to the site	Embodied energy
Building phase	Construction, installation, operation, and maintenance	Operational energy
Post-building phase	Demolition and recycling	Demolition energy

input or output [5]; (3) Environmental impact assessment (life cycle impact assessment): calculation of the flow to be assessed for an overall impact category [1]; (4) Interpretation: quantification and evaluation of the life cycle inventory and life cycle impact assessment study findings, and originating conclusions and suggestions [9]. The aim of this research work is to perform a life cycle assessment of building material from extraction to demolition stage. This can be done by integrating BIM and LCA for analysis of building frame and material.

2.1 LCA in the Building Sector

LCA has been applied to the rating of sustainable green buildings, which encouraged building sustainability assessment in practice [7]. Various stages of construction produce different negative impacts on the environment. From the study, it was observed that during the manufacturing and operating stages of building life cycle, the negative impact on the environment is more as compared to other stages [8]. The use of LCA in the construction sector is multifaceted and includes the ranking of sustainable green buildings, energy assessment, refurbishment of buildings, costs, social assessment, and carbon emissions [10]. With the ultimate goal of formulating strategies to reduce the use of primary energy in buildings, LCAs have been applied to the energy evaluation of buildings. The environmental impact of a building is dependent on the type of building frame. Steel building frames produce less negative impact on the environment as compared to concrete building frames [9]. Building materials can contribute significantly to achieving sustainable development goals. Use of modern building materials and removing typical building materials help us to achieve a sustainable design in the build environment. Modern building materials in building construction help to achieve 13 sustainable development goals and 25 targets of sustainable development goals [11].

2.2 BIM and LCA Integration

BIM is used to model energy-efficient building. Autodesk Revit has an extensive material library, which is helpful to find the most efficient building material. LCA helps to calculate the energy consumed in different stages of life cycle of a building right from raw material extraction to disposal and end of life of a product [3]. Najjar et al. [8] in their work integrated BIM and LCA for calculating the environmental impact of various building materials. To validate the results of the study, they take one real-life case study of an office building. Results show that during the manufacturing process and operation stage, impact of negative energy is more. Lu et al. [6] in their work integrated BIM and LCA for calculating carbon emissions. A case study of a hospital building is considered for validation. Results of this work show that RCC in the construction stage and HVAC in the operational stage contribute a large amount

of CO₂. Life cycle assessment helps in decision-making at the early design phase of the building by performing operational energy calculation and checking the impact of building material [9]. Najjar et al. [9] calculate operational energy throughout the life cycle of a building. To achieve this objective, one case study of three different profile buildings (low, normal, and high) was taken. Analysis results show that exterior wall and windows are most accountable for energy.

3 Research Methodology

The flowchart of the research work is shown in Fig. 2. It consists of six stages. Goal, scope, and system boundary is defined in the preliminary stage. After defining boundary, building design takes place in Revit, and quantity takeoff takes place for inventory analysis. This quantity takeoff file is then imported into One-Click LCA software for energy analysis. The results of energy analysis are compared in the interpretation stage.

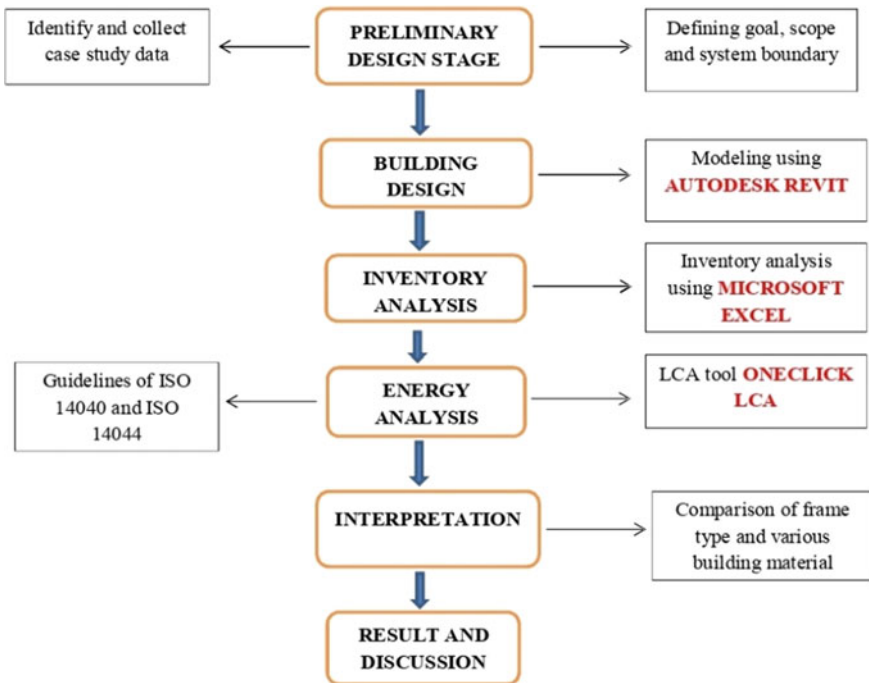


Fig. 2 Flowchart of research work

3.1 One-Click LCA

One-Click LCA operates on the basis of a web-based interface that can be integrated into compatible open standard applications and as a Revit software plug-in tool. This instrument follows the international criteria for the study of the LCA. For EN 15978, EN 15804, ISO 21931-1, ISO 21929-1, and ISO 14040, the One-Click LCA is independently accepted. In addition, an international database of Environmental Product Declarations has been developed to target the European market. It also enables the performance of building materials to be chosen, modified, and simulated. It has been used by researchers, who have researched LCA and BIM integration using various methods, such as the One-Click LCA and Tally.

3.2 Data Collection

Real-life case study data is collected which includes the bill of materials, each floor plan, section plan, and elevation obtained from the building's contractor and designer. Data related to material manufacturing and processing is obtained from international resources (international standards and guidelines) and from local resources. Climate data and other required data are considered according to the region of site.

4 Case Study

A case study of a residential apartment building named 'Gagan Nulife', which is located in Kamshet, Pune, India is taken. The gross floor area of the apartment building is 4400 m². The given building is G+10. There are 4 flats per floor and all of them are 2 BHK. A lift and staircase are provided for vertical circulation in the building. The climate type of the Pune region is semi-arid bordering tropical wet and dry with an average temperature ranging between 20 and 28°. Modelling of the apartment building is done using Autodesk Revit a BIM software. A pictorial representation of a typical plan and building model is shown in Fig. 3.

4.1 Goal and Scope

The goal of this research work is to determine the impact of building frames and building materials. The system boundary of LCA consists of stages right from raw material extraction, manufacturing, construction, operation, and end of life. Attention should be given to various impact categories and other data that need to be inputted. Scope of this work is to analyse buildings at the early design stage with

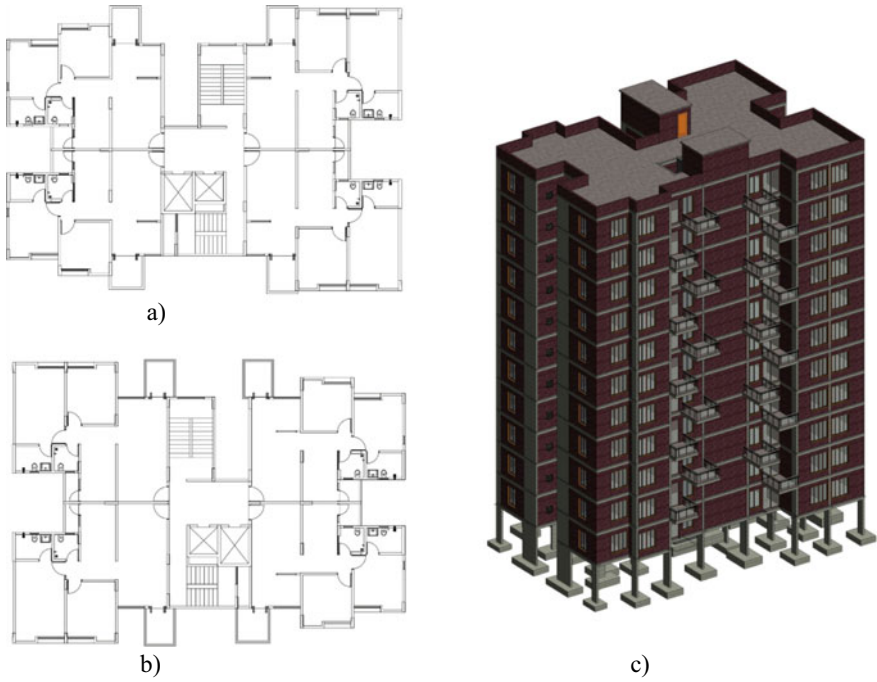
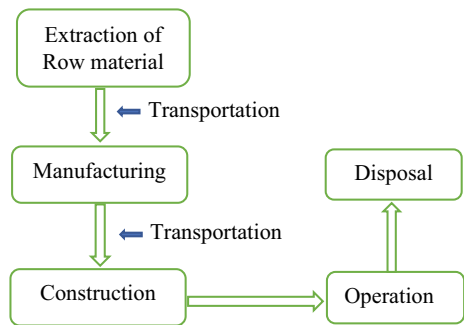


Fig. 3 a Plan of odd floor b Plan of even floor c Revit model

different materials to find out environment sustainable alternatives. It helps to get an environmental clearance certificate. The layout of the system boundary is shown in Fig. 4. The layout of the system boundary is defined from raw material extraction to the disposal stage.

Fig. 4 Layout of system boundary



4.2 Inventory Analysis

The initial phase modelling of building is done by assigning typical building material using Autodesk Revit. Quantity scheduling of various items of work is done in Revit and the report is generated in 'txt' format. Using Microsoft Excel, 'txt' file is converted into 'xlsx'. Environmental impact is assessed using One-Click LCA. The input given to One-click LCA software should be in gbxml, xml, and manual input format. Energy use, water use, building life, and other miscellaneous data need to provide to the software.

4.3 Calculation Result of the Building Frame

In this research work, comparison of steel frame and concrete frame of the building is done. Steel frame is analysed for load combination and optimum design of beam, column and connections are used for modelling. Modelling is done in Autodesk Revit. Similarly, reinforced concrete frame is also designed and modelled using Autodesk Revit with the use of Navigate plug-in. The pictorial representation of both the frame model is shown in Fig. 5.

Analysis of concrete and steel frame is done using One-Click LCA. Result of the analysis shows that the concrete frame produces 3.23 kg CO₂e/m²/year while the steel frame produces 2.55 kg CO₂e/m²/year. A comparison of both the frame is done using Microsoft Excel which is shown in Fig. 6.

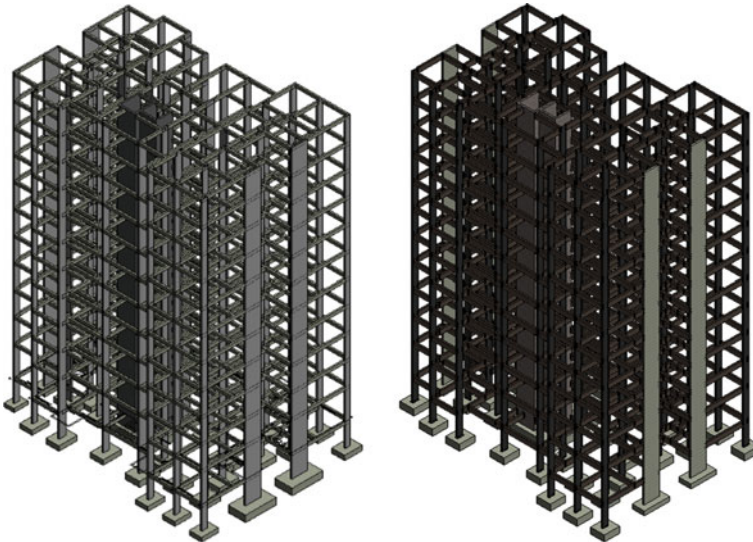


Fig. 5 a Concrete frame b Steel frame

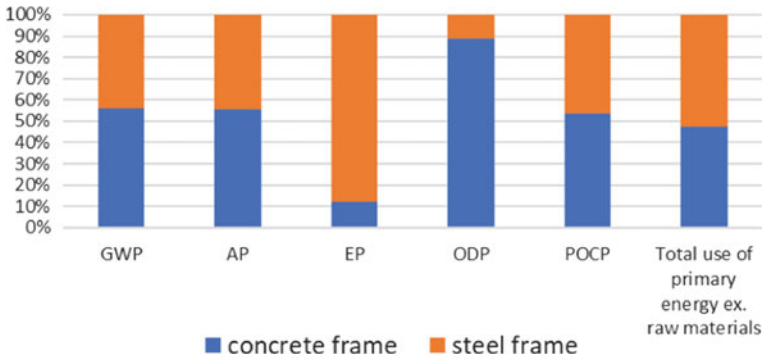


Fig. 6 Environmental impact comparison of concrete and steel frame

As per the above result data, it is observed that the impact of the steel frame is less than a concrete frame and the social cost of carbon is also minimum. But steel frame produces more impact in the category of eutrophication potential and total use of primary energy.

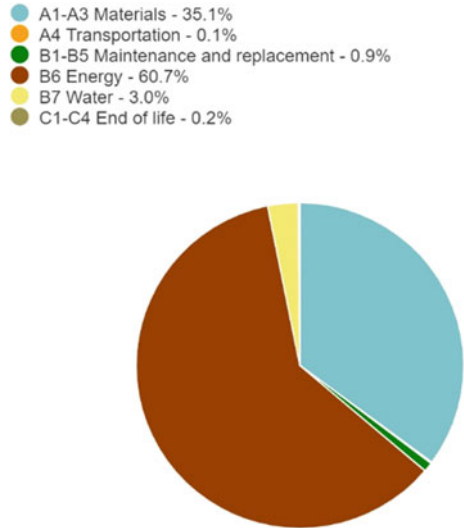
4.4 Calculation Result of Building Material

The whole building model with steel frame and typical building material is analysed and the result of the analysis shows that 45.46 kg CO₂e/m²/year is produced in the environment. The overall electricity use is 80,000 kwh/year. From all the devices, the electricity consumption by other types of machinery and HVAC is more. Fuel in the form of LPG consumption is at the rate of 7497.6 kg/year and in the form of diesel is 4559 l/year. Water consumption rate is 20,000 m³/year. Of all the life cycle stages, operational stage produces more impact on the environment. Global warming potential as per life cycle stage is shown in Fig. 7.

Of all typical building materials, clay bricks produce more impact on the environment. The most contributing material towards global warming is shown in Fig. 8.

To reduce the negative environmental impact of building materials, various material alternatives are analysed to find out the best sustainable option. Alternatives of wall, window, door, slab, insulation, and partition material are analysed for their embodied energy, and results are shown in the following figures.

Fig. 7 Global warming as per life cycle stage



No.	Resource	Cradle to gate impacts (A1-A3)	Of cradle to gate (A1-A3)
1.	Clay bricks 🏠 ?	2 576 tons CO ₂ e	73.3 %
2.	Structural steel profiles, generic 🏠 ?	449 tons CO ₂ e	12.8 %
3.	Ready-mix concrete 🏠 ?	282 tons CO ₂ e	8.0 %
4.	Slide-open aluminium frame window 🏠 ?	81 tons CO ₂ e	2.3 %
5.	Ready-mix concrete 🏠 ?	71 tons CO ₂ e	2.0 %
6.	Ready-mix concrete, normal strength, generic 🏠 ?	43 tons CO ₂ e	1.2 %
7.	External wood door 🏠 ?	13 tons CO ₂ e	0.4 %

Fig. 8 Most contributing materials towards global warming

5 Interpretation

Interpretation is the last stage of the LCA methodology. After energy analysis of various building materials and after doing their comparison, it is observed that sand-lime brick (13.1%), wood door (3.3%), double glazing window with wooden frame (13.4%), composite steel deck floor (6.6%), gypsum board partitioning system (3.3%), and cellulose insulation (0.7%) are the sustainable materials that produce less negative impact on the environment.

6 Results and Discussion

The 3D model of an apartment building is developed in Revit. Steel frame and concrete frame are analysed in One-Click LCA and the result shows that steel frame produces 2.55 kg CO₂e/m²/year and concrete frame produces 3.23 kg CO₂e/m²/year. The comparison of both the frame is shown in Fig. 6. Similarly, different material alternatives are analysed for their suitability for the environment and the result of the analysis is shown in Figs. 9, 10, 11, 12, 13 and 14. Sand lime brick, wood door, double glazing window with wooden frame, composite steel deck floor, gypsum board partitioning system, and cellulose insulation are the sustainable alternatives to the typical building material.

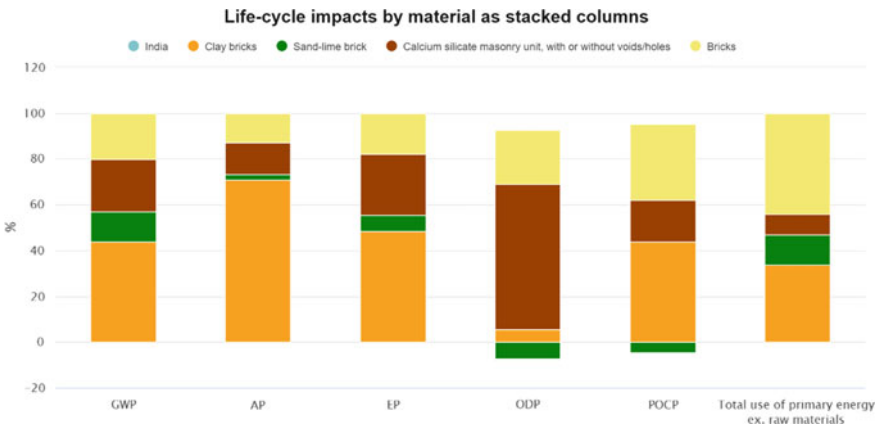


Fig. 9 Comparison of alternative brick materials

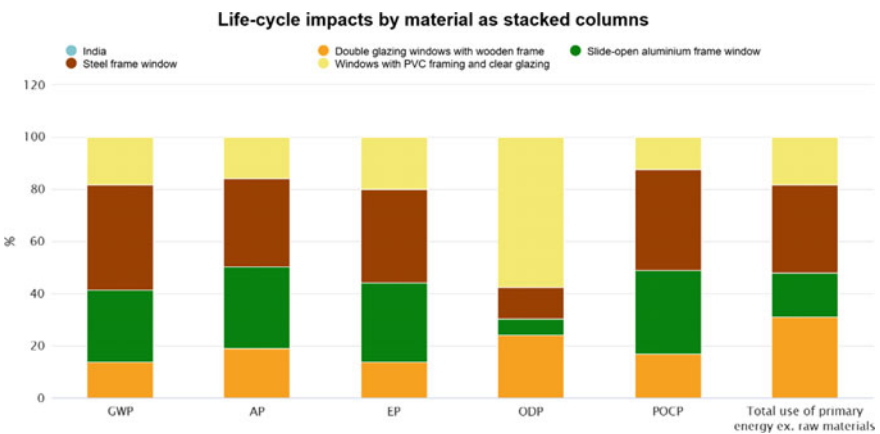


Fig. 10 Comparison of alternative window materials

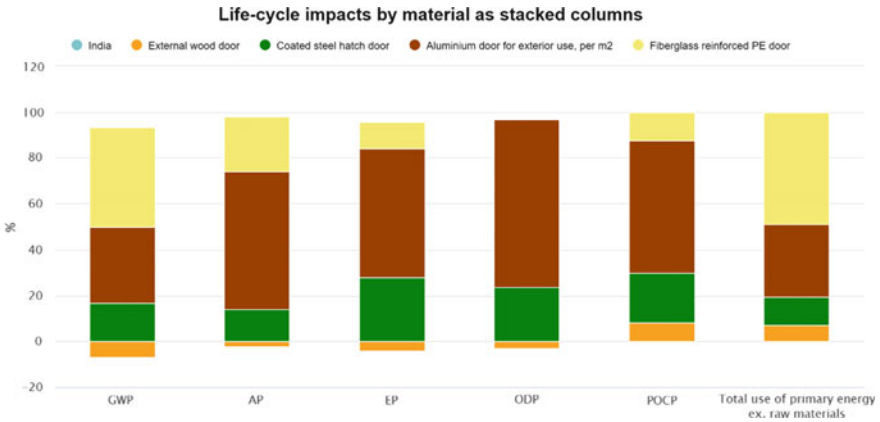


Fig. 11 Comparison of alternative door materials

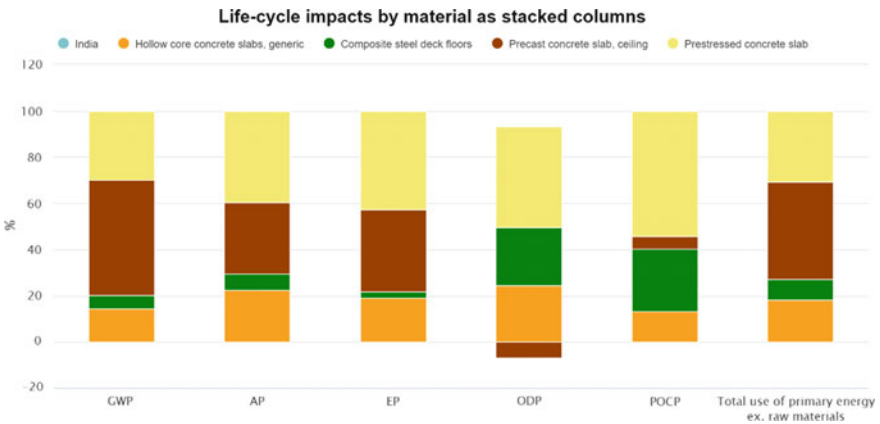


Fig. 12 Comparison of alternative slab materials

7 Conclusion

The impact of a wide range of building materials and building frame types are not analysed in previous research works. In this research work, the impact of concrete and steel frame is analysed for embodied energy and building material is analysed for life cycle energy consumption. To achieve this, integration of BIM and LCA is done and shortcomings are observed properly. Autodesk Revit helps to model a building using typical building material and LCA is used to evaluate environmental impact. Hence, the aim is to show the benefit of their integration to select sustainable building materials in the early design phase of the building.

A real-life case study is presented for the validation of all the results. This study highlighted the impact of building frames and building materials. One-Click LCA is

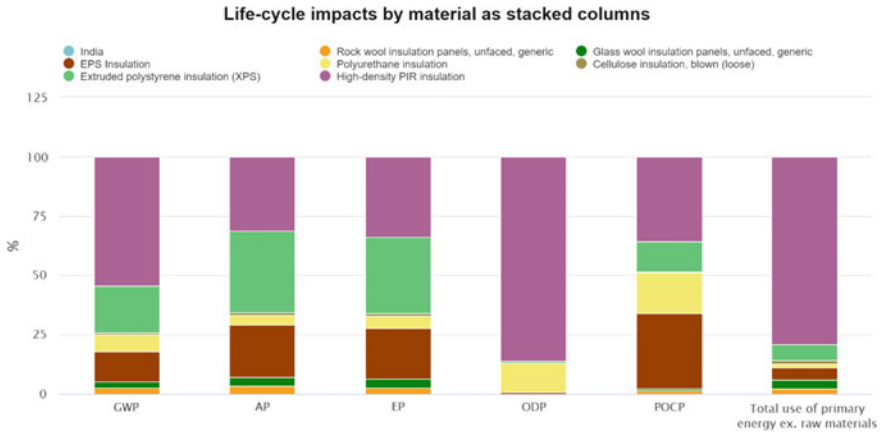


Fig. 13 Comparison of alternative insulation materials

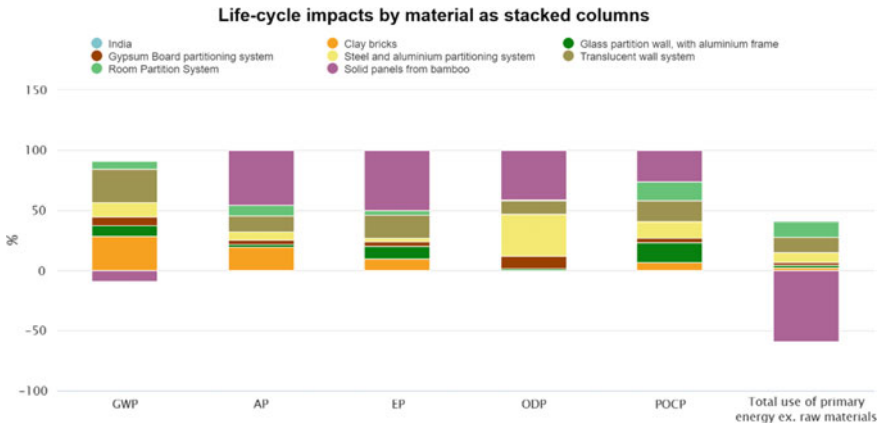


Fig. 14 Comparison of alternative partition material system

used to calculate impact which is a plug-in to Autodesk Revit. The problem regarding One-Click LCA software is that there is only a limited material database of India. This work is limited to the selection of building frame as well as building material at an early design phase of building. Future work should focus on the design aspect of building, the use of renewable energy resources and green building certification.

References

1. Gardezi SSS, Shafiq N (2019) Operational carbon footprint prediction model for conventional tropical housing: a malaysian prospective. *Int J Environ Sci Technol* 16(12):7817–7826. <https://doi.org/10.1007/s13762-019-02371-x>

2. ISO (2006) International Organization for Standardization. Environ Manage Life Cycle Assess Principles Framework 14044, Ruoyu J et al (2019) Integrating BIM with building performance analysis in project life-cycle. *Autom Constr.* <https://doi.org/10.1016/j.autcon.2019.102861>
3. Klöpffer W (2006) The role of SETAC in the development of LCA. *Int J Life Cycle Assess* 11(SPEC,1):116–22. <https://doi.org/10.1065/lca2006.04.019>
4. Kluppel HJ (1998) ISO 14041: environmental management—life cycle assessment goal and scope definition—inventory analysis. *Int J Life Cycle Assess* 3(6):301. <https://doi.org/10.1007/BF02979337>
5. Lee J et al (2018) A study on the analysis of CO₂ emissions of apartment housing in the construction process. *Sustainability (Switz)* 10(2):1–16. <https://doi.org/10.3390/su10020365>
6. Lu K et al (2019) Development of a carbon emissions analysis framework using building information modelling and life cycle assessment for the construction of hospital projects. *Sustainability (Switz)* 11(22):1–18. <https://doi.org/10.3390/su11226274>
7. Mateus R, Bragança L (2011) Sustainability assessment and rating of buildings: developing the methodology SBToolPT-H. *Build Environ* 46(10):1962–1971. <https://doi.org/10.1016/j.buildenv.2011.04.023>
8. Najjar M, Karoline F, Palumbo M et al (2017) Integration of BIM and LCA: evaluating the environmental impacts of building materials at an early stage of designing a typical office building. *J Build Eng* 14:115–26. <https://doi.org/10.1016/j.jobe.2017.10.005>
9. Najjar MK et al (2019) Life cycle assessment methodology integrated with BIM as a decision-making tool at early-stages of building design. *Int J Constr Manage* 1–15. <https://doi.org/10.1080/15623599.2019.1637098>
10. Nwodo MN, Anumba CJ (2019) A review of life cycle assessment of buildings using a systematic approach. *Build Environ* 162. <https://doi.org/10.1016/j.buildenv.2019.106290>
11. Omer MAB, Noguchi T (2020) A conceptual framework for understanding the contribution of building materials in the achievement of sustainable development goals (SDGs). *Sustain Cities Soc* 52:101869. <https://doi.org/10.1016/j.scs.2019.101869>
12. Sandberg M et al (2019) Multidisciplinary optimization of life-cycle energy and cost using a BIM-Based master model. *Sustainability (Switz)* 11:2. <https://doi.org/10.3390/su11010286>
13. Tushar Q et al (2019) Optimizing the energy consumption in a residential building at different climate zones: towards sustainable decision making. *J Cleaner Prod* 233:634–649. <https://doi.org/10.1016/j.jclepro.2019.06.093>

Enhancing the Building's Energy Performance through Building Information Modelling—A Review



Dhruvi Shah, Helly Kathiriya, Hima Suthar, Prakhar Pandya,
and Jaykumar Soni

Abstract Building Information Modelling (BIM) is a technique that facilitates the Architect, Engineering, Construction, and Operation (AECO) practitioners to model the building with detailed information in the early design phase. BIM is increasingly in demand as it provides a reliable platform for deciding the life cycle of a building at any time. We can say that BIM is the process of building a building twice. In the planning phase, the building is created in the virtual environment. All the procurement management phases, i.e., planning, building, scheduling, costing, operating and managing are simulated. The operation phase of any building has different aspects such as locating building components, facilitating real-time data access, space management, energy management, demolition and renovation. This paper focuses on the energy management segment. With ongoing increases in energy costs, rising climatic consequences and updating building guidelines worldwide, AECO practitioners progressively have to consider the building's energy performance while planning. The buildings' energy utilization pattern depends upon various factors like daylight, HVAC system, location, orientation, resident's behaviour, building material and weather. Current energy analysis systems are satisfactory up to limited levels; hence, there is a need for more efficient energy simulation systems. BIM-integrated energy simulation techniques can play a crucial role in efficiently analysing the building's performance and enhancing it. These methods are termed as Building Energy Modelling (BEM). Different BEM tools work based on input data and considerations, significantly affecting a particular tool's capacity. In this paper, different techniques are discussed accordingly. The energy modelling process is carried out by transferring the building data to a BEM tool in an acceptable file format. This research provides deep insights into the advantages and disadvantages of various

H. Kathiriya · H. Suthar · P. Pandya · J. Soni (✉)

Civil Engineering Department, L.J. Institute of Engineering and Technology, LJ University,
Ahmedabad, Gujarat, India
e-mail: jay.soni_ljiet@ljinstitutes.edu.in

D. Shah

Civil Engineering Department, Pandit Deendayal Energy University, Gandhinagar, India
e-mail: dhruvi.smtcl21@pdpu.ac.in

methods that contribute to future research and development of advanced methods and software programs.

Keywords Building information modelling (BIM) · Building energy modelling · Energy simulation · Energy performance

1 Introduction

The awareness that construction applications now face globalism, sustainability and atmospheric concerns other than that evolving legalization and skill requirements for the information era has triggered the technology known as Building Information Modelling (BIM) [12]. Building Information Modelling (BIM) is the technique of building a building twice. It is a process in which all the construction phases are simulated in a virtual environment. BIM is called the n-d process as it has many more dimensions along with 3D. 4 and 5 Ds stand for scheduling and cost evaluation of the project, respectively. 6th D is for facility management and 7th is for security and surveillance. It allows engineers to predict the building's performance in the early design stage [4]. BIM is quickly being adopted by the Architectural, Engineering, and Construction (AEC) industry as such techniques can boost productivity throughout the life cycle of the building. For example, the owner, design team and general contractor can use BIM to predict the requirements of the project, analyse the project scopes and intensify the coordination with a contractor and supplier, respectively. It can be a helping hand for facility managers by predicting the performance of the facility during the operation phase [5]. It is nowadays being used progressively as an arising technique to design, construct and operate the building in many countries [20]. BIM can be proven as a qualitative technique as it allows visualization, analysis, better documentation and easy modification in the design. Also, It allows different stack holders of the buildings to get valuable data from the model to fulfil efficient decision-making and economic project [4]. In short, BIM can be a handy tool for every building phase. In this article, the operation stage is taken under consideration as it contributes to about 60% of the total cost throughout the wheel of life of the building [18]. The operation phase of a building passes through various stages such as locating building components, visualization, marketing, space management and energy management. This article focuses on the energy management aspect.

Technological evolution affects social psychology, leading to variations in consumed energy [19]. The energy consumption pattern of a building is highly responsible for daylight and location [11], HVAC system, orientation, resident's behaviour, building material and weather. The overuse and misuse of energy resources are responsible for severe ecological and economic problems, including global warming [8]. With ongoing multiplying energy rates and the boosting concern about weather change, the idea of green building is a significant aspect of a sustainable energy future for the world. The significance of energy consumption evaluation has increased, but traditional statistics calculations are still done for estimation [16].

BIM-integrated energy simulation techniques can play a crucial role in efficiently analysing the building's performance and enhancing it. These methods are termed as Building Energy Modelling (BEM). A building energy model is a BIM model that performs energy consumption simulation. To prepare BEM models, various energy simulating tools have been developed and used. The building is first modelled using a modelling tool, this model is exported to the BEM tools in the accepted file format, and various design alternatives considering the energy utilization of the buildings are observed. The best alternative is finalized for the other construction process. This paper focuses on the file format for the data exchange between BIM and BEM. The focused formats are IFC (Industry Foundation Classes) and gbXML (Green Building Extensible Markup Language). These tools have been on the market since the 1980s. They are now improved to model and simulate more complicated and detailed systems. The energy modelling tool of a building can traditionally simulate the original structure and building materials along with complicated HVAC networks and innovative energy reservation techniques such as advanced window therapy for sun shading and renewable energy systems. But the interoperability between the BEM tool and 3D modelling tools is still challenging. The challenges are also discussed later in this article. The following segments of the article are literature review and methodology followed by discussion and conclusion.

2 Literature Review

It is believed that the planning stakeholders can be significantly benefited from BEM if BIM is implemented at the preliminary planning stage. The design alternatives in the context of energy utilization and thermal ease can be explored at this stage. The comparison between various available options can provide precise data regarding the energy consumption of the building. Dong et al. [7] said that BEM software programs could be segregated majorly into two parts. The one developed by the US Department of Energy and the other is private. For instance, eQUEST, Autodesk Green Building Studios (GBS), DesignBuilder and EnergyPlus are developed by the US Department of Energy. Whereas IES Virtual Environmental and Trace 700 are developed by private firms. Various BEM tools work according to different assumptions and details provided, influencing the performance and quality of results. For example, EnergyPlus is more flexible than BLAST and DOE-2 [6].

The BIM-based BEM can be considered a trending research topic. Some of the methods that have been developed are now used in practice. The main element of BIM-integrated BEM is data transfer. The building data such as geometry, thermal load, space heating, shading, daylight, space and thermal properties of materials are needed to be accurately transferred from BIM tool to BEM tool. There are four available primary methods for data transfer, i.e., Methods based on (1) Industry Foundation Classes (IFC), (2) Green Building Extensible Markup Language (gbXML), (3) Modelica Building Energy Modelling methods and (4) others. This article mainly focuses on the development and future research needed for the first two methods.

For the last decade, researchers and practitioners have been developing various methods to exchange the building data from BIM to the IFC-compatible BEM tools. A tool was developed to extract the data concerning the geometry of the facility from IFC to transfer it in ASCII format, preserving the data alteration rules of EnergyPlus [3]. Giannakis et al. [9] developed a semi-automatic technique using the IFC BIM model based on an algorithm to generate geometric data for EnergyPlus. An algorithm named 'Common Boundary Intersection Projection' (CBIP) was developed to produce the boundary of the geometry of the building from the IFC file. The results showed that this method provides accurate results [17]. For the transfer of material properties, an object-based technique was developed [13]. Kim et al. [14] developed an IFC-based converter that converts the building data within ArchiCAD and Revit. Laine et al. [16] developed an interface for EnergyPlus for the transformation of IFC-HVAC data to IDF and vice versa. These tools are efficient for data alteration but it is found that building geometry needs modification before simulation.

Abanda and Byers [1] examined the effect of orientation on the energy consumption process of building. The researchers used Revit and GBS for energy simulation. The results were relatively quick without regeneration of building geometry. The effect of window size, location and orientation on the energy performance of the building was examined in a study using GBS and Revit via the gbXML database [15]. To help the designer to estimate the daylight and energy usage, [2] innovated a system in Dynamo with gbXML format and a cloud-based program. Ham and Golparvar-Fard [10] developed a method for the ease of modifying thermal properties through 3D thermography using gbXML supported BIM tool. The methods compatible with the gbXML format are comparatively quick and do not require a large proportion of building geometry change. Also, to compare the results of energy consumption between various design alternatives, it is not required to get back to the BIM tool.

3 Methodology

To evaluate the building's energy behaviour through building Information modelling, the first step is to generate a BIM model of the facility to be constructed. The BIM model is not only a 3D model of a facility, but it also comprises material details, the building's location, type of building, the orientation of the building and all the aspects that affect the actual facility. After modelling, the building data are transferred to the BEM tool via accepted file format. BEM tool analyses the building's energy performance, gives results and compares the results of various design alternatives. The most possible and energy-efficient design is selected for the execution. IFC and gbXML are two various data extensions for data transfer.

IFC was initially proposed by the International Association for Interoperability (IAI). It is the only 3D object-oriented model used by BIM for information exchange and allows the exchange of details among collaborative groups. Autodesk Green Building Studios developed the gbXML based on the extensible markup language.

The XML represents a rich, generic, purposeful and validatable data format for storing and transmitting text and other details on and off the web service.

4 Discussion

Building Information Modelling is a technique evolving the decision-making segment of the construction sector. It can help enhance the collaboration between various stakeholders of a facility and provide a reliable base for decision-making during any building stage throughout its wheel of life. The operation phase of the building accounts for a large share of cost among all the phases so it is needed to enhance the performance of the building through various aspects. The overuse of energy has been increasing with the increase in demand and the time spent in the house. The construction sector is counted for considerable global energy utilization. Nowadays, Green Building has become a trending topic among researchers and practitioners due to the awareness and rising cost of energy sources. Building Energy Modelling Integrated with Building Information Modelling can perform a crucial part in analysing and enhancing the building energy performance. In this article, the methods of BIM-integrated BEM are focused. The exchange of information between BIM and BEM tools is an essential consideration as it is responsible for the accuracy of the results followed by decision-making. Both the medium, IFC and gbXML, are accurate up to a limited level. gbXML format is accurate for the simple building shapes. At the same time, IFC can deal with complex designs also. IFC requires comparatively more time for the analysis, and the gbXML format supports a rapid process. The gbXML file format is presently initiated to facilitate information exchange between BIM-supporting software programs and energy analysis tools. Compared to the IFC format which focuses on acquiring a complete and non-specific path to manage the information exchanging problems of a whole construction project, the gbXML format acquires particularity in the energy simulation discipline [7]. The literature review concluded that most of the gbXML-based techniques allow the successful exchange of geometrical, material and thermal data. It can be said that gbXML-based techniques have improved execution and touch a degree of semi-automated BIM-integrated BEM methods, where several building informations is altered from BIM, and the other necessary inputs need to be recorded by users in the user interface.

5 Conclusion

This article focuses on the methods of integrating BIM and BEM. Compared to manual methods used to date, BEM can provide accurate results for efficient decision-making concerning the building's energy performance. There are more than 400 tools for BIM and energy analysis. The BIM model data needs to be efficiently

transferred to the BEM tool to achieve accurate energy performance prediction of the building. The data that needs to be transferred is geometry, material, space type, thermal zone, space load and HVAC system. This paper discusses two methods (IFC-based and gbXML-based) for the information exchange. Many researchers have tried developing various tools in compliance with IFC or gbXML format, but in the end, it is needed to check and modify several BEM data manually for reliable energy modelling. The main reason is the lack of proper interoperability between BIM and BEM tools. A BIM model generally consists of high-level data, which is much more complicated for BEM to interpret. Future research should also focus on the design engineer's aspect of utilizing Building Information Modelling integrated with Building Energy Modelling and reliable transfer of BIM data to the BEM tool. This research gives an insight into the significance of BIM-integrated BEM. It is recommended that BEM should be an integral part of the design phase for economic and ecologic decision-making.

References

1. Abanda FH, Byers L (2016) An investigation of the impact of building orientation on energy consumption in a domestic building using emerging BIM (building information modelling). *Energy* 97:517–527. <https://doi.org/10.1016/j.energy.2015.12.135>
2. Asl MR, Bergin M, Menter A, Yan W (2014) BIM-Based parametric building energy performance multiobjective optimization. In: 32nd ECAADe conference, vol 224, p 10. <http://autodeskresearch.com/pdf/bimparametric.pdf>
3. Bazjanac V (2009) Implementation of semi-automated energy performance simulation: building geometry. In: *Managing IT in construction/managing construction for tomorrow*, pp 613–20. <https://doi.org/10.1201/9781482266665-84>
4. Borrmann A, König M, Koch C, Beetz J (2018) Building information modeling: Why? What? How? *Build Inf Model Technol Found Ind Pract* 1–24. https://doi.org/10.1007/978-3-319-92862-3_1
5. Bryde D, Broquetas M, Volm JM (2013) The project benefits of building information modelling (BIM). *Int J Project Manage* 31(7):971–980. <https://doi.org/10.1016/j.ijproman.2012.12.001>
6. Crawley DB, Lawrie LK, Winkelmann FC, Buhl WF, Joe Huang Y, Pedersen CO, Strand RK et al (2001) EnergyPlus: creating a new-generation building energy simulation program. *Energy Build* 33(4):319–331. [https://doi.org/10.1016/S0378-7788\(00\)00114-6](https://doi.org/10.1016/S0378-7788(00)00114-6)
7. Dong B, Lam KP, Huang YC, Dobbs GM (2007) A comparative study of the IFC and GbXML informational infrastructures for data exchange in computational design support environments. In: *IBPSA 2007—international building performance simulation association 2007*, pp 1530–37. https://www.researchgate.net/publication/285494452_A_comparative_study_of_the_IFC_and_gbXML_informational_infrastructures_for_data_exchange_in_computational_design_support_environments
8. Enshassi A, Ayash A, Mohamed S (2018) Factors driving contractors to implement energy management strategies in construction projects. *J Financ Manag Prop Constr* 23(3):295–311. <https://doi.org/10.1108/JFMPC-09-2017-0035>
9. Giannakis GI, Lilis GN, Garcia MA, Kontes GD, Valmaseda C, Rovas DV (2015) A methodology to automatically generate geometry inputs for energy performance simulation from IFC BIM models. In: *14th International conference of IBPSA—building simulation 2015, BS 2015, conference proceedings*, pp 504–11

10. Ham Y, Golparvar-Fard M (2015) Mapping actual thermal properties to building elements in GbXML-Based BIM for reliable building energy performance modeling. *Autom Constr* 49:214–224. <https://doi.org/10.1016/j.autcon.2014.07.009>
11. Hviid CA, Nielsen TR, Svendsen S (2008) Simple tool to evaluate the impact of daylight on building energy consumption. *Sol Energy* 82(9):787–798. <https://doi.org/10.1016/j.solener.2008.03.001>
12. Jaradat S (2014) Educating the next generation of architects for interdisciplinary BIM environments. *Charrette* 1(1):127–136
13. Kim H, Shen Z, Kim I, Kim K, Stumpf A, Jungho Y (2016) BIM IFC information mapping to building energy analysis (BEA) model with manually extended material information. *Autom Constr* 68:183–193. <https://doi.org/10.1016/j.autcon.2016.04.002>
14. Kim I, Kim J, Seo J (2012) Development of an IFC-Based IDF converter for supporting energy performance assessment in the early design phase. *J Asian Archit Build Eng* 11(2):313–320. <https://doi.org/10.3130/jaabe.11.313>
15. Kim S, Zadeh PA, Staub-French S, Froese T, Cavka BT (2016) Assessment of the impact of window size, position and orientation on building energy load using BIM. *Procedia Eng* 145:1424–1431. <https://doi.org/10.1016/j.proeng.2016.04.179>
16. Laine T, Karola A (2007) Benefits of building information models in energy analysis. *Energy* 8. <http://www.irbnet.de/daten/iconda/CIB8170.pdf>
17. Lilis GN, Giannakis GI, Rovas DV (2017) Automatic generation of second-level space boundary topology from IFC geometry inputs. *Autom Constr* 76:108–124. <https://doi.org/10.1016/j.autcon.2016.08.044>
18. Liu R, Issa RRA (2016) Survey: common knowledge in BIM for facility maintenance. *J Perform Constructed Facil* 30(3). [https://doi.org/10.1061/\(ASCE\)CF.1943-5509.0000778](https://doi.org/10.1061/(ASCE)CF.1943-5509.0000778)
19. Røpke I, Christensen TH (2012) Energy impacts of ICT—insights from an everyday life perspective. *Telematics Inform* 29(4):348–361. <https://doi.org/10.1016/j.tele.2012.02.001>
20. Wong AKD, Wong FKW, Nadeem A (2013) Comparative roles of major stakeholders for the implementation of BIM in various countries. *J Chem Inf Model* 53(9):1689–99

Analysis of Clashes and Their Impact on Construction Project Using Building Information Modelling



Samkit V. Gandhi and Namdeo A. Hedao

Abstract Building Information Modelling (BIM) is an intelligent digital database containing all required construction features that offer stakeholders, and AEC professionals the knowledge they can use across the project life cycle to plan, design, manage and make successful decisions. The cooperation between the teams by coordinating 3D designs through BIM is necessary for the final design to be free of clash. The literature indicates that the need for BIM has increased and that some countries have also mandated its use in their construction projects. This paper aims to investigate the root cause of clashes occurring in construction work and their quantification using building information modelling. The research method implemented in this study is the preparation of 3D architectural, structural and MEP (Mechanical, Electrical and Plumbing) Revit model and the analysis of clashes using BIM software for buildings in India. The result from the BIM software showed the different types of clashes that affect the construction mainly, hard clashes which occurs due to the intersection of the component from different disciplines, soft clashes due to lack of buffer space around equipment's and workflow, or 4D clashes focused on the conflict between workflow and scheduling of equipment. This study concludes with the detailed quantification of clashes, their causes and impact of occurrence on building construction projects.

Keywords Building information modelling · Clash · Detection · Quantification · Scheduling

1 Introduction

In the design stage, 70% of the cost of building construction is committed; therefore, it is necessary to incorporate multidisciplinary expertise throughout the building

S. V. Gandhi (✉)

Construction Management, College of Engineering Pune, Pune, India

e-mail: gandhisv19.civil@coep.ac.in

N. A. Hedao

College of Engineering Pune, Pune, India

e-mail: nah.civil@coep.ac.in

© The Author(s), under exclusive license to Springer Nature Singapore Pte Ltd. 2023

255

M. S. Ranadive et al. (eds.), *Recent Trends in Construction Technology*

and Management, Lecture Notes in Civil Engineering 260,

https://doi.org/10.1007/978-981-19-2145-2_21

construction process. The fact that there are so many diverse people working in the Architectural Engineering and Construction (AEC) industry is one of the problems according to a fragmented system of management in various sections of the project (structure, facilities, design, delivery, etc.). Each of these components must be based on a common concept and follow the same requirements as the others; they are a core component of the understanding that helps the project to be created together. If knowledge is not reliable and detailed enough, it will influence the next steps. Therefore, it is very common for existing buildings to lack suitable records, alter orders and a built-drawing. Because of its ability to cater to all stakeholders involved in the project, Building Information Modelling (BIM) is an important element in the integrated management of the project. BIM has the capacity to provide all stakeholders involved in the construction process with access to project-related information. BIM can assist owners, designers and builders to develop and coordinate the design of building systems and the planning of construction work, their manufacturing and construction processes and their operating and maintenance processes, as well as the decommissioning of their installations.

Building Information Modelling (BIM) is a sophisticated 3D model-based approach that offers architects, developers and construction practitioners the expertise and resources they need to help plan, design, create and maintain buildings and infrastructure. “The use of a shared digital representation of a built object (including buildings, bridges, roads, process plants, etc.) to facilitate design, construction and operation processes to form a reliable basis for decisions”. ISO 19650 (2019). In all stages of project implementation, BIM can be used. It also progresses through multiple so-called Levels of Development (LOD) as a project evolves through different delivery stages. The use of BIM as a way of promoting cooperation and enhancing implementation performance and project quality has been promoted by several governments in recent years (Fig. 1).

Clash Detection—In the film industry, the initial concept of detecting spatial conflicts with objects originated. Developers were immediately faced with an entirely new dilemma when programming the first video games. When modelling their trails, they realized the inevitability of the collision of solid elements. Therefore, when two entities were touching each other, they had to define what to do. This effectively led to the creation of a new program code that would describe the general actions of each object involved in the dispute. The fundamental idea was to see how two objects might collide in three-dimensional space. In the case of a collision with another entity being detected by the system, the solution was to add certain object attributes and compile behaviour rules. Civil engineers began to struggle with those concerns by using BIM as a result of the accelerated growth of information technology. Clash identification for the purpose of smooth collaboration consists of the process of examining and identifying disputes within various BIM models. Collision detection or teamwork are other expressions for collision detection. This method has an effect on significant design choices and, when used correctly, will help ensure a smooth building implementation. At various stages of the project, collisions will occur.

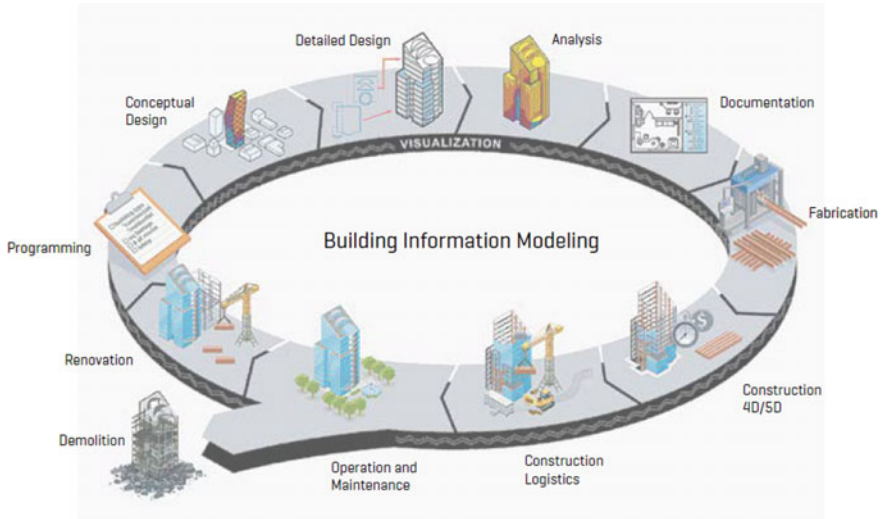


Fig. 1 BIM workflow. Courtesy Hagerman and Company

They are better resolved at the outset of the process, when it is most cost-effective. Some techniques were followed by the Built Environment to establish automatic clash identification and conflict element indicator. As time went by, this BIM clash detection system developed greatly. Today, science is actively designing tools that are more modern. These tools tend to assist in operations such as model processing and general concept making.

2 Literature Review

It is important to go for literature reviews from various journals, books, newsletters and magazines to find the attributes. By finding attributes, we will be able to know the efficiency, utilization of new technologies in construction for various purposes. BIM is a new trend which is changing the face of the construction industry. To move with the new trend, it is necessary to study and understands the impact of this adoption of new technologies in the construction sector. Impact on the construction sector, new policies to adopt, the main workforce to be recruited, cost effects of these types of various doubts will be cleared from the literature survey. Also, gaps find out in past research will be researched in this research.

BIM-based design collaboration was discussed in a recent publication with the involvement of designers, general contractors and engineers [1]. It is important to first set the team’s ground rules, and confirm that each trade can use the LOD, then the workflow of design coordination can be processed. A construction management team with proven positions specific to BIM, as well as the requisite expertise that should

be mapped out for each position in the BIM Project Execution Plan, is also required [2]. A questionnaire survey focused on the Technology-Organization-Environment (TOE) system examined the acceptance of building data modelling in the developing Indian markets [3], which broadly categorizes the influencing factors along these three dimensions. It was discovered that architectural companies in India had yet to completely leverage BIM's potential in the Indian market [4].

This paper aims to investigate the root cause of clashes occurring in construction work and their quantification using BIM. Traditionally overlaying of drawings on a light table was used for clash detection. It was a tedious and time-consuming process. Also, the results were less accurate compared to the software-based method. Thus, the use of BIM for clash detection enhances the efficiency of building construction and generate huge saving through early and accurate collision detection. The emerging use of BIM as a clash detection tool in the Indian construction sector is remarkable. In terms of design coordination, a 10-step method for 3D design coordination was proposed [5]. The design coordination workflow is split into just six steps, which enables tasks to be delegated to separate team members [1]. After the individual discipline-specific models have been developed, each BIM author must perform internal correspondence before sending their individual models to the BIM manager. After that, a federated model (which includes individual discipline-specific models) will be developed. It is also possible to define clashes as true positives, false negatives or false positives. Real positives are conflicts that have been identified as clashes that are in fact clashes, while false negatives are conflicts that have not been identified as clashes. It is also possible to define clashes as true positives, false negatives or false positives [6]. True positives are the conflicts identified as clashes as actually they are, false negatives are those which have not been registered as clashed, while false positives are clashes identified wrongly [7]. This designation aims to raise awareness of the accuracy of clash identification, either to minimize potential risks or to improve speed. The presence of positive relationships between clash identification and architecture, buildability and building efficiency is then confirmed [8].

The research carried out by Leite and Akinci [9] has compared types of clashes identified in their manual coordination process and through automatic clash detection using a BIM in Navisworks. Results from this study show a general high recall and low precision for the automatic clash detection process, and low recall and high precision for the manual approach. As a result, the root causes of clashes were investigated using the PAS 1192-2 design process requirements [10]. The isolated practice was shown to be the primary cause of high incidences of clashes related to 3D BIM Mechanical, Electrical and Plumbing (MEP) structures. They recommend that the common data environment should be unsegregated and capable of facilitating interdisciplinary and remote cooperation in an effective manner.

3 Types of Clashes

3.1 *Hard Clashes*

Hard clash is a type of conflict that involves only geometric issues. A collision in which the geometry of one part may or may not overlap that of another, but the distance between them is less than the tolerance. Hard conflicts, owing to both the specific sequence of components and their null dynamics, are perhaps the most readily recognizable of all forms of conflicts (Autodesk).

According to Seo et al. [11], these entities are assumed to be static and, thus, their permanent installation and sufficient interaction with the rest of the system can be predicted. Hard conflicts are, for example, piping system collisions with the walls or other structural components without identifying the opening.

3.2 *Soft Clashes*

Soft clash occurs when the element does not receive the required spatial or geometrical tolerance, or when its buffer zone is breached. In this case, in the control process, space, connection, installation and manipulation requirements are considered. “A clash in which the selection geometry of one component may or may not directly interfere with that of the selection of another component, but is less than the set tolerance gap” [12]. For example, for secure and simple maintenance access, an air conditioning unit can require buffer space from a beam. If left unattended, soft clashes can lead to maintenance issues as well as safety concerns.

3.3 *Workflow or 4D Clashes*

Contractor scheduling conflicts, delivery of equipment and services and conflicts over the general workflow timetable are all examples of workflow or 4D clashes. Unlike hard and soft clashes, 4D clashes result from scheduling clashes of interdisciplinary activities that eventually reduce the efficiency of the entire construction industry. Engineers may face challenges that can have a significant impact on ongoing work caused by different timetables or coordination plans. Since one dispute has a cascading effect on many fields and can bring work to a standstill, contractors cannot afford 4D disputes; it is necessary to prefer BIM. The control framework investigates these problems for 4D conflicts [13]. Basically, 4D collisions happen mostly during construction and have little to do with the structure’s design. An example of a 4D clash is insufficient distance between the crane and the structure during construction.

4 Research Methodology

From the literature survey, the need of using BIM in the design and coordination process was known and its benefits were identified. In order to illustrate the proposed clash detection work, the process is applied to the commercial office building in the central Maharashtra region. The building was designed as a multipurpose building for various office spaces. The data is collected in the form of 2D CAD drawings (structural, architectural, MEP) and other construction and interior details. The data available was analysed and separate 3D BIM models were developed from the 2D CAD drawings for all the 3 disciplines as architectural, structural and MEP. The ISO 19650 guideline, which was based on UK PAS 1192, specifies the criteria for achieving BIM Level 2 by developing a structure for collaborative working and knowledge requirements in BIM.

Considering LOD 300, the 3D architectural model was prepared using Revit 2020. As a base guide, the 2D plan was imported into the Revit. Using the reference, a plan is created taking into account the origin of the Revit to which the levels with the appropriate height and wall thickness have further been applied. The Revit families have allocated different building materials and architectural installations.

The 3D structural model is prepared using the same Revit 2020 software with the aid of the 3D architectural model and RCC plan available. The grid line for the creation of the model is mainly fixed. The location of columns and beams with the coordinates was then set with regard to the architectural model and the structural plan available. Then, as the slab height was determined by floor height, the roof was covered with galvanized sheets of iron. The connection between the beams, columns and all other structural members was provided in the Revit for RCC frame connections using the plug-in advance steel connection. The model prepared was then reviewed by the structural expert for maximum accuracy.

The preparation of the MEP model was the most critical and challenging modelling task. As it encompasses a wide range of components from various contractors, which is the primary reason for clashes. For ease of planning, separate 3D models were prepared for each system along with HVAC from the 2D drawings and information available for mechanical, electrical and plumbing systems. With the expert recommendations, other miscellaneous components such as cable trays, ducts, hangers were also added. In one federated model, these all-separate 3D models were integrated and all systems as a single model were linked together.

The clash detection analysis of these models was done using Navisworks Manage 2020 software. In this, the different models were merged clash detective test was carried out between two at a time as structural versus MEP, structural versus architectural, architectural versus MEP. The clash test between different components of the same model (i.e., piping with electrical) or different models from the same level also can be done. The clashes can be sorted based on hard, hard conservative, soft (clearance) and duplicate clash in the clash detective test. The elaboration of the clash test is shown in the data analysis part. The tolerance for each test can be set as per the requirement, it controls the severity of the clashes reported and filter out

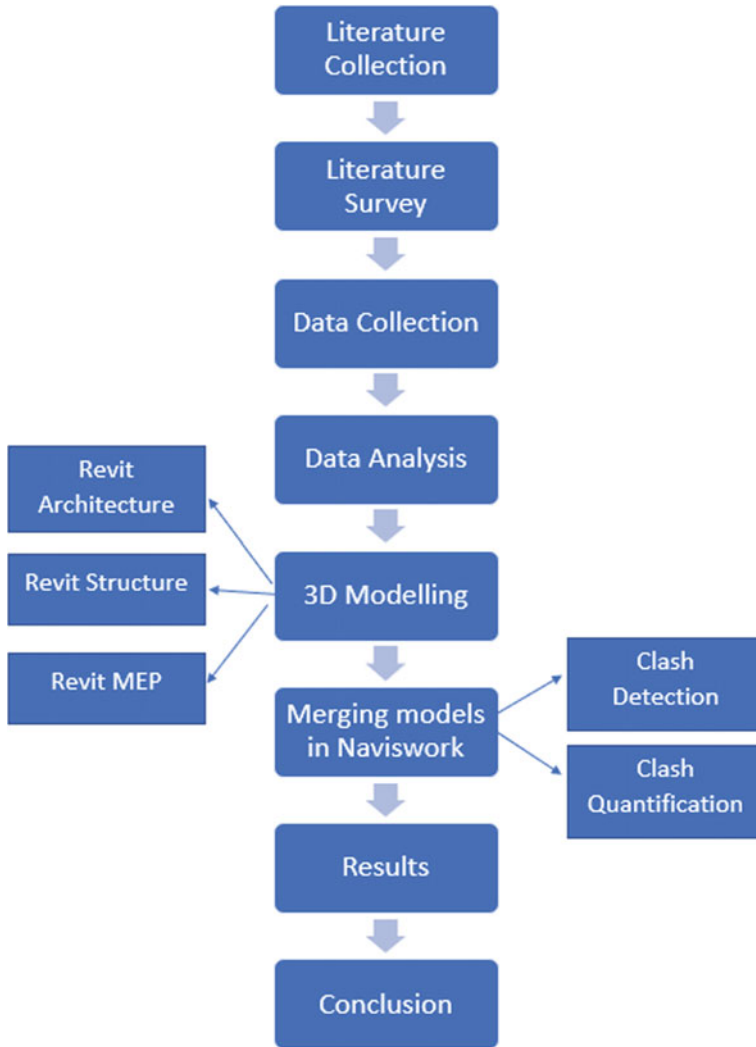


Fig. 2 Research framework

negligible clashes. Thus, after the clash test, the report of each test can be exported in excel format with the clash coordinates for ease of understanding (Fig. 2).

5 Data Collection

To study the effective use of BIM, a real-life case study of the multi-purpose buildings was selected. Details of the case study are as follows:

Location—Ahmednagar, Maharashtra India.

No. of Floors—G + 3.

Area of each Floor—1080 m².

Total Floor Area—4320 m².

Building type—Commercial office building.

Details Available—Floor Plan of all floors in 2D (Fig. 3).

6 Data Analysis

The collected data was categorized according to requirements and data analysis was carried out at various stages. Using Revit 2020 software, the 3D BIM-based Structural, Architectural and MEP modelling was primarily carried out. After the model was prepared, Navisworks Manage 2020 was used to conduct clash detection and further clash quantification based on various clashes and models (Figs. 4, 5 and 6).

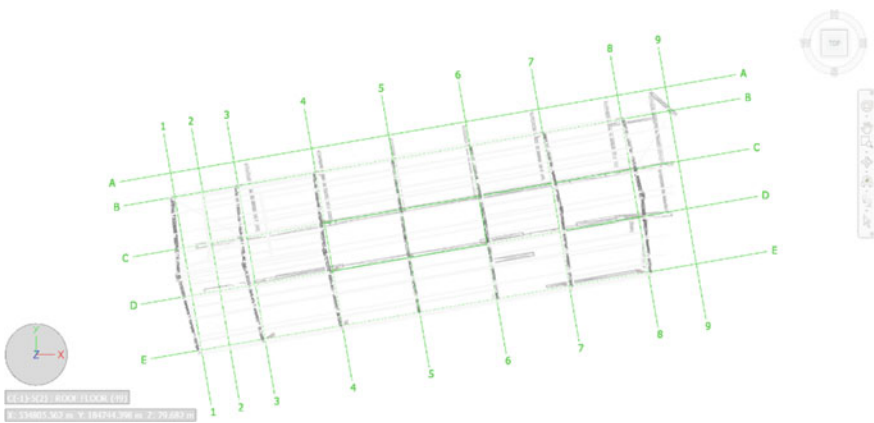


Fig. 4 BIM based 3-dimensional model of structural component

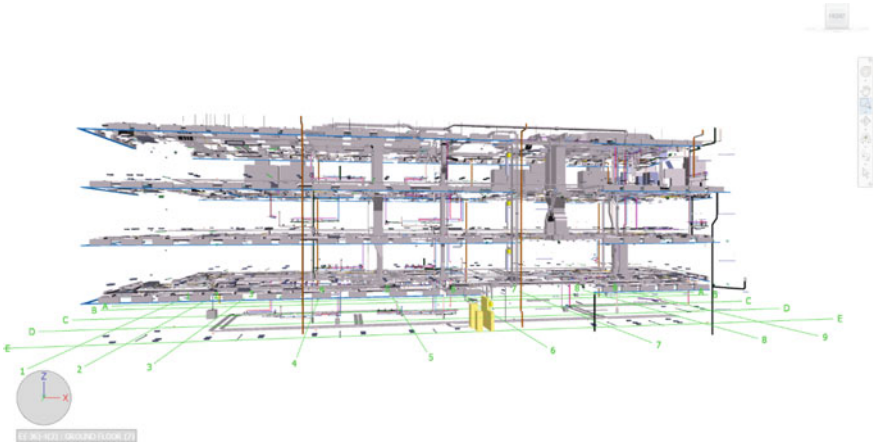


Fig. 5 BIM based 3-dimensional model of MEP components including HVAC system



Fig. 6 BIM-based three-dimensional model of architectural component

7 Result and Discussion

See Figs. 7, 8, 9, 10, 11, 12 and 13.

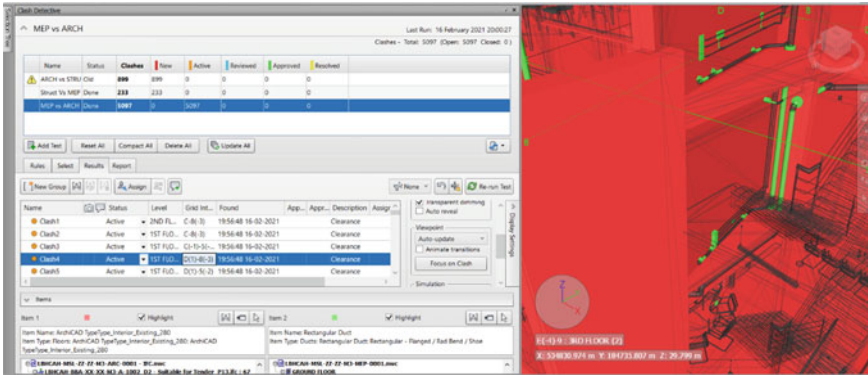


Fig. 7 Clash detection analysis between architectural and MEP models using Navisworks

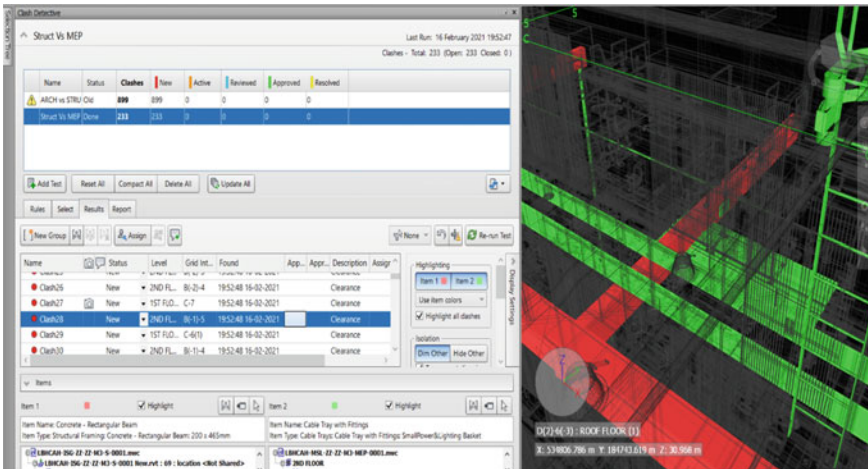


Fig. 8 Clash detection analysis between structural and MEP model using Navisworks

7.1 Observation from Results

From the data analysis and the results obtained from the data, we can observe that after the total 9 clash detection test between different models of architectural, structural and MEP using Navisworks out of total hard clashes maximum of 72% (2575) were caused between Architectural versus MEP models, 22% (793) between structural versus architectural models and only 6% (228) in structural versus MEP models. It can be seen that the maximum collision is between architectural and MEP components geometry and the lowest is between the structural and MEP components. The clash detective test for the soft/clearance clashes shows relatively same results showing 67% (2363) between architectural versus MEP, 26% (899) of structural versus

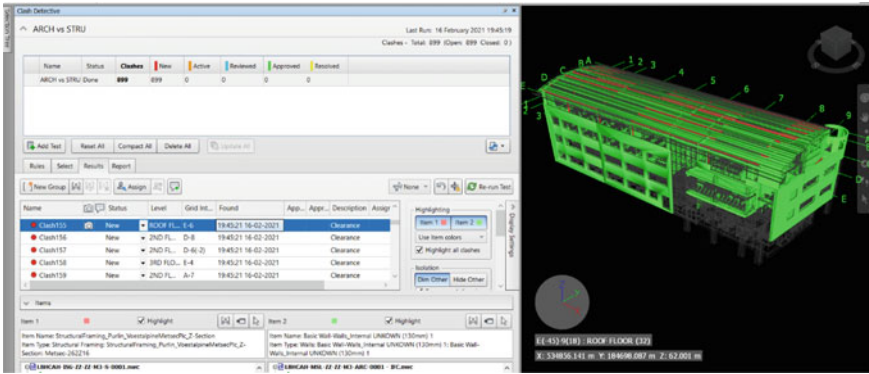
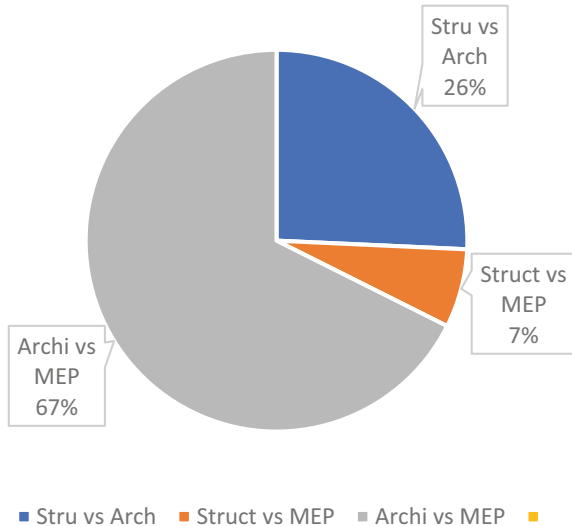


Fig. 9 Clash detection analysis between architectural and structural models using Navisworks

Fig. 10 Soft clash report



architectural, and only 7% (233) structural versus MEP. It shows that the geometry of the following clashes doesn't directly intersect but comes between the tolerance limit. We can further notice the occurrence of duplicate clashes having twin geometry and at the same location is also more for the architectural versus MEP test but comparatively negligible in numbers.

Thus, a comparative analysis of results shows that architectural and MEP components and their collision are the main reason for the occurrence of clashes and need to be focused primarily on designing and construction work.

Fig. 11 Hard clash report

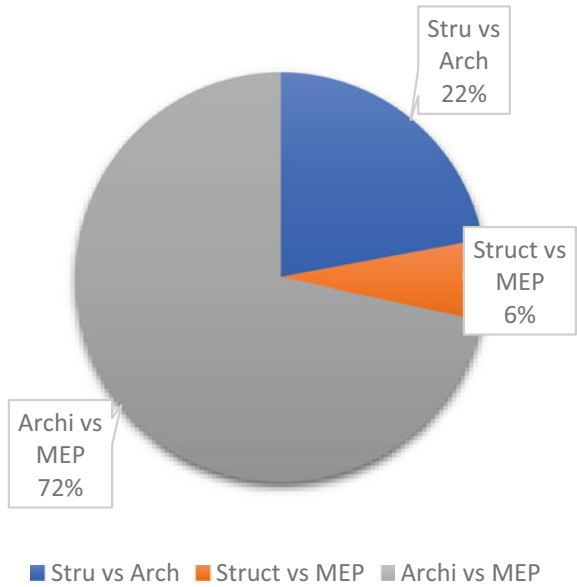
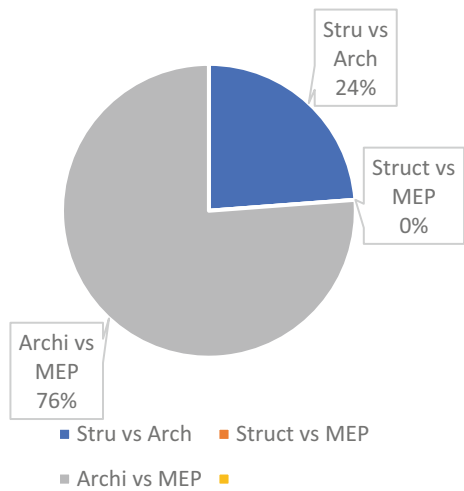


Fig. 12 Duplicate clashes report



8 Conclusion

After the review of the clash detection with the application of technology-based on BIM, the study shows that the incorporation of 3D models is important for better visualization in construction planning; therefore, pointless errors can be avoided to reduce the risk of cost overruns in the construction process. The clash detection terminology was explained with its types. 3D modelling was done for structural,

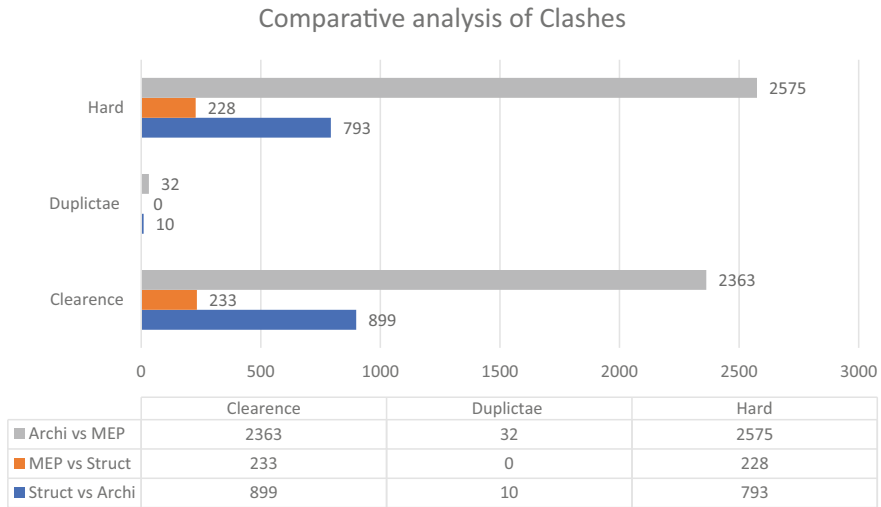


Fig. 13 Comparative analysis of clashes

architectural and MEP components using Revit2020 software. A Simple clash detection test was proposed using BIM-based Navisworks software. Clashes are sorted into three categories as hard, clearance and duplicate. Clash detective test identified the design collision and errors between the 3 models, with overall 3596 hard clashes detected in this study. Most clashes are detected between architectural and MEP (HVAC) component consisting of 2575 clashes caused. The main cause for the detected clashes was the lack of multidisciplinary coordination between different stakeholders. We can see that the count of the hard clash is nearly the same as the soft clashes thus can say circumstances that led to the hard clash may also cause the soft clash. The clashes pose possible risks, according to cited sources. High spending, significant delays, injuries and even deaths may be caused by them.

References

1. Arayici Y, Aouad G (2011) Building information modelling (BIM) for construction lifecycle management. In: Construction and building: design, materials, and techniques, March, pp 99–117
2. Abanda FH, Vidalakis C, Oti AH, Tah JHM (2015) A critical analysis of building information modelling systems used in construction projects. *Adv Eng Softw* 90:183–201. <https://doi.org/10.1016/j.advengsoft.2015.08.009>
3. Ahuja R, Sawhney A, Jain M, Arif M, Rakshit S (2020) Factors influencing BIM adoption in emerging markets—the case of India. *Int J Constr Manag* 20(1):65–76. <https://doi.org/10.1080/15623599.2018.1462445>
4. Sawhney A, Singhal P (2014) Drivers and barriers to the use of building information modelling in India. *Int J 3-D Inf Model* 2(3):46–63. <https://doi.org/10.4018/ij3dim.2013070104>

5. Staub-French S, Khanzode A (2007) 3D and 4D modeling for design and construction coordination: issues and lessons learned. *ITcon* 12(Sept 2006):381–407. <http://www.itcon.org/2007/26>
6. Tommelein ID, Gholami S (2012) Root causes of clashes in building information models. In: *IGLC 2012—20th conference of the international group for lean construction*, 1(510)
7. Tixier AJP, Hallowell MR, Rajagopalan B, Bowman D (2017) Construction safety clash detection: identifying safety incompatibilities among fundamental attributes using data mining. *Autom Constr* 74:39–54. <https://doi.org/10.1016/j.autcon.2016.11.001>
8. Hartmann T (2010) Detecting design conflicts using building information models : a comparative lab experiment. In: *Proceedings of the CIB W78 2010: 27th international conference—Cairo, Egypt*, 16–18 Nov
9. Leite F, Akinci B (2009) Identification of data items needed for automatic clash detection in MEP design coordination: construction research congress 2009, pp. 416–425
10. Akponeware AO, Adamu ZA (2017) Clash detection or clash avoidance? An investigation into coordination problems in 3D BIM. *Buildings* 7(3):1–28. <https://doi.org/10.3390/buildings7030075>
11. Seo J-H, Lee B-R, Kim J-H, Kim J-J (2012) Collaborative process to facilitate BIM-based clash detection tasks for enhancing constructability. *J Korea Inst Build Constr* 12(3):299–314. <https://doi.org/10.5345/jkibc.2012.12.3.299>
12. Reddy P (n.d.) BIM for building owners and developers: making a business case for using BIM on projects
13. Matejka P, Sabart D (2018) Categorization of clashes and their impacts on construction projects. In: *Engineering for rural development*, 17, pp 827–835. <https://doi.org/10.22616/ERDev2018.17.N102>

Predicting the Performance of Highway Project Using Gray Numbers



Supriya Jha, Manas Bhoi, and Uma Chaduvula

Abstract Earned Value Analysis is a methodology used to monitor project performance in terms of time, scope and cost and also to deal with uncertain situations that come within. Uncertainty is a part of construction project and sometimes these situations can cause a great loss in the project's success. Recently, to deal with uncertain situations a different approach has been developed to predict the project performance in a non-deterministic way, i.e., using gray interval numbers. A framework using gray interval numbers has been developed to predict the project performance and hence this study aims at using the framework to predict the performance of a real-life highway project of total duration of approximately 2 years. The analysis involves the verbal directed data from the site by the experts which were denoted as gray interval numbers. The results indicate that the project is under budget as the CPI is 1.06 and ahead of schedule as the SPI is 1.2. The results also show the worst case scenario that the project may exceed the budget as CPI is 0.83 and may run behind the schedule as SPI is 0.69. The outcomes of the study are in the form of range which provides the overall profile of the project and also helps the project team members to not always be accurate or deterministic with the outcomes. Since the construction sector was majorly hit by an uncertain event, i.e., COVID-19, this study can be very helpful in determining the performance after facing such a huge gap.

Keywords Project management · Earned value analysis · Gray numbers · Performance control

1 Introduction

Project management is an integral part of the construction sector and it involves making a project to be a success. Earned value analysis (EVA) is an important key to the project management which in turns predicts the overall performance of the project. Many methods of EVA have been developed like earned schedule, earned schedule

S. Jha (✉) · M. Bhoi · U. Chaduvula
Pandit Deendayal Petroleum University, Gandhinagar, India
e-mail: supriyajha534@gmail.com

© The Author(s), under exclusive license to Springer Nature Singapore Pte Ltd. 2023
M. S. Ranadive et al. (eds.), *Recent Trends in Construction Technology and Management*, Lecture Notes in Civil Engineering 260,
https://doi.org/10.1007/978-981-19-2145-2_22

271

min–max, earned duration management, etc., which are all deterministic methods. Timur et al. [1] discussed about the conventional Index-based (IB) EVM method, how it restricts the accuracy of forecasting Cost Estimate at Completion (CEAC) of a project by presuming that it only depends on the past available data and having insufficient amount of data at an early stage of the project, they suggested a new approach for CEAC which is a blend of index-regression technique to foresight the final cost of the impending projects. This strategy depends on ES-based IB equation altered by combination of Gompertz Growth Model (GGM) via non-linear regression analysis which gives more exact and detailed CEAC. Batselier et al. [2] compared three primary deterministic methods of EVM and their reciprocated blend on an actual project. The two methods i.e., ESM-1 and ESM-SPI(t) (where the performance index is selected as 1 and SPI respectively) were used as the addition in EVM and both of them combine rework and activity sensitivity in EVM time foresight, they both are performance-aimed techniques. Rupak [3] suggested a gray concept technique that will assist in acknowledging and creating project interrelationships and also to keep up with the uncertainty. This concept is believed to be an effective technique to work out the R&D project portfolio preferences.

Li et al. [4] aims at developing a different non-deterministic approach, i.e., gray-based approach for the selection of the ideal supplier. The outcomes show that gray theory works great with complex and uncertain situations and this proposed method is quite efficient and effective. Li et al. [5] discussed about the most common method for complex decision making process, i.e., TOPSIS (technique for order performance by similarity to ideal solution). They have proposed to extend this method by including Minkowski distance function to enhance the limitations of the TOPSIS method followed by the addition of gray numbers to deal with the uncertain situations involved and lastly to amalgamate it with the expert opinion decision process. Oztaysi [6] focussed on IT field to select the best communicating platform for both the internal and external affairs. They have proposed an amalgamation of Analytical Hierarchy Process (AHP) with Gray-TOPSIS model which enables the evaluation of the weightage of each factor and deals with the ranking including uncertainties. Li et al. [7] aims at developing a framework for assessing safety performance of the organizations that may involve all the risk-based factors. They aimed at broadening the conventional analytical hierarchy process to gray numbers systems to deal with the uncertain factors in the assessment. Amirian and Sahraeian [8] aims at approaching a different technique for project selection and scheduling. They have converted a pure integer model into gray model as gray numbers have distinctive type of relations with the variables other than the deterministic variables.

Durga et al. [9] compared the manual and computer-aided technique and showed that software could be easily managed and leads to time-saving and quicker decision making, also showed the track progress of the ongoing project. Paulo et al. [10] blended schedule performance and schedule adherence as an index to enhance the duration foresight precision where schedule adherence is an extension to EDM concept that leads to addition of c-factor with respect to schedule adherence which is not cost-related. Ibrahim et al. [11] discussed about the how the risk variables influence the EVM technique for evaluating the performance of infrastructure in the

Australian context, aims at recognizing the potential risk variables which influence the performance at the implementation stage, i.e., design and delivery stage. Perez et al. [12] suggested two new metrics and their related foresight techniques, i.e., ES_{min} and ES_{max} , these metrics highlight the preference of the activities and distribution of resources, these metrics can be separately used from EVM structure as they are not dependent on any primary metrics of EVM technique. Nadafi et al. [13] suggested a new approach to decide the project completion time and cost using verbal data. Nadafi et al. [13] introduced interval gray numbers for time and cost foresight of the project where the verbal data is assigned to gray numbers and the calculation is carried out accordingly.

Since project control is a major part of the construction project Earned Value Analysis (EVA) is very much necessary to monitor and track the project at different stages to predict the early warnings and how to cope up with them. Recently, gray numbers have been introduced in EVM technique to predict project performance where gray numbers are known for uncertain situations and unknown information. For uncertain situations, risk management for all the construction projects has been carried out but some uncertainties still remain which are unpredictable. For now-situation, due to COVID-19, construction projects were shut down for a long time and a great loss has been occurred in terms of time and cost. Hence, to have a bigger picture and insufficient amount information in hand, prediction of the projects' health condition is quite difficult. In such situation, gray numbers are of great use where partial information is known and from that much information foresight of the project condition in comprehensive view can be obtained.

Nadafi et al. [13] suggested a new approach to decide the project completion time and cost using verbal data and introduced interval gray numbers using a numerical example. This study contributes to improving the efficiency of the methodology by applying it to a real-life highway project and predicting the performance at different stages to avoid delays and shortage of resources. Since gray numbers are known for unpredictability and insufficient amount of data, this approach is quite useful for now-situation in the construction industry. Also, for more accurate results and indicating the effectiveness of gray numbers, intermediate values have also been considered in this study to show that the outcome will not cross the range, which will better assist the project members in making accurate decisions for management.

2 Research Methodology

This paper aims at predicting the performance of the project with a different approach which involves non-deterministic input, i.e., verbal directed data. The methodology involves gray interval numbers which will assist in predicting the performance of the project. Gray interval number is defined as a range of data that can be used in situations where data is incomplete or insufficient. Gray interval number can be defined by \otimes symbol and it provides the worst and best case scenarios of the project. Gray numbers provide a wholesome profile of the project progress with minimal

data and as a result, help the project members to be prepared for the worst and best case scenarios of the project. For the analysis, a real-life highway project with a total cost of approximately Rs. 680 (millions) and total duration of approximately 2 years has been taken into account. The progress of the activities was directed by the project members from the site verbally which will be denoted as gray interval numbers accordingly as shown in Table 1.

The verbal data for the progress of the activities on the site has been collected through project members and assigned to the gray numbers accordingly as shown in Table 2 [13].

The gray interval numbers are then multiplied with the cost of each activity and earned value of the activities was evaluated. The summation of the earned value of each activity gives the overall earned value of the project. Earned value indicates the actual work performed in the project at the particular tracking period. Similarly, the verbal data for the planned progress of the activities has been collected and gray interval numbers have been assigned accordingly as shown in Table 3.

The gray interval numbers are then multiplied by the cost of each activity and planned value of activities were evaluated. The summation of the planned value of each activity gives the overall planned value of the project at that particular tracking period. Planned value indicates the work scheduled to be completed at that particular period. After evaluation of the planned value and earned value, cost performance index (CPI) which indicates the cost regulation of the project has been evaluated. It determines how much we have earned for the work completed in comparison with the actual cost spent. It also indicates whether the project is under budget/ over budget or on budget. CPI can be calculated as shown below:

$$\otimes \text{CPI} = \otimes \text{EV} / \text{AC} \tag{1}$$

where AC = Actual cost spent in the overall project.

Similarly, schedule performance index (SPI) indicates the time regulation of the project has been evaluated. It determines how much work has been completed as compared to the planned schedule in terms of time. It also determines whether the project is behind schedule/ahead of schedule or on schedule. SPI can be calculated as shown below:

Table 1 Gray numbers and corresponding verbal terms

Gray numbers	Verbal term
[0.0–0.1]	Very low
[0.1–0.3]	Low
[0.3–0.4]	Less than Medium
[0.4–0.5]	Medium
[0.5–0.6]	More than medium
[0.6–0.9]	High
[0.9–1.0]	Very high

Table 2 Earned value estimation by gray numbers

Activity		Percentage of real progress as verbal	Cost (in millions)	Gray interval number	$\otimes EV = Cost \times P$
<i>Construction in Kesinga to Bhavanipatna</i>					
1.1	Culverts	Very high	15	[0.9–1.0]	[13.5–15]
1.2	Earthwork and Subgrade preparation	Very high	28	[0.9–1.0]	[25.2–28]
1.3	GSB	Very high	29	[0.9–1.0]	[26.1–29]
1.4	WMM	Very high	29	[0.9–1.0]	[26.1–29]
1.5	DBM	Very high	60	[0.9–1.0]	[54–60]
1.6	BC	Not started	0	[0–0]	[0–0]
1.7	Road side drain	Not started	0	[0–0]	[0–0]
1.8	Road signages and boards	Not started	0	[0–0]	[0–0]
<i>Construction of Amath to kesinga</i>					
2.1	Culverts	Low	134	[0.1–0.3]	[13.4–40.2]
2.2	Minor bridges	Not started	0	[0–0]	[0–0]
2.3	Embankment and subgrade preparation	Less than medium	22	[0.3–0.4]	[6.6–8.8]
2.4	GSB	Less than medium	22	[0.3–0.4]	[6.6–8.8]
2.5	WMM	Less than medium	22	[0.3–0.4]	[6.6–8.8]
2.6	DBM	Not started	0	[0–0]	[0–0]
2.7	BC	Not started	0	[0–0]	[0–0]
2.8	Road side drain	Not started	0	[0–0]	[0–0]
2.9	Construction of toll plaza and admin building	Not started	0	[0–0]	[0–0]
2.10	Road signages and boards	Not started	0	[0–0]	[0–0]
2.11	Protection work	Not started	0	[0–0]	[0–0]
2.12	Crash barriers	Not started	0	[0–0]	[0–0]
2.13	Miscellaneous work	Not started	0	[0–0]	[0–0]
<i>Acceptance</i>					
3.1	Testing	Not started	0	[0–0]	[0–0]
3.2	Handover	Not started	0	[0–0]	[0–0]
3.3	Finish	Not started	0	[0–0]	[0–0]

(continued)

Table 2 (continued)

Activity		Percentage of real progress as verbal	Cost (in millions)	Gray interval number	$\otimes EV = \text{Cost} \times P$
			406		[178.1–227.6]

$$\otimes SPI = \otimes EV / \otimes PV \tag{2}$$

Thus, by calculating CPI and SPI, we can predict the project performance using gray numbers in terms of cost and time which will assist the project members to be prepared for the worst and best case scenarios and act accordingly to avoid any uncertainties at any given point of time.

3 Analysis and Results

In this paper, we have aimed at approaching a different method for earned value analysis for predicting the project performance and avoid the uncertainties at various stages. For the analysis, a real-life highway project with total cost of approximately Rs. 680 (millions) and total duration of approximately 2 years has been taken into account and earned value analysis has been performed using gray interval numbers. Gray interval numbers were used to provide an overall satisfactory profile of the project when there is insufficient amount of data or there is shortage of time. Gray numbers assist in providing worst and best case scenarios for the project so that the project members will be prepared for both the scenarios and avoid any delays or resource losses in the project. As mentioned above, verbal data has been collected for the project progress from the site which is graphically shown in Fig. 1. Figure 1 shows the worst case scenarios of the percentage progress of the activities as per gray numbers based on verbal directed data for the ninth month of the project as tracking period.

From Fig. 1, it has been observed that progress of activity 6th seems to be planned to get completed by 10% for that particular tracking period but it has been not started yet and similarly for the progress of activity 12th seems to be planned to get completed by 60% but it has been completed till 30% for that particular tracking period. Thus, this progress shows the worst case scenarios of the project which may affect the completion time and cost of the project.

Figure 2 shows the best case scenarios of the percentage progress of the activities as per gray numbers based on verbal directed data for the ninth month of the project as tracking period. From this, it has been observed that the progress of activity 10th seems to be on schedule and similarly progress of activity 14th seems to be completed by 20% but it has been completed till 40% at that particular tracking period which indicates better performance of the project.

Calculation of CPI and SPI of the project using gray interval numbers:

Table 3 Planned value estimation by gray numbers

Activity		Percentage of planned progress as verbal	Cost (in millions)	Gray interval number	$\otimes PV = Cost \times P$
<i>Construction in Kesinga to Bhavanipatna</i>					
1.1	Culverts	Very high	15	[0.9–1.0]	[13.5–15]
1.2	Earthwork and subgrade preparation	Very high	28	[0.9–1.0]	[25.2–28]
1.3	GSB	Very high	29	[0.9–1.0]	[26.1–29]
1.4	WMM	Very high	29	[0.9–1.0]	[26.1–29]
1.5	DBM	Very high	60	[0.9–1.0]	[54–60]
1.6	BC	Low	65	[0.1–0.3]	[6.5–19.5]
1.7	Road side drain	Very low	14	[0–0.1]	[0–1.4]
1.8	Road signages and boards	Not started	0	[0–0]	[0–0]
<i>Construction of Amath to kesinga</i>					
2.1	Culverts	Low	134	[0.1–0.3]	[13.4–40.2]
2.2	Minor bridges	Not started	0	[0–0]	[0–0]
2.3	Embankment and subgrade preparation	High	22	[0.6–0.9]	[13.2–19.8]
2.4	GSB	Medium	22	[0.4–0.5]	[8.8–11]
2.5	WMM	Low	22	[0.1–0.3]	[2.2–6.6]
2.6	DBM	Not started	0	[0–0]	[0–0]
2.7	BC	Not started	0	[0–0]	[0–0]
2.8	Road side drain	Not started	0	[0–0]	[0–0]
2.9	Construction of toll plaza and admin building	Not started	0	[0–0]	[0–0]
2.10	Road signages and boards	Not started	0	[0–0]	[0–0]
2.11	Protection work	Not started	0	[0–0]	[0–0]
2.12	Crash barriers	Not started	0	[0–0]	[0–0]
2.13	Miscellaneous work	Not started	0	[0–0]	[0–0]
<i>Acceptance</i>					
3.1	Testing	Not started	0	[0–0]	[0–0]
3.2	Handover	Not started	0	[0–0]	[0–0]
3.3	Finish	Not started	0	[0–0]	[0–0]
			406		[189–259.5]

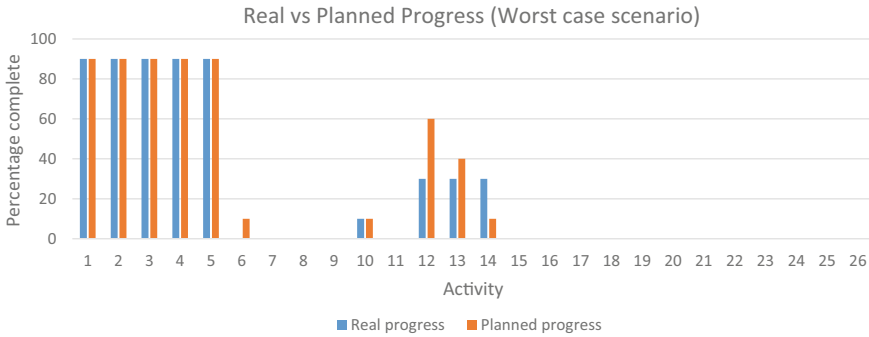


Fig. 1 Real versus planned progress of activities (worst case scenario)

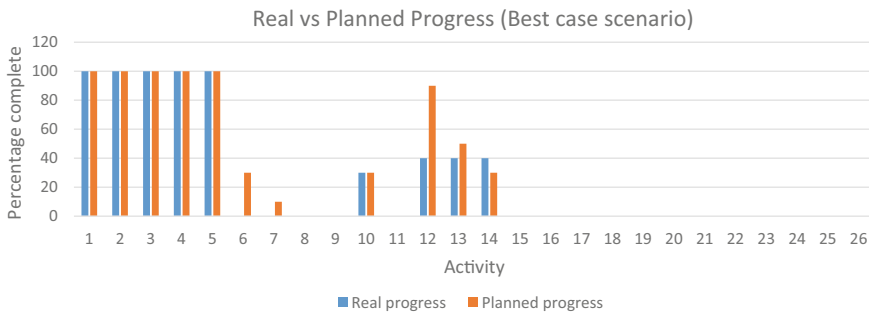


Fig. 2 Real versus planned progress of activities (best case scenario)

Taking into consideration the calculation of Tables 2 and 3 we have:

$$\otimes EV = [178.1 - 227.6]$$

$$\otimes PV = [189 - 259.5]$$

Figure 3 shows worst case scenario for Earned value versus Planned value of the activities for that particular tracking period and it has been observed that for activity 6th no value has been earned yet as per schedule some value was planned to be spent, hence such case shows the worst case scenario and assists the project members to be prepared with contingency plan.

Similarly, Fig. 4 shows the best case scenario for Earned value versus Planned value of the activities for that particular tracking period.

From EV and PV, we can further calculate the CPI and SPI and Estimate at completion (EAC) for predicting project performance and completion time and cost for the ninth month of the project as tracking period. Hence,

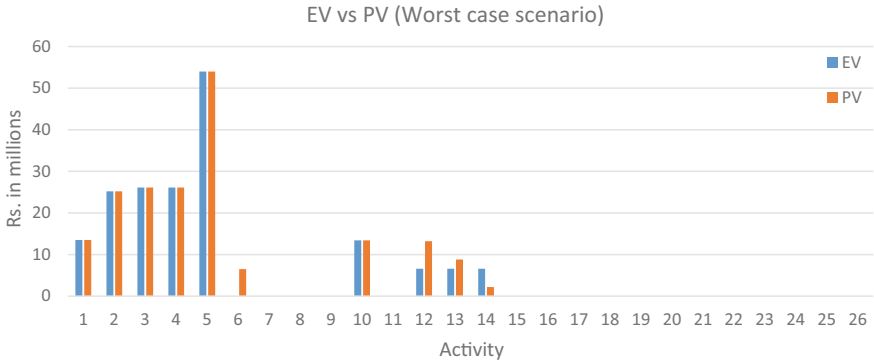


Fig. 3 EV versus PV of the activities (worst case scenario)

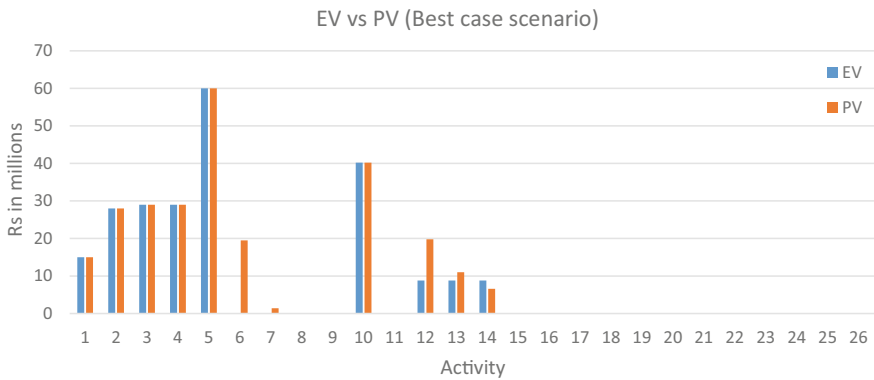


Fig. 4 EV versus PV of the activities (best case scenario)

$$\begin{aligned} \otimes \text{CPI} &= \otimes \text{EV} / \text{AC} \\ &= ([178.1 - 227.6]) / 214.7 = [0.83 - 1.06] \end{aligned} \tag{3}$$

$$\begin{aligned} \otimes \text{SPI} &= \otimes \text{EV} / \otimes \text{PV} \\ &= [178.1 - 227.6] / [189 - 259.5] = [0.69 - 1.20] \end{aligned} \tag{4}$$

$$\begin{aligned} \otimes \text{EAC} &= \text{BC} / \otimes \text{CPI} \\ &= [415.1 - 530.4] \end{aligned} \tag{5}$$

Thus, from the results of CPI and SPI, it has been observed that project is going under budget for that particular tracking period as CPI shows 1.06 on higher side which indicates under budget as $\text{CPI} > 1$. Similarly, project is going ahead of schedule for that particular tracking period as SPI shows 1.20 on higher side which indicates

ahead of schedule as $SPI > 1$. So overall it can be said that the project is under budget and ahead of schedule for that tracking period. Also, EAC seems to be out of the limit, i.e., 406 doesn't lie in between [415.1–530.4] which clearly shows the under budget scenario of the project. Thus, the outcomes determine that the project may worsen but not exceeding 0.69 and may perform better; it provides the overall satisfactory result so that the project members will be prepared for both worst and best-case scenarios. The project members can act accordingly to keep the project on track and avoid any serious uncertain situation without further loss.

4 Conclusion

This study aims at predicting the project performance of an infrastructure project using interval gray numbers. Interval gray numbers are used when determinant value, i.e., true value is not known, where data is insufficient. They assist in providing an overall view of the project profile and help in better decision-making process. Interval gray numbers are based on a non-deterministic approach other than the other methods, which are deterministic where determinate value, i.e., true value is known. Since lack of data availability is obvious in recent times; interval gray numbers are an effective way to predict the performance of the project and assist in better decision-making process.

Previously, using gray numbers to predict project performance has been carried considering a numerical example. Hence, this study covers the gap by applying the methodology on a real-life project by extending it to validate the theory to a better level by considering intermediate values to precisely provide the outcomes. A real-life commercial project has been considered and analysis has been done based on a non-deterministic approach, which indicated the project to be over budget and ahead of schedule as $CPI = [0.83–1.06]$ and $SPI = [0.69–1.20]$.

- Interval gray numbers are an effective way to predict the project performance and having a better decision-making process.
- Interval gray numbers are based on a non-deterministic approach unlike other methods which are deterministic in nature, i.e., true value or determinate value is known.
- Interval gray numbers provide the outcomes in a range which indicates the worst and best case situations of the project assisting the project members to be prepared for both situations and take better decision to keep the project on track.
- Considering intermediate values makes the interval gray numbers theory more efficient to understand the situation and precisely monitor and track the project performance to avoid any delays or shortages and losses of resources.

References

1. Narbaev T, Marco AD (2013) Earned value-based performance monitoring of facility construction projects. *J Facil Manage* 11(1):69–80
2. Batselier J, Vanhoucke M (2015) Evaluation of deterministic state-of-art forecasting approaches for project duration based on earned value management. *Inter J proj Manage* 4(3)
3. Bhattacharyya R (2015) A grey theory based multiple attribute approach for R&D project portfolio selection. *Fuzzy Inf Eng* 7(2):211–225
4. Li GD, Yamaguchi D, Nagai M (2007) A grey-based decision making approach to the supplier selection problem. *Math Comp Modell* 46:573–581
5. Li YH, Lee PC, Chang TP, Ting HI (2008) Multi-attribute decision making model under the condition of uncertain information. *Autom Constr* 17:792–797
6. Oztaysi B (2014) A decision model for information technology selection using AHP integrated TOPSIS-Grey: the case of content management systems. *Knowl Based Syst* 70:44–54
7. Li C, Chen K, Xiang X (2015) An integrated framework for effective safety management evaluation: application of an improved grey clustering measurement. *Exp Syst Appl* 42(13):5541–5553
8. Amirian H, Sahraeian R (2017) Solving a grey project selection scheduling using simulated shuffled frog leaping algorithm. *Comp Indus Eng* 107:141–149
9. Sruthi MD, Aravindan A (2019) Performance measurement of schedule and cost analysis by using earned value management for a residential building. *Mater Today: Proc* 33:524–532
10. Andrade PA, Martens A, Vanhoucke M (2019) Using real project schedule data to compare earned schedule and earned duration management project time forecasting capabilities. *Autom in Constr* 99:68–78
11. Ibrahim MN, Thorpe D, Mahmood MN (2019) Risk factors affecting the ability for earned value management to accurately assess the performance of infrastructure projects in Australia. *Constr Inno* 19(4):550–569
12. Pérez PB, Ablanado ES, Melià DM, Cruz MCG, Bagues JLF, Pellicer E (2019) Earned schedule min-max: two new EVM metrics for monitoring and controlling projects. *Autom Constr* 103:279–290
13. Nadafi S, Moosavirad SH, Ariaifar S (2019) Predicting the project time and costs using EVM based on gray numbers. *Eng Constr Arch Manage* 26(9):2107–2119

COVID-19—Assessment of Economic and Schedule Delay Impact in Indian Construction Industry Using Regression Method



Soniya D. Mahind and Dipali Patil

Abstract Coronavirus (COVID-19) is a Global pandemic and has severe impacts on the economy and schedule delay of the various industries including the construction sector. The construction industry is the second largest industry after agriculture in India. The current pandemic caused all projects and onsite construction work to halt abruptly which raised the need for the researcher to analyze and be prepared for such crises in the future. *This research investigates* the net impact of the effect of COVID-19 on Indian construction projects by considering essential aspects and their net impact on the total cost and delay of the project. The risk factors *impacting the construction industry* are gathered from available resources and observation. The empirical study was done using a questionnaire survey with 62 responses collected from well-known construction companies from India. The significance of the delay and cost factors was investigated using the relative importance index method and regression modeling. From factor analysis, we identified that cost factors such as conditions of clients, delay in handing over the project, transportation cost, unforeseen circumstances, cost for site hygiene, and delay factors like lockdown period, labor shortage, delay in supply, late payments for completed work and material shortage are majorly affecting on economy and delay of the project. The regression models established will help to predict the impact of a factor on the cost and delay of the project. This data will help the client, project manager, and contractor to confront such disruption in the future.

Keywords COVID-19 · Economy · Regression analysis · Schedule delay

S. D. Mahind (✉)

Construction Management, College of Engineering Pune, Pune, India
e-mail: mahindsd19.civil@coep.ac.in

D. Patil

College of Engineering Pune, Pune, India
e-mail: dlp.civil@coep.ac.in

1 Introduction

Coronavirus (COVID-19) was recognized as a pandemic by the world health organization (WHO) on 11th March 2020. This pandemic has severe impacts on the economy and delays on the various industries including the construction industry. This global pandemic not only caused illness and fatalities but also destroyed the global economy. India is also attempting to respond to the post-COVID-19 reality challenges, which have come to define a new normal for our economy and society as a whole, as in most parts of the world. After agriculture, the construction industry in India is the second-largest employer and is therefore vital to the economic stability of the country. It accounts for about 8% of the nation's GDP with an industry size of INR 10.5 trillion and employs close to 57.5 million people [1]. The infrastructure and construction industries, which are mainly responsible for the development of the nation, are already facing the headwinds of the COVID-19 pandemic and it cannot be assumed to be removed from its harmful effects. Besides, the unorganized and fragmented nature of the construction sector is likely to worsen this effect. The construction industry is expected to undergo a simultaneous downturn in both supply and demand due to this pandemic. Since the sector is mainly affected by infrastructure projects, it is predicted that current levels of uncertainty, weak business and consumer sentiments, loss of revenue, and the diversion of government funds to COVID-19 management would be seriously affected. The productivity of the construction sector mainly depends on man, material, and money and is directly related to the cost and time of the project. These key parameters were again subcategorized into various factors which were affected to various degrees due to COVID-19.

The study aims to analyze the impact of COVID-19 on construction projects by considering essential aspects and their net impact on the total cost and duration of the project and provide remedies or suggestions effectively to confront such disruption in the future. There are few factors that are majorly affecting the cost and the total duration of construction projects on the different construction phases. In this research, we are going to collect and assess those factors to understand their impacts on the Indian construction Industry.

2 Literature Review

There are ongoing challenges due to COVID-19 in the construction industries of Kabul, Afghanistan due to the COVID-19 pandemic. Research identifies the initiatives that should be taken by the government to overcome the situation. The mining sector is not immune to these impacts, and the crisis may have important short-, medium- and long-term repercussions for the industry. The productivity of the construction sector mainly depends on man, material, and money and is directly related to the cost and time of the project. COVID-19 is impacting construction and employment under various scenarios such as investment and economy. The survey

was done to check the influence of this pandemic on projects in India considering materials, man, and machinery [2]. The COVID-19 pandemic has placed labor-intensive industries at risk, including a typical one in the construction industry. Results obtained from the study give strategies to reduce and prevent the spread of COVID-19 in the construction industry of China [3]. COVID-19 Pandemic has slowed down the progress of industry because of reverse migration of labors causing the shortage, stoppage in various construction activities, the effect on order book execution rate, and working capital problems for firms that are financially vulnerable [1]. Time and cost overruns in Nigeria have been recognized as the most significant factors responsible for the abandonment and failure of contractors. Delay is a condition in which the contractor and the owner of the project contribute jointly or severally to the failure to complete the project during the initial or the contract duration stipulated or decided [4]. Factor analysis is performed for the study and quantitatively analyzed the underlying structure of the causes of variance [5]. The Relative Importance Index (RII) method is used by Larsen et al. [6] to check the effect of factors schedule delay, cost overrun, and quality level. The research explores, firstly through a questionnaire survey of construction professionals, the effects of construction delay on the implementation of the project and, secondly, the effects of delay on the cost and time of completion by an empirical approach. Doloi [7] identified the many factors that contribute to construction delays, use statistical methods to determine the relationship between these variables, and use a regression model to estimate the influence of these factors on construction delays in the Indian construction industry.

There is a lack of research availability due to the ongoing COVID-19 pandemic. The factors which were considered for the previous study of cost and duration of the construction project are not concerning the COVID-19 situation. Few findings are available on the impact of COVID-19 on the construction industry in Indian context. There is no mathematical model established to indicate the relationship of schedule delays and economy with their respective attributes in such a pandemic situation.

3 Research Methodology

See Fig. 1.

4 Data Collection

4.1 Preparation of Questionnaire

An important phase in the research's success is the identification of important attributes for the study and the creation of a questionnaire. The questionnaire survey is adopted as it is the most popular way of data collection, especially for large sample

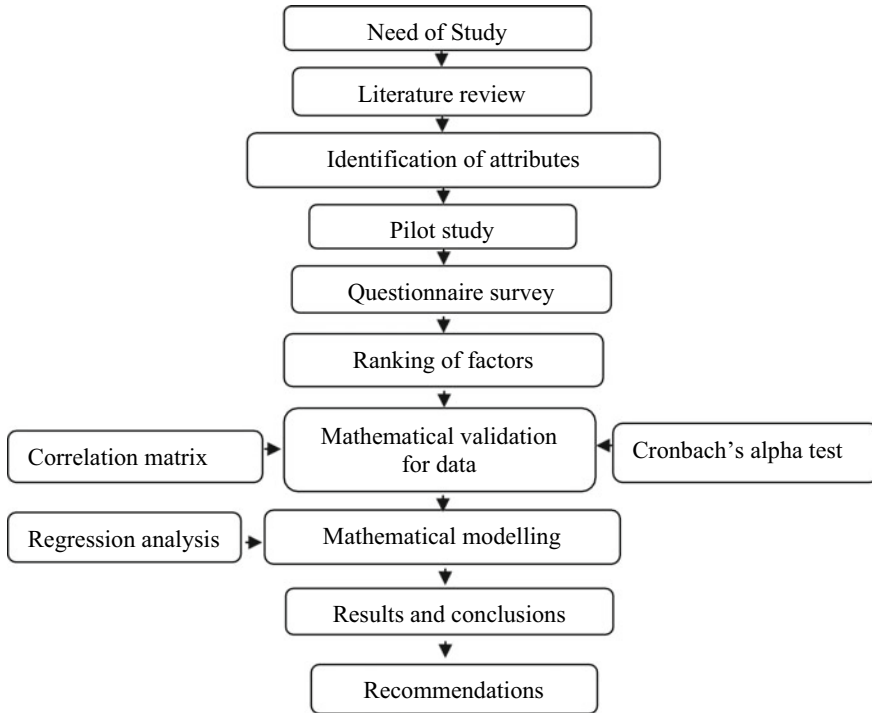
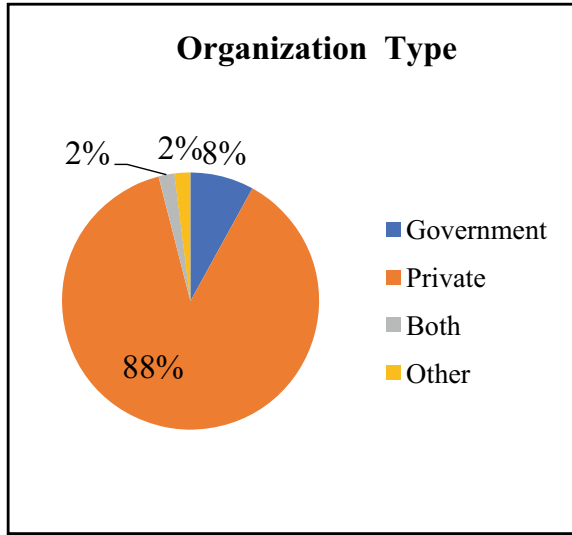


Fig. 1 Flow chart of research methodology

size. Total 17 attributes of schedule delay were identified under 5 broad categories such as materials and equipment related, manpower related, project management related, government related, owner related and 14 attributes of economy were identified under 4 broad categories materials and equipment related, Labor related, owner related, contractor related. We have used a structured questionnaire for this survey for easy analysis. It is the most helpful in a situation in which the score of the respondent can be compared to a distribution of scores from some well-defined category. Factor analysis was used to give rank to the attributes and regression analysis was used to develop a predictive model based on the best-fit attributes. The pilot study is mainly used for the identification of factors and validation and is done prior to the execution of the main study. To conduct this pilot study a small set of respondents having a sample size of sixteen including owners, contractors, Professional experts and developers will share their views on factors. For checking the influence of factors on the Economy and Schedule of the project, the questionnaire is prepared with the help of the Likert scale. It is most useful in a situation wherein it is possible to compare the respondent's score with a distribution of scores from some well-defined group. On a Likert scale, the respondent is asked to respond to each of the statements in terms of several degrees, here we have used a 5-point scale.

Fig. 2 Type of organization of respondents



4.2 Respondent’s Profile

The required quantitative data is obtained with the help of google form which is feasible and safe during this pandemic situation. Google form consists of three sections out of which 1st section is of general information of respondents including their name, type of organization, name of the organization, qualification, work experience. And remaining two sections asking to rate the impact of the factors affecting on Economy and Schedule Delay. Total 62 responses were considered from the project managers, construction managers, research scholars, and seniors engineers from well-known construction companies and institutes in India such as Larsen & Turbo, Shapoorji Pallonji & Co. Pvt. Ltd., B.G.Shirke Const. Tech Pvt (See Figs. 2, 3 and 4).

5 Data Analysis

5.1 Ranking of Attributes

According to Faridi and El-Sayegh [8] the mean and standard deviation of each attribute, are not suitable to judge overall rankings because they don’t represent any relationship between them. Hence the analysis was done by using the Relative Importance Index (RII) for providing ranks to the factors affecting on economy and delay of the construction industry collected and verified from literature. This method is used by Larsen et al. [6] to check the effect of factors schedule delay, cost overrun,

Fig. 3 Work experience of respondents

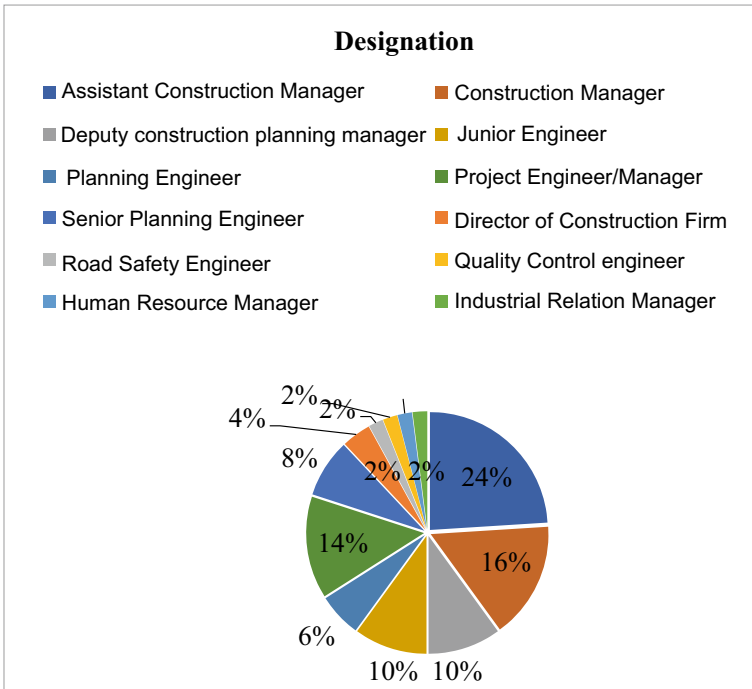
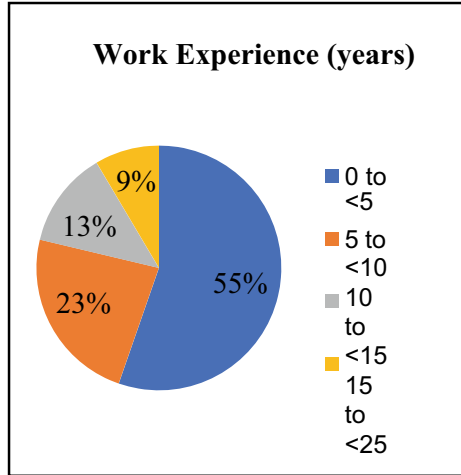


Fig. 4 Designation of respondents

Table 1 Thumb rule for Cronbach’s alpha test

$C\alpha$	Reliability
>0.9	Excellent
$0.9 > C\alpha > 0.8$	Good
$0.8 > C\alpha > 0.7$	Acceptable
$0.7 > C\alpha > 0.6$	Questionable
$0.6 > C\alpha > 0.5$	Poor
$0.5 > C\alpha$	Undesirable

and quality level (Table 1).

$$RII = \sum_{i=1}^5 W_i / (A \times N)$$

where W_i = Total sum of each factor (1 to 5 scale), A = highest possible weight used for study, N = Total number of respondents for each variable.

Tables 2 and 3 show the ranking of the project attributes in descending order based on their relative importance calculated using the equation above. Along with the ranks, the RII scores are displayed in the column. The most important traits are represented by the greatest RII values, while the least important traits are represented by the lowest RII values.

Table 2 Ranking of attributes affecting the economy of construction projects

Code	Risk factors	RII	Rank
E12	Economic conditions of clients (the main source of funding)	0.812	1
E11	Delay in handing over the project (penalties)	0.796	2
E3	Transportation cost (scarcity in the local availability)	0.768	3
E14	Unforeseen circumstances (if labors get infected)	0.764	4
E6	Cost for site hygiene (sanitization at a construction site)	0.752	5
E2	Labor cost (extra wages)	0.74	6
E1	Material cost (due to their shortage)	0.736	7
E13	Extent of variations (variation in market)	0.736	8
E8	Implementation of new policies (policies related to COVID-19)	0.716	9
E9	Liquidity risk (cannot meet short-term debt obligations)	0.716	10
E10	Interest rate during the project period (fewer investments)	0.708	11
E4	Medical cost (personal protective equipment)	0.692	12
E7	Hiring charges of plants and machinery (unavailability of operators and equipment)	0.68	13
E5	On-site labor accommodation cost (for migrant workers)	0.672	14

Table 3 Ranking of attributes affecting the schedule delay of the construction project

Code	Risk factors	RII	Rank
D7	Lockdown period (the total duration of projects ultimately increases)	0.868	1
D2	Labor shortage (causes pending of construction work)	0.82	2
D3	Delay in supply (supply chain is disturbed)	0.812	3
D17	Late payments for completed work (causes late start for next work)	0.78	4
D1	Material shortage (shortage of material turns into the halting of the project)	0.732	5
D5	Implementation of new safety guidelines (takes some time to implement causes delay)	0.732	6
D10	Delay in obtaining permits from the municipality (work was on halt in the period)	0.732	7
D4	Productivity at work (the efficiency of labor reduced due to fear)	0.724	8
D13	Inadequate client's finance (lack of funds available)	0.7	9
D6	Unavailability of plant and machinery (causes transportation from another place)	0.696	10
D9	Slow mobilization of equipment (the free movement of traffic is restricted)	0.692	11
D15	The complexity of the project (inexperienced contractors are not able to handle)	0.676	12
D16	Building permits approval (delay for approval)	0.668	13
D12	Suspension of work by owner (nonavailability of resources required to continue the project)	0.66	14
D14	Contractor's planning skills (inexperienced contractors are not able to handle)	0.66	15
D11	Poor communication and coordination with other parties (insufficient information and misunderstandings)	0.648	16
D8	Poor site management and supervision (due to such unforeseen situation)	0.644	17

5.2 Mathematical Validity of Factor Analysis

After the factors have been ranked, it is vital to double-check that factor analysis measured what was intended to be assessed, i.e. that the attributes in each factor describe the same measure within target dimensions collectively [7]. It is acknowledged that if attributes compose the specified factor, they should reasonably correlate with one another, but no need to be perfect. We can determine the level of correlation among distinct variables by using MS Excel to calculate Pearson correlation. Tables 4, 5 and 6 lists the Pearson correlation coefficients.

Table 4 Cronbach’s alpha test results

	Economy	Schedule delay
No. of risk factors	14	17
Sum of factor variances	9.299621297	21.92381377
Variance of the total score	98.9664	181.3316
Cronbach’s α	0.97572735	0.934038926

Table 5 Results of multiple regression analysis for economy factor

	Coefficients	Standard error	<i>p</i> -value		
Intercept	−0.891	0.221	0.0003	<i>R</i> Square	0.97397
E1	0.137	0.045	0.0042	Adjusted <i>R</i> Square	0.963558
E2	0.111	0.039	0.0068	<i>F</i>	93.54396
E5	0.178	0.046	0.0005		
E6	0.137	0.041	0.0019		
E7	0.101	0.044	0.0277		
E8	0.135	0.043	0.0033		
E9	0.088	0.033	0.0124		
E10	0.119	0.050	0.0231		
E11	0.146	0.044	0.0022		
E12	0.093	0.038	0.0215		
E14	0.157	0.045	0.0014		

Table 6 Results of multiple regression analysis for schedule delay factor

	Coefficients	Standard error	<i>p</i> -value		
Intercept	−1.641	0.2578	1.6E−07	<i>R</i> Square	0.95731
D3	0.143	0.0631	2.9E−02	Adjusted <i>R</i> Square	0.946365
D17	0.205	0.0502	2.1E−04	<i>F</i>	87.45812
D1	0.224	0.0583	4.4E−04		
D5	0.197	0.0609	2.5E−03		
D10	0.179	0.0571	3.3E−03		
D4	0.187	0.0377	1.4E−05		
D13	0.153	0.0393	3.8E−04		

5.2.1 Cronbach’s Alpha Test

Cronbach’s alpha test was done on the complete data as well as attributes in each component, as indicated in Table 1, for reliability analysis, which is essential to validate the build of the model over time (i.e. consistency of measured characteristics and scale). $C\alpha$ can have a value ranging from 0 to 1, with a higher value indicating

stronger internal consistency and vice versa. Doloi [7] suggested that the following ranges can be used as a thumb rule in most situations:

$$\text{Coefficient of Cronbach}(\alpha) = (N/(N - 1)) \times (1 - (V/A))$$

where N = Number of factors, V = Sum of the variance of all factors, A = Variance of the total score.

5.2.2 Regression Analysis

As previously stated, the factors that affect schedule delays and economy are further investigated using linear multiple regression to establish a prediction model in the Indian construction scenario. While factor analysis shows the presence of clusters of strong correlation coefficients with observable underlying dimensions, these dimensions (or factors) have no predictive value on the phenomena being studied. Multiple regression analysis, on the other hand, fits the complete dataset without taking into account the correlation matrix's common variance (R^2 value) [9]. R^2 is a useful criterion for evaluating the intensity of the relationship between the predictive or dependent variable and the independent variables. Some of the important underlying assumptions in the predictor variables should be met before conducting the regression analysis. Before starting the regression analysis, the parametric test was performed by analyzing the homogeneity of variance (Levene's test) on the selected attributes [9] Since the results of Levene's test are relevant ($p < 0.05$), the null hypothesis that the variances between variables are zero is rejected, and the regression analysis is viable. The attributes derived from the factor analysis, as shown in the analysis were used as independent variables.

6 Results

6.1 Impact of Attributes Affecting Economy

Out of the factors considered, the top five factors affecting the economy of the construction project, E12 (Economic conditions of clients (the main source of funding)) which has the highest RII, i.e. 0.812. As indicated by the decrease in RII values, this was followed by E11 (Delay in handing over the project), E3 (Transportation Cost), E14 (Unforeseen circumstances), E13 (Extent of variations) (Table 2).

6.2 *Impact of Attributes Affecting Schedule Delay*

Of the factors that affect schedule delay, the highest-ranked factor is D7 (lockdown period) with an RII of 0.868. As indicated by the decrease in RII values, this was followed by D2 (Labor shortage (causes pending of construction work)), D3 (Delay in supply), D17 (Late payments for completed), D1 (Material Shortage) (Table 3).

6.3 *Correlation Matrix of the Attributes*

Table 4 indicates the person bivariate correlations between different attributes in all components are more than 0.4 in the majority of cases. We can ensure that factors produced by factor analysis contain properties that are related based on these findings [7] The correlation matrices for factors, economy and schedule delay are helpful to determine the relationship between the attributes of respective categories.

6.4 *Cronbach’s Alpha*

From Table 4, the Cronbach’s alpha coefficient for the data related to the Economy of the construction is 0.976, and for data related to Schedule Delay is 0.934, which indicates that the consistency of data for both of them is excellent. Hence the data collected for this research is highly reliable. This test is applied to validate the consistency and reliability of the collected data.

6.5 *Regression Model*

The effects on the overall Economy and Schedule delay of the project are the dependent variables, which were asked separately to each respondent focusing on a specific project. For categorical variables, these attributes are added to the regression model in steps. As a result, the regression model used to assess the aggregate effect of individual attributes on delay can be summarized as follows:

$$Y_i = \beta_0 + \beta_1 X_{1i} + \beta_2 X_{2i} + \beta_3 X_{3i} + \dots + \beta_j X_{ji} + \varepsilon_i$$

where Y_i = Dependent term(one of the factors, economy, and delay); β_0 = Constant and intercept at Y-axis; β_i , i.e. (β_1 to β_j) = Determined regression coefficients; X_i , i.e. (X_1 to X_j) = Values of independent variables or attributes; ε_i = Error which is a random variable with mean 0; i = index of the performance of attributes being predicted; and k = number of predictor variables.

The adjusted R^2 values and the variation from R^2 values indicate how much the model generalizes the dependent variable's predictive power [7]. If the difference between R^2 and adjusted R^2 is less indicates the stronger model. Hence in an ideal case, the R^2 and adjusted R^2 should be the same values. The values in Tables 5 and 6 are acceptable for appropriate strengths based on the excellence of the model fit.

6.5.1 Economy Factor

The final regression model for the impact on Economy can be expressed as:

$$\begin{aligned} \text{Extra Cost}(\%) = & -0.891 + 0.137 * (\text{Material Cost}) + 0.111 * (\text{Labor Cost}) \\ & + 0.178 * (\text{On site labor accomodation}) \\ & + 0.137 * (\text{Cost for site hygiene}) \\ & + 0.101 * (\text{Hiring charges of plants and machinery}) \\ & + 0.135 * (\text{Implementation of new policies}) \\ & + 0.088 * (\text{Liquidity risk}) \\ & + 0.119 * (\text{Interest rate during project period}) \\ & + 0.146 * (\text{Delay in handing over the project}) \\ & + 0.093 * (\text{Economic conditions of clients}) \\ & + 0.157 * (\text{Unforeseen circumstances}) \end{aligned}$$

Where all the values of attributes causing extra cost are considered to be in percentage.

As the regression model in Table 5 demonstrates, on-site labor accommodation (E5) and unforeseen circumstances (E14) have maximum impact on the economy of the Indian construction projects in crisis due to COVID-19. Delay in handing over the project (E11) caused by unforeseen circumstances (E14). The Material cost (E1) and hiring charges of plants and machinery (E7) has been increased due to unstable market condition and shortage of locally available resources. The cost for site hygiene (E6) and Implementation of new policies (E8) is mainly because of the pandemic situation. Liquidity risk (E9), Interest rate during the project period (E10), Economic conditions of clients (E12) these costs are mainly related to the owners and affect the project economy as they are the source of funding. As labor is a key resource of the construction industry to continue the work which is on halt, an accommodation facility is provided. It seems that labor has more impact on the economy of the project, i.e. labor cost (E2).

6.5.2 Schedule Delay Factor

The final regression model for the impact on Schedule Delay of Indian construction Project can be expressed as:

$$\begin{aligned} \text{Delay (months)} = & -1.641 + 0.143 * (\text{Delay in supply}) \\ & + 0.205 * (\text{Late payments for completed work}) \\ & + 0.224 * (\text{Material shortage}) \\ & + 0.197 * (\text{Implementation of new safety guidelines}) \\ & + 0.179 * (\text{Delay in obtaining permits from municipality}) \\ & + 0.187 * (\text{Productivity at work}) \\ & + 0.153 * (\text{Inadequate client's finance}) \end{aligned}$$

Where all the values of attributes contributing to the delay of the project are considered to be in months. The above regression model implies material shortage (D1), late payment for completed work (D17), and Implementation of new safety guidelines (D5) is majorly affecting parameters on schedule delay of construction projects in India during the COVID-19 pandemic. Productivity at work (D4) is the attribute having an impact on the construction industry irrespective of any situation as previous findings [9] also show a similar impact. In this pandemic, poor productivity is mainly due to the fear of getting infected among laborers. The Lockdown situation causes a delay in obtaining permits from the municipality (D10). Delay in supply (D3) causes a delay in the schedule of the project. Money is an important resource in any project hence inadequate clients' finance (D13) has an impact on delays in the construction industry.

7 Conclusion

The findings from this study showed the significance of factors on the economy and schedule delay of projects in the Indian Construction industry. This pandemic situation hampered all four M's of the construction industry, i.e. man, material, money, and machinery. The lockdown period is mainly responsible for the scheduled delay of construction work and this is proved by both quantitative and qualitative data. And the extension of it causes an increase in the total duration and cost of projects. Late payments of completed work cause the late start of the successive activity. Since the construction industry is one of the labor-intensive industries, turned into their shortage which caused the proposed construction work to be pending or moving at a slow rate. Hence at some sites, on-site labor accommodations were provided which required extra investment. The economic conditions of clients have a great impact on the economy of the project. Though the RERA of various states in India has extended the completion period of all registered projects, delay in handing over the project has

majorly affected the economy as it causes penalties if unable to complete the project in time.

This study is validated by the available reports on the impact of COVID on Indian Construction. *Impact on Construction Sector in India Table of Contents* [2] indicates that in a pessimistic case increase in the total cost of the project 4.28% and the average value we have identified is 4.886%. According to the report, the underdevelopment projects were delayed by a minimum of 2–3 months and the findings from the study show the value of 3.465 months. The corresponding values are from June 2020 and have been increasing due to the extension of lockdown conditions.

Due to lockdown, the supply chain is disturbed and causing a delay in the construction industry. This data will help to construction manager, consultant, site engineer, and owner to get the idea of majorly affecting factors and prepare some mitigation strategies to confront such situation in the future.

8 Recommendations

1. Provide onsite accommodations facility for labors and motivate them, will help to reduce the reverse migration of labors and also to increase the productivity of their work.
2. Making small groups of workers and assigning work in alternate shifts to reduce the chances of infection and to implement new safety norms such as social distancing.
3. Establishment of the digital platform for office workers to reduce public gatherings and avoid direct contact.
4. Identifying alternate sources of resources so that the risk of their shortage can be minimized. The site should be flexible enough to store the resources to tackle possible supply chain interruptions.
5. Continuous evaluation of profitability in such situations will help to overcome financial crises with the help of mitigation strategies.
6. An alternative solution to minimize over-reliance on labor is the adoption of automation, mechanization and off-site production.
7. Design and enforcement of a risk management system for early detection of the infected worker to avoid further spread. This can be achieved with the help of daily health checkups.
8. For new projects to be sanctioned, impact factor of such situation and clause related to equal risk sharing should be considered in a contract.

References

1. Building again—brick by brick COVID-19: construction sector in India: growth paused temporarily (2020), 3(April)
2. Impact on construction sector in India Table of contents (2020), May
3. Zheng L, Chen K, Ma L (2021) Knowledge, attitudes, and practices toward COVID-19 among construction industry practitioners in China. *Front Public Health* 8(January):1–9. <https://doi.org/10.3389/fpubh.2020.599769>
4. Aibinu AA, Odeyinka HA (2006) Construction delays and their causative factors in Nigeria. *J Constr Eng Manag* 132(7):667–677. [https://doi.org/10.1061/\(asce\)0733-9364\(2006\)132:7\(667\)](https://doi.org/10.1061/(asce)0733-9364(2006)132:7(667))
5. Wambeke BW, Hsiang SM, Liu M (2011) Causes of variation in construction project task starting times and duration. *J Constr Eng Manag* 137(9):663–677. [https://doi.org/10.1061/\(asce\)co.1943-7862.0000342](https://doi.org/10.1061/(asce)co.1943-7862.0000342)
6. Larsen JK, Shen GQ, Lindhard SM, Brunoe TD (2016) Factors affecting schedule delay, cost overrun, and quality level in public construction projects. *J Manag Eng* 32(1):04015032. [https://doi.org/10.1061/\(asce\)me.1943-5479.0000391](https://doi.org/10.1061/(asce)me.1943-5479.0000391)
7. Doloi H (2009) Analysis of pre-qualification criteria in contractor selection and their impacts on project success. *Constr Manag Econ* 27(12):1245–1263. <https://doi.org/10.1080/01446190903394541>
8. Faridi AS, El-Sayegh SM (2006) Significant factors causing delay in the UAE construction industry. *Constr Manage Econ* 24(11):1167–1176. <https://doi.org/10.1080/01446190600827033>
9. Doloi H, Sawhney A, Iyer KC, Rentala S (2012) Analysing factors affecting delays in Indian construction projects. *Int J Project Manage* 30(4):479–489. <https://doi.org/10.1016/j.ijproman.2011.10.004>

Comparison of Afghanistan's Construction and Engineering Contract with International Contracts of FIDIC RED BOOK (2017) and NEC4—ECC



Mohammad Ajmal and C. Rajasekaran

Abstract Construction and engineering contracts are the core documents used to set out contractual relations, rights and obligations of parties, payment systems, communication lines, and dispute avoidance/resolution procedures in construction and engineering projects. Thus the importance of these documents is obvious. In this study, the Standard Bidding Document (SBD) for the Procurement of Small Works (PSWs) of the Government of Afghanistan (which's the approximate cost is up to AFN 500 million) is chosen. It is to be compared with the Conditions of Contract for Construction—FIDIC RED BOOK—2nd Edition (2017) and New Engineering Contracts (NEC4) Engineering and Construction Contract (ECC) 4th Edition (2017). This study was conducted using different research papers, theses and books, which were relevant to the research, and by deep study of the above three mentioned types of documents of contracts. After that, the comparison of Afghanistan's SBD for the PSWs with the FIDIC RED BOOK (2017) and NEC4—ECC (2017) in different parts with each other was carried out. After this comparison, the achieved results show that Afghanistan's SBD for the PSWs has shortcomings, lack of some essential clauses and/or sub-clauses, insufficient information in some clauses which may lead to disputes, errors and/or mistakes in naming of some clauses, lack of flexibility, and unbalanced risk-sharing.

Keywords Construction and engineering contracts · Standard bidding document · FIDIC RED BOOK (2017) · NEC4—ECC · Afghanistan's construction and engineering contract

M. Ajmal (✉) · C. Rajasekaran
Department of Civil Engineering, National Institute of Technology Karnataka, Surathkal,
Mangalore 575025, India
e-mail: mohammadajmalbah@gmail.com; mohammadajmal.192cm031@nitk.edu.in

C. Rajasekaran
e-mail: bcrasekaran@nitk.edu.in

1 Introduction

1.1 General

A contract is an agreement between two or more parties that gives rise to rights and responsibilities which will be applied according to the law system applying to the contract. Often, the law system applying to a contract will be specified within the contract itself [12].

Contracts may differ widely in type, from a very simple verbal contract to a very complicated written contract. In many cases, parties are going to take a standard form of contracts as an initial point. These contracts will typically set out the work to be performed under the contract in some detail, the price to be paid or the basis on which to measure the amounts due, and commonly the rights and obligations of the parties entering into the contract.

As far as possible, a properly written and well-prepared construction contract should aim to make sure clarification and assurance of the specific responsibilities and rights of the parties', provide the parties with the methods to be followed in certain cases or to achieve a particular outcome, and allocate the risk of damage or loss happening to the project precisely and thoroughly so that each party recognizes their risks and consequences of those risks accurately [12].

Unbalanced conditions in construction and engineering contracts have been identified as one of the significant problems in project execution. Traditionally, the text of contract documents is drafted by the owner (client). It usually results in a manual that is sometimes drafted to favor one of the parties—owner—entering into a contract. An unbalanced contract harms all parties at all times, and therefore, this type of contract is not a workable contract [18]. Accordingly, the related entities to procurement and those preparing contract documents may take in mind to draft it carefully and don't make any bias to any party in the contract.

1.2 Scope of the Study

The scope of this study is to compare the following standard contracts documents with each other:

- (1) SBD for the PSWs of the Government of Afghanistan (GoA) of unit price (admeasurement) contracts with BoQ (which's the approximate cost is up to AFN 500 million).
- (2) FIDIC RED BOOK 2nd edition (2017), according to unit price contracts.
- (3) NEC4—ECC (2017), main option B, priced contract with Bill of Quantities (BoQ).

In all the above contracts, the construction and engineering works are designed by the Owner (Employer/Client/Entity) without any small designs, i.e., design of temporary works, etc.

1.3 Research Problems

There are some questions that are to be answered by doing this research:

- (1) What are the similarities and differences of SBD for the PSWs of the GoA with FIDIC RED BOOK (2017) and NEC4—ECC (2017)?
- (2) What are the shortcomings of SBD for the PSWs of the GoA, according to FIDIC RED BOOK (2017) and NEC4—ECC?
- (3) What improvements can be made to SBD for the PSWs of the GoA, according to FIDIC RED BOOK (2017) and NEC4—ECC?
- (4) Which one of them is more useful, more flexible, and to complete the project with better performance?

1.4 Objectives of the Study

The objectives of this research which are to be achieved by this research, are as below:

- (1) to help with international engineering and construction entities and companies who are interested in getting contracts in Afghanistan,
- (2) help them to know about Afghanistan's engineering and construction contract and its differences and similarities with FIDIC RED BOOK (2017) and NEC4—ECC, and
- (3) to help the procurement authorities of the GoA and other countries to improve the process and conditions of contracts for better performance, good management, dispute avoidance, dispute resolution, and successful completion of projects.

1.5 Research Methodology

The methodology which is used in this study is as below:

- We did this study by using different research papers, theses, books, academic presentations, and some reliable electronic sources, which were relevant to our research, and
- by deep studying of SBD for the PSWs of Afghanistan, FIDIC RED BOOK (2017) and NEC4—ECC.

- After the above two steps, we compared SBD for the PSWs of the GoA with the FIDIC RED BOOK (2017) and NEC4—ECC (2017) in different parts with each other.

2 Literature Review

2.1 General

A good and well prepared Standard Contract Document (SCD) or Standard Bidding Document (SBD) will lead to reduce tendering cost, reduce the cost of negotiating the contract [25], improve co-operation between the parties entering into a contract, and other stakeholders, sense of responsibility, reduction in delays as well as improvement in productivity of the contract parties, reduce the incidence of disputes between them [18], provide a more significant stimulus to good project management [15], and can help to avoid the cost over-runs in some projects [16]. In fact, some conditions included in SBDs can cause conflicts and disputes, and some contracts could cause more disputes than others [7].

Internationally, many types of construction and engineering contracts are in use today, from which the two most commonly used forms are FIDIC and NEC3 [2]. Fortunately, we chose the latest editions of both of these two standard form contracts: FIDIC RED BOOK 2nd edition (2017) and NEC4—ECC 4th edition (2017). The FIDIC forms are commonly used and are well recognized as providing balanced forms of contract [12], and NEC3 is also used internationally. It is becoming a serious competitor to FIDIC [23]. More than 30 countries worldwide including the UK are using NEC. Thus, this indicates its reputation [3].

A study by Besaiso et al. [3], which evaluates the efficiency of FIDIC and NEC in reduction of disputes in the Palestine construction projects, compared FIDIC with NEC in six aspects: clarification and easiness, risk allocation and managing, force majeure and prevention occasions, physical and weather conditions risks, variations, and project organization (engineer vs. project manager).

It suggests that both standard contracts have admirable and necessary features for all parties of a contract and can be effectively used everywhere. Although, both contracts have certain areas of concern and sometimes restrictions. It expresses that NEC has possibly many benefits over FIDIC, mainly in clarification, variations, risk managing, and objective measurement of weather and field conditions risks. Its results reveal that disputes may be minimized by contract, and NEC seems to be more capable of doing so than FIDIC.

The engineer (FIDIC)/project manager (NEC) position has advantages and restrictions in both contracts; although, in Palestine, it appears that the role of project manager under NEC is more practical than the engineer in FIDIC. The force majeure or prevention occasions are unconvincing in both forms of contracts. The

authors further express that FIDIC has the advantages of precedence and familiarity, widespread reputation, and confirmation by many governments, international development banks and organizations [3].

A study by Rasslan and Nassar [22] compared the NEC and FIDIC standard forms of contracts and evaluated their suitability for Egypt's construction projects. It expresses that, FIDIC standard form of contract is used in a large number of the most important construction projects and in major infrastructure projects which are financed by the USAID (US Aid for International Development) and World Bank.

The authors express that variations, errors and omissions, and delays are the three most influential reasons for disputes arising during any construction project in Egypt.

Its results conclude that both FIDIC and NEC are well-designed, but NEC3 has more advantages over FIDIC. To manage a project's time and cost, the NEC3 provides a forward-looking proactive environment. It is a flexible, clear and easily understandable contract compared to FIDIC, which has many references to follow when reading any clause and contains lots of legal terminologies. The early warning system in NEC encourages identifying problems so that parties can establish an early resolution for upcoming issues [22].

Lord et al. [17] recommended three pillars of modern contract and examined specific provisions within the NEC3. These three pillars are: "fairness", "payment operating mechanism", and "functions and role of project participants". After examining, they found that the NEC is almost wholly compliant with these three pillars. Heaphy [13] comprehensively compared FIDIC and NEC3-ECC. He found that NEC3-ECC encourages collaborative behaviors, good project management and proactive risk management. Rooney and Allan [24] concluded that NEC3-ECC has performed better than other standard forms of contract in terms of time and cost predictability. He further discussed that NEC3-ECC has provided improved cooperation, flexibility, enhanced management practices and risk sharing in the UK highways projects [16].

2.2 Afghanistan Construction and Engineering Contracts

The National Procurement Authority (NPA) of the GoA has drafted and prepared two types of SBDs; the

- first one is SBD for the Procurement of Small Construction and Engineering Works (PSWs). Which's the approximate cost of procurement is up to AFN (500) millions [21].
- the second one is SBD for the Procurement of Large Construction and Engineering Works (PLWs). It is for procurements which's the approximate cost is more than AFN (500) millions.

It has been prepared to be used for the procurement of unit price or rate (admeasurement) type of works, through International Tender Process in projects, which the public funds finance.

These SBDs are not appropriate for lump-sum contracts without substantial changes to the method of payment and price adjustment, and the BoQ, Schedule of Activities, and so onward [20, 21].

In this study, we chose the SBD for the PSWs of the GoA (Unit Price Contract with BoQ). It is drafted and prepared by the NPA of the GoA according to International Multilateral Development Institutions' SBDs. The Procurement Entities of the GoA should use it for the PSWs financed by public funds.

2.3 FIDIC Contracts

The French acronym FIDIC corresponds to the Fédération Internationale des Ingénieurs-Conseils (in English; International Federation of Consulting Engineers) [4].

In 1957, for the first time, a contract was published by the FIDIC under the name of Conditions of Contract for Works of Civil Engineering Construction. It became popular because of its red cover as the RED BOOK. The latest edition of FIDIC RED BOOK was published in 2017.

There is a significant feature of FIDIC standard contracts that FIDIC does not generally allow its standard form contracts to be amended except a special license is negotiated. Generally in FIDIC, with the amending of Particular Conditions, the contract's standard form must be amended. With a logical arrangement of clauses, its standard contracts are consistent and coherent [25].

FIDIC RED BOOK is recommended for construction and engineering works designed by the owner (employer) or by his representative, the engineer. In this type, the contractor constructs the works according to a design provided by the owner. However, the works may have some part(s) that is(are) to be designed by the contractor [4, 9].

2.4 NEC4 Contracts

NEC is a wholly-owned subsidiary of the Institution of Civil Engineers (ICE), the NEC owner and developer.

The NEC contracts are the only suite of standard contracts designed to assist and encourage good management of the projects in which they are used. NEC standard contracts are used successfully around the world in both public and private sector projects; this trend seems set to continue at an increasing pace.

Each of the NEC standard forms of contract has the below characteristics:

- Its use facilitates and motivates good management of the relationships between the parties to the contract.
- It can be used for a wide variety of types of work and in any place.

- It is a simple and clear document, using a structure and language that is straightforward and easily understood.
- Its objective is far-sighted cooperation between all contributors to the project [10, 11, 15].

The existence of a number of optional clauses in NEC contract caused it to be adequately flexible in its terms to permit for any form of project delivery [14, 25].

3 Comparison of SBD for the PSWs of the GoA with FIDIC RED BOOK (2017) and NEC4—ECC

The above comparison is made in the below parts:

3.1 Structuring and Arrangement

There are some differences in structuring and arrangements of clauses and sub-clauses between these standard contracts. They are as follows.

3.1.1 SBD for the PSWs of the GoA

SBD for the PSWs of the GoA divided its General Conditions into five parts. The first part is General Issues. It has named the other three parts, like the triple constraint triangle of project management—time, scope, and budget—the three parts are Time Control, Quality Control, and Costs Control. The fifth part is about the Termination or Completion of the Contract. It has a total of 62 clauses.

3.1.2 FIDIC RED BOOK (2017)

FIDIC RED BOOK (2017) divided its General Conditions into 21 clauses which in the last edition of 1999 it was 20 clauses. One clause addition is the 20th Clause of the previous edition division into two separate clauses with some additions and subtractions. A good point is the Dispute Adjudication Board (DAB) changing in the previous edition to Dispute Avoidance and Adjudication Board (DAAB) in this edition. FIDIC has arranged its second to sixth clauses as the persons or groups involved in a project like the Employer, Contractor, Engineer, Subcontracting(Subcontractor), Staff and Labour. Employer or Contractor's Termination has separate clauses, but in NEC4—ECC, it is under one core clause, Termination. The structuring and arrangement are good, but if someone wants to know about any clause or sub-clause when he is reading one clause or sub-clause, it is referenced and linked with another clause or

sub-clause; when he/she refers there, it is referenced to another one, which creates a little bit confusion in some parts. SBD for the PSWs of the GoA also has this referencing, but not as much as in FIDIC, and even in referencing to the other clauses, there are several mistakes, and the number of referenced clauses and/or sub-clauses are wrong. Referencing to other clauses and/or sub-clauses is significantly less in NEC4—ECC, and more of their clauses and sub-clauses are written independently and clearly.

3.1.3 NEC4—ECC

NEC4—ECC has nine Core Clauses which are the same for every contract of NEC4. These clauses are General, The Contractor’s Main Responsibilities, Time, Quality Management, Payment, Compensation Events, Title, Liabilities and Insurance, and Termination. For the flexibility of this contract’s usage, it has six Main Option Clauses for the six different types of contracts from the point of view of funding the project and measuring and pricing the works done. Here in this study, our case is about the priced contracts with the BoQ because the SBD for the PSWs of the GoA is generally for this type of contracts. The part of Resolving and Avoiding Disputes has three Options, W1, W2, and W3. NEC4—ECC has added the new clause of W3 and with some changes in W1 and W2 from the last edition of NEC3. It has 21 Secondary Option Clauses, and it is not necessary to use any of them. Any combination may be used other than those stated there in NEC4—ECC [1, 6, 8–11, 21, 22].

3.2 Terminology and Expressions

There are some differences and similarities of some expressions and terminology between these standard contracts; they are as follows.

3.2.1 SBD for the PSWs of the GoA

SBD for the PSWs of the GoA uses Entity* instead of the owner, employer, or client. Entity’s representative for the project is the Project Manager. This SBD uses the word Bid and Bidding instead of Tender and Tendering in FIDIC RED BOOK and NEC4—ECC. In both this SBD and FIDIC RED BOOK (2017), the word Day means a calendar day.

3.2.2 FIDIC RED BOOK

FIDIC RED BOOK uses the word Employer (mostly), Owner (less) and sometimes Client. The Engineer represents the Employer (owner). FIDIC provides a central role

for the Engineer in the certification process during the performance of the works. It means that the certification process is performed by the Engineer. The Engineer can appoint a representative of him named as Engineer's Representative or Assistant. FIDIC uses the word Consultant instead of Designer in NEC.

3.2.3 NEC4—ECC

NEC4—ECC uses the word Client, but in NEC3, it was Employer. The Project Manager represents the Client and sometimes Supervisor can be the representative of the Project Manager. NEC4—ECC uses the expression of Scope instead of Works Information in NEC3—ECC, which is called the Specification and Drawings in the other two documents [1, 5, 6, 9–11, 21, 25].

*Entity: it is defined in Law on Procurement of the GoA as, Entity are the ministries, general departments, independent government commissions, municipalities, enterprises, their secondary units, other budgetary units, state-owned companies, and joint ventures [19].

3.3 *Errors or Mistakes about the Naming of some Clauses*

There are some errors or mistakes in SBD for the PSWs of the GoA about the naming of some clauses, some of them are as follow.

3.3.1 Certification by the Project Manager [18th Clause]

The name of the clause expresses that it will be about all certification that the Project Manager does, but it is not the case. It is about the Contractor's responsibility for designing temporary structures, preparing its specification and drawings, and submitting it to the Project Manager for approval and certification. And if needed to be certified by any third party, the Contractor should certify it. If it were named Contractor's Responsibilities about Temporary Structures, it would be better and express the actual meaning of the clause.

3.3.2 Safety [19th Clause]

It is better to be changed to Health and Safety Responsibilities of the Contractor. This clause of SBD for PSWs is discussed below in sub-sub Sect. 3.4.3.

3.3.3 Testing [32nd Clause]

It is about the tests which are not mentioned in the technical specifications and are beyond the contract. It is ordered by the Project Manager to be performed by the Contractor. If defects are detected, the contractor will pay its cost; if there was no defect, its cost will be paid by the Entity and counted in Compensable Events [42nd Clause]. The name of this clause shall change to Testing beyond Contract or Testing out of Contract. The new name will be most suitable for the information in this clause.

3.3.4 Tax [43rd Clause]

It is not about Tax, but about Changes in Tax and its result on the contract price.

3.3.5 Completion [53rd Clause]

It is not about the Completion or date of Completion, but about the Certification of Completion of Construction Works.

3.3.6 Dispute Resolution [62nd Clause]

If the amendments in the sub-sub Sect. 3.4.4 are added to this clause, then its name shall be changed to Dispute Avoidance and Resolution, which will express its comprehensive meaning [21].

3.4 Lack of some Essential Clauses and/or Sub-clauses

There are a lack of some essential clauses and/or sub-clauses in SBD for the PSWs of the GoA, which are as follows.

3.4.1 Subcontracting [7th Clause]

It has some information about the subcontracting and some are referenced to the Law on Procurement and Procurement Procedure of the GoA. One essential sub-clause that is not included in both SBD for the PSWs of the GoA and NEC4—ECC, but is in FIDIC RED BOOK (2017) is the duration for the response of the Engineer about the acceptance or rejection of the Subcontractor proposed by the Contractor. This duration is 14 days from the submission of the proposal about the Subcontractor. Suppose the Engineer does not respond within this duration after getting this proposal

by giving notice to the proposed Subcontractor. In that case, the Engineer shall be considered to have given his/her consent.

Notice to the Engineer should be given by the Contractor not less than 28 days before the commencement of each Subcontractor's work on the site, and not less than 28 days before the intended date of the commencement of work [9–11, 21].

3.4.2 Entity's Risks [10th Clause]

In this clause, besides the information included in it, it is missing some issues which are given in detail in NEC4—ECC. If it is added to this clause, it will complete the missing part of it. These are written as below:

- Damage to or loss of materials and plant provided by the Entity or others on the Entity's behalf to the Contractor; until the Contractor has received and accepted them.
- Damage to or loss of any equipment and the works, plant and materials retained on the site by the Entity after a termination, except damage or loss because of the activities of the Contractor on the site after the termination [10, 11, 21].

3.4.3 Safety [19th Clause]

It expresses that the Contractor is responsible for the safety of all activities on the site. It does not have sufficient information about safety. Also, it did not mention anything about the health issues of the personnel on the site. NEC4—ECC has also given less information in this case. FIDIC RED BOOK (2017) has given more detail in this part which, if added under this Clause of SBD for the PSWs of the GoA, it would make it better and clear. These are as follows:

The Contractor shall submit a health and safety manual to the Engineer for information, within 21 days of the start date and before starting any construction on the site; which has been mainly prepared for the works, the site, and other places (if any) where the Contractor intends to perform the works.

The Contractor shall:

- conform with all the applicable health and safety laws and regulations;
- conform with all the applicable health and safety responsibilities specified in the contract;
- take care of all persons' health and safety permitted to be on the site and other places where the works are being performed. Keep the site and other places where the works are being performed clear of unnecessary obstructions to avoid hazard to these persons;
- provide any temporary works (including fences, guards, footways, and roadways) that may be necessary, because of the execution of the works, for the use and safety of the owners and of public and occupants of adjacent property and land.

The name of this clause of SBD for the PSWs shall also be changed to express its clear meaning as written above in sub-sub Sect. 3.3.2 [9–11, 21].

3.4.4 Disputes Resolution [62nd Clause]

The second sub-clause of it is given as a separate clause—Disputes [24th Clause]—which should be removed, because it is already there in the 62nd Clause. The Dispute Resolution clause has some information, but not as much as to remove ambiguity and make it clear. This clause does not have any information for creating the Dispute Avoidance/Adjudication Board (DAAB), which can avoid or resolve the arisen disputes during the contract period. It also does not have any procedure to avoid the disputes or any stimulus for the cooperation between the Entity, Contractor, and Project Manager to lead to avoid the incidence of disputes between them. Both FIDIC RED BOOK (2017) and NEC4—ECC have good information and conditions; if added to the Dispute Resolution clause, it will improve [9–11, 21].

The name of this clause of SBD for the PSWs shall also be changed to express its comprehensive meaning as written above in sub-sub Sect. 3.3.6.

3.4.5 SBD for the PSWs of the GoA

The SBD for the PSWs of the GoA also lacks some of the essential clauses and/or sub-clauses as follows: staff and labor; delayed payment; suspension of works; contractor’s entitlement to suspend work; lacks some essential information about termination by the Entity; lacks information about force majeure or exceptional events; lacks sufficient information about measurement and evaluation; claims; lacks adequate details on testing and inspection [9–11, 21].

If these clauses and/or sub-clauses are added/amended in the SBD for the PSWs of the GoA. In that case, it will lead to a better standard form of contract, clear and easily understandable, and avoid or minimize the arising disputes due to the ambiguity and insufficiency of information.

3.5 Flexibility

Flexibility is a good and admirable feature of a standard contract. As mentioned in the last sections, the SBD for the PSWs of the GoA is for the admeasurement or unit price (priced contract with BoQ) contracts, which is in the scope of our study too. It can also be used for the lump sum contracts but considering some mentioned terms, which are to be amended in the SBD for the PSWs [21]. On the contrary, the NEC4—ECC is more flexible in this case and can be used for different types of contracts like; priced contract with Activity Schedules (AS), priced contract with BoQ, target contract with AS, target contract with BoQ, cost-reimbursable contract,

and management contract [10, 11]. If procurement authorities of the GoA make an effort, they can draft and prepare this SBD for the PSWs so that it can be more flexible and can be used for different types of contracts as NEC4—ECC is used.

3.6 Risk-Sharing

Balanced risk-sharing is also a desirable feature of a standard form of a contract. All modern contracts try to allocate the risk between the parties clearly. Good standard contracts allocate risk to the party who can best manage them [25]. The FIDIC RED BOOK (2017) and NEC4—ECC have balanced risk-sharing between the Employer and the Contractor. However, the SBD for PSWs' risk-sharing is approximately more in favor of the Entity, which increases the risk part of the Contractor. The SBD for the PSWs of the GoA shall be amended and prepared by the procurement authority of the GoA, to balance its risk-sharing between the Entity and the Contractor and to do not harm any party by unbalanced risk-sharing [9–11, 21].

4 Conclusion

The above study concluded that standard forms of contracts and their balanced conditions are of most importance.

In this study, the SBD for the PSWs of the GoA compared with the other two international standard forms of contracts FIDIC RED BOOK (2017) and NEC4—ECC. As a result of this research, the conclusion is written briefly as below:

- Balanced conditions are very essential for each contract, and unbalanced conditions led to arise disputes. FIDIC RED BOOK (2017) and NEC4—ECC are well prepared and balanced than the SBD for the PSWs of the GoA.
- The structuring and arrangement of Afghanistan's SBD for the PSWs is good but needs to be updated and amended to become better structured.
- There are some differences in terminology and expressions between these three standard forms of contracts.
- There are some errors and mistakes in the naming of some clauses in the SBD for the PSWs of the GoA, which the procurement authorities of the GoA should correct them for more clarity and easy understanding.
- There are a lack of some essential clauses and/or sub-clauses in the SBD for the PSWs of the GoA, which creates ambiguity and could cause disputes. The procurement authorities of the GoA may take in mind to add those clauses and/or sub-clauses mentioned in this research and other which are not mentioned here. It will cause to avoid or minimize the incidence of disputes and conflicts in the contract.

- NEC4—ECC is more flexible than FIDIC RED BOOK (2017) and SBD for the PSWs of the GoA. This flexibility is in case of usage of the standard form for different types of contracts from the aspect of its financing.
- The SBD for the PSWs of the GoA does not have balanced risk-sharing between the Entity and the Contractor, but FIDIC RED BOOK (2017) and NEC4—ECC are more balanced in this case.

References

1. Barnes M et al (2013) NEC3 engineering and construction contract, 3rd edn. Institution of Civil Engineers (Thomas Telford Ltd), Glasgow
2. Berry PA (2013) NEC3 or FIDIC? Which is most effective in managing the most commonly identified areas of dispute within construction?. Heriot-Watt University, Edinburgh
3. Besaiso H, Wright D, Fenn P, Emsely M (2016) A comparison of the suitability of FIDIC and NEC conditions of contract in Palestine. In: The construction, building and real estate research conference of the royal institution of chartered surveyors
4. Booen PL (2000) The FIDIC contracts guide (conditions of contract for construction, conditions of contract for plant and design-build and conditions of contract for EPC/Turnkey projects), 1st edn. FIDIC (International Federation of Consulting Engineers), Geneva
5. CMS (2017) NEC4; a closer look at the changes in the ECC. CMS Cameron McKenna Nabarro Olswang LLP, London
6. Cousins P, Reed C, Nicholson T (2006) Guidance notes for the engineering and construction contracts (NEC3), 3rd edn. Institution of Civil Engineers (Thomas Telford Ltd), Glasgow
7. Fenn P, Lowe DJ, Speck C (1997) Conflict and dispute in construction. *Constr Manage Econ* 6(15):513–518
8. FIDIC (1999) Conditions of contract for construction (for building and engineering works designed by the employer), 1st edn. FIDIC (International Federation of Consulting Engineers), Geneva
9. FIDIC (2017) Conditions of contract construction—for building and engineering works designed by the employer, 2nd edn. FIDIC (International Federation of Consulting Engineers), Geneva
10. Garratt M et al (2017) NEC4 engineering and construction contract, 4th edn. Bell & Bain Limited, Glasgow
11. Garratt M et al (2017, June) NEC4 engineering and construction contract, 4th edn. Institution of Civil Engineers (Thomas Telford Limited), Glasgow
12. Godwin W (2013) International construction contracts, 1st edn. Wiley-Blackwell, West Sussex
13. Heaphy I (2013). NEC versus Fidic. In: Proceedings of the ICE—management, procurement and law, vol 166, pp 21–30
14. Hughes K (2019) Understanding the NEC4 ECC contract. Routledge (Taylor & Francis Group), London and New York
15. Kilburn K, Cornelius A (2014) Using NEC3-what you need to know
16. Lau CH, Mesthrige JW, Lam PTI, Javed AA (2019) The challenges of adopting new engineering contract: a Hong Kong study. *Eng Constr Archit Manag* 26(10):2389–2409
17. Lord WE, Liu A, Zhang S, Tuuli, MM (2010). A modern contract: developments in the UK and China. In: Proceedings of the ICE—management, procurement and law, vol 163, pp 151–159
18. MoSPI (2005, April) Contract document for domestic bidding (Ministry of Statistics and Programme Implementation). Chandu Press, New Delhi
19. NPA (2016, Sept) Law on procurement. Ministry of Justice, Kabul
20. NPA (2017, May) Standard bidding document for procurement of large works. National Procurement Authority (NPA), Kabul

21. NPA (2018) Standard bidding document for procurement of small works. National Procurement Authority (NPA), Kabul
22. Rasslan ND, Nassar AH (2017) Comparing suitability of NEC and FIDIC contracts in managing construction project in Egypt. *Int J Eng Res Technol (IJERT)* 6(6):531–535
23. Roe M (2011) Presentation to the Danish society for construction and consulting law. Pinsent Masons, London
24. Rooney P, Allan R (2013) A case study of changing procurement practices on delivery of high-ways projects. In: Smith SD, Ahiaga Dagbui DD (eds) *Procs 29th annual ARCOM conference, 2–4 September 2013, Reading, UK. Association of Researchers in Construction Management*, pp 779–788
25. Shnookal T, Charrett D (2010) Standard form contracting; the role for FIDIC contracts domestically and internationally. In: *Australia, Society of construction law conference*, pp 1–30

Comparative Analysis of Various Walling Materials for Finding Sustainable Solutions Using Building Information Modeling



Amey A. Bagul and Vasudha D. Katare

Abstract In this modern age of the construction industry, the building sector has consumed around 35–50% of energy. Sustainable development has therefore become an essential factor to reduce the impact on the environment. The traditional brick used as a walling material has been a major contributor to the environmental adversity so finding an alternative has become the need of the hour. In this paper, the comparative analysis of various walling materials is done to determine the most suitable and sustainable one. The analysis is done using Building information modelling (BIM). The comparison is carried out by creating a 3D building model in Revit 2019. The sun-path analysis, heating and cooling load analysis, Wind analysis and shading/lighting analysis are performed. Technical, social, environmental, and economic aspects are also considered for comparative analysis. Analytic hierarchy process (AHP) is used as the decision-making process to determine the best walling material. The comparative analysis concludes that walling materials using waste are useful for achieving the goal of sustainable solution.

Keywords Sustainability · Walling materials · Building information modelling · Analytic hierarchy process · Revit

1 Introduction

In several countries, unsustainable growth in the construction industry is regarded as a major environmental hazard. [9] The construction industry in India alone accounts for 22% of overall greenhouse gas (GHG) emissions into the atmosphere. [17] To overcome this limitation, alternative construction materials are developed by using

A. A. Bagul (✉) · V. D. Katare
Department of Civil Engineering, COEP, Pune, Maharashtra 411005, India
e-mail: ameybagul@ymail.com

V. D. Katare
e-mail: vdk.civil@coep.ac.in

industrial and agro wastes are good options [6]. In building design and its construction, energy plays an important role. Many aspects like quantity and type of materials used, location and orientation of the building, parameters of spaces and zones are must be considered to estimate the overall energy need of a building [3, 13]. Materials play an important role in engineering design. Material selection is one of the most difficult problems in product design and production, and it is also crucial for the success and competitiveness of manufacturing organisations. Buildings use large quantities of raw materials that consume a significant amount of energy [20]. For sustainable building construction, the preference of building materials with a minimum amount of energy is of primary importance, as embodied energy in the manufacturing process contributes to a significant fraction of the overall energy usage of the building [19]. Clay bricks and fly ash bricks are significant sources of greenhouse gas emissions due to the use of coal and cement in its processing. For sustainable solutions, reusable and chip alternative options need to be studied [2, 4]. REVIT Architecture, based on parametric building modeling technology, is a purpose-built instrument for knowledge modeling [12]. As a result, it not only graphically portrays the design, but also collects and uses the data required to help sustainable design to deliver its optimum advantages. For analysis and documentation of various design choices, a model created in REVIT will be useful [7, 8, 10]. Building Information Modelling (BIM) is transforming the conventional way construction is delivered [1]. Therefore, the conversion of large energy-consuming structures into energy-efficient sustainable structures is important and it takes time to establish a system for sustainable building analysis using modern tools and technologies [16]. Sustainable construction meets social, environmental and economic needs in a balanced manner [5]. The present study evaluates the use of different wall bricks made up of industrial and agricultural waste to produce renewable and energy-efficient walling materials. The selected masonry units can be used as an alternative to the better thermal resistance and energy efficiency of traditional bricks. Technical, economic, environmental and social aspect were considered for comparison. The most sustainable brick along the selected is obtained by using analytic hierarchy process (AHP) method. The analytic hierarchy process (AHP) is one of the multi-criteria decision-making methods that can be used to help in the selection of the best strategic solution [18]. This study will assist in the identification of alternative, sustainable materials and technologies for walling materials that can minimise economic, environmental, and social impacts such as energy consumption and cost.

2 Methodology

2.1 Materials

For this study, five types of brick are selected with different material properties. Literatures are refried to find physical, thermal properties of the brick. Traditional

Table 1 Technical and social properties of selected bricks

Brick type	Technical properties			Social property
	Size (Inmm ³)	Compressive strength (MPa)	Density (Kg/m ³)	Thermal conductivity (W/m-K)
(Clay bricks) CB	230 × 105 × 75	03.10	1900	0.811
(Co-fired blended ash) CBA bricks	230 × 100 × 90	14	1330	0.55
(Paper and RHA waste bricks) RHAB	230 × 105 × 80	15.00	588	0.35
(Fly ash bricks) FB	230 × 105 × 75	03.12	1550	1.05
(Cotton and paper waste bricks) CWB	230 × 105 × 80	23.64	598	0.25

bricks like clay brick and fly ash bricks are considered along with cotton and paper waste bricks (CWB) [14], co-fired blended ash (CBA) brick [11], paper and RHA waste bricks (RHAB) [15]. Rate and environmental factors are calculated by survey and analysis. The standards of bricks are considered as per Bureau of Indian Standard (BIS), 2002. Table 1 shows the technical and thermal properties based on social comfort factor of selected Bricks.

2.2 Building Model

The location of study model is located in Aurangabad, Maharashtra, India. Single story building having a built up area of 71 m² is used as a study model. 24-hour usage residential unit is considered for building model. Figure 1 shows the plan view of building model. The location and building definition are considered to achieve accurate heating and cooling information.

Using Revit 2019; The 3D model of house is created (Fig. 2). For each type of selected brick, the properties of the wall were changed in Revit library. Remaining units were kept the same to justify the comparative analysis. The input data is taken from the literature. The rooms and spaces are provided for analysis purpose. The space-generated study model is shown in (Fig. 3). Energy analysis model is prepared in Autodesk Revit 2019 for performing sustainability analysis. The Energy analysis model is exported in gbXML, which will be analyzed for sun-path analysis, Wind analysis, Lighting/shading analysis and for calculating heating and cooling loads.

Using the data from result, heating and cooling loads analysis, wind analysis, and, finally, calculating energy usage building facility are performed in Autodesk Green building Studio.

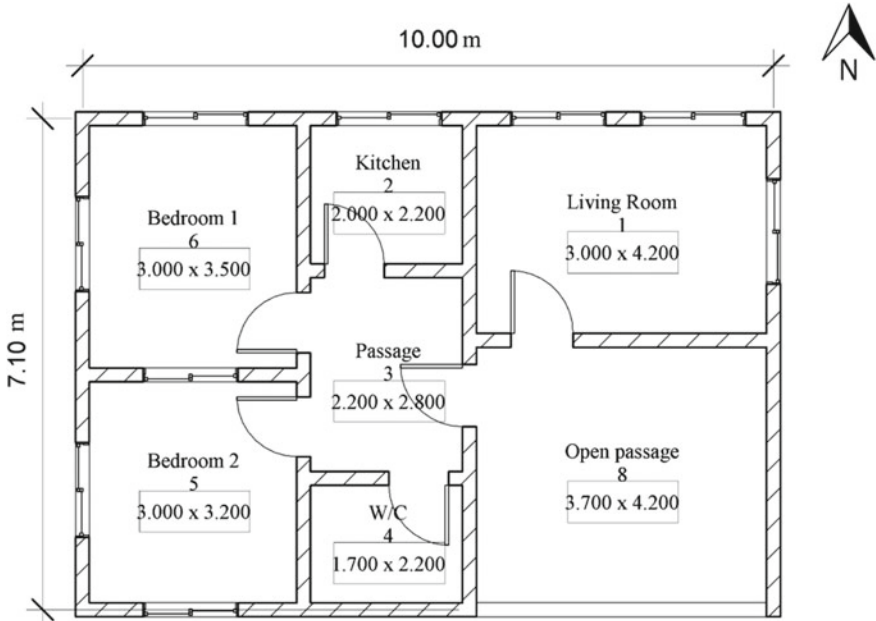


Fig. 1 2D view of floor plan of house

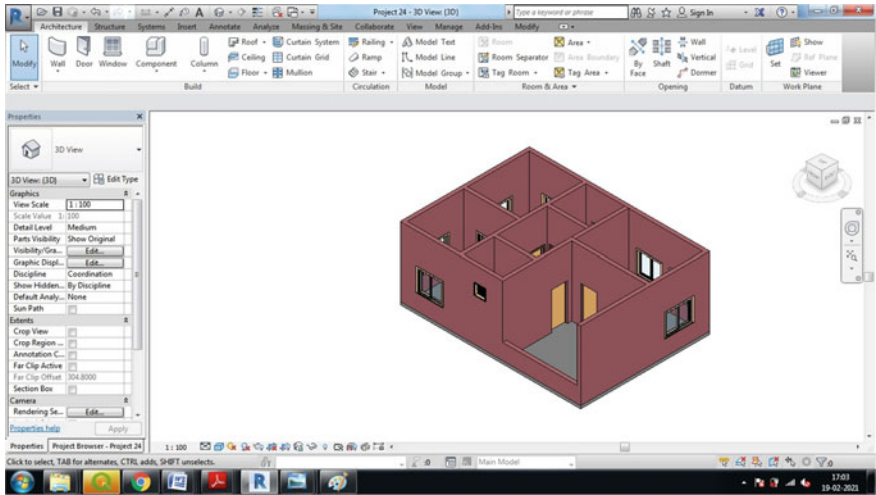


Fig. 2 BIM model

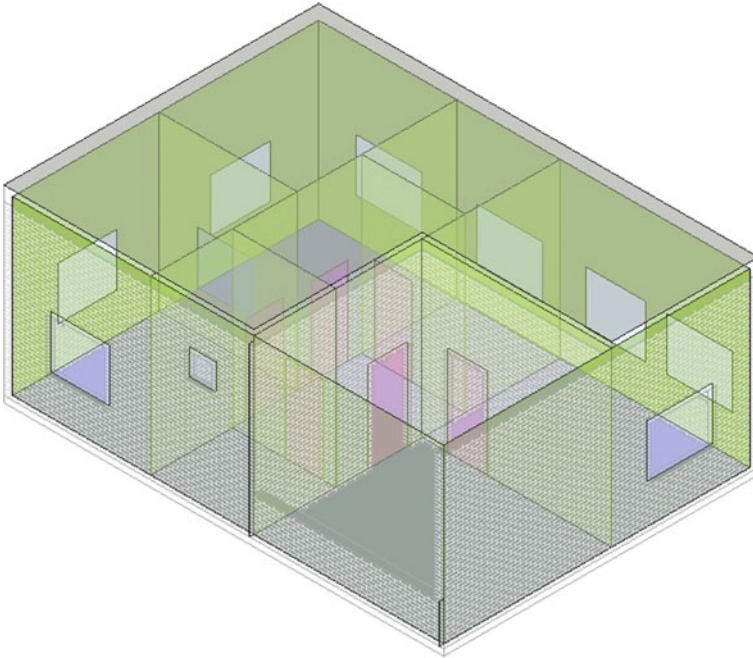


Fig. 3 Space generated study model in REVIT architecture

2.3 Analysis

For the comparative analysis of walling material Technical, social, environmental, and economic aspects are considered. Analytic hierarchy process (AHP) is used as a decision-making process to determine the best walling material. the four criteria that is technical, social, environmental, and economic aspect are considered with five alternative bricks. The matrix is formed and by using Saaty's Ratio Scale; the values are considered. A judgmental matrix is used to calculate the priorities of the corresponding criteria.

3 Result

3.1 Sun Path Analysis

The outcome of the sun path study will be useful for evaluating the suitable position for the electricity generation solar PV panel system, solar water heaters and other solar equipment mounted on the building facility to optimise the usage of solar energy. Sun path analysis is carried out using Autodesk Insight. To achieve thermal

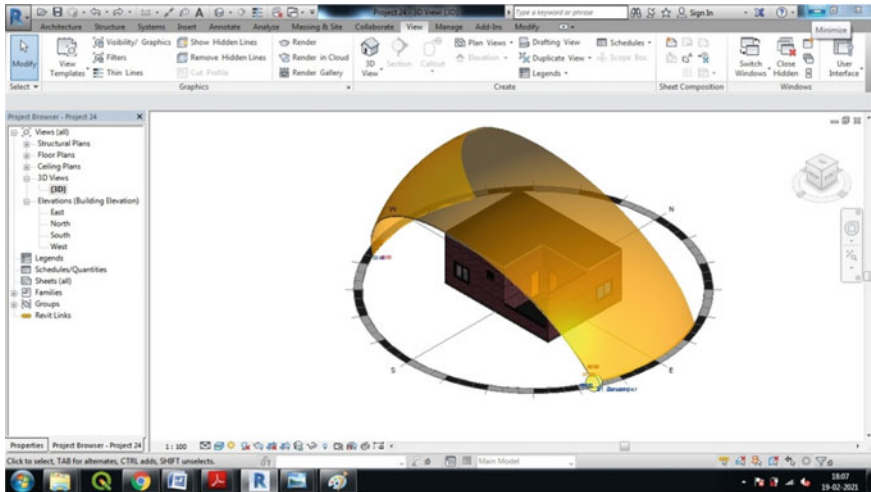


Fig. 4 Sun path analysis

and visual comfort in a construction facility, the effects of solar analysis may be used. Figure 4 shows the study of the sun’s direction.

3.2 Shading/Lighting Analysis

In any construction plant, for proper day lighting plan, the shading study is very helpful. It will minimise energy costs with little to no additional expenditure on systems. Also helps to decrease power costs, prevent eyestrain in the workplace and may be useful to avoid excessive absorption of summer heat. The location of openings such as doors, windows, etc., is determined using the shading analysis. Figure 5 shows the study of the shading/lighting analysis.

3.3 Wind Analysis

The most appropriate technique for inducing passive cooling is natural ventilation. Appropriate air circulation in a facility helps to maintain comfortable temperatures. In a building facility, proper air circulation and ventilation ensure that the contaminated air is replaced repeatedly by cleaner and fresher air. This analysis is based on the Annual wind roses study. Considering 16 cardinal directions, wind roses are made. On a radial scale, the wind frequency is represented with strength of 0, 2, 4, 6, 8, 10, 12, 14, 16 and 18% of the time as shown in Fig. 6.

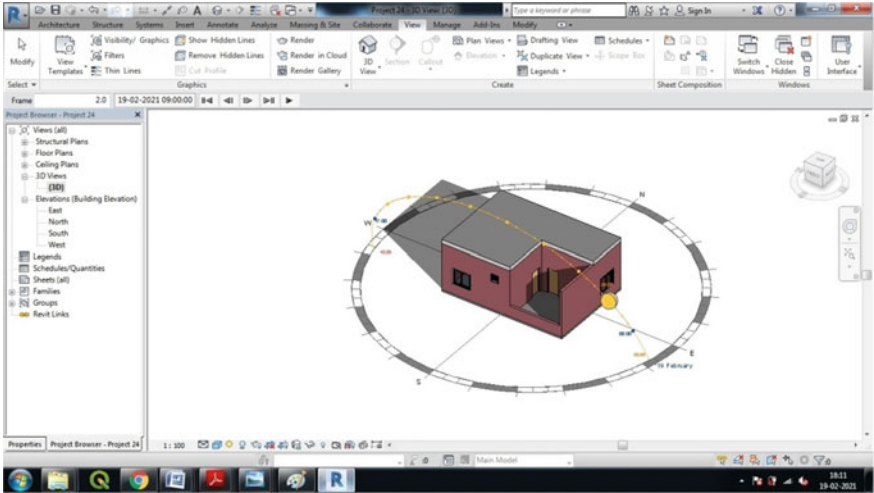


Fig. 5 Shading/lighting analysis

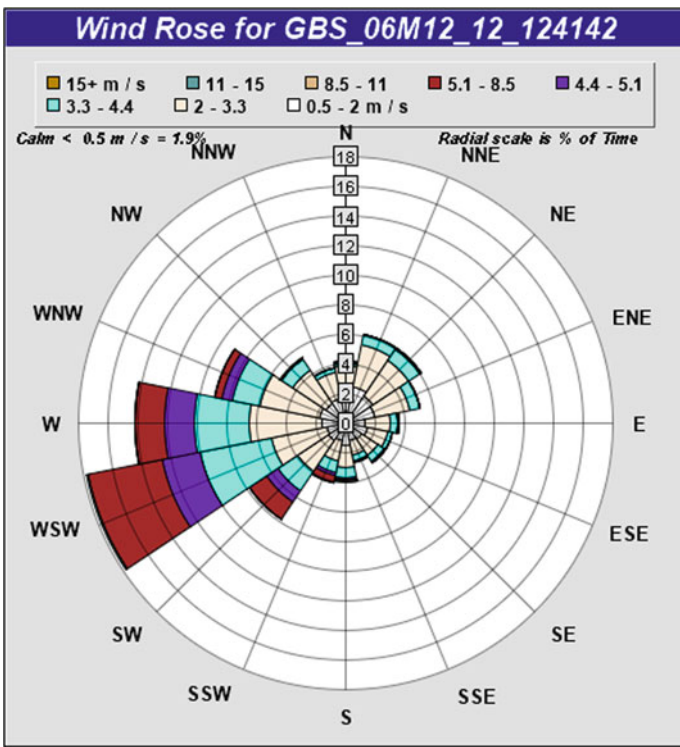


Fig. 6 Annual wind roses

3.4 Heating and Cooling Loads Analysis

The result from green building studio gives Heating and cooling analysis for the project which was carried out using BIM to build a better sustainable facility that naturally heated and cooled. The difference of the dry bulb and wet bulb temperature depending on the cooling and heating threshold is shown in Table 2.

The sustainability assessment is carried out only for brickwork. by changing and providing the properties such as brick density, thermal conductivity (k), dimension from wall library. Bricks are compared with the primary case model. peck cooling load for each case is found out. The market values of bricks are finding out by local survey. The average value is considered. For the value analysis, local brick distributor, contractor and civil industry are referred for the survey. The values are shown in Table 3.

Table 2 Heating and cooling load

Threshold (%)	Cooling		Heating	
	Dry bulb (°C)	MCWB (°C)	Dry bulb (°C)	MCWB (°C)
0.1	40.2	19.4	8.8	5.5
0.2	39.8	19.0	9.9	5.3
0.4	39.6	19.0	10.8	6.5
0.5	39.3	18.7	11.1	7.2
1	38.7	18.4	12.3	8.4
2	37.7	18.1	13.4	9.1
2.5	37.3	18.8	13.7	9.4
5	35.5	18.2	15	10.8

*Mean coincident wet bulb temperature (MCWB)

Table 3 Environmental and economic value of selected bricks

Brick type	Environmental properties		Economic Properties
	EE (MJ/Brick)	Peck cooling load demand (W)	Cost/unit (INR)
(Clay bricks) CB	4.19	11,243	7.61
(Co-fired blended ash) CBA bricks	1.71	9650	4.6
(Paper and RHA waste bricks) RHAB	0.078	7212	7.04
(Fly ash bricks) FB	0.09	8561	9.01
(Cotton and paper waste bricks) CWB	0.078	5418	5.68

Table 4 Saaty's ratio scale

Evaluation	Scale/Judgment
1	Equal importance of both elements
3	Moderate importance of one element over another
5	Strong importance of one element over another
7	Very strong importance of one element over another
9	Extreme importance of one element over another
2, 4, 6, 8	Compromises between the previous judgments
1/2, 1/3, 1/4, 1/5, 1/6, 1/7, 1/8, 1/9	If activity i has one of the above nonzero numbers assigned to it when compared with activity j, then j has the reciprocal value when compared with i

Source Saaty (1977, 1980)

Table 5 Ranking of brickwork

Rank	Technical	Social	Environment	Economic
1	CWB	CWB	CWB	CBA
2	CBA	CBA	RHB	CWB
3	RHB	CB	FB	RHAB
4	FB	RHB	CBA	CB
5	CB	FB	CB	FB

Using the obtained value the AHP method is used for analysis. AHP is a valuable method for dealing with tough choices, and it can help to set goals and make the best possible decision. AHP has the potential to use qualitative and quantitative criteria, the organised manner in which decisions are taken, which allows for good decision traceability, and the quality assurance offered by consistency indices are all benefits of this system. Five alternatives with four criteria are considered for AHP analysis. The Saaty's Ratio Scale is considered for comparative valuation as Shown in Table 4. The obtained result is shown in Table 5.

4 Conclusion

In The modern era of construction; sustainability becomes an essential part to balance energy and nature. The solid waste produced by agriculture and industrial waste can be a new solution for modern bricks. The Cotton and paper waste brick brick have the highest sustainability index. co-fired blended ash) CBA bricks and (Paper and RHA waste bricks) RHAB are also effective solutions on clay Brick. The Cotton and paper waste bricks have the highest sustainability index. which is 60% efficient in thermal conductivity, 26% cost efficient than Clay brick. (co-fired blended ash) CBA

bricks and (Paper and RHA waste bricks) RHAB are also effective solution on clay Brick. The Building Information Modelling (BIM) is the advanced tool that helps to understand the Problems and risk in panning and pre-construction stage. It provides accurate results with statically and visually. The AHP method helps to effectively deal with the issue so that it is easier for the decision maker to take appropriate actions. The comparative analysis concludes that walling materials using waste are useful for achieving the goal of sustainable solutions.

References

1. Abdelalim AM (2019) Integrating BIM-based simulation technique for sustainable building design. In: International congress and exhibition sustainable civil infrastructures: innovative infrastructure geotechnology. Springer, Cham
2. Adewale BA et al (2018) Dataset on cost comparative analysis of different walling materials in residential buildings in a developing economy. *Data Brief* 19:1918–1924
3. Ajayi SO et al (2015) Life cycle environmental performance of material specification: a BIM-enhanced comparative assessment. *Int J Sustain Build Technol Urban Dev* 6(1):14–24
4. Ashby MF et al (2004) Selection strategies for materials and processes. *Mater Des* 25(1):51–67
5. Azhar S, Brown J, Farooqui R (2009) BIM-based sustainability analysis: an evaluation of building performance analysis software. In: Proceedings of the 45th ASC annual conference, vol 1, No. 4
6. Ceranic B, Latham D, Dean A (2015) Sustainable design and building information modelling: case study of energy plus house, Hieron's Wood, Derbyshire UK. *Energy Procedia* 83:434–443
7. Charef R, Alaka H, Emmitt S (2018) Beyond the third dimension of BIM: a systematic review of literature and assessment of professional views. *J Build Eng* 19:242–257
8. Chong HY (2016) Comparative analysis on the adoption and use of BIM in road infrastructure projects. *J Manage Eng* 32(6):05016021
9. Dissanayake DMKW, Jayasinghe C, Jayasinghe MTR (2017) A comparative embodied energy analysis of a house with recycled expanded polystyrene (EPS) based foam concrete wall panels. *Energy Build* 135:85–94
10. Farghaly K et al (2018) Taxonomy for BIM and asset management semantic interoperability. *J Manage Eng* 34(4):04018012
11. Gavali HR, Ram S, Ralegaonkar RV (2018) Evaluation of energy efficient sustainable walling material. In: Urbanization challenges in emerging economies: resilience and sustainability of infrastructure. American Society of Civil Engineers, Reston, VA, pp 227–233
12. Jung I, Kim W (2014) Analysis of the possibility of required resources estimation for nuclear power plant decommissioning applying BIM
13. Kim H, Anderson K (2013) Energy modeling system using building information modeling open standards. *J Comput Civ Eng* 27(3):203–211
14. Rajput D, Bhagade SS, Raut SP, Ralegaonkar RV, Mandavgane SA (2012). Reuse of cotton and recycle paper mill waste as building material. *Constr Build Mater* 34:470–475
15. Raut SP, Sedmake R, Dhunde S, Ralegaonkar RV, Mandavgane SA (2012). Reuse of recycle paper mill waste in energy absorbing light weight bricks. *Constr Build Mater* 27(1):247–251
16. Sadeghifam AN et al (2016) Energy analysis of wall materials using building information modeling (BIM) of public buildings in the tropical climate countries. *J Teknologi* 78(10)
17. Shams S, Mahmud K, Al-Amin M (2011) A comparative analysis of building materials for sustainable construction with emphasis on CO₂ reduction. *Int J Environ Sustain Dev* 10(4):364–374
18. Saaty TL (2008) Decision making with the analytic hierarchy process. *Int J Serv Sci* 1:83–98

19. Thormark C (2006) The effect of material choice on the total energy need and recycling potential of a building. *Build Environ* 41(8):1019–1026
20. Udawattha C, Halwatura R (2017) Life cycle cost of different walling material used for affordable housing in tropics. *Case Stud Constr Mater* 7:15–29

Studies on Energy Efficient Design of Buildings for Warm and Humid Climate Zones in India



Santhosh M. Malkapur, Sudarshan D. Shetty, Kishor S. Kulkarni,
and Arun Gaji

Abstract In recent years, significant efforts have been made to improve energy efficiency and decrease energy consumption. The idea of energy efficiency in structures is related to the energy supply needed to achieve desirable environmental conditions that minimize energy consumption. The residential sector is liable for a significant piece of the energy consumption in the world. Most of this energy is used in cooling, heating and natural ventilation systems. In this work, the energy analysis of a residential building is carried out by varying building envelope parameters such as aspect ratio, orientation and window to wall ratio of the building in order to lessen the energy demand for the cooling and heating. The building is modeled in a software tool and various parameters are assigned to study the thermal efficiency in a warm and humid climate zone in India. The results indicate that a square building with an aspect ratio of 1:1 is more thermally efficient structure and North–South orientation of the building is better than East–West orientation. Also increasing window to wall ratio decreases the thermal efficiency of the building. The findings of this work would be helpful in design phase of an energy-efficient residential building.

Keywords Energy efficiency · Warm and humid climate · Orientation · Aspect ratio · Window to wall ratio

1 Introduction

Designing an energy-efficient structure is one of the best methods to reduce energy costs in buildings. To design energy-efficient buildings, structural components and building envelope parameters must be optimized. It is critical to recognize the basic factors that are directly related to heat transfer processes. The theoretical design phase

S. M. Malkapur (✉) · S. D. Shetty · A. Gaji
Department of Civil Engineering, Basaveshwar Engineering College, Bagalkot, Karnataka
585102, India
e-mail: smmcv@becbgk.edu

K. S. Kulkarni
AR & P Division, CSIR-CBRI, Roorkee, Uttarakhand 247667, India

© The Author(s), under exclusive license to Springer Nature Singapore Pte Ltd. 2023
M. S. Ranadive et al. (eds.), *Recent Trends in Construction Technology
and Management*, Lecture Notes in Civil Engineering 260,
https://doi.org/10.1007/978-981-19-2145-2_26

327

of a structure is the best ideal opportunity to incorporate feasible systems. Energy-efficient design methods provide additional value that benefits the end-user. An organized plan dependent on energy-saving standards diminishes economic expenses all through the lifecycle of the structure because of its lower energy consumption [1, 2]. Since there are additionally less CO₂ discharges into the environment all through the structure's yearly energy utilization, this is advantageous to society also. Energy saving is a high need in developed nations. Consequently, energy efficient measures are as a rule progressively executed in all possible areas.

2 Literature Review

The energy saving is a high need in the entire world. The residential sector is a major contributor to the total energy consumption. A large amount of energy is utilized in the cooling and heating systems. Energy efficient structures can be constructed by studying and applying the measures required for achieving it. The measures include shape of the building, building orientation, building envelope system, cooling, and heating, etc., of residential structures [3]. It is possible to improve the energy efficiency of buildings without any additional cost. Buildings should be oriented properly to get the maximum passive solar energy. Morrissey et al. [4] concluded that the concept of passive solar energy should be incorporated in design stage to improve the energy efficiency of buildings. The effect of passive parameters, for example, building shape and building orientation on heating demand has been theoretically examined by Aksoy and Inallib [5] by selecting a cold region (Elazig region) of Turkey. Building orientation was varied from 0° to 90°. It is concluded that structures with a square shape are more advantageous with respect to energy efficiency. Ourghi et al. [6] examined the effect of the shape for office building on its yearly cooling and total energy use. A streamlined examination technique is developed dependent on point-by-point investigations using a few blends of building geometry, glazing type, glazing area, and climate. An immediate connection has been made between relative minimization and complete structure energy use just as the cooling energy prerequisite.

Eskin and Turkmen [7] studied the electricity use in commercial buildings in Turkey. The interactions between various conditions, control systems, and heating/cooling loads in office buildings in the four significant climatic zones in Turkey were studied. This study is used to examine energy conservation opportunities on annual cooling, heating and total building load at four major climatic zones of Turkey. Jazayeri and Aliabadi [8] investigated energy efficiency in the cold and semi-arid climate of Shiraz, Iran. They evaluated energy efficiency in two stages. In the first stage, larger windows with NS facade were considered and in second stage all facades of equal window-to-wall ratio and different building aspect ratios were considered. When different facades are varied, the optimal aspect ratio of a building can be different for different Window to wall ratio (WWR). Friess et al. [9] studied the energy demand of residential villas in Dubai. Minimum insulation

levels for external wall and roof wall (U -value = $0.57 \text{ w/m}^2\text{-k}$) and reinforcement concrete frame was considered non-insulated. This work studied the effect of thermal impact on the structure’s energy consumption by using a software model. Simulation results showed that with suitable outside wall protection methodologies alone, energy savings of up to 30% are obtained. Studies were also carried out on energy simulation tools and the strengths and weaknesses of each tool were studied [10]. Most of the studies have focused on a particular envelope component in a generic building. There is a lack of comparative study of the relative efficiency and impact of passive design strategies.

3 Methodology

3.1 Model and Parameters

In this study, a residential single-family residence house is considered and the effects of different building envelope parameters are studied on the energy efficiency of the building. A single-family house with one floor and basement is modeled for study. Building overview details are provided in Table 1. The house is located at Gadag, Karnataka, which falls under climate Zone 1B: warm and humid as per ECBC [11]. Table 2 provides information on the geography and climate of Gadag. The floor plan is shown in Fig. 1 and the building envelope parameters which have been used as the input parameters in this study are presented in Table 3.

A residential building with three aspect ratios 1:1, 1:1.5 and 1:2 same building area 111.30 m^2 is considered for analysis. Hall, bedroom, kitchen, stairway, and

Table 1 Building overview details

Variable	Value
Total built-up area	111.3025 m ²
Building use	Single-family detached
Number of floors	Ground floor
Construction type wood-framed	Advance framing
Heating	Gas furnace + Electricity
Cooling	Air conditioner—ducted split system
Domestic hot water (DHW)	Electricity and Gas boiler with storage tank
Aspect ratio (building size)	1:1 (10.55 m × 10.55 m) 1:1.5 (8.62 m × 12.93 m) 1:2 (7.45 m × 14.96 m)
Orientation	North–South, East–West
Window to wall ratio (WWR)	30, 40, and 50%

Table 2 Details of geography and climate of Gadag

Variable	Value
City/state	Karnataka, Gadag
Climate zone	1B (warm and humid)
Latitude	N 15°53'
Longitude	E 76°02'
Elevation	650.0 m
Heating design	18 °C baseline
Cooling design	12 °C baseline
Building orientation	0° from the true north and 90° from east
Wind speed	8.2

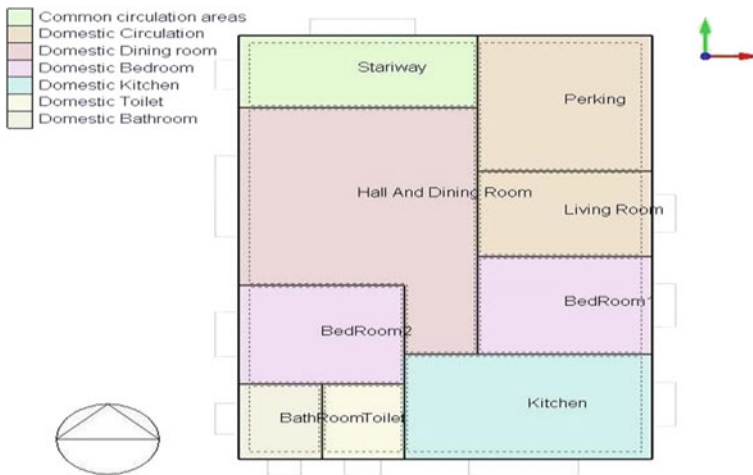


Fig. 1 Building floor plan

parking, etc., suitable dimensions of length and breadth are set out as given in Table 4.

3.2 Internal Loads and Schedules

The residential building of single-family with an occupancy of five people is considered for the present study. Details of activity, maximum occupancy, equipment load and lighting loads in each of the rooms are provided in Table 5.

Table 3 Building envelope parameters

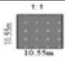
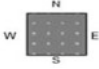
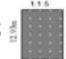

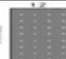

Building envelope parameters			
Model	Aspect ratio	Orientation North–South and East–West	Window to wall ratio %
Model 01	1:1 		30, 40, 50
Model 02	1:1.5 		30, 40, 50
Model 03	1:2 		30, 40, 50

Table 4 Building geometry

Room	Activity						
Aspect ratio		1:1		1:1.5		1:2	
Building size		10.55 m × 10.55 m		8.62 m × 12.93 m		7.45 m × 14.96 m	
Length in m	Breadth in m	L (m)	B (m)	L (m)	B (m)	L (m)	B (m)
Hall/dining room	Eating and Drinking Seated quiet	5.7	2.56	4.67	4.45	3.84	5.92
Master bedroom	Sleeping	4.2	3	3.45	3.0	3.05	3.2
Bedrooms	Sleeping	4.24	2.7	3.35	3.0	3.0	3.6
Kitchen	Cooking	4.24	2.2	4.57	3.2	3.84	3.5
Stairway	Light manual work	5.7	2.0	4.67	2.2	3.84	2.22
Parking and open	Light manual work	4.24	2.24	3.35	3.15	3.0	4.07
Living room	Entry	4.24	2.2	3.35	2.6	3.0	2.8
Bathrooms and toilet	Standing/Walking	2.025	2.0	1.65	2.3	1.475	2.5

3.3 Building Envelope

The building envelope is the physical boundary between the outside and inside environments encasing a structure. It is comprised of a series of components and frameworks that shield the inside space from the impacts of the environment such as

Table 5 Activities and schedules (general energy code or ECBC, 2017)

Room	Activity	Maximum occupancy	Equipment load (W/m ²)	Lighting load (W/m ²)
Hall/dining room	Eating and drinking seated quiet	5	3.06	5
Master bedroom	Sleeping	2	3.58	3
Bedrooms	Sleeping	1 per room	3.58	3
Kitchen	Cooking	2	30.28	5
Stairway	Light manual work	5	2.16	5
Parking	Light manual work	5	1.57	5
Living Room	Entrée	1 per room	1.57	2
Bathrooms and toilet	Standing/Walking	1 per room	3.28	3

precipitation, wind, temperature, humidity and also ultraviolet radiation. The internal environment is comprised of the occupants, building materials, lighting, machinery and the HVAC system. Improving the structure envelope of houses is perhaps the most ideal approach to improve energy efficiency. This home is modeled using advanced framing techniques. Layer-by-layer details of the wall, roof, and floors are provided. Using these details, creating custom layers and, if necessary, materials using the Design-Builder software. Building envelope construction details are considered as per ECBC 2017 (Fig. 2).

- Floors (ground) (ECBC)
- Roof (ECBC)
- Partition (ECBC)
- Door (ECBC)
- Wall (ECBC)
- Wooden door
- Uninsulated Glazing

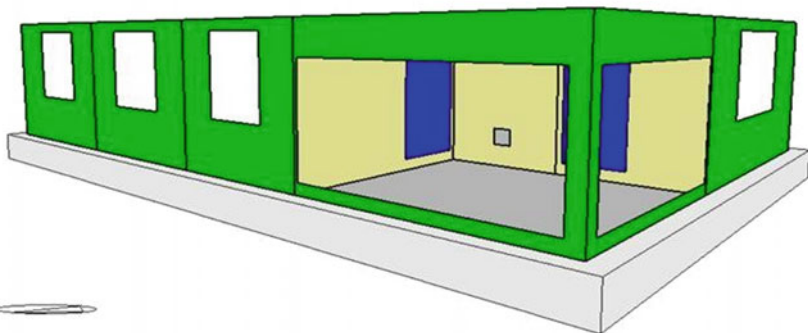


Fig. 2 Building envelope selected for the present study

3.4 Mechanical Systems

The building is considered to be centrally heated and cooled. The heating is provided through a gas furnace and the cooling system is a central split system. Efficiency details of the HVAC and SHW systems are provided as per ECBC 2017 (Table 6). The building is modeled in a software tool (Design builder) and various parameters are assigned to study the thermal efficiency in a warm and humid climate zone in India. Three envelope parameters namely aspect ratio (1:1, 1:1.5 and 1:2), orientation (North–South and East–West) and window-wall ratio (30, 40 and 50%) are varied by using three typical models and their energy efficiencies are evaluated.

Following are the details of the three models considered in this study:

Model 1—Single-family residential building with outer dimensions of 10.55 m × 10.55 m is considered for Model 1. Aspect ratio is kept as 1:1 and both orientations North–South and East–West are considered. Window to wall ratio is varied as 30, 40 and 50% (Fig. 3).

Model 2—Single-family residential building with outer dimensions of 12.93 m × 8.62 m is considered for Model 2. Aspect ratio of 1:1.5 and orientations in both

Table 6 Mechanical system details (general energy code or ECBC 2017)

Variables	Values
<i>Heating load</i>	
System type	Furnace
Fuel type	Electricity + Natural gas
Heating system efficiency (AFUE)	80%
Maximum supply air temperature (AT)	35 °C
Maximum supply air humidity ratio	0.0149
Heating capacity system	26 kW
<i>Cooling load</i>	
System type	Central air conditioning using a split system
Fuel type	Electricity
Cooling system EER	12.00
Cooling system SEER	17.50
Cooling system capacity	14 kW
<i>Domestic hot water system (DHW)</i>	
System type	A storage hot water system (standalone)
System fuel	Natural gas + Electricity
Energy factor	0.82
Hot-water delivery temperature	65 °C
Mains supply temperature	10 °C

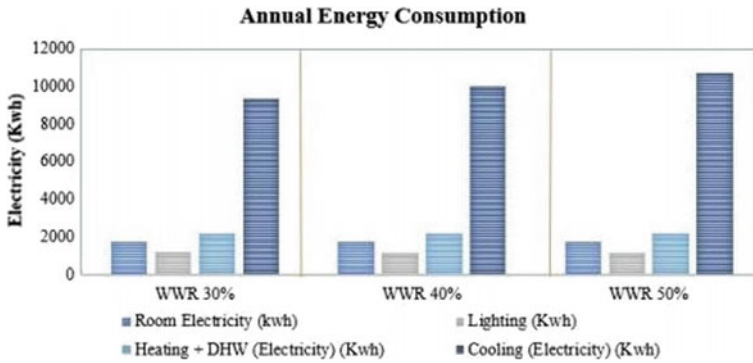


Fig. 3 Energy consumption for model-1

North–South and East–West direction are considered. Window to wall ratio is varied as 30, 40 and 50%.

Model 3—Single-family residential building with outer dimensions of 14.96 m × 7.45 m is considered for Model 3. Aspect ratio is kept as 1:2 and both orientations North–South and East–West are considered. Window to wall ratio is varied as 30, 40, and 50%.

4 Results and Discussions

In this section, the results of the thermal analysis of the three models are presented and discussed. The thermal efficiencies are discussed in terms of electricity consumption for lighting, heating, DHW, cooling, annual energy consumption and temperature.

4.1 Thermal Energy Efficiency of Model-01

The results of the thermal energy efficiency for model-1 are presented in Table 7. It is seen that the room electricity requirement of 1722.28 kWh is constant for different window to wall ratios. When lighting electricity is considered, small variations are seen for different window to wall ratios. It is observed that for window to wall ratio of 30% lighting electricity is found to be 1197.14 kWh, 1179.70 kWh for 40% and 1169.16 kWh for 50%. Heating and DHW electricity remained constant for different window to wall ratios. The cooling electricity is found to vary for different window to wall ratios. It is seen that for window to wall ratio of 30% cooling requirement is found to be 9314.08 kWh and for 40% and 50%, the cooling requirements are found to be 10007.93 kWh and 10699.93 kWh respectively. There is a large variation in the annual energy consumption for different window to wall ratios. The annual energy consumption is found to be 14405.11 kWh, 15081.55 kWh and 15762.98 kWh for

Table 7 Energy consumption results model-1

Description		Values		
Aspect ratio		1:1		
Orientation		NS and EW		
Window to wall ratio		30%	40%	50%
Room Electricity (kWh)		1772.28	1772.28	1772.28
Lighting (kWh)		1197.14	1179.70	1169.16
Heating + DHW (Electricity, kWh)		2171.61	2171.61	2171.61
Cooling (Electricity, kWh)		9314.08	10,007.93	10,699.93
Annual energy consumption		14,405.11	15,081.55	15,762.98
Temperature in °C	Outside	36.60	36.60	36.60
	Inside	33.10	33.51	34.00

window to wall ratio of 30%, 40% and 50%, respectively. In general, it can be seen that irrespective of the orientation, the energy consumption is found to increase with increasing window to wall ratios. This is true due to the fact that there will be increased thermal energy transfer between inside and outside environments with increased window to wall ratios and vice versa.

The energy consumption model is presented in Fig.4. The difference in the cooling electricity requirement is found to be lesser by 693.85 kWh and 693.85 kWh for a window to wall ratio of 30% and 40% respectively in comparison with 50%. It is observed that the annual energy electricity requirement is found to be reduced by 676.44 kWh and 681.43 kWh for window wall ratio of 30% and 40% as compared to 50%.

From Fig.4, it is observed that the inside temperature increases by increasing the window to wall ratio for a constant outside temperature of 36.6 °C. The inside temperatures observed are 33.1, 33.5 and 34 °C for window to wall area ratios of 30%, 40% and 50%, respectively.

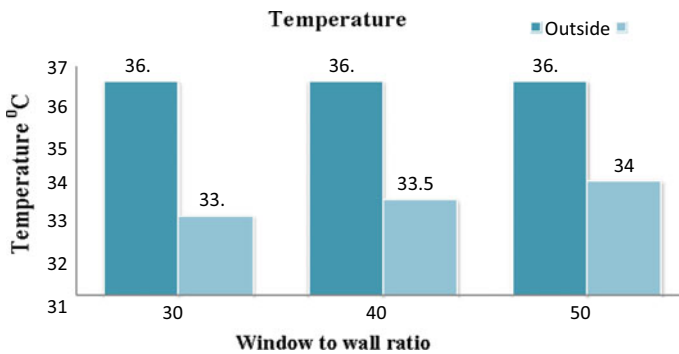


Fig. 4 Temperature variations between inside and outside environments (model-01)

Table 8 Annual energy consumption for WWR

Window to wall ratio (%)	Annual energy consumption (kWh)	Increase in %
30	14,405.11	–
40	15,081.55	4.7
50	15,762.98	4.5

Annual energy consumption for model-01 is found to increase for higher window wall ratios. The annual energy consumption is found to increase by 4.7 and 4.5% for window to wall ratios of 40% to 50% respectively as shown in Table 8. Also, daylight and sunlight dispersion map of model-01 is shown in Figs. 5, 6 and 7.

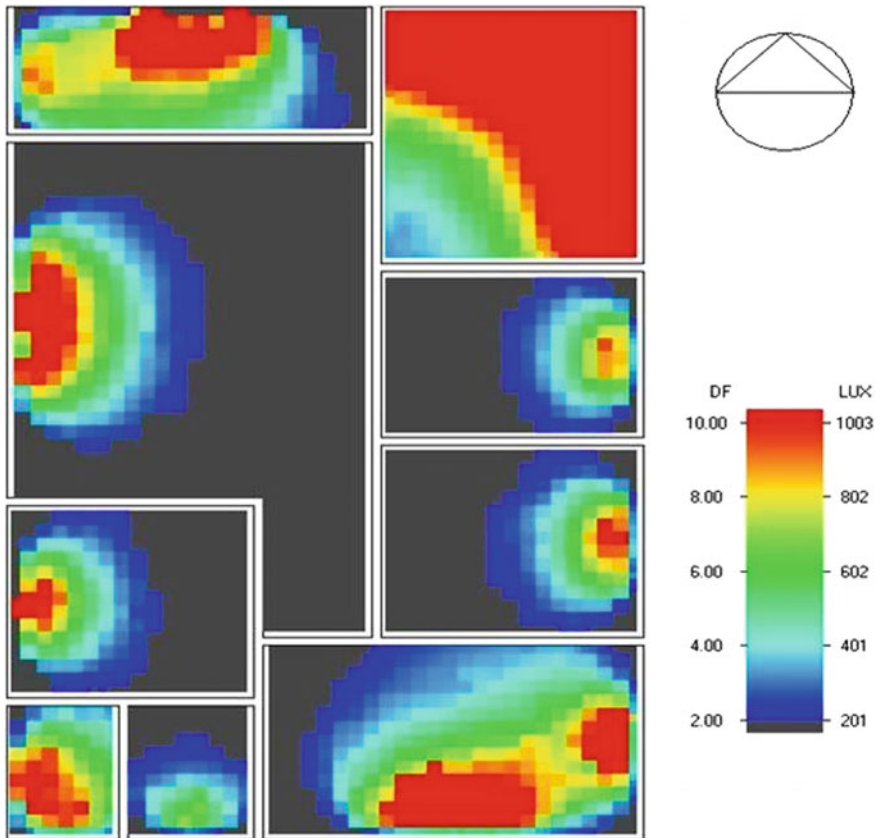


Fig. 5 Daylight inside the room (aspect ratio 1:1 and WWR30%)

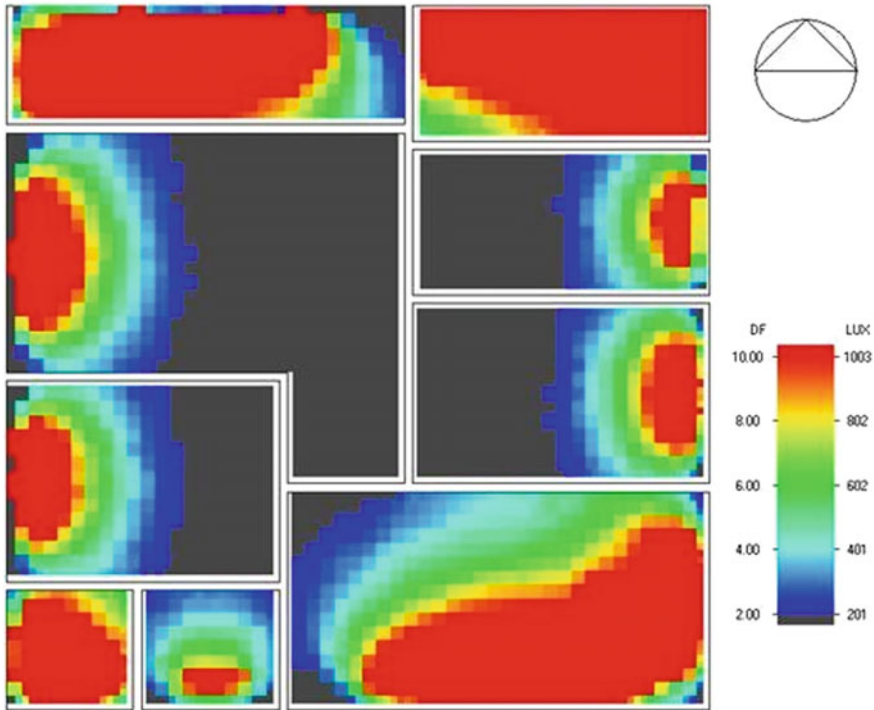


Fig. 6 Daylight inside the room (aspect ratio 1:1 and WWR40%)

4.2 Thermal Energy Efficiency of Model-02

The results of the thermal energy efficiency for model-2 are presented in Table 9 and Fig. 8. It is seen again that the room electricity requirement of 1530.4 kWh is constant for different window to wall ratios. Heating and DHW electricity did not vary for different window to wall ratios. When lighting electricity is considered, small variations are seen for different window to wall ratios. More variations are seen for cooling electricity for different window to wall ratios. It is seen that for window to wall ratio of 30%, cooling requirement is found to be 9314.08 kWh and for 40% and 50%, the cooling requirement are found to be 10007.93 kWh and 10699.93 kWh respectively. There is a large variation in the annual energy consumption for different window to wall ratios which can be seen in Table 9. The cooling electricity is found to increase significantly for increased window to wall ratios. Also with respect to orientation, North–South orientation is found to be better than the East–West orientation in improving the overall thermal efficiency of the building.

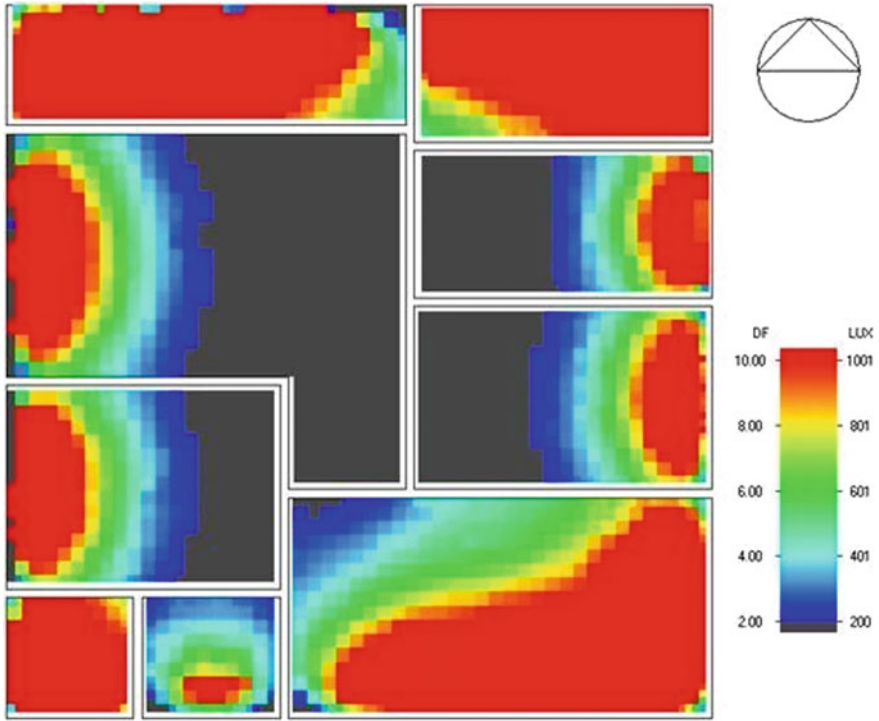


Fig. 7 Daylight inside the room (aspect ratio 1:1 and WWR50%)

Table 9 Energy consumption results of model-2

Description	Values					
Aspect ratio	1:1.5					
Orientation	North–South			East–West		
Window to wall ratio	30%	40%	50%	30%	40%	50%
Room electricity (kWh)	1530.4	1530.4	1530.4	1530.4	1530.4	1530.4
Lighting (kWh)	1158.5	1145.8	1139.5	1161.8	1146.7	1139.0
Heating + DHW (electricity, kWh)	2386.6	2386.6	2386.6	2386.6	2386.6	2386.6
Cooling (electricity, kWh)	10,937.0	11,429.1	11,893.9	11,352.5	11,764.6	12,180.4
Annual energy consumption (electricity, kWh)	16,012.5	16,491.9	16,950.3	16,431.3	16,828.3	17,236.4
Temperature (°C)	Outside	36.6	36.6	36.6	36.6	36.6
	Inside	34.25	34.50	34.75	33.77	34.0 1

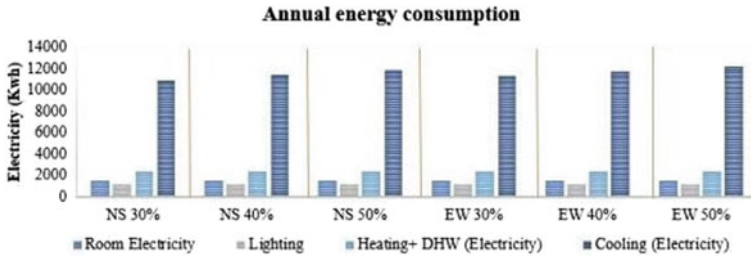


Fig. 8 Energy consumption model-2

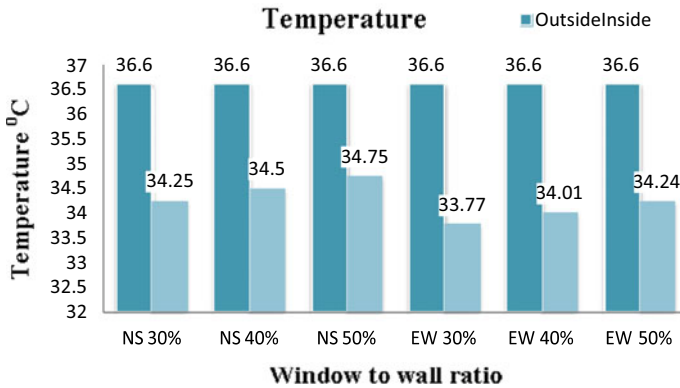


Fig. 9 Temperature variations between inside and outside environments for model-2

From Figure 9 it is observed that inside temperature increases with increasing window to wall ratio for constant outside temperature of 36.6 °C. Also, the North–South orientation is better than East–West orientation with respect to annual energy consumption (Fig. 10). On the other hand, East–West orientation is slightly better in reducing the inside temperatures of the building. Also, daylight and sunlight dispersion map of model-02 is shown in Figs. 11, 12 and 13 (Table 10).

4.3 Thermal Energy Efficiency of Model-03

The results of the thermal energy efficiency for model-3 are presented in Table 11. It is seen again that the room electricity requirement and heating and DHW electricity do not vary for different window to wall ratios. When lighting electricity is considered, small variations are seen for different window to wall ratios. For cooling electricity, considerable variations are seen for different window to wall ratios. It is seen that with increasing window to wall ratios, the cooling requirement increases irrespective of the orientation. There is a large variation in the annual energy consumption for

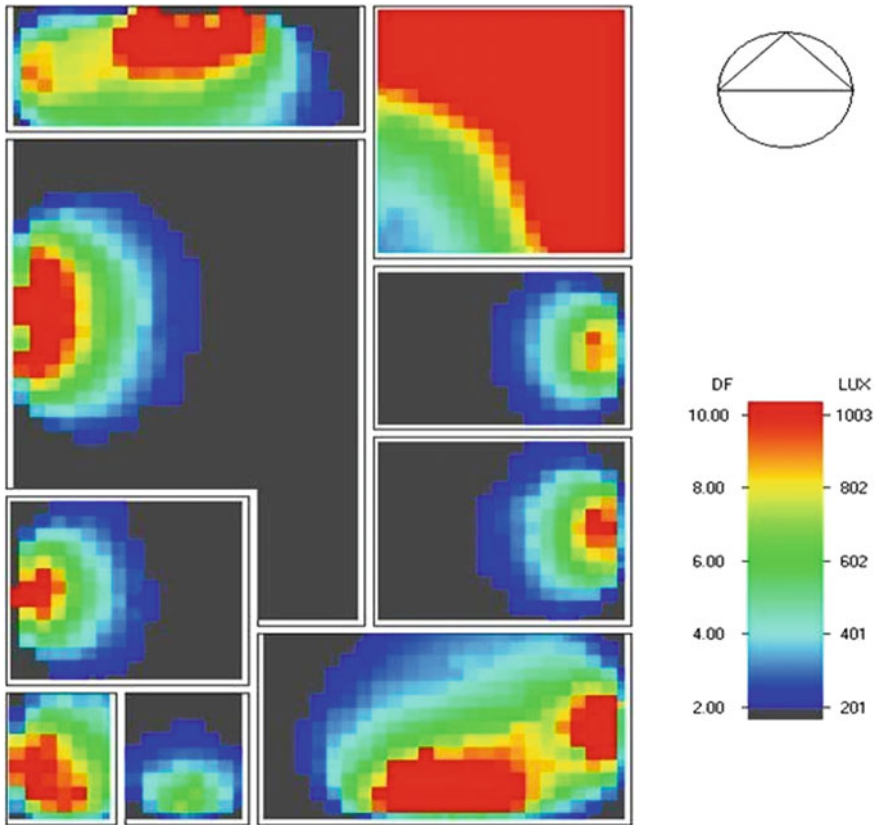


Fig. 10 Daylight inside the room (aspect ratio 1:1.5 and WWR30%)

different window to wall ratios, which can be seen in Table 11 and Fig 13. Also with respect to orientation, North–South orientation is found to be better than the East–West orientation in improving the overall thermal efficiency of the building.

The cooling electricity values of building with North–South orientation are found to be 12576.8 kWh, 13367.2 kWh and 14411.0 kWh for the window to wall ratio of 30, 40 and 50%, respectively. Similarly, for East–West orientation the cooling electricity values are found to be 12883.7 kWh, 13483.0 kWh and 14416.1 kWh for the window to wall ratio of 30, 40 and 50%, respectively (Fig. 14).

From Fig. 15, it is observed that inside temperature increases with increasing window to wall ratio for both North–South and East–West orientations for a given outside temperature. For the outside temperature of 36.6 °C, the inside temperatures are found to be 34.5, 34.61, and 34.65 °C for North–South orientation and for window to wall ratio of 30, 40, and 50% respectively. Similarly, for East–West orientation the inside temperatures are found to be 33.75, 33.9, and 34.1 °C for window to wall ratio

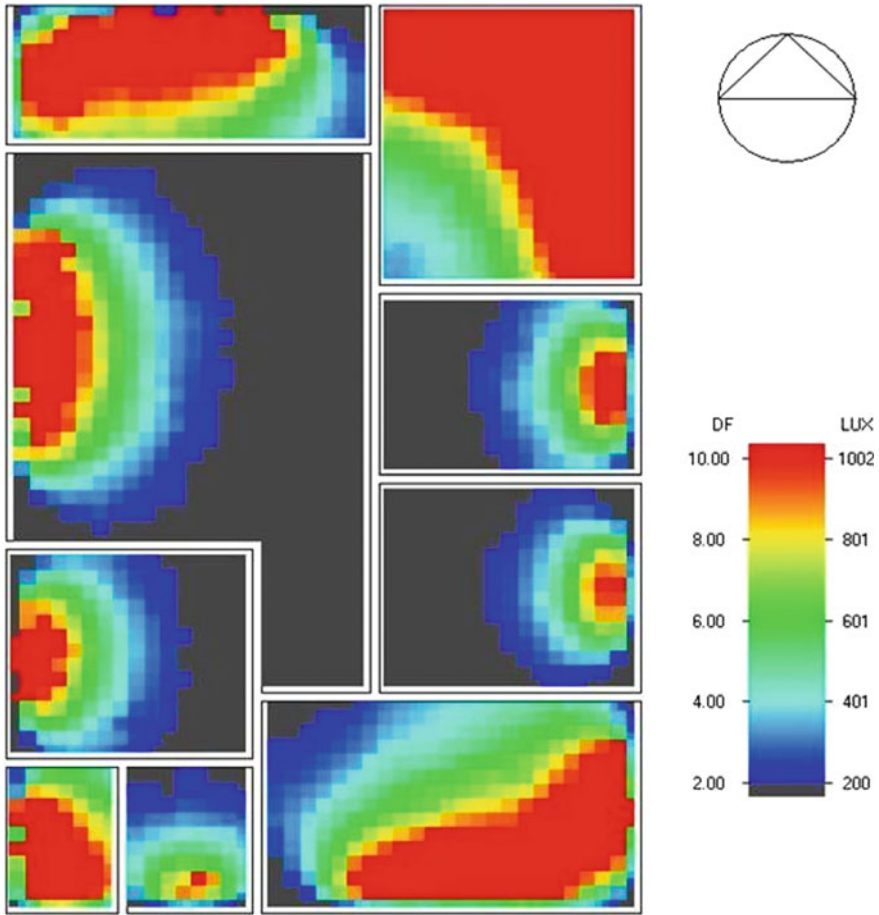


Fig. 11 Daylight inside the room (aspect ratio 1:1.5 and WWR40%)

of 30, 40, and 50%, respectively. Daylight and sunlight dispersion map of model-03 is shown in Figs. 15, 16 and 17.

Also, an overall comparison of electricity usage, annual energy consumption and temperature for different Aspect Ratios are presented in Figs. 18, 19 and 20 (Table 12).

5 Conclusion

- (1) In warm and humid climate conditions, the aspect ratio of 1:1, for a square building, energy consumption is 8–12% lesser in comparison with aspect ratio of 1:1.5.

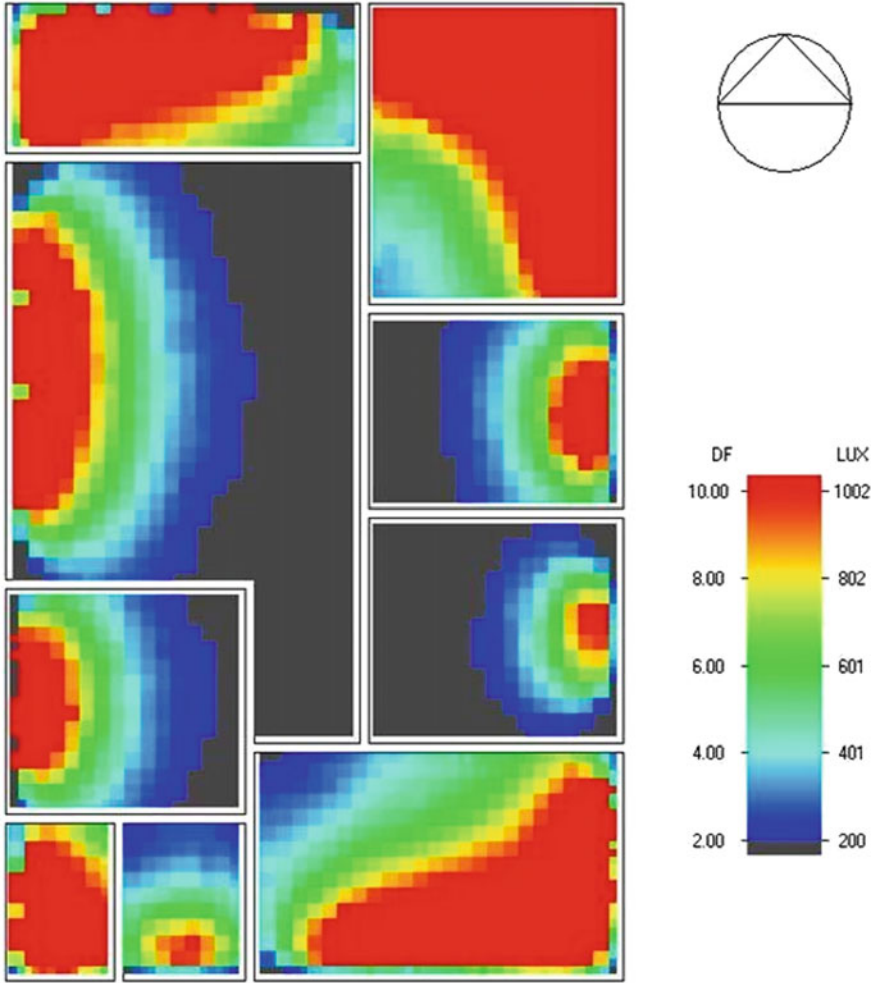


Fig. 12 Daylight inside the room (aspect ratio 1:1.5 and WWR50%)

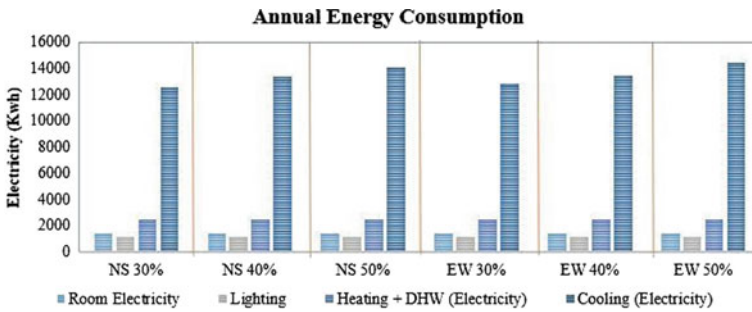


Fig. 13 Energy consumption chart model-3

Table 10 Annual energy consumption for NS and EW model-02

Window to wall ratio (%)	Annual energy consumption (kWh)		Difference in %
	NS	EW	
30	16,012.5	16,431.3	2.61
40	16,491.9	16,828.3	2.03
50	16,950.3	17,236.4	1.68

Table 11 Energy consumption results model-3

Description	Values					
Aspect ratio	1:2					
Orientation	North–South			East–West		
Window to wall ratio	30%	40%	50%	30%	40%	50%
Room electricity (kWh)	1448.9	1448.9	1448.9	1448.9	1448.9	1448.9
Lighting (kWh)	1131.9	1172.0	1167.83	1179.6	1170.9	1166.5
Heating + DHW (electricity, kWh)	2516.8	2516.8	2516.8	2516.8	2516.8	2516.8
Cooling (electricity, kWh)	12,576.8	13,367.2	14,111.0	12,883.7	13,483.0	14,416.1
Annual energy consumption (electricity, kWh)	17,674.4	18,504.9	19,244.5	18,029.0	18,619.6	19,548.3
Temperature (°C)	Outside	36.6	36.6	36.6	36.6	36.6
	Inside	34.5	34.61	34.65	33.75	33.9

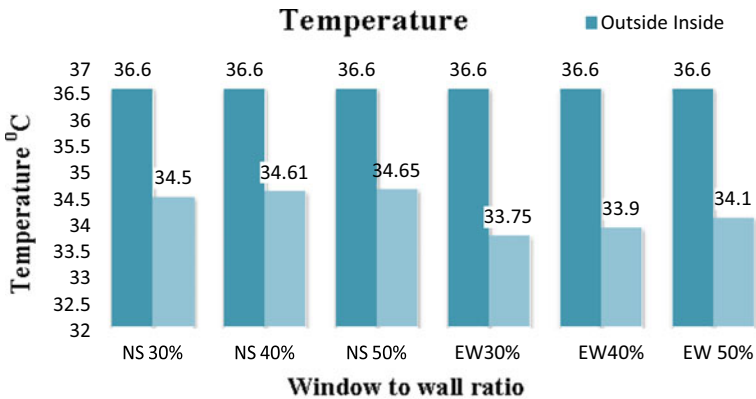


Fig. 14 Temperature variations between inside and outside environments for model-3

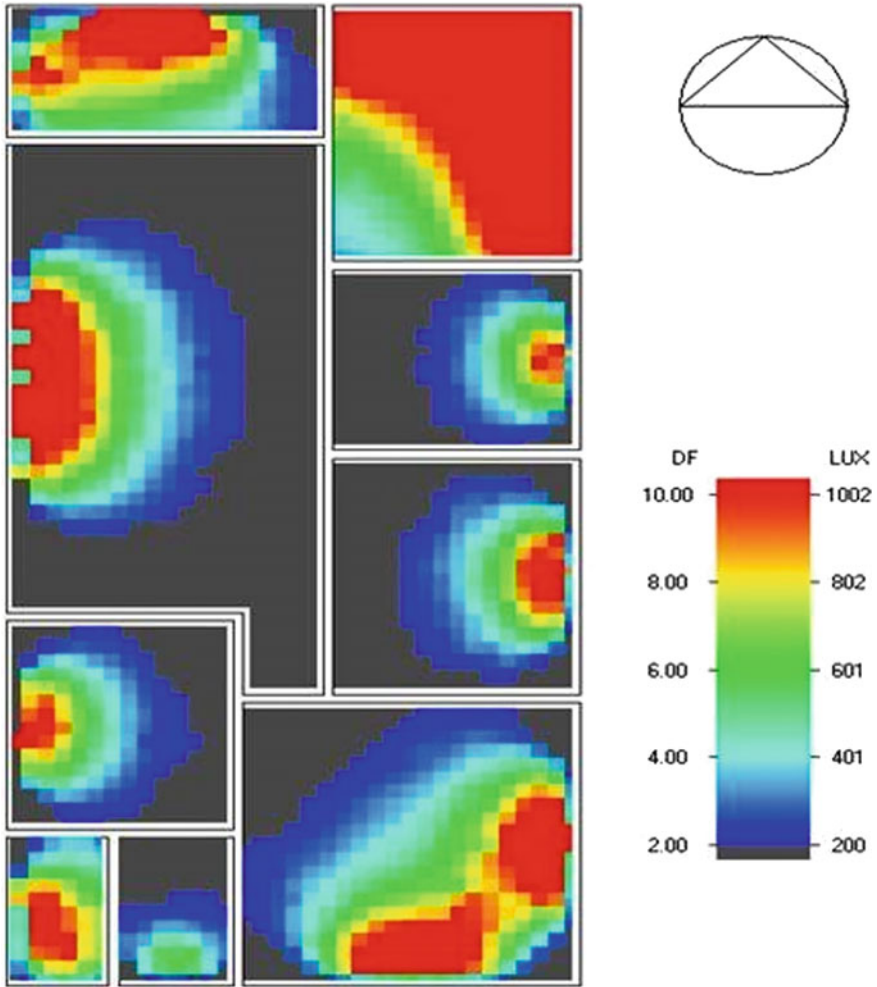


Fig. 15 Daylight inside the room (aspect ratio 1:2 and WWR30%)

- (2) Annual energy consumption for North–South orientation is found to be lesser as compared to the East–West orientation for window to wall ratio 30%, 40%, and 50% respectively. The trend remains same for increased aspect ratios of 1:1.5 and 1:2.
- (3) A window to wall ratio increases overall energy consumption of the building. However, the energy required for lighting decreases.
- (4) Every 10% increase in the window to wall ratio, the inside temperature increases by 0.25–0.5 °C.

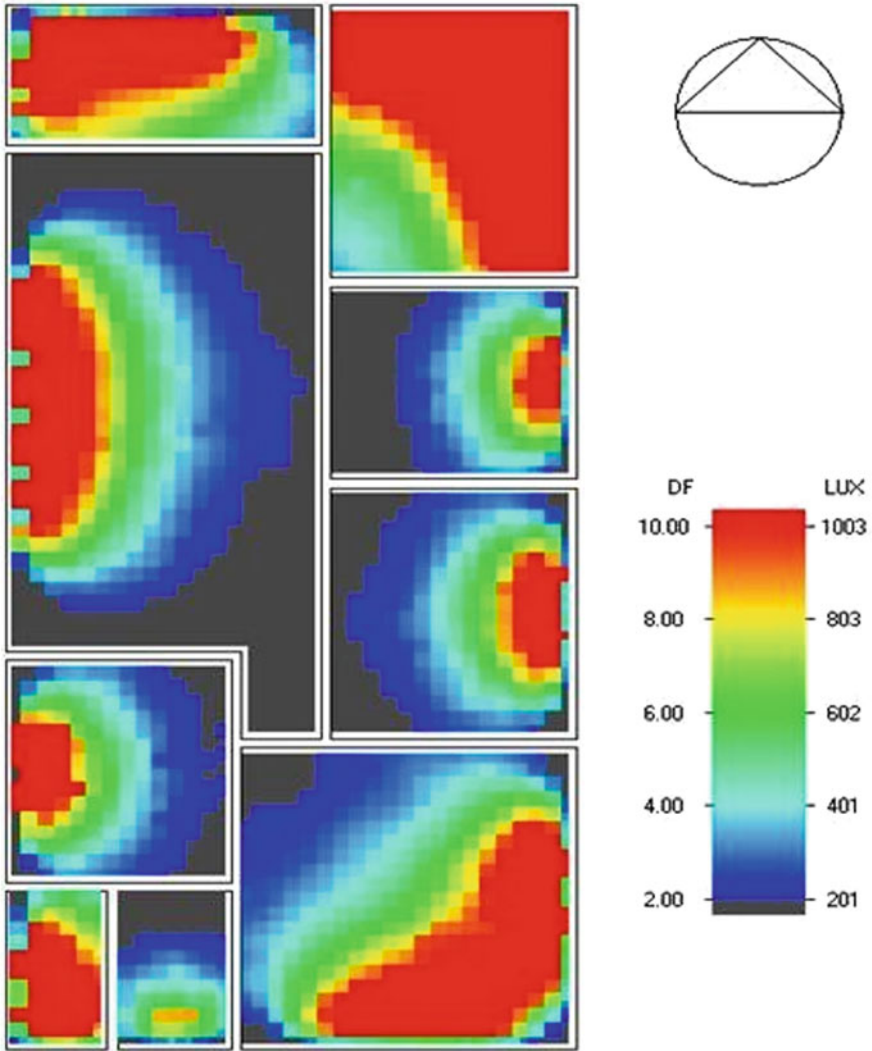


Fig. 16 Daylight inside the room (aspect ratio 1:2 and WWR40%)

The study is conducted based on the analytical approach using a software tool. Hence, further study involving actual experimentation can be conducted to validate the obtained results.

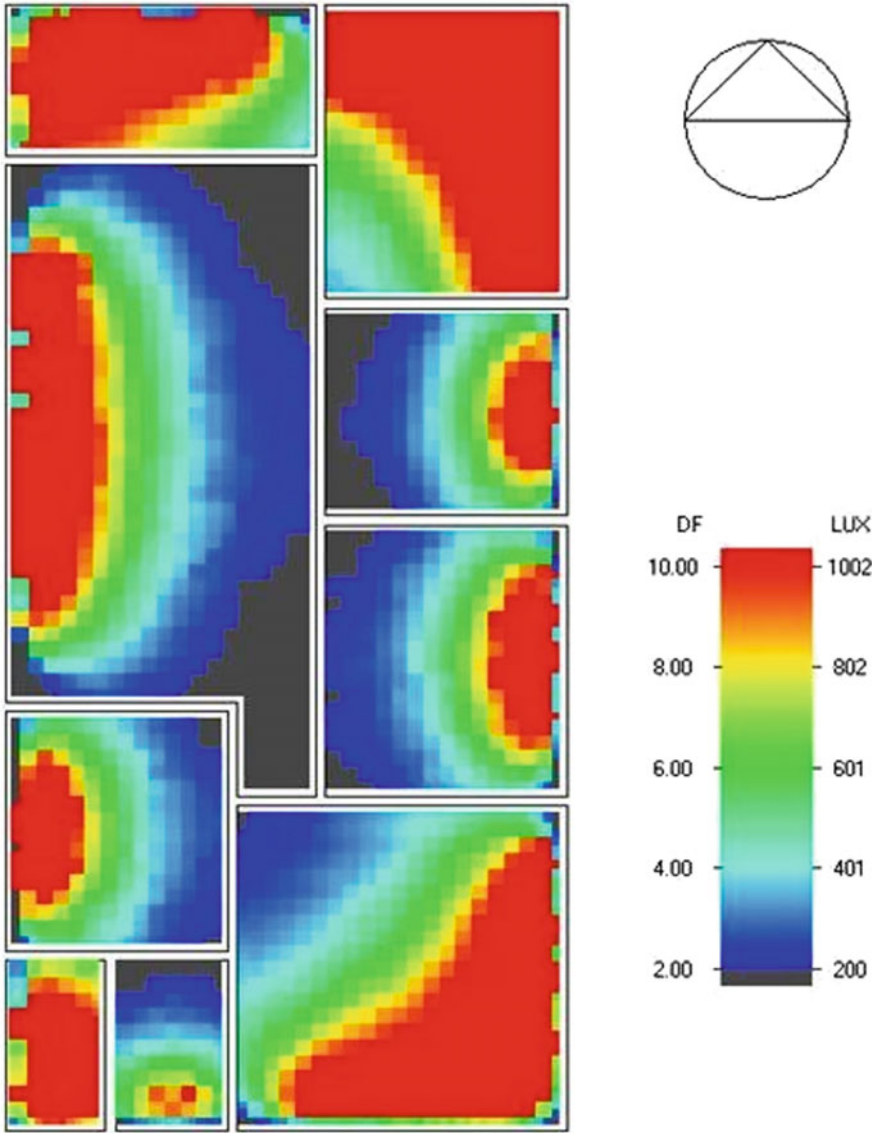


Fig. 17 Daylight inside the room (aspect ratio 1:2 and WWR50%)

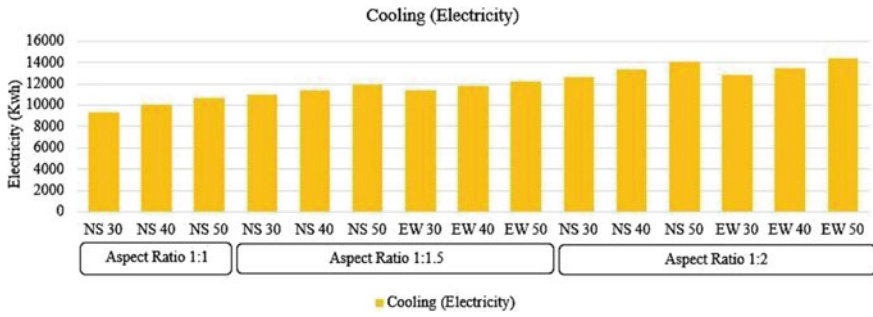


Fig. 18 Cooling load for all the models

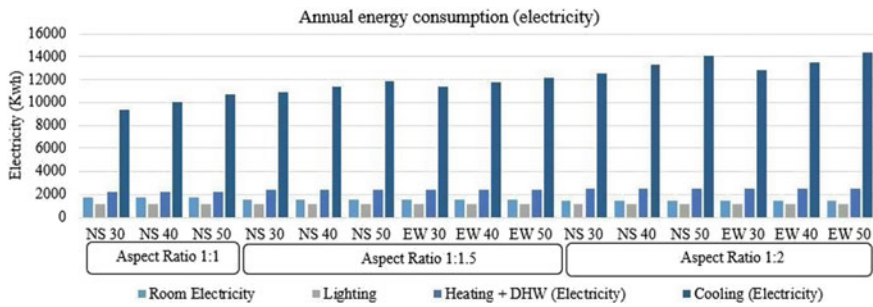


Fig. 19 Annual energy consumptions for all the models

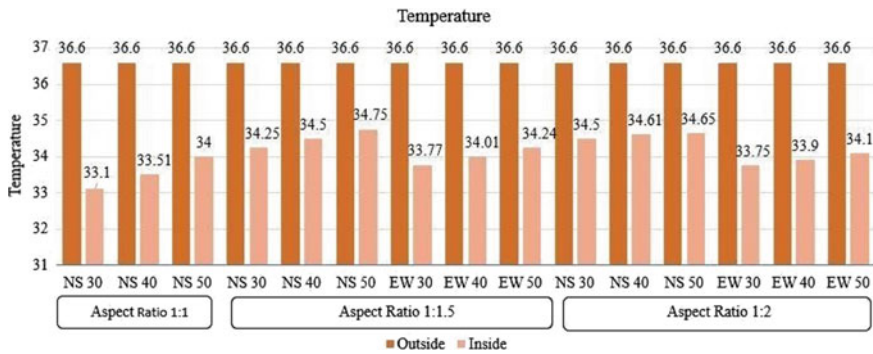


Fig. 20 Summary of temperature variations between inside and outside environments

Table 12 Annual energy consumption for NE and EW model-03

Window to wall ratio (%)	Annual energy consumption (kWh)		Difference in %
	NS	EW	
30	17,674.4	18,029	2.01
40	18,304.9	18,619.6	1.72
50	19,244.5	19,548.3	1.58

References

1. Aneesh NR, Shivaprasad KN, Das BB (2018) Life cycle energy analysis of a metro station building envelope through computer based simulation. *Sustain Cities Soc* 39:135–143
2. Snehal K, Das BB (2021) Experimental setup for thermal performance study of phase change material admixed cement composites—a review. In: *Smart technologies for sustainable development*, pp 137–149
3. Pacheco R, Ordóñez J, Martínez G (2013) Energy-efficient design of the building. *Renew Sustain Energy Rev* 16:3559–3573
4. Morrissey J, Moore T, Horne RE (2011) Affordable passive solar design in a temperate climate: an experiment in residential building orientation. *Renew Energy* 36:568–577
5. Aksoya UT, Inallib M (2006) Impacts of some building passive design parameters on heating demand for a cold region. *Build Environ* 41:1742–1754
6. Ourghi R, Al-Anzi A, Krarti M (2007) A simplified analysis method to predict the impact of shape on annual energy use for office buildings. *Energy Convers Manage* 48:300–305
7. Eskin N, Turkmen H (2008) Analysis of annual heating and cooling energy requirements for office buildings in different climates in Turkey. *Energy Build* 40:763–773
8. Jazayeri A, Aliabadi M (2018) The effect of building aspect ratio on the energy performance of dormitory buildings in cold and semi-arid climates of Iran. In: *International conference on sustainability, green buildings, environmental engineering & renewable energy*, pp 1–6
9. Friess WA, Rakhshan K, Hendawi TA, Tajerzadeh S (2012) Wall insulation measures for residential villas in Dubai: a case study in energy efficiency. *Energy Build* 44:26–32
10. Maile T, Fischer M, Bazjanac V (2007) Building energy performance simulation tools a life-cycle and interoperable perspective. *Center Integr Facility Eng Working Paper* 1–49
11. Energy Conservation Building Code (2017) ECBC, Bureau of Energy Efficiency

Recent Trends in Environmental and Water Resources Engineering

Spatial Variability of Organic Carbon and Soil pH by Geostatistical Approach in Deccan Plateau of India



N. T. Vinod, Amba Shetty, and S. Shrihari

Abstract Proper soil nutrient management is necessary to meet India's rising population without degrading the environment. However, the state of soil organic carbon (SOC) and soil pH is a concern, especially in Indian vertisols that are productive when well managed. Due to a lack of scientific knowledge and poor soil management among the small-scale farmers (most Indian farmers hold less than 2 ha), the crop yield has declined. The current study examines the correlation between soil pH and SOM and their spatial variability in vertisols (Black-Cotton soil). Geostatistics and conventional statistics are used to produce the spatial distribution maps, with the R software and the SpaceStat. Sixty-eight soil samples at the root zone level (0–15 cm depth) are collected from Gulbarga Taluk, Karnataka, India. The random sampling method is adopted according to the agriculture fields distribution, and each sample consists of five subsamples. The soil pH was estimated by pH meter and SOC by Walkley and black method. The violin plots indicate that most soil pH samples range from 8.5 to 7.5 and SOM 0.20–0.50%. The Pearson correlation indicated a negative correlation between the two parameters ($r = -0.21$). In semivariogram analysis, the spherical and exponential models were best fitted for soil pH and SOM, respectively. The ordinary kriging accomplished by a traditional estimator is adapted for generating spatial distribution maps. In line with the negative correlation of soil pH and SOC, the predictable maps are the mirror images. The spatial variability maps give an overview of how extrinsic and intrinsic factors affect the availability of soil pH and SOC. In this region, the parent materials, fertilizers application, and agricultural practices are affecting the soil variability. Small scale farmers should assess these spatial variability maps before applying the fertilizers.

N. T. Vinod (✉)

School of Civil Engineering, Reva University, Bengaluru, Karnataka, India
e-mail: vinodnayak2448@gmail.com

A. Shetty

Department of Water Resources and Ocean Engineering, National Institute of Technology Karnataka, Surathkal, India

S. Shrihari

Department of Civil Engineering, National Institute of Technology Karnataka, Surathkal, India

Keywords Vertisols · Sustainable environment · Spatial variability · Ordinary kriging

1 Introduction

Soil is an important parameter for agricultural practices. The main source of available soil nutrients. Soil health plays a vital role in agricultural practices. Soil is a renewable natural resource which is influenced by many factors that inexorably shift the soil towards future degradation, and it is difficult to reverse these processes without the start of a new geological erosion cycle. It is estimated that the soil depletion in India occurred on 147 Mha of land including 16 Mha of acidification and rest for water erosion, inundation, wind erosion and salinity. The acidification is due to inappropriate agricultural practices. Inappropriate practices by farmers incorporate extreme tillage, unbalanced usage of fertilizers and pesticide, poor irrigation, and poor crop cycle preparation [2]. To understand the variability in soil quality, the quantification of SOC content and soil pH is crucial. The most frequently reported attribute is SOM, and it is chosen as the most essential factor of soil quality and agricultural sustainability [10]. Understanding the complex existence of soil systems (such as SOC and pH) could help clarify soil quality changes that occur in the farmland.

Soil pH is a measurement of soil alkalinity or acidity, indicating the essential chemical and physical properties of soil quality. The alkalinity and acidity alter the presence of soil available nutrients. The SOC is a lively combination affecting a pattern of soil and nutrient properties. SOC content and consistency are known to be a critical factor in the soil's ability to sustain ecosystem services, maintain ecological quality, and improve plant health [13]. If SOC soil concentrations are too limited, then soil mechanics and disrupted soil nutrient cycling pathways can undermine the productive potential of agriculture [12]. With population rise and economy growth, land uses in rural areas have shifted dramatically, which has a big effect on the natural climate. PH and SOC are particularly sensitive to adverse agricultural practices.

In India, the Deccan Plateau is a large plateau in southern India, largely covered with vertisols. Vertisols are a type of soil noticeable by their clay texture and dark colour. Because of stickiness and swelling properties, vertisols are not suitable for agricultural practices; if properly handled, they are more productive. It contributes to disproportion of nutrients when intensively cultivated without understanding the soil state. It induces antagonism of nutrients under these conditions [5].

Proper land supervision is an important tool for increasing agricultural production in sustainable agriculture. Soil management also depends on knowledge of spatial soil variation, particularly soil nutrients. In countries where farms are operated by companies, the scale of the farm is comparatively high and precision farming methods are readily used for sustainable agriculture. In several developing nations, particularly India, a number of aspects, for instance small-scale (below two acres) agricultural

land, inadequate maintenance of innovative technical equipment attributed to financial constraints, and lack of technical information to farmers, are contributing to the decline in understanding of sustainable agriculture [16].

An appropriate strategy for assessing the spatial variability of soil properties is done through geostatistics. In India, the geostatistics are to be used for sustainable cultivation, although it has a long background in soil science activities [7, 19]. The spatial variability of soil nutrients in vertisol is vital to recognize. In this regard, it is recognized that soil pH and SOC play vital roles in agriculture, however determining their spatial variability is essential. There are several experiments carried using geostatistics around the world on spatial variation of soil pH and SOC [3, 4, 11] and few research on different areas of Indian farms [1, 6, 15, 17]. In specific, efforts to understand the spatial variations of soil properties on the Indian vertisol continents are marginal, despite poor crop productivity. In this analysis, certain soil samples were taken from small farms, and statistical and geostatistical techniques have been used to analyse soil pH values and SOC content data. The main objective of this work is to determine the spatial variability of soil pH and soil organic carbon, to characterize and recognize the spatial heterogeneity of the state of soil property, and to analyse the factors that influence the variability of soil properties.

2 Materials and Methodology

The study area, Kalaburagi taluk, is situated in north part of Karnataka, India, between 76°43' E and 77°4' E longitude and 17°27' N and 17°37' N latitude. The area of study is recognized as the tur bowl (pigeon pea vessel) of Karnataka (Fig. 1). The Hyperion satellite pass-over is the area selected for the collection of soil samples. The geographical area is 183.8 km². The region is completely covered with black cotton soil (vertisols). Pigeon pea and jowar are mostly cultivated in this region. The Hyperion satellite pass-over is the area selected for the collection of soil samples.

The sampling of the soil began during the harvest time on the second week of November 2016. Although the fields are distributed over a wide region and are random, the uniform sampling approach was difficult to implement. Topsoil samples (0–15 cm) are obtained at sixty-eight locations in the study area. These points are selected from the cultivated fields of pigeon pea. It was observed during sampling that few farmlands were waterlogged, and residual crops were burnt, as they prepare for another crops, those farmlands are not considered for sampling. The geographical coordinates of the sample positions are registered with Trimble Juno GPS with an accuracy of 2 m. Every soil sample comprises a mixture of five sub-samples with a range of 10 m, collected in plastic carry bag with a shipping label. The soil then air dried for chemical analysis and grounded through a 200-micron sieve. Soil pH is accordingly measured by the pH meter and SOC by Walkley–Black analysis [18].

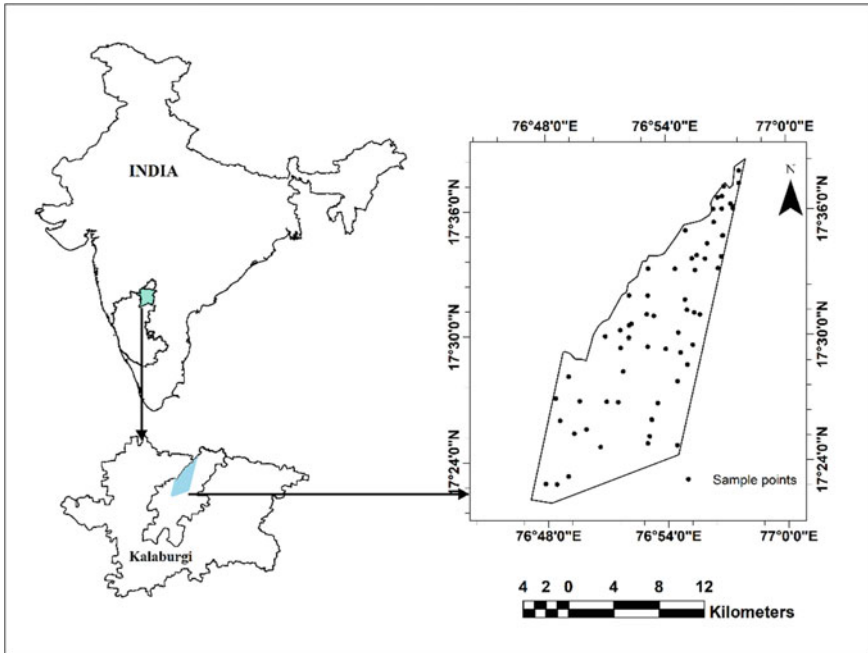


Fig. 1 Study area and sampling locations

2.1 Data Analysis

Descriptive analysis and soil data normality test is performed in R software. The violin plots are plotted. Parameters such as minimum, maximum standard deviation, mean and coefficient of variation are measured. The data were also tested for skewness and kurtosis. Geostatistical study is performed in SpaceStat 4.0[®] program. The semivariogram is determined using Eq. (1), the semivariance $\gamma(h)$ is calculated at various lags of h [7]. Semivariogram assesses the spatial correlation between data sets. The best semivariogram model is chosen based on the initial flatness of the curve and the lowest MSS error (mean sum of square error). Spatial dependence is determined by nugget to sill ratio.

$$\gamma(h) = \frac{1}{2N(h)} \sum_{\alpha=1}^{N(h)} [z(Y\alpha) - z(Y\alpha + h)]^2 \tag{1}$$

where $z(Y\alpha)$ and $z(Y\alpha + h)$ is the calculated value at α th sample location and at the point $(\alpha + h)$ th sample location, respectively [4]. Ordinary kriging process is used to obtain spatial heterogeneity maps, since it generates a non-sampled estimation with a low or no influence of outliers [11].

Spatial variability precision is verified by using Eqs. (2) and (3) respectively with a cross-validation procedure using Mean Absolute Error (MAE) and a Root Squared Error (RMSE) [16].

$$MAE = \frac{1}{N} \sum_{\alpha=1}^N z(y_{\alpha}) - \hat{z}(y_{\alpha}) \tag{2}$$

$$RMSE = \sqrt{\frac{\sum_{\alpha=1}^N [z(y_{\alpha}) - \hat{z}(y_{\alpha})]^2}{N}} \tag{3}$$

In above equations $\hat{z}(y_{\alpha})$ is the predicted value at location α .

3 Results

3.1 Descriptive Statistics of Soil pH and SOC

The descriptive statistics are presented in Table 1. The soil pH in the study region varied from 6.52 to 8.82 with mean value of 7.98. It is noted that soil pH varied from neutral to alkaline in nature. The violin plot of soil pH also indicates most of the data are densely accumulated towards alkalinity (Fig. 2). The alkalinity in soil is inherited due to presence of basalt rock as parent material in study area. The SOC varied from 0.03 to 0.86% with mean of 0.34%. The SOC in the study region is

Table 1 Descriptive statistics of SOC and soil pH

Soil property	Mean	Maximum	Minimum	Standard deviation	Coefficient of variation	Kurtosis	Skewness
Soil pH	7.98	8.82	6.52	0.48	6	0.59	-0.99
SOC (%)	0.34	0.86	0.03	0.203	58.2	-0.30	-0.88

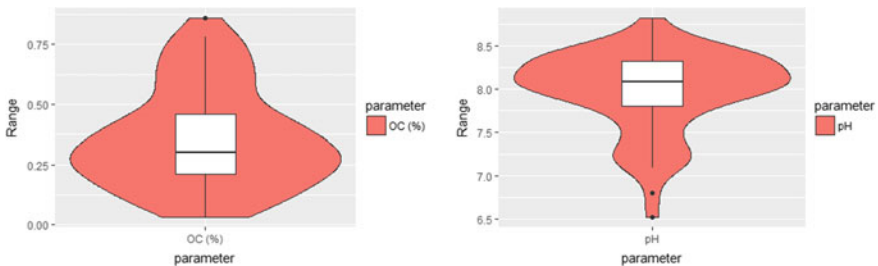


Fig. 2 Violin plots for soil properties

Table 2 Persons correlation for soil pH and SOC

Soil property	Soil pH	SOC
Soil pH	1	
SOC	-0.21	1

below the permissible limits (less than 0.5%), even violine plot indicates the data are accumulated in the lower range. is due to the extensive use of chemical fertilizers by farmers.

The CV is categorized as low (if CV is less than 15%), moderate (if CV ranges between 15 and 35%) and high (if CV is more than 35%) variability [15]. In the study region, soil pH was low and SOC was highly variable. The data were log transformed to reduce the negative skewness effect. The soil formation processes are influenced by topographical changes effects the variability of soil properties. The Pearson correlation analysis is used to identify the relationship between soil pH and SOC. The negative correlation indicates ($r = -0.21$) (Table 2) that maintaining the soil pH is essential to increase the SOC content. High pH soils also have poor chemical and physical conditions which are unfavourable for growth of crop and the production of the root system, resulting in a smaller amount of organic carbon input to the soil [8].

3.2 Geostatistics of Soil pH and SOC

The semivariogram tool is used to analyse the spatial structure for the soil properties. The well-established variograms (Gaussian, Exponential, Spherical, and Linear) are elevated for each property. The parameters included in the semivariogram model are nugget, sill, and range [13]. The degree of spatial dependence is calculated by taking nugget to sill ratio, it can be classified as strong (less than 25%), moderate (25–75%), and weak (more than 75%) [4]. The best semivariogram model is chosen based on the initial flatness of the curve and the lowest MSS error.

The results are tabulated in Table 3. The range is the maximal distance at which parameters are spatially associated. It shows the optimal sampling interval for correct spatial variability assessment. The obtained ranges indicate that the soil pH and SOC are ranged at 3347 m and 1051 m respectively, which also gives the future sampling distance strategy to be adopted. The nugget to sill ratio indicated moderate

Table 3 Geostatistical parameters for soil pH and SOC

Soil property	Nugget	Sill	N/S ratio	Range (m)	Spatial dependence	MSSE	Model	MAE	RMSE
Soil pH	0.089	0.17	0.52	3347.8	Moderate	0.32	Spherical	0.34	0.96
SOC (%)	0.004	0.082	0.04	1051.6	Strong	0.26	Exponential	0.24	0.83

and strong spatial dependency for spherical and exponential models, respectively. The different ranges, which are attributed to sampling intensity and study area size, have been compared by Laekemariam et al. [9]. The range recorded differs due to the cumulative impact of agricultural activities, environmental factors, and parental content. In our field of study, the range is varied due to agricultural activities.

The Ordinary kriging is carried for spherical and exponential models as they are the best-fitted models for generating spatial viability maps. The spatial variability maps show that soil pH usually ranged from neutral to alkaline in nature, the southern part of the region is mainly alkaline (Fig. 3), which may be due to the consistency of irrigation water, as well as the rich presence of calcium carbonate [14]. The SOC was

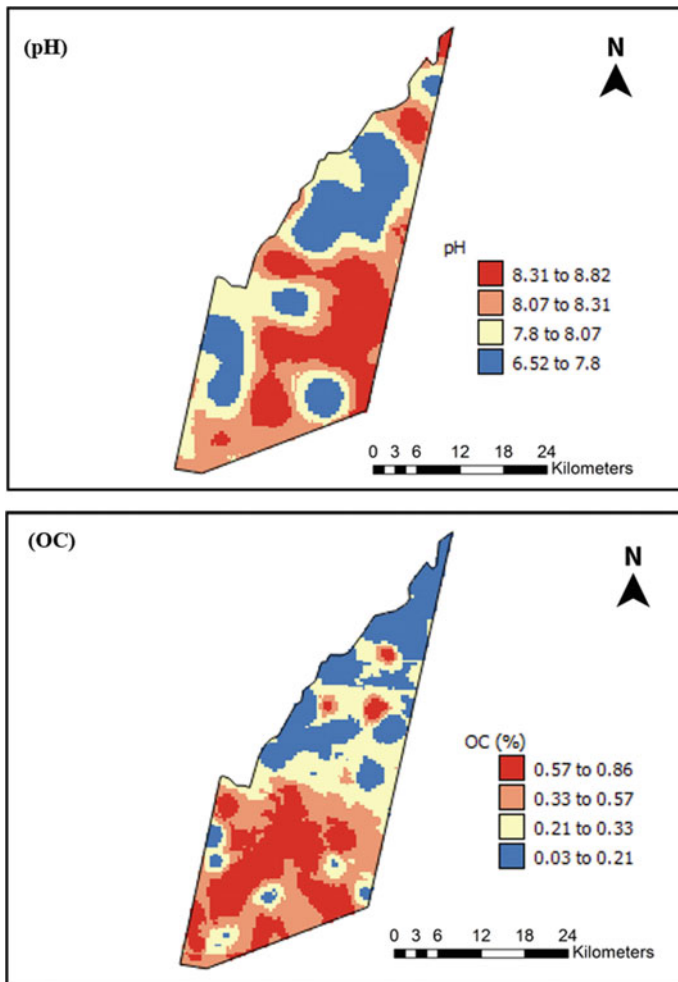


Fig. 3 Spatial variability maps for soil pH and SOC

comparatively higher on the south side of the study area, even though it is below the permissible limit (Fig. 3). This variability may be due to the use of organic manure and fertilizer application.

4 Conclusion

The Soil pH and the SOC are important soil properties to determine soil health. The soil in the study region is basically alkaline in nature and some parts are neutral. The SOC is below the permissible range in the study area. The correlation indicates maintaining the soil pH is vital, which regulates the SOC content. The geostatistics helps in a better understanding of the soil behaviour. The ranges obtained are helpful for researchers in future to maintain sampling distance. The spatial variability maps are useful to assess the soil pH and SOC variability for farmers. The status of soil health for crop cultivation and fertilizer applications will be monitored by these spatial variability maps. In developing countries like India practicing the geostatistical techniques will be benefited for small scale farmers.

References

1. Behera SK, Shukla AK (2015) Spatial distribution of surface soil acidity, electrical conductivity, soil organic carbon content and exchangeable potassium, calcium and magnesium in some cropped acid soils of India. *Land Degr Dev* 26(1):71–79
2. Bhattacharyya R, Ghosh B, Mishra P, Mandal B, Rao C, Sarkar D, Das K, Anil K, Lalitha M, Hati K, Franzluebbers A (2015) Soil degradation in India: challenges and potential solutions. *Sustainability* 7(4):3528–3570
3. Bogunovic I, Mesic M, Zgorelec Z, Jurisic A, Bilandzija D (2014) Spatial variation of soil nutrients on sandy-loam soil. *Soil Tillage Res* 144:174–183
4. Cambardella CA, Moorman TB, Novak JM, Parkin TB, Karlen DL, Turco RF, Konopa AE (1994) Field-scale variability of soil properties in central iowa soils. *Soil Sci Soc Am J* 58:1501–1511
5. Chatterjee S, Santra P, Majumdar K, Ghosh D, Das I, Sanyal SK (2015) Geostatistical approach for management of soil nutrients with special emphasis on different forms of potassium considering their spatial variation in intensive cropping system of West Bengal, India. *Environ Monit Assess* 187(4):1–17
6. Deb P, Debnath P, Denis AF, Lepcha OT (2019) Variability of soil physicochemical properties at different agroecological zones of himalayan region: Sikkim, India. *Environ Dev Sustain* 21(5):2321–2339
7. Goovaerts P (1999) Geostatistics in soil science: state-of-the-art and perspectives. *Geoderma* 89(1–2):1–45
8. Kemmitt S, Wright D, Goulding K, Jones D (2006) PH Regulation of carbon and nitrogen dynamics in two agricultural soils. *Soil Biol Biochem* 38(5):898–911
9. Laekemariam F, Kibret K, Mamo T, Shiferaw H (2018) Accounting spatial variability of soil properties and mapping fertilizer types using geostatistics in Southern Ethiopia. *Commun Soil Sci Plant Anal* 49(1):124–137

10. Liu X, Herbert SJ, Hashemi AM, Zhang X, Ding G (2011) Effects of agricultural management on soil organic matter and carbon transformation—a review. *Plant, Soil Environ* 52(12):531–543
11. Liu Z, Zhou W, Shen J, He P, Lei Q, Liang G (2014) A simple assessment on spatial variability of rice yield and selected soil chemical properties of paddy fields in South China. *Geoderma* 235:39–47
12. Loveland P, Webb J (2003) Is there a critical level of organic matter in the agricultural soils of temperate regions: a review. *Soil Tillage Res* 70(1):1–18
13. Mao Y, Sang S, Liu S, Jia J (2014) Spatial distribution of PH and organic matter in urban soils and its implications on site-specific land uses in Xuzhou, China. *CR Biol* 337(5):332–337
14. Srivastava P, Bhattacharyya T, Pal DK (2002) Significance of the formation of calcium carbonate minerals in the pedogenesis and management of cracking clay soils (Vertisols) of India. *Clays Clay Min* 50(1):111–126
15. Tamburi V, Shetty A, Shrihari S (2020) Characterization of spatial variability of vertisol micronutrients by geostatistical techniques in Deccan plateau of India. *Model Earth Syst Environ* 6(1):173–182
16. Tamburi V, Shetty A, Shrihari S (2020) Spatial variability of vertisols nutrients in the Deccan plateau region of North Karnataka, India. *Environ Dev Sustain* 23(2):1–14
17. Vasu D, Singh SK, Sahu N, Tiwary P, Chandran P, Duraisami VP, Ramamurthy V, Lalitha M, Kalaiselvi B (2017) Assessment of spatial variability of soil properties using geospatial techniques for farm level nutrient management. *Soil Tillage Res* 169:25–34
18. Walkley A, Black IA (1934) An examination of the Degtjareff method for determining soil organic matter, and a proposed modification of the chromic acid titration method. *Soil Sci* 37(1):29–38
19. Webster R, Oliver MA (2008) *Geostatistics for environmental scientists*, 2nd edn. John Wiley & Sons

Hydro-geo Chemical Analysis of Groundwater and Surface Water Near Bhima River Basin Jewargi Taluka Kalburgi, Karnataka



Prema and Shivasharanappa Patil

Abstract River Bhima is one of the major sources of water in the study area of the Jewargi taluka, Kalburgi district of Karnataka. The rural regions' major livelihood depends on agriculture, and the main water source for drinking irrigation purposes is the surface water of the Bhima River. The Hydro-geo chemical parameters are an important aspect of classifying the quality of water for irrigation and domestic purposes. Surface water analysis from the Bhima river basin near Jewargi taluka Kalburgi district Karnataka was carried out from five sampling points along the river for a five-meter stretches of the river. The samples were collected once a week at every 1 m distance approximately during February to May, which is pre-monsoon, and October to January, which is the post-monsoon season in the year 2019. All these five samples were analysed for pH, TDS, TH, Ca^{2+} , Mg^{2+} , Cl^- , Nitrate, Sulphate, dissolved oxygen (DO), Alkalinity, Sodium, Potassium as per the APHA manual. The concentration of ions of all the samples was determined by using hydro-geochemical analysis of Piper diagram, Gibb's diagram, and USSL diagram. From the analysis, it is noticed that all the samples were moderately hard water and rock dominance during both pre- and post-monsoon season. According to Piper's plots, the water samples belong to the permanent hardness that is $\text{Ca}^{2+}\text{-Mg}^{2+}\text{-Cl-SO}_4^{2-}$ types of water. As per USSL diagram, the surface water samples are of C_3S_1 type, which are not suitable for agriculture purposes because of its high salinity and low sodium water quality. Gibb's diagram shows that the samples belong to rock dominance in both the seasons. Due to this rock dominance, the surface water is also influencing the characteristics of groundwater. Rock Weathering is the main source for this chemical composition of the Bhima river basin in the study area. The results showed that water is having a medium hardness in both pre-monsoon and post-monsoon seasons in all the five points of the study area. This study improves to know the present situation and study can be referred to improve the surface water quality of Bhima River in Jewargi taluka of Kalburgi district of Karnataka.

Prema (✉) · S. Patil
PDA College of Engineering, Kalburgi, Karnataka, India
e-mail: prematengli52@gmail.com

Keywords Surface water · Piper diagram · Gibb's diagram · Hydro-geochemical · Bhima river

1 Introduction

A rapid increase in population has increased the demand for water by industrialization and urbanization. As per WHO, about 80% of diseases in living organisms especially in human beings are caused by water. As the demand for water increased nowadays leading to scarcity of water worldwide. The groundwater reservoir is a reliable source of drinking water than surface water as it is available almost everywhere and also less contaminated than surface water. As a result, groundwater analysis is also assumed a top priority nowadays [1]. From 1123 BCM (Billion cubic metre) of usable water, about 38.55% is groundwater in India [2]. Graphical interpretation of chemical analysis makes a complex water system simpler and quicker. Chemistry of water is represented by methods like Piper diagram, US salinity diagram, Gibb's diagram, etc. [3, 4]. Surface water is in use for domestic use, industrial use, water supply for agriculture throughout the world. Surface water bodies are the major natural resources for human development, which are being polluted by improper disposal of sewage, industrial wastewater, and abundance of human activities, that affects physical and chemical composition of water bodies. The study area is a zone with a dense population and agricultural activities. There is no proper drainage system in this region, hence the sewage water reaches directly into the surface water of the Bhima river and some part of it will join the groundwater through infiltration hence it has a large impact on groundwater quality. The present studies have been undertaken to estimate the health of the ecosystem of Bhima River with reference to physical and chemical properties of river water. The main objectives are to characterize the Physico-chemical analysis of ground and surface water and the Hydro-Geochemical analysis for irrigation water quality.

1.1 Study Area

Sahyadri is the origin of the Bhima river which is on the Western side of Western Ghats of Bhimashanaka hills near Karjat, Maharashtra state India. The flow of the Bhima River is southeast through Maharashtra and Karnataka states. The study area considered is the Bhima river basin near the Jewargi taluka Kalburgi district 25 km away from the Kalburgi district on NH218 [1]. Kalburgi is the divisional Head-Quarters of 6 Districts of Bidar, Gulbarga, Yadgir, Raichur, Koppal, and Bellary. The location map of the study area is shown in Fig. 1. Geographically, Jewargi is located between 17.02A, North latitude, and 76.77° East longitude at a height of 393 m (1289 ft) above mean sea level [5]. The black cotton soil is predominantly available due to weathering to basalt rocks in the study area [6]. The study area is comprised of

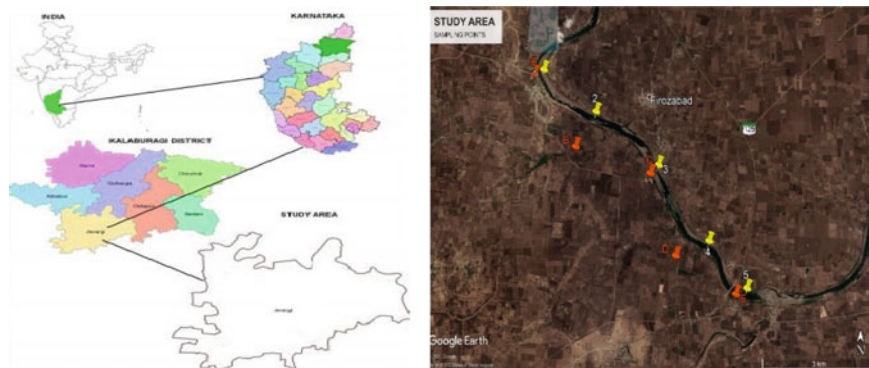


Fig. 1 Location map of the Bhima river basin

villages nearby the Bhima river basin of Jewargi taluka which are Kolkur village, Raddewadgi village, and Katti Sangavi village. The sampling locations are selected in such a way that they cover the study area uniformly.

2 Material and Methodology

All the reagents used for analysis are prepared by using the standard method prescribed in the NEERI manual [7]. Physico-chemical parameters such as Hardness, Calcium, Magnesium, Alkalinity, HCO_3 , DO, Cl, TDS, SO_4 , NO_3 , etc., are determined using standard methods prescribed in NEERI manual. The samples for the analysis of groundwater were collected from various points near the Bhima River basin. Figure 1 shows the location of sampling points A, B, C, D, and E are sampling points for groundwater and surface water sampling points are shown as point 1, 2, 3, 4 and 5. Table 1 shows the methods adopted and instruments used in the Physico-chemical analysis of samples. The samples were collected in pre-monsoon (Feb to May) and post-monsoon (Oct to Jan) seasons of the year 2019. Samples were collected using a grab sampling technique using 2.5liters of white polythene containers on every 6th day in the pre-monsoon and post-monsoon seasons. The samples were analysed for Physico-chemical analysis. Further, the analysed results are used to plot the hydro-geo chemical analysis like Piper diagram, US salinity diagram and Gibb's diagram with the help of AQQA software, Minitab software and MS Excel spreadsheet.

Table 1 Parameters, methods and equipment employed

Sl. No.	Parameters	Method	Equipment
1	pH	–	pH Meter
2	Total dissolved solids (TDS)	Gravimetric Method	China Dishes, Oven
3	Alkalinity	Titration by H ₂ SO ₄	–
4	Chloride	Titration by AgNO ₃	–
5	TH (total hardness)	Titration by EDTA	–
6	Ca ²⁺ (Calcium)	Titration by EDTA	–
7	Mg ²⁺ (magnesium)	Titration by EDTA	–
8	DO	Titrated by Na ₂ S ₂ O ₃	–
9	Nitrate	–	Spectrophotometer
10	Sulphate	Turbidimetric method	Spectrophotometer
11	Sodium	–	Flame photometer
12	Potassium	–	Flame photometer

* All the values are in mg/l except pH

3 Results and Discussions

Maximum, minimum values were for all samples during pre-monsoon and post-monsoon were calculated and tabulated in Table 2. For surface water and Table 3 for groundwater samples. From the analysis, it is found that pH is alkaline during both the season, there is a slight increase in total hardness, chloride, alkalinity, nitrate,

Table 2 Descriptive statistics of surface water samples during the year 2019

Parameters	Pre-monsoon season 2019		Post-monsoon season 2019	
	Max	Min	Max	Min
pH	8.6	7.5	8.5	7.5
TH	223	130	243	195
Ca ²⁺	156	124	168	130
Mg ²⁺	69	61	78	63
Cl ⁻	241	214	259	241
TDS	780	540	950	700
HCO ₃ ⁻	247	220	269	231
Na ⁺	99	74	88	52
K ⁺	13	10	15	12
SO ₄ ²⁻	99	90	109	95
NO ₃ ⁻	36	30	42	32
BOD	3.1	1.8	3.8	2.01
DO	9.6	7.3	8.8	7

Table 3 Descriptive statistics of groundwater samples during the year 2019

Parameters	Pre-monsoon season 2019		Post-monsoon season 2019	
	Max	Min	Max	Min
pH	7.9	7.2	8.3	7.2
TH	112.3	90.2	124.5	97
Ca ²⁺	46.9	39	55.9	41
Mg ²⁺	65.4	51	69.2	56
Cl ⁻	128	114	168	120
TDS	610	415	752	500
Alk(HCO ₃ ⁻)	228	210	248	214
Na ⁺	25.9	23	28	24.2
K ⁺	12.65	9.5	14.1	10.5
SO ₄ ²⁻	33.8	31	40.2	32
NO ₃ ⁻	28.6	26.3	32.8	26.3
DO	7.9	6.4	8.5	6.66

sulphate, and potassium from pre-monsoon to post monsoon season for groundwater samples and all the Characteristics are within the acceptable limit of BIS standards for drinking water. Whereas for the surface water TDS of all the sampling point increases from pre-monsoon to post-monsoon, the pH is between 6.5 and 8.5 and it represents that the surface water is suitable for domestic purposes, and all the samples were within the desirable limit in the selected study location.

3.1 Hydro-Geochemical Analysis of Groundwater

3.1.1 Piper's Diagram

The results of the Physicochemical analysis of samples were plotted in a piper plot, which is a trilinear diagram. Percentage epm (equivalent per millions) of principle cations and anions proportions are plotted in this diagram [1, 4] as shown in Figs. 2 and 3 for both surface and Groundwater samples. Figure 4 shows the subdivisions of piper plots. By comparing the piper plots with subdivisions it is observed that the chemical composition of the sample points, comes in the sub-divisions of 05 and 9 as shown in Table 4, which represents Secondary alkalinity with Carbonate hardness exceeds 50% and No cat ion-anion pair exceeds 50%. On Piper plot, it is seen that all samples belong to Ca²⁺-Mg²⁺-SO₄²⁻ type of water, which represents permanent hardness.

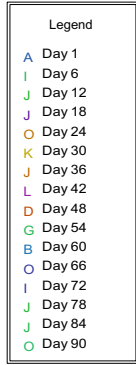
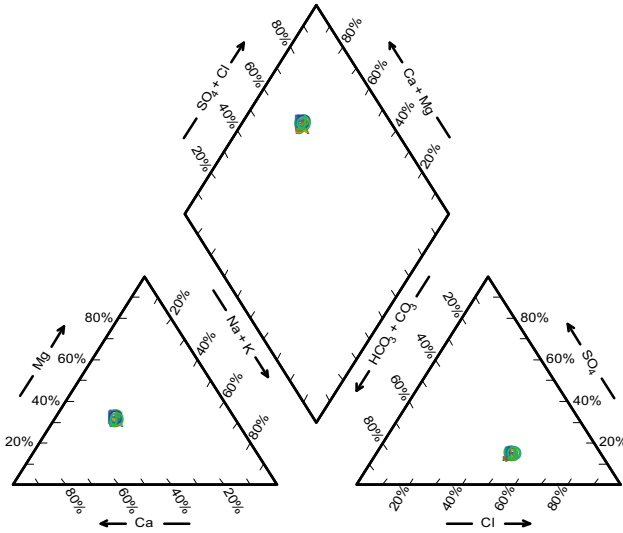


Fig. 2 Piper diagram for surface water samples

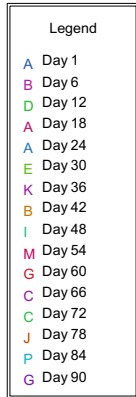
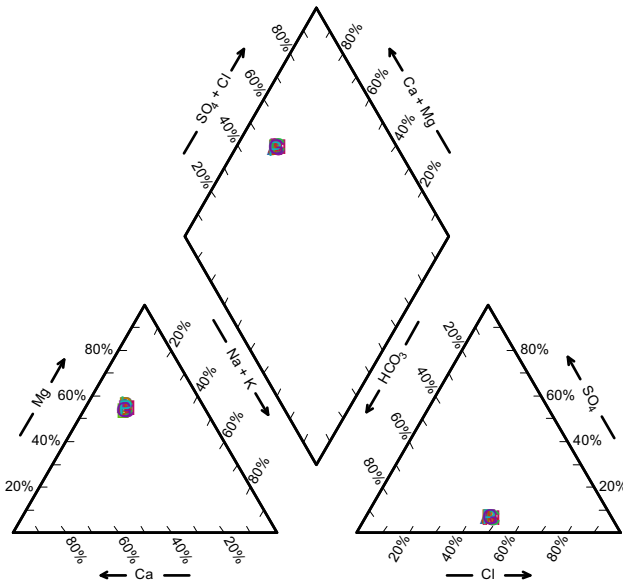


Fig. 3 Piper Diagram for groundwater samples

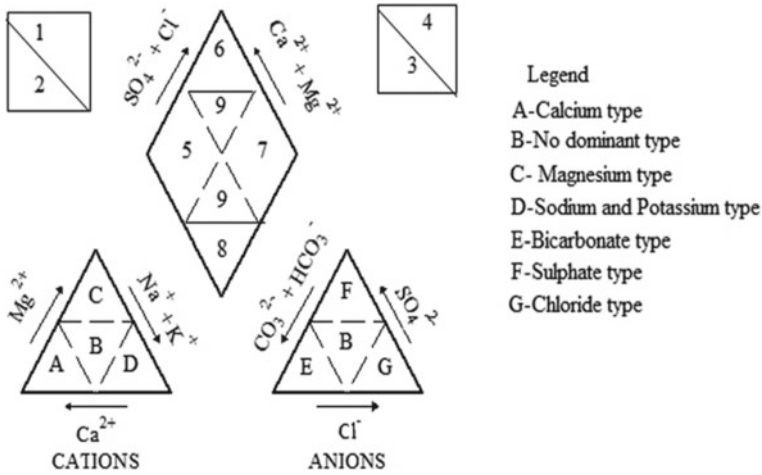


Fig. 4 Sub-divisions of Piper diagram

Table 4 Subdivisions of Piper’s diagram

Area	Subdivision
1	Alkaline earth exceeds alkalis
2	Alkalis exceed alkaline earths
3	Weak acids exceeds strong acids
4	Strong acids exceeds weak acids
5	Carbonate hardness (secondary alkalinity) exceeds 50%
6	Non carbonate hardness (secondary salinity) exceeds 50%
7	Non carbonate alkali (secondary salinity) exceeds 50%
8	Carbonate alkali (primary alkalinity) exceeds 50%
9	No one cation–anion pair exceeds 50%

3.1.2 Gibb’s Diagram

Gibb’s diagram represent the ratio of $(Na^+ / (Na^+ + Ca^{2+}))$ and $(Cl^- / (Cl^- + HCO_3^-))$ as a function of Total Dissolved Solids, are used to determine the major source of dissolved chemical-constituent; those are precipitation, rock and evaporation-dominance [8]. Gibb’s diagrams plotted for surface and groundwater are shown in Figs. 5 and 6. From the diagram, it is observed that most of the samples come under a rock- dominance type of the study area, and hence the rock types in all sampling points control water contamination in both seasons. Rock weathering is the main source for this chemical composition of the water in the study area.

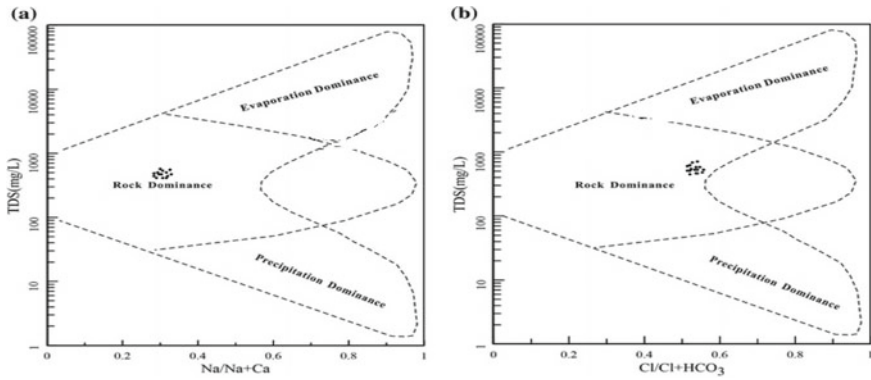


Fig. 5 Gibb’s diagrams for surface water samples

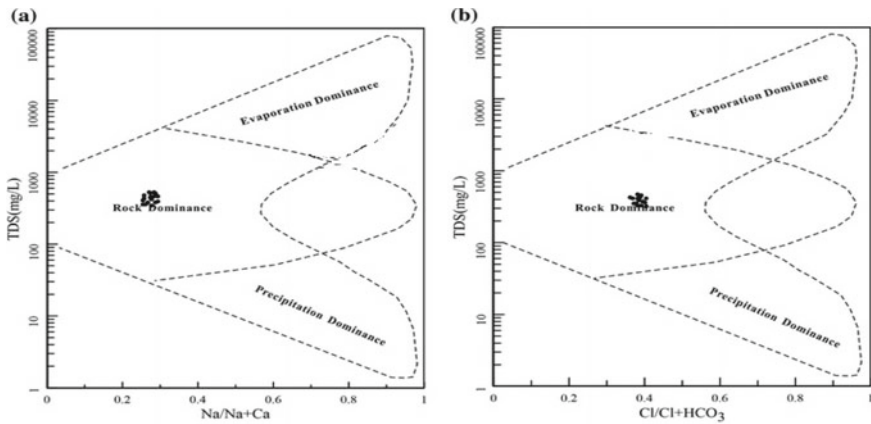


Fig. 6 Gibb’s diagrams for groundwater samples

3.1.3 U.S. Salinity Laboratory Classifications

The USSL diagrams plotted for pre-monsoon and post-monsoon season for ground-water are shown in Figs. 7 and 8 and USSL diagrams plotted for pre-monsoon and post-monsoon season for Surface water is shown in Figs. 9 and 10 for Pre-monsoon and Post-monsoon season. Which are plotted by taking SAR (Sodium Adsorption Ratio) verses EC (Electrical Conductivity). Groundwater sample of pre-monsoon belongs to C2S1 type, which represents 58.8% medium saline–low sodium water of the collected irrigated water samples, this type of water can be used if a moderate amount of leaching occurs with little danger of producing harmful levels of sodium. Where as in the post- monsoon 100% of samples belong to C3S1 type, that is high salinity and low sodium water. This class of water cannot be used on soils with restricted drainage otherwise, there is a possibility of development of harmful level

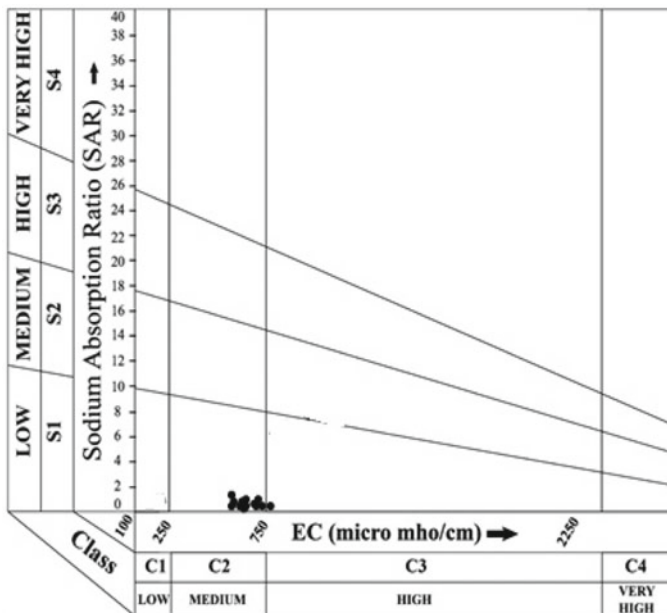


Fig. 7 USSSL diagram for groundwater during pre-monsoon

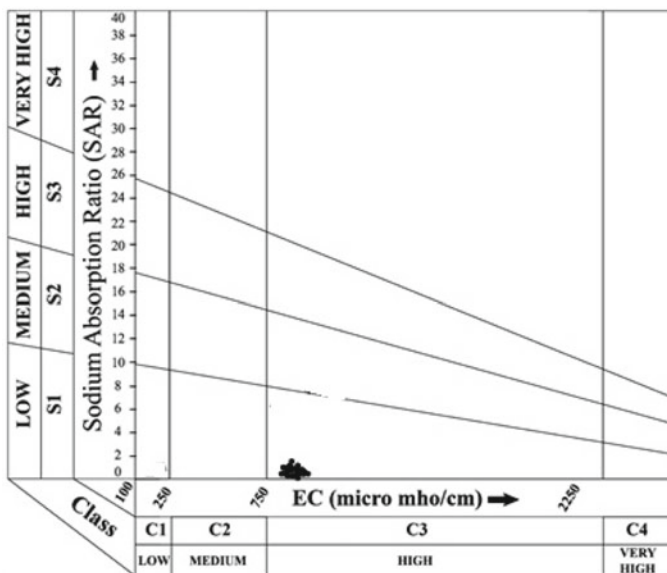


Fig. 8 USSSL Diagram for groundwater during post-monsoon

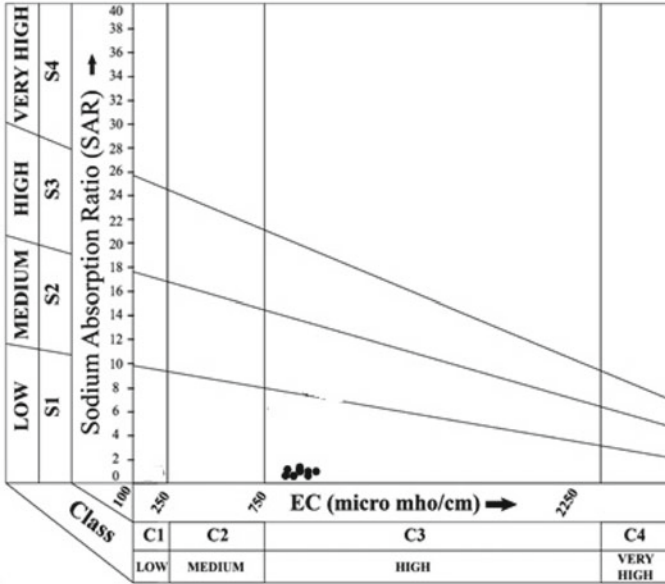


Fig. 9 USSL Diagram for surface water during pre-monsoon

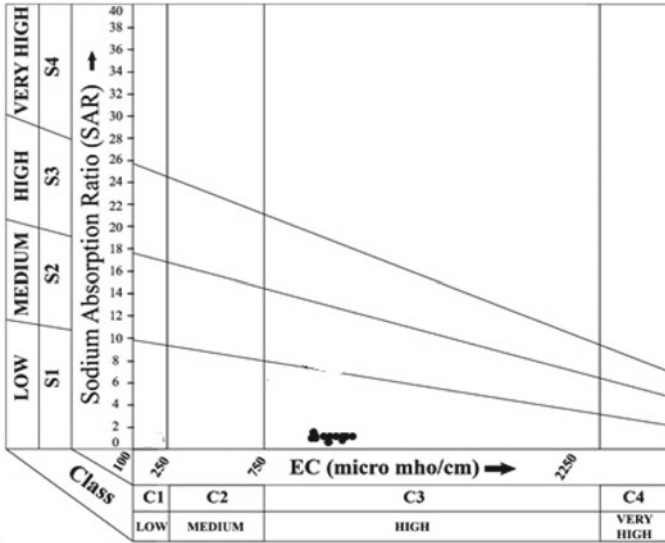


Fig. 10 USSL Diagram for surface water during post-monsoon

of sodium in the soil. Similarly, all the samples collected from surface water points are of C3S1 type both during pre-monsoon and post-monsoon seasons.

4 Conclusion

After the careful analysis of physico-chemical characteristics and hydro-geochemical analysis, the conclusions were drawn. Water has a medium hardness in both pre-monsoon and post-monsoon seasons in all five points of the study area. The concentrations of sulphate, nitrates, potassium and sodium in both seasons are within the permissible limit of the BIS standard for drinking water. In the Piper plot, the characteristics of the sampling points fall in chloride and magnesium domains. Based on Gibb's diagram, samples under the study area fall under the classification of rock dominance. Hence, it can be recommended to use for agriculture (irrigation) purposes in the study location. The groundwater proves to be the best alternative for drinking and agriculture purpose of Jewargi taluka. However, the surface water in the study area is contaminated due to excessive use of fertilizers, chemicals, domestic effluents and dumping of solid waste and faecal matters, etc. due to the self-cleansing capacity of river Bhima, the characteristics of the surface water quality are well within the permissible-limit and suitable for domestic and agriculture purposes. As per the USSL diagram in the post-monsoon, 100% of samples belong to the C3S1 type of high salinity low sodium water. This type of irrigation water cannot be used on soils with restricted drainage facility or else, harmful level of sodium may develop. All the surface water samples belong to C3S1 type during pre-monsoon and post-monsoon season, high salinity, and low sodium water. The present study can be referred to improve the surface water quality of Bhima River in the Jewargi taluka of the Kalburgi district of Karnataka.

References

1. Shivasharanappa, Yalkpalli A (2012) Hydro-geochemical analysis of Bhima River in Gulbarga district, Karnataka state, India. *IOSR J Eng* 2(4):862–882
2. Zolekar RB, Todmal RS (2020) Hydro-chemical characterization and geospatial analysis of groundwater for drinking and agricultural usage in Nashik district in Maharashtra, India. *Environ Dev Sustain*
3. Mirza A, Tanvir Rahman M, Saadat M, Islam MS, Al-mansur MA, Ahmed S (2017) Groundwater characterization and selection of suitable water type for irrigation in the western region of Bangladesh. *Appl Water Sci* 7(1):233–243
4. Lokhande PB, Mujawar HA (2016) Graphic interpretation and assessment of water quality in the Savitri River Basin. *Int J Sci Eng Res* 7(3):1113–1123
5. Shivasharanappa, Prema (2018) Ground water quality of Bhima River Basin near Jewargi Taluka Gulbarga district. *Int J Res Eng Technol* 7(8):42–44
6. Tamburi V, Shetty A, Shrihari S (2020) Spatial variability of vertisols nutrients in the Deccan plateau region of north Karnataka, India. *Environ Dev Sustain* 23(2):1–14

7. Laboratory manual on water analysis, National Environmental Engineering Research Institute (1987)
8. Chowdhury AK, Gupta S (2011) Evaluation of water quality, hydro-geochemistry of confined and unconfined aquifers and irrigation water quality in Digha Coast of West Bengal, India (a case study). *Int J Environ Sci* 2(2):576–589

Conjunctive Use Modeling Using SWAT and GMS for Sustainable Irrigation in Khatav, India



Ranjeet Sabale and Mathew K. Jose

Abstract The present study engages two powerful models viz., Soil and Water Assessment Tool (SWAT) and Groundwater Modeling System (GMS) to simulate groundwater and surface water conditions to aid conjunctive use applications. This work elaborates a robust coupling of these two models for conjunctive use studies. The study area, Khatav in Maharashtra, is mostly drought-prone, semi-arid and has an average annual rainfall of about 560 mm. In order to have a sustainable and efficient water resource management in this semi-arid region, conjunctive use of groundwater and surface water is essential. Therefore, the SWAT and GMS models were calibrated and validated by using observed data for a period of twelve years, from 2000 to 2012. The basin area considered for the study purpose is 470 km². After the SWAT model has been processed, study area was divided into 51 hydrological response units (HRUs) and 5 sub-basins. The methodology used in this work was, the Soil Conservation Service (SCS) curve number was used to estimate surface runoff. As the SWAT model cannot be used to predict groundwater levels in the basin, the Groundwater Modeling System (GMS) has been used to model the groundwater processes. The sensitivity of work was assessed by using SWAT-CUP tool and with SUFI-2 algorithm. The results showed that the average annual flow from the basin is $3.059 \times 10^3 \text{ m}^3$ and average curve number is 87.43. The study recommends recharging of the wells which are already available in the basin by operating them continuously to induce recharging by available surface water. The simulation shows that altogether due to reduction in evaporation and surface absorption, the groundwater level in basin is raised by 0.6 m. The validity of the simulations and acceptance of the SWAT model for the present study has been confirmed by values of RSR (0.60) and NSE (0.82) parameters.

Keywords Surface water · Groundwater · Conjunctive use · SWAT · GMS

R. Sabale (✉)
VTU, Belagavi, Karnataka, India
e-mail: ranjeetsabale123@gmail.com

M. K. Jose
National Institute of Hydrology, Regional Centre, Belgaum, India

1 Introduction

Conjunctive use of water means to use of surface and groundwater either in combination or separately to meet water demands. It is not a new technique but it is a less emphasized one. The conjunctive use term describes the integration of surface and groundwater through different hydrogeological processes like deep percolation, hydrological cycle, irrigation methods and water balance equation parameters [19]. The conjunctive use of water results in increase in water yield in low cost than different hydraulic structures like dam and reservoir. The conjunctive use projects are prominently categorized into (1) Stream diversion (2) Reservoir and Dams and (3) Total system [5]. The objectives of conjunctive use are to increase water yield, reliability of supply, improvement in water quality by dilution and overall efficiency of water management system. The conjunctive use of water resources can be used in space or in time. The strategies used in conjunctive use show that it is not necessary that all time groundwater and surface water has to use in conjunction but it can be used separately as per the command requirement. The conjunctive use technique was used to dilute the polluted water and to have systematic irrigation planning in Tehran plain, Iran [9]. The stormwater management model (SWMM) and Groundwater and Surface water Flow Model (GSFLOW) were together used to improve water resource management in water scare regions [23]. The water shortage problem can be minimized with the help of conjunctive use of groundwater and surface water [22]. As study area is semi-arid and water-stressed, the conjunctive use technique is suitable to alleviate the water shortage problem. Sabale and Jose [20] formulated a conjunctive use model using integration of SWAT and MODFLOW, the authors have adopted the artificial recharge technique. The study concludes that, conjunctive use of surface and groundwater leads to improvement in groundwater recharge. Moreover, the groundwater levels in study area were raised by 0.7 m.

In twenty-first century, it is difficult to build new dams and hydraulic structures because of environmental constraints and institutional issues. So, researchers and policymakers from around the globe are working on optimization/simulation of existing water resource systems. From the literature studies, the conjunctive use is the best tool which can be used to improve the hydraulic attributes of aquifers. Also it is able to reduce water logging, salination and pollutant contamination with the help of conjunctive use. So, in this study, an attempt was made to optimize water resources for sustainable water management through conjunctive use. To check feasibility and to optimize conjunctive use, the simulation model was developed by using SWAT and GIS software. The SWAT model works on data provided by remote sensing and GIS and model has been used since the last three decades for the betterment of water resource management [30]. The SWAT model was used to interpret the sediment yield and surface runoff for Lvohe river and according to the study the soil conservation management was adopted [13, 26, 29]. The evapotranspiration plays important role in surface water modeling [17] carried out the evaluation of evapotranspiration using SWAT. The authors concluded that SWAT is an efficient tool

although less data is available [27]. Pereira et al. [18] worked on hydrologic simulation on Pomba river basin in Brazil. SWAT model was used to simulate soil scenarios and climate; model was used on daily time step basis, results show runoff of 13.6 and 6.5 mm for two scenarios considered for study. For sustainable conjunctive use, groundwater behavior study is more important, Lee et al. [12] and Zhang et al. [28] formulated a new approach to assess the groundwater behavior under the influence of climate change. The SWAT model has limitations in well-managed watershed, e.g. canal irrigation command area, because the canal seepage is not included in SWAT [25] have tried the SWAT model with modifications and performed on 732 km² area of Arkansas river. The SWAT model simulates the runoff and sediment yield very precisely; it can be used to manage/plan and to develop water resources sustainably [1].

In this work, an attempt was made to integrate surface and groundwater resources in the Khatav area in Maharashtra, India to aid sustainable irrigation. The significance of conjunctive use is that it consists of the interaction between groundwater and surface water through the recharging process, so it implies the reliable water resources. Moreover, it reduces the waterlogging and soil salination problems. This approach will alleviate the water scarcity issue, Moreover; the net returns from agricultural sectors will be increased so in turn, it will reinforce the nation's economy. The methodology adopted in this study was, the data obtained from SWAT model was used for groundwater modeling in GMS. The SWAT model was used to calculate surface runoff, percolation and evaporation. The GMS model was used to find out groundwater level and its variation according to the suction and recharge process.

2 Study Area

Khatav (Vaduj) taluka of Satara district in Maharashtra state, India, having total area 1358 sq.km was selected for study (Fig. 1). The area lies between 17°15' and 17°45' north latitudes and 74°15' to 74°45' east longitudes. The Ner dam and Yeralwadi dam are the two principal water sources of the study basin. The study area is mostly water-stressed and has annual rainfall about 560 mm. The area was categorized as semi-critical by the Ground Water Resource estimation carried out in 2013 by CGWB. The study basin receives a maximum portion of rainfall from south-west monsoon. The annual temperature varies from minimum 140 to maximum 400 and average wind speed for area is 7.4 km/hr [4]. Agriculture is a major land use aspect of study area. The traditional crops like Jowar, Wheat, Soyabin and Maize with some cash crops like sugarcane and pulses are grown on the area. The current study basin is geomorphologically a part of the Deccan plateau. The physiographical features of study area are older flood plain of Yerala River and basaltic soil. For study area, it is considered that aquifer is single layered and mostly unconfined, so horizontal hydraulic conductivity is estimated for the aquifers.

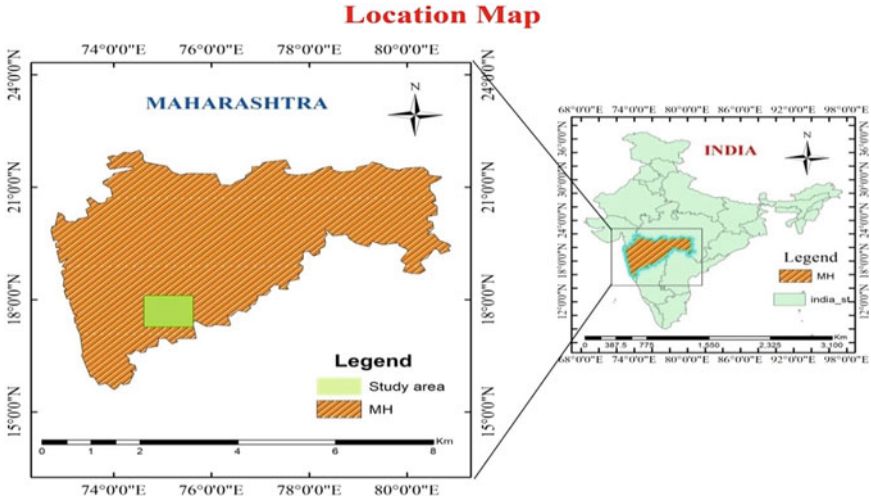


Fig. 1 Location map of study area

3 Materials and Methods

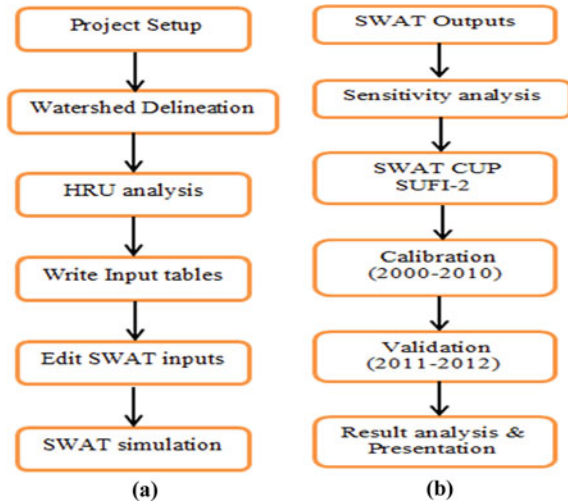
The methodology used in this work, Soil and Water Assessment Tool was calibrated and validated for a period 2000 to 2010 and 2011–2012, respectively. The sequential Uncertainty Fitting-2 algorithm from SWAT-CUP tool was used for sensitivity analysis. The GMS model was used to estimate the groundwater parameters.

The SWAT model requires Digital Elevation Model (DEM), Land use/Land cover map and global weather data and those were taken from USGS earth data center. The number of water wells available in study area are marked and used in GMS model.

3.1 SWAT Model

The SWAT model has been developed to simulate the impact of land use on hydro-geological parameters [3]. It was developed by US-Agriculture department and is mostly used to simulate environmental and ecological process [14]. It is semi-distributed, physically based and the conceptual model. The SWAT model encompasses sediment transport, weather, water quality and quantity and agriculture management. The literature shows that SWAT model was used for climate change study and to estimate the impact of climate change on hydrology [21]. The SWAT model and GMS was used by Kareem [10] for simulation of surface and groundwater to aid conjunctive water use in Jolak basin, North Iraq. The SWAT model and

Fig. 2 Flow chart of SWAT model: **a** run of model **b** model calibration



MODFLOW were successfully coupled and used for conjunctive water use simulation for Firoozabad watershed [6]. The suggestions of SWAT and MODFLOW study were, increase the rain gauge stations and temperature gauges in the basin.

The SWAT model is being semi-distributed, so it is unable to consider storage coefficient and hydraulic conductivity. Kim et al. [11] developed an integrated SWAT-MODFLOW model for sustainable groundwater management in Korea. The SWAT model was used by Venkatesh et al. [24] for hydrological modeling of Manimala river, in Kerala, India shows that the surface runoff was influenced by parameters like curve numbers and ESCO. The SWAT model uses input data such as digital elevation model (DEM), Soil map and land use/land cover (LULC) map of study area to delineate watershed into sub-basins. The sub-basins are again divided in to hydrologic response units (HRUs) that consist unique management of soil data and slope. The HRUs play a vital role in simulation and the data from each HRUs are added together to get basin parameters.

Based on the general rule and research studies, it is suggested to increase number of sub-basins than HRUs. Figure 2 shows the SWAT model flow chart including its run and Calibration–validation process.

3.1.1 DEM of Study Area

Digital elevation model explains the general topography and geometry of watershed. The Digital elevation model for current study area with 30 m resolution was downloaded from ASTER global dataset. The DEM data was available in two modules; by the mosaic tool the required DEM was created. The DEM was used to derive the parameters like percentage slope of basin, length of main channel, drainage pattern etc.

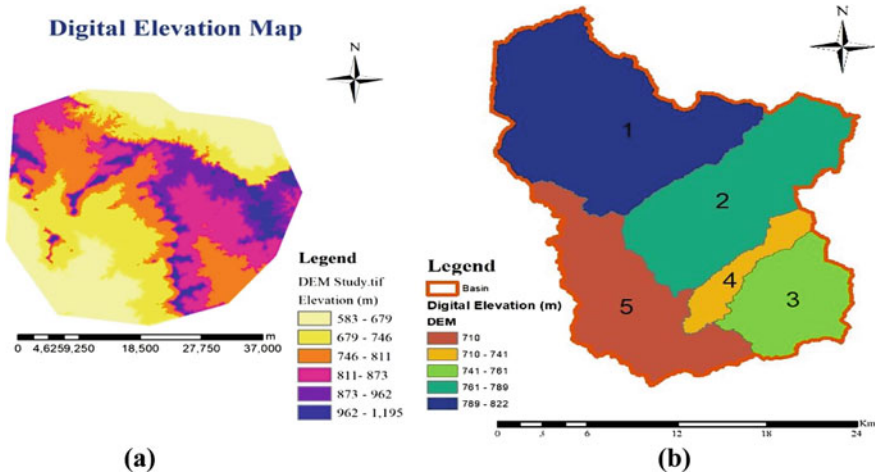


Fig. 3 a Digital elevations (m) of study area b sub-basins

After delineation of DEM it is divided into number of sub-basins and HRUs. For current study, the DEM was projected into WGS_1984_UTM_ZONE 43N. Figure 3a shows DEM of study area and Fig. 3b explains the number of sub-basins with elevation range.

3.1.2 LULC of Study Area

The land use and land cover map (LULC) of study area shows the physical use of area, e.g. forest, urban, bare land, etc., and reports how area is being used. The LULC data was taken from earth-explorer for period (2019–2020); data free from clouds were selected. The Landsat-8 images were used to prepare land use map for study area. For current study, LULC map of study area was developed with Arc SWAT (2012) version and classified according to maximum likelihood classification. Almost maximum study area was covered with high urban area (48.44%) and next to that with agriculture (26.64%), barren (17.73%), low urban (5.58%) and water bodies (1.60%). The maximum likelihood classification of LULC was verified manually from data available by local agriculture development authority. The verification showed good agreement between remote sensing data and manually available data. The authors reclassified the available LULC data into five groups (Fig. 4) for accurate analysis of curve numbers.

3.1.3 Soils in Study Area

The soil map for current study area was taken from NBSS and LUP, i.e. National Bureau of Soil survey and land use planning, department of India on the scale of

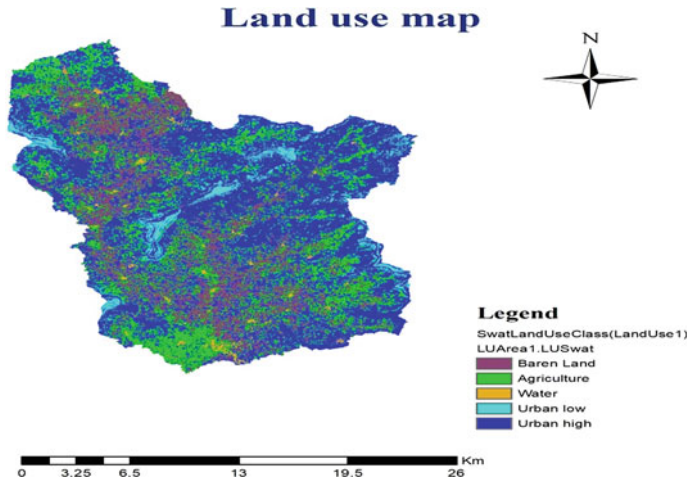


Fig. 4 Land-use map of study area

1:250,000. The data was available in detailed manner showing the texture profile of soil and then it was digitized according to model use. Figure 5 Shows details of soils present in study area. The Loam soil (Nd51-2b-3820, 56.98%) was major soil in basin and next to that Clay (Vc43-3ab-3861, 22.55%), Clay loam (Hh11-2bc-3711, 15.73%) and Loam soil (I-Hh-3721, 4.74%) were present in basin.

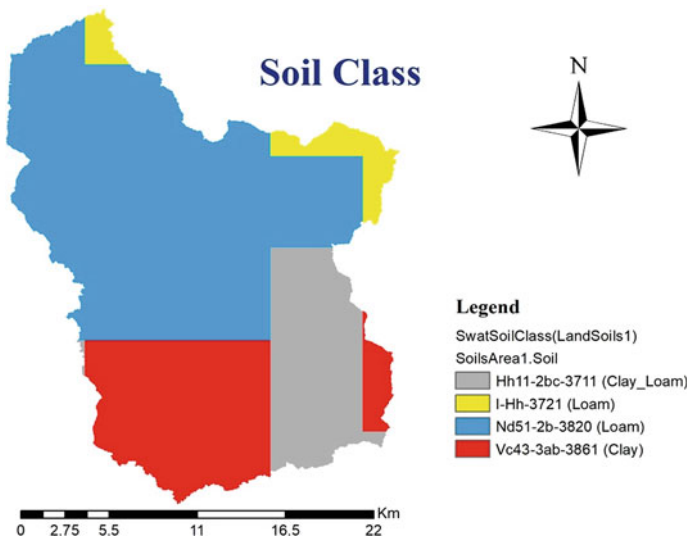


Fig. 5 Soil classification of study area

3.1.4 Meteorological Data

The daily based meteorological data namely precipitation, solar radiation, temperature (max and min),

relative humidity and wind was collected from global weather data for period (2000–2014). The IMD gridded data and CFSR world data were updated in SWAT database. In the current study, the SCS-CN method was used to simulate runoff.

3.1.5 SWAT Simulation

SWAT is Agro-hydrological, basin-scale model which works on daily and sub-daily time step. In current work, SWAT model was calibrated for 470 km² area in Khatav. The model encompasses the GIS data and gives outputs like surface runoff, sediment yield, evapotranspiration, soil properties and many more hydrological parameters. The meteorological data for the period (2000–2014) was used to run the model.

3.2 Groundwater Modeling System (GMS)

The GMS is a very effective pre- and post-processor and it offers various groundwater operations [7]. It works in three steps like conceptual model design, data and construction and calibration of model. The polygon, arc and points are used to define features like pumping wells, streams, boundaries, rivers and piezometers. The calibration of model is a process used to compare the outputs and observed data. The calibration facilitates the modification in input data until it does not match to outputs. Marnani [15] coupled MODFLOW with GMS for groundwater resource study and management in Firozabad plain. The study reveals that the numerical model was helpful to simulate the groundwater flows and outcomes were used to predict water levels in Firozabad plain for the next 5 years.

Gurwin and Poprawski [8] developed a numerical model for groundwater renewal in the Odra river basin. The MODFLOW was used to simulate groundwater flows and the results shows that renewal of shallow aquifers were rapid than deep aquifer. The average time for aquifer to recharge and discharge was about 130 years. The MODFLOW and GMS model were used by Aghlmand and Abbasi [2] with limited available data for Birjand plain in Iran to enhance the water management. The outcomes of study show, due to integration of models the water tables in study area were raised and the agreement between observed data and simulated values indicates the acceptance of model.

The SWAT has semi-distributed nature and has limitations for groundwater modeling. The groundwater levels are not mapped with SWAT also canal seepage is not analyzed. Therefore GMS model was used in this work to simulate groundwater characteristics. The GMS was developed (1998) by the department of defense, to facilitate groundwater modeling. The GMS is 3D model and the flow is explained

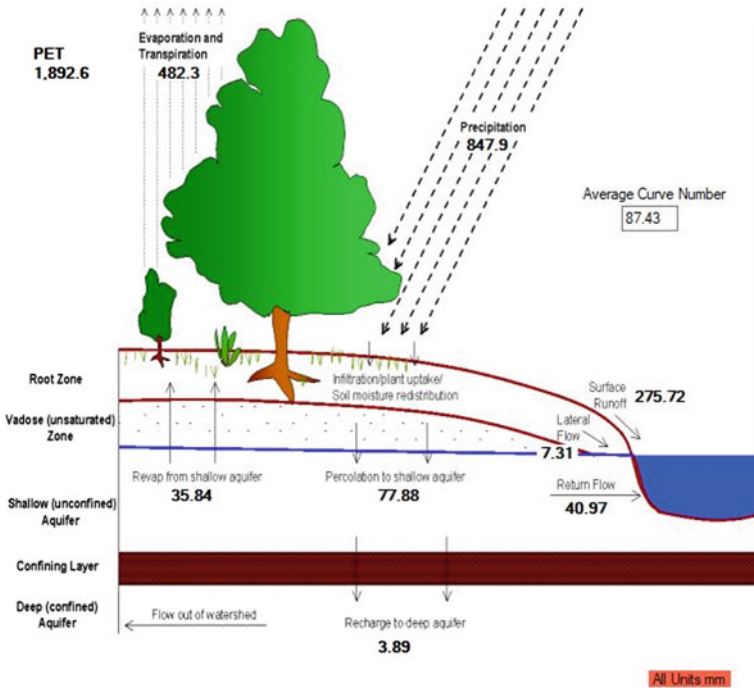


Fig. 6 Hydrology of study area

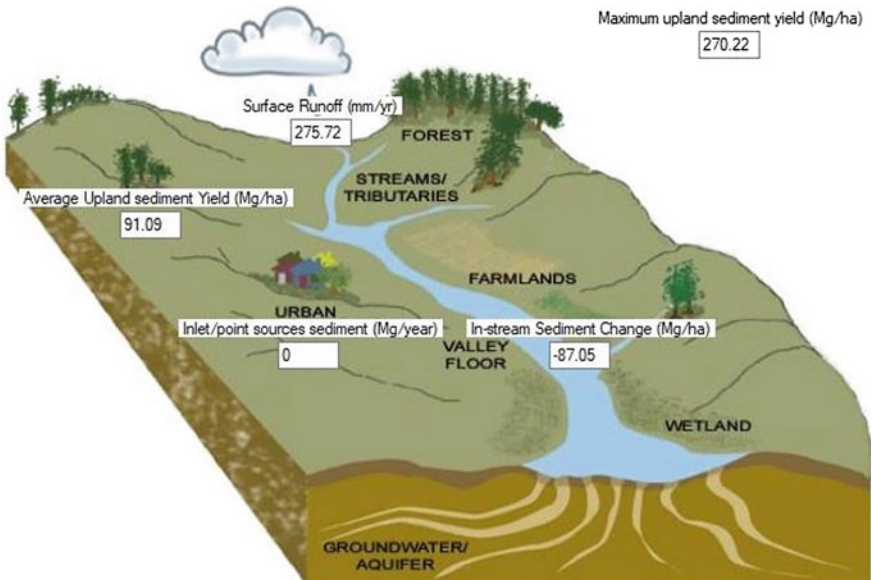


Fig. 7 Sediment yield in study area

by the following equations [16],

$$\frac{\partial}{\partial x} \left(K_{xx} \frac{\partial h}{\partial x} \right) + \frac{\partial}{\partial y} \left(K_{yy} \frac{\partial h}{\partial y} \right) + \frac{\partial}{\partial z} \left(K_{zz} \frac{\partial h}{\partial z} \right) - W = S_c \frac{\partial h}{\partial t} \quad (1)$$

where

- K_{xx}, K_{yy} and K_{zz} Hydraulic conductivity along X, Y and Z axes.
- h Hydraulic head (m).
- W Quantity of aquifer recharge.
- S_c Specific storage of aquifer.
- T Time.

3.2.1 GMS Input Data

In current work, the conjunctive water use practice was tried with the help of SWAT and GMS. The GMS model was used to trace groundwater levels and to suggest the recharge pits. The study suggests some wells which are already present in basin as a recharge point to accumulate surplus runoff. Figure 8, shows the available wells in basin and suggests the locations for recharge points. In the current work the value of the coefficient of transmissibility and storage coefficient was taken from the CGWB

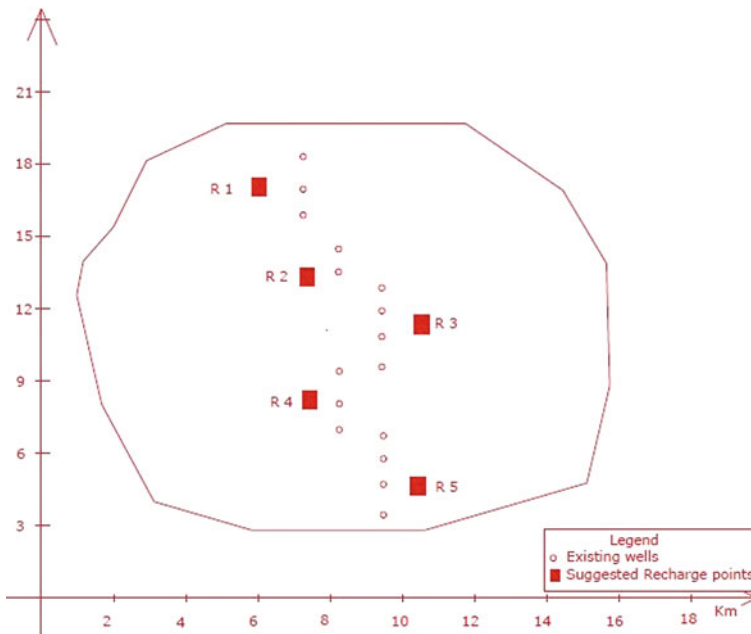


Fig. 8 Location of wells

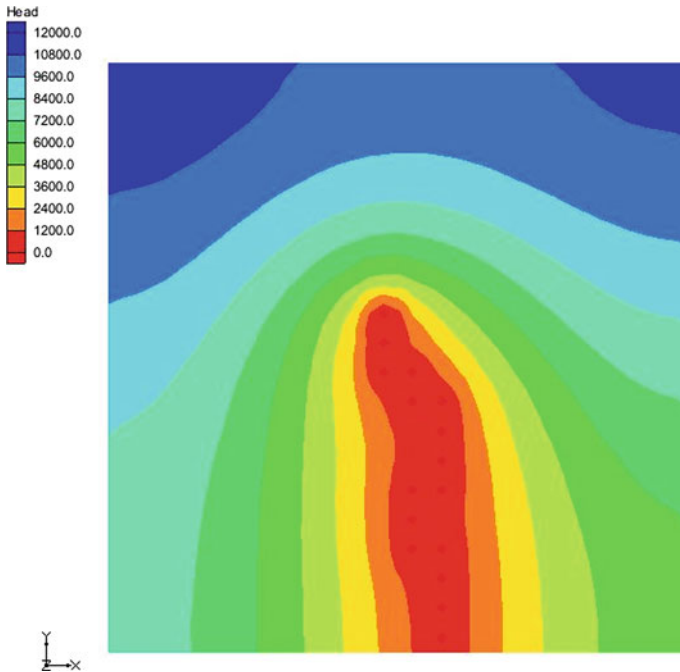


Fig. 9 Groundwater contour map of area

report [4], the values were 1800 m²/d and 0.1 respectively. The hydraulic head of area was decreasing with length of site as shown in Fig. 9. The GMS model use input data as elevations of bottom and top layers of aquifers, coefficient of transmissibility and storage coefficient. The Yerala river was considered as constant head boundary which recharges the aquifers of study area. The 16 available wells, as shown in Fig. 8, were assumed to be operating at a rate (10 lit/s). The time duration for well operation was considered as 12 h/ day.

4 Results and Discussions

The surface water model, physical-based and semi-distributed SWAT was prepared in this study by using GIS data. The aim of this work was to imply the conjunctive use process for sustainable and efficient irrigation management in Khatav area. The methodology used was SWAT model was coupled with GMS model, also authors have tried to evaluate interrelationship between surface and ground water. The outcomes will be useful to balance, store the runoff in aquifer and that can be used in water deficit period (Fig. 6). This study also suggests the five recharge pits nearby 16 well which are already available in basin (Fig. 8). The sensitivity analysis for 9 hydrological

Table 1 Sensitivity analysis (SWAT-CUP) with best-fitted values

Parameter name	Fitted value	Min value	Max value
CN2	45.45	35	98
ALPHA_BF	0.55	0.0	1
GW_DELAY	203	0.0	500
GWQMN	330	0.0	5000
ESCO	0.41	0.0	1
CH_N1	13.26	0.01	30
CH_N2	0.017	0.01	0.30
SOL_AWC	0.37	0.0	1
RCHRG_DP	0.20	0.0	1

parameters was carried out with SWAT CUP (2012 Version), SUFI-2 algorithm was used for statistical analysis. The details of parameters with fitted values are given in Table 1

The conjunctive water use technique will be helpful to bridge the time gap between rainy (monsoon) season and dry season; also it shows the benefits of aquifer recharge and reduces evaporation losses. The result reveals that, the surface runoff is greatly affected by size and shape of basin, curve numbers (CN) and Antecedent Soil moisture conditions (AMCs). The study area is being water stressed, the total runoff produced by basin was 3.059×10^3 cumec for (2003–2014), and that can be used to solve the water scarcity problem. The sediment yield from basin for time period (2003–2014) was 78.40×10^4 tones (Fig. 7). The average curve number (CN) of area was 87.43, annual average surface runoff was 275.72 mm and groundwater delay period was 203 days.

The land use aspect of present study area shows maximum proportion of urban and barren. Therefore curve number is more resulting sufficient runoff. The area suffers from critical soil erosion, so, SWAT will be useful to locate erosion-prone areas. The GMS simulates the groundwater flows, indeed, this conjunctive approach of SWAT and GMS will lead to plan and allocate water resource sustainably, to enhance crop production and also to mitigate environmental issues.

5 Conclusion

After the robust simulation work, this study concludes that the SWAT and GMS models can be efficiently used in data scarce and water stressed watershed like Khatav for efficient and sustainable irrigation management. The outcomes of this work will be helpful to stakeholders, water managers and policy makers to reinforce the current irrigation and water resource management in Khatav and for similar regions. At low laying areas, it was seen that the water level rose by 0.6 m after the steady state

is reached in one year. The sediment yield depicts the physical characters of basin as well as shows the critical basins for soil erosion. Altogether, this study was an attempt to alleviate the water scarcity issue in semi-arid region through conjunctive use modeling and to plan sustainable irrigation.

References

1. Abebe T, Gebremariam B (2019) Modeling runoff and sediment yield of Kesem dam watershed, Awash basin, Ethiopia. *SN Appl Sci* 1(5):1–13
2. Aghlmand R, Abbasi A (2019) Application of MODFLOW with boundary conditions analyses based on limited available observations: a case study of Birjand plain in East Iran. *Water (Switzerland)* 11(9)
3. Arnold JG, Moriasi DN, Gassman PW, Abbaspour KC, White MJ, Srinivasan R, Santhi C, Harmel RD, Van Griensven A, Van Liew MW, Kannan N, Jha MK (2012) SWAT: model use, calibration, and validation. *Trans ASABE* 55(4):1491–1508
4. CGWB 2017 (2017) Report of Central Ground Water Board 2017 Aquifer maps and ground water management plan
5. Coe JJ (1990) Conjunctive use—advantages, constraints, and examples. *J Irrig Drain Eng* 116(3):427–443
6. Dowlatabadi S, Ali Zomorodian SM (2016) Conjunctive simulation of surface water and groundwater using SWAT and MODFLOW in Firoozabad watershed. *KSCE J Civ Eng* 20(1):485–496
7. Gogu RC, Carabin G, Hallet V, Peters V, Dassargues A (2001) GIS-based hydrogeological databases and groundwater modelling. *Hydrogeol J* 9(6):555–569
8. Gurwin J, Poprawski L (1999) Groundwater renewal in the Middle Odra River catchment based on flow model and isotopic data—the Lubin Glogow Copper Region, Poland. *Acta Hydrochim Hydrobiol* 27(5):383–391
9. Karamouz M, Kerachian R, Zahraie B (2004) Monthly water resources and irrigation planning: case study of conjunctive use of surface and groundwater resources. *J Irrig Drain Eng* 130(5):391–402
10. Kareem IR (2015) Conjunctive use modeling of surface water and groundwater in The Jolak Basin, North Iraq. *J Kerbala Univ* 13(1):236–246
11. Kim NW, Chung IM, Won YS, Arnold JG (2008) Development and application of the integrated SWAT-MODFLOW model. *J Hydrol* 356(1–2):1–16
12. Lee J, Jung C, Kim S, Kim S (2019) Assessment of climate change impact on future groundwater-level behavior using SWAT groundwater-consumption function in Geum River Basin of South Korea. *Water (Switzerland)* 11(5)
13. Lingling L, Renzhi Z, Zhuzhu L, Weili L, Junhong X, Liqun C (2014) Evolution of soil and water conservation in rain-fed areas of China. *Int Soil Water Conserv Research* 2(1):78–90
14. Luo Y, He C, Sophocleous M, Yin Z, Hongrui R, Ouyang Z (2008) Assessment of crop growth and soil water modules in SWAT2000 using extensive field experiment data in an irrigation district of the Yellow River Basin. *J Hydrol* 352(1–2):139–156
15. Marnani (2010) Groundwater resources management in various scenarios using numerical model. *Am J Geosci* 1(1):21–26
16. McDonald MG, Harbaugh A (1988) A modular three-dimensional finite-difference groundwater flow model
17. Parajuli PB, Jayakody P, Ouyang Y (2018) Evaluation of using remote sensing evapotranspiration data in SWAT. *Water Resour Management* 32(3):985–996
18. Pereira DR, Martinez MA, da Silva DD, Pruski FF (2016) Hydrological simulation in a basin of typical tropical climate and soil using the SWAT model part II: simulation of hydrological variables and soil use scenarios. *J Hydrol: Reg Stud* 5:149–163

19. Ramesh H, Mahesh A (2012) Conjunctive use of surface water and groundwater for sustainable water management. In: Sustainable development—energy, engineering and technologies—manufacturing and environment, July 2016
20. Sabale R, Jose M (2021) Hydrological modeling to study impact of conjunctive use on groundwater levels in command area. *J Indian Water Works Asso* 53(3):190–197
21. Saraf VR, Regulwar DG (2018) Impact of climate change on runoff generation in the upper Godavari river basin, India. *J Hazard Toxic Radioactive Waste* 22(4):04018021
22. Singh A (2014) Conjunctive use of water resources for sustainable irrigated agriculture. *J Hydrol* 519(PB):1688–1697
23. Tian Y, Zheng Y, Wu B, Wu X, Liu J, Zheng C (2015) Modeling surface water-groundwater interaction in arid and semi-arid regions with intensive agriculture. *Environ Modell Softw* 63:170–184
24. Venkatesh B, Chandramohan T, Purandara BK, Jose MK, Nayak PC (2018) Modeling of a river basin using SWAT model. *Water science and technology library*
25. Wei X, Bailey RT, Tasdighi A (2018) Using the SWAT model in intensively managed irrigated watersheds: model modification and application. *J Hydrol Eng* 23(10):04018044
26. Yesuf HM, Assen M, Alamirew T, Melesse AM (2015) Modeling of sediment yield in Maybar gauged watershed using SWAT, northeast Ethiopia. *Catena* 127:191–205
27. Yu M, Chen X, Li L, Bao A, de la Paix MJ (2011) Streamflow simulation by SWAT using different precipitation sources in large arid basins with scarce rain gauges. *Water Resour Manage* 25(11):2669–2681
28. Zhang A, Zhang C, Fu G, Wang B, Bao Z, Zheng H (2012) Assessments of impacts of climate change and human activities on runoff with SWAT for the Huifua River Basin, Northeast China. *Water Resour Manage* 26(8):2199–2217
29. Zhang XS, Hao FH, Cheng HG, Li DF (2003) Application of swat model in the upstream watershed of the Luohe River. *Chin Geogra Sci* 13(4):334–339
30. Zhao WJ, Sun W, Li ZL, Fan YW, Song JS, Wang LR (2013) A review on SWAT model for stream flow simulation. *Adv Mater Res* 726–731:3792–3798

Modelling and Simulation of Pollutant Transport in Porous Media—A Simulation and Validation Study



M. R. Dhanraj and A. Ganesha

Abstract In this paper, the transport of pollutants is simulated with COMSOL multi-physics in a transition-based cross-sectional model to trace the path and flow of pollutants after infiltration from the point of discharge of treated domestic sewage. The study is investigated using soil columns with known porosity and permeability and with various other boundary conditions. The solutions are tested using a finite-element numerical model built with COMSOL Multi-physics. It is found that the simulation model holds good in pollutant removal in comparison with the physical pilot scale model. It is also found that there is a strong correlation between the inlet and outlet parameters in removing the pollutants with naturally available media (soil). Also, the removal efficiency in BOD and COD in soil media is 54.54 mg/l and 50.13 mg/l respectively. The results of the reliability check also showed good agreement between the measured and the simulated value for both BOD and COD with ($R^2 = 0.83$), ($R^2 = 0.99$), respectively. Hence the results obtained from horizontal transport of pollutant is more significant.

Keywords Transport of diluted species (TDS) · Infiltration · Biochemical oxygen demand (BOD) · Chemical oxygen demand (COD)

1 Introduction

Water is the main source for any creatures to survive on the planet earth. In a country like India due to the diversified culture people are adopted to a different lifestyle. Due to the consistent increase in population growth, mostly in urban areas, the managing of wastewater has become a tedious process. The water demand is increasing day by day and generation of the wastewater is increasing, with the lack of proper management of wastewater disposal is a burning issue in almost all the cities in the present scenario. Adopting a systematic way to attain sustainability in the present scenario is very important due to the pollution, climate change, and deforestation the natural

M. R. Dhanraj (✉) · A. Ganesha
International Center for Applied Science, MAHE, Manipal, India
e-mail: ghanraj1117@gmail.com

© The Author(s), under exclusive license to Springer Nature Singapore Pte Ltd. 2023
M. S. Ranadive et al. (eds.), *Recent Trends in Construction Technology and Management*, Lecture Notes in Civil Engineering 260,
https://doi.org/10.1007/978-981-19-2145-2_30

387

existing water sources are deteriorating day by day. In India presently, as per the estimation 61,754 million liters of water per day (MLD) of sewage is generated per day, 22,963 MLD of sewage is treated and 62% of sewage is discharged directly into the water bodies without the treatment. By 2025 demand for industry and domestic usage may increase to 29.2 BCM population is expected to cross the 1.5 billion mark by 2050 [1]. So therefore the aim is to utilize the treated sewage as an alternative source of the main source to replenish and conserve it for future purposes using artificial recharge technique. This may increase the efficiency in water use by the approach of conjunctive use of groundwater thereby reducing the demand for fresh-water sources. Though we have adopted the practice of stormwater recharge, the significant effects are still unknown after recharge for seasonal emerging pollutants. Water reuse plays a prominent role in future development, there are many forms of disposal of treated sewage the disposal is done either on surface or subsurface. Since because of the mandatory rules from the state pollution control board the disposal of the treated sewage has become a very big hectic planning. Zero effluent discharge for commercial, gated communities, institutions might be more troublesome to overcome such circumstances. Future this would not only be domestic, but even industry also treated waste would face problem is disposal of such a large quantity of water generated after treatment. A study was conducted to anticipate the reliability of the model using comsol to predict the outcome using the 2D model and its effectiveness for effective examination [2]. So, this research would give a solution to such problem of disposal which mega industries and domestic treatment plants are facing today. The amount of energy spent on treatment must reward back by some means, or in another way the treated sewage has to be utilized completely. There are many situations where the treated wastewater may be used completely, in developed countries after the tertiary treatment. But the stigma toward the developing countries for recycling and reuse is being present, due to a lack of concern. Therefore, adopting the groundwater recharge will overcome the disposal problem and also helps in replenishing as well as the withdrawal of water at any point in time for irrigation purposes [3]. For the present study, the water is being considered from the secondary clarifier, the considerations are being shown in the flowchart along with the treatment process (Fig. 1).

Analyzing the risk associated with the contamination of soils and identification of the sources of its propagation and fate processes is needed [4]. According to Jiang and Chen [5], their study suggested that both the physical (advection, diffusion,

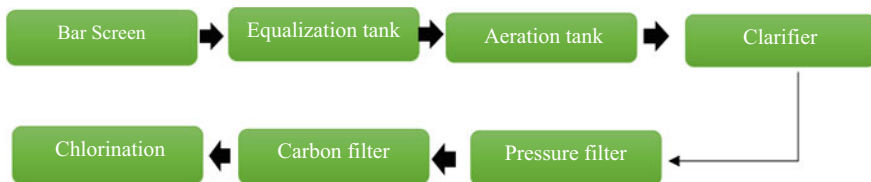


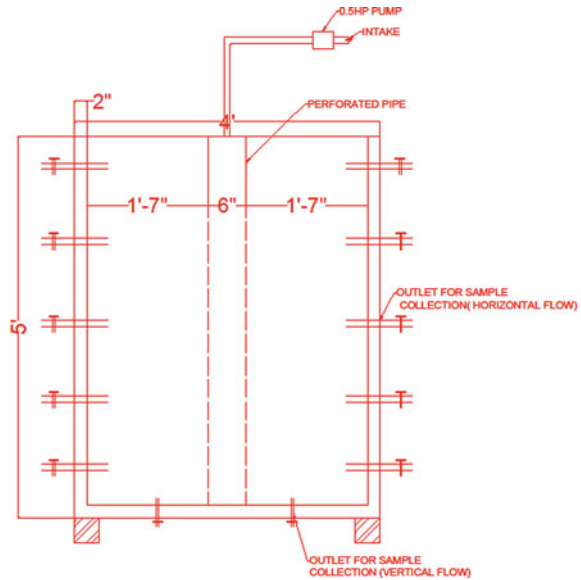
Fig. 1 Flowchart of STP

dispersion) and reaction (adsorption and degradation) process controlling contaminant transport should be analyzed in the numerical model. Lie et al. [6] in their study solved the one-dimensional advection-dispersion equation in a heterogeneous porous media coupled linear and nonlinear sorption or decay using the generalized integral transforms technique. Gao et al. [7] studied one-dimensional model convective diffusion in the soil contaminant transport subjected to time-dependent boundary conditions. Comsol multi-physics software based on a partial differential equation. It is to solve the linear or nonlinear problem, and the steady-state or transient problem which was related to geometry mode of 1D, 2D, 3D problems. Comsol was mainly used to study at present in earth science research of groundwater flow and the soil water infiltration applied the software to simulate the migration of pollutant in soil and unverified the applicability of comsol to simulate soil solute transport. In this study based on comsol 5.5, 3d transient cross-sectional models were used to investigate water and solute transport in the soil column denoting variable sand column forms. These research gap findings with horizontal transport of pollutants would help generate the baseline data on removal of pollutant concentration after infiltration and serve the purpose of disposal after the treatment. Also, this will help to find the distance of pollutant transport from the point of discharge in the same directions.

2 Methodology

The working model is made up of concrete with a diameter of 1.2 m and a height of 1.5 m consists of a perforated pipe at the center with a diameter of 0.15 m. This center pipe acts as a well for recharge, and it also includes outlets for sampling. The water is pumped from the clarifier using a 0.5HP pump with a controlled flow to the recharge well. The water is being allowed to percolate and tried with two types of media. The water which comes out of the model is tested for various parameters such as BOD, COD and then checked for efficiency under inlet flow conditions, with the same existing media of sand, followed by the same parameters. The water sample is collected using polyethylene cans. Further, it is being transported and stored in a deep freezer at 4 °C for further analysis. A total of 50 samples were collected to check the consistency in the media used for the study. BOD and COD are the two important water quality parameters required to assess the waste assimilative capacity in the soil media [8]. BOD is employed as a gross measure of the oxygen demanding potential of the effluent. Assimilative capacity varies following variations in hydrodynamic conditions and other ecological processes. COD is employed as an indicative measure of the amount of oxygen that can be consumed by reactions in a measured solution (Fig. 2).

Fig. 2 Pilot-scale model



2.1 BOD and COD Analysis

The analysis of water samples is done in the laboratory by collecting the water samples from both inlet and outlet. The collected water samples are stored in polyethylene bottles and stored at 5 °C while transportation. BOD₅ @20 °C is measured by the dilution method. Samples have undergone three trials and the best two values have been considered. The COD of the water is measured by the closed reflux method using potassium dichromate by colorimetric method (IS 10500:2012) (Fig. 3).

2.2 Model Characteristics

COMSOL Multi-physics modules were used to simulate and trace the pollutant transport in subsurface porous soil media. To verify the efficiency of the simulated model, experimental data is required. The COSMOL program, which simulates the velocity, pressure head, and the concentration distribution based on the boundary condition using an implicit iteration solution, has been used in developing and understanding the efficient working conditions of the model. A detailed description of the model is presented on the COMSOL website. In the following sections, a brief description of the main features of the model is presented (Tables 1 and 2).

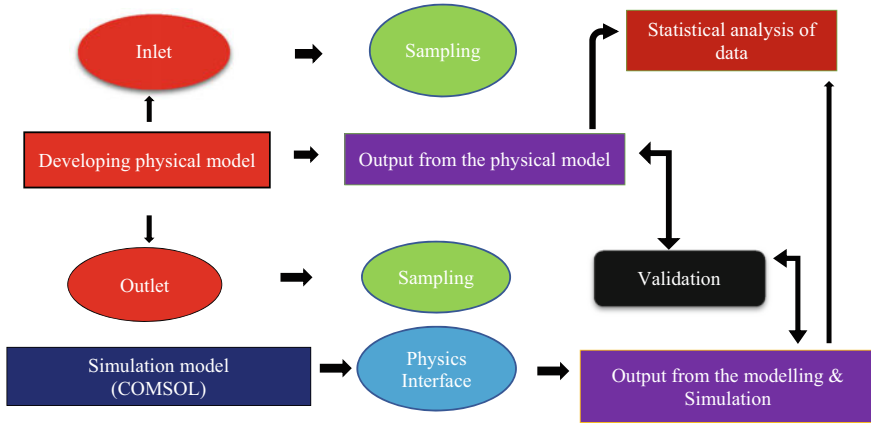


Fig. 3 Methodological flowchart of the study

Table 1 Boundary and initial conditions

Parameters	Soil
Permeability (cm/sec)	1.79×10^{-5}
Density (gm/cm ³)	1.46
Specific gravity	2.54
Grain size (uniformity coefficient)	1.44
Porosity	0.3

Table 2 Flow measurements

Parameters	Value
Velocity (m/s)	0.28
Discharge (m ³ /s)	0.044
Hydraulic head (m)	1.5
Pressure head (m)	1.38

2.3 Model Calibration and Governing Equations

Model calibration is a trial-and-error adjustment of parameters until the model solution matches the field physical model. In general, the calibration aims to design a steady state model for head distributions to be used as an initial condition for a transient state simulation after applying and trying different states of scenarios on it. Model calibration also includes a successive refinement for model input parameters from the initial condition to improve the fit between observed input and model predicted results. The calibration procedure typically begins with the definition of parameters also based on the availability of data with an initial conceptual model of the hydrogeology systems. The parameters chosen for the calibration process

include soil permeability, porosity and materials used for the study purpose. Several adjustments to the calibration parameters were made until the final calibration was achieved. Once calibrated then the physics used for the study purpose is applied to the model.

Phase transport in porous media for study controlled under time-dependent conditions is given by

$$\frac{\partial \varepsilon_p \rho_{s_i} s_i}{\partial t} + \nabla \cdot \mathbf{N}_i = 0 \quad (1)$$

By assuming the time-dependent equation this will be

$$\mathbf{N}_i = \rho_{s_i} \mathbf{u}_i, \quad \mathbf{u}_i = -\frac{\kappa_{r s_i}}{\mu_{s_i}} \kappa \nabla \rho_{s_i}$$

When the outflow is set for the model $-\mathbf{n} \cdot \mathbf{N}_i = -\mathbf{n} \cdot (\rho_{s_i} \mathbf{u}_i)$.

3 Results and Discussion

See Tables 3 and 4.

3.1 COMSOL Multi-physics for Simulation and Modelling

This study traced the contaminant transport in a horizontal direction and analyzed it using a 2D-model transport of pollutant in porous media with controlled discharge using COMSOL multi-physics created with soil matrix for water recharge of treated domestic sewage. The study's objective is to understand the concentration distribution in the saturated porous media of the system. Based on the different time the variations in the concentration is observed at the Outlet. A study using COMSOL multi-physics software for the Artificial recharge in Jordon compares the measured and the software modeling (Azad et al. 2010). The validation work has applied the same approach. A study was conducted in the vadose zone to model the solute transport and their travel times toward groundwater bodies. The study to understand the impact of the unique state of soil in terms of spatial infiltration of solute-rich water [9] is needed in COMSOL to trace the pollutant transport in soil concerning time (Fig. 4).

Table 3 Summary of the BOD results from the physical model

Parameter (mg/l)	Influent (mg/l)	Measuring range	Saturation time (min)	Effluent (mg/l)	Mean	Samples numbers	SD	SEM	Median
BOD ₅ @20 °C	30.06	30	30	15.96	10.26	10	7.34	2.32	6.20
COD	94.66	30	30	56.37	66.93	10	43.61	10.90	46.3

Table 4 Summary of the BOD results from the simulation model

Parameter (mg/l)	Influent (mg/l)	Measuring range	Saturation time (min)	Effluent (mg/l)	Mean	Samples number	SD	SEM	Median
BOD ₅ @20 °C	30.06	30	30	23	9.8	10	6.66	2.10	6.20
COD	94.66	30	30	39.06	39.05	10	22.62	5.19	26.2

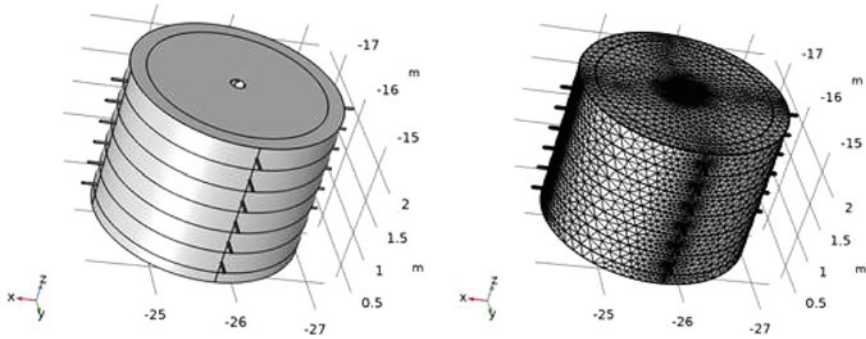
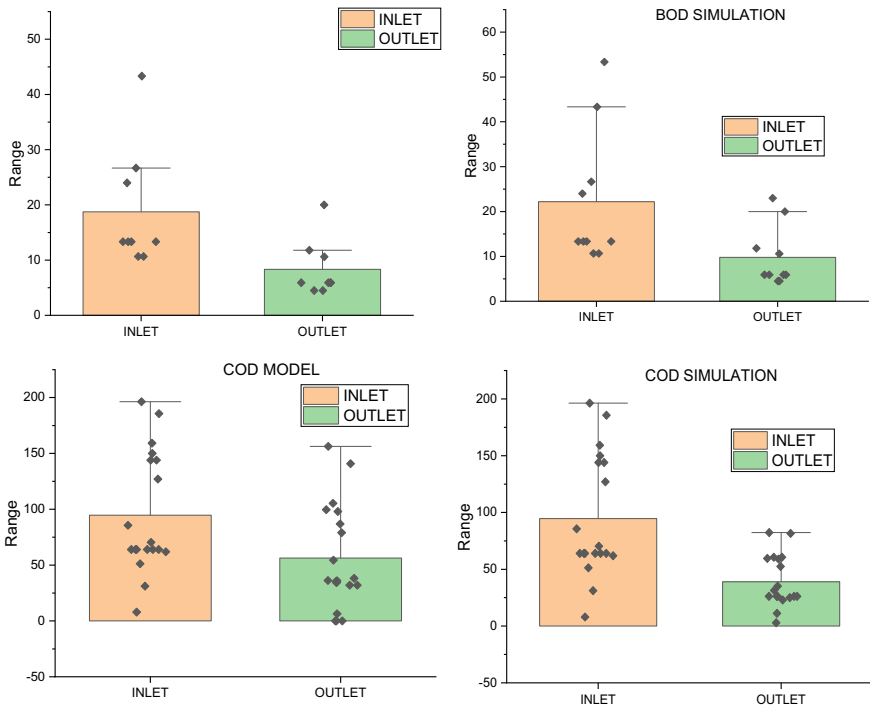


Fig. 4 Physical model developed using COMSOL

3.2 Performance Measures Between Measured Values and Simulated Values for BOD and COD

There is a significant reduction in the output of the model after the horizontal movement. The presented graph shows the variations at the inlet and outlet from the physical and simulation model of the study.



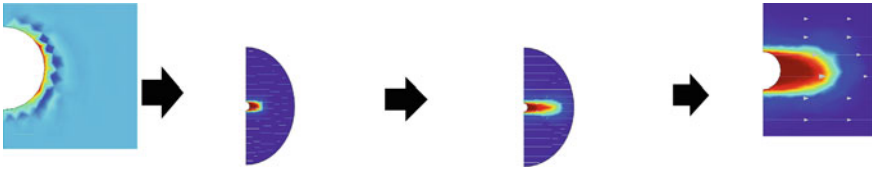


Fig. 5 Validation of pollutant transport in horizontal direction based on transient condition

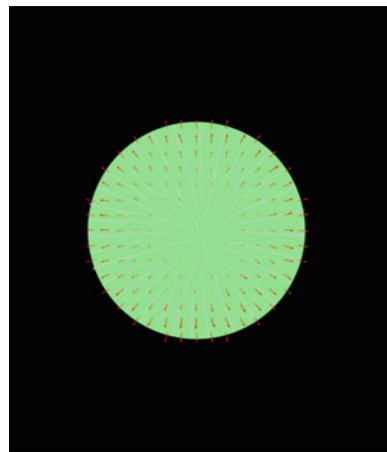
3.3 Particle Trace Trajectories for Validation Using Simulation

This Figure clearly shows the transport of pollutant in the horizontal direction. The distribution of concentration is observed at a time interval of $t = 30$ min (Fig. 5).

3.4 Dispersion of Pollutants

Horizontal displacement of the pollutant is not introspected well because the focus toward the recharge was always toward the vertical transport of species. Here Fig. 6 shows the horizontal transport from the point of discharge in different directions, this will be helpful in tracing the pollutant from the point of discharge.

Fig. 6 Particle dispersion in different directions

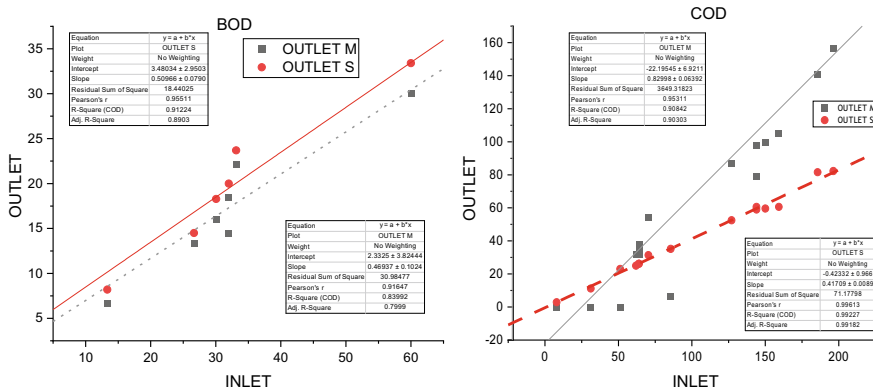


3.5 Numerical Analysis of BOD and COD Profiles

For data consisting of x and y subjected to each x corresponds to y and vice-versa which causes at least two distinct straight lines, correlation analysis, and various significance tests. The curve fitting is standardized with 95% confidence level. Therefore, from this analysis, the results obtained from the physical model and simulation model have a strong correlation with an R^2 value of 0.8 or more with good significance. Also, for all the measured value between the inlet and outlet samples has an R^2 value of 0.8 or more for the simulation value with good significance. The below-mentioned chart represents the graph drawn between the Inlet (influent) and Outlet (effluent) of measured value/Simulated value for soil media (Graph 1).

4 Statistical Analysis of Models

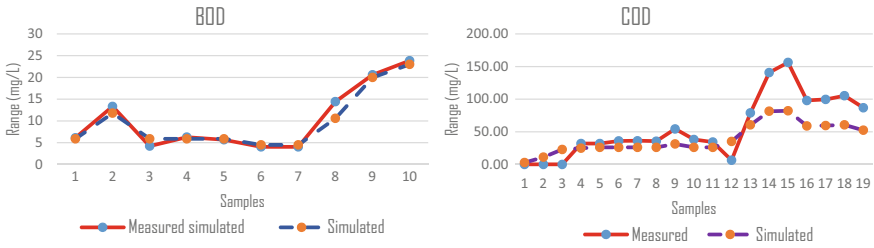
See Table 5.



Graph 1 Regression analysis of BOD and COD

Table 5 Regression

Models	Parameter	R^2
Measured value	BOD ₅	0.91
Simulated value	BOD ₅	0.83
Measured value	COD	0.90
Simulated value	COD	0.99



Graph 2 Validation between measured and simulated

4.1 Validation of the Results

In this paper, to tackle the common issues in the prediction process of simulation models the COMSOL multi-physics is used and validated with the measured values which are done on a pilot scale in the college campus. The main objective of the study was to prove the lateral movement in soil porous media. The forecasted data of pollutants for BOD and COD was measured for a year from January to December 2020. From the obtained results it is found that the measured and simulated are in good agreement with less than 10% error. The results from the simulation and measure are represented further using statistical analysis. Also, from the statistical analysis, it is found that there is a strong acceptance of data between measured data from the simulation model (Graph 2).

5 Discussion

The Effluent variations were closely observed and it is found that the influent has an impact and primly effected the target value at the Effluent. The comparison pertaining to pollutant removal efficiency between the measured and the Simulation holds good is contributing a good amount of pollutant removal after infiltration. The BOD removal concept remains the same as the water gets recharged. The retention time attained during transport reduces the pollutant concentration in the outlet and also in the simulation model. The chemical oxidations also go well during the horizontal infiltration after the recharge, which is also closely observed in BOD due to the relationship between BOD and COD. Therefore, the organic matter removal also takes place in the horizontal direction resulting in the impact of artificial recharge.

6 Conclusion

Artificial recharge and its removal of pollutants is the simplest form of disposal of treated domestic sewage. Where a high-quality consistent value is required. It is found that the permeability of the soil medium has a direct influence on the removal efficiency. The BOD removal is found to be 54.54 mg/l and COD removal is 50.13 mg/l. Also, the results obtained from the physical model and simulation model have a very strong correlation, i.e., $R\text{-square} = (0.7 < |r| \leq 1)$. The model can also be used to understand the pollutant travel distance for zero transport from the point of discharge. Therefore, artificial recharge of treated domestic sewage has an impact on unconfined aquifer with reduction of pollutant concentration from influent to effluent and hence artificial recharge can be used as a method of disposal for treated domestic sewage (used after secondary treatment). However, as a safety measure, regular monitoring of the recharge water quality and ground water quality in the surrounding area of recharge site is essential.

Acknowledgements The author and co-author are extremely thankful to the Civil engineering department for providing the software and also extremely grateful to the director, ICAS, and management for their perpetual support, encouragement, and inspiration along with the excellent library facilities, and accessibility for top indexed journals provided to the authors during this work.

References

1. Bhawan P, Nagar EA (2020) Central Pollution Control Board
2. Al-mansori NJ, Al-kizwini RS, Al-husseini FK (2020) Modeling and simulation of pollutants dispersion in natural rivers using comsol multiphysics. *J Eng Sci Technol* 15(2):1167–1185
3. Dhanraj AG (2019) Artificial recharge practice of treated domestic sewage—its challenges and opportunities in Indian perspective: a Mini systematic review. *Indian J Environ Protect* 39(12):1158–1165
4. Viccione G, Stoppiello MG, Lauria S, Cascini L (2020) Numerical modelling on fate and transport of pollutants in the Vadose Zone. *Environ Sci Proc* 2(34). <https://doi.org/10.3390/environsciproc2020002034>
5. Jiang WQ, Chen GQ (2019) Environmental dispersion in layered wetland: moment based asymptotic analysis. *J Hydrol* 569:252–264
6. Lei Y, Li Y, Su F, Li H (2019) Metabolomics study of subsurface wastewater infiltration system under fluctuation of organic load. In: *Current microbiology*. Springer
7. Gao G, Zhan H, Feng S, Fu B, Ma Y, Huang G (2010) A new mobile-immobile model for reactive solute transport with scale-dependent dispersion. *Water Resour Res* 46(8)
8. Thomann RV, Mueller JA (1987) *Principles of surface water quality modeling and control*. Harper and Row, New York
9. Cueto-Felgueroso L, Suarez-Navarro MJ, Fu X, Juanes R (2020) Interplay between fingering instabilities and initial soil moisture insoluble transport through the Vadose Zone. *Water (Switzerland)* 12(3). <https://doi.org/10.3390/w12030917>
10. Indian standard code book for analysis of water, IS 10500:2012
11. Omar K (2015) Treated wastewater use in Saudi Arabia: challenges and initiatives. *Int J Water Resour Dev*:799–809

Adsorptive Removal of Malachite Green Using Water Hyacinth from Aqueous Solution



Sayali S. Udakwar, Moni U. Khobragade, and Chirag Y. Chaware

Abstract Effluent from dye industries contains the reactive dye in large amount, which imparts color to the water and causes harm to the wellbeing of humans and aquatic animals. Malachite green (MG) is one of the dyes used in the dye industry, which is mutagenic, carcinogenic and therefore toxic. Water hyacinth (WH) is an aquatic weed, which is known for its proliferating growth. This leads to the eutrophication of water bodies. Water hyacinth (*Eichhornia crassipes*) powder is used as bio adsorbent to remove malachite green dye from aqueous solution. The adsorptive removal capacity of malachite green using water hyacinth powder was studied by carrying out the batch study on synthetic samples to assess malachite green removal efficiency. The effect on the removal was a function of various parameters like agitation speed, adsorbent dose, contact time, initial concentration, particle size and pH. At pH 7 adsorption reaches equilibrium at an agitation speed of 130 rpm at a contact time of 30 min at temperature of 27 °C. The pseudo-second-order kinetics and both Freundlich and Langmuir isotherms with R^2 0.9987, 0.9970 and 0.9923, respectively, fit the kinetics and isotherm models. The water hyacinth characterization was carried out with SEM and EDX, which suggests adsorption of malachite green. From the results obtained it can be observed that water hyacinth powder can adsorb the malachite green dye under optimum conditions which are easy to maintain. Therefore, water hyacinth can be potentially applied for the removal of malachite green dye from dye wastewater.

Keywords Bio adsorption · Malachite green dye · Water hyacinth · Kinetic study · Material characterization

S. S. Udakwar · M. U. Khobragade · C. Y. Chaware (✉)
Department of Civil Engineering, College of Engineering Pune, Pune 411005, India
e-mail: chawarecy19.civil@coep.ac.in

S. S. Udakwar
e-mail: udakwarss18.civil@coep.ac.in

M. U. Khobragade
e-mail: muk.civil@coep.ac.in

1 Introduction

One of the main sources of water on the earth is river water. About 97% water on the earth is saline in nature, 3% is fresh water. Out of 3, 69% is in the form of glaciers and ice cap; 30% is ground water and only 1% is surface water which is in the form of rivers, streams and lakes. The importance of water is known to one and all. However, despite being the limited resource on the earth and basic human need, this vital resource is being wasted, contaminated, and depleted [1, 2]. Therefore, it is necessary to conserve water and prevent pollution of water. Many cities in India and worldwide are already facing severe water shortage due to reduced rainfall, human-made climate change, reduced groundwater levels, pollution explosion, industrialization, and staggering water wastage. Water contamination, scarcity of drinking water, poor sanitation, open discarding of waste, and forest cover loss are some of India's problems. Fatal water borne-diseases leading to a higher mortality rate in infants and organs impairment is caused due to water pollution [3]. Animals drink water directly from the surface of water bodies, polluted water causes harm to the animal's health so, it is necessary to take care of this dye wastewater [4, 5].

Pollution of water due to dumping of dye waste water in the natural stream is a big concern nowadays as it imparts the color and toxicity to the water [6–8]. Many dyeing, fabrication, paper and textile industries use reactive dyes of imparting color to the products. These dyes are highly reactive and toxic [9]. If it is present in large amount causes damage to the nervous system of human beings. Textile industries dump this dye waste water directly into natural water bodies which imparts color to the water and forms toxic compounds [10]. This surface water in the natural stream is used for various purposes by human being and other living beings. So, treatment of dye wastewater is necessary before dumping into the natural water bodies [3]. Conventional filtration methods are less efficient in treating dye wastewater. Therefore, removal of dye from dye wastewater was studied using absorption technique. The abilities of water hyacinth are higher growth rate, pollutants absorption efficiency [11, 12], low operation cost and renewability which shows using this plant can be considered as a suitable technology for the treatment of dye waste water.

2 Materials and Methods

2.1 Adsorbate

Malachite green a cationic reactive dye was used as the model pollutant or reagent in the study. It was purchased from the market. This dye was selected because it was the most commonly used in cotton, acrylic, nylon, silk, wool, leather, plastic and paper dyeing textile industries. Considering this there is a possibility of bulk release of dye in effluents from the textile industry [13]. For the preparation of the stock solution

of 1000 mg/l 1 g malachite green as adsorbate was dissolved in 1000 ml of distilled water. By diluting the stock solution with adequate distilled water experimental solutions were prepared.

2.2 Preparation of Bio Adsorbent

In this study, water hyacinth leaves and stem powder was used as adsorbent, which is collected from Pashan Lake situated in Bavdhan, Pune. The collected adsorbents were washed thoroughly 2–3 times to clean the adsorbent from dust and mud. Leaves and stems were separated after washing. It was kept in 0.25 M EDTA solution for 24 h. at room temperature to removal, the metal and other surface impurities. It was rinsed with distilled water after 24 h. After washing with distilled water, it was soaked in sunlight for 2 h. After that keeping it in a hot air oven for 48 h at 110 °C which is an optimized temperature.

Crushed and dried water hyacinth leaves and stems were grinded in mixer grinder into a fine powder. Grinded powder is then sieved through 75 μm sieve to get fine powder. After sieving, water hyacinth leaves and stem powder were stored in airtight plastic bottles at room temperature 27 ± 2 °C and further used as the adsorbent in batch study.

2.3 Batch Bio Adsorption Experiments

The batch study experimentation was used to study the adsorption of malachite green using water hyacinth powder. Conical flask of 250 ml was used to perform batch study experiments and round bottom volumetric flask of 100 ml. A fixed volume and concentration of adsorbate solution were added in conical flask with the fixed amount of adsorbent powder. It was placed in orbital shaking incubator and temperature and agitation speed in orbital shaking incubator were fixed. After shaking in the orbital shaking incubator for a fixed time, conical flasks were removed from the orbital shaker and kept on a flat platform to rest so that suspended particles could settle down. As the suspended particles in the solution settled, the solution above the settled particles was removed to other conical flask. The sample was taken for analysis in the UV-spectrophotometer. By knowing absorbance, the concentration of the chemical substance in the solution was calculated. The results obtained from the spectrophotometer were used to find the removal percentage of malachite green and adsorption capacity of the adsorbent. This process was repeated by varying parameters such as contact time, pH, initial dye concentration, adsorbent dose, agitation speed and particle size. The calculation of adsorption efficiency $\eta\%$ and adsorption capacity q_e of the adsorbent was calculated by Eqs. 1 and 2.

$$q_e = (C_o - C_e)/m \quad (1)$$

$$\eta\% = [(C_o - C_e) / C_o] * 100 \quad (2)$$

where,

C_o Initial dye concentration in mg/L

C_e Final dye concentration in mg/L

m Mass of adsorbent in mg/L.

Adsorption efficiency and adsorption capacity are important parameters for evaluating the performance of adsorbents. q_e gives us the idea about the quantity of dye, adsorbed on the unit mass adsorbent, and the adsorption efficiency is just the removal efficiency of adsorbent irrespective of amount. The results were obtained by following the same procedure and were plotted to get the calibration curve that is used as basis for further calculations in the study.

2.4 Surface Characterization

SEM and EDX analysis

The removal of malachite green using water hyacinth leaves powder was examined a Scanning Electron Microscope (SEM) and Energy dispersive X-ray (EDX). A working solution of a malachite green dye having concentration 12 mg/L was prepared. The working solution was kept in orbital shaking instrument at temperature 27 °C and agitation speed of 130 rpm. It was then taken out and allowed to settle. The solution above the settled particles was removed from the top and solution at the bottom of the flask was allowed to dry. This dried powder was tested under a scanning electron microscope with 15 kV and 10,000 times magnification.

3 Results and Discussion

3.1 Adsorbent Material Testing

SEM and EDX analysis of water hyacinth water hyacinth leaves powder (Figs. 1, 2, 3 and 4):

The above graphs, images and table indicate the adsorption of malachite green on water hyacinth leaf powder. Dye molecules are visible on the adsorbent material surface in SEM images. The main constituent of malachite green oxalate is oxygen; there is a significant increase in oxygen percentage on the adsorbent surface after dye removal. Oxygen is increased by approximately 8%. This implies that adsorption takes place and water hyacinth leaves powder adsorbed the malachite green oxalate dye.

Fig. 1 SEM photograph of water hyacinth leaves powder before malachite green dye removal

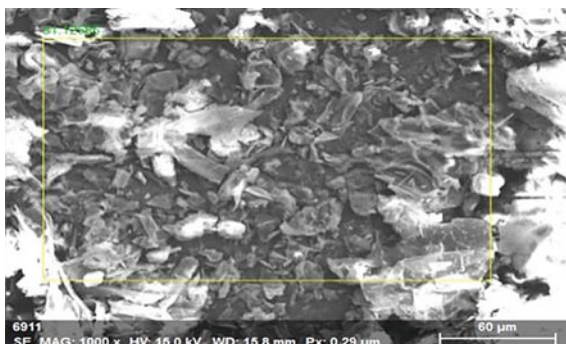


Fig. 2 SEM photograph of water hyacinth leaves powder after malachite green dye removal

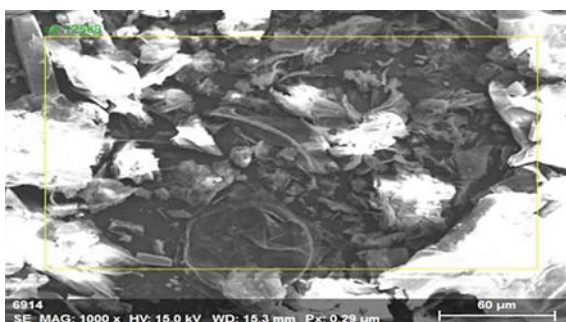


Fig. 3 EDX graph before removal using leaves powder

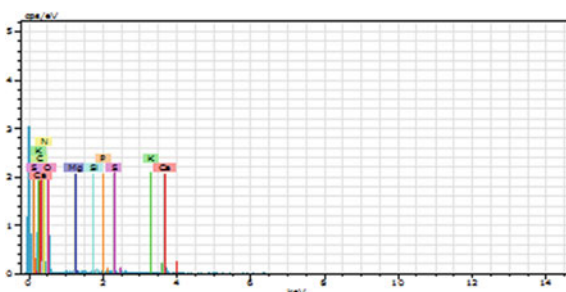
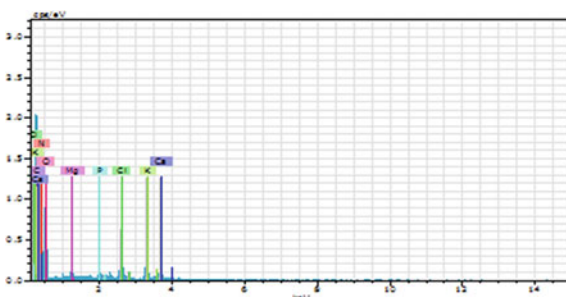


Fig. 4 EDX graph after removal using leaves powder



SEM and EDX analysis of water hyacinth water hyacinth stem powder (Figs. 5, 6, 7 and 8)

Water hyacinth stem powder shows similar behavior as that of water hyacinth leaves powder. The images, graphs, and tables proved that malachite green oxalate's adsorption takes place on the surface water hyacinth stem powder. There is an increase of 5% in the amount of oxygen after the removal of malachite green oxalate dye.

Fig. 5 SEM photograph of water hyacinth stem powder after malachite green dye removal

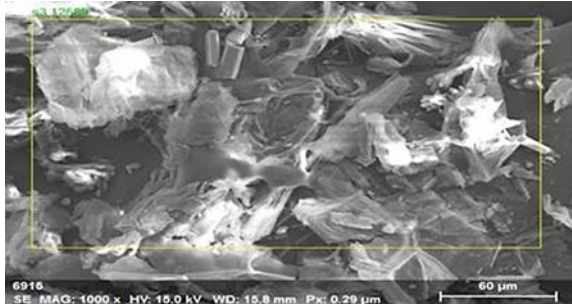


Fig. 6 SEM photograph of water hyacinth stem powder before malachite green dye removal

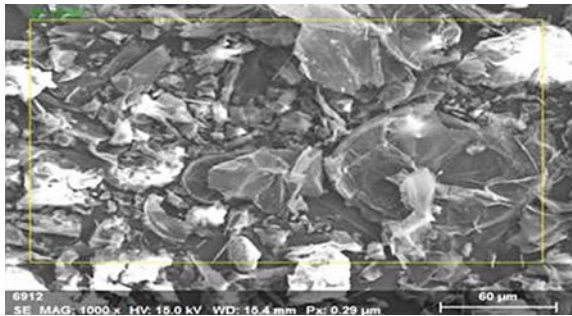


Fig. 7 EDX graph before removal using stem powder

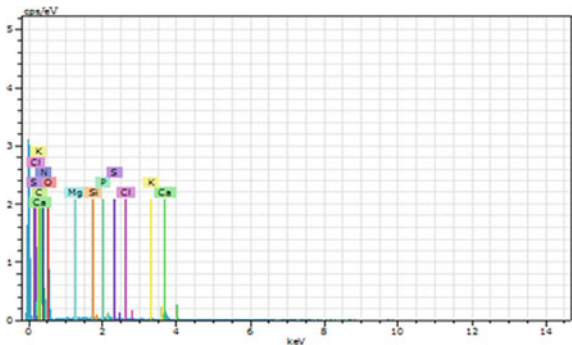


Fig. 8 EDX graph after removal using stem powder

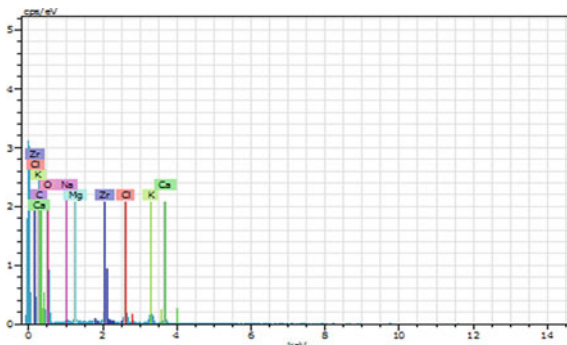
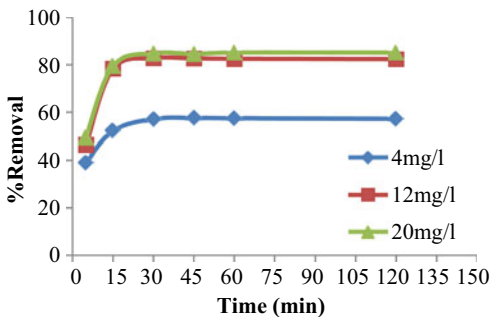


Fig. 9 Contact time effect on MG dye removal (Agitation speed = 150 rpm, PH = 7, Temperature = 27 °C, and adsorbent dose = 1.0 g/L)



4 Batch Adsorption Study for Water Hyacinth Leaves Powder

4.1 Effect of Contact Time

See Fig. 9.

From the above graph, it can be concluded that the contact time of 30 min is optimum for the adsorption of malachite green oxalate dye using WH leaves powder from the aqueous solution. Therefore, for the further experimental process, the optimum contact time was taken as 30 min.

4.2 Effect of Initial Dye Concentration

See Fig. 10.

From the above graph, it can be concluded that the initial dye concentration of 12 mg/L is an equilibrium concentration after which the rate of increase in removal

Fig. 10 Initial concentration effect on malachite green dye removal (Agitation speed = 150 rpm, pH = 7, Contact time = 30 min, Temperature = 27 °C and adsorbent dose = 0.5 g/L)

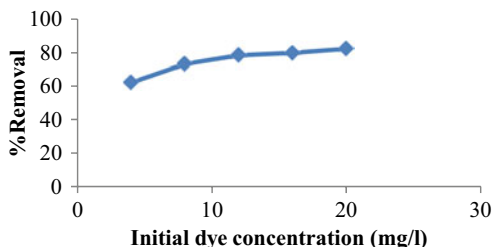
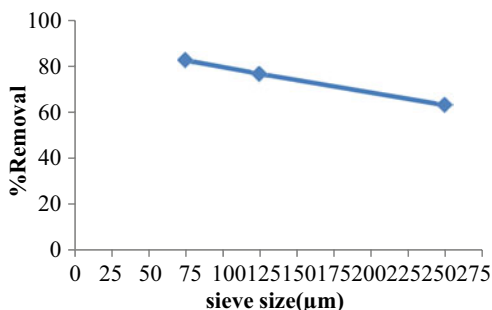


Fig. 11 Particle size effect on the removal of MG dye (Agitation speed = 130 rpm, Contact time = 30 min Initial concentration = 12 mg/L, PH = 7, Temperature = 27 °C and adsorbent dose = 1.0 g/L)



efficiency slows down. Therefore, for further study to get the optimum results solution having an initial concentration of dye at 12 mg/ L was taken.

4.3 Effect of Particle Size

Maximum removal efficiency of 82.73% is obtained at the adsorbent particle size of 75 μm . Smaller the particle more will be surface area and more will be the adsorption. Therefore, water hyacinth powder having 75 μm of particle size was used for the experimental work (Fig. 11).

4.4 PH Effect

At pH 7.5 the peak removal effectiveness of malachite green dye using water hyacinth powder was observed. From the above results, it can be concluded that neutral pH, i.e., 7 is an optimum pH for removal of malachite green oxalate dye from the aqueous solution. Therefore, neutral pH, i.e., 7 is adopted for further experimental procedures (Fig. 12).

Fig. 12 pH effect on malachite green dye removal (Agitation speed = 150 rpm, Initial concentration = 12 mg/L, Temperature = 27°C, Contact time = 30 min and adsorbent dose = 1.0 g/L)

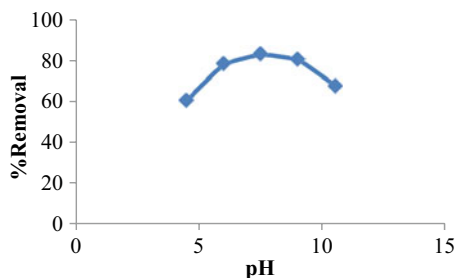
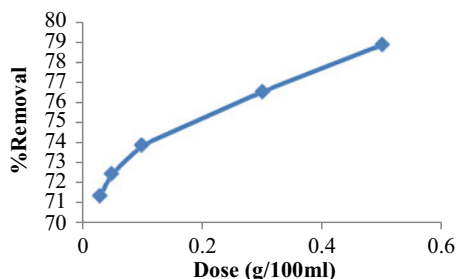


Fig. 13 Adsorbent dose effect on removal of MG dye (Initial concentration = 5 mg/L, pH = 7, Temperature = 27 °C, Contact time = 30 min and Agitation speed = 150 rpm)



Influence of Adsorbent Dose

See Fig. 13.

From the above graph, it can be concluded that 1 g/L of the adsorbent dose is required for optimal removal dye from an aqueous solution having initial dye concentration constant at 5 mg/L. Above dose 1 g/L or 0.1 g/100 ml removal efficiency do not increase by considerable amount. Therefore, for further study, adsorbent dose of 1 g/L was adopted.

4.4.1 Effect of Agitation Speed

See Fig. 14.

Fig. 14 Agitation speed effect on the removal of MG dye (Contact time = 30 min, PH = 7, Initial concentration = 12 mg/L, Temperature = 27 °C and adsorbent dose = 1.0 g/L)

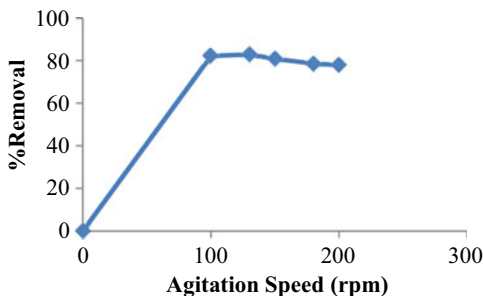
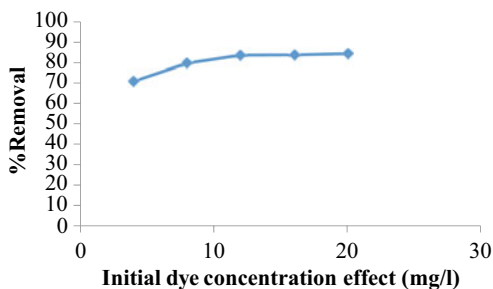


Fig. 15 Initial dye concentration effect on the malachite green dye removal using water hyacinth stem powder (Agitation speed = 130 rpm, pH = 7, Contact time = 30 min, Temperature = 27 °C and adsorbent dose = 1.0 g/L)



From the above graph, it can be concluded that as speed increases, detachment of dye molecules occurs therefore, with further increase in agitation speed removal efficiency decreases. For this study agitation speed of 130 rpm was optimum.

Batch Adsorption Study for Water Hyacinth Stem Powder

Effect of Initial Dye Concentration

See Fig. 15.

For this batch study adsorbent shows maximum removal efficiency 83.55% at an initial dye concentration of 12 mg/L like water hyacinth leaves powder. Therefore, the initial concentration of 12 mg/L is an equilibrium concentration.

Effect of Adsorbent Dose

See Fig. 16.

From the study, the optimum removal efficiency of 81.45% is obtained for an adsorbent dose of 1.5 g/L. Therefore, it can be concluded that water hyacinth stem powder is required in more quantity than that of leaves powder to remove malachite green dye from aqueous solution.

Adsorption Isotherms

The adsorption isotherms such as Langmuir isotherm and Freundlich isotherm model, depict the relationship between adsorbent and adsorbate. To carry out the analysis of these model's batch experiment was carried out by varying initial dye concentration

Fig. 16 Adsorbent dose effect on the MG dye removal using water hyacinth stem powder (Agitation speed = 150 rpm, Initial concentration = 12 mg/L, Contact time = 30 min, pH = 7 and Temperature = 27 °C)

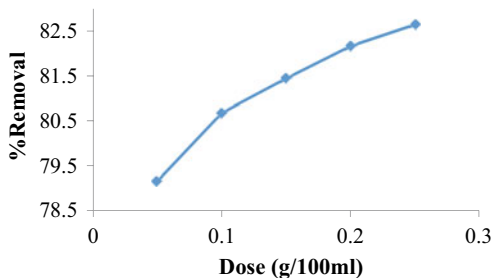


Table 1 Langmuir isotherm constants

Langmuir isotherm		
K_L (L/mg)	q_m (mg/g)	R^2
0.1113	16.9690	0.9923

Table 2 Freundlich isotherm constants

Freundlich isotherm		
K_F (L/g)	n	R^2
8.5729	20.03	0.9970

4, 8, 12, 16 and 20 mg/L and keeping constant adsorbent dose 1 g/L, contact time 30 min, agitation speed 130 rpm, pH 7 and temperature 27 °C. The values of constants in Langmuir and Freundlich isotherm are given in Tables 1 and 2,, respectively. The graph of Langmuir and Freundlich adsorption isotherm is shown in Figs. 17 and 18, respectively.

From Tables 1 and 2, it is clearly shown that the correlation coefficient (R^2) is almost similar in both isotherms Langmuir and Freundlich, which is 0.9923 and 0.9970, respectively. This depicts that the adsorption of malachite green dye using water hyacinth powder as adsorbent occurs in monolayer as well as a multilayer. Therefore, the adsorption of malachite green follows both Langmuir and Freundlich isotherm and adsorption technique is suitable for removing malachite green using water hyacinth powder from aqueous solution.

Fig. 17 Langmuir adsorption isotherm

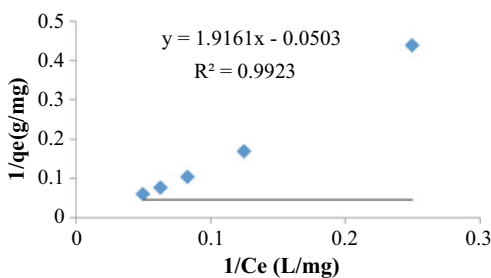


Fig. 18 Freundlich adsorption isotherm

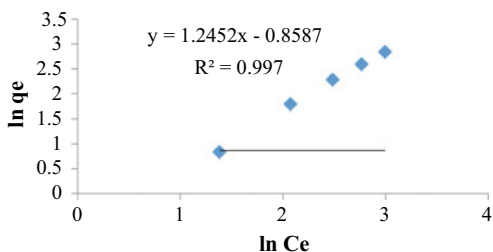
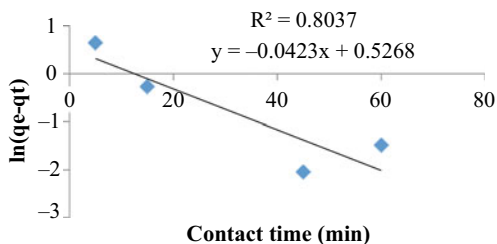


Fig. 19 Kinetic model
Pseudo-first-order



4.5 Adsorption Kinetics

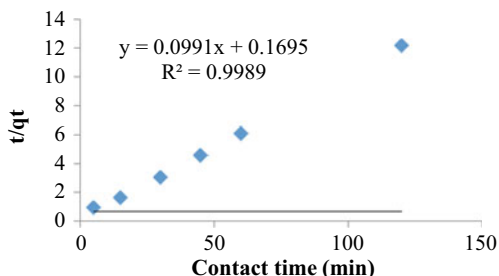
Pseudo-first-order and pseudo-second-order two kinetic models are utilized to analyze the dynamics of malachite green oxalate dye adsorption on the water hyacinth. The best fit for adsorption between pseudo-first-order and pseudo-second-order is examined using the coefficient of correlation. The correlation coefficient (R^2) for the pseudo-first-order is 0.8037 and for pseudo-second-order is 0.9989. It was observed that the adsorption process of malachite green oxalate dye using water hyacinth powder follows pseudo 2nd order kinetics. Therefore, for the removal of malachite green dye adsorption technique is water hyacinth powder (Fig. 19).

5 Conclusions

See Fig. 20.

It can be concluded from the study that an efficient adsorbent for malachite green dye removal was developed from water hyacinth plant and successfully used in the adsorption process. The adsorbent prepared from water hyacinth plant's leaves powder sieved through 75 μm IS sieve showed the optimum removal efficiency 81% at an agitation speed of 150 rpm, initial dye concentration 12 mg/L, adsorbent dose of 1 g/L, pH 7, contact time of 30 min, and temperature 27 ± 2 °C. The adsorbent prepared from the water hyacinth stem powder showed the same as that of water hyacinth leaves powder except the optimum removal efficiency of 83% at initial dye

Fig. 20 Kinetic model
Pseudo-second-order



concentration of 12 mg/L and adsorbent dose of 1.5 g/L. Therefore, both leaves and stem powder shall be utilized for malachite green dye removal as a bio adsorbent. The study concludes that water hyacinth is useful in removing dye solution Adsorption process follows both Langmuir and Freundlich adsorption isotherm as the value of the correlation coefficient of isotherms is 0.9923 and 0.997, respectively. In the kinetic study, this adsorption process follows a pseudo-second-order kinetic model with an R^2 value of 0.9989. which shows the significant amount of adsorption that occurred in the experiments. Therefore, the adsorption process is best suitable for the removal of malachite green dye.

6 Recommendation

The water hyacinth plant from the surface water bodies should be used for removing malachite green dye contaminants from dye wastewater with high efficiency. The separation of malachite green dye from the solution was observed between 80 and 83%. Thus, it is, recommended to modify the surface of water hyacinth powder chemically to improve the removal efficiency of malachite green.

References

1. Kumar B, Smita K, Flores LC (2017) Plant mediated detoxification of mercury and lead. Arab J Chem 10:S2335–S2342
2. Shokry H, Elkady M, Hamad H (2019) Nano activated carbon from industrial mine coal as adsorbents for removal of dye from simulated textile wastewater: operational parameters and mechanism study. J Mater Res Technol 8:4477–4488
3. Sukasem N, Khanthi K, Prayoonkham S (2017) Biomethane recovery from fresh and dry water hyacinth anaerobic co-digestion with pig dung, elephant dung and bat dung with different alkali pretreatments. Energy Procedia 138:294–300
4. Kulkarni MR, Revanth T, Acharya A, Bhat P (2017) Removal of crystal violet dye from aqueous solution using water hyacinth equilibrium, kinetics and thermodynamic study. Resource-Efficient Technol 3:71–77
5. Wanyonya WC, Onyarib JM, Shiunduc PM, Mulaad FJ (2017) Biodegradation and detoxification of malachite green dye using novel enzymes from bacillus cereus strain KM201428: kinetic and metabolite analysis. Energy Procedia 119:38–51
6. Elhalil A, Tounsadi H, Elmoubarki R, Mahjoubi FZ, Farnane M, Sadiq M, Abdennouri M, Qourzal S, Barka N (2016) Factorial experimental design for the optimization of catalytic degradation of malachite green dye in aqueous solution by Fenton process. Water Resour Ind 15:41–48
7. Sinha A, Lulu S, Vino S, Osborne WJ (2019) Reactive green dye remediation by Alternanthera philoxeroides in association with plant growth promoting Klebsiella sp. VITAJ23: a pot culture study. Microbiol Res 220:42–52
8. Abdelrahman EA, Hegazey RM, El-Azabawy RE (2019) Efficient removal of methylene blue dye from aqueous media using Fe/Si, Cr/Si, Ni/Si, and Zn/Si amorphous novel adsorbents. J Mater Res Technol 8:5301–5313
9. Jarusiripot C (2014) Removal of reactive Dye by adsorption over chemical pretreatment coal based bottom ash. Procedia Chem 9:121–130

10. Sousa HR, Silva LS, Sousa PAA, Sousa RRM, Fonseca MG, Osajima JA, Silva-Filho EC (2019) Evaluation of methylene blue removal by plasma activated palygorskites. *J Mater Res Technol* 8:5432–5442
11. Kanawade SM, Gaikwad RW (2011) Removal of methylene blue from effluent by using activated carbon and water hyacinth as adsorbent. *Int J Chem Eng Appl* 2(5):317–319
12. Sarkar M, Rahman AKML, Bhoumik NC (2017) Remediation of chromium and copper on water hyacinth (*E. crassipes*) shoot powder. *Water Resour Ind* 17:1–6
13. Rajabi M, Mahanpoor K, Moradi O (2019) Preparation of PMMA/GO and PMMA/GO-Fe₃O₄ Nano composites for malachite green dye adsorption: Kinetic and thermodynamic studies. *Compos B* 167:544–555

Sediment Yield Assessment of a Watershed Area Using SWAT



Prachi A. Bagul and Nitin M. Mohite

Abstract Soil erosion is a major concern and severe challenge for the sustainability and productivity of agricultural systems, land all over the world. It is directly and majorly impacting on storage capacity and life span of reservoir, dam. It is important to reduce soil loss from cultivated lands and minimize degradation in water quality. Sediment yield is the volume of sediment eroded from the ground surface by runoff and transferred to a stream system or basin outlet over time. Estimation of sedimentation yield is needed for studies of its impact on reservoir storage capacity, river morphology and planning of soil and water conservation measures. The present study has been carried out by using Soil Water Assessment Tool (SWAT), to develop model for watershed area which comes under Pawana Watershed, Maharashtra state, India. SWAT requires large number of input parameters which include digital elevation model, soil map, Land use land cover map, slope map, weather data. These inputs of SWAT have been prepared under the QGIS2.6.1 environment. All these inputs- thematic maps and attribute information of study area have been collected from various Government agencies and sources. The simulated result is obtained after successful run of SWAT which can be visualized statically, graphically, and numerically.

Keywords Pawana watershed · Sediment yield · Quantum geographic information system · Soil water assessment tool

P. A. Bagul (✉) · N. M. Mohite
Department of Civil Engineering, College of Engineering Pune, Pune, MH, India
e-mail: bagulaprachi@gmail.com

© The Author(s), under exclusive license to Springer Nature Singapore Pte Ltd. 2023
M. S. Ranadive et al. (eds.), *Recent Trends in Construction Technology and Management*, Lecture Notes in Civil Engineering 260,
https://doi.org/10.1007/978-981-19-2145-2_32

415

1 Introduction

Accelerated soil and water loss, seriously threaten land and water resources and ecological environment, by posing a severe challenge to the productivity of land by the loss of fertile soil and to the life of reservoirs by the deposition of sediment. If we see, Sedimentation is an important parameter to assess the life of a reservoir, sediments deposited in reservoir may affect the safety of reservoir and it also effect on hydropower production. For best watershed management practices, it might be to minimize the amount of sediment, to divert sediment around or through the reservoir, or to remove deposited sediments it is necessary to quantify and analyse the sedimentation yield.

In recent years, the study of soil erosion is more common by using geographic information system technology, remote sensing and Universal Soil Loss Equation (USLE) models like Revised USLE (RUSLE) and Modified USLE (MUSLE) are increasingly being used [1]. SWAT shows the efficient results in different scenarios like- to quantify the special and temporal runoff estimation from gridded rainfall data [2], Study areas of ungauged watersheds and which are closely located, having similar meteorological and hydrological characteristics [1]. SWAT shows efficient application of sediment yield in different scenario like Urbanized basin, highly urbanized basin, a temporary large basins management [3], in zone of semi-arid and arid catchments, though it is challenging due to unavailability of sufficient data, with gridded rainfall data and even in ungauged watershed area [4]. SWAT provides effective ways and methods for runoff and sediment simulation in different watersheds.

2 Study Area

The study area—Pawana dam lies between 73° 40' 30" E longitudes and 18° 21' 30" N latitudes and has an area of Pawana catchment is approximately 113.36 km². Pawana River (Pawana) is located in the western part of the state of Maharashtra, India, in the Pune district. It originates in the ghats of the West. It is a tributary of the Bhima River and merges into the Mula River in the city of Pune. Average annual rainfall in the catchment is 2800 mm. Figure 1 shows the location of study area.



Fig. 1 Location of study area Pawana watershed

3 Model Description and Methodology

The hydrological modelling of study area Pawana watershed is carried out by using SWAT. Digital Elevation Model (DEM), land use land cover (LULC), soil and slope maps are provided as inputs data to run the SWAT model. DEM of study area is extracted under QGIS environment, then delineation of the watershed is carried out. Soil map, slope map and land use land cover map are used to create hydrological response units. Figure 6 shows the Pawana watershed with 63 sub-basins by using stream network, where outlet point present at Pawana dam. Then using weather data as an input with hydrological response unit run the SWAT model.

Database preparation—For the hydrological runoff simulation, the SWAT model needs the following data which will work as input.

4 Digital Elevation Model (DEM)

From the Bhuvan website (<http://bhuvan.nrsc.gov.in/data/download/index.php>) a digital elevation model (DEM) was downloaded with a resolution of 30 m. Figure 2 depicts the various elevation bands, with high values suggesting higher elevations in the Western Ghats.

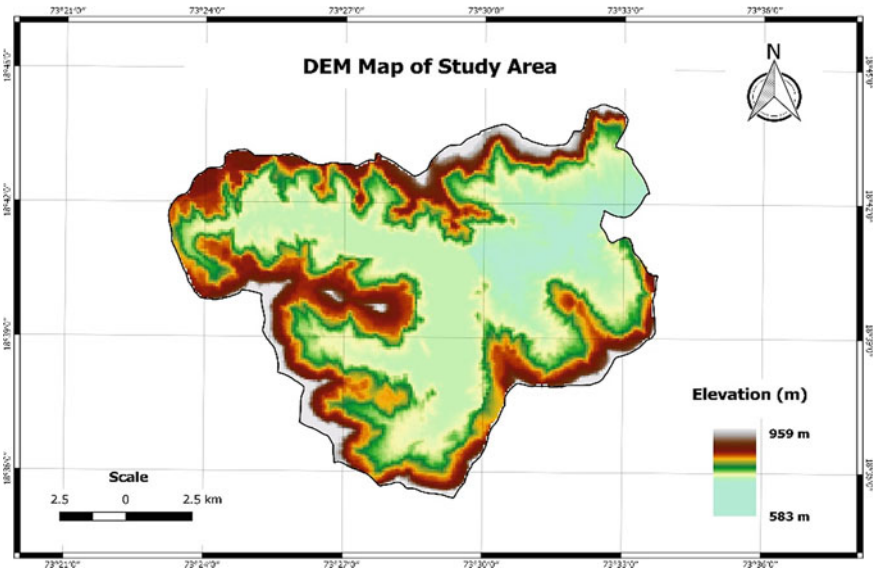


Fig. 2 Digital elevation module of study area

5 Weather Data

SWAT requires weather data which includes value of daily precipitation (mm), maximum and minimum air temperature (o C), solar, wind speed and relative humidity data with information on the location of the weather station (latitude and longitude). For the period 1978 to 2014 From India Meteorological Department (IMD) gridded precipitation data and from www.swat.tamu.edu. Maximum and minimum air temperature (°C), relative humidity, solar, wind data is collected and used.

6 Land Use Land Cover (LULC) Map

The land use land cover map of Pawana watershed was digitized and rasterized in QGIS, which was developed by adding web map service (WMS) layer provided by www.bhuvan.nrsc.gov. in QGIS. Figure 3 shows the type of land cover presented in the watershed area.

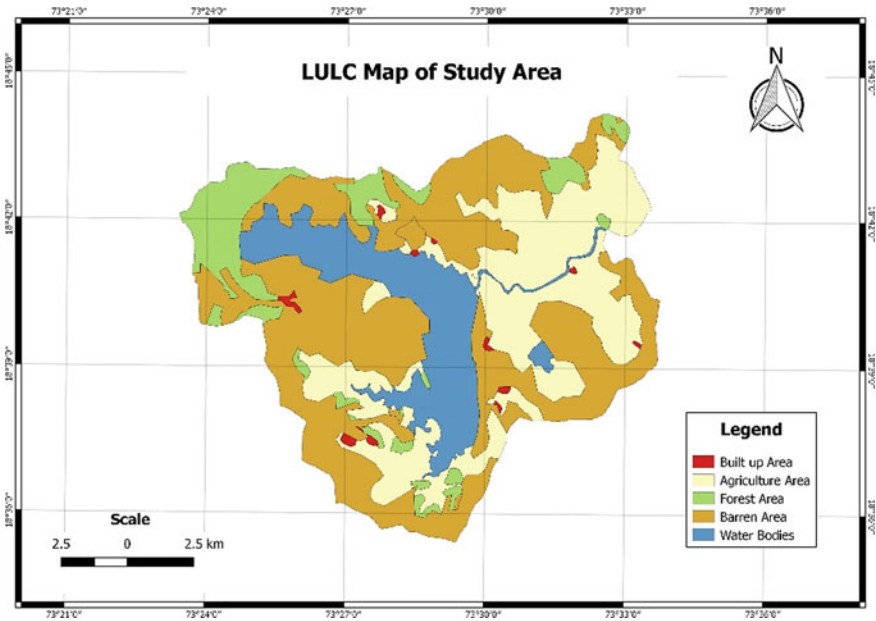


Fig. 3 LULC map of study area

7 Soil Map

Soil map of Maharashtra developed by NBSS, Nagpur was geo-referenced and used for digitized and rasterize soil map. The Pawana river basin is made up of three separate soil types: loamy soils (77), drained loamy soils (118), and fine soil (266), but the majority of the basin is made up of rocky/sandy loam. Figure 4 shows a soil map for study area.

8 Hydrological Response Units (HRU)

The regions with homogeneous soil, land use and topographical characteristics are known as hydrological response units (HRU). SWAT requires the soil map, land use and slope classification map for creating HRU, which are areas within a watershed that respond similar to the given input. It is a method of representing spatial heterogeneity of watershed. Nearly 292 HRUs were created from SWAT overlay analysis, shown in Fig. 5.

QSWAT Ref 2012.mdb file SWAT Code has been modified by copying useroil.xls to excel. Thirty-three years of daily weather data such as precipitation (mm), wind speed (m/s), solar radiation (MJ/m^2) and temperature ($^{\circ}\text{C}$) for the study area

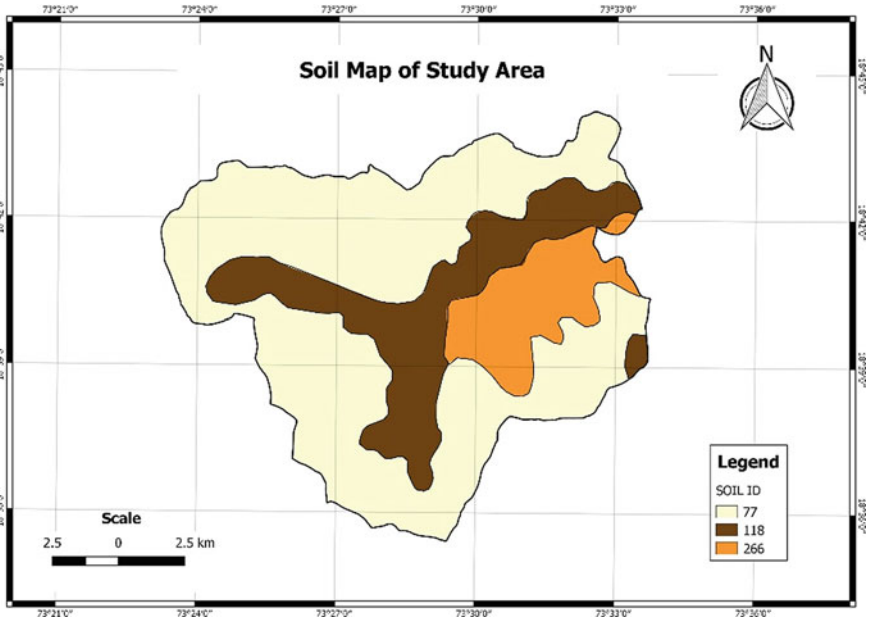


Fig. 4 Soil map of study area

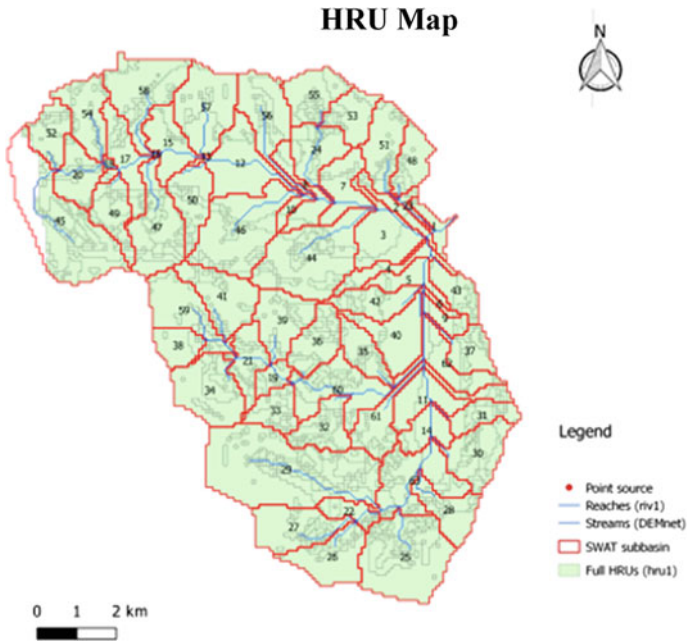


Fig. 5 HRU map of study area

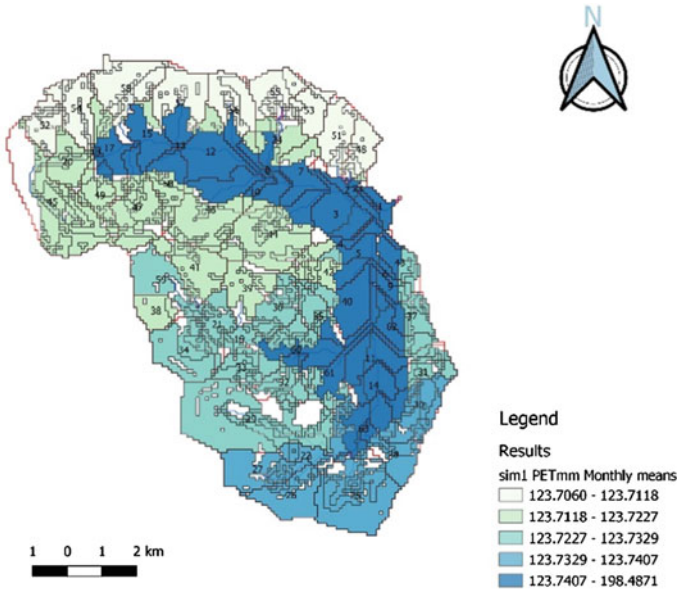


Fig. 6 Monthly evapotranspiration in mm

have been downloaded from the <http://globalweather.tamu.edu> site. Calculation of TMPMX (mean maximum temperature), TMPMN (mean minimum temperature), TMPSTDMX (deviation of max temperature), SOLARAV (mean solar radiation), WNDNAV (mean wind speed) was carried out with the help of Microsoft Excel. Precipitation-related parameters and dew point have been computed using custom software called pcpSTAT.exe and dewpoint.exe. All results are then copied to the WGEN WatershedGan.xls file. The SWAT model divides the watershed delineation into several sub-basins, and then determines the water balance components for each sub-basin.

9 Results

SWAT was run using the data obtained, analysed, and developed as mentioned above. The simulated result is obtained after successfully running SWAT. The outcomes can be presented on an overall, annual daily, monthly, and yearly basis. For each subbasin, it offers all types of hydrological components (Fig. 6).

The 63 subbasins were obtained in this analysis. Subbasins cover 10,763.73 km² of the total watershed area. Graphically, statically, and numerically, the output can be visualized. Figure 7 provides a graphic representation of the different parameters of subbasin 1.

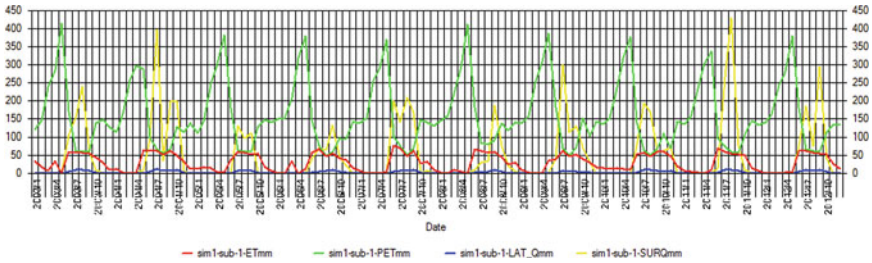


Fig. 7 Graphical presentation of variations of all the parameters for subbasin 1

Figure 8 illustrates the groundwater contribution of subbasins on a monthly basis which includes water yield average amount of precipitation, actual precipitation, surface runoff and potential evapotranspiration.

The 63 sub basins occupy a combined area of 10,763.73 km². SWAT Check is used to measure average monthly basin values for rainfall, water yield, sediment

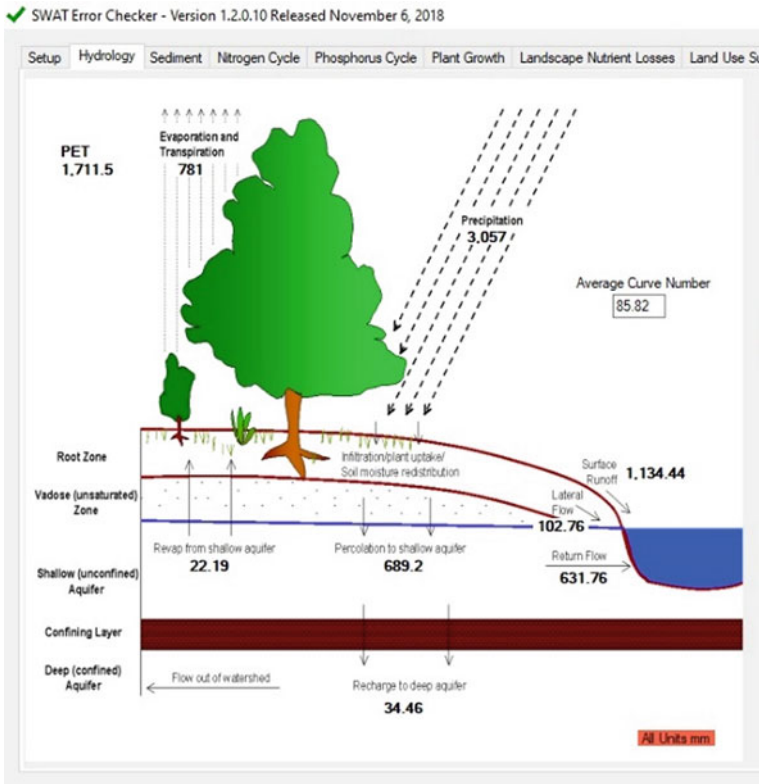


Fig. 8 Hydrology of study area

Table 1 Hydrological response unit analysis output

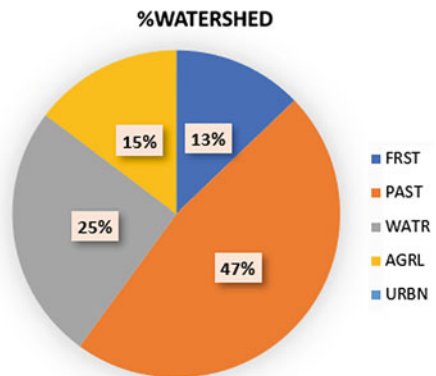
Land Use Pattern	Area (Ha)	% Watershed Area
Watershed (WATR)	2721.35	25.28
Agricultural Land (AGRL)	1581.59	14.69
Forest Area (FRST)	1380.65	12.83
Pasture (PAST)	5080.14	47.2

yield, surface runoff, evapotranspiration, and potential evapotranspiration (PET). The SWAT measures the amount of various land use areas covered by the watershed, which is shown in percentage in the following Tables 1 and 2 (Fig. 9).

Table 2 Average monthly basin values

MONTH	RAIN (mm)	SNOWFALL (mm)	SURFQ (mm)	LATQ (mm)	WATER YIELD (mm)	ET (mm)	SED. YIELD (mm)	PET (mm)
1	0.62	0	0	2.01	14.59	46.71	0	152.18
2	0.88	0	0	1	4.08	43.66	0	151.78
3	2.38	0	0	0.66	2.31	86.27	0	194.67
4	0.89	0	0	0.38	1.53	69.74	0	203.88
5	29.21	0	0.99	0.4	2.28	66.48	0.06	220.9
6	628.72	0	203.91	4.68	212.14	81.74	7.79	113.19
7	967.77	0	425.52	17.9	509.24	53.18	25.16	62.21
8	774.51	0	307.23	24.64	478.31	57.46	65.95	67.21
9	451.25	0	142.09	22.4	329.48	83.29	45.8	101.58
10	151.13	0	48.85	16.03	205.97	80.36	18.49	142.83
11	45.53	0	5.78	8.22	95.06	60.99	1.98	146.71
12	4.15	0	0.05	4.43	47.12	50.68	0.02	152.89

Fig. 9 Pie chart of presenting watershed area in percentage



From Table number 2, shows the average annual monthly basin values of rain, water yield and sediment yield, evapotranspiration (ET), potential evapotranspiration (PET). The results show that during wet months, discharge and sediment yield increase, while during dry months, they decrease.

10 Conclusions

The best way to assess the availability of water in various components of the hydrological cycle, as well as adjustments between these components, is to use water balance. The SWAT model has proved to be a valuable method for simulating the hydrology of large basins at the watershed scale. This shows the simulated outcomes for each parameter. This water balance study reduces the possibility of drought and mismanagement, resulting in more effective use of available water supplies. The best way to assess the availability of water in various components of the hydrological cycle, as well as variations between these components, is to use water balance. Open-source geospatial techniques like Q-GIS were used to construct various thematic maps of the study area's impact on land use, soil and slope, which were then fed into the SWAT model. This water balance study lessens the chances of drought and poor management, resulting in more effective use of available water supplies.

References

1. Prabhanjan A, Rao EP, Eldho TI (2015) Application of SWAT model and geospatial techniques for sediment-yield modeling in ungauged watersheds. *J Hydrol Eng* 20(6):C6014005
2. Jothiprakash V, Praveenkumar C, Manasa M (2017) Daily runoff estimation in Musi river basin, India, from gridded rainfall using SWAT model. *Eur Water* 57:63–69
3. Busico G et al (2020) Evaluating SWAT performance to quantify the streamflow sediment yield in a highly Urbanized Basin. *Environ Sci Proc* 2(1). Multidisciplinary Digital Publishing Institute
4. Mengistu AG, van Rensburg LD, Woyessa YE (2019) Techniques for calibration and validation of SWAT model in data scarce arid and semi-arid catchments in South Africa. *J Hydrol Reg Stud* 25:100621

“NDVI: Vegetation Performance Evaluation Using RS and GIS”



A. Khillare and K. A. Patil

Abstract Vegetation as an ecosystem’s crucial part, plays a key role in soothing global environment. Normalized Difference Vegetation Index (NDVI) is one such remote sensing technique that is widely used to compute vegetation cover change. Remote sensing and Geographical Information System methods are used often in examining natural resources, determination of land changes and related planning work. The methodology discussed in this study is based on association with vegetation remote sensed data in the form of Normalized Difference Vegetation Index (NDVI). The major application of this index is to monitor the vegetative cover. NDVI is a function of reflected Near Infrared (NIR) and Visible (VIS) radiance’s spectral contrast from a surface. A further study is made on the calculated NDVI to evaluate the agricultural drought index in the form of Vegetation Health Index. This index comprises of Vegetation Condition Index (VCI) and Land Surface Temperature (LST). Vegetation health is assessed based on VHI, which is suitable indicator of agricultural drought extent. A correlation is studied statistically between NDVI, VHI, precipitation and temperature. The present study is focussed on the Shirur and Khed talukas of Pune district for the years 2000, 2003, 2009, 2012, 2015 and 2018 for particular months. The use of data Landsat 7 ETM+ for the year till 2012 and data Landsat 8 OLI for 2015 and 2018 was made. Data was obtained from U. S Geological Survey. The precipitation data was taken from maharain.gov.in. Thus, vegetative cover over the specified area was studied including the drought severity. A liner regression analysis is performed using the evaluated data which can be used to forecast the vegetation condition as an early warning system for agricultural drought.

Keywords NDVI · VHI · Agricultural drought · Landsat · VCI

A. Khillare (✉) · K. A. Patil
Civil Engineering, College of Engineering, Pune, India
e-mail: khillareanjali21@gmail.com

K. A. Patil
e-mail: kap.civil@coep.ac.in

1 Introduction

Indian economy principally depends upon agriculture sector. Thus, agriculture can be entitled as a back bone of India. To develop these valuable asset-like landscapes, green open spaces is of a great concern. The way to advance in any field is to gain knowledge of advanced technology. With the help of advanced tools and a combination of educated and skilled employees, it is possible to perform better in various fields. Remote sensing and Geographical Information System are ways to enhance in the monitoring of vegetation, determination of land changes and planning work. The satellite imagery is used for yield and production forecasting, green cover inventory and assessment of drought-like catastrophe. By studying the temporal and spatial variations in the vegetative structure, monitoring and analysis can be performed. Vegetation indices are widely used in this field. There are numerous indices in use to study the changing pattern of the vegetation. These indices are the indicators of health and greenness of vegetation and a measure of density. To compute the vegetation indices the band combination is used which mainly comprises of red, green and infrared spectral bands.

One of the approved index is Normalized Difference Vegetation Index (NDVI) to monitor vegetation stress. Normalized Difference Vegetation Index (NDVI) offers better results to understand the vegetation change. It converts multi spectral data into a single image band which displays vegetation distribution. To quantify the healthy green vegetation based on satellite images, NDVI a graphical indicator makes use of the distinctive reflection of green vegetation in the visible and near infrared portions (NIR) portion of spectrum thus providing condition of the vegetation. NDVI value ranges from -1 to $+1$, value leaning towards $+1$ denoting healthier vegetation. Further, the remotely sensed data from satellite is adopted to analyse drought risk and has become widespread these days. Drought, a natural hazard causes noteworthy loss in the field of crop production, water supply and harness the well-being of humans. Recognition of such calamity becomes important to decrease its impact and severity in future. The way to mitigate drought effectively is to monitor such risk in advance with the help of remote sensing technology. Drought indices have been developed which comprise of spatial extent of vegetation, duration, intensity of meteorological factors. NDVI has an effective approach to monitor drought. A combination of NDVI in the form of Vegetation Condition Index (VCI) along with land surface temperature (LST) delivers a strong correlation thus providing information about agricultural drought beforehand.

Study aims to examine vegetation extent over the Shirur and Khed talukas of Pune District. The relationship between rainfall and NDVI in the context of these talukas Shirur and Khed is analysed for drought monitoring, rainfall being key factor in vegetative health. Use of Landsat dataset for examination of these indices is made and is explained in the methodology section.

2 Study Area

See Fig. 1.

Study is focussed on Shirur and Khed talukas of Pune district. Pune district is situated at 17.54–19.24-degree North latitude and 73.19–75.10-degree eastern longitude, located in western part of Maharashtra state, India with Shirur located at 18.8250° N, 74.3776° E and Khed at 18.8405° N, 73.9072° E. In arrears to the geographical conditions, Pune district has uneven rainfall distribution. The Western part of district adjoining West coast having mountainous area with forest cover. Hence, rainfall intensity is more in this region than the eastern parts. Mainly, southwest monsoon winds are responsible for rain in summer. About 87% of rainfall is during the monsoon months June to September with maximum intensity in the month of July and August. Around 73% of cropped area is cultivated under rainfed conditions. Agriculture is Rabi crop dominated in these areas and the second being the Kharif Crops. Summer crop production is comparatively less. Shirur is on the banks of the Ghod River on the eastern boundary of Pune District. Shirur is influenced by the semi-arid climate. Khed lies in the western region of Pune district with river Indrayani flowing through this taluka with a somewhat cool climate.

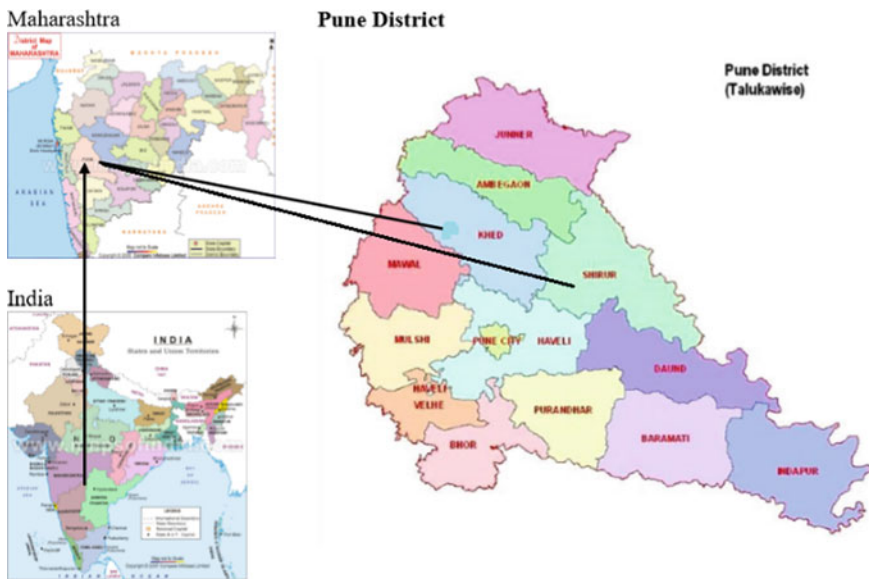


Fig. 1 Location map of study area

3 Methodology

In the following research, Vegetation condition is identified for long-term sequence for the year 2000, 2003, 2006, 2009,2012,2015 and 2018 of months January, May, September and December. For the analysis of NDVI and land surface temperature (LST) multispectral and thermal data from Landsat are used. The dataset used for the year 2000, 2003, 2006, 2009, 2012 is Landsat 7 ETM+ and for 2015 and 2018 is Landsat 8 OLI. The following flowchart describes the methodology briefly (Fig. 2).

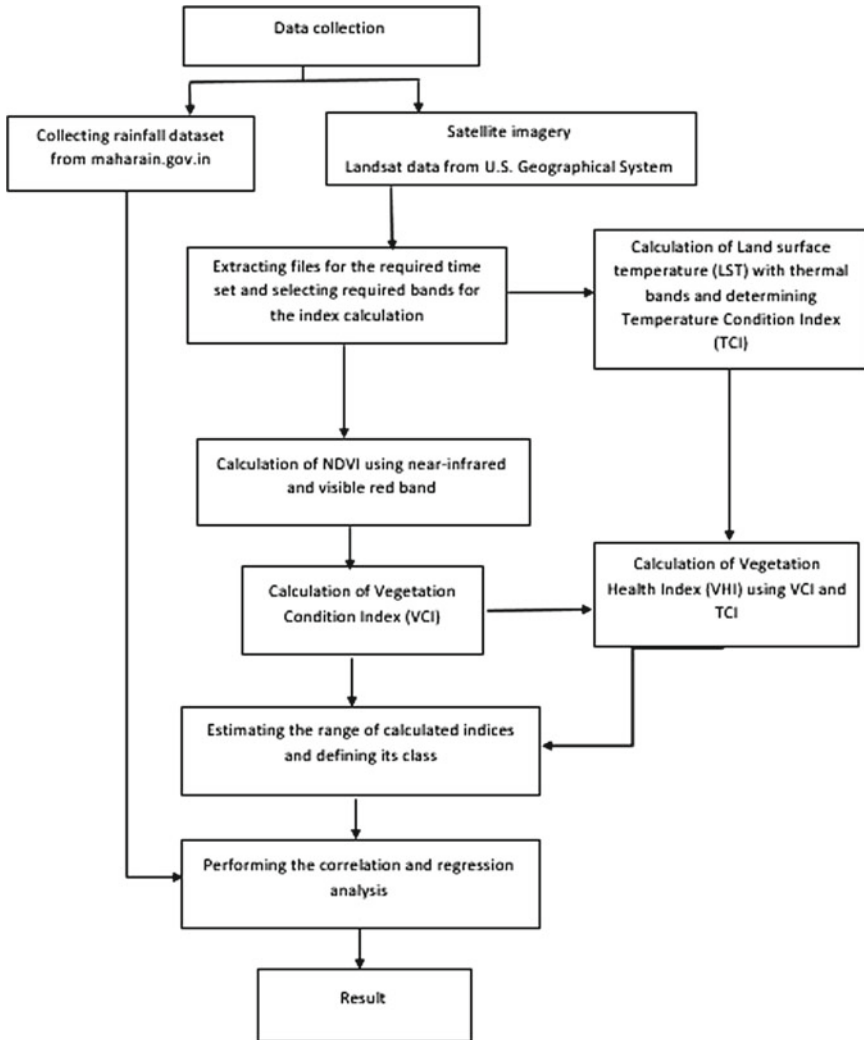


Fig. 2 Methodology flowchart

NDVI is expressed by the formula:

$$NDVI = \frac{NIR - VIS}{NIR + VIS} \tag{1}$$

NDVI calculation for the Landsat 7 ETM+ is calculated using relation:

$$NDVI = \frac{band4 - band3}{band4 + band3} \tag{2}$$

NDVI calculation for the Landsat 8 OLI is calculated using relation:

$$NDVI = \frac{band5 - band4}{band5 + band4} \tag{3}$$

where, NIR = Near Infrared Light, VIS = Visible Light.

Provided, bands are having their usual meaning according to the data set used. The classification of vegetative cover based on the NDVI values is according to the following Table 1 [1].

NDVI and LST time series have the capability to set out the various dynamics of dry conditions [2]. Landsat data sets are adopted for the calculation of vegetation condition index (VCI) and temperature condition (TCI). TCI is obtained from the calculated Land surface temperature which is calculated following the procedure in Landsat handbook provided by U.S Geological Survey. Combined VCI, TCI data is then used to compute VHI. The calculation of VHI is performed based on the relation shown below. VCI is determined from Normalized Difference Vegetation Index (NDVI) to monitor vegetation conditions [3]. The VCI data is obtained by the following equation.

$$VCI = \frac{(NDVI_a - NDVI_{min})}{NDVI_{max} - NDVI_{min}} \times 100 \tag{4}$$

Here, NDVI_a denotes the value of NDVI for current month, NDVI_{min}, NDVI_{max} represents the minimum, maximum NDVI values sequentially, during span of observation. VCI has been commended as drought tool. But, solely utilizing VCI is not sufficient to relate to drought analysis precisely. Thus, TCI is used to seize

Table 1 NDVI classification range

Cover type	NDVI range
Dense green leafy vegetation	0.500–1.000
Medium green leafy vegetation	0.140–0.500
Light green leafy vegetation	0.090–0.140
Bare soil	0.025–0.090
Swampy areas/wet lands	–0.046 to 0.025
Water bodies	–1 to 0.046

Table 2 VHI classification range

Drought class	VHI
Extreme drought	<10
Severe drought	10–20
Moderate drought	20–30
Mild drought	30–40
No drought	>40

various replication of vegetation together with in-situ temperature as supplementary data. This can be attained by using thermal channels for drought monitoring. TCI calculation is carried out using the following relation

$$TCI = \frac{(LST_{max} - LST_a)}{(LST_{max} + LST_{min})} \times 100 \quad (5)$$

where LST_a is the LST value for the current month, LST_{max} and LST_{min} represent maximum and minimum LST values respectively. VHI is calculated to analyse vegetation stress to define the drought severity. VHI is expressed as shown below

$$VHI = \alpha VCI + (1 - \alpha)TCI \quad (6)$$

VHI is expressed as a composition of VCI and TCI by parameter α . Here, parameter α in equation takes a value between 0 and 1. Since there is no foregoing information of its contribution for moisture and temperature conditions to the vegetation health, the value of α is generally taken as 0.5 [4, 5]. Following the classification of drought monitoring is used on the basis of following Table 2 [6]

Further, rainfall data is obtained from the Department of Agriculture, Maharashtra state for rainfall data. The annual precipitation was considered for the analysis. With the calculated data for NDVI, VHI, LST and rainfall data collected, correlation and linear regression analysis is carried out and the results of which are discussed below.

4 Results and Discussion

4.1 Results of NDVI

The NDVI image of Khed and Shirur are tabulated for month of January, May, September and December of the year 2000, 2006, 2009, 2012, 2015 and 2018 (Fig. 3).

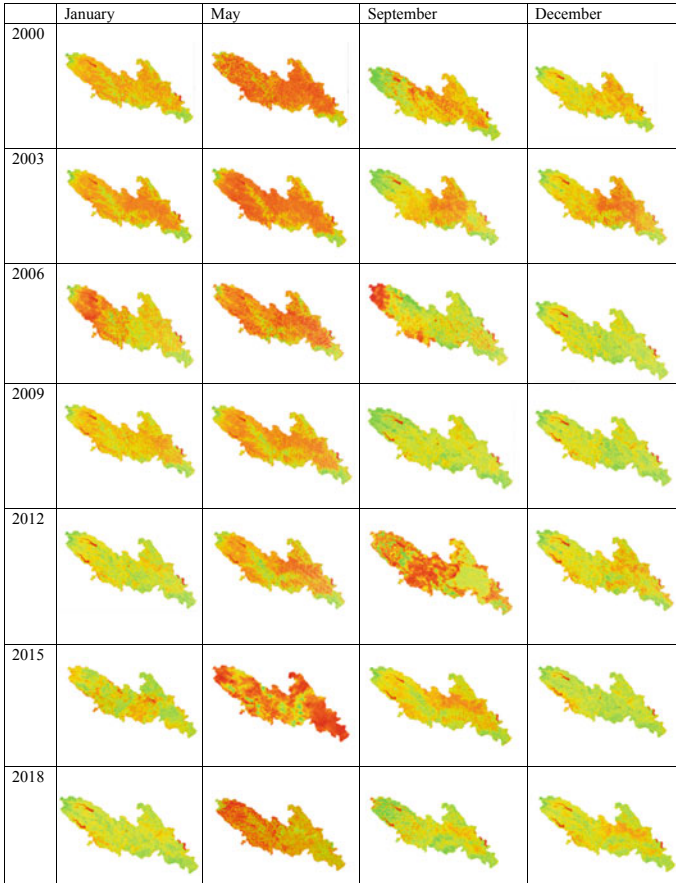


Fig. 3 NDVI images

4.2 Results of VHI

See Fig. 4.

4.3 Classification

See Table 3.

Here, the values tabulated clearly illustrate the class and severity of NDVI and VHI. Temperature being an important factor in the calculation of VHI, it is to be noted that in fact of having high NDVI values, its VHI value obtained can be less. In the year 2012, Shirur with NDVI value is having VHI in class of mild drought but

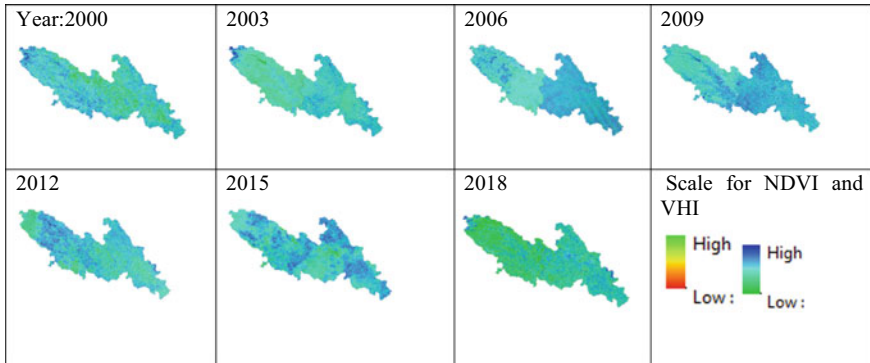


Fig. 4 VHI images

Table 3 Calculated NVDI and VHI values

Year	Block	NDVI Class (Based on the maximum values obtained)	VHI class
2000	Shirur	Medium green vegetation (0.55)	24.3–49.3 (No drought)
	Khed	Dense green vegetation (0.83)	23.6–74.32 (No drought)
2003	Shirur	Medium green vegetation (0.31)	25.4–30.4 (Moderate drought)
	Khed	Medium green vegetation (0.61)	29.4–53.55 (No drought)
2006	Shirur	Dense green vegetation (0.890)	26.3–52.3 (No drought)
	Khed	Dense green vegetation (0.897)	25.1–89.1 (No drought)
2009	Shirur	Dense green vegetation (0.942)	25.8–54.8 (No drought)
	Khed	Dense green vegetation (0.73)	25.16–68.96 (No drought)
2012	Shirur	Medium green vegetation (0.71)	10.42–36.6 (Mild drought)
	Khed	Dense green vegetation (0.69)	13.9–49.14 (No drought)
2015	Shirur	Medium green vegetation (0.579)	25.90–39.70(Mild drought)
	Khed	Dense green vegetation (0.81)	25.6–80.19 (No drought)
2018	Shirur	Light green vegetation (0.398)	29.32–30.9 (Moderate drought)
	Khed	Dense green vegetation (0.77)	31.76–75.68 (No drought)

Table 4 Correlation values

Block	NDVI and VHI	NDVI and Rainfall	VHI and Rainfall
Shirur	0.838127	0.890172	0.889107
Khed	0.909356	0.778066	0.8072

for Khed NDVI is 0.69 and having VHI in the class of no drought category, as Shirur has a hot and dry climate with Khed having somewhat cool climate.

4.4 Correlation and Liner Regression Analysis Results

Correlation between NDVI, VHI and annual Rainfall (in mm) for Shirur and Khed (Table 4).

It is found that these indices proficiently be used to identify the spatio-temporal extent of agricultural drought. Furthermore, it explains classes of drought severity in the research areas through combined examination of vegetation health through vegetation condition along with temperature condition of vegetation with the help of VHI. Thus, the variables under the study are correlated with the strength of their association with Shirur and Khed as shown above.

Correlation between NDVI and Temperature.

The result obtained for the correlation of NDVI and temperature is negative which is Shirur corr. factor = -0.396 and Khed corr. factor = -0.637 which denotes that the rise in temperature lowers the value of NDVI.

- (1) Regression analysis for NDVI and annual rainfall (in mm) (Table 5).
- (2) Regression analysis for VHI and annual rainfall (in mm) (Table 6).

Table 5 Regression analysis for NDVI and annual rainfall (in mm)

Block	r^2	Significance value	Equation
Shirur	0.7924	0.0072	$Y = 0.2428 + 0.000821 \times (X)$
Khed	0.60538	0.0398	$Y = 0.62179 + 0.0001998 \times (X)$

Table 6 Regression analysis for VHI and annual rainfall (in mm)

Block	r^2	Significance value	Equation
Shirur	0.7905	0.0074	$Y = 25.65103 + 0.03508 \times (X)$
Khed	0.6515	0.0281	$Y = 48.0341 + 0.03163 \times (X)$

- (a) r^2 value: The value of r^2 obtained is 0.7924 (for Shirur NDVI & rainfall), the value closer to the 1, better the regression line fits the data. To check the significance of the result obtained statistically, significance value is observed which is 0.0072 (<0.05 Pearson coefficient) and is ok.
- (b) Linear Regression equation: $Y = 0.2428 + 0.000821 \times (X)$ (for Shirur case). Here, Y = Shirur annual rainfall and X = NDVI values. The equation illustrates that 1 unit change in rainfall, changes NDVI value by 0.00821 units. Thus, these coefficients can be used to forecast the change in vegetative cover. The equations developed are useful in forecasting, crop insurance design and drought monitoring.

5 Conclusion

Study endeavours to identify the spatio-temporal extent of vegetative cover and agricultural drought for Shirur and Khed talukas with the use of remote sensing data based on NDVI, VHI and thus can be successfully used to identify the same. It explains the severity of drought with its class in the research areas by analysing both vegetation health by vegetation condition and temperature condition. Based on VHI values, Shirur area falls under medium green vegetation with moderate drought and Khed area with dense green vegetation with no drought. NDVI, VHI, rainfall and temperature under the study are correlated with the strength of their association for Shirur area and Khed area in the range of 77% to 90%. The estimated results of VHI lead to monitor the commencement of agricultural drought as an early warning system. The correlation and linear regression analysis can be made useful to forecast the vegetative cover condition. Results can further be useful for land use/ land cover database creation, identification of multiple crop and soil type.

Acknowledgements Authors are appreciatively grateful to US Geological Survey (USGS) for provision of Landsat dataset and Department of Agriculture, Maharashtra state for rainfall data used in the research.

References

1. Bisrat E, Berhanu (2018) Identification of surface water storing sites using Topographic Wetness Index (TWI) and Normalized Difference Vegetation Index (NDVI). *J Nat Resour Develop* 08:91–100. <https://doi.org/10.5027/jnrd.v8i0.09>
2. Wang H, Lin H, Liu D (2014) Remotely sensed drought index and its responses to meteorological drought in Southwest China. *Remote Sens Lett* 5(5):413–422
3. Kogan FN (1995) Application of vegetation index and brightness temperature for drought detection. *Adv Space Res* 15(11):91100
4. Rojas O, Vrieling A, Rembold F (2011) Assessing drought probability for agricultural areas in Africa with coarse resolution remote sensing imagery. *Remote Sens Environ* 115:343–352

5. Kogan FN (2001) Operational space technology for global vegetation assessment. Bull Am Meterological Soc 82(9):194964
6. Sholihah RI (2016) Identification of agricultural drought extent based on vegetation health indices of Landsat data. Procedia Environ Sci 33:14–20

Comparison of Suspended Growth and IFAS Process for Textile Wastewater Treatment



Sharon Sudhakar, Nandini Moondra, and R. A. Christian

Abstract Water is an essential commodity that is getting scarce due to its overuse. The primary consumers of water resources are the industries, and due to industrialization, the generation of wastewater is increasing. When discharged into water bodies, this wastewater contaminates the water bodies greatly, and thus its treatment is of utmost importance. The treatment facility is not economical for small and medium-scale industries. Hence, for such industries, a Common Effluent Treatment facility (CETP) is provided where the wastewater from a cluster of industries is collected, treated and finally discharged. The present study treats CETP wastewater using a sequencing batch reactor (SBR) with suspended biomass and an SBR-IFAS, which uses a combined suspended and attached growth process. The study was done on homogeneous textile wastewater from a CETP. HRT for the system was 10 h, with 9 h aeration and 1 h settling. The pre-treated wastewater was used as an influent in the study with an inlet COD concentration varying between 600 and 1160 mg/L. After the treatment in the SBR reactor, the maximum COD removal was 65.7% for homogeneous textile wastewater. Chromium removal was 48%, at a maximum suspended MLSS of 2852 mg/L with an SVI of 30 mL/g. In SBR- IFAS, maximum COD removal was 74.28%, chromium removal was 53.33% with a suspended MLSS of 2600 mg/L and attached biomass of 6.72 mg/m with SVI of 96 mL/g. Thus, the study indicates that the IFAS system incorporated in SBR will enhance the treatment efficiency while reducing the effluent concentration and help treat a larger volume of industrial wastewater for the same footprint.

Keywords Textile wastewater · SBR · SBR-IFAS · Ring lace · COD

1 Introduction

Water resources are getting reduced daily, so its sustainable use is considered one of the world's most critical environmental issues. Wastewater produced contains

S. Sudhakar (✉) · N. Moondra · R. A. Christian
Civil Engineering Department, SVNIT Surat, Surat, India
e-mail: sharonsudhakar6594@gmail.com

© The Author(s), under exclusive license to Springer Nature Singapore Pte Ltd. 2023
M. S. Ranadive et al. (eds.), *Recent Trends in Construction Technology and Management*, Lecture Notes in Civil Engineering 260,
https://doi.org/10.1007/978-981-19-2145-2_34

437

many pollutants like COD, phenols, heavy metals, etc., 12. The scarcity of water is increasing. Hence, the treatment of wastewater generated from various sources such as industries, agriculture, etc., is considered an effective solution for it to be reused or disposed of. Due to the growing industries globally, pollution from industries has become a significant concern that threatens the environment. It was seen that nearly 50% of small and medium scale industries are significant producers of industrial wastewater. In India, small-scale industries are very high, and these industries produce wastewater with very toxic pollutants, which makes treatment necessary before its disposal. Small scale industries cannot afford treatment systems because of space constraints, the need for skilled laborers for operation and maintenance, capital cost, etc. Hence, many other facilities were considered for the centralized treatment of such wastewater.

The aim of establishing CETP is to bring effluents of small and medium scale industries to a centralized treatment plant. CETP can be a better and economical option as equalization and neutralization are done more often. The effluent fluctuates in quality and quantity from different industries such as pharmaceutical, chemical, textile etc. The inlet characteristics of the wastewater vary depending on the industry and its processes. Therefore, this mixed wastewater treatment has gained more attention [1].

The effluent at CETP undergoes primary, secondary and tertiary treatment before being disposed. The CETP works continuously and has a series of operations like screening, equalization, primary clarifier for removing suspended solids present, biological treatment, secondary clarifier, advanced treatments, etc.

A wide variety of industries are present in India and along with the world. Industries produce wastewater based on the manufacturing process involved. Some major industries that use a significant amount of water for processing generate massive wastewater, including textiles, dairies, paper and pulp, chemicals, distillery, etc. The wastewater from the textile industry has high color, high organic and TDS load. The textile wastewater generated is highly polluted due to the presence of dyes, which are not readily amenable to biological treatment; hence primary treatment should be provided before secondary treatment. The color present in water causes scarcity of light, which is essential for developing aquatic organisms. Hence for the discharge of textile wastewater into the river, many treatment processes, including physical, chemical, biochemical, and hybrid treatment processes, have been developed to treat it economically and efficiently [2].

1.1 Integrated Fixed-Film Activated Sludge (IFAS) Process

The integrated fixed-film activated sludge (IFAS) process combines suspended and the attached growth systems. The biofilm in IFAS provides many advantages over conventional methods such as improved nutrient removal, larger solid retention time and high removal efficiency of anthropogenic pollutants. IFAS effectively removes

dissolved organic matter as carbon and offers high nitrification and de-nitrification [3].

The mode of operation for IFAS is similar to the conventional activated sludge process. The IFAS media is available in many types such as plastic elements, webs, sponges, string type, lace type, etc., and are manufactured by many companies. The biomass is attached to the media, which helps in reducing the loading on the secondary clarifier. Loading on secondary clarifiers is reduced due to biomass attachment on the media [4].

This present study compares the sequencing batch reactor (SBR) and sequencing batch reactor with an integrated fixed-film activated sludge process (SBR-IFAS) for pre-treated wastewater from CETP.

The study involves analysing pH, dissolved oxygen, COD and chromium for homogeneous textile wastewater in both reactors and analysing the mixed liquor suspended solids grown in suspended and attached form.

2 Materials and Methodology

2.1 Plant Setup

The setup of the experiment consisted of two reactors of 15 L each. One reactor is an SBR with suspended biomass and another reactor is with IFAS strips, as shown in Fig. 1. Both reactors were provided with outlets at 40, and 50% of the volume and 40% is utilized in the present study. Aeration in the reactor was provided with the help of aquarium pumps. IFAS reactor contained ring lace as fixed media made of PVC. Five media of 14.5 cm height were inserted such that they remained suspended and fixed. The reactors were covered with nets to prevent the breeding of mosquitoes. Influent feeding was done as a batch process daily to maintain the HRT of 10 h during the study.

2.2 Raw Wastewater Characteristics

The wastewater was analysed for parameters like pH, Dissolved Oxygen (DO), mixed liquor suspended solids (MLSS), chemical oxygen demand (COD) and chromium. Table 1 illustrates the initial characteristics of wastewater. The wastewater for the study was collected from CETP containing homogeneous textile wastewater coming from 150 dyeing and printing industry. The wastewater collected from the CETP used for the present study has undergone primary treatment such as screening and coagulation using lime, PAC, polyelectrolyte, etc.

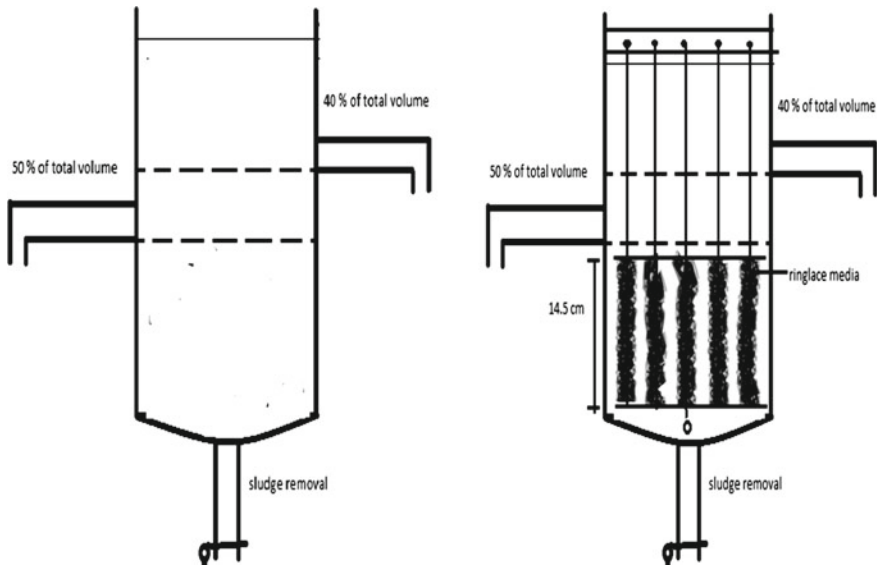


Fig. 1 Reactor setup for SBR and SBR-IFAS

Table 1 Initial characteristics of wastewater

Wastewater Sample	pH	TSS (mg/L)	DO (mg/L)	COD (mg/L)	Chromium (mg/L)
Textile wastewater	7.1–8.1	480–2000	0	600–1160	0.5–1

2.3 IFAS and Seeding

Seeding was done to acclimatize the bacteria in the new environment by aerating the reactor for a day followed by 1 h of settling. After settling, the supernatant was replaced by a fresh influent. MLSS of the seeded sample was around 1200 mg/L. Ring lace media is a fixed type of IFAS media used in biological wastewater treatment that will be submerged entirely even after decanting. It is a flexible PVC rope type of material attached to strands, as shown in Fig. 2. The strands contain loops that protrude out of them. Each loop has an approximate diameter of 5 mm, and aluminum frames were used to hold these media at the top and bottom of modules [5]. The strips were arranged so that it remained submerged after decanting to maintain the biomass grown on them.



Fig. 2 Ring lace media used before the growth of biomass and after the growth of biomass

2.4 Methodology

The biomass provided as seeding from aeration tank of CETP was aerated for 24 h, and 40% of the effluent decanted after 1 h settling and filled with homogeneous textile wastewater as an influent. The reactors were aerated for 9 h, and 1 h settled, and 40% of the reactor volume was collected as an effluent after settling. The treated effluent was collected and analysed for pH, DO, COD, MLSS and chromium. The reactors were operated for 35 days. All the parameters were analysed according to standard procedure as per APHA. The attached growth on Ring lace media, as shown in Fig. 2, was analysed for MLSS by oven drying method.

3 Result and Discussion

3.1 Variation of pH

pH is an essential factor in the wastewater treatment process. Still, it to be in the optimum range (6.5–8.5) is necessary to grow microorganisms (Metcalf and [6]. The inlet sample's pH is of the range 7–8.3, and after treatment in both SBR-IFAS and SBR reactor, pH is noted to have decreased as given in Fig. 3. Treatment did not impart considerable change in pH. A decrease in the pH of wastewater after the treatment process was probably due to the release of carbon dioxide on organic matter's biodegradation.

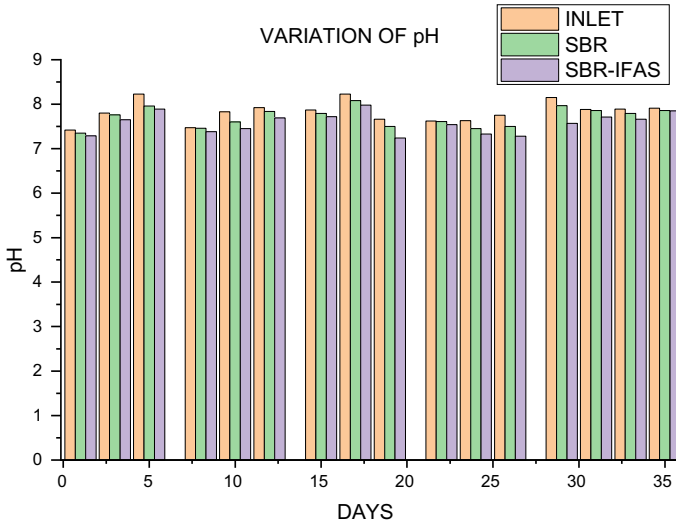


Fig. 3 Variation of pH

3.2 Variation of Dissolved Oxygen (DO)

DO being a vital parameter is necessary for the effluent to be discharged into water bodies as it affects their properties. It is seen that initially, DO in both SBR-IFAS and SBR reactors was nearly zero as the removal of organic matter in wastewater was significantly less due to the acclimatizing period of biomass. After treatment, DO in both reactors increased, which might be due to the increased degradation of organic matter present in wastewater by the biomass. But with further increase in MLSS, the COD removal reduced as the reactor has high biomass, and this biomass with less food can contribute to organics and start to degrade. Effluent DO was higher; this is basically due to a decrease in COD due to biological treatment. DO in the SBR-IFAS reactor varied from 0 to 2.8 mg/L, and in SBR, it varied from 0 to 2.4 mg/L. An increase of DO to 2.4 mg/L in IFAS caused good removal, and the decrease towards the end may have been due to the reduction in active biomass due to high MLSS, causing the reduction in F/M ratio. The excess biomass contributes to organic matter, which will degrade the quality and hence some amount of wasting of active biomass will be necessary. The variation in DO for both reactors is as given in Fig. 4.

3.3 Variation of Chemical Oxygen Demand (COD)

The wastewater, after undergoing pre-treatment, has an inlet COD in the range 600–1160 mg/L. The SBR-IFAS reactor showed a reduction in effluent COD varying from

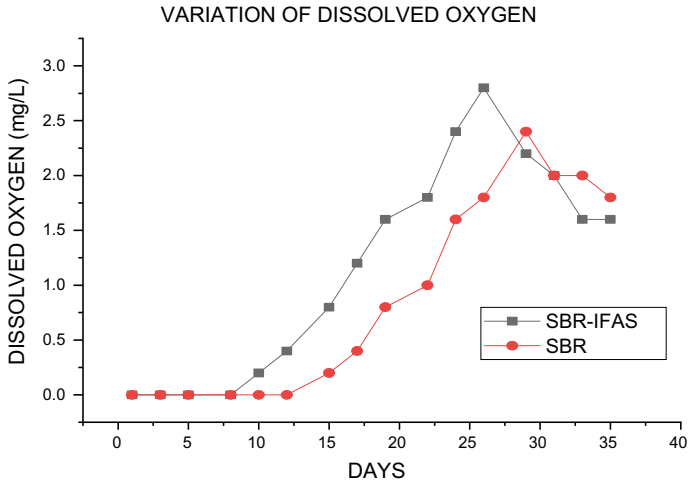


Fig. 4 Variation of dissolved oxygen

180 to 720 mg/L with a removal varying from 12.5% initially to maximum removal of 74% with the biological treatment provided for an HRT of 10 h, and SBR showed an effluent COD of 240–780 mg/L with a percentage removal of 10–65% as shown in Fig. 5. The biomass grown on the media might also contribute to the removal of organic matter in wastewater. After maximum removal of 74%, the COD removal decreased; this may be due to increased biomass, thus overloading the reactor. In the present study, the TDS of influent was in the range of 2000-2500 mg/L, and after

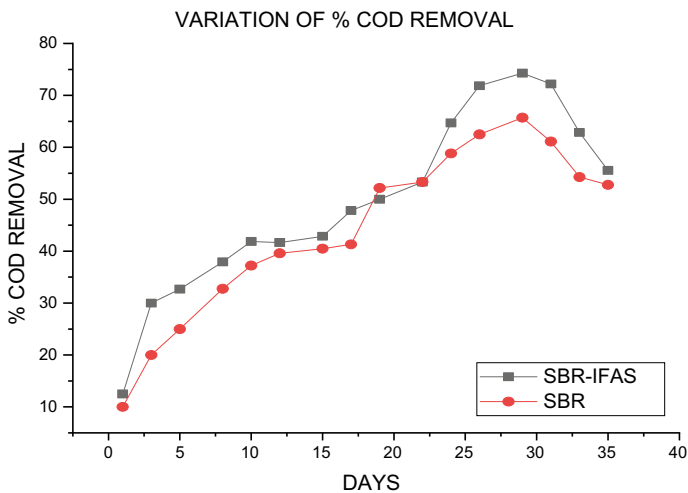


Fig. 5 Variation of % COD removal

treatment, there was no considerable reduction in TDS. This increased amount of TDS also might have reduced the COD removal efficiency. A study on the treatment of synthetic textile wastewater and raw was done based on variation in TDS, it was seen that a 24 h cycle time increase in TDS up to 5000 mg/L reduced the COD removal and COD removal was seen to be 59.44%. The study was seen to reduce the COD removal due to the increased TDS effect on activated sludge. In the present study, the TDS of influent was in the range of 2000-2500 mg/L, and after treatment, there was no considerable reduction in TDS. As per literature presence of TDS decreases the COD removal, and thus the overall efficiency of the reactor was less than 75% in the removal of COD. As per the literature study on activated sludge for textile wastewater treatment for an HRT of 18 h, the removal efficiency was 77% at MLVSS of 5000 mg/L. The study proved that with an increase in MLVSS and HRT, more removal could be obtained [7].

The present study was on a fixed HRT of 10 h at a maximum VSS of 1430 mg/L in the IFAS reactor and 1602 mg/L in the SBR reactor. But the maximum removal based on the figure was still considerably high; this can be because the wastewater obtained was already pretreated. The biomass on the IFAS media might be more volatile as more removal was obtained in the IFAS reactor. With a further increase in HRT and MLVSS, more removal can be achieved. Previous studies showed that for treatment using ASP, COD removal for textile wastewater was seen to be 89% at an HRT of 2 days [8]. The presence of dye can reduce removal efficiency and hence requires more HRT. HRT being 10 h gave maximum removal of 74% in SBR-IFAS and 65% in SBR. But in the present study, the presence of dye was not heavily visible and also the presence of heavy metals like chromium was less hence more removal.

3.4 Variation of Mixed Liquor Suspended Solids (MLSS)

In the present study, the variation of mixed liquor suspended solids (MLSS) was studied four times a week during the study period. It was seen that MLSS kept on increasing daily in both the reactors. This increase in MLSS caused an increase in COD removal. MLSS in the SBR-IFAS reactor increased from 660 to 2600 mg/L with a final MLVSS concentration of 1430 mg/L, and in the SBR reactor, it increased from 610 to 2852 mg/L and VSS of 1602 mg/L in suspended form and IFAS as attached growth it was seen to be 6.72 mg/m. The variation of MLSS in both reactors is given in Fig. 6. Initial seeding to the reactor was done from the CETP aeration basin, which had an MLSS concentration of 1200 mg/L, and after 24 h and 1 h, the settling sample from the aeration tank was replaced with 6 L of effluent. In the present study for MLSS of 2852 mg/L, the removal was 65.7% in the SBR reactor and 74% for a suspended MLSS of 2600 mg/L in SBR-IFAS. A literature study on textile wastewater also showed that COD removal was 60% for MLVSS concentration of 3500 mg/L [9]. The increased removal can also be due to the non-interference of harmful components like chromium that affect the efficiency of biomass in the removal of organics. In the IFAS reactor, some biomass attached to the media may have contributed to the

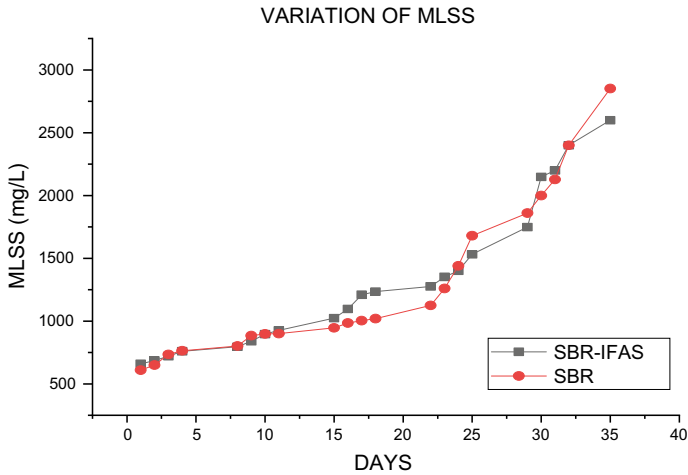


Fig. 6 Variation of mixed liquor suspended solids (MLSS)

removal. Analysis of the variation of MLSS in previous studies was compared with the present study. A study on textile CETP in Rajasthan showed removal of COD was at 75–85% at an MLSS concentration of 3500 mg/L for an HRT of 12–15 h in an aeration tank after primary treatment [10], which is similar to the removal efficiency in the present study.

3.4.1 Variation of Chromium (Cr^{6+})

If discharged into the river, chromium being a heavy metal, can damage the aquatic flora and fauna, and chromium consumption is harmful to humans. Textile wastewater supplied was colored. Thus, chromium was analysed as textile wastewater contains chromium due to dyeing. The wastewater was seen to have chromium in the range 0.5–1.02 mg/L, which is within limits per standards; this chromium reduction may be due to coagulants added. The effect of biomass in SBR-IFAS and SBR was analysed for the removal of chromium. After treatment using IFAS, chromium removal varied from 36.67% to 50%, and SBR reduction varied from 30 to 48.03%, as shown in Fig. 7. Studies have shown that activated sludge can remove chromium (Cr^{6+}) by 40% but is dependent on sludge acclimatization and a longer hydraulic retention time. According to the literature, as inlet chromium is less than 1 mg/L, it is proven that Chromium less than 5 mg/L will not affect COD removal [11]. The minimum value of effluent through IFAS treatment was 0.3 mg/L, limiting the discharge limit to 2 mg/L. The amount of chromium present is mainly due to the usage of dye for the coloring of textiles.

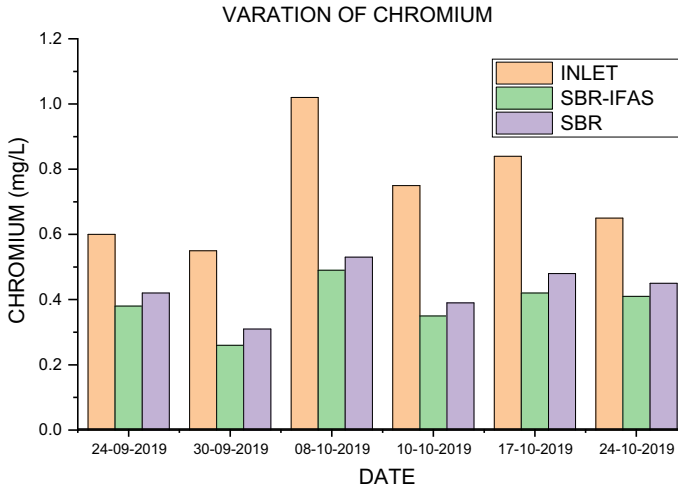


Fig. 7 Variation of chromium (Cr^{6+})

3.5 Sludge Volume Index

Sludge volume index (SVI) is used to analyse the sludge's settling characteristics in the present study. The sludge produced after treatment of CETP wastewater containing wastewater from textile industries was found in both SBR and SBR-IFAS. It was seen that SBR produced a sludge volume of 8 mL per 100 mL, thus giving an approximate sludge volume index (SVI) of 28 mL/g. For IFAS, a sludge volume of 25 mL per 100 mL, maintaining an SVI of 96 mL/g considering only the MLSS present in the suspended form for MLSS of 2852 and 2600 mg/L. The settling of sludge from the SBR-IFAS reactor was seen to be better than the SBR reactor.

4 Conclusion

Based on the study, the conclusions made were:

- A study was done to analyse the removal efficiency of SBR and SBR IFAS for textile wastewater.
- Based on the study, the SBR-IFAS treatment DO varied from 0 to 2.8 mg/L. The MLSS in suspended form was 2600 mg/L with a maximum COD removal of 74.28%, chromium removal of 53.33% and pH of 7.3–8; attached growth was measured by weight difference method obtained as 6.72 mg/m with an SVI of 96 mL/gm.

- For SBR, DO was in the range 0–2.4 mg/L with a maximum MLSS of 2852 mg/L and a maximum COD removal of 65.7%. Chromium removal was 48.03%, pH was maintained at 7.4–8.2, SVI was 30 mL/gm.
- Based on the removal efficiency of the COD SBR –IFAS reactor performed better than the SBR reactor, additional biomass grown on the Ring lace helped in improving the performance.
- The study was done without addition of nutrients; the IFAS reactor might have performed well if nutrients are supplied and also by maintaining the F/M ratio.

References

1. Popat A, Nidheesh PV, Singh TSA, Kumar MS (2019) Mixed industrial wastewater treatment by combined electrochemical advanced oxidation and biological processes. *Chemosphere* 237:124419
2. Holkar CR, Jadhav AJ, Pinjari DV, Mahamuni NM, Pandit AB (2016) A critical review on textile wastewater treatments: possible approaches. *J Environ Manage* 182:351–366
3. Waqas S, Bilad MR, Man Z, Wibisono Y, Jaafar J, Mahlia TMI, Khan AL, Aslam M (2020) Recent progress in integrated fixed-film activated sludge process for wastewater treatment: a review. *Journal Environ Manage* 268:110718
4. Hait S, Mazumder D (2008) Scope of improvement of treatment capacity of activated sludge process by hybrid modification. *J Environ Eng* 7:147–158
5. Sen D, Farren G, Sturdevant J, Copithorn RR (2006) Case study of an IFAS system—Over 10 years of experience 4309–4324
6. Metcalf & Eddy, Inc. (2017) *Wastewater engineering: treatment and reuse*. Boston :McGraw-Hill
7. Mirbolooki H, Amirmezahad R, Pendashteh AR (2017) Treatment of high saline textile wastewater by activated sludge microorganisms. *J Appl Res Technol* 15:167–172
8. Maddad M, Abid S, Hamdi M, Boullagui H (2018) Reduction of adsorbed dyes content in the discharged sludge coming from an industrial textile wastewater treatment plant using aerobic activated sludge process. *J Environ Eng* 223:936–946
9. Kumar K, Singh GK, Dastidar MG, Sreerishnan TR (2014) Effect of mixed liquor volatile suspended solids (MLVSS) and hydraulic retention time (HRT) on the performance of activated sludge process during the biotreatment of real textile wastewater. *Water Resour Ind* 5:1–8
10. Pophali GR, Kaul SN, Mathur S (2003) Influence of hydraulic shock loads and TDS on the performance of large-scale CETPs treating textile effluents in India. *Water Res* 37:353–361
11. Vaipoulou E, Gikas P (2012) Effects of chromium on activated sludge and on the performance of wastewater treatment plants: a review. *Water Res* 46:549–570
12. Mojiri A, Ohashi A, Ozaki N, Kandaichi T (2018) Pollutants removal from synthetic wastewater by the combined electrochemical, adsorption and sequencing batch reactor (SBR). *Ecotoxicol Environ Saf* 137–144

Innovative Arch Type Bridge Cum Bandhara for Economical and Quick Implementation of Jal Jeevan Mission



P. L. Bongirwar and Sanjay Dahasahasra

Abstract Total number of villages in India are 6,40,932, out of which 5,97,608 are inhabited villages having total 19.12 crore households. Jal Jeevan Mission (JJM) has been established by the government of India (GoI) with the provision of Rs 3.5 lakh crores to supply piped drinking water by functional household Tap connection (FHTC) by 2024 to all the rural population at the rate of 55 L per capita day. It can be noted that 75% of villages in India are below 1500 population. Due to inadequate water, especially in summer, tankers are required to be deployed at a very heavy cost. Generally, the water source at the village level is not reliable and assured, hence Regional Water Supply Schemes (RWSS) are planned at a cost of 150 lakhs to 200 lakhs per village and are executed to meet the need of cluster of villages. Each village is located near a natural stream, called Nalla which generally has a steep slope, hence rainwater drains off fast once the rain stops. They, therefore, do not help the ground recharging. Such villages are always connected by a small bridge which is proposed to be converted into bridge cum bandhara to act as a storage and crossing structure. After extensive model analysis and research, a new innovative affordable elliptical concrete arch is evolved which is permanently fixed to piers to create water storage up to a depth of 2.4 m. This water is proposed to be stored in nearby “Shet Tale” for meeting the need of drinking water and irrigation. Artificial recharging also can be adopted. Several structures have been constructed and it has revealed that besides meeting the drinking water need, we can have irrigation for 150–200 acres per village. Construction techniques are developed to complete structures in just 20 days and the cost of storage is 60% of norms as well 60% compared to the cost of cement weir/plug. The total cost per village (including BCB, solar pumps, Shet Tale, and filtering system) is on an average Rs 50 Lakhs per village against 150 lakhs to 200 lakhs in regional water supply scheme. Government intends to double the farmer’s income and this objective will be fulfilled with this innovative design. Objective of this paper is to discuss this innovative technique. It is recommended

P. L. Bongirwar (✉)

Public Works Department, Govt. of Maharashtra, Mumbai, India

e-mail: plbongirwar@rediffmail.com

S. Dahasahasra

Maharashtra Jeevan Pradhikaran, Mumbai, India

© The Author(s), under exclusive license to Springer Nature Singapore Pte Ltd. 2023

449

M. S. Ranadive et al. (eds.), *Recent Trends in Construction Technology*

and Management, Lecture Notes in Civil Engineering 260,

https://doi.org/10.1007/978-981-19-2145-2_35

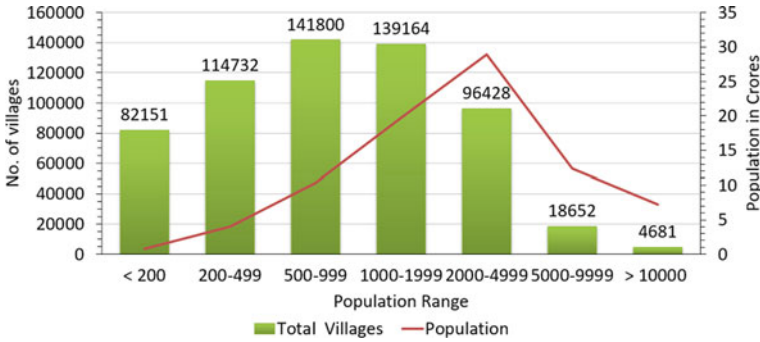


Fig. 1 Population wise grouping of villages

that this model be adopted by JJM to achieve FHTC at minimum cost and earlier than 2024.

Keywords Jal Jivan Mission · Bandhara · Drinking water · Irrigation

1 Introduction

Total number of villages in India are 6, 40, 932, out of which 5, 97,608 are inhabited villages having total of 19.12 crore households. Population-wise grouping of villages is shown in Fig. 1.

Jal Jeevan Mission (JJM) has been set by the GoI to supply piped water to all the rural population at the rate of 55 L per day. Out of 19.12 crores, as of 18 Jan 2021, there still remains 12.72 crore households to be supplied with Functional Household Tap Connections (FHTC). It can be noted that 75% of villages are below 1,500 populations. If water supply is provided to these villages, then the goal of JJM can be achieved.

Objective of innovative and cost-effective initiative is to make water supply schemes with sustainable water sources at village level using Arch Type Bridge cum Bandhara (BCB).

2 Scenario in Rural Water Supply

2.1 Supply of Water by Tanker

Due to inadequate water especially in summer, tankers are required to be deployed at a very heavy cost. In Nagpur district, Rs 175 lakhs was spent to supply drinking water by tankers to 45 thirsty towns/villages, out of which 15 are below 1500 population.

Fig. 2 Long queue for getting drinking water



Fig. 3 Rush for getting their buckets filled, when the tanker comes in the village



In Amravati, Rs 180 lakhs was spent for 65 villages, out of which 25 villages are below 1500 population. The supply by tanker creates a pathetic situation as can be seen from Figs. 2 and 3.

2.2 Regional Water Scheme

If the water source at the village level is not reliable and assured, Regional Water Supply Schemes (RWSS) are generally planned to meet the need of a cluster of villages. The source of RWSS is surface water from the reservoir of dam, major rivers, or natural lakes. Average cost per village is Rs 1.5–2 crore and per person the cost is Rs 5500–6000. Data of a few Regional Schemes are shown in Table 1.

Table 1 Data of a few regional scheme

SN	Name	No. of villages	Population rage	Below Population of 1500	Cost per village (Rs lakhs)	Per person (Rs)	Source
1	Pompbhurna	15	500–3200	10	192	5911	Wainganga river
2	Khambhora	60	140–3150	44	85	5654	Pick-up weir on Katepurna
3	Mul	24	120–4360	17	192	14,577	Wainganga river
4	Pombhurna Grid	15	471–2897	13	200	15,456	Wainganga river

3 Proposed Initiative

As the methods of water supply by tankers or by RWSS are too costly, there is a need to resolve this problem indigenously at an affordable cost to the villagers preferably at the village level.

3.1 Source of Water for Drinking Purposes

Groundwater sources of rural village schemes are mostly unsustainable due to dwindling of the water table (Fig. 4). To make it sustainable, recharging of groundwater should be carried out. This can be done by storing the rainwater (which otherwise goes waste) against the weir/bandhara and then allow it to percolate into the ground by various methods. But this action requires the first task to make water storages. The proposed initiative does the same (making of water storages) by constructing the *Bridge cum Bandhara* (BCB) across a small stream flowing near the village.

Source of water should preferably be developed near the village if feasible and possible as it proves to be a least cost solution. Generally, each village is situated

Fig. 4 Dried river near Piplagaon-14th August 18





Fig. 5 Typical innovative structures of BCB

near a small river called, Nalla. Such rivers have a steep slope of 1:250 and hence drain off once the rain stops. They, therefore, do not help ground recharging.

3.2 *Techniques of Water Storage Structures Within Banks of Rivers*

3.2.1 Arch Type Bridge Cum Bandhara (BCB)

A new model of constructing elliptical concrete arch (Fig. 5) abutting the bridge has now been evolved so that bridge serves dual purposes, i.e., crossing and storage. This type of arch type Bandhara is an almost permanent structure having a height up to 2.4 m in the form of an ellipse to create storage of water upstream. The design is evolved after extensive literature survey and model analysis.

3.2.2 Cement Plug/Cement Weir

It is the practice of agriculture/irrigation department to construct a permanent small weir known as cement plug/cement weir to store water within riverbank. Generally, storage planned is up to 2.5 m. These structures also create a pool of water which helps in increasing groundwater. The water is used as a source for drinking water, limited irrigation, etc. The typical structures are shown in the photographs in Figs. 6 and 7. Comparison is made in Table 2.

Fig. 6 Cement plug/Cement weir



(a)

(b)



Fig. 7 Anicuts/Cement plugs

4 Special Feature of Innovative Arch

4.1 Discharge Over Weir

IIT Roorkee [1] has done extensive research to find the discharge capacity of weir. This has helped us to evolve the most cost-effective shape to ensure maximum discharge with minimum afflux so that adjoining fields are not affected.

4.2 Obstruction to Waterway of Bridge

Basic question which is being raised is whether by creating a permanent storage, we are encroaching on waterway. This paper gives an explanation that we are just changing the direction of flow and not creating an obstruction to flow. By using the standard equations for discharge over weir after correcting for equivalent straight length as per the above findings, we can calculate afflux, highest flood level (HFL), and check whether it is likely to enter adjoining fields or touching the slab causing additional force for a high-level bridge. Storage depth has to be then readjusted.



4.3 Plan Area of Arch and Shape

Extensive model analysis was carried out at various places. The visual observation has revealed that if the plan area of the arch is 1.5 times the area of obstructed flow, then in that case the disturbance due to vortex formation is minimum.

4.4 Vortex Formation

During floods, water falls down from all sides of the arch and tries to rush out through the bridge opening. In this process, vortex is formed within the arch which kills all the

Table 2 Comparison

Sr. No	Element	Cement weir	Curved weir	Remarks
1	Shape			Being gravity structure, requires more materials while in arch being closed RCC structure, structurally efficient and requires much less materials
2	Length	More than width of minor river	Same width	To keep afflux low, length has to be increased in weir but due to curved shape same length is adequate
3	Wing wall	To channelize flow and to contain within banks	No need	Other elements of bridge channelize flow
4	Protection	Excessive protection required	No need	In cement weir, energy is killed by hydraulic jump requiring protection while in arch; it is killed by vortex formed inside the arch
5	Stability	By gravity	Shape makes it safe	Lever arm at base being more, dead load makes it safe. Cut off add resistance against sliding Virtually very minor force transferred to pier

energy. In conventional weir, the energy is killed by hydraulic jump requiring extensive protection measures while in the present case, virtually no protection measures are required.

4.5 Common Shape

To fulfill the condition of plan area of 1.5 times storage area, an ellipse shape is found to be ideal. With an objective of evolving common formwork, the shape for different spans is adjusted by keeping central straight portion.

4.6 Flow Characters of Small Rivers

Technology is developed for small villages to make them self-sufficient for drinking water by converting bridge as bridge cum bandhara to act as storage structures. Such small villages generally have nearby stream (nalla) having a width of 40–60 m and maximum flood depth of 5 m. We have already checked the stability for this condition, i.e., when stored water is 2.4 m and flood depth up to 8 m and found to be safe. Several completed BCB structures have been already subjected to maximum flood.

5 Cost of Structure

The structure is innovative cost-effective and affordable compared to the norms prescribed by the Government of Maharashtra (GoM). For storage structure, the cost is 50–60% only and similarly compared to cement weir/plug, the cost is 60–70%. Cost per running meter comes to about Rs 90,000 per running meter. As mentioned above, the cost of supplying drinking water under RWSS per village is 150 lakh to 200 lakh while in this innovative design, it can be brought down to 50 lakhs.

6 Model Study

Extensive model studies have been carried out at (1) Pune Engineering College [2], (2) Amravati Engineering College, and (3) “Chandrabhaga” Canal, at Amravati. To get a better understanding of the behavior of the flow, the arrangement is shown in Fig. 8, 9 and 10.

All these model studies have revealed that there are no adverse flow conditions such as heavy turbulence, hydraulic jump, etc. On the contrary, the vortex formed due to water falling on all sides creates a vortex and thereby kills energy. There is



Fig. 8 Lab study at Pune Engineering College

Fig. 9 Study at canal



Fig. 10 Study at Chandrabhaga canal



also a water bath within a span of bridge and arch which also absorbs the energy of falling water. As such, no separate protection measures are required. The photographs of the actual structure are as shown, and on the contrary, the flow is smooth. The model study also confirmed that afflux as calculated by the curved weir formula is reasonably correct. For multiple buried Hume pipe culverts with high face walls or buried boxes with high face well, we can plan storage even above the top of the pipe or top of the slab as seen in the model.

Table 3 Details of various villages

SN	Details of Village		
	Name	Population	Bridge details
1	Bothali	745	3 * 7 = 21
2	Peryl	1157	3 * 5 = 15
3	Gaurla	233	3 * 6 = 18
4	Jamkrdi	1226	5 * 2 = 10
5	Karambi	342	3 * 5 = 15
6	Dudha	320	1 * 7 = 7
7	Korgaon	1250	3 * 5 = 16
8	Umra Lahura	426	3 * 6 = 18

7 Water Required for Drinking Purpose

As per norms of JJM, each household should get 55 L of tap water and assuming 20% more the requirement of water for 1500 population is 42,000 cubic meters. As per the Irrigation department, 1 km² can give water of 14,197 cubic meters for 50% dependability and a 10 m waterway bridge can give at least 72,000 cubic meters minimum in the worst year. Table 3 indicates the quantity of water required for different population.

8 A Model for Supplying Drinking Water Through Water Stored in BCB

The overall water supply arrangement right from BCB to villages is shown in Fig. 11.

The total cost covering bandhara, Shet Tale, filtering system, solar, panels, pipe, pump, etc., works out to 50 lakhs. Solar panels are used to generate power to pump water to Shet Tale and later on to the elevated reservoir to distribute water. Excavation

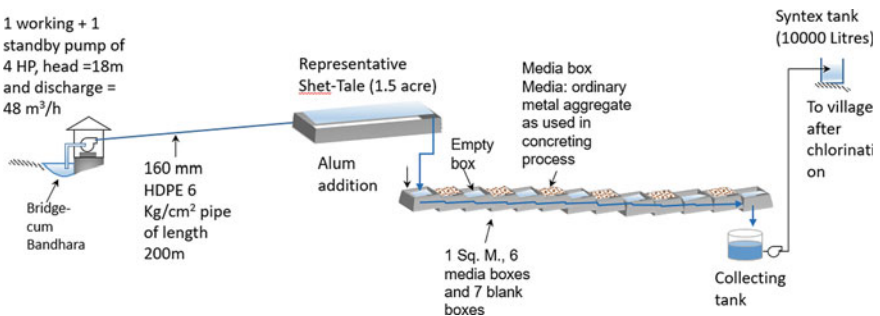


Fig. 11 Water supply arrangement from BCB to village

work of Shet Tale can be taken up under National Rural Employment Guarantee Act (NAREGA). Specially designed horizontal filter is used for designing filtering the water. Horizontal filter is easy to maintain. Water from the Bridge-Cum-Bandhara (BCB) as shown in Fig. 11 will be pumped by a pump of 5 HP which will be energized by a solar panel (Fig. 21). The rising main is 225 mm HDPE, PE100, 6 kg/cm² with length of 200 m.

9 Success Stories

Based on the proposed initiative, several structures have been constructed. Benefits of a few are described in Table 4.

10 Design of Structure

Guidelines for selection of site and data to be collected

The elliptical concrete cost-effective technology is developed to convert existing minor bridges into storage structures; standard designs are prepared for bridges of span up to 10 m. Drawings are now available to cover the following typical structures to BCB. The typical bridge shown in photographs can be converted into storage structures. Standard drawings are available for various spans and foundation condition. Tentative sites are shown in Figs. 12a–c.

11 Construction Technologies

Work is being executed in a remote area and as cost is low, big contractors are not expected to come forward for executions. We intend to construct a water-retaining structure, hence, the quality of concrete has to be good and the same should be dense without any honeycombing. This is only possible if good quality formwork is adopted which means higher cost. Experience has shown that the cost of formwork is comparable to that of concrete cost. It has also been decided to use M-30 self-compact concrete which may not require much vibration and thin sections can be casted having dense concrete. We have developed the precast construction technology which ensures good and dense concrete. A typical structure can be completed in 20 days using common equipment as it is now available even at talk level.

Table 4 Benefits of proposed BCB structures

SN	Village and Population	Bridge details	Slope	Storage in Bank (CuM)	Benefits/ remark
1	Kathrgaon, population = 600	5 Spans of 6 m	1:270	30,000	Irrigation for Kharip for the first time for 150 acres, Water level in wells rose by 25 m**
2	Ellora, population = 1500	6 spans of 5 m	1:370	35,000	Water level rose by 16 m in wells, more than 150 acres Kharip irrigation expected**
3	Kinh, population = 1500	3 spans of 6 m	1:500	20,000	At least 100 acres irrigation expected, totally in tribal area
4	Piri-kalga, population = 2250	3 spans of 7 m	1:260	20,000	Additional 25 acres irrigation in Kharip Fishing has an additional source of revenue
5	Mull Marodi, population = 1500	3 spans of 5 m	1:500	20,000	Expected 100 acres in this year
6	Sipna in Dharni Backwater of 2.5 km	Major bridge	1:1500	storage of 3 lakhs Cum	New Shet Tale constructed filled by solar pump to create irrigation for 60 acres. All tribal population 80% below BPL
7	Anhdari near chiroli	Major bridge	1:1400	Backwater of 4 km, storage of 4.5 lakh Cum	Four natural lakes which will be filled using solar panels to create storage of 16 lakh cubic meters to irrigate 1600 acres; 60% population is tribal and BPL; 70 acres irrigation in Kharip done from backwater. Average cost of irrigation is Rs 20,000 Rs per acre

(continued)

Table 4 (continued)

SN	Village and Population	Bridge details	Slope	Storage in Bank (CuM)	Benefits/ remark
8	Apoti, Population = 2500	3 spans of 6 m	1:600	30000 m ³	Saline track in Black cotton soil, groundwater not suitable for irrigation or drinking, 150 acres irrigation done in backwater for the first time, a natural tank of 54 acres is proposed to be filled using solar panels to create irrigation for 500 acres at an average cost of Rs 12,000 per acre. Sand filter being installed to supply drinking water at the rate of Rs one for 20 L

** The water supply for these two villages is part of RWSS for 114 villages at a cost of 221 crores. We can now supply water from our bandhara



(a) A typical bridge1



(b) A typical bridge2



(c) A typical bridge3

Fig. 12 Typical bridges

11.1 Precast Cut-off

Some of the precast cut off are shown in Figs. 13, 14, 15.

Fig. 13 Precast cut off



Fig. 14 Placing precast arch



Fig. 15 Completed structure



12 Details of Successful Projects

12.1 Success stories

The initiative was conducted at the following places:

- (1) Saline track village “Apoti”



Fig. 16 Village Apoti

The scheme is shown in Fig. 16. The benefits are: (a) 150 acres irrigation with sprinkler, (b) Pure drinking water—20 L per family at Rs one, (c) 50-acre lake to create irrigation for 500 acres.

(2) Village “Mul Marodi”

The scheme is shown in Fig. 17.

(3) Other Villages

The schemes are shown in Fig. 18, 19, 20.

(4) Economical Irrigation

Solar pumps are used in this project as shown in Fig. 21. BCB at Major Bridge Andhari Irrigation is shown in Fig. 22.

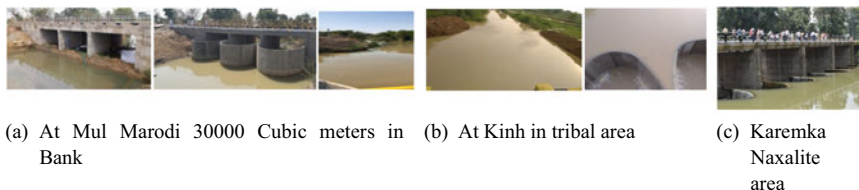


Fig. 17 Village Mul-Marodi



Fig. 18 BCB at Ellora and Kathargaon



Fig. 19 BCB at Pipri Kalga



Fig. 20 BCB at Apoti



Fig. 21 At Dharani Irrigation for 60 acres using solar panels

13 Comparison of Cost Economics

Comparison of cost, of this novel model prepared in this paper and discussed above, has been made with the Regional water supply scheme of “Pomphurna whose source for supply is the Wainganga River.

“Pombhurna” regional water supply scheme—The scheme is planned to supply drinking water to 15 villages having a total population of 20,000 at a cost of 28.82 crores, out of which, the cost of bringing filtered water up to the village is 17.30.



Fig. 22 BCB at Major Bridge Andhari Irrigation for 1600 acre by filling existing lakes for 16 lakh cub m using solar panels, cost 20,000 Rs per acre



Fig. 23 Photographs of BCBs near villages

Out of 15 villages, 11 villages have a population less than 1500, 3 villages have a population less than 1800, and balance one village has a population of 3200. The cost of the new design is 14.00 cores including irrigation for 1600 acres. Few photographs of bridges near these villages are attached in Fig. 23.

14 Conclusions

Jal Jeevan Mission (JJM) has a vision—“Har Guar Jal, every rural household has drinking water supply in adequate quantity of prescribed quality on regular and long-term basis at affordable service delivery charges leading to improvement in living standards of rural communities.” Main task of JJM is to make functional household tap connection (FHTC) to all these households. A provision of Rs 3.5 lakh cores is made to do this job of providing FHTC at the rate of 55 L per day per person and target is set to be achieved by the year 2024.

Suggestion for meeting the above mission.

- (1) The new design of elliptical concrete arch to convert bridges into storage structure, i.e., Bridge Cum Bandhara should be made a part of JMM.
- (2) The above innovative design is cost-effective, and can be completed in 20 days through local contractor. It does not require land acquisition and is cost-effective
- (3) Funds from JMM may be made available to water supply department for planning and execution.
- (4) As construction can be completed in a short period, cost of escalation is ruled out. The technology should be given first preference.
- (5) The additional benefit of irrigation in villages will help in doubling the income of the farmer.
- (6) Target to achieve 175 GW by 2022 through non-conventional energy sources has been planned and large-scale adoption of solar pumps (additional electricity in the national grid) in this innovative design for villages would help to achieve this target.
- (7) Draft national water policy 2020 gives importance to cost-effective sustainable option and discourage large-scale off-site storage and long-distance transport of water. As we are using rainwater near the villages, the objective of clean and safe water also will be fulfilled.
- (8) Advantage of NAREGA can be taken for constructing the Shet Tale.
- (9) More solar panels can be fixed to meet the power need of street lights, Gram Panchayat office, village health centers, and other government offices.
- (10) Government of India has taken a decision that on new National Highway and PMGSY works, BCBs can be constructed at their cost hence these funds also are available for JMM
- (11) Technology for water filtration being simple, the training classes can be arranged at village levels.

References

1. Kumar S et al (2012) Discharge characteristics of sharp crested weir of curved plan-form. Res J Eng Sci 1(4):16–20
2. Nilgunde P Study of Arch Type Bridge cum Bandhara. A mini Project Report Guided by Dr. A. D. Thube, COE, Pune
3. PMGSY guidelines P -1701 /S/2011-RC (part) (FMS-337815), dated 16 -10-4, "Provision of Bandhara on the bridges under construction under PMGSY roads", Amendment to Para 8.5 (V)
4. MORTH RW Construction of BCB Barrage Structure on NH serving dual purpose i.e. to cross water body as well as to store water
5. R&D Project on Development of standard design and drawings of Bridge Cum Bandhara System- Department of applied Mechanics ,VNIT, Nagpur

Green Synthesis of Zinc Oxide Nanoparticles and Study of Its Adsorptive Property in Azo Dye Removal



C. Anupama and S. Shrihari

Abstract Dyes are important colouring chemical compounds widely used in textile, paper, food, cosmetics and pharmaceutical industries. Most of the dyes are highly toxic and potentially carcinogenic. Exposure to high doses of these compounds can have severe effects in the human body. When untreated dye effluents are directly discharged into water bodies it leads to water contamination. Adsorption is an efficient method for the dye removal. It is also an economical technique. Green synthesis helps in the production of cost-effective and ecofriendly adsorbent. In this paper, green-synthesized zinc oxide nanoparticles were widely used for the removal of azo dye; methyl orange. Zinc oxide nanoparticles (ZnO NPs) were synthesized using *Plectranthus Amboinicus* leaf extract. The structure of nanoparticles was visualized using Field Emission Scanning Electron Microscope (FESEM). Nanoparticles due to their small size and thus large specific area are strong adsorbents. The effect of various parameters like dye dosage, zinc oxide nanoparticle loading, pH and contact time was evaluated. In batch adsorption study, maximum removal efficiency of 85.41% was obtained with zinc oxide nanoparticle dosage of 3 g initial dye concentration of 10 mg/l, pH 6 and contact time of 3 h. Adsorption parameters fitted well in the Langmuir isotherm model with a correlation coefficient (R^2) of 0.975. Adsorption kinetic studies revealed that adsorption strongly followed pseudo-second order. This paper suggests a safe, economical and environment-friendly technique for the removal of azo dyes.

Keywords Azo dye · Methyl orange · Zinc oxide nanoparticles · Adsorption

1 Introduction

Colour has always attracted human minds for aesthetic and social reasons. Dyes are colouring compounds that are used widely in paper, cosmetics, textile, pharmaceutical and food industries. To satisfy the demands and for marketing purpose

C. Anupama (✉) · S. Shrihari

Department of Civil Engineering, National Institute of Technology Karnataka, Mangaluru, India
e-mail: anupama23495@gmail.com

© The Author(s), under exclusive license to Springer Nature Singapore Pte Ltd. 2023
M. S. Ranadive et al. (eds.), *Recent Trends in Construction Technology and Management*, Lecture Notes in Civil Engineering 260,
https://doi.org/10.1007/978-981-19-2145-2_36

467

large variety of dyes are used to make different shades of fabrics. With the increasing demands, the environmental issues related to the production and applications of dyes are also increasing. Large quantities of wastewater with intensive colour and toxicity are being released in the environment during the production and manufacturing of dyes. About 200,000 tonnes of dyes are being released in textile effluents yearly due to the inefficiency in dyeing process. These dyes can be found in both suspended as well as dissolved state. They are very difficult to get degrade and are toxic, making the water fail to meet its purpose.

Coloured pollutants can be easily recognized in the environment. Textile industries in discharging effluents without any treatment contain chemicals that are toxic and which can lead to environmental issues like water pollution. It decreases the penetration of light into the water bodies which leads to decrease in the photosynthetic activities of aquatic plants. It also reduces the reoxygenation capacity of water bodies. Some of the synthetic dyes are carcinogenic. Dyes are resistant to biodegradation and are stable against temperature and light. Textile effluents also contain heavy metals that get accumulated in the body of organisms. It may affect the ecosystem adversely. Dyes are teratogenic or mutagenic in various species [8]. It may also damage the reproductive system, kidney, liver, nervous system and brain of human beings [9].

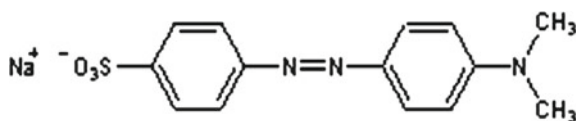
Dyes can be classified based on their chemical structure. Based on the chromophore present, they are classified as Nitro dyes, Azo dyes, Anthraquinone dyes, Indigoid dyes, Phthalein dyes, Nitroso dyes and Triphenyl methyl dyes [6]. Azo dyes are widely used dyes due to its productiveness, firmness and availability in a variety of colours. About 70% of total dyes used in industries are Azo dyes. The common structural feature of these dyes is the azo linkage ($-N=N-$) [2]. Azo dyes contain abundant organic compounds that can lead to various environmental issues. Effluents from various industries contain traces of dyes which may affect the water quality as well as human health because of its toxicity. Azo dyes are potentially carcinogenic and mutagenic. It is very difficult to remove these dyes by conventional treatment technologies [4]. In this paper, we study mainly about the azo dye; methyl orange.

Methyl orange is an anionic azo dye which is mostly used in pharmaceutical, textile industries, food, paper and printing industries and some research laboratories. It is a heterocyclic aromatic compound with molecular formula $C_{14}H_{14}N_3NaO_3S$ [1] (Fig. 1).

These dyes can cause eye irritation, gastrointestinal irritation with vomiting, nausea and diarrhoea. It may also cause skin irritation and respiratory tract irritation.

There are chemical, biological and physical methods for the removal of dyes from industrial effluents. Chemical method includes oxidation, electrocoagulation, photochemical oxidation, photocatalytic degradation, ozonation, etc. Biological method

Fig. 1 Methyl orange [1]



includes decolouration and degradation of azo dye either by biodegradation or by adsorption on to biomass. Physical methods of removal include filtration, flocculation and coagulation, ion exchange, reverse osmosis and adsorption.

Adsorption due to its high removal efficiency of pollutants had become a trending removal technique. Adsorption results in high-quality products and is also economically feasible [9]. In adsorption, the process involved is the transfer of soluble organic dye from wastewater to highly porous solid materials. Substances that get collected on the solid interface is referred as adsorbate and adsorbent is the solid on which adsorption occurs. Factors that influence the adsorption efficiency are particle size of adsorbent, surface area, temperature, pH, time of contact and the interaction between adsorbent and adsorbate. Optimizing these parameters will greatly help in improving the removal efficiency. Activated carbon is the most commonly used adsorbent.

Nanoparticles have good potential in wastewater treatment. Its characteristics like high surface area, catalysis activity and high reactivity make it a good treatment method. Nanoparticles due to its small size and large surface area act as a good adsorbent. Various organic and inorganic pollutants, heavy metals and bacteria are removed using varieties of nanoparticles.

Zinc oxide has been most frequently used for the degradation of many organic pollutants. Zinc oxides have strong activity even in small amounts. They have great heat resistance and durability [3]. Due to its high surface area to volume ratio, they have large number of active sites for the interaction of pollutant species for increased adsorption capacity. They also have antibacterial properties [7]. They also have potential application in heavy metal removal also. There are many methods for the synthesis of ZnO nanoparticles.

Green Synthesis of nanoparticles has been widely increased now since they are economical, safe and environment friendly. Bacterial extracts, plant extracts, certain enzymes and other organic sources are used for green synthesis. *Anisochilus carnosus*, *Tamarindus indica*, *Solanum nigrum*, *Vitex negundo*, *Plectranthus amboinicus* and *Hibiscus rosasinensis* are some of the plant extracts used for the synthesis of ZnO Nps [5]. Green synthesis can also help in the reduction of use of strong chemicals as reducing agents.

The main objectives of this paper include green synthesis of ZnO nanoparticles, study the effective removal of methyl orange dye by adsorption onto ZnO nanoparticles, understand the effect of various parameters like ZnO dosage, initial concentration of dyes, pH and contact time on adsorption.

2 Materials and Methodology

2.1 Materials

Methyl orange (MO), Zinc nitrate hexahydrate with purity of 98% for ZnO NP synthesis and ethanol were purchased from Gennext. *Plectroanthus amboinicus* leaves were collected from Kozhikode, Kerala.

2.2 Adsorbent Preparation and Analysis

Zinc oxide nanoparticles were selected as the adsorbent. It was synthesised biologically using *plectoranthus ambinicus* leaves.

2.2.1 Collection and Preparation of *Plectroanthus Amboinicus* Leaf Extract

Plectoanthus amboinicus leaves were collected and cleaned in distilled water. Then, 5 g of leaves were taken and cut into smaller pieces. The leaves were then boiled in 30 ml of distilled water for about 15 min. Then the cooled leaf extract was filtered through Whatman No. 41 filter paper and stored in the refrigerator for further use.

2.2.2 Biosynthesis of Adsorbent ZnO Nanoparticles

Zinc nitrate solution (0.1 M) was prepared using 30 mL of distilled water. To this solution 10 mL of leaf extract was added. It is continuously stirred at 80 °C for 4 h. Yellow colour paste will be obtained through centrifugation. This paste was collected in a crucible and kept in a hot air oven at 100 °C for 3 h. A pale yellow colour powder is obtained and it should be washed with ethanol and water. Zinc oxide Nanoparticles will be obtained after annealing the sample in a furnace for 2 h at 400 °C.

2.2.3 Characterization of Biosynthesized Zinc Oxide Nanoparticles

The biosynthesized ZnO NPs were characterized with the help of Field Emission Scanning Electron Microscope (FESEM). Instead of light, these microscope works with electrons. These electrons are liberated by a field emission source. It helps to obtain the surface morphology of the nanoparticles. The nanoparticles should be washed, dried and made free from any impurities before doing characterization.

2.3 Preparation of Adsorbate and Analysis

Methyl orange was the azo dye selected as adsorbate.

2.3.1 Preparation of Azo Dye

Synthetically prepared MO dye solution was used for the study. 100 mg/l of stock solution of the dye was prepared with 500 ml water. Sample solution was prepared by diluting this stock solution just before the study.

2.4 Adsorption Studies

2.4.1 Batch Adsorption Studies

Batch adsorption study was done by adding the required amount of ZnO nanoparticles to the prepared dye solution and mixed well on an orbital shaker for preferred time. Then the solution will be filtered and the residual concentration of dye will be monitored using UV–visible spectrophotometer. Effect of dosage of ZnO NPs, effect of initial concentration of dyes, effect of pH and effect of contact time on the adsorption rate was analysed.

The percentage removal of dye ZnO nanoparticles is calculated using,

$$\% \text{ Dye removal} = \frac{C_0 - C_e}{C_e} \times 100$$

C_0 is the initial concentration of dye and C_e is the concentration of dye at equilibrium.

3 Results and Discussions

3.1 Characterization of Zinc Oxide Nanoparticles

The morphology of the ZnO NPs synthesized was examined using Field Emission Scanning Electron Microscope (FESEM). The analysis gave a lotus petal-like flake-shaped structure. The average size of the ZnO NPs was 1 μm . Large surface area of ZnO NPs enables it to adsorb large amount of pollutants making it a good adsorbent (Fig. 2).

Fig. 2 FESEM image of ZnO NPs synthesised

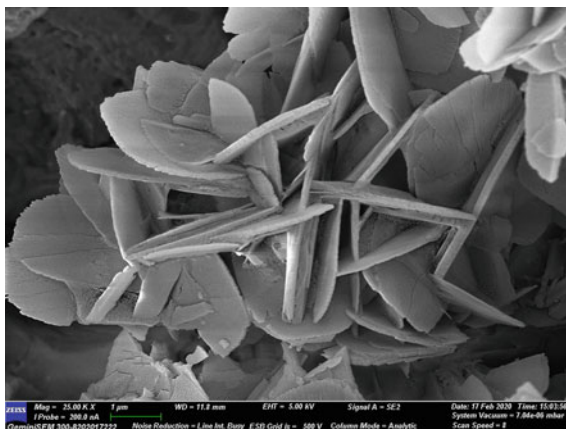
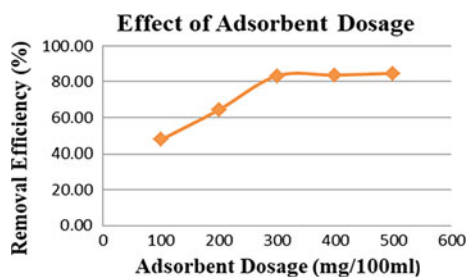


Fig. 3 Effect of ZnO NPs dosages on removal of methyl orange dye



3.2 Methyl Orange Dye Adsorption Analysis

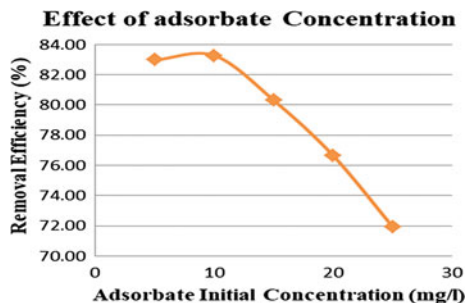
3.2.1 Effect of Adsorbent Dosage

For a fixed concentration of 10 mg/l and a volume of 100 ml, the percentage removal of methyl orange dye was examined by changing the dosage of ZnO NPs from 100 to 500 mg. Figure 3 shows that there was a good increase in the removal of dye from 100 to 300 mg dosage of ZnO NPs. This increase might be due to the availability of more sites and large surface area for adsorption with the increase in adsorbent dosage. But after 300 mg further increase in the adsorbent dosage didn't show much increase in the removal. This may be the result of formation of aggregation of particles. Since there was no significant increase in the removal efficiency with the further increase in adsorbent dosage, the optimum dosage was taken as 300 mg.

3.2.2 Effect of Initial Adsorbate Concentration

The initial concentration of methyl orange dye was varied from 5 to 25 mg/l at a constant pH and contact time. Then the efficiency in the removal of dye

Fig. 4 Effect of Initial adsorbate concentrations on removal of methyl orange dye



with the optimum dosage of ZnO NPs and was studied. Initially, there was good removal efficiency but with increase in concentration, the removal efficiency also decreased (Fig. 4). The initial increase in the removal might be due to the availability of large number of vacant active sites at lower concentrations. But when concentration increased the sites may have got saturated and difficult to capture the dye molecules.

3.2.3 Effect of pH

Optimum concentration of methyl orange dye was prepared at a varying pH of 2 to 12 and was allowed to react with ZnO NPs at a contact time of 3 h. Figure 5 shows the result of this adsorption study. Initially, there was an increase in the removal efficiency till a pH of 6 then the removal efficiency decreased. Maximum adsorption at pH 6 might be the result of good electrostatic attraction between the positively charged ZnO NPs and the anionic dye molecules. The low removal efficiency at very low pH may be because of the larger quantity of protons getting attached with $N=N$ and making methyl orange dye protonated and as a result repelling the positively charged ZnO NPs. When pH was increased there will be more negatively charged sites. They may repel the anionic dyes and reduce the adsorption. Also more OH^- ions may be available at higher pH which competes with the anionic dyes to occupy the positive sites which in fact reduces the removal efficiency.

Fig. 5 Effect of pH on adsorption of methyl orange dyes on to ZnO NPs

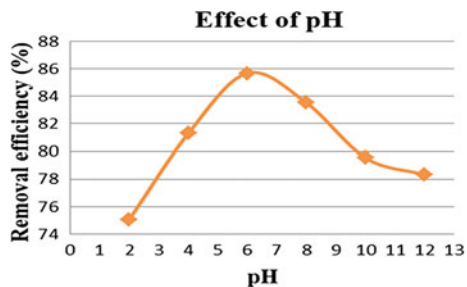
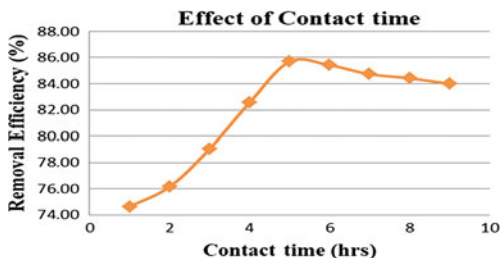


Fig. 6 Effect of contact time in the adsorption of methyl orange dye on to ZnO NPs



3.2.4 Effect of Contact Time

Optimum concentration of methyl orange dye with optimum pH was prepared and was allowed to react with a varying time interval of 1–5 h. The result of this adsorption study is shown in Fig. 6. The result shows a good increase in the removal efficiency up to 3 h, but later there was no considered change in the removal efficiency. This probably resulted from the saturation of active sites at 3 h and followed by adsorption and desorption process.

3.3 Adsorption Isotherms

At a constant temperature, the quantity of adsorbate adsorbed is a function of concentration of adsorbent. This function is called the adsorption isotherm. It is important to understand the adsorption behaviour to identify isotherm model. Isotherm models help us to identify the adsorption mechanism, surface properties and adsorption capacity. It helps to assess the efficiency of the synthesized adsorbent. The adsorption equilibrium data can be analysed using Langmuir and Freundlich isotherms.

3.3.1 Langmuir Isotherm

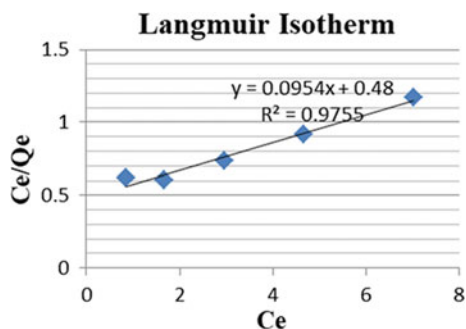
Langmuir isotherm was developed by some assumptions like the monolayer adsorption on a uniform surface with finite number of adsorption sites all having the same energy and the adsorption process is reversible. It is expressed as shown below.

$$Q_e = \frac{Q_{\max} K_L C_e}{1 + K_L C_e}$$

Langmuir equation is rearranged and isotherms were plotted between C_e/Q_e versus C_e and the Langmuir constants were found out from the slope and intercept.

$$\frac{C_e}{Q_e} = \frac{1}{Q_{\max} K_L} + \frac{C_e}{Q_{\max}}$$

Fig. 7 Langmuir isotherm



The important feature of Langmuir model can be defined by a dimensionless constant R_L (Separation factor).

$$R_L = \frac{1}{1 + K_L C_0}$$

Figure 7 shows the Langmuir isotherm plotted. Langmuir Constants,

$$Q_m, \text{ Maximum adsorption Capacity} = 10.482 \text{ mg/g}$$

$$K_L, \text{ Langmuir Isotherm Constant} = 0.198751/\text{mg}$$

$$R_L, \text{ Separation factor} = 0.1675$$

$$R^2, \text{ Coefficient of Determination} = 0.9755$$

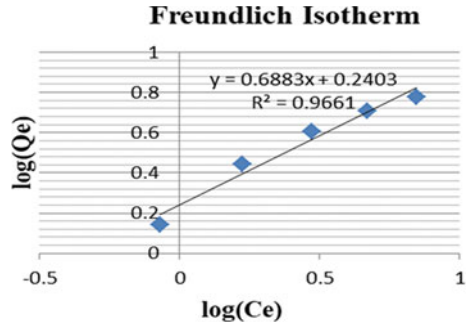
The maximum adsorption capacity obtained is 10.482 mg/g which is more than many other studies. The determination coefficient value ($R^2 = 0.9755$) shows strong positive correlation. Separation factor indicates whether the isotherm is irreversible ($R_L = 0$), favourable ($0 < R_L < 1$) or unfavourable ($R_L > 1$). It can be seen that R_L value obtained is less than 1 indicating the adsorption is favourable.

3.3.2 Freundlich Isotherm

It was developed based on some assumptions like heterogeneous surface energy. This isotherm defines reversible and non-ideal adsorption. It is not restricted to monolayer adsorption, multilayer adsorption can occur. It is expressed as below.

$$Q_e = K_f C_e^{1/n}$$

Fig. 8 Freundlich isotherm



Freundlich equation Freundlich isotherms were plotted between $\log(Q_e)$ versus $\log(C_e)$.

$$\log(Q_e) = \log K_f + \log C_e$$

Figure 8 shows the plotted Freundlich isotherm. Freundlich Constants,

$$K_f, \text{ Freundlich Capacity Factor} = 3.576\text{mg/g}$$

$$1/n, \text{ Freundlich Intensity Parameter} = 0.6883$$

$$n, \text{ Freundlich constant} = 1.4528$$

$$R^2, \text{ Coefficient of Determination} = 0.9661$$

Freundlich Capacity Factor K_F is a factor showing the adsorption capacity which is equal to 3.576 mg/g. $1/n$ indicates adsorption intensity or surface heterogeneity. When $1/n$ becomes closer to zero, it indicates more heterogeneous and when below 1, it shows a normal Langmuir isotherm and when greater than 1 indicates cooperative adsorption. n represents adsorption intensity. When $n < 1$, adsorbate was unfavourably adsorbed on the adsorbent and when $1 < n < 10$, adsorption was favourable. Here, $n = 1.4528$ which means adsorption is favourable. Coefficient of Determination obtained is 0.9661.

Comparing both the isotherms, R^2 value for Langmuir isotherm and Freundlich Isotherms are 0.9755 and 0.9661, respectively. This shows that the most appropriate isotherm that describes this adsorption study is the Langmuir isotherm. This shows that adsorption of methyl orange dye is predominantly by homogenous monolayer formation.

3.4 Adsorption Kinetics

The basics of kinetic studies are the kinetic isotherm obtained experimentally by tracking the adsorbate concentration against time. To study the mechanism of adsorption of the adsorbate onto the adsorbent kinetic studies are done.

3.4.1 Pseudo-First Order

The differential equation for pseudo first-order reaction is given by Lagergren equation,

$$\frac{dQ}{dt} = k_1(Q_e - Q_t)$$

Its linearized form is obtained by integrating the above equation under the boundary condition $Q_t (t = 0) = 0$,

$$\log(Q_e - Q_t) = \log(Q_e) - \frac{k_1}{2.303}t$$

The pseudo-first-order graph plotted between $\log(Q_e - Q_t)$ versus t is given in Fig. 9. The pseudo-first-order parameters were found out from the slope and y intercept of the graph.

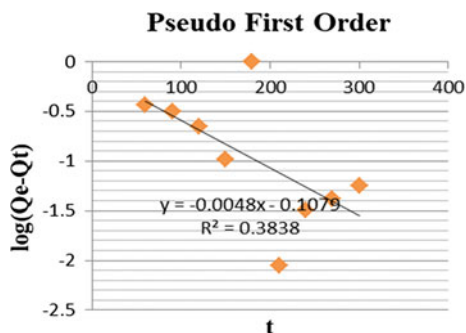
Pseudo-First-Order parameters,

$$\text{Rate constant, } K_1 = 0.0048 \text{ min}^{-1}$$

$$\text{Adsorption capacity at Equilibrium, } Q_e = 0.8977 \text{ mg/g}$$

$$\text{Coefficient of Determination, } R^2 = 0.3838$$

Fig. 9 Pseudo-first order



By analysis, it can be seen that the R^2 value is very less and also the experimental adsorption capacity at equilibrium did not match with the theoretical Q_e value obtained from the graph. It shows that adsorption of methyl orange dye on to ZnO NPs does not elucidate pseudo-first-order kinetics.

3.4.2 Pseudo-Second Order

This model assumes that the uptake rate is second order with respect to available sites. That is when the adsorbate reacts with two adsorption sites, the rate of adsorption is as follows,

$$\frac{dQ}{dt} = k_1(Q_e - Q_t)^2$$

Its linearized form is,

$$\frac{t}{Qt} = \frac{1}{k_2 Q_e^2} + \frac{t}{Q_e}$$

The graph plotted between t/Q_t versus t graph is shown in Fig. 10. The pseudo-first-order parameters were calculated from the slope and y intercept of the graph. Pseudo-Second Order Parameters,

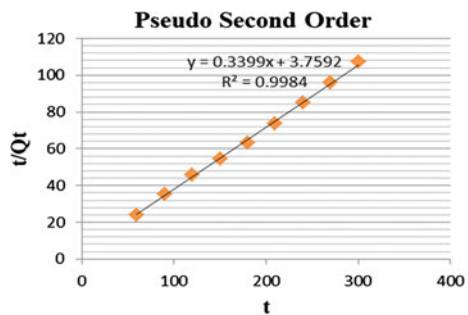
$$\text{Rate constant, } K_2 = 0.03073 \text{ min}^{-1}$$

$$\text{Adsorption capacity at Equilibrium, } Q_e = 2.942\text{mg/g}$$

$$\text{Coefficient of Determination. } R^2 = 0.9984$$

The correlation coefficient value of pseudo-second-order graph is very high and also the experimental Q_e value shows a good agreement with the Q_e value obtained

Fig. 10 Pseudo-second order



from graph. This shows that adsorption of MO dye onto ZnO NPs follows the pseudo-second-order adsorption kinetics.

4 Conclusion

The main aim of this study was to develop an ecofriendly and economical method for the removal of azo dyes from the wastewater. ZnO NPs were green synthesized followed by batch adsorption study was done for removal of methyl orange dye. Characterization using FESEM was done on green synthesized ZnO NPs and it showed a large surface area which is important for the adsorption. The optimum dosage, initial concentration of azo dye, pH and contact time of 0.3 g, 10 mg/L, 6 and 3 h gave a maximum removal of 85.41%. Adsorption isotherm studies clearly show that the adsorption of methyl orange dye on to ZnO NPs had strongly followed Langmuir adsorption isotherm and the maximum adsorption capacity was 10.482 mg/g. Adsorption had followed pseudo-second-order adsorption kinetics. Green synthesized ZnO NPs can be used for efficient removal of azo dyes in a cost-effective and ecofriendly manner.

References

1. Bazrafshan E, Zarei AA, Nadi H, Zazouli MA (2014) Adsorptive removal of methyl orange and reactive red 198 dyes by *Moringa peregrina* ash. *Indian J Chem Technol* 21(2):105–113
2. Benkhaya S, El Harfi S, El Harfi A (2017) Classifications, properties and applications of textile dyes. A review
3. Dimapilis EAS, Hsu CS, Mendoza RMO, Lu MC (2018) Zinc oxide nanoparticles for water disinfection. *Sustain Environ Res* 28(2):47–56
4. Ecology A, Bhatnagar P (2014) Assessing mutagenicity of textile dyes from pali (Rajasthan) using Ames bioassay
5. Fakhari S, Jamzad M, Kabiri Fard H (2019) Green synthesis of zinc oxide nanoparticles: a comparison. *Green Chem Lett Rev* 12(1):19–24
6. Mariselvam R, Ranjitsingh AJA, Thamaraiselvi C, Ignacimuthu S (2019) Degradation of AZO dye using plants based silver nanoparticles through ultraviolet radiation. *J King Saud Univ Sci* 31(4):1363–1365
7. Ngoepe NM, Mbita Z, Mathipa M, Mketo N, Ntsendwana B, Hintsho- Mbita NC (2018) Biogenic synthesis of ZnO nanoparticles using *Monsonia burkeana* for use in photocatalytic, antibacterial and anticancer applications. *Ceram Int* 44(14):16999–17006
8. Samchetshabam G, Hussan A, Choudhury TG (2017) Impact of textile dyes waste on aquatic environments and its treatment impact of textile dyes waste on aquatic environments and its treatment
9. Yagub MT, Sen TK, Afroze S, Ang HM (2014) Dye and its removal from aqueous solution by adsorption: a review. *Adv Coll Interface Sci* 55(209):172–184

Anthropogenic Impacts on Forest Ecosystems Using Remotely Sensed Data



Gaurav G. Gandhi and Kailas A. Patil

Abstract Modernizations are beneficial to the comfortable condition of living; they also negatively impact the world of which we belong. Human activity that causes environmental harm (either directly or indirectly) on a global scale include human reproduction, overconsumption, overexploitation, pollution, and deforestation, to name just a few. Normalized Difference Vegetation Index (NDVI) is a band ratio technique that helps to determine the health of the vegetation. NDVI has been extensively used to study land use and land cover changes, agricultural drought analysis, forest fire analysis, and climate change detection. In this study, NDVI of three forest areas in the Vidarbha region of India, namely, Pench National Park, Tadoba Tiger Reserve, and Gadchiroli forest are studied to determine the anthropogenic effects of Nagpur, Chandrapur, and Gadchiroli on the forest areas respectively for past twenty-one years. In the process, the land use and land cover of the cities have been studied and change in weather conditions has been predicted. On the other hand, the meteorological parameters, like the temperature and rainfall have been studied for the three forests and have been related to NDVI of these forests and then compared with the weather predictions from the land use and the land cover maps of the cities. The anomalies in these two are justified with probable justifications. The study revealed the effects of local anthropogenic activities on these forests. It is concluded that the local human activities have an impact on the forest vegetation along with the locational aspect of an area.

Keywords NDVI · Land use/Land cover · Climate change · Precipitation · Temperature

G. G. Gandhi (✉)

Environmental and Water Resources Engineering, College of Engineering, Pune, India

e-mail: gandhigg19.civil@coep.ac.in

K. A. Patil

Civil Engineering, College of Engineering, Pune, India

1 Introduction

Human beings have experienced numerous changes in the course of their culture since history has been documented. Although these modernizations are beneficial to the comfortable condition of living, they also negatively impact the human life. With great benefits that the advancement of technology has given us, it has also caused some environmental harm.

Anthropogenic practices have injected many toxins into the biosphere in the form of solids, liquids, and gases, which in turn degrade the environment in the short or long term. Biodiversity consists of several species of flora and fauna that are highly vulnerable to the slightest alteration in the nature of the biosphere and are in turn at risk of endangerment and destruction in a developed world subject to human activities. Certain human actions that directly or indirectly cause environmental damage on a global scale include human reproduction, overconsumption, overexploration, deforestation, and waste. Natural resources actively or indirectly caused by humans include anthropogenic environmental effects, including global warming and the atmosphere, biodiversity, biological hazards, and environmental failure.

To locate vegetation index, ground cover classification, vegetation, open field, farm area, woodland, with few band variations of the remote-sensed data, NDVI uses the multispectral remote sensing data technique. (Meera Gandhi et al. 2015). The highest monthly temperature and precipitation have greatly influenced the NDVI value (Fanghua Hao et al. 2011). The Landsat archive shows six GDE study areas, i.e., Annual NDVI vegetation, runoff, evaporative demand, groundwater depth, and land and water management (CUI Linli et al. 2010). The LULC map can be used as a base map to support the advancement of mine maintenance plans and sustainable development planning in the nearby local communities (Justin Huntington et al. 2016). The variance in fire patterns is related to both vegetation and precipitation variations (Susana Burry et al. 2017).

The combination of RS with GIS offers an excellent platform for data capture, preparation, synthesis, calculation, and interpretation, all of which are important for environmental interpretation. Satellite photographs are highly useful because they include regularly updated maps of remote regions with constantly evolving land-forms. Geographic Information Systems (GIS) and Remote Sensing (RS) have developed as important tools to support environmental monitoring assessments. Ecological surveillance is aimed to study the ecological structure of a given area in time and space, surveillance the environmental condition of the transition in key parameters, evaluating and forecasting the effect of human activities on the ecological system.

The current study intends to take an account of the effects on two different forest ecosystems which are affected and influenced by several anthropogenic activities in two cities located in close proximity, i.e., local influence is taken into consideration for these two forest ecosystems. The results are compared to another forest ecosystem which is so far not affected by any anthropogenic activities locally. Global effects of

several human for activities are predominant in all of these forests, considered in the study. The current understanding from this project is only based on local activities.

The goal of this initiative is the effect of anthropogenic behavior on the forest environment. In the current study, RS and GIS are incorporated to study and understand the effects of human activities on Tadoba-Andhari Tiger Reserve, Pench National Park, and Gadchiroli forest. The study also focuses on evaluating whether anthropogenic behaviors in surrounding urban areas have a beneficial or detrimental impact on vegetation.

The objectives of the study are as given below:

1. To find positive or negative effects of anthropogenic impacts of nearby urban areas on the vegetation.
2. To determine the impact of temperature and rainfall on surrounding vegetation using NDVI data.
3. To check the effectiveness of management activities undertaken by the government and forest management agencies.
4. To study change detection in the vegetation distribution in the study area and its temporal variation during the period 2000–2020.
5. To study the long-term trend of rainfall, temperature, and NDVI.
6. To determine the correlation between NDVI and different climatic parameters.

2 Study Area

The study is based on two forest areas, Pench National Park and Tadoba-Andhari National Park, which are situated next to two major cities, Nagpur and Chandrapur, respectively, of Maharashtra state of India. Nagpur is an industrial area, whereas mining activities are predominant in Chandrapur district. The results are compared with Gadchiroli forest, which is comparatively unaffected by any such activities. The full description of the area of the analysis is given in Fig. 1.

2.1 *Pench National Park:*

The forest is situated on the southern border of Madhya Pradesh and the state of Maharashtra. Nagpur district lies between 20.35 and 21.44 N latitude and 78.15 to 79.40 E longitude extending over an area of 9892 km². It is the closest extremely industrial city in the area of the Pench forest. Totladoh dam, adjacent to Madhya Pradesh in India, is a gravity dam on the Pench river near Ramtek in Nagpur district. The tank submerges 54 km² of the park district (Table 1).

Location Map of Study Area

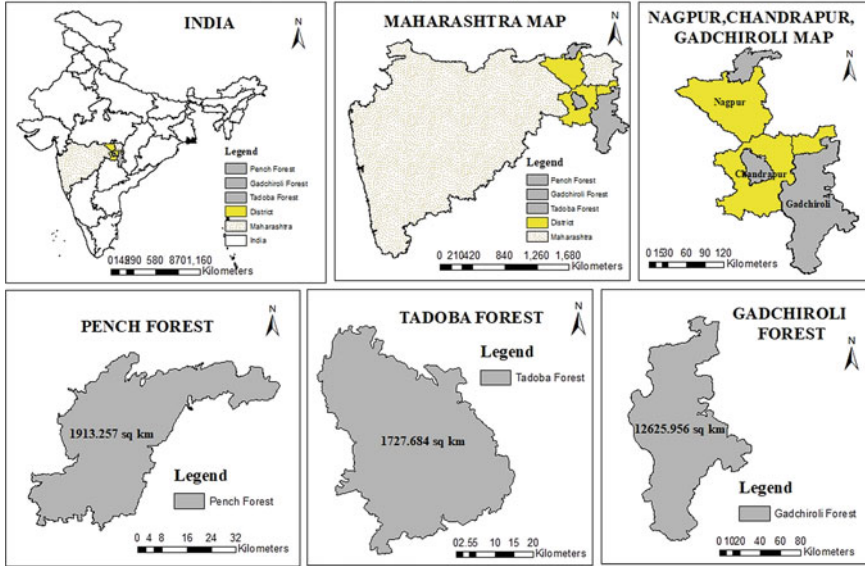


Fig. 1 Location of the study area

Table 1 Pench National Park Data

Total Pench National Park Area	1913.257 km ²
Latitude	21.64 N
Longitude	9.22 E
Temperature	6–31 °C in Winter to 25–48 °C in Summer
Average rainfall	1300

2.2 Tadoba Tiger Reserve

Chandrapur district is located between 19.30°N and 20.45°N latitude and at 78.46°E longitude extending over an area of 11,443 km². Chandrapur district is known for its thermal power stations and its vast reserves of coal in Wardha Valley coalfields (Table 2).

2.3 Gadchiroli Forest

It lies between 18° 08' and 20° 50' N latitudes and 79° 45' and 80° 54' E longitude. The district has a geographical area of 14915.54 km². Forests cover more than 79.36%

Table 2 Tadoba Tiger Reserve Data

Total Tadoba Tiger Reserve Area	1727.684 km ²
Latitude	20.16 N
Longitude	79.40 E
Temperature	25–30 °C in Winter to 47 °C in Summer
Average rainfall	1388

Table 3 Gadchiroli Forest Data

Gadchiroli Forest Area	12625.956 km ²
Latitude	20°50 N
Longitude	80°54 E
Temperature	14.6°C in Winter to 42.1°C in Summer
Average rainfall	1750

of the hilly geographical of the district. Several hill ranges span across the region of Gadchiroli. These hills provide the catchment area for valleys formed by the tributaries of rivers Pranhita, Vainganga, and Indravati (Table 3).

2.4 Data and Software Used

The data used, materials gathered, and software used for the completion of the goals and analysis for the study have been tabulated (Table 4).

3 Methodology

The methodology consists of collecting all the required data for the study, carrying out all the necessary correction and processing of the collected data to get the desired output and then finally determining the relation among the different climatic parameters and analyzing them carefully. An estimation of the health of forest vegetation was conducted by time series analysis using NDVI images (Fig. 2).

Table 4 Name of data and software used and their sources

Sr. No.	Description	Sources
1	Rainfall data	www.maharain.gov.in
2	Temperature data	www.globalweather.com
3	Arc-GIS	ESRI
4	LC/LU MAP	Arc-GIS

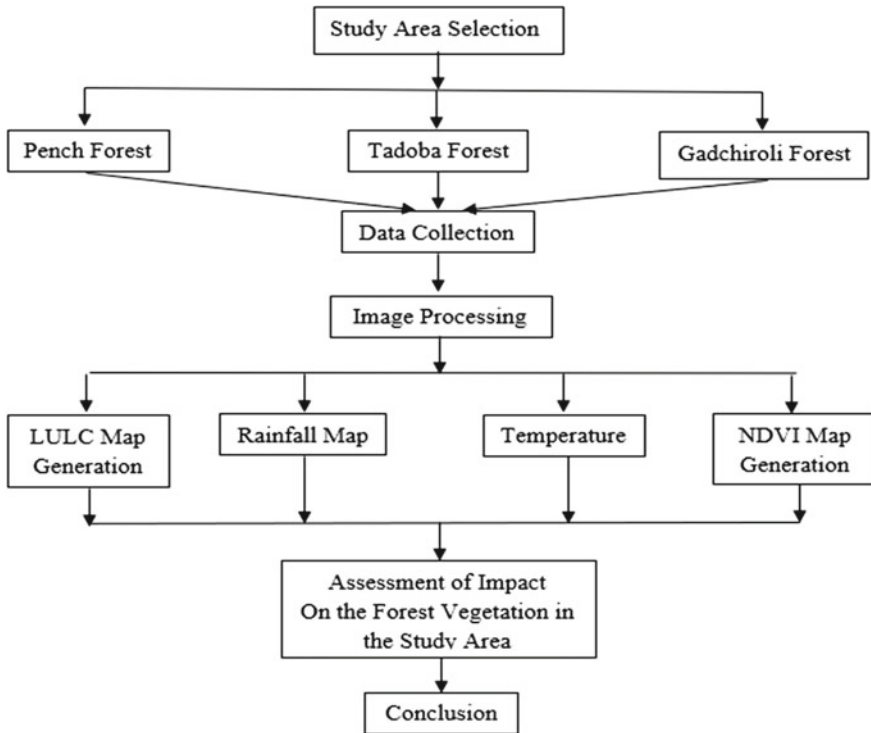


Fig. 2 Methodology flowchart

3.1 Preliminary Data Generation

It consists of acquiring satellite images, rainfall data, temperature data, boundary of study area, etc. Data generation process consists of generation of various maps needed for the study and also data needed for statistical analysis.

3.1.1 Collection of Satellite Images

Earth explorer has been used to observe and download the satellite images of the study areas Pench, Tadoba, and Gadchiroli, for different years and months.

For which, the procedure used is as follows:

- Set time of which the image is required.
- Locate the study area and mark it. Zoom it to the required resolution.
- Place four pins at corners and download the satellite images (Table 5).

Table 5 Datasets used in the present study and their source

Sr. No.	Data type	Sensor	Year	Resolution	Source
1	LANDSAT 5	TM	2000	30 m	USGS
2	LANDSAT 7	ETM+	2010	30 m	USGS
3	LANDSAT 8	OLI	2015	30 m	USGS
4	SENTINEL 2	MSI	2020	10 m	USGS

3.1.2 Projection System and Digitization of the Images

- a. Open Arc Map > Table of Contents > Right click on Layers > select Properties.
- b. Window named “Data frame properties” will open. Select coordinate system of “WGS 1984 UTM Zone 43N” > Apply > OK.

3.1.3 Rainfall data

Rainfall data were obtained from the Maharashtra State Department of Agriculture (<http://maharain.gov.in/>) Rainfall Recording and Review website. Average annual average rainfall data is obtained for the districts of Nagpur, Chandrapur, and Gadchiroli for the period 2000–2020. Then, around each rain gauge spot, Thiessen polygons were formed. Then Pench and Tadoba and Gadchiroli were found to have mean annual rainfall using the formula given below.

$$\bar{P} = \frac{P_1A_1 + P_2A_2 + P_3A_3 + \dots P_nA_n}{A_1 + A_2 + A_3 + \dots A_n} = \frac{\sum_{i=1}^n P_i A_i}{\sum_{i=1}^n A_i}$$

\bar{P} Mean precipitation

P_i Rainfall observed at the i th station inside or outside the basin

A_i In-region portion of the area of the polygon surrounding the i th station

N The number of areas
pagebreak

3.1.4 Temperature data

The Temperature data has been collected from the Global weather website for the study area for a duration of 21 years from 2000 to 2020. The data annual highest and lowest temperature has been calculated for the study. The annual average temperature has been calculated using the following formula,

$$T_{avg} = \frac{T_{max} + T_{min}}{2}$$

T_{avg} annual average temperature

Tmax maximum annual average temperature

Tmin minimum annual average temperature.

3.2 Land Use Land Cover Data

Using ArcMap software, the land use map for the years 2000 and 2020 was developed by raster-based supervised classification. The Land Use Land Cover satellite images were downloaded from United States Geological Survey (URL: <https://earthexplorer.usgs.gov>). Before supervised classification, images were projected. Then, the area was classified as:

- Built-up (Urban and Rural)
- Agriculture
- Forest
- Mining
- Water-body
- Wasteland.

3.3 NDVI Data Processing

The NDVI satellite data has been downloaded from USGS for a duration of 21 years from 2000 to 2020. The following processing is done on these images.

- a. The downloaded image for a particular time is opened in ArcMap.
- b. Now mosaic satellite data and from the processed image the desired area is clipped.
- c. Then go to the Windows>image analysis>image analysis option>select band R band; NIR band>NDVI>OK.
- d. The image is then classified for different break values (right click the NDVI image>go to symbology>click on classified>select number of classes>classify>ok.

$$NDVI = \frac{NIR - RED}{NIR + RED}$$

NIR Reflectance in Near-Infrared band for a cell

RED Reflectance in Red band for the cell (Table 6).

3.4 Analysis

Data obtained from the NDVI time series analysis in the form of NDVI value and area tables were then used to calculate the mean NDVI value of each vegetation class

Table 6 NDVI range for different features

NDVI range	Feature
-1 to 0	Water, snow, cloud
0 to 0.2	Built-up, barren land, rock
0.2 to 1	Vegetation

and the coverage area of that class, respectively. For the period 2000–2020, plots were made for the command areas.

The trends were identified and studied. Relation of climatic parameters upon the vegetation with the forest vegetation has been carried out on the basis of spatial and temporal variation

4 Results and Discussions

The LULC maps of Nagpur, Chandrapur, and Gadchiroli have been first studied in a chronological manner within the study time, i.e., 2000 and 2020. In the second part, the major focus of the study was on the forest area of Pench, Tadoba, and Gadchiroli and how the urban development has affected the climate and NDVI of the mentioned forests. The meteorological parameters are also related to the LULC change of the affecting urban areas; in this process, we can predict the effect of LULC changes of the urban areas on the NDVI of the study areas. Finally, the conclusion would be drawn on the effect of urban developments on the vegetation changes in nearby forest (Fig. 3, 4, 5 and 6).

The above study can help to understand the nature of effects that the anthropogenic activities in these cities can have on the forest ecosystem of the above-said forests. The study proved to be successful and some positive inferences were obtained about the anthropogenic activities and their effects on forest ecosystem. The land use and land cover map of the cities were studied in a time span and the probable meteorological effects were predicted that could occur in the close proximity of these cities which include the forest areas under study (Fig. 7, 8, 9, 10, 11, 12, 13 and 14).

The trend graphs provide a mathematical approach toward the understanding of the NDVI trends in the study area. The images were enough to understand the coarse patterns of NDVI. But, to understand the fine changes the graphs are necessary.

While from the NDVI graph it is evident that the vegetation has been decreasing through the years. All three forest areas including Pench, Tadoba, and Gadchiroli show similar trends of decreasing NDVI i.e., the density of the forest. But as compared to Pench and Tadoba, Gadchiroli show less decrement in vegetation.

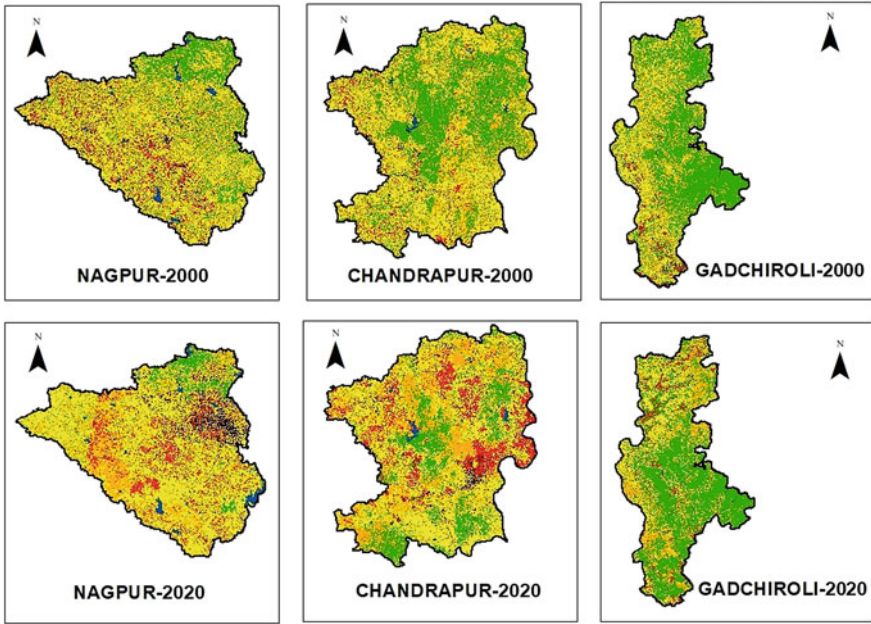


Fig. 3 LU/LC change in study area for year 2000 and 2020

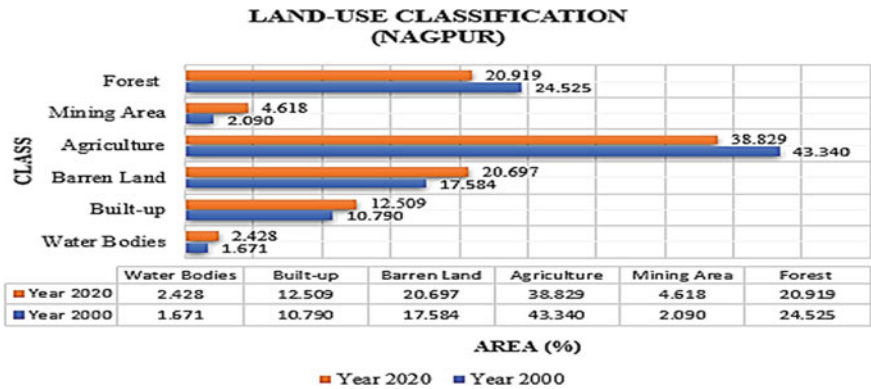


Fig. 4 Changes in LU/LC in Nagpur in 2000 and 2020

5 Conclusion

- In the last few years, there is a rapid rise in anthropogenic practices that have detrimental effects on the environment over time, so we have to consider the impact on the forest environment of human activities.

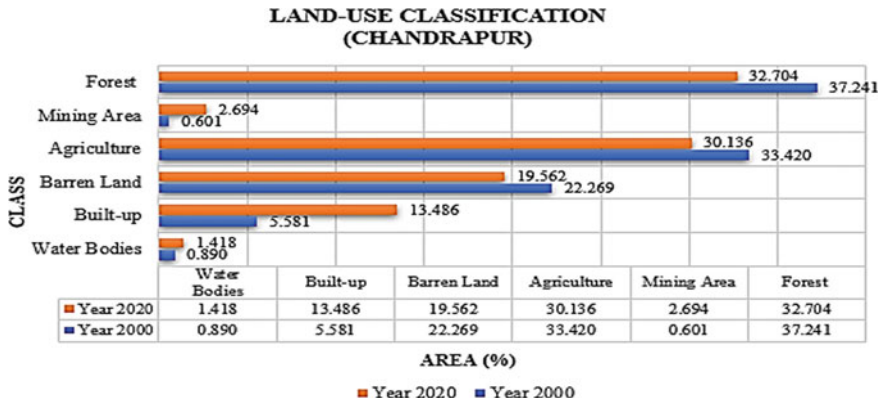


Fig. 5 Changes in LU/LC in Chandrapur in 2000 and 2020

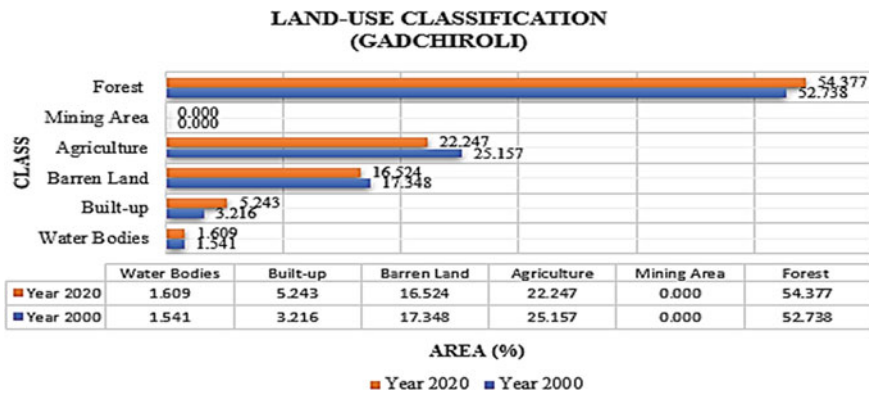


Fig. 6 Changes in LU/LC in Gadchiroli in 2000 and 2020

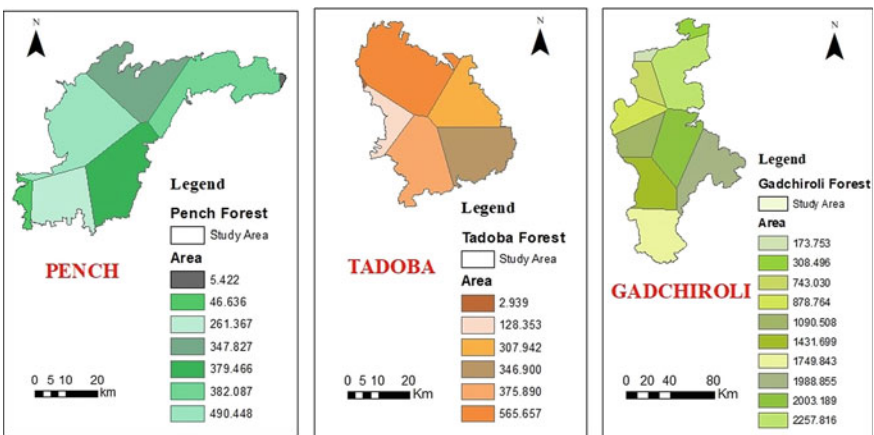


Fig. 7 Area of influence under each rain gauge station in the study area

RAINFALL MAP OF PENCH FOREST

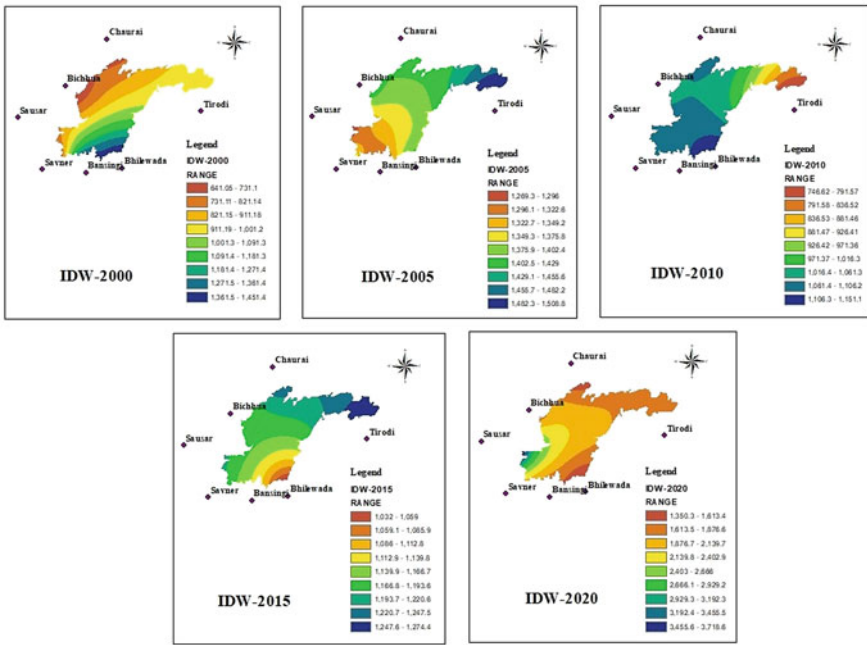


Fig. 8 Rainfall map of PENCH forest using IDW method

- The PENCH forest area has been decreased by 1.60% in the process of urbanization. The Tadoba forest area has been decreased by 4.53% in the process of urbanization. A drastic decrease of 4.53% has been monitored through the LULC maps. In the last twenty-one years, the Gadchiroli forest cover rises by 1.63%, because a small percentage in built-up area clearly states underdevelopment in Gadchiroli district. The positive scenario in the change of LULC of Gadchiroli is the increase in water bodies by 1.23%.
- This study aims to understand the impact of urbanization on three distinct Central Indian forests (Vidharba region of Maharashtra state). The target was to find out that if the development in these cities has been affecting the natural ecosystem adversely in last twenty-one years. This analysis can also clarify the understanding nature of effects that the anthropogenic activities in these cities can have on the forest ecosystem of near future.
- Through this study, it could have been understood that the protective measures taken by state and central government have been effective or not, and if not, then what are the probable measures that can be implemented.
- The land use and land cover map of the cities were analyzed over a period of time and the possible meteorological effects that could arise in the near vicinity of these cities, including the forest areas under study. Then, along with NDVI, the meteorological parameters (rainfall and temperature) were analyzed in these

RAINFALL MAP OF TADOBA FOREST

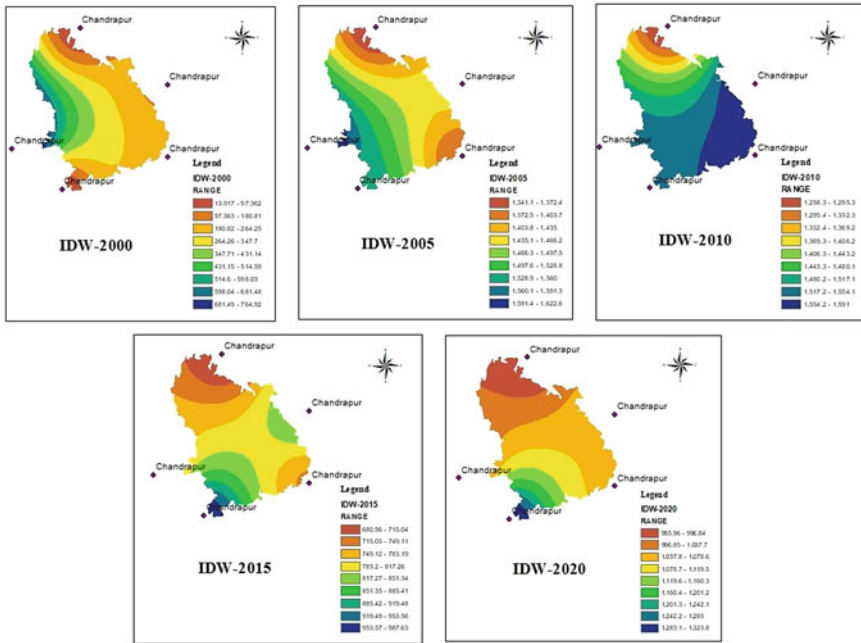


Fig. 9 Rainfall map of Tadoba forest using IDW method

forests to explain the patterns in the last twenty-one years and the patterns are then contrasted with the estimates of the transition from the previously collected causative cities on land use and land cover maps.

- In order to validate the predictions and inferences mathematically, a thorough analysis can be performed on the same, and this method can be pursued anywhere in other areas to figure out the impact of anthropogenic behavior on forest ecosystems.

RAINFALL MAP OF GADCHIROLI FOREST

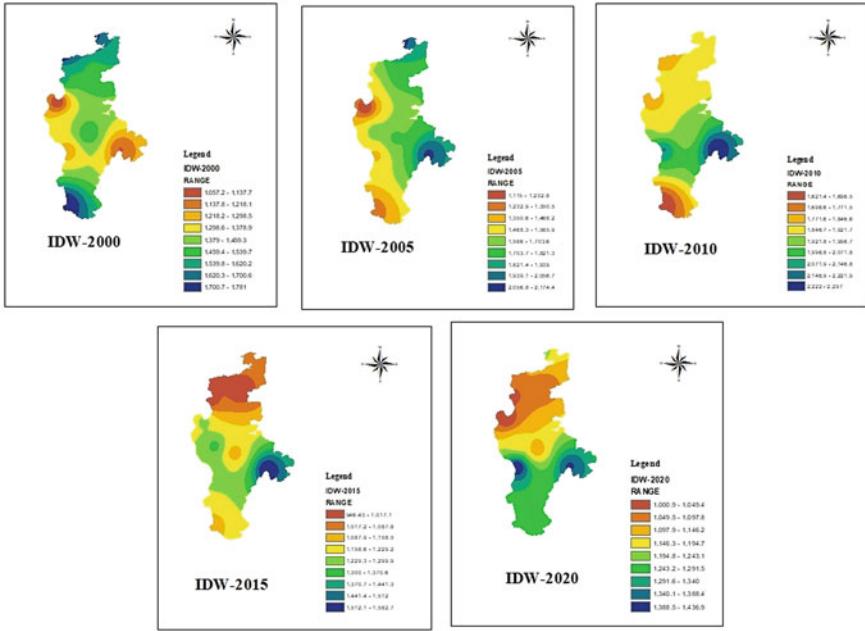


Fig. 10 Rainfall map of Gadchiroli forest using IDW method

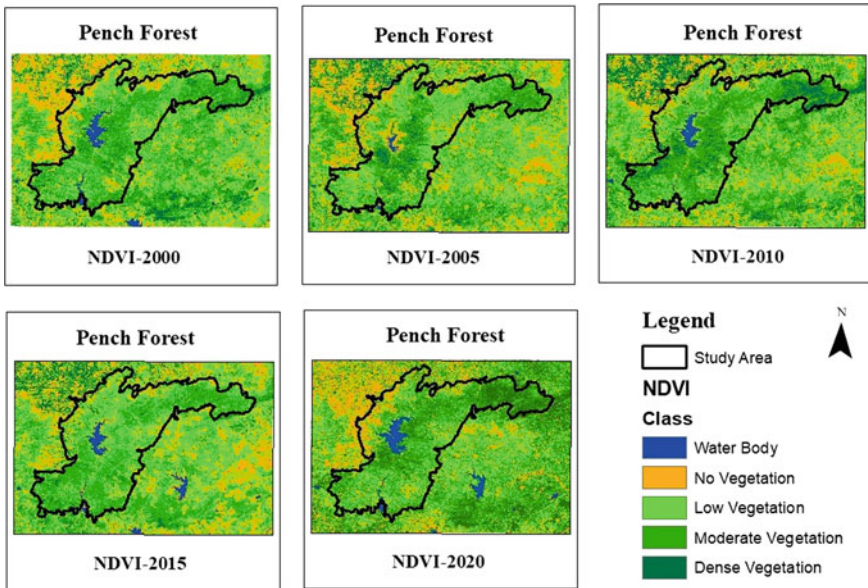


Fig. 11 NDVI image of Pench forest

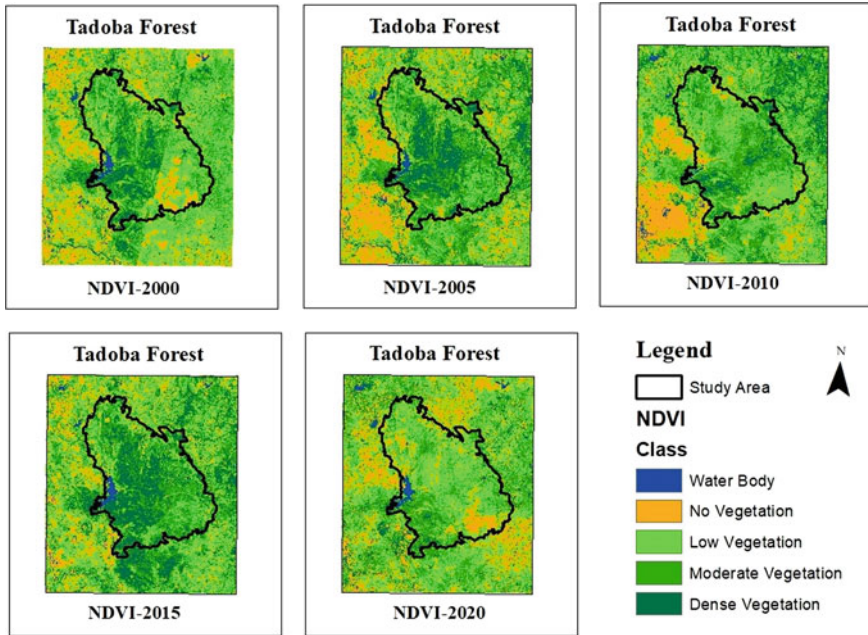


Fig. 12 NDVI image of Tadoba forest

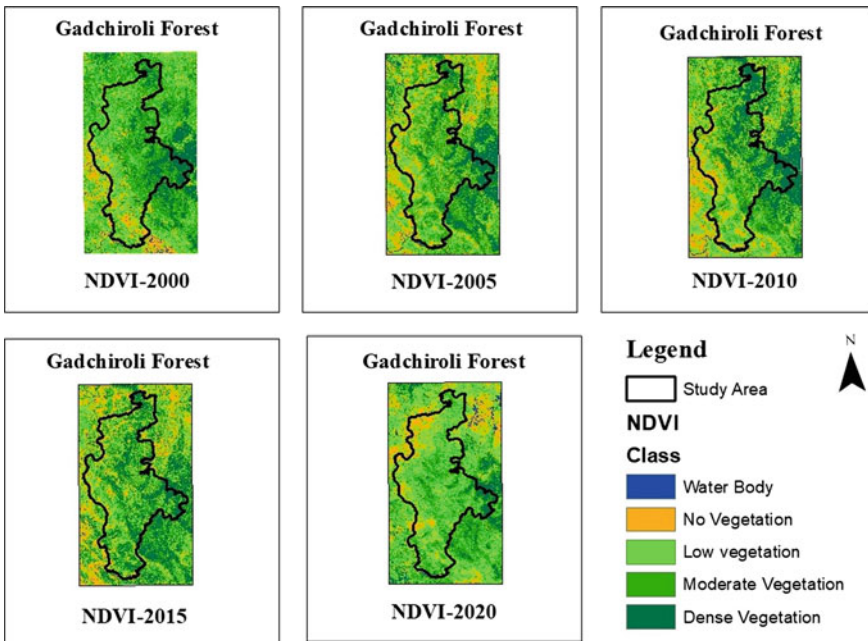


Fig. 13 NDVI image of Gadchiroli forest

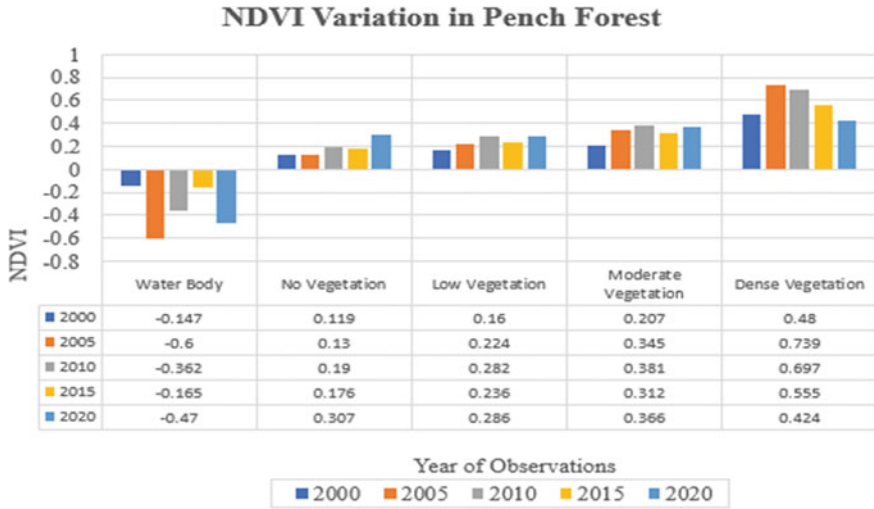


Fig. 14 Trend in NDVI variation in Pench forest

Seasonal and Lockdown Effects on Air Quality in Metro Cities in India



K. Krishna Raj and S. Shrihari

Abstract Air pollution is one of the worst avoidable threats in developing nations across the world. India has undergone a substantial number of infrastructure changes during recent years due to the ever-increasing population. This and the consequent industrialization, the air quality of Indian cities became worsened. The changes in climatic conditions across various cities in India also contribute to air pollution. To control the air pollution within the acceptable limit several control measures have been imposed in India, despite these efforts the air pollution level has not decreased considerably. In India, the first COVID-19 case has reported on 30th January 2020 in the state of Kerala. To control the quick spread of COVID-19 in India, the central government executed a three-week nationwide lockdown from 24th March 2020, and further, it has extended into several phases. It was the first time in India a long-term shutting down of all the sectors happening and which resulted in positively on the environment. This study is dealing with the lockdown effect on air quality in metro cities in India and is compared with the pre-existing conditions. Also, the seasonal variations in air quality in the course of the past two years are compared. The data of pollutants PM₁₀, PM_{2.5}, SO₂, NO₂, O₃, CO, and NH₃ from metro cities were collected and by adopting the National Air Quality Index to depict the variations in overall air quality. During the lockdown period, most of the cities experience a considerable improvement in overall air quality and PM₁₀, NO₂, PM_{2.5}, and CO concentrations. Whereas, the Ozone shows some increasing trend in a few cities might be due to the increment in the temperature caused by the exposure of sun during the summer season.

Keywords Lockdown · Metro cities · India · Air quality · COVID-19

K. Krishna Raj (✉) · S. Shrihari
Department of Civil Engineering, NITK Surathkal, Mangaluru, Karnataka, India
e-mail: krishnarajk1621@gmail.com

© The Author(s), under exclusive license to Springer Nature Singapore Pte Ltd. 2023
M. S. Ranadive et al. (eds.), *Recent Trends in Construction Technology and Management*, Lecture Notes in Civil Engineering 260,
https://doi.org/10.1007/978-981-19-2145-2_38

497

1 Introduction

Air pollution is one of the serious issues that developing nations like India face nowadays. The impacts of the abnormal population boost, urban growth, industrialization, and increment in vehicular count have created serious environment degradation, particularly, the deterioration of air quality in Indian cities. Along with the anthropogenic activities, the seasonal changes, differing climatology, and geography across the various regions also affect air pollution. According to Indian Meteorological Department (IMD), the winter season starts from December to February, summer season from March to May, monsoon season from June to September, and autumn season from October to November are the four major seasons in India [1]. Thus, air pollution causes serious health-associated difficulties related to organs like lung, heart, liver, etc. Therefore, effective air quality assessment at the city level could be a chief method for knowing the air pollution levels and might help to select appropriate schemes for opposing the condition. Identification of sources, technique adopted by the governing officials to reduce the emission, and checking the advancement in the technique adopted frequently are the chief elements of effective air quality [2].

Air Quality Index (AQI) is used to express the magnitude of air pollution of a region. In India, the monitoring of air quality was started in 1984 to quantify integrated air quality and in 2015 the CPCB revised the National Air Quality Index (NAQI) based on the maximum operator perspective [3]. Few of the Indian cities exceeding the air quality standards recommended by the World Health Organization (WHO) and Central Pollution Control Board (CPCB) for the past few years and thus falling into the list of most polluted cities of the world [4]. Non-local sources contribute around 70% of particulate matter in the North Indian region [5] and the activities like transportation, industrial, power generation and domestic fuel combustion, etc. helps to originate pollutants such as NO_x , CO, and SO_2 [6].

The Ministry of Environment, Forest, and Climate Change (MoEFCC) runs as the focal organization in collaboration with the UN Environment Programme for controlling air pollution and thus to protect the nature. The CPCB runs as a statutory body that obliged under the Air Act 1981. The Air Act (1981), Environment Act (1986), The Motor Vehicles Act (1988), The Public Liability Insurance Act (1991), National Environmental Tribunal Act (1995), National Environment Policy (2006) are also helping to protect the environment [3]. The biofuels scheme aimed to transform a minimum of 20% conventional fuel engines into biofuel engines by 2017 and the National Clean Air Programme introduced in 2016 focused on reducing particulate matter by 30% nationwide by the end of 2021 [7]. In addition to these, strategies like odd and even system in Delhi, introduced Metros to improve public transport, etc., were tried to reduce the air pollution in various cities. Despite these regulation measures, the air quality is not much improved across India.

From 24th of March 2020 to a period of three weeks a nationwide lockdown was forced in India due to the spread of pandemic COVID-19. During this period, activities related to transportation, industries, constructions, commercial, institutional, administrative, etc., have been restricted nationwide. As a result, the emission of

chief pollutants associated with these activities gets reduced in metro cities and which ultimately helped to improve the overall air quality of the cities during the lockdown as per the data from the CPCB. The current work is intended to know the degree of air quality change due the lockdown and also the variations in air quality during different seasons for the past two years at metro cities in India. Also, it is to evaluate the functionality of the lockdown as an approach for the reduction of air pollution in metro cities. The current work has focused on Delhi, Noida, Gurugram, Lucknow, Kolkata, Jaipur, Mumbai, Hyderabad, Bangalore, and Chennai. The objective of the study is to collate the chief atmospheric pollutant concentrations in metro cities from 24th of March to 14th of April in recent past years, to know the seasonal variations in air quality in metro cities, to estimate the general air quality due to the restrictions made during lockdown period and to assess the usefulness of the lockdown as an approach for reduction of air pollution in metro cities.

2 Materials and Methodology

The data From CPCB portal (<https://app.cpcbcr.com/ccr/#/caaqm-dashboard-all/caaqm-landing>) for air quality data dissemination, the concentrations of pollutants were obtained [8]. The pollutants selected for the analysis were $PM_{2.5}$, PM_{10} , SO_2 , NO_2 , CO , O_3 , and NH_3 . To compare the overall air quality of cities NAQI was used. The sub-indices for pollutants at a monitoring station were computed centered on 24-h average for $PM_{2.5}$, SO_2 , PM_{10} , NO_2 , and NH_3 and eight hours for O_3 and CO . Also, it is not possible to monitor all seven pollutants at all the locations concurrently. In order to measure NAQI, data of minimum of three pollutants concentration is necessary and it include either one among PM_{10} or $PM_{2.5}$ is requisite within those. Else, the data are inadequate for the calculation of NAQI. Similarly, for the estimation of subindex of a pollutant, a minimum of 16 h data is necessary and the air quality of a pollutant is the subindex value calculated for that pollutant.

3 Results and Discussion

3.1 Changes in NAQI During Lockdown

The metro cities have witnessed a substantial reduction of the pollutants after the declaration of the lockdown measures. During the three-week lockdown in the year 2020, the sectors like industries, mass transportation, construction, commercial, and institutional establishments were remains closed. Thus, the lockdown helped the cities to reduce the emission rate of air pollutants. As a result, the average NAQI of metro cities had shown a considerable reduction during the lockdown period (Fig. 1). The North Indian cities had shown a maximum depletion in air pollution

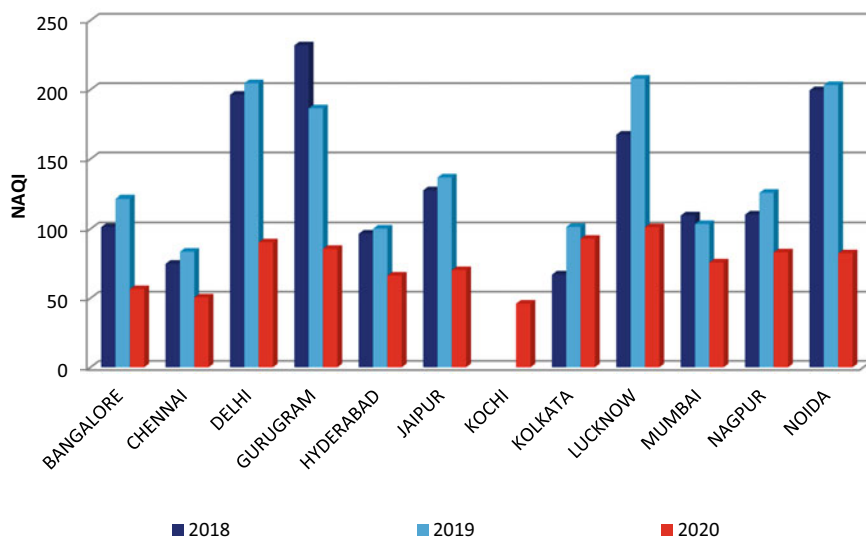


Fig. 1 Changes in average NAQI during 24 March–14 April in recent past years at metro cities

during the study period. The overall air quality of cities Noida and Gurugram had been improved by about 59.12% during the lockdown in comparison with the average of previous years. Similarly, the cities Delhi, Jaipur, and Lucknow had undergone 54.98%, 46.85%, and 46.12% improvements in NAQI, respectively. Whereas, metro cities located other than North India also had considerable enhancement in overall air quality. During the lockdown period, the average NAQI values of all cities except Lucknow fall below 100. The cities Chennai, Hyderabad and Nagpur NAQI was falls under the category of satisfactory or good throughout the lockdown period. This improvement in air quality is primarily due to the depletion in the concentration of PM_{10} , NO_2 , $PM_{2.5}$, and CO.

3.2 Changes in Pollutant Concentration During Lockdown

The closure of all sectors during the lockdown period helped to reduce the emission of Particulate Matters (PM) drastically. The average concentration of significant pollutants at different metro cities during the period starting from 24th of March–14th of April during the past years is indicated in Table 1. Table 1 outlines the slight increment in the concentration of pollutants in the year 2019 than that of 2018. Whereas, during the lockdown, the PM_{10} concentration reduced by more than 60% in cities Delhi and Noida in comparison to 2018 and 2019. Thus, the cities located in the northern part of India have undergone a maximum declination in pollutant concentration during the lockdown period in comparison with the previous years. It

Table 1 Variations of average concentration of dominant pollutants during 24 March–14 April in recent past years at metro cities

Span	24 March–14 April											
	2018				2019				2020			
Cities	Average pollutants concentration ($\mu\text{g}/\text{m}^3$)											
	PM ₁₀	PM _{2.5}	NO ₂	O ₃	PM ₁₀	PM _{2.5}	NO ₂	O ₃	PM ₁₀	PM _{2.5}	NO ₂	O ₃
Bangalore	92.7	30.5	26.0	46.2	113.1	51.3	35.7	55.1	46.8	25.9	11.3	43.2
Chennai	–	39.2	18.3	33.1	32.8	38.5	13.7	25.6	145.4	22.6	8.5	35.4
Delhi	219.0	87.6	46.7	51.2	225.9	86.2	34.9	44.7	84.8	40.7	20.0	39.5
Gurugram	173.0	70.5	24.8	25.9	213.7	82.5	9.0	32.6	73.8	35.3	14.7	55.8
Hyderabad	99.3	45.1	41.1	44.2	109.0	43.6	36.7	38.3	64.3	33.8	19.5	32.1
Jaipur	132.4	50.9	34.3	74.1	154.4	49.4	33.0	61.4	59.1	23.0	13.4	48.2
Kochi	–	–	–	–	–	–	–	–	23.2	39.3	2.5	1.32
Kolkata	77.7	46.0	12.5	49.3	94.2	48.5	42.4	31.0	65.3	37.3	12.6	56.9
Lucknow	–	85.5	42.1	33.1	–	102.4	47.7	39.2	49.9	34.5	13.3	32.8
Mumbai	–	–	–	–	95.7	25.8	18.5	26.4	74.0	25.4	8.8	27.7
Nagpur	103.3	48.9	38.9	46.4	105.2	52.5	46.7	115.3	45.7	22.5	22.9	57.7
Noida	271.6	68.4	27.5	43.3	237.0	90.1	35.2	28.0	77.0	34.7	14.3	41.5

is primarily because of the restriction given on transportation and industrial activities during the span. Due to the prevailing local conditions in the course of the lockdown span in Chennai, the PM₁₀ concentration has increased more than fourfold upon comparing with the average of the same period in 2019. Similar to the trend of PM₁₀, the pollutant PM_{2.5} has also declined drastically in North Indian cities and moderate to slight in other cities during the lockdown period. About 53.12% reduction in PM_{2.5} has been observed in Delhi in the course of the lockdown period upon comparing with the average concentration for same period in 2018–2019. Table 2 shows the area-wise concentration of particulate matter in typical metro cities. In metro cities, industrial and transportation sectors play a vital role in the increment of pollution rate. In Delhi, the pollutant concentrations from industrial and transportation sector has reduced more than 60% in case of PM₁₀ and more than 50% in the case of PM_{2.5}. Thus, this data opens our eyes to the need for restriction implementation on anthropogenic activities. During the lockdown period, vehicle counts on the road decreased, the manufacturing processes paused in industries helped to reduce the dust resuspension in metro cities.

In metro cities, the source for NO₂ and CO is from vehicles on road, combustion practice, manufacturing industry, and power plants. The lockdown also reduced the concentration of pollutants NO₂ by more than 60% in cities like Lucknow, Bangalore, and Jaipur upon comparing with the average value of 2018–2019 for the same period. Gurugram was the only city which shows increment in NO₂ during the lockdown period by about 63.3% during the lockdown in comparison with the average value of 2019. Figure 2 shows the trends of variations of CO in metro cities from

Table 2 Area wise variation of concentration of chief pollutants during 24 March–14 April in recent past years at typical metro cities

Cities	pollutants	Span from 24 March–14 April										Overall variations		
		Average concentration of 2018–2019					Average concentration during lockdown 2020					Residential and other areas	Net	%
		Avg	Industrial area	Transport area	Residential and other areas	Avg	Industrial area	Transport area	Residential and other areas					
Delhi	PM ₁₀	222.5	246.5	244.8	203.7	84.8	96.1	90.4	79.7	–137.7	–61.9			
	PM _{2.5}	86.9	94.3	93.2	81.84	40.7	45.9	43.4	39.0	–46.2	–53.2			
Hyderabad	PM ₁₀	104.2	113.9	110.0	99.6	64.3	60.9	80.6	61.7	–39.9	–38.3			
	PM _{2.5}	44.4	47.3	51.7	44.2	33.8	31.1	47.0	33.5	–10.6	–23.9			
Bangalore	PM ₁₀	102.9	–	138.4	94.9	46.8	–	39.5	48.5	–56.1	–54.5			
	PM _{2.5}	40.9	–	50.5	39.9	25.9	–	30.6	24.9	–15.0	–36.7			
Lucknow	PM _{2.5}	94.0	112.5	100.9	88.3	34.5	72.6	65.2	33.6	–59.5	–63.3			

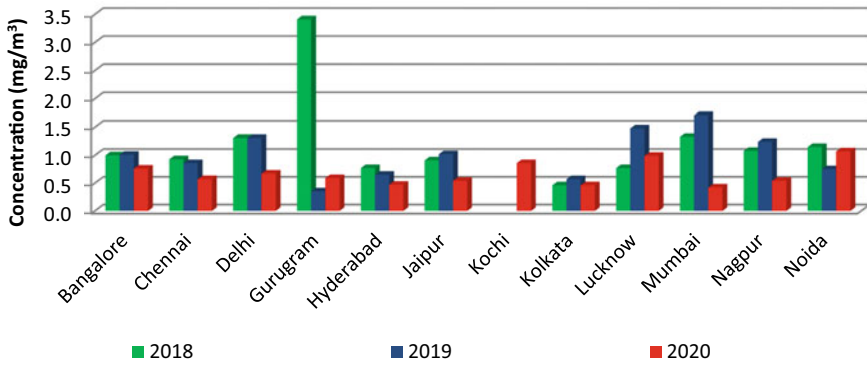


Fig. 2 Average variation of concentration of CO at different metro cities during 24 March–14 April in recent past years

24th of March–14th of April in recent past years. The mean concentration of CO in cities Mumbai and Gurugram has declined by about 72.37% and 68.62% respectively during the lockdown than that of the averaged value of 2018–2019 for the same duration. Whereas, Noida is the only city which shows increment in concentration of CO by about 12.63% in comparison with the averaged value of 2018–2019. Significant declining trends in NO₂ and CO were observed in the first two weeks of lockdown period, afterward, it shows some increase in the concentration of these pollutants. The reason for the increase might include the open burning of nonbiodegradable materials at households and intermittent checking of parked vehicles such as buses and heavy motors.

On the other hand, the pollutant Ozone shows a slight rise in the course of the lockdown span in majority of cities. Whereas, few cities like Bangalore, Delhi, Hyderabad, etc., show decreasing trends too. The reason for the changes in O₃ concentration might be because of the usual rise or fall of exposure of sunlight and temperature during the summer period in different cities. The pollutants SO₂ and NH₃ experience a slight fall in the mean concentration in the course of the lockdown. The major emission source for SO₂ in metro cities includes fossil fuel combustion at power plants and industries, burning of materials that contain sulfur, metals processing, and smelting facilities, and vehicles. Whereas, sources of NH₃ include industrial processes, vehicular emissions, and uses of NH₃-based fertilizers. The lockdown helps to reduce the pollutants in metro cities due to the closure of these sectors during the period.

3.3 Seasonal Variations in NAQI

The differing climates in metro cities have a dominant part in making the air quality of a city poor. The majority of cities exceed the permissible levels of NAQI during the

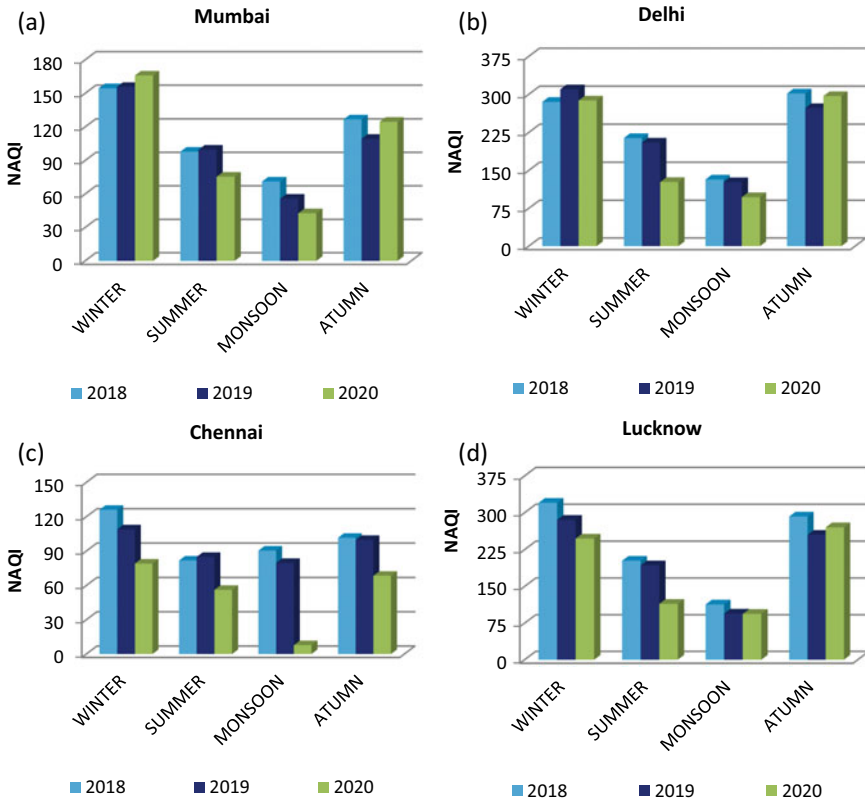


Fig. 3 Seasonal changes in average NAQI in typical metro cities for the recent past years

autumn and winter seasons (Fig. 3). It is primarily because of the practice of open-burning biodegradable and nonbiodegradable materials. The direction of wind plays a crucial role in transporting pollutants from one place to another. Thus, along with the anthropogenic activities, the natural phenomenon also had a prominent role in deciding the air quality of a city. During the autumn season, farmers burn agricultural wastes like straw stubble that makes the air quality very poor in North Indian cities. Similarly, the burning of agricultural straw stubble happens during the end of the winter season in Southern India. Whereas in monsoon season, the continuous rain and cyclonic winds help to improve the air quality. The overall air quality became improved exceptionally than that of other seasons because of the flowing of pollutants with rainwater in the monsoon season. The average NAQI during the monsoon season in the year 2020 is nearly equal to or more improved than that of the lockdown period in selected cities. The reason for the extra enhancement in air quality in the course of the monsoon season in 2020 is due to the extension of restrictions on certain activities into several phases. Similarly, the phased unlock procedure also helped to improve the air quality during this season. On the other hand, the average NAQI during the

summer season has much above the monsoon season but falls below the average values of the autumn and winter season. The North Indian cities had poor air quality in all seasons than that of the other locations might be due to the increased number of vehicular sources, manufacturing industries, and power plants located nearby cities. There are not many changes observed in the NAQI in 2018 and 2019 in all seasons. Similarly, during the winter and autumn season in the year 2020, the air quality becomes worsened equal to or more than that in the same seasons in previous years. Thus, it may be indicating the need for a strategy to improve the overall air quality levels in metro cities during the winter and autumn seasons.

3.4 Seasonal Variations in Dominant Pollutants

The concentrations of air pollutants have a drastic increment during the autumn and winter season in metro cities due to various reasons (Fig. 4). The prevailing local condition in different cities during the autumn and winter season plays a vital role in the variation of air pollutants. As a result, the particulate matter, NO_2 , and O_3 levels have shown high variation than those in the monsoon and summer seasons. Open burning of biomass during the autumn and winter season increasing the concentration of PM_{10} and $\text{PM}_{2.5}$ far above the acceptable limits. In North Indian cities like Delhi, Noida, Gurugram, etc., particulate matter has been deteriorating the air quality during the autumn and winter season. The yearly average concentration of PM_{10} for the city Delhi was 244.3, 188.9, and 160.9 $\mu\text{g}/\text{m}^3$ for 2018, 2019, and 2020, respectively. Whereas, the average seasonal concentration of PM_{10} for the winter and autumn lies far above the annual average values for the past years from 2018 to 2020 in Delhi. Similarly, in the case of $\text{PM}_{2.5}$, the trends of variation were identical as that of PM_{10} . Other cities also had more or less identical behavior that of the city Delhi in the case of particulate matters. On the other hand, the concentration of CO, NO_2 , and O_3 was almost having same value during the autumn and winter seasons in all cities. Upon comparing with other seasons, the concentration of these two pollutants were high in the winter and autumn season. Along with anthropogenic activities, the natural phenomenon like wind direction, wind velocity, moisture content, etc., has a significant role in maintaining the air quality very poor. Thus, during the autumn and winter season, it is a must to introduce some strategies to control the pollutants within the acceptable limits.

Similar to the trend of NAQI, the air pollutants concentration has also shown declining trends during the monsoon season. Upon comparing with other seasons, during monsoon, all the pollutants have shown declining trends in cities. The average monsoon season concentration for the year 2020 for most of the selected cities falls below the three-week average value during the lockdown period. It is because of the continued number of lockdown phases followed by a number of unlocking phases. Even in the years 2018 and 2019, the average monsoon season concentration of air pollutants were almost equal to or slightly more than the corresponding average concentration of pollutants in the lockdown period. Thus, during monsoon season,

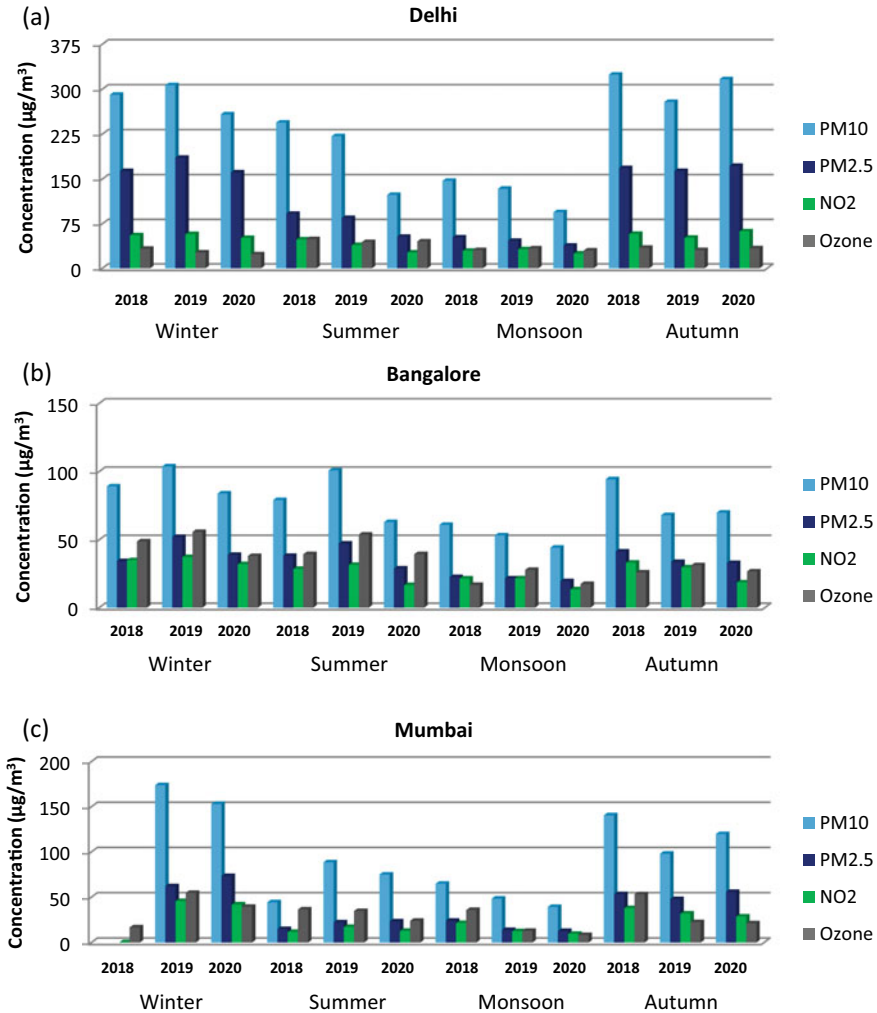


Fig. 4 Seasonal changes in average concentration of chief pollutants at typical metro cities **a** Delhi **b** Bangalore **c** Mumbai

every city has shown a minimum level of concentration of pollutants. Due to the decline in the natural exposure of sunlight and temperature during monsoon season, the concentration of O₃ has shown decreasing trend than that of the other seasons. Similarly, other pollutants also had reducing trend during the monsoon season.

Whereas in summer, the concentration of pollutants except O₃ has a value greater than the concentration of corresponding pollutants in monsoon and less than that of the autumn and winter. The pollutant Ozone has shown maximum concentration during the summer season. It might be due to the increment in the natural exposure of sunlight and temperature during the summer season. Due to the dust resuspension

and open burning the PM_{10} and $PM_{2.5}$ remains high value in the course of summer also. Upon comparing the North Indian cities with other cities, the cities located in North India have high concentration of particulate matter. Whereas, in certain cities located in Southern India, low concentration of PM might be due to the intermittent summer rain and cyclonic winds.

3.5 Annual Average Variation of Particulate Matter

Particulate matter (PM) decides the overall air quality in terms of NAQI in a city most of the time. Table 3 has shown the variation in annual mean of PM_{10} and $PM_{2.5}$

Table 3 Annual average concentration of particulate matter in recent past years at metro cities

Cities	Pollutants	Average concentration ($\mu\text{g}/\text{m}^3$)			Variation between 2020 and 2019		Variation between 2020 and 2018	
		2018	2019	2020	Net	Percentage	Net	Percentage
Bangalore	PM_{10}	79.6	77.3	63.6	-13.7	-17.7	-16.0	-20.1
	$PM_{2.5}$	34.4	35.8	29.2	-6.6	-18.4	-5.2	-15.11
Chennai	PM_{10}	-	50.1	80.6	+30.5	+60.87	-	-
	$PM_{2.5}$	53.3	42.7	30.7	-12.0	-28.1	-22.6	-42.4
Delhi	PM_{10}	244.3	217.2	160.9	-56.3	-25.9	-83.4	-34.1
	$PM_{2.5}$	114.7	108.2	81.4	-26.8	-24.8	-33.3	-29.0
Gurugram	PM_{10}	233.0	188.9	148.5	-40.4	-21.4	-84.5	-36.3
	$PM_{2.5}$	111.5	93.2	81.9	-11.3	-12.1	-29.6	-26.6
Hyderabad	PM_{10}	95.6	91.7	77.6	-14.1	-15.4	-18.0	-18.8
	$PM_{2.5}$	43.2	41.5	35.8	-5.7	-13.7	-7.4	-17.1
Jaipur	PM_{10}	141.5	114.6	102.7	-11.9	-10.4	-38.8	-27.4
	$PM_{2.5}$	62.1	49.1	45.1	-4.0	-8.2	-17	-27.4
Kochi	PM_{10}	-	-	59.4	-	-	-	-
	$PM_{2.5}$	-	-	32.8	-	-	-	-
Kolkata	PM_{10}	104.6	125.2	88.6	-36.6	-29.2	-16.0	-15.3
	$PM_{2.5}$	61.3	68.4	48.6	-19.8	-29.0	-12.7	-20.7
Lucknow	PM_{10}	-	-	210.3	-	-	-	-
	$PM_{2.5}$	116.4	97.4	89.3	-8.1	-8.3	-27.1	-23.3
Mumbai	PM_{10}	88.4	96.5	90.8	-5.7	-5.9	+2.4	+2.7
	$PM_{2.5}$	33.1	34.8	37.5	+2.7	+7.8	+4.4	+13.3
Nagpur	PM_{10}	88.4	79.2	56.1	-23.1	-29.2	-32.3	-36.5
	$PM_{2.5}$	44.5	42.4	29.3	-13.1	-30.9	-15.2	-34.2
Noida	PM_{10}	252.7	225.1	184.8	-40.3	-17.9	-67.9	-26.9
	$PM_{2.5}$	116.8	110.6	97.2	-13.4	-12.1	-19.6	-16.8

in metro cities. In general, the annual average concentration of particulate matters in most of the cities had a decreasing trend from 2018 to 2020. Upon comparing the annual average concentration of PM_{10} in 2020, Chennai is the only city which shows an increase of about 60.87% than that of 2019. Similarly, in Mumbai, the annual mean of $PM_{2.5}$ in 2020 has increased beyond 7% than that of 2019. Whereas, in 2020, about 2.7% and 13.3% increment has been observed in PM_{10} and $PM_{2.5}$, respectively, in Mumbai than that of the year 2018. Mumbai is the only city which has shown increasing trend in the concentration of $PM_{2.5}$ both in 2019 and 2020 than that of the annual average concentration in the year 2018. All other cities have shown declining trend in the level of particulate matter in the year 2020. The decrease in PM_{10} and $PM_{2.5}$ was primarily due to the lockdown measures implemented to control the rapid spread of COVID-19. Also, the extended lockdown measures and phased unlock of lockdown during the monsoon season drastically reduced the particulate matters.

The cities located in North India have undergone a maximum reduction in concentration of particulate matter in the year 2020. Upon comparing the average concentration of PM_{10} in 2018–2019 with 2020, about 30.27%, 29.60%, 15.89%, and 22.65% reduction has observed in cities Delhi, Gurugram, Jaipur, and Noida respectively. Similarly, in the case of $PM_{2.5}$ about 26.96%, 19.98%, 18.88%, and 14.51% reduction has observed in cities Delhi, Gurugram, Jaipur, and Noida respectively.

4 Conclusions

The study was conducted to determine the seasonal and lockdown effect on air quality in metro cities in India. The result reveals that the metro cities undergo significant improvement in overall air quality in terms of NAQI during the lockdown duration. The reason for the improvement in NAQI is due to the reduction in concentration of chief pollutants such as PM_{10} , $PM_{2.5}$, NO_2 , and CO. This improvement in overall air quality directly reveals the role of anthropogenic activities on air pollution. Similarly, the overall air quality in terms of NAQI becomes worsened during the autumn and winter season. Therefore, this study is a helpful addendum to the governing authorities to plan a new measure like short duration lockdown (say up to 7 days) in an aim to improve the air quality, especially, during the autumn and winter season.

References

1. Roy SS (2019) Spatial patterns of trends in seasonal extreme temperatures in India during 1980–2010. *Weather Climate Extremes* 24
2. Brauer M, Guttikunda SK, Nishad KA, Deye S, Tripathig SN, Weagleh C, Martin RV (2019) Examination of monitoring approaches for ambient air pollution: a case study for India. *Atmos Environ* 216:116940

3. Mahato S, Pal S, Ghosh KG (2020) Effect of lockdown amid COVID-19 pandemic on air quality of the megacity Delhi, India. *Sci Total Environ* 730:139086
4. Garaga R, Sahu SK, Kota SH (2018) A review of air quality modeling studies in India: local and regional scale. *Current Pollution Reports*
5. Guo H, Kota SH, Sahu SK, Zhang H (2019) Contributions of local and regional sources to PM_{2.5} and its health effects in north India. *Atmos Environ* 214:116867
6. Sunil Gulia SM, Nagendra S, Khare M, Khanna I (2015) Urban air quality management-A review. *Atmos Pollut Res* 6:286–304
7. Sharma S, Zhang M, Anshika JG, Zhang H, Kota SH (2020) Effect of restricted emissions during COVID-19 on air quality in India. *Sci Total Environ* 728:138878
8. Central Control Room for Air Quality Management Delhi NCR, CAAQMS Information, <https://app.cpcbcr.com/ccr/#/caaqm-dashboard-all/caaqm-landing>, Accessed date: June 2020 to Dec 2020

Inter-Basin Pipeline Water Grid for Maharashtra



Raibhann Sarnobbat, Pritam Bhadane, Vaibhav Markad,
and R. K. Suryawanshi

Abstract Maharashtra is facing water crises of unprecedented nature. There are floods during monsoon but in the same area, there is no water during the summer season. Some regions conically face years of droughts and the rivers' current have webbed. Some reservoirs spill during monsoon whereas some do not get filled. On the other hand, water demands are continuously increasing. To overcome these issues, in this paper an attempt is made to develop an inter-basin water transfer pipeline grid for the river basins in the state of Maharashtra with the objective of transfer of water from surplus to deficits for both spatial and temporal scales. Major storages in all the river basins in the state are located at the georeferenced locations on the Digital Elevation Model (DEM) of Maharashtra. Using the DEM to contour map and FRL and DSL of each of the reservoirs, pipeline water grid is delineated. The pipeline grid is filled during monsoon so that surplus waters can be transferred to deficit reservoirs. This also can be done during non-monsoon to serve the scarcity regions. Since the pipeline grid is designed for gravity flow and no major land acquisition issues are involved, the inter-basin pipeline water grid can be an effective solution to mitigate the water problems in the state.

Keywords Water crises · Pipeline water grid · Gravity flows · ArcGIS

1 Introduction

State of Maharashtra in India faces varied rainfall conditions. The north–south small strip of Konkan region experiences very high rainfall whereas the widely spread Marathwada region receives very less rainfall compared to the national average. Rainfall is restricted to monsoon months of June to September only. Rest of the period is practically dry. Thus, the spatial and temporal distribution of surface water resources is highly skewed [1, 2]. Major portion of the state includes river basins of Krishna, Godavari, and Tapi and west-flowing rivers and a small portion in north falls

R. Sarnobbat · P. Bhadane · V. Markad · R. K. Suryawanshi (✉)
Emeritus Prof COEP, Pune, India
e-mail: rksurya2000@yahoo.com

© The Author(s), under exclusive license to Springer Nature Singapore Pte Ltd. 2023
M. S. Ranadive et al. (eds.), *Recent Trends in Construction Technology and Management*, Lecture Notes in Civil Engineering 260,
https://doi.org/10.1007/978-981-19-2145-2_39

511

in the Narmada basin. The major rivers flowing through the state include Godavari, Krishna, Tapi, Indravati, Wardha, Manjara, Penganga, Purna, and the west-flowing rivers of Konkan strip. Many times, there is excess water in some basins whereas other basins face high water scarcity. Water demands are also varying spatially as well as temporally in view of increasing population, rapid urbanization, and industrialization. Thus, it has become highly essential to have long-term planning for water resources management to meet the rapidly changing supply and demand scenario [3–5]. The inter-basin water transfer is an alternative to balance the non-uniform temporal and spatial distribution of availability of water resources and water demands [6, 7].

2 The Need

Generally, inter-basin water transfer is attempted by linking two or more rivers by creating a network of canals to transfer the water from surplus river basin to the deficit river basin which can mitigate the droughts and floods situations to some extent. In this study, an attempt is made to analyze the feasibility of the inter-basin water transfer in Maharashtra using pipeline grid with gravity flow. Accordingly, the main four river basins of Godavari, Krishna, Tapi, and west-flowing rivers are considered for transfer of water from basin to basin. Some of the major reservoirs in these basins are interconnected so that the excess water in the reservoir can be transferred to the deficit reservoir under gravity flow using a pipeline. The tools used include ArcGIS with Google Pro [1, 8].

3 Study Area

The objective is to study the feasibility of establishing a water transfer grid under gravity flow using pipes instead of conventional canal grid for the state of Maharashtra. The basins selected include Krishna, Godavari, Tapi, west-flowing rivers as depicted in Fig. 1. The major reservoirs in these basins are selected for the establishment of pipeline links.

The Krishna basin with catchment area of about 258,948 km² has average annual rainfall of 921 mm. Total of 11 major storages are selected from this basin for the pipeline grid. The Godavari basin has a catchment area of about 312,811 km² with average annual rainfall of 947 mm. Total of 15 reservoirs are selected from this basin. The Tapi basin has a catchment area of about 51,504 sq. km having average annual rainfall of 709 mm and total 5 dams are selected from this basin. West flowing river basins have a catchment area of about 33,017 sq. km with average annual rainfall of 3145 mm and 4 reservoirs are selected from this basin for pipeline grid. The basin wise reservoirs selected and their relevant characteristics such as FRL, MDDL, storage capacity are shown in Tables 1, 2, 3, and 4.



Fig. 1 River basins in Maharashtra

Table 1 Krishna basin reservoirs

Sr No	Reservoir	FRL (m)	MDDL (m)	Gross storage (MCM)	Height of dam (m)
1	Dhoni	747.70	725.0	382.97	50.00
2	Dimbhe	719.15	711.9	380.00	67.21
3	Pimpalgaon Joge	686.80	678.4	235.53	28.60
4	Koyna	657.90	609.5	2797.40	103.00
5	Varasgaon	639.50	628.7	374.00	63.40
6	Panshet	635.81	609.8	303.00	63.56
7	Kasarsai	626.60	610.6	17.38	17.27
8	Pawana	613.26	602.0	305.00	42.37
9	Radhanagari	590.00	566.1	236.79	42.68
10	Khadakwasla	582.87	578.6	86.00	32.90
11	Ujjani	497.58	491.0	332.00	56.40

Table 2 Godavari basin reservoirs

Sr. No	Reservoir	FRL (m)	MDDL (m)	Gross storage (MCM)	Height of dam (m)
1	Bhandardara	744.74	720.7	312.4	82.35
2	Karanjvan	661.00	553.0	248.0	39.61
3	Nilwande	660.00	640.0	236.0	73.91
4	Manjara	642.37	633.4	250.7	25.00
5	Gangapur	612.50	606.0	215.0	36.57
6	Darna	593.00	570.0	226.9	28.00
7	Mula	552.30	534.2	738.9	48.17
8	Nandur-Madhyameshwar	533.53	529.3	29.9	10.90
9	Totladoh	490.00	464.0	1241.0	74.50
10	Jayakwadi	483.91	441.6	2909.0	41.30
11	Yeldari	461.67	455.6	934.0	51.20
12	Isapur	441.00	418.7	1241.5	57.00
13	Upper wardha	342.00	332.5	786.5	46.20
14	Gosekhurd	245.00	241.3	1146.1	22.40
15	Erai	207	200.5	144.69	30.0

Table 3 Tapi basin reservoir

Sr No	Reservoir	FRL (m)	MDDL (m)	Gross storage (MCM)	Height of dam (m)
1	Chankapur	673.52	658.1	79.7	39.00
2	Girna	398.07	382.8	608.9	54.56
3	Akkalpada	390.00	370.0	369.0	33.00
4	Wagur	234.10	223.6	325.0	13.60
5	Hatnur	214.00	207.7	388.0	25.50

Table 4 West flowing rivers basin reservoirs

Sr No	Reservoir	FRL (m)	MDDL (m)	Gross storage (MCM)	Height of dam (m)
1	Upper vaitarna	663.5	580.0	353.96	41.0
2	Tillari	462.0	437.0	462.20	73.0
3	Bhatsa	142.7	79.2	976.10	88.5
4	Talamba	142.4	100.0	308.75	57.4

Table 1 shows the reservoirs selected in the Krishna basin. Among the storages considered in this study, it can be observed that from the point of view of feasibility of water transfer with gravity pipe flow, the highest FRL elevation in Krishna basin

is for Dhom reservoir, and lowest FRL is for Ujjani reservoir. The largest storage capacity is of Koyna reservoir with gross storage of 2797.4 MCM.

Table 2 shows the reservoirs selected in the Godavari basin. Among the storages considered in this study, the reservoir with the highest elevation in the Godavari basin is Bhandardara and at lowest being Gosekhurd. The largest storage capacity is of Jayakwadi reservoir with gross storage of 2909 MCM.

Table 3 shows reservoirs selected in Tapi basin. Among the storages selected it is seen that the storage with highest FRL elevation in Tapi basin is Chanakapur and at lowest being Hatnur. The largest storage is Girna with a gross storage capacity of 608.9MCM.

Table 4 shows reservoirs selected in west-flowing river basins. Among the storages selected, the highest FRL elevation in west-flowing rivers basin is of Upper Vaitarna reservoir and the lowest is for Talamba. The largest storage is of Bhatsa having gross storage capacity of 976.1 MCM.

4 Methodology

The study is conducted as per the study flow chart as depicted in Fig. 2. For establishment of pipe water grid in the state of Maharashtra, total of 35 major reservoirs in four river basins are selected representing all the regions of the stat.

Methodology followed mainly includes the following assumptions:

- This water grid is based on purely technical aspects related to the flow of water in the pipeline grid. Interstate water agreements for sharing of water, etc., are beyond the scope of this study [7].
- Water is taken out at MDDL of the upper reservoir and is to be emptied at FRL of the connection lower reservoir considering that the reservoir whose MDDL

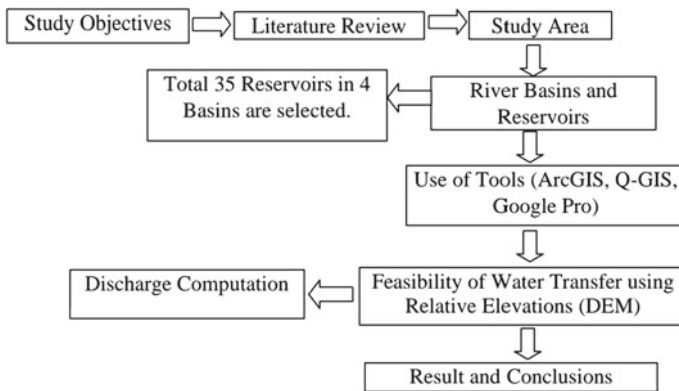


Fig. 2 Methodology flow chart

is higher than FRL of the lower reservoir so that water can be transferred under gravity flow.

- To save land acquisition cost, pipelines are proposed along either side of state and national highways.
- Wherever local height is greater than MDDL of the upper reservoir, such lengths can be under cuttings or tunnels which can be identified and computed.
- The maximum diameter of the pipeline is 1.8 m to restrict the water transfer from basin to basin.
- Only selected major projects are considered to represent all the basins in the state.
- The idea is to transfer water from water surplus to water deficit reservoirs at any point of time especially during monsoon months when reservoirs are spilling or to mitigate the drought situation. with respect to time and regions [5].

5 Analysis and Results

Tools used include mainly ArcGIS with images from Google Pro. SRTM 90 m DEM (Fig. 3) is used for the entire state of Maharashtra. Using ArcGIS morphological analysis is carried out and the drainage basins are delineated and the locations of the selected major projects in each basin are marked (Fig. 4) The reservoir-to-reservoir



Fig. 3 DEM image of Maharashtra



Fig. 4 Location of selected reservoirs

pipeline grid within the basins and inter basins are digitized using the alignments of State and National Highways using google images. The results are as per Figs. 5, 6, 7, 8 and 9 for all respective intra basins grids as well as for inter-basin grid. The maximum possible discharges in each of the links are computed using the Darcy–Weisbach equation.

To calculate discharge through the pipeline using head loss.

$$H_l = f \frac{L}{D} \frac{v^2}{2g} \tag{1}$$

where

H_l = Head Loss,

f = friction factor = $64/Re$, $Re = 1500$ for laminar flow condition,

L = Length of Link,

D = Diameter of pipe,

v = Velocity of flow = Discharge(Q)/area(A) = Q/A ,

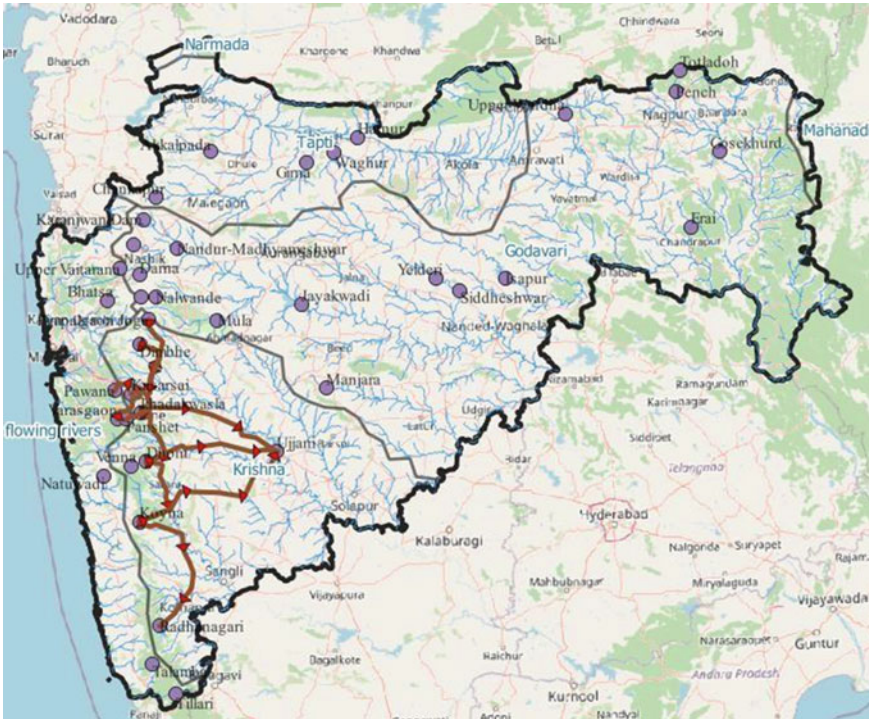


Fig. 5 Krishna basin links

$g = \text{acceleration due to gravity} = 9.81 \text{ m/s}^2,$

$$H_l = f \frac{L}{D} \frac{Q^2}{2gA^2} \tag{2}$$

Using the Eq. (2), the Discharge (Q) in each of the links is computed.

The links selected include intra basin as well as inter-basin. The results of the link and the respective maximum discharges for Krishna basin are as per Table 5. In Krishna Basin, the selected 11 reservoirs are linked depending on the relative elevations of MDDL and FRL. The ten links having maximum discharge of 1.93 cumecs between Dhom and Khadakwasla with many links having lengths more than 100 km.

In Godavari basin, selected 15 reservoirs with total storage capacity of 43,662 MCM are linked and depending on the relative elevations of MDDL and FRL the links are studied and results are depicted in Table 6. It is seen that maximum discharge of 2.51 cumecs is observed in the link between Darna to Mula reservoirs. Some of the links show lengths over 200 km with minimum lengths of about 50 km.

In the Tapi basin, selected five major reservoirs are linked depending on the relative elevations of MDDL and FRL. The suggested four links with their respective lengths



Fig.6 Godavari basin links

and maximum discharges possible are depicted in Table 7. It can be seen that the maximum length is 142 km whereas the maximum possible discharge is 2.61 cumecs in Girna to Waghur link.

In West Flowing River basins, selected four reservoirs are linked depending on the relative elevations of MDDL and FRL, The three links possible are depicted in Table 8 It can be seen that the maximum discharge possible is 3.90 cumecs between Upper Vaitarna to Bhatsa and the maximum length observed is of 297 km.

For Inter Basin Water Transfer many of the above reservoirs are considered. Depending upon the relative elevations of MDDL and FRL 18 possible links as depicted in Table 9 are analyzed. It can be seen that most of the links have discharge of more than 1 cumec with maximum discharge of 3.85 cumecs. The maximum length observed is 379 km between Koyana to Jayakwadi.

6 Conclusion

The scope of this study is to analyze the feasibility of a pipeline water grid for the state of Maharashtra using modern tools of RS-GIS for terrain analysis. Using the basin-wise existing data of various reservoirs, modern geospatial tools available the

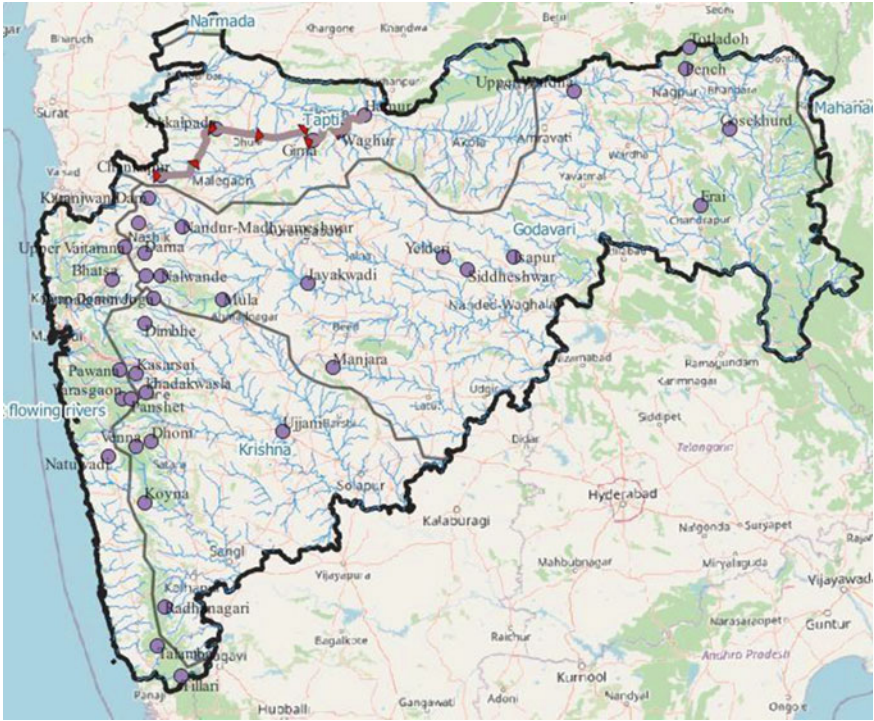


Fig. 7 Tapi basin links

analysis is conducted. From the results obtained, the following conclusions can be drawn.

- Considering the reservoir levels in the intra or inter-basins, it is seen that waters can be generally transferred from higher reservoir to lower reservoirs using pipelines placed along the sides of the existing road network. The transfer of water can be mostly under gravity though in a few cases pumping is essential.
- It is to indicate that using modern technological tools of terrain analysis, depending upon the relative elevations of the storages, the existing reservoirs can be linked by pipeline networks in order to transfer water from surplus to deficit during floods or drought situations.
- The links analyzed in this study are purely based on topographical/ terrain analysis in the entire state of Maharashtra. There can be many more links which can be more feasible which have not been studied here. The links considered are representative only.

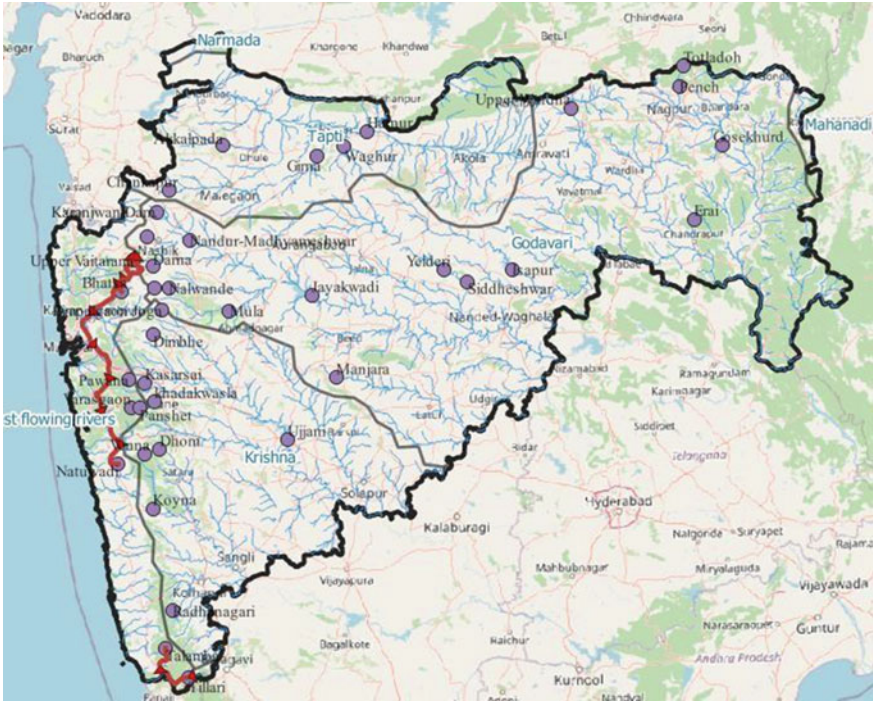


Fig. 8 West flowing rivers basin links

- Scope of this study is macro analysis. There are several other major/ medium reservoirs in the basins which have not been included in this study. Thus, there is further scope for consideration of these reservoirs for such links.
- Considering the relative elevations, it can be seen that there is scope for transfer of water from West flowing rivers and Krishna basin to deficit regions of Godavari and Tapi Basins
- From the analysis it can be seen that the pipeline network interconnecting large number of possible existing reservoirs along the existing roads is feasible option for uniform supply of water for all regions which can eliminate the land acquisition cost, reduce the evaporation and theft of precious water resources with faster implementation and less R&M expenditure.

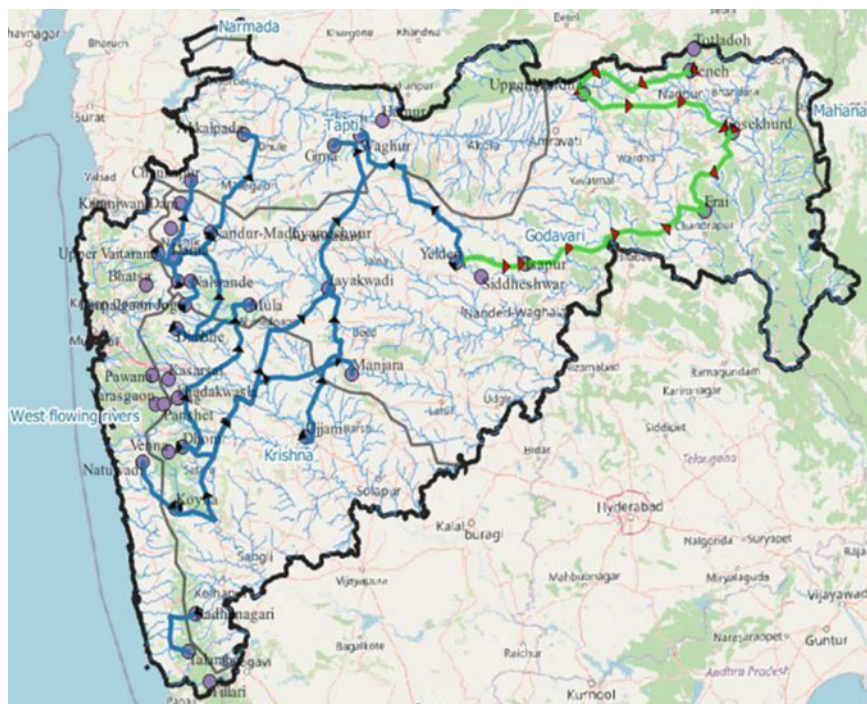


Fig. 9 Inter basin links

Table 5 Krishna basin links

No	From	To	Length (m)	Head Loss (m)	Pipe Diameter(m)	Discharge (m ³ /s)
1	Dimbhe	Khadakwasla	97,804.29	129.03	1.8	1.67
2	Dimbhe	Ujjani	234,015.84	214.32	1.8	1.39
3	Dhom	Khadakwasla	80,491.44	142.13	1.8	1.93
4	Dhom	Koyana	104,256.68	67.10	1.8	1.17
5	Koyana	Radhanagari	160,867.19	19.50	1.8	0.51
6	Dhom	Ujjani	145,088.23	227.42	1.8	1.82
7	Koyana	Ujjani	186,320.33	111.92	1.8	1.13
8	Pimpalgaon Joge	Kasarsai	112,227.12	52.40	1.8	0.99
9	Varasgaon	Pawana	82,929.28	15.44	1.8	0.63
10	Dimbhe	Panshet	116,837.46	76.09	1.8	1.17

Table 6 Godavari Basin links

No	From	To	Length (m)	Head Loss (m)	Pipe Diameter (m)	Discharge (m ³ /s)
1	Mula	Jayakwadi	97,677.57	50.3	1.8	1.04
2	Yeldari	Isapur	76,757.13	21.0	1.8	0.76
3	Upper Wardha	Gosekhurd	183,636.19	87.5	1.8	1.00
4	Gosekhurd	Erai	117,619.38	34.3	1.8	0.78
5	Isapur	Erai	231,224.15	211.7	1.8	1.39
6	Manjara	Jayakwadi	108,012.87	149.5	1.8	1.71
7	Gangapur	Nandur-madhyameshwar	51,528.45	72.5	1.8	1.72
8	Darna	Mula	125,101.71	22.7	1.8	0.62
9	Bhandardara	Nalwande	20,305.84	60.7	1.8	2.51
10	Nalwande	Mula	103,945.86	87.7	1.8	1.33
11	Karanjwan	Gangapur	37,934.31	47.5	1.8	1.63
12	Gangapur	Darna	44,419.35	14.0	1.8	0.82
13	Manjara	Yeldari	205,678.33	148.4	1.8	1.23
14	Totaladoh	Upper Wardha	146,664.14	122.0	1.8	1.32

Table 7 Tapi Basin Links

No	From	To	Length (m)	Head Loss(m)	Pipe Diameter(m)	Discharge (m ³ /s)
1	Girna	Waghur	46,052.26	148.7	1.8	2.61
2	Waghur	Hatnur	40,548.04	9.6	1.8	0.71
3	Chankapur	Akkalpada	99,564.04	315	1.8	2.58
4	Akkalpada	Waghur	142,103.1	135.9	1.8	1.42

Table 8 West flowing rivers links

No	From	To	Length (m)	Head Loss(m)	Pipe Diameter(m)	Discharge (m ³ /s)
1	Upper Vaitrana	Bhatsa	60,509.24	437.3	1.8	3.90
2	Tillari	Talamba	70,721.67	297	1.8	2.98
3	Upper Vaitrana	Natuwadi	297,530.7	460	1.8	1.81

Table 9 Inter-basin links

No	From	To	Length (m)	Head Loss(m)	Pipe Dia (m)	Discharge (m ³ /s)
1	Dhom	Mula	234,224.2	172.7	1.8	1.25
2	Dimbhe	Mula	116,405.7	159.6	1.8	1.70
3	Dimbhe	Nandur-Madh'war	166,427.1	178.4	1.8	1.50
4	Jaikwadi	Girna	200,168.8	43.5	1.8	0.68
5	Yeldari	Waghur	230,344.7	227.9	1.8	1.44
6	Upper Vaitrana	Nandr- Madh'war	86,299.27	130.0	1.8	1.78
7	Nandr-Madh'war	Akkalpada	140,361.9	125.3	1.8	1.37
8	Pimpalgaon Joge	Nalwande	34,098.57	18.4	1.8	1.07
9	Dhom	Manjara	276,328.9	82.6	1.8	0.79
10	Bhandardara	Chankyapur	122,583.4	15.7	1.8	0.52
11	Ujjani	Jayakwadi	207,652.9	7.1	1.8	0.27
12	Radhanagari	Talamba	81,856.03	426.1	1.8	3.31
13	koyana	Natuwadi	69,717.31	489.5	1.8	3.85
14	koyana	Jayakwadi	379,187.8	125.6	1.8	0.84
15	Totaladoh	Upper Wardha	146,664.14	122.0	1.8	1.32
16	Yeldari	Isapur	76,757.13	21.0	1.8	0.76
17	Upper Wardha	Gosekhurd	183,636.19	87.5	1.8	1.00
18	Gosekhurd	Erai	117,619.38	34.3	1.8	0.78
19	Isapur	Erai	231,224.15	211.7	1.8	1.39

References

1. Suryawanshi RK, Gavhale SH (2019) River rejuvenation by adopting continuous stream storage approach in mula-mutha basin using geospatial and simulation tools. In: Proceedings of Sixth India Water Week, 24–28 Sept 2019, Vigyan Bhavan New Delhi
2. Jain SK, Reddy NSRK, Chaube UC (2009) Analysis of a large inter-basin water transfer system in India. *Hydrol Sci J*
3. Tian J and others (2019) Impacts of inter-basin water transfer projects on optimal water resources allocation in the Hanjiang River Basin, China. *State Key Laboratory of Water Resources and Hydropower Engineering Science. Wuhan University, Wuhan (MDPI J)*
4. Yano S, Okazumi T, Iwasaki Y, Yamaguchi M (2018) How inter- basin transfer of water alters basin water stress used for water footprint characterization. *MDPI J*
5. Strategic analyses of inter-linking of rivers in drought- prone tehsils of Jalgaon district—Maharashtra (2018) *Asian J Sci Technol*
6. Karamouz M, Ali Mojahedi S, Ahmadi A (2010) Inter-basin water transfer: economic water quality-based model. *J Irrig Drainage Eng*

7. Anupriya, Chamat LR (2018) Study of interlinking of rivers by using geographic information system (GIS) With Quantum-GIS. Int J Eng Res Technol (IJERT)
8. Prakash I, Patel AK, Singh NP Planning of river inter- linking canal system between Shetrunji River and Dhatarwadi River, Saurashtra, India, using Remote Sensing and GIS

Removal of Heavy Metals from Water Using Low-cost Bioadsorbent: A Review



Praveda Paranjape and Parag Sadgir

Abstract Current review paper presents the performance of natural low-cost (economical) bioadsorbent, i.e., plant biomass and agricultural waste used for the removal or extraction of copper and other heavy metals. The current study focuses on use of various leaves, seed, peel, root, bark, husk, shell, fiber, and other bioadsorbents in their raw, pretreated as well as modified forms. This review paper objects to evaluate the applicability of said biomass for single and multimetal removal from water/wastewater. Researchers' variations in different experimental parameters such as contact time, initial concentration, adsorbent mass, speed of agitation, temperature and pH, etc., are considered along with isotherm, kinetics, thermodynamic, and desorption studies. Researchers using various instruments such as UV vis. spectrophotometer, transmitted electron microscope (TEM), atomic absorption spectroscopy (AAS), molecular absorption spectrophotometer, SEM–EDX analyses, XDR spectroscopy and FTIR analysis, etc., to obtain the characterization of bioadsorbent. In this review, an extensive summary of previous literature on plant biomass, agricultural waste, and other biomass were compiled to provide information on experimental and equilibrium conditions and their potential as a low-cost sorbent.

Keywords Copper removal · Plant-based bioadsorbents · Agricultural waste · Adsorption mechanism

1 Introduction

In India, nowadays, the quality of environment is deteriorating due to extensive industrial processes or operations which particularly include pharmaceuticals, mining, processing of metals, tanneries, pesticides, organic chemicals manufacturing, processing of plastics and rubber industries, wood products manufacturing, agricultural processes, and disposal of industrial waste materials, etc. The wastewater and its effluents which are released from most of the industries contain toxic materials

P. Paranjape (✉) · P. Sadgir
Department of Civil Engineering, College of Engineering Pune, Pune 411005, India
e-mail: pnp20.civil@coep.ac.in

© The Author(s), under exclusive license to Springer Nature Singapore Pte Ltd. 2023
M. S. Ranadive et al. (eds.), *Recent Trends in Construction Technology and Management*, Lecture Notes in Civil Engineering 260,
https://doi.org/10.1007/978-981-19-2145-2_40

527

and heavy metals into rivers without appropriate treatment hence heavy metals are major pollutants in marine water, groundwater as well as treated wastewater. Heavy metals in industrial wastewater comprise Cd, Pb, Fe, Cr, Cu, Hg, Ag, Zn, Ni, etc. These metals are very responsive even at very less concentrations and can accumulate in the food web, causing adverse effects on community health. Adverse effects on heavy metals on human health have been regularly looked over by international bodies like the World Health Organization (WHO) and problems arise due to metal toxicity are anemia, arthritis/rheumatoid arthritis, hypertension, nausea/vomiting, schizophrenia, insomnia, heart problem, cystic/pulmonary fibrosis, inflammation and enlargement of liver, thyroid dysfunction, genetic defects, muscle weakness, skin, lung, and bladder cancer, etc., and many more. Various chemical, physical, and biological treatments are area unit accessible for the removal of harmful toxic metals like chemical oxidization, reduction, chemical precipitation, ultrafiltration, reverse diffusion, electrochemical analysis, and adsorption. Most of those standard ways suffer from some limitations like low potency, high operational price, generation of huge quantity of sludge and their disposal issues, etc. Among these standard techniques, adsorption looks low price operating, efficient, straightforward in style, and effective at lower concentrations. In adsorption, especially bioadsorption (usually uses inactive waste biomass) is one among the in effect method for removal of noxious or toxic heavy metal ions from water or waste material because it offers the most potency even at lower concentrations. The purpose of the current paper is to review info supported, varied plant biomass and agricultural waste as bioadsorbents that are employed in recent studies for copper and alternative serious metals removal from completely dissimilar media. Current paper conjointly purposes to review the pertinence of the plant biomass and agricultural waste bioadsorbents, factors poignant the bioadsorption method, metal removal potency of adsorbents in numerous experimental conditions, etc.

2 Plant Biomass Used for Heavy Metal Removal

Plant biomass is made up of logs and agricultural waste and is available in leaf, seed, root, bark, peel, and other biomass formats. Lignocellulosic constituents are the structural fundamentals of wood and other plant materials that are existing in abundant amounts in the biosphere, are reasonable and have little to low cost-effective value, and these are very promising for the future.

2.1 Leaves Biomass

Leaves are in the group of abundantly available natural resources, often non-toxic and renewable. In adverse situations, most plants shelter their leaves and these leaves can be used as bioadsorbents in the form of raw powder or with some modifications. The

adsorption potential of leaf biomass, in the bioadsorption of metal ions is compiled in Table 1.

Work carried out on the separation of Cu (II) ions from aqueous solution by means of spent-tea-leaves improved with Ca (OH)₂ by Ghosh et al. [21]. Mathematical models were used to investigate the simulation and optimal adsorption conditions for adsorbent dose, pH, and reaction time and concluded that RSM gives superior predictions than ANN. Also, the author discovered that adsorption equilibrium statistics were close-fitting with Langmuir isotherm and follows the pseudo-second-order kinetics. Maximum removal efficiency of Cu (II) was observed to be 96.12% using modified spent tea leaves. For the separation of cadmium, copper, zinc, and lead from aqueous solution, activated carbon prepared from olive branches (H₃PO₄ treated) were used as raw material [15]. They found that the process of bioadsorption depends on the pH and increases with rise in temperature and the initial concentration of metal ions. Maximum bioadsorption for Pb (II), Cu (II), and Cd (II) was obtained at pH 5 and at pH 3 for Zn (II). The overall adsorption potential in mg/g for Pb (II) was 41.32, 34.97 for Zn (II), 43.10 for Cu (II) and for Cd (II), respectively. The author also set up that for all metal ions, adsorption equilibrium statistics were best described with Freundlich isotherm model, and progress of bioadsorption was observed to be non-spontaneous.

2.2 Seed Biomass

Researchers have analyzed seed biomass as resourceful bioadsorbent for extraction of many heavy metals from water and wastewater and summarized it as follows.

Oboh et al. [35] observed the elimination of Pb, Cu, Zn, and Ni using Luffa cylindrical (sponge and seeds) as a bioadsorbent from aqueous solution. The FTIR and SEM analysis used for characterization of bioadsorbents and found that the carboxylic and amine groups were accountable for metal complex formation in the adsorption of all metal ions. The maximum bioadsorption was reported 98.2% for lead, 95.2% for zinc, 87.6% for copper, and 43.5% for nickel at pH 5 with 1 g dose of adsorbent. Within 120 min of time of contact, the adsorption equilibrium was reached and obeys the pseudo-second-order kinetics model for all metals. Garba et al. [17] studied prime conditions using defatted papaya seeds (DPS) as a bioadsorbent for the removal of copper (II) and lead (II) from the solution. The optimal bioadsorption conditions for adsorbent dose, shaking speed, and initial metal concentration were examined by applying central composite design (CCD) which is a subgroup of response surface methodology (RSM) and 97.55% removal of Cu (II) and 99.96% removal of Pb (II) were acquired at bioadsorbent dose of 0.30 gm, shaking speed of 180rpm, and primary metal concentration of 150mg/L. Langmuir isotherm model provides the best result with monolayer adsorption capacities measured in mg/g was 17.29 for copper (II) and 53.02 for lead (II).

Table 1 Summary of heavy metals removal using leaf biomass

Leaf biomass	Metal	pH	Adsorbent dose (g/l)	Contact time (minutes)	Adsorption capacity (mg/g)	Isotherm model	KINETICSMODEL	References
Caesalpinia bonducella	Cu (II)	5	0.7	120	76.92	Langmuir	Pseudo-second-order	[54]
	Cu (II)	4	15	12 (hr)	15.87	Langmuir	Pseudo-second-order	[27]
Syzygium cumini leaves	Ni (II)	6			15.60			
	Cr (VI)	2			16.07			
	Cu (II)	4	15	12 (hr)	17.76			
Populus deltoides leaves	Ni (II)	6			16.45			
	Cr (VI)	2			18.31			
Lawsonia Inermis Leaves	Cu (II)	5	0.5	90	6.06	Langmuir	Pseudo-second-order	[7]
	Cu (II)	6	10	120	5.74	Langmuir	Pseudo-second-order	[26]
Dry cabbage leaves	Cd (II)				5.06			

2.3 Peel Biomass

The feasibility of peel biomass (peel is considered waste material) as bioadsorbents in the removal of metals has been demonstrated in recent studies. Table 2 summarizes some of the adsorption parameters of peel biomass in the bioadsorption of heavy metal ions.

Chowdhury et al. [11] investigated the use of skins of garlic and onion for elimination of Cu (II) from aqueous solution and observed that onion skin has maximum adsorption capacity (76.9 mg/g) as w.r.t. garlic skin (66.7 mg/g) at optimum pH of 5.3 at 303 K. Endothermic and spontaneous cycles of bioadsorption of Cu (II) on both onion and garlic skin was recorded. The adsorption equilibrium data was close-fitting with the Langmuir isotherm model and follows the pseudo-second-order kinetics for both bioadsorbents. Later on, *Lagenaria siceraria* (LS) peel has been explored for the elimination of Fe, Hg, Cr, Ag, Co, Zn, and Cu from industrial wastewater [2]. The untreated and Formaldehyde treated *Lagenaria siceraria*-LS biomass were used for elimination of the said metal ions and concluded that said biomass has notable affinity toward copper ions (99% removal efficiency) followed by iron and silver (95% removal efficiency). The removal efficiency of metallic ions at pH 4–5 is in order mercury < zinc < silver < chromium < cobalt < iron < copper. The adsorption equilibrium of all metal ions follows Langmuir model except Iron (follows Freundlich model). Extreme adsorption capacity in mg/g was observed to be 7.34 for Cu, 8.54 for Co, 5.03 for Zn, 8.92 for Cr, 6.05 for Hg, 4.34 for Ag, and 11.36 for Fe.

2.4 Root Biomass

The use of water hyacinth roots as an economical bioadsorbent for deduction of Cu (II) from the water-based solution was scrutinized [55] and concluded that the bioadsorption of Cu (II) on water hyacinth roots was both a chemisorption method and a quick and endothermic one. The adsorption potential in mg/g of Cu (II) was found to be 22.7 and equilibrium is best fitted with Langmuir isotherm model. From FTIR analysis they have concluded that the –OH and C = O groups have more affinity towards Cu (II) ions. Sorghum root (SR) powder has been explored as bioadsorbent [10] for bioadsorption of copper (II) and chromium (VI) from dissolvable water solution. The author found that optimum pH 2 with a bioadsorbent dosage of 0.45 mg/100 ml for 50 mg/l of initial concentration of metal ions has maximum separation efficiencies of 93% for copper (II) and 91.98% for chromium (VI) within a duration of 60 min at 20°C. The highest adsorption capacities for Cu (II) and Cr (VI) were observed to be 18.6 and 18.39, respectively, measured in mg/g. The adsorption process follows the pseudo-second-order kinetic model with Langmuir isotherm model for both said metal ions. The bioadsorption of copper (II) and chromium (VI) on SR powder was possible, exothermic, and spontaneous.

Table 2 Summary of heavy metals removal using peel biomass

Peel biomass	Metal	pH	Adsorbent dose (g/l)	Contact time (minutes)	Adsorption capacity (mg/g)	Isotherm model	Kinetics model	References
Zalacca edulis peel	Cu (II)	5	0.1	24 (hr)	27.03	Langmuir and Freundlich	Pseudo-second-order	[47]
Orange peel	Cd (II)	5	4	30	13.7	Langmuir and Freundlich	Pseudo-second-order	[29]
	Cu (II)				15.27			
	Pb (II)				73.53			
	Pb				116.2			
Sweet lime peel	Cu (II)	5	1	30	37.45	Langmuir	Pseudo-second-order	[37]
Pomegranate peel	Cu	5.8	3	120	30.12	Langmuir	Pseudo-second-order	[6]

2.5 *Bark Biomass*

Bark is a by-product of the timber industry and abundantly available at a very cost-effective value. The use of bark in water/wastewater treatment converts the agricultural waste byproduct into a cost-effective adsorbent and reduces the cost of residue disposal. Bark biomasses have been suggested for its effectiveness as bioadsorbents for metals removal as follows.

Chakravarty et al. [8] carried out a study on the separation of Cu (II) ions from aqueous solution utilizing heartwood powder of *Areca catechu* as a bioadsorbent and concluded that optimum pH is 5.5 with bioadsorbent dose of 0.5 g/l having maximum removal efficiency within a duration of 30 min. The FT-IR and SEM characterization of the bioadsorbent concluded that N–H, C–O, and O–H groups were primary binding groups for Cu (II) ions. The bioadsorption method was physical in nature and balance is ideally well-matched with the Langmuir isotherm model having extreme bioadsorption potential of 9.578 in mg/g and follows the kinetic model of the pseudo-second-order. Cutillas-Barreiro et al. [12] observed the removal of Cd, Cu, Ni, Pb, and Zn utilizing Pine bark powder as a bioadsorbent and effectively removed Pb (98–99%) and Cu (83–84%) followed by Cd (78–84%), Zn (77–83%) and Ni (70–75%) for 1–48 h of the time of the contact. The bioadsorption equilibrium statistics was close-fitted with Langmuir isotherm model for all said metals. The maximum uptake was 39.4, 65.9, 39.7, 87.9, and 38.1 mmol/kg for Cd, Cu, Ni, Pb, and Zn, respectively.

3 *Agricultural Waste Used for Heavy Metals Removal*

Agricultural products and by-products like husk, stalk, fiber, and shell are the abundantly available waste materials and their proper disposal is necessary. When disposed of by burning, they produce carbon dioxide and other sources of emissions. As a consequence, it is important to transform agricultural products and by-products into useful and value-added products. As described below, the usage of different agricultural products and byproducts for the separation of heavy metal from the solution was discovered by the number of researchers and proved to be economical [19].

3.1 *Husk/ Hull*

Husk is the dried form of outer shell or coating of grains generated from various agricultural processes, which contains cellulose, hemicelluloses, lignin, mineral ash, and silica. It can be chemically improved to increase adsorption capacity also coconut waste contains hydroxyl and carboxyl group which also helps in bioadsorption of

heavy metals. The summary of removal of heavy metals by husk/hull reported in the literature is compiled in Table 3.

Marula seed husk was utilized as bioadsorbent for extraction of Pb (II) and Cu (II) ions from water-based solution [32]. The Langmuir model defined the equilibrium data well and it was found that the maximum bioadsorption abilities in mg/g were 20 and 10.20 for lead (II) and copper (II), respectively. In current studies, adsorption kinetics follows the pseudo-second-order model. The optimal pH for the removal of lead (II) is 5 and for copper (II), it is 6. The equilibrium was accomplished within 60 min of contact time for Pb (II) ions while 180 min was required for Cu (II) ions. Bioadsorption of both the ions on marula seed husk was endothermic, spontaneous, and feasible. A proportional studies on removal of zinc (Zn) and copper (Cu) from aqueous solution by using sunflower hull/husk (SFH) and durian leaves (DL) as a bioadsorbent was carried out by Abood et al. [1]. The ideal pH required for the removal of both metals was 8 for sunflower husk and 9 for durian leaves. The equilibrium was reached within 120 min of contact time in case of SFH and within 60 min in case of DL for both the metals and close-fitted with Freundlich isotherm model. The removal efficiency of copper and zinc was found to be 83% and 93% correspondingly using SFH while using DL it was 70% and 78%, respectively at 10 mg/l of initial metal concentration, agitated at 150 rpm at 25 °C. The maximum bioadsorption capacities of copper was found to be 0.39 mg/g (SFH), 0.06 mg/g (DL) and for zinc 0.27 mg/g (SFH), 0.15 mg/g (DL).

3.2 Shell

Shells are byproducts of various agricultural activities which mostly contain Lignocellulosic material. These materials are highly porous, with more surface area and thus easily used to extract heavy metals (because of the attraction of water molecules to cell wall components) as summarized as follows.

Utilization of cashew nut shells as an operative bioadsorbent for removal of Cu (II) ions was studied by SenthilKumar et al. [46]. The maximum removal efficiency obtained was 82.11% with best suitable pH of 5 having dosage of 3 g/l in 20 mg/l copper (II) solution. Adsorption equilibrium was reached at 120 rpm agitation speed in 30 min of contact time and the ability of monolayer adsorption in mg/g was observed to be 20. The bioadsorption equilibrium statistics was upright provided by the Langmuir and Freundlich isothermal models at 30 °C. Mechanism of bioadsorption was feasible, exothermic, and spontaneous and follows the model of kinetics of the pseudo-second-order. Hossain et al. [24] explored the use of palm oil fruit covering as bioadsorbent for the removal of copper ions from water. They have concluded that an extreme removal efficiency obtained is 98.5% with the best suitable pH of 6.5 and adsorption capacity is between 28 and 60 mg/g at room temperature. The adsorption kinetics obeys pseudo-second-order model. Further, [22] investigated the use of ultrasound in bioadsorption procedure for the removal of Cu (II) ions using watermelon shells make activate with citric acid (AWS) and calcium hydroxide

Table 3 Summary of heavy metals removal using Husk/Hull biomass

Husk biomass	Metal	pH	Adsorbent dose (g/l)	Contact time (minutes)	Adsorption capacity (mg/g)	Isotherm model	Kinetics model	References
watermelon seed hulls	Cu (II)	5	2	60	33.90	Langmuir	Pseudo-first order	[3]
	Pb (II)	5	2	80	42.19			
Cicer arietinum husk	Cu (II)	5	20	120	9.7	Langmuir	Pseudo-second order	[38]
	Cd (II)	7			8.58			
Moringa oleifera seed husk	Cd	6	1	60	13.1	Langmuir	Pseudo-second order	[18]
	Cu							
Pigeon pea hull	Cu (II)	5	0.4	60	20.83	Langmuir	Pseudo-second order	[48]
	Cd (II)				19.81			
Pigeon pea hull AC	Cu (II)	6	0.6		37.39			
	Cd (II)				35.85			
Sesame husk	Cu (II)	6	10	30	10.83	Langmuir	Pseudo-second order	[14]
Maize hull	Cu (II)	6	5	90	19.6	Langmuir	Pseudo-second order	[20]

(SWS). The author observed that in the existence of ultrasound the adsorption rate increases and equilibrium was reached early as compared to conventional process. At pH 5, 90 W ultrasonic power, and contact time of 20 min and 30 °C temperature, the maximum removal efficiency was attained. The maximum potential for adsorption was 27.027 mg/g for ASW and 31.25 mg/g for SWS. For both adsorbents, adsorption system obeys the kinetic model of pseudo-second-order and is ideally equipped with the isotherm model of Langmuir.

4 Other Biomass

Other than plant biomass and agricultural waste biomass like cone biomass, flower, and fruit waste can also be utilized as a bioadsorbent for the removal of heavy metals as shown in Table 4.

Pretreated black tea waste has been used to extract Cu(II) from water-based solution as a bioadsorbent [50]. The NaOH treated black tea waste proved to be more efficient than other pretreatments. The maximum removal efficiency was nearly 90% for a duration of 10 min with optimum pH of 4.4 at a temperature of 26°C. FT-IR research reveals that the responsible groups of black tea waste for copper adsorption were the -CH, -OH, and -C = C groups and adsorption governs diffusion and reaction follows physisorption. The adsorption of copper on NaOH treated black tea waste was spontaneous and endothermic. The Langmuir isotherm was well represented in the adsorption equilibrium data and follows pseudo-second-order kinetics model with the maximum bioadsorption potential in mg/g of 43.18. (Yusoff et al., 2014) investigated the removal of Cu (II), Pb (II), and Zn (II) ions from aqueous solution by exploiting diverse types of agricultural waste materials like sawdust of Durian tree (DTS), coconut coir (CC) and oil palm empty fruit bunch (EFB) as economical bioadsorbents. The utmost adsorption was obtained at pH 5 and the bioadsorption of all metal ions to all adsorbents was favorable. The maximum bioadsorption capacities in mg/g was obtained to be 18.42 (DTS), 18.38 (CC), and 26.95 (EFB) for Cu(II), 20.37 (DTS), 37.04 (CC), and 37.59 (EFB) for Pb (II) while 22.78 (DTS), 24.39 (CC), and 21.19 (EFB) for Zn (II) calculated by Langmuir isotherm model.

5 Mechanism of Bioadsorption

The elimination of elements from solution by biological materials is well defined as biosorption/bioadsorption (Insoluble or soluble and gaseous inorganic or organic forms can be such substances). Bioadsorption is a physicochemical system that can involve processes such as adsorption, ion exchange, precipitation, absorption, and texture of the surface [16]. The mechanism of bioadsorption is very complex and, under some circumstances, a number of mechanisms can be operative. Because of the concentration gradient and diffusion across cell walls and membranes, primarily

Table 4 Summary of heavy metals removal using different biomass

Other biomass	Metal	pH	Adsorbent dose (g/l)	Contact time (min)	Adsorption capacity (mg/g)	Isotherm model	Kinetics model	References
Pine cone	Cu (II)	5	0.3	120	19.27	Langmuir	Pseudo-second-order	[13]
	Cd (II)	7			26.11			
Olive stone waste (AC)	Fe (II)	5	0.3	180	57.47	Langmuir	Pseudo-second-order	[4]
	Pb (II)				22.37			
	Cu (II)				17.83			
	Cu (II)				124.21			
Tomato waste	Cu (II)	8	4	60		Langmuir	Pseudo-second-order	[52]
Moringa pods	Cu	1		40	6.07	Freundlich and Temkin	Pseudo-second-order	[31]
	Ni			30	5.53			
	Cr			40	5.49			

ion exchange, adsorption by physical forces, chelation, and trapping in inter and intrafibrillary capillaries and spaces of the structural polysaccharide network occurs. The variety of structural components found in biomass contributes to the numerous functional groups that can interact with metal types and improve their affinity, e.g., carboxyl, phosphate, hydroxyl, amino, amido and thiol, etc. (for strong or weak bond with ions). The existence of such functional groups does not guarantee bioadsorption [43]. X-Ray Diffraction (XRD), X-Ray Photo Electron Spectroscopy (XPS), Fourier Transform Infrared spectroscopy (FTIR), Scanning Electron Microscopy (SEM), Elemental analysis and Energy Dispersive, X-ray fluorescence spectroscopy (EDX) can also help to determine the process of bioadsorption [5].

6 Bioadsorption Isotherm Modeling

Isothermal adsorption is the process by which the amount of material adsorbed is calculated as a function of concentration (at a constant temperature). Adsorption isotherms are created by exposing a fixed amount of adsorbate to varying amounts of adsorbent in a fixed volume of liquid. The amount of adsorbate that can be taken up by an adsorbent depends on both the temperature and the adsorbate's characteristics and concentration. The isotherms do not provide any information about the adsorption process, but they do aid in determining adsorption ability (Metcalf and Eddy, Inc., 2003). The following equation is used to develop adsorption isotherm.

$$q_e = \frac{(C_o - C_e)V}{m}$$

where, q_e = adsorbent phase concentration after equilibrium in mg/g.

C_o = initial concentration of adsorbate in mg/l.

C_e = final equilibrium concentration after absorption has occurred in mg/l.

V = Volume of liquid in the reactor in lit.

m = mass of adsorbent in g.

Langmuir, Freundlich, Braunaure-Emmett Telleri (BET), Temkin, and Dubinin-Rudushkevich (D-R) models can explain the equilibrium isotherm. Among them, Langmuir and Freundlich are the most ordinarily used isotherm equilibrium models. Table 5 shows the isotherm equations and assumptions for commonly used isotherms.

Table 5 Isotherm equations and Assumptions

Sr. No	Model	Equation	Remark/Assumptions
1	Freundlich isotherm	$q_e = KC^\beta$ or $\log q_e = \log K + \beta \log C$	<ol style="list-style-type: none"> 1. Defines adsorption on Surfaces which are heterogeneous, i.e., surfaces with different affinities having adsorption sites 2. Only at a constant pH value they can be implemented
2	Langmuir isotherm	$q_e = Q^0KC/1 + KC$	<ol style="list-style-type: none"> 1. The adsorbate has an equal affinity for all binding sites 2. Adsorption is restricted to monolayer formation 3. The number of surface sites does not exceed the total number of adsorption species 4. Only at a constant pH value they can be implemented

7 Factors Affecting Bioadsorption

7.1 Effect of pH

The metal ions uptake in adsorption is intensely dependent on pH and as pH increases metal ion adsorption increases because of competition between metal cation and proton at low pH. Along with this positive surface charge is decreases as pH increases which leads to the dropping of Coulombic repulsion of metal ions [49]. Yargıç et al. [52] observed the impact of pH on extraction of Cu (II) ions using tomato waste and found that adsorption capacity changes from 9.34 to 46.04 mg/g as pH increases from 2 to 8 at 293 K. Pandey [38] explored the use of Cicer arietinum husk as bioadsorbent for separation of copper (II) and cadmium (II) ions and results indicates that adsorption to be influenced by the pH of the sorbent media. The experimental investigation indicates that at lower pH, bioadsorbent surface is positively charged due to preferential adsorption of H⁺ ions but on increasing pH concentration of H⁺ ions decrease and metal uptake increases. The best pH for removing Cu (II) and Cd (II) was determined to be 5 and 7, respectively. Kamar et al. [26] found that the ideal pH for removal of Cadmium (II) and Copper (II) was 6 using dry cabbage leaves as a bioadsorbent. The trials were carried out between pH 3 and 8 and observed that removal increases as pH rises up to 6 and then decreases due to decrease in the H⁺ ions in the solution which form some facilities with metal ions and precipitate as metals hydroxide.

7.2 Effect of Dose of Adsorbent

A significant parameter for studying the quantitative absorption of contaminants/metal ions is the adsorbent dose i.e. pollutant or metal ions retention was observed in relation to the adsorbent dose. The percentage of removal increases as the adsorbent dose increases, after which it remains constant as the number of active sites rises as the dose bioadsorbent of increases [4]. The impact of adsorbent dose on adsorption was studied [42] and observed that percentage adsorption of Cu (II) on Stalk powder of Jerusalem artichoke (*Helianthus tuberosus* L.) rises with rise in adsorbent dose, then decreases and after that becomes constant at 5 g/l of dose. Değirmen et al. [13] performed a number of experiments to determine the effect of bioadsorption dose on the percentage removal of Cu (II) and Cd (II) from pine cones. The bioadsorbent concentration varies between 1 and 10 g/l keeping temperature and pH constant and found that as bioadsorbent dose increases yield increases because more active sites will be available but adsorption capacity decreases because of unsaturated adsorption sites or might be due to particle interaction (i.e., aggregation, resulting in a reduction in surface area).

7.3 Effect of Initial Metal Concentration

The bioadsorption efficiency would be reliant on the initial metal concentration. The percentage of bioadsorption tends to decrease as the initial metal concentration increases, but the ability to adsorb increases. At lower initial concentrations, the surface area available for initial moles of metal ions was limited, and fractional adsorption was independent of initial metal concentration [44]. The increase in the potential for adsorption is proportional to the enhancement of the initial concentration of metals. The concentration gradient's driving forces are stronger at higher initial concentrations, which aids in increasing the initial adsorption rate [37, 51]. The effect of initial metal concentration on the removal of Cu (II), Pb (II), and Zn (II) using durian tree sawdust was investigated, and it was discovered that as the initial metal concentration accumulated upto 200 mg/L, the adsorption potential increased from 2.09 to 16.62 mg/g for Copper (II), 2.37 to 20.01 mg/g for Lead (II), and 1.57 to 15.65 mg/g for (II) (Yusoff et al., 2014).

7.4 Effect of Contact Time

Metal ion bioadsorption rates are initially higher being the accessibility or availability of more surface area adsorbents, but they gradually decrease over time until they reach equilibrium (equilibrium state happens when adsorbent is saturated with the adsorbate i.e. metal ions). As the number of active sites decreases over time/exhaustion,

the rate of uptake is governed by the rate of adsorbent transport from the outside to the inside site. In monolayer adsorption, each active adsorbent site can only adsorb one metal ion as it has a fixed number of sites, so surface metal absorption is initially rapid and subsequently decreases, resulting in metal ions remaining in the media [46]. Pavan et al. [40] observed that adsorption of nickel (II), cobalt (II), and copper (II) from solution by utilizing waste ponkan mandarin peel was increased with time and reach equilibrium within 5 min of contact time in case of Ni (II) (Also, 5 min of contact time to reach equilibrium was reported by Ofomaja et al. [36] utilizing pine cone powder for removal of Cu (II), this time was very low as related to the other research conclusions), while it takes 10 min for Co(II) and 15 min for Cu (II). Paulino et al. [39] observed that elimination of Cu (II), Zn (II), Cd (II), and Pb (II) by using citric acid-treated natural cotton fibers from aqueous solution was very fast at early stage and gradually increases with time and within 10 min of contact, equilibrium was achieved.

7.5 Effect of Temperature

The thermodynamic factors such as variation in Gibb's free energy (ΔG°), variation in enthalpy (ΔH°) and variation in entropy (ΔS°) should be considered in order to identify the essence of the adsorption procedure. Both entropy and energy variables are considered to determine the spontaneity of the operation [13]. The negative value of ΔG° specifies the viability and random nature of the adsorption, while the negative value of (ΔH°) indicates the exothermic nature. (positive value specifies adsorption process is endothermic) where as positive value of ΔS° specifies the increasing uncertainty at the solid/liquid boundary [30, 33]. At high temperatures, the adsorption is faster and more beneficial because temperature changes will travel along the driving force of diffusion through the external interface layer and increase the diffusion rate inside the pores, making it easier for metal ions to reach the inner pores of bioadsorbents [51]. Most of the process of bioadsorption shows the exothermic nature, but some research shows that, for example, adsorption of copper on chemically treated rice husk is mostly physical adsorption and absorbs energy, i.e., endothermic [25]. The adsorption of copper and nickel ions decreases with rise in temperature indicates exothermic nature while adsorption of chromium ions increases with increase in temperature specifies endothermic nature using Moringa pods as a bioadsorbent [31]. Hossain et al. [24] observed that ΔG° decreases as temperature rises from 30 to 70 °C and positive value of ΔH° presented that the adsorption of Cu (II) ions on banana peels was endothermic.

7.6 *Effect of Size of Particles*

In the adsorption procedure, size of particles plays a significant role. Yuvaraja et al. [54] studied the impact of particle size (50, 75, 100, and 125 μm) of *Caesalpinia bonducella* leaf powder on the bioadsorption of Cu (II) and found that as particle size increases removal efficiency decreases due to decrease in surface area and binding probability between metal ions and bioadsorbent functional groups. The variation of particle size from 75 to 125 μm gives decrease in efficiency from 85.22, to 72.46, to 32.23%. Hossain et al. [24] performed the batch experiment to study the effect of particle size (six particle sizes varies between 600 and <75 μm) on removal of copper using banana peel and observed that as particle size reduce from 600 to <75 μm the removal efficiency increased from 74 to 96%. Also [6] reported that as particle size of pomegranate peel powder reduced from 1.6 mm to 630 μm , the removal efficacy of Cu (II) ions increases from 57.39 to 89.99%.

7.7 *Effect of Agitation Speed/rate*

The speed of agitation develops the potential for adsorption. Choudhary et al. [10] was discovered that as agitation speed increased from 80 to 120 rpm, copper and chromium adsorption ability increased from 17.55 to 18.60 mg/g and 16.75 to 18.39 mg/g, respectively. The author also reported that increasing the agitation speed promoted bulk quantity transfer of metal ions from the bulk solution to the adsorbent surface and shortened the adsorption equilibrium time. Similar trend was observed by Banerjee [28] in adsorption of Cu (II) on watermelon shells and [34] during utilization of biomass of *Thuja orientalis* for bioadsorption of Cu (II) from water-based media.

8 Desorption

Desorption of loaded biomass, regardless of the fact that the desorbing mediator does not significantly harm or destroy biomass, encourages biomass reuse and the recovery and/or containment of the adsorbed material. Desorption therapies may result in a loss of biomass efficiency in some cases, but they may also result in increased sorption capability in others. Acids, alkalis, and other complexing agents are the most commonly used desorbents, depending on the material sorbed, procedure conditions, and economic factors; selective desorption (e.g., for certain metals) is also possible. The desorption processes in continuous flow system occur without significant interruption as, columns in parallel allow easy sorption and desorption [16]. *Cinnamomum camphora* leaves powder (CLP) was used [9] to extract copper ions from solution. They inferred from EDS and FTIR study that the basic removal

mechanism was ion exchange and a certain amount of surface complexation mechanism also coexisted. At pH 4 and 30–60 °C temperature, the bioadsorption power of Cu (II) ions was found to be 16.76–17.87 mg/g. Further, [37] utilized sweet lime peel (SLP) as the bioadsorbent for extraction of Cu (II) from water-based solution and concluded that max removal is obtained at pH 5 and 20°C temperature. The adsorption balance is best equipped with monolayer adsorption Langmuir isotherm with an extreme potential of 37.45 mg/g at 293 K and kinetics obey the model of pseudo-second-order. The maximum desorption efficiency of Cu(II) is observed to be 90% with 0.1 N HCL.

9 Conclusion

The bioadsorption process is economical and more efficient within a short contact time but limitation is that bioadsorbents are not available in readily usable form and pretreatment or modification (it is required to increase bioadsorption properties by alkali or acidic solutions) may increase the overall cost. Although researching various bioadsorbents, much of the research performed has limited batch experimentation, but there is still limited application to real wastewater on a large scale. Adsorption equilibrium data for copper removal is ideally suited to the isotherms of both Langmuir and Freundlich, which showed single and multilayer bioadsorption. Bioadsorption is firmly influenced by physiochemical constraints (parameters) such as solution pH, size of adsorbent and dosage, initial concentration of metals, surface chemistry, etc. The desorption studies and successful recovery and reuse of bioadsorbent is still challenge.

References

1. Abood MM, Istiaque F, Azhari NN (2019) Remediation of heavy metals using selected agricultural waste: sunflower husk and durian leaves. *IOP Conf Ser Mater Sci Eng* 557. <https://doi.org/10.1088/1757-899X/557/1/012080>
2. Ahmed D, Abid H, Riaz A (2018) *Lagenaria siceraria* peel biomass as a potential biosorbent for the removal of toxic metals from industrial wastewaters. *Int J Environ Stud* 75:763–773. <https://doi.org/10.1080/00207233.2018.1457285>
3. Akkaya G, Güzel F (2013) Bioremoval and recovery of Cu(II) and Pb(II) from aqueous solution by a novel biosorbent watermelon (*Citrullus lanatus*) seed hulls: kinetic study, equilibrium isotherm, SEM and FTIR analysis. *Desalin Water Treat* 51:7311–7322. <https://doi.org/10.1080/19443994.2013.815685>
4. Alslaibi TM, Abustan I, Ahmad MA, Foul AA (2014) Kinetics and equilibrium adsorption of iron (II), lead (II), and copper (II) onto activated carbon prepared from olive stone waste. *Desalin Water Treat* 52:7887–7897. <https://doi.org/10.1080/19443994.2013.833875>
5. Arief VO, Trilestari K, Sunarso J, Indraswati N, Ismadji S (2008) Recent progress on biosorption of heavy metals from liquids using low cost biosorbents: characterization, biosorption parameters and mechanism studies. *Clean - Soil, Air, Water* 36:937–962. <https://doi.org/10.1002/clen.200800167>

6. Ben-Ali S, Jaouali I, Souissi-Najar S, Ouederni A (2017) Characterization and adsorption capacity of raw pomegranate peel biosorbent for copper removal. *J Clean Prod* 142:3809–3821. <https://doi.org/10.1016/j.jclepro.2016.10.081>
7. Bhatia, Amarpreet Kour FK (2015) Biosorptive removal of copper (II) ion from Aqueous solution. *J Environ Earth Sci* 5:21–30
8. Chakravarty P, Deka DC, Sarma NS, Sarma HP (2012) Removal of copper (II) from wastewater by heartwood powder of Areca catechu: kinetic and equilibrium studies. *Desalin Water Treat* 40:194–203. <https://doi.org/10.1080/19443994.2012.671167>
9. Chen H, Dai G, Zhao J, Zhong A, Wu J, Yan H (2010) Removal of copper(II) ions by a biosorbent-Cinnamomum camphora leaves powder. *J Hazard Mater* 177:228–236. <https://doi.org/10.1016/j.jhazmat.2009.12.022>
10. Choudhary S, Goyal V, Singh S (2015) Removal of copper(II) and chromium(VI) from aqueous solution using sorghum roots (*S. bicolor*): a kinetic and thermodynamic study. *Clean Technol Environ Policy* 17:1039–1051. <https://doi.org/10.1007/s10098-014-0860-2>
11. Chowdhury A, Bhowal A, Datta S (2012) Equilibrium, thermodynamic and kinetic studies for removal of copper (II) from aqueous solution by onion and garlic skin. *Water* 4:37–51. <https://doi.org/10.14294/WATER.2012.4>
12. Cutillas-Barreiro L, Ansias-Manso L, Fernández-Calviño D, Arias-Estévez M, Nóvoa-Muñoz JC, Fernández-Sanjurjo MJ, Álvarez-Rodríguez E, Núñez-Delgado A (2014) Pine bark as bio-adsorbent for Cd, Cu, Ni, Pb and Zn: Batch-type and stirred flow chamber experiments. *J Environ Manage* 144:258–264. <https://doi.org/10.1016/j.jenvman.2014.06.008>
13. Değirmen G, Kiliç M, Çepelioğullar Ö, Pütün AE (2012) Removal of copper(II) and cadmium(II) ions from aqueous solutions by biosorption onto pine cone. *Water Sci Technol* 66:564–572. <https://doi.org/10.2166/wst.2012.210>
14. El-Araby HA, Ibrahim AMMA, Mangood AH, Abdel-Rahman AA-H (2017) Sesame husk as adsorbent for copper(II) ions removal from aqueous solution. *J Geosci Environ Prot* 05:109–152. <https://doi.org/10.4236/gep.2017.57011>
15. Elsherif KM, Alkheraz AM, Ali AK (2020) Removal of Pb(II), Zn(II), Cu(II) and Cd(II) from aqueous solutions by adsorption onto olive branches activated carbon: equilibrium and thermodynamic studies. *Chem Int* 6:11–20
16. Gadd GM (2009) Biosorption: Critical review of scientific rationale, environmental importance and significance for pollution treatment. *J Chem Technol Biotechnol* 84:13–28. <https://doi.org/10.1002/jctb.1999>
17. Garba ZN, Bello I, Galadima A, Lawal AY (2016) Optimization of adsorption conditions using central composite design for the removal of copper (II) and lead (II) by defatted papaya seed. *Karbala Int J Mod Sci* 2:20–28. <https://doi.org/10.1016/j.kijoms.2015.12.002>
18. Garcia-Fayos B, Arnal JM, Piris J, Sancho M (2016) Valorization of Moringa oleifera seed husk as biosorbent: isotherm and kinetics studies to remove cadmium and copper from aqueous solutions. *Desalin Water Treat* 57:23382–23396. <https://doi.org/10.1080/19443994.2016.1180473>
19. Ghaedi M, Mosallanejad N (2013) Removal of heavy metal ions from polluted waters by using of low cost adsorbents: review. *J Chem Heal Risks* 3:7–22
20. Ghasemi SM, Mohseni-Bandpei A, Ghaderpoori M, Fakhri Y, Keramati H, Taghavi M, Moradi B, Karimyan K (2017) Application of modified maize hull for removal of Cu(II) ions from aqueous solutions. *Environ Prot Eng* 43:93–103. <https://doi.org/10.5277/epe170408>
21. Ghosh A, Das P, Sinha K (2015) Modeling of biosorption of Cu(II) by alkali-modified spent tea leaves using response surface methodology (RSM) and artificial neural network (ANN). *Appl Water Sci* 5:191–199. <https://doi.org/10.1007/s13201-014-0180-z>
22. Gupta H, Gogate PR (2016) Intensified removal of copper from waste water using activated watermelon based biosorbent in the presence of ultrasound. *Ultrason Sonochem* 30:113–122. <https://doi.org/10.1016/j.ultsonch.2015.11.016>
23. Hossain A, Ngo H, Guo W, Nguyen V (2012) Biosorption of Cu(II) from water by banana peel based biosorbent: experiments and models of adsorption and desorption 2:87–104. <https://doi.org/10.11912/jws.2.1.87-104>

24. Hossain MA, Ngo HH, Guo WS, Nguyen TV (2012) Palm oil fruit shells as biosorbent for copper removal from water and wastewater: experiments and sorption models. *Bioresour Technol* 113:97–101. <https://doi.org/10.1016/j.biortech.2011.11.111>
25. Jaman H, Chakraborty D, Saha P (2009) A study of the thermodynamics and kinetics of copper adsorption using chemically modified rice husk. *Clean—Soil, Air, Water* 37:704–711. <https://doi.org/10.1002/clean.200900138>
26. Kamar FH, Nechifor AC, Nechifor G, Sallomi MH, Jasem AD (2016) Study of the single and binary batch systems to remove copper and cadmium ions from aqueous solutions using dry cabbage leaves as biosorbent material. *Rev Chim* 67:1–7
27. Kaur R, Singh J, Khare R, Cameotra SS, Ali A (2013) Batch sorption dynamics, kinetics and equilibrium studies of Cr(VI), Ni(II) and Cu(II) from aqueous phase using agricultural residues. *Appl Water Sci* 3:207–218. <https://doi.org/10.1007/s13201-012-0073-y>
28. Banerjee K et al (2012) A novel agricultural waste adsorbent, watermelon shell for the removal of copper from aqueous solutions Iran. *J Energy Environ* 3:143–156. <https://doi.org/10.5829/idosi.ijee.2012.03.02.0396>
29. Lasheen MR, Ammar NS, Ibrahim HS (2012) Adsorption/desorption of Cd(II), Cu(II) and Pb(II) using chemically modified orange peel: equilibrium and kinetic studies. *Solid State Sci* 14:202–210. <https://doi.org/10.1016/j.solidstatesciences.2011.11.029>
30. Farhan AM, Salem NM, Ahmad AL, Awwad AM (2013) Kinetic, equilibrium and thermodynamic studies of the biosorption of heavy metals by *Ceratonia Siliqua* Bark. *Am J Chem* 2:335–342. <https://doi.org/10.5923/j.chemistry.20120206.07>
31. Matouq M, Jildeh N, Qtaishat M, Hindiyyeh M, Al Syouf MQ (2015) The adsorption kinetics and modeling for heavy metals removal from wastewater by Moringa pods. *J Environ Chem Eng* 3:775–784. <https://doi.org/10.1016/j.jece.2015.03.027>
32. Moyo M, Guyo U, Mawenyiyo G, Zinyama NP, Nyamunda BC (2015) Marula seed husk (*Sclerocarya birrea*) biomass as a low cost biosorbent for removal of Pb(II) and Cu(II) from aqueous solution. *J Ind Eng Chem* 27:126–132. <https://doi.org/10.1016/j.jiec.2014.12.026>
33. Munagapati VS, Yarramuthi V, Nadavala SK, Alla SR, Abburi K (2010) Biosorption of Cu(II), Cd(II) and Pb(II) by *Acacia leucocephala* bark powder: kinetics, equilibrium and thermodynamics. *Chem Eng J* 157:357–365. <https://doi.org/10.1016/j.cej.2009.11.015>
34. Nuhoglu Y, Oguz E (2003) Removal of copper(II) from aqueous solutions by biosorption on the cone biomass of *Thuja orientalis*. *Process Biochem* 38:1627–1631. [https://doi.org/10.1016/S0032-9592\(03\)00055-4](https://doi.org/10.1016/S0032-9592(03)00055-4)
35. Oboh IO, Aluyor EO, Audu TO (2011) Application of *Luffa cylindrica* in natural form as biosorbent to removal of divalent metals from aqueous solutions—kinetic and equilibrium study. *Waste Water—Treat Reutil* 546. <https://doi.org/10.5772/16150>
36. Ofomaja AE, Naidoo EB, Modise SJ (2009) Removal of copper(II) from aqueous solution by pine and base modified pine cone powder as biosorbent. *J Hazard Mater* 168:909–917. <https://doi.org/10.1016/j.jhazmat.2009.02.106>
37. Panadare DC, Lade VG, Rathod VK (2014) Adsorptive removal of copper(II) from aqueous solution onto the waste sweet lime peels (SLP): equilibrium, kinetics and thermodynamics studies. *Desalin Water Treat* 52:7822–7837. <https://doi.org/10.1080/19443994.2013.831789>
38. Pandey G (2016) Removal of Cd(II) and Cu(II) from aqueous solution using Bengal gram husk as a biosorbent. *Desalin Water Treat* 57:7270–7279. <https://doi.org/10.1080/19443994.2015.1026280>
39. Paulino ÁG, da Cunha AJ, da Sliva Alfaya RV, da Sliva Alfaya AA (2014) Chemically modified natural cotton fiber: a low-cost biosorbent for the removal of the Cu(II), Zn(II), Cd(II), and Pb(II) from natural water. *Desalin Water Treat* 52:4223–4233. <https://doi.org/10.1080/19443994.2013.804451>
40. Pavan FA, Lima IS, Lima ÉC, Airoidi C, Gushikem Y (2006) Use of Ponkan mandarin peels as biosorbent for toxic metals uptake from aqueous solutions. *J Hazard Mater* 137:527–533. <https://doi.org/10.1016/j.jhazmat.2006.02.025>
41. Prasanna Kumar Y, King P, Prasad VSRK (2006) Equilibrium and kinetic studies for the biosorption system of copper(II) ion from aqueous solution using *Tectona grandis* L.f. leaves powder. *J Hazard Mater* 137:1211–1217. <https://doi.org/10.1016/j.jhazmat.2006.04.006>

42. Prokopov T (2015) Removal of copper (ii) from aqueous solution by biosorption onto powder of jerusalem artichoke. *Ecol Eng Environ Prot* 1:24–32
43. Rao LN, Prabhakar G (2011) Removal of heavy metals by biosorption—an overall review. *J Eng Res* II:17–22
44. Rathnakumar S, Sheeja RY, Murugesan T (2009) Removal of copper (II) from aqueous solutions using teak (*Tectona grandis* L. f) Leaves. *World Acad Sci Eng Technol* 3:880–884
45. Romero-Cano LA, García-Rosero H, Gonzalez-Gutierrez LV, Baldenegro-Pérez LA, Carrasco-Marín F (2017) Functionalized adsorbents prepared from fruit peels: equilibrium, kinetic and thermodynamic studies for copper adsorption in aqueous solution. *J Clean Prod* 162:195–204. <https://doi.org/10.1016/j.jclepro.2017.06.032>
46. SenthilKumar P, Ramalingam S, Sathyaselvabala V, Kirupha SD, Sivanesan S (2011) Removal of copper(II) ions from aqueous solution by adsorption using cashew nut shell. *Desalination* 266:63–71. <https://doi.org/10.1016/j.desal.2010.08.003>
47. Sirilamduan C, Umpuch C, Kaewsarn P (2011) Removal of copper from aqueous solutions by adsorption using modify *Zalacca edulis* peel modify. *Songklanakarın J Sci Technol* 33:725–732
48. Venkata Ramana DK, Min K (2016) Activated carbon produced from pigeon peas hulls waste as a low-cost agro-waste adsorbent for Cu(II) and Cd(II) removal. *Desalin Water Treat* 57:6967–6980. <https://doi.org/10.1080/19443994.2015.1013509>
49. Villaescusa I, Martínez M, Miralles N (2000) Heavy metal uptake from aqueous solution by cork and yohimbe bark wastes. *J Chem Technol Biotechnol* 75:812–816. [https://doi.org/10.1002/1097-4660\(200009\)75:9%3c812::AID-JCTB284%3e3.0.CO;2-B](https://doi.org/10.1002/1097-4660(200009)75:9%3c812::AID-JCTB284%3e3.0.CO;2-B)
50. Weng CH, Lin YT, Hong DY, Sharma YC, Chen SC, Tripathi K (2014) Effective removal of copper ions from aqueous solution using base treated black tea waste. *Ecol Eng* 67:127–133. <https://doi.org/10.1016/j.ecoleng.2014.03.053>
51. Weng CH, Wu YC (2012) Potential low-cost biosorbent for copper removal: Pineapple leaf powder. *J Environ Eng (United States)* 138:286–292. [https://doi.org/10.1061/\(ASCE\)EE.1943-7870.0000424](https://doi.org/10.1061/(ASCE)EE.1943-7870.0000424)
52. Yargıç AS, Yarbay Şahin RZ, Özbay N, Önal E (2015) Assessment of toxic copper(II) biosorption from aqueous solution by chemically-treated tomato waste. *J Clean Prod* 88:152–159. <https://doi.org/10.1016/j.jclepro.2014.05.087>
53. Yusoff SNM, Kamari A, Putra WP, Ishak CF, Mohamed A, Hashim N, Isa IM (2014) Removal of Cu(II), Pb(II) and Zn(II) Ions from aqueous solutions using selected agricultural wastes: adsorption and characterisation studies. *J Environ Prot (Irvine, Calif)* 05:289–300. <https://doi.org/10.4236/jep.2014.54032>
54. Yuvaraja G, Subbaiah MV, Krishnaiah A (2012) *Caesalpinia bonducella* leaf powder as biosorbent for Cu(II) removal from aqueous environment: Kinetics and isotherms. *Ind Eng Chem Res* 51:11218–11225. <https://doi.org/10.1021/ie203039m>
55. Zheng JC, Feng HM, Lam MHW, Lam PKS, Ding YW, Yu HQ (2009) Removal of Cu(II) in aqueous media by biosorption using water hyacinth roots as a biosorbent material. *J Hazard Mater* 171:780–785. <https://doi.org/10.1016/j.jhazmat.2009.06.078>

Adsorptive Removal of Acridine Orange Dye from Industrial Wastewater Using the Hybrid Material



Vibha Agrawal and M. U. Khobragade

Abstract In recent years, a lot of development and industrialization has led to the environmental pollution to a greater extent. Water pollution resulting due to toxic and non-biodegradable dyes present in the effluent of many industries related to textile, rubber, plastics, paper, cosmetics, leather is frequently seen nowadays. This research study uses hybrid material, combination of Surfactant Modified Alumina (SMA) and Surfactant modified Silica (SMS) for the removal of acridine orange dye (ACO) using the concept of adsolubilization. ACO dye is an organic dye capable of binding to the nucleic acid of various organisms. The surfactant which is used to modify the surface of alumina is Sodium Dodecyl Sulphate (SDS) which is anionic in nature whereas cationic surfactant Cetyl Trimethyl Ammonium Bromide (CTAB) is used to modify the surface of silica. The mode of analysis was batch study and the various parameters affecting the batch study of adsorption were studied. The batch studies indicated that as the dye concentration of ACO increased, the sorption capacities increased while percentage removal efficiency decreased and achieved equilibrium at 120 min contact time with 120 rpm agitation at 29 ± 2 °C. The removal efficiency of hybrid adsorbent material was around 92.5% and 81% for synthetic and real wastewater sample respectively with adsorption capacity of 46.25 mg/gm for synthetic sample and 40.5 mg/gm for the sample of real textile industry wastewater sample at adsorbent dose of 2 g/l. EDX and SEM analysis was carried out to determine the elemental composition of the adsorbent as well as to check the removal of the dye. It was concluded that the removal took place through pseudo-second-order kinetic mechanism ($R^2 > 0.99$) and data was a good fit to the Freundlich isotherm model ($R^2 > 0.998$).

Keywords Surfactant modified alumina · Surfactant modified silica · Acridine orange dye · Adsorption · Batch study

V. Agrawal (✉) · M. U. Khobragade
Department of Civil Engineering, College of Engineering Pune, Pune 411005, India
e-mail: vibhagrwl071@gmail.com

© The Author(s), under exclusive license to Springer Nature Singapore Pte Ltd. 2023
M. S. Ranadive et al. (eds.), *Recent Trends in Construction Technology and Management*, Lecture Notes in Civil Engineering 260,
https://doi.org/10.1007/978-981-19-2145-2_41

547

1 Introduction

In recent years, a lot of development and industrialization has led to the environmental pollution to a greater extent. Water pollution resulting due to the dyes present in the effluent of many industries related to textile, rubber, plastics, paper, cosmetics, leather is frequently seen nowadays. The ecosystem poses threats due to these dyes as many dyes are toxic and non-biodegradable [4]. Some dyes are also mutagenic, toxic, and carcinogenic [10]. Variety of treatment methods such as membrane separation technologies, electrochemical method, ion exchange, photocatalytic degradation, adsorption are explored by various scientists [13]. Adsorption technique is the most efficient one to remove various dyes. The most commonly used adsorbent is activated carbon but it requires high energy and cost in its synthesis and regeneration [3]. Thus, researchers are finding alternative adsorbent materials.

Acridine Orange Dye (ACO) is a basic cationic dye used in textile industry for coloring textiles. The dye also had wide applications in various fields. The biological affects of ACO including mutagenic actions are another wide area of research [12].

Nanomaterials have special physical and chemical properties thus it has received impetus for adsorption in research work. But the hydroxyl group on their surface causes them to agglomerate and leads to poor dispersion capacity [6]. Thus, using surfactant-modified metal oxides as adsorbent for adsorption has been in trend in recent years [11]. Depending on the surfactant concentration, the single layer or double layer structure of ionic surfactants forms on the surface of charged metal oxide [9]. These surfactant layers formed known as micelles have the ability to remove the organic molecules and solubilize them within its structure and this concept is called adsolubilization [2]. There are not much studies on engineering application of surfactant modified metal oxides for treatment of wastewater. The preliminary study has shown less efficiency of individual adsorbents SMA and SMS for the removal of dye. Since this study is out of the scope of this research paper it is not mentioned here.

In this research, we have worked towards the removal of acridine orange dye (ACO) from textile industry wastewater using adsorption process. The adsorbents used are hybrid materials—combination of surfactant modified alumina (SMA) and surfactant modified silica (SMS). The batch study of adsorption is used in this work. The various entities affecting the batch study such as adsorbent dose, time of contact, temperature, agitation speed as well as concentration of dye are studied and analyzed. The isotherm studies as well as the kinetic studies are carried to check the pollutants uptake rate and also to study the removal mechanism. The Scanning Electron Microscopy (SEM) and Electron Dispersive Xray (EDX) analysis are also carried out to determine the modification of the adsorbent material and removal of the contaminants.

2 Materials, Instrumentation, and Methodology Adopted

2.1 Materials

2.1.1 Chemicals Used

Acridine orange dye ($C_{17}H_{19}N_3$, molecular weight—265.360 $g\cdot mol^{-1}$), cationic surfactant cetyltrimethylammoniumbromide (CTAB— $C_{19}H_{42}BrN$), anionic surfactant Sodium Dodecyl Sulphate (SDS— $NaC_{12}H_{25}SO_4$), Alumina (Al_2O_3 —molecular weight 101.96 gm), Silica gel and all other chemicals of high purity were obtained from a chemist in Pune and used as received.

2.1.2 Instrumentation

High-end precision instruments such as electrical balance for measurement, digital pH meter, oven for drying, orbital incubator shaker was used. UV spectrophotometer was used to measure the concentration of ACO dye in the solution by simple principle of measuring light absorbed. Glassware used was made up of borosil. The distilled water was used to wash all the glassware thoroughly several times and later on dried in oven.

2.1.3 Preparation of Synthetic Adsorbate Solution of ACO Dye

Working solution of 100 mg/l of ACO dye was prepared from the stock solution of 500 mg/l. The wavelength of 463 nm was used for testing the absorbance by acridine orange dye in the UV spectrophotometer.

2.1.4 Preparation of Adsorbent

Surfactant Modified Alumina (SMA)—The positive charge is present on the surface of the alumina so the surfactant Sodium Dodecyl Sulphate (SDS) which carries negative charge on surface is used to modify its surface. The anionic surfactant forms micelles on its surface which solubilize the organic molecules. The alumina of 70–290 mesh ASTM and Zero Point of charge of 9.15 is used. Alumina of weight 200 g was shaken with SDS concentration of 20,000 mg/l for 24 h. After shaking for 24 h in orbital shaker, the supernatant obtained was discarded and the alumina was washed with distilled water and dried at 60 °C for 24 h. The final product obtained was the surfactant modified alumina (SMA) and it was further used for adsorption process [1].

Surfactant Modified Silica (SMS)—The surface of the negatively charged silica gel was modified using the cationic surfactant cetyltrimethylammoniumbromide

(CTAB). 180 g silica gel with the dose of 30 g/l was shaken with the CTAB solution of 6 L for 24 h which had 7500 mg/l concentration. The supernatant was again discarded and the silica gel was washed thoroughly with the distilled water and later on dried at 60 °C to obtain Surfactant Modified Silica (SMS) [2].

The SMA and SMS were taken in 1:1 proportion to form hybrid adsorbent material for the removal of ACO dye.

2.2 Methodology

2.2.1 Batch Study of Adsorption

The batch study of adsorption was used in this research work. The various factors affecting the batch study were analyzed. The adsorbent dose was varied from 0.1 g to 0.5 g to find the optimum dose for removal of dye. The variation of the contact time was done in the range from 30 to 180 min and agitation speed varied from 90 to 180 RPM. The inlet concentration was varied from 20 mg/l to 100 mg/l and even variation of temperature was studied.

2.2.2 Removal Efficiency and Adsorption Capacity

The UV–Vis Spectrophotometer was used to study the removal of the ACO dye. The adsorbent efficiency of the removal and the capacity of adsorption of the hybrid adsorbent material (mg/gm) were calculated using Eqs. (1) and (2), respectively [12, 14].

$$\% \text{ Removal} = \frac{C_0 - C_e}{C_0} * 100 \quad (1)$$

$$\text{Adsorbent Capacity} = \frac{C_0 - C_e}{M} \quad (2)$$

where,

C_0 represents the initial concentration (mg/l) of ACO dye

C_e represents the final concentration (mg/l) of ACO dye

M is the mass (g/l) of SMA adsorbent.

2.2.3 Adsorption Isotherms

Isotherms for adsorption process are plotted to describe the mechanisms of adsorption process. They describe the relationship between the adsorbate and adsorbent. The

Langmuir isotherm and Freundlich isotherm models are the two most used isotherm models.

Langmuir adsorption Isotherms—The assumption of the Langmuir isotherm is that the adsorbent surface has active sites with uniform monolayer formation. Here it is assumed that at every point on adsorbent there is same affinity for the adsorbate. Equation (3) below is the non-linearized form of Langmuir isotherm [7, 14].

$$\frac{1}{q_e} = \left[\frac{1}{K_L * q_e} * \frac{1}{C_e} \right] + \frac{1}{q_m} \tag{3}$$

where,

- q_e is equilibrium capacity in mg/gm
- K_L is Langmuir constant (l/mg)
- C_e is concentration at equilibrium (l/mg)
- q_m is the maximum concentration at equilibrium (mg/gm).

Freundlich adsorption isotherms—The Freundlich isotherm is valid for multi-layer adsorption based on the assumption that adsorption of ions occur on a heterogeneous adsorbent surface. It can be represented in linear form by Eq. (4) and its modified form by Eq. (5). The value of n and K_f is found by plotting the graph between $\ln C_e$ and $\ln q_e$.

$$q_e = K_f + (C_e^{1/n}) \tag{4}$$

$$\ln q_e = \log K_f + 1/n \ln C_e \tag{5}$$

where,

- q_e is equilibrium capacity in mg/gm
- K_f is freundlich constant (l/mg)
- C_e is concentration at equilibrium (mg/l)
- n indicates the affinity towards the adsorbent.

2.2.4 Adsorption Reaction Kinetics

Reactions that are time-dependent are called as kinetic reactions. Adsorption kinetics are used to test linearity between time and adsorption capacity. The rate of adsorption of ions on adsorbent material can be analyzed using two kinetic models.

Pseudo first-order kinetic model—This model suggested by Lagergren is given below in its integrated form (Eq. 6) [12].

$$\log (q_e - q_t) = \log(q_e - K_{s1}) \tag{6}$$

where,

q_e is equilibrium capacity in mg/gm
 q_t is equilibrium capacity at any time t
 K_{s1} is rate constant in $l/min = 2.303 K$.

Pseudo-second-order kinetic model—The pseudo-second-order kinetic model based on the sorption equilibrium capacity is suggested in 1999. Following Eq. (7) gives the integrated linearized form of the model [5].

$$\frac{t}{q_t} = \frac{1}{K_{s2}q_e^2} + \frac{1}{q_e}t \quad (7)$$

where,

K_{s2} is pseudo-second-order rate constant in gm/mg-min.

3 Analysis, Results, and Discussion

3.1 SEM and EDX Analysis

Scanning Electron Microscopy (SEM) rasters a focused electron beam toward the surface and detect backscattered electrons providing detailed high-resolution images of the sample. An Energy Dispersive X-Ray (EDX or EDA) gives identification of element and information about composition of the sample. The SEM image of hybrid adsorbent material after removal of ACO dye (Fig. 2) is darker than the previous image before removal (Fig. 1) which shows the adsorption of dye on surface of hybrid material [8].

SEM indicated the large surface area and rough surface texture of adsorbent before adsorption of dye, which provides suitable binding sites for ACO molecules. The change in the surface texture of the adsorbent material was found before and after the adsorption process. After adsorption, dye molecules led to coverage of most of the pores to become saturated.

The EDX analysis showed the chemical composition of dye adsorbed on hybrid material -mixed modified alumina and silica. It was observed that the amount of oxygen, bromium, carbon, nitrogen, aluminium, silicon has increased significantly which indicates the adsorption of dye on the surface of hybrid material and its removal from the wastewater. The results clearly indicated the increase in atomic percentage of carbon and nitrogen (main chemical composition of ACO dye).

Fig. 1 SEM image of hybrid adsorbent material before treatment of dye

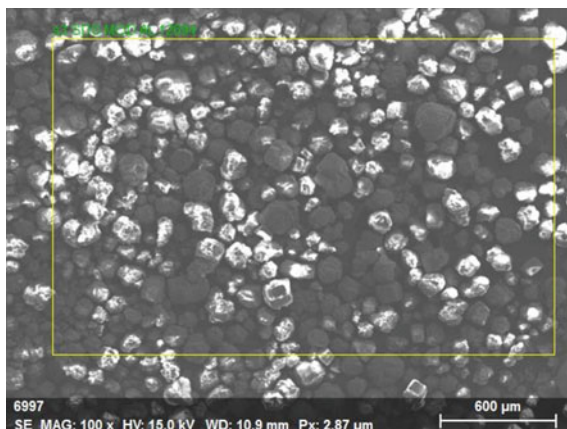
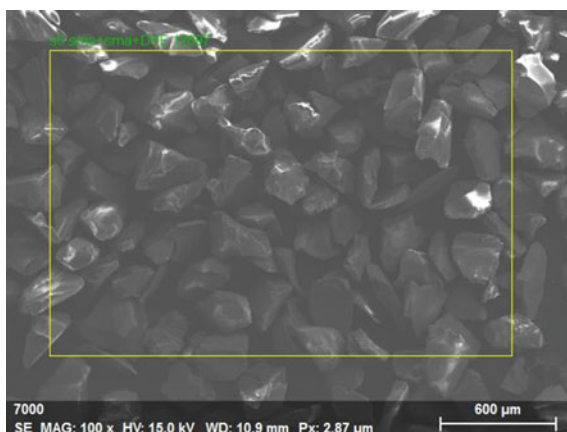


Fig. 2 SEM image of hybrid adsorbent material after treatment of dye

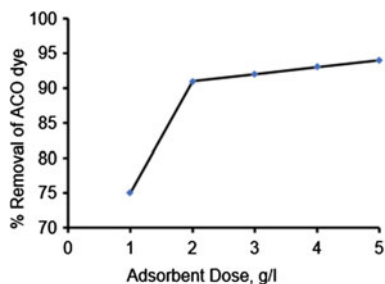


3.2 *Effect of Various Parameters*

3.2.1 **Effect of Dose of Adsorbent**

The dose of the adsorbent is an important parameter which affects the process of adsorption. The removal efficiency increases as the active adsorbent site increases after increasing the dose of adsorbent. The adsorbent dose effect on the efficiency is illustrated below in Fig. 3. The adsorbent dose was varied from 1 g/l to 5 g/l and it was observed that at dose of 2 g/l, the percentage removal of ACO dye was 91%. It was also seen that after 2 g/l dose, the efficiency was not increasing significantly. The other operating conditions were as mentioned, pH was fixed at 5.3 at 29 °C with agitation of 120 RPM for 120 min for 100 mg/l concentration of dye.

Fig. 3 Effect of adsorbent dose on the removal of ACO dye



3.2.2 Effect of Time of Contact and Initial Concentration

Figure 4 represents adsorption of ACO dye onto hybrid material. It was realized that removal of ACO dye onto the combination of SMA and SMS reached to the equilibrium in 120 min. It was observed that at the initial stage of adsorption of ACO dyes, the removal is less than 30 min and was about 64.46% for combination of SMA and SMS. When the contact time of adsorption was increased, there was gradual increase in the removal of ACO dye and was reached upto 82.56% at contact time 120 min. The further increase in the contact time between the adsorbent and the dye showed that there was a slight increase in the percentage removal of ACO. Thus, 120 min is treated or used as equilibrium time for further experiments.

The other operating conditions were as mentioned, pH was fixed at 5.3 at 29 °C with agitation of 120 RPM for dose of adsorbent of 2 g/l for 100 mg/l concentration of ACO dye.

The concentration of ACO dye was varied from 20 mg/l to 100 mg/l under the controlled operating conditions (Speed of agitation = 120 rpm at 29 °C for 120 min contact time). It was noticed that the percentage removal efficiency decreased with the increase in the dye concentration. The decrease observed was in the range of 99.8–92.4% for concentration of 20–100 mg/l of ACO dye.

Fig. 4 Effect of time of contact on the efficiency of ACO dye

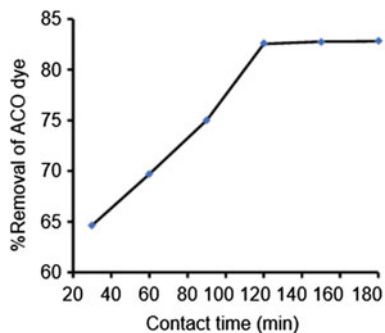
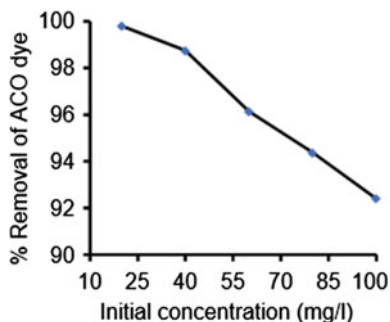


Fig. 5 Effect of concentration on the removal of ACO dye



3.2.3 Effect of Speed of Agitation and Temperature

Figure 6 shows the effect of speed of agitation on efficiency of removal of ACO dye. The range of agitation speed was 90RPM-180RPM and the efficiency of ACO dye removal was studied in this range. The highest removal efficiency of 92.41% was observed for 120 RPM agitation speed. This shows that after a particular speed of agitation the adsorbed contaminant dye is removed from the surface of the adsorbent due to excess speed.

Figure 7 shows the effect of temperature on removal efficiency of ACO dye. Temperature changes the capacity of adsorption so it is another important physiochemical parameter. The temperature varied was in the range of 293, 302, and

Fig. 6 Effect of speed of agitation on the removal of ACO dye

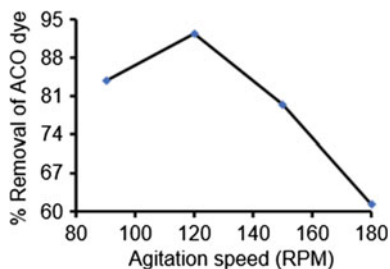


Fig. 7 Effect of temperature on the removal of ACO dye

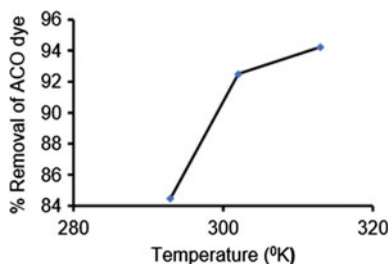
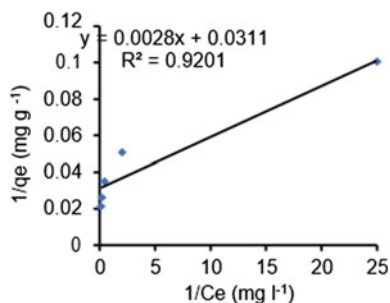


Fig. 8 Langmuir adsorption isotherm



313 °K. The other parameters used are agitation speed (120 rpm) with concentration of 100 mg/l at 120 min time of contact and adsorbent dose (2 g/l). The 302 °K (29 degrees) was the optimum temperature with the maximum removal efficiency of around 95%. The increase in removal was not much on increasing the temperature beyond 302 °K.

3.2.4 Real Wastewater Analysis

When the real wastewater was analyzed by the above-optimized parameters of adsorbent dose of 2 g/l at agitation speed of 120 RPM at temperature of 29 degrees for 120 min contact time in 100 mg/l dye concentration, the removal efficiency observed was 81% with adsorption capacity of 36.5 mg/gm.

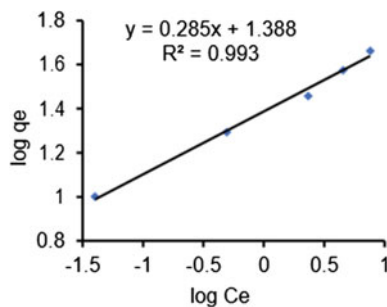
3.3 Adsorption Isotherms

We plot adsorption isotherms in order to establish the relationship between the adsorbate and the adsorbent. Langmuir and Freundlich adsorption isotherms are plotted in this study. The best fit of these isotherms was checked using the data of varying concentration. The plots indicated that the value of correlation coefficient R^2 was more for (Fig. 9) Freundlich isotherm (0.993) as compared to the (Fig. 8) Langmuir isotherm (0.9201). Thus, Freundlich isotherm was a good fit to the data indicating the adsorption of the dye in multilayers on the adsorbent. It also displays that the adsorption has taken place in heterogenous manner.

3.4 Kinetic Model

The adsorption kinetic model represents the pollution uptake rate. The pseudo-first order and pseud-second-order kinetic model are analyzed here for the study. The

Fig. 9 Freundlich adsorption isotherm



R^2 value of first-order kinetic model (Fig. 10) is less than the R^2 value of second-order model (Fig. 11). From this we concluded that adsorption is a chemisorption controlled mechanism. The contaminant dye particles are attached to the surface of the adsorbent by means of chemical forces, which are harder to desorb as compared to ones attached through physical forces.

Fig. 10 Pseudo first order kinetic model

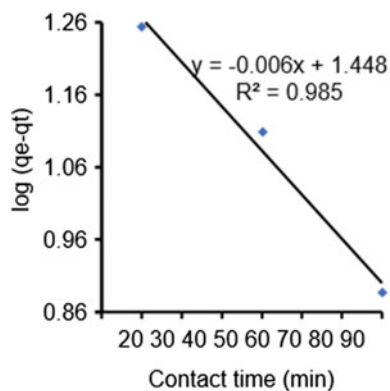
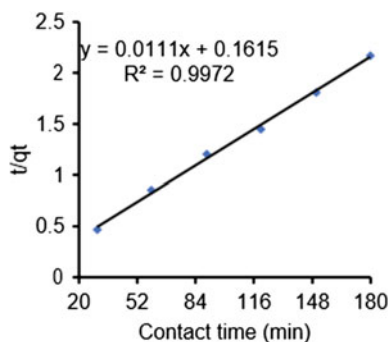


Fig. 11 Pseudo second order kinetic model



4 Conclusions

The percentage removal of ACO dye molecules from synthetic as well as real wastewater sample using hybrid adsorbent material made of combination of SMA and SMS is 92.5% and 81% respectively. For synthetic sample, the adsorption capacity is 46.25 mg/gm as well for real wastewater sample the adsorption capacity is 40.5 mg/gm. The adsorbent dose of 2 g/l of hybrid material along with the contact time of 120 min at speed of agitation of 120 RPM at 29 °C for the 100 mg/l ACO dye concentration is reported to be the optimum experimental condition. The removal followed Freundlich isotherm model and pollution uptake was controlled by pseudo-second-order mechanism. It was seen that the combination of SMA and SMS could provide the effective and efficient way to remove the ACO dye. Thus, it is suggested to explore the concept of hybrid adsorbent material for the removal of other contaminants and dyes from wastewater.

References

1. Adak A, Bandyopadhyay M, Pal A (2005) Removal of crystal violet dye from wastewater by surfactant-modified alumina. *Sep Purif Technol* 44(2):139–144. <https://doi.org/10.1016/j.seppur.2005.01.002>
2. Adak A, Koner S (2016) Adsolubilization of organic dye through surfactant modified silica gel waste from aquatic environment batch and fixed bed studies wastewater treatment. 26684561:1–5. <https://doi.org/10.15224/978-1-63248-114-6-12>
3. Alnajjar M, Hethnawi A, Nafie G, Hassan A, Vitale G, Nassar NN (2019) Silica-alumina composite as an effective adsorbent for the removal of metformin from water. *J Environ Chem Eng* 7(3):102994. <https://doi.org/10.1016/j.jece.2019.102994>
4. Gupta VK, Suhas Tyagi I, Agarwal S, Singh R, Chaudhary M, Harit A, Kushwaha S (2016) Column operation studies for the removal of dyes and phenols using a low cost adsorbent. *Global J Environ Sci Manage* 2(1):1–10. <https://doi.org/10.7508/gjesm.2016.01.001>
5. Kasprzyk-Hordern B (2004) Chemistry of alumina, reactions in aqueous solution and its application in water treatment. *Adv Coll Interface Sci* 110(1–2):19–48. <https://doi.org/10.1016/j.cis.2004.02.002>
6. Khan AM, Shafiq F, Khan SA, Ali S, Ismail B, Hakeem AS, Rahdar A, Nazar MF, Sayed M, Khan AR (2019) Surface modification of colloidal silica particles using cationic surfactant and the resulting adsorption of dyes. *J Mol Liq* 274:673–680. <https://doi.org/10.1016/j.molliq.2018.11.039>
7. Khobragade MU, Pal A (2016) Adsorptive removal of Mn(II) from water and wastewater by surfactant-modified alumina. *Desalin Water Treat* 57(6):2775–2786. <https://doi.org/10.1080/19443994.2014.982195>
8. Khobragade MU, Pal A (2016) Fixed-bed column study on removal of Mn(II), Ni(II) and Cu(II) from aqueous solution by surfactant bilayer supported alumina. *Separat Sci Technol (Philadelphia)* 51(8):1287–1298. <https://doi.org/10.1080/01496395.2016.1156698>
9. Koner S, Pal A, Adak A (2012) Use of surface modified silica gel factory waste for removal of 2,4-D pesticide from agricultural wastewater: a case study. *Int J Environ Res* 6(4):995–1006. <https://doi.org/10.22059/ijer.2012.570>
10. Koner S, Pal A, Adak A (2010) Cationic surfactant adsorption on silica gel and its application for wastewater treatment. *Desalin Water Treat* 22(1–3):1–8. <https://doi.org/10.5004/dwt.2010.1465>

11. Nguyen TMT, Do TPT, Hoang TS, Nguyen NV, Pham HD, Nguyen TD, Pham TNM, Le TS, Pham TD (2018) Adsorption of anionic surfactants onto alumina: characteristics, mechanisms, and application for heavy metal removal. *Int J Polym Sci* 2018:5–9. <https://doi.org/10.1155/2018/2830286>
12. Qadri S, Ganoë A, Haik Y (2009) Removal and recovery of acridine orange from solutions by use of magnetic nanoparticles. *J Hazard Mater* 169(1–3):318–323. <https://doi.org/10.1016/j.jhazmat.2009.03.103>
13. Wang H, Zhao W, Chen Y, Li Y (2020) Nickel aluminum layered double oxides modified magnetic biochar from waste corncob for efficient removal of acridine orange. *Biores Technol* 315(May):123834. <https://doi.org/10.1016/j.biortech.2020.123834>
14. Yadav S, Asthana A, Chakraborty R, Jain B (2020) Cationic dye removal using novel magnetic/activated charcoal/ β -cyclodextrin/alginate polymer nanocomposite 1–20

Basin Delineation and Land Use Classification for a Storm Water Drainage Network Model Using GIS



Kunal Chandale and K. A. Patil

Abstract Due to rapid urbanization and the recent trends in climate change there is a need for an efficient and sustainable storm water drainage network. In order to design a storm water drainage network there are some preliminary studies to be taken into consideration. This paper aims at using ArcMap 10.3 for GIS based basin delineation, supervised classification and nodal elevation extraction. The study area covers about 13 km² which spans over villages Handewadi, Wadachiwadi, and Pisoli in the South-Eastern region of the Pune city. Digital Elevation Models (DEM) were used for basin delineation which helped in identification of ridge line for the study area. To identify the percentage of impervious area supervised classification was performed using the Landsat 8 images, upon analysis which concluded in 43.37% of area being impervious, i.e., (buildings and roads). 660 plus nodes were digitized for an area using MIKE Urban + which were then exported, and then imported in ArcMap 10.3. Elevation values were extracted for each node using the DEMs.

Keywords Basin delineation · Land classification · GIS

1 Introduction

Storm water modelling plays a significant role in checking issues such as urban flooding, water logging and urban water-quality problems [1]. Before designing a storm water drainage network there are some prerequisite tasks which are mandatory and help design a sustainable drainage network. Rapid construction and land development causes an increase in the imperviousness of land which leads to increased surface runoff causing risk of urban flooding. To mitigate risks of urban flooding, an efficient storm water drainage system is mandatory. In order to administer and

K. Chandale (✉) · K. A. Patil
Department of Civil Engineering, College of Engineering Pune, Pune 411005, India
e-mail: chandaleka19.civil@coep.ac.in

K. A. Patil
e-mail: kap.civil@coep.ac.in

understand the landscape modifications, the quantitative assessment of land use and land-cover and the transformations in it must be performed [2]. The various factors operating either on local, regional, or global scale define the land use changes which are basically dynamic in nature [3]. The land use pattern is dynamically being affected by the swift and unrestrained population growth, along with rapid industrialization and the continuously growing economy [4].

Remote Sensing (RS) and Geographic Information System (GIS) are the most acknowledged tools being used for estimating and quantifying these changes in the land use. In order to gather, store, recover, analyze, influence or exploit, and display any georeferenced or spatial data for a particular development-oriented program, GIS proves to be an efficient tool capable of performing the required tasks [5]. Recent advances in remote sensing technology allow to acquire data at spatial and temporal resolutions beyond the human capability, at any point in space and time. Remote sensing data along with geographic information systems has made more-compendious analysis of spatial information feasible [6]. Among various Land use land cover classification techniques, supervised and unsupervised classifications are used the most [7].

2 Study Area

Pune located in state of Maharashtra is one of the eight most populous city of India. Known as the “Oxford of the East,” it is an education hub since decades and in the recent times has become a booming IT hub. It is situated 560 m above mean sea level on the Deccan Plateau on the banks of Mutha River. Given the scenario, there is a massive hike in the population of the city in the recent years. According to the Pune Municipal Corporations (PMC) development plan the population of the city in the next 20 years is projected to be thrice of what it was in the year 2011 (PMC City Development Plan 2012). The villages Handewadi (18°45' N, 73°93'E), Pisoli (18°44'N, 73°90'E), and Wadachiwadi (18°43'N,73°91'E) situated in the South-Eastern region of the city of Pune together forming an area of 13 km², is considered in this study.

3 Data Collection

ArcMap 10.3 software was used for basin delineation and land use classification studies. Cartoset-1 Digital Elevation Model (CartoDEM) was downloaded from the Indian Space Research Organization's (ISRO) bhuvan.nrsc.gov.in website. Landsat 8 OLI (Operational Land Imager) and TIRS (Thermal Infrared Sensor) with 15–30 m multispectral data images downloaded from United States Geological Survey (USGS) website.

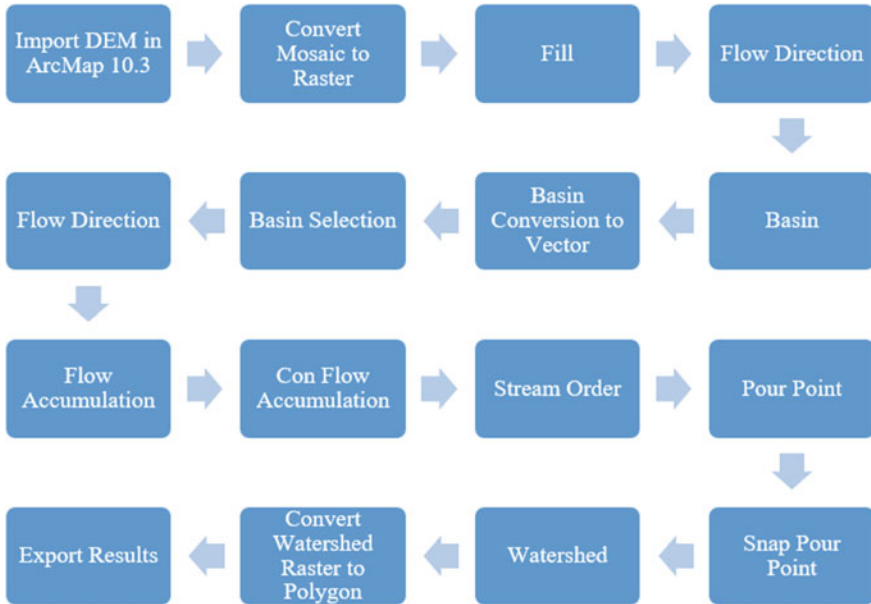


Fig. 1 Flowchart for basin delineation process

4 Methodology

4.1 Basin Delineation

To design a storm water drainage network, there is a need to first identify the boundary or ridge line of that particular region which shows the area that will be contributing the runoff to the drainage network. Spatial Analysis Tools and Data Management Tools of the ArcToolbox were primarily used for basin delineation. The following flowchart shows the commands used in order to obtain the desirable results (Fig. 1).

4.2 Land Use Classification

Urban floods are caused due to an increase in the recent trends of population density, haphazard development of urban infrastructure without paying due consideration to drainage aspects and increase in paved surfaces. Paved surfaces are relatively more impervious than unpaved surfaces which restrain surface infiltration and cause increased surface runoff. To identify the percentage of paved or impervious land use classification is necessary. Supervised classification of Landsat eight images was done using ArcMap 10.3. The remote sensing images are displayed in three primary

Fig. 2 Flowchart for supervised classification process



colors (red, green, and blue) known as color composite images. It means associating each spectral band to primary color results in a color composite image [8]. False Color Composite (FCC) scheme was used to detect various classes.

Red = Short Wave Infrared (SWIR) band (SPOT4 band 4, Landsat TM band 5)

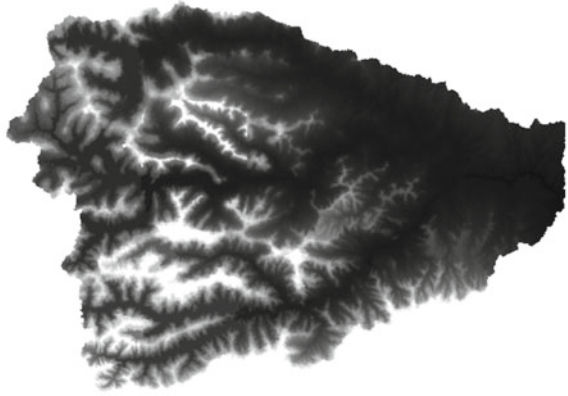
Green = Near Infrared (NIR) band (SPOT4 band 3, Landsat TM band 4)

Blue = Red band (SPOT4 band 2, Landsat TM band 3)

Sample training was done for five classes, i.e., buildings, roads, barren land, water bodies, and vegetation. Interactive supervised classification was carried out accordingly. The following flowchart shows the process for supervised classification (Fig. 2).

4.3 Nodal Elevations

For regular inspection, cleaning, and maintenance of the drainage line, there has to be some sort of access available. This access is provided by constructing orifices along the drainage line which are called Manholes. At every change of orientation, slope of land, change in diameter of pipe, at the origin of all pipes and branches, and at every intersection of two or more pipes, a manhole must be provided mandatorily [9]. In the software, these manholes are represented as nodes. 660 nodes were digitized along the road network for the study area using MIKE Urban+ software. MIKE Urban+

Fig.3 Fill clip raster

features complete high performing MIKE 1-D multicore engine for modeling large stormwater and sewerage systems with fast execution, extracting model data directly from a high-performing database. The node shapefile was imported to ArcMap 10.3 and elevation values for each node were extracted using extraction tool of the ArcToolbox from the DEM.

5 Results and Discussion

5.1 Delineated Basin

The resulted delineated basin will form the boundary for the area contributing to surface runoff and eventually contributing to the stormwater drainage network. The basin's area is 29.49 km² and the perimeter of the basin is 32.43 km. The resultant shapefiles of each and every command generated shapefiles in ArcMap are as follows (Figs. 3, 4, 5, 6 and 7).

5.2 Supervised Classification

In the composite stacked image, after using the 4-3-2 FCC, water bodies resembled black color. The buildings showed pink color and the roads showed dark pink color. The barren land was seen in shades of blue. The aim of the classification was to get percentage of paved area, i.e., roads and buildings. The composite image shows bifurcation of landmass with respect to different classes in ArcMap (Figs. 8, 9 and Table 1).

The classification results above in the classified image states that approximately 45% of study area comprises of barren land and vegetation. Around 43.37% of study

Fig. 4 Flow direction raster

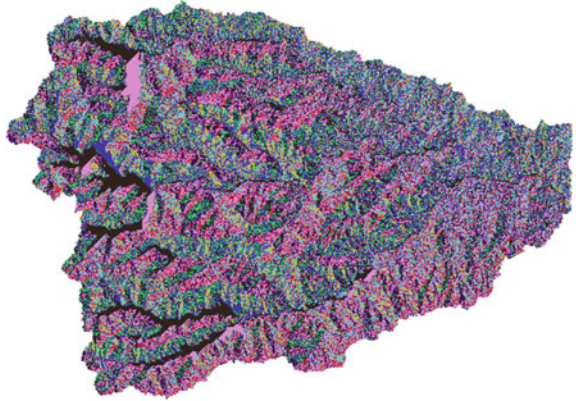


Fig. 5 Vector polygon

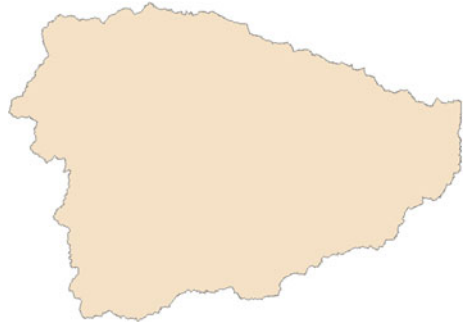


Fig. 6 Stream order



area comprises of impervious land and the remaining consists of water body. Visual inspection was done for verification of these classification results which was in favor of the results (Table 2).

Fig. 7 Delineated basin



Fig. 8 Composite image

5.3 Node Elevation

Post importing the node shape file from MIKE Urban+ , Extract Values to Points command from the Arc Toolbox was used which is quite user-friendly. The elevation values efficiency majorly depend on the accuracy of the DEMs used to extract these values. Figure 10 shows node shapefile in ArcMap whereas Fig. 11 shows imported node shapefile in MIKE Urban+ with elevation values.

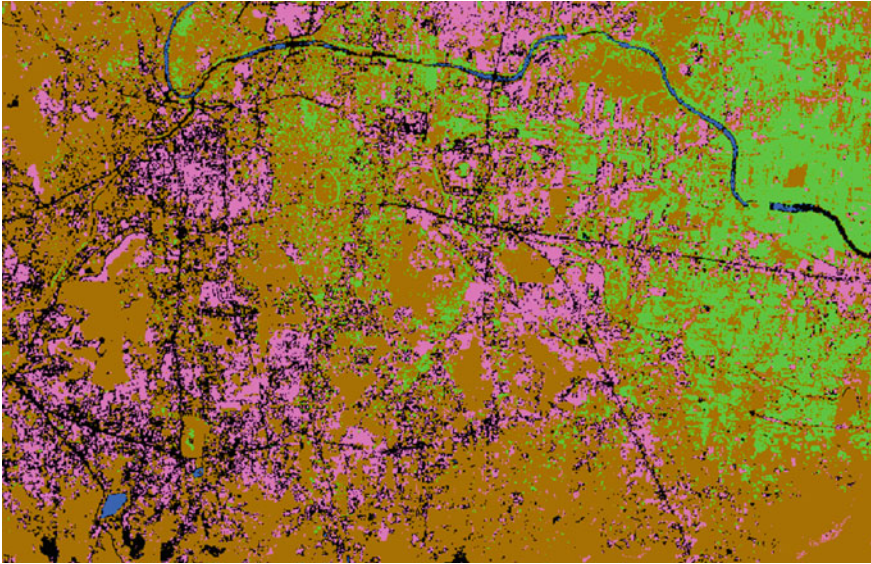


Fig. 9 Classified image

Table 1 Class name and value

Sr. No.	Value	Class name
1	27	Vegetation
2	1	Water bodies
3	7	Barren land
4	41	Buildings
5	40	Roads

Table 2 Classification results

Sr. No.	Class value	% of area	Class name
1	27	1.815175	Vegetation
2	1	0	Water bodies
3	7	54.80489	Barren land
4	41	23.58139	Buildings
5	40	19.79855	Roads

6 Conclusions

Based on the study carried out different conclusions drawn are as given below.

Fig. 10 Node shapefile in ArcMap 10.3

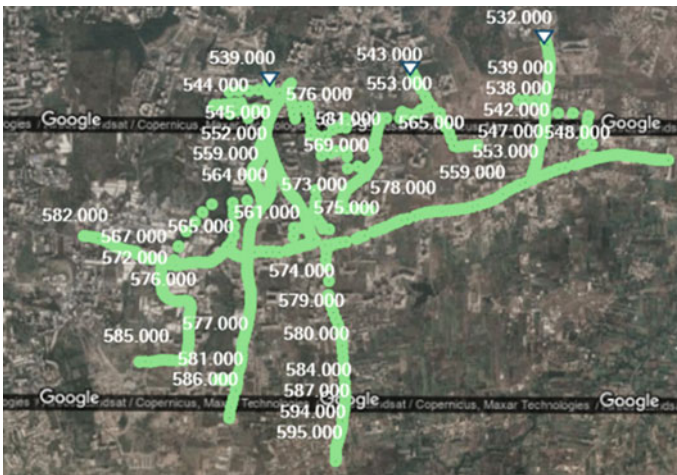


Fig. 11 Nodes with elevation values

1. The resultant shape file of basin delineation is useful as a foundation layer for study area and to understand the topography.
2. Resultant shape file is useful to demarcate the study area, digitize nodes, land use classification, delineate catchments, and countoring.
3. The land use classification helps to find the magnitude of the imperviousness of the land. Percentage imperviousness helps to calculate the groundwater abstractions from the surface runoff which gives the net runoff contributing to the drainage system.
4. The percentage area of vegetation, barren land, buildings, and roads in the study area found to be 1.82%, 54.80%, 23.58%, and 19.80%, respectively.
5. The flow in a collection system or drainage system is always Freudian, i.e., under the influence of gravity. The nodes and its elevations define the pipe network.

6. The orientation and the direction of pipe flow are governed by the elevations of nodes.

References

1. Rangari VA, Prashanth SS, Umamahesh NV, Patel AK (2018) Simulation of urban drainage system using a storm water management model (SWMM). *Asian J Eng Appl Technol* 7(S1):7–10
2. Singh SK, Mustak S, Srivastava PK, Szabó S, Islam T (2015) Predicting spatial and decadal LULC changes through cellular automata Markov chain models using earth observation datasets and geo-information. *Environ Processes* 2:61–78
3. Rahman A, Kumar S, Fazal S, Siddiqui MA (2012) Assessment of land use/land cover change in the north-west district of Delhi using remote sensing and GIS techniques. *J Indian Soc Remote Sens* 40:689–697
4. Dutta D, Rahman A, Paul SK, Kundu A (2019) Changing pattern of urban landscape and its effect on land surface temperature in and around Delhi. *Environ Monit Assess* 191:551
5. Mallupattu PK, Sreenivasula Reddy JR (2013) Analysis of land use/land cover changes using remote sensing data and GIS at an urban area, Tirupati, India. *The ScientificWorld J* 2013(268623)
6. Quinn NWT, Kumar S, Imen S (2019) Overview of remote sensing and GIS uses in watershed and TMDL analyses. *J Hydrol Eng* 24(4)
7. Naikoo MW, Rihan M, Ishtiaque M (2020) Analysis of land use land cover (LULC) change and built-up expansion in the suburb of a metropolitan city: spatio-temporal analysis of Delhi NCR using landsat datasets. *J Urban Manage* 09:347–359
8. Imam E (2019) Remote sensing and GIS module: colour composite images and visual image interpretation. University Grand Commission (UGC), MHRD, Government of India
9. Manual on Storm Water Drainage Systems, Central Public Health and Environmental Engineering Organisation (CPHEEO), Ministry of Housing and Urban Affairs (MoHUA), Government of India
10. Shukla H, Watershed management: it's role in environmental planning and management. *IOSR J Environ Sci Toxicol Food Technol* 1(5):8–11
11. Pune Municipal Corporation (2013) Draft city development plan 2012/2013. Pune Municipal Corporation, Pune

Prediction of BOD from Wastewater Characteristics and Their Interactions Using Regression Neural Network: A Case Study of Naidu Wastewater Treatment Plant, Pune, India



Sanket Gunjal, Moni Khobragade, and Chirag Chaware

Abstract Analysis of variance (ANOVA) results were used to analyze the behavior of various water quality parameters like Total Suspended Solids, Biochemical Oxygen Demand, and Turbidity. The turbidity is not a recommended water testing parameter for wastewater testing, still it was measured on experimental basis. The datasets used in this work were derived from a detailed experimental investigation of inlet and outlet water parameters of Naidu wastewater treatment plant, a major conventional treatment plant in Pune City, India. It has an average flow rate of 115 MLD. The samples were collected daily for over three months. Statistical data analysis methods such as correlation coefficient, regression analysis, and graphical representation of the data were used to find the interrelations between selected parameters. The regression neural network model obtained from the analysis of data was used to predict BOD parameter considering standard error. The p -value obtained by ANOVA analysis was observed to be significant at $p < 0.05$. The ANN model predicted the results at maximum accuracy of 96% and average accuracy of 94%. Good interrelation between the selected parameters was observed and it was observed that BOD can be predicted using suspended solids and turbidity of water sample.

Keywords BOD prediction · Turbidity · TSS · ANN

1 Introduction

The wastewater systems are very complex systems and difficult to model in any statistical relations. The time consumption of the environmental experiments greatly

S. Gunjal · M. Khobragade · C. Chaware (✉)
Department of Civil Engineering, College of Engineering Pune, Pune 411005, India
e-mail: chawarecy19.civil@coep.ac.in

S. Gunjal
e-mail: sanketdg1996@gmail.com

M. Khobragade
e-mail: muk.civil@coep.ac.in

needs to be reduced to make fast decisions and increase the wastewater treatment efficiencies. The legitimate operation and regulation of wastewater treatment plants (WWTPs) are increasing due to concerns regarding environmental problems. Inappropriate activity of a WWTP may achieve genuine ecological and general well-being issues, as its gushing to an accepting water body can spread different diseases to individuals. A good control of a wastewater treatment plant could be accomplished by building up a powerful numerical tool, for predicting plant execution, based on previous interpretations of such critical boundaries. “The measurement of complex physical, biological and chemical processes engaged with wastewater treatment displays non-linear behaviour and is hard to depict by direct numerical models” [1]. Be that as it may, demonstrating a WWTP is a troublesome errand because of the multifaceted nature of the treatment measures. The artificial neural network is tasted to be best to model various non-uniform, and complex systems. This study focuses on prediction of water quality parameters like BOD which are time and resource consuming. This paper presents prescient models dependent on the idea of artificial neural network (ANN), a generally utilized use of fake insight that has demonstrated a serious guarantee in an assortment of utilizations in designing, design acknowledgment, and monetary market investigation. The experimental work was conducted for more than three months to get more than 90 data sets from November 2020 to February 2021. The created models are appeared to perform reliably well in the face of changing precision and size of information. Though turbidity is not a recognized parameter for wastewater quality testing, it was used for analysis on experimental basis. The methods like ANN are being used progressively in water and wastewater area. As it has been observed to be great while handling nonlinear and non-uniform datasets.

2 Material and Methods

The standard procedures for measurement of the desired parameters BOD, TSS, and turbidity were used. The APHA manual was referred for the experimental procedures. Analytical grade chemicals were used for the experimental work. The chemicals were purchased from the Aishwarya chemicals. The standard procedure for measuring the parameters like BOD and TSS takes huge time. The prediction method that we are targeting to develop will be helpful in getting the Bod value in just few minutes once we get the TSS and turbidity values ready for fresh analysis. The main disadvantage of this system is that it needs good quality data or else the system will end up predicting very random value of the targeted parameter, in our case the BOD. The huge amount of data sets doesn't seem to be required in this kind of analysis, as the readings of a particular plant mostly lie in a particular range. The seasonal variations are unavoidable and hence should be tackled by collecting the datasets all over the year and creating seasonal models will help solving this issue. Although this problem has not solved in our work. Validation of the results will be done by using 10% of the data selected randomly from the collected data sets. The unique thing about this work

is that we have tried establishing the interrelation between TSS and Turbidity with respect to BOD for the selected wastewater treatment plant for a case study. There are various limitations regarding sample collection and constraints to perform the study or carry out the experimentations which are tried to be eliminated with current work. The prediction of the BOD from less time-consuming parameters, TSS and turbidity will save most of the resources such as chemicals, manpower, machines and the most valuable and important time. Conventionally the parameters are analyzed by the lab experimental procedures of the respective parameters. The conventional methods are pretty time-consuming and cannot be used on the field. The final artificial neural network that was ready after training on the data that was generated by us gave the average accuracy of 95% and maximum prediction accuracy of 96%.

2.1 Case Study

The created ANN models were used for Naidu wastewater treatment plant. This plant is an important WWTP on the bank of the Mula stream, India. It is being developed in three phases to serve an extreme populace of 1 million (115 MLD). It is an nitrifying actuated overflow type plant. It incorporates fine coarse and fine screening and grit removal, sedimentation, diffused aeration, last explanation, and chlorination offices. The records taken over the time of 3 months collected for BOD concentration and TSS at the inlet station, and at the stream from the last stage.

2.1.1 Model Development

The steps shown in Fig. 1 were carried out for ANN model development process.

Collection of Data and Preprocessing of Data

Data collection was done for over 90 days. The fundamental target of the information preprocessing is to filter out the data which will help improving the predicted results. For excluding the outlier datasets, we used regression line and buffer zone of 20% around the line. Generally, the preprocessing also includes the filling of missing data in the datasets, but in our case, there was no any missing data so that we skipped the step of filling the missing values. Dependent and independent variables were



Fig. 1 ANN model development

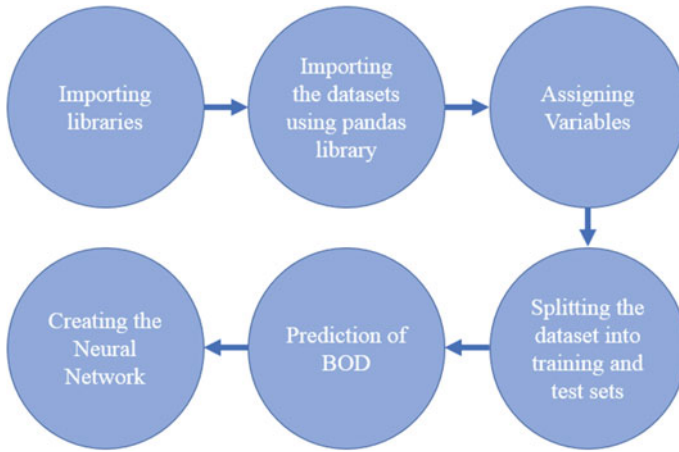


Fig. 2 ANN model steps

decided logically as the BOD is a parameter dependent on the solids present in the water so that TSS and Turbidity were chosen as independent parameters and BOD as a dependent parameter. The dissolved solids were not considered as the dissolved impurities are mostly minerals and they contribute very less in the BOD and that's why can be neglected for our current project work (Fig. 2).

Model Design and Network Training

Multivariate linear regression (MLR)

It has multiple independent variables contributing to the value of dependent variable and has multiple coefficients and complex in nature. In our case turbidity and TSS are considered to be independent variables and BOD is considered to be a dependent variable.

Libraries such as Numpy, Sklearn, Pandas, and Tensorflow were used for the pre-processing and actually building the neural network.

NumPy is a Python library used for working with arrays, domain of linear algebra, Fourier transform, and matrices. Travis Oliphant created This open-source library in 2005. NumPy stands for Numerical Python.

The scikit-learn (sklearn) library is used to deal with machine learning and statistical problems including clustering of data, classification of data, regression, and dimensionality reduction of the data. Scikit-learn is an open-source library.

Pandas is also an open-source library created for the Python programming language and it is used for data analysis and data manipulation. The data for our work was imported and exported in the model using pandas library.

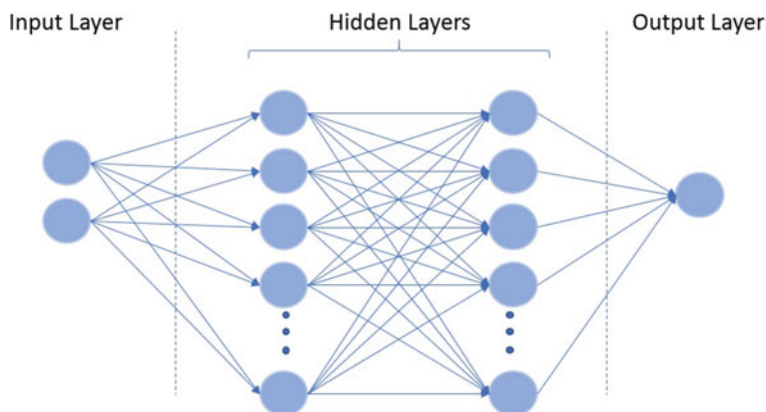


Fig. 3 Neural network

TensorFlow: TensorFlow is an open-source library developed by Google. This beautiful library is primarily developed for deep learning applications. It also supports traditional machine learning.

The ANNs are tools of mathematical modeling that are especially helpful in the field of prediction and in dynamic environments forecasting. The ANN accomplishes this by a vast number of strongly integrated computing components (neurons) working together to solve particular challenges, such as predicting and pattern detection (Fig. 3).

Each neuron has different coefficients or weights related to some of its neighbors, which reflect the relative effect of the various neuron inputs to other neurons. The Python coding language was used for the coding the neural network. The model engineering, preparing strategy, and preparing rates were resolved utilizing an experimentation approach. The BOD, TSS and turbidity values (100 sets for every parameter) were used for training and initial testing of model. 90% (90 entries) of total datasets were used to train the model and remaining 10% datasets (10 entries) were used for validation of constructed ANN model. Feedforward-error back-propagation type neural network was constructed with the help of TensorFlow library design by google. The loss function used for the network was “Root Mean Squared Error” and various optimization functions like Adagrad, Adadelta, Adam, Nadam were used while constructing the neural network and were observed to obtained the best results. Various neuron activation functions like sigmoid, Relu, selu, leaky-relu were used and observed till getting the best results. To arrive at the reasonable organization engineering, a few preliminaries for every gathering were led till the appropriate learning rate, number of hidden layers, and number of neurons per each layer were reached. Reasonable arrangements are those that have delivered an insignificant blunder term in the training and testing of data. The reasonable design for BOD prediction was resolved to comprise an input layer with two neurons (for input TSS and Turbidity). The hidden layer has five hundred neurons. The output layer has one neuron (for

anticipated BOD).To arrive at this network structure, various network structures were tested and were assessed. Network structures with four layers containing five hundred neurons were observed to be perform great.

Model Testing

The observed ANN model average accuracy for the Naidu wastewater treatment plant was 94% and It reached a maximum value of 97% for inlet properties and 85–89% for outlet water quality parameters. The activation functions, loss functions, and optimizer functions along with a number of epochs affect the accuracy of model greatly. We should also observe carefully while testing the model that mistakenly we have not got the local minima of the error surface otherwise the readings will appear to be very random and diverted instead of occurring in certain range (e.g., range of 4–6% from the estimated values) of BOD. Graphs of testing are as shown (include graphs of testing errors, etc. Also include descriptions of the graphs in this paragraph). Various combinations of number of neurons and number of layers were checked and the behavior of the model was noted to optimize the number of neurons and number of layers by trial and error method. The model was behaving weird at lower neuron count but higher epochs, so that number of neurons were set to five hundred to get stable outcomes.

3 Results and Discussion

The ANN model constructed for the prediction of inlet water quality parameters performed really well. The observed values (Red color line) and predicted values (Blue color line) by ANN model for inlet water parameter are as shown in Fig. 4. The accuracy of the model was observed in between 94 and 97%. The ANN model constructed for prediction of outlet water quality parameters didn't performed well as our selected parameters were not sufficient to predict the outlet BOD. The model's accuracy was observed to be in between 85 and 89%. The observed values (Orange

Fig. 4 Plotted values of BOD observed and predicted for inlet water

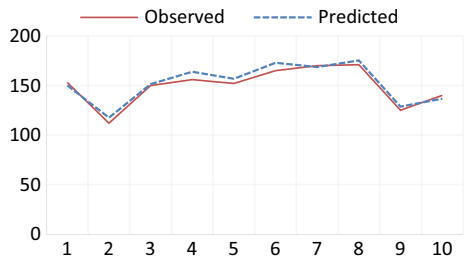
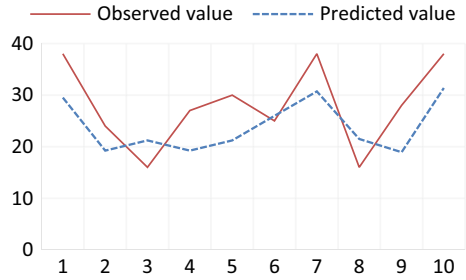


Fig. 5 Plotted values of BOD observed and predicted for outlet water



color line) and predicted values (Blue color line) by ANN model for inlet water parameter are as shown in Fig. 5.

The p -value for the ANOVA analysis at $p < 0.05$ was observed to be $p < 0.00001$ and the F-ratio was observed to be 1347.95699. These values signify that the data that we collected doesn't have much randomness. P -values for all the intermediate interrelationships of all three parameters taken two at a time was observed to be less than 0.00001. The mean value of Turbidity, TSS, and BOD for inlet water are 40.79, 214.375, and 149.67, respectively.

4 Conclusion

The ANN-dependent model was created to predict the influent and effluent-BOD concentration for a WWTP in Pune. The neural network model gave great prediction to the BOD values. The datasets we used for the prediction covered a wide range of data for training and testing the model. The error variations were very less and observed to be smooth over the range of data. The limitations in data, in any case, ought to be highlighted. On the off chance that more data sets were gathered, if the information were less noisy, it would have brought about an improved prediction capacity of the model. In any case, the ANN is observed to be a great tool for the prediction of BOD.

Reference

1. Hamed MM, Khalafallah MG, Hassanien EA (2004) Prediction of wastewater treatment plant performance using artificial neural networks. *Environ Model Softw* 19:919–928

Floodplain Mapping of Pawana River Using HEC-RAS



Tejas R. Bhagwat and Aruna D. Thube

Abstract A flood is catastrophic natural high stage at which the stream overflows its banks and inundates the surrounding area of river banks. It is a natural hazard and threat to life and property. In this study, flood inundation mapping is done for the downstream of Pawana dam located on Pawana river in Upper Bhima sub-basin of Krishna basin in Pune district. Flood mapping has been done for entire river stretch of 58 km till its confluence with the Mula river. Mapping involves locating blue line, orange line, and red line which are the extent of the inundated area for the discharges of 25-year, 50-year, and 100-year return period flood and identification of the most affected villages as they come under prohibitive and restrictive regions. The study utilizes the Digital Elevation Model (DEM) data for the procurement of cross-section and HEC-RAS software developed by USACE for the steady flow analysis. which provides the water surface profiles and water depths obtained are further utilized to create the floodplain map. For model calibration, Manning's roughness coefficient is varied between 0.015 to 0.045 for channel and 0.010–0.050 for floodplain. The Coefficient of determination (R^2) and Nash Sutcliffe Coefficient (NSE) values is found to be above 0.60 and 0.75 for both calibration and validation. The locations coming under the flood lines are identified by importing the flooding map to Google Earth as a layer. The significant findings found from the study was that under prohibitive zone, up to river station 29,966, i.e., Godumbre village, there is not much urbanization present. But there are urbanized locations downstream of river station 27,965, i.e., Gahunje village. From this river station 27,965, there are residential sectors, buildings, and small slums located on the banks of river which are getting flooded even for 25-year return period flood and fall under prohibitive zone. Such type of construction is strictly prohibited in this zone, but structure exists, so government agencies should monitor existing structures and should be well prepared in advanced with Emergency Action Plan (EPA) and Disaster Management Plan if the flooding situation arises.

T. R. Bhagwat (✉)

Environmental and Water Resources Engineering, College of Engineering Pune, Pune, India
e-mail: bhagwatr19.civil@coeep.ac.in

A. D. Thube

College of Engineering Pune, Pune, India

Keywords HEC-RAS · DEM · Return period · Pawana river · Floodplain mapping

1 Introduction

India is one of the most disaster-prone countries in the world due to its geoclimatic conditions. Out of 329 million hectare of total geographical area, 40 mha of area is flood-prone. Every year on an average 75 lakh hectares of land is getting affected. Nowadays, floods have also been occurring in areas which was not considered to be flood prone earlier. Flooding is a condition of partial or complete inundation by water. It is temporary covering of land by water due to heavy rainfall when capacity of water bodies to hold water exceeds. Among all the disasters, floods are the most common and cause damages to infrastructure apart from the loss of lives. It also affects the economy due to reconstruction costs, shortage of food which causes increase in prices, etc. The flood disaster cannot be controlled completely but many methods have been practiced to mitigate the flood. Flooding is one of the world's most severe threats and accounts for 40% of all-natural disaster casualties, with many flood events occurring in developing and tropical regions. According to Abhas et al. (2012), 178 million people were affected by floods in 2010 alone and total financial losses in the exceptional years such as 1998 and 2010 exceeded \$40 billion. There are four types of floods, specifically river floods, flash floods, tidal floods, and storm surge floods, which cause tremendous loss to property and lives [1]. Flood zone recognition has been used extensively in river management studies by defining high-risk flooding areas, set mandatory limits in high-risk areas, avoid flood risk, coordinate, and optimize rivers by deciding flood zones with different return periods (Forgani et al. 2016). Floodplain mapping and river cross-sectional boundaries play a major role in planning and optimizing the utilization of the floodplain areas on the banks of river in order to reduce flood damage. Due to the complexity of rivers during floods, modeling using software is one of the cost-effective tools for studying and simulating the behavior of rivers during floods (Parsa et al. 2016). According to [2], through floodplain maps, areas that are vulnerable to flooding hazards can be identified and floodplain analysis indicated that more than 400% area is likely to be inundated as compared to the normal flow of the river, hence there is a need of policymakers and planners for the development of flood mitigation measures.

India is facing the same global challenges of droughts and floods resulting from extreme climate change. In India, the majority of floods occur due to excessive rainfall that leads to the bursting of river banks, causing flood and the consequent high discharge of rivers damages crops and infrastructure. They also result in silta-tion of reservoirs and hence limit the capacity of existing dams to control floods. There are several factors which are responsible for occurrence of floods and droughts which including climatic changes, global warming, urban development and popula-tion density in exposed areas. In the recent past, Maharashtra too have witnessed many flood situations. The recurring flood losses hinder the state's economic growth. The

population living in the region where flooding frequently occurs is constantly threatened. Unplanned growth and increased floodplain invasions have contributed to the intensity of river floods. A call for better flood preparedness to ensure that adequate and efficient flood emergency preparedness steps are taken in order to prevent the loss of life, property, and the environment. In order to reduce vulnerability, it is crucial to have an effectual flood prevention plan and mitigation strategy, in addition to effective disaster response management plan. For planning and relief operations, flood inundation mapping plays a vital role for conveying the available flood risk information to decision-makers, evacuation teams, and to the general public.

Main objective of this study is to perform steady flow analysis and to develop floodplain inundation maps for the segment of the Pawana river and to develop flood line marking for 25-year, 50-year, and 100-year return period flood and determining critical locations affected due to flooding.

1.1 Flood Lines

Flood lines are lines indicating the maximum water level likely to be reached and delimits the area that would get inundated by floodwaters once every 25, 50, or 100 years.

1.1.1 Blue Line

For the discharge of 25-year return period flood or 1.5 times river capacity whichever is more. The area which gets flooded on either side of river bank comes under this line and zone is called prohibitive zone. Under this zone, any type of construction is prohibited and should be left open and can be used for gardens, playgrounds, or light crops.

1.1.2 Orange Line

For the discharge of 50-year return period flood, the area which gets flooded on either side of the banks of river comes under this line.

1.1.3 Red Line

For the discharge of 100-year return period flood or the design flood for dam, the area which gets flooded on either side of the banks of river comes under this line and the zone is called restrictive zone. The area under restrictive zone can be used for constructions having their plinth at safe levels from which evacuation can be facilitated and the construction can be such that it will not get demolished in floods.

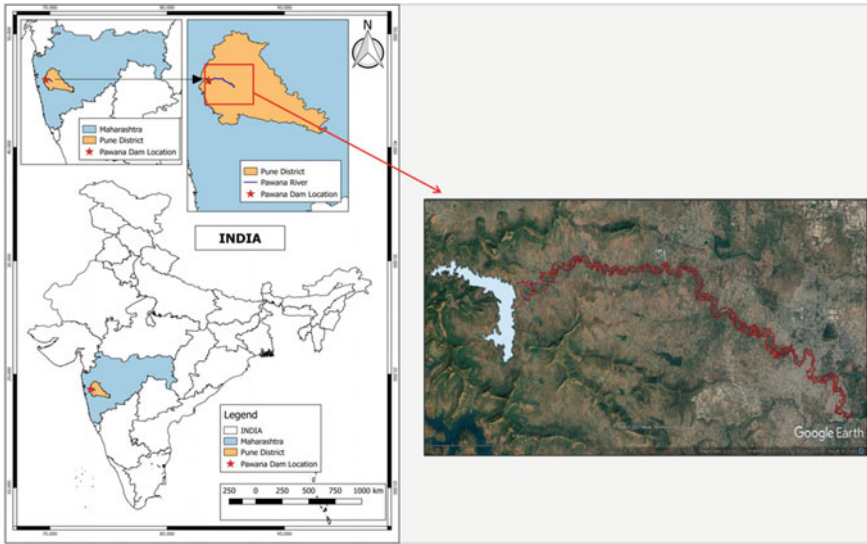


Fig. 1 Study area map of Pawana river

2 Materials and Procedures

2.1 Selection of Study Area

Pawana river originates in south of Lonavala in Pune district and is located on the western side of Maharashtra, India. Pawana river confluences with the Mula river at Pimpale Gurav and further flows downstream as the Mula-Mutha river, which further meets Bhima River around 54 km east of the city. The Pawana dam an Earth fill gravity dam has been built on the Pawana river in Pune district of Maharashtra state. The latitude of dam is $18^{\circ} 21' 30''$ and longitude is $73^{\circ} 40' 30''$. Dam has a height of 38.10 m and length of 1329 m. Water of this dam is used for hydroelectricity generation and for water supply to the area of Pimpri-Chinchwad city. The study area of Pawana river is covered between $18^{\circ} 40' 55''$ N and $18^{\circ} 34' 18''$ N latitudes and $73^{\circ} 29' 56''$ E to $73^{\circ} 49' 58''$ E longitudes. The location of the study area of Pawana river in India, has been shown in Fig. 1.

2.2 Data Collected and Processing

The necessary data needed for this study was obtained from different sources. Among the collected data, type of data, sources of data, and location has been listed in Table 1.

Table 1 Data collected list

Type of data	Source of data	Location
Discharge data	Irrigation Division, Pune	Pawana river
Gauge water level	Hydrology Project, Nashik	Pimpale-Gurav
Return flood period data	Irrigation Division, Pune	Pawana river
DEM (30 m * 30 m)	Bhuvan site	Pune, Maharashtra

The major inputs to HEC-RAS model are Digital Elevation Model (DEM) of 30 m × 30 m resolution, Manning’s roughness coefficient, and spillway discharge for calibration and validation of model.

2.3 Analysis Process for HEC-RAS

HEC-RAS uses multiple number of input parameters for hydraulic analysis of river channel geometry and water flow. With the help of these parameters cross-section are created along the stream center line. At each cross-section, stream bank lines are identified so as to divide the cross-section into section of left floodplain channel, and right floodplain channel as visualized in Fig. 2.

For open channel flow, the total energy per unit weight has three components: elevation head, pressure head, and velocity head as shown in Fig. 3.

$$H = Z + Y + \frac{\alpha V^2}{2g} \tag{1}$$

where:

- H = Total head or Energy head in m.
- Z = Elevation head or potential head in m.

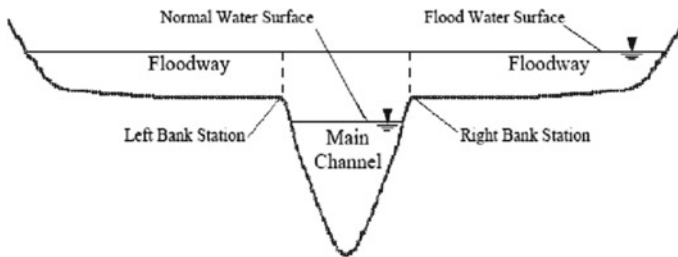


Fig. 2 Schematic view of stream cross-section [3]

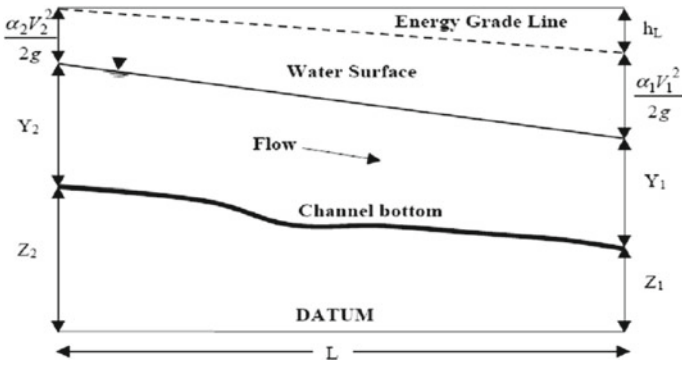


Fig. 3 Representation of energy equation parameters [3]

Y = Depth of water above channel bed in m.

α = Energy correction factor = 1 for Gradually varied flow.

Analysis has been done to get water depths, velocity, and water encroachment over the bank lines for different flood discharges which will be used further for purpose of mapping. In Arc-GIS, each attribute, i.e., cross-sections, river banks lines, etc., are created and saved in different features called as RAS layer, these layers are imported in HEC-RAS to make geometric files for HEC-RAS. In HEC-RAS software input the geometric data, steady flow data, boundary condition, etc. The schematic representation of geometry created and imported in HEC-RAS has shown in Fig. 4.

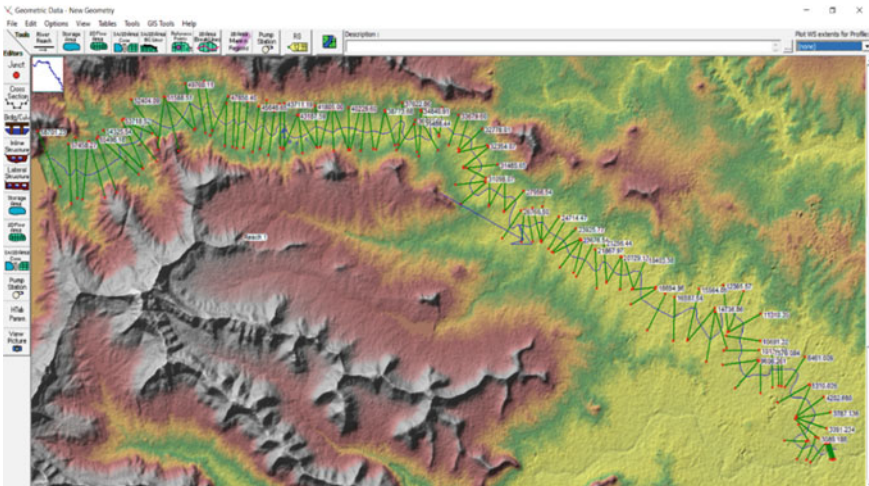


Fig. 4 The schematic representation of Pawana River in HEC-RAS

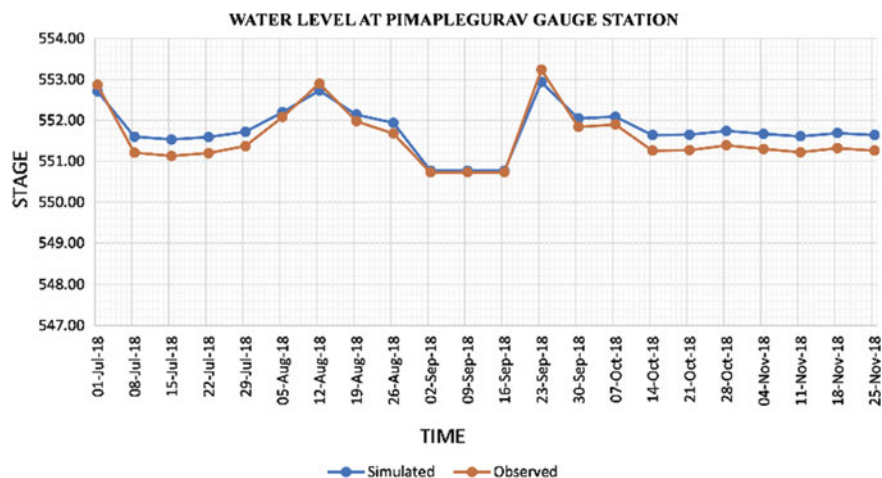


Fig. 5 Model calibration observed and simulated hydrograph at Pimpale Gurav

2.4 Model Calibration for Steady Flow

For HEC-RAS model calibration the daily spillway discharge of four months from July to November of 2018 has been used for this study. The model has been calibrated using measured water level data at Pimpalegurav gauging stations and effort has been made to calibrate Manning's roughness coefficient to a single value. Manning's roughness coefficient was varied between 0.015 and 0.045 for the channel and 0.010 and 0.050 for floodplain in order to justify the adequacy of simulation of flow in the Pawana River. Finally, "n" value as 0.030 for main channel and 0.037 for flood plain has been calibrated. After calibration, the comparison of observed and simulated stage hydrograph at Pimpale Gurav gauging stations has shown in Fig. 5. Coefficient of determination (R^2) and Nash–Sutcliffe Efficiency (NSE) have been found as 0.63 and 0.81, respectively, for the steady flow calibration.

2.5 Model Validation for Steady Flow

For validation of model the daily spillway discharge of four months from July to October of 2017 has been used. After validation, the comparison of observed and simulated stage hydrograph at Pimpale Gurav gauging stations is in close accord with each other and have been shown in Fig. 6. Coefficient of determination (R^2) and Nash–Sutcliffe Efficiency (NSE) has been found as 0.61 and 0.76 respectively for the steady flow validation.

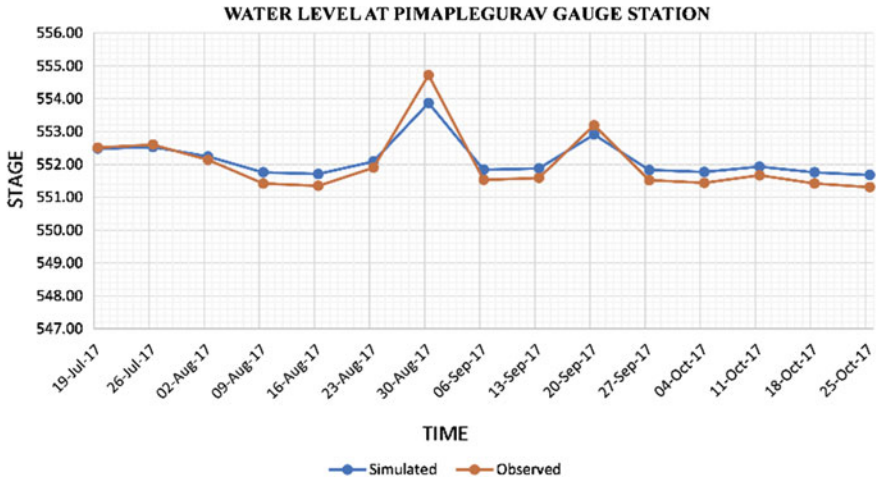


Fig. 6 Model validation observed and simulated hydrograph at Pimpale Gurav

2.6 Running Steady-State Simulation

After the model has been calibrated and validated, then the model is simulated for 25-year, 50-year, and 100-year return flood period data. For the Blue line, 25-year return period flow or 1.5 times river capacity whichever is higher is chosen for simulation. The 1.5 times river capacity is 811 m³/s and 25-year return period flood is 929 m³/s as per provided by Irrigation Division, Pune, therefore, flow values for Blue lines are taken as 929 m³/s. For the orange line, discharge value is 1061 m³/s and for red line discharge value is 1261 m³/s by taking these values as input model was run to perform steady flow analysis. Normal depth for boundary condition of bed slope is specified as 0.001. Once the steady flow data and boundary conditions are completed the model is simulated.

2.7 Visualize the Results

The model will take a few minutes for simulation and then visualization of the results, the cross-section, 3-D perspective plots, depth of water, water surface level, velocity, summary output table, and floodplain map can be viewed in each respective tab. The detailed flood inundation map can be exported to Google-Earth to view the areas which are getting affected. The detailed methodology in the form of flowchart in Fig. 7.

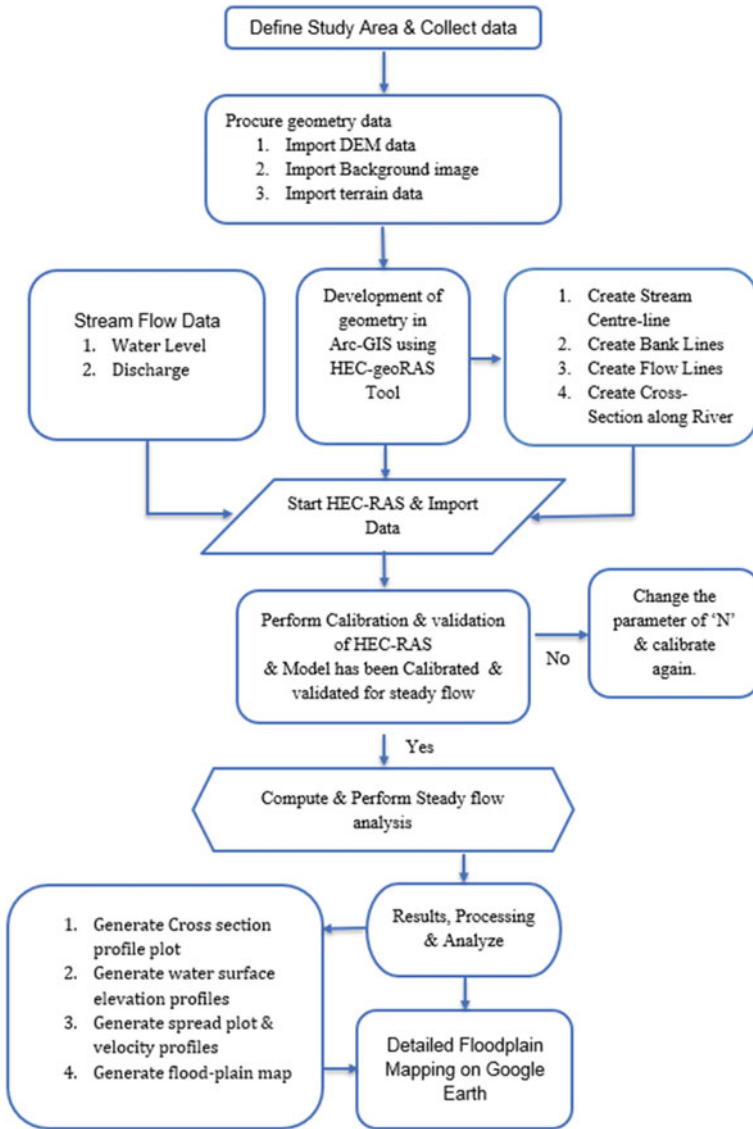


Fig. 7 General method for modeling floodplains using Arc-GIS and HEC-RAS

3 Results and Discussion

Floodplain inundation mapping is a valuable task to be performed by government agencies, planners, and engineers, and with the help of the map we can understand the extent of flooding caused and floodplain inundated, so in the best way, we can allocate resources to prepare for emergency action plans and be well prepared in

advance if the situation arises. The analysis for the floodplain areas inundated for 25-year, 50-year, and 100-year return period floods has been performed using HEC-RAS software. River cross-sections were inputted at around 500 m distance from each other. Total 115 cross-sections were plotted for 58 km long Pawana river, out of which 31 important cross-sections which are nearer to villages, settlements, etc., are selected. The coefficient of determination (R^2) and Nash Sutcliffe Coefficient (NSE) values are found to be above 0.60 and 0.75 for both calibration and validation. Then the results of maximum water depth, maximum velocity, and water spread on left and right of banks on each cross-section of Pawana river has been tabulated and shown in Table 2.

The floodplain map created using HEC-RAS has been imported to Google Earth and blue line, orange line, and red line for 25-year, 50-year and 100-year return period flood are marked. Once the floodplain map has been generated the affected locations, settlements, etc., are identified (Figs. 8, 9, 10, 11 and Table 3).

Table 2 Maximum water depth and maximum velocity for affected locations on the banks of the river for 25-year, 50-year, and 100-year return period flood

River station	Affected location on left of bank	Affected location on right of bank	25-year return period flood		50-year return period flood		100-year return period flood	
			Max water depth (m)	Max velocity (m/s)	Max water depth(m)	Max velocity (m/s)	Max water depth (m)	Max Velocity (m/s)
57,437	Pawanagar	–	2.98	0.48	3.18	0.49	3.47	0.52
52,898	Kadadhe village	–	2.19	1.21	2.4	1.22	2.68	1.24
42,233	–	Pimpalkhunte	5.84	1.81	6.06	1.91	6.38	2.02
37,536	–	Bebadohal	3.9	1.25	4.15	1.33	4.5	1.5
34,856	Parandwadi	Dhamaane	6.99	0.99	7.22	1.05	7.55	1.13
31,516	Shirgaon		7.25	0.95	7.48	1.01	7.8	1.08
29,966		Godumbre	4.57	1.1	4.8	1.16	5.1	1.28
27,965	Gahunje	–	5.81	1.04	6.01	1.13	6.29	1.15
25,487	Lodha-towers	–	2.92	1.16	3.1	1.23	3.31	1.33
22,917	Dattawadi	–	0.86	0.32	1.02	0.42	1.23	0.53
19,997	Ravetgaon	BuddhaVihar	6.9	0.65	7.06	0.73	7.28	0.83
19,431	Sector 32 A	Vishnudev nagar	6.59	1.14	6.74	1.24	6.95	1.38
18,300	Walhekarwadi	Newale wasti	2.82	0.55	2.96	0.61	3.17	0.69
15,612	Keshvanagar	Bijlinagar	5.23	2.93	5.45	3.16	5.74	3.48
14,772	Deowada		5.14	1.71	5.41	1.7	5.8	1.67
14,035	Moryarajpark	–	6	1.46	6.27	1.52	6.66	1.64
12,386	Manik colony	Pawanagar	7.26	1.03	7.52	1.1	7.88	1.19
11,900	Yashopram housing soc	Shanti colony	6.98	1.31	7.23	1.4	7.58	1.52
11,304	Ambedkar colony	Nirmalnagar	4.26	2.02	4.48	2.16	4.8	2.36
10,129	Mali Ali	Shraddha colony	4.75	1.4	4.91	1.49	5.13	1.63
9002	Pimprigaon	Rahatnigaon	5.29	1.27	5.44	1.37	5.63	1.51
7053	–	Krantinagar	8.16	1.17	8.46	1.21	8.88	1.29
6442	Kasarwadi	–	8.77	1.68	9.07	1.8	9.46	2
4589		Kadamwada	5.54	2.59	5.78	2.75	6.13	2.93
4228	Sevanagar	Agarsenagar	7.49	1.44	7.74	1.53	8.1	1.64
3785	Devkarnagar	Dapodi	9.03	1.1	9.27	1.19	9.63	1.31
3399	Devkarnagar	Ganeshnagar	7.57	0.9	7.81	0.97	8.17	1.03

(continued)

Table 2 (continued)

River station	Affected location on left of bank	Affected location on right of bank	25-year return period flood		50-year return period flood		100-year return period flood	
			Max water depth (m)	Max velocity (m/s)	Max water depth(m)	Max velocity (m/s)	Max water depth (m)	Max Velocity (m/s)
3097	Pimpalegurav road	Gangotri nagar	2.25	1.63	2.49	1.67	2.85	1.73
2754	–	Shivramnagar	3.53	5.07	3.76	5.27	4.08	5.54
2269	–	Samarthnagar	6.39	1.64	6.64	1.76	7	1.89
826	Budhvihar	Mamtanagar	6.65	1.08	6.84	1.18	7.1	1.32

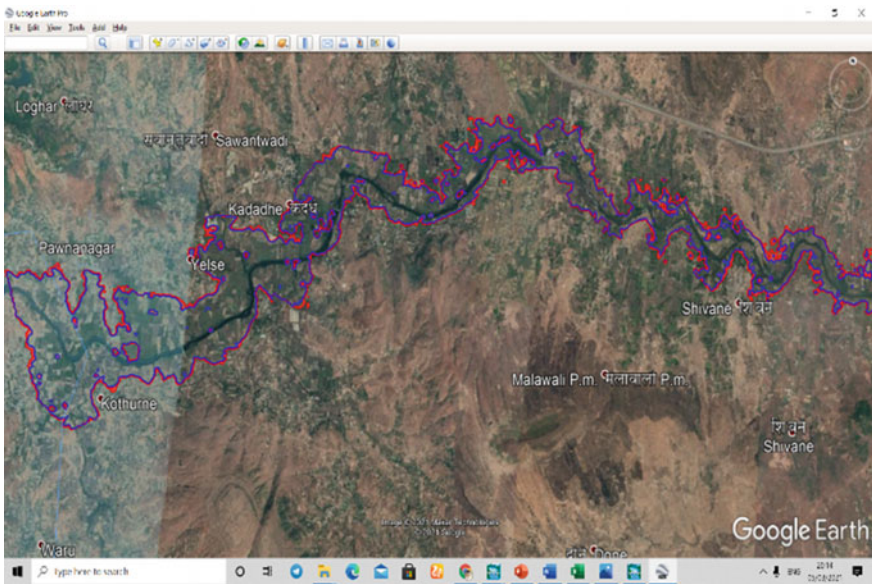


Fig. 8 Floodplain map from river station 57,437 to river station 42,233

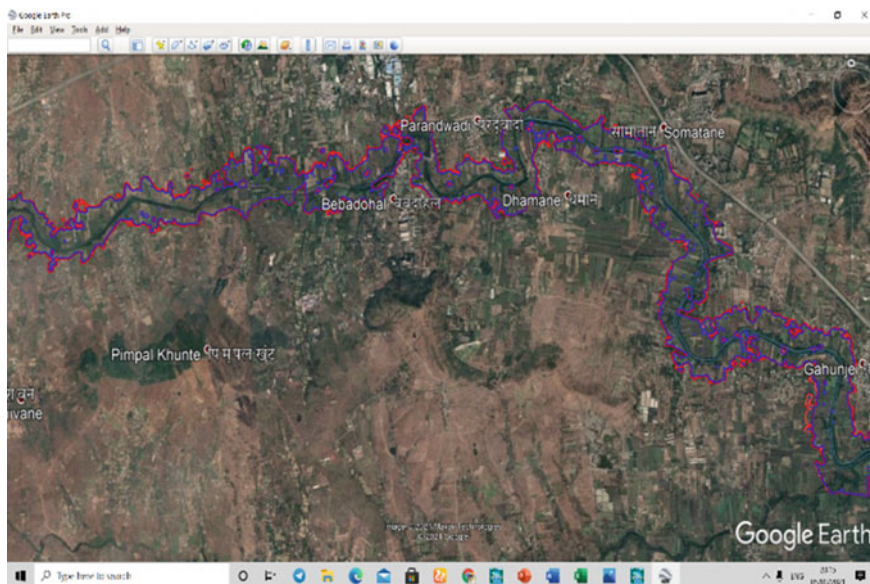


Fig. 9 Floodplain map from river station 42,233 to river station 25,487

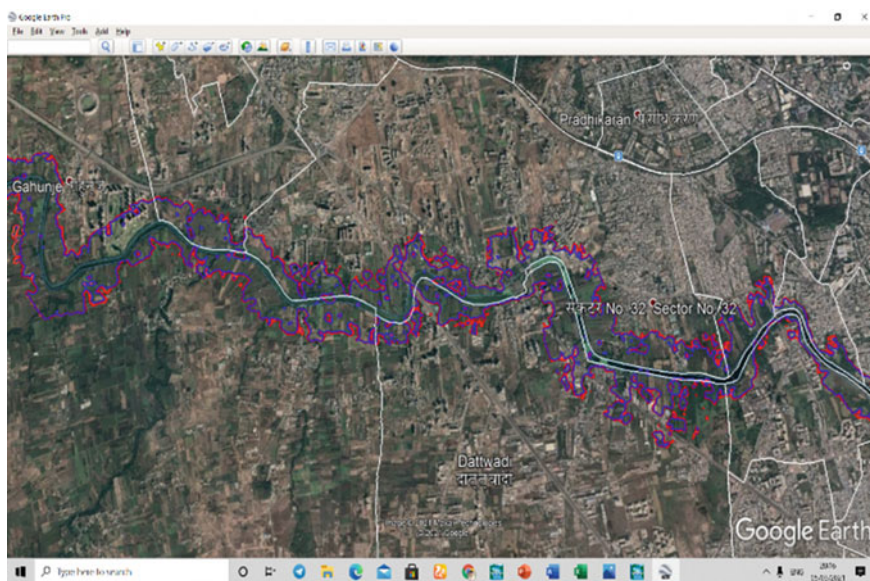


Fig. 10 Floodplain map from river station 25,487 to river station 11,900

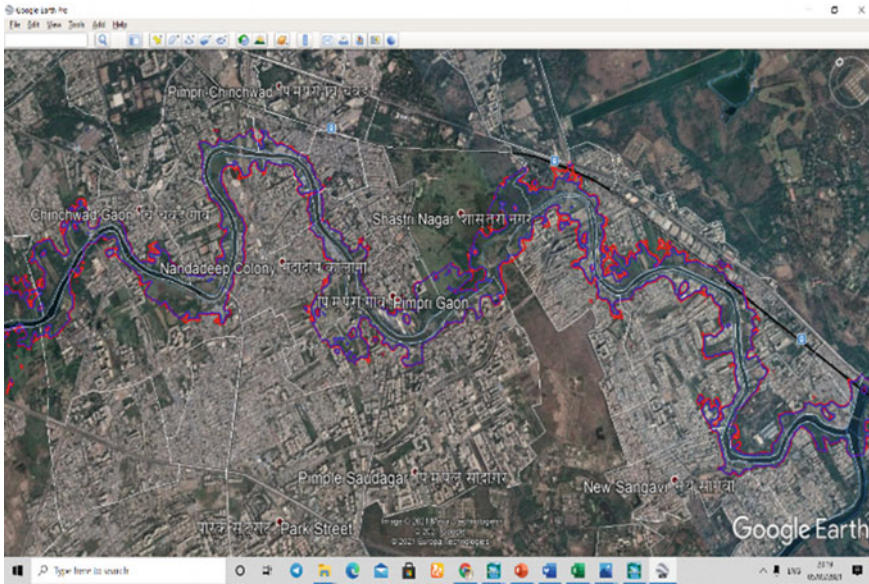


Fig. 11 Floodplain map from river station 11,900 to river station 826

Table 3 Spread plot for affected locations on the banks of river for 25-year, 50-year, and 100-year return period flood

River station	Affected location on left of bank	Affected location on right of bank	25-year return period flood		50-year return period flood		100-year return period flood	
			Water spread on LOB (m)	Water spread on ROB (m)	Water spread on LOB (m)	Water spread on ROB (m)	Water spread on LOB (m)	Water spread on ROB (m)
57,437	Pawananagar	–	578	679	578.8	691.7	600	696
52,898	Kadadhe village	–	557	46	561.2	48.7	580	53.1
42,233	–	Pimpalkhunte	218	47	231.8	55.5	238	61
37,536	–	Bebadohal	113	153	120.5	160.7	125	185
34,856	Parandwadi	Dhamaane	70	334	81.2	336.1	83	342
31,516	Shirgaon		264.1	257.1	270.7	255.9	282.1	262.2
29,966		Godumbre	371.4	133.7	382.5	137.8	392.9	140.2
27,965	Gahunje	–	119.4	353	131.1	363.1	142.9	374.9
25,487	Lodha-towers	–	286.5	200.5	289.1	214.5	294.6	220.7
22,917	Dattawadi	–	286.7	406.9	311.5	407.1	357	410.3

(continued)

Table 3 (continued)

River station	Affected location on left of bank	Affected location on right of bank	25-year return period flood		50-year return period flood		100-year return period flood	
			Water spread on LOB (m)	Water spread on ROB (m)	Water spread on LOB (m)	Water spread on ROB (m)	Water spread on LOB (m)	Water spread on ROB (m)
19,997	Ravetgaon	BuddhaVihar	482.5	71.3	494.9	72.6	533.1	74.4
19,431	Sector 32 A	Vishnudev nagar	66.9	426.8	67.4	432.1	70.1	436.8
18,300	Walhekarwadi	Newale wasti	421.7	340.1	427.8	348	433.9	351.6
15,612	Keshvanagar	Bijlinagar	100.8	18.8	76.9	20.1	101.6	69.9
14,772	Deowada		210.3	194.1	211.1	195	211.7	195.3
14,035	Moryarajpark	–	222.7	224.2	227.7	227.6	232.8	231.1
12,386	Manik colony	Pawanagar	139	185.1	143.1	190.3	145.2	197
11,900	Yashopram housing soc	Shanti colony	201.5	57.8	205.1	60.8	208.4	71.2
11,304	Ambedkar colony	Nirmalnagar	36.3	78	38.3	79.7	42.4	86.3
10,129	Mali Ali	Shraddha colony	233.1	156.4	241.7	160.8	256.6	165.6
9002	Pimprigaon	Rahatnigaon	246.7	194.2	253.3	197.7	261.7	202.6
7053	–	Krantinagar	378.1	86.8	383.4	88.5	420.3	99.9
6442	Kasarwadi	–	101.8	182.4	120.4	192.9	193	201.1
4589		Kadamwada	91.6	60.7	97.1	63.4	203.9	65.8
4228	Sevanagar	Agarsenagar	113.1	175	116.7	176.8	121.5	182.7
3785	Devkarnagar	Dapodi	117.4	168.1	120.3	177.7	124.9	188.5
3399	Devkarnagar	Ganeshnagar	137.9	355.7	176	363.1	189.3	375.2
3097	Pimpalegurav road	Gangotri nagar	219.6	47.6	223	53.3	225.4	58.2
2754	–	Shivramnagar	3.4	32	5.1	33.7	7	36.2
2269	–	Samarthnagar	97	35	106.7	37	116	40.8
826	Budhvihar	Mamtanagar	194	19	195.2	20.8	200	22

4 Conclusion

1. The floodplain mapping for 25-year, 50-year, and 100-year return period floods has been done, by calibrating and validating the model on HEC-RAS with the real-time observed data to get accuracy of the flooding caused.
2. The extent of the flooding caused has shown with the help of the flood lines, i.e., blue line, orange line, and red line marking have been done for the Pawana river at the downstream of Pawana dam.
3. It is observed that there are many critical locations that are affected due to this flooding. Under prohibitive zone, up to river station 29,966, i.e., Godumbre village, there is not much urbanization present. Hence under prohibitive zone there are structures mainly temples, small industrial, and few temporary structures.
4. The urbanized locations at downstream of river station 27,965, i.e., Gahunje village. From this river station 27,965, there are residential sectors, buildings, and small slums located on banks of river which are getting flooded even for 25-year return period flood and fall under prohibitive zone.
5. Flood control measures such as construction of dykes and levees, structures which can absorb water or divert the floodwater away from banks, repair, and maintenance of the embankments are suggested. Also, government agencies should monitor existing structures and should be well prepared in advanced with Emergency Action Plan (EPA) and Disaster Management Plan if a flooding situation arises.
6. It is recommended to do floodplain mapping and investigate flood risk management for dams and rivers, well in advance using suitable measures to tackle the situation in an effective and efficient way.

References

1. Rahman MM, Ali MM (2016) Floodplain mapping of the Jamuna River using HEC-RAS and HEC-GeoRAS. *J. Presidency University, Part: B* 3(2):24–32. ISSN: 2224–7610
2. Shahzad Khattak M, Anwar F, Saeed TU, Sharif M, Sheraz K, Anwaar A (2016) Floodplain mapping using hec-ras and ArcGIS: a case study of Kabul River. *Arab J Sci Eng* 41:1375–1390
3. Tate E, Maidment DR (1999) Floodplain mapping using HEC-RAS and ArcView GIS. Master's Thesis, Department of Civil Engineering, the University of Texas at Austin
4. Forghani MR, Irandoust M, Jalalkamali N (2016) Flood plain analysis and flow simulation of river using HEC-RAS model. *Sci Arena Publ Spec J Agri Sci* 2(2):27–36
5. ShahiriParsa A, Qalo N, Heydari M, bt Mohd Amin NF (2013) Introduction to floodplain zoning simulation models through dimensional approach. *Int J Adv Civil Struct Environ Eng* 1(1):20–23
6. Tate EC, Maidment DR, Olivera F, Anderson DJ (2002) Creating a terrain model for floodplain mapping. *J Hydrol Eng* 7:100–108

7. USACE, River Analysis System HEC-RAS, Hydraulic Reference Manual version 5.0.7, <https://www.hec.usace.army.mil/software/hecras/>
8. USACE, User's Manual of HEC-RAS version 5.0.7

Performance Evaluation of Varying OLR and HRT on Two Stage Anaerobic Digestion Process of Hybrid Reactor (HUASB) for Blended Industrial Wastewater as Substrate



Rajani Saranadagoudar, Shashikant R. Mise, and B. B. Kori

Abstract The study was carried out to evaluate the performance of a two-stage pilot-scale hybrid up-flow anaerobic sludge blanket reactor (HUASB) of 9.5-L capacity treating blended Industrial Wastewater as substrate under varying organic and hydraulic loading conditions under ambient laboratory conditions. The reactor was operated for around 6 months with four different hydraulic retention times of 48, 36, 24 and 12 h. Imposed organic loading rates (OLR) ranged from 2.4, 3.2, 4.8, and 9.6 (kgCOD/m³·d). The steady-state performance of HUASB reactor showed a tremendous performance on the treatment of blended industrial wastewater, with an average COD and BOD₅ removal efficiency of 94.4% and 92.7%, respectively, with a maximum biogas production of 12600 cc/d. The results show that the HUASB reactor could serve as a good alternative for anaerobic digestion of Blended industrial wastewater and methane production.

Keywords Anaerobic · COD · HUASB reactor · Blended industrial wastewater · Biogas

1 Introduction

The dairy industry is a food processing industry which is one of the major polluting industries, both in terms of quality and quantity of waste generated. It is estimated that about 120 million tons of the milk and approximately 275 million tons of wastewater will be produced every year from the Indian dairy industries by the year 2020. A series of operations involved in dairy industry are receiving, Pasteurizing, bottling, condensing, dry milk manufacturing, cheese production, butter, and Casein making.

R. Saranadagoudar (✉) · S. R. Mise
Department of Civil Engineering, Poojya Dodappa Appa College of Engineering, Kalaburagi,
Karnataka 585102, India
e-mail: rajanigndecb@gmail.com

B. B. Kori
Department of Civil Engineering, Guru Nanak Dev Engineering College, Bidar, Karnataka
585403, India

Wastewater is mainly generated from the following actions such as cleaning of equipment, tankers, and washing of containers, floor washing, water softening unit, boiler house, and refrigeration plant waste [1]

Distillery industries are included under the category of most polluting Industries in regard with water pollution. The total volume of wastewater may vary from 70–120 L per liter of alcohol produced. Distillery using molasses for the production of alcohol by fermentation and distillation processes produces a very high organic and inorganic effluent. The manufacturing processes are feed preparation, yeast propagation, and continuous fermentation, multipurpose distillation with isolated spent-wash evaporator, stillage processing, molecular sieve dehydration for fuel alcohol, and packaging unit. The waste streams comprise of spent wash, which in turn is one of the major source of wastewater. Spent wash, contains dissolved salts and has persistent dark brown color. It also contains acids and alkalies in traces which are produced from cleaning and sanitizing.

Aerobic processes, which are widely used for the treatment of wastewater have two distinct disadvantages like high energy requirement and excess sludge production, which require handling, treatment, and disposal [2]. In contrast, anaerobic processes generate energy in the form of biogas, and produce sludge in significantly lower amounts than those resulting from aerobic systems [3].

2 Experimental Section

2.1 Hybrid UASB Reactor Setup

- A laboratory-scale Hybrid UASB reactor is fabricated using a 5 mm thick acrylic pipe with external diameter of 34 cm. The reactor has a working volume of 9.5 L. Height of the hybrid reactor is 251 cm which includes GLSS separator. To create electrolysis process in the reactor, two electrodes (zinc rods) are provided with a diameter of about 10 mm and with the height of about 150 mm, One rod is connected to anode and other rod to cathode, these rods are connected to DC power supply with the volt of about 4.5, resulting in continuous supply of oxygen and hydrogen. At high inter-electrode distances, removal efficiency decreases due to reduced rate of mass transfer and due to elevated ohmic drop which reduces the anodic oxidation [4].
- The settler consists of baffles, which help, in guiding the gas bubbles to enter into the separator, to capture the evolved gas, and to allow the settling of suspended solids.
- Bedding media made up of PVC material in the form of Circular Rings (Diameter—1 cm, Thickness—0.1 cm, Height—0.2 cm) was added up to 30 cm height into the reactor to enhance granulation process by increasing the surface area. Gas collected was measured by water displacement method. The arrangement

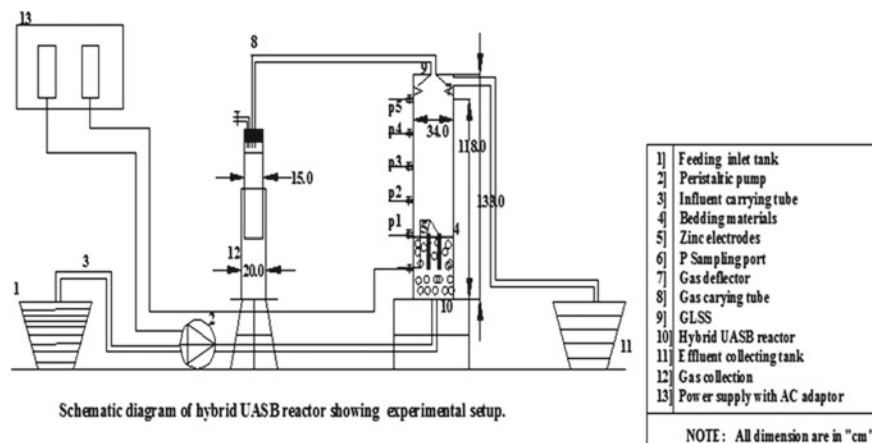


Fig. 1 Schematic representation of hybrid UASB reactor

consists of a 15 cm diameter internal cylinder, 20 cm diameter external cylinder with capacity of 20 L.

- The reactor was mounted on a mild steel-framed structure. The Schematic representation of Hybrid UASB reactor is as shown in Fig. 1.

2.2 Wastewater and Seed Sludge

The study was carried out under ambient environmental conditions. The dairy wastewater is collected from Karnataka Milk Federation (KMF) milk processing plant, Kalaburagi, Karnataka. The distillery industry wastewater is collected from Sanjeevani Sahakari Sakharkharkhana limited, Shingnapur, At: Kolpewadi, Tal-Kopergaon, Dist. Ahmednagar, Maharashtra. The general characteristics of blended industrial wastewater (dairy and distillery) and seed sludge are given in Table 1 [2, 5].

Table 1 Physico-characteristics of blended industrial wastewater and seed sludge

S.No.	Parameters	Unit	Seed sludge (distillery)	Blended industrial wastewater
1	COD	mg/L	1,33,200	7200
2	BOD ₅	mg/L	82,947	4380
3	pH		4.2	7.10
4	DO	mg/L	Nil	Nil
5	Alkalinity	mg/L	8658	2600
6	Total solids	mg/L	60,040	16,624
7	Dissolved solids	mg/L	44,377	13,182
8	Suspended solids	mg/L	15,662	3442

2.3 Reactor Operation

For initial startup and acclimatization the hydraulic retention time (HRT) was 48 h for organic loading rate 2.4 (kgCOD/m³·d) subsequent organic loading rates are 3.2, 4.8, and 9.6 kgCOD/m³·d at subsequent hydraulic retention time 36 h, 24 h, and 12 h, respectively. COD:N:P ratio of Blended wastewater is 480:9.6:1, COD:N:P should be maintained between 250:5:1 to 500:5:1 for good methanogenic activity.

2.4 Analytical Procedure

The effluent from the reactor was daily analyzed for various parameters such as Biogas production, pH, alkalinity, TS and TVS, alkalinity, and suspended solids (TS) analysis was carried out in accordance with Standard Methods (APHA 2017).

3 Results and Discussion

The reactor was operated continuously for 131 days. Initially, reactor was operated at a loading rate of 2.4 (kgCOD/m³·d) and Hydraulic-Retention-Time of 48 h. The reactor was operated for varying OLR of 2.4, 3.2, 4.8, and 9.6 (kgCOD/m³·d) by changing HRTs 48 h to 36 h, 24 h, and 12 h, respectively. During the operation, COD removal efficiencies were observed by performing tests. Due to the presence of large granules, accumulations of hydrolytic fermentative bacteria around the granules were more in number. Due to this complex, organic matter is converted into simpler dissolved form. After achieving the successful granulation the COD removal efficiency increased. During the operation, optimum COD removal efficiency recorded was 94.5%.

BOD₅ removal efficiency is the major parameter to study the performance of a reactor. The BOD₅ removal efficiency in the beginning was 73.06% later it increased up to 92.6%. During the operation pH was maintained within the range (6.7–8.0) which resulted in the optimum BOD removal efficiency and also due to successful granulation, BOD removal efficiency was increased. The Solid removal is the most important parameter to study the performance of the reactor, as hybrid reactor is provided with bedding media to improve the sludge settling characteristics. Initially, the total solids removal was 49%, Dissolved solids removal was 50.7% and suspended solids removal was 43.3% for aOLRof 2.2 kgCOD/m³·d. Later, it increased to 95.4%, 97.3%, and 87.8% for a OLRof 9.6 kgCOD/m³·d.

Fig. 2 Variation of biogas with OLR

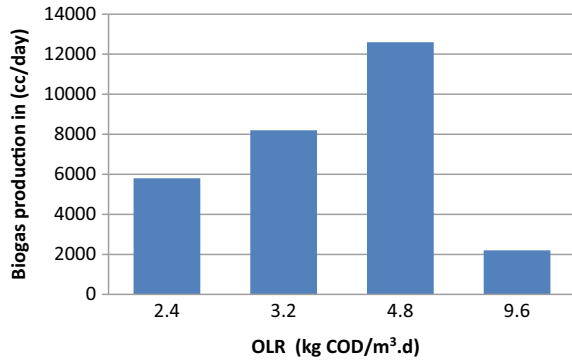
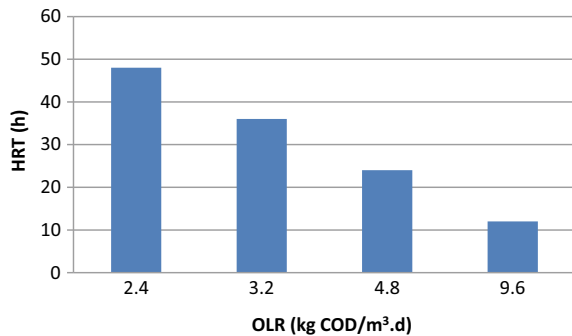


Figure 2 illustrates variation of Biogas with OLR. At an OLR of 2.4 (kgCOD/m³.d), biogas production of 5800 cc/d. At an increased loading of 3.2 (kgCOD/m³.d), it was 8200 cc/d, at OLR 4.8 (kgCOD/m³.d) biogas production was maximum 12600 cc/d, as the loading was increased to 9.6 (kgCOD/m³.d) biogas production was reduced to 2200 cc/d. An increase in OLR had shown increase in the biogas production. When the OLR was increased to 9.6 (kgCOD/m³.d) biogas production decreased to 2200 cc/d and the reactor became unstable, this indicates that the HRT of the reactor was not to be reduced to 12 h or less than 12 h.

The COD concentration of 7200 mg/L was maintained in the reactor at an HRT of 48 h and later HRT were reduced to 36 h, 24 h, and 12 h respectively. The COD concentration was maintained constant throughout until the COD removal efficiency has reached steady-state conditions for varying organic-loading rates 2.4, 3.2, 4.8, and 9.6 (kgCOD/m³.d). Figure 3 shows the variation of organic loading rate along with HRT.

Fig. 3 Variation of HRT with OLR



4 Conclusions

- The reactor was operated for various OLRs and HRTs. The maximum COD removal efficiency was 76%, 84%, 87.8%, and 94.5% after 50th, 75th, 100th, and 120th day, respectively, from the start up at a loading rate of 2.4, 3.2, 4.8, and 9.6 (kgCOD/m³·d) respectively.
- The maximum biogas produced was 12,600 mL after 120th day from the start-up of the reactor at an O.L.R of 4.8 (kgCOD/m³·d). The BOD₅ removal efficiency was 92.6% for a loading rate of 4.8 (kgCOD/m³·d).
- Hence, It can be concluded that, as the daily feed ratio was increased from 2.4, 3.2, 4.8, and 9.6 (kgCOD/m³·d), the gas production and percentage COD removal increased.
- However, as the O.L.R was increased to 15.36 (kgCOD/m³·d), reactor became instable with an increase in VFA/Alkalinity ratio of 0.44–0.89.

References

1. Patyal V, Lallotra B (2015) Study of USAB method of treatment of distillery wastewater. IOSR J Mech Civil Eng (IOSR-JMCE) 27-32, e-ISSN: 2278-1684, p-ISSN: 2320-334X
2. Bhatti ZA (2014) UASB reactor startup for the treatment of municipal wastewater followed by advanced oxidation process. Brazil J Chem Eng 31(03):715–726, ISSN 0104-6632
3. Venkatesh KR, Rajendran M, Murugappan A (2013) Start-up of an upflow anaerobic sludge blanket reactor treating low-strength wastewater inoculated with non-granular sludge. Int Ref J Eng Sci (IRJET) 2(5):46–53
4. Fayad N (2017) The application of electrocoagulation process for wastewater treatment and for the separation and purification of biological media. Chem Process Eng. Université Clermont Auvergne, 2017. English. fNNT: 2017CLFAC024ff. fftel-01719756f
5. Shirule PA (2013) Treatment of dairy waste water using UASB reactor and generation of energy. Pratibha: Int J Sci Spirit Bus Technol (IJSSBT) 2(1):2277–7261

Analysis of Morphometric Parameters of Watershed Using GIS



Bhairavi Pawar and K. A. Patil

Abstract Watershed management is the study for sustainable development of water bodies as well as land in the watershed region. Morphometric parameters of watershed act as a yardstick in analyzing, planning, and maintaining of watersheds. In this paper, data acquired from LANDSAT and NASA satellites was interpolated, supervised, and classified in order to obtain DEM and delineate watershed boundary in Arc GIS 10.3. Pour point was taken on dam wall of Palkhed dam to delineate watershed on the upstream region of the dam. Area of 811.15 sq. km of watershed was obtained. Various topographic, geomorphometric, and geological parameters of the watershed were extracted and analysed using GIS as a tool.

Keywords Watershed · GIS · Arc map · Morphometric parameters

1 Introduction

Watershed is a hydrological unit and is an exemplary unit for management of resources like water and land. According to National Water Mission (NWM), Govt. of India, the estimated usable surface water is 690BCM. Most of this water precipitated is lost in the form of excessive surface flow due to the absence of management of water. Watershed management aims at storing this excess water and utilizing it for various onsite purposes. Watershed regions have a huge extent of area and thus the study of various morphological parameters becomes tedious. Morphological parameters are obtained by using satellite imagery data and by processing this obtained data using GIS and remote sensing software like Arc-GIS.

In this era of digitization, most of the manual and traditional systems of analysis of data collection, software, and tools like remote sensing and GIS replace data analysis

B. Pawar (✉) · K. A. Patil
Department of Civil Engineering, College of Engineering Pune, Pune 411005, India
e-mail: pawarbv19.civil@coep.ac.in

K. A. Patil
e-mail: kap.civil@coep.ac.in



Fig. 1 Location of study area

and data interpretation. Remote sensing tool has made it possible to gain detailed information without even having physical contact with that place.

2 Study Area

Dindori is a town and taluka located in Nashik District of Maharashtra, which is also known as the “Wine capital of India” because of its grape farming. Palkhed dam is a significant water resource project that falls in this region. It is an earth-fill dam on Kadwa river with gross storage capacity of 230,100.00 cu km. This study considers watershed region of 811.15 sq km on upstream side of Palkhed dam (20.1911225°N 73.8834431°E) as the study area. This region marks the presence of River Kadwa which is the tributary of Godavari river. The significance of this region is the purpose of the dam, which is solely for irrigation, and it meets the needs of almost 1.77 lakh population receding in the watershed region. Figure 1 shows the study area location.

3 Data Collection

DEM (30 m resolution) from ASTER DEM of the study region downloaded from the earth explorer website of USGS. Hydrological soil group data from ORNL DDAC Sponsored by NASA downloaded from daac.ornl.gov website. Landsat 8 OLI, i.e., Operational Land Imager and TIRS, i.e., Thermal Infrared Sensor with 30 m multi-spectral data images downloaded from USGS website, Bhukosh portal of Geological survey of India and toposheet from Survey of India Website.

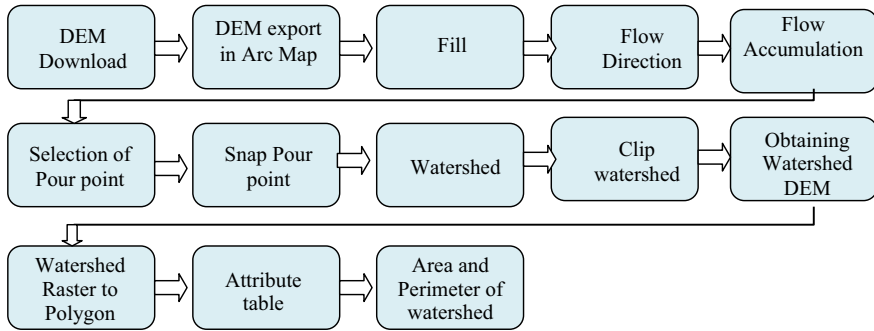


Fig. 2 Flowchart for watershed delineation process

4 Methodology

4.1 Watershed Delineation

The delineation of watershed includes the use of Digital Elevation Models (DEMs) obtained from earth explorer web portal of U.S. geological survey website. The DEMs obtained are of 30 m resolution and act as a source of stored data that help us to obtain spatial information related to the selected study area. Prerequisite for spatial study of watershed is to delineate that watershed from the given DEM. Arc Map10.3 version facilitates the user to clip the watershed raster from the DEM. It has Spatial Analysis Tool (SAT) and Data Management Tool (DMT) that are used for watershed delineation. Following are the steps (Fig. 2).

4.2 Morphometric Parameters

Morphometric analysis is the practice of geomorphology that aims at quantitative description and analysis of landforms of drainage basins. One such basic parameter under morphometry is the stream order. According to the method put forward by Strahler (1964), stream orders of the given basin are further classified into five stream orders. Most of the streams are stream order 1 present in the basin. All other morphometric parameters are further obtained using stream order data. Following are the steps to obtain stream order. Figure 3 shows a flow chart of morphometric parameter analysis.

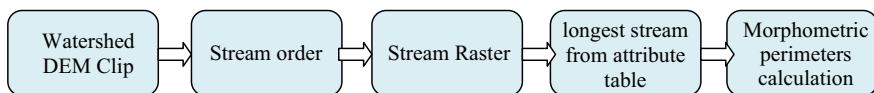


Fig. 3 Flowchart for morphometric parameters analysis

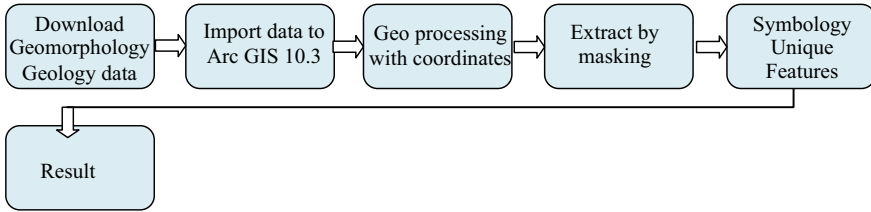


Fig. 4 Flowchart for geomorphology and geological analysis

4.3 Geomorphology and Geology

Geomorphology is the scientific study of effects of physical, chemical, or biological processes on the topographic and bathymetric features of the region. Geomorphology data and geology data of India were obtained from “Bhookosh” portal of Geological Survey of India website. The data is imported into Arc Map 10.3 and terrain features are extracted using masking tool and assigning unique values and unique color codes to each feature. Raster file is geo-referenced with WGS 1984 UTM Zone 43 N coordinate system. Figure 4 shows the flow chart of for geomorphology and geological analysis.

4.4 TIN Model Generation

TIN an acronym for **Triangulated Irregular Network** is a portrayal of a continuous surface consisting completely of triangular facets, used mainly as Discrete Global Grid in primary elevation modeling. TIN model gives a 3D feel of real features on grounds. It is generated using Arc Map and can be simulated in Arc Scene. TIN Model also provides with Slope and Aspect of the region, which is essential in formulating discharge accumulation sites and depressions and elevations in the given region. Figure 5 shows steps to formulate TIN model.

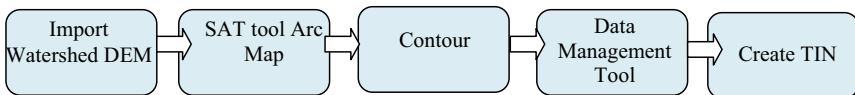


Fig. 5 Flowchart for TIN analysis

5 Results and Discussion

5.1 Watershed and Watershed Parameters

The Watershed obtained is having an area of 811.15 sq. km and a perimeter of 131.34 km. The length of the longest stream is 46.26 km. Figure 6 shows DEM clip of watershed. Figures 7, 8, and 9 show flow direction raster, drainage density, and longest stream, respectively. Figure 10 shows stream orders the values of which are ranging between 1 and 5 and Fig. 11 shows TIN model of the watershed.

Fig. 6 DEM clip watershed

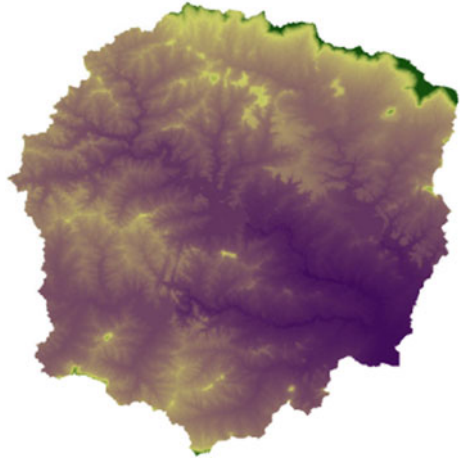


Fig. 7 Flow direction raster

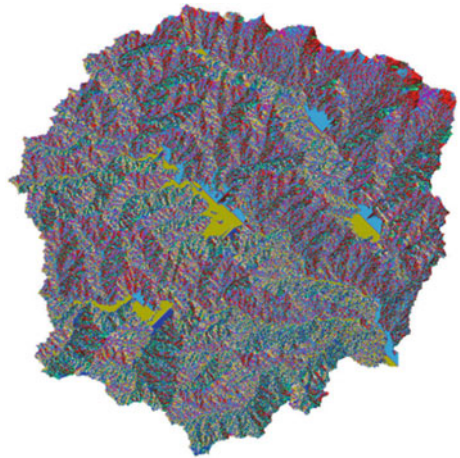


Fig. 8 Drainage density

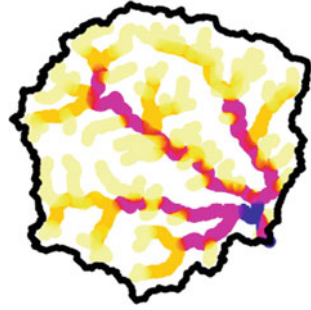


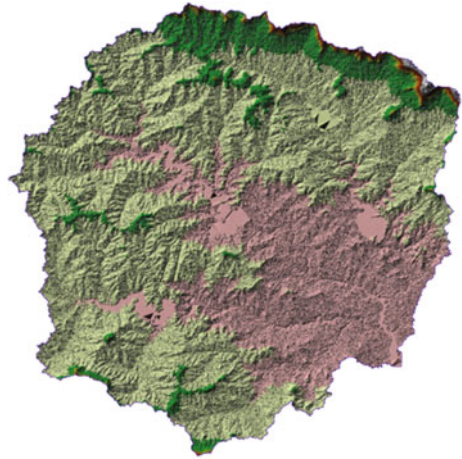
Fig. 9 Longest stream



Fig. 10 Stream order



Fig. 11 TIN model



5.2 Geology and Geomorphology Results

Figure 12 shows geology of the watershed and Fig. 13 shows geomorphology of the watershed. From these figures, it is seen that the region has a late cretaceous—Palaeocene, Deccan trap type of geological features where the rock is Deccan Trap Basalt.

It is seen in the geomorphology of the watershed that the watershed has dissected plateau region. There are four reservoirs in the catchment.

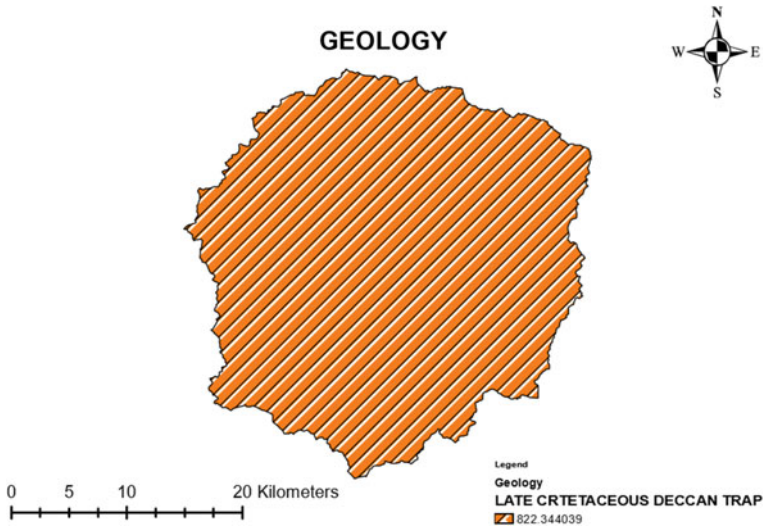


Fig. 12 Geology of the watershed

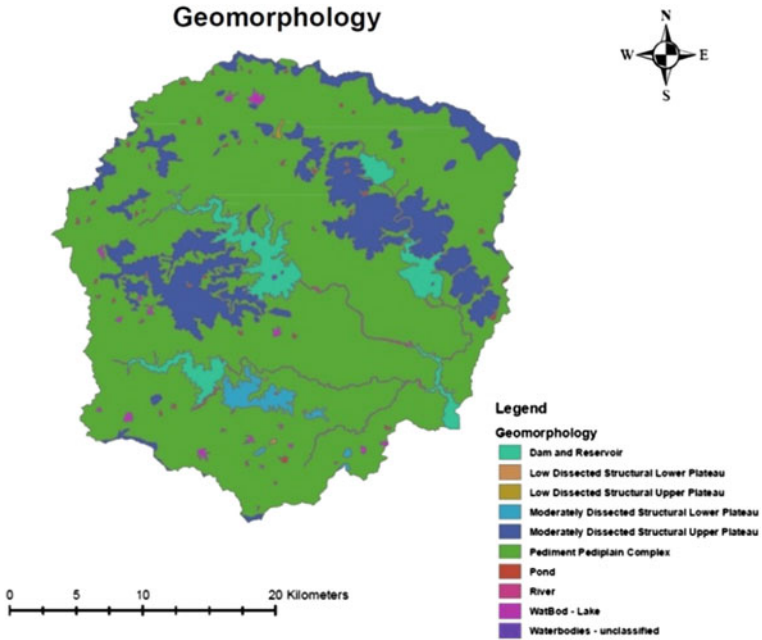


Fig. 13 Geomorphology of the watershed

5.3 Morphometric Parameters Analysis

A table is formulated containing various watershed parameters like stream order, stream length, stream ratio, bifurcation ratio, stream frequency, length of overland flow, form factor, circulatory ratio, texture ratio, drainage density, etc.

1. **Stream Order: u**
2. **Stream Length: Lu**
3. **Elongation Ratio (Re)**

$$Re = (2/Lb) * (A/\pi)^{0.5}$$

Where A = Area of Basin

Lb = Length of Basin

P = Perimeter

4. **Circularity Ratio (Rc)**

$$Rc = 4 \pi A/P^2.$$

Where A = Area of Basin

P = Perimeter

5. **Texture Ratio (T)**

Table1 Morphometric parameters

Sr No.	Parameters	Stream orders				
		I	II	III	IV	V
1	Stream order (U)	5050	2633	2342	132	102
2	Stream length (LU)	173.00	90.49	80.99	4.4	3.68
4	Stream length ratio (RL)	1.0058	1.0112	1.0125	1.2941	1.3731
5	Bifurcation ratio (Rb)		1.918	1.124	17.742	1.294
7	Perimeter (P) (in km)	141.34				
8	Basin length (Lb) (km)	46.26				
9	Basin area (sqkm)	811.15				
12	Elongation ratio (Re)	0.69				
13	Length of over land flow (L _g) (km)	4.5977				
14	Drainage density (D) (km/km ²)	0.43				
15	Stream frequency (Fs) (per sq. km)	12.64				
16	Texture ratio (Rt)	72.5				
17	Form factor (Rf)	0.37				
18	Circulatory ratio (Rc)	0.51				

$$T = Nu/P$$

Where P = Perimeter

Nu = Total number of stream segments of order u

6. Drainage Density (Dd)

$$Dd = Lu/A$$

Where Lu = Total stream length of order u

A = Area of Basin

7. Bifurcation Ratio (Rb)

$$Rb = Nu/Nu_0 + 1$$

Where Nu = Total number of stream segment of order u (Table 1).

6 Conclusions

Following conclusions based on analysis of morphometry:

1. Most of the streams in the study area are found to be of order 1.
2. The elongation ratio of watershed is below 0.7, thus the basin is elongated.
3. Drainage density of watershed is less than two, so the basin is coarse in nature.

4. Length of overland flow is greater than 0.4, this indicates a gentle slope and a long flow path.
5. The elongated watershed has high relief and young geomorphic stage, thus the watershed is prone to erosion.
6. The erosion causes silting of the dam and affects its storage capacity.
7. The rock type is—Palaeocene, Deccan trap type and hence it has low permeability.
8. The stream order is inversely proportional to the number of obtained streams.

References

1. Bisht BS, Kothiyari BP (2001) Land-cover change analysis of garur ganga watershed using GIS/remote sensing technique. *J Indian Soc Remote Sens* 29(3):2001
2. Ramakrishnan D, Durga Rao KHV, Tiwari KC (2001) Delineation of potential sites for water harvesting structures through remote sensing and GIS techniques: a case study of Kali watershed, Gujarat, India. *Geocarto Int* 23(2):95–108
3. Singh JP, Singh D, Litoria PK (2008) Selection of suitable sites for water harvesting structures in soankhad watershed, Punjab using remote sensing and geographical information system (RS&GIS) approach—a case study. *Springer, J Indian Soc Remote Sens* (March 2009) 37:21–35
4. Al Marsumi KJ, Al Shamma AM (2017) Selection of suitable sites for water harvesting structures in a flood prone area using remote sensing and GIS—case study. *J Environ Earth Sci* 7(4). www.iiste.org ISSN 2224–3216(Paper) ISSN 2225–0948 (Online)
5. Khan MA, Gupta VP, Moharana PC (2001) Watershed prioritization using remote sensing and geographical information system: a case study from Guhiya, India. *J Arid Environ* 49:465–475. <https://doi.org/10.1006/jare.2001.0797>, available online at <http://www.idealibrary.com>
6. Quinn NWT, Kumar S, Imen S (2019) Overview of remote sensing and GIS uses in watershed and TMDL analyses. *J Hydrol Eng* 24(4)

Mapping Ground Water Potential Zone of Fractured Layers by Integrating Electric Resistivity Method and GIS Techniques



R. Chandramohan and B. Kesava Rao

Abstract This research summarizes the results of integrating GIS with electric resistivity methods to draw awareness to the significance, understanding and improving groundwater governance and management. Schlumberger Vertical Electrical Sounding (VES), the electric resistivity method was selected to examine earth's sub-layers in the selected zone. Later, the collected resistivity data was explicated by IPI2WIN software to establish Earth's subsurface zones of different regions such as top soil, weathered rocks, first and second fractured layers. The results obtained from geophysical method were exported to GIS software for identifying the most favourable and favourable groundwater-potential areas. In Palani taluk, most of the groundwater potential zones falls under hornblende-biotite gneiss. In Palani taluk 25.51 Km² area was covered with the most favourable groundwater zones and 31.32 km² was covered with favourable groundwater potential zone. The result showed that the integration of GIS and the method of electrical resistivity can be effectively used for categorizing potential groundwater areas. By using proper water recharge arrangements, the areas of the most favourable and favourable zone can be made more capable of accumulating more groundwater. This research can be useful to identify either to build or avoid constructing recharge structure in selected area. These results are useful to develop, monitor and manage groundwater resources in different hydro-geological environments.

Keywords GIS · VES survey · Hydrology · Fractured zone · Groundwater potential areas

R. Chandramohan · B. Kesava Rao (✉)
Department of Civil Engineering, RVR & JC College of Engineering (A), Chowdavaram, Guntur
522019, India
e-mail: kesava.battena@gmail.com

© The Author(s), under exclusive license to Springer Nature Singapore Pte Ltd. 2023
M. S. Ranadive et al. (eds.), *Recent Trends in Construction Technology and Management*, Lecture Notes in Civil Engineering 260,
https://doi.org/10.1007/978-981-19-2145-2_47

613

1 Introduction

Water is one of the earth's natural resources required for the survival of man, animals and plants. Water is distributed unevenly on the earth's surface and the earth's subsurface. Among the few foremost resources for drinking water, groundwater plays a vital role. Without groundwater, humanity cannot survive in this world. It is a foremost resource for three significant requirements of day-to-day life such as the cultivation of crops, manufacturing industries and human consumption. Insufficient groundwater may result in setbacks to the nation in the key profitable activities. Along with identification suitable groundwater potential areas, nowadays it has become essential to conserve and monitor this important resource. Overlay GIS analysis is used to locate potential groundwater area [1–3]. When compared to all geophysical method, the Schlumberger VES resistivity ground survey is an economical, less time-consuming and suitable technique for arid and semi-arid areas. Understanding the earth's various subsurface layers, especially in a fractured zone in semi-arid and arid areas, is still a very difficult task. The above-mentioned techniques are attempted by many authors [4–6]. Most of the hydrologists and geologists [7, 8] used GIS tool to identify, monitor and conserve the groundwater. The present effort involved a comprehensive electric resistivity study of the study region. Later the geophysical results were taken into GIS. In GIS, multiple thematic maps were produced such as the first fractured thickness, first fracture resistivity, second fracture thickness, second fractured resistivity and geological map. All thematic maps were overlaid to identify the apt groundwater-potential region. Overlaying all thematic maps, the most favourable, favourable and unfavourable groundwater potential zones are identified. By integrating GIS and resistivity techniques any location within the study area can be easily recognized whether it is having good or poor groundwater potential zone as well as it is possible to construct an appropriate artificial recharge structure in the study area.

2 Methodology

The review area lies between $10^{\circ}20'2''$ N and $10^{\circ}38'24''$ N and longitudes and $77^{\circ}18'6''$ E to $77^{\circ}35'41''$ E. Study area covers 766.83 km^2 , of which 116.85 km^2 are occupied by hilly landforms. The study region falls in Tamil Nadu state, Dindigul District. Recharge of groundwater here depends on monsoon rainfall. The average rainfall of a Palani Taluk is 690 mm (1980–2013) [9, 10]. The review area is mostly covered by Archean crystalline rocks and surrounded by hillocks. Groundwater is found mostly in the fractured zones easy.

Palani taluk base map was collected from the Statistical Department of Dindigul district, and the map was geo-referenced with SOI (Survey of India) toposheet number 58f of 1:50,000 scale. Geo-referencing was performed in GIS software. The geological map was obtained from Bhuvan website, traced and digitized and then imported to

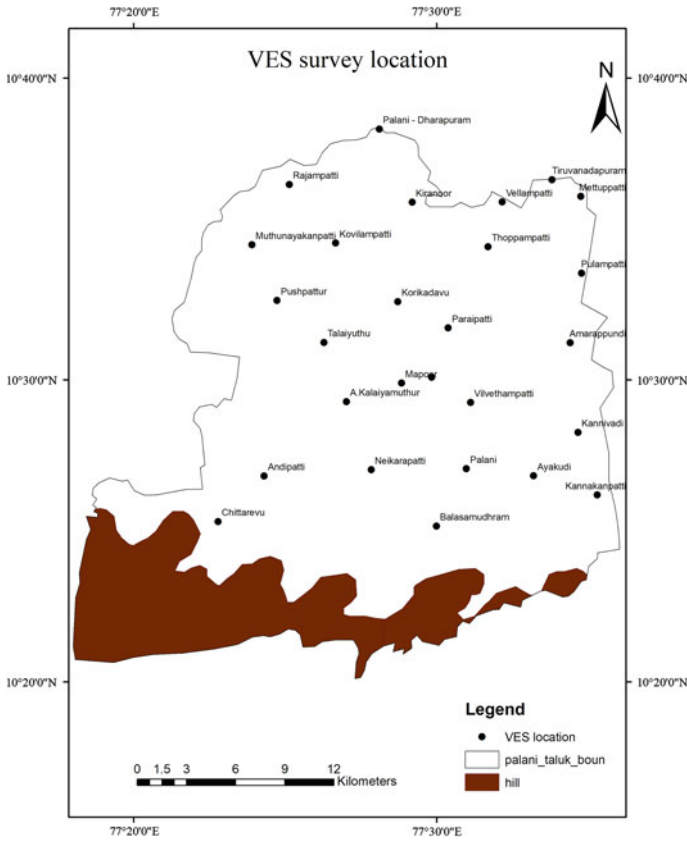


Fig. 1 VES survey location

a GIS platform. Schlumberger VES (Vertical Electrical Sounding) ground survey was conducted at 27 locations in Palani Taluk as shown in Fig. 1. The map coordinates of the locations were confirmed with a GPS device. The geophysical Schlumberger VES ground survey was performed at 250 m maximum electrode spacing. The potential electrode and current electrode spacing vary from 0.2 m to 15 m and 0.5 m to 125 m. The collected data was exported to IPI2WIN software to evaluate the different layers of the earth’s subsurface by its resistivity and thickness. The results obtained from IPI2WIN software were imported into attribute table. The ground survey coordinates and attribute data were exported in GIS software. By IDW (Inverse Distance Weight) techniques in GIS software, the spatial interpolation map was drawn for thickness and resistivity values of all earth sub-layers. This technique was used for the fractured layers to prepare the corresponding thickness and resistivity map. Later the above map was overlaid with the geological map. The suitable zones for groundwater were identified by low resistivity and greater thickness. Figure 1 shows the VES Survey

location, and Fig. 2 shows the methodology of integrating the most favourable and favourable-groundwater-potential zones identified by electric resistivity method.

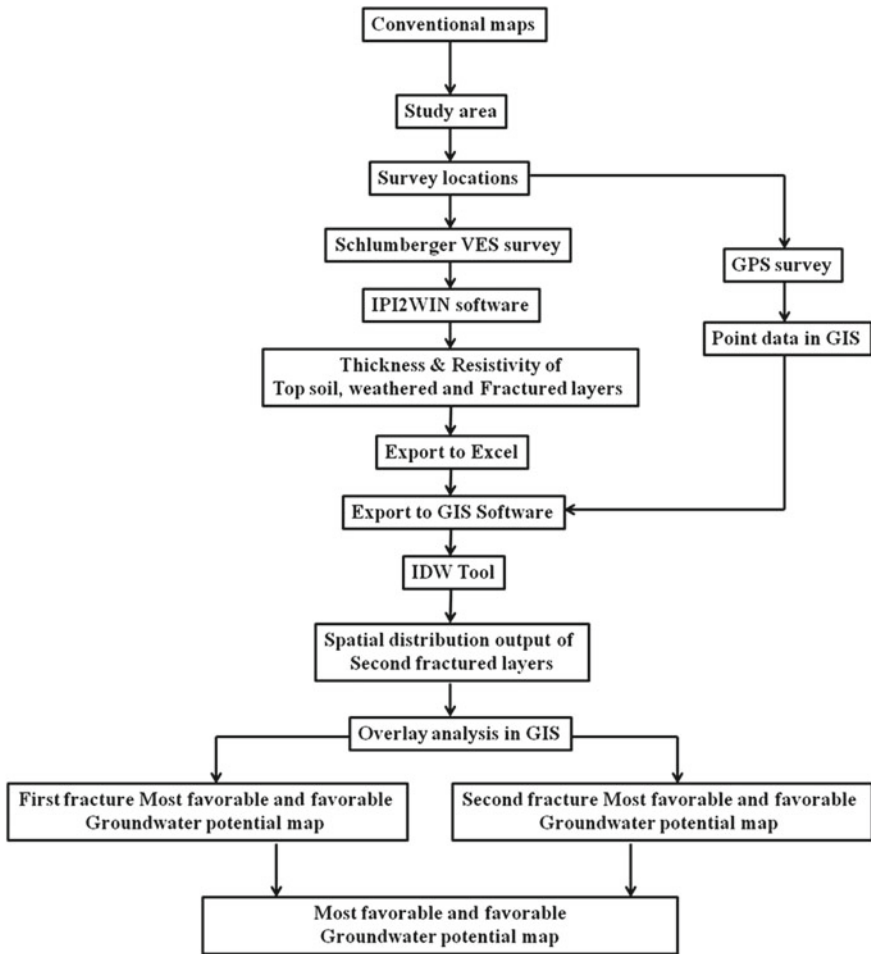


Fig. 2 Methodology to identify the favourable and most favourable groundwater potential zone by electric resistivity

3 Results and Discussions

3.1 Groundwater-Potential Zone Using Geophysical Survey

The field survey results of VES Schlumberger are shown in Fig. 3 (thickness) and Fig. 4 (resistivity) furnish the topsoil; weathered, fractured zones (first and second). The obtained geophysical results are added to the GIS environment as a point feature for further analysis. The maximum resistivity value in Paraipatti, Mappoor, etc.

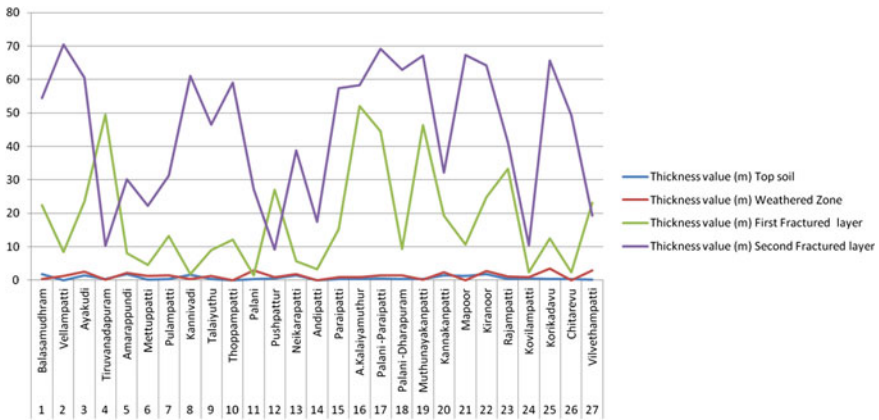


Fig. 3 Thickness values for various VES survey location

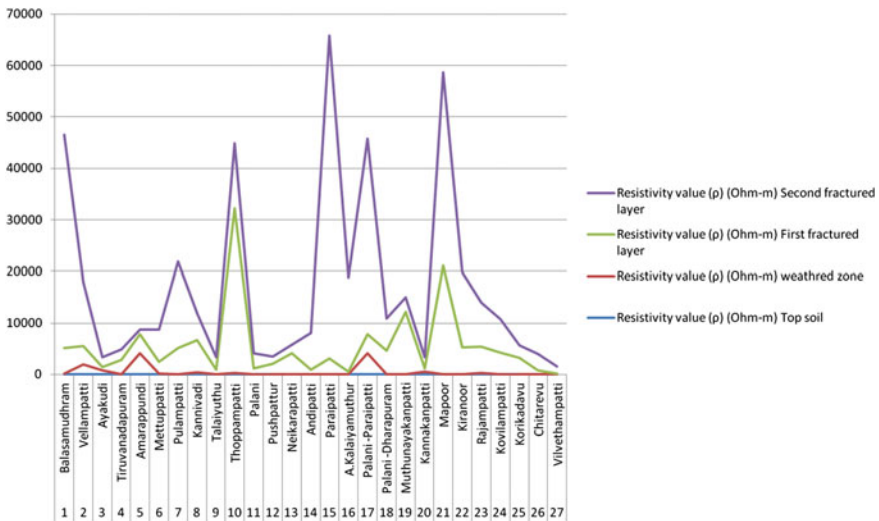


Fig. 4 Resistivity values for various VES survey location

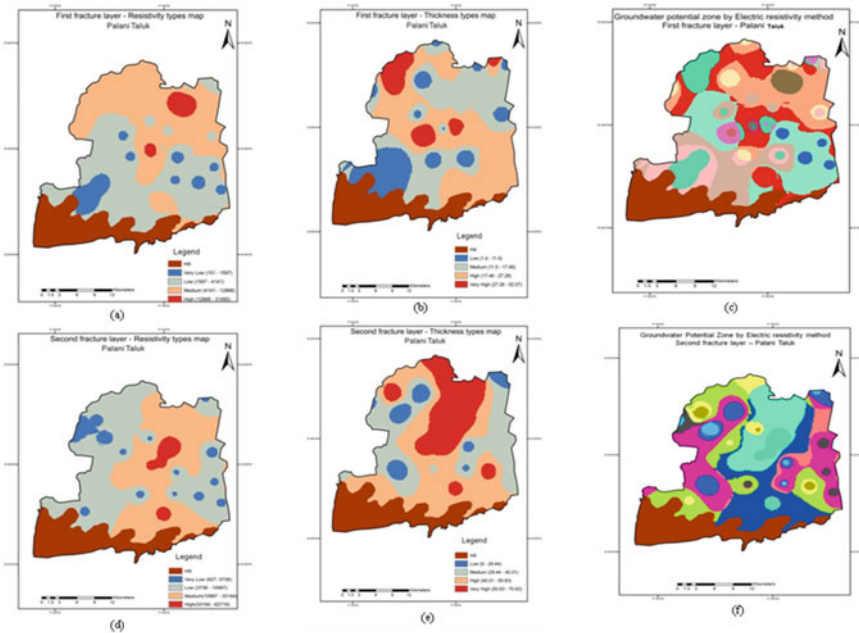
confirms compact rock formation. It was also evident in the survey that the borehole drilled closer to this area doesn't have a good quantity of groundwater. Low resistivity values in Amarapundi, Neikarapatti, etc. show the availability of good quantity of groundwater. The areas falling in high thickness with low resistivity value will yield a good quantity of groundwater. In the study area, high thickness, i.e. 52.14 m with low resistivity 507 Ω m value falls in the first fracture zone in a village named A. Kalaiyamuthur. By conducting the field check in A. Kalaiyamuthur, the area has good groundwater quantity. Therefore, the high thickness zone indicates a good sum of groundwater storage.

3.2 GIS Analysis

All VES surveyed locations' point coordinate values were captured by the GPS device. Later, the coordinate points are added as a layer into GIS software as point data and the resulting VES survey values were imported and related to the appropriate locations to generate various thematic maps. The fracture zone of the first layer resistivity, shown in Fig. 5a, was superimposed over the fracture zone of the first layer thickness, as shown in Fig. 5b. The first fractured groundwater potential zone map was derived and shown in Fig. 5c. Figure 5c gives the 15 combinations value; it was shown in Fig. 5g. Among these combinations, the values are indicated by abbreviations as follows: LT means Low Thickness, MT means Medium Thickness, HT means High Thickness, VHT means Very High Thickness, LR means Low Resistivity, MR means Medium Resistivity, HR means High Resistivity and VLR means Very Low resistivity.

Among these, HT & LR combination value covers a huge area of 97 km². Due to its shallow depth, this area is suitable for dug well construction. Similarly, The fracture zone of the second layer resistivity Fig. 5d was superimposed over the fracture zone of the second layer thickness map, shown in Fig. 5e. The Second fracture zone resistivity and thickness were derived and shown in Fig. 5f. Results show 13 number of the combination, represented in Fig. 5h. Among these MT & LR combination value covers a large area of 97.16 km². This combination shows water to be at greater depth and boring tube wells needs to be considered.

The groundwater potential zone of first fractured (Fig. 5c) was superimposed with groundwater potential zone of second fractured (Fig. 5f), which was overlaid with geological map and the resultant map was shown in Fig. 6 and it represented 107 combinations value. Of these, a few combinations value are shown in Fig. 7. The first and second fracture most favourable and favourable-groundwater-potential zone were identified; it was shown in the corresponding Figs. 8 and 9. Table 1 provides the combination of values of favourable and most favourable groundwater-potential zones by electric resistivity method for Palani Taluk. The results show that the combinations of most favourable and favourable locations in groundwater potential zone



Legend

- Palani taluk boundary
 - Hill
 - Low thickness, Medium resistivity
 - Medium thickness, Medium resistivity
 - High thickness, Medium resistivity
 - Very high thickness, Medium resistivity
 - Very high thickness, Low resistivity
 - High thickness, Low resistivity
 - Medium Thickness, Low resistivity
 - Low thickness, Low resistivity
 - Medium Thickness, High resistivity
 - Medium Thickness, Very Low resistivity
 - Low thickness, Very low resistivity
 - High thickness, High resistivity
 - Low thickness, High resistivity
 - Very high thickness, Very low resistivity
 - High thickness, Very low resistivity
- (g)

Legend

- Palani taluk boundary
 - Hill
 - Very high thickness, Low resistivity
 - High thickness, Low resistivity
 - Very high thickness, Medium resistivity
 - Low thickness, Very low resistivity
 - Low Thickness, Low resistivity
 - Medium Thickness, Low resistivity
 - High thickness medium resistivity
 - Very high thickness, Very low resistivity
 - High thickness, Very low resistivity
 - Medium Thickness, Medium Resistivity
 - Medium thickness, Very low resistivity
 - Very high thickness, High resistivity
 - High thickness, High resistivity
- (h)

Fig. 5 First and second fracture layer thickness, resistivity, groundwater potential zone and its legends

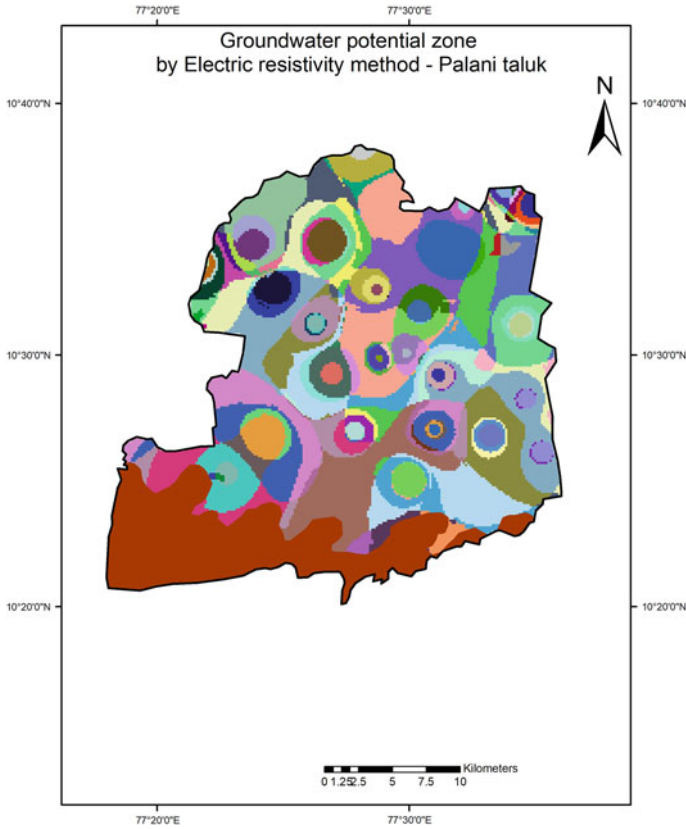


Fig. 6 Integrated groundwater potential map of first and second fractured layer

fall on geology type of hornblende-biotite gneiss, because most of the study area comes under this type. High Thickness and Low Resistivity, Medium Thickness and Low Resistivity and hornblende-biotite gneiss cover 27.02 km²; these are high groundwater potential zones. This was also verified in the field. The most favourable-groundwater-potential zone covers 25.51 km² and favourable groundwater potential zone covers 31.32 km². Figure 10 shows the integration of the most favourable and favourable groundwater potential zones of the first and second fractured layers of study area. By integrating GIS and electric resistivity method government, farmers, etc. can easily identify the location where the groundwater potential is more and where the groundwater potential is very poor. After identifying the most favourable and favourable groundwater potential zone government appropriate artificial recharge structure can be constructed in the selected locations to increase groundwater level.

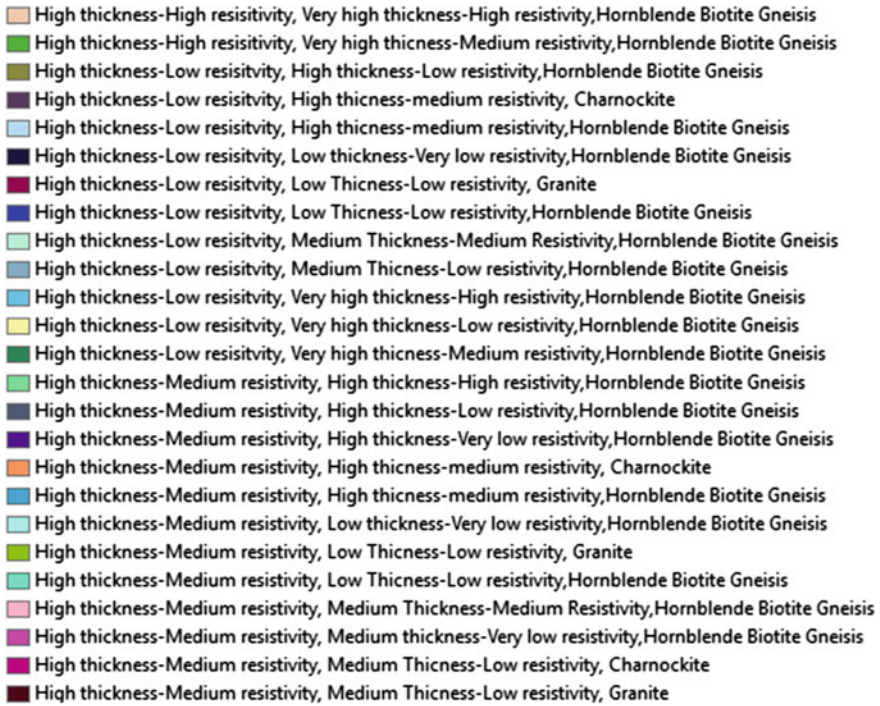


Fig. 7 Few combination values of potential groundwater zone by electric resistivity method

In recent years, most of the researchers performed VES survey to identify ground-water potential zone; this may help to identify potential groundwater region of a specific sample point location, etc. But very few researchers such as [11, 12] imported the result of geophysical method into GIS environment and applied interpolation techniques. In GIS IDW (Inverse Distance Weighted) interpolation techniques are used to estimate pixel values by averaging the values of VES survey sample points. These techniques may be useful especially in arid and semi-arid areas to identify suitable groundwater potential zone.

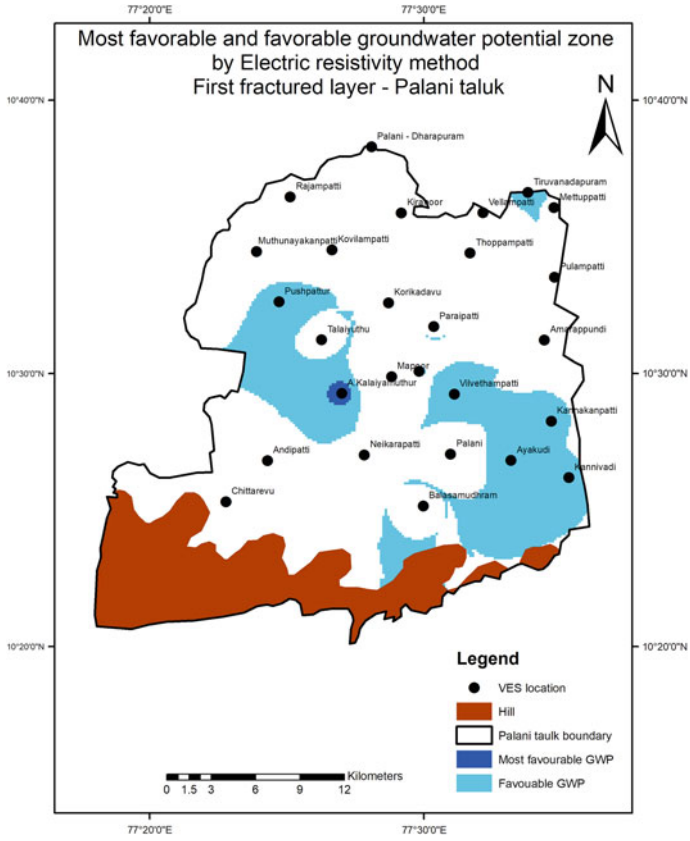


Fig. 8 First fractured layers most favourable and favourable groundwater potential

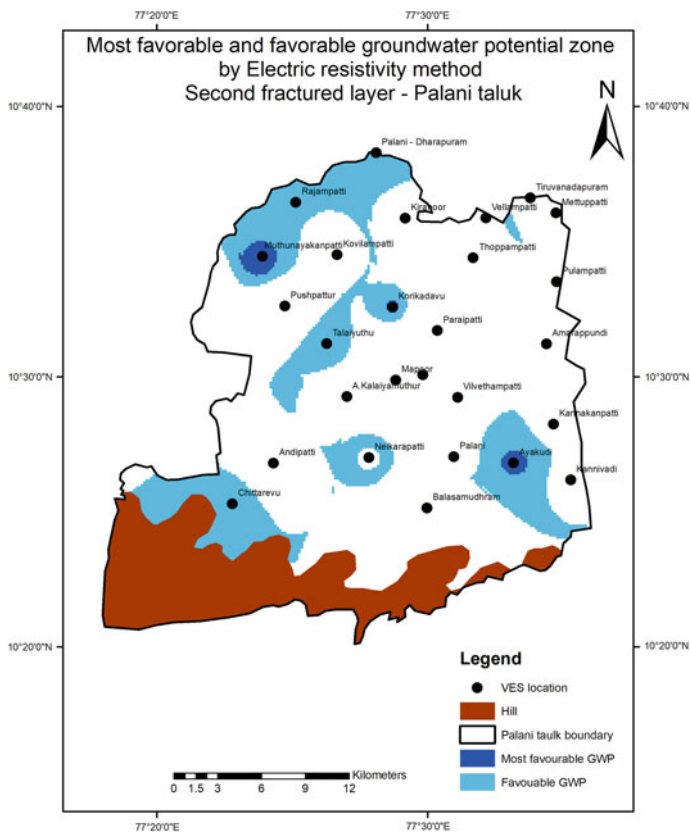


Fig. 9 Second fractured layers most favourable and favourable groundwater potential

Table 1 Combination values of favourable and most favourable-groundwater-potential zone by electric resistivity method

S. No.	Combination values of groundwater potential zone by electric resistivity	Electric resistivity GWP type	
		Most favourable GWP	Favourable GWP
1	HT-LR, HT-LR, Hornblende—biotite gneiss	MF-GWP	
2	HT-LR, MT-LR, Hornblende—biotite gneiss		F-GWP
3	HT-LR, VHT-LR, Hornblende—biotite gneiss	MF-GWP	
4	HT-VLR, MT-VLR, Hornblende—biotite gneiss		F-GWP
5	HT-VLR, MT-LR, Hornblende—biotite gneiss		F-GWP
6	HT-VLR, VHT-LR, Hornblende—biotite gneiss	MF-GWP	
7	HT-VLR, VHT-VLR, Hornblende—biotite gneiss	MF-GWP	
8	MT-LR, HT-LR, Hornblende—biotite gneiss		F-GWP
9	MT-LR, MT-LR, Hornblende—biotite gneiss		F-GWP
10	MT-LR, VHT-LR, Hornblende—biotite gneiss		F-GWP
11	MT-LR, VHT-LR, Hornblende—biotite gneiss		F-GWP

a. GWP—Groundwater potential zone

b. MF-GWP—Most favourable-groundwater-potential zone

c. F-GWP—Favourable-groundwater-potential zone

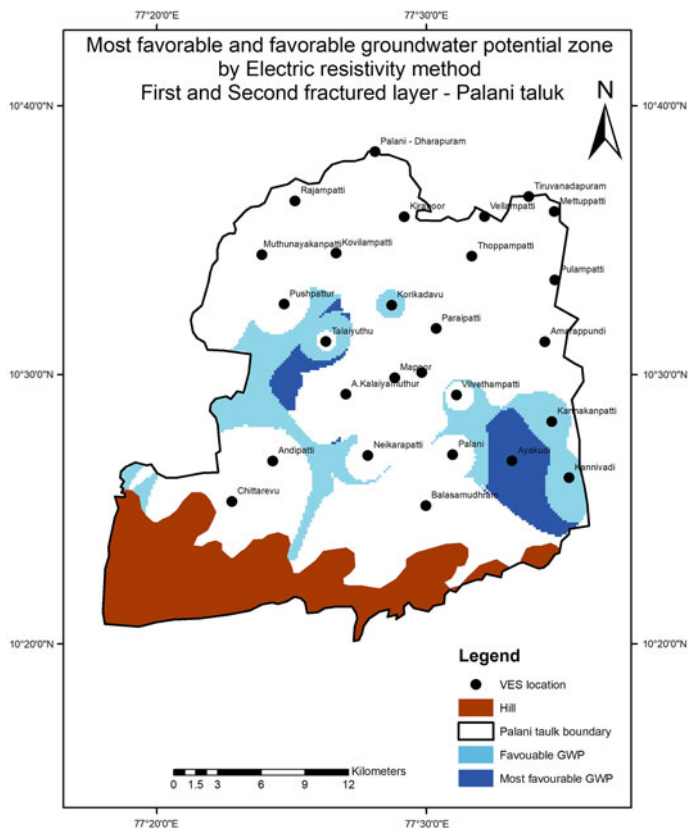


Fig. 10 Integrated most favourable and favourable-groundwater-potential zone of first and second fracture layer

4 Conclusions

In the study area, the favourable and most favourable area is suitable for constructing dug and bore wells. By integrating electric resistivity and GIS techniques, we can easily locate, monitor and preserve the good groundwater potential zones. By integrating GIS and resistivity technique any location within the study area can be easily recognized whether it is having good or poor groundwater potential zone as well as it is possible to construct appropriate artificial recharge structure in the study area. With appropriate water recharge arrangements, the areas of high thickness and very low resistivity can be made more capable of accumulating more groundwater. This research can be useful for government to identify either to build or avoid constructing recharge structure in the selected area. The government can also focus poor groundwater potential zone and they can avoid constructing recharge structures in particular in that region. The government can also address this issue to farmers and need to carry out alternative arrangements to the farmers or they can suggest crops, vegetables, etc. to the farmers which utilized less quantity of water to grow. By building various rainwater harvesting techniques, demand for groundwater can reduce especially in poor groundwater potential zone.

References

1. Rokade VM, Kundal P, Joshi AK (2007) Groundwater potential modelling through remote sensing and GIS: a case study from Rajura Taluka, Chandrapur District, Maharashtra. *J Geol Soc India* 69:943–948
2. Adeyeye OA, Ikpokonte EA, Arabi SA (2019) GIS-based groundwater potential mapping within Dengi area, North Central Nigeria. *Egyptian J Remote Sens Space Sci* 22(2):175–181
3. Allafta H, Opp C, Partra S (2020) Identification of groundwater potential zones using remote Sensing and GIS techniques: a case study of the Shatt Al-Arab-Basin. *Remote Sens* 13
4. Gurugnanam B, Prabhakaran N, Suvetha M, Vasudevan S, Gobu B (2008) Geographic information technologies for hydrogeomorphological mapping in parts of VellarBasin, Central Tamilnadu, South India. *J Geol Soc India* 72:471–478
5. Ravindran A, Ramanujam A, Somasundaram P (2012) Wenner array resistivity and sp logging for groundwater exploration in Sawerpuram Teri deposits, Thoothukudi District, Tamil Nadu, India. *ARPN J Earth Sci* 1(1):1–5
6. Gopalan CV (2011) A comparative study of the groundwater potential in hard rock areas of Rajapuram and Balal, Kasaragod, Kerala. *J Indian. Geophys Union* 15(3):179–186
7. Venkateswaran S, Prabhu MV, Karuppannan S (2014) Delineation of groundwater potential zones using geophysical and GIS techniques in the Sarabanga Sub Basin, Cauvery River, Tamil Nadu, India. *Int J Curr Res Academ Rev* 2:58–75
8. Omolaiye GE, Oladapo IM, Ayolabi AE (2020) Integration of remote sensing, GIS and 2D resistivity methods in groundwater development. *Appl Water Sci* 10(129)
9. Chandramohan R, Kanchanabhan TE, Siva VN, Krishnamoorthy R (2017) Groundwater fluctuation in Palani Taluk, Dindigul District, Tamilnadu, India. *Int J Civil Eng Technol* 8(7):1041–1049

10. Chandramohan R, Kanchanabhan TE, Siva VN (2018) Identification of artificial recharges structures using remote sensing and gis for arid and semi-arid areas. *Nat Environ Pollut Technol* 18(1):183–189
11. Mohamaden MII, El-Sayed HM, Hamouda AZ (2016) Combined application of electrical resistivity and GIS for subsurface mapping and groundwater exploration at El-Themed, Southeast Sinai, Egypt. *Egyptian J Aquatic Res* 42(4):417–426
12. Byamungu M, Ngenzebuhoro C, Kiro K, Shungu L (2018) The application of vertical electrical sounding (ves) for the hydrogeological and geophysical investigations in kibumba area. *Int J Innov Appl Stud* 24(1):9–16

Sustainable Development in Circular Economy: A Review



Mohnish Waikar and Parag Sadgir

Abstract Circular Economy (CE) is the new sustainable policy by which we can reduce waste generation by reusing and recycling the products to form a loop. The new resources are utilized less in this policy and the waste generation is minimized. This reuse and recycling will influence the business models to emerge and contribute to the country and nature. Based on the existing investigations, the current work builds up an orderly financial model in agreement with the attributes, destinations and standards of CE. Also, government mediation is basic to building a waste administration division in its beginning phase. This paper suggests the model for CE research in Pune Metropolitan Regional Development Authority (PMRDA) region for the holistic development of the industry and the betterment of society.

Keywords Circular economy · Water · Wastewater

1 Introduction

Circular economy (CE) is the sustainable use of resources while making less waste. It's all about making growth sustainable. It involves making the most use of our natural resources and constructing our goods so that processed raw materials are reused as much as possible. They ought not to wind up in a dump, however, in another item.,we create a closed loop by reusing and recycling the resources. By doing this, we can save a lot on the use of primary resources and stop generating waste, pollution and carbon emissions. The transition to CE involves action to be taken at all stages of the life cycle, beginning with product design, through raw material procurement, refining, manufacturing, use, collection of waste and ending with its management. If waste is already produced in the CE approach, it should be treated as secondary raw materials and used for re-production. This is to be achieved through mechanisms implemented at earlier stages of the life cycle. The CE approach is inextricably linked to the growth of innovation, the emergence of new business models and the growing

M. Waikar (✉) · P. Sadgir

Department of Civil Engineering, College of Engineering Pune, Pune 411005, India
e-mail: waikarmm20.civil@coep.ac.com

© The Author(s), under exclusive license to Springer Nature Singapore Pte Ltd. 2023
M. S. Ranadive et al. (eds.), *Recent Trends in Construction Technology and Management*, Lecture Notes in Civil Engineering 260,
https://doi.org/10.1007/978-981-19-2145-2_48

629

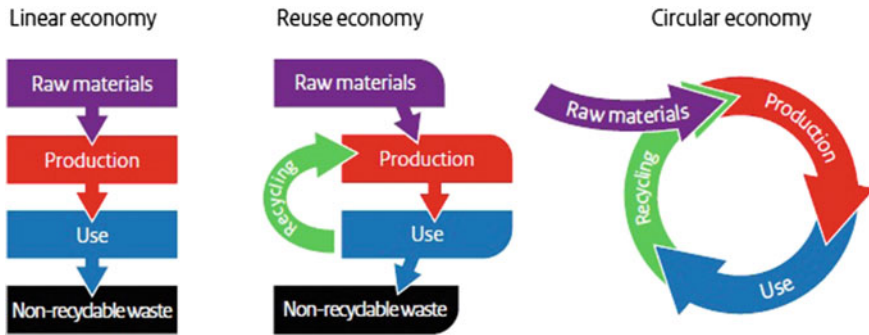


Fig. 1 Difference between linear economy and circular economy

environmental consciousness of society. Thus, CE differs from the linear economy model, based on the “take-produce-use-throw away” concept. As the government of Netherlands has mentioned in their circular “A Circular Economy in the Netherlands by 2050” the biggest challenge of the twenty-first century is the raw materials, as the population is increasing day by day the extraction is increasing so, aside from the increased environmental impact it will likewise include expanding harm to and fatigue of common capital a deficiency of biodiversity, a danger of depleting the inventory of raw materials, and climate change. The ministry of environment and food of Denmark has also launched a strategy for CE as “Danish Strategy for Circular Economy” in which they have stated that “It is the objective of the government to promote circular economy, including better use and recycling of resources and the prevention of waste.” Geissdoerfer et al. states that there are various objectives related to the CE and supportability in the writing. While it appears clear to most authors that the CE is focusing on a closed loop, taking out all asset information sources and waste and outflow spillages of the framework, the objectives of manageability are open-ended what’s more, various authors address a significant huge number of objectives, which additionally move contingent upon the thought about specialists and their interests (Fig. 1).

2 Studying Different Models Used for CE

2.1 France

The government of France has announced a law, i.e. “anti-waste law for a circular economy” which proposes a more calm day by day life wherein producers are more responsible, local specialists are soothed and buyers are better educated to turn out to be more engaged with the change during their buys. There is a period when manufacturing for the purpose of destroying is no longer appropriate.

The law provides for a ban on all single-use plastics by 2040. They have implemented five-year plans for a progressive and reasoned method for phasing out which is, plastic reduction, reuse and recycling targets. Their goal is to reduce disposable tableware in the fast-food sector, by using reusable tableware, they can save up to 180,000 tonnes of packing products. The government issued a ban on polystyrene boxes, plastic confetti, etc. while promoting the use of biodegradable plastics.

Disposal, in other words, the landfilling and incineration, of unsold non-food products will be prohibited. From now on, companies will have to donate or recycle their unsold products. These include items such as daily hygiene products, clothing, electronics, shoes, books and household appliances, among others. This is according to the publication “A French act of law against waste and for a circular economy” published by The Ministry of the Ecological Transition in February 2020.

2.2 *Netherlands*

The government aims to be fully practicing CE by the end of 2050 as per their strategy “A Circular Economy in the Netherlands by 2050” published by The Ministry of Infrastructure and the Environment and the Ministry of Economic Affairs, also on behalf of the Ministry of Foreign Affairs and the Ministry of the Interior and Kingdom Relations in September 2016. In practical terms, this ensures that by 2050, raw materials can be easily used and reused, with no harmful emissions into the atmosphere. If new raw materials are needed, they will be obtained in a sustainable manner, preventing further harm to the social and physical living environments as well as public health.

They deduced that, if the CE is involved, then the extra turnover of 7.3 billion can be generated, and the use of raw materials can be reduced by 100,000 kilo tonnes, i.e. one-fourth of their total annual import for raw materials. The use of bioplastics should be increased to reduce the non-degradable plastic. With the help of students from Amsterdam and some entrepreneurs, they have started manufacturing skateboards from disposed plastic bottles and caps and are making carpets out of discarded fishing nets.

2.3 *Denmark*

Ministry of Environment and Food and Ministry of Industry, Business and Financial Affairs of Denmark, in 2018, published with state of green the publication “Strategy for Circular Economy”. They have taken the following steps to achieve CE.

Empower organizations to go about as impetuses for the CE. Organizations can improve their primary concern by planning items and parts with long valuable life and the capacity to be effectively fixed, reused, and reused. This is to give SMEs induction to accurately that data and those resources that can help them convert their

endeavour to the use of a more circular plan of action. Creating a typical mark of correspondence with government offices for firms that utilize circular plans of action. For organizations with roundabout plans of action, the public authority will make a solitary resource with specialists so that they can find a quicker solution on whether another innovation, plan of action, or creation strategy can be utilized under current guidelines. Increasing the inventory of financing for roundabout plans of action, The Danish Green Pension Fund will actually want to have responsibilities because of the public authority's endeavours. Thus, the asset will want to subsidize a more extensive assortment of activities. This will give new green endeavours, including circular organizations, extra decisions for finding the imperative financing for the creation, headway and creating of their game plan. The public authority is attempting to guarantee that products are planned so that they add to a circular economy indeed while guaranteeing an elevated requirement of ecological and general wellbeing security while growing Danish presence in European circular standards work. Circular procurement is promoted. Denmark's government will ensure that the country is a leader in renewable and circular public procurement. This can be achieved, among other items, by widening and improving the Relationship between Green Public Procurement and the Forum on Fair Procurement, all of which have recently been granted a joint Secretariat for Procurement to ensure co-thinking and cooperation. The government needs to see a more uniform waste collection in order to ensure improved environmental waste management while also releasing industry economic benefits from a more effective waste collection into a wider and more efficiently operating sector. For creating a fair playing field for waste and recycled raw materials on the market, the government needs to ensure that companies operate on an equal basis regardless of where they are based. Simultaneously, the government would foster a better-functioning market for waste and recycled raw materials without jeopardizing efficiency, public health, or the environment.

2.4 *Spain*

In order to address this situation, the Spanish Strategy for the Circular Economy, called *Espada Circular 2030*, has been launched in June 2020. *Espada Circular 2030* establishes the bases to advance another creation and utilization model in which the estimation of items, materials and assets are kept up inside the economy for as far as might be feasible, with negligible waste and reusing however much as could be expected the waste that can't be stayed away from.

The overall standards which are the foundation of this Strategy, motivated by the European and Spanish legitimate systems, are accompanying:

- (i) Waste progressive system: Successful implementation of the waste order law, progressing waste anticipation, reusing and demonizing waste that cannot be reused for power production or other purposes.

- (ii) **Production quality:** Adopting suggestions to improve worldwide proficiency and imagination of effective cycles; this should be possible by the utilization of computerized administrations and foundations, just as the presentation of natural administration plans, with the general objective of encouraging business intensity and long-haul development.
- (iii) **Sustainable usage:** Promoting inventive models for cognizant and practical utilization, including things and organizations, similar to the use of modernized establishments and organizations.
- (iv) **Collaboration and mindfulness:** Promoting the value of moving towards a circular economy, as well as encouraging and motivating effective networks for cooperation among organizations and data sharing between public bodies, financial and social partners, as well as creative and conventional academics, to build mutual energies that can fuel this transition.

Before 2030, they intend to keep greenhouse gas emissions under 10 million tonnes CO₂eq.

2.5 Finland

The government has a goal of implementing the CE by 2025 as mentioned in their Sitra journal, “Sitra studies 121” published in 2016. The following steps need to be taken:

- (i) Rather than maximizing the amount of timber, the national forest policy should concentrate on the total benefit of Finnish forest-based goods and services.
- (ii) Encourage the utilization of wood-based and different items produced using renewables in open acquisitions.
- (iii) Create a business opportunity for natural reused supplements
- (iv) Minimize food waste by removing obstacles and providing rewards.
- (v) Promote the use of biogas systems and other green energy technologies in agriculture to minimize the use of fossil fuels.
- (vi) Develop motivating forces and strategy instruments to hasten the transition to a more service-based transportation structure.
- (vii) Create tax and other measures to encourage the phase-out of fossil fuels in private vehicles by 2040 and the use of renewable biofuels.

2.6 Germany

The publication of the government of Germany “Federal Ministry for the Environment, Nature Conservation, Building and Nuclear Safety” has been studied for the CE work. They have been in this system for a long time from about 2012 and their

goal of taking resources efficiently has been on the radar. They implemented the law for procuring raw materials sustainably in 2016 and looking for the supply, fortifying natural, social and straightforward principles globally and making supply chains more supportable. The government has not drafted a combined report or policy for the whole country, whereas divided it into the city level so that optimization and increase in efficiency are possible for the cities and towns.

Different laws and goals are provided for the respective city.

2.7 Greece

The Ministry of environment and energy of Greece has published “National strategy for Circular Economy” in December 2018 which is referred for the CE work in Greece. Due to the variety of possibilities and potential for using the country’s capital, the expertise and specialization of young Greek professionals, and the recent developments in our country’s economy and development, in general, as well as the waste management industry, in particular, the circular economy concept can be easily adapted to the Greek economy. The emergency our nation has been encountering as of late, joblessness—and youth joblessness specifically—and underdevelopment set out more open doors for Circular Economy. The lack of funds to procure raw materials, the versatility of SMEs and social businesses, the need to provide jobs for young professionals, as well as environmental legislation’s commitments, all lead to recycling and reuse programmes. It has the ability to generate new jobs, help small and medium-sized enterprises, grow new trades and improve the social economy.

Implementation actions taken by them:

- (i) Completion of the waste management regulatory process.
- (ii) Convincing execution of prioritization of waste organization, propelling the contravention of making waste and engaging in reuse and reusing are significant.
- (iii) Processing proposals for reducing food loss.
- (iv) A strong difference between waste and goods, making for a seamless transition to secondary raw materials.
- (v) Using recycled water and sludge from wastewater treatment plants
- (vi) Developing a methodology for calculating and monitoring food waste.
- (vii) Promoting the utilization of waste as optional fuel in the industry.

2.8 Poland

The Polish government has published “Road Map towards the Transition to Circular Economy” in September 2019. Their aim for transitioning to CE is:

- (i) Development of guidelines for Zero Waste Coal Power (ZWCP) aimed at minimizing the environmental impact associated with coal mining and electricity and heat generation from coal combustion.
- (ii) Feasibility study on creating a dedicated platform for secondary raw materials.
- (iii) Monitoring the effectiveness and efficiency of the current regulations and developing recommendations for adapting and amending national regulations on municipal waste.
- (iv) Preparation of proposals for regulations concerning hazardous waste.
- (v) A feasibility report on the creation and advancement of neighbourhood biorefineries.
- (vi) A public awareness programme targeted at farmers, with the intention of educating them and steering their efforts towards CE.
- (vii) Drawing up standards and guidelines for specific classifications of items produced using biomass.

2.9 Ireland

“A Waste Action Plan for a Circular Economy” prepared by the Department of Communications, Climate Action and Environment in September 2020 has been referred. They have drafted Ireland’s National Waste Policy 2020–2025 in which they have included:

1. For Household and Business
 - (a) Recycling targets should be given to waste collectors so that they will work efficiently
 - (b) Standardized bin colours should be used across the state: green for recycling, black for residual and brown for organic waste.
 - (c) A body to regulate waste control and customer protection.
 - (d) A waste segregation education and awareness drive.
2. Plastic, Packaging and Single-Use Plastic (SUP)
 - (a) A scheme for depositing the plastic and aluminium cans should be developed for the encouragement of people.
 - (b) Single-use items will be banned from July 2021.
 - (c) Significantly reduce sups being available in the market by 2026 so that the waste generation can be reduced.
 - (d) All packaging should be reusable or recyclable by 2030 for the minimization of waste.

3 Methodology

By referring to the mentioned documents, we can carry out the CE planning and implementation work for PMRDA. In terms of the developing community, this is important for moving forward, continuing with the framework and setting targets for waste minimization, product reuse, recycling and compliance with the CE. We should primarily concentrate on issues such as agriculture, manufacturing and the Air Quality Index as tools for assessing whether the process is being applied or not. Waste management, such as electronic waste, biomedical waste, industrial waste, urban waste and so on, is also an important step in ensuring CE compliance.

3.1 Data Collection and Analysis

The data used for the PMRDA work is referred from the annual Environmental Status Report (ESR) 2018–2019. As PMRDA majorly consists of Pune and Pimpri Chinchwad, the ESR from Pune Municipal Corporation (PMC) and Pimpri-Chinchwad Municipal Corporation (PCMC) of 2018–2019 is used for reference.

The waste generated from the city is categorized as given below. By seeing the data, we can definitely say that the waste that is going into the landfill is more, i.e. 1100 MT. So, if we develop a method where the waste generation is minimized and the reuse of products is increased, then the landfill mass will be less. If goods are to be reused, careful segregation is necessary. A policy for the consideration of waste and what constitutes a secondary product should be given. The biodegradable waste should also be used to generate energy using biogas plants, etc. The wet waste can also be used for making compost and used as fertilizers for farming. Sludge from the wastewater treatment can also be used for the same. Treated water can also be used for gardening, washing, in industry for cooling towers and so on.

As we can see, the daily production of waste around 2000–2200 MT is generated, and from that, around 50% goes to landfills. If we reduce the amount of waste generated first-hand at the primary stage, then we can save on the land of the landfill, we can also save the vehicles needed to transport the waste to the site, thus helping nature in multiple ways. The larger part of the daily waste generated is that of the household waste in comparison to others (Figs. 2 and 3).

The utilization of inexhaustible resources like sun-based energy, wind energy ought to likewise be focus on as the essential resources for other energy creation for example petroleum derivatives, etc. will be minimized and there will be reduction of the extraction of resources from nature. Using rainwater harvesting, the extraction of water can be minimized and load on the water distribution system can be shared. The data shows that the usage of rainwater harvesting, vermicomposting and solar heaters have increased in the present year as people are becoming more aware of

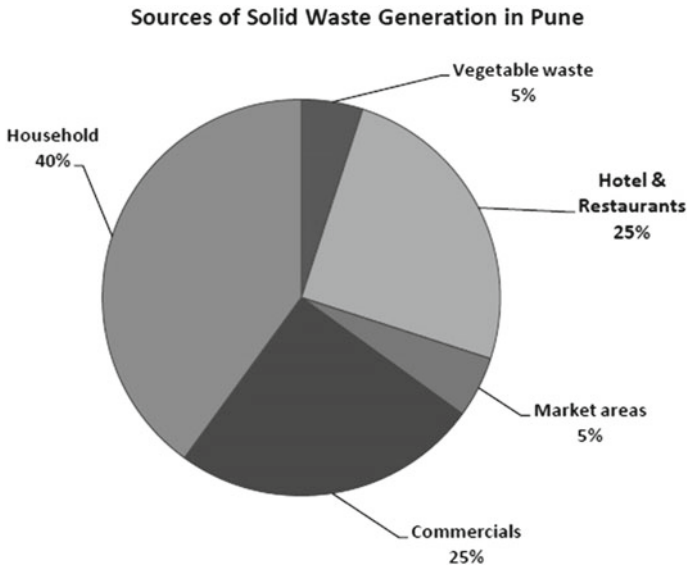


Fig. 2 Generation of solid waste in Pune (Source ESR 2018–2019)

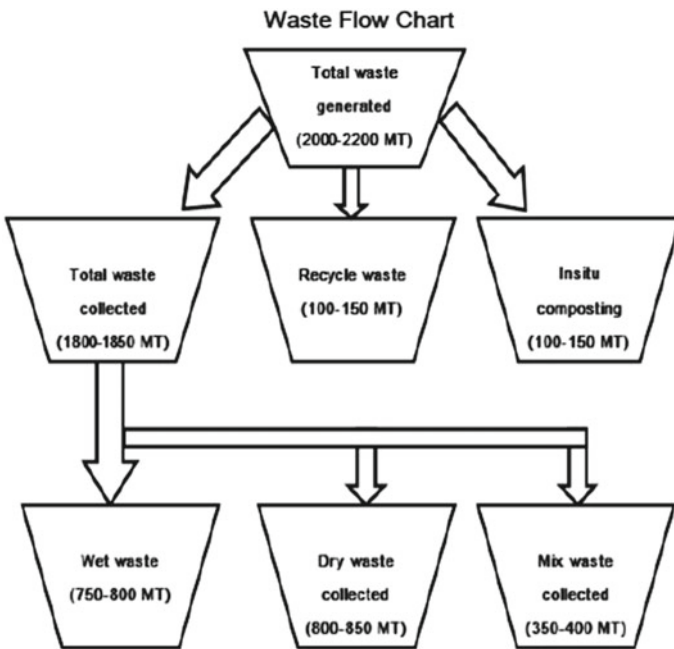


Fig. 3 Collected waste categorized (Source ESR 2018–2019)

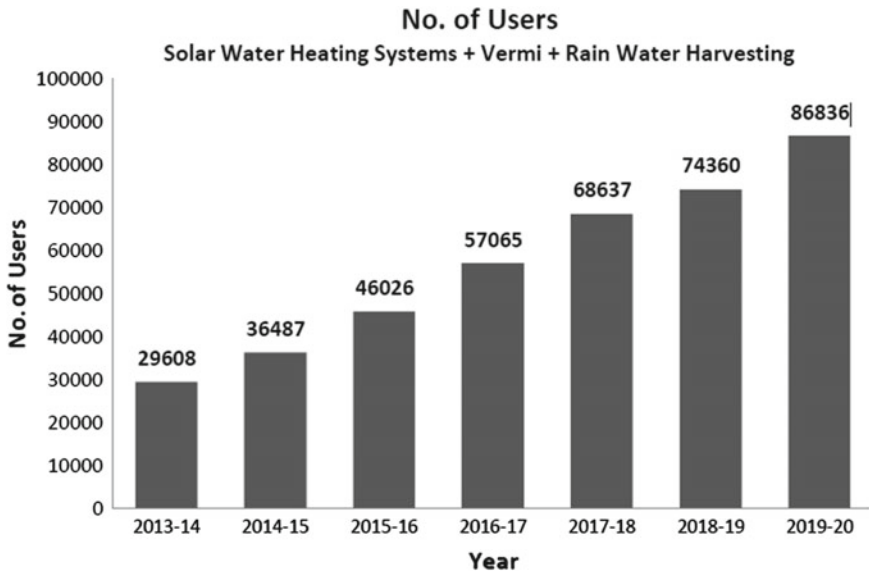


Fig. 4 Number of users using solar water heating systems, vermicomposting and rainwater harvesting (*Source* ESR 2018–2019)

the nature and are trying to protect it by using renewable resources as their sources (Fig. 4).

3.2 Suggestion

As we can compare different models from the European countries, we can also achieve CE if we start implementing the norms and start focusing on how to manage our city properly. Management of water resources (water and wastewater), municipal solid waste, industrial waste, electronic waste should be done considering the effect of products on the environment, and recycling and reuse of materials should be increased, such as water, solid waste, metals, etc. to reduce the raw material load and depletion of resources from natural habitat. If succeeded, the CE will give a boost to the economy while taking care of nature.

4 Conclusion

This paper has talked about the Circular Economy idea which is presently pervasive in the arrangement and business advancement banter on the economic advancement

of modern creation. CE is seen by strategy improvement offices and business relationships as a significant component to advance economical creation and is seen as a potential or potential future paradigmatic move, which will, therefore, bring about mechanical changes. Besides, the paper tended to the subsequent examination question—How is the Circular Economy thoughtfully identified with sustainability? We found that the Circular Economy is seen as a condition for sustainability, an advantageous connection, or a compromise in writing. This can be separated into eight distinct connections. In light of the examined writing, this paper contends that the subset relationship is by all accounts proper to keep up variety while, correspondingly, revealing insight into the wide scope of correlative techniques that managers and policymakers can adopt. In the current conditions, a Circular Economy can reinforce business and advancement, along with a significant level of natural preservation. Putting resources into circular economy, energy productivity and confronting environmental change may turn into a switch for changing the profitable model, in this way, turning around the pervasive patterns of de-venture, while likewise advancing new speculation and making new openings all through the inventory network of industrial items.

Biogas Generation Through Anaerobic Digestion of Organic Waste: A Review



Vaishali D. Jaysingpure and Moni U. Khobragade

Abstract The main aim of the present study is to focus on the generation and optimization of methane gas from organic waste by using anaerobic digestion (AD) technique. Anaerobic digestion is a traditional method that is in use for decades. It is the biggest source of renewable energy. It gives an optimal solution to the treatment of organic waste by giving useful byproducts. The byproducts of AD, mainly biogas, are directly used as an energy resource. It can be transformed into any form of energy. The efficiency of the AD process and the amount of gas production fully depend on parameters such as pH, temperature, holding time and recirculation of leachate (Gopal in J King Saud Univ Sci 33, 2021). Recently, a concept of co-digestion came into focus in which two organic wastes are digested together to enhance the efficiency of the digestion process. The results obtained by different researchers proved that co-digestion of two substrates produces a large quantity of biogas than a single substrate. Results obtained by experimental analysis can be optimized by using different types of software like MATLAB, RSM, i.e. Response Surface Methodology and ANN, i.e. Artificial Neural Network.

Keywords Anaerobic digestion (AD) · Co-digestion · Biogas

1 Introduction

Nowadays, the whole world is facing the most threatening issue, i.e. Solid waste disposal. Approximately 980 million tonnes of waste generation is observed annually in India, which includes waste generated from households, commercial, industries and agriculture waste. Anaerobic Digestion (AD) is a traditional method used for organic solid waste treatment in an efficient manner. It is a technology in which

V. D. Jaysingpure (✉) · M. U. Khobragade
Department of Civil Engineering, College of Engineering Pune, Pune 411005, India
e-mail: vaishalij18.civil@coep.ac.in

M. U. Khobragade
e-mail: muk.civil@coep.ac.in

waste is stored in an air-tight tank for some specific duration. Therefore, this technology has been successfully used to stabilize the organic sludge produced from municipal wastewater treatment. Recently, a number of researchers are using this technology for treating many organic solid wastes such as wastes from energy crops. Goapl et al. [1] studied the AD for flower waste. Wang et al. [2] used AD concept for waste-activated sludge digestion. Chandra et al. [3] studied methane production from anaerobic digestion of oil cakes of jatropha and pongamia. Nowadays, mixed anaerobic digestion, i.e. mixing of one organic waste with other organic wastes (2 or 3 wastes) appears to be an efficient technique for enhancement of biogas production. Biogas, which is one of the most useful byproducts of the anaerobic digestion process, is a type of biofuel resulting from the disintegration of organic matter. It is a mixture of various gases like CO_2 , H_2S and Methane. Biogas is considered as the largest energy source. It is a key source of green energy in the terms of electricity and heat for the local grid. Korai et al. [4] studied the mono-, co- and tri-digestion of fruits, vegetables and yard waste. He recorded the data for three different seasons. He reported that tri-digestion of fruits, vegetables and yard waste with an equal mixing ratio gives the highest methane production. Cheng et al. [5], in his study, added food waste with rusted iron shavings to improve the process of digestion. He recorded a significant increase in daily methane yield and rate of methane production after addition of rusted iron shavings to the food waste. Co-digestion of food waste with vegetable waste is performed in a leach bed reactor [6].

Nguyen et al. [7] tested anaerobic digestion (AD) of various organic wastes, such as wastes from livestock farms, a cattle slaughterhouse waste and waste streams from the agricultural zone, to check its ability to produce methane. The studies are carried out under thermophilic conditions. He studied the highest methane yield of $110.83 \text{ mLCH}_4/\text{g VS}$ added from animal carcasses on the 4th day. The experimental results proved the model organic wastes to have the good potential to produce biomethane. To overcome the deficiency of nitrogen in rice straw, it is digested anaerobically with co-substrate which is rich in nitrogen named, *hydrilla verticillata* [7].

2 Materials and Methods

2.1 Feedstocks and Inoculums

Various types of organic wastes called as feedstocks, also called as substrates are used for biogas production by anaerobic digestion. Different researchers used a variety of organic feedstocks which includes agricultural waste, kitchen waste, garden waste, dairy waste, vegetable and fruit waste, industrial sludges, etc. [8]. The biogas potential of each feedstock is different. Kainthola et al. [9] carried out the anaerobic co-digestion of *hydrilla verticillata* with rice straw. Ranjithav [10] explained the results of the anaerobic co-digestion of vegetables and flower wastes.

The process of addition of a suitable number of active microbes into the feedstock during anaerobic digestion to convert the organic material into biogas is called inoculation. Therefore, the success of digestion process mostly depends on the proper selection of inoculums. The best inoculum consists of a large count of active microbes. The factors such as rate of degradation, composition of biogas, time taken for complete digestion and stability of reactor are directly influenced by the proper selection of inoculums. Commonly used inoculums include industrial sludges or sludge from wastewater treatment plants and cow dung.

Nguyen et al. [7] collected cow dung from Amingaon, Assam, India, from the outlet of operating biogas plant through a fixed dome and used it as an inoculum. He observed that the cow dung consisted of abundant anaerobic microorganisms and analyzed it for various parameters like VS% of 32.63%, sCOD of 8.81 g/L and a pH of 7.75.

2.2 *Pretreatment of Feedstock*

Treatments given to the feedstock prior to feeding in the digester are called as pretreatments. Pretreatment improves the AD treatment of organic waste. It improves biogas production. The main advantage of pretreatment is that it breaks the lignin layer which protects the cellulose and hemicelluloses, which, in turn, make the organic material easily accessible to the microorganisms and thus improves the digestion process. Pretreatment also helps to decrease the crystalline nature of cellulose which increases its porosity.

Main pretreatments given to the substrates include physical, chemical and biological treatments [1]. Physical pretreatment includes mechanical and thermal or microwave pretreatments. Mechanical pretreatment includes particle size reduction of the substrate which increases the speed of the digestion process by making a large surface area available for the microorganisms to feed on the organic matter. Thermal pretreatment maintains the required temperature of the digester by using different techniques. In Chemical pretreatment, some chemicals such as acids, alkalis and oxidizers are added to the feedstock. Whereas in biological pretreatment, few microorganisms are introduced into the substrate. The most commonly used pretreatments include Physical and chemical methods, whereas biological treatment methods are used rarely. These pretreatments can be used in combination with Physical-chemical and thermo-chemical methods. Wang et al. [2] carried out combined alkaline/acid pretreatments to waste-activated sludge using bipolar membrane electrodialysis to produce equal concentrations of acid and alkali.

The co-digestion of wheat straw and chicken manure was carried out with the waste-activated sludge. Initially, it was thermally pretreated before being sent into the digester. It was analyzed for different four C/N ratios: 35:1, 30:1, 25:1 and 20:1. After experiments, he studied that the composition having C/N value of 20:1 as the optimum value [11].

2.3 Substrate to Inoculum Ratio (S/I Ratio)

The substrate to inoculum ratio can be expressed as the amount of volatile solids present in the substrate per the amount of volatile solids or amount of volatile suspended solids (VSS) present in the inoculum. The rate of the anaerobic digestion process is highly influenced by the S/I ratio. It is considered one of the most important parameters in biomethane potential testing. Sri Bala Kameswari et al. [12] studied the optimization of I/S ratio for co-digestion of fleshings with the sludge from the tannery. He carried out batch studies and maintained 6 different reactors with 6 different I/S ratios: 0.25, 0.50, 0.67, 1.00, 1.50 and 2.20. Biogas generation was monitored daily. It was noted that methanogenic activity slow down as the I/S ratio decreased, which results in a decrease in the generation of biogas. But with an increased I/S ratio from 0.25 to 2.30, 1846 ml of increase in biogas generation was observed. Gopal et al. [1] studied the AD of flower waste by running 3 experimental setups with 3 different S/I ratios 1:2, 1:1 and 2:1, respectively.

Korai et al. [4], while studying co-digestion and combined digestion of 3 substrates including fruit (FW), Vegetables (VW) and yard (YW) waste, prepared the samples by using different ratios on a weight basis such as FW:VW (1:1), FW:YW (1:1) and VW:YW (1:1). And for combined digestion of 3 substrates, the samples were prepared by using different ratios on a weight basis such as FW: VW: YW (0.5:1:1), Fr: V: Y (1:0.5:1), FW: VW: YW (1:1:0.5) and FW: VW: YW (1:1:1).

Co-digestion of kitchen waste and black water in the ratio of 2:1 gives a larger amount of biogas than single digestion of kitchen waste. Also, by the addition of granular activated carbon by maintaining the same ratio, biomethane potential (BMP) is enhanced [13]. Food waste is digested with raw sludge (co-digestion) but with a higher concentration of food waste gives higher methane production. Okoro-Shekwaga et al. [14] in his study used two different food waste samples with less particle sizes of 1 mm and 2 mm, using two different inoculum to substrate ratios for testing biomethane potential. He studied that the two inoculums to substrate ratios, i.e. 3:1 and 4:1 were helpful to stabilize experiment reactors, respectively. For the co-digestion of vegetable and flower waste, pig manure is used as an inoculum [8].

3 Experimental Analysis

The biological process, with zero presence of oxygen, in which bacterial breakdown of organic materials occurs resulting in the generation of biogas, which is composed of different gases including methane, carbon dioxide and hydrogen sulphide, etc. is called as anaerobic digestion. Feedstocks used to produce gas include organic solid wastes from different sources, manure resulting from live stocks and wet organic materials. Anaerobic digestion has two stages, namely: fermentation and methanogenesis. Fermentation includes hydrolysis, acidogenesis and acetogenesis. In fermentation, 10 to 20 % of the energy of the substrate is transformed into gaseous products

such as hydrogen and carbon dioxide. Whereas, as the name suggests, in methanogenesis, 80 to 90 % energy of the substrate gets transformed into gaseous products, i.e. methane. The complete anaerobic digestion process takes approximately 21 days [15]. On the basis of stages of operation, anaerobic digestion is carried out in two ways, batch and continuous process.

3.1 Batch Mode Technique of Anaerobic Digestion

In a batch mode anaerobic digestion process, the reactor vessel is fed with raw feedstock and inoculum in proper ratio. Then it is sealed to maintain the anaerobic condition and kept undisturbed until complete digestion is over. Biomethane potential called as BMP test is conducted to check the biodegradability of feedstocks and their capacity to produce methane gas. It is carried out in small bottles called as BMP bottles varying from size 125 ml to 2000 ml. Wang et al. [2] studied biomethane potential for sludge treatment. Acid and alkaline pretreatment were given to the waste and the experiments were conducted in 250 ml serum bottles. To mix the substrate and inoculums thoroughly, the shaker was operated at a shaking speed of 150 rpm maintaining a temperature of 30 °C.

Korai et al. [4] studied the biomethane potential of wastes arising from fruits, vegetables and yards with combinations of one, two and three substrates. Anaerobic digestion is carried out in fifteen reactors, each having a capacity of 500 ml. The tests are carried out under mesophilic conditions by maintaining the temperature up to 38 ± 1 °C or under thermophilic conditions by maintaining the temperature up to 50–58 °C. The digesters are expected to be agitated manually or automatically 3 to 4 times per day for the proper bacterial contact with the waste and to avoid the sedimentation of solid particles. According to studies for statistical analysis, BMP should be carried out in triplicates [16]. BMP of inoculums is measured separately to identify the BMP of substrate individually. Accumulated gas collection can be done daily by using the liquid displacement method. The percentage of methane, carbon dioxide and hydrogen sulphide content are estimated by using Gas chromatography.

3.2 Continuous Mode Anaerobic Digestion

In a continuous digestion process, the reactor is continuously fed with feedstock and the sludge, i.e. digested material is removed continuously at a specific interval. Continuous mode anaerobic digestion process is carried out on a magnifying scale. The main difference between batch and continuous methods is that in the batch process, the reactor is fed only once at the beginning and operated under required controlled conditions, whereas, in the continuous process, it is fed daily. A batch process is technically simple and less capital intensive. Still, the land required for the batch process is comparatively larger. Besides, as waste generation is a continuous

process, the batch system is not practical. Also, another major concern in the batch process is its hectic loading and unloading. Having these short comings, the batch process has got some restrictions on the users for their study.

3.3 Characterization of Waste

The biodegradability of organic matter completely depends on its composition. Hence, it is essential to know the exact characteristics of a substrate and inoculum before carrying out a BMP test of the substrate [8]. As per [7], food/microorganism (F/M) ratio, carbon/nitrogen (C/N) ratio and pH are the main environmental parameters that have a large influence on biogas generation includes.

Generally, the feedstocks and inoculums are analyzed for total solids (TS), Suspended solids (SS), moisture content (MC), Volatile solids (VS), pH, total alkalinity and COD. Elemental analysis is carried out for the presence of C, H, N, O and S. Surface morphology of the substrate is studied by using SEM, i.e. Scanning electron microscopy.

Korai et al. [4] analyzed feedstocks, inoculums and material for TS, VS, pH, total alkalinity, volatile fatty acids and ammonia nitrogen ($\text{NH}_3\text{-N}$) according to the standard methods defined in APHA, 2005. Elemental analysis for C, H, O, N, was carried out as per the method prescribed in BBOT23122013. Wang et al. [2] studied the surface morphology of pretreated sludge and *E. coli* cells by scanning electron microscopy, SEM USA make. Nguyen et al. [7] has studied elemental composition (C, H, N, O) of each by an elemental analyzer Italy make, which is used to study the elemental composition C, H, N, O of substrates.

3.4 Measurement of Biogas

Techniques involved in gas measurements evaluates gas either by using manometers maintaining the volume constant and increase in the pressure indicates the volume of gas. Another method measures gas by volume maintaining constant pressure conditions and measuring the volume of gas [8]. Low permeability gas sampling bags can be the alternative biogas collection method that nullifies the absorption problem during long periods of contact with a barrier solution.

Measurement of biogas generated from lab scale models is done either by water displacement method or by using lubricated syringes. Liquid displacement is the most commonly used method for the collection of biogas [17]. Other instruments such as manometers, pressure transducers and low pressure flow meters are also used for the measurement of biogas. For large-scale models, it can be measured by using automatic gas flow meters. The water displacement method includes the arrangements of three tanks placed in sequence connected to each other. The first one is a digestion tank in which feeding material is added for a particular period. The

second is the water displacement tank. This tank is filled with water and is connected to the digester through a small pipe. The third unit is the collection tank which is again connected to the displacement tank through a pipe. By this method, gas generated in the digestion tank is measured in terms of ml of water displaced by the displacement tank. The water displacement method is used to measure biomethane production. Instead of water, 1.5 ml of normal sodium hydroxide solution is used in the displacement tank, and an indicator, named thymol blue is used. The displaced sodium hydroxide volume is measured by measuring cylinder which gives the per day quantity of biomethane generated [9].

In the syringe method, normally a 1000 ml syringe is used to measure biogas. A gas tight syringe is used in each digester at regular intervals of time and measures the volume of biogas production. By injecting the needle through the butyl bung, the syringe is connected to the reactors. Pressure in the headspace is dropped to ambient pressure by drawing the plunger out and the amount of biogas is collected, and thus the volume of gas in the syringe gives the measurement of the gas produced. After collection, a gas chromatograph is used to analyze the biogas for its contents. A gas chromatograph is equipped with a capillary column having split ratio 3:1 and dimensions: 30 m length, inner diameter 0.53 mm, 40 μm film and having a thermal conductivity detector to measure the methane concentration [6, 8].

3.5 Optimization of Biogas

Optimization is the process of enhancing system capabilities and integration of all the parameters to the extent that all components operate with maximum efficiency. It is done by using different types of software. These software provide standardized, efficient, accurate and comprehensible 2D and 3D graphs which gives clarity to the results obtained from experiments. Nowadays different types of software are used to optimize biochemical methane potential (BMP) of various substrates including MATLAB, RSM (Response Surface Methodology), ANN (Artificial Neural Network), etc.

Nguyen et al. [7] used RSM, a central composite design (CCD) for optimization of the design and performed twenty trials for this experimental design. The three important variables selected for the optimization and modelling include $X_1 = \text{C/N ratio}$, $X_2 = \text{F/M ratio}$ and $X_3 = \text{pH}$.

Sharma et al. [17] used response surface methodology for optimization of various combinations of flower waste with cow dung. For defining the experimental design in an anaerobic co-digestion of rice straw with hydrilla verticillata, a central composite design, response surface methodology was used efficiently [18]. The stability of the digestion, potential of biomethane production and rate of biomethane production for waste from farms of livestock, slaughterhouse waste and streams of waste generated from agricultural lands were assessed followed by the experimental analysis of results using four kinetic models [7].

4 Discussion and Concluding Remarks

The current research primarily focuses on the processes and methods of the anaerobic digestions through various well-known researchers' work into consideration. This study has focused on detailed methods available for anaerobic digestion, its significance and limitations. An effort is paid to find the optimum conditions required for an efficient digestion process. Rigorous insights into the study yield the following conclusions:

- Anaerobic digestion is an efficient technology which has remarkable advantages compared to other waste stabilization techniques. It converts the organic waste into useful byproducts like biogas which is the cheapest source of energy. Digestate resulting from the process have the highest nutritive value and is used as a fertilizer.
- It is studied that anaerobic digestion of multi substrates gives higher methane production as compared to anaerobic digestion of a single substrate. Rather the productivity of biogas reactors can be improved further by a mix-digestion strategy, as compared to mono-digestion and co-digestion of organic waste.
- Temperature, pH and Mixing rate of waste/agitation, and Hydraulic retention time are the major controlling parameters of the anaerobic digestion process.
- Proper inoculum to substrate ratio (I/S ratio) has a significant influence on biogas generation in the anaerobic digestion process.
- After a detailed review of the work of researchers, it was observed that the pretreatment of substrates gives more favourable results than that of untreated waste. Also, it is noted that thermal alkaline pretreatment enhances biogas production significantly.
- Optimization of parameters influencing the anaerobic digestion process gives accurate predictions, thus improving the efficiency of the digestion process to a large extent.

References

1. Gopal LC et al (2021) Optimization strategies for improved biogas production by recycling of waste through response surface methodology and artificial neural network: sustainable energy perspective research. *J King Saud Univ Sci* 33(1). <https://doi.org/10.1016/j.jksus.2020.101241>
2. Wang S et al (2019) Development of an alkaline/acid pre-treatment and anaerobic digestion (APAD) process for methane generation from waste activated sludge. *Sci Total Environ* 134564. <https://doi.org/10.1016/j.scitotenv.2019.134564>
3. Chandra R, Vijay VK, Subbarao PMV, Khura TK (2012) Production of methane from anaerobic digestion of jatropha and pongamia oil cakes. *Appl Energy* 93:148–159. <https://doi.org/10.1016/j.apenergy.2010.10.049>
4. Korai MS, Mahar RB, Uqaili MA (2018) The seasonal evolution of fruit, vegetable and yard wastes by mono, co and tri-digestion at Hyderabad, Sindh Pakistan. *Waste Manag* 71:461–473. <https://doi.org/10.1016/j.wasman.2017.09.038>

5. Cheng J, Zhu C, Zhu J, Jing X, Kong F, Zhang C (2020) Effects of waste rusted iron shavings on enhancing anaerobic digestion of food wastes and municipal sludge. *J Clean Prod* 242:118195. <https://doi.org/10.1016/j.jclepro.2019.118195>
6. Chakraborty D, Venkata Mohan S (2019) Efficient resource valorization by co-digestion of food and vegetable waste using three stage integrated bioprocess. *Bioresour Technol* 284(January):373–380. <https://doi.org/10.1016/j.biortech.2019.03.133>
7. Nguyen DD et al (2019) Thermophilic anaerobic digestion of model organic wastes: evaluation of biomethane production and multiple kinetic models analysis. *Bioresour Technol* 280(February):269–276. <https://doi.org/10.1016/j.biortech.2019.02.033>
8. Raposo F, De La Rubia MA, Fernández-Cegrí V, Borja R (2012) Anaerobic digestion of solid organic substrates in batch mode: an overview relating to methane yields and experimental procedures. *Renew Sustain Energy Rev* 16(1):861–877. <https://doi.org/10.1016/j.rser.2011.09.008>
9. Kainthola J, Kalamdhad AS, Goud VV (2019) Optimization of methane production during anaerobic co-digestion of rice straw and hydrilla verticillata using response surface methodology. *Fuel* 235. <https://doi.org/10.1016/j.fuel.2018.07.094>
10. Ranjithav J (2014) Production production of bio-gas from flowers and vegetable wastes using anaerobic digestion of bio-gas from flowers and vegetable wastes using anaerobic digestion. *Int J Res Eng Technol* 03(08):279–283. <https://doi.org/10.15623/ijret.2014.0308044>
11. Hassan M, Ding W, Shi Z, Zhao S (2016) Methane enhancement through co-digestion of chicken manure and thermo-oxidative cleaved wheat straw with waste activated sludge: a C/N optimization case. *Bioresour Technol* 211:534–541. <https://doi.org/10.1016/j.biortech.2016.03.148>
12. Sri Bala Kameswari K, Kalyanaraman C, Porselvam S, Thanasekaran K (2012) Optimization of inoculum to substrate ratio for bio-energy generation in co-digestion of tannery solid wastes. *Clean Technol Environ Policy* 14(2):241–250. <https://doi.org/10.1007/s10098-011-0391-z>
13. Zhang Q, Li R, Guo B, Zhang L, Liu Y (2021) Thermophilic co-digestion of blackwater and organic kitchen waste: impacts of granular activated carbon and different mixing ratios. *Waste Manag* 131(June):453–461. <https://doi.org/10.1016/j.wasman.2021.06.024>
14. Okoro-Shekwa CK, Turnell Suruagy MV, Ross A, Camargo-Valero MA (2019) Particle size, inoculum-to-substrate ratio and nutrient media effects on biomethane yield from food waste. *Renew Energy* 151:311–321. <https://doi.org/10.1016/j.renene.2019.11.028>
15. Cremiati R, Mastellone ML, Tagliaferri C, Zaccariello L, Lettieri P (2018) Environmental impact of municipal solid waste management using Life cycle assessment: the effect of anaerobic digestion, materials recovery and secondary fuels production. *Renew Energy* 124:180–188. <https://doi.org/10.1016/j.renene.2017.06.033>
16. Filer J, Ding HH, Chang S (2019) Biochemical methane potential (BMP) assay method for anaerobic digestion research. *Water (Switzerland)* 11(5), MDPI AG. <https://doi.org/10.3390/w11050921>
17. Sharma D, Yadav KD, Kumar S (2018) Biotransformation of flower waste composting: optimization of waste combinations using response surface methodology. <https://doi.org/10.1016/j.biortech.2018.09.036>
18. Kainthola J, Kalamdhad AS, Goud VV (2019) Optimization of methane production during anaerobic co-digestion of rice straw and hydrilla verticillata using response surface methodology. *Fuel* 235:92–99. <https://doi.org/10.1016/j.fuel.2018.07.094>

Recent Trends in Geotechnical Engineering

A Cost Comparison Study of Use of Cased and Uncased Stone Column in Marshy Soil



Starina J. Dias and Wilma Fernandes

Abstract Over the past decade, there is a lot of growth in infrastructure and now it is becoming very difficult to find suitable soils for construction purpose, hence this has forced geotechnical engineers to take up the challenge of constructing structures even on weak soft soils. The characteristics of soft clay are highly compressible low shear strength and low permeability. General construction problems in this soil are insufficient bearing capacity, instability on excavation and excessive post-construction settlement. Among various technologies implemented by engineers, stone columns are the most beneficial method for the modification of weak soil. For the present study, at a bridge site in Goa, we encountered extremely soft soil where a sufficient number of stone columns were used, thus in this study, an attempt was made to reduce the number of stone columns by wrapping the granular pile with geotextile which will enhance the performance of stone column by increasing the bearing capacity which will help in reducing the number of stone columns. This proposed improvement by encasement with a geotextile was done by using a finite element software called Plaxis 2D. It can be seen that for a given area, the stone column numbers were reduced from twelve to nine columns.

Keywords Geotextile · Stone columns · Soft soil · Encased stone column

S. J. Dias (✉)

Civil Engineering Department, Don Bosco College of Engineering, Fatorda, Goa, India
e-mail: starina23@gmail.com

W. Fernandes

Civil Engineering Department, Goa College of Engineering, Farmagudi, Goa, India
e-mail: wilma@gec.ac.in

1 Introduction

Ground improvement is one of the most applicable methods for improving soil condition and humankind till date has pursued ground improvement techniques to improve soil condition. This method is the most useful and economic than other kinds. Ground improvement has numerous methods and a suitable method is selected based on the soil type, bearing condition and structure type. Several ground improvement techniques have been developed to convert weak soil into a stratum of desired strength and compressibility as per the design requirements with adequate safety. The soil can be improved by using various ground improvement techniques like Dry soil mixing, Dynamic compaction, Injection systems, Vibro compaction, Vacuum Consolidation, Heating, Ground freezing, Soil nailing, Stone columns, etc.

Nowadays, in Goa, land is slowly getting exhausted and there is a decrease in good construction sites. There are a number of soil types in Goa and each one has unique characteristics like colour, texture, structure, and mineral content. There are certain types of soils that are problematic as they are collapsible, liquefiable and some soils are even expansive in nature. One of these types of soil is weak compressible soil like soft clay and marshy soil which is a classic example of soil found along the coastal areas in India and along the perimeters of river bays. In places like Goa, soft soils are often found near the mouths of rivers and can be especially troublesome. The problems of soft soil are low bearing capacity, low shear strength, high settlements and low permeability. Hence, these soils have to be improved in order to construct building, storage tanks, embankments, etc. Hence, ground improvement techniques in recent times have now become a necessity and thus this particular field is branded as a fast-improving one. In the present study, by using a finite element software called PLAXIS we are studying the effect of encasing a Stone column with geosynthetic.

2 Concept of Stone Column

2.1 Introduction of Stone Columns

Stone column is basically a technique where granular material is compacted in long cylindrical holes that are mostly used for improving the soil characteristic of soft clay. When a stone column is subjected to vertical loading, it undergoes a tremendous vertical compression caused by the lateral bulging of the aggregates mostly seen in the top portion of the column. Figure 1 shows the behaviour of a stone column where we can see that the column bulges almost four times the diameter of the column and the granular material present in the stone column penetrates into the surrounding soft soil and transfers the stress to the surrounding soil. The bulge, in turn, increases the lateral stress within the clay which provides additional confinement for the stones.

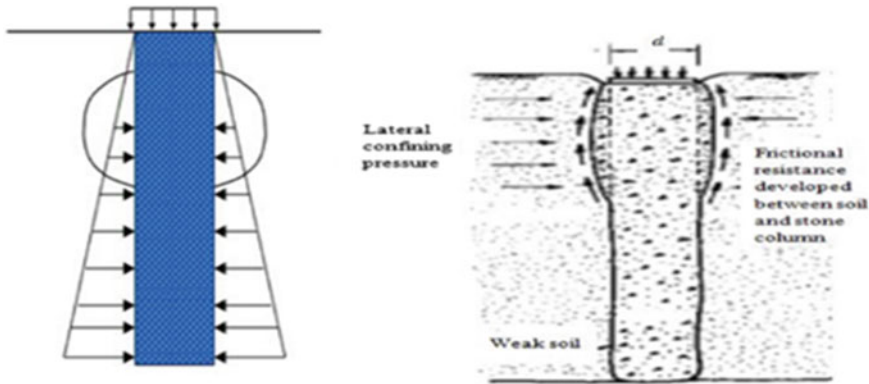


Fig. 1 Behaviour of a stone column (Rajagopal K.—IIT Madras)

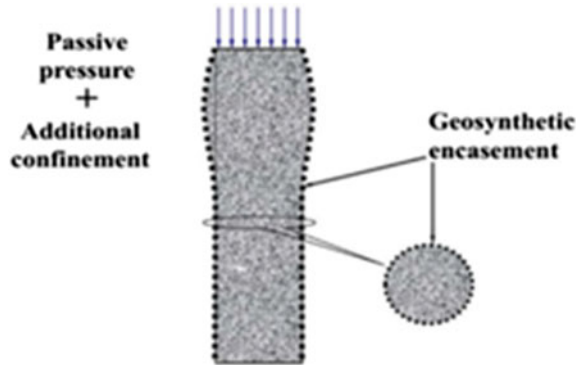
The passive pressure from the neighbouring clay allows the column to resist the vertical load on the stone column. It can be said that the strength of the surrounding clay is the main factor that contributes to the load-carrying capacity of the stone column (Malarvizhi and Ilamparuthi).

3 Concept of Encased Stone Column (ESC)

3.1 Introduction of Encased Stone Columns

Mostly stone columns have found to be effective for soils having undrained strength that is $C_u \geq 15 \text{ kN/m}^2$, but for very soft soil having undrained shear strength that is $C_u \leq 15 \text{ kN/m}^2$, the ordinary stone column technique may not be feasible either due to excessive bulging of the stone column in the clay or due to clay clogging in the pores of the aggregates of the stone column. Hence, when such a situation arises, the performance of a stone column can be enhanced by using a high tensile strength geosynthetic that is placed around the stone column and such stone columns are termed as called as Geosynthetic Encased Stone Column [ESC]. Basically, this method is an extension of the well-known stone or sand column foundation improvement techniques. Encased stone columns consist of inserting continuous, seamless, high strength geotextile tubes into soft soil with a mandrel. The tube is then filled with either sand or fine gravel to form a column with a high bearing capacity. Their load carrying capacity varies from 20 to 40 tonnes (Murugesan S. and Rajagopal K).

Fig. 2 Concept of encased stone column (Rajagopal K.—IIT Madras)



3.2 Schematics of the Encased Stone Column

Generally, it is seen in a stone column that the bearing capacity of the treated ground is mostly derived from the passive resistance offered by the surrounding soil due to lateral bulging of stone column material under applied loads, but the behaviour of geosynthetic encased stone column is thought out to be entirely different from that of the conventional stone column. The vertical deformations and the load distribution between the encased stone column and the soft soil are defined by the tensile strength and the stiffness of the encasing material used for encasement. Hence, the encasement provides passive pressure and additional confinement to the stone column. Figure 2 explains the concept of encased stone columns.

3.3 Site Details

The present study is chosen in the Tiswadi taluka of Goa at a site named Manduras seen in Fig. 3. At this site, in the past, there existed a small bridge that was used by the locals to commute to the other side of the tributary of the Zuari river, which had collapsed in due course of time. Hence, a single-lane bridge construction was proposed. This bridge, if constructed, could be of use to connect this small village of Mandur to Kundaim which lies close to it, and would reduce the travelling distance mainly from Vasco-Agacaim–Mandur to Kundaim, which is a prominent industrial estate of Goa. Table 1 shows the Travel distance which the proposed single lane bridge would reduce.

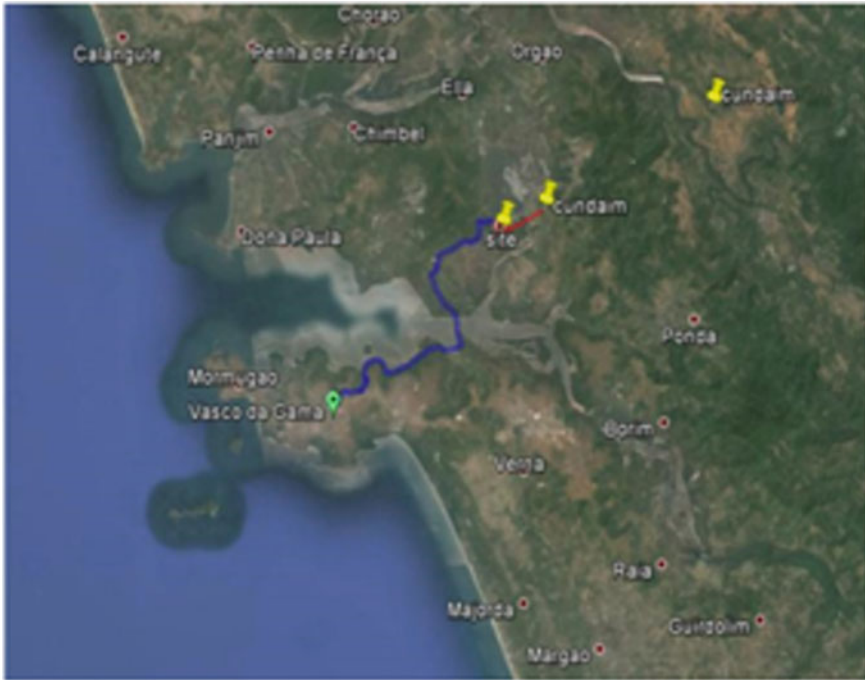


Fig. 3 Distance from Vasco to Kundaim with proposed bridge

Table 1 Travel distance which the proposed single lane bridge would reduce

Destination	Travel time (minutes)	Distance (Kilometer)	Route
Margao to kundaim	49	30.1	Via Borim, Priol
Vasco to Kundaim	53	34.8	Via Agaciam, Neura, Ella, Corlim
Vasco to Kundaim	36	20.84	Via Agaciam, Neura, Proposed Dongrim-Madur bridge

The present bridge site in Goa falls along the floodplains of the tidal estuary and the soil encountered here is mostly soft marine clay. The report of the soil investigation carried out at the site suggested very weak soft saturated soil having poor strength and having SPT potential (N) between $N = 1-3$. Also, the water table was encountered at ground level. Presently, the soil is improved by stone columns in the western approach way to the bridge site, resulting in a hundred and six stone columns, thus an attempt is made in reducing the number of stone columns by wrapping the granular pile with geotextile. It may be noted that geosynthetics are being used nowadays to a great extent in the environment of increasing land scarcity (Fig. 4).

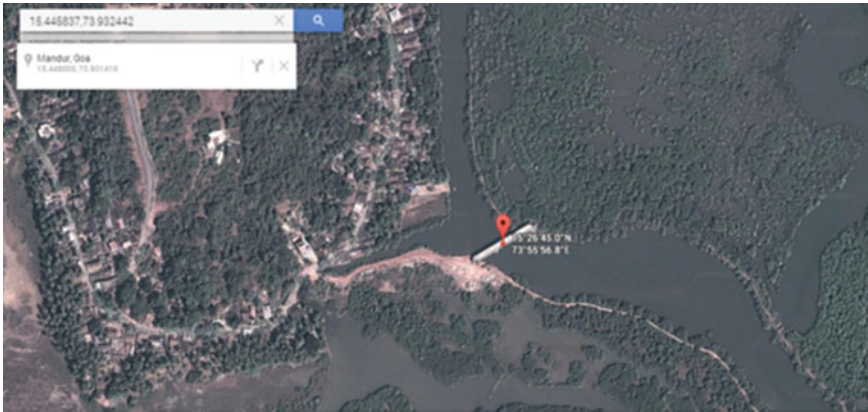


Fig. 4 Coordinates showing the proposed bridge at Mandur site

4 Parametric Study on Ordinary Stone Column (OSC) and Encased Stone Column (ESC) for Mandur

It was decided to propose to construct stone columns to improve the ground below the proposed approach way to the bridge. The diameter of the stone columns existing at the site is 900 mm, length of the stone column is 1500 mm, centre-to-centre spacing that was used was 2700 mm and load of 165 kN was used on the column. The geosynthetic used in the Plaxis software is used to show the effect of encasement and is modelled as a geogrid element having tensile stiffness only. The input parameters required by the software for clay and sand are given in Table 2.

Table 2 Material properties used in PLAXIS software

Properties	Clay	Stone
γ_{unsat} (unsaturated unit weight)	15 kN/m ³	17 kN/m ³
γ_{sat} (saturated unit weight)	18 kN/m ³	18 kN/m ³
K_x (Permeability in x direction)	2×10^{-4} m/day	12 m/day
K_y (Permeability in y direction)	1×10^{-4} m/day	6 m/day
E (Elastic Modulus)	2000 kN/m ²	30,000 kN/m ²
ν (Poissons ration)	0.45	0.3
C (cohesion)	9.81 kN/m ²	0 kN/m ²
ϕ (friction angel)	0°	40°
Ψ (Dilation angel)	0°	10°
LL (%)	39	
PL (%)	21.52	
PI (%)	17.48	

In the present case, at Mandur, taking an area of 57.6 m², there exist twelve ordinary stone columns at centre-to-centre spacing of 2700 mm. An attempt is made to reduce the number of stone columns in the said area with appropriate encasement stiffness and also check its cost feasibility (Fig. 5).

The centre-to-centre spacing of the stone column was varied from the existing spacing of 2700–3500 mm along with the stiffness to achieve the optimum spacing and appropriate stiffness. The geogrid material found satisfactory for Mandur is a biaxial geogrid called TechGrid Biaxial (TGB)-40, having a stiffness of 333.33 kN/m. Below is the property of the geogrid (Table 3).

Fig. 5 Present case at Mandur-Twelve ordinary stone columns at center to center spacing of 2700 mm for an area of 57.6 m²

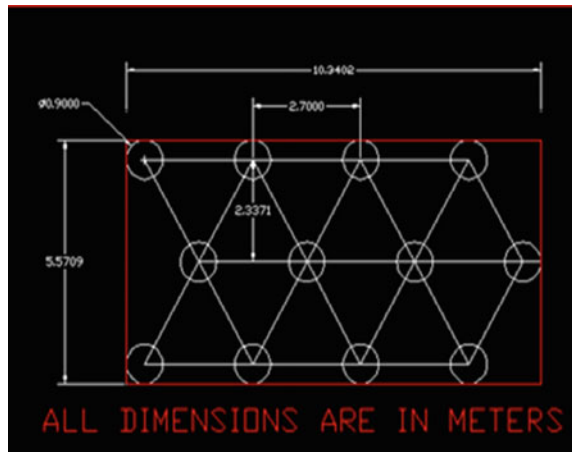


Table 3 Specification for tensile geogrid biaxial (TGB-40)

Property		TGB-40	Test method
Ultimate tensile strength	MD	40 kN/m	ASTM
	CD	40 kN/m	D 6637
Elongation at maximum load	MD	12%	EN
	CD	12%	SO 10,319
<i>Physical property</i>			
Aperture size (+/- 3 mm)	25 × 25		
<i>Roll dimensions</i>			
Roll length	50 m/100 m		
Roll width	2.5 m/3.9 m/5.0 m		
MD—Machine direction	CD—cross direction		

Source Techfab—India

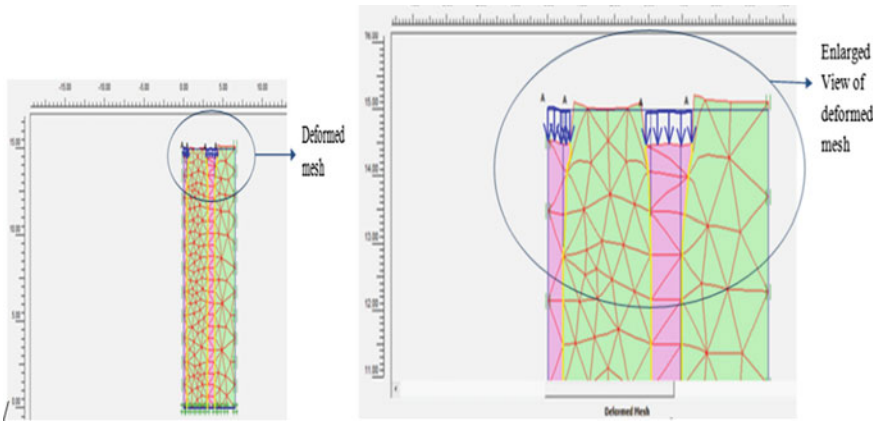


Fig. 6 Deformed mesh of the failed encased stone column at spacing of 3500 mm center to center. *Source* Plaxis-output

The following is a figure of a deformed mesh of a failed ESC at a spacing of 3500 mm (Fig. 6).

The following is a figure of a deformed mesh of a failed ESC at a spacing of 3200 mm (Figs. 7 and 8).

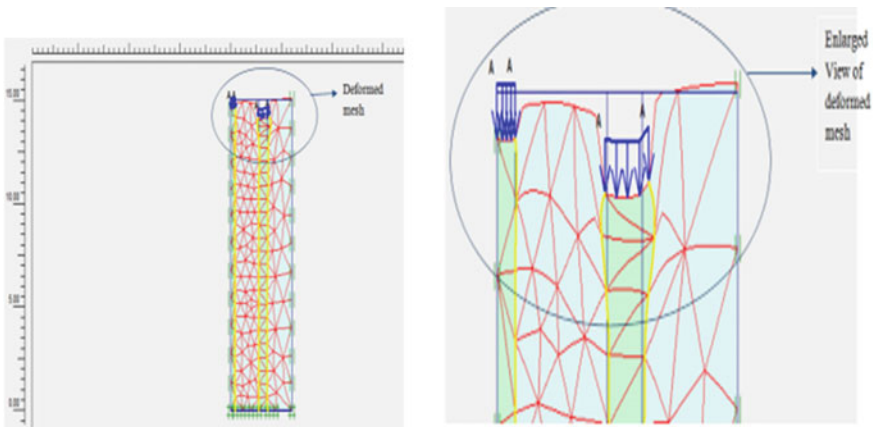
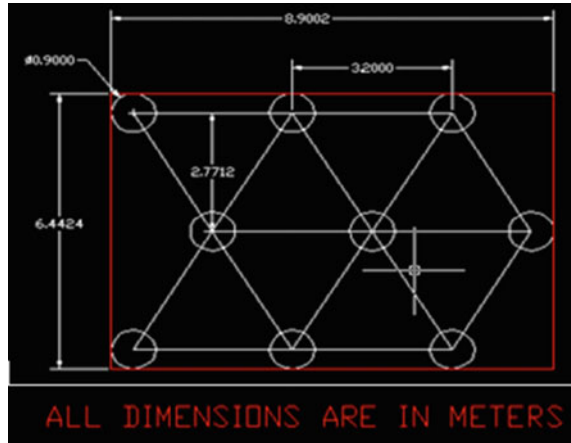


Fig. 7 Deformed mesh of the successfully passed encased stone column using a stiffness of 333.33 kN/m at spacing of 3200 mm center to center. *Source* Plaxis-output

Fig. 8 After analysis-nine stone columns at center-to-center spacing of 3200 mm with a geogrid stiffness of 333.33 kN/m for an area of 57.35 m²



After doing the analysis in the software with the said geogrid, it is found that for an area of 57.35 m², nine stone columns at centre-to-centre spacing of 3200 mm with a geogrid of stiffness of 333.33 kN/m were found satisfactory for a given load of 165 kN. It can be noted that the stiffness of encasement plays a role in transferring the stresses to the surrounding soil. It was seen that, for the given stiffness of 333.33 kN/m, the spacing of the encased stone column could be increased to 3200 mm centre-to-centre, but for the same stiffness, the spacing could not be increased more than 3500 mm as the encasement is not able to sustain the given load.

5 Cost Feasibility

The costing was done to determine the cost factor between OSC and ESC. The Table 4 has the breakup of the cost involved in setting up a single OSC.

Table 4 Nature of work and cost

Sr. No.	Nature of work	Units of measurement	Cost (rupees)
1	Cost of drilling-which includes bailing out of soil, operator charges	per meter	3000
2	Quantity of stone 6-40 mm	cum	1400
3	Labour cost per person	per day	500
4	Rental of drilling machine	per day	4000
5	Geogrid-TGB-40	per meter	200

Assuming it takes three days to construct a single stone column of diameter 900 mm and length of 1500 mm and taking into consideration eight labourers per day, we arrive at a cost of approximately Rs. 75,000/- for a single OSC. Using geogrid-TGB-40 for a single encased stone column for an outer circumferential area of 42.5 m² and using the same criteria mentioned above, we arrived at a cost of approximately Rs. 83,500/-.

In an area of 57.6 square metres, an OSC having twelve columns has a cost of Rs. 9,00,000/-, while an ESC for an equivalent area has nine columns, having a cost of Rs. 7,51,500/-. Hence, by comparing the cost of construction of an ordinary stone column and Encased stone column, it was found that the cost reduces by 16.5% for an Encased stone column.

6 Conclusions

It can be concluded for the present site where stone columns are used in the embankment for the approach for the single-lane bridge that:

By encasing the stone column by a geogrid of stiffness of 333.33 kN/m and maintaining a centre-to-centre spacing of 3200 mm for the existing diameter at the site, the stone columns reduce from twelve to nine columns for a given area. Generally, the spacing between stone columns is generally 2–3 times the diameter, but after analysis, it may be seen that for a particular stiffness of encasement, the spacing between the stone columns could be increased to 3.5 times the diameter, hence reducing the number of constructed stone columns in an equilateral pattern for the said area.

Also, upon comparing the cost of construction of an ordinary stone column and encased stone column for the area of 57.6 m², it was found that the cost reduced by 16.5%. Hence, considering the type of soil at the site, it would be advantageous to use this type of encasing method of stone column to reduce the overall cost of the project.

Bibliography

1. Murugesan S, Rajagopal K (2010) Studies on the behavior of single and group of geosynthetic encased stone columns. *J Geotech Geoenviron Eng* 136(1):130
2. Nayak S, Vibhoosha MP, Bhasi A (2019) Effect of column configuration on the performance of encased stone columns with basal geogrid installed in lithomargic clay. *Int J Geosynth Ground Eng*

3. Murugesan S, Rajagopal K (2006) Geosynthetic-encased stone columns: numerical evaluation. *Geotext Geomembr* 24:349–358

Review on Field Direct Shear Test Methodologies



Kakasaheb D. Waghmare and K. K. Tripathi

Abstract This paper reviews the techniques used for in situ testing of soil shear strength. Conventional laboratory direct shear test has problems like the simulation of field conditions, particle size restriction, etc. Therefore, many researchers have tried to perform in situ testing for the shear strength of soil to get reliable results. But because of the soil's heterogeneous nature and heavy designs of the set-up, these tests are not popular. The study will help to identify the advantages and limitations of existing in situ direct shear testing set-ups currently being used. With the help of this review, it has been concluded that there is a need for simpler and strain-controlled in situ direct shear testing on the soil.

Keywords Shear strength · In situ direct shear test · Cohesion · Angle of internal friction

1 Introduction

Assessment of the bearing capacity of soil is mainly influenced by its shear strength ($c-\phi$) parameters. Various tests, such as triaxial test, vane shear test, direct shear test, etc. are available for the determination of bearing capacity from shear strength parameters. Whereas tests such as standard penetration test and plate load test are available for the determination of bearing capacity from settlement criteria. The present study focuses on the study of work done on In situ direct shear test standards and some other modified methods. Laboratory direct shear test is one of the simplest and fastest tests to know the shear strength parameters of soil. But the field direct shear test is not very popular due to the requirements of the heavy set-up, the problems of applying shear and normal load, the test controls, etc. Laboratory tests are carried

K. D. Waghmare (✉)
College of Engineering Pune, Pune, India
e-mail: kdwaghmare3@gmail.com

K. K. Tripathi
Civil Engineering Department, College of Engineering Pune, Pune, India

out under controlled conditions, which may differ from actual on-site conditions. Due to technical constraints such as scale effect and quality of sampling, there are considerable potential limitations to the on-field testing techniques in the form of sampling and testing anomalies. Therefore, the study aims to compare the various methods and techniques used for in situ shear testing to better understand their accuracy, consistency, and adoptability. In this study, standard procedures like the ASTM code tests and I.S. code tests, modifications in the ASTM and I.S. code field direct shear tests have been explained and compared.

2 Objective

To study various methods of field direct shear test of soil and do a comparative assessment of their suitability for wide-scale adoption.

3 Literature Survey

The various techniques as recommended by the ASTM code and the I.S. code and their respective modifications have been studied and published. The following section includes brief notes on such previous investigations carried out for in situ direct shear tests to measure shear strength and shear strength parameters of soil.

3.1 *Field Direct Shear Strength Test to Measure Rock Discontinuities (ASTM D 4554-02)*

In this technique of field shear strength testing, ASTM D 4554-02 recommends that during the performance of the in situ shear test on rectangular-shaped blocks of rock, the blocks to be isolated on all surfaces, except for the shear plane surface. The size of blocks for which this technique is deemed suitable is of size 700 mm × 700 mm × 350 mm. The detailed set-up of the equipment is shown in Fig. 1. Care should be taken that the blocks are not to be disturbed during preparation operations and that the base of the block shall coincide with the plane to be sheared. A normal load is applied perpendicular to the shear plane, and then a lateral load is applied to induce shear along the plane of discontinuity. This technique requires the placement of the test specimen in concrete, which considerably increases the test's conduct duration. While the technique is useful for checking the discontinuities of rock, it does not help in checking the soil's shear strength.

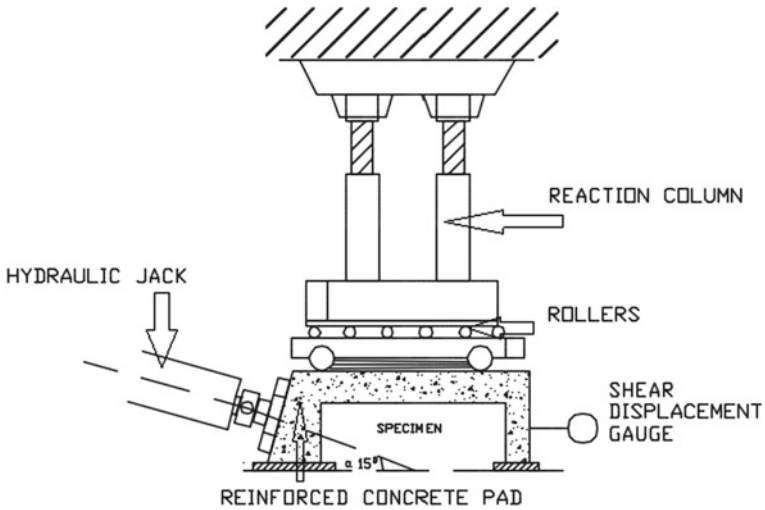


Fig. 1 Typical arrangement of equipment for in situ direct shear test

3.2 Direct Shear Test for Soils Containing Gravel IS 2720-1979 Part 39/2

Using this technique, as recommended in IS 2720-1979 part 39/2, the shear strength of soils containing gravel and cobblestone can be determined using the direct shear test. In this technique, a 1500 mm² box is lowered into the ground with the help of a hydraulic jack. The soil around the box is excavated step-by-step till the box reaches the desired position. After the digging is complete, an assembly is placed on the top of the blocks for the application of normal load. This assembly is made up of rolled steel joists, wooden sleepers and sandbags. The shear load is applied with a controlled hydraulic jack and proving ring arrangement, taking reaction from the adjacent box (Fig. 2). This method can be used even for soils where the particle size

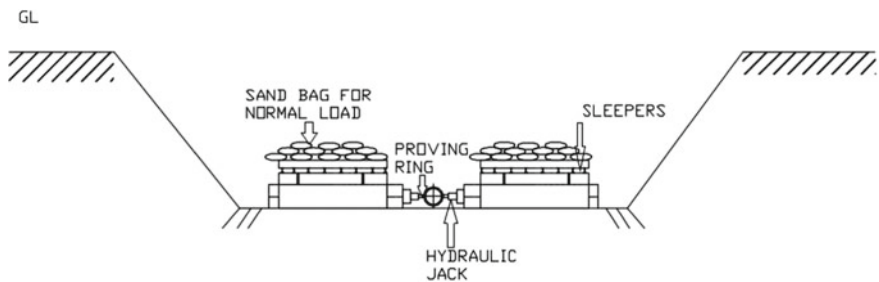


Fig. 2 Typical arrangement I.S. code method for in situ direct shear test

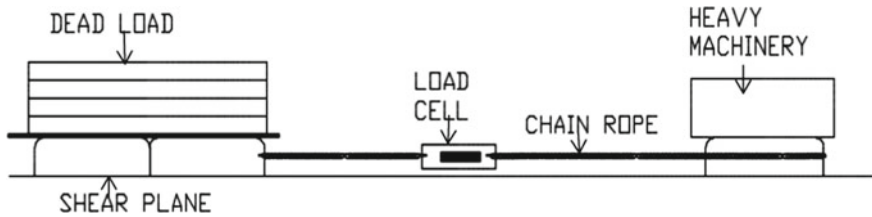


Fig. 3 Arrangement for modified in situ direct shear test device

is greater than 30 mm. However, the method is complicated to perform as it requires heavy excavation work leading to more human resource requirements.

3.3 Shear Test Using Modified In Situ Direct Shear Device

Liu [3] proposed a modified version of the direct shear on-field test device similar to the I.S. code version. In this test, the upper part of the shear box, as presented in the IS Code test, is replaced by the lattice shear box. The lattice shearing box frame is placed directly on the ground. The box is then pulled with a flexible chain while a dead load is applied onto the shearing frame. Validation is done by carrying out tests on trials with similar gradations under normal stress (up to 880 kPa) (Fig. 3). As can be understood, this test has no control of strain rate, as the shear load is applied by pulling the chain with heavy machinery.

3.4 Field Testing of Shear Strength of Soil with the Help of an Open-Sided Shear Box

A paper by M. Cross, July 2010, presents an open-sided shear box with a 300 mm² basal shearing zone and two 300 mm × 150 mm horizontal shearing areas. Lead weights are used to provide normal loads that simulate natural geostatic forces, and a shearing force is induced by a winch/cable system. This field open-sided direct shear box (Fig. 4) was used to assess the shear strength parameters of the Derbyshire shallow residual and colluvial soil. Some locations were chosen for shear testing by dividing the total slope profile into three equal parts, from the slope crest to the slope foundation, the higher, middle and lower slope sections. The soil sample was pulled by winch and wire rope, thereby making it a strain-controlled test. This test is a strain-controlled test, however, the strain control is crude and unprecise as the winch is manually operated.

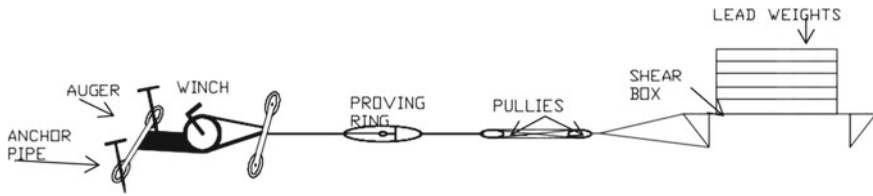


Fig. 4 Schematic view of open-sided shear box test

3.5 Shear Testing Using Modified Standard Operation of Rock Piles

Another modification of the direct shear test technique was used to measure the rock pile materials' cohesion and friction angle. Two test apparatuses had been designed, 300 and 600 mm² Shear boxes. The test apparatus also included a manufactured roller plate, a metal top plate, shear dial gauges with support services and two hydraulic pistons and cylinders with a maximum hydraulic cylinder of 70 MPa (10,000 psi) for normal loading (Fig. 5).

The Questa Rock Pile Stability Study SOP 82v4 made use of this method. This Questa Rock Pile Stability Study SOP 82v4 was developed to provide technical guidance and practices to test rock pile materials during mines' environmental investigations. The test aimed to determine how much cohesion exists in the rock pile material and to check the weathering impact on the material's shear strength properties, such as cohesion and friction angle. A trench was excavated with the help of a shovel up to a specified layer of rock. With the help of a nail board and nail cage, the required shape was given to the rock pile to fit into the shear box. A roller plate was then placed over the rock pile and a dead load was applied with the help of machinery

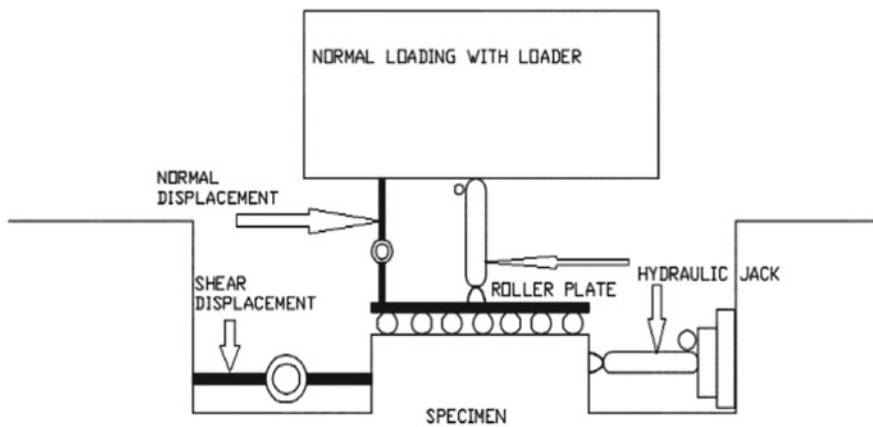


Fig. 5 Modified in situ direct shear test technique of rock piles

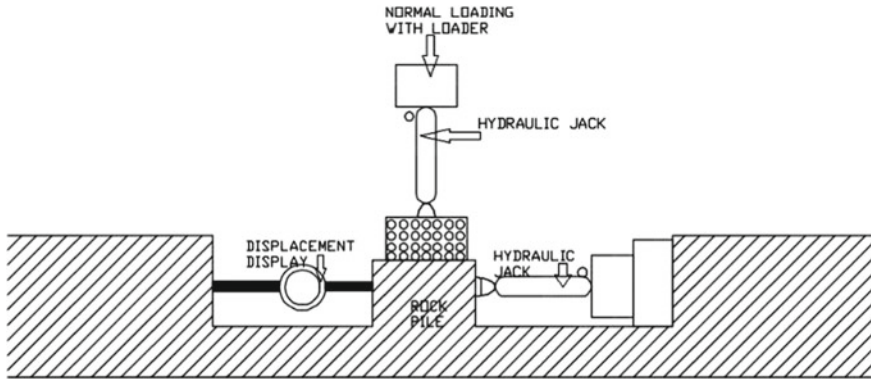


Fig. 6 Arrangement of SOP for testing rock pile

or dead plates. The normal load was applied with the help of a hydraulic jack and a horizontal shear load was applied with the help of another hydraulic jack. As can be seen, this method of testing soil shear strength is a stress-controlled test and requires heavy support (Fig. 6).

3.6 Effect of Strain rate on Shear strength of soil.

This paper [7] shows the relationship between shear strength and shear rate of the soil. The test was carried out on the Ring Shear Test apparatus. The test consists of eight stages with four different shear rates: 0.01, 0.1, 1 and 10 mm/s. The specimens were saturated and consolidated at 100 kPa and the total normal stress was maintained at 100 kPa during the tests. After the residual energy was formed, the shear rate was reduced significantly and the pore pressure was dissipated under wet conditions. The specimen was re-extracted at 1 mm per second (phase 2). This shearing process removed the pore water pressure, and re-shearing was repeated until the eighth stage. The relationship between the remaining active collision angles and shear values was recorded.

The paper demonstrated that the shear strength value changes with the change in strain rate. Many other papers have also studied the effect of strain rate on the shear strength of soil and have shown that this effect is owing to the fact that pore water pressure rate takes time to dissipate in the clayey soil.

4 Comparison Between Devices

Table 1 shows the tabular comparison of the above literature and shows the limitations of the same.

Table 1 Comparison of various field direct shear test

Method	Type of soil test	Mould size	Test type	Limitations
Field direct shear strength test to measure rock discontinuities (ASTM D 4554-02)	Rock	700 × 700 mm	Stress controlled test	(1) The test requires the emplacement of the test specimen in concrete
Direct shear test for soils containing gravel I.S. 2720-1979-part 39/2	Gravel	1500 × 1500 mm	Stress controlled test	(1) Heavy set-up (2) Require a lot of excavation
Shear test using modified in situ direct shear device by Liu [3]	Coarse-grained	122.5 × 122.5 mm	Stress controlled test	(1) Heavy construction machinery (2) Disturbance in soil (3) Calculations complicated
Field testing of shear strength of soil with help of an open-sided shear box	Coarse-grained	300 × 300 mm	Partially strain-controlled test	(1) Sample disturbance is not eliminated (2) Shallow depth testing
Shear testing using modified standard operation of rock piles (Questa Rock Pile Stability Study SOP 82v4)	Rock pile	300 × 300 mm and 600 × 600 mm	Stress controlled test	(1) Heavy set-up (2) Require more than five labourers (3) Normal load with a front end loader

5 Discussion

From the results shown in Table 1, it can be seen that the most available techniques and methods that have been studied and recommended were stress-controlled, and even in the strain-controlled tests, the strain control is crude and partial. It is also seen that the strain rate influences the shear strength of soil and hence poor control of strain rate while conducting the tests can lead to inaccurate results. It is worth noting here that the most popular test, i.e. the laboratory direct shear test, is a strain-controlled test. The reason for wide-scale acceptability and adoption of laboratory direct shear test is its simplicity, speed of conduction, consistency and reliability of results. Most of the trials of the above literature have been done on the rock piles and very few tests or modifications have been done on soil samples. It is also observed

that no tests have introduced a testing depth of more than one metre. All the present in situ tests require heavy set up and human resources to perform, thereby making them expensive.

6 Conclusion

In light of the above literature review and comparative analysis of different types of tests for shear strength, it can be concluded that further research and experimentation are required in order to make field shear testing of soil more acceptable in routine practice. Considering that the current practices are heavy set-ups, it is necessary to devise lightweight set-up tests to perform field direct shear tests on the soil. As the strain rate is found to influence the results of shear strength testing, it must be ensured that the newly devised tests have better, preferably complete strain control. Most existing field tests entail a high requirement of manpower, especially labourers. This dependence on manual labour needs to be reduced in order to make the tests efficient, cost-effective and easily replicable. The above factors will ensure that the field direct shear testing technique has all the virtues of a laboratory direct shear test device, thus making it widely acceptable and adoptable.

References

1. *ASTM D 4554-02* (2006) Standard test method for in situ determination of direct shear strength of rock discontinuities. ASTM, Philadelphia
2. *I.S. 2720-1979 part XXXIX/2*, Direct shear test for soils containing gravel. Bureau of Indian Standards, New Delhi
3. Liu S (2009) Application of in situ direct shear device to shear strength measurement of rockfill materials. *Water Sci Eng* 2(3):48–57
4. Cross M (2010) The use of a field open-sided direct shear box for the determination of the shear strength of shallow residual and colluvial soils on hillslopes in the south Pennines, Derbyshire. *North West Geogr* 10(2):8–18
5. Fakhimi A, Boakye K, Sperling DJ, McLemore VT (2007) Development of a modified in situ direct shear test technique to determine shear strength parameters of mine rock piles. *Geotech Testing J* 31(3):1–5
6. Standard Operating Procedure (2008) In-situ direct shear tests. Questa Rock Pile Stability Study, SOP 82v4
7. Saito R, Fukuoka H, Sassa K (2006) Experimental study on the rate effect on the shear strength. Disaster mitigation of debris flows, slope failures, and landslides, pp 421–427

Numerical Prediction of Tunneling Induced Surface Settlement of a Pile Group



B. Swetha, S. Sangeetha, and P. Hari Krishna

Abstract Tunnel construction below or adjacent to the piles of Existing Building Structure (EBS) will affect the performance and eventually the stability of piles due to ground deformation which may result in the settlement of piles. A two-dimensional finite element analysis using PLAXIS 2D was performed to study the behavior of a pile group due to tunnel construction beneath the ground. A 15-noded plane strain model was used to simulate the soil structure. The Mohr–Coulomb (MC) model was used to simulate the soil–structure interaction at the tunnel–soil interface. An embedded beam row element was used to simulate the pile embedded in mixed soil conditions. An isotropic elastic plate element was used for modeling the existing building. A twin tunnel circular in shape was considered to be constructed underneath the building. Different tunnel locations are considered vertically and horizontally away from the building. A contraction volume loss of 0.5% during tunnel construction was adopted for analysis. The settlement of the building was found to decrease with an increase in tunnel depth from the ground surface. The settlement was also observed to decrease on moving the tunnels horizontally away from the building at a given depth. Compared to tunnel depth increment, an increase in horizontal distance between tunnels and the building has a greater influence on decreasing settlement. A 45° pressure distribution line was drawn to understand the settlement decrement pattern. Tunnel cross-sectional area overlapping with the influence region of building load was determined for each twin tunnel location. The settlement of the building was found to increase or decrease similar to the changes in the overlapping area. Differential settlements of pile group were observed in all the tunnel locations. But the difference in settlement of individual piles was found to decrease with an increase in the horizontal distance and vertical depth from the pile group.

B. Swetha (✉) · S. Sangeetha
VNR Vignana Jyothi Institute of Engineering and Technology, Hyderabad, Telangana 500090,
India
e-mail: b.swetha1828@gmail.com

P. Hari Krishna
Department of Civil Engineering, NIT, Warangal 506004, India

Keywords Pile group settlement · Existing building settlement · Tunneling · Numerical analysis · PLAXIS 2D

1 Introduction

Tunneling is being considered the best option to avoid increasing traffic congestion in urban areas. Tunnels can be used to take heavy traffic from one point in city to another so that local roads can be freed up. In practical, tunnels can rebuild the city, generate returns in long term by letting networks of roads to be born-again, and collectively improve the livability of whole urban areas. For high-rise buildings supported by deep foundations, the construction of tunnel induces ground movements, which, in turn, affect the bearing capacity as well as the settlement of the existing piles [1]. The surface settlements during the tunneling and optimum tunnel depth could be predicted based on the numerical methods that are accurate [2], economical, and time-saving. The present work was aimed to evaluate the effect of tunneling on an existing building with piled foundation [3, 4] by adopting the numerical finite element method, PLAXIS 2D [5]. For its to avail the saving time, men and machine power and accuracy for observing the deformation of soil mass while tunneling. There has been considerable research examining the behavior of the soil–tunnel–pile interaction and the possible damage to an existing piled foundation caused by tunneling. The objective of this study is to investigate the surface settlement behavior of piled foundations due to twin tunnel construction.

2 Methodology

2.1 Data Collection

A study by Raghavendra et al. [6] has given the following salient features of the Bangalore underground metro tunnel:

- The total length of the Bangalore metro line is 42.3 km, which is divided into two corridors. The first one runs along the east–west corridor extending up to 18.1 km and the other running along the north–south corridor is 24.2 km long.
- The focus of this study is confined to the underground section with a twin tunnel for a length of 4.8 km along the east–west section (See Fig. 1).
- Tunnels are bored using an inner diameter of 5.6 m which is reinforced with a concrete lining of thickness 280 mm.

The properties such as Young's modulus, Poisson's ratio, and density, for the different layers of soil in Bangalore, along with their depths, and some of the elastic properties are taken from a study conducted by Sitharam and Anbazhagan [8] based on Multichannel analysis of surface waves (MASW) survey and tabulated as shown

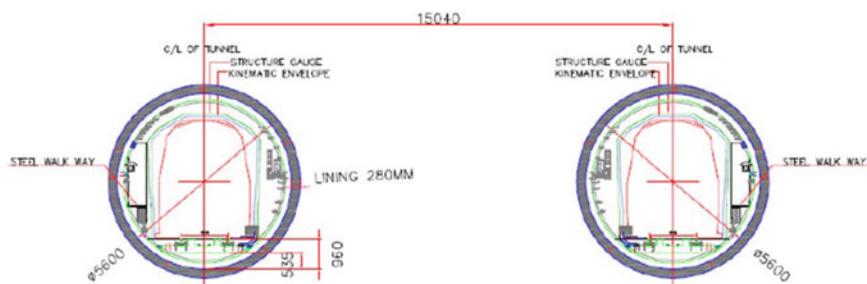


Fig. 1 Cross section of Bangalore Metro Underground Tunnel [6, 9, 10]

Table 1 Input properties of soil layers adopted in the numerical analysis

Properties	Identification				Units	Model
	Layer 1	Layer 2	Layer 3	Layer 4		
Drainage type	Drained	Drained	Drained	Drained	–	Mohr–coulomb
Unsaturated unit weight (γ_{unsat})	15	15	16	26	kN/m ³	
Saturated unit weight (γ_{sat})	16	16	17	26	kN/m ³	
Young’s modulus (E')	325×10^3	111×10^3	408×10^3	523×10^3	kN/m ²	
Poisson’s ratio (ν')	0.3	0.3	0.3	0.2	–	
Cohesion (C_{ref})	5	20	15	4000	kN/m ²	
Friction angle (φ)	35	30	35	42		
R_{inter}	1.0	1.0	1.0	1.0	–	

in Table 1. The properties of the foundation, tunnel lining, and pile foundation are given in Tables 2 and 3.

2.2 Finite Element Modeling and Boundary Conditions

Finite element plane strain model with 15 noded triangular elements was used for modeling the building which is supported by a group of 6 piles of length 10 m with a spacing of 3 m, carrying a line load of 80 kN/m², and twin tunnels with 5.6 m diameter and 15 m c/c are constructed under the preexisting building which was modeled to study the settlement behavior of the pile foundation. Preexisting elements like Elastic plate element, embedded beam row [7], and interface structures were adopted to simulate the Existing Building Structure (EBS). The model dimensions were 80

Table 2 Material properties of building plate and lining adopted in the numerical analysis

Properties	Identification		Units	Model
	Building plate	Tunnel lining		
Diameter (D)	–	5.8	m	Elastic
Thickness (t)	1	0.28	m	
Normal stiffness (EA_1)	300×10^6	351×10^6	$kN\ m^2/m$	
Flexural rigidity (EI)	25×10^6	966×10^6	kN/m	
Unit weight (γ)	25	25	kN/m^3	
Poisson's ratio (ν)	0.15	0.15	–	

Table 3 Material properties of the pile

Properties	Identification model pile (embedded beam row)	Units	Model
Diameter (D)	0.3	m	Elastic
Predefined beam type	Massive circular beam	–	
Young's modulus (E)	20×10^6	kN/m^2	
Unit weight (γ)	25	kN/m^3	
Poisson's ratio (ν)	0.15	–	
$L_{spacing}$	3	m	

$\times 40\ m$. Figure 2 shows the two-dimensional finite element model. The boundary conditions of the geometry model are enabled in staged construction mode. The boundary conditions are as follows, Boundary X_{min} : horizontally fixed, Boundary X_{max} : horizontally fixed, Boundary Y_{min} : fully fixed, Boundary Y_{max} : free.

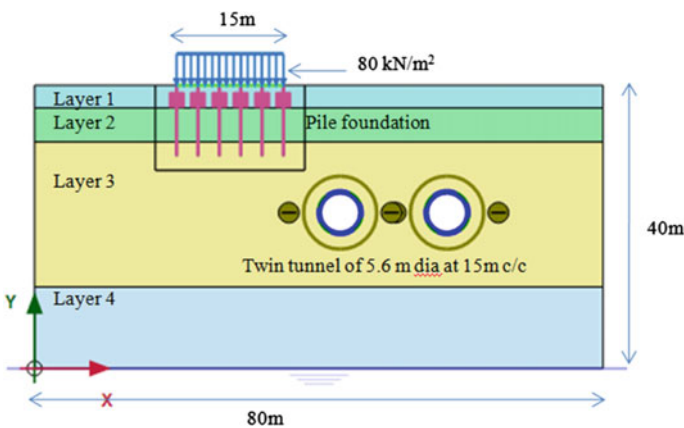


Fig. 2 The geometric model of pile foundation and twin tunnels

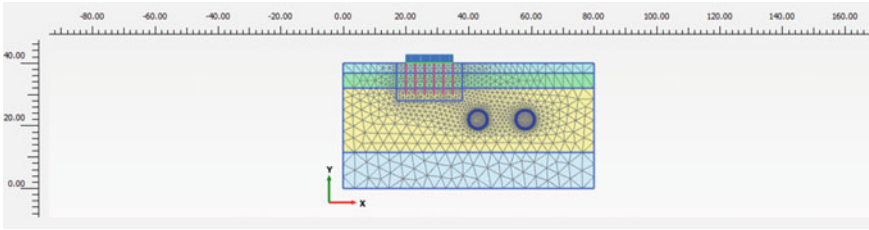


Fig. 3 The finite element mesh of the numerical model

An automated mesh was generated in PLAXIS 2D, with fineness ranging from fine to very fine mesh. In the model, very fine mesh was enabled near structures and tunnels to obtain more accurate results, and the fine mesh for the remaining model (Fig. 3) gives the automated mesh generated in numerical analysis.

2.3 Procedure of Simulation and Analysis in Staged Construction

Staged construction is a powerful PLAXIS feature that enables a realistic simulation of construction and excavation processes by activating and deactivating soil clusters and elements, application of loads, etc. This procedure allows a realistic assessment of stresses and displacements as caused (PLAXIS 2D manual), for example, soil excavation during an underground construction project.

The flowchart given in Fig. 4 shows the procedure adopted for the simulation of the model having twin tunnels construction under EBS with pile foundation.

Initially, only soil layers were in an activated state and the remaining structures were deactivated. Then the piles and building plate were activated and loads were applied to the plate. Construction of tunnel 1 was simulated by activating the tunnel lining and deactivating the soil cluster inside tunnel 1. A contraction value of 0.5%

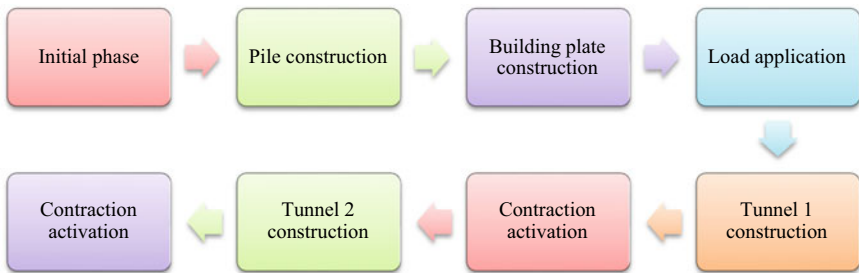


Fig. 4 Flow chart showing procedure used for simulation and analysis of project

was given for tunnel lining and was activated. Then the tunnel 2 construction process was simulated similar to that of tunnel 1.

3 Results and Discussions

The results obtained through the output window after the calculation in staged construction mode are discussed in the section. Figure 5 shows the deformation of mesh due to tunneling activity and Fig. 6 gives the intensity of settlements near tunnels and building plates.

To find the effect of twin tunnel location on pile group, the location of the tunnel was shifted in the transverse direction and vertical direction from the first pile of foundation. A contraction value of 0.5% was given to account for volume losses as per FHWA-NHI-09-010. The settlement values of the building plate were found to vary with different tunnel locations. Table 4 represents the settlement values for the tunnel location from exactly below the building and just beside the pile to 6 m away from the edge pile, and vertically 15 m from GL up to 21 m from GL. Figure 7 represents the variations of surface settlements along with tunnel depth and were explained based on the tunnel area under the influence of building load.

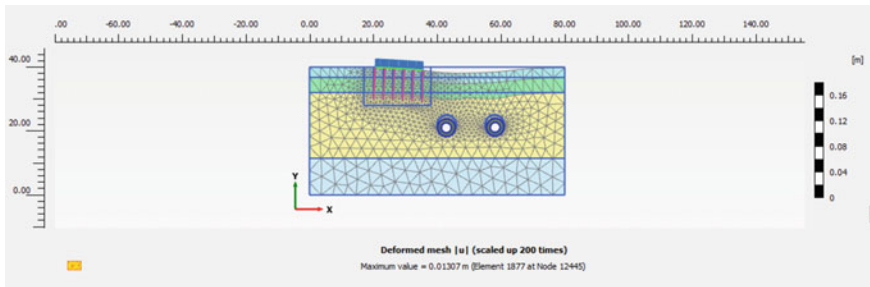


Fig. 5 Deformed mesh after performing calculation

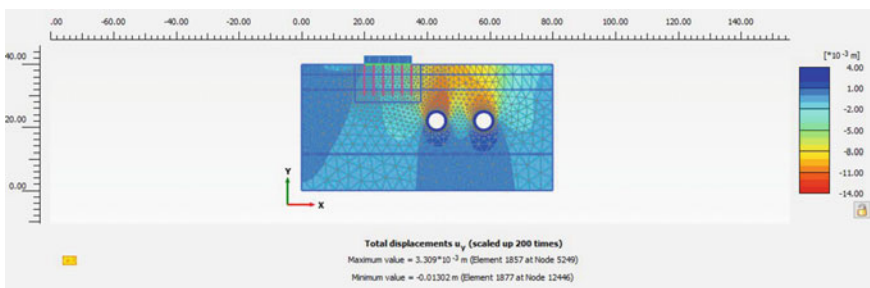


Fig. 6 Maximum settlement after calculations

Table 4 Maximum surface settlements (mm) values of building plate for different tunnels locations

Depth below ground surface (m)	Distance of tunnels from the edge of pile foundation							
	Exactly below the EBS	0 m	1 m	2 m	3 m	4 m	5 m	6 m
15	12.8	9.8	8.7	7.5	6.6	5.4	4.4	3.7
16	12.5	9.7	8.7	7.8	6.5	5.8	4.5	3.9
17	12.2	9.5	8.6	7.5	6.5	6	4.9	4.1
18	11.8	9.3	8.4	7.6	6.9	5.9	4.9	4.1
19	11.7	9.3	8.4	7.5	6.7	5.8	5.1	4.4
20	11.4	8.9	8.3	7.5	6.7	6.1	5.1	4.5
21	11	8.9	8.2	7.3	6.5	5.8	5.2	4.6

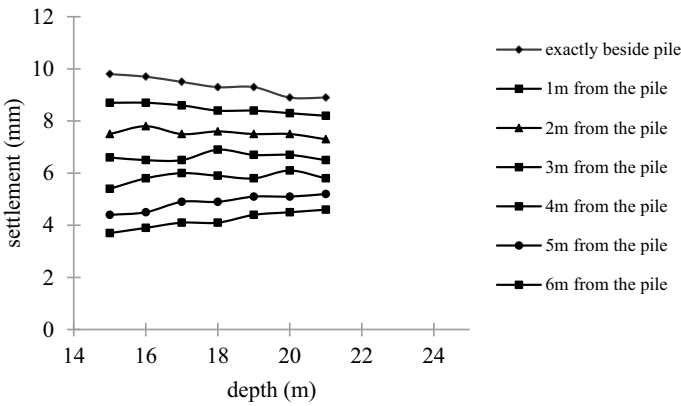


Fig. 7 Maximum surface settlement (mm) values of building plate for different tunnels locations

Figure 8 shows one of the graphs obtained for varying tunnel depths and depicts the differential settlement of piles due to varying tunnels location at 18 m depth below ground level. Similar graphs were drawn for various other depths. Table 5 gives the

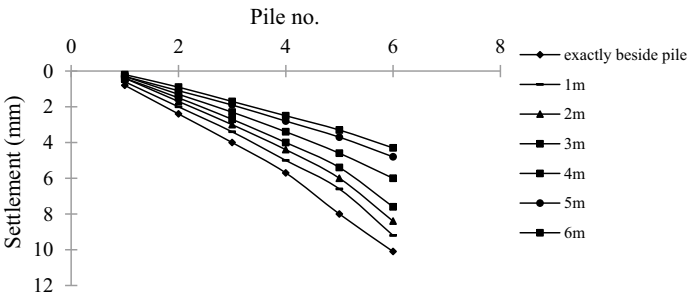


Fig. 8 Differential settlement of piles for different tunnel locations at 18 m below GL

Table 5 Distortion values of piles for 0.5% contraction value

Depth below GL (m)	Distortion values of pile for different tunnel locations						
	Beside the edge pile (0 m)	1 m	2 m	3 m	4 m	5 m	6 m
15	1/1415	1/1562	1/1829	1/2173	1/2727	1/3488	1/4054
16	1/1470	1/1612	1/1764	1/2272	1/2542	1/3409	1/3947
17	1/1546	1/1648	1/1875	1/2205	1/2459	1/3191	1/3846
18	1/1612	1/1744	1/1875	1/2083	1/2631	1/3333	1/3658
19	1/1648	1/1764	1/1973	1/2205	1/2678	1/3191	1/3658
20	1/1785	1/1875	1/2027	1/2238	1/2678	1/3125	1/3658
21	1/1851	1/1948	1/2142	1/2380	1/2727	1/3125	1/3571

calculated distortion values of piles for all tunnel locations. The distortion values were varying from a maximum of 1/1415 to a minimum 1/4054 and are within the permissible limits.

In this study, for a better understanding of the settlement values obtained from numerical analysis and to understand the increment and decrement pattern of settlements, a 45° stress distribution line is drawn from the last pile tip of the pile group to hard strata as shown in Fig. 9. For example, tunnels at 5 m horizontal distance are taken to explain the tunnel area coming under the influence of the building load area shaded in Fig. 10 for different tunnel depths. Similar drawings were made for other locations as well. It is observed that if the area of the tunnel cross section is increasing within the stress line, the settlements were observed to be increasing. This may be the reason for increasing settlement value with depth, beyond 3 m horizontal distance from the edge pile. If the area of a tunnel under the influence zone remains

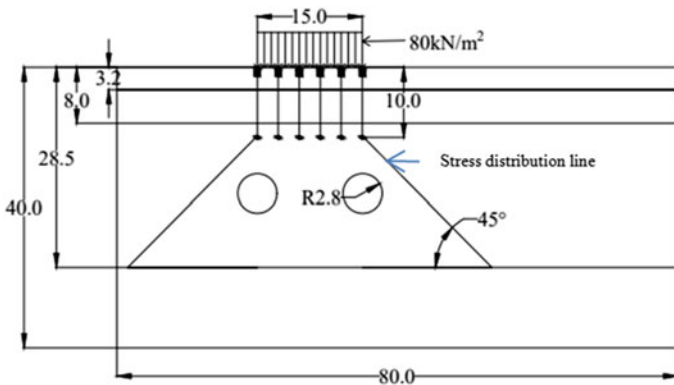


Fig. 9 A typical model showing the stress distribution line and dimensions of the model (All dimensions are in m)

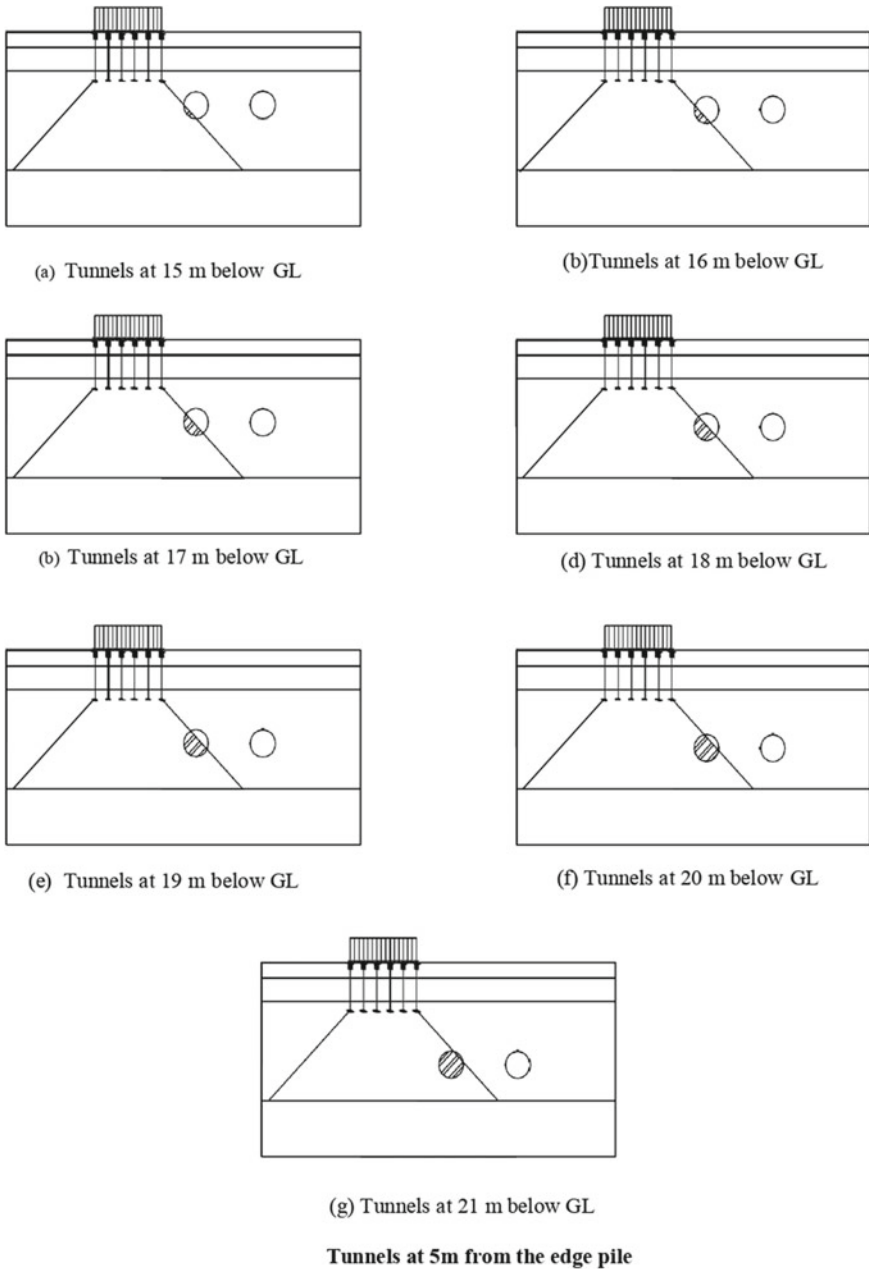


Fig. 10 Tunnel area within stress distribution region for 5 m horizontal distance from the edge pile

Table 6 Area (m^2) of tunnel cross section falling under stress distribution zone of the building for varying tunnel locations

Depth below GL (m)	Distance from the edge pile						
	0 m	1 m	2 m	3 m	4 m	5 m	6 m
15	21	17.5	13.7	9.7	5.9	2.6	0.2
16	23.7	21	17.5	13.6	7.1	5.9	2.5
17	24.6	23.7	21	17.4	13.6	9.6	5.8
18	24.6	24.6	23.7	20.9	17.4	13.5	9.6
19	24.6	24.6	24.6	23.7	20.9	17.4	13.5
20	24.6	24.6	24.6	24.6	23.6	20.9	17.3
21	24.6	24.6	24.6	24.6	24.6	23.6	20.8

constant such that the first tunnel lies entirely within the influence zone, settlements were observed to decrease with an increase in depth.

Table 6 shows the cross-sectional area of the tunnel coming under the influence region of building load for different tunnel locations. From the above table, it was observed that the area of the tunnel falling under the influence of building is decreasing with an increase in the lateral distance, but it is found to be increasing with an increase in vertical depth. The variation of building foundation settlement is found to be in line with this tunnel area under influence of building load.

When tunnels are placed exactly below the building, surface settlement decreases with an increase in depth. At a given horizontal distance of up to 3 m from the edge pile, the settlement decreases with an increase in depth. When tunnel c/s area under building influence remains almost constant, tunnel settlement decreases with an increase in depth. Beyond 3 m horizontal distance, tunnel area within building load intensity increases significantly with depth. Hence, surface settlement increases with an increase in tunnel depth. Due attention has to be given to the load distribution pattern from the building while deciding the location of the tunnel.

4 Conclusion and Recommendations

The surface settlement during the tunneling and optimum tunnel depth could be based on the analytical, empirical or numerical methods. The present work was aimed to evaluate the effect of tunneling on surrounding piled foundation structures by observing the deformation of soil mass while tunneling.

From the above study, the conclusions arrived are as follows:

- Tunnel construction causes significant settlement on the surface structure supported by a pile foundation. Settlement decreases with an increase in horizontal distance from the EBS and decreases with an increase in depth of the tunnel.

- Tunnel-induced settlement pattern of existing building structure follows the tunnel area under influence of existing building load.
- Beyond 3 m horizontal distance, the computed settlements are found to increase in depth as much of the tunnel cross-sectional area comes under the building load distribution zone.
- Differential settlements were observed on piles and are within allowable limits.
- Tunnel-induced settlement pattern of existing building structure follows the tunnel area under influence of existing building load.
- Beyond 3 m horizontal distance, the computed settlements are found to increase in depth as much of the tunnel cross-sectional area comes under the building load distribution zone.
- Care must be taken while constructing the tunnel underneath the immediate vicinity EBS foundation. The zone of influence to create surface settlement must be decided considering vertical load distribution from the EBS.
- In order to maintain the deformation of EBS within the permissible limit, the tunnel has to be located outside the building load distribution region. In the absence of an alternate route, preventive measures are to be followed to secure EBS from undesirable structural damage.

References

1. Pastore A, Bhadauria SS (2017) Numerical modelling of building response to underground tunnelling—a case study of Chennai Metro. *Int J Civil Eng* 4(10):7–17
2. Raja K, Premalatha K, Hariswaran S (2015) Influence of tunneling on adjacent existing pile foundation. *Int J Eng Res And*4(08):477–483
3. Khabbaz H, Gibson R, Fatahi B (2019) Effect of constructing twin tunnels under a building supported by pile foundations in the Sydney central business district. *Undergr Space (China)* 4(4):261–276
4. Basile F (2014) Effects of tunnelling on pile foundations. *Soils Found* 54(3):280–295
5. El-kasaby EA (2017) Numerical analysis of tunnel boring machine in soft ground. *Jokull J*
6. Raghavendra V, Jose S, Arjun Shounak GH, Sitharam TG (2015) Finite element analysis of underground metro tunnels. *IJCIET* 6(2):06–15. ISSN 0976-6316
7. Sluis J, Bos W (2013) Validation and application of the embedded pile row. *Plaxis*, (December), 10–13
8. Sitharam TG, Anbazhagan P (2006) Measurements of dynamic properties and soil profiling using multichannel analysis of surface waves. In: *Invited Keynote in 4th Karl Terzaghi Memorial Workshops (November 2016)*, p 6
9. U.S. Department of Transportation Federal Highway Administration ‘Technical manual for design and construction of road tunnels—civil elements’ Publication No. FHWA-NHI-09-010 March 2009
10. PLAXIS 2D Manual for General Information, Reference and Scientific Manual

Numerical Study of Pile Supported Embankment Resting on Layered Soft Soil



Uzma Azim and Siddhartha Sengupta

Abstract Adaption of construction on soft soil is coming into the picture with the increased demand for developing infrastructure. Since soft grounds are characterized by low permeability and high compressibility as well as low shear strength, the construction needs to be accompanied by ground strengthening methods. This paper studies settlement study of a 4 m high pile supported embankment resting on layered soft soil with respect to change in depth of pile penetration, the influence of altering slope and geometry of the embankment, effect of varied pile spacing and surcharge, variation of mesh size involved in simulation and effect of simulating model. Commercially available finite element software PLAXIS-2D was employed in the investigation. Increasing the depth of penetration of piles from 6 to 9 m resulted in a deduction in maximum displacement in the underneath soft soil layers from 0.3052 to 2.982 m due to transmission of load to a comparatively deep stiff soil layer. Decreasing the spacing between the piles from 4 m c/c spacing to 2 m c/c spacing, lowered the deformation in the soft soil layer and the time taken for consolidation due to homogenization of soil particles caused due to surcharge load and efficient load transfer platform in combination with friction acting on the surface of the piles. Also, widening the embankment and increasing the number of piles resulted in a decrease in the total displacement because of the larger area endured under an efficient load transfer platform. With regard to mesh size, fine mesh types with r_e of 0.50 gave accurate output but resulted in increased computational time due to the involvement of higher densification of elements. Therefore, a medium mesh size composed of r_e equivalent to 1.00 was employed in order to obtain desirable results in nominal time. Modified Cam Clay model (MCC) and Soft Soil model (SS) were used to perform a comparative study to observe the characteristics of soft soil with respect to the total displacement and dissipation of excess pore pressure. The total displacement when Modified Cam Clay (MCC) model was used to simulate the problem was 0.3052 m; modeling with the Soft Soil (SS) model with decreased stiffness resulted in an over prediction of the settlement to almost 3.154 m. This was attributed to the difference in the way Modified Cam Clay (MCC) and Soft Soil (SS)

U. Azim · S. Sengupta (✉)

Civil & Environmental Engineering, Birla Institute of Technology, Mesra, Ranchi 835215, India
e-mail: siddhartha@bitmesra.ac.in

model represented the failure surface on the left side of the critical state line and also on the modification in the compression indices involved in the calculation of simulating parameters. Further, the MCC model incorporates the capability of modeling the elasto-plastic behaviour of the soil medium which assists in efficiently analyzing the simulated model under hardening, softening and critical state behaviour.

Keywords Pile supported embankment · Finite element · Modified Cam Clay model · Soft Soil model · Excess pore water pressure

1 Introduction

With the increasing need for developing infrastructure in the era of paucity in land availability and increasing land costs results in the unavailability of stiff grounds for creating a firm foundation for huge roadway and railway networks. Thereby it's high time to look for sustainable construction on unpropitious ground conditions such as soft soil. But the risks involved with soft ground comprising of low bearing capacity, inadequate shear strength, high permeability and compressibility raises obstacles during and post construction activities. In order to rectify the instability of embankments during the construction phase and to safeguard long service life, various researches have been done to make soft soils compatible for construction by accompanying with other conventional construction methods or by creating a medium for transferring embankment and surcharge loads to stronger soil stratum at a deeper depth.

Al-Neami et al. [1] observed that relative density of sand was found to have a proportional effect on bending moments of pile group whereas pile spacing to diameter ratio had less effect on the same. Bagavasingam [2] analyzed the behaviour of soft clays undergoing consolidation. Sudden high settlement occurred with a sudden increase in stress whereas the application of constant stress for a considerable time leads to a decrease in the rate of instant settlement. Borthakur and Dey [3] analyzed the group capacity of micropile in weak clayey soil and concluded that the settlement to micropile cap size ratio to be the most appropriate parameter to predict the load carrying capacity and micropile cap position with respect to the ground position to be the least effective parameter. Dang et al. [4] concluded that Fibre Reinforced Load Transfer Platform (FRLTP) thickness enhanced Stress Concentration Ratio (SCR) between columns and surrounding soil thereby decreasing lateral deformation and effectively improving embankment system stability. Esmaeili et al. [5] compared two experimental models of a high embankment with and without micropiles reinforcement with respect to the bearing capacity of the embankment fill material, axial strains in the micro piles and resulting displacements. Pham and Dias [19] numerically inspected pile supported embankment by employing FLAC-3D software and concluded that in this case soil arching is the main contributor towards reducing settlements which acts on the pile cap thereby causing a deduction in the load reaching the soft subsoil layer. The arching was computed by the parameter named efficacy

given by $E_a = \frac{P_c}{(\gamma H + q)A}$, where P_c is the load acting upon the pile cap due to arching, H denotes the embankment height, A is the area influenced due to piles, q represents surcharge and γ is the unit weight of soils composing the embankment.

Fattah et al. [6] carried out experiments to record the response of pile models under the presence of cavities. Juran and Guermazi [9] studied the effect of compacted sand column reinforcement in soft soils on the settlement by performing laboratory experiments and observed that the group effect, consolidation and replacement factor caused a substantial reduction in settlement and vertical stress concentration on columns. Karim et al. [10] carried out creep analysis of soft foundation soil underlying geogrid reinforced embankment associated with Pre-fabricated Vertical Drains (PVD's) using the Modified Cam Clay (MCC) model. They distinguished between two creep analyzes:- Creep A analysis employed an elliptical yield surface and Creep B analysis was based on upgraded and modified yield surface criteria. Creep B analysis gave more accurate results for lateral displacement profile, displacement profiles and critical settlement profiles with about 3% over prediction as compared to 7% in creep A analysis. Kumar et al. [13] investigated stability, the effect of height and slope angle, stresses, strains and displacement occurring in embankments constructed of laterite soil in the Karnataka region. The results showed that strains decreased and stresses remained constant as embankment height was increased. For a constant height, steep slopes gave higher stresses and strains. Ghosh et al. [8] evaluated embankment resting on soft soil supported by columns injected with concrete. Consolidation analysis was performed to take into account the variation in soil permeability with respect to void ratio along with settlements and lateral movements in the subsoil layer. It was seen that the settlements in the columns decreased with depth and the columns resting on stiff clay layer experienced maximum shear forces and bending moments and arching caused the column heads to carry higher amount of load. Pham et al. [21] performed an analytic and numerical 3D discrete element analysis to study the contrivances involved in pile supported embankments. They concluded discrepancies between both the analysis in envisaging stress reduction ratio, efficacy and differential settlement due to the complex load transfer mechanism involved.

Moni and Sazzad [17] analyzed homogeneous and layered slopes with the shear strength reduction (SSR) technique. Rise to a certain level was seen in factor of safety (FOS) with an increase in point of application of surcharge from the crest of soil slope and beyond that the effect of surcharge remained constant. Sadaoui and Bahar [23] concluded that Young's modulus of stone columns relied upon the compaction and lateral confinement of improved soil. Said et al. [24] performed settlement analysis for soft soil reinforced by a floating soil-cement column and it was seen that the reinforcement had led to an increase in the bearing capacity and stiffness of the composite ground thereby reducing settlements. Sazzad and Haque [25] studied the effect of surcharge acting on a homogeneous slope and observed an inverse proportional relation between the factor of safety (FOS) and slope angle whereas high FOS values were obtained for low surcharge loads. Tai et al. [28] performed a parametric analysis which showed that by increasing foundation stiffness, time taken for completion of 90% degree of consolidation decreases, differential settlement

reduces and the steady stress concentration ratio increases. Zhang et al. [35] prepared 3D numerical models to carry out a comparison analysis between the deformation caused due to uniform and localized load acting on the pile supported embankment and it was observed that the soil arching effect acting on the pile cap enhanced during uniform loading conditions resulting in reduced settlements whereas it tarnished under localized loading conditions causing failure. Pham and Dias [20] prepared 25 full scale models and performed 6 series of experiments in order to analytically analyze the design of pile supported embankments. They concluded that the analytical design methodologies correctly interpret the deformation in the case of cohesionless fill soils as compared to cohesive fill materials and it is less appropriate to be employed in the case of low rise embankments. These deformities are due to inconsistent assumptions involved with respect to the subsoil support and arch shape.

Wen et al. [29] found post grouting to be effective in the improvement of skin friction of soft clay by 48.7% and 30.8% under compression and tension respectively. Wu et al. [30] concluded that maximum horizontal displacement occurred amidst the toe and center line of embankment resulting in bending failure of piles. Yan-hui et al. [32] performed experiments on soft ground enhanced by the vacuum-surcharge preloading method and concluded the rate of surcharge application to have a great impact on ground deformation. Soil parameters such as void ratio, Poisson's ratio and compression modulus also had a profound influence on the deformation characteristics. Zhang and Wang [34] prepared centrifuge model tests to observe slope stability strengthened by piles and concluded that reduced pile spacing enhanced the factor of safety of the reinforced slope. Zhang et al. [33] investigated the effect of spacing amid piles on surrounding soil press, press on top of piles and pile strain by preparing 3 different centrifugal models of cement-fly ash-gravel (CFG) pile composite foundation. The foundation was found to undergo shear failure with large pile spacing and was affected by pile quality, embankment height and cushion strength. Zhou et al. [36] summarized factors affecting the stability of uplift resistance of foundations in soft clay which included the soil's anisotropy with respect to strength, depth of soil under foundation, the type, size and shape of foundation pit. Pham [18] analytically studied geosynthetic reinforced pile supported embankment in order to understand the interaction amidst the linked elements such as foundation, granular platform, fill soil and geological media around the embankment foundation. They suggested that the overall efficacy of the system can be improved by augmenting the degree of consolidation in the subsoil, increasing the height of the embankment, rising the angle of friction in the embankment soils and reducing the subsoil modulus.

Based on the study done in the literature review with principal findings summarized in Table 1, it can be observed that with the rise in the demand to improve infrastructure and increase in land costs due to scarcity of land availability, it is an urgent need to check for alternatives for construction on soft soil preferably accompanied with other conventional construction methods. It can be seen that studies have been done to observe the stability of structures on different types of soils and to check the variance of the factor of safety under different circumstances. Research needs to be done in the area of deformation analysis underlying an embankment constructed on layered soft soil strata. A study on pile supported embankments over soft soils

Table 1 Summary of literature review

S. No.	Name of author	Description	Principal findings
1	Esmaeili et al. [5]	Prepared models with and without micropiles to observe the difference in bearing capacity of the embankment and displacements of the foundation and the embankment	Embankment settlement reduced by 40–45%, FOS increased by 30% and bearing capacity of high embankment increased by 65%
2	Fattah et al. [6]	Carried out experiments to record the response of pile models under the presence of cavities	Presence of cavities in close proximity to piles caused a reduction in soil density and shaft friction along the pile thereby decreasing the pile failure load.
3	Firat et al. [7]	Investigated the effect of soil type, height and water table level on embankment stability	Concluded that the fill properties for embankment and sub base highly affected stability. Medium semi stiff clay gave high factor of safety than soft clay fill and increasing the height of embankment lowered the factor of safety
4	Ghosh et al. [8]	Evaluated embankment resting on soft soil supported by columns injected with concrete and performed deformation and consolidation analysis	Settlements in the columns decreased with depth and the columns resting on a stiff clay layer experienced maximum shear forces and bending moments and arching caused the column heads to carry higher amount of load
5	Laskar and Pal [14]	Researched on consolidation effects due to increase in surcharge	Increasing surcharge pressures reduced the values of compression index and coefficient of consolidation for silty clayey soil
6	Leeworthy and Asr [15]	Performed a comparison study between LEM and FEM slope analysis	Each loading condition was found to affect slope stability contrarily due to varied load distribution on soil and instances of displacement decrease with an increase in load indicated a local failure in both the analysis

(continued)

Table 1 (continued)

S. No.	Name of author	Description	Principal findings
7	Manna et al. [16]	Numerically studied model slopes prepared from Yamuna sand	Observed a similar slip failure with bulging in all the models and concluded slope stability to be dependent on slope angle, soil cohesion and surcharge loads
8	Moni and Sazzad [17]	Analyzed homogeneous and layered slopes with the shear strength reduction (SSR) technique	Rise to a certain level was seen in FOS with an increase in point of application of surcharge from the crest of soil slope and beyond that the effect of surcharge remained constant
9	Pham [18]	Analytically studied geosynthetic reinforced pile supported embankment in order to understand the interaction amidst the linked elements such as foundation, granular platform, fill soil and geological media around the embankment foundation	The overall efficacy of the system can be improved by augmenting the degree of consolidation in the subsoil, increasing the height of the embankment, rising the angle of friction of the embankment soils and reducing the subsoil modulus
10	Pham and Dias [19]	Numerically inspected pile supported embankment composed of both cohesive and non-cohesive soils in order to incorporate the study of fill cohesion effect, the height of the embankment and ground elastic modulus	Soil arching effect was seen to be influenced by the fill soil cohesion by increasing the loading efficacy. The ratio of the embankment height to pile spacing, subsoil stiffness and embankment fill soil properties are the crucial parameters required to be considered while designing the depth and spacing of the piles supporting the embankment
11	Pham and Dias [20]	Prepared 25 full scale models and performed 6 series of experiments in order to analytically analyze the design of pile supported embankments	The analytical design methodologies correctly interpret the deformation in the case of cohesionless fill soils as compared to cohesive fill materials and it is less appropriate to be employed in the case of low rise embankments. These deformities are due to inconsistent assumptions involved with respect to the subsoil support and arch shape

(continued)

Table 1 (continued)

S. No.	Name of author	Description	Principal findings
12	Rajput et al. [22]	Analyzed the deformation under load in soft soil strengthened with sand piles	Bearing capacity increased to 3.25 times in comparison to that of unreinforced soil at the optimum spacing of 2.5 times the piles diameter
13	Souria et al. [27]	Experimented with various pile group configurations and analyze their impact on the lateral resistance of pile groups using numerical simulations	Battered piles had the highest group efficiency of 70–80%, followed by 60–85% for the mixed pile group and 40–80% for the vertical pile group
14	Xie et al. [31]	Performed research on combined retaining wall structure (CRS) to support an embankment constructed on a steep slope of soft soil	CRS platform effectively reduced the bending moment acting on piles and thereby prevented potential sliding

should be performed considering their impact on hastening construction and diminishing deformations. This paper addresses to the study of deformation characteristics in a pile supported embankment resting on layered soft soil strata has been studied by varying simulating parameters and doing a comparison analysis. The comparisons have been done with respect to the penetration depth of piles, the consequence of variation in geometry and slope of the embankment, spacing between piles, the effect of surcharge on the settlement characteristics, effect of employed mesh size and the model used for simulation of the soft soil.

2 Methodology

In the paper, finite element based software, PLAXIS-2D has been employed to analyze the deformation characteristics in order to study pile supported embankments resting on layered soft soil. The plot for simulation was set by fixing, the horizontal extent of 40.0 m, soft soil depth of 9.0 m with each soil layer of 3 m each and embankment height of 4.0 m. The contours for the simulation were set as $x_{\min} = 0.0$ m, $x_{\max} = 40.0$ m, $y_{\min} = -9.0$ m, $y_{\max} = 4.0$ m. The road embankment having a crest width of 20 m and side slope of 1:3 was supported by 9 pile elements with a spacing of 2 m amidst the piles (Fig. 1). The top most layer, very soft clay (shown in blue), had the weakest geotechnical properties underlain by comparatively stiffer layers of Soft clay (1) and Soft clay (2) (shown in green and yellow respectively). The properties used for the simulation were referred from [12] and are listed in Table 2. The water table was located at 1 m below the ground level in order to take into

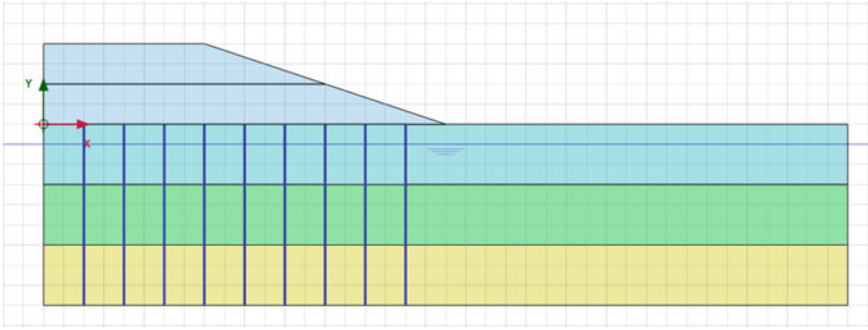


Fig. 1 Geometrical modeling of an embankment resting on pile reinforced soft soil up to base depth

Table 2 Parameters considered for embankment resting on pile supported soft soil strata

Description	Embankment fill	Very soft clay	Soft clay (1)	Soft clay (2)	Pile
Model	Mohr–Coulomb (MC)	Modified Cam Clay	Modified Cam Clay	Modified Cam Clay	Linear-elastic
Drainage	Drained	Undrained	Undrained	Undrained	–
γ_{unsat} (kN/m ³)	15	8.19	12.55	10.76	–
γ_{sat} (kN/m ³)	18.90	12.82	14.72	14.27	–
k_x (m/day)	4.32E–3	3.825E–4	1.3E–3	2.125E–4	–
k_y (m/day)	2.16E–3	1.912E–4	6.5E–4	1.062E–4	–
Λ	–	0.075	0.057	0.068	–
K	–	0.025	0.032	0.03	–
M	1.2	1.2	1.2	1.2	–
c' (kN/m ²)	10	7	10	5	–
Φ' (°)	30	27	30	30	–
ν'	0.3	–	–	–	0.3
R_{inter}	1	1	1	1	1
EA (kN/m)	–	–	–	–	7.5E6
EI (kN-m)	–	–	–	–	1E6
E (kN/m ²)	8500	–	–	–	–

Source Kasim et al. [12]. “Simulation of Safe Height Embankment on Soft Ground using Plaxis.” *Asia–Pacific Chemical, Biological & Environmental Engineering Society*, Vol 5, 152–156. And Sengupta and Azim [26]. “Numerical modelling of a pile-supported embankment”. Constrofacilitator

consideration the dissipation of excess pore pressure caused during the installation of pile elements during the staged construction method.

3 Load Transfer Mechanism in Pile Supported Embankment

The load transfer mechanism in an embankment resting on pile supported soft soil comprises of two steps of shearing resistance and soil arching. The load coming from the superstructure is partly repelled by the shearing resistance of the soft soil. Due to the stiffness difference between the materials used in pile caps and that of adjacent soil, there is a difference in the load taking capacity causing a larger concentration of load at the pile caps in comparison to the soil present in the foundation amid the pile caps which undertakes reduced stress in contrast to the overburden stress, ultimately resulting in the differential settlement at the foundation level. The stresses in granular embankment are redistributed and re-oriented to form arches. This mechanism transfers embankment load above arches and external load to the piles. This mechanism is referred to as 'soil arching' which decreases the load reaching the soft soil layers thereby reducing the settlement in the soft soil layers.

4 Numerical Simulation

After fixing the contours and incorporating the properties of the soils and pile elements, plane strain analysis was used to model the pile supported embankment in order to study the displacement and stress characteristics in the pile along with lateral movement exhibited by soil due to load application. In order to perform precise finite element calculations, the model was medium meshed and was discretized into 150 elements by keeping the relative element size (r_e) as 1.

To investigate the impact of depth of pile penetration, the embankment was made to rest on 9 m layered soft soil with the depth of each layer being 3 m. Two pile depths of 6 m and 9 m were modeled and studied (refer Fig. 2a, b) so as to study the deformation characteristics at the mid soil layer depth and the stiffest bottom most soft soil layer respectively. Consolidation analysis was adopted for the calculation of stresses in the staged construction mode of the software by taking into account the water table situated 1 m below the ground level.

To analyze the influence of variance in slope and geometry of the embankment, two embankment models were prepared to rest on the soft soil layers having the same properties. The first model incorporated an embankment with a slope of 1:3 and crest width of 40 m supported by 9 pile supports with amid pile spacing of 2 m and depth of 9 m (refer Fig. 2b). The second model was prepared with an embankment slope of 3:5 and a crest width of 60 m. Accordingly, the number of pile supports got increased

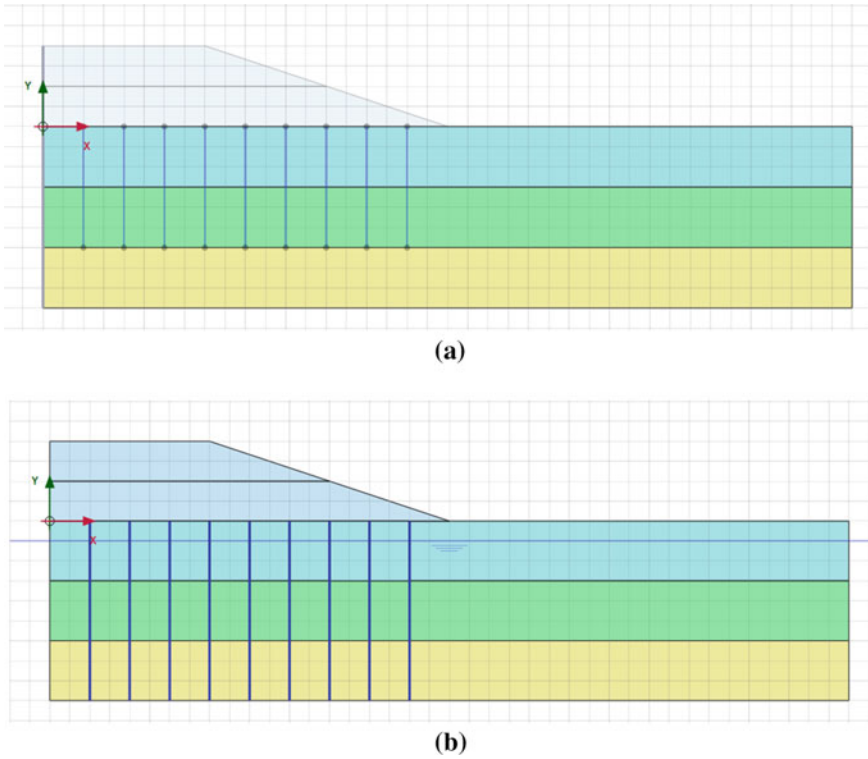


Fig. 2 Simulating geometry to study effect of depth of pile penetration **a** pile depth of 6 m **b** pile depth 9 m

to 17 with 2 m centre to centre spacing (refer Fig. 3). Water level was considered to be positioned at 1 m below the surface level so as to carry out consolidation analysis and incorporate the dissipation of excess pore pressure.

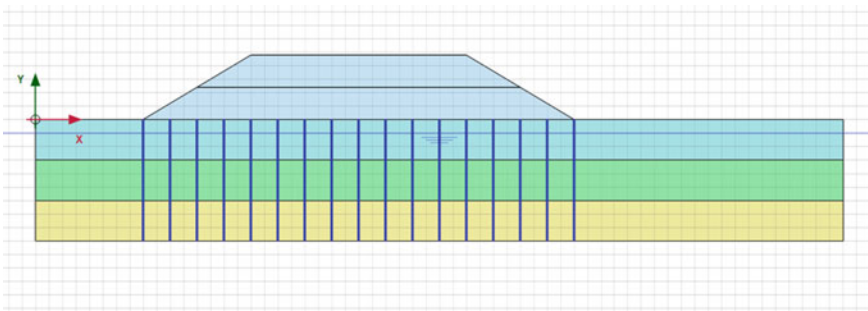


Fig. 3 Modeling of embankment with slope 3:5

Apart from the self-weight of the embankment with 1:3 slope and crest width of 40 m acting on the layered soft soil, the effect of surcharge loaded upon the embankment was taken into account along with change in pile spacing. In the case of 2 m pile spacing, 9 pile elements were considered with pile depth of 9 m and surcharge in the form of static line load was increased gradually from 10 to 150 kN/m (refer Fig. 4a) and the structure was found to fail at load of 150 kN/m. 5 pile elements of depth 9 m were considered when pile spacing was increased to 4 m and static line load was varied from 10 to 120 kN/m (refer Fig. 4b) and settlement failure was observed to occur at 100 kN/m in this case.

After drawing the geometry and assigning properties to the soil and pile elements in the soil stratigraphy mode, the finite element software PLAXIS-2D involves meshing of the structure in order to perform a precise calculation. In contemplation to study the influence of varying mesh sizes on the deformation characteristics, excess pore pressure variation and time taken for consolidation, 5 mesh sizes, namely, very coarse mesh, coarse mesh, medium mesh, fine mesh and very fine mesh, were analyzed and compared based on the meshing parameter target element size or average element size (I_e) which is globally required to generate a mesh. In the used

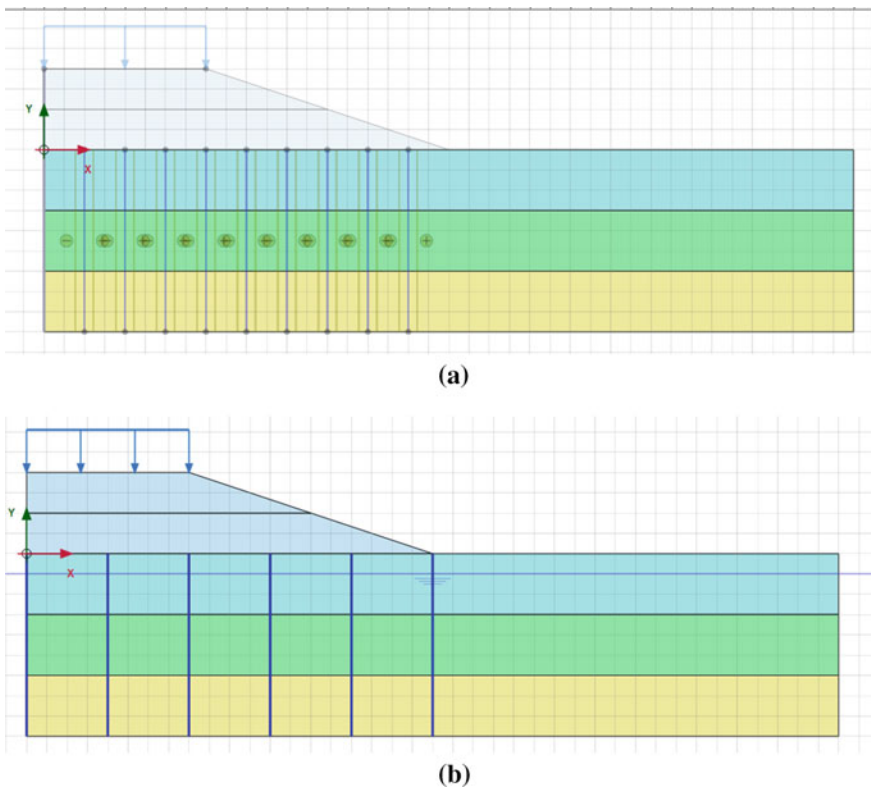


Fig. 4 Simulating model of embankment with surcharge **a** 2 m pile spacing **b** 4 m pile spacing

software, it was calculated using the outer boundary dimensions, x_{\min} , x_{\max} , y_{\min} and y_{\max} , as:

$$I_e = r_e \times 0.06 \times \sqrt{(x_{\max} - x_{\min})^2 + (y_{\max} - y_{\min})^2} \quad (1)$$

I_e is based on a parameter called ‘relative element size factor (r_e)’ referring to the ratio of the sides of the triangular mesh adopted in the software according to which the number of elements into which the model will be discretized is decided. Discretization of the model in very coarse meshing was keeping r_e as 2.00 (Fig. 5a), r_e as 1.33 for the coarse mesh (Fig. 5b), r_e was kept at 1.00 for the medium mesh (Fig. 5c), fine mesh adopted r_e as 0.67 (Fig. 5d) and r_e was kept 0.5 for very fine mesh (Fig. 5e).

To study the effect of models adopted to simulate the behaviour of soft soil, Modified Cam Clay (MCC) and Soft Soil (SS) model were employed in the analysis to model the layered soft soil. In the case of the MCC model, 3 soil layers were adopted (refer Fig. 1) and the properties involved in the analysis are summarized in Table 2, whereas for the SS model, 2 soil layers were used, Soft clay-3 and Soft clay-4 (shown in green and yellow respectively) (refer Fig. 6) and the properties were referred from Karstunen et al. [11] and are encapsulated in Table 3. The same embankment geometry was considered for both the models with a height of 4 m and slope of 1:3.

5 Results and Discussions

5.1 Depth of Penetration of Piles

Deformation analysis was done to study the settlement in embankment resting on layered soft soil with pile reinforcement resting up to 6 m of the soil strata and up to a base depth of 9 m. When the piles were made to rest at the mid soil layer at a depth of 6 m, no soil collapse occurred but a slight deviation of the end piles was observed in the deformation analysis (refer Fig. 7). At a pile depth of 9 m, the structure was analyzed to be stable as efficient load transfer took place with reduced displacement in soft soil with no displacement of piles from its original position (refer Fig. 8). The maximum deformation was reduced to 0.3052 m from 2.982 m in the case of piles resting at a depth of 6 m (refer Figs. 9 and 10). This was because the entire embankment load was supported by the pile resistance thereby decreasing the settlement.

Figure 11a shows the variation of total displacements (u) (m) with time (days) with a pile depth of 6 m. The displacement–time curve usually consists of 3 components: (a) Resulting immediate settlement during load application (b) deformation caused due to consolidation as the transpiration of excess pore pressures occurs under loads (c) Secondary consolidation settlement is restrained by the structure and soil

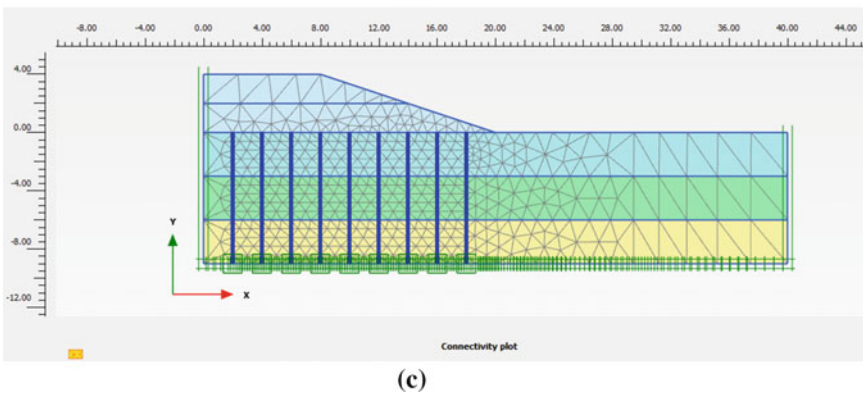
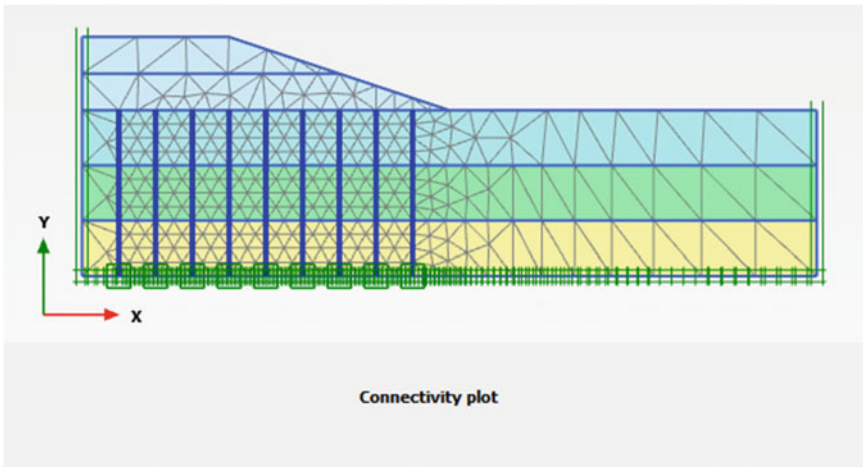
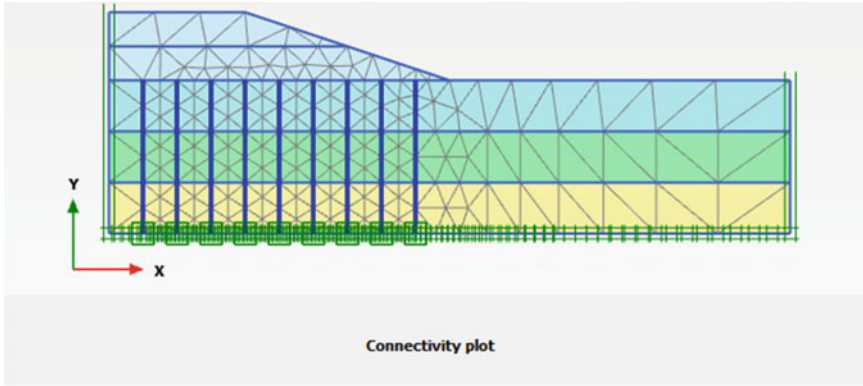
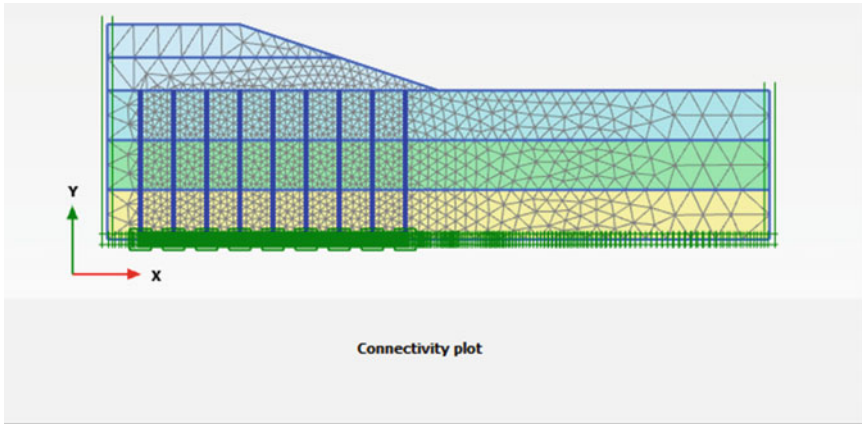
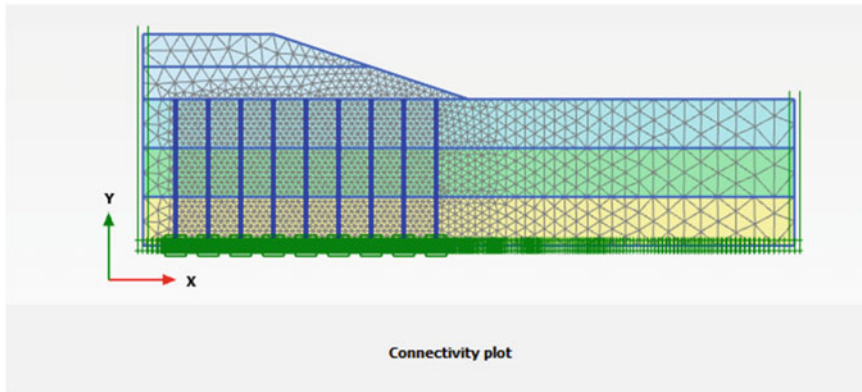


Fig. 5 Meshing in PLAXIS 2-D **a** very coarse mesh **b** coarse mesh **c** medium mesh **d** fine mesh **e** very fine mesh



(d)



(e)

Fig. 5 (continued)

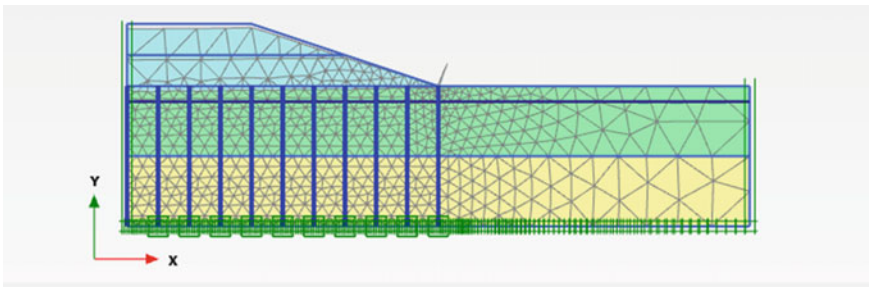


Fig. 6 Simulating geometry for soft soil modeled with SS model

Table 3 Parameters considered for embankment resting on pile supported soft soil strata simulated using Soft Soil model

Description	Embankment fill	Soft clay-3	Soft clay-4	Pile
Model	Mohr–Coulomb	Soft Soil	Soft Soil	Linear-elastic
Drainage	Drained	Undrained	Undrained	–
γ_{unsat} (kN/m ³)	15	12.55	10.76	–
γ_{sat} (kN/m ³)	18.90	14.72	14.27	–
k_x (m/day)	4.32E–3	From data set	From data set	–
k_y (m/day)	2.16E–3	From data set	From data set	–
c' (kN/m ²)	10	0	0	–
Φ' (°)	30	30	30	–
ν'	0.3	0.2	0.2	0.3
R_{inter}	1	–	–	1
E (kN/m ²)	8500	–	–	–
λ^*	–	0.24	0.24	–
κ^*	–	0.01	0.01	–
K_o^{NC}	–	0.67	0.5	–
EA (kN/m)	–	–	–	7.5E6
EI (kN-m)	–	–	–	1E6

Source Karstunen et al. [11] “Modeling the behaviour of an embankment on soft clay with different constitutive models.” *International Journal for Numerical and Analytical Methods in Geomechanics*, Vol 30, 953–982

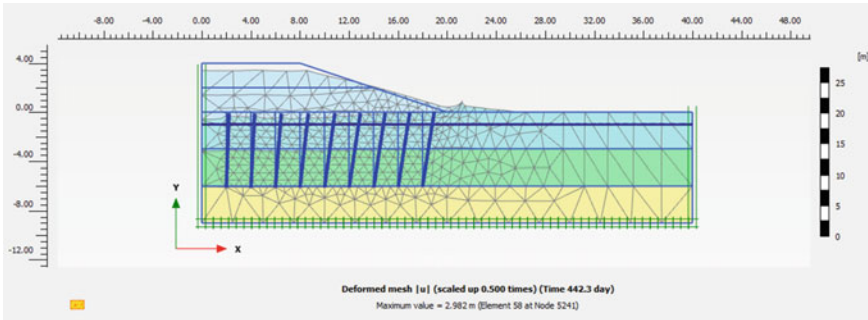


Fig. 7 Deformed mesh at pile depth of 6 m

composition. In this case, a small deviation from the original trend is observed due to the displacement of the end piles while taking the load. The graph for 9 m pile depth depicted a perfect smooth curve for the immediate settlement indicating that the load acting on the embankment was efficiently engrossed by the piles followed by the curve reaching a constant state to depict the secondary settlement state depicting complete dissipation of the excess pore water pressures (refer Fig. 11b).

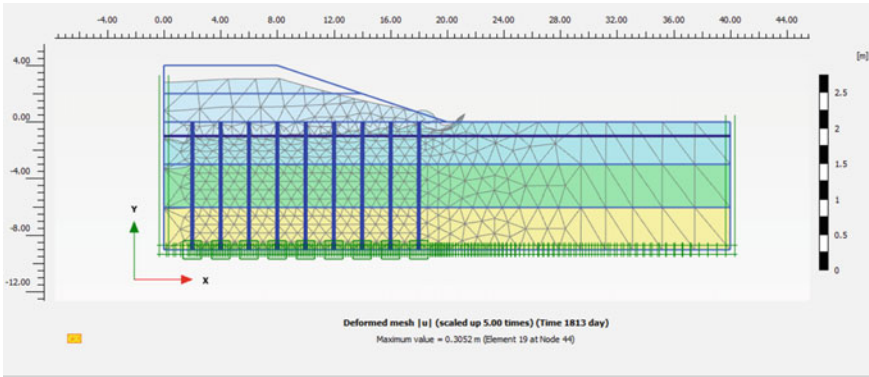


Fig. 8 Deformed mesh at pile depth of 9 m

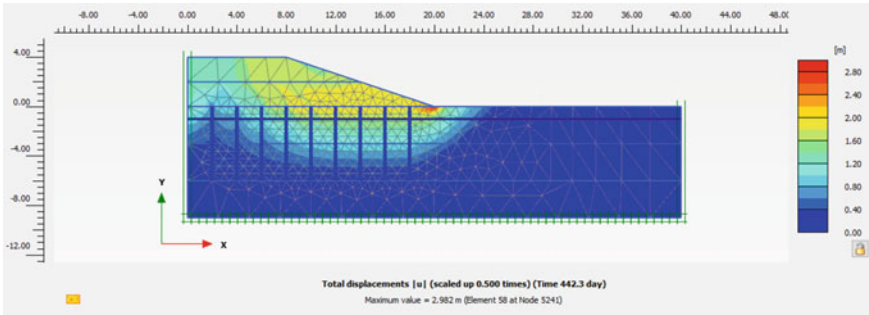


Fig. 9 Settlement distribution in the case of pile resting at a depth of 6 m

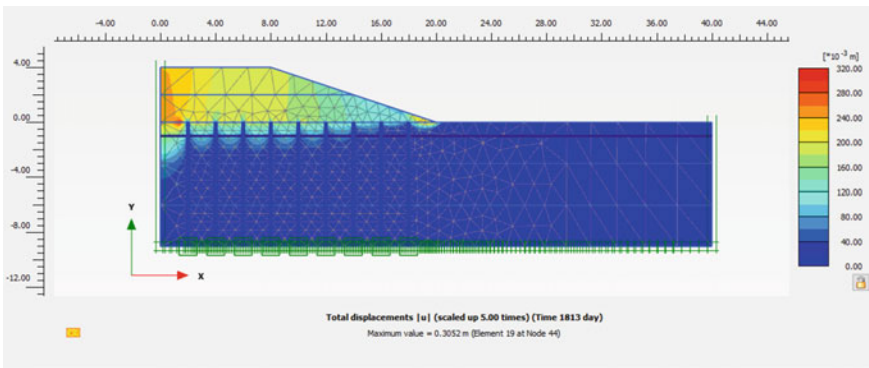


Fig. 10 Settlement distribution in the case of pile resting at a depth of 9 m

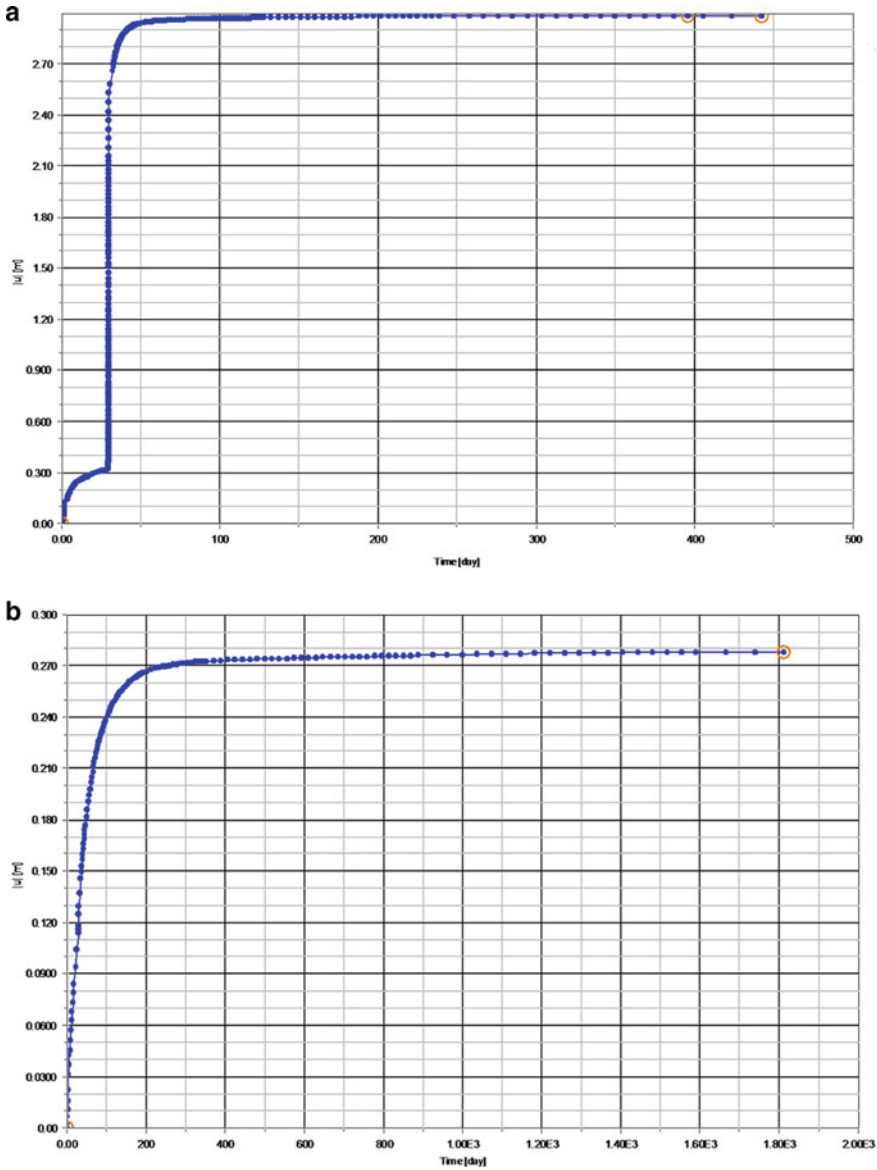


Fig. 11 Variation of total displacements (u) (m) with time (days): **a** 6 m pile depth **b** 9 m pile depth

Figure 12a, b illustrates alteration of excess pore pressure with time for pile depth of 6 m and 9 m respectively. The two peaks in Fig. 7a, symbolizes the peaks of the construction phase and consolidation phase respectively. In the case of 6 m pile depth, the maximum excess pore pressure reached was 20 kN/m² during the initial days of construction and 50 kN/m² in the consolidation phase. It took almost

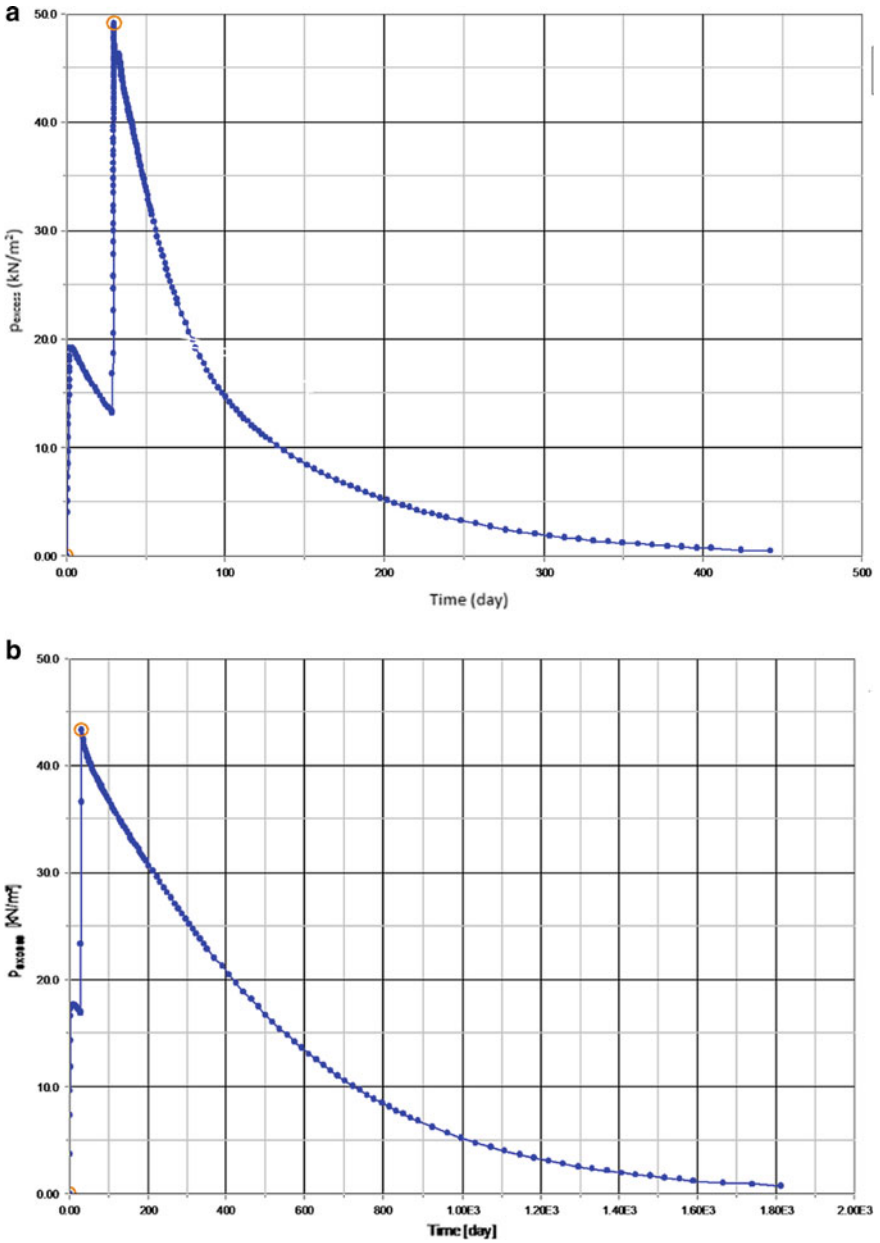


Fig. 12 Variation of excess pore pressure (p_{excess}) (kN/m^2) with time (days): **a** 6 m pile depth **b** 9 m pile depth

442.3 days to complete the consolidation phase in this simulation. The difference in excess pore pressure peaks between the construction phase and the consolidation phase was due to increased weight from the superstructure which leads to a rise in the rate of consolidation. For 9 m pile depth, the peak excess pore pressure reached during the construction phase was around 19 and 43 kN/m^2 for the consolidation phase. 1813 days were taken according to the simulation for complete transpiration of excess pore pressures thereby reducing the deformation in the soft soil strata.

Owing to the results, it can be deduced that the depth and type of soil below the level at which the pile reinforcement rests affect the settlement characteristics. This is because of the geotechnical properties of the soft soil and the strength anisotropy affecting the stability of uplift resistance offered by the soil adjoining at the pile. When the piles were at 6 m, the piles did not rest at the stiffest layer and acted as floating piles and as the load from the embankment was increased in the staged construction mode, displacement of the end piles occurred to take up the load and complete the simulation. When the piles were made to rest at 9 m, there was a reduction in the maximum displacement, as increasing the length of pile resulted in homogeneous dissemination of the settlement in the soft soil attributable to the efficient load transfer platform which caused the entire embankment load to be taken by the pile resistance.

5.2 Effect of Geometry and Slope of the Embankment

In pursuance of analyzing the effect of variation in geometry and slope of the embankment, the results of the above model of the embankment with a side slope of 1:3 (refer Fig. 1) was compared with the model of the embankment with a side slope of 3:5 supported by 17 piles and resting on layered soft soil strata bearing the same geotechnical properties as summarized in Table 2. The maximum deformation in the case of embankment with a 3:5 slope was 0.1420 m (refer Fig. 13) and 0.3052 m for embankment with a 1:3 slope (refer Fig. 10). Figure 14 depicts the distribution of plastic points in the simulation which illustrate the concentration of stresses with respect to

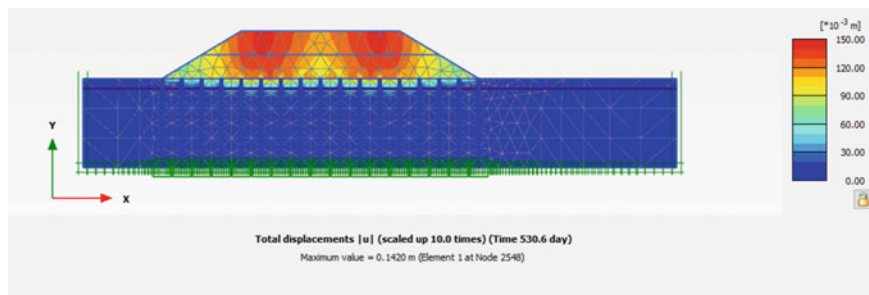
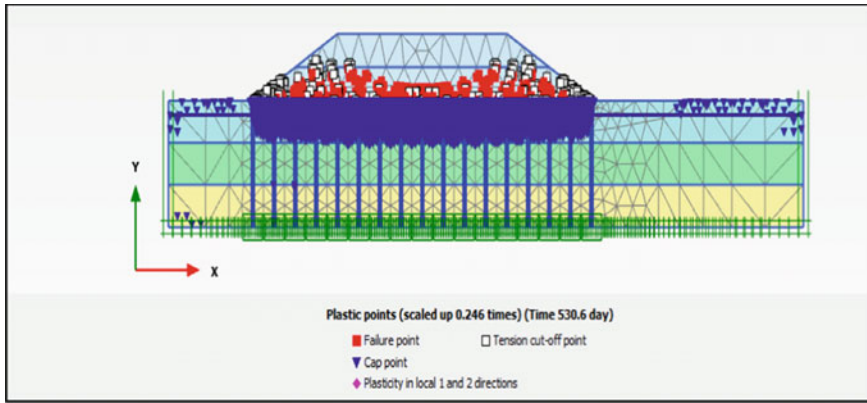
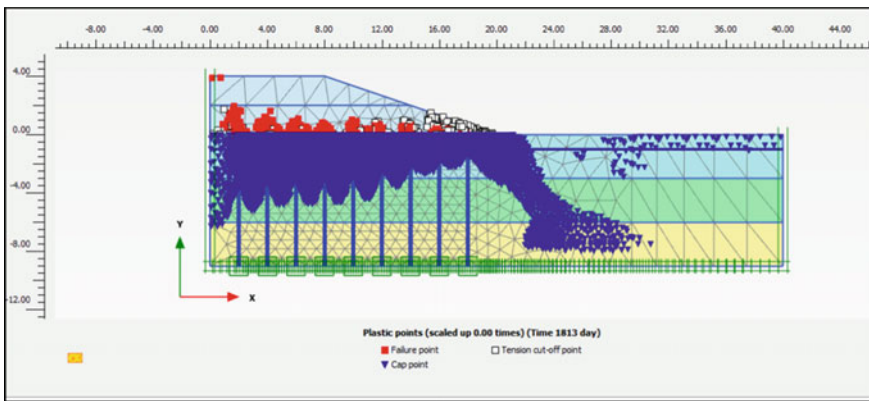


Fig. 13 Deformation analysis of embankment with 3:5 slope



(a)



(b)

Fig. 14 Location of failure points a 3:5 slope b 1:3 slope

critical failure points (shown in red), tension cut-offs (shown in white blocks) and state of consolidation (shown in blue). Embankment with a 3:5 slope showed greater uniformity in the distribution of failure points. The red failure points appropriately signified the soil arching phenomenon as the stress points were located at the pile caps. The blue cap points indicating the state of consolidation in also homogeneously distributed to indicate the p_{excess} dissipation. The tension cut off points was observed to be located at the zones of increased slope in the figure.

Therefore, the study leads to the inference that increasing the height and lateral spread of the embankment with increased slope resulted in a decrease in the total displacements. The reduction in total displacements was because by changing the geometry of the embankment, the width increased thereby increasing the number of pile supports passing through the soft soil. This increased the area available for soil arching with more efficient load transfer mechanism which resulted in evenly

distribution of the load. Researchers have also reported that the soil arching effect is responsible for the decrease in the deformation of the soft soil layers enhances with the increase in the embankment dimensions up to a certain limit.

5.3 Effect of Spacing Between Piles and Surcharge

Owing to the study of effect of variation of pile spacing on the deformation and time taken for consolidation, a 4 m high embankment was made to rest on pile supported soft soil with 2 and 4 m centre to centre spacing. Static line load acting on the embankment was increased in increments. Table 3 summarizes the results obtained by varying the pile spacing and surcharge for maximum deformation and time taken for consolidation.

It was observed that the settlement and settlement rate increases with the increase in the spacing between the piles. Increasing the number of piles by decreasing the centre to centre spacing from 4 to 2 m gave the advantage of about application of 50 kN/m static line load. This can be related to the overlapping of soil pressures resulting from lateral friction acting on the piles due to decreased spacing causing densification of soil adjoining the piles thereby magnifying the pile load taking capacity. Further, reducing the spacing between piles caused an increase in the number of piles for the same embankment width which resulted in an efficient load transfer platform by increasing the interaction mechanism between the embankment material, the piles extending from the load transfer platform to the stiff subsoil and the underlying soil medium. The homogenization of soil particles caused due to surcharge load and efficient load transfer platform in combination with friction acting on the surface of the piles accounts for the deduction in the maximum deformation in the case of pile spacing of 2 m.

From Table 4, it was also observed that the time taken for consolidation is reduced when 2 m spacing was adopted. This is because with the increase in surcharge pressure and decreased pile spacing increases the speed of pore water extraction from soil.

Table 4 Comparison of pile spacing and surcharge variation

Load (kN/m)	Maximum deformation		Time taken for consolidation	
	2 m c/c pile spacing	4 m c/c pile spacing	2 m c/c pile spacing	4 m c/c pile spacing
10	0.219 m	0.3725 m	605.5 days	1198 days
50	0.3253 m	1.319 m	670.2 days	1255 days
100	0.4353 m	25.38 m (failed)	726.9 days	1334 days (failed)
120	16.67 m	29.64 m (failed)	827.1 days	49.82 days (failed)
150	37.22 m (failed)	–	days (failed)	–

This in turn causes re-arrangement of soil particles instigating a depletion in the void ratio of the adjoining soil. This triggers a decline in the lateral movements of the consolidating soil particles along with deduction in the lateral pore water movement which reduces the time taken for consolidation. Therefore, the decreased compression and rate of consolidation in the case of increased surcharge in 2 m spacing increases the load taking capacity with less settlement in the soft soil layer.

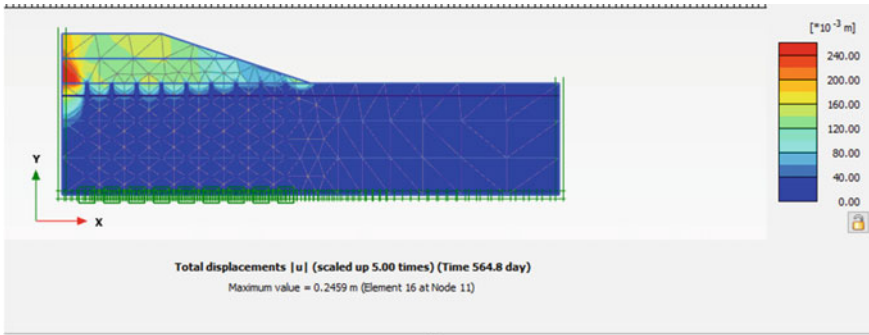
5.4 Effect of Mesh Size

Regarding the element distribution, there are 5 distinct mesh sizes, namely, very coarse, coarse, medium, fine and very fine, the analysis of which are discussed below (refer Table 5).

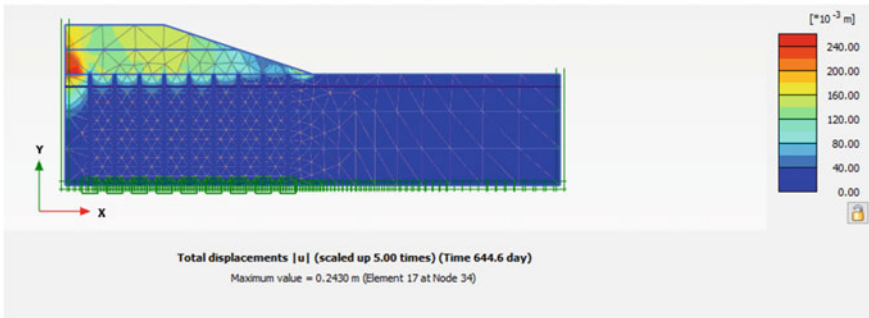
In finite element numerical analysis, different mesh sizes accounts to precision in the estimation of physical and mechanical properties of the simulated model. Figure 15a–e illustrates the deformation analysis in the different mesh sizes. It can be seen that the fine meshing with decreased element size shows a better concentration of stresses and accurate deformation (refer Table 5). It can be clearly observed that mesh size relates to the accuracy of the results. Simulating a model in fine meshing resulted in critically investigating each node for the geotechnical properties of the soils along with the interface, the pile behaviour and the configuration of each meshing node. Therefore, fine meshing gave highly accurate results due to decreased element size and increased number of elements for the simulation analysis. The only drawback associated with fine meshing is that it intensifies the complexity thereby increasing the time required for computation and therefore fine meshing is utilized when highly precise results are required. It can also lead to over-estimating the results. Coarse meshing resulted in less accurate estimation for deformation and p_{excess} analysis due to increased element size and therefore required less computational time. Therefore,

Table 5 Mesh comparison

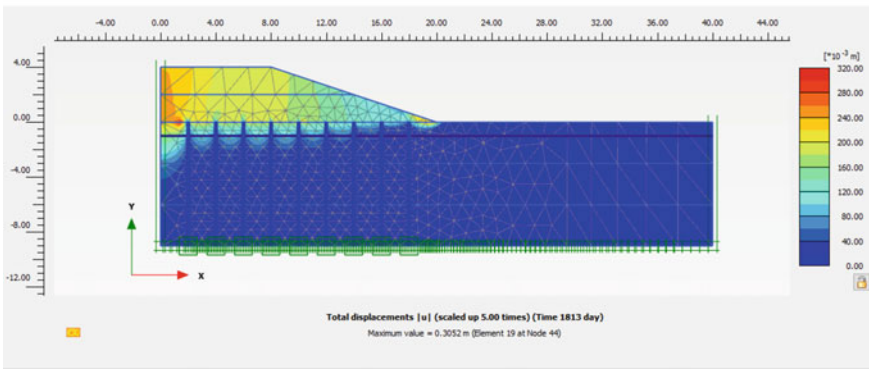
Mesh type	Relative element size	No. of elements	Maximum deformation (m)	Maximum p_{excess} (kN/m ²)	Minimum p_{excess} (kN/m ²)	Time taken for consolidation (days)
Very coarse	2.00	30–70	0.2459	6.954E–3	–0.8987	564.8
Coarse	1.33	50–200	0.2430	3.781E–3	–0.9565	644.6
Medium	1.00	90–350	0.3052	5.754E–3	–0.9229	1813
Fine	0.67	250–700	0.3019	0.9858E–3	–0.9780	774
Very fine	0.50	500–1250	0.2245	0.7456E–3	–0.8990	477.1



(a)



(b)

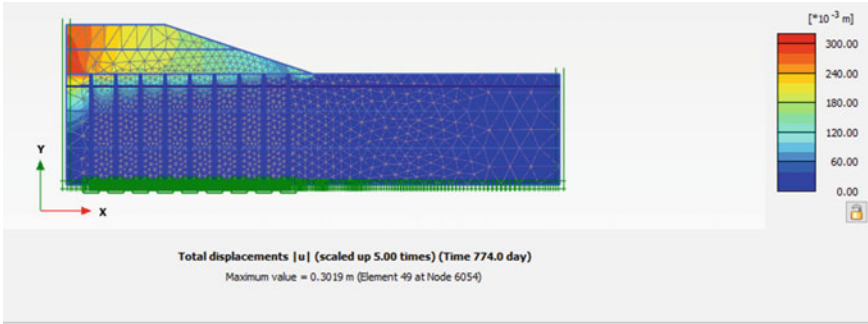


(c)

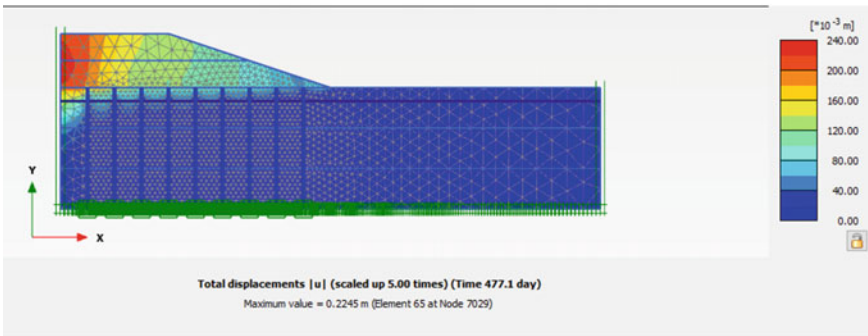
Fig. 15 Deformation analysis in various mesh sizes: **a** very coarse meshing **b** coarse meshing **c** medium meshing **d** fine meshing **e** very fine meshing

coarse meshing employed a large element size thereby reducing the finite element model's size and can be utilized for rough and quick estimation of results.

Figures 16 and 17 depict the variation of displacement (u) (m) with time (days) and excess pore pressure (kN/m²) with time (days) respectively. Increasing mesh



(d)



(e)

Fig. 15 (continued)

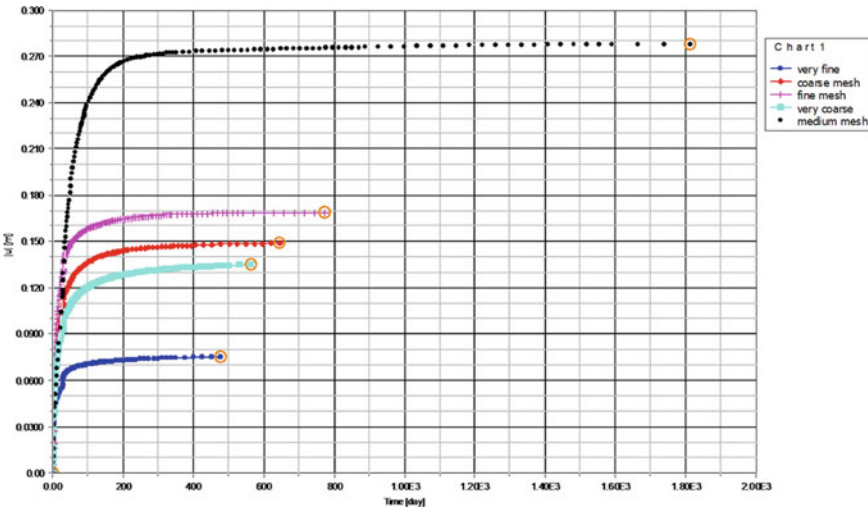


Fig. 16 Variation of displacement (u) (m) with time (days)

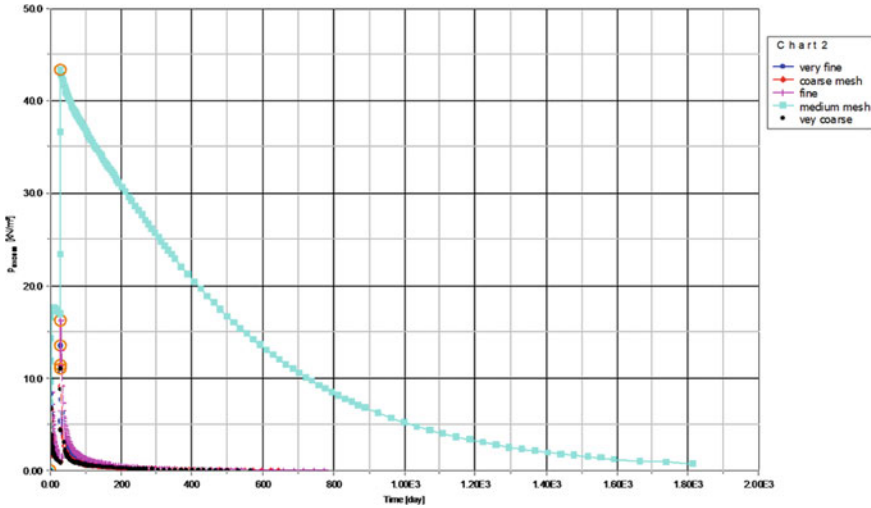


Fig. 17 Variation of excess pore pressure (p_{excess}) (kN/m^2) with time (days)

sizes showed a decrease in maximum deformation in the pile supported embankment resting on layered soft soil strata. It can be concluded that increasing mesh density leads to over-estimation of analysis whereas large element size leads to under-estimation of results in less computational time. Therefore, it is advisable to employ medium mesh to achieve the average results in normal computational time.

5.5 Effect of Simulating Models

MCC and SS models were adopted to study the effect of simulating models as both the models are designed to be used for soft consolidated clays. The difference lies in which the used parameters are computed. There exists a logarithmic relationship between void ratio (e) and mean effective stress (p') in MCC model as:

$$e - e^o = -\lambda \ln(p'/p_o) \text{ (for isotropic compression under virgin condition)} \quad (2)$$

$$e - e^o = -\kappa \ln(p'/p_o) \text{ (for isotropic unloading/reloading)} \quad (3)$$

where e : final void ratio, e^o : initial void ratio, p' : mean effective stress, p_o : stress corresponding to initial void ratio.

The SS model considers volumetric strain (ϵ_v) to vary logarithmically with changes in and mean effective stress (p') as:

$$\varepsilon_v - \varepsilon_v^o = -\lambda^* \ln\left(\frac{p' + c \cot \varphi}{p^o + c \cot \varphi}\right) \text{ (for virgin compression)} \tag{4}$$

$$\varepsilon_v - \varepsilon_v^{eo} = -\kappa^* \ln\left(\frac{p' + c \cot \phi}{p^o + c \cot \phi}\right) \text{ (for unloading/reloading)} \tag{5}$$

where ε_v : volumetric strain, c : cohesion, φ : angle of internal friction.

λ and κ denotes the indices for Cam clay compression and swelling respectively. λ^* and κ^* are Modified compression and swelling indices respectively and are attained from unloading isotropic compression test. On concocting a graph of mean stress on a logarithmic scale against volumetric strain for clayey matter, the graph is proximated to two straight lines. λ^* is derived from the gradient of the primary loading and the slope of the unloading line gives κ^* . Analogous to a specific estimate of isotropic pre-consolidation stress (p_p) there exists an enormous number of unloading and reloading lines. The peak stress level undertaken by soil is denoted by p_p . It remains constant in the course of the unloading/reloading process and hikes with stress levels during primary loading which causes irreparable plastic volumetric strains.

Table 6 enlists the comparative results obtained after modeling the soft soil layers with the two models. Simulation with the MCC model showed the settlement of the embankment material with maximum deformation of 0.3052 m (refer Fig. 10) whereas modeling using the SS model resulted in a maximum deformation of 3.154 m (refer Fig. 18). This can be due to the parameter of modified compression index (λ^*) and modified swelling index (κ^*) (refer Eqs. 2–5) been incorporated for the calculations in the SS model which employs volumetric strain for computation whereas the void ratio is used for calculating λ and κ in MCC model. Therefore, the inference drawn indicates that the SS model over-predicted the deformation and did not predict the settlement pattern in the simulation appropriately. The difference arises in the assumptions involved in the computation of the deformation behaviour on the left fringe of the critical state line. The MCC is based on elasto- plastic deformation characteristics in which the nonlinear elasticity and critical state conditions are administered by the volumetric strains thereby taking the incremental strains and deformations into account. Moreover, MCC predicts the deformation by applying

Table 6 Simulation model comparisons

Analysis	Modified Cam Clay (MCC) model	Soft Soil (SS) model
Total displacement (m)	0.3052	3.154
Maximum excess pore pressure (kN/m ²)	5.754E-3	-0.9229
Minimum excess pore pressure (kN/m ²)	0.06719	-80.68
Time taken for complete consolidation (days)	1813	957.3

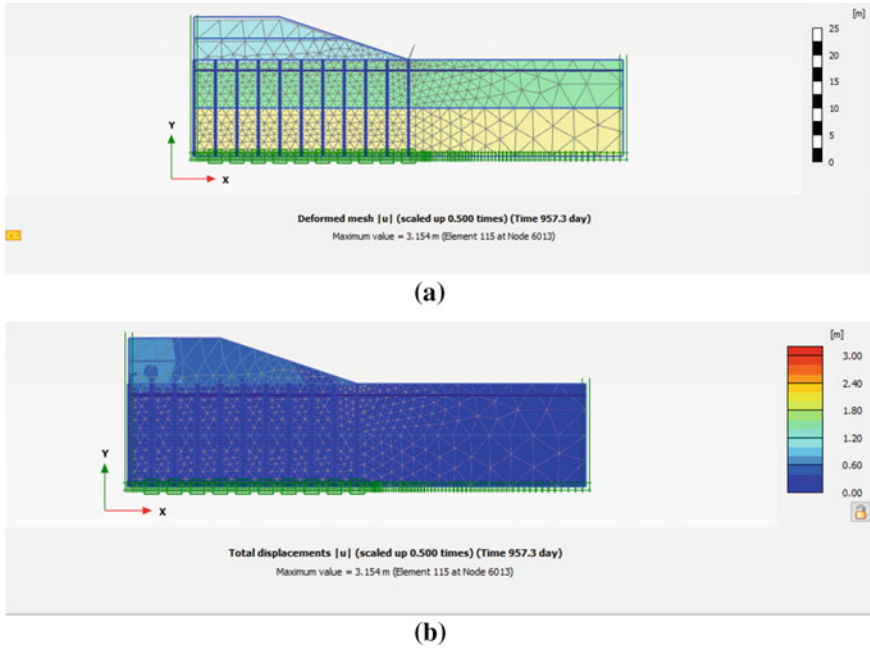


Fig. 18 a, b Deformation analysis in the case of SS model

notable strain softening whereas in the SS model the behaviour is controlled by Mohr–Coulomb failure slope and is perfectly plastic.

6 Conclusions

In this paper, pile supported embankment resting on layered soft soil was numerically studied by incorporating results of varying parameters such as pile depth, pile spacing, surcharge, slope and geometry of embankment and simulating models. The main results obtained from the analysis are summarized herewith:

1. Settlement and settlement rate increase with the increase in the spacing between the piles. This can be related to the overlapping of soil pressures resulting from lateral friction acting on the piles due to decreased spacing causing densification of soil adjoining the piles thereby enhancing the piles load taking capacity. By reducing the spacing between the piles, the rate of load penetration increases but pile-soil stress shearing ratio and negative skin friction acting on the piles decreases which result in a decrease in the load acting on the pile thereby increasing the load taking capacity by the piles.

2. Increasing the height and lateral spread of the embankment with increased slope resulted in a decrease in the total displacements due to a more efficient load transfer platform.
3. Further, increasing the depth of piles penetration resulted in efficient load transfer platform by increasing the interaction mechanism between the embankment material, the piles extending from the load transfer platform to the stiff subsoil and the underlying soil medium. The homogenization of soil particles caused due to increase in the depth of the pile resulted in efficient load transfer platform in combination with friction acting on the surface of the piles accounts for the deduction in the maximum deformation when the pile rested at 9 m.
4. Simulating a model in fine meshing resulted in critically investigating each discretized node for the geotechnical properties of the soils along with the interface, the pile behaviour and the configuration of each meshing node. As a result, fine triangular meshing gave accurate results but took more time for computation because of the increased density and complexity involved in the simulation.
5. SS model over-predicted the deformation and did not predict the settlement pattern in the simulation appropriately. The difference arises in the assumptions involved in the computation of the deformation behaviour. The mathematical reckonings involved in the MCC model critically consider the elasticity, plasticity and critical state conditions which assist in accurately interpreting the settlement in the soft soil medium.

References

1. Al-Neami MA, Samueel ZW, Al-Noori M (2019) The influence of pile groups configuration on its stability in dry sand under lateral loads. *IOP Conf Ser Mater Sci Eng* 579(1). IOP Publishing
2. Bagavasingam T (2015) Secondary consolidation and the effect of surcharge load. *Int J Eng Res Technol* 4(11):695–699
3. Borthakur N, Dey AK (2020) Evaluation of group capacity of micropile in soft clayey soil from experimental analysis using SVM-based prediction model. *Int J Geomech* 20(3)
4. Dang LC, Dang C, Khabbaz H (2017) Numerical modeling of embankment supported by fiber reinforced load transfer platform and cement mixed columns reinforced soft soil. *International Congress and Exhibition “Sustainable Civil Infrastructures: Innovative Infrastructure Geotechnology”*. Springer, Cham
5. Esmaeili M, Nik MG, Khayer F (2013) Efficiency of micro piles in reinforcing embankments. *Institution of Civil Engineers-Ground Improvement*, vol 167(2), pp 122–134
6. Fattah MY, Al Helo KH, Abed H (2017) Load distribution in pile group embedded in sandy soil containing cavity. *Korean Soc Civ Eng J Civ Eng* 22(2):509–519
7. Firat S, Işık NS, Yamak S (2018) Effect of height and water table level on stability analysis of embankments. In: *3rd International Sustainable Buildings Symposium (ISBS)*, *Geotechnique Journal* (2018). https://doi.org/10.1007/978-3-319-63709-9_43
8. Ghosh B, Fatahi B, Khabbaz H, Nguyen HH, Kelly R (2021) Field study and numerical modelling for a road embankment built on soft soil improved with concrete injected columns and geosynthetics reinforced platform. *Geotext Geomembr* 49:804–824. <https://doi.org/10.1016/j.geotextmem.2020.12.010>

9. Juran B, Guermazi A (2013) Settlement response of soft soil reinforced by compacted sand columns. *J Geotech Eng* 114(8):930–943
10. Karim MR, Manivannan G, Gnanendran CT, Lo SR (2011) Predicting the long-term performance of a geogrid-reinforced embankment on soft soil using two-dimensional finite element analysis. *Can Geotech J* 48(5):741–753
11. Karstunen M, Wiltafsky C, Krenn H, Scharinger F, Schweiger HF (2006) Modeling the behaviour of an embankment on soft clay with different constitutive models. *Int J Numer Anal Meth Geomech* 30:953–982
12. Kasim F, Marto A, Othman BA, Bakar I, Othman MF (2013) Simulation of safe height embankment on soft ground using Plaxis. *Asia-Pacific chemical, biological & environmental engineering society*, vol 5, pp 152–156. <https://doi.org/10.1016/j.apcbee.2013.05.027>
13. Kumar A, George V, Marathe S (2016) Stability analysis of lateritic soil embankment sub-grade using plaxis-2D. *Int J Res Civ Eng* 2(1). <https://www.researchgate.net/publication/313442092>
14. Laskar A, Pal SK (2017) The effects of different surcharge pressures on 3-D consolidation of soil. *Int J Appl Eng Res* 12(8):1610–1615
15. Leeworthy T, Asr AA (2020) Effects of various surcharge loading conditions on the stability of soil slopes. Loughborough's Research Repository. https://repository.lboro.ac.uk/articles/conference_contribution/
16. Manna B, Rawat S, Zodinpuui R, Sharma KG (2014) Effect of surcharge load on stability of slopes—testing and analysis. *Electron J Geotech Eng* 19:3397–3409. http://www.ejge.com/Index_ejge.htm
17. Moni MM, Sazzad MM (2015) Stability analysis of slopes with surcharge by LEM and FEM. *Int J Adv Struct Geotech Eng* 4(4):216–225
18. Pham TA (2020) Analysis of geosynthetic-reinforced pile-supported embankment with soil-structure interaction models. *Comput Geotech* 121:103438
19. Pham TA, Dias D (2021a) Comparison and evaluation of analytical models for the design of geosynthetic-reinforced and pile-supported embankments. *Geotext Geomembr* 49(3):528–549
20. Pham TA, Dias D (2021b) 3D numerical study of the performance of geosynthetic-reinforced and pile-supported embankments. *Soils Found*. <https://doi.org/10.1016/j.sandf.2021.07.002>
21. Pham TA, Tran Q, Villard P, Dias D (2021) Geosynthetic-reinforced pile-supported embankments—3D discrete numerical analyses of the interaction and mobilization mechanisms. *Eng Struct* 242:112337
22. Rajput D, Kumar R, Jain PK, Chandrawanshi S (2016) Load-settlement behaviour of soft soil reinforced with sand piles. *Int Res J Eng Technol (IRJET)* 3(11). <https://www.irjet.net/volume3-issue11>
23. Sadaoui O, Bahar R (2017) Field measurements and back calculations of settlements of structures founded on improved soft soils by stone columns. *Eur J Environ Civ Eng*, 1–27. <https://doi.org/10.1080/19648189.2016.1271358>
24. Said KN, Rashid AS, Osouli A, Latifi N, Yunus NZ, Ganiyu AA (2018) Settlement evaluation of soft soil improved by floating soil cement column. *Int J Geomech* 19(1) (2018). [https://doi.org/10.1061/\(asce\)gm.1943-5622.0001323](https://doi.org/10.1061/(asce)gm.1943-5622.0001323)
25. Sazzad MM, Haque MF (2014) Effect of surcharge on the stability of slope in a homogeneous soil by FEM. In: 2nd International conference on advances in civil engineering. <https://www.cuet.ac.bd/icace2/>
26. Sengupta S, Azim U (2020) Numerical modelling of a pile-supported embankment. *Constrofacilitator*. <https://www.constrofacilitator.com/numerical-modelling-of-a-pile-supported-embankment/>
27. Souria A, Abu-Farsakha MY, Voyiadjis GZ (2020) Evaluating the effect of pile spacing and configuration on the lateral resistance of pile groups. *Mar Georesour Geotechnol*. <https://doi.org/10.1080/1064119X.2019.1680780>
28. Tai P, Indraratna B, Rujikiatkamjorn C (2020) Consolidation analysis of soft ground improved by stone columns incorporating foundation stiffness. *Int J Geomech* 20(6). [https://doi.org/10.1061/\(ASCE\)GM.1943-5622.0001668](https://doi.org/10.1061/(ASCE)GM.1943-5622.0001668)

29. Wen L, Kong G, Li Q, Zhang Z (2020) Field tests on axial behaviour of grouted steel pipe micropiles in marine soft clay. *Int J Geomech* 20(6). [https://doi.org/10.1061/\(ASCE\)GM.1943-5622.0001656](https://doi.org/10.1061/(ASCE)GM.1943-5622.0001656)
30. Wu JT, Ye X, Li J, Li GW (2019) Field and numerical studies on the performance of high embankment built on soft soil reinforced with PHC piles. *Comput Geotech* 107:1–13. <https://doi.org/10.1016/j.compgeo.2018.11.019>
31. Xie M, Zheng J, Zhang R, Cui L, Miao C (2020) Performance of a combined retaining wall structure supporting a high embankment on a steep slope: case study. *Int J Geomech* 20(6). [https://doi.org/10.1061/\(ASCE\)GM.1943-5622.0001644](https://doi.org/10.1061/(ASCE)GM.1943-5622.0001644)
32. Yan-hui GE, Shu-cai LI, Chuan-fu L, Guo-fu S, Wang MB (2009) The settlement analysis of soft ground improved by vacuum-surcharge preloading method. In: *International conference on engineering computation*. <https://doi.org/10.1109/ICEC.2009.67>
33. Zhang J, Guo C, Xiao S (2012) Analysis of effect of CFG pile composite foundation pile spacing on embankment stability based on centrifugal model tests. *Appl Mech Mater* 178–181:1641–1648
34. Zhang G, Wang L (2017) Simplified evaluation on the stability level of pile-reinforced slopes. *Soils Found* 57:575–586. <https://doi.org/10.1016/j.sandf.2017.03.009>
35. Zhang Z, Tao F, Han J, Ye G, Liu L (2020) Numerical analysis of geosynthetic-reinforced pile-supported embankments subjected to different surface loads. In: *Geo-congress 2020: engineering, monitoring, and management of geotechnical infrastructure*. American Society of Civil Engineers, Reston, VA
36. Zhou A, Shen H, Sun J (2017) Effects of inserted depth of wall penetration on basal stability of foundation pits. *AIP Conf Proc* 1839:020012-1–020012-9

A Review on Application of NATM to Design of Underground Stations of Indian Metro Rail



Sandesh S. Barbole, M. S. Ranadive, and Apurva R. Kharat

Abstract This paper describes the advanced concepts used for the underground construction of tunnels i.e., the New Austrian Tunneling Method (NATM) in Indian Metro Rail. Many areas of Indian cities are highly congested and populated. Hence, elevated metro rail construction is not always feasible. Therefore, the Metro Rail system in India is elevated as well as underground also. Underground tunnel construction below highly congested urban area is another challenge in itself. It was constructed by using various tunneling methods. Some most popular methods used for tunnel construction in urban areas are Tunnel Boring machines (TBM), Cut & Cover Method, NATM, etc. The construction of a complete tunnel by using a single method does not only consume more time but also results in uneconomical construction. NATM is commonly adopted on both sides of underground stations for providing a safe opening for TBM launching and outbreaks. It is also used for providing cross-passage between up-line and down-line tunnels. In this paper, the methodology of applications of NATM in Indian Metro Rail is explained. The NATM method has been used to construct all underground metro tunnels in India. A comparative aspect of the construction of an underground tunnel by using NATM in Pune Metro and Mumbai Metro is also discussed in this paper. In addition, challenges like heavy groundwater seepage, application of NATM in soft ground, etc. are presented here.

Keywords New Austrian Tunneling Method (NATM) · Cut & Cover Method · Tunnel Boring Machine (TBM) · Metro stations · Cross passage

S. S. Barbole (✉) · A. R. Kharat
Rail & Metro Technology, College of Engineering Pune (COEP), Pune, India
e-mail: barboless19.pgdrmt@coep.ac.in

A. R. Kharat
e-mail: kharata19.pgdrmt@coep.ac.in

M. S. Ranadive
Civil Engineering Department, College of Engineering Pune (COEP), Pune, India
e-mail: msr.civil@coep.ac.in

1 Introduction

The first metro rail system in India was Kolkata Metro, which started in 1984. As technology was not much developed in the nineteenth century, 16.45 km of underground construction was constructed in 14 years using the ‘Cut & Cover Method’ and ‘Shield Tunneling’. ‘Elattuvalapil Sreedharan’, is a Metro Man of India who took great efforts and constructed this masterpiece. His great efforts and hard work resulted in the development of the metro rail grid in many Indian cities. Delhi Metro was the first advanced and modern metro that started its operation in 2002. It was constructed using modern technological methods like TBM and NATM. Most preferably, TBM is used for metro tunnel construction. But, for Station Construction, cross-passage construction, exit, and launching of TBM at both ends of stations, NATM is used. Furthermore, Chennai Metro, Bangalore Metro, Mumbai Metro, and Pune Metro were also constructed with these technologies and advanced concepts were used for the underground metro network [1, 2]. Currently, Kolkata Metro Rail Corporation (KMRC) is constructing underwater metro. The metro will run under the foothills of the river [3]. Now, the yellow line of the Delhi Metro is the longest underground tunnel in India with a total length of around 33–35 km with 34 metro stations [4].

Pune Metro Rail Project consists of two routes, currently, which are under construction. The first route is Pimpri Chinchwad (PCMC)—Swargate and another is Vanaz (Kothrud)—Ramvadi, the first route consists of an 8.2 km length of underground metro tunnel construction. It is constructed by using NATM, TBM, and the Cut & Cover Method. There is a total of five underground stations namely Swargate, Mandai, Budhwar Peth, Civil Court, and Shivajinagar, which are constructed by using the Cut & Cover Method. In Mumbai Metro Rail Project, the aqua line (line three) is a complete underground metro tunnel passing from Cuffe Parade Station (South Terminal Station) to SEEPZ station (North Terminal Station), which is of length 33.5 km. It is also constructed by using NATM, TBM, and the Cut & Cover Method. A description of all underground metro is given in Table 1.

Table 1 Underground Metro Rail in India

S. No.	Underground Metro Rail	Present length (KM)	Under-construction (KM)
1	Delhi Metro	48.06	41.044
2	Chennai Metro	31.3	45.81
3	Kolkata Metro	10.8	–
4	Banglore Metro	8.82	21.386
5	Mumbai Metro	–	33.5
6	Pune Metro	–	8.2

1.1 NATM Concept

The New Austrian Tunneling Method (NATM) appeared between the years 1957–1961. NATM was invented by Von Rabcewice, Pacer, and Muller-Salzburg. Their main idea was to use conventional tunneling methods by following the principles of the observation method to apply the support system. The NATM requires minimum loss of strength to avoid the softening of rock mass and it is achieved by minimum distortion of ground. Parallely, a sufficient amount of deformation of the ground is necessary to achieve a sufficient amount of strength of rock mass. In addition, there is no use of thick and stiff lining in NATM [5].

NATM is a misnomer as it is not a method but it is a concept with uniformity and sequence. NATM is used by continuous conduction of ground parameters while driving the tunnel. In NATM, the response of the already excavated portion of the tunnel is continuously monitored, and according to results, ahead tunnel construction is carried out [6]. NATM is often referred to as the “design as you go” approach of tunneling. It is not a bunch of excavation methods and support systems. More precisely it can be described as a “design as you monitor” approach but it depends on observation of surrounding rock mass, produced stresses inlining, etc. In this method, a tunnel is constructed using the open face excavation method and support system as wire mesh, rock bolt, lattice girder, etc. with shotcrete lining to provide ground support. The main aim of this method is to the utilization of strength of the surrounding ground. NATM is very useful in adverse and difficult geological ground conditions. It proves an economical as well as a less time-consuming method of tunneling in unfavorable conditions. In congested urban areas, it is the safest method for underground tunnel construction.

1.2 Elements of NATM

Following are the main elements of NATM:

1. Mobilization of the strength of rock mass.
2. Protection of tunnel by using shotcrete lining.
3. Measurements of deformations in the lining.
4. Providing flexible supports by a combination of rock bolts, wire mesh, and lattice girder.
5. Closing of inverts and creating load-bearing rings.
6. Contractual measurements for changes if necessary.
7. Rock mass classification for determination of support parameters.

1.3 Principles of NATM

Following are some of the major principles on which the NATM works:

1. First and most important principle is to take maximum advantage of the surrounding rock mass.
2. Most of the original rock strength should be retained, so the cutting of rock should not be less or more.
3. Loosening of surrounding rock mass must be avoided as maximum as possible.
4. Create triaxial condition i.e., the load distribution should continue in all directions.
5. Minimum deformation of surrounding rock mass to form supporting envelopes.
6. Preliminary support must be provided at the right moment i.e., not so early or not too late.
7. Calculation of time factor for rock mass and rock mass plus preliminary support.
8. To avoid large deformations or loosening of rock, shotcrete is provided to get active support.
9. For the least bending moment provide thin and flexible preliminary support.
10. Avoid sharp corners in profile as they develop stresses and damages surrounding rock.
11. Release the seepage pressure by drainage and filters.

2 Literature Review

Xen Ren et al. (2019), have described a case study on Beijing Subway's extensive expansion plan, the refined model is applied to Beijing Subway Line 6 project and a series of risk control measures were taken. The risk control system was shown to be effective and ensure the success of tunnel excavation. This model is believed to serve as a valuable reference for future subway construction in Beijing using NATM in the congested urban area [7].

Aejaz Ahad et al. (2019), have presented a paper on a case study on Udhampur-Srinagar-Baramulla Rail Link Project (USBRL Project) and this project hence was monitored by PMO (Prime Minister's Office). The steps in the construction of this tunnel by using the NATM method were explained according to the geology of the Himalayan Region in the described manner. Each step is described with construction details and the latest technologies used in this project. The focus is on construction steps, geological mapping, 3D Mapping, etc.

Young-Chul Han et al. (2013), have described a new tunnel load evaluation method (Ground Lining Interaction model) that was presented and discussed while considering the rock grade, tunnel depth, and in-situ stress ratio. Moreover, a new equation that evaluates the tunnel load acting on the concrete lining is proposed using the results obtained from the GLI model.

Palmstrom et al. [8], states that NATM involves a combination of several tunneling aspects from ground characterization via rock mechanics and tunnel design to construction principles, rock support design, and monitoring during tunnel excavation. The main principle of the method is, however, utilization of the bearing

capacity of the ground surrounding the tunnel. This is practically done by letting the weak ground around the tunnel deform in a controlled way by applying a flexible rock support.

Wayne Clough et al. (1992), have described that the construction process of NATM tunnels is analyzed using the finite element method. The softening technique, currently used for the analysis of NATM tunnels, is improved and applied to a parametric study of ovoid transportation tunnels constructed in undrained clays. Based on this study, a simplified method is provided for the preliminary design of the NATM tunnel support [9].

3 Geological and Geotechnical Properties

Geology plays a very significant role in the cost of a tunnel. It is important to frequently gather necessary data of tunneling after each small step. It is collected by pilot tunneling or probe drilling method. During the excavation process, the stability of the surrounding ground depends on strength of rock mass, faults zones, discontinuities in the ground, available groundwater, etc. Mostly, the worst conditions occur in soft ground, which may travel, flow, squeeze or swell.

Pune City is a part of Deccan volcanic province consisting of layers of basalt rock. Around, 7–45 m thickness of layers of basalt is occupying more than 45% of the region of Pune. The top layer is vesicular basalt rock and the bottom layer consists of massive basalt rock in this area [10]. It is a very good quality rock for construction purposes. Mumbai's geology is somewhat different from that of Pune. Mumbai is also part of the Deccan plateau. Parent rocks of Mumbai are Basalt, Breccia and Tuff. In Mumbai, the strength of rock varies in a similar grade of rock in various locations and groundwater is close to ground level [11].

Generally, geological and geotechnical parameters are studied by drilling boreholes along the alignment of the tunnel including laboratory as well as field tests. The number of boreholes and test pits is excavated, soil samples are taken out and the groundwater level is checked. Field tests conducted on-site are the Standard Penetration Test (SPT) and Plate Load Test (PLT). Laboratory tests conducted are uniaxial & triaxial tests, direct shear test, consolidation test, sieve analysis, Atterberg limit test, and chemical tests on a soil sample. After studying these tests, the properties of geological and geotechnical parameters are determined.

4 Construction Sequence of NATM

Below diagram shows the steps involved in NATM tunnel construction (Fig. 1).

Sequence of NATM tunneling is as follows:

1. Profile Making

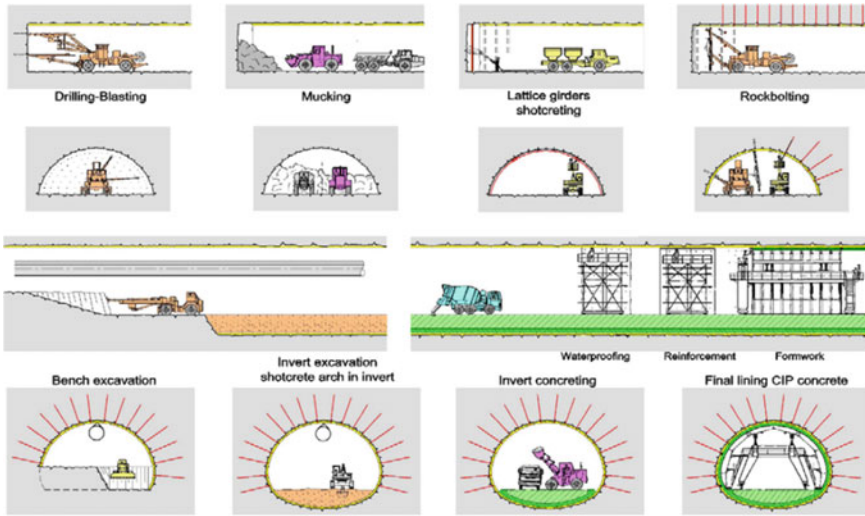


Fig. 1 NATM sequence [12]

2. Face Drilling
3. Charging and Blasting
4. De-fuming
5. Mucking
6. Scaling
7. Geological Face Mapping
8. Shotcrete Protection
9. Lattice Girder
10. Fore Poling
11. 3D Monitoring
12. Initial Lining (Shotcrete)
13. Rockbolt
14. Grouting.

5 Applications of NATM in Metro Rail

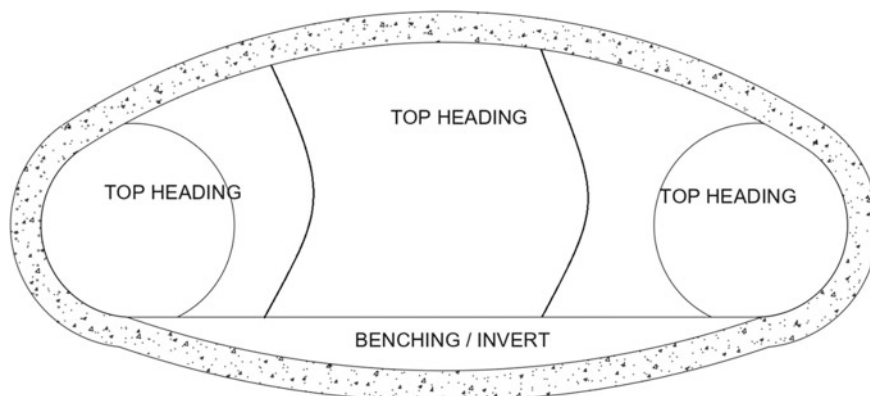
NATM is used in the underground construction of every metro rail project in India. Two metro rail systems are selected which have different geology namely Pune Metro and Mumbai Metro. In the below table (Table 2), the comparison of the application of NATM in tunneling is given briefly.

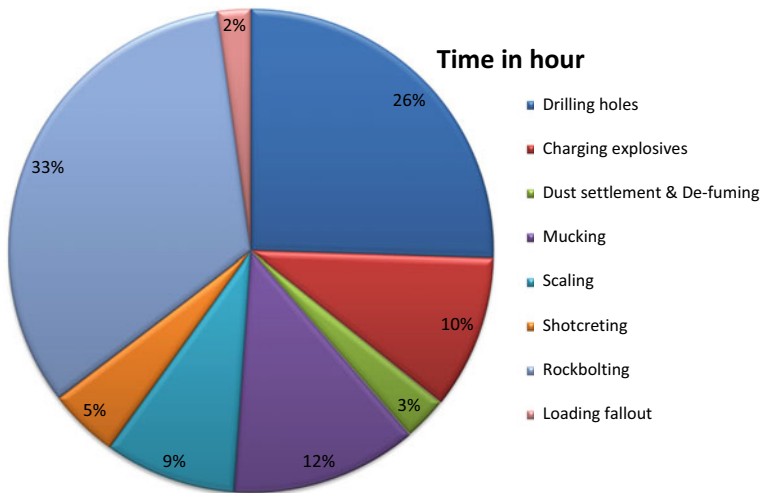
In underground metro construction, the beginning of the NATM tunnel mostly starts with the earlier construction of a vertical shaft or with a station box. The shaft is used for access of people, material, and equipment, and for the removal of muck. A typical cross-section of NATM or face of tunnel is divided into several small portions,

Table 2 Comparison of NATM in Pune and Mumbai Metro Rail Project (8, 9, 11, 12, 13, 14)

Description	Pune Metro	Mumbai Metro
Geology	Basalt Rock (Strong to moderately strong rock)	Basalt, Breccia, Tuff (Moderately strong to weak rock)
Shape of tunnel	Horizontal egg shape, 22.35 m × 7.50 m	Circular shape
Excavation method	Heading and Benching method (3 heading + 1 Benching) with Drilling and Blasting method	Heading and benching method with mechanical excavation
Explosive type	Emulsion explosive (83 and 23 mm cartridge with electric detonator)	Not used
Fore poling pipes	Dia. 101.6 and 5.4 mm thick (only at face)	Dia. 101.6 and 5.4 mm thick
Shotcrete	Wet mix, M30 grade and cylindrical strength—125 MPa	Wet mix, M30 grade and cylindrical strength—125 MPa
Rockbolt	Sn-bolts and Self-drilling (SD) Bolts, 25 mm dia.	Sn-bolts, 25 mm dia.
Wire Mesh	150 × 150 mm × 6 mm dia. of wire	150 × 150 mm × 6 mm dia. of wire
Lattice Girder	Not used	Used
Grouting	w/c ration = 0.35–0.7	w/c ratio = 0.35–0.45
Major problems	High groundwater seepage	Weak geology, risk of collapse of rockmass, water seepage with high pressure

which are excavated one by one i.e., heading and benching method as shown in Fig. 2. In Pune Metro Project, excavation is conducted in a sequence of three headings and one benching. It is proceeding in small sequential portions because; the entire face

**Fig. 2** Typical NATM profile for two-way metro tunnel



Graph 1 Activity time analysis

area is too large for simultaneous blasting. This simultaneous blasting may lead to the generation of a huge amount of vibrations, which will damage structures in the surrounding locality. The umbrella fore-poling method is used only when rock strength is weak. Either it is commonly used at the face of a tunnel to avoid the risk face falling at the beginning of tunnel operation. In Pune Metro NATM work, fore-poling is used only at the face of the tunnel.

In hard rock, ‘Drilling and Blasting Methods’ are typically used and on the weak ground, mechanical excavators like ‘Roheaders’ are used along with the heading and benching method. Basalt is typically found in Pune region, hence in Pune Metro underground construction drilling and blasting method is used for tunnel excavation. However, in Mumbai rock is basalt, breccia & tuff, which are weak rocks leading to the application of mechanical excavation for metro tunneling. Drilling of holes as per blast patterns conducted with the use of ‘Hydraulic jumbos’. This machine has one or more arms mounted with a drilling rig, which can drill vertical, horizontal, and angled holes. The drilling pattern is different for every sequential face of the tunnel. The drilling pattern and type of explosive is depended on strength of the rock, stand up time, shape & size of the tunnel, depth of the tunnel, etc. Mostly emulsion explosives are used in metro tunneling in urban areas. The blast parameters will change according to the geology at face. All pre-determined blasting patterns are subjected to change according to rock conditions encountered in the tunnel. Blasting shall take place, only when all people will discharge from the tunnel. The time required for tunnel ventilation is approx. 45 min. After de-fuming, blast holes must be checked alone by a blaster.

Scaling and trimming of the blasting profile will be done to remove loose rocks resulting from the blast and ensures the excavated profiles conform to the design

Table 3 Activity sequence and time

S. No.	Activities	Time in hour
1	Drilling holes	6.61
2	Charging explosives	2.66
3	Dust settlement and de-fuming	0.75
4	Mucking	3.23
5	Scaling	2.28
6	Shotcreting	1.21
7	Rockbolting	8.60
8	Loading fallout	0.58
	Total Time =	25.92

profile of the tunnel. Then all excavated material or muck is collected and transported out of the tunnel. Usually, geological mapping is executed before shotcreting. Depending on the data collected by geological mapping, the parameters of the support system are decided. After every excavation step, shotcreting is performed with high pressure on the tunnel surface. Shotcrete supports wire mesh, rock bolt, lattice girder, etc. It serves as arching support around the face of the tunnel. Shotcrete is usually applied in three layers, the first layer and last three layers are reinforcing with wire mesh and without wire mesh respectively. Combining all three layers makes the primary lining wall of the tunnel. After sufficient time rock bolting, lattice girder, etc. are installed at specified locations. Lattice girders are typically used of a crown shape or circumferential and are mostly used when rock quality is poor. It provides assistance in tunnel profiling and in achieving correct shotcrete thickness. In danger zones, a support system must be placed before geological mapping. The support system changes according to the strength of the rock and surrounding conditions. About 40% cost of NATM tunnel construction is required for support systems. The activities in NATM construction and the time required for it is shown below (Table 3) and analyzed graphically.

Graphical representation on the previous page shows that rock bolting and drilling require maximum time in all NATM activities. More than 50% of the time is required only for these two activities. The time required for rock bolting or drilling is totally depending on strength of the rock. More the strength of the rock more will be the time required for both activities. For the blasting purpose, a number of holes are required to drill as per the drilling pattern. One drilling pattern includes 100–1000 holes, which consumes huge time. Similarly, rock bolts are inserted in sidewalls as well as in the roof of the tunnel. So many numbers of holes are drilled into the wall and roof of the tunnel. Grouting in all holes also needs more time.

6 Comparison of NATM with Other Methods of Tunnel Excavation

There is a variety of tunneling methods used in this world. There is nothing like any single method that is the best method of tunneling. The selection of tunneling method is mostly depending on the geology of the site, choice of technology, available funds, etc. The most advanced and commonly used methods of tunneling are TBM, NATM, and the Cut & Cover Method. In the given tables (Tables 4 and 5), a comparison of NATM with TBM and Cut & Cover is described.

6.1 NATM Versus TBM

In this table (Table 4), a comparative analysis of the New Austrian Tunneling Method (NATM) with Tunnel Boring Machine (TBM) is described.

Table 4 NATM versus TBM

Description		NATM	TBM
Cross-section		Any shape can be achieved	Limited to circular shape only
Longitudinal curves		Any tunneling radius can be achieved	Tunneling radius is limited
Requirement of geological investigation		Good amount of investigation required	Way more detailed investigation is required. Lack of investigation may lead to a breakdown
Requirement of ventilation		High because of blasting activity	Less
Mechanism		Not completely mechanized	Completely mechanized
Electricity requirement		Moderately high	Very high
Automatization		Lacking as many equipments are handled manually	Completely automatized
Time	Preparation time	3–4 months	1–1.5 years
	Familiarization time	Almost negligible	3–4 months
	Performance time	2–3 to 12–15 m/day	10–50 m/day, largely depend on geology and surrounding conditions
	Breakdown time	Can be solved within a limited time	Lead to a major delay in project
Cost		Not so high cost	Very high cost

Table 5 NATM versus TBM

Description	NATM	Cut & Cover method
Diversion of traffic	Not much required	Compulsory required
Impact on environment	Less	More as it is open to ground surface
Freedom of alignment	Provides more options for an alignment	Limited options for alignment due to traffic, surface infrastructure, etc.
Dust and noise production	Less as it is surface	More as it is open to surface
Production of construction and demolition (C & D) material	Lesser quantity as compared to Cut & Cover Method	Larger quantity is needed to excavate up to the ground surface
Depth suitability	Can use as any depth	Not suitable for very deep excavations
Skilled manpower	Highly required	Not much as it is frequently in use from a long time
Cost	Less costly	More costly
Time	Consumes less time as compared to the Cut & Cover Method	Consumes more time as the volume of excavation is more

Even though TBM is costly, and required high technology and skilled people, it is preferred for metro tunneling. Because it has almost two to five times more speed of tunnel construction than other methods. However, NATM is used where highly unfavorable conditions are present.

6.2 NATM Versus Cut and Cover Method

In this table (Table 4), a comparative analysis of the New Austrian Tunneling Method (NATM) with the Cut and Cover Method is described.

NATM has many advantages over the Cut and Cover Method. NATM is a safe, less time-consuming, and economical method in an urban locality. It does not disturb surface traffic as well as there is a small possibility of disturbance or damage to the surrounding structures due to settlement.

7 Groundwater Seepage in Tunnel

It is very necessary to control groundwater seepage as continuous groundwater seepage can trigger fractures in the rock and will result in ground settlement. It will damage buildings and infrastructure in the surrounding locality. Groundwater

seepage is a problem, which cannot be avoided in tunneling. Under the presence of high groundwater table, it is very difficult to control the seepage of water. The small seepage of water can trigger the closure of pores and fractures. It will cause heavy damage to the tunnel and surrounding structures.

7.1 Countermeasures for Groundwater Seepage

Water leakage is depending on various physical attributes of the rock joints. In high water ingress areas, pre-injection or grouting is the only reasonable solution, as this process seals open joints in the rock before the water starts to flow. The objective of grouting is to fill the open voids using a liquid matter that will be harder later. Grouting creates a dry tunneling environment, which reduces the tunneling cycle and total construction time. Ultimately it leads to saving the cost of the project.

There are two main functions for the pre-grouting of tunnels:

- (a) To prevent the ingress of water into the tunnel,
- (b) To make the working of tunneling more precise. So that there will be an improvement in the rock mass quality.

There are many conditional situations in which severe water leakage problems are faced in shotcrete-lined or unlined water tunnels, which not only cause a reduction in the stability of rock mass but also create a water loss in tunneling systems. Therefore, the leakage leads to high safety risks and thus leads to an incremental economical loss of the project. Whereas, the application of the full concrete lining for the support causes a rise in the time and cost of the construction. So to reduce the leakage and prevent the rise in construction cost and time pre-grouting injection in the tunnels is the most suitable solution.

It can be categorized into either cement or chemical grout. There are various methods of grouting like open-end tube grouting, Tube a manchette grouting, double packer grouting, etc. Nowadays the use of the new technique has been increased i.e., Pre Excavation Grouting (PEG). PEG provides effective prevention of ingress of groundwater in advance of the excavation. It not only provides a dry underground environment but also improves ground stability. Modern PEG includes high-pressure injection of non-bleeding stable grout with low viscosity and fixes the water-cement ratio. In addition, the use of suitable Microfine Cement and Colloidal Silica in grouting is also quite useful and effective to avoid problems associated with groundwater.

7.2 *Interruptions to Groundwater Flow and Countermeasures*

The underground transportation system solves the problems of traffic above the surface. However, it may cause other problems in the surrounding environment. The big size of the tunnel may interrupt the flow in the aquifers at the sites. Sometimes, in NATM tunnels, walls are of higher length, or in the Cut and Cover method, deep walls secant piles are constructed. These deep and long walls of the tunnel interrupt the flow of groundwater from upstream to downstream at the site. It causes the rise and level down of groundwater at upstream and downstream sides, respectively. This change in the nature of the flow of groundwater affects the surrounding environment. It may result in excess seepage of groundwater in a tunnel. The change also leads to dehydration or the death of plants on the downstream side.

Groundwater flow prevention is very important to prevent these problems associated with flow interruption. It is necessary to collect interrupted water upstream and transport it through siphon or pipes laid in or beneath the structure and is recharged downstream. Another method is to collect groundwater in a tunnel inside the sump and discharge it at the downstream side with pumps.

8 Conclusions

Observation plays a very significant role in NATM tunnel construction as the outcomes of observations decide the NATM support system. Observations depend on data obtained from geological mapping and 3D monitoring. Analysis of tunnel profile at every face at regular intervals is a key to safe and productive NATM tunneling. NATM allows a higher amount of flexibility for fixing the alignment in a congested urban region. NATM is a safe, economic, and time-consuming method of tunnel construction. It plays a vital role in providing a safe opening for TBM launching and outbreaks. It is also used for the construction of the cross passage. The problem of high ingress of underground water is observed in every Indian Metro underground tunnel construction. The problem of water ingress can be solved by the use of applications of effective grouting.

References

1. Chaudhary P, Saha G (1995) Calcutta Metro—construction by “Cut & Cover” and “Shield Tunnelling” methods, ICI Bulletin No. 53
2. METRO RAIL: FACTS & HISTORY, Indiatimes, December 2014. <https://www.indiatimes.com/culture/travel/metro-rail-facts-history-313969>
3. Kolkata set to start India’s first Underwater Metro, Metro Rail News, January 2020. <https://www.metrotrainnews.in/kolkata-set-to-start-indias-first-underwater-metro/>

4. India's Longest Underground Tunnels of Metro Lines, Walkthrough India. <http://www.walkthroughindia.com/walkthroughs/trains/indias-longest-underground-tunnels-of-metro-lines/>
5. Springer, Chapter—7, New Austrian Tunneling Method. https://doi.org/10.1007/3-540-28500-8_7
6. Boldini D, Lackner R, Mang H (2005) Shotcrete interaction of NATM tunnels with high overburden. *J Geotech Geoenviron Eng. American Society of Civil Engineering (ASCE)*
7. Ren X, Han Y, Fu C, Liu B, Du W (2019) Management for Beijing subway tunnel construction using the New Austrian tunneling method: a case study. In: International conference on transportation and development. American Society of Civil Engineering (ASCE)
8. Palmstrom A, Stpndiat (1993) New Austrian Tunneling Method (NATM), FJELL-SPREAIKK/GEOTEKNIKK
9. Leca E, Wayne Clough G (1992) Design for NATM tunnel support in soil. *J Geotech Eng. ASCE*
10. Groundwater of Pune: an over-exploited and ungoverned lifeline, South Asia Network on Dams, Rivers, and People (SANDRP), July 2016
11. What Lies Beneath The Earth, METRO CUBE—Mumbai Metro Rail Corporation Newsletter, issues February 2018–December 2018
12. Ahmad A, Ashirwad N, Sinha M (2019) New Austrian Tunneling Method (NATM) in Himalayan Geology: emphasis on execution cycle methodology. *Int J Eng Res Technol (IJERT)* 8(06). ISSN: 2278-0181
13. Detailed Project Report (DPR) of Pune Metro Rail Project
14. Detailed Project Report (DPR) of Mumbai Metro Rail Corporation Ltd (MMRCL)
15. Pune Metro: Official site of Pune Metro Rail Project. www.punemetrorail.org
16. Official site of Mumbai Metro Rail Corporation Ltd (MMRCL). www.mmrc.com
17. Metro dig tells the story of the ground beneath our feet, December 2016. http://timesofindia.indiatimes.com/articleshow/55881989.cms?utm_source=contentofinterest&utm_medium=text&utm_campaign=cppst

Slope Stability Analysis of Artificial Embankment of Fly Ash and Plastic Recycled Polymer Using Midas GTS-NX



Prajakta S. Chavan, Kalyani G. Patil, and Sariput M. Nawghare

Abstract Artificial embankments are constructed to make provisions for infrastructure such as roads, railways, canals and to protect low lying ground from flooding. The slope stability analysis of the embankments should be carried out to know the nature of the underlying material. Careful study and consideration of topographic features along with the site investigation, testing, sampling, modelling monitoring and slope stability analysis is required for the construction of any artificial embankment. In this study, an artificial embankment of fly ash and recycled plastic polymer (RPP) is analysed. The plastic recycled polymers were mixed with fly ash at different proportions to inspect its influence on the slope stability of the artificial embankment. The fly ash was mixed with various proportions of plastic recycled polymers, i.e., with 0, 25, 50 and 75%. In this regard, the laboratory study included Atterberg limits, standard proctor test, unconfined compressive strength, and direct shear test. The various parameters (modulus of elasticity, cohesive strength, internal angle of friction, unit weight, saturated unit weight) of embankment mix were obtained from the experimental testing. The slope stability of the artificial embankment of fly ash and recycled plastic polymers analysed using MIDAS GTS-NX software. MIDAS GTS-NX is a FEM based modelling software which carries out slope stability analysis by the strength reduction method. Embankment models of only fly ash and fly ash with recycled plastic polymer mix have been accounted and simulated using MIDAS GTS-NX software to understand the failure mechanism and the changes in factor of safety. The maximum factor of safety is obtained at a mix percentage of 50% of recycled plastic polymer with fly ash. Further increase in the polymer content decreases the overall factor of safety of the artificial embankment.

P. S. Chavan (✉) · K. G. Patil · S. M. Nawghare
Civil Engineering Department, College of Engineering Pune, Pune, India
e-mail: chavanprajakta21@gmail.com

K. G. Patil
e-mail: kalyanigpatil12@gmail.com

S. M. Nawghare
e-mail: smn.civil@coep.ac.in

Keywords Slope stability · Finite element method · Fly ash · Plastic recycled polymer · MIDAS GTS-NX

1 Introduction

Slope stability problems are extensively important in engineering applications and notably within the construction and operation of surface transportation facilities. The stability of the fill slopes, natural slopes, embankments, and excavations are the crucial issues not only for geotechnical designing but also important in assessing the effect of these phenomenon on safety of humans. Slopes fail consequently due to the soil strength and faulty slope geometry. In some cases, the slope cannot sustain disturbing forces resulting from soil weight and surcharge loads, high groundwater conditions or seismic loading. In order to quantify stability of any slope, the general factor of safety is appropriated. Factor of safety (F.O.S.) is ratio of the sum of maintaining forces (friction, cohesion of the material) to the sum of disturbing forces (gravitation and filtration forces). Based on the value of this ratio, we can approximate the stability of the slope or embankment into consideration as follows:

$$\text{F.O.S} = \frac{\text{Shear strength of soil}}{\text{Shear stress required for sliding}} \quad (1)$$

- F.O.S. < 1—unstable slope/unstable embankment
- F.O.S. = 1—slope/embankment in temporal stability
- F.O.S. > 1—stable slope/stable embankment.

Conversely, in India, the disposal of fly ash has become an issue of concern [1]. Our country largely depends on thermal power plants for production of energy. Such thermal power plants are largely coal based. Hence, fly ash disposal issue will be the topic of apprehension for the years to come. The residual fly ash is disposed of in places, which creates a menace of land management and danger to human health. Plastic waste is also becoming extremely threatening to the environment as they are generated in high quantities and jeopardize the environment and its inhabitants [2, 3]. Therefore, this study is intended considering both these issues. The stability of the artificial embankment of plastic polymer and fly ash thus proposed is analysed by using MIDAS GTS-NX software and the failure reports are studied.

Table 1 Fly ash: physical properties

S. No.	Property	Value
1	Specific gravity	2.18
2	Maximum dry unit weight	12.20 kN/m ³
3	Optimum Moisture Content (OMC)	18.6%
4	Young's Modulus of elasticity (E)	4200 kN/m ²
5	Cohesion (c)	23.14 kN/m ²
6	Angle of internal friction (ϕ)	20.4 ⁰
7	Coefficient of uniformity (cu)	15
8	Coefficient of curvature (cc)	1.45
9	Poisson's ratio (μ)	0.27
10	Unit weight (γ)	14.47 kN/m ²
11	Saturated unit weight (γ_{sat})	16.41 kN/m ²
12	D ₆₀	0.045 mm
13	D ₃₀	0.014 mm
14	D ₁₀	0.003 mm
15	Liquid limit	23.6%
16	Plastic limit	NP

2 Materials

2.1 Fly Ash

Fly ash is a waste by-product extracted by mechanical or electrostatic precipitator, obtained from coal-based power plants. Fly ash consists of alumina, silica, and iron. Fly Ash of class F was obtained from Tata thermal power plant, Trombay, Mumbai for the experimental program. The fly ash sample was screened through a 12 mm sieve, to get rid of the foreign materials, vegetation, and other deleterious material. The samples were dried in the oven for about 24 h before any further usage [4]. Table 1 represents the physical properties of the fly ash used.

2.2 Plastic Recycled Polymer

Plastic recycling is the process of recovering waste plastic material and converting them into useful products. Basically, all types of plastic can be recycled except those made from recycled plastics are usually unrecyclable. Plastic Recycled Polymers (PC) employed in the research lab work were obtained from R R Petroplast Pvt. Ltd., Pune. These are produced by reprocessing plastic waste from organic

Table 2 Specification of plastic recycled polymers

S. No.	Parameter	Specification
1	Type	Recycled plastic polymer
2	Colour	White and Yellow
3	Diameter (mm)	3.0
4	Specific gravity (<i>G</i>)	2.154
5	Density (kg/m ³)	1300

compounds producers, molders, extruders, fabricators, and utilization corporations. The properties of recycled plastic polymer (RRP) are mentioned in Table 2.

3 Methodology

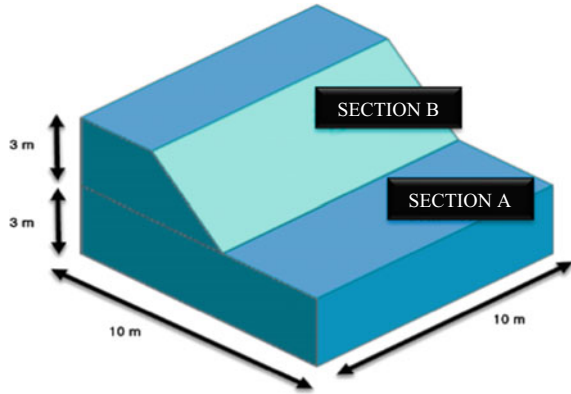
3.1 Laboratory Testing

In order to obtain parameters required for slope stability analysis, series of tests were conducted on fly ash with various proportions of recycled plastic polymer, i.e., 25, 50, and 75%. During the conduction of experimental laboratory tests, following Indian Standard codes [5] were followed:

- (i) Standard Proctor Test—IS: 2720 (Part 7)—1980
- (ii) Unconfined Compressive Strength (UCS) Test—IS: 2720 (Part 10)—1991
- (iii) Direct Shear Test—IS: 2720 (Part 13)—1983
- (iv) Unconsolidated Undrained Test—IS: 2720 (Part 11)—1993
- (v) Permeability Test—IS: 2720 (Part 17)—1986
- (vi) Liquid limit and Plastic limit test—IS: 2720 (Part 5)—1985.

3.2 Midas GTS-NX

The experimental results are typically accurate and reliable since they replicate the precise behaviour of the tested structure. It is an incontrovertible fact that the experimental testing of structures is time overwhelming and expensive. Therefore, it is desirable to rely on numerically simulated models which might replace the experimental investigation in a fairly accurate manner. Finite Element Method (FEM) could be a sensible choice for the numerical simulation of complex structures. Midas GTS-NX software is based on the finite elements method (FEM). It is accustomed to simulate actual phenomena occurring within the soils. Midas GTS-NX software uses the Strength Reduction methodology to deduce the kind and reason behind slope failure [6]. In the strength reduction methodology, the shearing strength of the soil material is decreased gradually, till the point where convergence does not occur [7,

Fig. 1 Embankment model

8]. This point is taken into consideration and the maximum decrease in the strength of that soil material is considered as the least factor of safety.

4 Embankment Model Description

4.1 Geometry of Embankment

Geometric details of the embankment are shown in Fig. 1. The overall length of section A and B is 1000 mm. The width of section A is 1000 mm, and its depth is 300 mm. The top width of section B is 300 mm, and the bottom width is 600 mm. The angle of slope is 45° .

4.2 Material Properties

The summary of properties of the materials comprising the artificial embankment used for the stability analysis are mentioned in Table 3.

Table 3 Artificial embankment: material properties

S. No.	Mixture	Modulus of elasticity (kN/m ²)	Poisson's ratio (μ)	Unit weight (kN/m ³)	Saturated unit weight (kN/m ³)	Cohesion 'c' (kN/m ²)	Friction angle ' ϕ '
1	Fly ash only	4200	0.27	14.47	16.41	23.14	20
2	Fly ash + 25% RPP	5200	0.32	16.45	16.98	17.65	27
3	Fly ash + 50% RPP	5200	0.32	17.39	16.97	12.94	39
4	Fly ash + 75% RPP	5200	0.32	16.32	16.98	16.47	29

Table 4 Midas GTS-NX slope stability analysis results

S. No.	Material	Factor of safety (FOS)	Maximum displacement (mm)
1	Fly ash only	0.9672	451.343
2	Fly ash + 25% RPP	1.2680	693.701
3	Fly ash + 50% RPP	2.1148	122.212
4	Fly ash + 75% RPP	1.4910	427.823

5 Results and Discussion

5.1 Software Results

The factor of safety obtained from the software are given in Table 4. The displacement of the artificial embankment for the various mix proportions of fly ash and recycled plastic polymer are shown in Figs. 2, 3, 4 and 5.

5.2 Graphical Results

Graph 1 shows the variation of the embankment material mix with respect to factor of safety predicted by the software.

From the results, it is evident that the amount of recycled plastic polymer influences the factor of safety of the fly ash embankment. The maximum factor of safety is obtained at a mix percentage of 50% of plastic recycle polymer with fly ash. Further

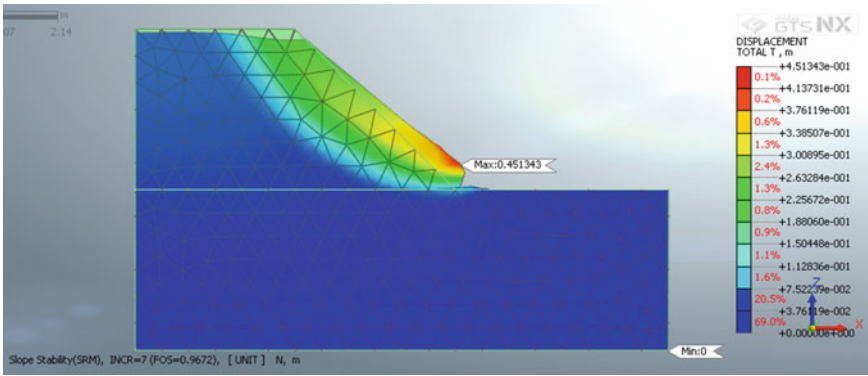


Fig. 2 Total displacement (in m) for fly ash only model

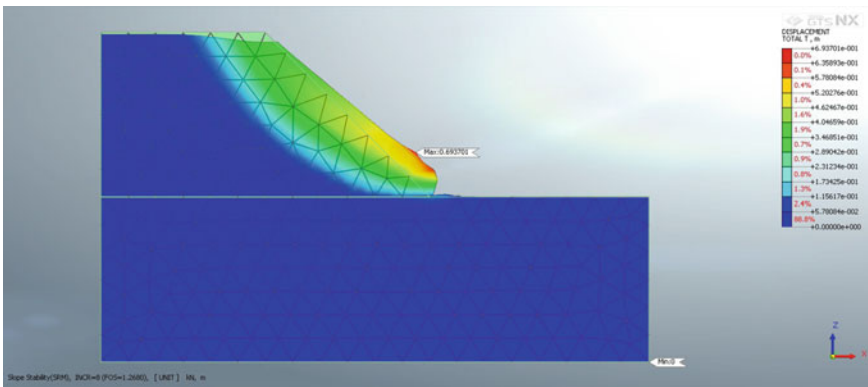


Fig. 3 Total displacement (in m) for FA and 25% RPP model

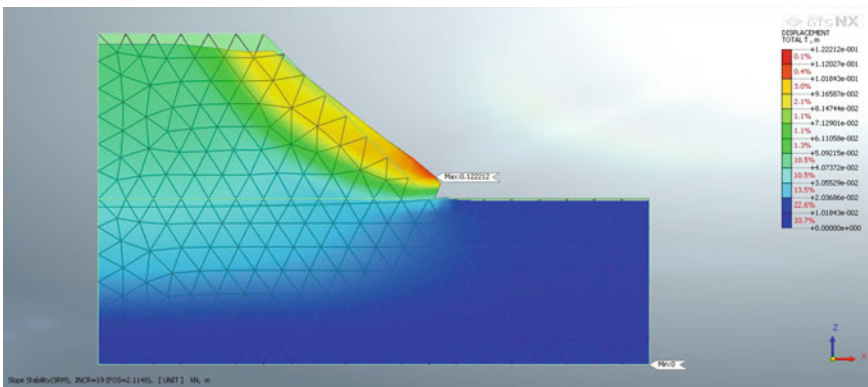


Fig. 4 Total displacement (in m) for FA and 50% RPP model

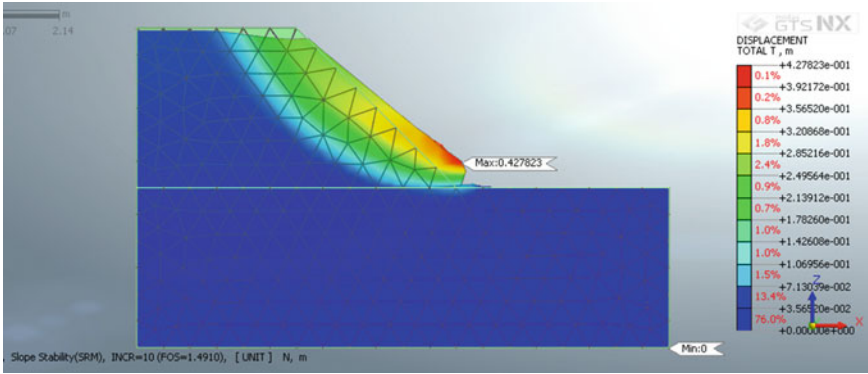
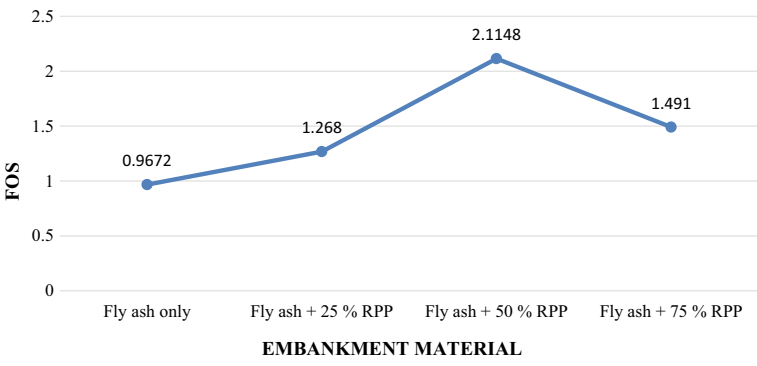


Fig. 5 Total displacement (in m) for FA and 75% RPP model



Graph 1 Embankment mix material versus factor of safety

increase in the polymer content decreases the overall factor of safety of the artificial embankment.

6 Conclusion

An artificial embankment of fly ash and varying percentage of recycled plastic polymer (RPP) as described in Sect. 3 was modelled in Midas GTS-NX. The embankment was analysed based on its properties as described in Sect. 2. The following conclusions are drawn:

1. Embankment made of fly ash only is not stable and requires admixtures/additives to improve the stability.
2. Fly ash along with 50% of recycled plastic polymer gives the maximum factor of safety in comparison with other mix percentages.

3. Thus, 50% recycled plastic polymer by weight of fly ash, acts as ideal mix percentage for achieving optimum factor of safety for the proposed embankment.
4. Finally, we can stabilize slopes, make fly ash slopes stable and steeper with the use of recycled plastic polymer. Such slopes take large loads and result in lower deformations, due to its improved confinement and inclusion property.

References

1. Salunkhe T, Nawghare S, Padade A, Mandal JN (2014) Stabilization of fly ash slope using plastic recycled polymer. *Int J Sci Eng Res* 5(7):248–252. ISSN 2229-5518
2. Salunkhe TV, Mandal JN (2014) Behavior of fly ash at different mix ratios with plastic recycled polymers. *Int J Res Appl Sci Eng Technol (IJRASET)* 2(III):190–198. ISSN: 2321-9653
3. Awoyera PO, Adesina A (2020) Case study: plastic wastes to construction products: status, limitations, and future perspective. *Case Stud Constr Mater* 12:30–41
4. IRC: SP: 58-1999, Guidelines for use of fly ash in road embankments. The Indian Roads Congress, New Delhi, India
5. IS 2720 (1983) Methods of test for soils, Part 1-14, 17, Bureau of Indian Standards, New Delhi, India
6. Goyal T, Sonthwal VK (2017) A review on slope stability analysis by strength reduction method using Midas GTS. *Int J Innovative Res Sci Eng Technol (IJIRSET)* 6(8):17050–17053
7. Saikia R, Kanti Dey A (2016) Slope stability analysis of slides at Sonapur using strength reduction method. In: *Proceedings of Indian geotechnical conference IGC2016*, pp 15–17
8. Ankur N, Sonthwal VK (2018) Assessment of a failed slope on Mandi Pathankot highway, Himachal Pradesh using Midas GTS NX. *Int J Tech Innovation Mod Eng Sci (IJTIMES)* 4(7):561–564. e-ISSN: 2455-2585

Lateral Capacity of Step-Tapered Piles in Sand Deposits



K. V. S. B. Raju, K. S. Rajesh, L. Dhanraj, and H. C. Muddaraju

Abstract Many structures on pile foundations, especially in the marine environments are subjected to lateral loads from the impact of berthing ships, sea waves, wind, etc. Piles are mostly used with straight-sided walls or circular ones. However, in recent days enlarged, top cross-section, step-tapered piles are found to be of interest and advantageous over traditional deep foundation systems. Step-tapered pile foundation is a relatively new structure and is such a kind of pile foundation having its cross-section decreased in steps. In this study, the characteristics of step-tapered piles were established from the experimental investigation, under lateral loadings. The tests were carried out on straight and step-tapered piles of different segments, 650 mm long embedded in homogenous and layered sand deposits. The piles were instrumented along their length to know their behaviour along with the depth. In order to examine the ultimate lateral capacity and the deflection, the tests were carried out to failure. The test results indicated a non-linear response and a substantial increase in lateral capacity of the pile with decreased deflections for step-tapered piles. The provision of providing steps or segments for piles with five segments resulted in an increase in the load capacity ranging between 44 and 73% in a layered condition and 42–63% in a homogenous sand condition. Providing segments shows a significant effect on load-bearing capacity. Step-tapered piles experienced lesser deflection at the pile head and also along the shaft when compared to the uniform diameter pile and they have better material distribution leading to overall efficiency.

Keywords Step-tapered piles · Homogenous sand · Layered sand · Ultimate lateral capacity · Deflections

K. V. S. B. Raju · K. S. Rajesh (✉) · L. Dhanraj · H. C. Muddaraju
Department of Civil Engineering, UVCE, Bangalore University, Bengaluru 560056, India
e-mail: rajeshksra@gmail.com

© The Author(s), under exclusive license to Springer Nature Singapore Pte Ltd. 2023
M. S. Ranadive et al. (eds.), *Recent Trends in Construction Technology and Management*, Lecture Notes in Civil Engineering 260,
https://doi.org/10.1007/978-981-19-2145-2_56

739

1 Introduction

Piles are slender structural members in a foundation that transfers the load from the superstructure to a stiffer medium. Structures on pile foundation, especially in an offshore environment, are subjected to both axial and lateral loads, and the ultimate capacity under lateral loads is important and maybe the controlling factor in foundation design. Nowadays, the shape of the pile can be varied from pile to pile. One such is a step-tapered pile foundation, a relatively new structure and in its kind cross-section decreased in steps.

Step-tapered piles feature favourable formation applicability and lateral load-carrying capability, indicating that they are flexible in layout and may have significant economic benefits. They were broadly utilized in latest years, especially in large bridge pile foundations in deep water, such as the pile foundations of the main piers of the Sutong Yangtze River Bridge. These piles have various advantages in terms of driving efficiency, flexibility, installation, load-carrying capacity, inspection, etc. Also, a wide range of configurations is available to best satisfy subsoil conditions and loading requirements.

2 Literature Review

The literature on step-tapered piles is still not systematic or comprehensive. Ismael [1] conducted a load test on straight and step-tapered bored piles in the sand under compression. The analysis included both the base capacity and the shaft friction at ultimate loads. The results showed that step-tapered piles have large lateral resistance with an increase in the axial bearing capacity compared to straight piles with the same base area. Ghazavi and Lavasan [2] studied the bearing capacity under axial loads of cylindrical, step and tapered piles. The results indicated an increase in the capacity of both step and tapered piles. Also, the bearing capacity was less than 10% between stepped and fully tapered piles.

The behaviour of step-tapered and straight bored piles in calcareous sand by lateral loads was examined in field tests by Ismael [3]. The piles were 5.3 m long embedded 5 m below the ground level. The straight piles were 0.2 and 0.3 m in diameter and step-tapered piles are 0.3 m along with the upper 10, 20 and 40% segment changing to 0.2 m for the lower section. Test results indicated a non-linear response and a substantial increase in lateral capacity, and at working loads, the deflections for the step-tapered piles were less compared with the straight shaft piles.

Load transfer mechanism of step tapered hollow pile analyzed by Ming et. al [4], Fang and Ming [5] studied the deformation and load-bearing characteristics of step tapered piles under lateral load using physical model tests and theoretical analysis. The results indicated that a step-tapered pile are more effective against lateral loads. The behaviour of step-tapered bored piles under static lateral loading in the sand was tested at a particular site in Kuwait [6]. Results indicated an increase

in load-carrying capacity and deflections decreased at specified applied loads to the step-tapered piles due to the strengthening of the top sections of the piles. Tavaroli and Ghazavi [7] studied the same length and volume of stepped and tapered piles as offshore piles driven by hammer blows and concluded that an increase in shear strength parameters of soil increases the bearing capacity in step-tapered piles and this is suitable for stiff soil strata.

Since there is limited knowledge of the performance of these kinds of piles under lateral loads, more research and investigation need to be performed to know the behaviour of these piles in homogenous and layered soils under horizontal loads.

3 Test Preparation

3.1 Description of Equipment

The test tank was made of mild steel and the walls of the tank were 10 mm thick with dimensions 1.2 m \times 0.75 m \times 1.5 m. In order to apply the lateral load, the tank is provided with a hand-winch arrangement. The load applied to the model piles was measured using a proving ring. The pile head deflection along the length was recorded using sensitive dial gauges with the least count of 0.01 mm.

3.2 Soil Medium

In the present investigation commercially available dry sand was chosen as a soil medium. Laboratory tests were conducted as per IS code and the properties are presented in Table 1.

The tests were conducted in two different soil systems, i.e., homogenous and layered systems. In the first case, the compactness of sand is loose and dense (Fig. 1). In the second case, the compactness of sand is medium dense between loose and dense states, respectively. Another case is loose between dense and medium dense states, respectively (Fig. 2). The relative densities for the loose, medium and dense states were 30%, 50% and 70%, respectively, for the tests on model piles in a sand medium.

3.3 Model Piles

The dimension of piles was selected as per the similitude law proposed by Wood [8]. The model piles selected were made of aluminium, and a scale factor of 1/18 is adopted. This simulates a prototype pile made from steel of Young's modulus $E = 210$ GPa, diameter = 600 mm and length = 12 m.

Table 1 Properties of soil sample

Properties		Values
Specific gravity (G)		2.64
Particle size	D_{10}	0.5
	D_{30}	0.7
	D_{60}	1.1
Uniform coefficient, C_u		3.2
Curvature coefficient, C_c		0.89
Classification		Poorly graded sand (SP)
Maximum unit weight ($\gamma_{d,max}$), e_{min}		16.19 kN/m ³ , 0.62
Maximum unit weight ($\gamma_{d,min}$), e_{max}		13.63 kN/m ³ , 0.9
Peak friction, ϕ_{peak}		28° ($D_r = 30\%$) 34° ($D_r = 50\%$) 39° ($D_r = 70\%$)

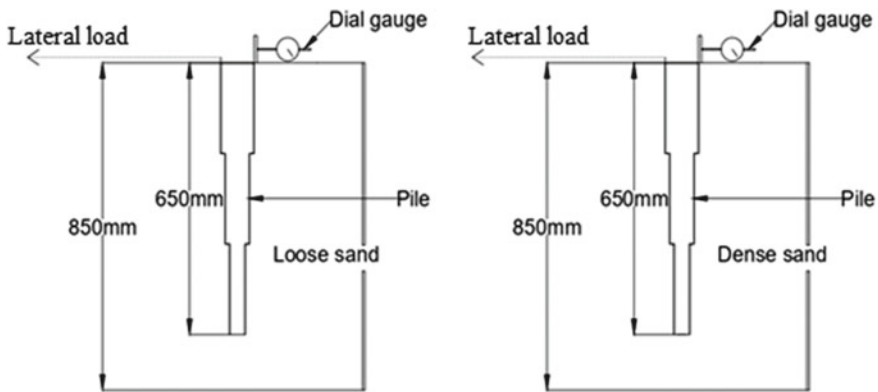


Fig. 1 Homogenous sand system

In order to produce the step-tapered piles, the pile is divided into appropriate increments of length of constant diameter having the same total perimeter area as that of a cylindrical pile. The model pile dimensions and schematic view are shown in Table 2 and Fig. 3.

4 Test Procedure

The placement of sand plays an important role to achieve reproducible density. In this study, sand raining technique is adopted. Initially, sand was allowed to fall freely

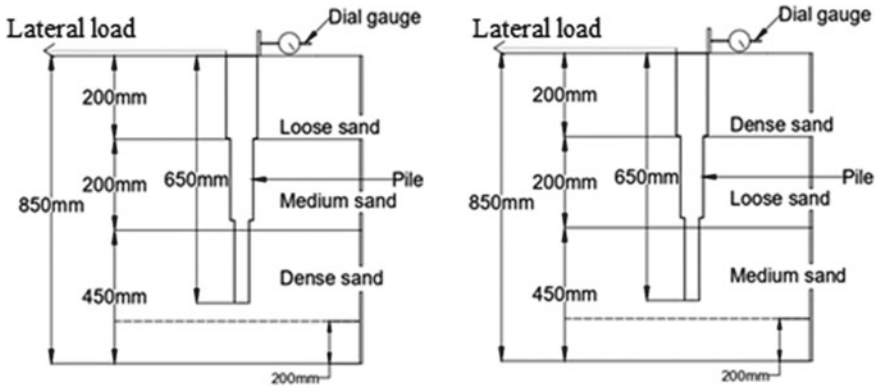


Fig. 2 Layered sand system

Table 2 Model pile dimensions

Pile type	Length of pile (mm)	Number of segments	Length of each segment (mm)	Diameter of each segment (mm)	Wall thickness of the pile (mm)	% increase in diameter of each segment
Straight (SP)	650	0	650	27	5	0
Step-tapered	650	2	325	40	5	48
				27	5	0
Step-tapered	650	3	216.67	40	5	48
				33.5	5	24
				27	5	0
Step-tapered	650	5	130	40	5	48
				36.75	5	36
				33.5	5	24
				30.25	5	12
Straight (SP)	650	0	650	40	5	48

in the tank continuously through the raining mesh from a particular height and the density with which the sand is deposited is determined. For a particular height of fall, the density that can be achieved is predetermined. The schematic view of the experimental setup is shown in Fig. 4.

The raining platform initially was positioned directly over the tank to the required height to achieve the desired density of sand. The sand was allowed to fall freely into the tank. At the pile base, the surface of the sand is levelled with the help of a straight edge. The pile was placed with the help of a clamp; the pile is held vertical. Again the sand was placed at the required height. The raining platform position was changed

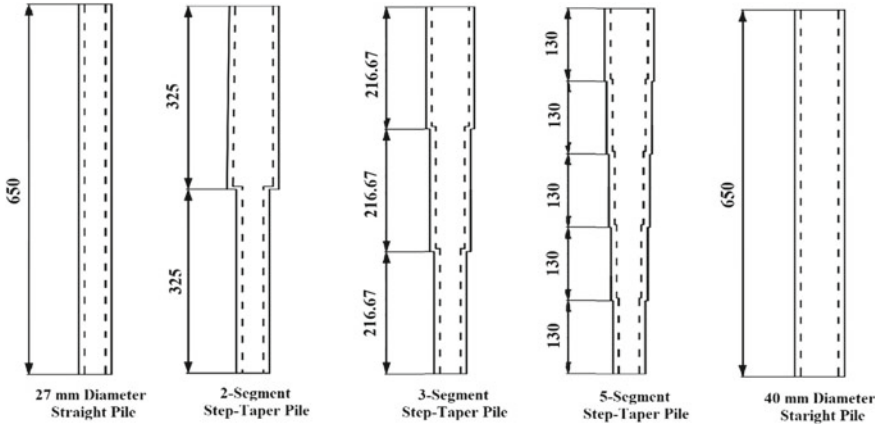


Fig. 3 Schematic view of model piles

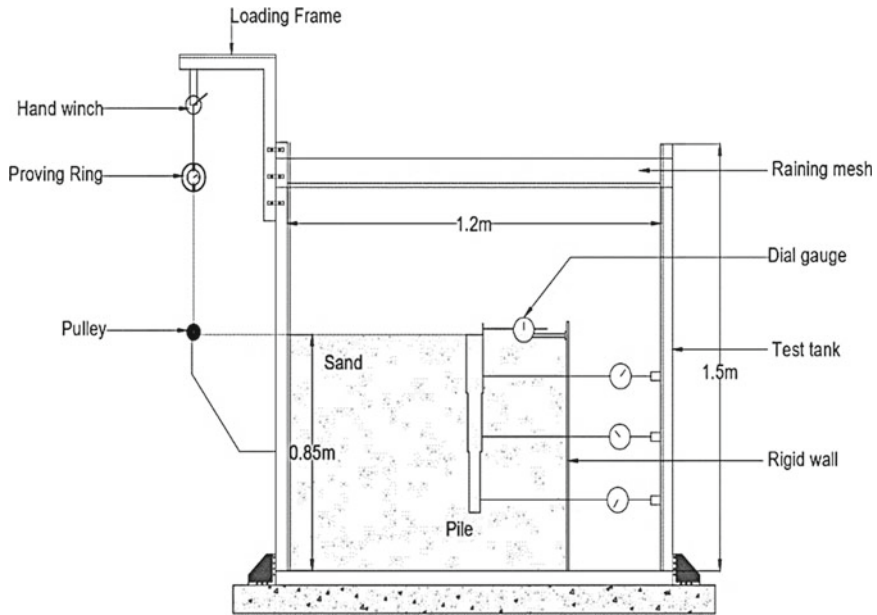


Fig. 4 Schematic representation of test setup

regularly to the needed height to make sure that the intended density is achieved. Dial gauges were attached to the pile throughout the length to know the deflection along with the depth and corrected to zero lateral displacements. The corresponding loads and lateral displacements were measured and recorded during the load test. The test has been continued till the proving ring reading becomes constant or starts decreasing or up to a minimum displacement of 25 mm. The test is repeated with

different pile combinations and the corresponding load–displacement graphs were plotted and the capacities of piles were determined. For each model test, the soil was removed from the tank and was replaced with the required depth and density.

5 Results and Discussions

Soil layers and the number of segments of step-tapered piles on lateral resistance of straight and step-tapered piles were tested. In the present study, at a lateral displacement of 25 mm, failure is considered. The corresponding load–deflection response graphs were plotted for all straight and step-tapered piles. The following section discusses the obtained results in detail.

5.1 Load–Deflection Response

Load–deflection curves for all the model piles in loose sand are shown in Fig. 5. It shows that enlarging the upper part of the pile section for the step-tapered piles has significantly decreased the pile head deflection. Enlarging pile diameter from 27 to 40 mm for upper 50% of the length of pile has reduced the head displacement with increased lateral capacity from 20.36 to 28.9 N, approximately a 45% increase. Also, corresponding to an enlargement of 100%, the diameter of 40 mm, there was no significant improvement in deflection and the load capacity was around 29 N, indicating no increase in capacity over the 50% enlargement.

The pile-head deflection curve for straight and step-tapered piles is shown in Fig. 6. It can be seen that step-tapered piles showed lesser pile head deflection than a

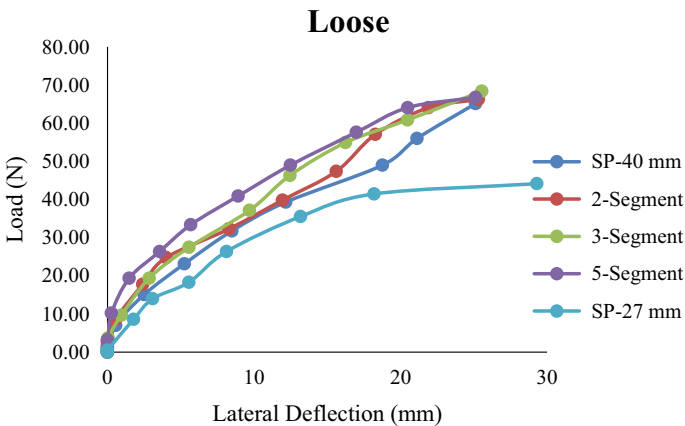


Fig. 5 Load–deflection curve in loose sand

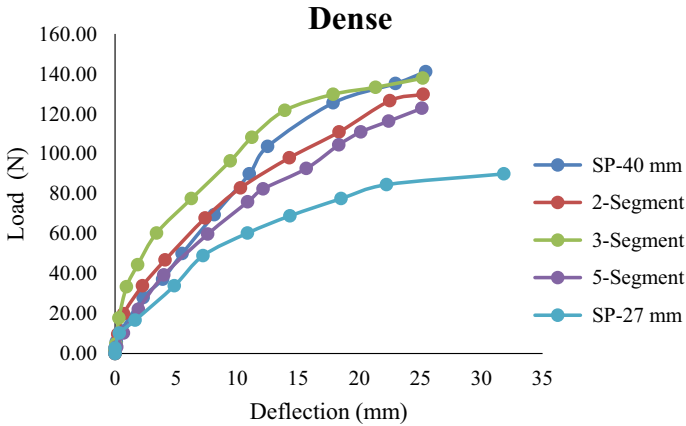


Fig. 6 Load–deflection curve in dense sand

straight or cylindrical pile. An increase in pile diameter to the upper 50% of the pile length decreased head deflection with an increased load-carrying capacity of around 63%. But the case is not so when the enlargement was 100% since the load capacity is reduced with the deflection.

The five-segmented pile showed better performance compared to other piles (Fig. 7a). The pile-head deflection is reduced for step-tapered piles than the straight piles. In the latter case, loose between dense and medium-dense state, Fig. 7b, comparatively the three-segmented pile showed better performance. Also with enlarging the pile cross-section, the head deflection is increased with decreased pile’s load-carrying capacity. However, it can also be noted from the figure that as the number of segments increases, the deflection is reduced. This increment is limited to piles up to three segments, beyond which increment had no beneficial effect.

5.2 Ultimate Load Capacity

There are no such failure criteria to access the ultimate capacity of the pile under lateral loads, as recommended by Sharma and Prakash [9]. The ultimate lateral load capacity is defined as the load corresponding to a lateral displacement of 6.25 mm.

The displacement of 6.25 mm in the loose sand condition is shown in Fig. 8. The figure clearly shows that the five-segment step-tapered pile carries the maximum ultimate load than other piles. It is about a 10% increase in ultimate capacity of the straight pile of 40 mm diameter pile, which corresponds to 100% enlargement. There is a significant difference in the behaviour of SP-40 mm and two-segment piles. It shows that by increasing the steps in pile models, the load-carrying capacity was found to be increased.

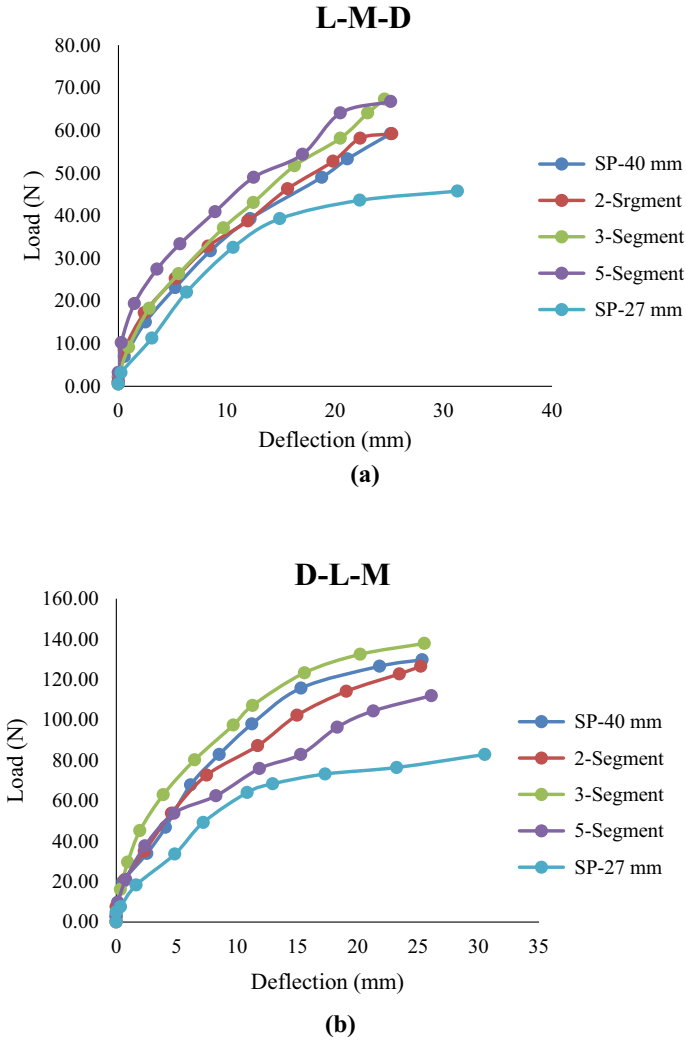


Fig. 7 Load–deflection curve in layered sand

The ultimate load capacity of straight and step-tapered piles for the dense sand conditions is shown in Fig. 9. It can be noted that a three-segment step-tapered pile carries a maximum ultimate lateral capacity than other piles and an increase of 12.5% in the lateral capacity than a pile of 40 mm diameter, which corresponds to 100% enlargement. Also beyond three segments, there will be no significant improvement in pile’s lateral capacity.

In this case of medium-dense between loose and dense state, Fig. 10a, a five-segment step-tapered pile carries the maximum ultimate load than other piles. It is about a 25% increase in 40 mm diameter for a straight pile. Figure 10b shows

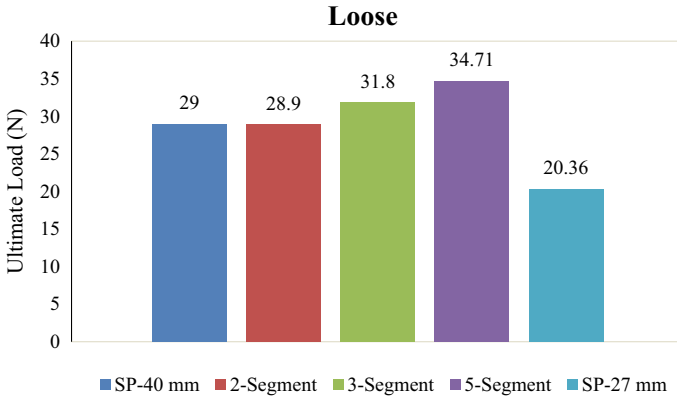


Fig. 8 Ultimate load capacity in loose sand

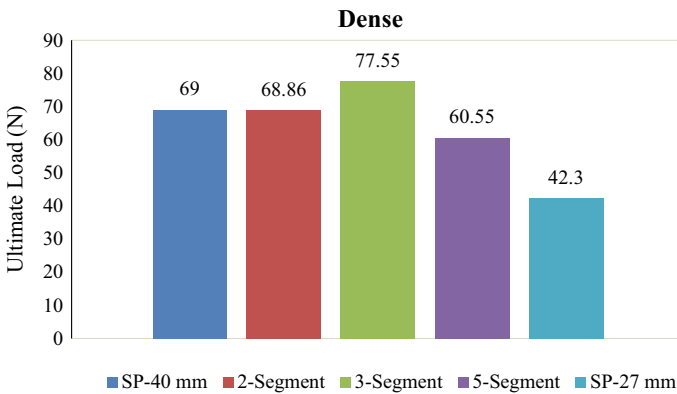


Fig. 9 Ultimate load capacity in dense sand

the ultimate load capacity of piles in dense–loose–medium dense sand, respectively. It can be noted from the figure that the three-segment step-tapered pile carries the maximum ultimate load than other piles. The increment in the load capacity is around 17% compared to that of a straight pile of 40 mm diameter.

The deflection for all the piles is reduced in dense sand conditions compared to loose sand cases. Also, the same can be observed for the top dense conditions than top loose conditions (layered sand case), respectively. Compared to the straight pile, step-tapered piles experienced lesser pile head deflection. This is due to the increased stiffness of step-tapered piles due to changes in cross-sectional area. In order to know the effectiveness under lateral load conditions of step-tapered piles, the ultimate load capacity was expressed in terms of pile load capacity ratio, given in Table 3. The ratio of capacity is defined as the load-carrying capacity of step-tapered piles to the load-carrying capacity of a straight pile of 27 mm diameter.

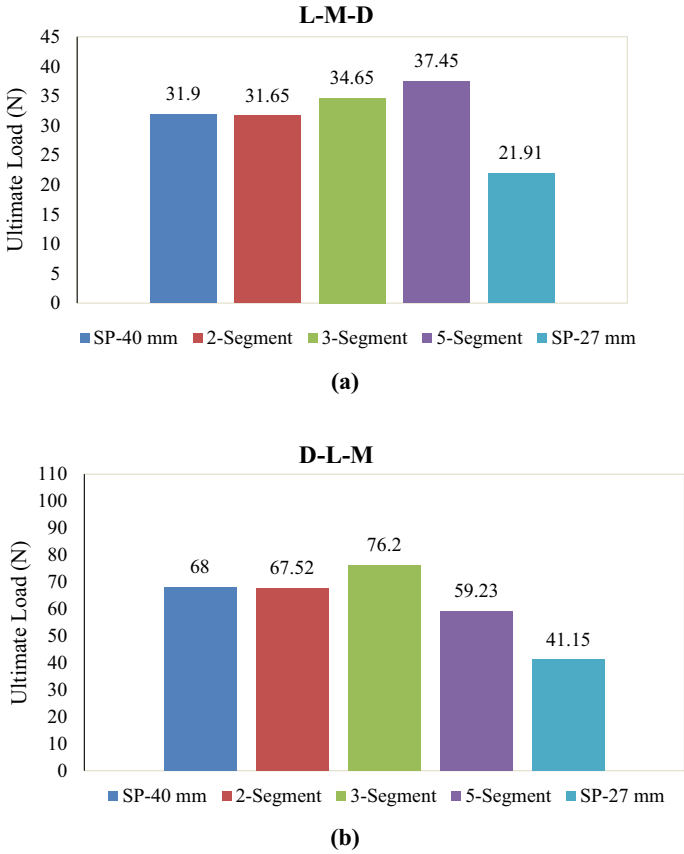


Fig. 10 Ultimate load capacity in layered sand

Table 3 Ultimate lateral load capacity and ratio of capacity

Pile	Condition	SP-27 mm	2-Seg	3-Seg	5-Seg	SP-40 mm
Lateral load capacity (N)	Loose	20.36	28.9	31.8	34.71	29
	Dense	42.3	68.86	77.55	60.55	69
	L-M-D	21.91	31.65	34.65	37.45	31.9
	D-L-M	41.15	67.82	76.2	59.23	68
Ratio of capacity	Loose		1.42	1.56	1.7	1.42
	Dense		1.63	1.83	1.43	1.63
	L-M-D		1.44	1.58	1.73	1.46
	D-L-M		1.65	1.85	1.44	1.65

It can be observed from Table 3 that the three-segment pile displayed an increase in the ultimate lateral load ranging between 58% in loose–medium–dense and 85% in dense–loose–medium condition. In dense and loose conditions, a maximum increase of 83% and 56% can be seen, respectively. Five-segment pile displayed an increase in the ultimate lateral load ranging between 44% in dense–loose–medium and 73% in loose–medium–dense condition. In dense and loose conditions, a maximum increase of 43% and 70% can be seen, respectively. A similar trend was observed for other piles, two-segment and SP-40 mm piles. It can be noted that for top dense sand conditions, the pile with three-segment was found to be favourable. However, beyond this, increment in the segment has no influence on the pile's capacity.

6 Conclusions

Step-tapered piles are versatile and innovative pile foundation system for accessing lateral loads. These piles are an ideal foundation for structures carrying larger lateral loads, jetties, lighthouses, etc. An attempt is made in the present study to evaluate the lateral response of uniform diameter and step-tapered pile in the homogenous bed of sand and in layered sand of different densities that correspond to loose–medium dense–dense and dense–loose–medium dense (three layers). By varying the number of segments to 2, 3 and 5, the diameter varied from 40 mm at the top to 27 mm in the homogenous and layered sand. Tests were conducted on the straight pile and step-tapered pile by varying densities corresponding to loose and dense in the case of homogenous sand and loose–medium dense–dense and dense–loose–medium dense in the case of layered sand. The following conclusions were drawn from the study:

1. The response of the pile under the lateral loads was affected by soil fabric, soil density, and shape of pile characteristics.
2. The provision of providing steps or segments for piles with five segments resulted in an increase of the load capacity ranging between 44 and 73% in layered condition and 42 and 63% in homogenous sand condition. Providing segments shows a significant effect on load-bearing capacity.
3. It was observed that when compared to a uniform diameter pile, step-tapered pile carries more lateral load and lesser pile-head deflection. Also in the case of uniform diameter piles in homogenous sand beds, the dense state of sand carries the more lateral load when compared to the loose state of sand. In a loose state of sand as the number of segments increases lateral load was found to increase. In the case of a dense state of sand, the lateral load increases significantly till three segments, and thereafter for five segments, it was found to decrease because as the number of segments increases the overall surface area was found to decrease and the corresponding mobilization of passive resistance. Also in the case of the loose bed of sand, there will be slippage of sand particles surrounding the pile, thereby decreasing the adhesion between the pile–soil interface.

4. It was observed that in layered sand when compared to uniform diameter pile, step-tapered pile carries more lateral load and lesser pile-head deflection. In layered sand when compared to loose–medium dense–dense state, the strata consisting of dense–loose–medium dense state was observed to offer more lateral resistance and lesser pile-head deflection due to mobilization of more passive resistance in dense strata (top one-third of pile length), and it was also observed that three segments carry more lateral load than five segments due to overall decrease in surface area in the case of five segments and decrease of pile–soil adhesion.
5. Compared to the straight pile, step-tapered piles experienced lesser deflection at the pile head and also along the shaft. Also, step-tapered piles have better material distribution leading to overall efficiency.
6. The present study is helpful in accessing foundations for the structures where larger lateral loads are anticipated, such as tall buildings, wharves, and structures in the marine environment.

References

1. Ismael NF (2003) Load tests on straight and step tapered bored piles in weakly cemented sand. Field measurements in geomechanics. ISBN 9058096025
2. Ghazavi M, Lavasan AA (2006) Bearing capacity of tapered and step-tapered piles subjected to axial compressive loading. In: 7th International conference on coastal, ports & marine structures (ICOPMAS)
3. Ismael NF (2006) Analysis of lateral load tests on step tapered bored piles in calcareous sands. ASCE, GeoCongress
4. Ming H, Song J, Dexiang X, Tao D, Xing S, Tao F (2018) Load transfer mechanism and theoretical model of step tapered hollow pile with huge diameter. *Chin J Rock Mech Eng*2018(10):2370–2383
5. Fang T, Huang M (2019) Deformation and load-bearing characteristics of step-tapered piles in clay under lateral load. *Int J Geomech* 19(6):04019053
6. Ismael NF (2010) Behavior of step tapered bored piles in sand under static lateral loading. *J Geotech Geoenviron Eng* 136:669–676
7. Tavasoli O, Ghazavi M, Driving behavior of stepped and tapered offshore piles due to hammer blows. *Mar Geores Geotechnol*. ISSN:1064-119X (P) 1521-0618
8. Wood DM (2004) Geotechnical modelling. CRC Press
9. Prakash S, Sharma HD (1990) Pile foundations in engineering practice. Wiley, New York, NY

Strength and Dilatancy Behaviour of Granular Slag Sand



K. V. S. B. Raju and Chidanand G. Naik

Abstract This paper focuses on the shear strength and dilatancy properties of granular slag sand. Direct shear tests were conducted on sample slag sand collected from the JSW steel plant, Toranagallu of Bellary district. The different relative densities at which tests were conducted are 20%, 50%, and 80% respectively, with corresponding unit weights are 14.58 kN/m³, 15.27 kN/m³, and 16.03 kN/m³, respectively. All the direct shear tests were continued till the shear strain equals 40% in order to achieve the critical state. The dilatancy and shear strength characteristics of the slag sand sample were observed at different relative densities under different normal stresses ranging from 50 to 400 kPa. It was found that both the friction angle and dilatancy angle reduced with the decrease in the applied normal stress. Also based on a series of test results critical state frictional angle was evaluated, which is independent of normal stress and relative density. For the chosen slag sand sample, a correlation is established between the peak friction angle and the critical state friction angle in the present work. The study can be useful in assessing the stability of geotechnical structures, wherein granular slag sand is used to enhance engineering performance. The established correlation was finally compared with those established by various researchers.

Keywords Dilatancy · Peak friction angle · Density index · Correlations · Critical state · Slag sand

K. V. S. B. Raju · C. G. Naik (✉)
UVCE, Bangalore University, Bangalore 560056, India
e-mail: naik.aec@gmail.com

© The Author(s), under exclusive license to Springer Nature Singapore Pte Ltd. 2023
M. S. Ranadive et al. (eds.), *Recent Trends in Construction Technology and Management*, Lecture Notes in Civil Engineering 260,
https://doi.org/10.1007/978-981-19-2145-2_57

753

1 Introduction

Almost all granular materials undergo volume change when they are subjected to shearing. This behaviour is termed dilatancy. While the factors causing this dilation behaviour of soil are very well known, there is no practical solution based on in situ conditions to measure the dilation angle. The strength of the granular materials is generally denoted by two important factors, namely, critical state friction angle and peak friction angle. The present work focuses on the shear strength and dilation characteristics of slag sand. The experimental programme consists of numerous direct shear experiments on slag sand maintained at different relative densities. In terms of the stress–dilatancy relationship and shear strength parameters, test results were interpreted. The main aim of the present study is to find a correlation between the peak friction angle (φ_p), dilation angle (ψ_p), and critical state friction angle (φ_{cv}) for the chosen slag sand sample.

2 Literature Review

Several researchers have worked on the strength and dilation characteristics of various granular materials; a few of them are highlighted here.

In order to establish a correlation between stress and dilatancy of coarse aggregate used for base course construction in Poland, Katarzyna [1] employed a large direct shear apparatus. The standard pressures used for the experimental work were 55.5–59.6, 130.9–133.9, and 254.6–258.2 kPa [1]. At a horizontal displacement of 60 mm, all experiments were interrupted (i.e. about 12% of the sample diameter). For tested coarse granular soil, the critical state frictional angle was estimated to be $\varphi_p = 41.2^\circ$ and the measured critical state frictional angle was found to be independent of compaction and soil moisture condition. Wang et al. [2] have investigated the shear strength of sandstone–mudstone mixture by conducting numerous direct shear tests in a laboratory [2]. For the study, lightly weathered blocks of rock collected from a mountain situated near the Yangtze River in Chongqing of China were used. Six different combinations of mixtures were used for the study, namely, 0, 20, 40, 60, 80, and 100% mudstone. Effective vertical normal stresses were applied in the range between 50 and 400 kPa. Variations of shear stress against relative horizontal displacement were plotted for the study material. Four major influence factors were recognised, namely, the distribution of particle size, particle composition of mudstone in the mixture, initial dry bulk unit weight, and water content. Dry sand maintained at various density indices (i.e. 20, 50, and 80%) was subjected to a direct shear test by Raju and Khan [3]. Vertical normal stress ranging from 50 to 400 kPa was applied

to the prepared sample. It was observed that with an increase in effective normal stress, the peak frictional angles and dilation angles were found to decrease [3]. Also, it was found that an increase in density leads to an increase in peak friction angle and dilation angle [3]. Also, it is found that as the grain size of sand decreases from coarse to fine, there is a substantial reduction in peak frictional angle, critical state friction angle, and dilation angle. In the study, critical state friction angle was found for the three different types of graded sand. It was found that φ_{cv} for coarse sand was 35.34° , φ_{cv} for medium sand was 27.07° , and φ_{cv} for fine sand was 24.08° . Bolton [4] explored shear strength and dilatancy characteristics of almost 17 different types of sands maintained at various densities and normal stresses. By performing axisymmetric and plane-strain tests, a variation in shear stress and volumetric strains with respect to axial strains was found. The new term “relative density index” has been established in terms of density index and effective stress level. Also, he has indicated a much simpler correlation among φ_p , φ_{cv} , and ψ_p . The established correlations are mentioned below:

$$\varphi_p = \varphi_{cv} + 0.8\psi_p \quad (1)$$

$$\varphi_p = \varphi_{cv} + 5 \text{ IR for plain strain condition} \quad (2)$$

$$\varphi_p = \varphi_{cv} + 3 \text{ IR for triaxial condition} \quad (3)$$

The correlation between dilatancy index (IR), relative density (DR), and effective stress (σ_v) is given by the relationship:

$$\text{IR} = \text{DR}(Q - \ln(\sigma_v)) - R \quad (4)$$

In the above expression, Q and R are constants; vertical normal stress (σ_v) is expressed in kPa and relative density (DR) in decimal number. According to observations made by [4], the values of Q and R were taken as 10 and 1, respectively. Later another researcher, Salgado et al. (2000) took values of Q and R as 9 and 0.49, respectively [5]. Jayant [6] studied the characteristics of Bangalore sand and provided empirical relations mentioned as follows [6]:

$$\varphi_p = \varphi_{cv} + 0.932\psi_p \quad (5)$$

$$\varphi_p = \varphi_{cv} + 3.5 \text{ IR for plane-strain condition} \quad (6)$$

Strength–dilatancy relationships of almost 17 types of sands were extensively studied by Bolton and other researchers.

For the present experimental study, slag sand is taken as study material. The scarcity of natural building materials has necessitated the use of alternative materials. In most applications requiring fine aggregate, slag sand is used and is especially suitable for structural fills and embankments, road base layers, asphalt hot mix, and flowable lightweight fill.

The established strength–dilatancy relation plays an important role in:

1. modelling of stress–strain behaviour of slag sand
2. the design of shallow foundation placed on slag sand fill
3. slope stability calculation of embankment made up of slag sand.

3 Materials and Methods

3.1 Materials Description

Iron ore, fluxes (dolomite and/or limestone), and iron scrap along with coke or fuel are fed into a blast furnace during the production of iron. Carbon monoxide is released as the coke undergoes combustion, which reduces the ore to molten iron. Molten slag is floating on the upper surface of molten iron. Molten iron is channelised to a vessel after separating it from molten slag using a weir. Cooling and solidification of molten slag are done by rapid water quenching. This process leads to the formation of sand size fragments with friable material very similar to clinker called slag sand. The slag sand used in this analysis was collected from the JSW Steel Plant, Toranagallu, Bellary district.

3.1.1 Properties of Slag Sand

The slag sand sample selected for the present study comprised sub-angular grains and was found to be poorly graded as per the Indian Standard [7]. The properties of chosen slag sand sample are mentioned in Table 1. The slag sand sample used in the present study is shown in Fig. 1. The scanning electron microscope photographs of slag sand taken from NITK, Surathkal are shown in Figs. 2 and 3.

Table 1 Properties of slag sand

Parameter		Slag sand
D_{10} (mm)		0.25
D_{30} (mm)		0.41
D_{60} (mm)		0.57
Coefficient of uniformity, C_u		2.28
Coefficient of curvature, C_c		1.18
Specific gravity, G		2.654
% Uncompacted volume of voids		41.48% (Sub-angular)
Relative density, I_d %	20%	14.58 kN/m ³
	50%	15.27 kN/m ³
	80%	16.03 kN/m ³



Fig. 1 Slag sand sample

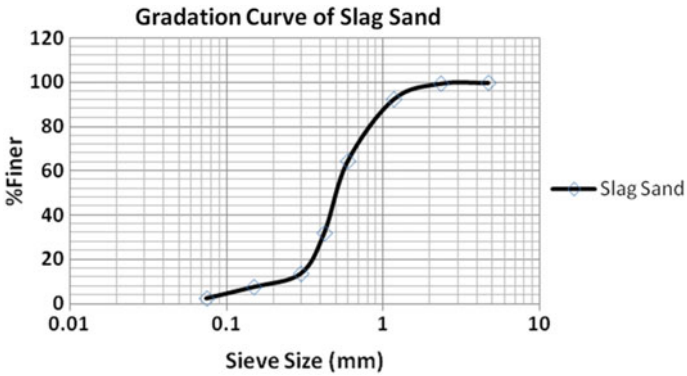


Fig. 2 Gradation curve

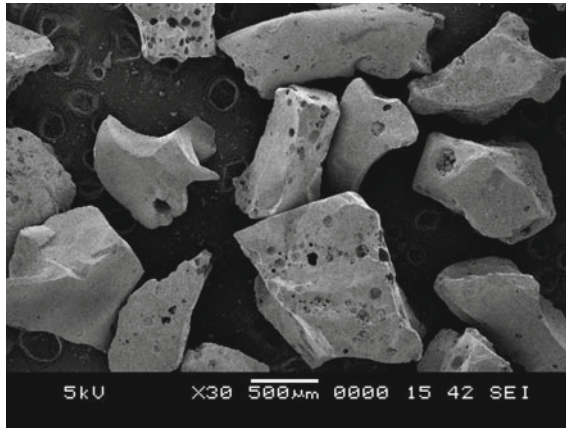


Fig. 3 A microscopic view of a portion of the slag sand sample by SEM

3.2 Direct Shear Tests

The slag sand sample selected for the study was subjected to a series of direct shear tests under five different vertical effective normal stresses between 50 and 400 kPa. Three distinct density indices were maintained, namely, 20% for loose state, 50% for medium dense state, and 80% for the very dense state. The required density was achieved by either raining the material from constant height (to achieve a loose to medium dense state) or by a tamping technique using a fixed number of blows (to achieve dense–very dense state) [3]. A shear box of size 60 mm × 60 mm × 25 mm was used for the present study. A uniform strain rate of 0.05 mm/min was maintained. The process of shearing was carried up to $u/H = 40\%$, where H is the initial height of the sample and u is the horizontal displacement at any time [3].

4 Results and Discussion

4.1 Presentation of Test Results with Graphs

The magnitude of shear force and the corresponding difference in height of the slag sand sample was continuously observed by increasing the horizontal displacement at regular interval of time. The corresponding test results conducted on slag sand sample are indicated in Figs. 5, 6 and 7 in terms of (i) variation in stress ratio (Ph/Pv)

with shear strain (u/H), and (ii) variation in volumetric strain (v/H) with u/H , where Ph and Pv are the magnitude of horizontal and vertical force, respectively [3]. From these plots the values of friction angles (φ) and dilatancy angles (ψ) were determined using the following expressions [3]:

$$\varphi = \tan^{-1}(Ph/Pv) \quad (7)$$

$$\psi = \tan^{-1}(\delta v/\delta u) \quad (8)$$

In the above expressions, φ_p and ψ_p are the peak friction and peak dilation angles, respectively. Figure 9 shows φ_p and ψ_p variations with normal stress (σ_v) for the chosen slag sand. Critical observations made by researchers [3, 7] from a similar study were referred for Figs. 5, 6, 7 and 10.

4.2 Correlation Between φ_p and ψ_p

A linear relationship is established between peak friction angle and peak dilation angle as shown in Fig. 8. As a critical state friction angle (φ_{cv}), the intercept produced corresponding to the zero-dilatation state is taken. It is a unique parameter, which remains independent of density, stress level, and type of test conducted. It depends only on the grain size and minerals comprising the granular material. The values φ_p were plotted against corresponding values of ψ_p , for different values of density index (DR) and σ_v values.

The relationship between ψ_p and φ_p is better describable by the following equation. All data points are shown in Fig. 8.

$$\varphi_p = \varphi_{cv} + 1.393\psi_p \quad (9)$$

Figure 8 shows that the value of φ_{cv} for the selected sample of slag sand equals 27.40° .

From Fig. 8 and regression analysis it is evident that Eq. (9) is suitable to express the correlation between shear strength and dilatancy of slag sand with $R^2 = 0.88$, where R^2 is the coefficient of correlation. Hence, from the regression of φ_p on ψ_p , it is observed that both the φ_p and ψ_p values are positively correlated. From Fig. 8, it is found that $\varphi_{cv} = 27.40^\circ$ (i.e. stress ratio $Ph/Pv = 0.52$). Also, an achievement of the critical state is observed close to $Ph/Pv = 0.52$ in all tests at a shear strain range of 35–40%, which is seen in Figs. 5a, 6a, and 7a.

4.3 Correlation Between φ_p and σ_v

The plot of φ_p versus σ_v is shown in Fig. 9. It is evident that σ_v increases as the φ_p value reduces. The following Eqs. (10) and (11) are given by Bolton [4] and Kumar [6], respectively. Kumar [6] took the values of Q and R as 10 and 1, respectively.

$$\varphi_p = \varphi_{cv} + 5 IR \quad (10)$$

$$\varphi_p = \varphi_{cv} + 3.5 IR \quad (11)$$

In the above expressions, IR is termed as dilatancy index, whose magnitude is dependent on density index (DR) and effective vertical normal stress (σ_v). The expression for determining IR is mentioned below:

$$IR = DR(Q - \ln(\sigma_v)) - R \quad (12)$$

σ_v expressed in kPa and DR in decimal.

The following relationship is suitable for the chosen slag sand sample:

$$\varphi_p = \varphi_{cv} + 3.204 IR \quad (13)$$

where $IR = DR(Q - \ln(\sigma_v)) - R$.

σ_v expressed in kPa and DR in decimal.

Figure 10 shows the prediction of $(\varphi_p - \varphi_{cv})$ by different formulae given by various researchers against measured values of $(\varphi_p - \varphi_{cv})$ for the granular materials. It is clearly indicated from the graph that the recommendations proposed by Salgado [5] and Bolton [4] falls on the higher end. On the other hand, the estimation from Eq. (13) seems to be better. Additionally, from the regression analysis, it is found that the value of coefficient of correlation, i.e., R^2 is equal to 0.963. From this, it can be interpreted that there exists a strong positive correlation between the estimated values $(\varphi_p - \varphi_{cv})$ and measured values of $(\varphi_p - \varphi_{cv})$ for the present data.

5 Conclusions

On the basis of shear tests conducted on slag sand at various density and stress conditions, correlations have been suggested close to those established by Kumar et al.

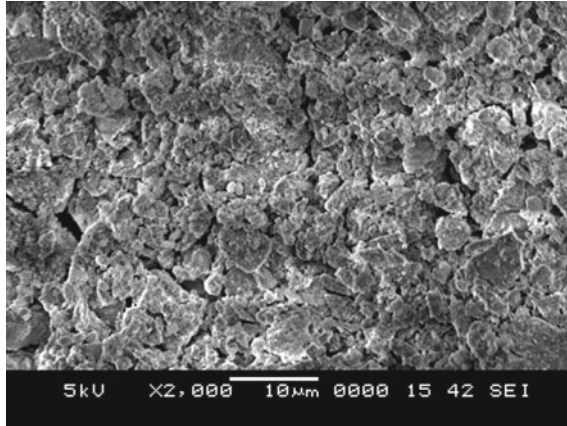


Fig. 4 SEM image of the surface texture of slag sand

[6], Salgado et al. [5] and Bolton [4]. The φ_p value can be estimated corresponding to any known values of φ_{cv} and DR at any magnitude of applied vertical stress. Furthermore, to estimate the value of φ_p an expression correlating ψ_p with φ_{cv} and φ_p is provided from the present experimental work. The expressions suggested fit the test findings well. On the basis of test data, it can be concluded that (i) reduction in σ_v values results in an improvement in both ψ_p and φ_p values. (ii) The value of φ_{cv} is independent of density and stress levels (Fig. 4).

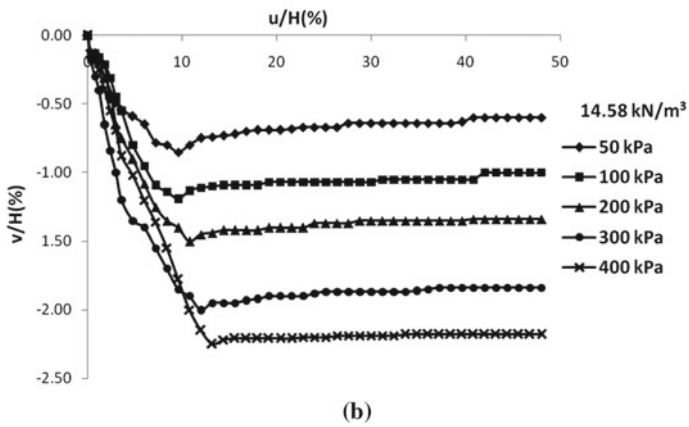
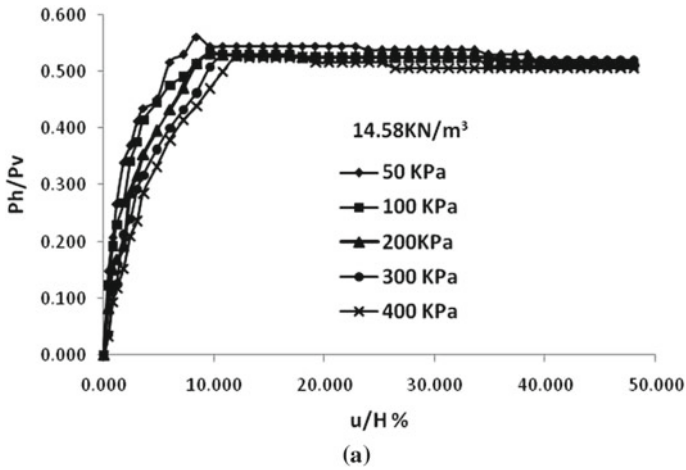


Fig. 5 For $\gamma = 14.58 \text{ kN/m}^3$ slag sand, the observed variation of **a** stress ratio (Ph/Pv) with shear strain (u/H), and **b** volumetric strain (v/H) with shear strain (u/H)

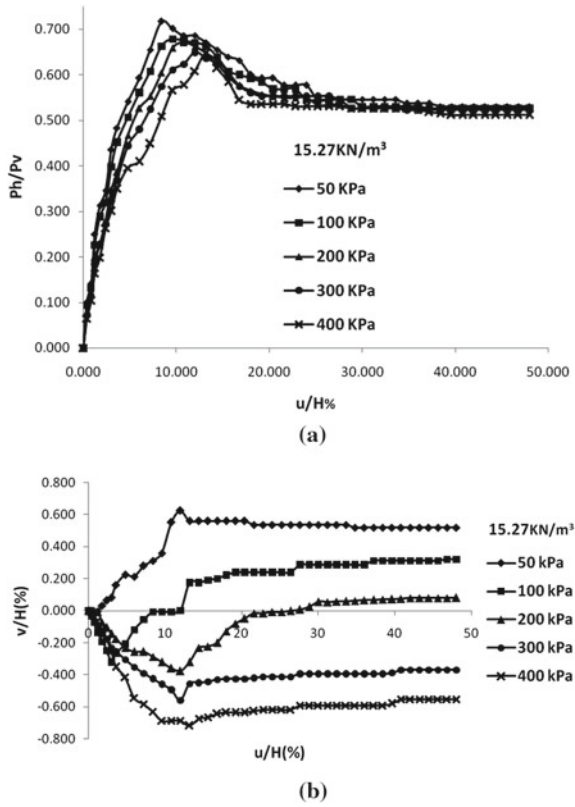


Fig. 6 For $\gamma = 15.27 \text{ kN/m}^3$ slag sand, the observed variation of **a** stress ratio (Ph/Pv) with shear strain (u/H), and **b** volumetric strain (v/H) with shear strain (u/H)

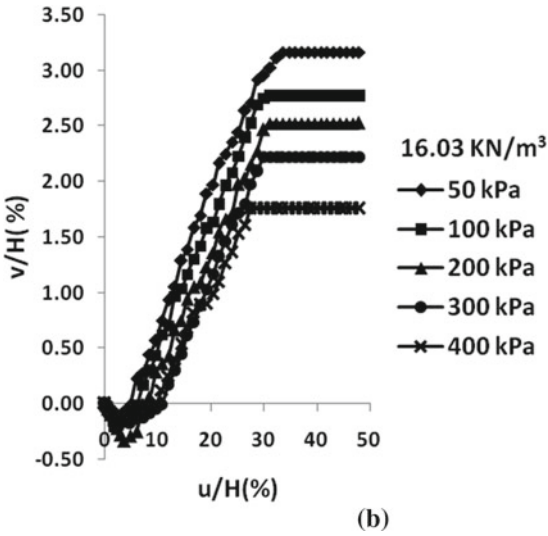
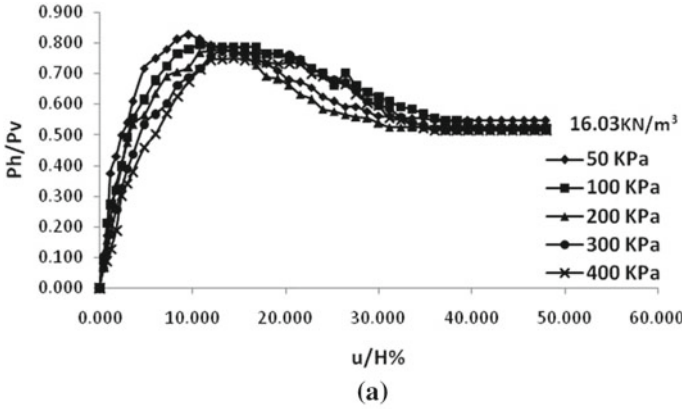


Fig. 7 For $\gamma = 16.03 \text{ kN/m}^3$ slag sand, the observed variation of **a** stress ratio (Ph/Pv) with shear strain (u/H), and **b** volumetric strain (v/H) with shear strain (u/H)

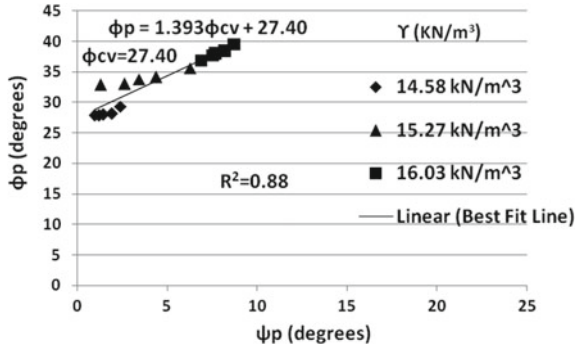


Fig. 8 Established relationship between peak friction angle (ϕ_p) and maximum dilation angle (ψ_p)

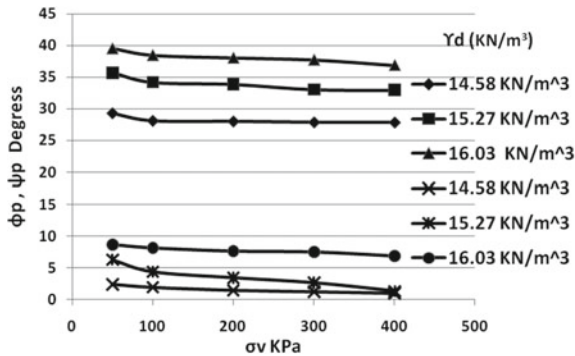


Fig. 9 The variation of ϕ_p and ψ_p with σ_v for slag sand

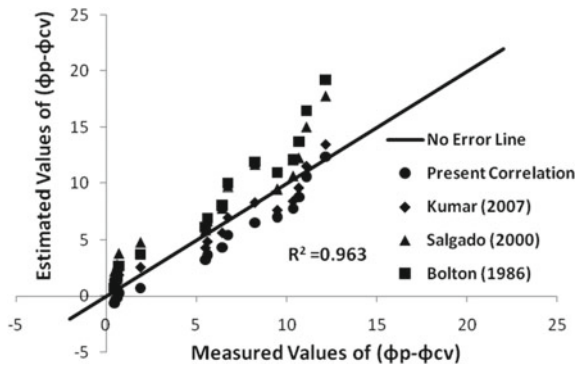


Fig. 10 The prediction of $(\phi_p - \phi_{cv})$ by different formulae against measured values of $(\phi_p - \phi_{cv})$ for all the tests for slag sand

References

1. Dolzyk-Szypcio K (2019) Direct shear test for coarse granular soil. *Int J Civ Engi* 17(12):1871–1878
2. Wang J-J, Guo J-J, Bai J-P, Wu X (2018) Shear strength of sandstone–mudstone particle mixture from direct shear test. *Environ Earth Sci* 77(12), Article 442
3. Raju KVS B, Khan S (2014) The effect of grading on strength and dilatancy parameters of sands. In: *Proceedings of Indian geotechnical conference-2014, December 18–20, 2014, Kakinada*
4. Bolton (1986) The strength and dilatancy of sands. *Geotech J* 36(1):65–78
5. Salgado, Bandini, Karim (2000) Shear strength and stiffness of silty sand. *J Geotech Geoenviron Eng, ASCE*, 451–462
6. Kumar J, Raju KVS B, Kumar A (2007) Relationships between rate of dilation, peak and critical state friction angles. *Indian Geotech J* 37(1):53–63
7. IS:1498-1970, Classification and identification of soils for general engineering purposes
8. Rowe PW (1962) The stress-dilatancy relation for static equilibrium of an assembly of particles in contact. *Proc R Soc London* 269:500–527

Parametric Study of the Slope Stability by Limit Equilibrium Finite Element Analysis



Prashant Sudani, K. A. Patil, and Y. A. Kolekar

Abstract Slope stability analyses of both natural and artificial slopes are an issue and need to be taken care of as they can affect both economic and infrastructure development. Water is the main factor that often leads to slope instability. Numerous studies are available in this direction, and it shows that the presence of the water harms the shear parameter, and it should increase the groundwater table, which further leads to loss of shear strength. The slope's stability depends on the shear parameter, cohesion, and angle of internal friction. If we can develop the relationship of this parameter with the instability, it can monitor the slope. This research's prime objective is to analyze the effect of the different controlling parameters on slope instability. The stability analysis has been done through the limit equilibrium finite element slope stability model. The slope was modeled in the commercial package GeoStudio SEEP/W, slope/w, and analyzes the stability. The stability factor was evaluated utilizing fully coupled flow deformation analysis compared with the various controlling parameters such as cohesion and angle of internal friction. For slope stability analysis, slopes were modeled with only one type of soil called the homogeneous fill. The influence of each parameter on slope instability was analyzed, and the results are discussed in this paper. It was also studied whether the relationship between the slope's instability and the controlling parameter existed. The research output shows that all chosen parameters' value negatively affects slope stability if their variations were favorable.

Keywords Slope stability · Landslide warning · Finite element analysis

P. Sudani (✉)
College of Engineering Pune, SPPU, Pune, India
e-mail: sudaniprashant93@gmail.com

K. A. Patil · Y. A. Kolekar
Civil Engineering Department, COEP, Pune, India

© The Author(s), under exclusive license to Springer Nature Singapore Pte Ltd. 2023
M. S. Ranadive et al. (eds.), *Recent Trends in Construction Technology and Management*, Lecture Notes in Civil Engineering 260,
https://doi.org/10.1007/978-981-19-2145-2_58

767

1 Introduction

Rainfall-induced slope instability is widespread worldwide, and it depends upon the geology, topography, and geotechnical properties of the slope strata; instability leads to several hazardous effects on human beings and infrastructure development. There are numerous cases of massive destructive landslides present in the literature worldwide, triggered by intense rainfall [9–11, 13].

In a tropical country like India, heavy rainfall after the hot and humid climate condition leads to the formation of the residual soils in a state of unsaturated previously due to lower groundwater table in the summer season [6]. In unsaturated soil, the suction pressure is present, which increases the slope's shear strength by suction effect in the slope's soil strata. During the rainfall, precipitation water is infiltrating into the slope geometry through the voids of the soil, and it depends on the properties of the material forming the slope. Infiltrating water leads to saturating the ground, and hence the suction will be reduced soon; moisture has a significant effect on the shear parameter, which further results in lowering the shear strength and increase in the stress; the factor of safety is reduced. When saturation reached 100%, it would reduce the suction pressure to zero and increase positive pore water pressure [4, 5]. Fredlund found that matric suction is the main parameter responsible for the slope's instability [3]. The development of the instability through the formation of the slip surface depends on more than one factor, including slope geometry (height, width, and inclination of the slope), topography and morphology of the area, stratification of the slope, material properties of the soil consisting of the slope, effect of the moisture, geotechnical analysis, and mechanical behavior. Since the slope's failure resulting from the heavy rainfall is in massive debris fall, it can make colossal destruction to both life and properties. Thus the precise physical analysis for the slope stability is essential.

In the present study, by keeping various hazardous landslides (such as the Malin landslide of Maharashtra, which caused an entire village burial and reported 161 lives losses [1, 2, 8, 12], into the center, the controlling parameter was analyzed. According to Rahardjo et al. [7], the slope geometry and the initial water table determine the initial safety factor, and the actual failure conditions are much affected by rainfall characteristics and properties of the soils on the slope. Ering et al. also presented the rainfall slope instability phenomenon in his study by back analysis assuming the slope as a fully saturated and on the verge of the failure factor of safety. They concluded that the rainfall effect on the slope has significant losses in the shear strength which can be evaluated through shear parameter cohesion and angle of the internal friction. Hence here in this study, the extensive analytical analyses were made to find out the effect of this crucial parameter on the slope stability.

To analyze the factor of safety with varying the controlling factors, the soil's geometry and profile were very simple to complex in this research. Slope stability was analyzed using the limit equilibrium finite element analysis using the GeoStudio Seep/W, Slope/W module. For the material model, the Mohr–Coulomb model was used in the analysis, and for stability analysis, phi-ci reduction analysis was employed

for better results. The slope was modeled and analyzed by adopting two different cases, often presented in the field. In the first case, the entire slope was made up of one material, a so-called homogeneous slope, which can help stimulate the slope’s result. While on the second case, the slope was modeled in the two-layer with different soil properties and analyzed. For analysis purposes, the slope stability controlling parameters, i.e., cohesion and angle of internal friction, were varied and the slope instability effect was observed.

2 Slope Geometry and Material Properties

In this study, slope geometry was used, as shown in Fig. 1. The inclination of the slope 26.56° (2:1) is considered. The height of the slope is 60 m. The groundwater table was encountered at the base, which was then varied to the top of the slope to analyze the groundwater table’s effect on the slope instability. The Morgenstern-price method is used to analyze the slope stability as this method can simulate the effect of both vertical and horizontal interaction force between the slice.

The surface soil’s behavior was modeled as linear and elastic–plastic soil material using the Mohr–Coulomb material model.

The surface soil behavior was modeled as linear and elastic–plastic soil material using the Mohr–Coulomb material model and analyzed using soil parameters derived from undrained tests. The dilatancy effect on the slope was not considered in the physical model simulation and soil dilation angle is negligible as per the empirical relationship ($\Psi = \phi - 30^\circ$).

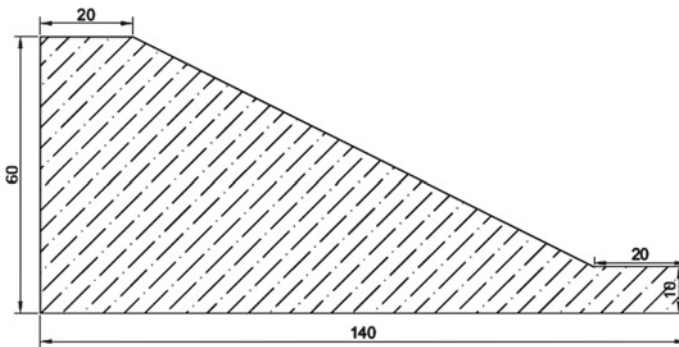


Fig. 1 Geometry of the slope model and initial groundwater condition

Table 1 Properties of the soil were used in the study

Soil type	γ_{unsat}	γ_{sat}	K_x	K_y	E	ν	C	ϕ
Clayey loam	15.8 kN/m ³	17.8 kN/m ³	0.4 kN/m ³	0.4 m/day	2000 m/day	0.33 kN/m ²	25 kN/m ²	40°

2.1 Finite Element Method (FEM)

Finite element analysis is a technique used to solve differential equation problems in engineering science (Vinod et al. 2020). Finite element analysis is best suited for mechanical and physical analysis as it can solve the problem by discretizing the large elements into smaller ones and then analyze them. FEA is a computational method used for engineering design and analysis purposes. The method used the mesh generation, which was then calculated based on the program coded with FEM. The basic theory in the analysis of finite elements is (1) discretization of the area being scrutinized in FE. These discrete constituents are thought to be interconnected exclusively at the joints, which are called nodes. (2) The use of familiarizing polynomials defines a field variable's difference within an element (Vinod et al. 2020). For slope stability analysis through FEM, there are two approaches to deal with the breakdown of the instability. The first is by building a gravity load, and the other is to diminish the quality characteristics of the soil mass, also known as c - ϕ reduction techniques. The “ c - ϕ reduction approach” for slope stability analysis is received in a fantastic commercial package known by GeoStudio.

2.2 Homogeneous Fill

Here the slope was used to be with the same kind of fill called the homogeneous fill. The properties of the soil used in the model are shown in Table 1. The analysis started from the initial soil properties, making them complex by gradually varying the controlling parameters and analyzing the yield.

2.3 Modeling of the Slope

A sample study has been carried out on assumed slope geometry. The slope was modeled with a homogeneous fill of the clayey loam. The slope's current condition was determined using limit equilibrium finite element slope stability modeling through the SLOPE/W program. The influence of the stability with the cohesion, angle of internal friction, and groundwater table soil was also examined.

The modeling sequence includes the path like geometry input—material definition—mesh generation—boundary condition—loading condition—construction sequence definition—analyze case—check results.

3 Result and Discussion

The entire study here divides into four cases, including (i) cohesive soil would analyze where the angle of internal friction would be zero and would observe the effect of the cohesion on the slope instability, (ii) frictional soil where cohesion would be made zero and would observe the effect of the friction angle on the slope stability, (iii-a) cohesive frictional soil with constant cohesion and varying the frictional angle, (iii-b) cohesive frictional soil with constant frictional angle and varying the cohesion, and (iv) effect of the rainfall simulation on the slope.

3.1 Case 1: Cohesive Soil, Where $\Phi = 0$ and Different Values of Cohesion

In this case, cohesive soil is modeled in the SLOPE/W to know the effect of the cohesion on the slope stability. Here, we used to vary the cohesion from 45 to 15 kN/m². The results of the simulation are shown in Table 2 and Fig. 2.

Observation of case one where the cohesion effect was analyzed, and the result is shown in Table 2. It shows that as the value of the cohesion reduced from its base value and the slope’s safety factor got disturbed significantly, which often seems during the rainfall infiltration.

Table 2 Effect of the cohesion on the slope stability

S. No.	ϕ	C	FOS
1	0	45	1.384
2	0	40	1.231
3	0	35	1.077
4	0	30	0.922
5	0	25	0.772
6	0	20	0.615
7	0	15	0.462

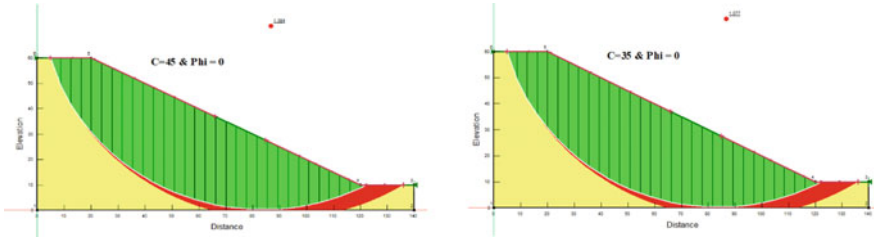


Fig. 2 SLOPE/W output for case, cohesion = 45 kN/m² and $\phi = 0$ (Left), and cohesion = 35 kN/m² and $\phi = 0$ (Right)

3.2 Case 2: Frictional Soil, Where $C = 0$ and Varying Frictional Angle

In this case, cohesive soil is modeled in the SLOPE/W to know the frictional angle’s effect on the slope stability. Here, we used to vary the value of the frictional angle from 45° to 15°. The results of the simulation are shown in Table 3 and Fig. 3.

The output of the analysis shows that the internal friction angle has a remarkable effect on slope stability. Results show that the variation of the slope’s safety factor with the variation of the friction angle is linear.

Table 3 Effect of the friction angle on the slope stability

S. No.	C	ϕ	FOS
1	0	45	2.002
2	0	40	1.680
3	0	35	1.402
4	0	30	1.156
5	0	25	0.772
6	0	20	0.729
7	0	15	0.536

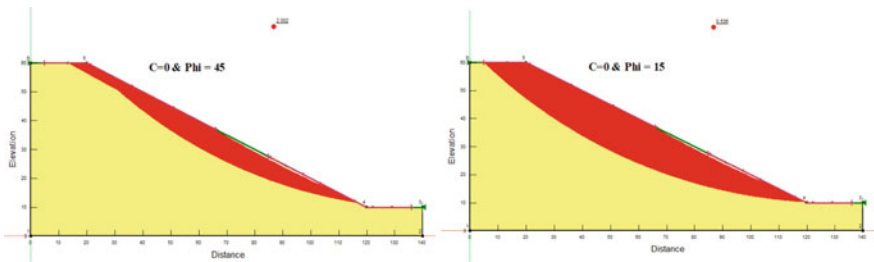


Fig. 3 SLOPE/W output for case, cohesion = 0 and $\phi = 45^\circ$ (Left), and cohesion = 0 and $\phi = 15^\circ$ (Right)

3.3 Case 3 (a): Cohesive Frictional Soil with Constant Cohesion and Varying Frictional Angle

In this case, frictional cohesive soil is modeled in the SLOPE/W to know the frictional angle’s effect on slope stability. Here, in this case, the cohesion’s value would make constant as 25 kN/m². Here, in this case, we used to vary the value of the frictional angle from 45° to 0°. The results of the simulation are shown in Table 4 and Fig. 4.

The result of variation of the friction angle in cohesive frictional soil has a severe effect on the slope instability compared to the cohesion.

Table 4 Effect of the friction angle on the slope stability in cohesive frictional soil

S. No.	C	ϕ	FOS
1	25	45	3.474
2	25	40	3.077
3	25	35	2.723
4	25	30	2.401
5	25	25	2.110
6	25	20	1.842
7	25	15	1.591
8	25	10	1.316
9	25	00	0.772

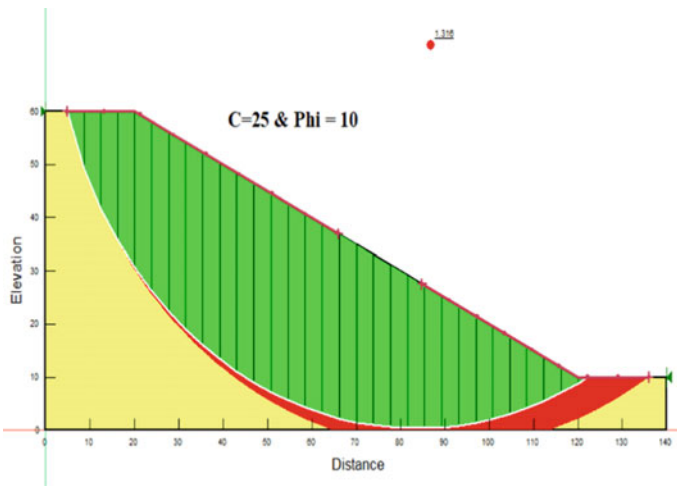


Fig. 4 SLOPE/W output for case, cohesion = 25 kN/m² and $\phi = 10^\circ$

3.4 Case 3 (B): Cohesive Frictional Soil with Constant Frictional Angle and Varying Cohesion

In this case, frictional cohesive soil is modeled in the SLOPE/W to know the effect of the cohesion on the slope stability with $C-\phi$ soil. Here, in this case, the value of the friction angle would make constant as 30° . We used to vary the cohesion value from 55 to 0 kN/m^2 . Results of the simulation are as shown in Table 5 and Fig. 5.

It has been seen that the cohesion can change negatively after coming into contact with the water at a faster rate than the friction angle. Hence, in this case, the cohesive frictional soil is considered for the study with varying cohesion, and it is observed that the safety factor makes their value from nearly five to less than one.

Table 5 Effect of the cohesion on the slope stability in cohesive frictional soil

S. No.	C	ϕ	FOS
1	55	30	3.460
2	50	30	3.283
3	45	30	3.106
4	40	30	2.929
5	35	30	2.751
6	30	30	2.574
7	25	30	2.401
8	20	30	2.221
9	15	30	2.026
10	10	30	1.825
11	00	30	1.156

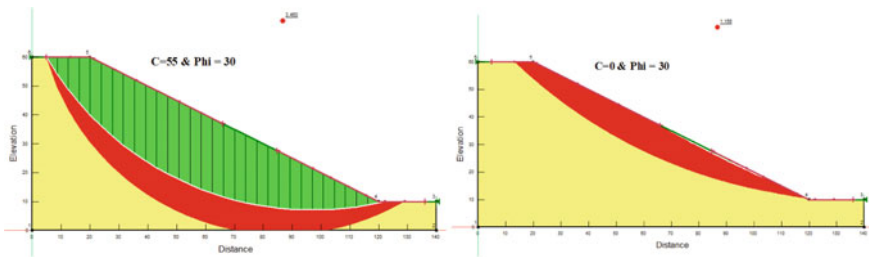


Fig. 5 SLOPE/W output for case, cohesion = 55 kN/m^2 and $\phi = 30^\circ$ (Left), and cohesion = 0 kN/m^2 and $\phi = 30^\circ$ (Right)

3.5 Case 4: Rainfall Simulation in the Slope

Here in Case 4, we simulate the rainfall in the slope by applying the flux on the slope’s surface at a 9 and 90 mm/h rate. The slope is modeled with the composite fill with geometry, as shown in Fig. 6. A two-layered slope profile is used to simulate the rainfall infiltration effect on the slope stability. For the hydrological simulation of the slope, the SEEP/W module of GeoStudio is used, and then SLOPE/W is used to keep SEEP/W as the parent simulation so that hydrological modeling can be incorporated into the slope stability analysis. The soil properties of the modeled two-layered slope are shown in Table 6.

As shown in Fig. 6 of the modeled slope, different boundary conditions are used to analyze slope stability. Zero boundary flux is provided on the 9-2-1-6 node of the slope on that boundary, and the rain will not infiltrate. 5-4-3-8-9 is open to get the rainfall, so boundary flux with 9 mm/h is provided here. This can vary according to the expected rainfall and infiltration properties of the modeled slope. For the sleep surface entry and exit method, the GeoStudio is used to simulate.

Further, for the SLOPE/W module Morgenstern-price method is used to analyze the problem. SEEP/W, SLOPE/W combination yields the FoS for the composite two-layered soil as 1.710 and 0.846 for 9 mm/h and 90 mm/h rainfall simulation, respectively, which indicates the transformation of instability of the safe slope. The output of the same is shown in Fig. 7.

Fig. 6 Modeled slope geometry with rainfall simulation on the slope

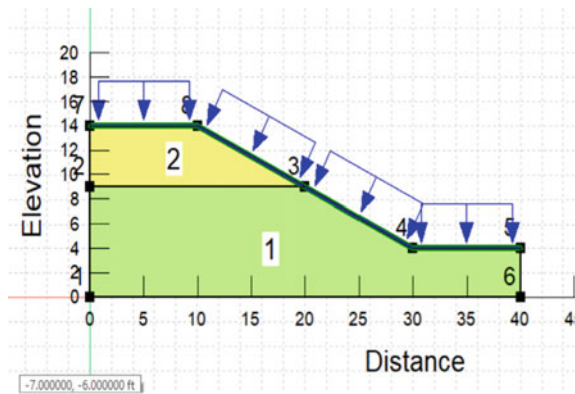


Table 6 Material properties used for Case 4 rainfall simulation

Soil type	γ_{unsat}	γ_{sat}	K_x	K_y	E	ν	C	ϕ
Upper layer	17	17.8	0.4	0.4	1500	0.25	4	20
Lower layer	18 kN/m ³	19 kN/m ³	0.4 kN/m ³	0.4 m/day	2500 m/day	0.23 kN/m ²	8 kN/m ²	25 Degree

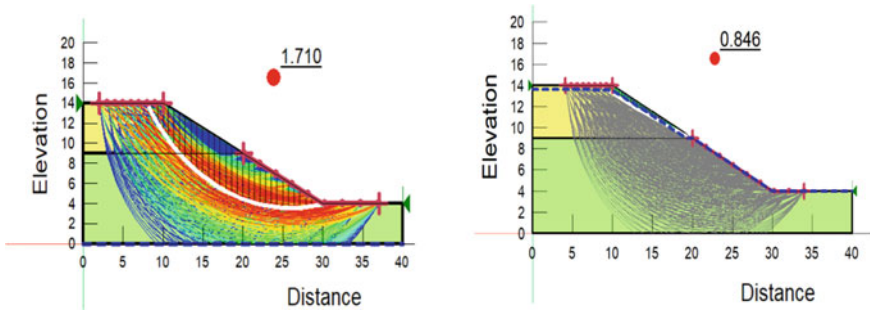


Fig. 7 Rainfall simulation SEEP/W, SLOPE/W output with 9 mm/h (Left) and 90 mm/h (Right) rainfall simulation

4 Conclusions

The parametric study for instability status of the land slope found helpful to understand and assess the effect of the stability governing parameters i.e., cohesion, angle of internal friction and rainfall. Results of the study represents the how the stability could vary once the shear strength parameters decay their values, which is seems often during saturation of the soil. Inference of the research are as presented below:

- The output of the analysis shows that as cohesion decreased from their undrained value, which is often seen when soil sample got saturated, the safety factor reduced and made the slope unstable.
- Other shear parameter, angles of internal friction also greatly influence slope stability; the higher the value, the safer the slope.
- Simulation of the rainfall infiltration into the slope model yields the hydrological model.
- The shear parameter significantly influences slope stability, especially cohesion, which can reduce slope stability if it varies negatively in the soil.

Fundamental research and their observation show that the variation of the shear parameter and other factors, including rainwater infiltration, saturation evolution, and rise in groundwater, can reduce the slope's safety. Monitoring of the landslide could be possible through developing relationship between the shear parameters, and saturation of the soil, which further could be possible to link with the stability of the landmass.

Acknowledgements We are thankful to AICTE-NDF Scheme (Application number 60400) for providing a research fellowship. We are also thankful to the College of Engineering Pune for providing a research facility.

References

1. Ering P, Sivakuma Babu GL (2016) Probabilistic back analysis of rainfall induced landslide—a case study of Malin landslide, India. *Eng Geol* 208:154–164
2. Ering P, Kulkarni R, Kolekar Y, Murty Dasaka S, Sivakuma Babu GL (2015) Forensic analysis of Malin landslide in India. *IOP Conf Ser Earth Environ Sci* 26(1)
3. Fredlund DG, Xing A (1994) Equations for the soil-water characteristic curve. *Can Geotech J* 31(4):521–532
4. Keefer DK, Wilson RC, Mari RK, Brabb EE, Brown Iii WM, Ellen SD, Harp EL, Wieczorek GF, Alger CS, Zatkint RS (1987) During heavy rainfall (November)
5. Krahn J (2004) Stability modeling with SLOPE/W an engineering methodology
6. Rahardjo H, Li XW, Toll DG, Leong EC (2001) The effect of antecedent rainfall on slope stability. *Geotech Geol Eng* 19(3–4):371–399
7. Rahardjo H, Ong TH, Rezaur RB, Leong EC (2007) Factors controlling instability of homogeneous soil slopes under rainfall. 133(December):1532–1543
8. Sarvade SM, Sarvade MM, Khadatare PS, Kolekar MR (2017) 30/7 Malin landslide: a case study (October 2014)
9. Schuster RL, Fleming RW (1986) Economic losses and fatalities due to landslides. *Bull Assoc Eng Geol* 23(1):11–28
10. Schuster RL, Highland LM (2007) The third Hans Cloos lecture. Urban landslides: socio-economic impacts and overview of mitigative strategies. *Bull Eng Geol Env* 66(1):1–27
11. Shah MV, Sudani P (2020) Strength and deformation characteristics of laterite rock with different rock matrix's using triaxial system, 85–102
12. Singh TN, Singh R, Singh B, Sharma LK, Singh R, Ansari MK (2016) Investigations and stability analyses of Malin village landslide of Pune district, Maharashtra, India. *Nat Hazards* 81(3):2019–2030
13. Thiebes B, Bell R, Glade T, Jäger S, Mayer J, Anderson M, Holcombe L (2014) Integration of a limit-equilibrium model into a landslide early warning system. *Landslides* 11(5):859–875

Model Testing on PET Bottle Mattress with Aggregate Infill as Reinforcement Overlaying on Fly Ash Under Circular Loading



Shahbaz Dandin, Mrudula Kulkarni, and Maheboobsab Nadaf

Abstract The consumed PET bottles which are readily cellular restrict lateral movement. Comprehensive studies surface every day with alarming statistics on the most pressing environmental issues. By recycling, an attempt is made to lay down the effective procedure for reinforcement in fly ash fills, for which the subsurface and mountains are excavated for the purpose of backfill in the infrastructure construction. The objective of this work is to know the practical behavior of fly ash (a coal combustion residue) backfill overlaying reinforcement of consumed water bottle mattresses which are customized with reasoning and bottle pockets filled with various aggregate grading. By placing 1000 and 500 ml PET bottle mattress on fly ash bed, a sequence of plate load tests would be performed. The varying parameters considered for these series are four varying cellular infill aggregate grading (A_d , A_3 , A_6 , and A_{12}); two different PET bottle cell aperture sizes (P_d 50 mm and P_d 73 mm); and three varying sizes of circular footing plate for loading ($B' = 80, 160, \text{ and } 240$ in mm). A total of 36 trial procedures are noted to analyze the retort of the system. As a result, the reinforced fly ash system indicated a higher bearing capacity than the non-reinforced condition by 432%; the optimum ratio of the diameter of the cell (P_d) to the aggregate grading (A) is $P_d/A = 16$, and also it is known that the effective ratio of the diameter of the cell (P_d) to the width of footing (B') values should be lower than 0.5 times the footing width (B') for achieving the highest possible stability and reliability under vertical loading.

Keywords Plate load test · PET bottle mattress · Fly ash · Cellular reinforcement · Aggregate infill

S. Dandin (✉) · M. Kulkarni
School of Civil Engineering, MIT World Peace University, Pune, India
e-mail: shahbaz.dandin@mitwpu.edu.in

M. Nadaf
Department of Civil, ADCET, Astha, Sangli, India

© The Author(s), under exclusive license to Springer Nature Singapore Pte Ltd. 2023
M. S. Ranadive et al. (eds.), *Recent Trends in Construction Technology and Management*, Lecture Notes in Civil Engineering 260,
https://doi.org/10.1007/978-981-19-2145-2_59

779

Abbreviations

CD	Consolidated drain
PET	Polyethylene terephthalate
P_d	Diameter of the cell pocket
ϕ	Angle of internal friction
c	Apparent cohesion
A_d	Quarry dust as aggregate
A_3, A_6, A_{12} (3/6/12)	Size of aggregate in mm
PLT	Plate load test
F	Footing plate size
B	Width of the PET bottle mattress reinforcement
D_b	Buried depth from a top surface of cell mattress
Q_{ult}	Ultimate bearing capacity
δ_{ult}	Ultimate deformation
B'	Width of the footing plate
A	Aggregate

1 Introduction

The reinforcement of backfill material in various civil engineering projects like retaining wall, low-lying areas, plinth filling, and reinforced earth wall are experienced based on the performance, stability, and usage in practice, as well as in prototype model research. The consumption of natural resources for earth fills, majorly in infrastructure construction, is leaving a serious impact on the environment [28]. Nevertheless, the utilization of fly ash as a concern is to be effectively replaced with a conventional system of backfilling proposal. The performance is based on the following factors, which include the material used, type of installation, mode of practice, drainage pattern, and type of loading. Previous research works worked on the effects, behavior, and bearing capacity of fly ash backfill, with and without providing reinforcement [2, 12, 15, 16, 27, 30, 31]. The alarming statistical data of water bottle generation is booming with greater demand [13]. The overflowing landfill capping system with millions of tons of discarded water bottles has been an environmental hazard. The usage and recycling have been effectively settled up with design procedures as of the conventional procedure of earth filling for stability. Among all the reinforcement concerning function, the geocell reinforcement is more advantageous and beneficial; it has reduced settlement and has increased the bearing capacity [28]. Such honeycomb structured reinforcement is to be replaced by a consumed water bottle mattress as the functional role is similar. Some researchers have worked on the laboratory experimentations on large and small-scale model studies on the parameters like settlement, bearing capacity resistance, and stability with various procedures laying down, like the studies by Ghosh and Subbarao [1], Kim and Prezzi [22], Xu

and Shi [17] experimentally remarked that the fly ash as a mass can be worked in geotechnical engineering application.

Choudhary et al. [12] provided geogrid reinforcement in fly ash slope under strip loading. The different series of patterns of reinforcement by geogrid were placed with varying layer thickness within fly ash with respect to burial depth for varying footing widths. The load versus settlement characters were observed experimentally and concluded that the increase in geogrid layers within the fly ash fill enhances the bearing capacity and sustains the fly ash slope. Moreover, the alternative reinforcement was experimented with by the author Nadaf et al. [27] with plastic bottle arrangement in fly ash slope by considering 60° to the horizontal. The parameters considered were coverage ratio, varying edge distance with a series of strip footing widths and cell heights of 10, 20, and 30 mm, and wall thickness of the cell was 0.15 mm of the plastic bottles. The fly ash slope was placed with different burial depths and layers of bottle strips were placed by considering the coverage ratio for achieving the desired density of fly ash bed with steel strips mixture. The vertical strip loading was experimented; results and observations were made; and bearing capacity incremental behavior was observed with an increase in coverage ratio, reducing the spacing of burial depth. A 30–60% settlement reduction was observed compared with the unreinforced fly ash slope. Tavakolo Mehrjardi et al. [33] experimentally concluded that the subgrade with weak strength over overlaid reinforcement ends up with higher settlement exerting more tension through the reinforcement plane. Dutta and Mandal [15] examined the efficiency of unreinforced and reinforced fly ash backfill that underlays soft clay, with particular emphasis on the behavior of the fill material. Different types of techniques were adopted in the tank study; fly ash column was embedded into marine clay with fly ash column perforated with plastic encasement of 105 mm diameter with inner wrapping with jute geotextile (end bearing column). A layer of woven jute geotextile is placed as a function of separators between marine clay and fly ash fill in a geocell mattress made up of plastic bottles and experimented with impinged to vertical loading of a circular plate of varying sizes. The study determines maximum efficiency for the group column situation and efficiency of triangular and square patterns. They observed that the four columns had good footing capacity than the single and three columns. The literature reviewed indicates that encasing the stone columns with suitable geosynthetic reinforcement enhances its capacity to a greater extent. Ram Rathan et al. [30] have noted that minimizing the coverage ratio of reinforcement reduces load-bearing capacity. Fly ash as cell infill material is less efficient as it causes larger backfill material sliding down due to its smaller grain size alongside the cell walls during settlements, which in turn restricts the effectiveness of bottle mattress on increasing bearing capacity [24]. The consumed water bottles should also be considered for laboratory testing [15].

Based on the above-stated views on the reuse of fly ash and PET bottle in mass quantity, the following areas have been identified and considered in the present research. The response of plastic bottle mattress reinforced fly ash bed is directly affected by coverage area, so laying down plastic bottle mattress (100% coverage) is considered in the present research. The primary study aims to prove that the behavior

of compacted fly ash bed ($H = 750$ mm) subjected to vertical loading with varying sizes of footing plate ($B' = 80, 160, \text{ and } 240$ in mm); to examine the compression behavior of fly ash bed overlying customized plastic bottle mattress with varying ratios of cell diameter (P_d 50 mm and P_d 73 mm) to the aggregate size ($A_d, A_3, A_6,$ and A_{12}) and also to decide the ratio of the diameter of a plastic bottle (P_d) to the width of the footing (B').

In view of the fact that, as claimed by Maghadas et al. [24], the ratio of burial depth of geocell to the loading plates diameter was considered 0.1 and Tavakoli et al. [34] claimed that the loading plate's diameter was selected as 0.25 times the width of geocell (in our case it is B) which is considered in this present research.

2 Test Article

2.1 Fly Ash

Class “F” Grade II fly ash is considered for this experimental study. Fly ash was collected from Nashik thermal power station, Eklahare, Maharashtra, India. The physical characteristics and chemical properties of the fly ash are summarized in Tables 1 and 2.

Table 1 Physical and mechanical characteristics of fly ash

Properties	Value	
Color	Tan-brownish	
Specific gravity (G_s)	2.1	
Fine sand size particles	20%	
Silt size particles	70%	
Clay size particles	10%	
Liquid limit; W_L	26%	
Plasticity; W_p	–	
Dry unit weight; γ_d	13.5 kN/m ³	
Optimum moisture content; OMC	18.5%	
Classification	IS 3812–1981	Grade II
	ASTM C618	Class F
The angle of shearing resistance; Triaxial-CD test (φ)	12.04°	
Apparent cohesion; Triaxial-CD test (c)	7 kN/m ²	

Table 2 Major chemical characteristics of fly ash (X-ray fluorescence)

Components	Measure (%)
SiO ₂	56
Al ₂ O ₃	25
Fe ₂ O ₃	8
CaO	2
LOI	4

2.2 Cellular Reinforcement-Consumed PET Bottles

The polyethylene terephthalate bottles considered for this study have the cells of diameter and height of 50/100 and 73/150 in mm, mentioned aspect ratio between 2 and 2.2 (500 and 1000 ml mineral water bottle), respectively, and are collected from our university garbage yard. There are various diameters of water bottles which are available for packed mineral water from manufacturers. Among all the sizes most widely consumed are of 500 and 1000 ml.

Figure 1a, b illustrates a view of a customized PET bottle, individually and a group of bottles forming a mattress with a pocket diameter of 50 mm (P_d 50); P_d is the “diameter of the pocket”. The aspect ratio of the cell pocket’s diameter to the medium grain size varies from 3.4 to 36.7. To make a cellular mattress, plastic water bottles of 500 and 1000 ml capacity with 50 and 73 mm diameter are used in the tank study. These bottles were cut from the cap side with a height of 100 mm and

Fig. 1 **a** A view of the customized single plastic bottle with aspect ratio = 2.
b A view of the customized PET bottle mattress



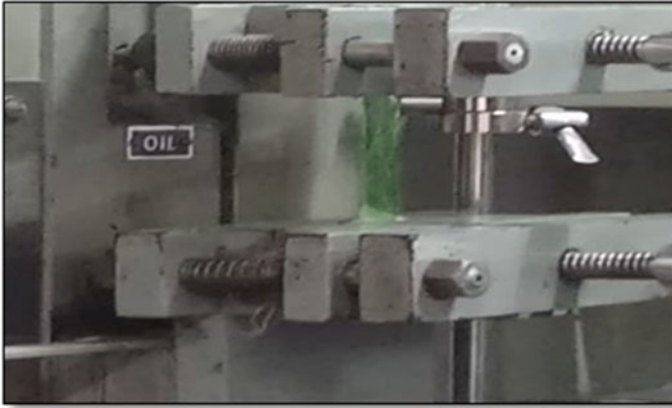
(a)



(b)

Table 3 Characteristics of a plastic water bottle

Reinforcement	Property	Average value
PET bottle (strip of 15 × 2 cm) ASTM D638-2014	Tensile strength (ISO 527-1; Dutron testing machine)	150.57 MPa
	Tensile modulus	2349.63 MPa
	Wall thickness	0.25–0.30 mm

**Fig. 2** Testing setup of PET bottle strip of 15 cm × 2 cm in Dutron testing machine

150 mm for 500 ml and 1000 ml bottles, respectively. Holes of diameter 5 mm at equal spacing intervals from the side and bottom face were made with the help of a soldering machine for drainage purposes. These bottles were joined together by a manual 26/6 stick stapler to form a mattress. The engineering properties of the PET bottle are specified in Table 3. The ultimate tensile strength and tensile modulus of a plastic bottle are tested by preparing the strip of 15 × 2 cm, firmly fixed in the frame (see Fig. 2), and tension is created in Dutron testing machine. The reading is recorded for three numbers of samples till failure, and the mean value was taken into account. The total modulus is equal to (tensile strength × total length)/change in length (Fig. 2).

2.3 Aggregate Infill in the Cellular PET Bottle Pockets

For cellular pocket fill, four grading of uniform aggregate with the size of A_d , A_3 , A_6 , and A_{12} is taken into account for the study, underlying fly ash bed. Further, more than 12 mm size of aggregate gives self-lateral restrain because of a higher void ratio, so restricted to 12 mm aggregate (A_{12}) as cellular fill material. The physical

characteristics of these pocket infill materials are classified as per the Indian Standard Soil Classification System (ISSCS) and are described in Table 4.

A_d is stone quarry dust as aggregate; A_3 is ≤ 3 mm aggregate grading; A_6 is ≤ 6 mm aggregate grading; A_{12} is ≤ 12 mm aggregate grading (Fig. 3).

Table 4 Physical properties of aggregate used as infill in PET bottle mattress

Description	Aggregate quarry dust	Aggregate 3 mm	Aggregate 6 mm	Aggregate 12 mm
Specific gravity	2.6	2.52	2.43	2.33
Coefficient of curvature, C_c	0.62	1.24	1.03	0.93
Coefficient of uniformity, C_u	13.8	2.7	2.13	1.3
Medium grain size, D_{50} (mm)	–	4	5.9	12.4
Water content	–	–	–	–
Fractured particles (%)	–	90	88	85
Crushing value (%)	–	26	29	34
Soundness (%) NaSO_4	–	7	9	9



Fig. 3 A view of the plastic bottle mattress “ $P_d 73$ ” with cellular pocket infill with 3, 6, 12 in mm and quarry dust aggregate grading

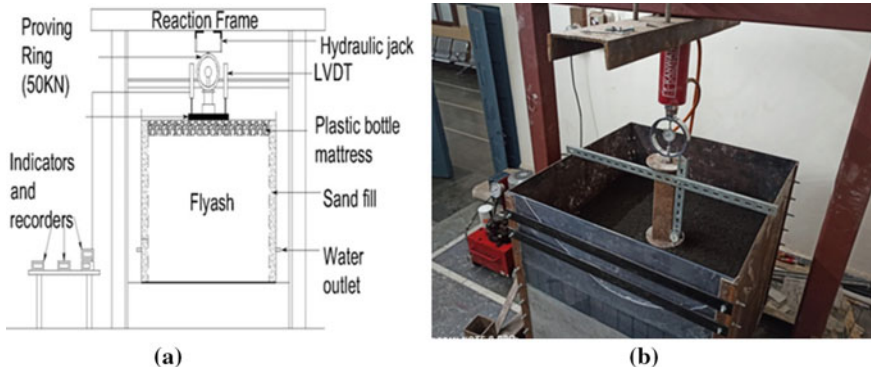


Fig. 4 **a** Schematic representation of the test setup with reinforcement (not to scale). **b** Model test tank experimental setup in the laboratory

3 Experimental Setup, Instrumentation, and Test Approach

Tankage was used to execute the experimental test series. It exemplifies a schematic view, notifications, and dimension; “ z ” is the burial depth from the top of the mattress to the vertical loading surface; B' is the loading plate width; H is the height of the fly ash fill in the tank; and B is the width of PET bottle mattress.

3.1 Geometry of the Tankage

The view of the experimental model testing setup is shown in Fig. 4a, b. Mild steel plate cube of 8 mm thickness; in-to-in dimensions of 1000 mm³. The front view face of the tankage was fitted with an acrylic sheet for visual observation and behavioral change has been seen. Vertical loading is imposed till the failure to ensure the rigidity of the tankage. The complete cube was fixed by the bolting system. Sidewalls were additionally supported by steel columns at equal spacing.

3.2 Loading Arrangement

The reaction loading frame was fabricated, as shown in Fig. 4b. A hydraulic jack was supported by a reaction beam and a detachable setup was made on the jack for proving ring placement; in turn, the proving ring had been given a detachable connection to the square loading plate of 20 mm thickness. The three different sizes of circular loading plate were considered, i.e., 80, 160, and 240 in mm such that the vertical loading is imposed on the center of the tankage; the size of the circular loading plate was chosen such that the stress should be within the tankage, i.e., semi-infinite

condition. Selig and Mckee [32] and Chummer [13] stated with their experimental analysis that in the foundation bed the failure wedge is extended over a distance of about 2–2.5 times the width of the footing from the center. The uniform vertical load is imposed via a hydraulic jack and the proving ring measures the applied pressure having the capacity of 50 kN; uniform incremental loading is maintained throughout the series of the test as per the laid procedure for plate load test (PLT) IS:1888-1982. In the entire reinforcement experiment series or pattern on fly ash fill, the incremental loading has increased to workable stress up to 179 kN/m², but it was not the same in all the testing program patterns. If the failure pattern was not observed, the deformation was restricted to 40 mm settlement or 0.25 times the diameter of the loading plate. The LVDTs were placed diagonally on the loading plate to avoid tilting of footing with an accuracy of 0.01%; due to the diagonal placing of LVDTs, tilt was easily known so that appropriate balance can be maintained and an average of deformation can be noted on each incremental loading.

3.3 Fly Ash in the Tankage

The tankage is filled with fly ash at the height of 750 mm, which is compacted in three layers of equal height with respect to an optimum moisture content of 18.5%. Each layer is compacted with the compaction effect of around 600 kJ/m³ to achieve the maximum dry density of 13.5 kN/m³ as per IS-2720 part7. In order to ensure maximum, a dry density proctor needle is used as obtained from the calibration curve (water content in % vs. penetration resistance in kN/m²). All the sides of the tankage are filled with coarse material for drainage purpose and compaction is also achieved effortlessly. Once the desired height of 750 mm of fly ash fill is achieved, then the implementation of the plastic bottle mattresses is introduced.

3.4 Bottle Pocket Infill

Once the customized bottle mattresses are placed on a compact fly ash fill surface, covering the area of 0.75 m², the aggregates are poured into the bottle pocket and after the desired height of the aggregate is achieved, i.e., the height of the bottle plus 20 mm (z , the burial depth), the compaction is carried out by vibratory plate to achieve relative density (D_r) of 84%.

4 Test Program

The series of reinforcement patterns overlaying fly ash bed were performed on cellular pocket diameter, loading plate area, and aggregate grading to check the

failure behavior on loading. Plate load tests of 36 trials are carried out as mentioned in Table 4. Examination parameters were a cellular bottle of diameters 50 and 73 mm; the aggregate of 3, 6, and 12 in mm and quarry dust, respectively, and loading plate size (B') is 80, 160, and 240 mm. Each trial is experimented with to investigate the influence of one parameter, whereas the diverse parameter continued to be persistent. Results were drawn on load–settlement. While conducting the test procedures few test trials were reiterated to ensure the reliability of the result. The present research considers the conclusions of Tafreshi and Dawson [24] that the buried depth of cellular reinforcement (geocell) with varying burial trials was analyzed and concluded that the buried depth should be 0.1 times of loading plate width and also considered the remark of the research by Tavakoli et al. [34] that the geocell mattress should be laid such that it must be four times the vertical loading plate width; the length of bottle cell size is considered as constant with length by diameter (L/D) ratio of 2:2.2 (Table 5).

5 Results and Discussions

The following results and analysis are related to the bearing capacity of the foundation in the fly ash bed without reinforcement, plastic bottle fly ash bed reinforced by P_d 50 and P_d 73. Figure 5 outlines the bearing capacity for each reinforced and unreinforced fly ash foundation which is on load–settlements. The feedback could be contracting due to poorly graded aggregate size and backfill surface having different diameters of loading areas.

Series 1: Fly ash fill as foundation bed without reinforcement. The basic findings of this experimental tank study are to know the behavior of fly ash subjected to vertical loading with varying sizes of footing plate, the fly ash as foundation bed, load versus settlement data were recorded. As predicted initially the behavioral observation report was similar. The increase in footing plate size and incremental values of Q_{ult} were observed, as shown in Fig. 6. The settlement was drawn down rapidly within the small loading of a maximum of 41.6 kN/m² for three cases. As the vertical deformation was observed the particles were showing lateral movement toward the phase of the tank which ensures and teaches us that confinement is needed to sustain higher loads. The above observation was seen as similar in all the three footing plate trials. The graph seen in Fig. 6 named load–settlement behavior for fly ash fill is to be represented as Q_{ult} by the use of Table 6 so that values of Table 6 are achieved. Let us recall Terzaghi's bearing capacity equation that as we increase the breadth of the footing, the bearing capacity increases. The results were not so shocking as they were predicted (Figs. 7 and 8).

Series 2: Fly ash fill as foundation bed overlaying P_d 50 PET bottle mattress with various aggregate grading within the cell. The coverage area of 100% laid as plastic bottle mattress was more efficient than reducing the coverage area. The bottles were used with two intentions in mind; lateral confinement and end bearing

Table 5 Testing program

	Test trials			Reinforcing condition	Footing plate diameter (mm) B'	Burrial depth (D_b) = $0.1 \times B'$ (mm)	Width of reinforcement (B) = $4 \times B'$ (mm)	Fly ash fill height (H) (mm)
	Aggregate grading							
	A_4	A_3	A_6					
Series 1	1	10	19	Unreinforced	80	-	-	750
	2	11	20		160	-	-	750
	3	12	21		240	-	-	750
Series 2	4	13	22	Reinforced by P_d 50	80	8	320	750
	5	14	23		160	12	480	750
	6	15	24		240	15	600	750
Series 3	7	16	25	Reinforced by P_d 73	80	8	320	750
	8	17	26		160	12	480	750
	9	18	27		240	15	600	750

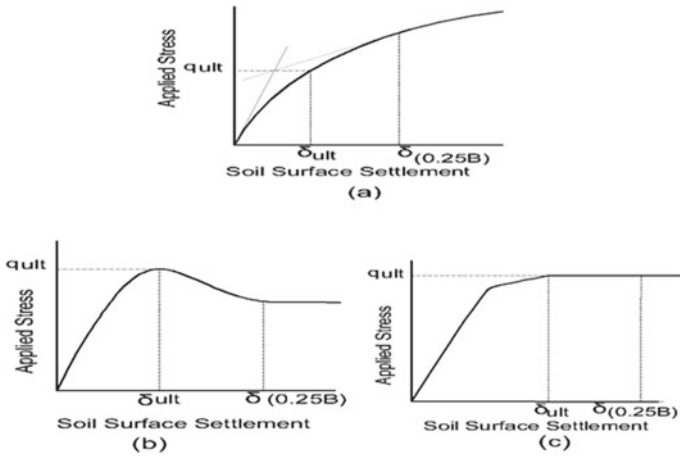


Fig. 5 Behavior of load versus settlement curve and representation of q_{ult} . **a** Toughening action, **b** soften action, **c** flexible ideal plane action

Fig. 6 Load–settlement behaviors for fly ash fill bed (F is the footing plate)

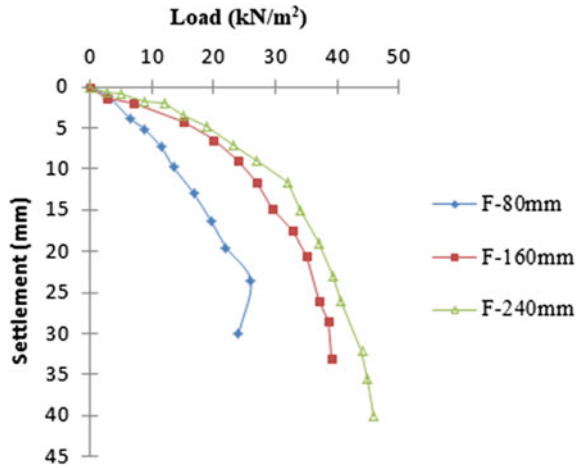


Table 6 Fly ash fill as foundation bed values of load and settlement

Loading plate diameter (mm)	Q_{ult} kN/m^2	δ_{ult} (mm)
80	21.3	28.5
160	38.3	32.6
240	41.6	35.2

Fig. 7 Response of Q_{ult} —aggregate size (reinforced condition P_d 50)

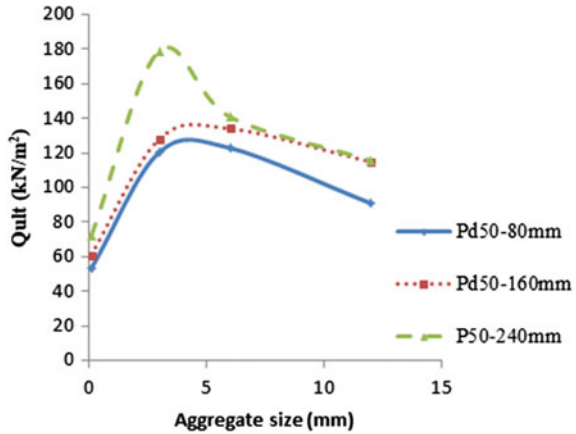
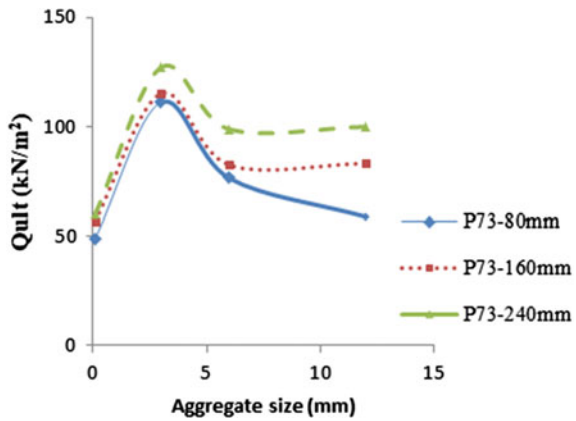


Fig. 8 Response of Q_{ult} —aggregate size (reinforced condition P_d 73)



to the aggregate as an infill into the pocket so that aggregate won't penetrate into the fly ash and, in turn, sustain less load and rapid settlement. The learnings of vertical loading behavior of plastic bottle mattresses by varying ratio of the diameter of cell aperture (P_d) to the aggregate size (P_d/A) were obtained 16, i.e., 16 times of aggregate size to that of an aperture of the bottle. Table 6 shows the values of load versus settlement with the reinforced condition of two aperture sizes of bottle with footing plate diameters 80, 160, and 240 in mm and fly ash in micron as cell infill (Table 7).

A_3 showed greater values compared to other sizes of aggregate infill. A_d , quarry dust infill, also showed excellent bearing resistance against loading but slight heaving was observed on the surface that leads to large settlement, as the loading plate was circular with a maximum of 240 mm, so heaving was predicted in quarry dust infill because of the lower weight of surcharge pocket infill, but it was not the same in other cases, due to larger deadweight of heavy aggregate heave was negligible. Once

Table 7 Values of load–settlement at Q_{ult} for reinforced patterns of P_d 50 and P_d 73

Reinforced condition	Footing diameter (mm) B'	A_d		A_3		A_6		A_{12}	
		Q_{ult} kN/m ²	δ_{ult} (mm)	Q_{ult} kN/m ²	δ_{ult} (mm)	Q_{ult} kN/m ²	δ_{ult} (mm)	Q_{ult} kN/m ²	δ_{ult} (mm)
P_d 50	80	83	35	120.4	28	122.8	26.2	90.8	28
	160	91	33	128	39	134	30	114.8	38
	240	109	40	179	33	140/8	44	115.6	33
P_d 73	80	89	32	111.2	25.6	76.4	29	58.8	25
	160	97	30	115.2	36	82.4	29.2	83.2	36
	240	101	37	127.2	32	98.8	32.8	100	32

the most efficient is known, the ratio of individual pocket cell size to the aggregate size (P_d/A) is observed as 16. In short, small size aggregate grading ≤ 3 mm screen was effective when we look at the observational results.

Series 3: Fly ash fill as foundation bed overlaying P_d 73 PET bottle mattress with various aggregate grading within the cell. Figure 9 describes the response of plate size once loaded in reinforced condition, and a gradual increment is observed with respect to loading plate size. The initial plate size is 80 mm, and as the plate size is doubled with the size of 160 mm, the bearing capacity increases. Now it is understood that reducing the loading plate size with the phase as aggregate reduces Q_{ult} , i.e., brings down around 200% with respect to the maximum Q_{ult} . The ratios of individual pocket size to the loading plate size are remarked. The loading plate should be 0.5 times more than the individual plastic bottle pocket when taken into account in the form of mattress. In the entire fly ash reinforced condition pattern the bottom portion of the bottles was not punctured, which means the bottle has the capability to sustain higher loading. Due to this without failure the entire load was taken by aggregates and lateral support by plastic bottles; this was a good combination needed to sustain higher stress (Fig. 10).

Fig. 9 Response of plate size once loaded (reinforced condition P_d 50)

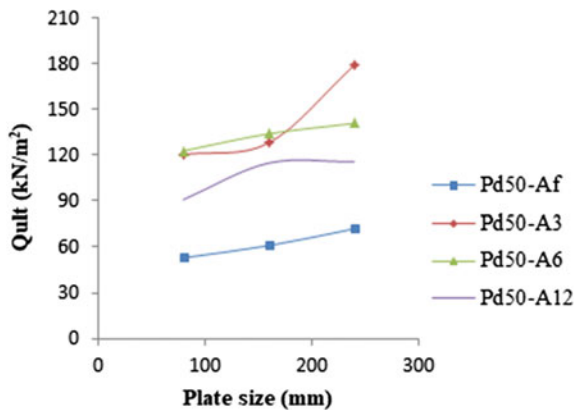
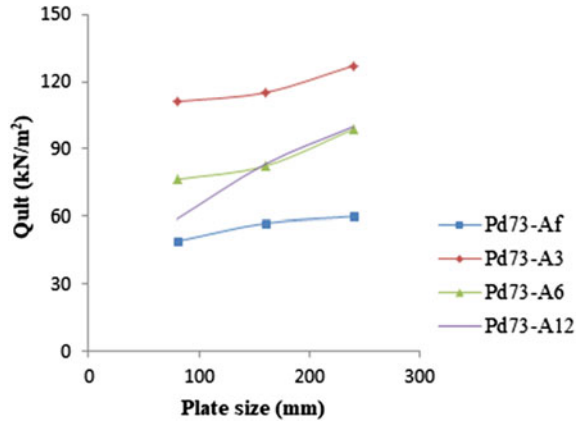


Fig. 10 Response of plate size once loaded (reinforced condition P_d 73)



Limitations The model tankage is 1 m^3 , where the surface area was 1 m^2 ($100 \text{ cm} \times 100 \text{ cm}$). The loading plate diameter (B') was restricted to 240 mm due to the plain strain footing concept, in the view of the semi-infinite boundary condition; the stress shall be within the fly ash foundation. The aggregate grading considered in this research as infill material in PET bottle pockets is limited to A_{12} because $>12 \text{ mm}$ aggregate can self withstand the lateral movement once loaded vertically; in short, no cellular support is required. The saturated condition of fly ash fill with and without reinforcement is not practiced due to the lack of prerequisites held on drainage arrangement while installation of model tankage in the laboratory.

6 Conclusions

In plate load tests, a series of trials are carried out to evaluate the consumed plastic bottles as reinforcement underlying fly ash bed as these stated materials (fly ash and PET bottle mattress) are the major contributors to lower the environmental hazards. An attempt to utilize these materials has a positive impact on replacing the conventional earth filling. This view of transportation of fly ash from the nearby thermal power stations will be economical in utilization for infrastructure constructions.

The detailed results obtained from this experimentation with respect to systems are presented below:

- It is an upright method to intensify the bearing capacity and reduce settlement. In some situations, proper selection of effectual parameters for cellular reinforcements can boost the reinforced fly ash backfill up to 5.2 times when compared with non-reinforcement; the mass utilization of fly ash compaction bed is effective and resistant to shear failure.
- By maintaining the footing width (B') in the range of 13–27 (20 on average) times, the aggregate size (A) of $\leq 3 \text{ mm}$ pocket fill material has benefitted in the usage

of the plastic bottle as reinforcement and also it is suggested that the size of cell opening (P_d) is chosen in such a way that it should be less in size than 0.67 times of footing width, in order to obtain more balanced and dependable plastic bottle mattress reinforcements fly ash backfill.

- This work also demonstrates the delicacy of the significant variables on the plastic bottle mattress-reinforced fly ash system and thus allows stimulating the applications of their most appropriate span. Though the experimentation results were restricted to the span of the size of the loading plate, just two types of cross-section areas of plastic bottles with the same height and four types of gravel grading. Particular execution of practice in the field must only be made after taking into account the above limitations.

Lastly, it is concluded that this research work provides vision and awareness to the basic mechanics that establishes the performance of waste plastic bottle mattress as reinforcement underlying partially saturated fly ash fills under vertical loading.

Funding and Acknowledgements This experimental research was funded by the Directorate of Minorities, Bengaluru, India. Grant ID: PhD/CR-35/2018-19. We are also thankful to Abhishek Mandlik, Onkar Madane, Rushikesh Lokhande, Shadab Shakil, and Raunak Walekar—UG students, School of Civil Engineering, MITWPU, Pune, India for the assistance in the overall journey of the experimentation.

References

1. Anand A, Sarkar R (2020) A probabilistic investigation on bearing capacity of unsaturated fly ash. *J Hazard Toxic Radioact Waste (ASCE)* 24(4):06020004. [https://doi.org/10.1061/\(ASCE\)HZ.2153-5515.0000547](https://doi.org/10.1061/(ASCE)HZ.2153-5515.0000547)
2. Kumara A, Mandal JN (2017) Effect of reinforcement on multi-tiered fly ash wall. *Transportation Geotechnics and Geoecology*, TGG 2017, 17–19 May 2017, Saint Petersburg, Russia. <https://doi.org/10.1016/j.proeng.2017.05.072>
3. ASTM (1995) Standard test method for measuring pH of soil for use in corrosion testing. ASTM G51-95, West Conshohocken, PA
4. ASTM (2010a) Standard test method for measuring mass per unit area of geotextiles. ASTM D5261, West Conshohocken, PA
5. ASTM (2011a) Standard test method for breaking force and elongation of textile fabrics (strip method). ASTM D5035-11, West Conshohocken, PA
6. ASTM (2010b) Standard test methods for specific gravity of soil solids by water pycnometer. ASTM D854-10, West Conshohocken, PA
7. ASTM (2011b) Standard test method for consolidated drained triaxial compression test for soils. ASTM D7181-11, West Conshohocken, PA
8. ASTM (2011c) Standard test method for tensile properties of geotextiles by the wide-width strip method. ASTM D4595-11, West Conshohocken, PA
9. ASTM (2012a) Standard specification for coal fly ash and raw or calcined natural pozzolan for use in concrete. ASTM C618-12, West Conshohocken, PA
10. ASTM (2012c) Standard test method for measuring nominal thickness of geosynthetics. ASTM D5199-12, West Conshohocken, PA
11. Biabani MM, Indraratna B, Ngo NT (2016) Modelling of geocell-reinforced subballast subjected to cyclic loading. *Geotext Geomembr* 44(4):489–503

12. Choudhary AK, Jha JN, Gill KS (2010) Laboratory investigation of bearing capacity behavior of strip footing on reinforced fly ash slope. *Geo text Geomembr* 28(4):393–402
13. Chummer AV (1972) Bearing capacity theory from experimental results. *J Soil Mech Found Div ASCE* 98(12):1311–1324
14. Capital D (2011) *Plastics commodity to custom products: Redefining perception*. Mumbai, India
15. Dutta S, Mandal JN (2016) Model studies on geocell reinforced fly ash bed overlying soft clay. *J Mater Civil Eng*. [https://doi.org/10.1061/\(ASCE\)MT.1943-5533.0001356,04015091](https://doi.org/10.1061/(ASCE)MT.1943-5533.0001356,04015091)
16. Dutta S, Mandal JN (2017) Model studies on encased fly ash column-geocell composite systems in soft clay. *J Hazard Toxic Radioact Waste Manage*. [https://doi.org/10.1061/\(ASCE\)HZ.2153-5515.0000353,04017001](https://doi.org/10.1061/(ASCE)HZ.2153-5515.0000353,04017001)
17. Xu G, Shi X (2018) Characteristics and applications of fly ash as a sustainable construction material: a state-of-the-art review. *Resour Conserv Recycl* 95–109
18. Ghosh KP, Mukherjee K, Saha S (2015) Fly ash of thermal power plants: review of the problems and management options with special reference to the Bakreshwar thermal power plant, Eastern India. *Int J Geol Earth Environ Sci* 5(2):74–91
19. Gill KS, Choudhary AK, Jha JN, Shukla SK (2013) Experimental and numerical studies of loaded strip footing resting on reinforced fly ash slope. *Geosynth Int* 20(1):13–25
20. Hegde A, Sitharam TG (2015) Joint strength and wall deformation characteristics of a single-cell geocell subjected to uniaxial compression. *Int J Geomech*. [https://doi.org/10.1061/\(ASCE\)GM.1943-5622.0000433,4014080](https://doi.org/10.1061/(ASCE)GM.1943-5622.0000433,4014080)
21. Hegde AM, Sitharam TG (2014) Effect of infill materials on the performance of geocell reinforced soft clay beds. *Geomech Geoeng Int J* 10(3):163–173
22. Kim B, Prezzi M (2008) Evaluation of the mechanical properties of class-F fly ash. *Waste Manag* 28(3):649–659
23. Kim B, Prezzi M, Salgado R (2005) Geotechnical properties of fly and bottom ash mixtures for use in highway embankments. *J Geotech Geoenviron Eng*. [https://doi.org/10.1061/\(ASCE\)1090-0241\(2005\)131:7\(914\),914-924](https://doi.org/10.1061/(ASCE)1090-0241(2005)131:7(914),914-924)
24. Moghaddas Tafreshi SN, Dawson AR (2010b) Comparison of bearing capacity of a strip footing on sand with geocell and with planar forms of geotextile reinforcement. *Geotext Geomembr* 28(1):72–84
25. Nadaf MB, Dutta S, Mandal JN (2016) Fly ash as backfill material in slopes using waste pet bottles as reinforcement. In: *Proceedings of 6th IconSWM, International Society of Waste Management, Air and Water, Kolkata, India*, pp 1209–1215
26. Nadaf MB, Mandal JN (2014) Triaxial behavior of steel grid reinforced fly ash. In: *Proceedings of Indian Geotechnical Conference, Indian Geotechnical Society, Kakinada, India*, pp 50–54
27. Nadaf MB, Mandal JN (2017) Model studies on fly ash slopes reinforced with planar steel grids. *Int J Geotech Eng* 11(1):20–31
28. NPCS (NIIR Project Consultancy Services) (2020) *Pet bottle recycling*. <http://www.niir.org/profiles/profile/2045/pet-bottle-recycling.html> (Dec. 9, 2020)
29. Ram Rathan Lal B, Mandal JN (2012) Feasibility study on fly ash as backfill material in cellular reinforced walls. *Electron J Geotech Eng* 17(J):1437–1458
30. Ram Rathan Lal B, Mandal JN (2014a) Behavior of cellular reinforced fly-ash walls under strip loading. *J Hazard Toxic Radioact Waste Manage*, 45–55. [https://doi.org/10.1061/\(ASCE\)HZ.2153-5515.0000201](https://doi.org/10.1061/(ASCE)HZ.2153-5515.0000201)
31. Ram Rathan Lal B, Mandal JN (2014b) Model tests on geocell walls under strip loading. *Geotech Test J* 37(3):477
32. Dash SK, Majee A (2021) Geogrid reinforcement for stiffness improvement of railway track formation over clay subgrade. *ASCE* 21(9). [https://doi.org/10.1061/\(ASCE\)GM.1943-5622.0002128](https://doi.org/10.1061/(ASCE)GM.1943-5622.0002128)
33. Tavakoli Mehrjardi G, Behrad R, Moghaddas Tafreshi SN (2019) Scale effect on the behavior of geocell-reinforced soil. *Geotext Geomembr* 47(2):154–163
34. Yoo C (2001) Laboratory investigation of bearing capacity behavior of strip footing on geogrid-reinforced sand slope. *Geotext Geomembr* 19(5):279–293

Recent Trends in Structural Engineering

Sustainable Project Planning of Road Infrastructure in India: A Review



Appa M. Kale and Sunil S. Pimplikar

Abstract Road infrastructure in India is growing speedily. Vision (2030) anticipates a quality, dependable, sustainable, resilient infrastructure, and sound technology. Road infrastructure can be built by using the sustainability concept. A conventional road causes environmental and social issues as well as affects the economy of road infrastructure. To overcome this problem sustainable planning is a very prominent solution. By reviewing research papers of the previous 30 years, life cycle cost analysis seems to be a key method for achieving required growth. Further, along with life cycle cost analysis, various other techniques such as Project Definition Rating Index (PDRI) and Project Rework Reduction Tool (PRRT) suggested by the researchers are also inferred.

Keywords Road infrastructure · Sustainable development · Life cycle cost analysis · Sustainable planning · Sustainable development goals

1 Introduction

After the Paris Convection of the United Nations Climate Change Conference (2015), the usage of 17 development goals for a developing nation like India has opened the doors just as difficulties. The Government of India, by and large, and the Ministry of Road Transport and the Highway (MoRT&H) have specifically focused on an absolute fulfillment of 200,000 km of national highways by 2022, including on venture of 7 trillion for the commitment of other roads and highways throughout the following 5 years.

India is practically seeing a proceeded with advancement in sustainable development. The improvement business has been an onlooker to a strong advancement wave

A. M. Kale (✉) · S. S. Pimplikar
Dr. Vishwanath Karad, MIT World Peace University, Pune 411038, India
e-mail: appakale297@gmail.com

S. S. Pimplikar
e-mail: sunil.pimplikar@mitpune.edu.in

fuelled by huge spending on housing, streets, ports, water supply, and air terminal progression. The advancement division has enlisted twofold digit improvement in the midst of the several years and its proposal as a degree of GDP has extended stunningly when diverged from the latest decade. The Planning Commission of India has proposed a theory of around US\$ 1 trillion in the Twelfth 5-year plan (2012–2017), which is twofold that of the Eleventh 5-year plan.

The report on Indian urban infrastructure and services MoUD (2011) investigated the three primary elements affecting income contrarily, for example, deficit in granting projects according to design, setback in financing, and wasteful venture execution which adds to a US\$ 200 million misfortune to GDP by 2017 (100 + 20 + 80).

India's logistic infrastructure is lacking, unfit, and ill-designed to help the expected development pace of 7–8% throughout the following decade. Expected 2.5-overlap development in dismay traffic will additionally press India's infrastructure.

Gaining from the past and embracing worldwide accepted procedures seek after a calculated foundation system that limits speculation, expands cost-effectiveness for clients, and is energy productive.

2 Literature Review

Vision (2030) expects a quality, reliable, sustainable, and resilient infrastructure which is affordable as well as even more having increased resource use efficiency, and use of clean, environmentally sound technology, and industrial processes, further demanding a focus on greater research and development efforts as well as restoring to the innovative approaches (Achieving Sustainable Development in India: The study of Financial Requirement and Gaps 2015) [21].

NHAI with 40% equity and the remaining 60% annuity model investment from Canada, Malaysia, Japan, and Asian Development Bank is accelerating the infrastructure development in India. Sapatnekar et al. [31] have emphasized the need of regulating infrastructure development in India based on the modeling and anticipating various risks arising due to the gap existing between the planning and execution, adopting world standards as against their effective implementation, improper coordination and communication among various stakeholders, uncontrolled wrong professional practices, and the like.

The report on Indian Urban Infrastructure and Services MoUD (2011) has analyzed the three main factors impacting revenue negatively, such as shortfall in awarding projects as per plan, shortfall in funding, and inefficient project execution which contribute to a US\$ 200 million loss to GDP by 2017 (100 + 20 + 80).

India's logistic infrastructure is lacking, unfit, and ill-designed to help the expected development pace of 7–8% throughout the following decade. Expected 2.5-overlap development in dismay traffic will additionally press India's infrastructure.

Gaining from the past and embracing worldwide accepted procedures seek after a calculated foundation system that limits speculation, expands cost-effectiveness for clients, and is energy productive [23].

It examines how India's present logistic infrastructure is lacking to meet its development goal and gauge the current and future grouping of freight traffic streams in the country to characterize strategic prerequisites and monetary ramifications (McKinsey & Company 2015).

Life cycle analysis appears to be a very promising solution which will enable to reduce the aforementioned gap [1, 4, 5, 7, 8, 10–12, 14, 15, 17, 24–27]. Nevertheless, for determining the research gap the following points need to be considered.

These include:

1. Clarifying enhancing and achieving optimum combination of life cycle cost analysis and value engineering and an objective of developing comprehensive guidelines or standards, thus enabling the inclusion of hidden and social costs [5].
2. Raghuram et al. [10] have recommended measures to reduce time and cost overrun related to environmental clearance and land acquisition being identified as a major reason for delays in the road sector. Researchers further suggest scope for improvement in the use of technology, transparent assessment, appointment of an independent trustworthy land evaluator, decentralization in decision making, and special capacity building so as to crack global business opportunities.
3. Extension of the sustainable engineering infrastructure model suggested by Okon et al. [13] for applicability under Indian conditions and for further facilitating decision making based on risk [22, 28 (Chi, Bunker, Teo 2016) and return evaluation, stakeholder's perspective, and sustainability issues in the highway project.
4. Ikpe and Hammon [15] have recommended a potential area for further research in construction industries with respect to establishing effective health and safety on construction sites.
5. Alam et al. [17] have presented a qualitative model which identifies the impact levels of various life cycle analysis components associated with road projects, thus establishing a comprehensive system boundary for life cycle analysis of the road. Researchers have suggested for the work in regards to the quantitative assessment of parameters so as to facilitate objectivity in decision making.
6. Buneo et al. [18] recognize significant difficulties in improving life cycle assessment of transport projects, like the requirement for normalization and using between the fleeting accumulation of substantial and immaterial environmental, social and economic impacts, fixing the markdown rate for its maintainability thing distinguished as the zone of additional exploration. Specialists further accentuate that particular attributes and worries of society have not been remembered for and utilized by practical examination instruments.

7. Mishra et al. [20] suggest further research to identify critical success factors converting current issues of PPP project as essential for the sustainability of PPP of road projects.
8. Godinho and Dias, Alam [14, 24] has incorporated the impact of road user's greenhouse gases (RUG factor), has recommended the determination of global warming potential (GWP) based on life cycle analysis, has used a research framework in determining the road sustainability index, suggested a universal concept of standard carbon vehicle (SCV), further advocated that road agencies develop albedo matrix different types of pavement surfacing based on the age of payment, for assessing GWP on real-time field measurements, and has finally observed that infrastructure rating schemes show inadequate consideration to life cycle aspect of road infrastructure in terms of credit items and weights.
9. Babashamsi et al. [25] have suggested including preventive maintenance treatment as a part of strategic management for bettering the performance of existing pavement life cycle cost analysis models, further quantifying them, and if possible, standardizing the value associated with user cost.
10. Castro [26] accentuates consideration of risk and sensitivity analysis in the existence cycle cost examination to build the degree of dependability and certainty assessed model.
11. Yu et al. [29] suggest the use of sustainable project planning (SPP) which has been used for predicting project success of Chinese construction projects for other sectors as well (applicability to road sector performance in the Indian context may be explored).

3 Conclusion

1. Based on the literature review conducted, it appears that sustainable highway infrastructure can be achieved with help of Sustainable Project Planning Model (SPPM).
2. This in turn is expected to contribute to social, environmental, and economic aspects of the society.

References

1. Fwa, Sinha (1991) Pavement performance and life cycle cost analysis. *Am Soc Civ Eng*, 1–5
2. Cottell (1993) Facilitating sustainable development: Is our approach correct? *J Prof Issues Eng Educ Pract ASCE*, 21–24
3. Feis (1994) Sustainable development issues: industry, environment, regulation and competition. *J Infrastruct Syst ASCE*, 51–59
4. Ravirala, Grivas (1995) State increment method of life cycle cost analysis for highway management. *J Infrast Syst ASCE*, 151–159

5. Arditi, Messiha (1999) Life cycle cost analysis (LCCA) in municipal organizations. *J Infrastruct Syst ASCE*, 1–10
6. Horvath, Matthews (2004) Advancing sustainable development of infrastructure systems. *J Infrastruct Syst ASCE*, 55–63
7. Feng, Wang (2008) Integrated cost–benefit analysis with environmental factors for a transportation project: case of Pinglin interchange in Taiwan. *J Urban Plann Dev*, 161–167
8. Gho, Yang (2009) Extending life-cycle costing analysis for sustainability considerations in australian road infrastructure projects, Rethinking sustainable development: planning, infrastructure engineering, design and managing urban infrastructure. Faculty of Built Environment and Engineering, Queensland University of Technology, Queensland University of Technology, Brisbane, Queensland, pp 324–331
9. Raghuram, Bastian, Sundaram (2009) Mega projects in India: environmental and land acquisition issues in the road sector. Indian Institute of Management Ahmedabad, pp 2–15
10. Madanu et al (2010) Life-cycle cost analysis of highway intersection safety hardware improvements. *J Transp Eng ASCE*, 25–33
11. Okon, Ekpo, Elhag (2010) Cost-benefit analysis for accident prevention in construction projects. *J Transp Eng ASCE*, 103–111
12. Gho, Yang (2010) Responding to sustainability challenge and cost implications in highway construction projects. *J Transp Eng ASCE*, 236–245
13. Okon, Ekpo, Elhag (2010) A sustainable engineering infrastructure model for the 21st century. In: Proceedings of the world congress on engineering, pp 35–46
14. Godinho P, Dias J (2012) Cost-benefit analysis and the optimal timing of road infrastructure. *J Transp Eng ASCE*, 99–107
15. Ikpe, Hammon (2012) Cost-benefit analysis for accident prevention in construction project. *J Constr Eng Manag ASCE*, 64–69
16. Hwang, Tan (2012) Sustainable project management for green construction: challenges, impact and solutions. In: Ciob construction conference, WCC, pp 39–47
17. Alam, Kumar, Dawes (2012) Life cycle analysis for sustainability assessment of road projects. CIB World Building Congress, pp 76–88
18. Buneo, Vassello, Cheung (2013) Sustainability assessment of transport infrastructure projects: a review of existing tools and methods, 1–28
19. Meyer, Kassa (2013) Sustainable streets and highways: an analysis of green roads rating systems. Georgia Transportation Institute Report, pp 1–23
20. Mishra, Narendra, Kar (2013) Growth and infrastructure, investment in India: achievements, challenges, and opportunities. *Econ Anal*, 51–70
21. Envision 2030 (2015) 17 Goals to transform the world for persons with disabilities, Department of Economic and Social Affairs, United Nations-Disability, pp 57–81
22. Mohapatra (2015) An economic analysis of improvement of road infrastructure: a case study. *Eur Acad Res*, 14637–14650
23. Achieving Sustainable Development in India: The Study of Financial Requirement and Gaps, Build Resilient Infrastructure, Promote Inclusive and Sustainable Industrialization and *Foster Innovation Report*, 5–34
24. Alam (2016) Developing life cycle environmental indicators for road infrastructure. Ph.D. thesis, Queensland University of Technology, Australia, pp 10–28
25. Babashamsi et al (2016) Sustainable development factors in pavement life-cycle: highway/airport review. *Sustainability*, 3–8
26. Castro (2016) Life cycle cost analysis of road infrastructures using LCC Am/Qm software. *Tecnico Lisboa*, 1–9
27. Chi, Bunker, Teo (2017) Measuring impacts and risks to the public of privately operated toll road projects by considering perspectives in cost-benefit analysis. *J Transp Eng ASCE*, 77–76
28. Agarchand (2017) Sustainable infrastructure development challenges through Ppp procurement process: Indian perspective. *Int J Proj Manage*, 53–59
29. Yu, Zhu, Yang, Wang, Sun (2018) Integrating sustainability into construction engineering projects: perspective of sustainable project planning. *Sustainability*, 1–17

30. Demand for Grants 2018–19 Analysis; Road Transport and Highways, PRS Legislative Report, pp 1–6
31. Sapatnekar, Patnaik, Kishore (2018) Regulating infrastructure development in India. NIPFP Working Paper Series, pp 23–33

Behaviour of Space Frame with Innovative Connector



Pravin S. Patil and I. P. Sonar

Abstract The hollow circular tube is the most efficient section of space structure because of its lightweight and load resistance. Flatted end tube with a bolted connection is being the most economical connection with fast assembly, easy to transport, easy to maintain and easy to repair for space truss. This flatted end tube is connected with welded plates by bolting jointly, provided that welded plates are in the direction of force to avoid eccentricity in the space truss. A connector is an extremely important part of a prefabricated system and the final commercial of structural connections of all types has been the subject of intensive research during the last decade. Investigation into the behaviour of flatted, flattened and tapered flattened end tube is the main objective of the present work. Flatted, flattened and tapered end tube of 3-D space structure with an innovative connector is modelled in Catia. The performance is checked by Ansys analysis and results are discussed. The research on flattened and tapered end tube connector for steel tube space structure is the main contribution to this research work. The flattened and tapered flattened end tube connector shows better performance as compared to flatted end tube connector.

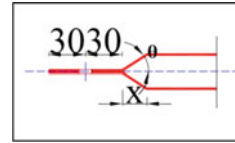
Keywords Flatted end tube · Flattened end tube · Tapered flattened end tube · Deflection of space frame

P. S. Patil (✉)

Assistant Professor @ Department of civil Engineering, DY Patil University Ambi Pune, Pune, Maharashtra, India
e-mail: pravinspatil154@gmail.com

I. P. Sonar

Associate Professor @ Department of Civil Engineering, College of Engineering Pune, Pune, India

Fig. 1 Flattened end tube

1 Introduction

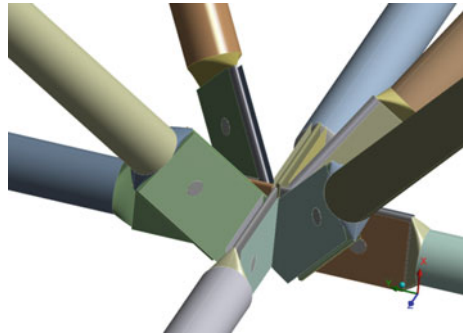
End flattened connectors are a type of bolted connection. The hollow sections used for space frame elements are pressed and flattened at their ends. The flattened ends are connected with a single bolt. This type of connector is economic and gives a pleasing appearance in the space frame. This type of connector is more common in Brazil, where it is used in many large textile industries, churches, sports gymnasiums, and soccer stadiums and in infrastructures such as warehouses for grain storage, bus and railway stations and airports. The structural components are end flattened structural elements of a bolt. Since the structural elements are less, it is easy to assemble. For space structure flattened, flattened and tapered flattened members have been used. The flattened end tube is the hollow circular tube that has been pressed at the ends ($\theta = 90$ as shown in Fig. 1). In flattened end tube give a particular angle for smooth load path analysis ($\theta = 30$ as shown in Fig. 1). Tapered flattened end thickness has to be increased at the end to reduce the stresses, and after this, it should be called a tapered flattened end tube.

From the literature review, this paper contains a newly developed space truss system with reduced cost but the same behaviour and ease of construction [1]. Two new approximately analysing methods favourable for dynamic analysis of space trusses have been presented in this paper [2]. The paper introduces a space truss system newly developed as an attempt to reduce the cost of space trusses without compromising their behaviour or ease of construction [3]. In this paper, efficient neural networks are analyzed for the design of a double-layer grid. Square diagonal on diagonal with a span varying 26.5–75 m was considered [4]. The results conclude that 68% raise in local collapse is associated with the serviceability limit state and a 17% increase in global collapse is associated with the ultimate limit state in the truss load-carrying capacity [5, 6]. The structural behaviour up to the collapse of reinforced eccentric and simple eccentric nodes was discussed on the basis of the experimental. To improve the structural load-carrying capacity and minimize deflection, a structural reinforcement is created [7].

2 Innovative Connector

The innovative connector has been employed consisting of the use of tubular members with flatted and flattened ends, but connected to a device composed of welded steel

Fig. 2 Innovative connector



plates in the direction of force referred to in Fig. 2. This innovative connector allows for the elimination of node eccentrics.

3 Assembly of Space Frame Connector

After creating all the necessary component parts, each model is assembled in Catia Assembly. Each member is assembled to form a node. In each assembly, the datum plane is given three references in x , y and z to match its exact position. After assembling the horizontal and inclined (bracing) parts, the node is bolted. To check if there is an interface between the members in that particular node, then that node is analysed for ‘global interface’. When global interface is there, then meshing will not be made in ANSYS. Therefore, if any parts are overlapping, it is to be corrected at each node. Level complete model is assembled as in Fig. 3, checked for interface and exported for analysis in ANSYS, as shown in Fig. 4.

Meshing has done in such a way that there is no connection with each other. That gives unstructured mesh generation for all parts (Fig. 5).

Fig. 3 Space frame

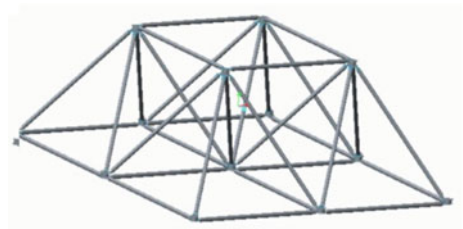


Fig. 4 Space frame with innovative connector

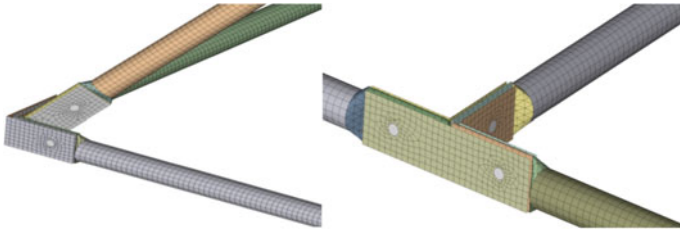


Fig. 5 Meshing of space frame

4 Analysis Setup

To perform a better finite element analysis, our work was done by ANSYS 14.5. However, SAP analysis is made for a space frame without flattening the tube. This is performed to check the member forces and deflection theoretically.

Modelled space frame and analysis setup details are furnished below:

Long span: 2 m

Short span: 2 m

Grid size: 1 m

Grid type: Square on square

Bracing angle: 45°

Member CHS (Circular Hollow section)

Member size: CHS 50 mm OD, 2 mm thick

Connector type: Innovative connector with flatted, 30° flattened end tube ($\theta = 30^\circ$) and tapered flattened end tube ($\theta = 30^\circ$)

Material: Fe250

Support condition: Fixed at four ends. Node 1, 3, 7 and 9 (Ref Fig. 7)

Loading: incremental up to 50 kN

Bolt diameter: 16 mm (Fig. 6).

Fig. 6 Space frame analysis setup

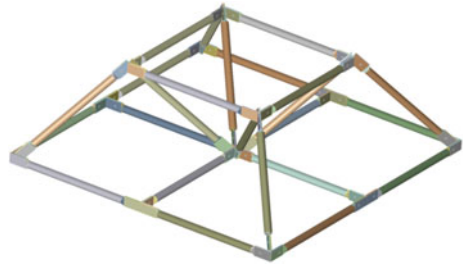
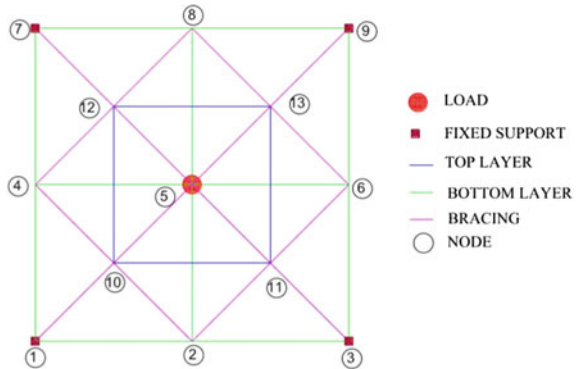


Fig. 7 Space frame analysis setup SAP2000



5 Analysis of Space Frame in SAP2000

Analysis setup is made in SAP2000. AutoCAD line diagram prepared is exported in SAP. For all the lines, the geometry of the hollow section with a size of 50 mm outer diameters and 2 mm thickness is assigned. Material steel with a yield strength of 250 MPa (Fe250) is assigned to all the tubes. End nodes in the bottom layer are fixed, while the centre node is loaded from 5 to 50 kN. The analysis model in SAP is shown in Fig. 7.

6 Loading on Space Frame

Load is applied in node 5 (Fig. 8). Properly the load is applied in the bolt fixed at node 5 in 'y' direction. In ANSYS, the y direction acts as the vertical direction. Load is applied from 5 to 50 kN in an incremental order of 5 kN. Totally, in 10 s, 10 loads were applied. This is performed to study the behaviour of the space frame for an incremental load.

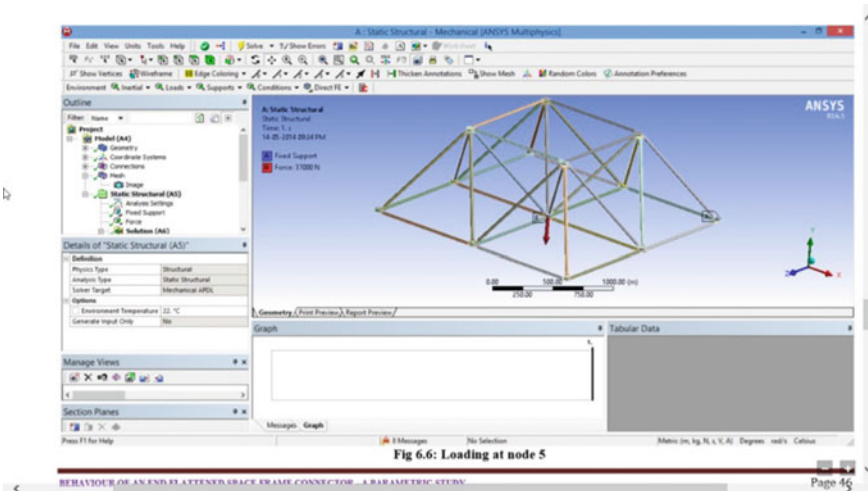


Fig. 8 Loading on space frame

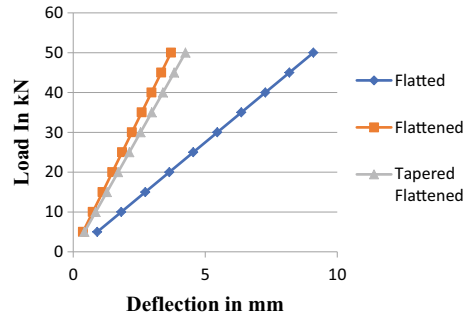
7 Performance of Simple Tube, Flatted, Flattened and Tapered Flattened End Tube of Space Frame

In any structure, the displacement of nodes must be less. Due to local effects, a structure shall experience positive or negative deflections. Globally, a structure with minimum deflection is considered as a safe structure.

7.1 Deflection for Flatted, Flattened and Tapered Flattened End Tube

Load vs displacement shows the elastic performance of a structure. It depends on the material property of the structure. Our space frame is of steel Fe250, so yielding is expected. In Fig. 9, load versus deflection of the 2 mm thick model is seen. It is observed that flatted end tube model experiences more deflection than other models. Minimum deflection is very essential to select a good model since deflection is a criterion of limit state of serviceability. When deflection is less, then the structure is stiff enough to resist loads. It is observed that flatted end tube experiences more deflection than flattened and tapered flattened end tubes. If we see the slope of load–deflection curve for flattened and tapered flattened model, it is linear, with an inclination nearly equal to 85°. Minimum deflection is very essential to select a good tube since deflection is a criterion of limit state of serviceability. When deflection is less, then the tube is stiff enough to resist loads. The flattened end tube model experiences less deflection (load application point of flatted end tube).

Fig. 9 Load versus deflection of space frame



From load–displacement figures, minimum deflection is seen in flattened end tube. It shall be justified that when load path is smooth in a member then secondary effects like torsion and moment in that member will be less which gives negative effects and reduces deflection. At flattened end tube, the load path is smooth; therefore, these models experience less deflection. Other models have a sudden change in load path due to flattening angle, which increases the secondary effects. So, these models experience much displacement.

The deformed shape of the space frame of flatted end tube with an innovative connector for incremental loading is shown in Fig. 10. The red colour shows maximum deflection in the space frame.

The deformed shape of flattened end tube with an innovative connector for incremental loading is shown in Fig. 11. In this tube, the proper angle for smooth load path analysis is given at the end of the tube.

The deformed shape of tapered flattened end tube with an innovative connector for incremental loading is shown in Fig. 12. End thickness has been increased to reduce the stresses (Table 1).

8 Comparisons of Flatted, Flattened and Tapered Flattened End Tube

A comparison between flatted, flattened and tapered flattened models for the 5–50 kN is plotted in Fig. 13. In this comparison, at all loadings from 5 kN to 50 kN, the flattened end tube model experiences less deflection, while flatted end tube undergoes maximum deflection, so the flattened end tube gives good performance compared to flatted and tapered flattened end tube.

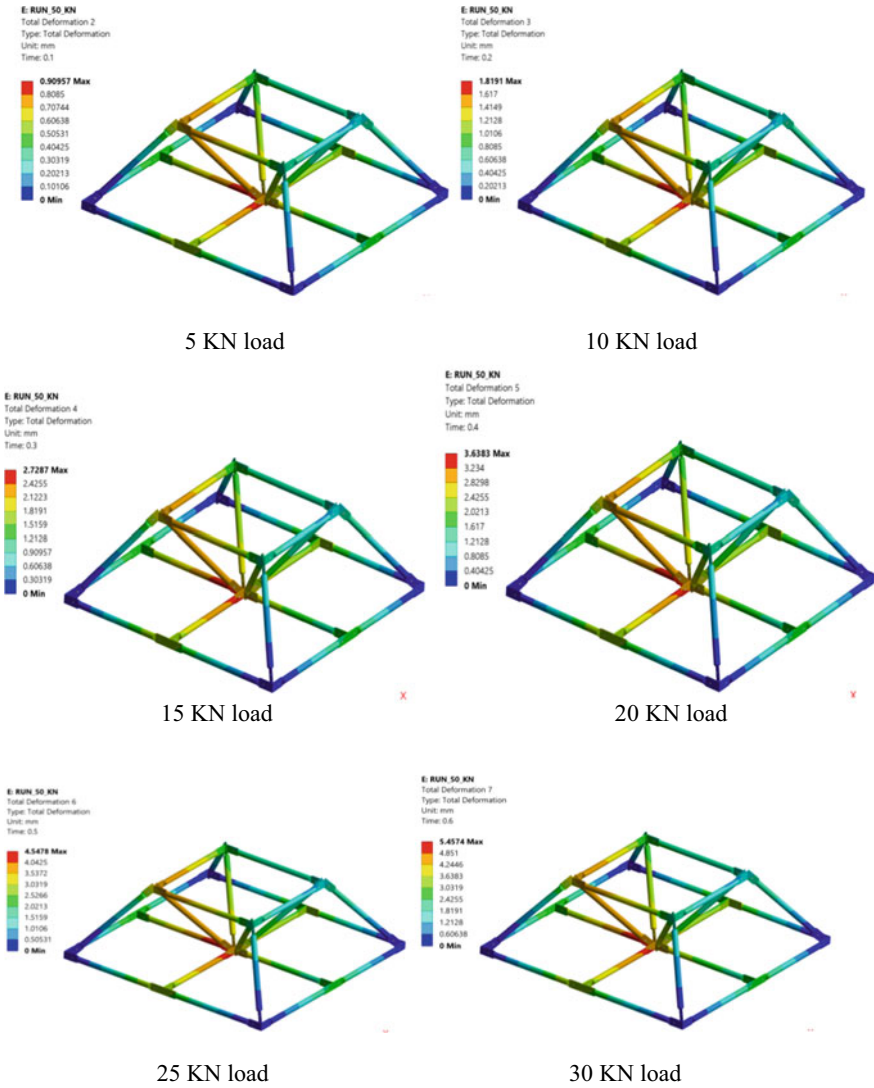


Fig. 10 Deformed shape of flatted end tube

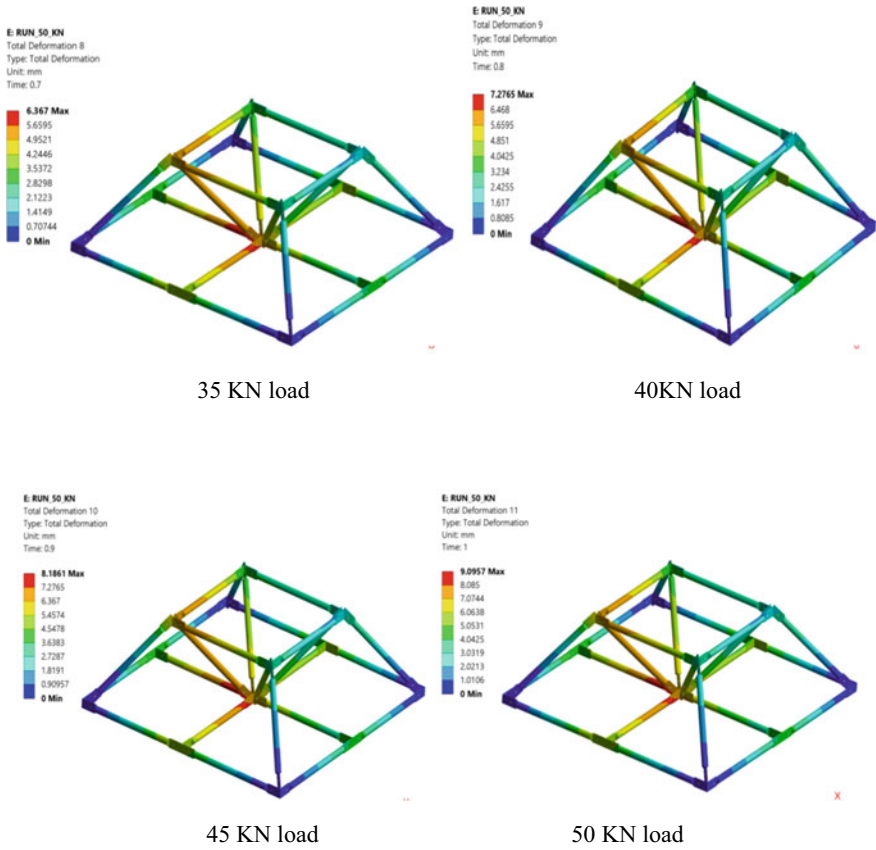


Fig. 10 (continued)

9 Conclusion

Space frame with end-flattened hollow sections connected with one bolt is easy to manufacture and economic. But, it does have some disadvantages like nodal eccentricities which produce secondary effects. In the case of space structure to avoid eccentricity and for easy connections, it is suggested to use an innovative connector. In the space frame model with an innovative connector, flattened end tube gives good performance compared to tapered flattened and flatted end tube.

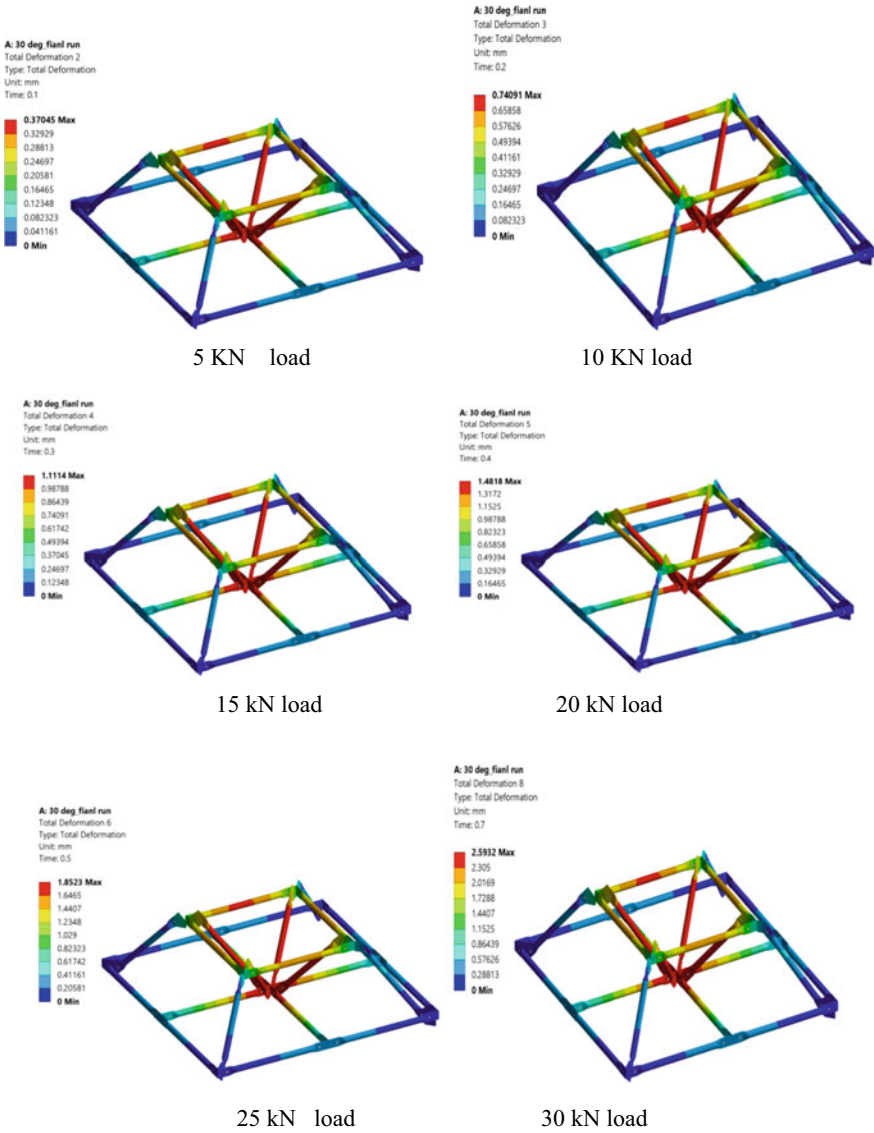


Fig. 11 Deformed shape of flattened end tube

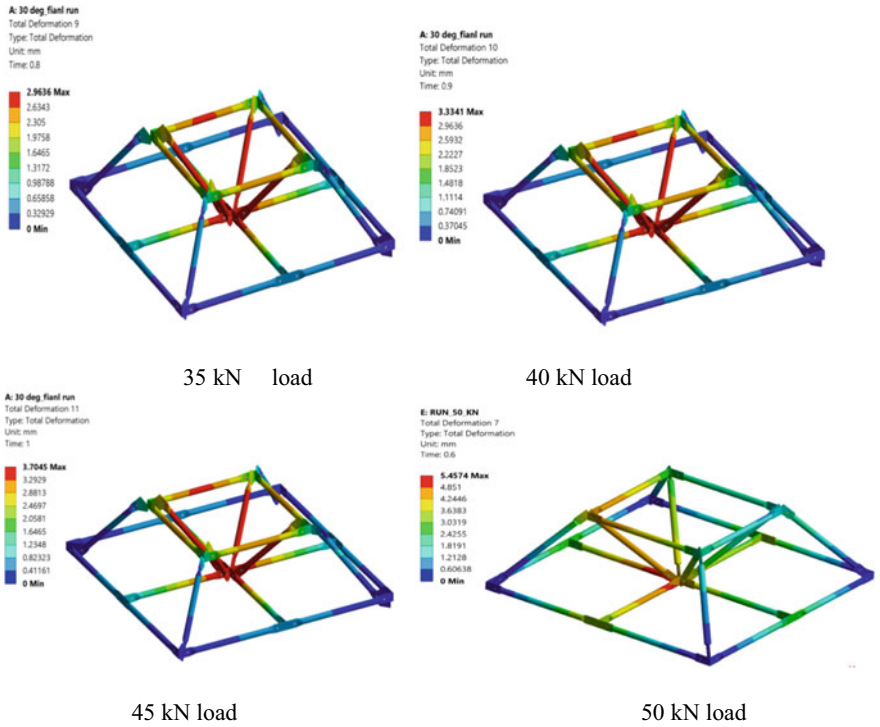


Fig. 11 (continued)

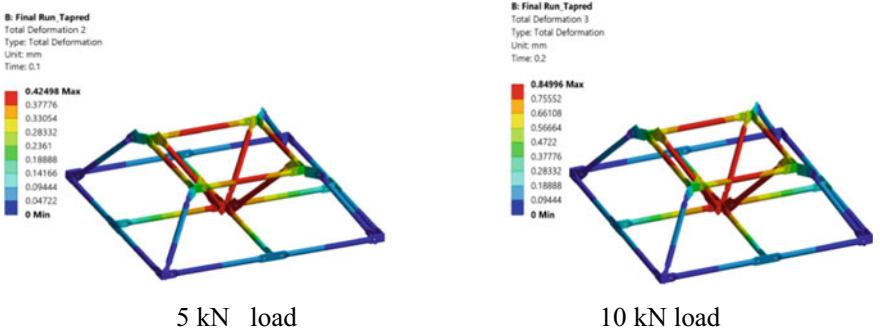
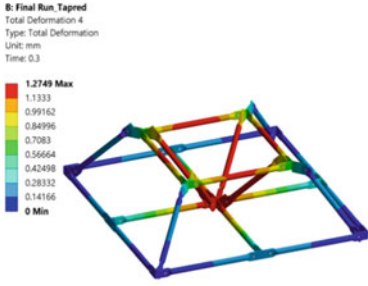
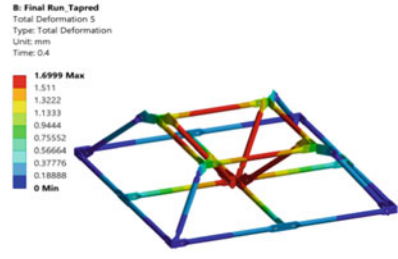


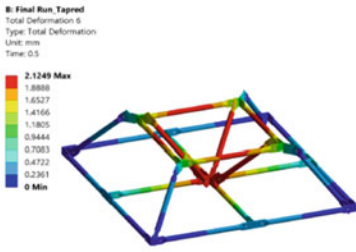
Fig. 12 Deformed shape of tapered flattened end tube



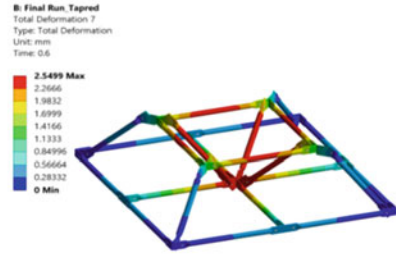
15 kN load



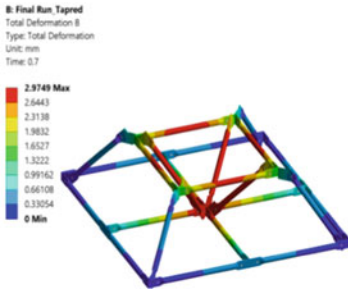
20 kN load



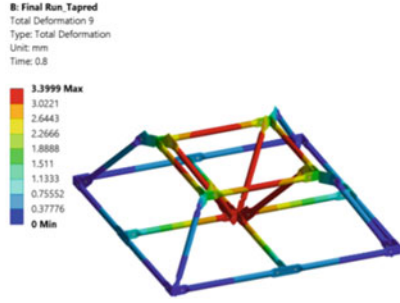
25 kN load



30 kN load



35 kN load



40 kN load

Fig. 12 (continued)

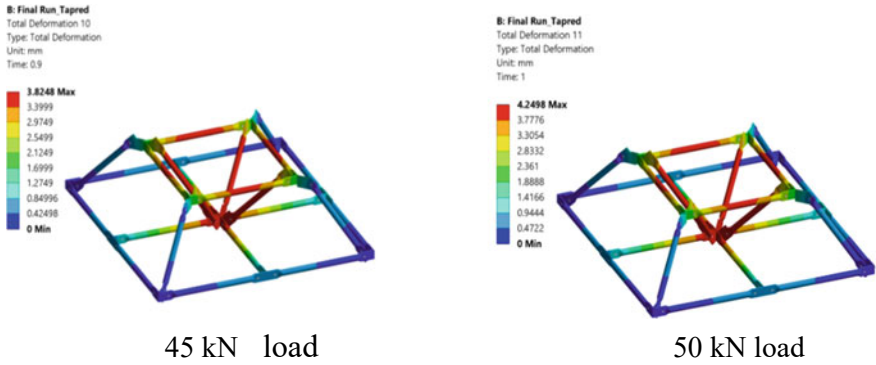


Fig. 12 (continued)

Table 1 Deflection of space frame for flatted, flattened and tapered flattened end tube

End tube	Deflection in mm									
	5 kN	10 kN	15 kN	20 kN	25 kN	30 kN	35 kN	40 kN	45 kN	50 kN
Simple tube	0.013	0.027	0.04	0.054	0.067	0.081	0.094	1.08	1.21	1.35
Flatted end tube	0.909	1.819	2.728	3.638	4.547	5.457	6.367	7.276	8.186	9.095
Flattened end tube	0.3704	0.740	1.111	1.481	1.852	2.593	2.963	3.334	3.704	3.704
Tapered flattened end tube	0.424	0.849	1.274	1.699	2.124	2.549	2.974	3.399	3.824	4.2498

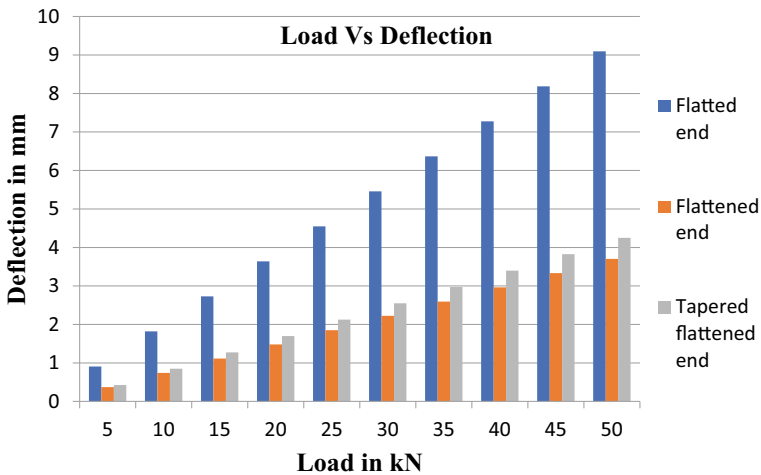


Fig. 13 Load versus deflection of flatted, flattened and tapered flattened end tube

References

1. El-Sheikh A (1996) Development of a new space truss system. *J Constr Steel Res* 37:205–227
2. El-Sheikh A (2000) Approximate dynamic analysis of space trusses. *J Eng Struct* 22:26–38
3. El-Sheikh A (2000) New space truss system from concept to implementation. *J Eng Struct* 22:1070–1085
4. Kaveh A, Servati H (2001) Design of double layer grid using back propagation neural networks. *J Comput Struct* 79:1561–1568
5. de Freitas CAS, Bezerra LM, Araujo RM, Araújo GM (2013) Experimental and numerical investigation of the space-truss with reinforce of the stamped connection. *J Exp Trusses, Roofs, Connections; ICSDEC 2012 ASCE 2013*
6. Bezerra LM, de Freitas CAS, Matias WT, Nagato Y (2009) Increasing load capacity of steel space trusses with end- flattened connections. *J Constr Steel Res* 65:2197–2206
7. de Andrade SAL, Vellasco PCGDS (2005) Tubular space trusses with simple and reinforced end-flattened nodes-an overview and experiments. *J Constr Steel Res* 61:1025–1050

Seismic Analysis of Base Isolated Building Frames with Experimentation Using Shake Table



Mahesh Kalyanshetti, Ramankumar Bolli, and Shashikant Halkude

Abstract Base isolation is the most effective and widely used technique for protecting a structure against seismic forces. The base isolation substantially decouples a structure from its base resting on the shaking ground, thus safeguarding the integrity of the structure by making them sustain the seismic forces without damage and also protect the lives of occupants. In the present study, an investigation is done to assess the seismic response of the structure with conventional fixed base and isolated base conditions. The isolation is configured with an elastomeric rubber isolator analyzed and designed in accordance with the International Building Code, IBC:2000. The analytical study is performed using ETAB application software and the experimentation is done using a uniaxial shake table on 1:12.5 scaled-down steel model developed using similitude laws corresponding to G + 3 and G + 5 prototype building frame. The study is carried out by applying three time histories, namely El-Centro, Uttarkashi and Indo-Burma. The fixed base condition is simulated in the laboratory by directly bolting the model on the shake table. The isolated base condition is simulated by mounting the model on an elastomeric rubber isolator. The study reveals that the acceleration produced in the base-isolated structure is reduced in the range of 40–60% in comparison with the fixed base condition. Pseudo spectral acceleration corresponding to fixed and isolated base conditions is obtained, which reveals that the time period of base-isolated structure increased to almost 2.5 s from 0.5 s. The shift in time period resulted in depletion in various parameters such as energy demand, pseudo acceleration and reinforcement requirement. The cumulative energy demand throughout the event of an earthquake is also studied. The reduction in energy demand for the isolated base condition is observed to be 50–90% lesser than in the fixed base condition. The reinforcement demand is reduced to 50% in isolated base condition. Thus, the study reveals that base isolation reduces the seismic demand of structure and enhanced safety, thereby reducing the cost of the structure.

M. Kalyanshetti (✉) · R. Bolli
Civil Engineering Department, Walchand Institute of Technology, Solapur, Maharashtra, India
e-mail: mgkalyanshetti@gmail.com

S. Halkude
Walchand Institute of Technology, Solapur, Maharashtra, India

Keywords Shake table · Base isolation · Scaled-down model · Elastomeric rubber · Time history · Time period · Pseudo acceleration

1 Introduction

The base isolation reduces earthquake forces by prolonging the time period of building. Different types of isolation systems used are friction pendulum bearing (FPB), elastomeric bearing, high damping bearing and lead core bearing. Elastomeric isolation system is used widely. Design of structure conventionally in seismic hazard regions would result in heavy costs. Provision of base isolation will prolong the time period, hence seismic demand will be reduced. The peak lateral acceleration was reduced by over 40% during dynamic tests carried out by Falborski and Jankowski [1]. Base isolation does not make a building earthquake-proof, but it can make the structure more flexible to control its frequency from dangerous resonance range [2]. The reduction in acceleration reduces the forces acting upon each story and the structure will move relatively less. The whole building frame during the earthquake tries to remain rigid. Base isolation reduced bending moment almost by four times as compared to fixed base structure [3]. This reduces the demand for reinforcement in the structure, hence making it cost-effective in heavy seismic zones. The base isolation is not effective in high-rise buildings as it produced large overturning moments and subsequently more tensile forces at the base [4]. Considering the effect of overturning and tilting, the tension resisting device arrangement is made to restrict the model from overturning and tilting. Low stiffness rubber isolators provide satisfactory structural behavior than moderate or high stiffness rubber isolator [5]. The elastomeric rubber bearing with hardness IRHD 60 is provided under each column which provides better stability and damping during the event of an earthquake, and also it can sustain the huge axial loads acting on it [6].

2 Objectives

The study is carried out to investigate the response of structure corresponding to fixed and isolated base conditions by carrying out analytical and experimental studies subjected to various time histories. Following are the specific objectives:

- i. To study seismic performance of structure subjected to various time history motions;
- ii. To study the effect of base isolation systems on seismic performance of building frame analytically using application software and experimentally using shake table;
- iii. To know the effect of isolation for two different configurations of building frames;

Table 1 Details of prototype R.C. building frame

S. No.	Particulars	Details	
1	Configuration	G + 3	G + 5
2	Height of story (m)	3.5	3.5
3	Concrete grade	M 25	M 25
4	Steel grade	Fe415	Fe415
5	Width of bay (both directions) (m)	4	4
6	Thickness of slab (m)	0.15	0.15
7	Column size	0.45 m × 0.3 m	0.40 m × 0.25 m (above third story) 0.45 m × 0.45 m (up to third story)
8	Beam size	0.4 m × 0.23 m	0.4 m × 0.23 m

- iv. To study the energy demand for the structures considering fixed and isolated base conditions;
- v. To study the change in time period of the structure due to base isolation;
- vi. To compare analytical results with experimental results to validate the experimental setup.

3 RC Building Frame Used for the Study

The study is carried out on G + 3 and G + 5 building frame with a single bay in both directions. In view of the feasibility of the experimental study, an appropriate geometry of the building frame is considered which is shown in Table 1.

4 Scaled-Down Steel Model

The important aspect of an experimental study is to configure an experimental model, which will produce identical behavior to that of the prototype structure. It is also observed that every aspect of the structure is not possible to be scaled due to payload capacity limitation of the shake table. But it should not be considered as a matter of big concern, since the objective of the test is not to qualify the prototype structure by testing but to study the behavior of structures, in general, subjected to dynamic loading. The most important task in scaling down is to achieve “dynamic similarity” so that the prototype and model experience homologous forces. For this purpose, the method suggested by Meymand [7] is adopted. Many of the scaling factors can be achieved by three principal test conditions. The first condition is a 1-g environment for testing, which ensures prototype and model accelerations to be the same. Secondly, the density of prototype and model should be similar by maintaining

Table 2 Scale factors

Parameters	Mass density	Acceleration	Frequency	Time	Length	EI	Strain
Scale factor	1	1	$S^{-1/2}$	$S^{1/2}$	S	S^5	1

other components of the scaling relations. Thirdly, appropriate scaling relation for natural frequency of prototype and model should be used. The scaling conditions are expressed in terms of the geometric scaling factor (S) for length, mass, acceleration, density and time.

4.1 Model Scale Factor

Selection of geometric scale factor is the critical step in the modeling process. In view of shake table specifications and the arrangements of holes on the table to hold the specimen, the spacing between two columns is kept as 0.32 m, which will lead to a linear scale factor of ' S ' = $4.0/0.32 = 12.5$ (corresponding to 4 m spacing in prototype structure). Therefore, a geometric scaling factor of 1:12.5 is adopted, and accordingly height, length, and width of the model are determined as 1.12 m, 0.32 m and 0.32 m, respectively. Table 2 shows various scale factors used for various parameters.

4.2 Scaling of Building Frames

The scaled-down models of both the building frames are prepared based on similitude laws. As a representative case, the scaled-down procedure of G + 3 building frame is discussed here.

The relationship between the natural frequency of model and prototype corresponding to $S = 12.5$ as per Table 2 is given in Eq. (1).

$$\begin{aligned} f_m/f_p &= S^{-1/2} \\ &= 3.54 \end{aligned} \quad (1)$$

Using the application software (modal analysis) natural frequency of the G + 3 prototype building is found, $f_p = 1.4792$ Hz. Therefore, according to Eq. (1), the required frequency of the model is 5.24 Hz.

The density of the prototype structure (ρ_m) is 264 kg/m^3 . Therefore, as per the second condition, the mass of the model (M_m) is calculated as

$$\begin{aligned} M_m &= \rho_m \times V_m \\ &= 30.269 \text{ kg} \end{aligned} \quad (2)$$

Table 3 Details of scaled-down model

S. No.	Particulars	Details	
1	Configuration	G + 3	G + 5
2	Height of story (mm)	280	280
3	Steel grade	Fe250	Fe250
4	Width of bay (mm)	320	320
5	Thickness of slab (mm)	4	3
6	Column size	10 mm × 10 mm	12 mm × 12 mm

The column and slab dimensions of scaled-down model are determined so that the weight of the model nearly equals to 30.269 kg and also it satisfies stiffness and flexural rigidity as required by simulated laws and produces a natural frequency of 3.54 Hz. The details of both the scaled-down models are presented in Table 3.

4.2.1 Scaling of Time History Input Motion for Scaled-Down Model

The study is carried out on time histories relevant to the Indian and global contexts. Two Indian time histories which are generally used by many researchers, i.e., Indo-Burma and Uttarkashi are used as these have produced high-intensity shaking, resulting in the destruction of thousands of homes. In the global context, El-Centro time history is very significant as it is characterized as a typical moderate-sized destructive event with a complex energy release. Thus, in view of all the above, the study is carried out on three time histories, namely Indo-Burma, Uttarkashi and El-Centro. It is essential to scale the input time history motion for the experimental study. The input provided to shake table is displacement time history. Hence in the case of scaling for the input motion of the shake table, the displacement and time has to be scaled with a linear scale factor. The representative calculations are shown below for El-Centro time history. Figure 1 shows the original time history motion of El-Centro 1940 earthquake with maximum displacement input of 131 mm. The scale factor for displacement and time is calculated in accordance with Table 2. The scale factor for displacement is ‘S’, i.e., 12.5 and the scale factor for time is ‘S^{1/2}’, i.e., 3.535. Accordingly, the time history is scaled which is shown in Fig. 2. Similarly, Indo-Burma and Uttarkashi time histories are scaled.

5 Experimental Setup on Shake Table

The servo-hydraulic uniaxial shake table size is 2 m × 2 m with a maximum payload capacity of 30 kN with a frequency range of 0.01–50 Hz. The experimental setup

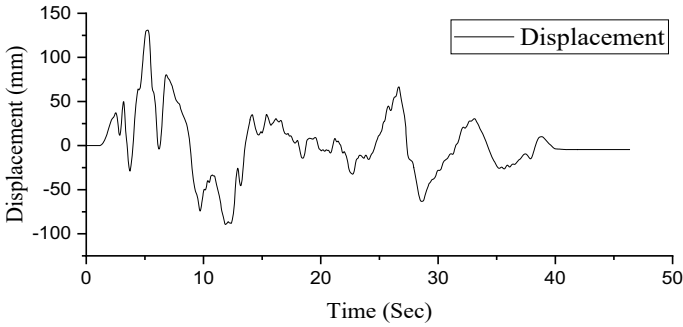


Fig. 1 Original El-Centro time history

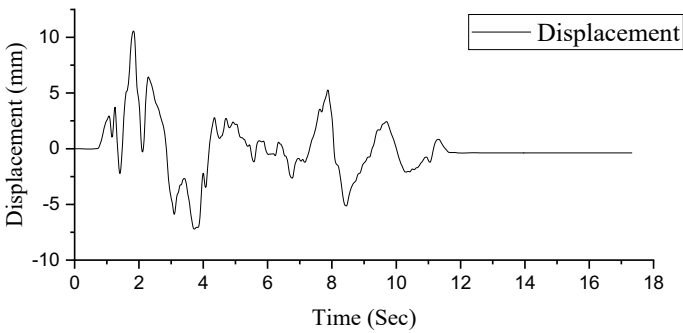
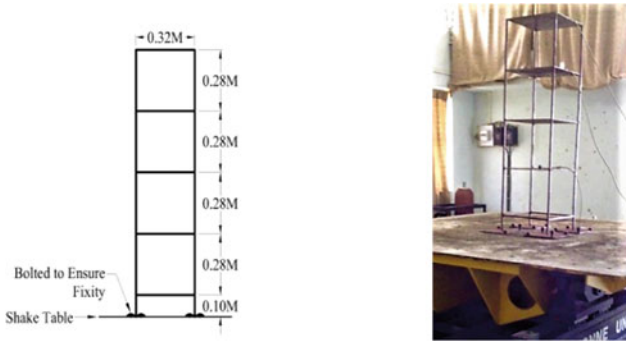


Fig. 2 Scaled El-Centro time history

corresponding to fixed and isolated base conditions is developed in the laboratory described in the following sections.

5.1 Fixed Base Condition

The fixed base condition is established by directly bolting the scaled-down model to the platform of the shaking table. Four accelerometers are used to record the acceleration. Accelerometer no. 1 is placed at the actuator of the shake table. Accelerometer nos. 2, 3 and 4 are used to record accelerations of various floor levels. The fixed base setup for G + 3 model is shown in Fig. 3. A similar setup is done for G + 5 model.



(a) Typical details of G+3 model (b) Experimental setups of G+3

Fig. 3 Fixed base condition setup

5.2 Isolated Base Condition

Elastomeric rubber is used as an isolator. These are placed below each column footing. The size of the elastomer is determined based on International Building Code:2000 [8]. The details of the isolator are presented in the following subsections.

5.2.1 Design of Elastomeric Rubber Isolator

Seismic isolation systems are difficult to design and require complex analysis to produce the ideal design for the structure which is meant to achieve the desired target time period [9]. International Building Code (IBC) made provisions for the guidelines and design criteria for the isolation systems. The IBC:2000 is referred for design. The horizontal effective stiffness of the rubber required to achieve the target time period of 2.5 s is obtained by making various trials in the computer application. The effective stiffness for G + 3 model is worked out to be 105 kN/m. Similar calculations are done for G + 5 model.

The thickness of rubber is governed by the design displacement and it is calculated referring the Sect. 1623.2.2.1 of IBC:2000. Usually we need to achieve this displacement at about 150% shear strain. The dimensions of rubber for model worked out to be 35 mm × 35 mm in plan and 15 mm in thickness. The design of isolator for G + 5 models is also done similarly.

5.2.2 Laboratory Setup of Isolated Base Model

The experimental setup for isolated base condition is done by decoupling the structure from the shaking table. The rubber pad of the required size is prepared. The wooden

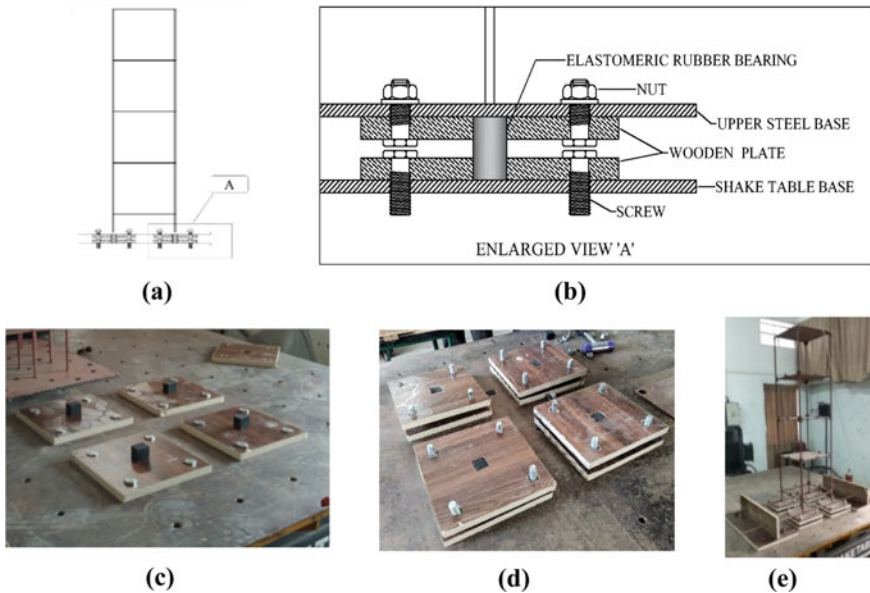


Fig. 4 **a** Typical sectional elevation of isolated base setup. **b** Enlarged detailed view 'A' of setup of isolator at base. **c** Rubber isolator without top plate at base. **d** Rubber isolator with top plate at base. **e** G + 3 isolated base model on uniaxial shake table

planks under each column have been used to hold the rubber isolator properly. The detailed setup is shown in Fig. 4a–e.

6 Analytical Study

The analytical study is carried out using the software ETABS which provides integrated features to do time history analysis on building frames and extract the results quickly and precisely. The original time history motions are given as input for the prototype structure shown in Fig. 5c. The fixed and isolated base G + 3 model and G + 5 model developed using application software are shown in Fig. 5a, b, respectively.

7 Results

The scaled-down models of G + 3 and G + 5 buildings with the fixed base condition and isolated base condition are subjected to El-Centro, Indo-Burma and Uttarkashi time histories. The models are fitted with an accelerometer at all the stories to

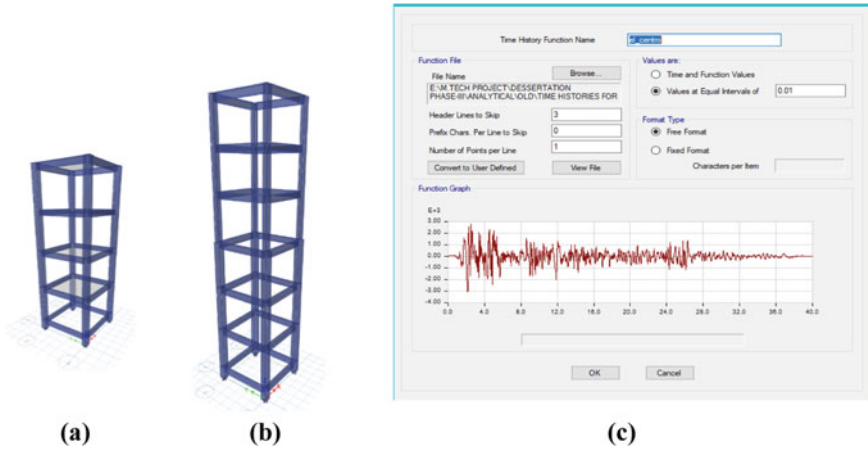


Fig. 5 a 3D model of G + 3 building. b 3D model of G + 5 building. c El-Centro time history function definition in ETABS

record the acceleration. The acceleration responses are presented below for fixed and isolated base conditions.

7.1 Response of G + 3 Building

Time history responses of roof story are shown in Sect. 7.1.1 and the response of all stories are illustrated in Sect. 7.1.2 for G + 3 building.

7.1.1 Comparison of Roof Acceleration of G + 3 Building Frame

The analytical and experimental results of roof acceleration for El-Centro time history for G + 3 model are presented in Fig. 6a, b, respectively. The response of the experimental study is presented on scaled time. The acceleration time history of the analytical study is presented in Fig. 6a, which shows that the maximum acceleration is @9.64 m/s², whereas for isolated base condition maximum acceleration is @3.41 m/s². Thus, the acceleration of the isolated base is reduced by almost 64% that of acceleration corresponding to the fixed base. The acceleration time history of the experimental study is presented in Fig. 6(b), which shows that the maximum acceleration is @10.70 m/s², whereas for isolated base condition maximum acceleration is @4 m/s². Thus, the acceleration of isolated base is reduced by almost 62% that of acceleration corresponding to the fixed base. It is also revealed that the acceleration obtained by analytical and experimental studies is within close agreement. The acceleration produced in the experimental study is almost 9–11% higher than the

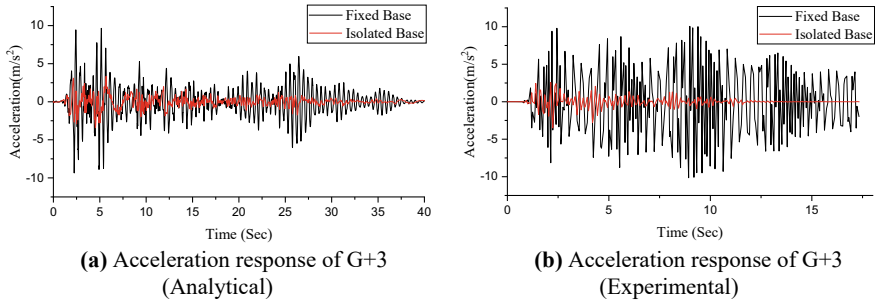


Fig. 6 a Acceleration response of G + 3 (analytical). b Acceleration response of G + 3 (experimental)

analytical study, which may be considered reasonably marginal. Thus, it is inferred that the experimental setup is simulated precisely in the laboratory.

7.1.2 Variation of Acceleration of All the Stories of G + 3 Building

The acceleration response of all stories subjected to all three time histories corresponding to fixed and isolated base are presented in Table 4 and subsequently shown in Fig. 7. The reduction in roof acceleration for isolated base condition in analytical study is almost 65% for El-Centro (from 9.64 to 3.42 m/s²), 73% for Indo-Burma (from 4.40 to 1.27 m/s²) and 64% (from 7.19 to 2.60 m/s²) for Uttarkashi time history, shown in Fig. 7a, b, c, respectively. Similarly, in experimental study, reduction in acceleration for isolated base condition is almost 66% for El-Centro (from 10.70 to 3.59 m/s²), 73% for Indo-Burma (from 4.88 to 1.34 m/s²) and 66% (from 7.98 to 2.73 m/s²) for Uttarkashi time history. So, it is revealed that the base isolation is causing almost 64–73% reductions in acceleration.

It is observed from Fig. 7a–c that the accelerations increase with a higher rate (almost nonlinear) in the case of fixed base condition, whereas in the case of isolated base condition the acceleration is observed to be increasing with a lower rate (almost

Table 4 Variation of acceleration of G + 3 building for all time histories

Acceleration for G + 3 building (m/s ²)												
Time history	El-Centro				Indo-Burma				Uttarkashi			
Story	IV	III	II	I	IV	III	II	I	IV	III	II	I
FA	9.64	7.62	6.09	4.00	4.40	3.47	2.78	2.50	7.19	5.68	4.54	4.20
FE	10.70	8.46	6.76	4.30	4.88	3.85	3.08	2.66	7.98	6.30	5.04	4.33
IA	3.42	2.70	2.16	1.80	1.27	1.01	0.80	0.76	2.60	2.05	1.64	1.45
IE	3.59	2.84	2.27	2.00	1.34	1.06	0.84	0.78	2.73	2.15	1.72	1.52

FA Fixed analytical; FE Fixed experimental; IA Isolated analytical; IE Isolated experimental

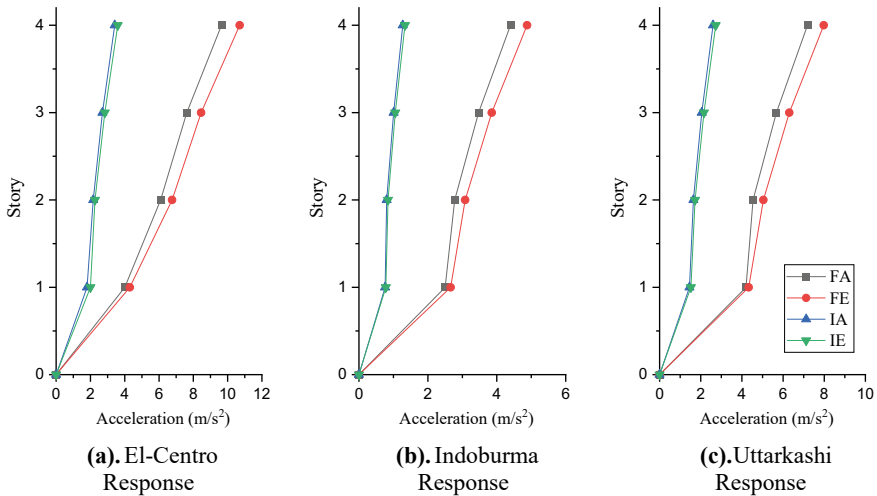


Fig. 7 Variation of acceleration for G + 3 building

linear). The same trend is observed in analytical and experimental studies. In the fixed base condition, the difference in acceleration for the experimental and analytical studies is observed to be in the range of 10–12%, whereas in the isolated base condition it is in the range of 4–6%.

7.2 Response of G + 5 Building

Time history responses of roof story are shown in Sect. 7.2.1 and the response of all stories are illustrated in Sect. 7.2.2 for G + 5 building.

7.2.1 Comparison of Roof Acceleration of G + 5 Building Frame

The analytical and experimental results of roof story acceleration for El-Centro time history for G + 5 model are presented in Fig. 8a, b, respectively. The response of the experimental study is presented on scaled time. The acceleration time history of the analytical study is presented in Fig. 8a, which shows that the maximum acceleration of the fixed base is @9.17 m/s², whereas for the isolated base condition the maximum acceleration is @3.64 m/s². Thus, the acceleration of the isolated base is reduced by 61% that of acceleration corresponding to the fixed base. The acceleration time history of the experimental study is presented in Fig. 8b, which shows that the maximum acceleration of the fixed base is @10.59 m/s², whereas for the isolated base condition maximum acceleration is @4.35 m/s². Thus, the acceleration of the isolated base is reduced by almost 60% that of the acceleration corresponding to the

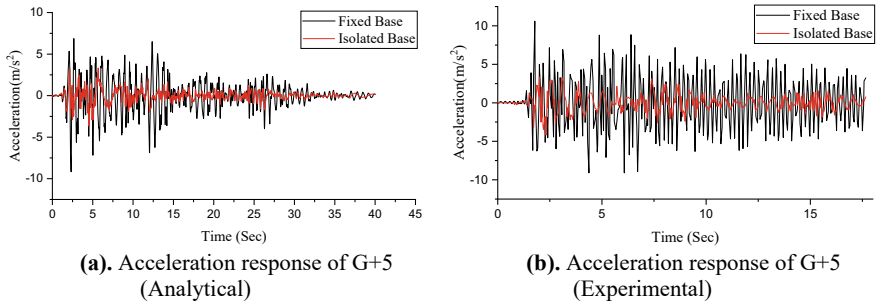


Fig. 8 a Acceleration response of G + 5 (analytical). b Acceleration response of G + 5 (experimental)

fixed base. The acceleration obtained from the analytical and experimental studies is in close agreement. The acceleration produced in the experimental study is almost 15–20% higher than the analytical study.

7.2.2 Variation in Responses of All the Stories of G + 5 Building

The acceleration responses of all stories subjected to all three time histories corresponding to the fixed and isolated base conditions are presented in Table 5 and subsequently shown in Fig. 9. The reduction in roof acceleration for isolated base condition in the experimental study is almost 59% for El-Centro (from 10.59 to 4.35 m/s²), 65% for Indo-Burma (from 4.43 to 1.57 m/s²) and 48% (from 5.67 to 2.97 m/s²) for Uttarkashi time history, shown in Fig. 9a–c, respectively. Similarly, in analytical study, reduction of acceleration for isolated base is almost 60% for El-Centro (from 9.17 to 3.64 m/s²), 65% for Indo-Burma (from 3.80 to 1.32 m/s²) and 55.71% (from 5.60 to 2.48 m/s²) for Uttarkashi time history, shown in Fig. 9a–c, respectively. So, it is revealed that the base isolation is causing almost 48–65% reductions in acceleration. In the fixed base condition, the difference in acceleration

Table 5 Acceleration response of G + 5 building for all time histories

Acceleration for G + 5 building (m/s²)

Time history	El-Centro							Indo-Burma						Uttarkashi				
	VI	V	IV	III	II	I	VI	V	IV	III	II	I	VI	V	IV	III	II	I
FA	9.2	7.0	5.9	5.3	3.3	3.0	3.8	2.9	2.7	2.4	1.7	1.5	5.6	5.4	5.1	4.4	3.3	3.0
FE	10.6	8.2	6.9	6.0	3.9	3.3	4.4	3.3	2.5	2.0	2.5	1.7	5.7	5.5	5.2	5.0	3.7	3.3
IA	3.6	3.6	3.5	3.3	3.2	2.5	1.3	1.3	1.3	1.3	1.2	1.2	2.5	2.5	2.5	2.5	2.5	2.2
IE	4.4	4.1	4.1	3.5	3.3	2.7	1.6	1.4	1.4	1.4	1.3	1.3	3.0	2.9	2.8	2.7	2.7	2.4

FA Fixed analytical; FE Fixed experimental; IA Isolated analytical; IE Isolated experimental

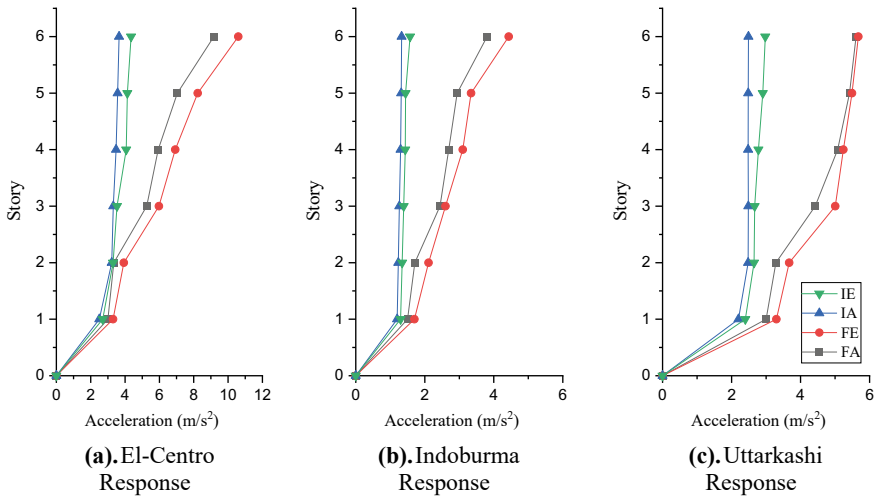


Fig. 9 Variation in acceleration for G + 5 building

for the experimental and analytical studies is observed to be in the range of 10–12%, whereas in the isolated base condition it is 4–6%.

7.3 Pseudo Spectral Acceleration

Response spectrum curves for the three time histories have been obtained for both the buildings at different damping ratios from 0 to 10%. The time period for isolated model has to be shifted to the desired target time period to which the structure is designed. The isolator is designed considering the IBC:2000 code which recommends achieving a target time period of 2.5 s for having little or no ductility demand.

The typical plot showing pseudo spectral acceleration on Y-axis vs the time period on X-axis for G + 3 building subjected to El-Centro is shown in Figs. 10 and 11 for fixed and isolated base conditions, respectively. It is observed that the time period is 0.5 s and peak pseudo acceleration is 190 m/s² for G + 3 fixed base building shown in Fig. 10, which is after isolation observed to be approximately 2.5 s with peak velocity being 13 m/s² as shown in Fig. 11. Hence the isolation of the base increased the time period of the structure to have little or no ductility demand.

The PSA for all time histories for G + 3 building is shown in Figs. 12, 13 and 14 for fixed and isolated base conditions, respectively. The PSA is plotted at different damping levels. The maximum pseudo acceleration is observed at 0% and 2% damping for El-Centro time history shown in Fig. 12. A reduction of 88–97% in peak pseudo acceleration is observed. The time period is consistent and it is close to 2.5 s for isolated base model.

Fig. 10 Pseudo spectral acceleration for G + 3 fixed base building (El-Centro)

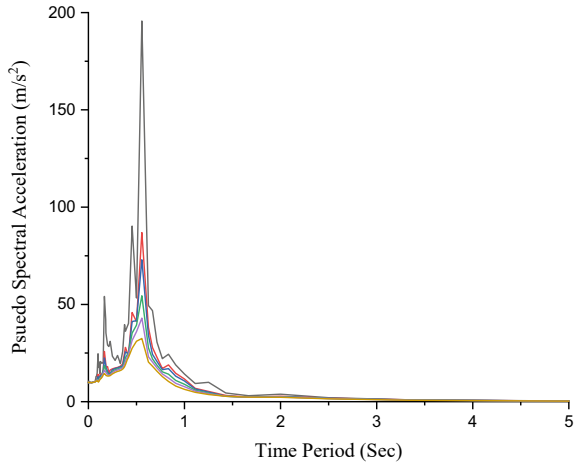
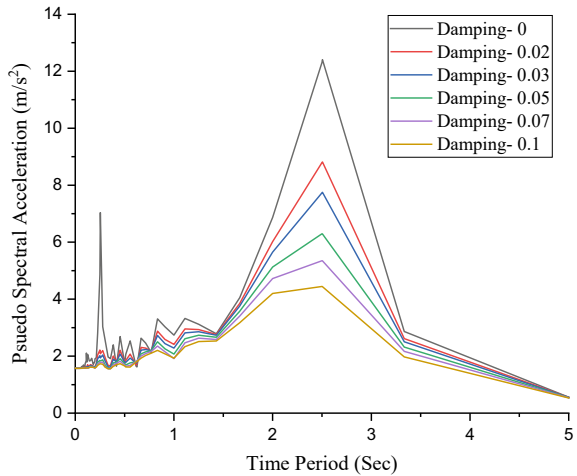


Fig. 11 Pseudo spectral acceleration for G + 3 isolated base building (El-Centro)



The PSA for G + 5 building for all time histories is shown in Figs. 15, 16 and 17. The maximum pseudo acceleration is observed at 0 and 2% damping for El-Centro time history. A reduction of 82–97% in peak pseudo acceleration is observed and shown in Fig. 15. The pseudo acceleration is observed to be 13% more in G + 5 building than in G + 3 building. However, the isolated base model was producing almost similar results in peak accelerations. The time period is shifted approximately to 2.5 s for isolated base model, resulting in reduced accelerations and increased time period.

Fig. 12 Pseudo spectral acceleration of G + 3 isolated base building at various damping levels for El-Centro

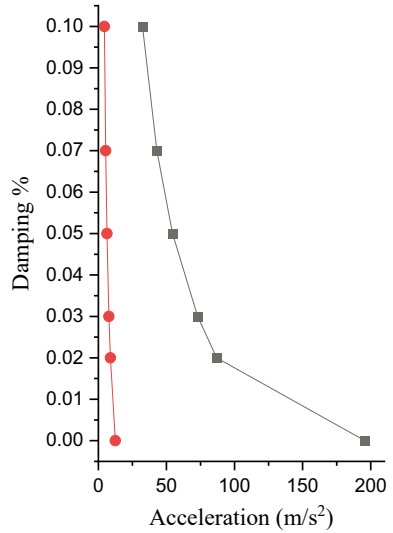
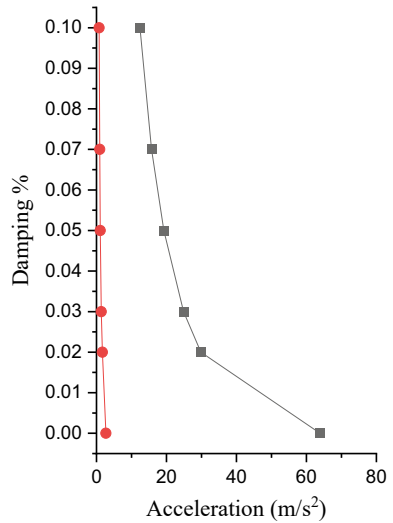


Fig. 13 Pseudo spectral acceleration of G + 3 fixed base building at various damping levels for Indo-Burma



7.4 Energy Demand

The conventional structures have evolved a lot to resist the seismic forces and are more capable of distributing the load evenly while maintaining a sustained energy demand. In the regions where an earthquake has more dominance than any other load, the conventional structure even designed very efficiently will require higher energy, hence the demand will be higher. The most efficient solution to sustain an earthquake while maintaining low energy demand is the introduction of an energy dissipation

Fig. 14 Pseudo spectral acceleration of G + 3 fixed base building at various damping levels for Uttarkashi

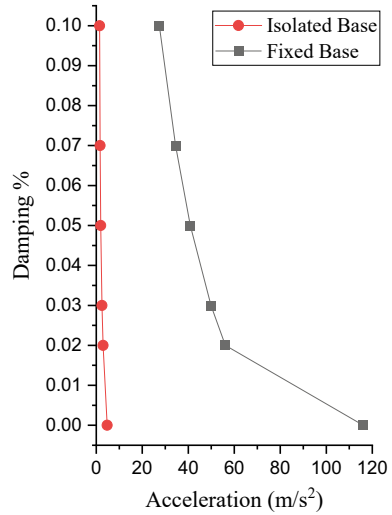
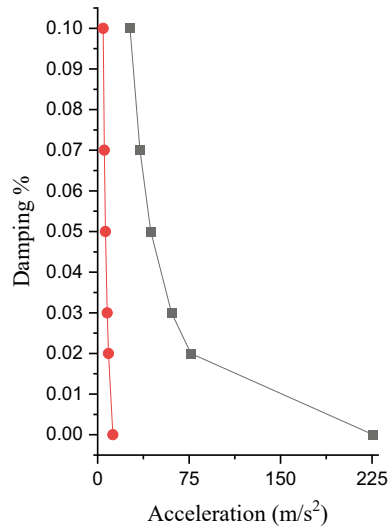


Fig. 15 Pseudo spectral acceleration of G + 5 fixed base building at various damping levels for El-Centro



device (i.e., base isolation). The energy demand for both the conventional, i.e., fixed base and isolated base conditions have been found in the analytical study in ETABs and compared.

The typical plot showing the energy demand of G + 3 building for El-Centro time history is shown in Figs. 18 and 19 for fixed and isolated base conditions, respectively. It is observed that the fixed base building is demanding almost 78% more energy than the isolated base condition.

Fig. 16 Pseudo spectral acceleration of G + 5 isolated base building at various damping levels for Indo-Burma

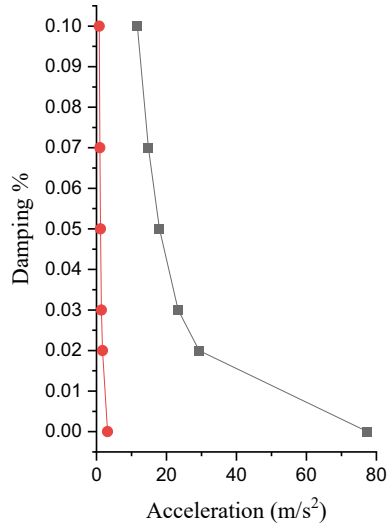
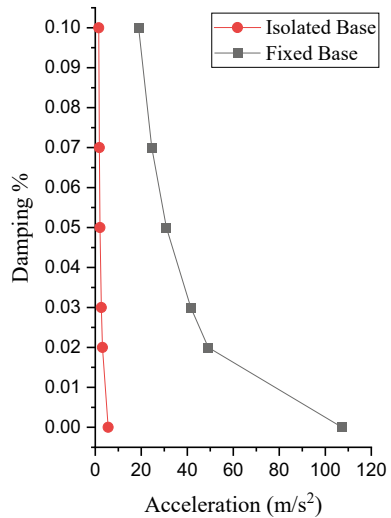


Fig. 17 Pseudo spectral acceleration of G + 5 fixed base building at various damping levels for Uttarkashi



The cumulative energy required to sustain an earthquake through the entire event for all time histories is shown in Fig. 20 for G + 3 building and in Fig. 21 for G + 5 building. It is observed that the energy demand in the fixed base condition is 78.57% more for El-Centro time history for G + 3 building shown in Fig. 20. Similarly, for Indo-Burma and Uttarkashi approximately 90% more energy is required as compared to the isolated base condition.

For G + 5 building the energy demand is reduced by 44.23% compared to the fixed base condition shown in Fig. 21. The reduction in Indo-Burma and Uttarkashi

Fig. 18 Energy demand for fixed base G + 3 building (El-Centro)

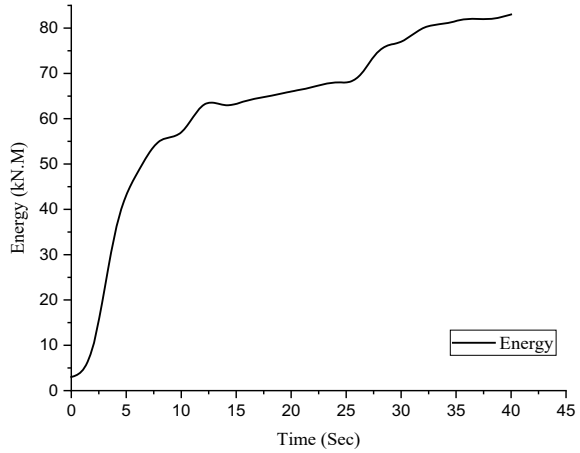
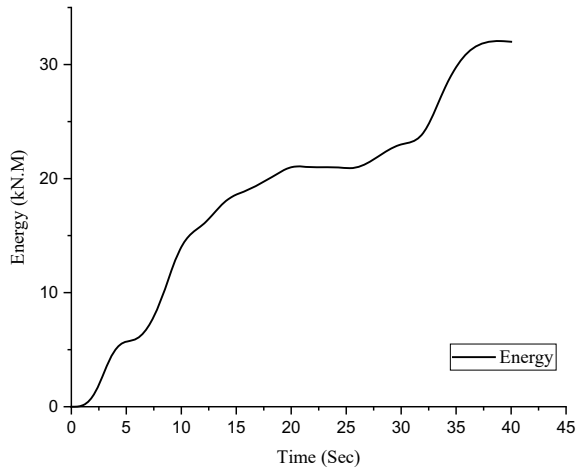


Fig. 19 Energy demand for isolated base G + 3 building (El-Centro)



is 90% and 68%, respectively. The reduction in energy demand is more for G + 3 building compared to G + 5 building.

8 Conclusion

In this study, the effect of base isolation is investigated experimentally and analytically for two scaled-down steel building frames of G + 3 and G + 5 which are designated as low-rise and high-rise buildings, respectively. The results of each building are compared and the conclusions are drawn as follows:

Fig. 20 Energy demand for G + 3 building

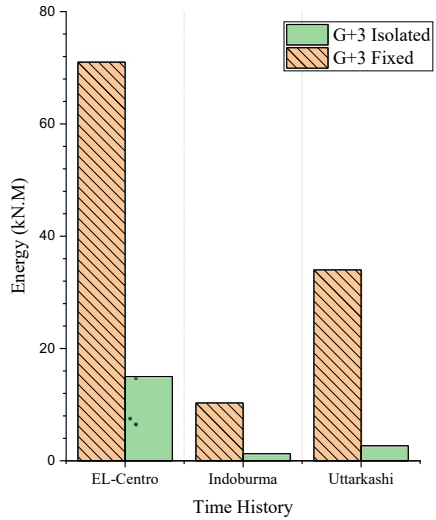
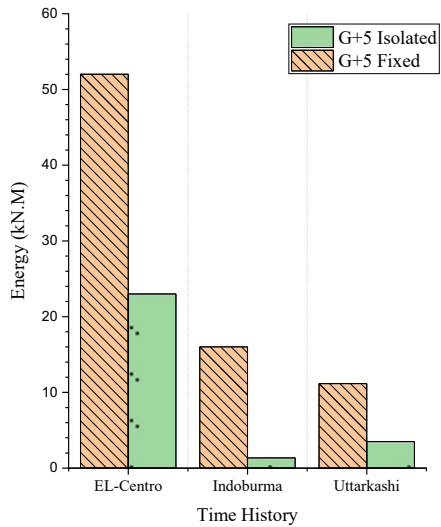


Fig. 21 Energy demand for G + 5 building



- i. Base isolation is observed to be distinctly effective as acceleration has been reduced by almost 60% and displacement is reduced by @40%. This trend is observed to be almost the same for all time histories.
- ii. Base isolation effect is more significant in low-rise buildings as the percentage reduction in the acceleration and displacement is higher than high-rise building. So, it is inferred that base isolation is beneficial in low-rise buildings.
- iii. The base isolation increases the time period so as to have no or little ductility demand which is achieved at all damping levels.

- iv. Energy demand in the isolated base buildings is reduced by almost 40–90% showing the effectiveness of isolation to keep the structure from deterioration. The G + 3 building is consuming less energy and also a reduction in consumption of energy is more than that of G + 5 building.
- v. The present study is carried out by using an elastomeric rubber isolator. However, the effect of different isolation systems may be studied to access the effectiveness of various isolation methods.
- vi. In the present work, the analytical and experimental study produces the acceleration and displacement with minimal difference which is quite obvious due to the difficulty to simulate the field conditions in the laboratory due to the limitations of the experimental facility.

Acknowledgements The authors express their gratitude to All India Council for Technical Education (AICTE), New Delhi, for providing financial assistance under Research Promotion Scheme (RPS) to procure a uniaxial shake table and to create an experimental facility in the structural dynamics lab of the institute.

References

1. Falborski T, Jankowski R (2017) Experimental study on effectiveness of a prototype seismic isolation system made of polymeric bearings. *MDPI Appl Sci* 7(808):7–16
2. Zahura FT, Javed SA, Naznin R. Effect of base isolation & different bracing system to improve building performance under earthquake excitations. In: International conference on advances in civil engineering, pp 359–363
3. Seranaj A, Garevski M (2015) An analysis of reinforced concrete buildings with different location of seismic isolation system. *Int J IJERT* 4(1). ISSN: 2278-0181
4. Hu K, Zhou Y, Jiang L, Chen P, Qu G (2017) A mechanical tension-resistant device for lead rubber bearings. *Eng Struct* 152:238–250
5. Aydin E, Ozturk B, Kilinc OF (2012) Seismic response of low-rise base isolated structures. In: 15WCEE LISBOA 2012
6. Maalek S, Akbari R, Ziaei-Rad S. Estimation of elastomeric bridge bearing shear modulus using operational modal analysis
7. Meymand PJ (1998) Shaking table scale model tests of nonlinear soil-pile-superstructure interaction in soft clay. PhD Dissertation, University of California, Berkeley
8. International Building Code, IBC:2000
9. Naeim F, Kelly JM. Design of seismic isolated structures: from theory to practice

Critical Study of Wind Effect on RC Structure with Different Permeability



Ankush Asati and Uday Singh Patil

Abstract Wind load is one of the significant loads that affect the design of a structure. Therefore, to analyze and design a building considering the effect of wind load, it is necessary to calculate the wind speed and pressure for different heights of buildings with different geometry. In the current building codes and design standards, internal stresses are insufficiently defined, primarily due to the complexities involved in their assessment, but play an important role in the design of buildings and cladding. The category of the building with a single dominant opening is usually considered critical for wind load design. However, the correct assessment of internal pressure behavior for buildings with cross-openings of realistic wall porosities is essential. In this paper, the reinforced concrete framed structure is analyzed for three classes of structure, i.e., Class A, B, and C with the constant base dimension; with varying heights of the structure; having four bays in each direction, and ceiling height of 3 m. All the models are analyzed for three different basic wind speeds, i.e., 33, 44, and 55 m/s with three different permeabilities, i.e., <5, 5–20, and >20% for different terrain categories specified in respective standards. The influence of the wind load response in terms of axial force, bending moment, and peak deflections are calculated and compared. It is observed that the effect of terrain category and permeability is not significant in centrally located columns. However, in corner columns, the axial forces are not constant. It increases with the increase in wind speed, permeability, and reduces from terrain category 1–4. Also, significant co-relation between forces and displacement was observed for less than 5% permeability, wind speed of 33 m/s, and terrain category 1.

Keywords Permeability · RC structure · Terrain category · Wind load

A. Asati · U. S. Patil (✉)

Department of Civil Engineering, Yeshwantrao Chavan College of Engineering, Nagpur, India

e-mail: patil.udaysingh4@gmail.com

1 Introduction

Structural designers refer to relevant standards on wind loads while designing tall buildings for wind loads to arrive at correct values of wind forces that will be acting at different floor levels of the structure. One of the significant loads that affect the design of the structure is wind load. To analyze the structure considering the effect of wind load, it is necessary to calculate the wind speed and pressure for different heights of buildings and different geometry. Various major standards and codes give us the procedures and coefficients required for the calculation of wind load for particular parameters, like the importance of building, surrounding terrain, the topography of building size, pressure, and force coefficients for different geometric shapes and sizes of buildings. (IS: 875-Part-3,1987) provides the values of coefficient of external pressure for rectangular and square plan shape clad buildings with rectangular corners for wind incidence angle normal to the surfaces. As per the historical wind speed data, India is divided into several zones, and design wind speed is considered according to the wind map of India. In the current building codes and design standards, internal stresses are insufficiently defined, primarily due to the complexities involved in their assessment, but play an important role in the design of buildings and cladding. While designing the structure subjected to wind load, generally wall with a foremost opening is considered important but the correct assessment of internal pressure behavior for structure with cross-openings of realistic wall porosities is also essential. Many researchers have used various methods to evaluate the equivalent static wind load. Ranjitha et al. analyzed buildings with different shapes for zone I and IV of India from linear static and dynamic analysis. Naved Ahmed and Rajeev Banerjee studied the effect of wind load on buildings with different H/B ratios. Sidhh et al. compared IS 875 Part 3: 1987 and IS 875 Part 3: 2015 on an existing structure. Nakul et al. carried out an analytical study to calculate the R factor for RCC and industrial structures to check its feasibility as given in Indian standards. In the present study, the critical study of the effect of wind loading on various sizes and shapes of the building with different permeability as per IS 875-part 3 is considered. The wind loads were applied to three different structures of class A, class B, and class C. The influence of the wind load response in terms of axial force, bending moment, and peak deflections is calculated and compared. As per the Indian standards, the static load is calculated for various structures and the acting forces depend largely on the basic wind speed, terrain category, class of structure, the height of the structure, and permeability. There is also a need to develop a mathematical model and investigate if there is a close relationship between the coefficient specified in various tables in the code. Accordingly, the problem statement of the present study is to critically analyze structure subjected to wind load with variable input parameters such as wind velocity, class of structure, the height of the structure, permeability and to investigate the possibility of development of co-relation/mathematical model among the forces and displacement. The results of a parametric study will show the variation in the forces of the structural member of the RC buildings with the change in the

permeabilities and terrain categories. Thus, subsequently will help in the efficient design of structures that are both cost-effective and safe.

2 Literature Review

Raj and Ahuja studied the variations of base shear, base moments, and twisting moments with wind incidence angle on 3 models, i.e., A, B, and C [1–18]. On a building structure, wind load is maximum when it is exposed to a maximum area. It is found that with the change in the wind incidence angle, wind loads get affected and modified accordingly. It is also observed that for the same floor area of the building the shape of the building affects the wind load to a great extent. Thus compared to the square shape of the building, the percentage increase in the values of these forces depends on the building's cross-sectional shapes. Verma et al. carried out an experimental investigation on a wind tunnel with a plan of square shape and tall structure with boundary layer flow.

The values of coefficients of wind pressure were obtained from the various pressure point on the surfaces of the wall of the model. The goal of the research was to produce and create data for the designers to be able to safely design structural frames and wall claddings subjected to wind loads [19]. The internal airflow field has been found to have a major effect on the values of the internal pressure. It is seen that this field is not uniform for a wall that has porosity configurations greater than 10% and openings that are located on the neighboring walls. For the building of category 3, the values of peak internal pressure coefficients were found to surpass design values. Stathopoulos et al. analyzed models of low-rise structures with various geometries and experimentally evaluated the induced internal pressures in it for different volumes. It is found that magnitudes of internal pressures obtained are lesser than the values of local external pressure. Internal pressure coefficients for windward are found to be positive and found to be negative or zero for high porosity with small openings. A good relation between components of external and internal pressures has been established. Seavhai and Narayanan compared the value of roof pressures of the low-rise rectangular plan building with a dominant, non-dominant opening, and canopies with the help of 4 standards, namely, MS 1553-2002, EC 1991-1-4:2005, IS 875-3-1987, and BS 6399-2:1997 on various roof types. The maximum wind speed of 33.5 m/s as stated in MS 1553-2002 was used for the analysis. Reference height of buildings, averaging time for wind speed, and pressure coefficient values are some of the factors that are found to vary with different codes. Chauhan et al. estimated the wind forces acting on tall buildings for the design of structural elements. Using the Force coefficient method and Gust Factor Method, the influence of static and dynamic velocity fluctuations on the along wind loads for the structures was determined. A 60 and 120 m buildings are analyzed by ETABS Software with 4 different Terrain Categories and 6 basic wind speeds. Holmes et al. compared 3 buildings using 15 different codes and standards from the Asia–Pacific Region. The comparisons showed varying degrees of agreement.

3 Mathematical Model and Analytical Parameter

3.1 Computational Model

In this study, an analysis of the multi-storied building subjected to wind forces for all-terrain categories is carried out. 3-D model is prepared for G + 5, G + 14, and G + 24 multi-storied buildings in STAAD-Pro. The reinforced concrete frame structure is modeled for three classes of structure, i.e., Class A, B, and C having constant base dimensions with varying heights of structure; having four bays in each direction, and a ceiling height of 3 m. All the models are analyzed for basically three different basic wind speeds, i.e., 33, 44, and 55 m/s with three different permeability, i.e., <5, 5–20, and >20%, for four different terrain categories. The structural details used in the present study are cross-sectional dimensions of columns (450 × 450) mm, dimensions of beams (300 × 500) mm, 150 mm slab thickness, infill walls in the buildings are assumed to be 230 mm thick, storey height is 3 m, live load considered as 3 KN/m², plan size is 16 m × 16 m. Wind parameters considered are terrain category: 1, 2, 3, and 4; risk coefficient: 1; wind in X-direction and Z-direction. For analysis, the corner column and center column of the building are considered.

4 Results and Discussions

The member forces, bending moment, and displacement are calculated for a load combination of 1.2(DL + LL + WL), for Class A, Class B, and Class C structures.

4.1 Class A Structure

From Figs. 1, 2, 3, 4, 5, 6, 7, 8, 9 and 10, it can be seen that the axial force in the corner column for class A structure is increasing with the increase in wind speed and permeability. Also, it reduces from terrain category 1 to terrain category 4. The shear force FY and FZ in the corner column for class A structure are found to increase with an increase in wind speed with an increase in permeability. Shear force value is found to reduce from terrain category 1 to terrain category 4. The displacement in the X, Y, and Z directions in the corner column for class A structure is increasing with an increase in wind speed, permeability and reduced from terrain category 1 to terrain category 4. Since the corner columns are more exposed to wind thus the maximum response in X, Y, and the Z directions is observed that explains the increase in the displacement in the corner columns.

Fig. 1 Class A structure with wind speed = 33 m/s, permeability < 5%, and different TC—corner column

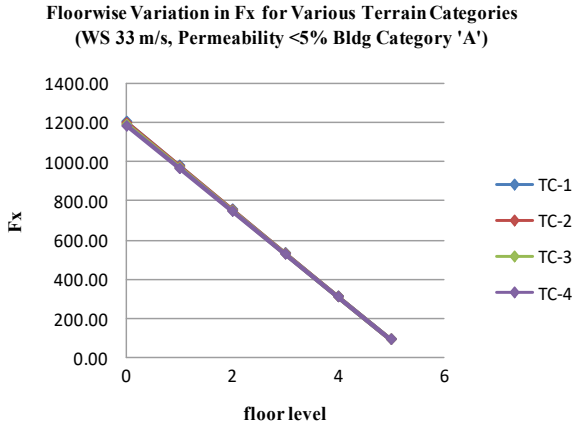


Fig. 2 Class A structure with TC-1, wind speed = 33 m/s, and different permeability—corner column

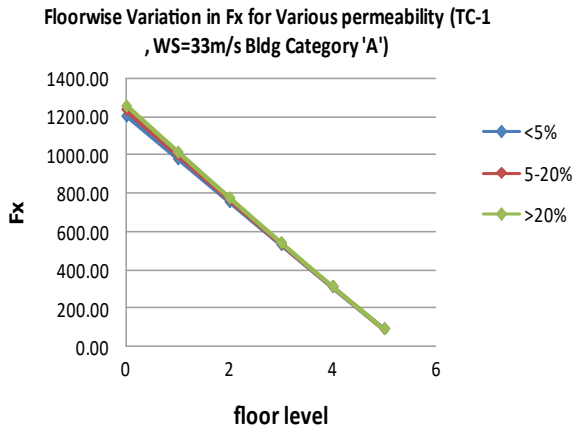


Fig. 3 Class A structure with TC-1, permeability < 5%, and different wind speeds—corner column

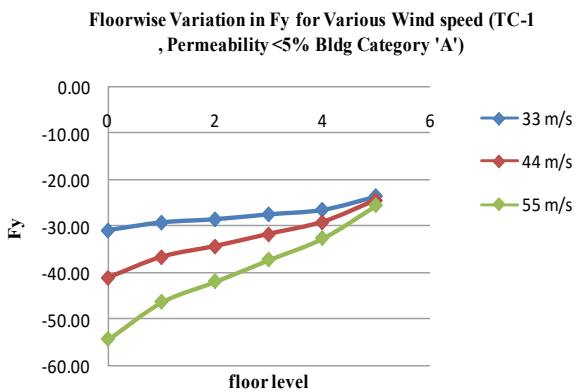


Fig. 4 Class A structure with wind speed = 33 m/s, permeability < 5%, and different TC—corner column

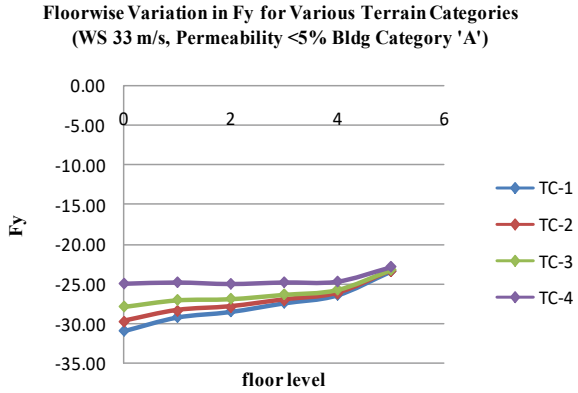


Fig. 5 Floor level and M_x for class A structure with wind speed = 33 m/s, permeability < 5%, and different TC—corner column

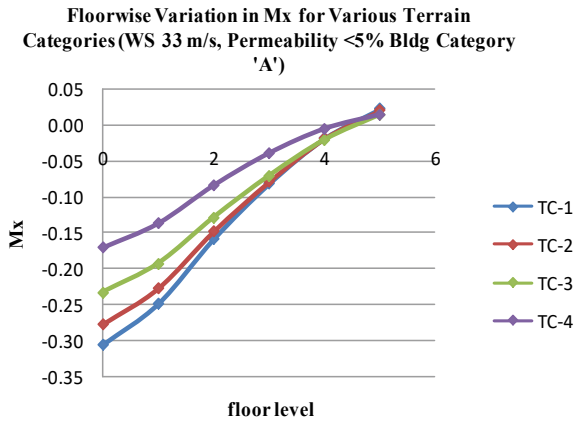


Fig. 6 Floor level and M_y for class A structure with TC-1, permeability < 5%, and different wind speeds—corner column

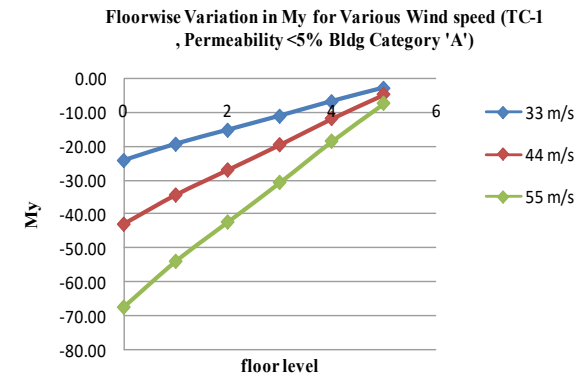


Fig. 7 Floor level and MZ for class A structure with wind speed = 33 m/s, permeability < 5%, and different TC—corner column

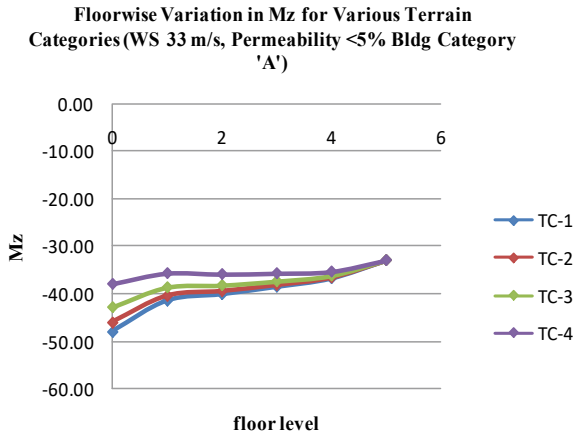


Fig. 8 Floor level and DX for class A structure with TC-1, permeability < 5%, and different wind speeds—corner column

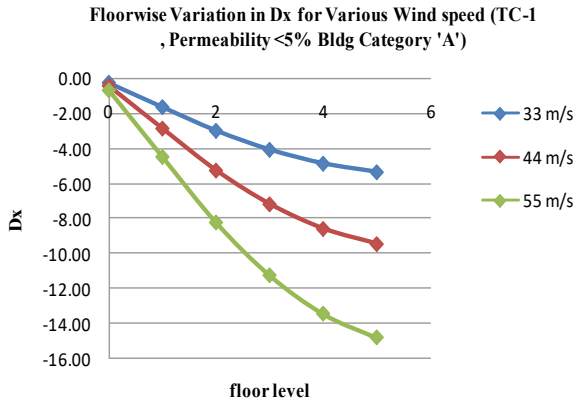


Fig. 9 Floor level and DY for class A with wind speed = 33 m/s, permeability < 5%, and different TC—corner column

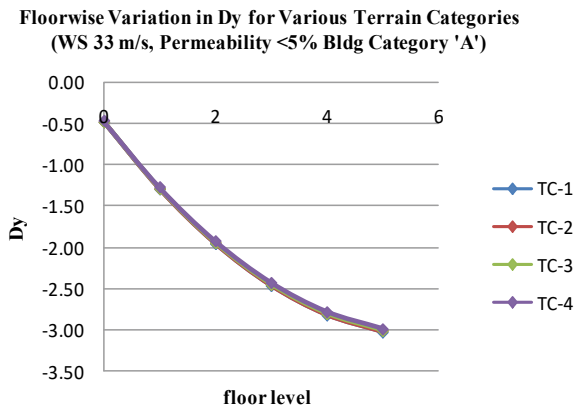
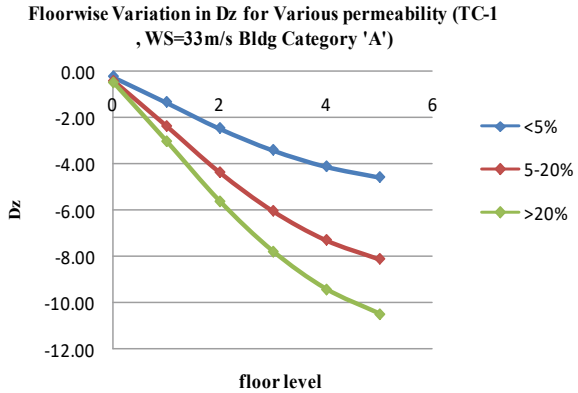


Fig. 10 Floor level and DZ for class A structure with TC-1, wind speed = 33 m/s, and different permeability—corner column



4.2 Class B Structure

From Figs. 11, 12, 13, 14, 15, 16, 17 and 18, it can be seen that a similar trend has been observed as that of class A structure, i.e., axial force in the corner column for class B structure is found to increase with an increase in wind speed and permeability. The axial forces were found to decrease from terrain category 1 to terrain category 4 since the terrain and height multiplier reduces with an increase in the terrain category. The shear force FY and FZ in the corner column for class B structure has increased with the increase in wind speed and permeability and reduced from terrain category 1 to terrain category 4. Again the reason behind this increased response is attributed to the more exposure of corner columns. Thus, it can be inferred that dynamic effects of structure vary drastically with the class of structure, permeability, and terrain categories.

Fig. 11 Floor level and FX for class B structure with wind speed = 33 m/s, permeability < 5%, and different TC—corner column

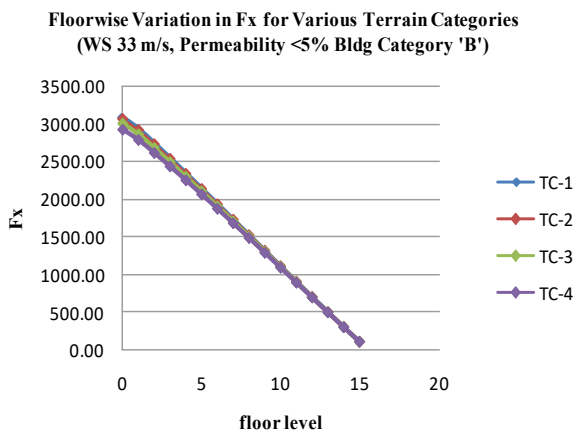


Fig. 12 Floor level and FY for class B structure with wind speed = 33 m/s, permeability < 5%, and different TC—corner column

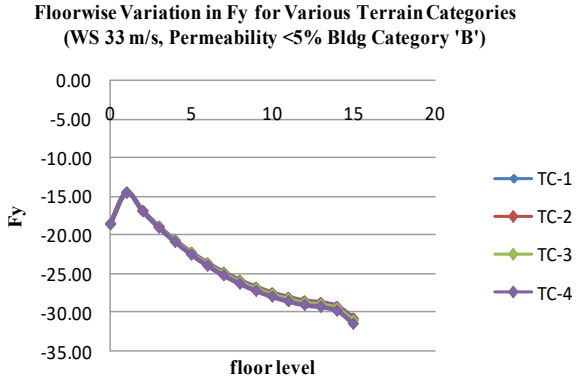


Fig. 13 Floor level and FZ for class B structure with wind speed = 33 m/s, permeability < 5%, and different TC—corner column

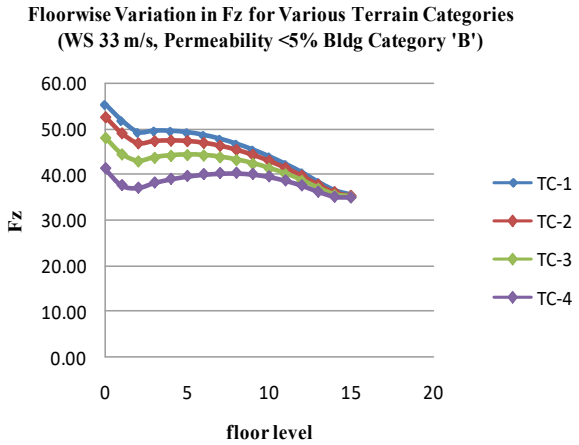


Fig. 14 Floor level and MX for class B structure with wind speed = 33 m/s, permeability < 5%, and different TC—corner column

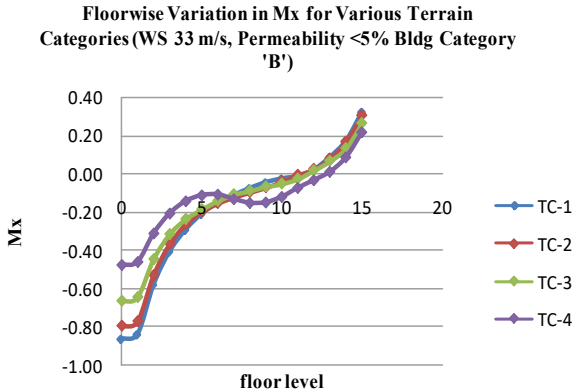


Fig. 15 Floor level and MY for class B structure with wind speed = 33 m/s, permeability < 5%, and different TC—corner column

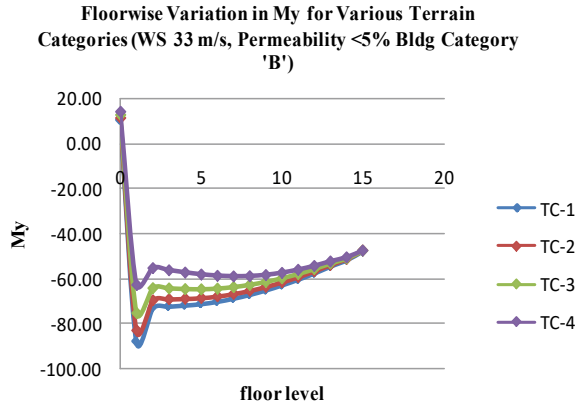


Fig. 16 Floor level and MZ for class B structure with wind speed = 33 m/s, permeability < 5%, and different TC—corner column

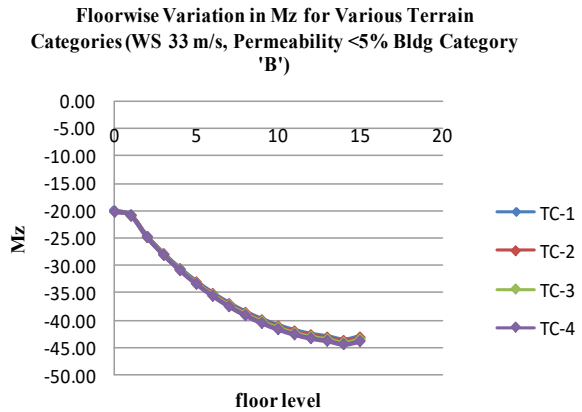


Fig. 17 Floor level and DX for class B structure with wind speed = 33 m/s, permeability < 5%, and different TC—corner column

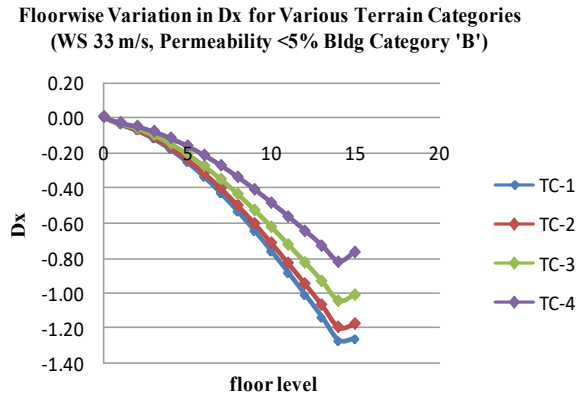
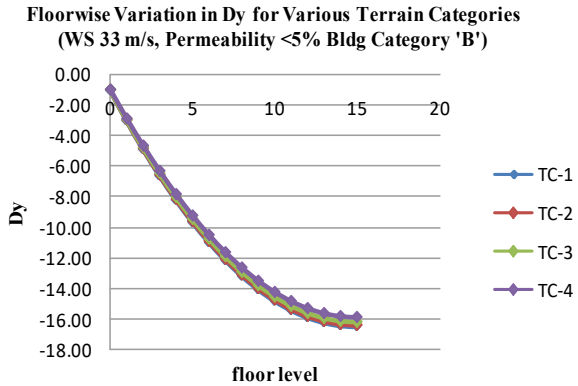


Fig. 18 Floor level and DY for class B structure with wind speed = 33 m/s, permeability < 5%, and different TC—corner column



4.3 Class C Structure

Figures 19, 20, 21, 22, 23, 24, 25, 26, 27, 28, 29 and 30, axial force in the corner column for class C structure is found to increase with the increase in wind speed, permeability and started reducing from terrain category 1 to terrain category 4. The shear force FY and FZ in the corner column for class C structure are increasing with the increase in wind speed, permeability, and reducing from terrain category 1 to terrain category 4. Thus, it can be inferred that the variation in wind speed with height is also influenced by the roughness of the ground, and so differs for each terrain category (IS: 875(Part3): Wind Loads on Buildings and Structures—(Proposed Draft and Commentary)).

Fig. 19 Floor level and FX for class C structure with TC-1, permeability < 5%, and different wind speeds—corner column

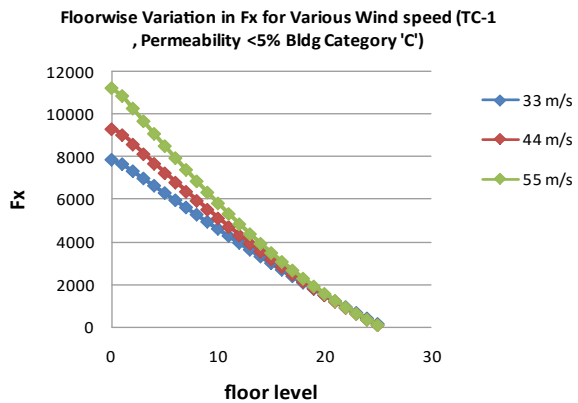


Fig. 20 Floor level and FY for class B structure with TC-1, permeability < 5%, and different wind speeds—corner column

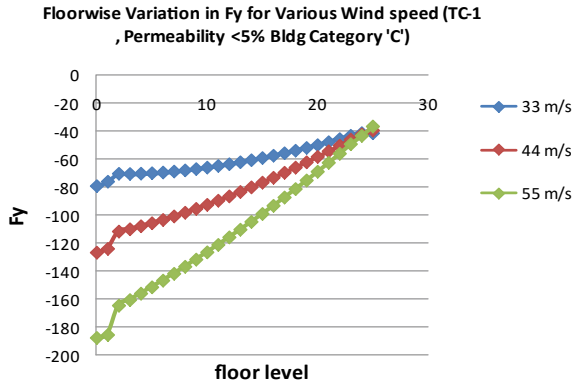


Fig. 21 Floor level and Fz for class C structure with wind speed = 33 m/s, permeability < 5%, and different TC—corner column

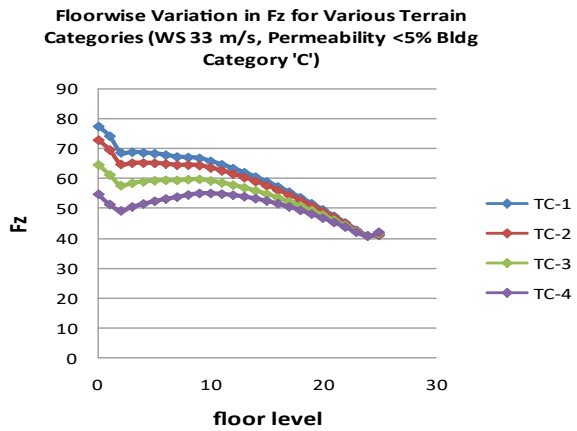


Fig. 22 Floor level and Mx for class C structure with wind speed = 33 m/s, permeability < 5%, and different TC—corner column

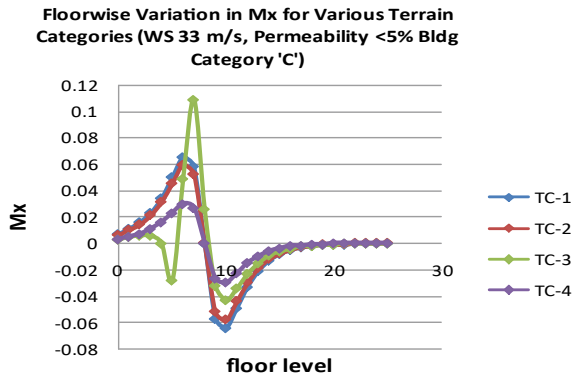


Fig. 23 Floor level and MY for class C structure with TC-1, permeability < 5%, and different wind speeds—corner column

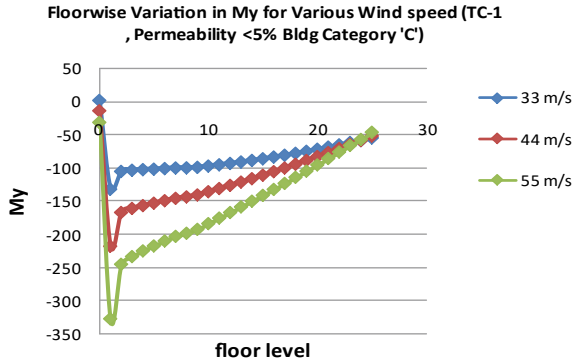


Fig. 24 Floor level and MZ for class C structure with TC-1, permeability < 5%, and different wind speeds—corner column

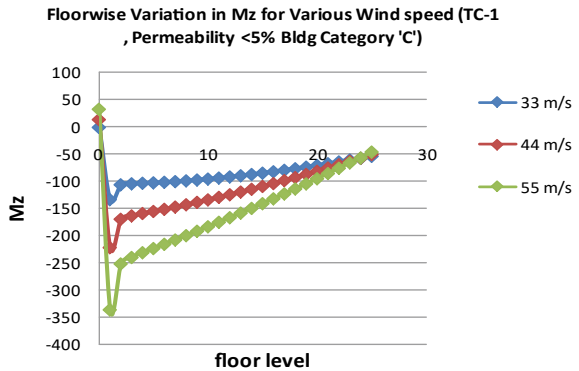


Fig. 25 Floor level and DX for class C structure with TC-1, permeability < 5%, and different wind speeds—corner column

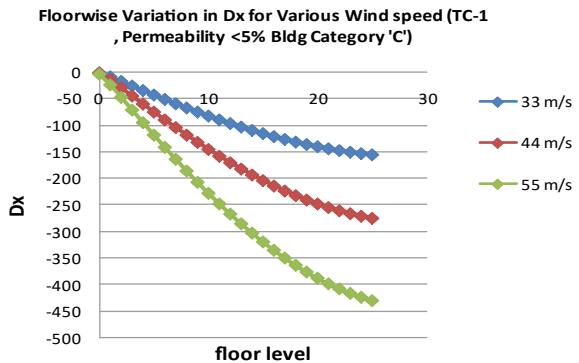


Fig. 26 Floor level and DY for class C structure with TC-1, permeability < 5%, and different wind speeds—corner column

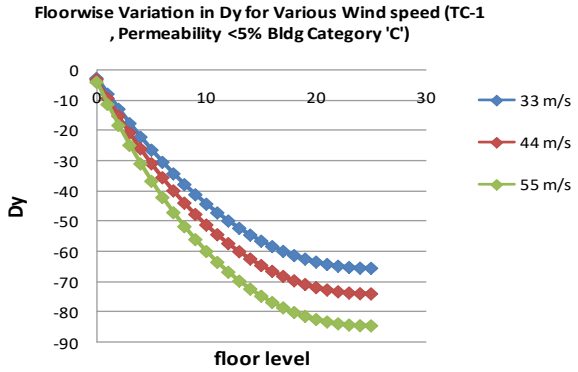


Fig. 27 Floor level and DZ for class C structure with wind speed = 33 m/s, permeability < 5%, and different TC—corner column

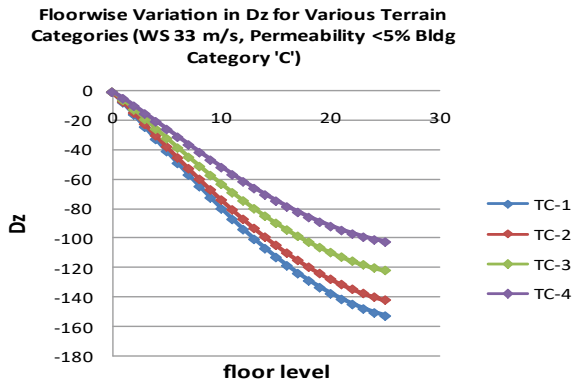


Fig. 28 Floor level and DZ for class C structure with TC-1, permeability < 5%, and different wind speeds—corner column

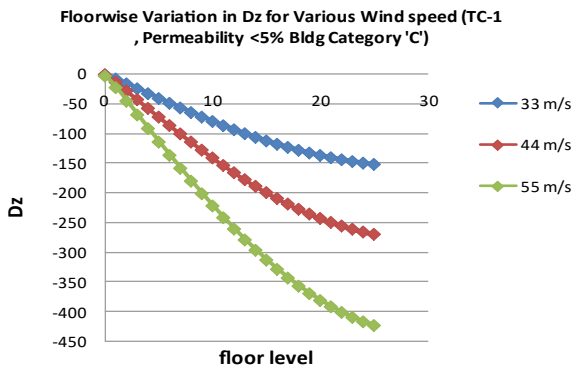


Fig. 29 Floor level and DZ for class C structure with TC-1, wind speed = 33 m/s, and different permeability—corner column

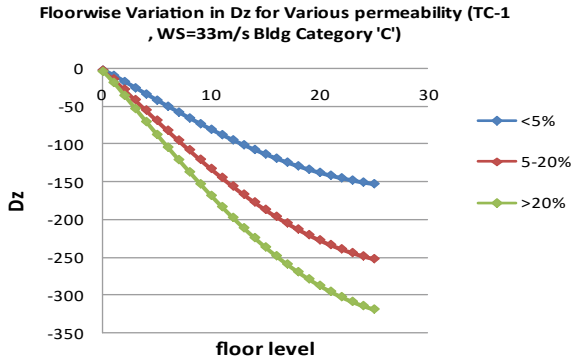
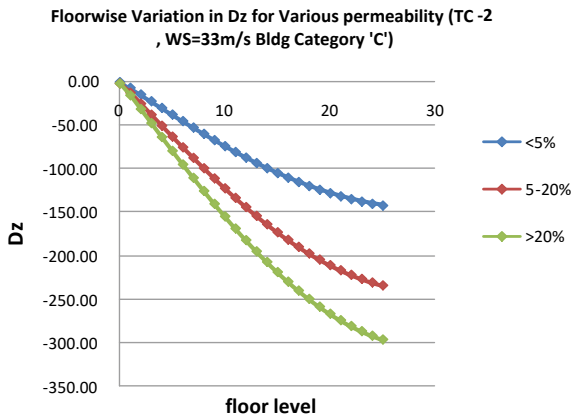


Fig. 30 Floor level and DZ for class C structure with TC-2, wind speed = 33 m/s, and different permeability—corner column



4.4 Co-relation Between Forces, Moments, Displacement with Terrain Categories, Permeabilities, and Wind Speed

To understand the correlation between various parameters like forces, moments, and displacement among the condition specified in IS 875 (Part-3), the data for all buildings are clubbed together. Graphs are plotted, and the trained line equation along with R^2 values was noted. Corresponding values are shown in Tables 1, 2 and 3 and observed that there exists an excellent relation between forces, moments, and displacements with terrain categories, permeabilities, and wind speed.

Table 1 Co-relation between forces, moments, and displacement for terrain categories

Parameter	Force/Displacements	Correlation between	Mathematical relation	R ² value	Observation
Terrain category	Fx	TC1 × TC2	Force(TC2) = 0.9804 × Force(TC1) + 25.27	0.9999	Excellent correlation
		TC1 × TC3	Force(TC3) = 0.9427 × Force(TC1) + 72.83	0.9991	
		TC1 × TC4	Force(TC4) = 0.906 × Force(TC1) + 116.4	0.997	
Terrain category	Fy	TC1 × TC2	Force(TC2) = 0.925 × Force(TC1) – 2.799	0.999	
		TC1 × TC3	Force(TC3) = 0.790 × Force(TC1) – 7.791	0.996	
		TC1 × TC4	Force(TC4) = 0.639 × Force(TC1) – 13.70	0.978	
Terrain category	Mx	TC1 × TC2	Force(TC2) = 0.900 × Force(TC1) – 0.008	0.999	
		TC1 × TC3	Force(TC3) = 0.741 × Force(TC1) – 0.017	0.993	
		TC1 × TC4	Force(TC4) = 0.492 × Force(TC1) – 0.042	0.909	
Terrain category	My	TC1 × TC2	Force(TC2) = 0.926 × Force(TC1) – 1.027	0.999	
		TC1 × TC3	Force(TC3) = 0.795 × Force(TC1) – 2.032	0.999	

(continued)

Table 1 (continued)

Parameter	Force/Displacements	Correlation between	Mathematical relation	R ² value	Observation
		TC1 × TC4	Force(TC4) = 0.651 × Force(TC1) – 2.730	0.995	
Terrain category	Dx	TC1 × TC2	Force(TC2) = 0.930 × Force(TC1) + 0.27	1	
		TC1 × TC3	Force(TC3) = 0.799 × Force(TC1) + 0.413	1	
		TC1 × TC4	Force(TC4) = 0.665 × Force(TC1) + 1.308	0.999	
Terrain category	Dy	TC1 × TC2	Force(TC2) = 0.984 × Force(TC1) – 0.078	0.999	
		TC1 × TC3	Force(TC3) = 0.952 × Force(TC1) – 0.249	0.999	
		TC1 × TC4	Force(TC4) = 0.924 × Force(TC1) – 0.313	0.997	

5 Conclusion

Following are the conclusions from the present study:

1. It is observed that the forces bear a constant proportionality ratio with various terrain categories, wind speeds, and different permeability conditions for class A, class B, and class C structures.
2. The moment and displacement were found to vary with a constant ratio for all-terrain categories, wind speed, and different permeability in all classes of structures, i.e., class A, class B, and class C.
3. No significant effect is observed in the axial force in the center column of the structure due to wind loads.
4. Displacements and Moments are significant to wind loads for all-terrain categories, especially for corner columns.

Table 2 Co-relation between forces, moments, and displacement for permeability

Parameter	Force/Displacement	Correlation between	Mathematical relation	R ² value	Observation
Permeability	Fx	<5% × 5–20%	Force(5–20%) = 1.111 × Force(<5%) – 132.7	0.997	Excellent correlation
		<5% × >20%	Force(>20%) = 1.185 × Force(<5%) – 220.4	0.993	
Permeability	Fy	<5% × 5–20%	Force(5–20%) = 1.615 × Force(<5%) + 20.60	0.985	
		<5% × >20%	Force(>20%) = 2.022 × Force(<5%) + 34.17	0.975	
Permeability	Mx	<5% × 5–20%	Force(5–20%) = 1.673 × Force(<5%) + 2E–05	0.998	
		<5% × >20%	Force(>20%) = 2.122 × Force(<5%) + 0	0.997	
Permeability	My	<5% × 5–20%	Force(5–20%) = 1.649 × Force(<5%) – 0.413	0.999	
		<5% × >20%	Force(>20%) = 2.082 × Force(<5%) – 0.712	0.999	
Permeability	Dx	<5% × 5–20%	Force(5–20%) = 1.649 × Force(<5%) + 0.169	1	
		<5% × >20%	Force(>20%) = 2.077 × Force(<5%) + 0.147	1	
Permeability	Dy	<5% × 5–20%	Force(5–20%) = 1.094 × Force(<5%) + 0.454	0.997	

(continued)

Table 2 (continued)

Parameter	Force/Displacement	Correlation between	Mathematical relation	R ² value	Observation
		<5% × >20%	Force(>20%) = 1.156 × Force(<5%) + 0.752	0.994	

Table 3 Co-relation between forces, moments, and displacement for wind speed

Parameter	Force/Displacement	Correlation between	Mathematical relation	R ² value	Observation
Wind speed	Fx	33 × 44	Force(44) = 1.113 × Force(33) – 119.3	0.997	Excellent correlation
		33 × 55	Force(55) = 1.259 × Force(33) – 272	0.991	
Wind speed	Fy	33 × 44	Force(44) = 1.708 × Force(33) + 24.32	0.974	
		33 × 55	Force(55) = 2.615 × Force(33) + 55.39	0.945	
Wind speed	Mx	33 × 44	Force(44) = 1.777 × Force(33) – 4E–05	1	
		33 × 55	Force(55) = 2.774 × Force(33) – 0.00	0.999	
Wind speed	My	33 × 44	Force(44) = 1.778 × Force(33) + 0.022	1	
		33 × 55	Force(55) = 2.776 × Force(33) + 0.027	1	

(continued)

Table 3 (continued)

Parameter	Force/Displacement	Correlation between	Mathematical relation	R ² value	Observation
Wind speed	Dx	33 × 44	Force(44) = 1.778 × Force(33) – 0.004	1	
		33 × 55	Force(55) = 2.763 × Force(33) – 0.359	0.996	
Wind speed	Dy	33 × 44	Force(44) = 1.094 × Force(33) + 0.284	0.998	
		33 × 55	Force(55) = 1.213 × Force(33) + 0.627	0.993	

5. Corner columns are more significant to all the parameters, viz., axial force, moments, and displacements than center columns for all conditions and terrain categories.
6. Effect of terrain category and permeability is not significant in centrally located columns of the structures.
7. Significant correlation exists between forces and displacement in less than 5% permeability with forces and displacement in other permeability.
8. Significant correlation exists between forces and displacement developed with basic wind speed of 33 m/s with other wind speeds chosen.
9. Significant co-relation exists between forces and displacement developed considering terrain category 1 with that in other terrain categories, however, the R² value is more than 0.9 for Mx between terrain categories 1 and 4.

References

1. Raj R, Ahuja AK (2013) Wind loads on cross shape tall buildings. *J Acad Indus Res* 2(4):111–113
2. Al-Tamimi M, Ahmed N et al (2011) The effects of orientation, ventilation, and varied WWR on the thermal performance of residential rooms in the tropics. *J Sustain Dev* 4(2):142–149. <https://doi.org/10.5539/jsd.v4n2p142>
3. Verma SK, Ahuja AK, Pandey AD (2013) Effects of wind incidence angle on wind pressure distribution on square plan tall buildings. *J Acad Indus Res* 1(12):747–752
4. Siddh SP Dr, Pagaria P, Hiwase PD Dr, Patil U. Comparative study of old and new Indian seismic and wind codes for analysis of existing high rise structure. *Int J Adv Sci Technol* 29(7):12546–12551

5. Patil U, Kabra N, Hiwase PD Dr, Siddh SP Dr (2019) Analytical study of response reduction factor of RCC structures. *Helix Scien Explorer* 9(6):5768–5770
6. Hiwase PD Dr, Patil U, Kabra N, Asati A (2019) Response reduction factor for industrial structures. *Helix Scien Explorer* 9(6):5775–5778
7. Stathopoulos T, Surry D, Davenport AG (1980) Internal pressure characteristics of low-rise buildings due to wind action. *Zement-Kalk-Gips* 1:451–463
8. Kumar BD, Swami BLP. Critical gust pressures on tall building frames-review of codal provisions. *Int J Adv Technol Civil Eng* 1(2):141–147
9. Wang K, Stathopoulos T (2006) The impact of exposure on wind loading of low buildings. In: Structures congress 2006, American Society of Civil Engineers, pp 1–10. [https://doi.org/10.1061/40889\(201\)9](https://doi.org/10.1061/40889(201)9)
10. Chauhan HM, Pomal MM, Bhuta GN (2013) A comparative study of wind forces on high-rise buildings as per is 875-iii (1987) and proposed draft code (2011). *Glob J Res Anal* 2(5)
11. Mehta KC (1984) Wind load provisions ANSI a58.1-1982. *ASCE J Struct Eng* 110(4), Paper No. 18758
12. Faysal RM (2014) Comparison of wind load among BNBC and other codes in different type of areas. *Int J Adv Struct Geotech Eng* 03(03):265–271
13. Holmes JD, Tamura Y, Krishna P (2008) Wind loads on low, medium and high-rise buildings by Asia-Pacific codes. In: The 4th international conference on advances in wind and structures, 29–31 May, 2008
14. Das NK. A comparative study of wind load standards. B.C.E Graduate Faculty of Texas Tech University
15. Ambadkar SD, Bawner VS (2012) Behaviour of multistoried building under the effect of wind load. *Int J Appl Sci Eng Res* 1(4):656–662. <https://doi.org/10.6088/ijaser.0020101066>
16. Kumar KS (2011) Commentary on the Indian standard for wind loads. In: 13th International conference on wind engineering, Amsterdam, The Netherlands, July 10–15, 2011
17. Ellingwood BR, Tekie PB (1999) Wind load statistics for probability-based structural design. *J Struct Eng* 125(4):453–463. [https://doi.org/10.1061/\(ASCE\)0733-9445\(1999\)125:4\(453\)](https://doi.org/10.1061/(ASCE)0733-9445(1999)125:4(453))
18. Ranjitha KP, Khan KN, Kumar NS Dr, Raza SA (2014) Effect of wind pressure on R.C tall buildings using Gust factor method. *Int J Eng Res Technol (IJERT)* 3(7)
19. Karava P, Stathopoulos T (2012) Wind-induced internal pressures in buildings with large façade openings. *J Eng Mech* 138(4):358–370. [https://doi.org/10.1061/\(ASCE\)EM.1943-7889.0000296](https://doi.org/10.1061/(ASCE)EM.1943-7889.0000296)

Performance Assessment of SMA-LRB Isolated Building Structure Due to Underground Blast-Induced Ground Motion



Sonali Upadhyaya, Narendranath Gogineni, and Sourav Gur

Abstract Blast-induced ground motions (BIGM) are highly damaging to structural and infrastructural systems, as it imparts a large amount of energy to the system over a small duration of time. Thus, it is very important to use high-energy dissipating materials in the vibration control device, which will show quick response during blast loading. In this context, shape memory alloy (SMA) material shows its capability of high-energy dissipation and auto-recentering through the phase transformation process. Therefore, the current research work considers base-isolated building structure, and aims to study the vibration control efficiency of SMA supplemented lead rubber bearing (SMA-LRB) under BIGM. Nonlinear time history analyses are executed to estimate the response quantities of interest, and the results are compared with the responses of LRB isolated building structures. To represent the LRB and SMA Bouc-wen and Graesser–Cozzarelli models are used, respectively, and the BIGM input is modeled as an exponentially decaying function with acceleration time history. Finally, to demonstrate superior control efficiency of SMA-LRB over LRB, parametric study results are provided for a wide range of isolator and structure properties, and different loading cases. Study results show that, for a wide range of parameters, the SMA-LRB isolation system can substantially reduce maximum floor acceleration and maximum isolator displacement than the LRB isolation system. Also, it has been found that the presence of SMA significantly reduces the residual deformation of the isolator at the end of BIGM. Thereby, SMA-LRB provides a much higher recentering capability of isolator than convention LRB isolation system.

Keywords BIGM · Building structure · Vibration control · SMA-LRB isolator · Residual displacement

S. Upadhyaya (✉) · N. Gogineni · S. Gur (✉)
Department of Civil and Environmental Engineering, Indian Institute of Technology, Patna, Bihar
801106, India
e-mail: sonali_2021ce21@iitp.ac.in

S. Gur
e-mail: sgur@iitp.ac.in

1 Introduction

Over time, blast-induced ground motion (BIGM) gained a lot of importance due to the increased activities of the blast. Though earthquake and the underground blast both produce ground vibration, blast pulses are widely different from the earthquake motion, due to their characteristics of high frequency and large amplitude wave over an extremely small duration. Also, due to the very less distance of epicenter for BIGM, than the seismic motion, the attenuation, as well as the spatial variation of BIGM, are more important, for the same propagation distance. Further, in the case of seismic loading, the structural response is mainly dominated due to the lower modes, without any higher modes' contribution; whereas, during BIGM, the higher frequency modes are primarily excited. In this regard, Su et al. [1] put forward that lead rubber bearing (LRB) when used as a base isolator (BI) is more effective for a higher frequency that matches with the blast pattern of loading. As well as, it has been observed that the LRB has a larger tolerance to peak acceleration as compared to sliding type BI. Other studies Kangda and Bakre [2, 3] use LRB without or with fluid viscous damper for vibration control of regular or vertically irregular buildings under BIGM with seismic loading.

In the case of near-fault earthquake motion (similar to the pulse type of BIGM), which leads to large isolator displacement, traditional elastomeric bearings are not very much suitable as they have no recentring capacities. Therefore, a recent study Gur et al. [4, 5] presented a view that smart material shape memory alloy (SMA) outperforms LRB under the ground motion of near-fault and pulse type. Other studies on SMA supplemented conventional isolation system for buildings and bridges [4–8] show superior seismic vibration control efficiency, under deterministic and stochastic ground motion. A similar comparison study of the performance of various base isolators due to underground BIGM is studied by Mondal et al. [9, 10]. The study result demonstrates that the New Zealand (NZ) type isolation system provides good response reduction with a small amount of peak bearing displacement. However, Mondal et al. [11] found there is a substantial amount of permanent deformation with the NZ bearing system, and this is one of the critical isolator design parameters. Thus, to reduce this permanent deformation or residual deformation, among various materials, SMA is more promising due to their super-elastic effect and its flag shape hysteric curve, which provides great energy absorption capacity. In some other research work [9, 10], a comparison study of SMA mounted RB (SMARB) with NZ bearing is carried out. Interestingly the results of this study showed that the SMARB has negligible residual deformation, whereas it is quite higher and unpredictable for NZ bearing for different blast loading. Various underground blast energy produced during a nuclear explosion, mining activities, military activities, etc., threaten human life and essential instruments. For high-risk facilities like public and commercial building design consideration against extreme events such as blasts is very important [12]. They cause catastrophic failure of structures depending upon their intensity. Thus, the design of structure due to underground blast loading is gaining importance in the engineering field.

In a past study [13], SMA supplemented LRB (i.e., SMA-LRB) employed as BI under the stochastic ground motion and optimal performance is assessed. Other studies [14] focus on understanding the properties of SMA-LRB, investigating peak and residual isolator displacements, ultimate shear resistance, recentering capabilities, and enhancement of energy dissipation capacity. In another study [15], using a new constitutive model called SC-BKH (Self-centering bilinear kinematic hardening) which gives greater accuracy in predicting self-centering behavior, but the response behavior of any structure isolated via SMA-LRB due to underground BIGM is still unfamiliar. The present study focuses on the vibration suppression efficiency of the SMA-LRB isolator, during underground BIGM, and compares the results with the LRB isolation system.

2 Material Modeling of Isolator

This section will provide the hysteresis behavior of LRB and super-elastic SMA isolation system through various force–deformation (f – δ) behavior.

2.1 Modeling of Lead Rubber Bearing (LRB)

Under the cyclic loading, LRB dissipates energy through yielding and shows a stable bilinear f – δ hysteresis loop. The parametric Bouc-Wen model [4, 5] is used to describe the f – δ hysteresis loop. According to the model, non-linear constitutive relation is stated as

$$F_z(x, Z) = \alpha_z k_z x + (1 - \alpha_z) F_{yz} Z \quad (1)$$

$$\dot{Z} = \left(\frac{\delta}{q_z} \right) \dot{x} - \left(\frac{\gamma}{q_z} \right) |\dot{x}| Z |Z|^{\eta-1} - \left(\frac{\beta}{q_z} \right) \dot{x} |Z|^\eta \quad (2)$$

where k_z is the initial elastic stiffness, α_z is the ratio of post-yield to pre-yield stiffness (i.e., rigidity ratio), F_{yz} and q_z are respectively the yield strength and yield displacement, the parameters δ , γ , and β in Eq. (2) are the controlling parameters for the shape of the hysteresis loop. Here, x and \dot{x} are, respectively, the relative displacement and velocity of the yield damper, variable Z is a non-dimensional quantity, which represents the hysteretic behavior of metallic material in the yield damper. δ , γ , β , and η are the parameters controlling the shape of the hysteresis curve. The parameter η controls the transition from elastic to plastic state and parameter β control the nature of the loop.

2.2 Modeling of Shape Memory Alloy (SMA)

Shape Memory Alloys (SMAs) are such materials, which can regain large percentages (almost 8%) of strain upon heating above a critical temperature. It happens due to stress-free and thermally driven phase transition in the microstructure. However, another property of the SMA material, known as super-elasticity (SE), is the primary focus of interest and is mainly related to the phase transformation of microstructure due to applied mechanical loading. During the loading cycle, this austenite (A) phase transforms into the martensite (M) phase through stress-free microstructure orientation, causes a stress plateau. During unloading, martensite SMA recovers its deformed shape through a backward transformation process from martensite (M) to austenite (A) phase and leaves no residual deformation. This process of loading-unloading cycle produces flag shape hysteresis loop, dissipates a large amount of energy, and leaves no residual deformation. Out of several alternatives, for super-elastic SMA, the Graesser–Cozzarelli material model [4, 5] has been predominantly used for the analysis of the dynamic response of the SMA-based control system. The one-dimensional material model is given as

$$\dot{F}_{\text{SMA}}(\dot{x}, \beta) = k_{\text{SMA}} \left[\dot{x} - |\dot{x}| \left| \frac{F_{\text{SMA}} - \beta}{F_{y\text{SMA}}} \right|^{(\eta-1)} \left(\frac{F_{\text{SMA}} - \beta}{F_{y\text{SMA}}} \right) \right] \quad (3)$$

$$\beta = \alpha_{\text{SMA}} k_{\text{SMA}} \left[x - \left(\frac{F_{\text{SMA}}}{k_{\text{SMA}}} \right) + f_T |x|^{c'} \operatorname{erf}(a'x) \right] \quad (4)$$

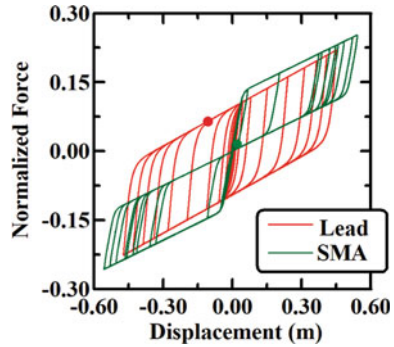
$$\operatorname{erf}(z) = \frac{2}{\sqrt{\pi}} \int_0^z (e^{-t^2}) dt \quad (5)$$

where x is the displacement, F_{SMA} is the restoring force in SMA, k_s is the stiffness of SMA in the austenite phase, $F_{y\text{SMA}}$ is the force causing the forward curve of transformation from the austenite to the martensite phase. Here, α_s is a constant definition of pre- to post-transformation stiffness ratio, a' is a constant controlling the amount of shape recovery during unloading. Parameter η also controls the sharpness of the transformation curve, c' decides the slope of unloading path, β is one-dimensional back stress given by Eq. (4), f_T is a controlling parameter of type and size of hysteresis. Here, $\operatorname{erf}(z)$ is the error function with argument z , as defined by Eq. (5).

2.3 Force Deformation Hysteresis of LRB and SMA

A comparison of typical f – δ characteristics of the lead core of LRB and the SMA wire is shown in Fig. 1. As can be observed, hysteresis energy dissipation of capacity (i.e., area under the hysteresis curve) of lead core and SMA wire are almost comparable.

Fig. 1 Comparison of the hysteresis loop of lead core and SMA material



However, compared to the lead core, SMA leaves almost no residual deformation upon unloading. In the case of the lead core, after yielding plastic strain accumulates and thus provides large residual deformation. Whereas for SMA, above austenite finish temperature (A_s), upon unloading, complete microstructure transforms take place and SMA regains its original shape. This phenomenon has been depicted in the flag shape hysteresis loop and recentring capability of SMA material, which ultimately helps to provide better control efficiency. Thus, such a remarkable behavior of super-elastic SMA material makes it very much pertinent for blast application as the recentring device.

3 Numerical Modeling and Analysis

This section provides the important details of the simulation process in terms of the equation of motion and modeling of the BIGM, as discussed below.

3.1 Blast Loading

The present section deals with the modeling of underground blast loading as an exponentially decaying function, suggested by the previous study [16]. Blast load $F(t) = m\ddot{x}_g(t)$, is used and time history records are developed for the ground acceleration, $\ddot{x}_g(t)$ based on charge wets and distance of blast.

$$\ddot{x}_g(t) = -(1/t_d)\bar{x}_g \exp(t/t_d) \tag{6}$$

where \bar{x}_g is the peak particle velocity (PPV), $t_d = R/C_p$ is the time of arrival. Here, R is the radius of the charge center and $C_p = \sqrt{E/\rho}$ denote the velocity of the

blast wave in soil or rock medium, E represents Young’s modulus and ρ is the mass density of the medium.

Among numerous empirical formulae of prediction of PPV, here relation suggested by Wu and Hao [17] is used in following Eqs. (7) and (8) considering granite site.

$$PPV = 2.981 f_1 (R/Q^{(1/3)})^{-1.3375} \tag{7}$$

$$f_1 = 0.121(Q/V)^{0.2872} \tag{8}$$

Here, f_1 is the decoupling factor for PPV, Q is Trinitrotolium (TNT) weight in kilogram, V is the volume of the TNT in cubic meter, and R is the distance in meters. In this study, the distance of charge center R is 50 m and the TNT charge weight Q is 20 tons. The volume of charge chamber V and propagation velocity C_p are considered as 1000 m³ and 5280 m/s, respectively [17].

3.2 Dynamic Analysis

In the present study, a two-dimensional shear-type building (non-isolated) and isolated via LRB and SMA-LRB has been considered for the analysis, as shown in Fig. 2a, b, respectively. The mechanical model of the LRB and SMA-LRB systems are shown in Fig. 2c, d, respectively.

Since the input blast energy dissipation occurs through the hysteresis curve of LRB or SMA-LRB isolation, thus they will behave non-linearly, and the building will stay linear-elastic domain. With linear superstructure and non-linear isolator behavior, the dynamics building and isolator are written as

$$[M]\{\ddot{x}\} + [C]\{\dot{x}\} + [K]\{x\} = -[M]\{r\}(\ddot{x}_g + \ddot{x}_b) \tag{9}$$

$$m_b \ddot{x}_b + c_b \dot{x}_b + F_b - (c_1 \dot{x}_1 + k_1 x_1) = -m_b \ddot{x}_g \tag{10}$$

$$F_b = k_r x_b + F_H(\dot{x}_b, x_b) \tag{11}$$

Here, $[M]$, $[C]$, and $[K]$ are the mass matrix, damping matrix, and elastic stiffness matrices of the building structure; $\{r\}$ is the vector containing stories deformation due to unit deformation of the ground, i.e. $\{r\} = \{1 \ 1 \ 1 \ \dots \ 1\}^T$; $\{\ddot{x}\}$, $\{\dot{x}\}$ and $\{x\}$ are acceleration, velocity, and displacement vector of the building; \ddot{x}_g and \ddot{x}_b are acceleration due to BIGM and isolator, m_b and $c_b = 4\pi \xi_b m_b / T_b$ are the isolator mass and damping of the isolator, ξ_b and T_b are the damping ratio and time period of the isolator, and F_b is the restoring force of the isolator which consists of two parts liner force due to rubber and non-linear hysteresis force lead core or SMA wires.

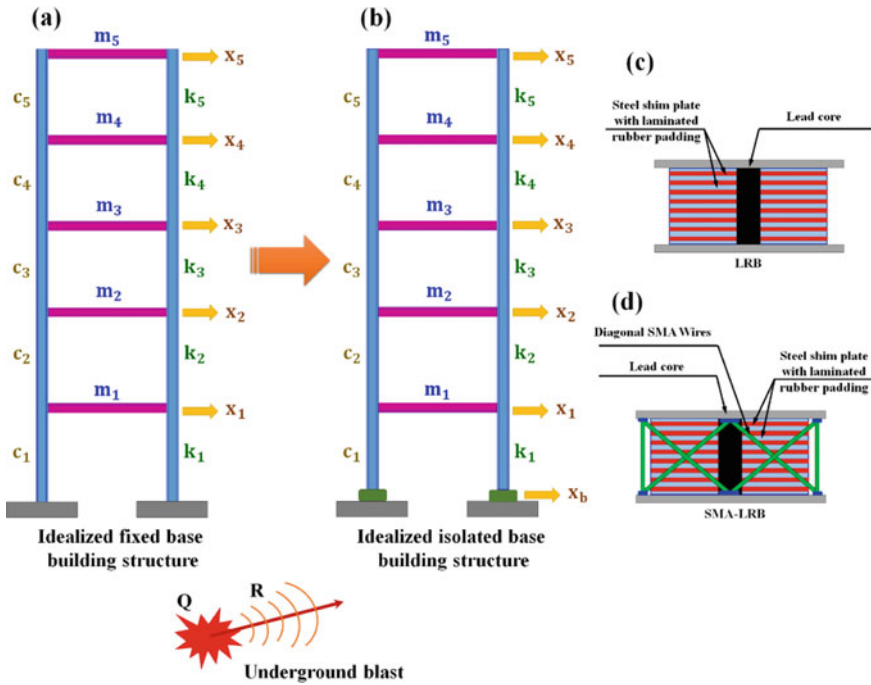


Fig. 2 Model of **a** fixed base and **b** isolated building. Mechanical model of isolator **c** Lead-Rubber-Bearing (LRB) and **d** Shape-Memory-Alloy-Lead-Rubber-Bearing (SMA-LRB)

The time period of the isolator is calculated as

$$T_b = \begin{cases} 2\pi \sqrt{M_t / (k_r + \alpha_z k_z)} & \text{for LRB} \\ 2\pi \sqrt{M_t / (k_r + \alpha_z k_z + \alpha_{SMA} k_{SMA})} & \text{for SMA-LRB} \end{cases} \quad (12)$$

where k_r is the rubber stiffness, $\alpha_z k_z$ and $\alpha_{SMA} k_{SMA}$ are the post-yield stiffness of lead core and SMA wire, $M_t = m_b + \sum_{i=1}^n m_i$ is the total system mass, and m_i is the each floor mass. Here the mass of the isolator is set the same as floor mass, i.e., $m_b = m_i$, stiffness of the lead core and SMA wires are calculated as $k_z = F_{yz}/q_z$ and $k_{SMA} = F_{ySMA}/q_{SMA}$, respectively, and finally using Eq. (12), stiffness of the rubber (k_r) is calculated. The time period and damping ratio of the isolator are adopted as $T_s = 2.00$ s and $\xi_s = 2\%$, respectively. This provides the default value of the total stiffness of the isolator as 177.65 kN/m.

The response of the non-isolated/ isolated building structure under the BIGM excitation is obtained via the step-by-step numerical integration method (Newmark-beta average acceleration technique) with the time step Δt of 0.0001 s. It is well known that the isolation system will dissipate input energy from the blast loading, through a non-linear force deformation hysteresis loop. Thus, the building structure will stay in the linear-elastic domain. Thus, to obtain the correct solution at each time

Table 1 Values of different parameters adopted for buildings, LRB and SMA-LRB isolator

Building structure	LRB isolator	SMA-LRB isolator
Floor mass: $m_i = 3000$ kg Floor stiffness: $k_i = 5830$ kN/m Time period: $T_s = 0.50$ s Damping ratio: $\xi_s = 2\%$ proportional damping for the first mode	Normalized yield strength: $F_{0yz} = 0.075$ Hysteresis parameter of lead core: $\alpha_z = 0.05, q_z = 0.025$ m $\beta = 0.5, \gamma = 0.5$ $\delta = 1.0, \eta = 1.0$	Normalized transition strength: $F_{0SMA} = 0.075$ Hysteresis parameter of lead core: same as LRB isolator Hysteresis parameter of SMA wire: $\alpha_{SMA} = 0.10,$ $q_{SMA} = 0.035$ m $a' = 2500, c' = 0.001$ $f_T = 0.07, \nu = 3.0$

step, the equation of motion of the building structure with isolation system needs to be solved iteratively. At any time steps, the iteration process will continue until the error in any response quantity become less than the tolerance limit δ_{tol} , and in the present study, it is taken as 10^{-5} . It is important to note that, to capture the non-linear force–deformation response of isolator under sudden blast loading such small-time step and tolerance limit has been adopted. To determine the responses MATLAB code is developed using the equation of motion of building, isolator, and BIGM as a non-linear material model of the isolator. Different parameters for the numerical solution are adopted from Table 1 and are also available in other studies [4–8].

4 Results and Discussion

Performance of the isolated and non-isolated building structures is studied through the numerical simulation, during underground BIGM, as mentioned in the above section. The isolation efficiency of LRB and SMA-LRB isolators is demonstrated by comparing the top floor acceleration and isolator displacement. In the parametrical study, maximum top floor acceleration, ultimate and residual isolator displacement are adopted for comparing the vibration control efficiency and performance of LRB and SMA-LRB isolator building structures.

4.1 Numerical Illustration

A typical time history analysis result is shown in Fig. 3, for non-isolated building structures and LRB or SMA-LRB isolated building structures. Figure 3a, b shows responses of top floor acceleration and displacement for the fixed base and isolated (via LRB and SMA-LRB) building structures. Compared to the non-isolated building, the isolated building substantially reduces the top floor acceleration and displacement, but the response control efficiency of SMA-LRB is more than the LRB isolator.

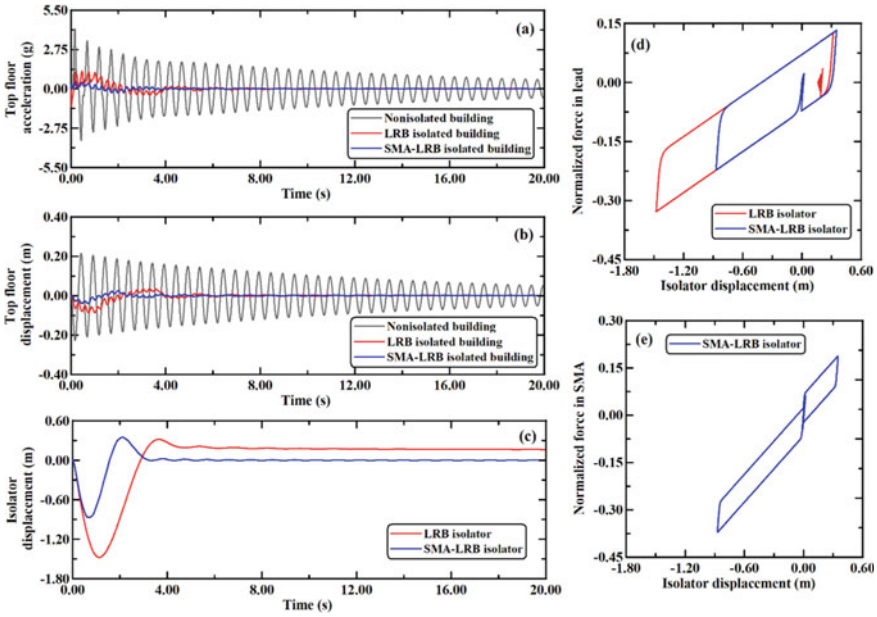


Fig. 3 Response of top floor **a** acceleration and **b** displacement of fixed base, LRB isolated, and SMA-LRB isolated building, **c** isolator displacement. Hysteresis loop of isolator **d** Lead and **e** SMA material

It is because of the added hysteresis loop of the SMA wire, as shown through the hysteresis loop area in Fig. 3e. Displacement time history of isolator response is shown in Fig. 3c, where due to the proximity of the blast site both the LRB and SMA-LRB isolator undergoes a large level of non-linear deformation, and thereby dissipate a significant amount of blast loading energy. Further, this can be observed from the hysteresis loop of lead core and SMA material as shown in Fig. 3d, e, respectively. Another important observation from Fig. 3c is that, in contrast to the LRB, due to the presence of SMA wires in SMA-LRB, it substantially reduces the peak displacement of the isolator, as well as residual displacement of the isolator. Thus, the super-elastic SMA wires in the SMA-LRB isolation system act as the auto-recentering device and thereby reduces the damage possibility of the isolator.

4.2 Parametrical Study

At first, the effect of the isolator strength on the different response parameters is provided in Fig. 4. The maximum value of top floor absolute acceleration (Fig. 4a) increases with increasing normalized strength of LRB and SMA. Isolator peak displacement and residual displacement for LRB and SMA-LRB are provided in Figs. 4b, c. As observed, incorporation of SMA material up to a critical value (i.e.,

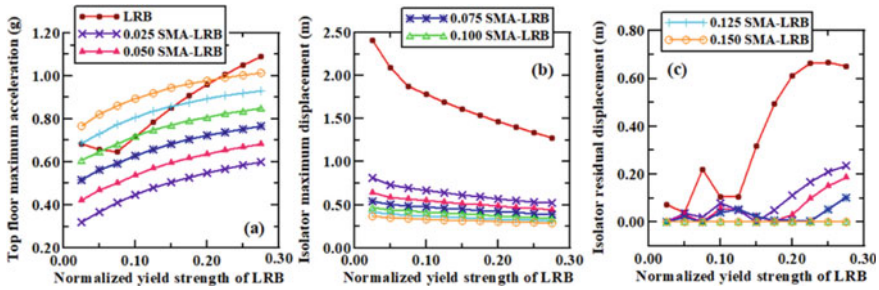


Fig. 4 Maximum **a** absolute acceleration of top floor, **b** displacement of isolator, and **c** residual displacement of isolator for normalized strength of LRB and SMA wire

normalized strength 0.10) reduces top floor acceleration than LRB. This is because, at a lower value of SMA transformation strength, the isolator goes into the non-linear domain. Thus, the SMA wires dissipate a large amount of energy from the blast loading through the hysteretic deformation and thereby reduce the acceleration. When the higher value of SMA transformation strength is used, it either stays in the liner domain or undergoes small non-linear deformation i.e., shows a small hysteresis loop. Therefore, SMA wires do not dissipate a large level of blast loading energy and make the isolator stiff which transfers more blast loading energy to the building and therefore it increases top floor acceleration. Figure 4b shows that the maximum value of isolator displacement decreases with increasing normalized strength of isolators (LRB or SMA-LRB). Figure 4c shows that residual displacement of the isolator reduces with increasing normalized transformation strength of SMA, whereas the LRB isolator shows a high level of residual displacement. The addition of SMA wires makes the SMA-LRB isolator stiff and thus it reduced the peak displacement and residual displacement (due to the shape recovery property of SMA), compared to the LRB isolator.

Figure 5 shows the control efficiency of both the isolation system under different isolator time periods. Figure 5a shows that the maximum value of top floor absolute acceleration decreases with increasing time period of isolator in the case of

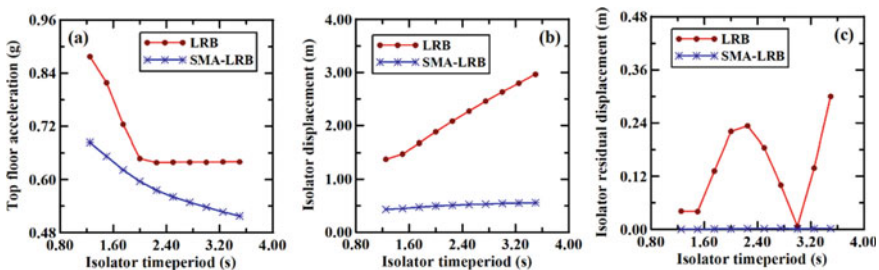


Fig. 5 Maximum **a** absolute acceleration of top floor, **b** displacement of isolator, and **c** residual displacement of isolator for the time period of LRB and SMA-LRB isolator

SMA-LRB, but for LRB it shows initially decreasing and then staying constant. The decrease in acceleration is because of the increased isolator flexibility which transfers less force to the structure. However, in the case of LRB, this effect is not significant after 2 s of the isolator time period. According to Fig. 5b, with an increase in isolator time period, the maximum value of isolator displacement increases at a much higher rate in the case of LRB than the SMA-LRB. Here as the base of the structure becomes flexible, thus this leads to an increase in the building displacement. However, it can be observed that the SMA-LRB isolator is showing better control of displacement than LRB. Figure 5c shows that residual displacement of the isolator is much high for LRB than SMA-LRB for all the values of the isolator time period.

Effect of structure time period on isolation efficiency of the LRB and SMA-LRB isolator is shown in Fig. 6. As it can be observed from Fig. 6a, with the increasing time period of the structure, the maximum value of top floor absolute acceleration drastically increases for LRB isolated buildings than SMA-LRB isolated buildings. Figure 6b shows that the maximum value of isolator displacement stays almost constant with varying structure time periods, but overall the isolator displacement is more for LRB than SMA-LRB. Thus, when the structure time period is increasing and it became more flexible, this can be said from Fig. 6a, b that the SMA-LRB isolator has better control efficiency of reducing both structural and isolator response than only LRB isolated structure. Figure 6c shows that the residual displacement of the isolator is much high for LRB than SMA-LRB for all the values of the structure time period. This is due to the recentering capacity of SMA which can be shown from the hysteresis loop of SMA material in Fig. 3e.

Next, the effect of BIGM characteristics on the vibration control efficiency of LRB and SMA-LRB is studied. The first influence of blast loading intensity on the structure and isolator response has been shown in Fig. 7, where the distance from the blast site is kept as 50 m. Figure 7a show that, with increasing blast loading intensity, the maximum value of top floor absolute acceleration increases for both LRB and SMA-LRB isolated building. As the BIGM act as pulse type loading to structure, thus it creates sudden impact loading, consequently, it excites the higher modes of the structure. Thus, an increase in blast loading intensity leads to a drastic increase in the response of the structure. However, this increase in top floor acceleration is

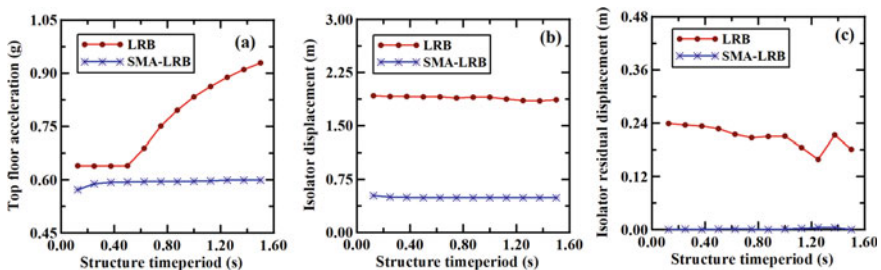


Fig. 6 Maximum **a** absolute acceleration of top floor, **b** displacement of isolator, and **c** residual displacement of isolator for the building structure time period

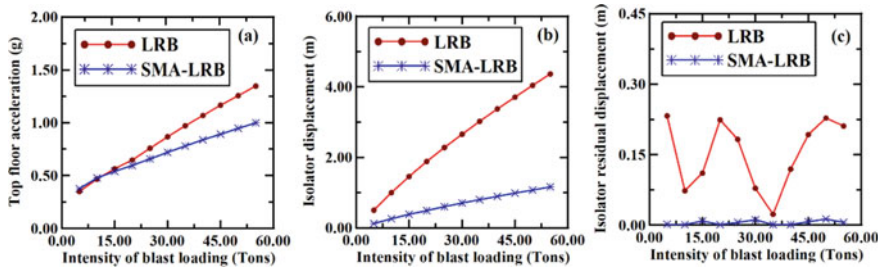


Fig. 7 Maximum **a** absolute acceleration of top floor, **b** displacement of isolator, and **c** residual displacement of isolator for the intensity of blast loading

more for LRB isolated buildings than SMA-LRB isolated buildings. Figure 7b, c shows the variation of isolator peak displacement and residual displacement (for both LRB and SMA-LRB) with blast loading intensity, respectively. It is shown in Fig. 7b that the maximum value of LRB isolator displacement increases largely with increasing blast loading intensity and always much higher SMA-LRB isolator displacement. Figure 7c shows that the residual displacement of the isolator is much high for LRB than SMA-LRB, for all the values of blast loading intensity. It can be observed that even at very high blast intensity, the SMA-LRB isolator leaves no residual displacement. This proves the robustness of SMA material.

Figure 8 shows the effect of the distance from the blast site to the structure on the peak floor acceleration isolated structure and isolator peak and residual displacement for the LRB and SMA-LRB isolation system. Here the intensity of blast loading is kept as 20 tons. Figure 8a shows that, with the increasing blast site distance from the structure, the maximum value of top floor absolute acceleration drastically decreases for both LRB and SMA-LRB isolated buildings. But more reduction can be observed for SMA-LRB isolated building cases than LRB isolated buildings. Figure 8b, c shows the variation isolator peak and residual displacement with varying distance from the blast site, respectively. Figure 8b shows that the maximum value of isolator displacement decreases largely with increasing blast site distance from structure, but more reduction is observed for SMA-LRB than LRB. As provided in the formulae

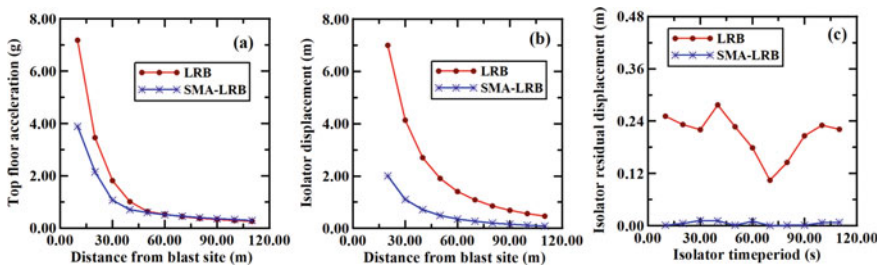


Fig. 8 Maximum **a** absolute acceleration of top floor, **b** displacement of isolator, and **c** residual displacement of isolator for the distance from the blast site

of Eqs. (6) and (7), it can be found that the blast radius R is inversely related to the ground acceleration \ddot{x}_g . Thus, with an increase in distance of the blast site, both structural and isolator responses are reducing at a decreasing rate. Figure 8c shows that residual displacement of the isolator is much high for LRB than SMA-LRB for all the values of blast site distance.

5 Conclusion

This paper presents the vibration control efficiency of the SMA-LRB isolator under blast loading and compares the results with the LRB isolation system. To this end, a parametrical study has been performed for varying isolator property, structure–property, and various loading cases. The time history analysis results reflect that the acceleration and displacement response of isolated structures is much lower than non-isolated ones. In addition, it has been observed that the reason for superior control efficiency of SMA-LRB is due to its better energy dissipation capacity, via a large hysteresis loop.

Parametrical study results show that, at the lower value of SMA normalized transformation strength (i.e., 0.1), the SMA-LRB isolator provides higher floor acceleration control efficiency than the LRB isolator. With the increase in the intensity of blast loading the reduction in top floor acceleration and isolator displacement is much more in the case of SMA-LRB than LRB and this reduction is very significant for smaller loading ($Q < 30$ tones). Furthermore, the maximum isolator displacement increases with the increased blast loading intensity, but the rate of increase is negative. In contrast to the LRB isolator, the residual displacement of the SMA-LRB isolator is very negligible, irrespective of blast intensity. This is due to the recentring (due to shape recovery property) ability of SMA that makes it very attractive to use in case of such BIGM. For a wide range of isolator time periods and structure time period, the top floor acceleration, isolator displacement, and residual displacement of SMA-LRB are much lower than LRB. Hence, the SMA material behaves very promisingly under blast loading application.

Acknowledgements The authors acknowledge the SERB under the DST Government of India for providing the research funding under the SRG scheme (SRG/2020/000892).

References

1. Su L et al (1989) Comparative study of base isolation systems. *J Eng Mech* 115(9):1976–1992
2. Kangda MZ, Bakre S (2018) The effect of LRB parameters on structural responses for blast and seismic loads. *Arab J Sci Eng* 43(4):1761–1776
3. Kangda MZ, Bakre S (2020) Performance evaluation of moment-resisting steel frame buildings under seismic and blast-induced vibrations. *J Vib Eng Technol* 8(1):1–26

4. Gur S et al (2013) Performance assessment of buildings isolated by shape-memory-alloy rubber bearing: comparison with elastomeric bearing under near-fault earthquakes. *Struct Control Health Monit* 21(4):449–465
5. Gur S et al (2013) Multi-objective stochastic-structural-optimization of shape-memory-alloy assisted pure-friction bearing for isolating building against random earthquakes. *Soil Dyn Earthq Eng* 54:1–16
6. Gur S et al (2014) Stochastic optimization of shape-memory-alloy rubber bearing (SMARB) for isolating buildings against random earthquake. *Struct Control Health Monit* 21(9):1222–1239
7. Gur S et al (2017) Thermally modulated shape memory alloy friction pendulum (tmSMA-FP) for substantial near-fault earthquake structure protection. *Struct Control Health Monit* 24(11):e2021
8. Mishra S et al (2016) Response of bridges isolated by shape memory–alloy rubber bearing. *J Bridge Eng* 21(3):04015071
9. Mondal PD et al (2017) Control of underground blast induced building vibration by shape-memory-alloy rubber bearing (SMARB). *Struct Control Health Monit* 24(10):e1983
10. Mondal PD et al (2017) Performances of various base isolation systems in mitigation of structural vibration due to underground blast induced ground motion. *Int J Struct Stab Dyn* 17(4):1750043
11. Mondal PD et al (2013) Performance of N-Z systems in the mitigation of underground blast induced vibration of structures. *J Vib Control* 20(13):2019–2031
12. Ngo T et al (2007) Blast loading and blast effects on structures—an overview. *Electron J Struct Eng* 7:76–91
13. Shinozuka M et al (2015) Shape-memory-alloy supplemented lead rubber bearing (SMA-LRB) for seismic isolation. In: *Probabilistic engineering mechanics*, vol 41, pp 34–45
14. Hu JW (2016) Seismic analysis and parametric study of SDOF lead-rubber bearing (LRB) isolation systems with recentering shape memory alloy (SMA) bending bars. *J Mech Sci Technol* 30(7):2987–2999
15. Dezfuli FH et al (2017) Effect of constitutive models on the seismic response of an SMA-LRB isolated highway bridge. *Eng Struct* 148:113–125
16. Carvalho EML, Battista RC (2003) Blast-induced vibrations in urban residential buildings. *Struct Build* 156(3):243–253
17. Wu C, Hao H (2005) Numerical study of characteristics of underground blast induced surface ground motion and their effect on above-ground structures. part i. ground motion characteristics. *Soil Dyn Earthq Eng* 25(1):27–38

Research Progress on the Torsion Behavior of Externally Bonded RC Beams: Review



Rajesh S. Rajguru and Manish Patkar

Abstract Externally strengthened reinforced concrete beams (RCB) are subjected to torsional loading having different properties of the externally bonded (EB) material and bond conditions. These conditions make it more complex compared to the normal beams. In the previous decade, a substantial number of investigation is been recounted on the utilization of various types of material for strengthening of RC beams under flexural and shear loading using EB method. A very few works have been reported on torsional behavior. This paper represents a state of review of the various materials utilized for strengthening RC beams using the EB practice and their assessment measures. The behavior of the strengthened beams (SB) is contested in relation with load carrying ability under different geometrical, power-driven characteristics of the RC beam, composite wrapping configuration, and different modes of failure. In the present paper, analytical methods described to calculate the torsional response of RC beams strengthened with EB technique are also discussed. This critical review will help to develop a database of strengthening systems of RC beams and will act as footprint for further research.

Keywords Reinforced concrete · Torsions · Strengthening · Mode of failure · External bonding

R. S. Rajguru (✉)

Assistant Professor, Civil Engineering Department, SRES's Sanjivani COE, Kopergaon, Maharashtra, India
e-mail: rajgururs25@gmail.com

Assistant Professor, Civil Engineering Department, Savitribai Phule Pune University, Pune, Maharashtra, India

Research Scholar, Civil Engineering Department, Oriental University, Indore, Madhya Pradesh, India

M. Patkar

Associate Professor, Civil Engineering Department, Oriental University, Indore, Madhya Pradesh, India

1 Introduction

Nowadays globalization is at its peak. Many infrastructural projects are going on in the world. It includes high-rise buildings, bridges, and water tanks. Structural members are generally subjected to flexural, compression shear loading and barely subjected to torsion loading. However, RC beam located along the periphery of structures, ring beam of the circular slab, subjected to cantilever loading may have a torsional effect. The behavior of such member and its strengthening is more complicated and need to study. Many researchers have been working on strengthening of RC beam by using externally bonded fiber reinforced polymer (FRP) [1–16]. FRP's good strength to mass proportion, good opposition to chemical and corrosion attack, flexible to use make it more popular for strengthening work [17]. FRP is continuous fiber strip that can be warped on beam surface by using different polymer matrices to transfer stresses. To eradicate the limitations of the well-established FRP strengthening system, a new type of amalgamated method, denoted as fiber reinforced cementitious matrix (FRCM) composite, has been inspected lately. It has been investigated in view of providing a substitute strengthening practice [18]. Numerous forms of fibers have been utilized in FRCM composite practices which include basalt, steel, carbon, glass, and polyparaphenylene benzobisoxazole (PBO). Very few researches are available in the literature on its usage for torsional firming [19].

The last two decades literature has been split into four groups or zones as shown in Fig. 1. From the year 2000 to 2005, only 0.04% of investigation has been done on strengthening of RC beams under torsion. From 2006 to 2010, 2011 to 2015, and 2016 to 2020 progress on the same area was 22.44, 16.33, and 57.14%. Ghobarah et al. in 2002 carried out experimental investigation on glass fibers as well as carbon fibers utilized in the torsional opposition. The outcomes or results reveals that completely wrapped beams from all sides executed better than that by utilizing the strips. The investigation suggested that the material is efficiently utilized under 45° orientation of the fibers. From the year 2007, various authors propose various analytical models. Beams reinforced with carbon-Fiber reinforced polymer bars and transverse reinforcement under torsional loading studied in 2014 show good agreement with normal beam [20]. Epoxy adhesive has poor performance as it is allied with fumes with high toxicity and in elevated thermal atmospheres. To overcome this issue, a novel adhesive with cement base has been established and utilized as a substitute to

Fig. 1 Research progress

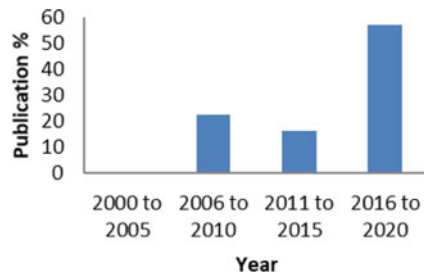
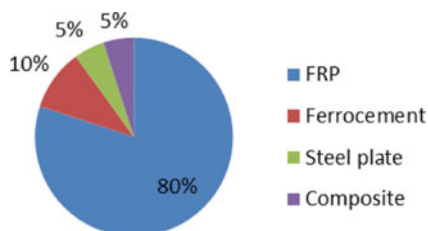


Fig. 2 Strengthening material



epoxy in numerous readings [9]. Figure 2 indicates that many researchers used FRP as strengthening material, although its high cost makes its strengthening process completely an expensive affair. Apart from this Ferrocement is more economical alternative. Still, there is an unavailability of codes for ferrocement compounds [21].

Though many researchers have focused on this issue, still many constraints need to be explored. Ferrocement is known to have good resistance to impact, good ductility, and superior in crack resisting ability [22–31]. High rich mortar matrices in ferrocement laminates seem to improve the considerable positive impact in the load carrying potential and ductility [22, 32] [22]. Revathy et al. [31] carried out experimental investigation on a rich and flowable nanosilica-based cementitious matrices of ferrocement which increase the compressive strength by 7.5 to 50% compared to control cement mortar [32]. CFRP strengthened beam increases cracking and ultimate strength in torsion up to 40% and 75%, respectively, compared to normal beams [33]. To increase the torsional enactment of RC beam members, utilization of high performance fiber reinforced cementitious composite mortar was found to be a beneficial technique [34].

The current paper presents the progress of investigation done on torsional strengthening of RC beams with EB composites. From a comprehensive literature study, a databank of investigational trials is established and debated. The usefulness of the strengthening scheme is inspected in regard to mechanical and geometrical properties, amalgamated wrapping configuration, and its categories. Various approaches to failure of the SB are also conferred in the present study. Later, various analytical systems established to calculate the torsion strength reaction of strengthened RC beams by using EB methods are presented.

2 Experimental Investigation

Table 1 displays the experimental data of beam strengthening under torsion loading. Table 1 summarizes the data related to cross section of specimen along with percentage of reinforcement used, strengthening material used and experimental results obtained. Geometrical properties and reinforcement used in RC strengthened beams may affect the strength of RC beam as compared to control specimens. Strength also depends on percentage of main reinforcement used and center-to-center spacing of stirrups. As compressive strength of concrete, shape, and type of

Table 1 Experimental data base

References	External bounded fiber											Results			
	BN	Sh	W	D	Pt%	Co	Si	NL	W	S	T	An	T_c kN.m	Tu kN.m	FM
[39]	C1	SR	150	350	0.33	Ca	4	1	-	-	0.165	N	12.01	32.1	F
	C2	SR	150	350	0.33	Ca	2	1	100	100	0.165	N	9.88	24.93	CF
	C3	SR	150	350	0.33	Ca	1	1	100	-	0.165	N	16.75	21.95	C
	C4	SR	150	350	0.33	Ca	2	1	200	100	0.165	N	11.74	28.27	C
	C5	SR	150	350	0.33	Ca	2	1	100	150	0.165	N	10.49	23.96	C
	C6	SR	150	350	0.33	Ca	4	1	100	-	0.165	N	-	30.05	F
[7, 40]	G1	SR	150	350	0.33	Gl	4	1	-	-	0.353	N	12.81	33.81	F
	G2	SR	150	350	0.33	Gl	2	1	100	100	0.353	N	11.23	23.48	C
	CS1	SR	500	350	0.40	-	-	-	-	-	-	-	68.4	62.9	C
	FS050D2	SR	500	350	0.40	Ca	4	2	50	175	0.176	N	73.7	93.8	CF
	FH050D2	BR	500	350	0.94	Ca	4	2	50	175	0.176	N	22.2	87.7	D
	Ra-FC(1)	SR	100	200	0.5	Ca	4	1	-	-	-	N	2.8	4.87	F
	RaS-FS150(2)	SR	100	200	0.5	Ca	4	2	150	150	0.11	N	2.35	4.33	C
	Rb-FC(1)	SR	150	300	0.22	Ca	4	1	-	-	-	N	8.79	10.05	F
	Rb-FS200(1)	SR	150	300	0.22	Ca	4	1	200	200	0.11	N	6.73	9.32	C
	Rb-FS300(1)	SR	150	300	0.22	Ca	4	1	300	300	0.11	N	6.96	7.52	C
[42]	RbS-FS200(1)	SR	150	300	0.22	Ca	4	1	200	200	0.11	N	6.93	9.8	C
	Ra-c	SR	100	200	0.5	-	-	-	-	-	-	-	2.389	-	C
	Ra-F(1)	SR	100	200	0.5	Ca	4	1	-	-	0.11	N	2.8	4.868	F
	Ra-F(2)	SR	100	200	0.5	Ca	4	2	-	-	0.11	N	2.83	6.65	F

(continued)

Table 1 (continued)

References	External bounded fiber													Results		
	BN	Sh	W	D	Pt%	Co	Si	NL	W	S	T	An	ζ_c kN.m	Tu kN.m	FM	
[5]	Ra-Fs150(2)	SR	100	200	0.5	Ca	4	2	150	300	0.11	N	2.219	3.018	F	
	Rb-F(1)	SR	150	300	0.22	Ca	4	1	-	-	0.11	N	8.794	10.05	F	
	T-FU(2)	T	150	300	0.22	Ca	3	2	-	-	0.11	N	8.775	9.45	D	
	Control	SR	200	300	1.29	-	-	-	-	-	-	N	10.4	16.8	C	
	NP3S1	SR	200	300	1.29	CF	3	1	101.6	101.6	0.046	N	11.6	18.1	C	
	NP4S1	SR	200	300	1.29	CF	4	1	101.6	101.6	0.046	N	14.3	21.8	C	
	NP4C1	SR	200	300	1.29	CF	3	1	-	-	0.046	N	13.7	27.2	C	
	NP4C2	SR	200	300	1.29	CF	4	2	-	-	0.046	N	14.5	35.1	C	
	U4H	SR	125	250	0.54	FE	3	4	-	-	25	N	6.424	7.68	CFE	
	L04H	SR	125	250	2.17	FE	3	4	-	-	25	N	6.675	7.87	CEF	
[25, 26]	T04H	SR	125	250	0.54	FE	3	4	-	-	25	N	6.618	8.66	CFE	
	CO4H	SR	125	250	2.17	FE	3	4	-	-	25	N	6.71	12.91	CFE	
	F1	SR	150	300	0.22	Ar	4	1	-	-	0.25	N	4.235	4.675	C	
[43]	F2	SR	150	300	0.22	Ar	4	1	-	-	0.25	N	4.070	4.620	C	
	F3	SR	150	300	0.22	Ar	4	1	-	-	0.25	N	4.097	4.207	C	

BN = Beam name, Sh = Shape, W = Width, D = Depth, Pt% = Percentage main steel, Co = Composite, Si = Side, NL = No. of layers, S = Spacing, T = Thickness, An = Anchorage, ζ_c = Cracking strength, Tu = Ultimate strength, FM = Failure mode, Ca = Carbon fiber, Gl = Glass fiber, CF = Composite fiber, C = Concrete, F = fiber, CF = Concrete and fiber, D = Debonding, SR = Box rectangular, BR = Tee, FE = Ferrocement, Ar = Aramid fiber

composite fiber changes, the mode of failures also changes accordingly. Data in Table 1 shows that approximately 50% increment in the strength was achieved when beam was strengthened by FRP. Kim et al. [35] conducted eleven experimental tests were conducted to study the effect of reinforcement and cross section on torsional strength. His results revealed that solid cross section and hallow cross section has similar level of strength also smaller amount of torsion reinforcement increased the ductile behavior regardless of cross section [35]. Maalej and Leong [36] stated that the size of beam doesn't have any significant effect on the strengthening proportion and deflection. According to Lee et al. [37] carbon fiber reinforced polymer when used as a strengthening material for deep beam, its length parameter has a noteworthy effect on the performance of deep beams. Sole form of reinforcement is ineffectual in increasing the torsion strength [22]. It is perceived that all the beams enveloped with aramid fiber strips upsurge torsion carrying ability. The FRP strip spacing and torsional moment carrying ability is inversely proportional to each other [38].

Experimental database included total of thirty-five beam specimen details. Out of that 82% of the test were performed on RC beam having 0.22–0.5% main steel as represented in Fig. 3a. The transverse reinforcement in the RC beam samples is found to be less significant in enhancing the torsion strength [34]. Therefore, CFRPs are found to be more practicable strengthening practice.

Copiously enfolded RCB aramid fiber grosses 140% extra ultimate torsional moment, compared with controlled beam [44]. The ultimate torsional strength increased by up to 150% with the utilization of 90° orientated entirely wrapped glass fibers. Composite fibers are also effective in order to increase the torsional capacity of RC members as that of Glass-FRP and Carbon-FRP combinations [5]. The maximum torsional moment is highly sensitive to the area of steel and yield strength parameters used in RC beams [45]. Brittle failure of concrete in RC beam can be reduced by designing RC beam as a under reinforced section. As percentage of transverse reinforcement increases torsional strength and stiffness enhances, regardless of beams size parameters [35]. A steel-below balance section with three side ferrocement covering showed better torsional strength when matched to over reinforced beams [30]. Ferrocement wrapped RC beam without steel in longitudinal direction is not

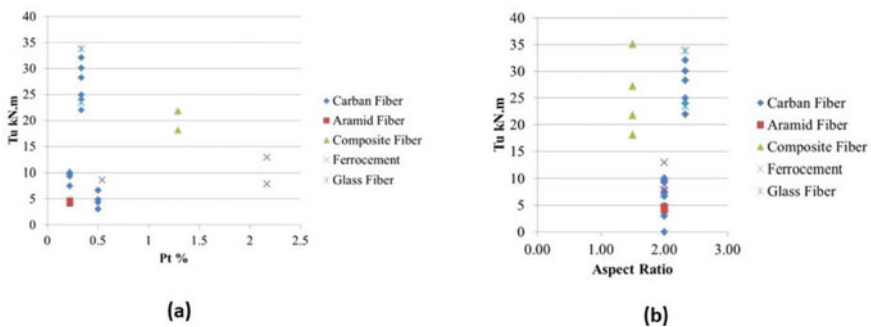


Fig. 3 Graphs showing a percentage steel (Pt %) versus Tu and b aspect ratio versus Tu

actual mode of improving the torsional strength, while growth in toughness is found to be negligible [46]. Figure 3b shows that strength can be enhanced under any aspect ratio depending upon the type of composite used and warping configuration. Carbon fiber is mostly preferred fiber for various aspect ratios. It might be due to its high tensile strength of up to 3900 MPa and better in mechanical properties over the other fibers. Maximum research work has been carried out on aspect ratio between 1.5 and 2.5 and more research need to be carried out for different aspect ratios.

3 Warping Configuration

Figure 4 shows typical warping configuration used by many researchers. Practically four side warping around the cross section is not feasible although full side warpped strengthening system is the only configuration that shows fiber rupture failure [42]. Therefore, 3-side, 2-side, and 1-side warping configurations have been explored. The prolonged three side jacket bands were very much operative strengthening ways compared to the un-anchored three side jacket bands due to excessive fiber slippage in 2-side and 1- side warping [4, 47, 48]. For 0-degree alignment, the critical strength was found to be not much more than the strength at first crack. FRP rupture of beams is controlled when fibers are oriented in the 90° direction [49]. Though 90-degree alignment of fibers were established to be quite operative in rising the strength (torsion) than 45-degree alignment, still de-bonding of fiber occurs at the end. The SBs in rectangular form and enveloped uninterrupted FRP sheets achieved improved torsional ability compared to SBs with FRP strips [42]. PBO-FRCM composite-strengthened beams show that the 90-degree fiber alignment is far too operative in rising the strength (torsion) than the 0-degree alignment [19]. Database shows that majority of test were conducted on single layer and two layers of fibers. When a more amount of films are provided, the efficacy of strengthening system declines. Properly anchored number of fiber layers forced failure mode in fiber rupture instead of debonding of fibers [19]. The complete wrap of a RCB is quite efficient in strengthening the torsional resistance compared to the beams in which strips of different patterns are used for the purpose of strengthening [39].

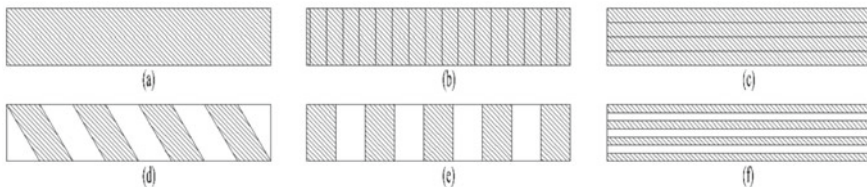


Fig. 4 Typical warping configurations

4 Mode of Failure

Deifalla et al. [4] divided mode of failure into three modes. The first mode includes concrete failure due to crushing caused by compressive loads or slanting cracking caused due to oblique tensile loads. The second mode includes the steel stirrup yielding tailed by end debonding of fiber reinforced polymer and lastly oblique failure. Third mode is characterized by steel yielding tailed by flaking off of fiber reinforced polymer and lastly slanting failure [4]. Though the samples had main fissures that obliquely flew on three verges of the sample, the main depreciations were observed on the bottom part of the back face [50]. The initial fissures were introduced at the intermediate of the lengthier faces [20]. Two layers of FRCM composite with 4-sided continuous wrapping configuration improved the post cracking stiffness and torsional strength quite efficiently compared to single film composites [5]. The fiber reinforced polymer strips break at the final strain in succession to the yielding of strengthening steel rebar under tensile forces [17] PBO-FRCM complex was unsuccessful because of the fiber estrangement at the beam junctions tailed by crushing of concrete [5]. A detachment of the CFRP-sheet was detected at the final value of force after the process of concrete deafening [51]. In the case of plain beams, the crack is originated on the lengthier side, but in this case a mono-latent crack established in the center was responsible for the failure of unwrapped concrete side [26, 30, 46]. This may be due to the slight detention provided by the fiber. Untimely de-bonding of the fiber films happened due to a substantial cracking of concrete [39]. Sometimes it may be because of epoxy bonding complications linked with toxicity of fumes and reduction in performance in elevated thermal atmosphere [9]. The beams in absence of bars and stirrups displayed an unexpected failure and parted in two numbers [52]. Crack width and pattern of this failed specimen sample specifies that the width was 13.6 mm for regulator beam. Beam strengthened with carbon fiber has smaller fissure width of 3.1 mm as matched to beam strengthen with glass fiber was of 4.1 mm [53].

5 Analytical Models

Extraction of analytical outcomes for RC beam subjected to torsion is greater tough work. Analytical calculation concerned compatibility equations under deformation and relation of concrete, reinforcement, and strengthening materials impact. The results confirmed the feasibility of the softened membrane model for torsion (SMMT) used to calculate the torsional reaction of fully wrapped fiber reinforced cementitious matrix (FRCM) and composite-strengthened beams with the fiber rupture failure mode [18]. Ameli and Ronagh [54] proposed analytical method in which the relations of different parameters are allowed by fulfilling equilibrium and compatibility conditions throughout the loading. Whereas the maximum torque of the beam is designed accurately using compression field theory (CFT) [54]. Deifalla and Ghobarah [47] established an analytical prototype constructed on the basics of the

modified compression field theory. Model accounted for the effect of various parameters including various strengthening techniques, FRP influence, and various failing types. This model displayed decent relationships with the investigated outcomes [55]. The Generalized Softened Variable Angle Truss-Model is reconstructed in an integrated way and efficiently utilized to reinforced concrete and plain concrete beam. (Constantin E. Chalioris) has proposed distinct truss model, which uses Fiber reinforced polymer restrained concrete interaction of the EB Fiber reinforced polymers to the torsional ability. Accountable compression and tension interaction with Fiber reinforced polymer strengthened concrete are showed in the projected model [56].

6 Conclusions and Future Scope

The key findings from this comprehensive review are mentioned as follows.

1. The experimental data shows that maximum performance of RC beam under torsion was achieved by providing four side wrapping configuration and is explored by many researchers.
2. Fibers with 0-degree, 45-degree, and 90-degree alignments with respect to the longitudinal axis of beam are examined. Fibers wrapped with 90° orientations have good agreement with the result. 45°-orientated fibers are also good in diagonal crack arresting. Fiber with 0° orientation has less contribution in improving the torsional strength.
3. Fibers wrapped in strips are not much effective as compared to the fully wrapped continuous fibers; however, they prove effective in arresting the cracks.
4. Failure of strengthening beam occurred either due to failure of concrete or failure of fibers. Failure of concrete lead to the de-bonding of fibers.
5. Literature survey revealed that Analytical models such as softened membrane model for torsion (SMMT), Softened Variable Angle Truss-Model (GSVATM), and special truss model were proposed to strengthened RC beam under torsion.

Present work can be extended in the following areas to know in-depth behavior of RC beam strengthened with externally bonded (EB) composites:

1. Very few studies were noticed on proper anchorage system, which can effectively resist the slippage between fiber and concrete joint with three side wrapping configuration.
2. Additional work is needed on torsional strengthening with FRCM composite to know its response under FRCM strengthening beams with different fiber types.
3. Experimental work can be carried out on large size beam in large scale to evaluate the effect of size on externally strengthened RC beam under torsion.
4. Future investigation can be carried out on different strengthening configurations along with different types of composite FRP'.
5. Analytical model on RC beam strengthened with FRCM composite needs to be explored.

References

1. Sundarraja MC, Rajamohan S (2009) Strengthening of RC beams in shear using GFRP inclined strips—an experimental study. *Constr Build Mater* 23(2):856–864. <https://doi.org/10.1016/j.conbuildmat.2008.04.008>
2. Almusallam TH, Al-Salloum YA (2001) Ultimate strength prediction for RC beams externally strengthened by composite materials. *Compos Part B Eng* 32(7):609–619. [https://doi.org/10.1016/S1359-8368\(01\)00008-7](https://doi.org/10.1016/S1359-8368(01)00008-7)
3. Anania L, Badalà A, Failla G (2005) Increasing the flexural performance of RC beams strengthened with CFRP materials. *Constr Build Mater* 19(1):55–61. <https://doi.org/10.1016/j.conbuildmat.2004.04.011>
4. Deifalla A, Awad A, Elgarhy M (2013) Effectiveness of externally bonded CFRP strips for strengthening flanged beams under torsion: an experimental study. *Eng Struct* 56:2065–2075. <https://doi.org/10.1016/j.engstruct.2013.08.027>
5. Alabdulhady MY, Sneed LH, Carloni C (2017) Torsional behavior of RC beams strengthened with PBO-FRCM composite—an experimental study. *Eng Struct* 136:393–405. <https://doi.org/10.1016/j.engstruct.2017.01.044>
6. Rizzo A, De Lorenzis L (2009) Behavior and capacity of RC beams strengthened in shear with NSM FRP reinforcement. *Constr Build Mater* 23(4):1555–1567. <https://doi.org/10.1016/j.conbuildmat.2007.08.014>
7. Hii AKY, Al-Mahaidi R (2006) Experimental investigation on torsional behavior of solid and box-section RC beams strengthened with CFRP using photogrammetry. *J Compos Constr* 10(4):321–329. [https://doi.org/10.1061/\(asce\)1090-0268\(2006\)10:4\(321\)](https://doi.org/10.1061/(asce)1090-0268(2006)10:4(321))
8. Gao B, Kim JK, Leung CKY (2004) Experimental study on RC beams with FRP strips bonded with rubber modified resins. *Compos Sci Technol* 64(16):2557–2564. <https://doi.org/10.1016/j.compscitech.2004.05.016>
9. Al-Bayati G, Al-Mahaidi R, Kalfat R (2016) Experimental investigation into the use of NSM FRP to increase the torsional resistance of RC beams using epoxy resins and cement-based adhesives. *Constr Build Mater* 124:1153–1164. <https://doi.org/10.1016/j.conbuildmat.2016.08.095>
10. Rizzo A, De Lorenzis L (2009) Modeling of debonding failure for RC beams strengthened in shear with NSM FRP reinforcement. *Constr Build Mater* 23(4):1568–1577. <https://doi.org/10.1016/j.conbuildmat.2008.03.009>
11. Maalej M, Bian Y (2001) Interfacial shear stress concentration in FRP-strengthened beams. *Compos Struct* 54(4):417–426. [https://doi.org/10.1016/S0263-8223\(01\)00078-2](https://doi.org/10.1016/S0263-8223(01)00078-2)
12. Guenaneche B, Krour B, Tounsi A, Fekrar A, Benyoucef S, Adda Bedia EA (2010) Elastic analysis of interfacial stresses for the design of a strengthened FRP plate bonded to an RC beam. *Int J Adhes Adhes* 30(7):636–642. <https://doi.org/10.1016/j.ijadhadh.2010.06.003>
13. Goudar SK, Shivaprasad KN, Das BB (2019) Mechanical properties of fiber-reinforced concrete using coal-bottom ash as replacement of fine aggregate. In: *Sustainable construction and building materials*. Springer, Singapore, pp 863–872
14. George RM, Das BB, Goudar SK (2019) Durability studies on glass fiber reinforced concrete. In: *Sustainable construction and building materials*. Springer, Singapore, pp 747–756
15. Srikumar R, Das BB, Goudar SK (2019) Durability studies of polypropylene fibre reinforced concrete. In: *Sustainable construction and building materials*. Springer, Singapore, pp 727–736
16. Yadav S, Das BB, Goudar SK (2019) Durability studies of steel fibre reinforced concrete. In: *Sustainable construction and building materials*. Springer, Singapore, pp 737–745
17. Gao B, Leung CKY, Kim JK (2007) Failure diagrams of FRP strengthened RC beams. *Compos Struct* 77(4):493–508. <https://doi.org/10.1016/j.compstruct.2005.08.003>
18. Alabdulhady MY, Aljabery K, Sneed LH (2019) Analytical study on the torsional behavior of reinforced concrete beams strengthened with FRCM composite. *J Compos Constr* 23(2):04019006. [https://doi.org/10.1061/\(asce\)cc.1943-5614.0000927](https://doi.org/10.1061/(asce)cc.1943-5614.0000927)

19. Alabdulhady MY, Sneed LH (2018) A study of the effect of fiber orientation on the torsional behavior of RC beams strengthened with PBO-FRCM composite. *Constr Build Mater* 166:839–854. <https://doi.org/10.1016/j.conbuildmat.2018.02.004>
20. Mohamed HM, Chaallal O, Benmokrane B (2015) Torsional moment capacity and failure mode mechanisms of concrete beams reinforced with carbon FRP bars and stirrups. *J Compos Constr* 19(2):04014049. [https://doi.org/10.1061/\(asce\)cc.1943-5614.0000515](https://doi.org/10.1061/(asce)cc.1943-5614.0000515)
21. Kaish ABMA, Jamil M, Raman SN, Zain MFM, Nahar L (2018) Ferrocement composites for strengthening of concrete columns: a review. *Constr Build Mater* 160:326–340. <https://doi.org/10.1016/j.conbuildmat.2017.11.054>
22. Adhikari A, Bagal DK, Student BT (2019) Torsional strength of ferrocement ‘U’ wrapped RC beams: a comparative study. *Int J Appl Eng Res* 14(13):146–155
23. Mandal A, Nigam MK (2018) A review report on mechanical properties of ferrocement with cementitious materials. *Int J Eng Res Technol* 1(9):46–54
24. Deepak MS, Surendar M, Aishwarya B, Beulah Gnana Ananthi G (2020) Bending behaviour of ferrocement slab including basalt fibre in high strength cement matrix. *Mater Today Proc*:8–11. <https://doi.org/10.1016/j.matpr.2020.08.074>
25. Behera GC, Rao TDG, Kameswara CB (2014) Study of post-cracking torsional behaviour of high-strength reinforced concrete beams with a ferrocement wrap. *Slovak J Civ Eng* 22(3):1–12. <https://doi.org/10.2478/sjce-2014-0012>
26. Behera G, Dhal M (2018) Torsional behaviour of normal strength RCC beams with ferrocement ‘U’ wraps. *Facta Univ—Ser Archit Civ Eng* 16(1):1–16. <https://doi.org/10.2298/fuace160514001b>
27. Li B, Lam ESS, Wu B, Wang YY (2013) Experimental investigation on reinforced concrete interior beam-column joints rehabilitated by ferrocement jackets. *Eng Struct* 56:897–909. <https://doi.org/10.1016/j.engstruct.2013.05.038>
28. Ganesan N, Indira PV, Irshad P (2017) Effect of ferrocement infill on the strength and behavior of RCC frames under reverse cyclic loading. *Eng Struct* 151:273–281. <https://doi.org/10.1016/j.engstruct.2017.08.031>
29. Shaaban IG, Shaheen YB, Elsayed EL, Kamal OA, Adesina PA (2018) Flexural characteristics of lightweight ferrocement beams with various types of core materials and mesh reinforcement. *Constr Build Mater* 171:802–816. <https://doi.org/10.1016/j.conbuildmat.2018.03.167>
30. Behera GC, Rao TDG, Rao CBK (2016) Torsional behaviour of reinforced concrete beams with ferrocement U-jacketing—experimental study. *Case Stud Constr Mater* 4:15–31. <https://doi.org/10.1016/j.cscm.2015.10.003>
31. Revathy J, Gajalakshmi P, Aseem Ahmed M (2020) Flowable nano SiO₂ based cementitious mortar for ferrocement jacketed column. *Mater Today Proc* 22:836–842. <https://doi.org/10.1016/j.matpr.2019.11.020>
32. Sankar K, Shoba Rajkumar D (2020) Experimental investigation on different high rich cement mortar for ferrocement application. *Mater Today Proc* 22:858–864. <https://doi.org/10.1016/j.matpr.2019.11.033>
33. Al-Mahaidi R, Hii AKY (2007) Bond behaviour of CFRP reinforcement for torsional strengthening of solid and box-section RC beams. *Compos Part B Eng* 38(5–6):720–731. <https://doi.org/10.1016/j.compositesb.2006.06.018>
34. Kim J, Kwon M, Seo H, Lim J (2015) Experimental study of torsional strength of RC beams constructed with HPFRC composite mortar. *Constr Build Mater* 91:9–16. <https://doi.org/10.1016/j.conbuildmat.2015.05.018>
35. Kim MJ, Kim HG, Lee YJ, Kim DH, Lee JY, Kim KH (2020) Pure torsional behavior of RC beams in relation to the amount of torsional reinforcement and cross-sectional properties. *Constr Build Mater* 260:119801. <https://doi.org/10.1016/j.conbuildmat.2020.119801>
36. Maalej M, Leong KS (2005) Effect of beam size and FRP thickness on interfacial shear stress concentration and failure mode of FRP-strengthened beams. *Compos Sci Technol* 65(7–8):1148–1158. <https://doi.org/10.1016/j.compscitech.2004.11.010>
37. Lee HK, Cheong SH, Ha SK, Lee CG (2011) Behavior and performance of RC T-section deep beams externally strengthened in shear with CFRP sheets. *Compos Struct* 93(2):911–922. <https://doi.org/10.1016/j.compstruct.2010.07.002>

38. Kandekar SB, Talikoti RS (2018) Study of torsional behavior of reinforced concrete beams strengthened with aramid fiber strips. *Int J Adv Struct Eng* 10(4):465–474. <https://doi.org/10.1007/s40091-018-0208-y>
39. Ghobarah A, Ghorbel MN, Chidiac SE (2002) Upgrading torsional resistance of reinforced concrete beams using fiber-reinforced polymer. *J Compos Constr* 6(4):257–263. [https://doi.org/10.1061/\(asce\)1090-0268\(2002\)6:4\(257\)](https://doi.org/10.1061/(asce)1090-0268(2002)6:4(257))
40. Hii AKY, Al-Mahaidi R (2006) An experimental and numerical investigation on torsional strengthening of solid and box-section RC beams using CFRP laminates. *Compos Struct* 75(1–4):213–221. <https://doi.org/10.1016/j.compstruct.2006.04.050>
41. Chalioris CE (2007) Behavioural model of FRP strengthened reinforced concrete beams under torsion. In: *Proceedings of the 1st Asia-Pacific conference on FRP in structures, APFIS 2007*, vol 1, no December 2007, pp 111–116
42. Chalioris CE (2008) Torsional strengthening of rectangular and flanged beams using carbon fibre-reinforced-polymers—experimental study. *Constr Build Mater* 22(1):21–29. <https://doi.org/10.1016/j.conbuildmat.2006.09.003>
43. Kandekar SB, Talikoti RS (2020) Torsional behaviour of reinforced concrete beams retrofitted with aramid fiber. *Adv Concr Constr* 9(1):1–7. <https://doi.org/10.12989/acc.2020.9.1.001>
44. Kandekar SB, Talikoti RS (2019) Torsional behaviour of reinforced concrete beam wrapped with aramid fiber. *J King Saud Univ—Eng Sci* 31(4):340–344. <https://doi.org/10.1016/j.jksues.2018.02.001>
45. Ilkhani MH, Naderpour H, Kheyroddin A (2019) A proposed novel approach for torsional strength prediction of RC beams. *J Build Eng* 25(January):100810. <https://doi.org/10.1016/j.jobe.2019.100810>
46. Behera GC, Gunneswar RTD, Rao CBK (2013) Torsional strength of ferrocement ‘U’ wrapped normal strength beams with only transverse reinforcement. *Procedia Eng* 54:752–763. <https://doi.org/10.1016/j.proeng.2013.03.069>
47. Deifalla A, Ghobarah A (2010) Full torsional behavior of RC beams wrapped with FRP: analytical model. *J Compos Constr* 14(3):289–300. [https://doi.org/10.1061/\(asce\)cc.1943-5614.0000085](https://doi.org/10.1061/(asce)cc.1943-5614.0000085)
48. Alabdulhady MY, Sneed LH, Abdelkarim OI, ElGawady MA (2017) Finite element study on the behavior of RC beams strengthened with PBO-FRCM composite under torsion, vol 179. Elsevier Ltd
49. Panchacharam S, Belarbi A (2002) Torsional behavior of reinforced concrete beams strengthened with FRP composites. *First FIB Congr.*, no. September, pp 1–11, 2002, [Online]. Available: <http://rb2c.mst.edu/media/research/rb2c/documents/torsional.pdf>
50. Jeng CH, Chao M, Chuang HC (2019) Torsion experiment and cracking-torque formulae of hollow prestressed concrete beams. *Eng Struct* 196(July):109325. <https://doi.org/10.1016/j.engstruct.2019.109325>
51. Capozucca R, Nilde Cerri M (2002) Static and dynamic behaviour of RC beam model strengthened by CFRP-sheets. *Constr Build Mater* 16(2):91–99. [https://doi.org/10.1016/S0950-0618\(01\)00036-8](https://doi.org/10.1016/S0950-0618(01)00036-8)
52. Chalioris CE, Karayannis CG (2009) Effectiveness of the use of steel fibres on the torsional behaviour of flanged concrete beams. *Cem Concr Compos* 31(5):331–341. <https://doi.org/10.1016/j.cemconcomp.2009.02.007>
53. Tibhe SB, Rathi VR (2016) Comparative experimental study on torsional behavior of RC beam using CFRP and GFRP fabric wrapping. *Procedia Technol* 24:140–147. <https://doi.org/10.1016/j.protcy.2016.05.020>
54. Ameli M, Ronagh HR (2007) Analytical method for evaluating ultimate torque of FRP strengthened reinforced concrete beams. *J Compos Constr* 11(4):384–390. [https://doi.org/10.1061/\(asce\)1090-0268\(2007\)11:4\(384\)](https://doi.org/10.1061/(asce)1090-0268(2007)11:4(384))
55. Bernardo LFA, Andrade JMA (2020) A unified softened truss model for RC and PC beams under torsion. *J Build Eng* 32(April):101467. <https://doi.org/10.1016/j.jobe.2020.101467>
56. Shen K, Wan S, Mo YL, Jiang Z (2018) Theoretical analysis on full torsional behavior of RC beams strengthened with FRP materials. *Compos Struct* 183(1):347–357. <https://doi.org/10.1016/j.compstruct.2017.03.084>

Study on Static Analysis and Design of Reinforced Concrete Exterior Beam-Column Joint



Yogesh Narayan Sonawane and Shailendrakumar Damodar Dubey

Abstract In reinforced cement concrete, the beam-column joint is always considered as critical structural elements. Therefore, the analysis, design and construction of beam-column joint are indeed a very important task. Due to the geometrical conditions and the basic complexity of the load transfer mechanism, the design code on seismic behavior of moment-resisting frame received many conflicting reviews on the beam-column joint design to date. In fact, the overall structural performance of the entire building components in an earthquake majorly depends on the load-bearing capacity of the beam-column joint. During such an earthquake action, the beam-column becomes more vulnerable and unable to achieve its desired efficiency. The earthquake so far has shown that there are two major failures that occur at the beam-column joint such as (i) Joint shear failure (ii) End anchorage failure due to inadequate reinforcement detailing. This paper focuses on the experimental study of exterior beam-column joint casted as per IS 456:2000 and tested on loading frame.

Keywords Beam-column joint · Anchorage mechanism · Joint shear failure · End anchorage failure

1 Introduction

1.1 Beam-Column Joint

In reinforced cement concrete frame structure, beam-column joint is a really complicated and insecure area, where the beam and column elements come together in all three directions [1], such a joint always confirms the continuation of the entire

Y. N. Sonawane (✉)
KBCNMU, Jalgaon, Maharashtra, India
e-mail: yogeshsonawane789@gmail.com

S. D. Dubey
Department of Civil Engineering, SSVPS, Dhule, Maharashtra, India

structure and helps to transfer various forces that are induced at the end of all structural members. Therefore, considering the safety of the building, in places where there is an earthquake-affected area, the buildings are to be designed in such a way that to minimize their damage after the earthquake. The structural behavior of reinforced cement concrete moment-resisting frame structure seen in the latest earthquake around the world has emphasized the performance of the beam-column joints [2]. Therefore, over the few last decades, the researches on the reinforced concrete beam-column joints have been focused on its seismic behavior, because such joints are a major source of energy dissipation. In order to maintain proper connection of all the members after the earthquake, it is necessary to create the proper design of the beam-column joint. If not designed properly, then due to load reversal can lead to a drastic reduction in both strength and stiffness. Still in India, the design guidelines for structural steel and reinforced concrete construction practices used in earthquake-resistant construction have not been effectively revised. Studies so far have shown that the deficiency of these beam-column joints is mainly due to insufficient transverse reinforcement and anchorage capacity in the beam-column joints. Due to the lack of reinforcement details, the constituent material is partly strong, resulting in inadequate structural performance with beam-column joint ability to carry limited strength even in moderate earthquakes.

1.2 Classification of Reinforced Concrete Beam-Column Joint

In reinforced cement concrete moment-resisting frame structure majorly three types of the beam-column joint can be recognized are as follows as shown in Figs. 1 and 2.

- (a) Exterior beam-column joint
- (b) Interior beam-column joint
- (c) Corner beam-column joint.

According to ACI 352 R-02, classifications of the beam-column joint based on various loading conditions are Type-1 and Type-2.

Type-1 beam-column joint is made of a member designed to satisfy ACI 318-02 strength requirement for a member without significant inelastic deformation, i.e., without considering special ductility requirement. Type-1 is to design for resist gravity load and normal wind load.

Type-2 connection, frame members are designed to maintain a constant strength under structural deformation reversal into the inelastic range. This joint is specially designed to resist lateral load due to earthquake, blast, and cyclonic windfall [4].

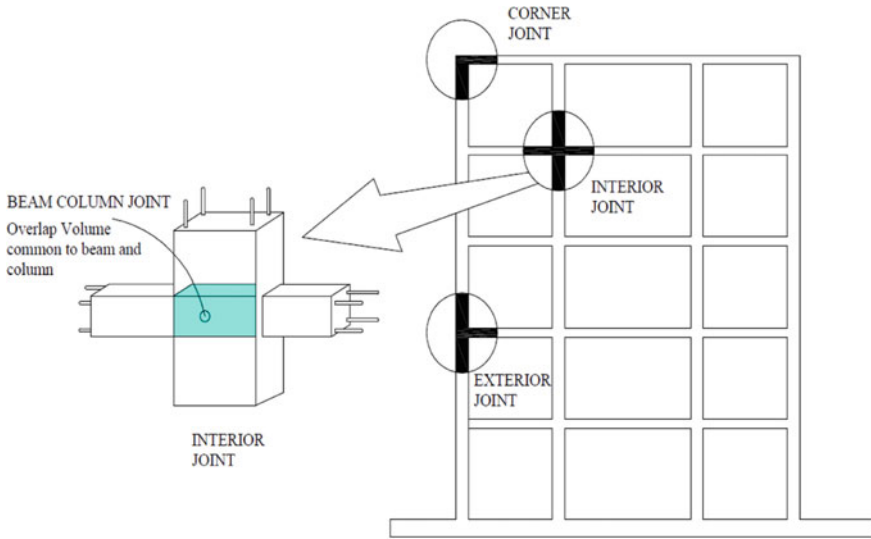


Fig. 1 Beam-column joints are critical part of reinforced framed structure

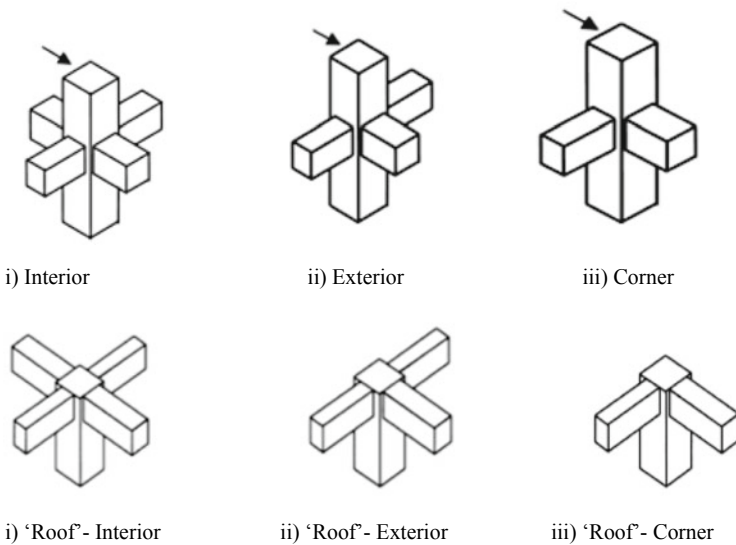


Fig. 2 Classification of Joints in moment-resisting frame structure. Source ACI-352R-02 [3]

2 Review of Codes

In India, the Indian Standards Code does not include the necessary recommendations for a reinforced concrete beam-column joint. If such joint does not design properly,

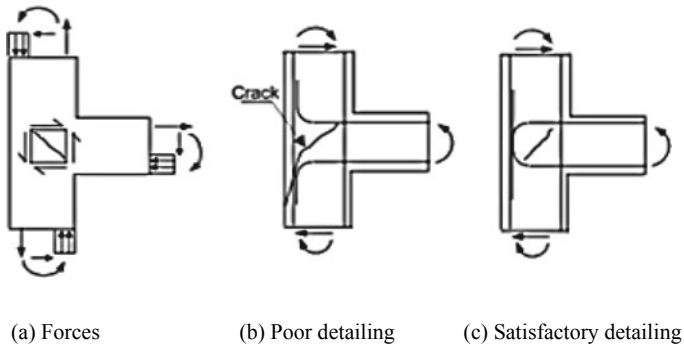


Fig. 3 Reinforcement details at exterior joint [8]

earthquakes will cause a lot of damage to entire structures and human lives. We have many standard codes along with Indian code of practice (i.e., IS 456:2000 and IS 13920:2016, ACI 352-2002, ACI 318.2011, NZS 3101:2006, EN 1998:2003, etc., association with the beam-column joints [5, 6, 7]

2.1 Forces Acting on the Exterior Beam-Column Joint

The shear and flexural stresses have produced simultaneously in the reinforced concrete beam-column core region. To resist large amount of lateral loads without occurring severe damages, the strength and energy dissipation capacity are needed. It is highly uneconomical to design a reinforced concrete framed structure for most potential seismic ground motion without any damage (Fig. 3).

Symbol refers to stress resultant are

C_c = Compression in the concrete

C_s = Compression in the reinforcement

T = Tension force in reinforcement

V = Sum of shear stress.

3 Experimental Investigation

3.1 Design and Detailing of Exterior Beam-Column Joint Specimen as Per IS—456:2000 for M20 Concrete

The test specimen of exterior beam-column joint has column cross section 225 mm \times 150 mm and height 800 mm connected with cantilever beam portion having the

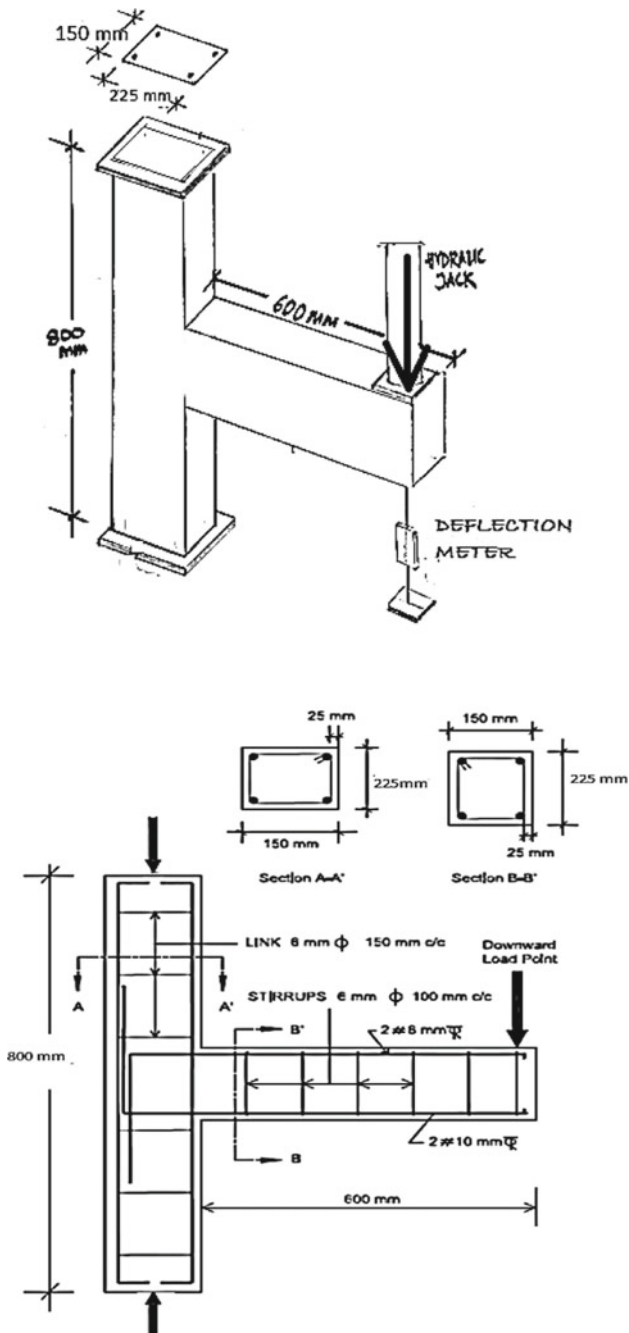


Fig. 4 Specimen details for test

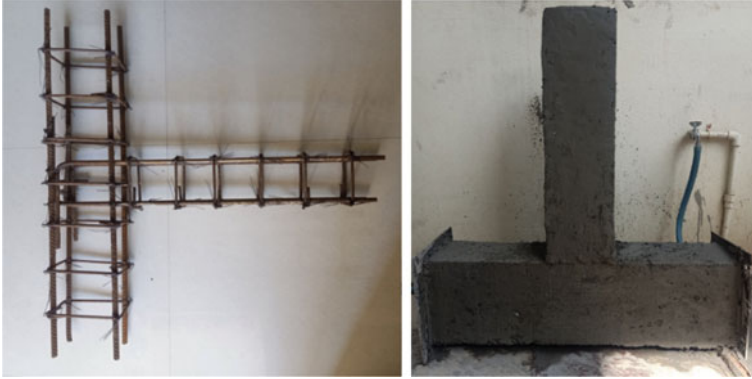


Fig. 5 Casting of specimen



Fig. 6 Experimental setup for test

same cross section with length of 600 mm. For the present study grade of concrete is M20 and Fe 415 grade steel reinforcement is used (Figs. 4, 5, 6 and 7).

3.2 *Result Discussion*

See Table 1 and Fig. 8.

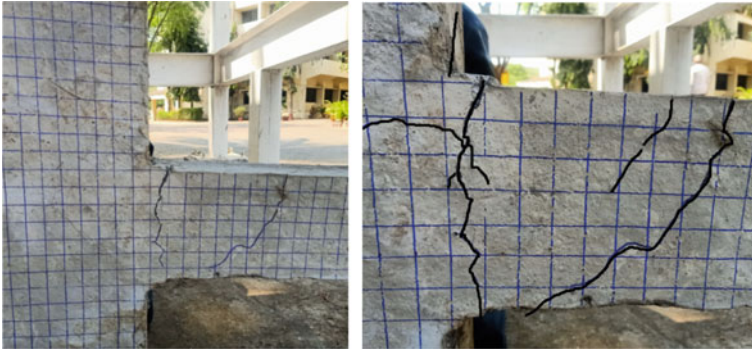


Fig. 7 Crack pattern

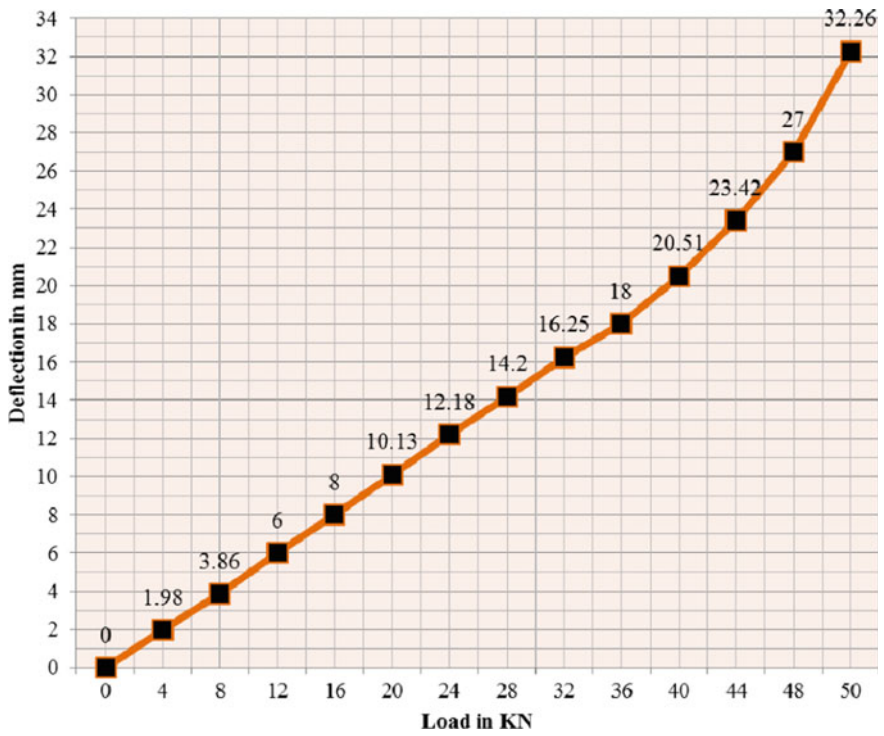


Fig. 8 Load versus deflection graph

Table 1 Reinforcement-beam and column [9]

Reinforcement	Numbers	Area (A_{st})	Clause no. (IS456:2000)
Tension reinforcement in beam	2 bars of 10 mm Φ	$A_{st} = 157 \text{ mm}^2 > A_{st \text{ min}} = 0.85 \text{ bd}/f_y = 69 \text{ mm}^2$	Cl. 26.5.1.1 (a)
Shear reinforcement in beam	2-legged 6 mm Φ	$A_s = 56.52 \text{ mm}^2$	Cl. 26.5.1.6
Spacing of shear reinforcement	6 mm Φ stirrups	100 mm c/c	Cl. 26.5.1.5
Anchorage length (L_d)	for the tension rod 10 mm	470 mm	Cl. 26.2.1
Reinforcement in column (longitudinal)	5 bars of 12 mm Φ	$A_{sc} = 452 \text{ mm}^2 > 0.8 \text{ bd} = 270 \text{ mm}^2$	Cl. 26.5.3.1 (a)
Lateral ties in column	6 mm Φ	150 mm c/c	Cl. 26.5.3.2 (c)

Table 2 Load versus deflection readings

Load in KN		Deflection in mm	Load in KN	Deflection in mm
0	0		28	14.20
4	1.98		32	16.25
8	3.86		36	18.00
12	6.00		40	20.51
16	8.00		44	23.42
20	10.13		48	27.00
24	12.18		50	32.26

4 Summary and Conclusion

The beam-column joint plays an important role in various loading conditions as the stability of the whole structure. In the present study, its deflection is calculated by creating a beam-column joint pattern using the IS code 456: 2000 guidelines.

An experimental test was performed to study the crack pattern subject to static loading. After setting up the experimental setup, we read the deflection at every 4 KN intervals. This study showed that the model failed a maximum load of 50 KN with a deflection of 32.26 mm. More study is required to obtain proper results.

References

1. Kaliluthin AK, Kothandaraman S, Suhail Ahamed TS (2014) A review on behavior of reinforced concrete beam-column joint. *Int J Innov Res Sci Eng Technol* 3(4):11299–11312
2. Rajaram P, Murugesan A (2010) Experimental study on behaviour of interior RC beam column joints subjected to cyclic loading. *Int J Appl Eng Res Didigul* 1(1):49–59
3. ACI-ASCE Committee 352R-02, Recommendations for design of beam-column connections in monolithic reinforced concrete structure
4. American Concrete Institute (ACI) (1985) Building code requirements for structural concrete and commentary. ACI 318-95, Farmington Hills, Mich
5. IS 13290:2016 (2016) Ductile design and detailing of reinforced concrete structures subjected to seismic forces-code of practice (First Revision), BIS
6. IS 13290:1993, Ductile design and detailing of reinforced concrete structures subjected to seismic forces-code of practice
7. IS 1893 (Part 1):2016 (2016) Criteria for earthquake resistant design of structures (Sixth Revision), BIS
8. Uma SR, Prasad AM, Seismic behavior of beam column joints in reinforced concrete moment resisting frames. Final report—a earthquake codes
9. Indian standard code of Plain and Reinforced Concrete—Code of Practice IS 456 (2000) Bureau of Indian Standards, New Delhi
10. Bindhu KR, Jaya KP (2010) Strength and behaviour of exterior beam column joints with diagonal cross bracing bars. *Asian J Civ Eng (Build Hous)* 11(3):397–410
11. Padmanabham K, Rambabu K (2019) Design improvements of non-seismically detailed R/C beam-column joints during seismic transformation. *Int J Tech Innov Mod Eng Sci* 5(3):701–709
12. Dhake PD, Patil HS, Patil YD (2015) Role of hoops on seismic performance of reinforced concrete joints. In: *Proceedings of the Instituion of Civil Engineers-Structures and Buildings*, vol 168, no 10, pp 708–717 (Magazine of Concrete Research)
13. Jain SK, Murty CVR (2005) Proposed draft provisions and commentary on ductile detailing of RC structures subjected to seismic forces, Final report—a earthquake codes

Refined Methodology in Design of Reinforced Concrete Shore Pile: A Design Aid



Mahesh Navnath Patil and Shailendra Kumar Damodar Dubey

Abstract Shore piles with rock anchors are considered as distinct types of retaining walls. The idea behind the erection of shore piles is to protect structures surrounding the construction site from collapse due to the formation of a slip circle. A very limited guidelines and solutions are available in the existing literature for the design of shore piles. The earth pressure distribution differs along the depth of excavation from ground level depending upon the density of soil and occurrence of the water table below the ground surface. This paper represents a finite element analysis of shore piles with *Staad Pro. V8i*. Experimental investigation of earth pressure and surcharge load on shore piles from opposite sides of excavation with two platforms in the case of breaking loads with case study are discussed. A parametric study was conducted to enable a discussion of the effects of the distribution of active lateral earth pressure and surcharge and fixity generated due to rock anchors on maximum flexural moment generated on shore pile, which is analyzed as a rectangular beam. Updated practice is suggested to enrich the manual calculation with software aid in the bending moment of the wall.

Keywords Shore piles · Rock anchors · Finite element analysis · *Staad pro. V8i* · Earth pressure

1 Introduction

The deep excavation in the middle of the civic requires an alternate arrangement to handle the lateral pressure of surrounding structures. The lateral pressure is normally distributed in the form of a pressure bulb underneath soil [1]. An artificial structure such as a retaining wall is constructed to bear the lateral load of backfill and surcharge.

M. N. Patil (✉)

Research Scholar, Kavyitri Bahinabai Chaudhari North Maharashtra University, Jalgaon, India
e-mail: m.patil123@gmail.com

S. K. D. Dubey

Professor and Head of the Civil Engineering Department SSVPS BSD COE, Dhule, India
e-mail: dubey.dhule@gmail.com

© The Author(s), under exclusive license to Springer Nature Singapore Pte Ltd. 2023
M. S. Ranadive et al. (eds.), *Recent Trends in Construction Technology and Management*, Lecture Notes in Civil Engineering 260,
https://doi.org/10.1007/978-981-19-2145-2_67

897

In the case of large plan dimensions and deep excavations, a retaining wall is not a wise choice and we have to adopt heavy structures such as shore piles [2]. Shore piles are the segment of interlocked piles designed to carry lateral and/or hydrostatic pressure arising due to the formation of slip circles, formed due to differences in elevations because of excavation, dredging, backfilling, or a combination of these [3]. A sealed shore pile provides a safe and economical solution in the places with the intrusion of groundwater to inhibit the seepage into the construction site and minimize the risk of settlement. The shore piles provide the anchorage with surrounding soil through rock anchors.

When excavation exceeds 6–10 m below ground level, a fencing of interlocking shore piles is needed to resist heavy lateral loads [2]. It includes active earth pressures, passive earth pressures, surcharge loads, and hydrostatic pressure [4]. In such conditions, reinforced shore piles are the best suited as the boundary of excavation. Moreover, the cross-sectional properties and spacing of shore piles depend on present site conditions such as geotechnical properties of soil, depth of water table below ground level, and magnitude of surcharged lateral pressure [2]. Specification of shore piles should include general instruction issued by the project manager, architect, structural engineer, and owners, setting out of shore pile position on site, boring and piling, protection of boreholes against collapse, specification on concrete and reinforcement to be used, and specification of the casing for shore piles. Onsite shore piling and its design should be done in compliance with IS code guidelines.

This paper presents a methodology to design shore piles. The theoretical analysis is a complex process; thus, for precise and speedy analysis, the case study is considered and modeled in STAAD. Pro V8i. The shore pile is analyzed for two different conditions. The first condition is non-yielding support at the top (in place of rock anchor) with spring supports at the base end and the second condition is yielding support at the top (in place of rock anchor) with fixed support at the bottom (midpoint of the support socket length). The analysis includes the lateral loading conditions from the opposite side of the excavation. This study provides guidelines for the design of shore piles as the direct procedure is not available anywhere.

2 Specifications for Shore Piles

Onsite construction of shore piles should be done in compliance with the following guidelines.

2.1 General

The drawings shall be read in conjunction with relevant architectural drawings, soil investigation reports, survey drawings, services drawings, tender conditions, specifications and item descriptions in the bill of quantities, and instructions issued by the

project manager, architect, structural engineer, and owners. Any discrepancy among any of the above shall be immediately brought to the notice of the project manager before proceeding to execute the work. No claim shall be entertained if the work is carried out without obtaining a guideline decision in case of discrepancy. Piling design and detailing have been carried out based on the information given in the soil investigation report. In case the contractor discovers site conditions differing from those mentioned in the soil report, they shall be instantly brought to the notice of the structural engineer through the project manager before proceeding to execute the work. Failure to obtain clarification/approval to proceed for execution in such cases shall impose the responsibility of any consequences arising out of taking unilateral decision solely on the contractor.

2.2 Setting Out

The contractor shall follow the architectural centerline drawings to set out the column centers from the given baseline. The contractor shall obtain written approval for the setting out of column centers from the project manager as per the architectural drawings. Before commencing with boring for any pile, removable casings shall be driven up to ground level and their center lines checked jointly by the contractors and Project Manager.

2.3 Boring and Piling

The construction of the shore pile should be carried out as per guideline of IS: 2911 similar to the pile foundation. The casting of shore piles must be cast in situ. The sequence of construction of shore piles should be such that the previously constructed piles should not be affected by the construction of subsequent ones. The sequence of construction should be decided by contractors and proceed with the work only after obtaining approval.

2.4 Allowances and Tolerances

The shift or eccentricity of piles from their theoretical position shall not be more than 75 mm for piles up to and including 1200 mm. Out of plumb of the piles shall not be more than 2%. All consequences of noncompliance with these requirements shall be to the contractor's account.

2.5 Protection of Bore Whole Sides

The contractor should be responsible to protect the sides of the borehole and prevent them from collapsing. Bentonite slurry should be used to stabilize the walls of the boreholes by circulating bentonite slurry if required. Bentonite shall be solution based and conform to relevant IS codes. Bentonite shall be used after mixing with water, and a thick slurry shall be generated with a specific gravity of 1.08–1.10 and a pH value of 6–9. Boring shall be carried out as per the recommendations of the geotechnical investigation report and as per the results obtained during the first pile test results. The depth of the boring shall depend upon desired capacity. The contractor shall be responsible to keep the site clean by carting away mud while boring is in progress. In the case of marine clay, liquid sand, and any other soil in which bentonite clay cannot be used for stabilizing the sides of boreholes, mild steel liners shall be used for the entire length of the borehole. M.S. liner shall be sufficiently strong such that it withstands the soil and water pressure for the full length of the bore even when concrete is not poured. The liner shall not form any gaps and shall be placed properly to withstand all forces while installation, concreting, and retrieval operations.

2.6 Reinforcement

All reinforcement used in the shore piles shall be high yield strength deformed bars with a yield strength of 500 N/mm² conforming to IS 1786. All steel shall be tested as per standard norms for physical and chemical tests. Reinforcement should be as per the drawing issued by the structural engineer. The binding wire shall be galvanized. Reinforcement shall be protected against corrosion if exposed to the atmosphere by any standard method approved by the project manager. Clear cover to main reinforcement shall be 50 mm made up of PVC/Plastic material. Provisions of IS 1786:2008 [5], IS 228:1992 [6], IS 1387:1993 [7], and IS 1599:1985 [8] should be followed.

2.7 Concrete

Concrete shall conform to the specifications as per IS 456:2000 [9]. Admixtures such as superplasticizer shall be used for workability requirements. Concrete shall be deposited in the pile using a tremie pipe.

2.8 *Dewatering*

Dewatering shall be carried out continuously or as directed by the project manager in order to keep the borehole completely dry to retain the consistency and composition of concrete poured in the bores.

2.9 *Casing*

Temporary steel casing of adequate thickness shall be used if necessary to avoid the sides from collapsing and to maintain the alignment and position of the pile. Use of permanent liners may be permitted if the soil condition demands their use. All such liners shall be prescribed by the contractor in advance and permission obtained from the project manager before installing them.

2.10 *Material*

2.10.1 *Cement*

53 grade ordinary Portland cement is recommended. Some basic parameters such as strength, setting, and time should be tested after receiving a batch of cement. Onsite field test should be performed on cement if it is stored over for a longer period as per instructions of the project manager.

2.10.2 *Coarse Aggregate*

Coarse aggregate shall be obtained from authorized and approved quarries. Aggregate shall be clean, free from vulnerable impurities which affect the strength as well as durability characteristics of the concrete and reinforcement. The coarse aggregates shall be uniformly graded with the size of all the particles should be greater than 4.75 mm. The limits of the impurities shall be within the permissible limit given by IS 2386:1963 [10] and IS 383:2016. The soundness of aggregate, impact value, abrasion value, and crushing value shall be as per norms and limits laid down by IS 383:2016. The source of supply of coarse aggregates is never allowed to change without permission and approval of the competent authority [11].

2.10.3 Fine Aggregate

Grading of fine aggregates used shall be restricted to the size of particles less than 4.75 mm and should lie within zone 1st and 2nd as per IS 383:2016. It should be free from the impurities which affect the durability of concrete. It should not contain impurities which can attack and corrode steel reinforcement. Depending on the situation, crushed sand may be added to natural sand within the permissible limit [12].

2.10.4 Water

Water used while concreting shall be potable water free from impurities such as alkalis and salts which adversely affect the useful life of the concrete and may cause deterioration of reinforcement within the concrete. Water should not affect the hydration reaction of cement and consequently hardening properties of concrete. The level of harmful impurities within water should be limited to the restriction prescribed by IS 456:2000 [9]. Testing of water should be done in accordance with IS 3025 [13]. The average compressive strength of a 15 cm mortar cube should vary more than 10% as compared with a mortar cube prepared using distilled water in accordance with IS 516:1959. The pH value of water shall be within the range of 6–9.

2.10.5 Admixture

Admixture conforming to IS 9103:1999 [14] (Clause no. 5.5 of IS 456) shall be permitted to be used without affecting the strength and durability characteristics of concrete. Admixtures shall be free from impurities (e.g. chlorides, sulphates, etc.) which deteriorate concrete. Reinforcement should not be affected by admixtures used within concrete. The admixtures may be accelerators or retarders depending upon situations. If more than one admixtures are suggested at a time, then their compatibility must be assured.

2.10.6 Cover Block

Cover blocks shall be made up of non-corrosive material such as mortar, plastic, and stones. The strength of the cover block shall be nearly equal to the strength of concrete used for shore piles. If cover blocks are made up of concrete or mortar, they should be fully cured before concreting.

2.10.7 Binding Wire

Galvanized iron wires of 18 gauge shall be used as winding wire. It shall not be corroded. It shall not contain a composition that may obstruct the bonding of reinforcement with concrete.

2.10.8 Ready Mix Concrete (R.M.C.)

In the construction of shore piles, concrete from ready mix concrete plants is preferred as mass concreting is required to be done and quality should be assured. Proportions and quality of ingredients of concrete should be as per IS 10262:2019 [15].

The continuous flow of concrete shall be required to be maintained as mass concreting is required at the time of shore piling. A stationary or mobile concrete pump shall be deployed for maintaining the continuous flow of concrete. All the accessories of the pump such as bends and chutes shall be organized in such a manner that concreting shall not be interrupted.

2.11 Bentonite

Boring is to be done before concreting of shore piles. The sides of the boreholes are required to be protected from collapse. Bentonite slurry plays a vital role in stabilizing the walls of the boreholes. Water-based slurry of bentonite clay shall be used for stabilizing walls of boreholes.

2.12 Delivery and Storage of Reinforcement

Care should be taken while loading and unloading steel on site, and it should not bend. Rebar shall be covered with a coating of some suitable material such as turpentine to protect it against corrosion. Reinforcement shall be not stored directly on the ground, and it can be isolated from the ground with the use of a timber rack or by plain cement concrete surface. The minimum yield strength of reinforcement shall not be less than 500 N/mm². Rebar of ISI mark shall be preferred.

2.13 Design of Shore Piles

This section consists of the design of shore piles for the basement of the construction site. The design comprises 750 mm diameter shore piles at 800 mm c/c spacing. A 20 KN/m² of the live load has been assumed to represent the vehicular load

(construction activity). Water pressure is not considered, as there is a 50 mm gap between the shore piles, which will allow the water to seep through it. The angle of internal friction within soil particles is 300 [16].

3 Calculation for Earth Pressures

Based on the thickness of different layers of soil, the calculation of lateral earth pressure is shown below [17].

3.1 Layer-I Sand or Backfill Material, Ground Level to 1.5 m, I.E. 0–1.5 m

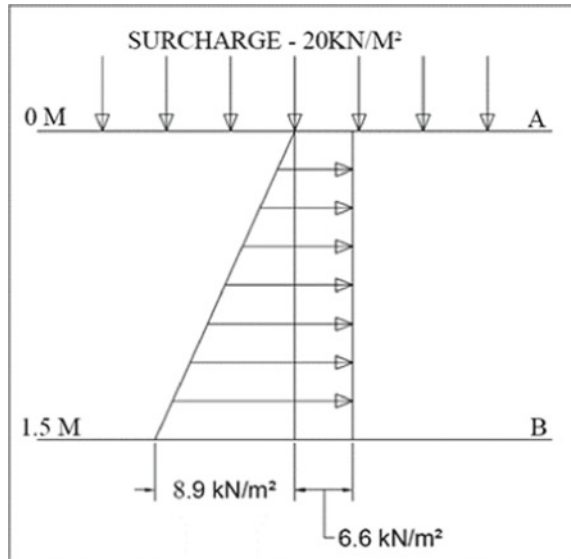
With reference to Fig. 1

$$\text{Coefficient of active pressure}(K_a) = (1 - \sin\theta)/(1 + \sin\theta)$$

where θ = Angle of internal friction = 30⁰

$$\text{Dry unit weight of soil}(\gamma_d) = 18 \text{ kN/m}^2$$

Fig. 1 Soil pressure in zone-I (0–1.5 m)



$$\text{Surcharge}(q) = 20 \text{ kN/m}^2$$

$$\text{Pressure at top(A)} = K_a \times q = 0.33 \times 20 = 6.6 \text{ kN/m}^2$$

$$\begin{aligned} \text{Pressure at bottom(B)} &= (K_a \times q) + (K_a \times \gamma \times H) \\ &= (0.33 \times 20) + (0.33 \times 18 \times 1.5) \\ &= 15.50 \text{ kN/m}^2 \end{aligned}$$

3.2 Layer-II Stiff Clay (1.5–5.5 m)

With reference to Fig. 2

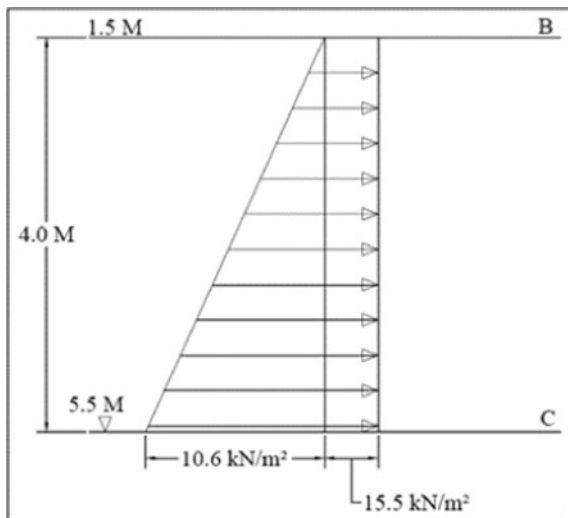
$$\text{Coefficient of active pressure}(K_a) = 0.33$$

$$\text{Dry unit weight of soil}(\gamma_d) = 18 \text{ kN/m}^2$$

$$\text{Surcharge}(q) = 20 \text{ kN/m}^2$$

$$\gamma_{\text{submerged}} = 8 \text{ kN/m}^2$$

Fig. 2 Soil pressure in Zone-I (1.5–5.5 m)



$$\text{Pressure at top} = 15.50 \text{ kN/m}^2$$

$$\begin{aligned} \text{Pressure at bottom(C)} &= (K_a \times \gamma_{\text{sub}} \times H) + 15.50 \\ &= (0.33 \times 8 \times 4) + 15.50 \\ &= 26.10 \text{ kN/m}^2 \end{aligned}$$

As water table depth is at 1.5 m from ground level, water Pressure (hydrostatic pressure) is calculated as follows:

$$\gamma_w = 10 \text{ kN/m}, \text{ Water pressure} = \gamma_w \times H = 10 \times 4 = 40 \text{ kN/m}^2$$

3.3 Layer III-Highly Weathered Volcanic Breccia with Shale (5.5–12.60 m)

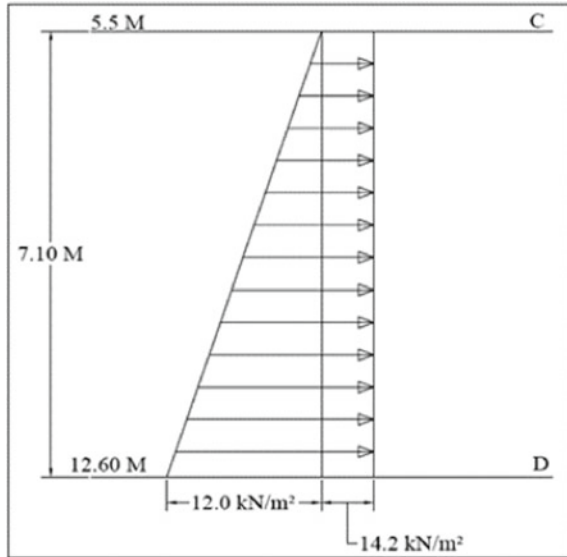
With reference to Figs. 3 and 4

Angle of internal friction is given 45° as per soil testing report

$$\text{Coefficient of active pressure}(K_a) = (1 - \sin\phi)/(1 + \sin\phi),$$

where $\phi = 45^\circ$

Fig. 3 Soil pressure in Zone-I (5.5 m–12.60 m)



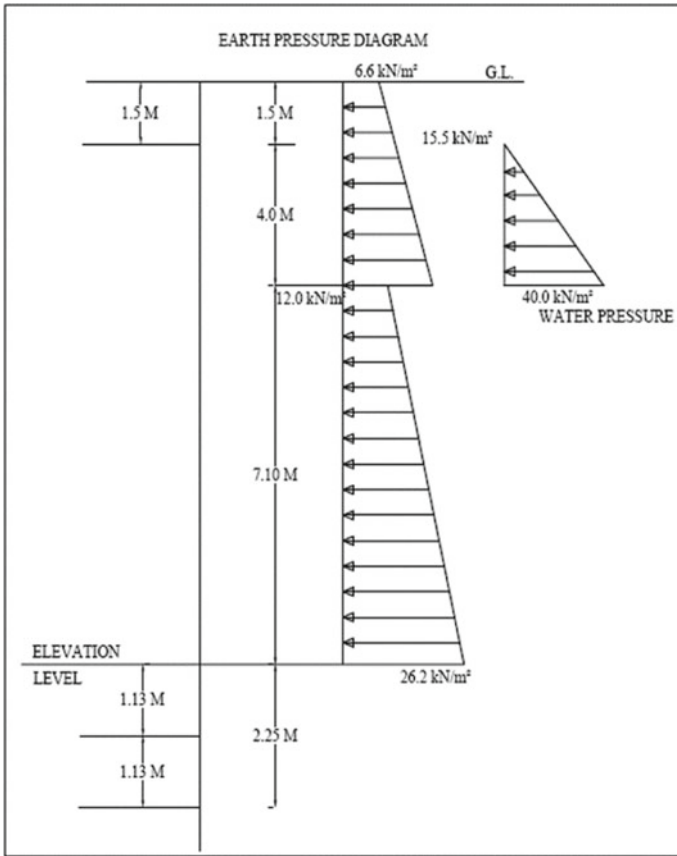


Fig. 4 Soil pressure distribution from ground level to socket length

$$\text{Coefficient of active pressure}(K_a) = 0.1$$

$$\text{Dry unit weight of soil}(\gamma_d) = 20 \text{ kN/m}^2 \text{ (For Rock)}$$

$$\text{Surcharge}(q) = 20 \text{ kN/m}^2$$

$$\begin{aligned} \text{Surcharge}(q) &= 20 + (18 \times 1.5) + (8 \times 4) + (10 \times 4) \\ &= 119 \text{ kN/m}^2 \end{aligned}$$

$$\begin{aligned} \text{Pressure at top}(C) &= K_a \times q \\ &= 0.1 \times 119 = 12 \text{ kN/m}^2 \end{aligned}$$

$$\begin{aligned}
 \text{Pressure at bottom(D)} &= (K_a \times q) + (K_a \times \gamma \times H) \\
 &= (0.1 \times 119) + (0.1 \times 20 \times 7.1) \\
 &= 26.20 \text{ kN/m}^2
 \end{aligned}$$

4 Material Properties

Grade of the concrete = M 25 (Characteristics Strength of Concrete = 25 N/mm²)

Grade of rebar = Fe 500 (Yield strength of 500 N/mm²)

Modulus of elasticity = E = 5000 $\sqrt{f_{ck}}$ = 25,000 N/mm²

5 Condition 1

The shore pile has been designed for two cases depending on the support conditions. In this condition, non-yielding support is at the top (in place of a rock anchor) and spring supports at the base (reference Figures 5, 6 and 7). Staad Pro. V8i software for structural analysis and design is used. A 2D frame representing a single pile (750 mm dia.) is modeled in STAAD.

5.1 Calculation of Spring Constant for Pile in Socketing Zone

Subgrade Modulus (as per soil testing report) = 37,500 KN/m³

Three spring supports (joints) are assigned in the region of socket length

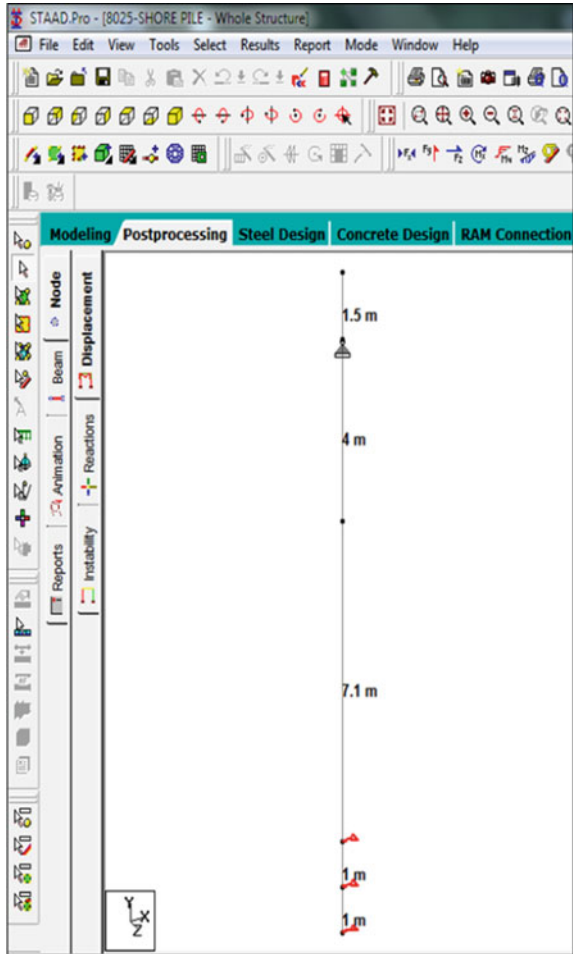
Spring constant for central spring support (joint)

$$\begin{aligned}
 &= \text{exposed area of shore pile} \times \text{subgrade modulus} \\
 &= \text{socket length} \times \text{diameter of pile} \times \text{subgrade modulus} \\
 &= 1.125 \times \text{Pile Diameter} \times 37,500 \\
 &= 1.125 \times 0.75 \times 37,500 = 31640.625 \text{ kN/m}
 \end{aligned}$$

Assigned to end support in the region of socket length in STAAD. Pro Modeled as spring constant

Spring constant for external joint

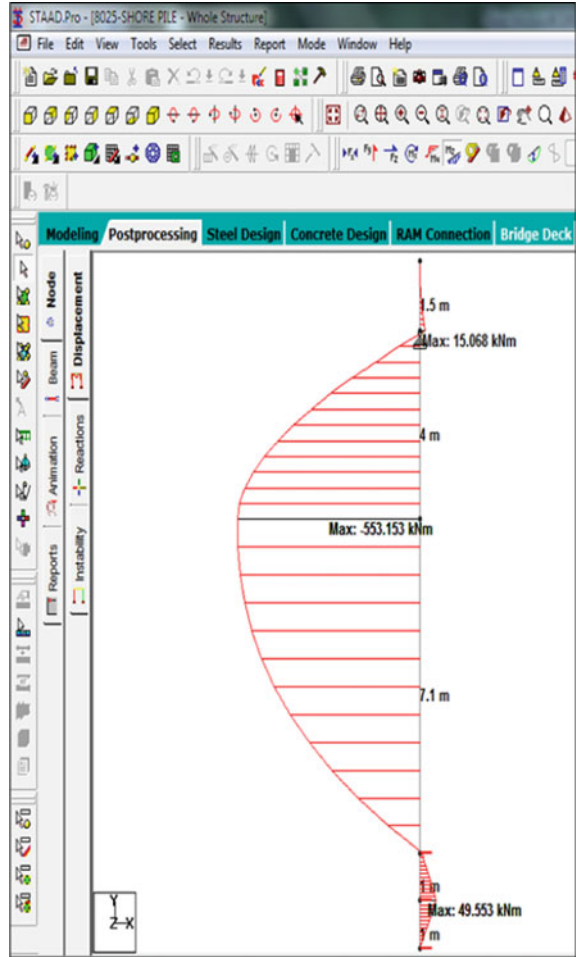
Fig. 5 Condition 1-Staad.
Pro. model



$$\begin{aligned}
 &= \text{exposed area of shore pile} \times \text{subgrade modulus} \\
 &= \text{socket length} \times \text{diameter of pile} \times \text{subgrade modulus} \\
 &= 1.125/2 \times \text{Pile Diameter} \times 37500 \\
 &= (1.125/2) \times 0.75 \times 37,500 = 15820.31 \text{ kN/m}
 \end{aligned}$$

Assigned to central support in the region of socket length in Staad Model as spring constant

Fig. 6 Condition 1 free BMD, after application of load



5.2 Design Calculations

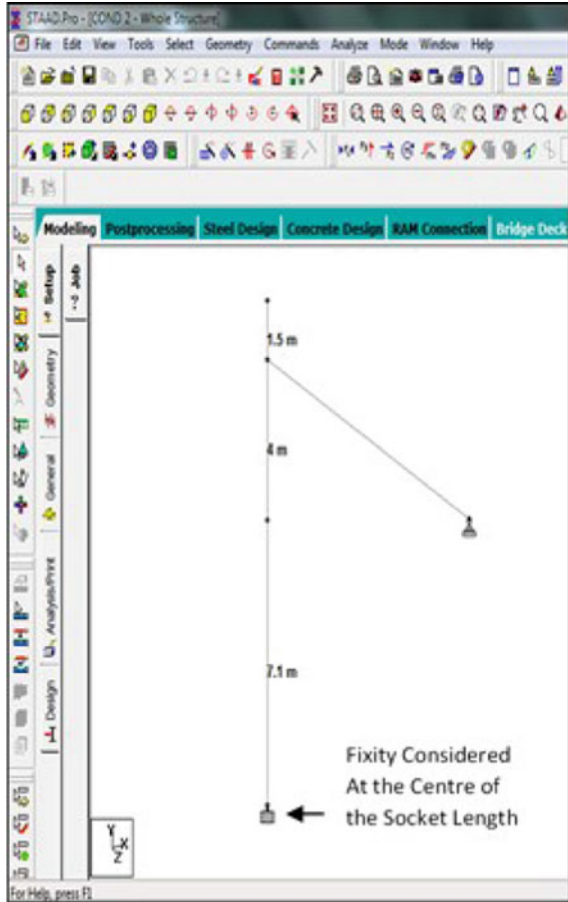
Detail calculations for reinforcement of shore piles on both the faces of piles, i.e. face exposed to excavation and its opposite face are elaborated in the following sections.

5.2.1 Design for Flexure

As in the STAAD model, loads are calculated for 1 m strip, thus to convert to the actual load on the pile multiplying by 0.8 m

$$\text{Maximum B. M. (Positive)} = 0.8 \times 554 = 444 \text{ kN-m}$$

Fig. 7 Condition 2 Staad.
Pro. model



$$\text{Area of 750 diameter pile} = \pi/4 \times 750^2 = 441786 \text{ mm}^2$$

For design purpose, a rectangular beam with width 500 mm and depth 600 mm is considered in place of the 750 Ø piles

$$\frac{M_u}{b.d^2} = \frac{444 \times 10^6}{500 \times 600^2} = 2.47$$

From SP 16 [18], Table no.3, Page No. 49, the Percentage steel P_t can be calculated as $P_t = 0.65$

$$P_t = \frac{100.A_{st}}{b.d}$$

$$A_{st} = 1950 \text{ mm}^2 \text{ or } A_{st_{req}} = \frac{0.85}{100} \times 600 \times 500 = 2250 \text{ mm}^2 \text{ whichever is greater}$$

Let us provide 8 numbers of bars of 20 mm dia. Tor steel is on the excavated side of the pile.

5.2.2 Design and Check for Shear

$$V_{u \max} = 0.8 \times 233 = 187 \text{ kN}$$

$$\tau_v = \frac{V_u}{b.d}$$

$$\tau_v = \frac{187 \times 10^3}{500 \times 600} = 0.623 \text{ N/mm}^2$$

$$\tau_{\text{permissible}} = 0.5 \text{ N/mm}^2$$

Shear reinforcement is required to be provided for surplus stress of 0.123 N/mm². Shear reinforcement provided should be T-8 @ 200 mm c/c in the form of circular stirrups.

5.2.3 Provision of Pre-stressed Rock Anchor

Maximum reaction at top = 256 kN (horizontal)

Adopt spacing = 4 m c/c

Total horizontal force = 256 × 4 = 1024 kN

Force in 45° inclined rock anchor

COS 45° = 1024/r,

r = 1024/COS 45°

r = 1448 kN

≈ 145 T

According to calculations, one can provide 150 T rock anchor at (45°) with 4 m c/c.

6 Condition II

As discussed in the previous section, the whole analysis is divided into two conditions. Let us discuss the conditions in detail. Yielding support at the top (in place of rock anchor) and fixed support at the bottom (midpoint of the support socket length). In this case, instead of considering a rigid pinned support at the top, we have modeled a tie rod (which represents the rock anchor) with the fixity at the anchor length [19].

With reference to Figs. 8, 10, 11 and 12

Maximum Negative BM = $0.8 \times 866 \text{ kN-m} = 693 \text{ kN-m}$

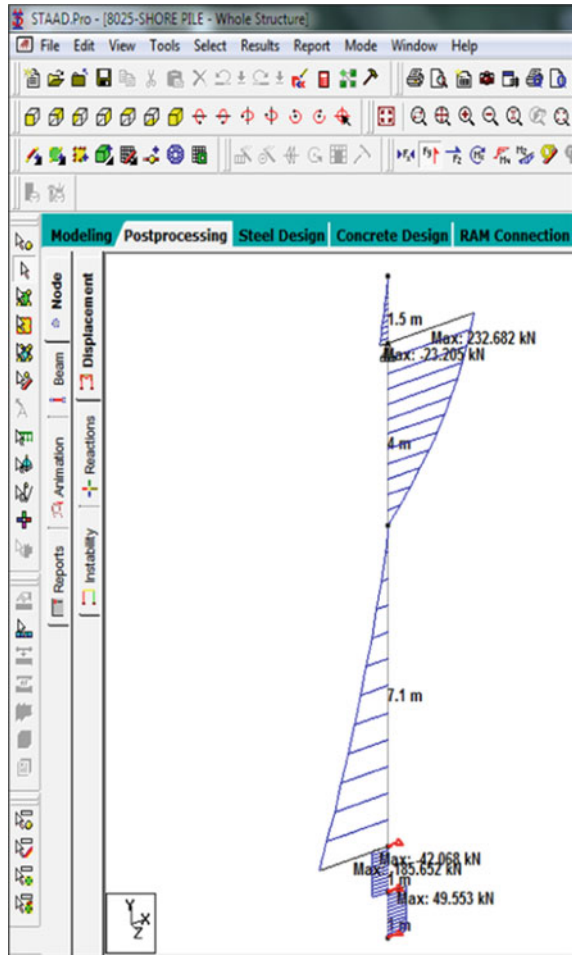
$$\frac{Mu}{b.d^2} = \frac{693 \times 10^6}{500 \times 600^2} = 3.85$$

$$A_{st_{req}} = \frac{1.43}{100} \times 500 \times 600 = 4290 \text{ mm}^2$$

Let us provide T 25 – 8 Bars + T16 – 2 Bars

Let us provide 8 numbers of bars of 25 mm dia. bars and 2 numbers of bars of 16 mm dia. bars for steel on opposite sides of excavation side in shore piles.

Fig. 8 Condition 1 SFD after application of load



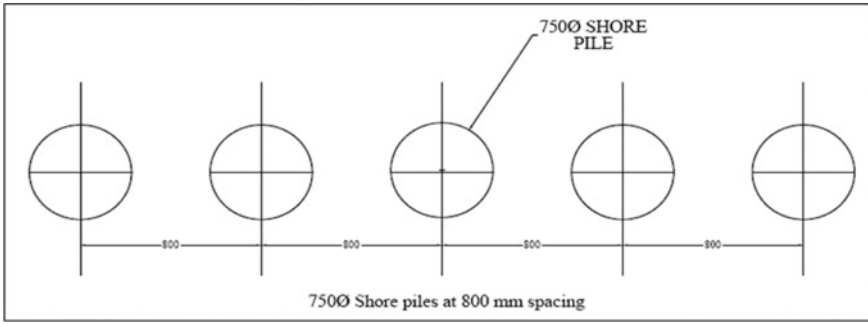


Fig. 9 750 mm diameter shore piles at 800 mm c/c (site condition)

Fig. 10 Condition 2 free BMD after application of load

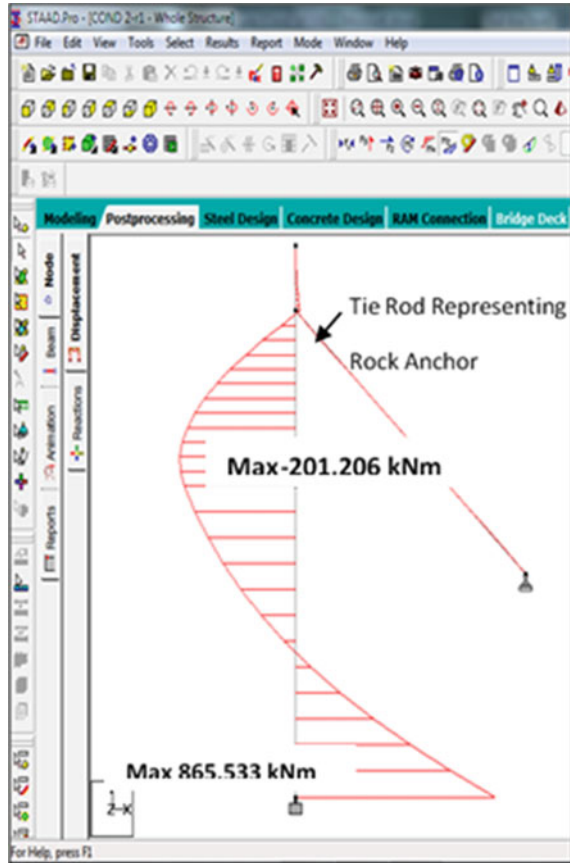


Fig. 11 Condition 2 SFD after application of load

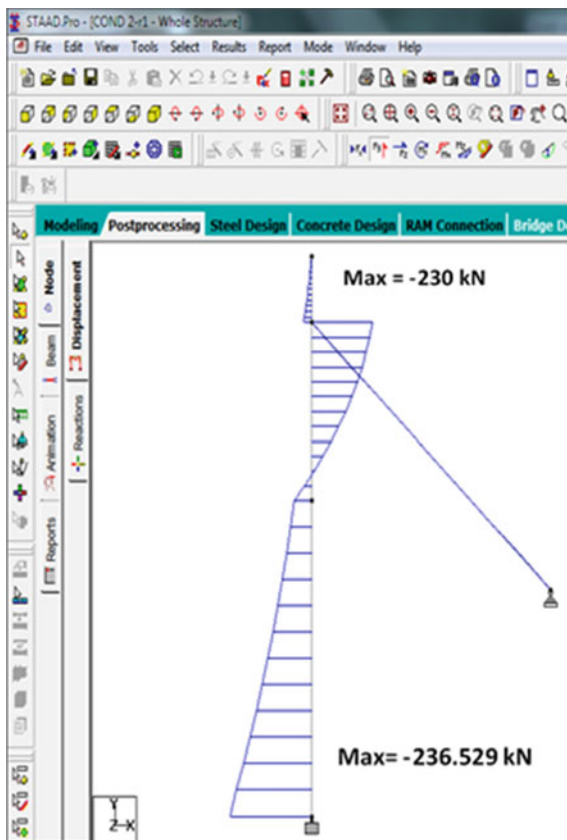
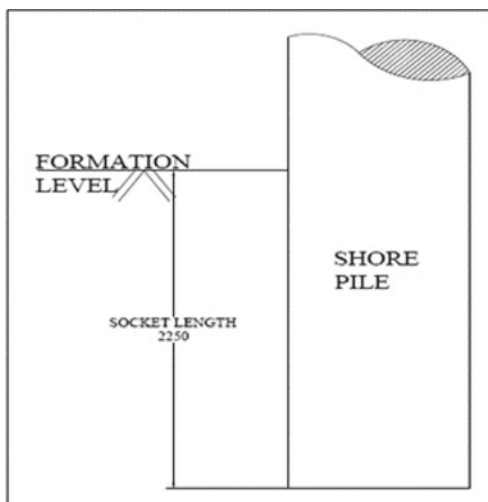


Fig. 12 Representation of socket length



7 Conclusion

The objective of shore piles is to resist lateral pressure in addition to support the vertical load. Methodology for design of shore pile is not elaborated anywhere. This research paper aims for the same. Concluding remarks are as follows.

1. Deformation, cracking, or failure of structure occurs if large excavation is carried out besides high-rise buildings or other important structures such as highways due to slip circle formation.
2. Shore pile is the solitary key to resist lateral pressure due to soil adjacent to the excavation exceeding the depth of 6 m.
3. Analysis of shore piles is tedious, and it can be effectively and accurately done with a finite element-based software like STAAD. Pro V8i.
4. The spacing of shore piles should be planned based on design calculations.
5. The position and capacity of rock anchors depend on the designed lateral load.
6. Shore piles are designed as flexural members.

References

1. Ranjan G, Rao ASR (2005) Basic and applied soil mechanics. New age international publishers, ISBN 81-224-1223-8
2. Basit MA., Shouki, SA, Rahman SMR, Rahman MA, Hanafi BM (2016) Analysis of shore pile for deep excavations. In: Proceedings of 3rd international conference on advances in civil engineering, CUET, Chittagong, Bangladesh, December 2016, pp. 21–23
3. Murthy VNS (2007) Advance foundation engineering. CBS publishers and distributors, ISBN: 9788123915074
4. Choudhury D, Chatterjee S (2006) Dynamic active earth pressure on retaining structures. *Sadhana*, 31(6):721–730
5. IS 1786:2008, Indian Standard high strength deformed steel bars and wires for concrete reinforcement— specification (fourth revision)
6. IS 228 (Part 15): 1992, Methods for chemical analysis of steels.
7. IS 1387:1993, General requirements for the supply of metallurgical materials
8. IS 1599–1985, Method for bend test
9. IS 456:2000, Plain and reinforced concrete-code of practice.
10. IS 2386 (Part I)-1963, Methods of test for aggregates for concrete
11. IS 383: 2016, Coarse and fine aggregates for concrete-specification
12. IS 516:1959, Methods of test for strength of concrete
13. IS 3025-1:1987: Methods of sampling and test physical and chemical) for water and wastewater Sampling
14. IS 9103:1999 Concrete admixtures—specification
15. IS 10262:2019, Concrete mix proportioning—guidelines (Second Revision)
16. IS 2911 (Part 1/Sec 1): 2010, Design and construction of pile foundations-code of practice
17. Mittal S, Garg KG, Saran S (2006) Analysis and design of retaining wall having reinforced cohesive frictional backfill. *Geotechnical Geological Eng* 24(3):499–522

18. SP 16:1980, Design aids for reinforced concrete to IS 456-1978
19. Koopialipoor M, Murlidhar BR, Hedayat A, Armaghani DJ, Gordan B, Mohamad ET (2020) The use of new intelligent techniques in designing retaining walls. Eng Computers 36(1):283–294

Investigating the Efficacy of the Hybrid Damping System for Two-Dimensional Multistory Building Frame Using Time History Analysis



A. P. Kote and R. R. Joshi

Abstract Nonlinear analysis is the response of nonlinear structure by the base simulation method. The simulation consists of numerical techniques and mathematical modeling. In the dynamic analysis, we need the consideration of elastic as well internal forces along with energy dissipating devices such as damping. The most powerful technique is the time history analysis for the determination of the nonlinear dynamic response of structures; in this paper, nonlinear dynamic analysis of multi-storey steel moment-resisting frame is found out by using different cases such as V.F.D. only, B.R.B. only, and Hybrid damping models (both V.F.D. and B.R.B.). It is found that by using the above-mentioned models, the base shear is reduced when it is compared with a steel moment-resisting frame without any P.E.D. The joint displacement was decreased by 80% and inter-story drift was reduced to 40%.

Keywords Time history analysis · Viscous fluid damper · Buckling restrained braces · Steel moment resisting frame · Hybrid damping · SAP2000

1 Introduction

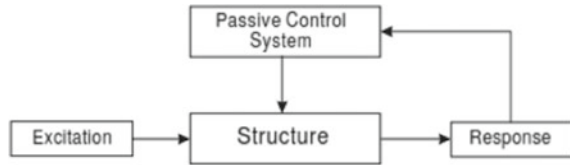
The safety of life is an important criterion for a structural engineer while designing any structure. Gupta and Krawinkler (1999) critically mentioned that to provide consistency and predictability, there is a necessity for seismic analysis and design of the structure. The seismic codes provide very simplified criteria for simple seismic design but the practical design of any structure involves complications. Seismic design of structure requires various parameters to be taken into consideration before actual design consideration. The earthquake has peculiar characteristics such as amplitude, duration, and frequency. The performance-based seismic design (PSBD) is emerging to be efficient to capture the inelastic behavior of materials and to reduce the effects of earthquakes installation of dampers which are energy dissipating devices used in the lateral force-resisting system of the structure. The passive

A. P. Kote (✉) · R. R. Joshi
Department of Civil Engineering, College of Engineering Pune, Pune, India
e-mail: apk21.civil@coep.ac.in

© The Author(s), under exclusive license to Springer Nature Singapore Pte Ltd. 2023
M. S. Ranadive et al. (eds.), *Recent Trends in Construction Technology and Management*, Lecture Notes in Civil Engineering 260,
https://doi.org/10.1007/978-981-19-2145-2_68

919

Fig. 1 Workflow of passive hybrid damping system.
Source Earthquake resistant and design of steel structures



hybrid dampers as shown in Fig. 1 absorb a large amount of energy due to earthquake so it does not undergo inelastic deformation. It also reduces the inter-story drift. The various dampers such as viscous fluid dampers, buckling restrained braces, viscoelastic dampers, and friction dampers are very useful in reducing energy dissipation during an earthquake. Mostly in a highly prone area where the earthquake is a risk factor, the use of a damper is very useful. When there is a heavy earthquake, structure undergoes inelastic deformations; therefore, it depends on ductility and hysteretic energy dissipation to avoid such damage to structures as mentioned by Jinbiao [6].

2 Passive Damping in the Buildings

The purpose of using a passive energy system is to prevent damage to structural components. Damping systems reduce the amplitude of vibration. The passive control system is designed to dissipate a huge portion of earthquake input energy. This depends on the inherent properties of the basic nature. This can also be used for a wide variety of structural components. Buckling restrained braces, viscous fluid dampers (H. K. Miyamoto, A. S. J. Gilani, and A. Wada), and hysteretic dampers (V.F.D. and B.R.B.) are some of P.E.D. types devices. Reference [13] has done a lot of research on buckling restrained braces and has devised B.R.B. for use. The vibratory system has some energy that is dissipated during the motion. The rate of decreasing the amplitude depends upon the amount of damping. V.F.D. works on the principle of dissipation of energy since the fluid is flowing through the orifice as shown in Fig. 2 as given by Taylor and devices (2007) below; in this mechanism, the fluid flows from the chamber. There is another type of energy dissipation system known as buckling restrained braces (B.R.B.) which is having a steel core, bond preventing layer, and a casing. Buckling restrained braces as shown in Fig. 3 are designed to withstand cyclic loadings, and this prevents buckling under axial compression. B.R.B. can absorb a large amount of energy during cyclic loading as shown in Fig. 4 in case of an earthquake. B.R.B. provides a large amount of ductility.

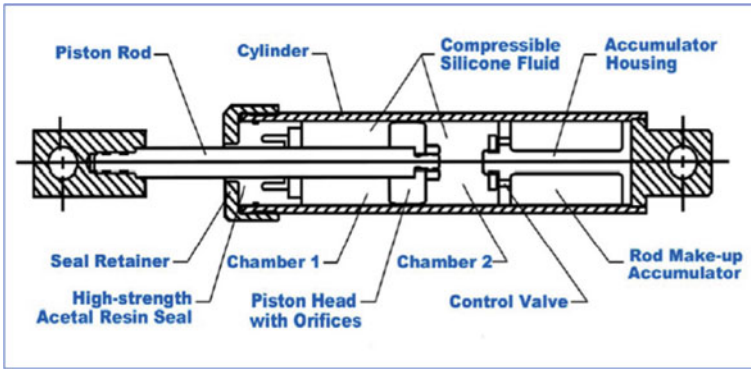


Fig. 2 Viscous fluid damper. Source Taylor Devices Inc.

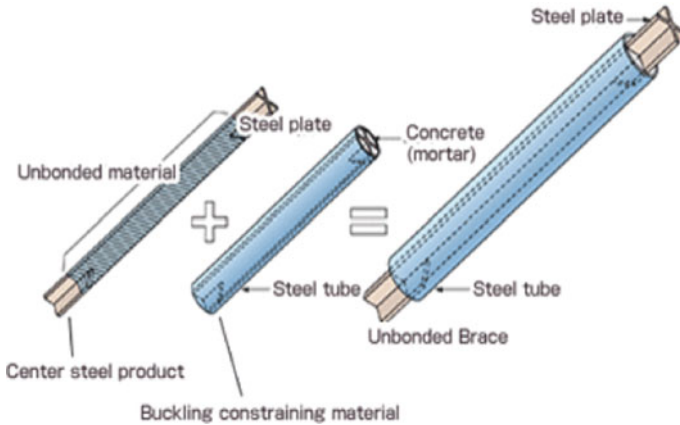


Fig. 3 Schematic sketch of B.R.B.

3 Example Building for Seismic Analysis

A three-dimensional steel moment-resisting frame is considered with 5 bays in the x- and y-directions with 5 m spacing each. The seismic analysis is performed for an intermediate frame as shown in Fig. 5 due to symmetry. The considered building is analyzed and designed for a dead load of 3.0 kN/m^2 and a live load of 5 kN/m^2 along with a floor finish load of 1.5 kN/m^2 on the intermediate story and 3 kN/m^2 on the roof floor. The time history analysis of the building is performed using SAP2000 with bilinear material properties. The material properties for the steel frame considered are given below.

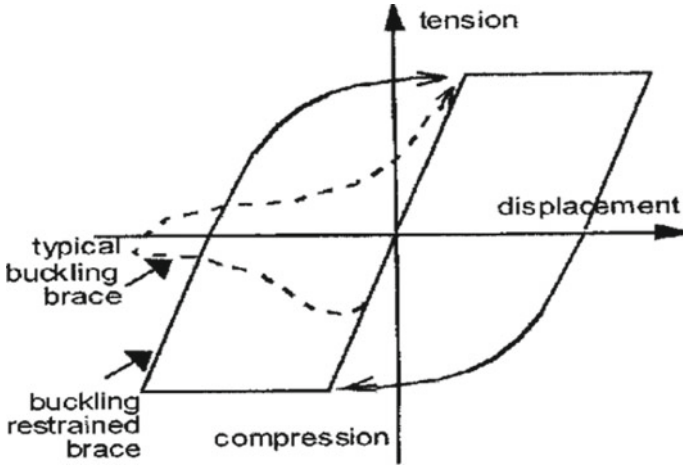


Fig. 4 Hysteretic behavior of B.R.B.

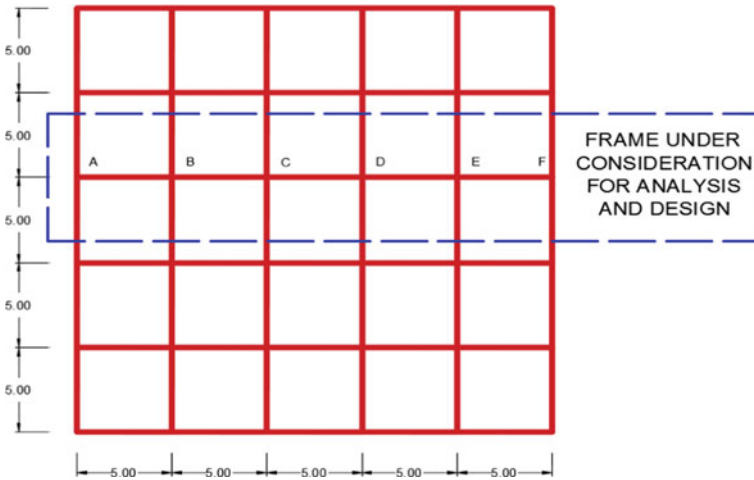


Fig. 5 Structural plan of building considered for analysis. All dimensions are in (m)

3.1 Seismic Data

The typical example building is assumed to be located in the Pune City of India. As per the current seismic code of India, the site seismic zone is categorized as Zone-III. The structural plan of the building was considered for analysis as shown in Fig. 5. To perform the seismic analysis through the time history solution, the plots for selected time history records for the three earthquake records and details of these earthquake records are given in Fig. 6 and Table 1, respectively.

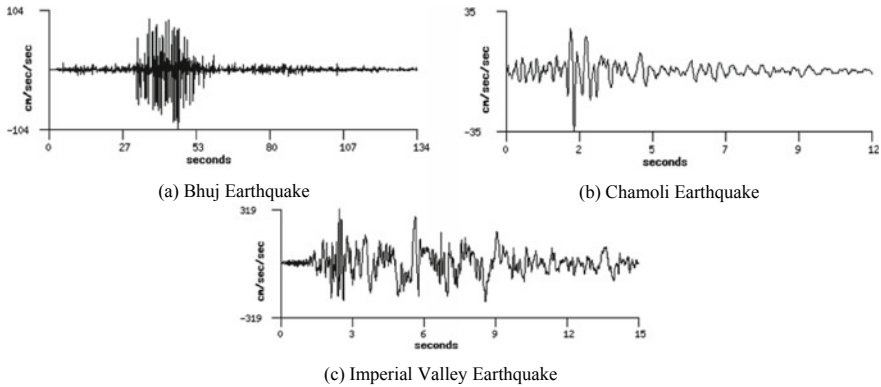


Fig. 6 Selected time history records

Table 1 Selected time history records

Sr. no.	Name of earthquake	Recording station	EQ component	PGA (m/s^2)
1	Bhuj earthquake EQ	Ahmedabad [AMD]	N 78 E	-1.038
2	Chamoli earthquake EQ	Gopeshwar [GOP]	N 20 E	-3.5283
3	Imperial valley EQ	UCSD station [US6616]	N 45 E	-3.2059

3.2 Different Frame Cases

For the comparative study, the considered frame of the example building is considered without any damping system, i.e., Bare frame; to evaluate the effectiveness of the passive hybrid damping system, the frame is installed with B.R.B. and V.F.D., and this damping system is termed as Hybrid Damping. Further, to verify the individual effects of the B.R.B. and V.F.D. on the frame, two cases with installed B.R.B. and V.F.D. only are considered for seismic analysis. The four different cases of frames as mentioned are shown in Figs. 7, 8, 9 and 10.

4 Results and Discussions

1. Buckling restrained braces (B.R.B.) and Viscous Fluid Dampers (V.F.D.) are modeled in the frame with built-in link elements in SAP200.
2. Figs. 11, 12, 13 and 14 show the yielding of these elements; thus, the full potential utilization of these dampers is achieved.
3. The results for column base shear, story displacements, and inter-story drifts are shown in the table below.

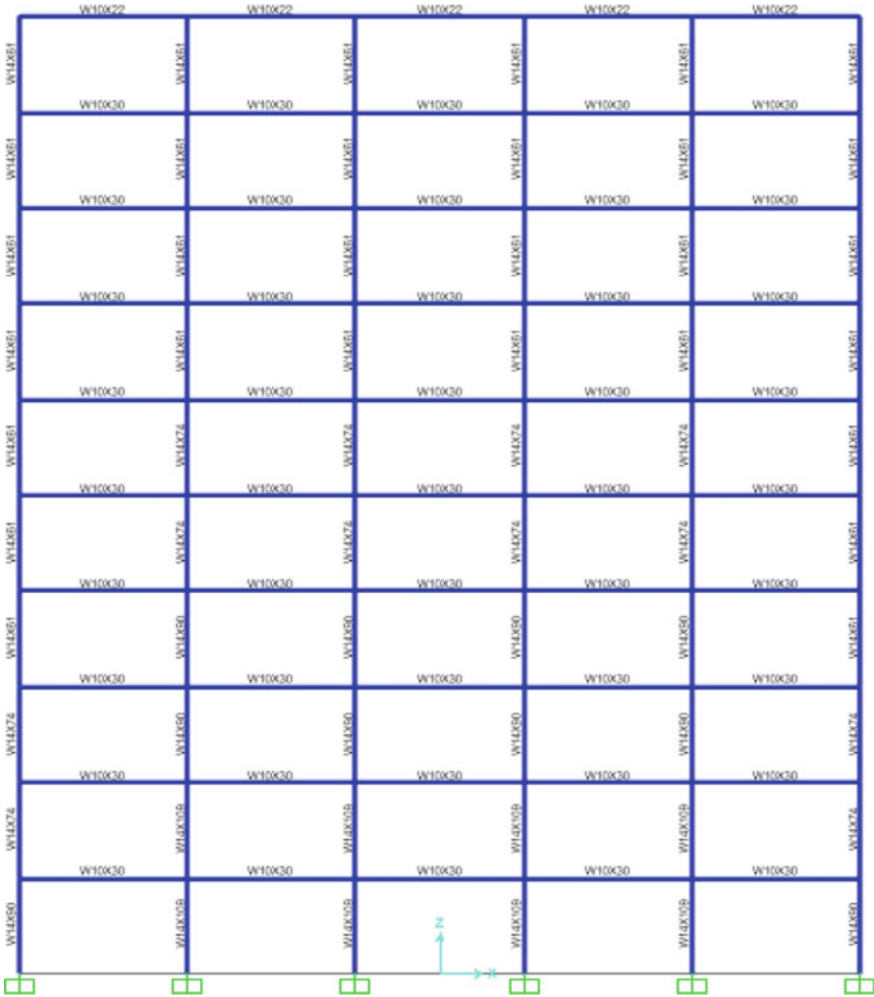


Fig. 7 Building frame without dampers (frame-1)

4.1 Hysteresis Behavior

4.2 Base Shear

The response results for the seismic base shear for the four cases of the frames with and without damping are shown in Table 2. The seismic base shear as per the Indian IS:1893-2016 code is also computed. It is seen that installing the hybrid damping system results in ductile behavior of the frame, and the resulting base shear is less than

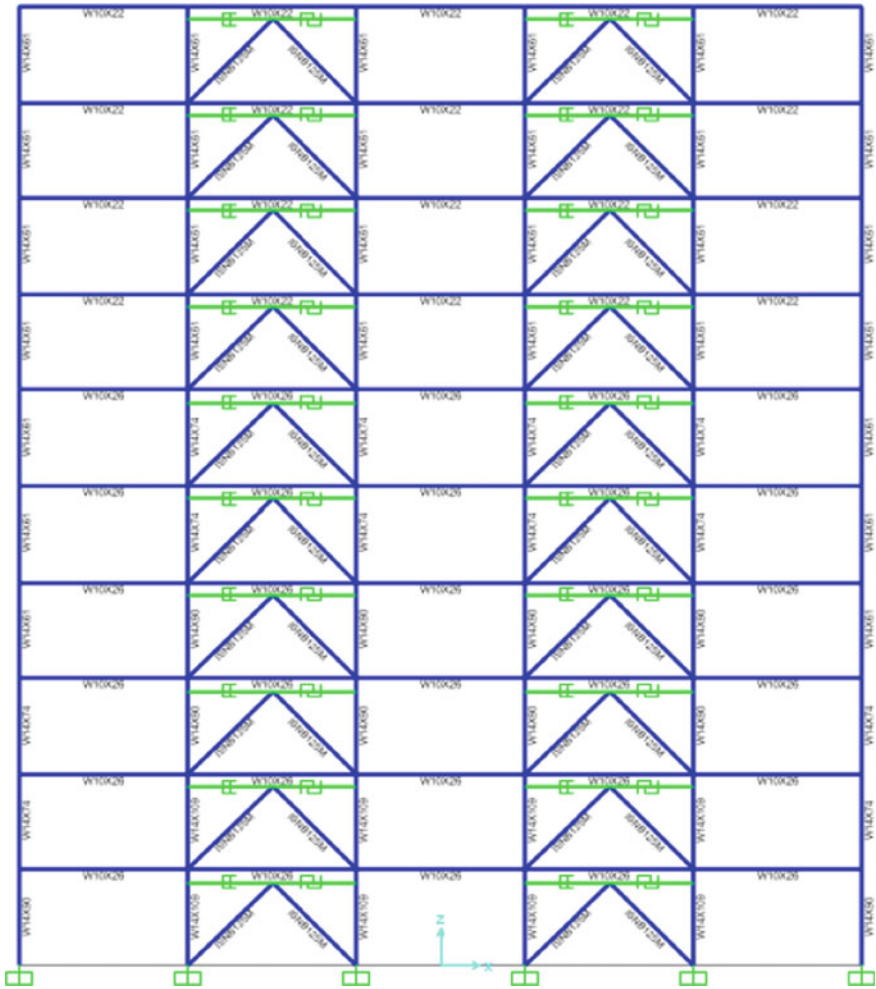


Fig. 8 Frame with hybrid damping system installed in 2nd and 4th bay (frame-2)

the frame without any damping systems. Installing B.R.B. made the frame highly stiff resulting in higher base shear.

4.3 Story Displacement

The calculated floor displacements are shown in Table 3 with plots for all four frames in Fig. 15. It is seen that the bare frame undergoes large deformation at the

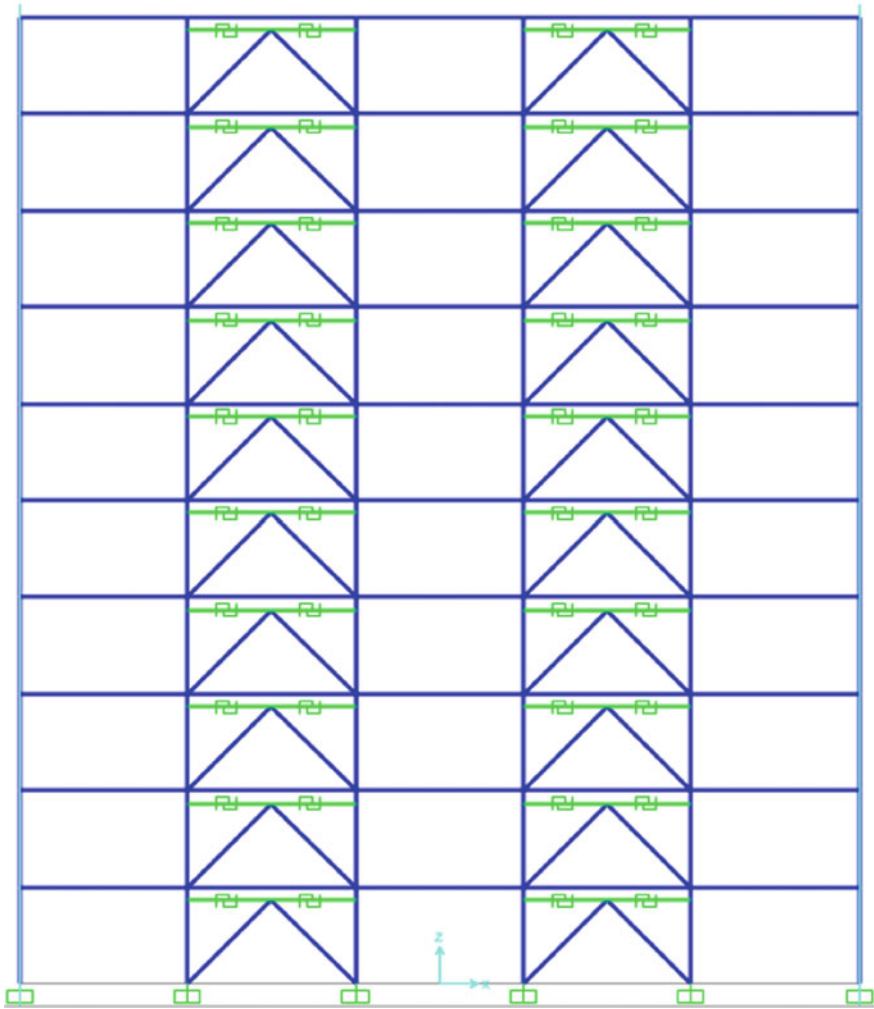


Fig. 9 Frame installed with B.R.B. in 2nd and 4th bay (frame-3)

roof. However, the other three frames with a damping system result in lower roof displacements.

4.4 Story Drift

The calculated story drifts along with the plots are shown in Table 4 and Fig. 16, respectively. The story drift for the damped model frames is significantly reduced when compared with the frames without a damping system.

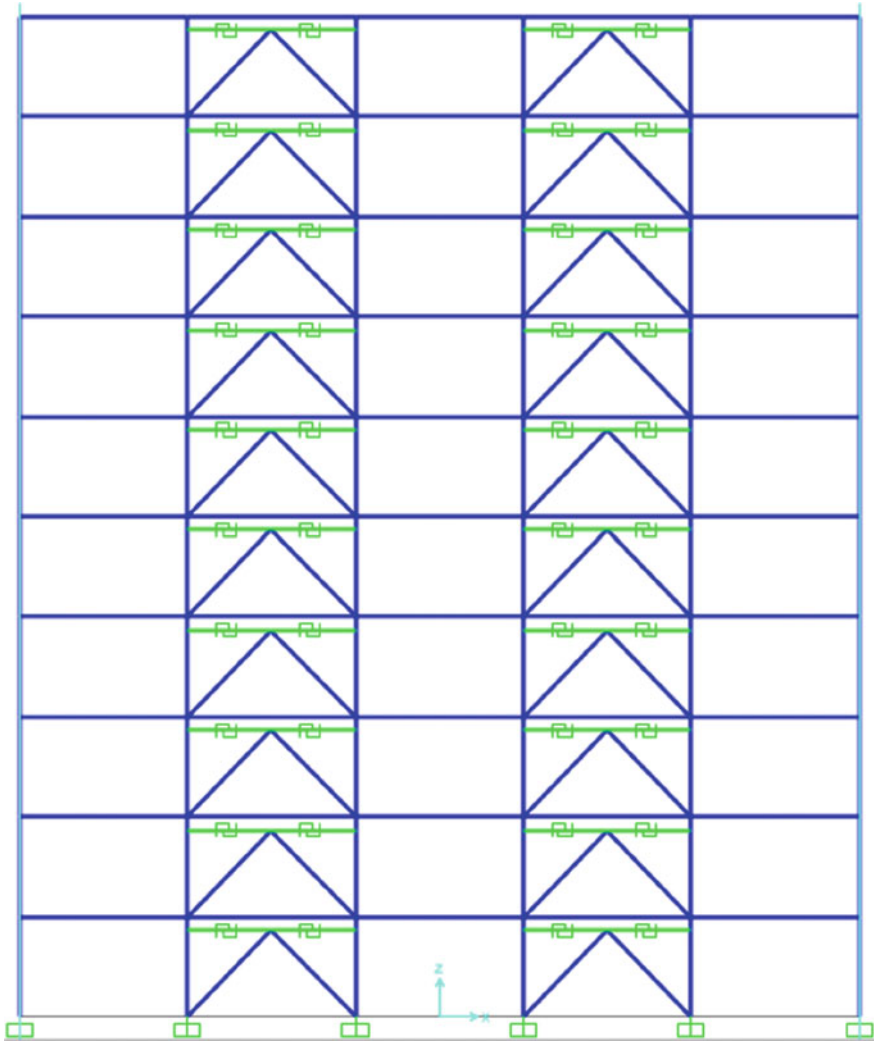


Fig. 10 Frame installed with V.F.D. in 2nd and 4th bay (frame-4)

5 Conclusions

The example building is analyzed and designed using the three earthquake records. For seismic analysis, the interior frames with four different cases with and without passive damping are considered, viz. Bare Frame, Frame with V.F.D., Frame with B.R.B., and frame with Hybrid damping (V.F.D. and B.R.B.). It is seen that the frame without any damping system performs poorly in terms of the large displacements at the roof story. There is also a slightly higher base shear force observed for the bare

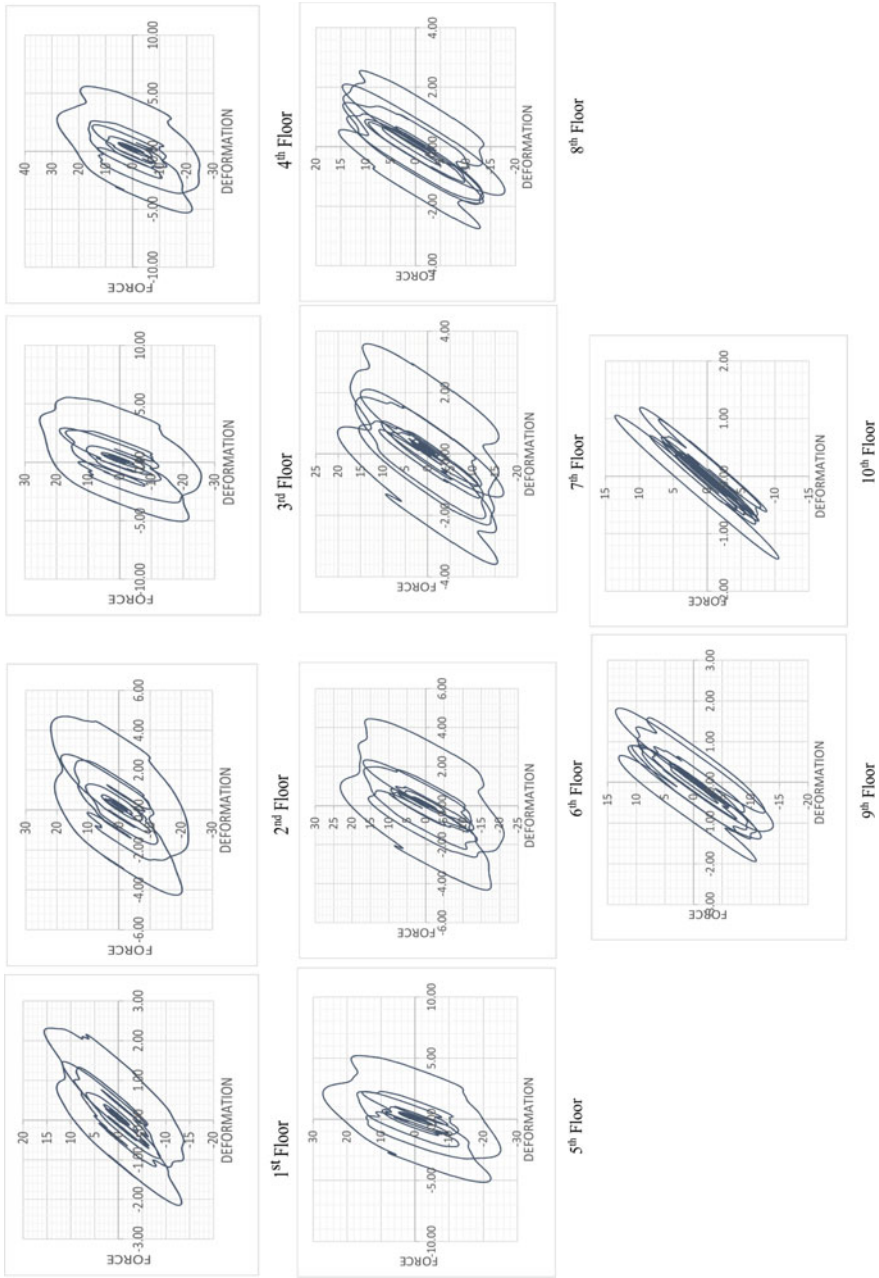


Fig. 11 Hysteretic plots for V.F.D. in hybrid damping frame

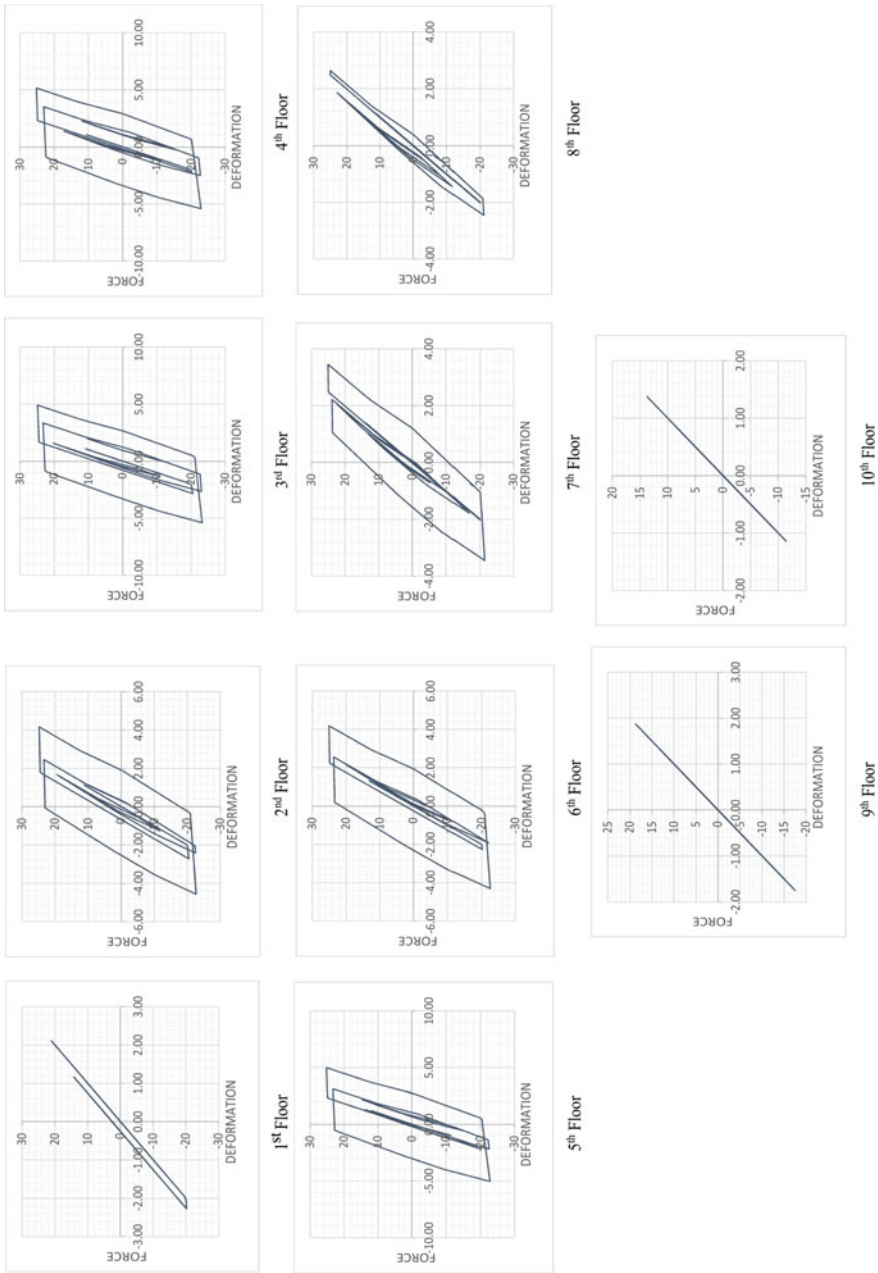


Fig. 12 Hysteretic plots for B.R.B. in hybrid damping frame

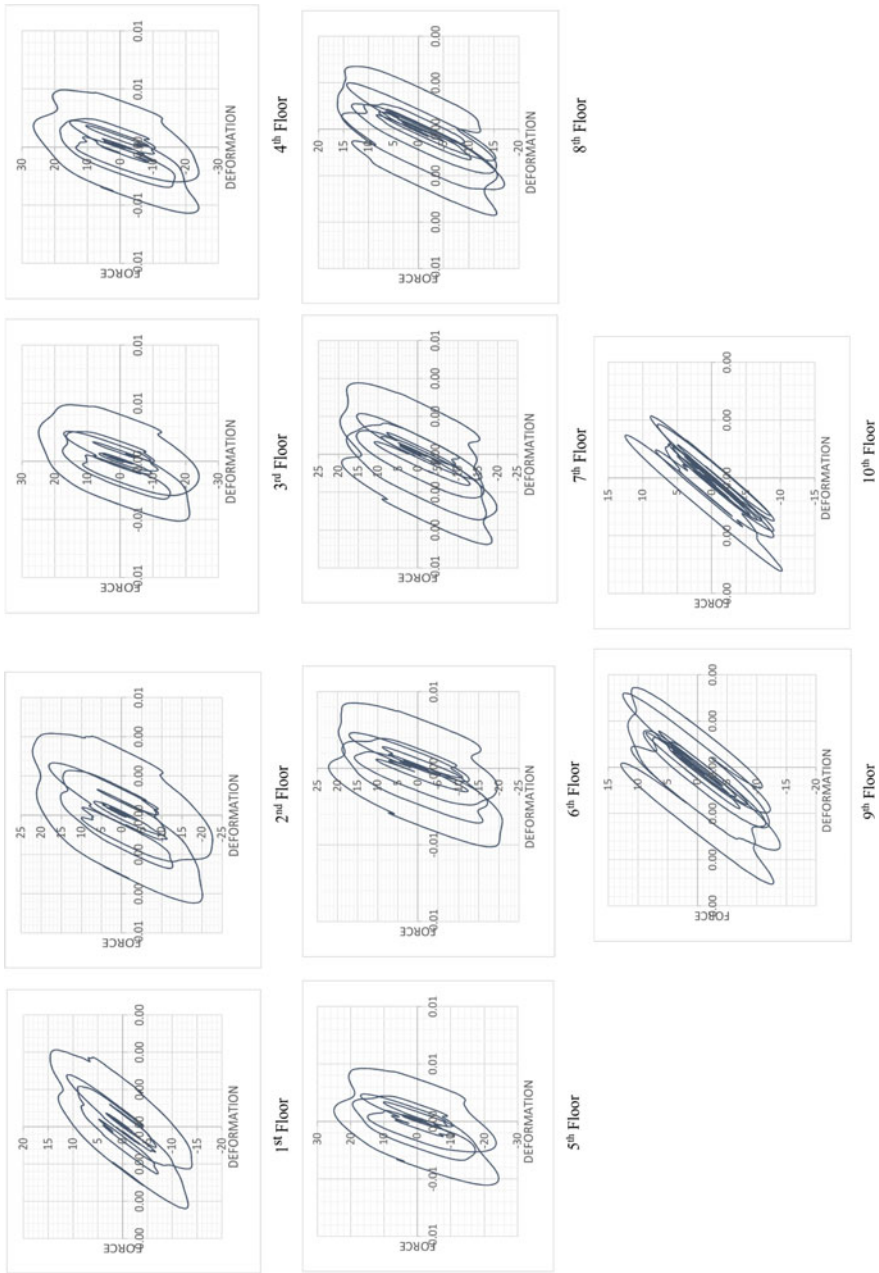


Fig. 13 Hysteretic plots for frame with V.F.D. only frame

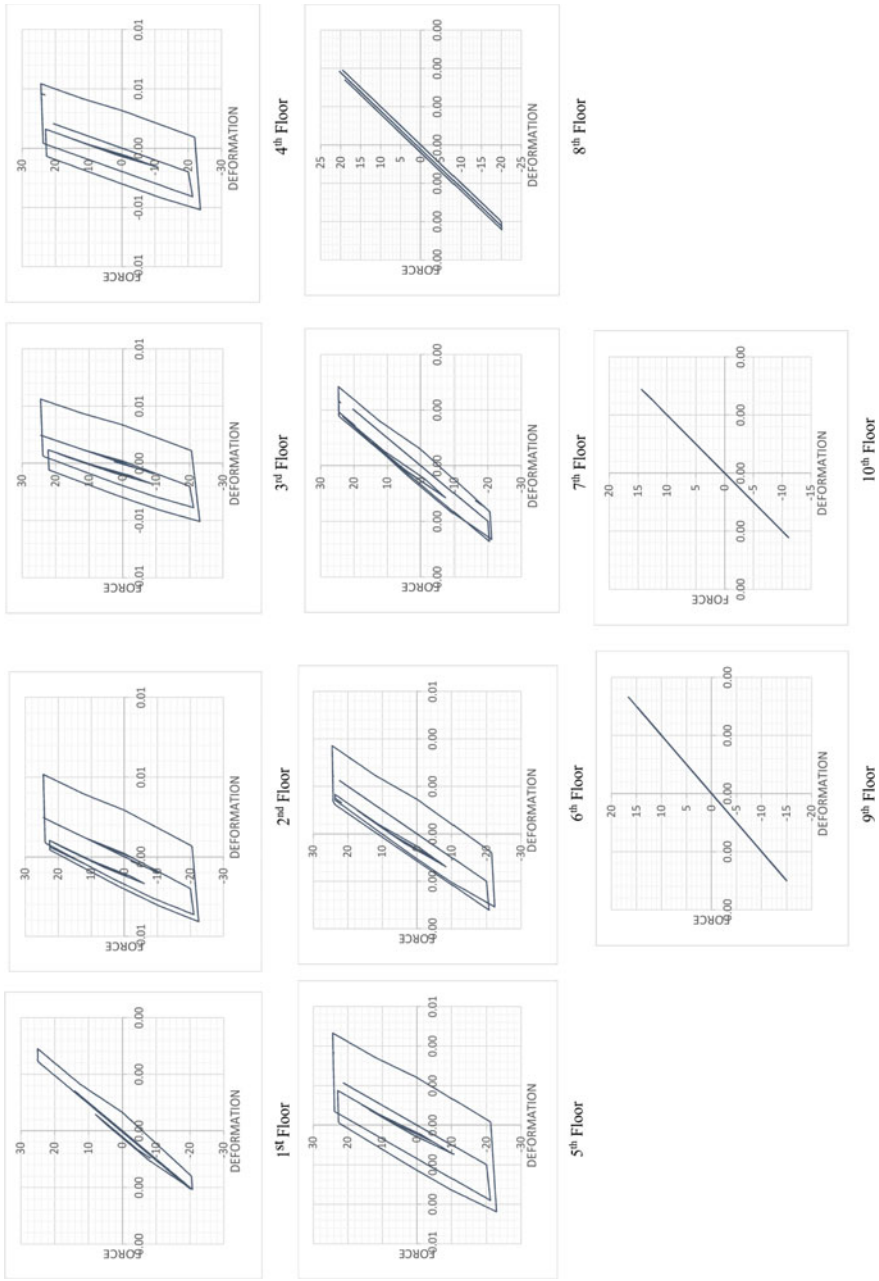


Fig. 14 Hysteretic plots for frame with B.R.B. only frame

Table 2 Base shear response

Frame #	Observed base shear (kN)	Seismic weight (kN)	% of seismic weight	As per IS1893:2016
1	251.986	12,624.453	1.996	1.99808%
2	204.508	12,618.243	1.620	
3	373.111	12,642.353	2.951	
4	136.947	12,629.709	1.084	

Table 3 Story displacement (mm)

Story no.	Frame-1	Frame-2	Frame-3	Frame-4
1	7.209	4.390	6.683	4.105
2	20.935	13.097	18.343	11.868
3	35.592	23.026	30.582	20.244
4	48.982	33.215	42.189	28.550
5	59.766	42.867	52.049	36.732
6	68.783	51.000	59.633	43.963
7	81.702	57.604	65.759	49.984
8	92.470	62.302	70.821	54.387
9	100.428	65.095	74.655	57.186
10	107.087	66.759	77.158	58.691

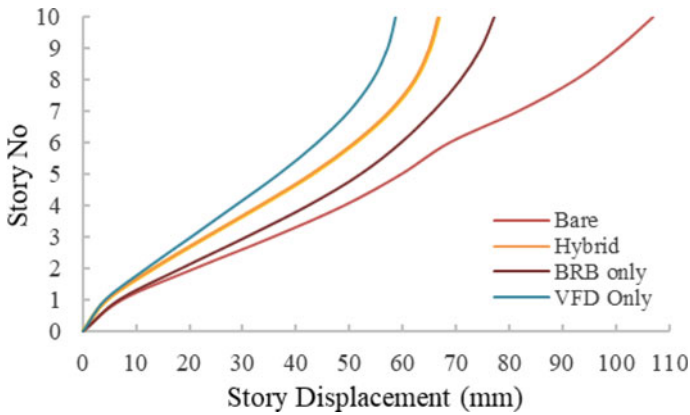


Fig. 15 Story displacements

Table 4 Roof drift (mm)

Frame #	Roof drift	Allowable as per IS1893:2016
1	107.87	$\Delta = 0.4\%$ of H $\Delta = 0.004 * 30 * 1000$ $\Delta = 120$ mm
2	66.759	
3	77.158	
4	58.691	

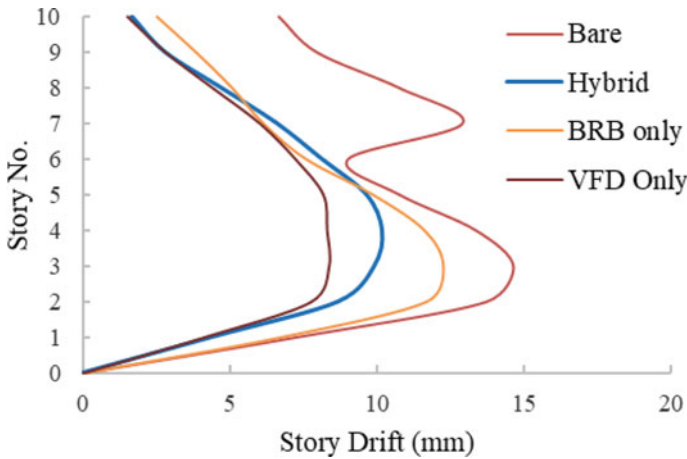


Fig. 16 Story drifts

frame. However, in the frames with damping systems, the lateral stiffness are lower except for the frame with B.R.B. For the frame with installed V.F.D., improvements with low roof displacements are observed. The base shear was also reduced to a large extent in the case of the V.F.D. only frame as compared to other frames. The joint displacement is reduced by 80% and the inter-story drift is decreased by 45% when compared with Frame-1. A roof displacement of 59 mm was seen when the damping and stiffness properties were changed accordingly. Finally, by reducing the displacement and drift, the effect for non-structural elements can be reduced to quite a large extent.

References

1. Gupta A, Krawinkler H (1999) Seismic demands for performance evaluation of steel moment resisting frame structures. Report 132, Stanford University
2. Taylor DP (1983) Seismic protection with fluid viscous dampers for the Torre Mayor a 57-story office tower in Mexico City, Taylor Devices, Inc, 90 Taylor Drive, North Tonawanda
3. FEMA - 355 C (2000) State of the art report on systems performance of steel moment frames subject to earthquake ground shaking. SAC Joint Venture
4. Miyamoto HK, Gilani AS, Wada A (2008) State of the art design of steel moment frame buildings with dampers. WCEE 2008, Beijing, China
5. Miyamoto HK, Gilani ASJ, Wada A, Viscous damper limit states and collapse analysis of steel frame buildings with dampers. Paper no-146, July 25–29, Toronto, Ontario, Canada
6. Liu J (1986) Earthquake analysis of steel moment-resisting frames. South China University of Technology, China
7. Rajendran K, Rajendran CP, Thakkar M, Tuttle MP (2001) The 2001 Kutch (Bhuj) earthquake: seismic surface features and their significance. *Curr Sci* 80(11)
8. Magar Patil HR, Jangid RS (2013) Seismic vulnerability assessment of steel moment resisting frame due to infill masonry walls, variation in column size and horizontal buckling restrained braces. *ACEE* 2(1)

9. Kharmale SB, Patil VB, Revankar VS (2012) Seismic performance of steel moment-resisting frames designed with displacement-based and strength-based approaches. ISET paper no. D013, 20–21 Oct 2012
10. Kojic S, A design analysis of the Imperial country services building. Yugoslavia
11. Soong TT, Constantinou MC (2010) Passive and active structural vibration control in civil engineering. Department of Civil Engineering State University of New York at Buffalo, NY 14260
12. Symans MD, Whittaker AS, Kircher CA, Charney FA, Johnson MW, McNamara RJ, Constantinou MC (2008) Energy dissipation system for seismic applications current practice and recent developments. ASCE 134(1)
13. Taylor (2007) Structural applications of fluid viscous dampers. Taylor Devices Inc., North Tonawanda
14. Dogan T, Goodno BJ, Craig JI (2004) Hybrid passive control in steel moment frame buildings. In: 13th world conference on earthquake engineering, Paper no 2387, 1–6 Aug 2004, Vancouver B.C., Canada
15. López WA, Sabelli R (2004) Seismic design of buckling-restrained braced frames
16. Pandey Y, Dharmaraju R, Chauhan PKS (2001) Estimation of source parameters of Chamoli Earthquake, India. Indian Acad Sci (Earth Planet Sci) 110(2)

Thermal Buckling Analysis of Stiffened Composite Cutout Panels



K. S. Subash Chandra, T. Rajanna, and K. Venkata Rao

Abstract In aeroplanes, ships, and hypersonic space vehicles, stiffened plates with cutouts are often used. Aerodynamic heating produced by the interaction between the environment and the vehicle's surface quickly heats up this structural component. These activities affect the buckling characteristics of perforated plates and may result in an early failure due to the presence of cuts. This impact is avoided by properly stiffening the area surrounding the cutout. Thermal buckling effects must, thus, be taken into account when designing and analyzing thin-walled structural components. Using finite-element techniques, the effect of high temperatures on the buckling stresses of composite laminates with and without reinforced cuts is studied. This is accomplished via the use of a nine-noded heterosis element and a three-noded quadratic beam element. A transformation matrix ensures the displacement compatibility of the plate and stiffener. Thermal buckling of layered panels with cutouts is analyzed by employing eccentric stiffeners. It is witnessed from this investigation that various parameters significantly affect the buckling behavior of stiffened plates. These factors include cutout size, material anisotropy, thermal expansion ratio, modulus ratio, and boundary conditions.

Keywords Thermal buckling · Cutout · Stiffener · Laminates · Nine-noded heterosis

K. S. S. Chandra (✉)

Department of Technical Education, Government Polytechnic, Bagepalli, Karnataka, India
e-mail: subashks.17pm@bmsce.ac.in

T. Rajanna

Department of Civil Engineering, BMS College of Engineering, Bengaluru 560 019, India

K. V. Rao

Department of Mechanical Engineering, BMSE College of Engineering, Bengaluru 560 019, India

© The Author(s), under exclusive license to Springer Nature Singapore Pte Ltd. 2023

935

M. S. Ranadive et al. (eds.), *Recent Trends in Construction Technology and Management*, Lecture Notes in Civil Engineering 260,
https://doi.org/10.1007/978-981-19-2145-2_69

1 Introduction

The composite materials' qualities are known for their more excellent strength/weight ratio, high specific rigidity, and improved fatigue life. The inclusion of stiffeners to a panel, without significantly impacting its total weight, further enhances these features. There is an enormous increase in a minor weight penalty's strength and stability aspects of the constructions. Plates with a pattern of stiffeners are usually discovered in an aircraft's fuselage, including wings, a ship's hull and its deck, maritime drilling gears, pressure containers, roofing members, and the thrusting plinth of the missile. The extensive acceptance and utilization of the before-mentioned materials, under various incidents, are governed by severe environmental circumstances throughout their service life. The raised heat is one thing that dangerously influences the buckling properties of layered laminae, mainly in the geometrically ceased panels. These discontinuities may complicate the in-plane thermic stress concentration in the plates. Deficient stresses produce a deterioration of stability due to non-uniformity in the stress field. The fiber-reinforced composite constructions remain exposed to high-temperature loads throughout the operational cycle, leading to significant strength degeneration, including additional damaging consequences. Hence, the entire understanding of thin panels with cutouts is essential to prevent premature breakdown and utilize their full strength, which can be explored tremendously in thin-walled structures. Two kinds of buckling are customarily probable. They are local buckling due to cutout and the overall buckling essentially the another. The first is attributed to local and the global as the other. The local mode is observed across the cutout. However, panels are more cost-effective if they appear to buckle globally compared to those that buckle locally. Rigid reinforcing around the cutout removes the local mode. Thus, construction engineers need to consider composited laminates' stability behavior to achieve a practical design with reinforced cutouts.

In many literary works, the mechanical buckling of composites plates under in-plane compression is studied (for example, [1, 2]). Laminated composites cause thermal buckling due to extreme temperature changes. In some situations, the thermal load is the critical load for designing such plates. The three-dimensional layer-wise research analysis has helped predict composite laminated angles' thermal bending reaction [3]. Buckling of composite laminates plates in a thermal environment is carried out by many researchers, and a few studies are by References [4–12]. The maximum of the works was conducted without any discontinuities or cutouts. Panels with cutouts become a part of an integral component of complex structures. These perforations are present mainly to access the pipeline, electric cables, doors, or window structures. Research has been done for laminated panels considering the cutouts by References [13, 14]. Such perforated plates' thermal analysis can undergo thermal buckling mainly due to local buckling near the cutouts. Hence, various stiffeners strengthen the cutout panels [15] against thermal buckling.

In contrast, it is very much essential to consider weight addition due to stiffeners practically. Considering the total volume removed by the cutout portion being added as stiffeners around the cutouts, such work is done for various mechanical in-plane

compressive loadings by Reference [16]. Nevertheless, thermal buckling for panels with cutouts and stiffeners considering the same is yet to be done. There are very few works available on the thermal buckling of laminated plates with cutouts. Studies with thermal buckling of laminates with stiffeners placed around the cutout, considering the total volume remaining the same throughout, are not detected within the open literature. While, in the current article, a nine-noded heterosis plate element is applied, the finite-element program is established in MATLAB to analyze the thermal buckling of laminates with and without stiffeners. The thermal buckling behavior for different lamination angles, cutout ratios, and modular ratios is analyzed only after verifying with the current formulation with previous studies. The effects of panels with an eccentrically placed stiffener around the circular cutouts are analyzed, investigated, and compared with the panels without stiffeners for various parameters under consideration.

2 Theoretical Formulation

In this study, the first-order shear deformation theory, including a shear rectification determinant of 5/6, is considered for the non-linear distribution of shear strains within the thickness. Reddy and Phan [2] express the equations for laminates. The displacement field is

$$\{\bar{u}, \bar{v}, \bar{w}\}^T = \{u(x, y), v(x, y), w(x, y)\}^T + \{z\theta_x, z\theta_y, 0\}^T \tag{1}$$

where \bar{u} , \bar{v} , and \bar{w} are displacements ingredients in the x -, y -, and z -paths correspondingly. u , v , and w are associated mid-plane displacements in the x -, y -, and z -axis, sequentially, plus θ_x and θ_y perform rotations of normal regarding y - and x -axis, sequentially, being presented within Fig. 1a. A typical mesh is shown in Fig. 1b.

Green–Lagrange’s strain–displacement relationship exists and is appropriated during the formulation. The strain–displacement association consists of (i) linear strain expressions applied to derive the elastic stiffness matrix also and (ii) non-linear strain concerning the geometrical stiffness matrix.

$$\{\varepsilon\} = \{\varepsilon_l\} + \{\varepsilon_{nl}\} \tag{2}$$

2.1 Constitutive Relations

Constitutive relations of the composite panel subjected to the present buckling analysis’s temperature are described as follows. The stress–strain association for laminate is given by equation and is explained in detail in Subash Chandra et al. [18].

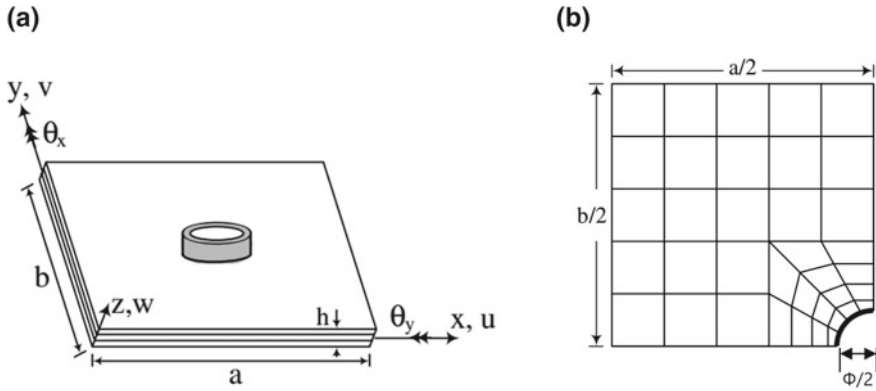


Fig. 1 a Plate geometry with cutout and eccentric stiffener b detailed mesh over quarter plate

$$\{F\} = [D]\{\varepsilon\} - \{F^N\} \tag{3}$$

The constitutive matrix in the above Eq. (3) is given by

$$[D] = \begin{bmatrix} [A_{ij}] & [B_{ij}] & 0 \\ [B_{ij}] & [D_{ij}] & 0 \\ 0 & 0 & [S_{ij}] \end{bmatrix} \tag{4}$$

The extension–extension, extension–bending, and bending–bending stiffness components exist presented in Eq. (4) as

$$(A_{ij}, B_{ij}, D_{ij}) = \sum_{k=1}^n \int_{z_{k-1}}^{z_k} (\overline{Q_{ij}})_k (1, z, z^2) dz, \quad i, j = 1, 2, 6 \tag{5}$$

and

$$[D_{ij}] = \alpha \sum_{k=1}^n (\overline{Q_{ij}})_k (z_k - z_{k-1}); \quad i, j = 4, 5 \tag{6}$$

where $(\overline{Q_{ij}})$ in the above equation is

$$\begin{aligned} (\overline{Q_{ij}}) &= [T_1]^T (Q_{ij}) [T_1] (i, j = 1, 2, 6) \\ (\overline{Q_{ij}}) &= [T_2]^T (Q_{ij}) [T_2] (i, j = 4, 5) \end{aligned}$$

in which,

$$[T_1] = \begin{bmatrix} \cos^2 \theta & \sin^2 \theta & \sin \theta \cos \theta \\ \sin^2 \theta & \cos^2 \theta & -\sin \theta \cos \theta \\ -2 \sin \theta \cos \theta & 2 \sin \theta \cos \theta & \cos^2 \theta - \sin^2 \theta \end{bmatrix} \text{ and}$$

$$[T_2] = \begin{bmatrix} \cos \theta & \sin \theta \\ -\sin \theta & \cos \theta \end{bmatrix}$$

$$[Q_{ij}]_k = \begin{bmatrix} Q_{11} & Q_{12} & 0 \\ Q_{12} & Q_{22} & 0 \\ 0 & 0 & Q_{66} \end{bmatrix} (i, j = 1, 2, 6) \text{ and}$$

$$[Q_{ij}]_k = \begin{bmatrix} Q_{44} & 0 \\ 0 & Q_{55} \end{bmatrix} (i, j = 4, 5)$$

in which,

$$Q_{11} = \frac{E_{11}}{1 - \nu_{12}\nu_{21}}, Q_{12} = \frac{\nu_{12}E_{22}}{1 - \nu_{12}\nu_{21}},$$

$$Q_{22} = \frac{E_{22}}{1 - \nu_{12}\nu_{21}}, Q_{44} = G_{13}, Q_{55} = G_{23}$$

The non-mechanical strength and moment resultants concerning temperature implication are shown as

$$\{N_x^N, N_y^N, N_{xy}^N\}^T = \sum_{k=1}^n (\overline{Q}_{ij})_k \{e\}_k (z_k - z_{k-1}).$$

$$\{M_x^N, M_y^N, M_{xy}^N\}^T = \frac{1}{2} \sum_{k=1}^n (\overline{Q}_{ij})_k \{e\}_k (z_k^2 - z_{k-1}^2).$$

Where

$$\{e\}_k = \{e_x e_y e_{xy}\}^T = [T] \{\alpha_1 \alpha_2\}_k^T (\Delta T)$$

while $[T]$ = Transformation matrix fit to temperature and denotes

$$[T] = \begin{bmatrix} \cos^2 \theta & \sin^2 \theta \\ \sin^2 \theta & \cos^2 \theta \\ \sin 2\theta & -\sin 2\theta \end{bmatrix}$$

$e_x, e_y,$ and e_{xy} are the non-mechanical strains of the k th lamina, oriented at an arbitrary angle θ ; α_1 and α_2 are the thermal coefficients in longitudinal and lateral directions.

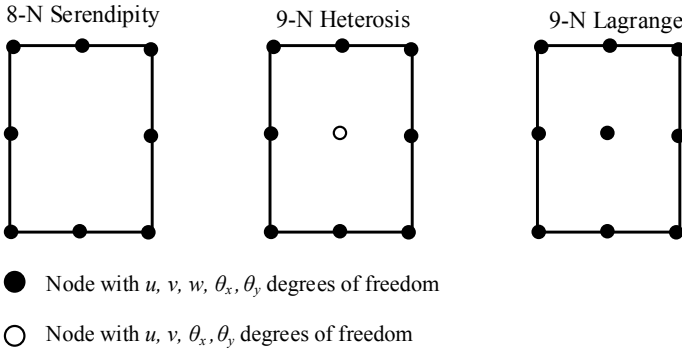


Fig. 2 Plate element types

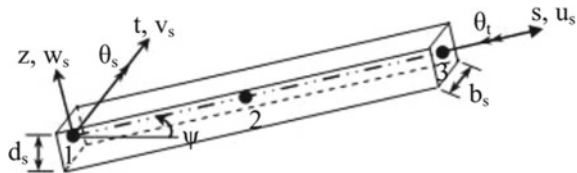
2.2 Formulation of a Plate Element

In this plate element, there are nine nodes, and each has five degrees of freedom (three translational and two rotational). As shown in Figure 2, the heterosis element is a derivation of the Serendipity elements with eight nodes and the Lagrange elements with nine nodes. The full mathematical expression for the heterosis plate element and the corresponding stiffness matrices have been discussed by Subash Chandra [18] and have not been shown here for brevity.

2.3 Stiffener Element Formulation

Figure 3 shows the standard geometrical arrangement of an isoparametric three-nodal beam element with b_s in width and d_s in depth with a positive co-ordinate configuration. The stiffer is constructed as a laminated strip in the current formulation and is positioned at a different angle ψ to the x -axis in some arbitrary directions. Timoshenko beam principle is the basis of the stiffener formula. In the original hypothesis, only the consequence of shear deformation is considered. The principle is updated to handle the torsional effect into account as well. The displacement field “ z ” from the stiffener mid-plane is given according to a modified beam theory and is given as in [16].

Fig. 3 Geometry of stiffener with arbitrary orientation



$$\begin{aligned} \bar{u}_s &= u_s + z\theta_s \\ \bar{v}_s &= z\theta_t \\ \bar{w}_s &= w_s \end{aligned} \tag{7}$$

where θ_s and θ_t imply bending and torsional rotations along each plane concerning t - and s -axis, and u_s and w_s of axial and transverse displacements. The relationship between the laminated stiffener is given as

$$\{N_s^1\} = [D_s]\{\epsilon_s^1\} \tag{8}$$

where $\{N_s^1\} = [N_s \ M_s \ M_{st} \ Q_{sz}]^T$ and $\{\epsilon_s^1\} = [\epsilon_s \ \chi_s \ \chi_{st} \ \gamma_{sz}]^T$ indicate both stress and strain vectors, on sequence. $[D_s]$ is the stiffener, constitutive matrix comparable to Patel and Sheikh concept [17].

Applying Green–Lagrange’s strain–displacement expression [17], elastic stiffness matrix $[k_{es}]$ and geometric stiffness matrix $[k_{Gs}]$ can be expressed as follows:

$$[k_{es}] = b_s \int_{-1}^{+1} [T_e]^T [T_o]^T [B_s]^T [D_s] [B_s] [T_o] [T_e] d\xi \tag{9}$$

$$[k_{Gs}] = b_s \int_{-1}^{+1} [T_e]^T [T_o]^T [B_{Gs}]^T [D_s] [B_{Gs}] [T_o] [T_e] J_s d\xi \tag{10}$$

where $[T_e]$ and $[T_o]$ are matrices of transformation, taking account of eccentricity and random orientation of stiffener, $[B_s]$ and $[B_{Gs}]$ are the linear and non-linear strain–displacement matrix, whose details are found in [16].

2.4 Governing Equations

The following eigenvalue problem may be used to describe the stability equation.

$$([K] - \lambda[K_g])\{q\} = 0 \tag{11}$$

where $[K]$ and $[K_g]$ indicate the global stiffness plus geometric matrix in order. Furthermore, $\{q\}$ is a generalized displacement vector.

Specific critical buckling temperature ΔT_{cr} exists and is collected from the lowest eigenvalue λ .

3 Results and Discussion

On a thin laminated squares panel, thickness ratio is considered to be $h/b = 0.01$. Numerical results are shown for stiffened panel with d_s/b_s is known as the ratio of the stiffener (d_s) depth to width (b_s), which is taken as 2 for all problems, except for where stiffener depth to width ratio is taken into consideration. The overall stiffener volume taken into account is proportional to the material quantity withdrawn by the cut; that is to say, the stiffeners form from the material extracted from the cut-over. The panel’s lamination scheme varies from $\theta = (\pm 0^0)_{2s}$ to $(\pm 90^0)_{2s}$. In the stiffener’s case, the fiber orientation remains impartial toward each stiffener’s axis; nevertheless, the existing stiffener formulation is fit toward several assigned ply-orientation. Material properties analyzed toward both panel as well as stiffener denote $E_{11} = E_{22} = 25$; $G_{12} = G_{13} = 0.50 E_{22}$; $G_{23} = 0.20 E_{22}$ and $\nu_{12} = 0.25$, $\alpha_1 = 0.02 \times 10^{-6} \text{ } ^\circ\text{C}^{-1}$, $\alpha_2 = 22.52 \times 10^{-6} \text{ } ^\circ\text{C}^{-1}$, unless stated. The two sets of boundary conditions examined during the aforementioned study do the same as Rajanna et al. (2008).

3.1 Comparison and Convergence Study

The comparison investigations ensure the exactness of the outcomes obtained, and convergence studies for the present study with and without stiffener are done to meet the precise convergence during this current work and get relevant results. Comparison studies in Tables 1 and 2 show excellent rapport amidst this present finite-element formulation and previous studies. Convergence studies show the number of elements required to converge for the current formulation in Table 3. The value within the

Table 1 Comparison of thermal buckling with previous studies for laminate under simply supported boundary condition

Laminate [mesh size]	Shi et al. [8] [12 × 12]	Shi et al. [11] [12 × 12]	Ounis et al. [14] [12 × 12]	Zhao et al. (2016) [32 × 24]	Present [12 × 12]
[0/90/90/0] _s	12.26	12.2610	12.2612	12.25	12.261
[0/45/-45/90] _s	13.71	13.7519	13.7357	13.65	13.724

Table 2 Thermal buckling with ten-layered angle-ply laminate composite plates

Source/laminate ($\pm\theta$) _{5s}	Minimum critical buckling temperature (ΔT_{cr})			
	$\theta = 0^0$	$\theta = 15^0$	$\theta = 30^0$	$\theta = 45^0$
Present	0.7464×10^{-3}	0.1115×10^{-2}	0.1502×10^{-2}	0.1674×10^{-2}
Noor and Burton	0.7464×10^{-3}	0.1115×10^{-2}	0.1502×10^{-2}	0.1674×10^{-2}
Ounis et al.	0.7464×10^{-3}	0.1133×10^{-2}	0.1540×10^{-2}	0.1720×10^{-2}

Table 3 Mesh convergence for present investigations of ΔT_{cr} of the laminate including and without reinforcement around the circular cutout

Cutout ratio (ϕ/b)	No. of elements	Critical buckling temperature (ΔT_{cr})	
		Without stiffener	With stiffener
0.5 [laminate sequence (45/-45) _{2s}]	100	946.05	1492.02
	132	939.06	1487.03
	164	925.52	1478.21
	196	921.70	1477.22
	228	921.60 (921.70)	1477.19 (1477.20)

bracket in Table 3 indicates the thermal buckling value obtained through ABAQUS software.

3.2 Parametric Studies on Thermal Buckling of Cutout Panels with and Without Stiffeners

The various effects such as a change in cutout ratios, modulus ratio, thermal expansion ratios, and different boundary conditions are studied. Furthermore, analysis is done in detail for the square ($a/b = 1$) panels having centrally placed cutouts and is compared with the reinforced panel around the cutout with a stiffener depth (d_s) to width (b_s) ratio equal to 2.

3.2.1 Effect of Cutout Ratios on Panels with and Without Stiffener

The effect of different cutout ratios (ϕ/b) ranging from 0.1 to 0.7 is studied for the variations in the thermal buckling of square panels. A similar study is analyzed for panels with stiffener ($d_s/b_s = 2$) placed at the cutout surrounding, which amounts to equal to the volume of the cutout portion of the panel, as shown in Figure 4a and b, sequentially. It is found that $(\pm 45)_{2s}$ have the highest thermal buckling for cutout panels either with and without stiffeners. The Von-misses stress plot for $(\pm 45)_{2s}$ ply angle has been shown for cutout panel $\phi/b = 0.5$, with and without stiffener in Figure 5a and b sequentially. It signifies from Figure 5a that the panel without stiffener has a higher stress concentration near the hole, leading to local buckling. However, such a phenomenon is not seen for panels with reinforcement, as the stresses get redistributed, hence higher thermal buckling resistance.

The difference in thermal buckling between each cutout size increased with the rise in the cutout ratio. Larger the cutout size is found to have higher ΔT_{cr} irrespective of fiber orientation. However, the percentage change has increased between with and without stiffeners. For example, in $(\pm 45)_{2s}$ ply panel, with $\phi/b = 0.1$, percentage variations are 11.7%. In contrast, with $\phi/b = 0.7$, 169% change between the panels

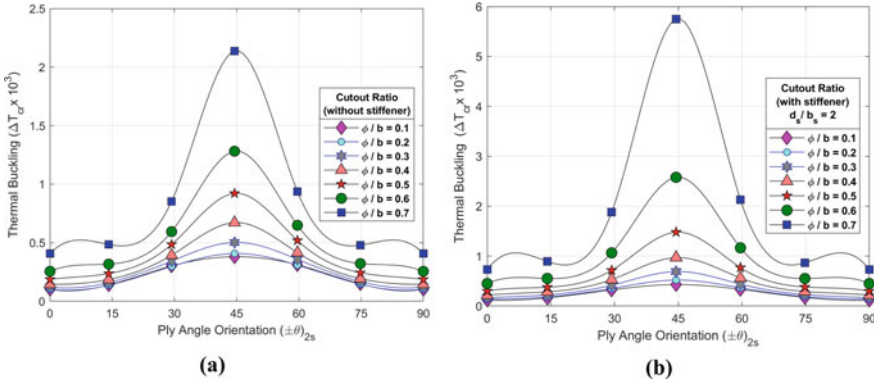


Fig. 4 Variation in the thermal buckling for different ply angles with increasing cutout ratios **a** without stiffener and **b** with stiffener

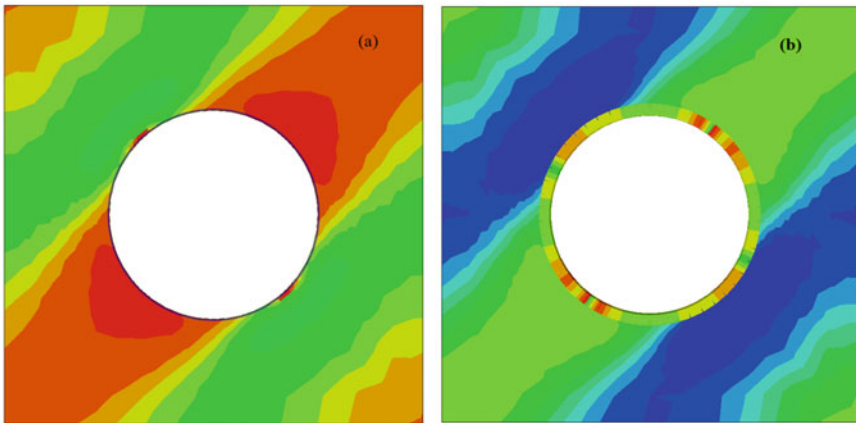


Fig. 5 Von-mises stress distribution for panels with cutout ratio $\phi/b = 0.5$, for ply angle $(\pm 45)_{2s}$ **a** without and **b** with stiffener, respectively

with and without stiffeners. Hence, adding stiffeners around the cutout for larger cutout sizes improved the thermal buckling resistance significantly.

3.2.2 Effect of Modulus Ratio on Cutout Panels with and Without Stiffener

The effect of change of modulus ratio observed for cutout panels ($\phi/b=0.5$), with and without stiffener, is as seen in Figure 6a and b. It implies that as the modulus ratio increased, the ΔT_{cr} increased for both cutout panels with and without stiffeners.

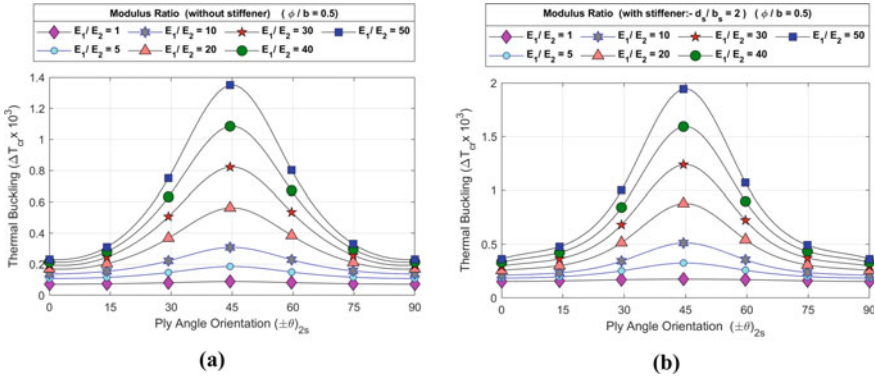


Fig. 6 Variation in the thermal buckling for different ply angles with increasing modulus ratios with cutout ratio $\phi/b = 0.5$ **a** without stiffener and **b** with stiffener around the cutout

However, the percentage change in thermal buckling between stiffened and unstiffened panels decreased at higher modulus ratios. For example, in $(\pm 45)_{2s}$ ply-angle laminate, with modulus ratio = 1, the percentage change in ΔT_{cr} is 96%, while with modulus ratio = 50, it is 44.2%. It is also observed that ply-angle variations have no meaningful effect on ΔT_{cr} for modulus ratio = 1 (i.e., isotropic), which agrees with the [20] studies, which are also valid for cutout panels with and without stiffeners.

3.2.3 Effect of Boundary Conditions and Thermal Expansion Ratios (α_1/α_2) for Cutout Panels with and Without Stiffeners

The effect of change in boundary conditions with varying thermal expansion ratios (α_1/α_2) for $(\pm 45)_{2s}$ panels with and without stiffeners is analyzed with a cutout ratio = 0.5, as shown in Table 4. That denotes that as the α_1/α_2 ratio raised, the thermal buckling decreased irrespective of boundary restrictions. However, it was also observed that the higher the α_1/α_2 ratio, the lower the thermal buckling rate. It is found that for clamped conditions, the thermal buckling resistance is most elevated. For stiffened cutout, panels have higher ΔT_{cr} than without, irrespective of α_1/α_2 . However, the percentage change increased with higher α_1/α_2 ratios. For example, in the supported boundary condition, for α_1/α_2 ratio = 1, the percentage change is found to be 36%, while for α_1/α_2 ratio = 35, it is 45%. Moreover, this change is found to decrease with boundary constraints.

3.2.4 Effect of Stiffener Depth Ratio (d_s/b_s) for Different Ply-Angle Orientations

The ply-angle orientation $(\pm\theta)_{2s}$ for different stiffener depth ratios (d_s/b_s) in the range of 1–10 is studied and analyzed for panel with $\phi/b = 0.5$ and is shown in

Table 4 Variations in ΔT_{cr} for $(\pm 45)_{2s}$ cutout panels ($\phi/b = 0.5$) with and without stiffener under different boundary conditions and α_1/α_2 ratios

Thermal expansion ratio (α_1/α_2)	SSSS		CCSS		CCCC	
	Without stiffener	With stiffener	Without stiffener	With stiffener	Without stiffener	With stiffener
1	714.8	970.8	723.07	979.44	752.73	1003.8
5	601.34	831.4	608.3	838.9	633.25	860.27
10	501.78	704.85	507.59	711.29	528.41	729.73
15	430.51	611.72	435.49	617.35	453.35	633.55
20	376.96	540.32	381.32	545.33	396.96	559.76
25	335.26	483.84	339.14	488.35	353.05	501.35
30	301.87	438.05	305.36	442.14	317.89	453.97
35	274.53	400.18	277.7	403.93	289.09	414.77

Table 5. The study is carried out for the same volume, equal to the cutout portion of the panel. It is understood that as the ply angle increases from $\theta = 0^0$ to $\theta = 45^0$, the percentage change in thermal buckling between any two successive d_s/b_s ratios decreases. It may be because the reduction in thickness of stiffener increases the thermal exposed area. It also signified that the minimum thermal buckling difference was observed at $\theta = 45^0$. Further, increase in ply angle from $\theta = 45^0$ to $\theta = 90^0$, the percentage change in thermal buckling increases and is determined to hold a maximum in $\theta = 90^0$.

Table 5 Variations in ΔT_{cr} for $(\pm\theta)_{2s}$ cutout panels ($\phi/b = 0.5$) with different stiffener d_s/b_s ratios

d_s/b_s ratio	$\theta = 0^0$	$\theta = 15^0$	$\theta = 30^0$	$\theta = 45^0$	$\theta = 60^0$	$\theta = 75^0$	$\theta = 90^0$
1	307.81	385.68	754.56	1477.7	755.51	386.04	307.96
2	304.38	382.71	751.04	1477.2	752.08	383.08	304.53
3	301.96	380.4	748.4	1475	749.51	380.77	302.11
4	300.42	378.9	746.62	1473.2	747.79	379.27	300.58
5	299.4	377.89	745.36	1471.8	746.5	378.27	299.56
6	298.69	377.19	744.43	1470.7	745.69	377.57	298.85
7	298.18	376.69	743.71	1469.9	745.01	377.07	298.35
8	297.81	376.32	743.15	1469.3	744.48	376.7	297.97
9	297.53	376.04	742.7	1468.7	744.05	376.43	297.7
10	297.33	375.84	742.34	1468.3	743.71	376.22	297.5

4 Conclusions

The comparison of thermal buckling has been made with the previous studies and holds good agreement for the laminated plates. The tasks are carried out with heterosis plate element and quadratic beam element in the present formulation. The square panels with centrally placed circular cutout are compared with the panels with stiffener (with its depth to width ratio equal to 2) placed encompassing the circular cutout corresponding to that volume separated of panel's cutout part. A few noteworthy points are extracted from the present study and are detailed as follows:

- The buckling variation within smaller cutouts with/without stiffener is not that significant, and hence, the smaller-sized cutouts may be neglected within the plate.
- The modular ratio and ply-orientation notably influence the thermal buckling resistance concerning plates with and without stiffeners. Toward any given ply angle, the thermal buckling detention progresses beside an increase in the modular ratio, which is significant for $(\pm 45)_{2s}$ ply-orientation. It is insignificant for $(\pm 0)_{2s}$ and $(\pm 90)_{2s}$ ply-orientations.
- An increase in boundary constraint significantly increases the thermal buckling resistance. Simply support boundary condition has the least thermal buckling, while clamped experienced the highest.
- Higher the value of α_1/α_2 , the higher the thermal buckling resistance for stiffened panels.
- The panel with $(\pm 45)_{2s}$ has the highest thermal buckling resistance for either cutout panels with and without stiffener. However, for modulus ratio = 1, it does not affect either the ply angle or the panels with and without stiffener.
- The stiffener depth ratio notably influences the thermal buckling aspects of each panel. The plate's thermal buckling stability diminishes by increasing the stiffener depth ratio for a given cutout size.

References

1. Timoshenko SP, Gere JM (1961) Theory of elastic stability. New York, McGraw-Hill
2. Reddy JN, Phan ND (1985) Stability and vibration of isotropic, orthotropic and laminated plates according to a higher-order shear deformation theory. *J Sound Vibration* 98(2):157–170
3. Noor AK, Burton WS (1992) Three dimensional solutions for thermal buckling of multilayered anisotropic plates. *J Eng Mech* 18(4):683–701
4. Wu CH, Tauchert TR (1980) Thermoelastic analysis of laminated plates in symmetric specially orthotropic laminates. *J Therm Stress* 3(2):247–59
5. Chen L-W, Chen L-Y (1987) Thermal buckling of laminated composite plates. *J Therm Stress* 10(4):345–356
6. Chen WJ, Lin PD, Chen LW (1991) Thermal buckling behavior of thick composite laminated plates under non-uniform temperature distribution. *Comput Struct* 41(4):637–45
7. Prabhu M, Dhanaraj R (1994) Thermal buckling of laminated composite plates. *Comput Struct* 53(5):193–204

8. Shi YC et al (1999) Thermal postbuckling of composite plates using the finite element modal co-ordinate method. *J Therm Stress* 22(6):595–614. doi: <https://doi.org/10.1080/014957399280779>
9. Matsunaga H (2005) Thermal buckling of cross-ply laminated composite and sandwich plates according to a global higher-order deformation theory. *Compos Struct* 68(4):439–54. doi: <https://doi.org/10.1016/j.compstruct.2004.04.010>
10. Topal U, Uzman Ü (2008) Thermal buckling load optimization of laminated composite plates. *Thin-Walled Struct* 46(6):667–75. doi: <https://doi.org/10.1016/j.tws.2007.11.005>
11. Shiau L-C et al (2010) Thermal buckling behavior of composite laminated plates. *Compos Struct* 92(2):508–14. doi: <https://doi.org/10.1016/j.compstruct.2009.08.035>
12. Ounis H et al (2014) Thermal buckling behavior of laminated composite plates: a finite-element study. *Front Mech Eng* 9(1):41–49. doi: <https://doi.org/10.1007/s11465-014-0284-z>
13. Topal U, Uzman Ü (2010) Effect of rectangular/circular cutouts on thermal buckling load optimization of angle-ply laminated thin plates. *Sci Eng Compos Mater* 17(2). doi: <https://doi.org/10.1515/SECM.2010.17.2.93>
14. Ounis H, Belarbi MO (2017) Thermal buckling behaviour of laminated composite plates with cut-outs. *J Appl Eng Sci Technol* 3(2):63–69
15. Devarajan B, Kapania RK (2020) Thermal buckling of curvilinearly stiffened laminated composite plates with cutouts using isogeometric analysis. *Compos Struct* 238:111881. doi: <https://doi.org/10.1016/j.compstruct.2020.111881>
16. Rajanna T et al (2018) Effect of reinforced cutouts and ply-orientations on buckling behavior of composite panels subjected to non-uniform edge loads. *Int J Struct Stab Dyn* 18(04):1850058. doi: <https://doi.org/10.1142/S021945541850058X>
17. Patel SN, Sheikh AH (2016) Buckling response of laminated composite stiffened plates subjected to partial in-plane edge loading. *Int J Comput Meth Eng Sci Mech* 17(5–6):322–38. doi: <https://doi.org/10.1080/15502287.2016.1231235>
18. Subash Chandra KS, Rao KV, Rajanna T (2021) Hygro-thermo-mechanical vibration and buckling analysis of composite laminates with elliptical cutouts under localized edge loads. *Int J Struct Stab Dyn* 2150150. doi: <https://doi.org/10.1142/S0219455421501509>
19. Subash Chandra KS, Rao KV, Rajanna T (2020) A parametric study on the effect of elliptical cutouts for buckling behavior of composite plates under non-uniform edge loads. *Latin American J Solids Struct* 17(8):e328. doi: <https://doi.org/10.1590/1679-78256225>
20. Jones RM (2005) Thermal buckling of uniformly heated unidirectional and symmetric cross-ply laminated fiber-reinforced composite uniaxial in-plane restrained simply supported rectangular plates. *Composites. Part A, Appl Sci Manuf* 36(10):1355–1367

Effect of Isolated Wind Incidence on Local Peak Pressure



Supriya Pal, Ritu Raj, and S. Anbukumar

Abstract This paper presents the results of the experimental investigations carried out on a Modified triangle shape tall building to evaluate its aerodynamic performance of such. The purpose is to study the associated environment arising due to wind forces in isolated conditions on a building model of scale 1:300 with a prototype having 180 m height. Local peak pressure coefficients for the isolated tall building are studied by using boundary layer wind tunnel experiments. Two wind incidences, 0° and 180° , are considered for the current isolated study. From the perspective of cladding as well as structural design, the experimental findings are analyzed and presented. A higher number of critical positions facing maximum peak pressure and maximum peak suction are observed at 180° of wind incidence as compared to that at 0° wind incidence. The highest suction at 180° wind incidence is -1.25 , which is nearly 36% stronger than the highest suction at 0° wind incidence (-0.92). The maximum fluctuation between maximum peak pressure (0.85) and minimum peak pressure (-0.85) is observed at Face-I of 180° of wind incidence. Due to the difference in the direction of wind incidence, the test results showed significant variations in the related wind environment around the building model. Isolated wind incidence condition at 180° is critical as compared to 0° wind incidence.

Keywords Tall buildings · Peak pressure coefficient · Turbulence · Suction · Vortex

1 Introduction

Building materials and practices have advanced recently, resulting in a new generation of taller and flexible constructions [1]. Tall buildings are more exposed to wind oscillations and dynamic loading [2], and that is why shape optimization is considered to increase wind resistance [3]. Wind-induced lateral movement of tall structures can agitate residents (especially those who are on the higher levels) and inflict structural

S. Pal (✉) · R. Raj · S. Anbukumar
Delhi Technological University, New Delhi, India
e-mail: supriya8788@gmail.com

© The Author(s), under exclusive license to Springer Nature Singapore Pte Ltd. 2023
M. S. Ranadive et al. (eds.), *Recent Trends in Construction Technology and Management*, Lecture Notes in Civil Engineering 260,
https://doi.org/10.1007/978-981-19-2145-2_70

949

damage [4] and, thus, is considered as one of the main serviceability criteria while designing tall buildings [5]. Underspecification can have massive impacts, necessitating extensive experimental and analytical research to better comprehend more realistic wind-induced situations [6].

With the development of structural systems and building materials, the possibility of the construction of unconventional shape tall buildings is very high. Wind-induced effects on various unconventional shape isolated tall building models have been investigated through a series of experimental and numerical work, including “+” [7–9], “H” [10–12], “Z” [13], “L” and “U” [14], “L” and “T” [15], “C” [16], “L” [17], “E” [18, 19] and “Triangle” shape building with various configurations [20–23] have investigated “Fish Shape” model; [24] have studied Remodel triangle shape building; [25] investigated two Fish-plan shape buildings, “Triangle” and “Y” [26], “Triangle”, “Y”, and “Circular” [27] shape buildings. In addition to studying the aforementioned unusually shaped tall building models, research has been conducted to better grasp the notion of aerodynamic shape optimization [28–31]. Despite the fact that many peculiar shaped structures are being investigated these days due to the versatile requirements, the majority of the studies are limited to the examination of mean coefficients of pressure and forces. Wind analysis is a project of tremendous unconventionality if the building’s plan is unique because of the flow patterns originating from the exchanges of the wind with the elements. Because of the building’s unique shape, peak pressure and suctions on the walls must be investigated, since they frequently cause damage in high-wind scenarios [21, 32, 33].

The formation of high turbulence in the wind at the principal building model causes the fluctuation in wind-induced load. The goal of researching wind flow characteristics surrounding any altered building plan is to compare the wind flow pattern on all of the building’s walls to that of typical square or rectangular-shaped buildings [34]. The research concentrated on the experimental investigation of peak pressure and suctions coming at a face on an isolated Modified triangular shape building model for various isolated wind incidence directions of 0° and 180° . Isolated Modified triangle plan buildings are adapted triangular plan shape buildings that are typically erected on triangular plots; the best example being the Flatiron Building in New York (see Fig. 1). Small adjustments to the exterior building shape, according to [35], could result in force and moment diminution. Modified triangle-shaped buildings (Fig. 2) that are modified triangular plan shaped buildings provide better room availability as compared to triangular plan shaped buildings. The results demonstrate that understanding the position of high pressure and high suction zones is critical for cladding surface design since it creates considerably huge compression and strong tension on the external surface, resulting in cladding failure. Furthermore, the findings of this study can help structural designers choose from a variety of recent technologies in order to meet a structure’s failure and serviceability standards in severe wind conditions.



Fig. 1 New York City's flatiron building

2 Experimental Work's Setup

Experiments were conducted in Roorkee's boundary layer wind tunnel in the Department of Civil Engineering at IIT Roorkee. The studies were conducted at a geometric scale of 1:300 in a simulated wind flow of terrain category II as per IS 875: part 3, where the mean wind velocity profile followed the power-law with a power exponent of 0.22. Figure 3 depicts the mean wind velocity profile. The average wind velocity at the building model's roof height was 10 m/s.

Measurements are made on a pressure model made of a transparent Perspex sheet for conditions of isolated wind incidence at 0° and 180° as shown in Fig. 4c. $H/D = 3$ was the height-to-breadth ratio. The models depicted full-size buildings with a height of 180 m at the specified geometric scale of 1:300. A total of 273 pressure taps, 39 on each level (Fig. 4b), are installed on the walls of the principal building. The pressure points are located at seven different heights levels of 10, 60, 180, 300, 420, 540, and 590 mm from the bottom as shown in Fig. 4a to obtain a proper distribution of wind pressure on all the faces of models.

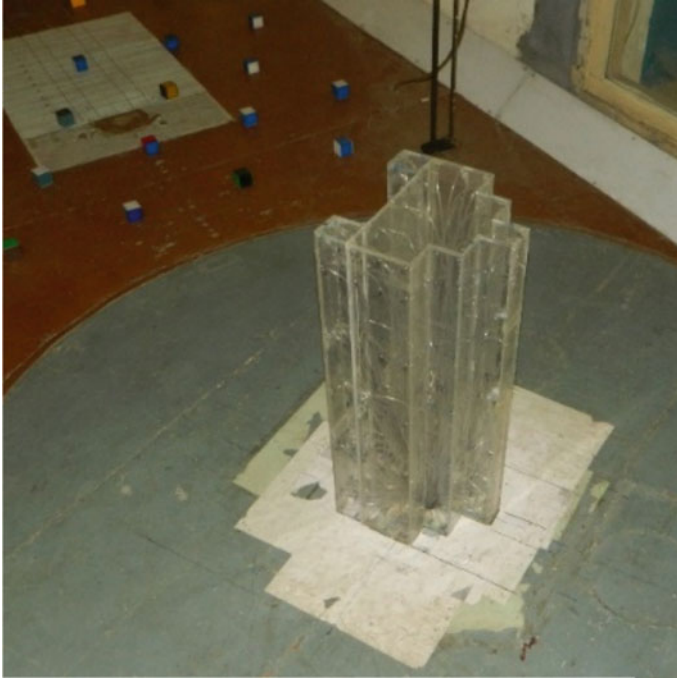


Fig. 2 Downscale model in the wind tunnel

3 Results and Discussions

The peak pressure is the maximum and minimum pressure coefficients that come at a pressure point over the time of pressure observation. The peak maximum pressure coefficient ($C_p^\Delta(i, \theta)$) is determined for each pressure tapping point using the formula Eq. (1):

$$C_p^\Delta(i, \theta) = \frac{\text{Peak maximum } P_a \text{ pressure point "i", at wind direction } \theta}{0.6 V^2} \quad (1)$$

The peak minimum pressure coefficient ($C_p^\nabla(i, \theta)$) is determined for each pressure tapping point using the formula Eq. (2):

$$C_p^\nabla(i, \theta) = \frac{\text{Peak minimum } P_a \text{ pressure point "i", at wind direction } \theta}{0.6 V^2} \quad (2)$$

where P_a denotes the pressure at the corresponding pressure tapping point, and V is the mean wind velocity in m/s at the top of the building model, which in this case is 10 m/s.

Fig. 3 Mean wind velocity profile

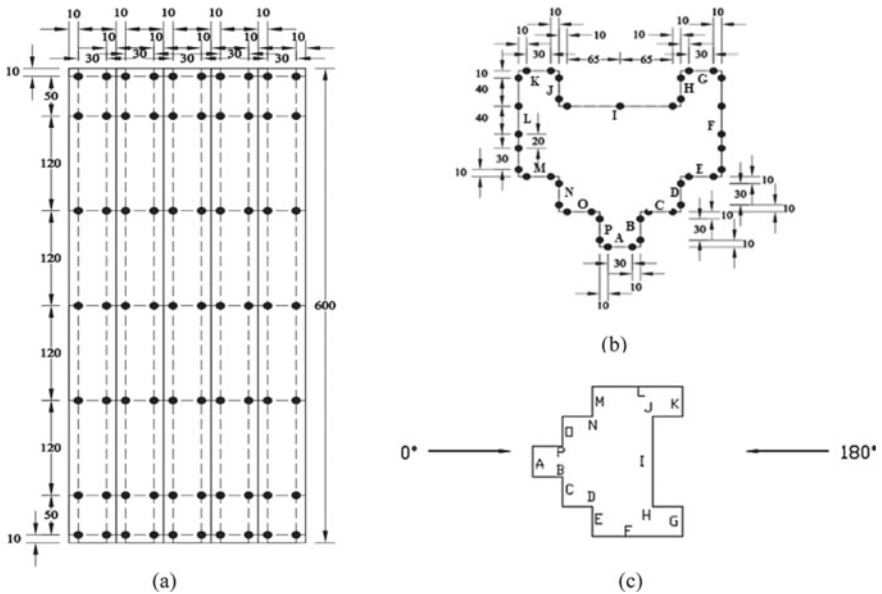
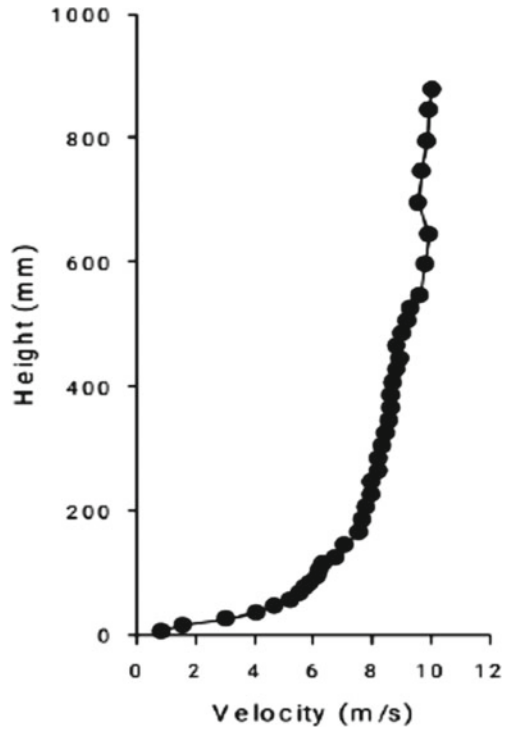


Fig. 4 Pressure tapping layout of modified triangular-shaped model **a** elevation, **b** plan view, and **c** directions of wind incidence (all units: mm)

Peak pressure coefficients show the fluctuating component of induced pressure over a period. A thorough comparative study of the distribution of peak maximum and peak minimum pressure coefficient along the building periphery at certain observation height levels is presented in the present study. This study is mainly carried out to check the critical points for wind conditions at both the 0° and 180° isolated wind incidence directions. H is the total height of the building model, i.e., 600 mm. Figure 5 shows the variation of peak maximum and minimum C_p along the building periphery at observation height levels of 0.9H, 0.5H, 0.3H, and 0.1H for 0° isolated wind incidence conditions. Face-E and Face-M at all the observation levels show both positive and negative peak pressures, and hence, the face has maximum turbulence. High fluctuation is seen due to flow turbulence prior to flow separation from the edges of Face-E and Face-M. At 0.3H, large fluctuation is seen at Face-G and Face-K with a large difference between peak pressure coefficients due to the converging stream of fluid flow. Face-A to Face-E and Face-M to Face-P show positive peak C_p at all the observation levels, whereas, due to positioning of faces, Face-F to Face-L show negative peak C_p . Maximum peak suction at all the observation levels is shown by Face-F and Face-L.

Figure 6 shows the variation of peak maximum and minimum C_p along the building periphery at observation height levels of 0.9H, 0.5H, 0.3H, and 0.1H for

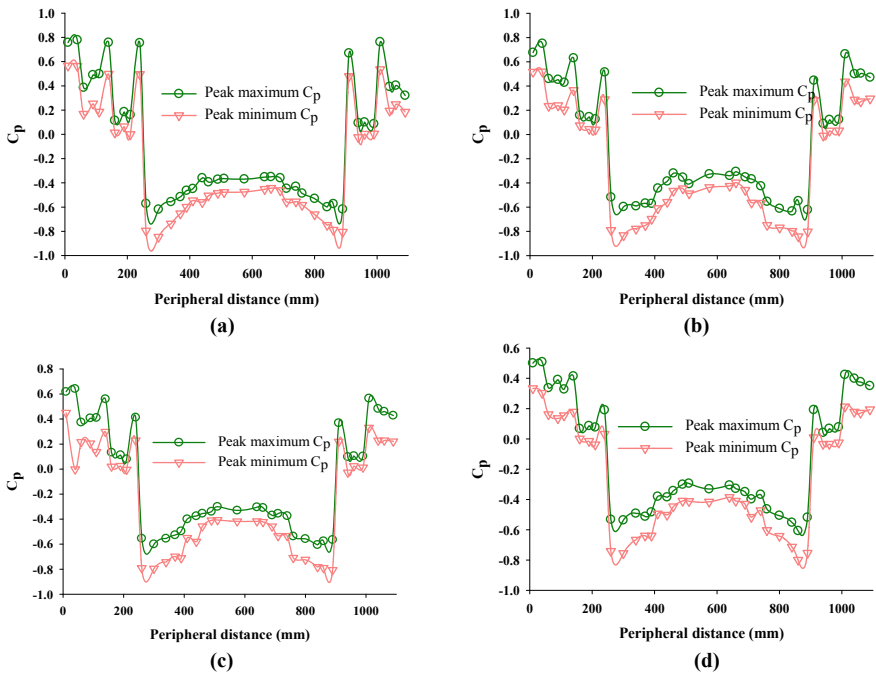


Fig. 5 Peak C_p along building periphery at **a** 0.9H, **b** 0.5H, **c** 0.3H, and **d** 0.1H for 0° isolated wind incidence

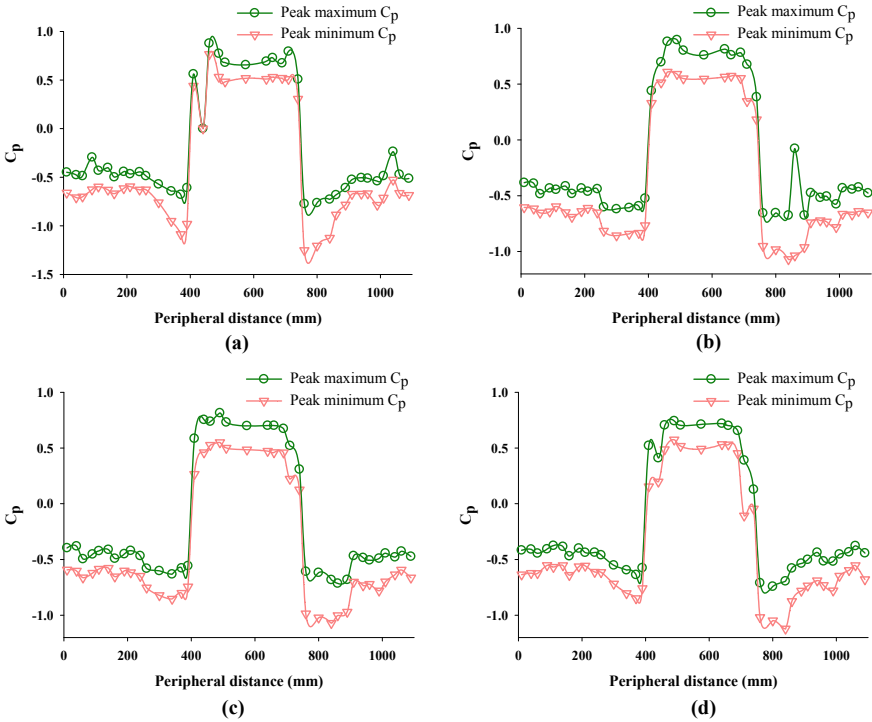


Fig. 6 Peak C_p along building periphery at **a** 0.9H, **b** 0.5H, **c** 0.3H, and **d** 0.1H for 180° isolated wind incidence

180° isolated wind incidence conditions. At this angle of wind incidence, no face shows transient behavior with both positive and negative peak C_p magnitudes due to the orientation of the model to the incoming wind. Due to the orientation of the model, Face-A to Face-F and Face-L to Face-P show negative magnitudes in peak maximum C_p and peak minimum C_p showing that the faces totally lie in the wake region. Maximum peak C_p is shown by Face-H at most of the observation levels as the wind is getting trapped between the adjacent edge of Face-H and Face-I, whereas, Peak minimum C_p of -1.25 is seen at Face-L at 0.9H.

For (a) 0° incident wind and (b) 180° incident wind circumstances, Fig. 7 displays the fluctuation of highest peak C_p and lowest peak C_p along the model’s faces. Figure 7a shows a significant disparity between the highest and lowest peak C_p magnitudes at Face-N and Face-D, owing to the highest turbulence at the face due to the faces’ depressed placement. Because Face-H and Face-J are on the leeward side and at depression, the difference in peak C_p between the highest and lowest magnitudes is the smallest. Because flow separation occurs from the faces, creating a suction area at the faces due to face orientation, Face-F and Face-L have the lowest peak C_p .

In Fig. 7b because of the windward orientation of the faces in the current circumstance, the highest peak C_p is seen at Face-H, followed by Face-I and Face-J. Given

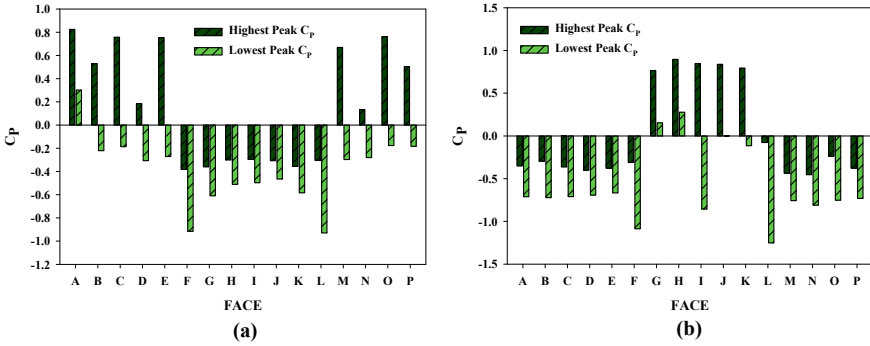


Fig. 7 Highest and lowest peak C_p along building façade for a 0° and b 180° wind incidences

that the incident wind forms eddies due to flow separation from these faces due to their direction, the lowest peak C_p is seen at Face-L, followed by Face-F. Face-I has the most turbulence, as evidenced by the difference in peak C_p between the highest and lowest magnitudes. The leeward Face-A, on the other hand, has a very steady condition with the least difference in the highest and lowest peak pressures.

Figures 8 and 9 show the critical points that are unfavorable pressure points for isolated 0° and 180° wind incidences, respectively. In Fig. 8, maximum peak pressure at Face-C and Face-E of 0.76 and 0.75, respectively, is seen at 540 mm height at 40 mm from the edge. Also, maximum peak pressure at Face-O of 0.76 is seen at 540 mm height at 40 mm from the edge. The highest peak maximum pressure is produced mainly due to the positioning of faces. The highest peak suction of -0.92 is produced at Face-F at 590 mm height and 10 mm from edge mainly due to top wash. Maximum fluctuation, i.e., the difference between peak maximum and minimum C_p is seen at Face-C at 540 mm height and 10 mm from the edge, at Face-B at 10 mm height and

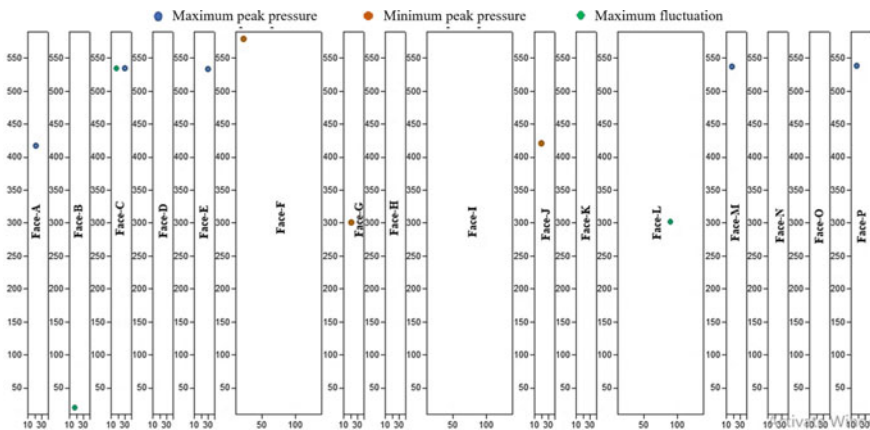


Fig. 8 Unfavorable positions on model for isolated 0° wind incidence condition

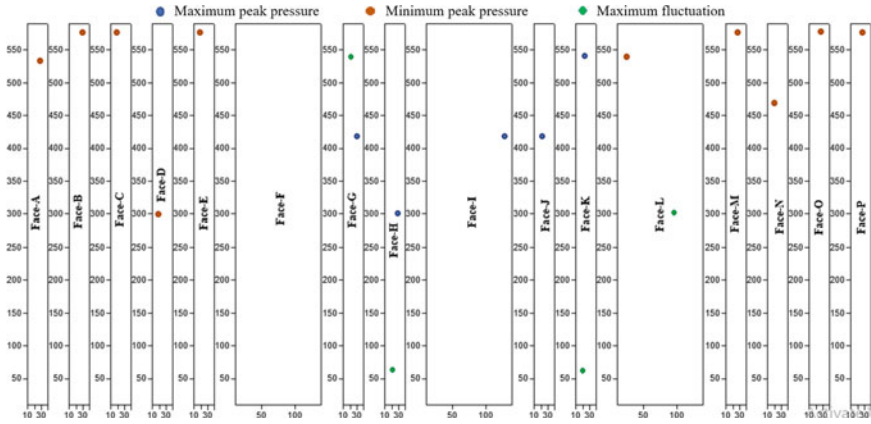


Fig. 9 Unfavorable positions on model for isolated 180° wind incidence condition

10 mm from the edge, and at Face-L at 300 mm height and 100 mm from the edge. The maximum difference between the peak values shows high turbulence areas in certain wind directions.

Figure 9 shows the critical points that are unfavorable pressure points for isolated 180° wind incidence conditions. Due to the orientation of the isolated model to the wind direction, higher peak pressure and peak suction are observed at the faces. The highest suction of -1.25 is manifested by Face-L at 540 mm height and 10 mm distance from the edge. Whereas, maximum peak pressure of 0.90 is manifested by Face-H at 300 mm height and 40 mm distance from the edge. The maximum fluctuation between peak pressures is seen at Face-F at 540 mm height and 10 mm distance from the edge.

4 Conclusion

Experiments are carried out to investigate the effects of varied wind directions on an isolated Modified triangle shape model. Peak pressure coefficients are calculated to find out the effect of fluctuating wind forces on various walls of the model at 0° and 180° wind incidence conditions. Due to the positioning of both faces and the fact that flow separation is prevalent at the faces, the smallest minimum peak pressure at both wind incidences is obtained at Face-F and Face-L. Critical positions in terms of maximum peak pressure and maximum peak suction are shown in order to highlight the unfavorable positions in both directions of wind incidences. A higher number of critical positions facing maximum peak pressure and maximum peak suction are observed at 180° of wind incidence as compared to that at 0° wind incidence. The highest suction at 180° wind incidence is -1.25 , which is nearly 36% stronger than the highest suction at 0° wind incidence (-0.92). The maximum fluctuation between

maximum peak pressures (0.85) and minimum peak pressure (-0.85) is observed at Face-I of 180° of wind incidence mainly due to the higher dimension of the exposed face as compared to that at 0° wind incidence condition. Due to the difference in the direction of wind incidence, the test results showed significant variations in the related wind environment around the building model. Isolated wind incidence condition at 180° is critical as compared to 0° wind incidence.

References

1. El-Heweity MM, Abdelnaby MH, Eshra EM (2019) Numerical simulation of buffeting longitudinal wind forces on buildings. *Alex Eng J* 58:225–236. <https://doi.org/10.1016/j.aej.2018.08.001>
2. Xu A, Xie ZN, Fu JY, Wu JR, Tuan A (2014) Evaluation of wind loads on super-tall buildings from field-measured wind-induced acceleration response. *Struct Design Tall Spec Build* 23:641–663. <https://doi.org/10.1002/ta.1065>
3. Zheng C, Xie Y, Khan M, Wu Y, Liu J (2018) Wind-induced responses of tall buildings under combined aerodynamic control. *Eng Struct* 175:86–100
4. Aly AM (2013) Pressure integration technique for predicting wind-induced response in high-rise buildings. *Alex Eng J* 52:717–773. <https://doi.org/10.1016/j.aej.2013.08.006>
5. Farouk MI (2016) Check the comfort of occupants in high rise building using CFD. *Ain Shams Eng J* 7:953–958
6. Raj R, Jha S, Singh S, Choudhary S (2020) Response analysis of plus shaped tall building with different bracing systems under wind load. *Int J Adv Res Eng Technol (IJARET)* 11(3):371–380
7. Chakraborty S, Dalui SK, Ahuja AK (2014) Wind load on irregular plan shaped tall building—a case study. *Wind Struct* 19(1):59–73
8. Chakraborty S, Dalui SK, Ahuja AK (2013) Experimental and numerical study of surface pressure on ‘+’ plan shape tall building. *J Civ Eng* 8:251–262
9. Raj R, Ahuja AK (2013) Wind loads on cross shape tall buildings. *J Acad Indus Res (JAIR)* 2(2)
10. Cheng L, Kit ML, Wong SY (2015) POD analysis of crosswind forces on a tall building with square and H-shaped cross sections. *Wind Struct an Int J* 21(1):63–84
11. Nagar SK, Raj R, Dev N (2020) Experimental study of wind-induced pressures on tall buildings of different shapes. *Wind Struct* 31(5):441–453. doi: <https://doi.org/10.12989/was.2020.31.5.441>
12. Nagar SK, Raj R, Dev N (2021) Proximity effects between two plus-plan shaped high-rise buildings on mean and RMS pressure coefficients. *Scientia Iranica*. doi: <https://doi.org/10.24200/SCI.2021.55928.4484>
13. Paul R, Dalui SK (2016) Wind effects on ‘Z’ plan-shaped tall building: a case study. *Int J Adv Struct Eng* 8:319–335
14. Gomes MG, Rodrigues AM, Mendes P (2005) Experimental and numerical study of wind pressures on irregular-plan shapes. *J Wind Eng Ind Aerodyn* 93:741–756
15. Amin JA, Ahuja AK (2011) Experimental study of wind-induced pressures on buildings of various geometries. *Int J Eng Sci Technol* 3(5):1–19
16. Mallick M, Kumar A, Patra KC (2019) Experimental investigation on the wind-induced pressures on C-shaped buildings. *KSCE J Civ Eng* 23(8):3535–3546
17. Li Y, Li SQ, Chen F (2017) Wind tunnel study of wind-induced torques on L-shaped tall buildings. *J Wind Eng Ind Aerodyn* 167:41–50
18. Bhattacharyya B, Dalui SK, Ahuja AK (2014) Wind induced pressure on ‘E’ plan shaped tall buildings. *Jordan J Civ Eng* 8(2). <https://doi.org/10.1016/j.engstruct.2018.08.031>

19. Bhattacharyya B, Dalui SK (2020) Experimental and numerical study of wind-pressure distribution on irregular-plan-shaped building. *J Struct Eng* 146(7):04020137. [https://doi.org/10.1061/\(ASCE\)ST.1943-541X.0002686](https://doi.org/10.1061/(ASCE)ST.1943-541X.0002686)
20. Bandi EK, Tamura Y, Yoshida A, Kim YC, Yang Q (2013) Experimental investigation on aerodynamic characteristics of various triangular-section high-rise buildings. *J Wind Eng Ind Aerodyn* 122:60–68
21. Bandi EK, Tanaka H, Kim Y, Ohtake K, Tamura Y (2013b) Peak pressures acting on tall buildings with various configurations. *Int J High Rise Build* 2:229–244
22. Pal S, Raj R, Anbukumar S (2021) Comparative study of wind induced mutual interference effects on square and Fish-plan-shape tall buildings. *Sādhanā, Indian Acad Sci* 46:86. <https://doi.org/10.1007/s12046-021-01592-6>
23. Tamura Y, Tanaka H, Ohtake K, Kim YC, Yoshida A, Bandi EK, Xu X, Yang Q, Aerodynamic control of wind-induced vibrations and flow around super-tall buildings. In: Proceedings of the 6th international conference advance experience structural engineering international working advance smart mater, smart structures technology, Urbana-Champaign
24. Pal S, Raj R, Anbukumar S (2021) Bilateral interference of wind loads induced on duplicate building models of various shapes. *Latin American J Solids Struct* 18(5):e386. <https://doi.org/10.1590/1679-78256595>
25. Pal S, Raj R (2021) Evaluation of wind induced interference effects on shape remodeled tall buildings. *Arab J Sci Eng*. <https://doi.org/10.1007/s13369-021-05923-x>
26. Ming G (2010) Wind-resistant studies on tall buildings and structures. *Sci China Technol Sci* 53(10):2630–2646. <https://doi.org/10.1007/s11431-010-4016-2>
27. Hayashida H, Iwasa Y (1990) Aerodynamic shape effects of tall buildings for vortex induced vibration. *J Wind Eng Ind Aerodyn* 33:237–242
28. Ahmed E, Bitsuamlak G, Damatty AE (2017) Enhancing wind performance of tall buildings using corner aerodynamic optimization. *Eng Struct* 136:133–148
29. Sharma A, Mittal H, Gairola A (2018) Mitigation of wind load on tall buildings through aerodynamic modifications: review. *J Build Eng* 18:180–194
30. Stathopoulos T, Zhou Y (1993) Numerical simulation of wind induced pressures on buildings of various geometries. *J Wind Eng Ind Aerodyn* 46–47:419–430
31. Xie J (2012) Aerodynamic optimization in super-tall building designs. In: The Seventh International Colloquium on Bluff Body Aerodynamics and its Applications (BBAA7) Shanghai, China (2012), pp 2–6
32. Stathopoulos T, Saathoff P (1991) Wind pressure on roofs of various geometries. *J Wind Eng Ind Aerodyn* 38(2–3):273–284. [https://doi.org/10.1016/0167-6105\(91\)90047-z](https://doi.org/10.1016/0167-6105(91)90047-z)
33. Surry D, Djakovich D (1995) Fluctuating pressures on models of tall buildings. *J Wind Eng Ind Aerodyn* 58(1–2):81–112. [https://doi.org/10.1016/0167-6105\(95\)00015-j](https://doi.org/10.1016/0167-6105(95)00015-j)
34. IS: 875-Part-3 (2015) Code of practice for design loads (other than earthquake loads) for buildings and structures-wind loads. India 2015
35. Gaur N, Raj R (2020) Wind load optimisation by aerodynamic mitigation techniques for tall buildings—a review. *Solid State Technol* 63(2s):5968–5986

Investigation of Performance of Perforated Core Steel Buckling Restrained Brace



Prajakta Shete, Suhasini Madhekar, and Ahmad Fayeeg Ghowsi

Abstract Energy Dissipating Devices (EDDs) are used to control structural vibration. Buckling-Restrained-Braces (BRBs) are observed as one of the most effective structural techniques used for resisting lateral forces generated due to earthquakes as they exhibit symmetric load-deformation behavior. The use of all-steel BRB is getting widespread because of its advantages over the traditional concrete BRB. All-steel BRB is entirely made of steel by sandwiching the core plate with the outer restraining element. Perforated core plate BRB is a recently innovated EDD. The steel core segment is perforated in different configurations along the length to dissipate the seismic energy. In this study, a numerical investigation is carried out to predict all-steel perforated core BRB (PBRB) cyclic response. The numerical models are validated with the previous experimental study. Numerical finite element modeling is carried out using ABAQUS software. This validated model is further used to carry out the investigation of the cyclic performances of PBRBs. Various configurations are considered to study the cyclic performance of PBRBs. Axial strength, hysteresis response, and energy dissipation are observed to evaluate the cyclic performances of PBRBs. Results show that the configuration of PBRB has a substantial impact on the stability of perforated BRB.

Keywords Buckling restrained brace · Perforated buckling restrained brace · Finite element analysis · Axial strength · Hysteresis response

1 Introduction

Buckling restrained brace (BRB) is one of the most effective lateral load resisting systems. BRB is a structural brace component designed to permit the structure

P. Shete (✉) · S. Madhekar
Department of Civil Engineering, COEP, Pune, Maharashtra 411005, India
e-mail: ps15.civil@coep.ac.in

A. F. Ghowsi
Department of Civil Engineering, IIT Delhi, New Delhi 110 016, India

© The Author(s), under exclusive license to Springer Nature Singapore Pte Ltd. 2023
M. S. Ranadive et al. (eds.), *Recent Trends in Construction Technology and Management*, Lecture Notes in Civil Engineering 260,
https://doi.org/10.1007/978-981-19-2145-2_71

961

to survive earthquake-induced cyclic lateral loadings. Traditional concrete BRB involves a steel core, casing, and bond-preventing layer or unbonding layer. The unbonding layer separates the outer casing from the inner steel core. This permits the steel core to take the axial forces in the bracing component. The encasing member restrains the brace from buckling in compression. It comprises a square, rectangular, or circular hollow structural steel casing filled with mortar or concrete [1]. By preventing the buckling action of the brace, a symmetric and stable hysteresis curve is achieved that dissipates a high amount of energy in every single cycle. As the steel core is restrained from buckling action, it experiences nearly uniform axial strains. The core cross-sectional area can be considerably less than that of conventional braces as its behavior is not restricted by buckling. BRB is a displacement-dependent EDD that works after yielding. The middle portion of the core is designed to yield inelastically and rigid; the non-yielding lengths are provided on either end of the core plate. The enlarged cross-sectional area of the non-yielding segment confirms that it stays elastic, and thus plasticity is focused in the central portion of the steel core. The plastic hinges related to buckling do not form in properly designed and detailed BRBs. A significant numerical study has been done to reduce the seismic response using BRB frames [2, 3]. Celik and Bruneau [4] highlighted the potential of BRBs for the rehabilitation of existing buildings and bridges. The overall behavior of the BRB core is affected by its length; moderate length BRB can efficiently dissipate energy [5]. Khampanit et al. [6] show that the friction among the core and the restraining segment of BRB may cause overstrength in compression and may cause overall flexural buckling of the outer core. An extensive numerical and experimental study has been carried out in the past, which distinguishes the promising seismic performances of BRBs.

All-steel BRB is getting widespread because of its lightweight, easy maintenance, inspection, simple fabrication, and erection [7]. All-steel BRB is entirely made of steel by sandwiching the core plate with the outer restraining element. A gap is required between the steel core and the restraining element to cater Poisson's expansion. The stoppers are provided to keep the outer casing in its proper position. Jiang et al. [8] demonstrated that buckling load and buckling mode are affected by the core length of BRB. Comprehensive research has been carried out by Ghowsi and Sahoo [9] to study the influence of loading sequence and the restraining parameters of all-steel BRBs. They concluded that the loading history affects the energy dissipation demand. Shete et al. [10] carried out a detailed numerical analysis of all-steel BRBs on varying core lengths and gaps and concluded that the interaction of these influencing parameters must be considered to obtain a stable hysteretic performance.

The research work by Zhou et al. [11] reveals the requirement to keep the yielding of the core limited within the specific portion and keep the ends elastic and stable. This can be achieved by weakening the yielding portion, and weakening can be done by perforating the yielding steel core plate. [12] were the first to use the perforated core in BRB. Perforated core plate BRB is a recently innovated EDD. The core steel segment is perforated in different configurations along the length to dissipate the seismic energy. The previous study shows improper perforated plate configuration may cause premature buckling of the strong axis and cracks in the perforated zone.

Perforations in the BRB can be arranged as per the strength requirement, and hence there is a need for further research to investigate the best suitable arrangement and configuration.

In the present study, the research is carried out to evaluate the impact of the configuration of PBRB, location, and size of the perforated zone on the cyclic behavior of the PBRB. The evaluation compares the hysteresis response, axial strength, core fracture pattern, and energy dissipation.

2 Numerical Study

To explore the influence of perforated core and its configuration on the cyclic performance of BRB, finite element analysis has been carried out in ABAQUS software. In this study, a numerical investigation has been conducted to observe the cyclic behavior of all-steel perforated core BRB. The numerical models are calibrated with the previous experimental study, and the particulars of finite element simulation are discussed in the subsequent section. Three different configurations, hexagonal, circular, and rectangular, are considered to evaluate the cyclic effect of PBRB. The yielding core length of PBRB is kept constant for all cases. Further to study the effect of the size of perforation, two configurations, namely circular and rectangular, are considered.

2.1 *Finite Element Analysis*

To evaluate the impact of the perforations and different configurations on the cyclic behavior of the PBRB, rectangular, circular, and hexagonal shapes are considered to keep the cross-sectional area of the core plate constant. The numerical finite element model used for the parametric study is calibrated with the previous experimental work conducted by Wu et al. (2014). All-steel BRB with the core cross-section 160 mm \times 20 mm is considered with a uniform core length of 1600 mm, as considered in the experimental work. The stoppers on either side of the steel core segment in the central portion along the length are provided, as shown in Fig. 1. The gap size between the steel core and the restrainers is provided as 1 mm along the strong surface and 2 mm along weak surfaces. The results of the experimental work done by Wu et al. [13] are used to validate the BRB model. Further, this BRB model is perforated in a different configuration to study the effect of the perforated BRB core and its configuration, as discussed earlier.

General-purpose eight-noded hexahedral first order (C3D8R) element with Hourglass control and reduced integration technique is used to model the brace in ABAQUS. Each node of C3D8R elements has three degrees of freedom. In case of the hexahedral element throughout, constant volumetric strain is considered. Hexahedral elements offer the solution of equal precision at less cost. The convergence rate is

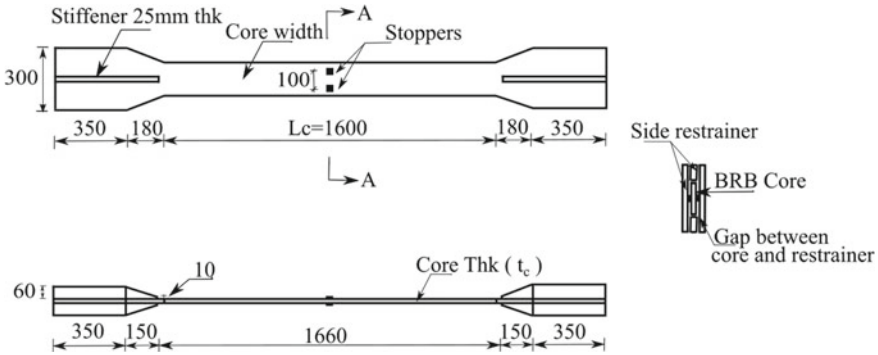


Fig. 1 Details of all-steel BRB

high, and their mesh sensitivity is less than the tetrahedral elements. The reduced integration technique decreases the computational time by using the lower order integration to form the element stiffness. Hourglass control prevents shear locking and volumetric control. Similar to past numerical modeling techniques [14, 15] are adopted in the present work.

The primary purpose of the restrainer segment is to offer adequate constraint to the buckling of the BRB core segment prior to compression yielding; hence at the restrainer interfaces, perfect contact with tie constraints has been assumed. In the experimental work by Wu et al. [13], the restrainers are connected with high-strength bolts. The fundamental research by [14] shows that the transverse flexural distortion of the restraining elements between the bolts is substantial compared to the axial distortion of bolts. Hence, they are not modeled in the finite element analysis. For surface-to-surface contact between the core and the restrainer segment, friction coefficient 0.15 in the tangential direction and the hard contact in the normal direction are considered. The BRB behavior under cyclic loading conditions is modeled using the damage plasticity model, including the nonlinear isotropic and kinematic hardening behavior. Combined isotropic and kinematic hardening behavior is applied to model the elastoplastic material properties of the steel core element. All other casing portion is modeled as perfectly elastic. The loading direction effect on the inelastic cyclic behavior of material is considered by the combined isotropic and kinematic hardening model. Kinematic hardening represents the yield surface translation in stress space through back stress α . The change in the size of the yielding surface is described through isotropic hardening. Back stress represents the constant kinematic shift of the yield surface and is beneficial to model the effect of residual stresses. The kinematic hardening component $\dot{\alpha}$ is expressed as the combination of a linear kinematic term and a nonlinear relaxation term [16]

$$\dot{\alpha} = C \frac{1}{\sigma_0} (\sigma - \alpha) \dot{\epsilon}^p = \gamma \alpha \dot{\epsilon}^p \tag{1}$$

Table 1 Calibrated kinematic hardening parameters of steel core

σ_Y (MPa)	C (GPa)	γ	Q_∞ (MPa)	b
330	8	52	25	10

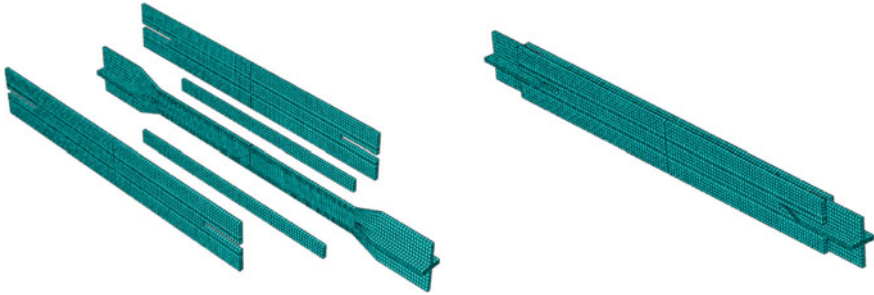


Fig. 2 All-steel BRB finite element model and assembled configuration

In Eq. (1), C represents the initial kinematic hardening modulus, and σ^0 is the initial yield stress, γ defines the rate at which the kinematic hardening modulus decreases with an increase in plastic deformation, $\dot{\epsilon}^p$ signifies the equivalent plastic strain rate, which considers the hardening and softening of the material as follows:

$$\sigma_0 = \sigma_Y + Q_\infty(1 - e^{-b\dot{\epsilon}^p}) \tag{2}$$

where σ_Y is the yield stress when plastic strain is zero, Q_∞ and b are the material parameters. Q_∞ is the maximum change in the size of the yield surface, and b is the rate at which the size of the yield surface changes as plastic straining develops. The calibrated kinematic hardening parameters of the steel core used in the present research work are given in Table 1. Young’s modulus of 200 GPa and Poisson’s ratio of 0.3 is used. Based on the first buckling mode, the initial global imperfection factor of Length/1000 is considered [17]. The typical finite element model used for validation purpose and the perforated BRB model is shown in Fig. 2.

2.2 Loading Protocol and Validation

The loading protocol considered for the experimental work by Wu et al. [13] has been selected for the present work, as shown in Fig. 3. Loading protocol signifies the gradually rising core displacements till a maximum of 3.5% core strain in an interval of 0.5%, monitored by constant fatigue cycles equivalent to 2% core strain. The loading protocol includes all possible effects on BRBs, such as the gradually increasing, decreasing, or constant displacements during a seismic event. For validation of finite

Fig. 3 Loading protocol

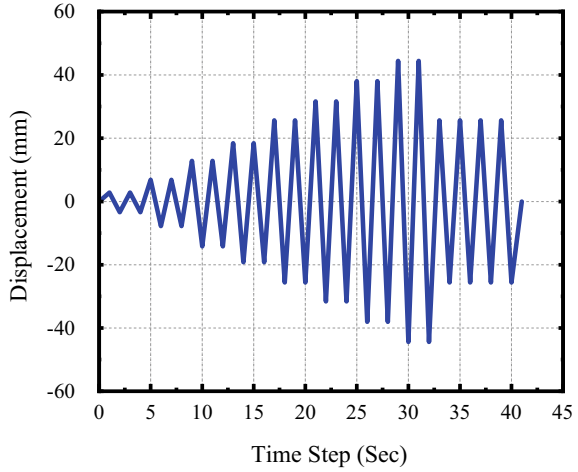
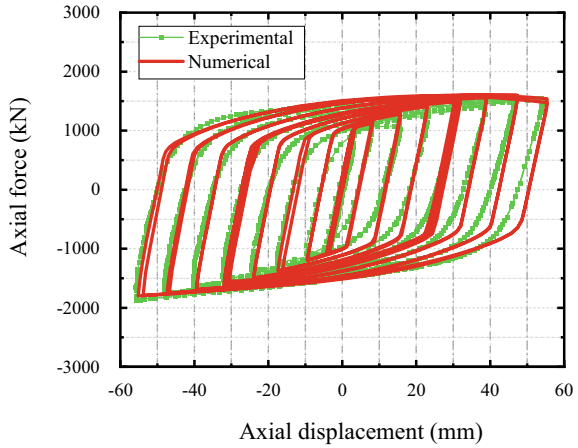


Fig. 4 Matching of hysteresis response



element models, the predicted hysteresis response of BRB is compared with the experimental work as discussed earlier. The hysteresis response, peak values of axial load, and hardening response at each cycle of the finite element model match the experimental results very well. 'Fig. 4' shows the hysteretic response of the validated numerical model and experimental result.

3 Results and Discussion

In the present research work, the influence of the configuration of PBRB is studied, and their seismic performances are evaluated with the hysteresis response, axial

strength, fatigue pattern, and energy dissipation. In past studies by Zhou et al. [11], the influence of perforated core plate configuration on the strong axis stability is evaluated and determined the suitability of semi-circle configuration in enhancing the strong axis stability and performance during fatigue. A limited study is available on PBRB and its configuration. In this study, an attempt has been made to evaluate the various configuration to study their seismic response. Perforated cores with hexagonal, circular, and rectangular configurations are considered by keeping the yielding length of the core constant. The percentage openings are found to decide the performance of PBRB. Details of the perforated configuration are shown in Fig. 5. The

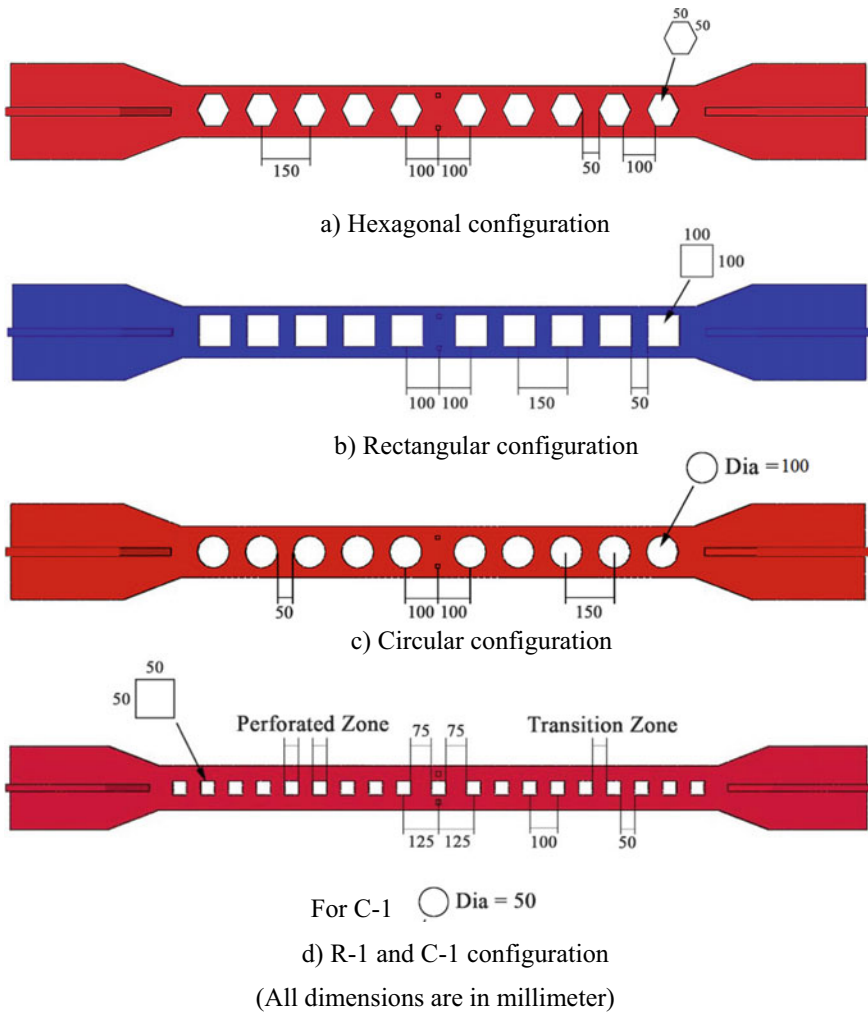


Fig. 5 Details of PBRB configuration

effect of reduced area perforation on BRB performance is studied by reducing the size of perforations. Model C-1 and R-1 are the PBRBs with reduced size of perforation. According to the configurations, the percentage of openings has been found. Hexagonal configuration has 25% area opening; rectangular configuration has 39% area opening; circular configuration has 31% area opening. R-1 and C-1 have 19% and 15% area of the opening, respectively.

3.1 Effect of the Configuration of PBRB on Hysteresis Response

Figure 6 shows the hysteresis response of PBRB with hexagonal, rectangular, and circular configurations. Stable and symmetric hysteresis performances are observed for hexagonal and circular PBRB. Hexagonal and circular configurations can able to sustain a higher number of fatigue cycles as compared to rectangular configurations. For the rectangular configuration, buckling of the strong axis core has been observed. In the rectangular PBRB, as the transition length is less and the perforated zone width is more, strong axis buckling has been observed. As buckling of the strong axis in the perforated core is observed, it cannot sustain the higher deformation. For the hexagonal configuration, stress concentration is observed in the end segment. Also, sufficient width is available between each perforation to distribute the stress, whereas, in the circular configuration, stress concentration is observed only in the center portion of the core. The results show that circular type configuration performs better considering the percentage of opening and energy dissipation.

The result of model R-1 and C-1 shows the size of perforation influences the cyclic performances of PBRBs. Stable and symmetric hysteresis response with no strength reduction has been observed for the reduced size PBRB. Circular PBRB can able to sustain the higher cyclic deformation.

3.2 Effect of the Configuration of PBRB on Axial Strength and Energy Dissipation

Figure 7 shows the axial strength and energy dissipation comparison for the hexagonal, rectangular, and circular configurations of PBRB. For all three configurations, the same elastic stiffness has been observed. High post elastic stiffness is observed for the circular configuration PBRB. The area covered under the corresponding hysteretic loops gives the dissipated energy by a member under cyclic loading. Higher energy dissipation is observed for circular and hexagonal PBRB. As a result of the strong axis buckling of the perforated core, the rectangular configuration cannot sustain all the given cyclic loading sequences. Hence low energy dissipation, as well as post-yield stiffness, are observed.

Table 2 summarises the results obtained for all described configurations. It is observed that the circular configuration PBRBs are the most promising PBRB. An overall improvement in the cyclic response has been observed. Enhancement in the strong axis stability, as well as fatigue performance, increases the energy dissipation capacity of circular configuration PBRB. To control the strong axis buckling of PBRB, the area of the perforated zone and the width of the transition segment must be designed carefully. In the case of hexagonal configuration, stress concentration at the edges is observed, hence as far as possible, make the edges round.

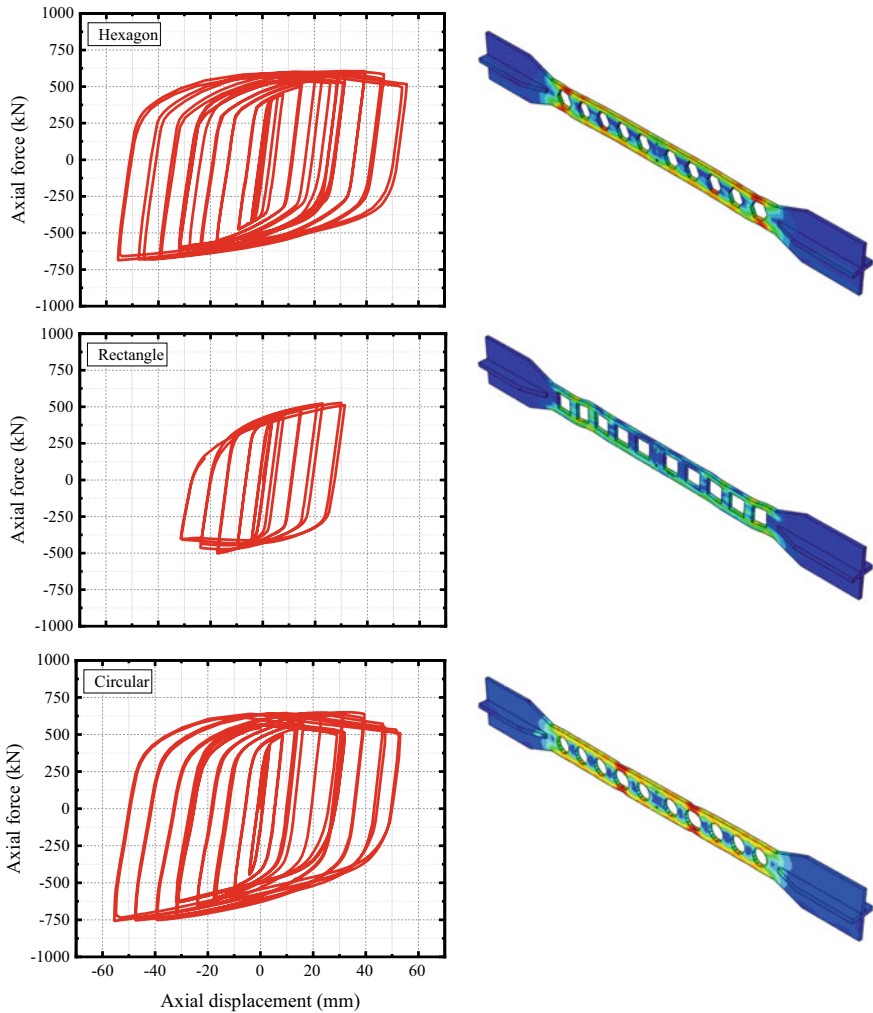


Fig. 6 Hysteresis response and PBRB yielding pattern

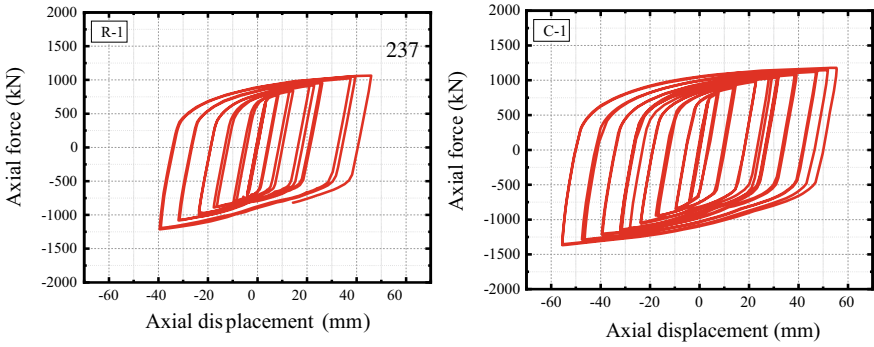


Fig. 6 (continued)

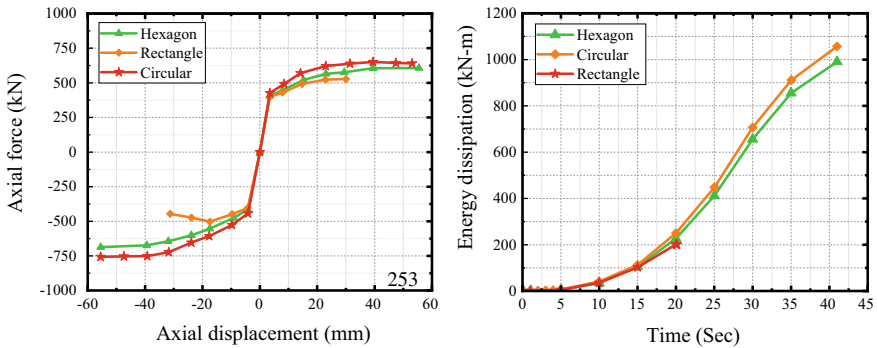


Fig. 7 Backbone curve and energy dissipation of PBRB configuration

Table 2 Details of axial strength and cumulative energy dissipation

Sr. No.	PBRB configuration	Max tension force (kN)	Max compression force (kN)	Energy dissipation (kN-m)
1	Hexagon	606.17	686.68	990.35
2	Rectangle	527.17	502.33	201.13
3	Circular	650.38	756.73	1056.73
4	C-1	1178.84	1367.65	1775.37
5	R-1	1063.76	1214.06	497.81

4 Conclusions

In this study, an analytical investigation has been conducted to predict the cyclic response of all-steel PBRB. The influence of the configuration of the PBRB core has been studied. It is concluded that the configuration and area of perforation have a significant impact on the overall performance of PBRB. Configuration, area, and

the perforation location must be selected judiciously in order to achieve the required performance of PBRB. PBRB is a lightweight and economical option where less axial strength is required. In PBRB, post-yield stiffness changes with the change in the configuration, which significantly impacts strong axis stability, fatigue performance, and energy dissipation capacity. The strong axis buckling of the perforated core depends on the selection of the length of the transition zone. Further, the perforated yielding core length and the perforated configuration and their interaction effect can be studied. Hexagonal and circular PBRB configurations are the most suitable configurations.

References

1. Wu B, Mei Y (2015) Buckling mechanism of steel core of buckling-restrained braces. *J Construct Steel Res* 107:61–69
2. Sabelli R, Mahin S, Chang C (2003) Seismic demands on steel braced frame buildings with buckling-restrained braces. *Eng Struct* 25(5):655–666
3. Fahnestock LA, Sause R, Ricles JM (2007) Seismic response and performance of buckling-restrained braced frames. *J struct Eng* 133(9): 1195–1204
4. Celik OC, Bruneau M (2009) Seismic behavior of bidirectional-resistant ductile end diaphragms with buckling restrained braces in straight steel bridges. *Eng Struct* 31(2):380–393
5. Mirtaheri M et al (2011) Experimental optimization studies on steel core lengths in buckling restrained braces. *J Construct Steel Res* 67(8):1244–1253
6. Khampanit A, Leelataviwat S, Kochanin J, Warnitchai P (2014) Energy-based seismic strengthening design of non-ductile reinforced concrete frames using buckling-restrained braces. *Eng Struct* 81:110–122
7. Dusicka P, Tinker J (2013) Global restraint in ultra-lightweight buckling-restrained braces. *J Compos Constr* 17(1):139–150
8. Jiang Z, Guo Y, Zhang B, Zhang X (2015) Influence of design parameters of buckling-restrained brace on its performance. *J Constr Steel Res* 105:139–150
9. Ahmad Fayeq G, Ranjan Sahoo D (2019) Effect of loading history and restraining parameters on cyclic response of steel BRBs. *Int J Steel Struct* 19(4):1055–1069
10. Shete P, Madhekar S, Ghowsi F (2022) Numerical analysis of steel buckling restrained braces with varying length, gap, and stoppers. *Pract Period Struct Des Construct* 27(1):04021051. Doi: [https://doi.org/10.1061/\(ASCE\)SC.1943-5576.0000629](https://doi.org/10.1061/(ASCE)SC.1943-5576.0000629)
11. Yun Z, Gong C, Zhao J, Zhong G, Tian S (2020) Strong-axis stability and seismic performance of perforated core plate buckling-restrained braces. *Thin-Walled Structures* 156:106997
12. Zhou Y, Qian H, Chu H (2009) A study on the design principle and performance of a new type of buckling-resistant brace. *China Civil Engg J* 42(4): 64–71
13. Wu A, Lin P, Tsai K (2014) High-mode buckling responses of buckling-restrained brace core plates. *Earthquake Eng Struct Dyn* 43(3):375–393
14. Korzekwa A, Tremblay R (2009) Numerical simulation of the cyclic inelastic behaviour of buckling restrained braces. In: International specialty conference on behaviour of steel structures in seismic area (STESSA), 2009
15. Hoveidae N, Tremblay R, Rafezy B, Davaran A (2015) Numerical investigation of seismic behavior of short-core all-steel buckling restrained braces. *J Construct Steel Res* 89–99

16. Chaboche JL, Dang Van K, Cordier G (1979) Modelization of the strain memory effect on the cyclic hardening of 316 stainless steel
17. Zhao J, Wu B, Ou J (2011) A novel type of angle steel buckling-restrained brace: cyclic behavior and failure mechanism. *Earthquake Eng Struct Dyn* 40(10):1083–1102
18. Prestandard FEMA (2000) Commentary for the seismic rehabilitation of buildings (FEMA356). Washington, DC: Federal Emergency Management Agency 7 (2000), 2

A Method for Evaluating Maximum Response in Multi-storied Buildings Due to Bi-directional Ground Motion



P. B. Kote, S. N. Madhekar, and I. D. Gupta

Abstract In the present paper, a method is proposed to evaluate the maximum response of multi-story buildings under the effect of simultaneous action of bi-directional components of earthquake ground motion using the concept of critical response spectrum. The critical response spectrum is computed using the resultant response of a bidirectional single degree of freedom system at each time step under the simultaneous action of the two horizontal components of ground motion. For an illustration of the proposed method, steel building asymmetric in the plan is analyzed using critical response spectra of the three different pairs of recorded earthquake ground motion, and the results obtained are validated by comparison with the exact time-history solution. The exact response is taken as the maximum of the responses estimated by applying the horizontal components of time-histories of ground acceleration at different angles from 0° to 180° at an interval of 10° . On the other hand, in the response spectrum method, two values of the desired response quantity are obtained by applying the critical response spectrum along the structural x and y directions and the multi-component seismic response is combined using the SRSS method. It has been found that the use of the critical spectrum provides a very convenient method for estimating the maximum response under bi-directional earthquake excitation without the need for computation of the critical incident angle of incidence.

Keywords Multi-component seismic excitation · Time-history · Critical earthquake response · Critical response spectrum

P. B. Kote (✉) · S. N. Madhekar
Department of Civil Engineering, College of Engineering Pune, Pune 411005, India
e-mail: kpb18.civil@coep.ac.in

I. D. Gupta
Central Water and Power Research Station (CWPRS), Pune 411024, India

© The Author(s), under exclusive license to Springer Nature Singapore Pte Ltd. 2023
M. S. Ranadive et al. (eds.), *Recent Trends in Construction Technology and Management*, Lecture Notes in Civil Engineering 260,
https://doi.org/10.1007/978-981-19-2145-2_72

973

1 Introduction

In seismic design practice, the translational components in the 3 orthogonal directions are considered and rotational components are usually ignored. The critical orientation of the earthquake components with the structural axes, as well as the multi-component response combination methods for combining individual effects, has been studied in the past by several researchers. In usual seismic design, structures are analyzed and designed for horizontal translational components of acceleration. However, for the seismic design of the bridges, the vertical component of ground motion is also considered. Penzien and Watabe [6] stated that recorded components of ground motion may not be necessarily uncorrelated, therefore based on the concept mechanics they proposed a procedure to compute three mutually perpendicular directions, resolving the recorded components in these principal directions results in the uncorrelated earthquake ground motion components. The axes to which these resolved components are uncorrelated are later termed principal axes. These idealized major and intermediate principal axes are horizontal. The major principal axis approximately gives the direction of the epicenter of the earthquake, the horizontal intermediate principal axis is perpendicular to the major principal component of ground motion, and the third minor principal axis is vertical. In general, when the principal components of ground motion are applied in the structural axes of the buildings the maximum seismic response of that building can be obtained.

In usual design practice, the seismic response of the structure is performed using the response spectrum method. In the response spectrum method, the spectra are applied along the structural axis of the buildings and multi-component seismic response is computed using different combination rules, the details of these combination rules are discussed in Sect. 2.2. Various researchers proposed rules for combining multicomponent seismic response, Newmark [5] was the first researcher to propose a simplified percentage rule, later Rosenblueth and Contreras [8] proposed a similar rule to estimate the approximate seismic response of the structure due to the application of the multi-component seismic ground motion. They assumed a linear combination of 100% of the response due to one seismic component and some percentage (β) of the responses resulting due to application of the other two components of ground motion. Newmark suggested $\beta = 40\%$ of the actual response and Rosenblueth and Contreras suggested $\beta = 30\%$ of the actual response. Smeby and Der Kiureghian [11] assumed the Penzien and Watabe idealized model of uncorrelated ground motions, and they proposed the CQC3 rule (the extension of the CQC) modal combination rule [1] for the combination of the multi-component seismic response. This rule was derived using elementary concepts of stationary random vibrations and accounts for the correlation between the components of ground motion and the structural response.

Many studies have investigated to relative performances of these rules, but to the best of the author's knowledge, none of them have compared the maximum response with the exact time-history solution. Wilson et al. [12] stated that the percentage

combination rules in most of the cases underestimate the design forces in the structural members when compared with the SRSS rule of combining multi-component seismic response. Menun and Der Kiureghian [4] carried out a comparative study for the CQC3 response results with SRSS, the 30% ($\beta = 0.3$), and the 40% ($\beta = 0.4$) rules, assuming CQC3 results to provide a benchmark. The studies by Fernández-Dávila et al. [2] and Zaghlool et al. [13] have pointed out that percent rules, and the SRSS rules are inappropriate and do not take into account the orientation effects of horizontal orthogonal components of ground motion. Salazar et al. [10] showed that the percentage rule i.e. 30%, and the SRSS rule of combining multi-component responses underestimate when compared with the CQC3 rule. Reyes-Salazar et al. [7] studied the response of moment-resisting steel frames and observed that for the bi-directional seismic ground motion if combined with the SRSS rule, in most cases this method produces a lower estimate of response than the Max + 30%. They showed that maximum seismic response could be obtained for different orientations than that of the principal components of ground motion.

Sadhu and Gupta [9] formulated a new modal combination rule using the ordered peak seismic response of multi-storied buildings under the effects of the multi-component seismic ground motions. They have shown that their method performs better than the CQC3 rule for stiffer buildings. However, the structure considered for the analysis was not appropriate. The authors have also pointed out the method suggested by them underestimates the response. Secondly, this rule requires the response spectrums in principal directions, which may not be always available.

In the present study, an investigation of the various spatial combination rules for the computation of seismic response is performed, and a new method is proposed to estimate the maximum seismic response for multi-storied buildings under the simultaneous action of bi-directional components of seismic ground motion using the proposed concept of critical response spectrum. The critical response spectrum is computed using the resultant response of a single degree of freedom at each time step under the simultaneous action of the two horizontal components of motion. For illustration, a steel moment-resisting building, asymmetric in the plan, is analyzed using the proposed critical response spectrum of the three different pairs of recorded ground motion, and the results obtained are validated by comparison with the exact time-history solutions.

The exact response is taken as the maximum of the responses estimated by applying the two horizontal time histories of ground acceleration at different angles from 0° to 180° with respect to the structural axis. On the other hand, in the response spectrum method, two values of the desired response quantity are obtained by applying the critical response spectrum along the x - and y -directions of the structure and are combined using the SRSS method. It will be shown that the proposed critical spectrum provides a very good estimate of maximum response without the need for the computation of the critical incident angle. The proposed method evaluates the maximum response of multi-storied buildings subjected to bi-directional ground motions using the concept of the critical response spectrum, rather than the traditional principal components. The proposed method seismic response results are compared with the existing combination rules such as CQC3 rule, MAX + 30%, MAX +

40%, and SUM method of combining response for multi-component seismic ground motion.

2 Theoretical Background

2.1 Time History Method

The equation of motion for a linear, multi-degree of freedom system (MDF) due to the three input recorded components of ground motion is given by

$$M\ddot{U} + C\dot{U} + KU = -MI\ddot{X} \tag{1}$$

where M , C , and K are the lumped story mass matrix, modal damping matrix, and stiffness matrix respectively, U is the nodal relative displacements vector, $X = [X_1 X_2 X_3]^T$ is components of ground motion in three translational directions, includes components in the horizontal $X_1(t)$ and $X_2(t)$ vertical $X_3(t)$, and $I = [I_1 I_2 I_3]^T$ is the mass influence matrix. Usually, the response quantity of interest, $R(t)$, the nodal displacements are written in the generic form such that $R(t) = q^T U$, where q constants vector. To obtain the response of internal forces in a member q represents the stiffness matrix of that member. Transformation to the normal coordinate system such that $U = \Phi Y$, and the i th uncoupled modal equation is given by

$$\ddot{Y}_i + 2\zeta_i \omega_i \dot{Y}_i + \omega_i^2 Y_i = -\Gamma_i^T \ddot{X} \tag{2}$$

where $Y = [Y_1 Y_2 \dots Y_n]^T$ is the vector of normal coordinates, $\Phi = [\Phi_1 \Phi_2 \dots \Phi_n]$ is the eigenvector matrix. ω_i and ζ_i are the structural natural frequency and corresponding modal damping ratio of i th mode, respectively, and $k = 1, 2, 3$ are the three input ground motion components. Time-history solution for multi-component excitation is as per Eq. (3)

$$U(t) = \sum_{k=x,y} \sum_{l=x,y} \sum_i \sum_j \psi_{ki} \psi_{lj} Y_i(t) Y_j(t) \tag{3}$$

where $Y_i(t)$ is the required modal solution of Eq. (2) for i th mode, which is like the equation of motion for a single degree of freedom oscillator.

The time history solution procedure given above is applicable when the earthquake ground motion is applied along the structural axis of the buildings, however, to find the maximum response the ground motion is required to be applied in the all-possible orientations. This process involves a large number of computations thus practically for design purposes it is not adopted.

2.2 Response Spectrum Method

For the seismic analysis and design of the buildings for a particular location, the actual site-specific earthquake time history is required, however, the availability of such records for every location may not be possible. Further, the seismic analysis of the structures depends on the amplitude of ground acceleration as well as the frequency content and the structure’s dynamic properties. Therefore, in most cases, the response spectrum method is used for seismic analysis. This method provides a computational advantage as the prediction of the response involves the calculation of the maximum values of the response quantities in each mode of vibration. These maximum values of the response for the element forces in each mode are obtained from the smooth design spectrum which is based on the average of several earthquakes. The maximum modal response is obtained from Eq. (4).

$$Y_{i,max} = |Y_i(t)|_{max} = \Gamma_i S_d(\zeta_i, \omega_i) \tag{4}$$

where Γ_i is the modal participation factor for i th mode and $S_d(\zeta_i, \omega_i)$ is the i th mode nodal displacement. The final maximum displacement response Y_{max} is evaluated using the modal combination rules. The commonly used method for combining the modal maximum final response is given by Complete Quadratic Combination (CQC) method [1] given by

$$Y_{max} = \sqrt{\sum_{i=1}^n \sum_{j=1}^n \rho_{ij} Y_i Y_j} \tag{5}$$

here Y_i and Y_j are the i th and j th modal responses respectively and ρ_{ij} is the modal correlation coefficient [1] given by Eq. (6)

$$\rho_{ij} = \frac{8(\zeta_i \zeta_j)^{1/2} (\zeta_i + \beta \zeta_j) \beta^{3/2}}{(1 - \beta^2)^2 + 4\zeta_i \zeta_j \beta (1 + \beta^2) + 4(\zeta_i^2 + \zeta_j^2) \beta^2} \tag{6}$$

The response due to multi-component seismic ground motion is determined using simplified combination methods such as the percentage rules (e.g. Max + 30%, Max + 40%), square root of the sum of squares (SRSS), and Complete Quadratic Combination (CQC3) rules the details of these methods are given below.

2.2.1 CQC-3 Rule

This method is proposed by Smeby and Der Kiureghian [11] and later by Menun and Der Kiureghian [4] for finding the critical response under the simultaneous action of ground motion. This method requires the ground motion in the principal directions.

The incident angle-dependent response is given by Eq. (7)

$$\begin{aligned}
 R_\theta = & \left[\sum_{k=1,2,3} \sum_{i=1}^n \sum_{j=1}^n \rho_{ij} \psi_{ki} \psi_{kj} S_{ki} S_{kj} \right. \\
 & - \sum_{i=1}^n \sum_{j=1}^n \rho_{ij} [\psi_{1i} \psi_{1j} - \psi_{2i} \psi_{2j}] [S_{1i} S_{1j} - S_{2i} S_{2j}] \sin^2 \theta \\
 & \left. + 2 \sum_{i=1}^n \sum_{j=1}^n \rho_{ij} \psi_{1i} \psi_{2j} [S_{1i} S_{1j} - S_{2i} S_{2j}] \sin \theta \cos \theta \right]^{1/2} \tag{7}
 \end{aligned}$$

where, ψ_{ki} is the effective participation factor in the k th structural axis, ρ_{ij} is the modal correlation coefficient [1], S_{1i} and S_{2i} are the horizontal principal components [6]. The θ in the equation represents the angle between the principal components w.r.t the structural axis. The critical angle for the response can be obtained by differentiating Eq. (7) w.r.t. θ . The critical angle is given by Eq. (8)

$$\theta_{cr} = \frac{1}{2} \tan^{-1} \left(\frac{2 \sum_{i=1}^n \sum_{j=1}^n \rho_{ij} \psi_{1i} \psi_{2j} [S_{1i} S_{1j} - S_{2i} S_{2j}]}{\sum_{i=1}^n \sum_{j=1}^n \rho_{ij} [\psi_{1i} \psi_{1j} - \psi_{2i} \psi_{2j}] [S_{1i} S_{1j} - S_{2i} S_{2j}]} \right) \tag{8}$$

Equation (8) has two roots between 0° and 180° corresponding to those values of θ gives the maximum and minimum multi-component seismic response.

2.2.2 SRSS Rule

This method of combining response due to bi-directional seismic components of ground motion is given by Eq. (9)

$$R_{crit} = \left[\{R^x\}^2 + \{R^y\}^2 \right]^{1/2} \tag{9}$$

where R^x and R^y is the response due to application of the critical response spectrum in x th structural and y th structural axis respectively. The response quantities R^x and R^y are computed as given in Eq. (10)

$$\begin{aligned}
 \{R^x\} &= \left\{ \sum_{i=1}^n \sum_{j=1}^n \rho_{ij} \psi_{xi} \psi_{xj} S_{xi} S_{xj} \right\}^{\frac{1}{2}} \\
 \{R^y\} &= \left\{ \sum_{i=1}^n \sum_{j=1}^n \rho_{ij} \psi_{yi} \psi_{yj} S_{yi} S_{yj} \right\}^{\frac{1}{2}} \tag{10}
 \end{aligned}$$

where ψ_{xi} , ψ_{yi} are the effective modal participation factor in the x th and y th structural axis, ρ_{ij} is the modal correlation coefficient [1], S_{xi} and S_{yi} are the i th modal response spectral acceleration values of the x th and y th components.

2.2.3 Max + 30% Rule

As per the discussion in the introduction section [8] suggested the simplified percentage rule to estimate the approximate multi-component seismic response. This method is further recommended by ATC-3(1978), IS-1893:2016, and many other seismic codes. The response is given by Eq. (11)

$$R = \max\{R^x + 0.3R^y \text{ or } 0.3R^x + R^y\} \quad (11)$$

2.2.4 Max + 40% Rule

Newmark [5] proposed this method with a higher percentage of contribution from the other two components of ground motion. This method produces a higher estimate of response compared to the earlier rule. This method is recommended by ASCE (1986), ATC-32, for seismic analysis of nuclear structures. The response is given by Eq. (12)

$$R = \max\{R^x + 0.4R^y \text{ or } 0.4R^x + R^y\} \quad (12)$$

2.2.5 SUM Method

This method assumes the contribution of the response due to multi-component seismic ground motion occurs simultaneously hence, the response is combined as absolute sum of the response contribution as given in Eq. (13)

$$R = R^x + R^y \quad (13)$$

This method usually yields conservative results hence this method is not recommended by various design codes.

3 Response Spectrum Used for Analysis

The response spectra are the smooth curves of the absolute maximum response of an SDOF system (for a fixed damping ζ and natural frequency ω) due to earthquake

ground motion to its natural time period (or frequency). The various types of response spectra considered for the present analysis for the structures are given below.

3.1 Response Spectra of Recorded Components [SAX, SAY]

The response spectra of the originally recorded components of the seismic ground motion for a given damping ratio (ζ) are considered as SAX and SAY.

3.2 Response Spectra of Principal Components [SAXP, SAYP]

The SAXP and SAYP are obtained by resolving the recorded earthquake components in the two horizontal major and intermediate principal direction θ_1, θ_2 respectively. The angles of the major and minor principal directions θ_1 and θ_2 are computed from [6] idealization.

3.3 Critical Response Spectra [SACRIT]

The proposed Critical Response Spectrum is obtained by the resultant response $R_{(t)}$ of an SDOF system obtained from SRSS of the response in the x -and y -directions are $R_{x(t)}$ and $R_{y(t)}$ respectively for each natural period (T) and damping ratio (ξ). The resultant response of the SDOF system is computed by Eq. (14)

$$SA_{crit(T,\xi)} = R_{(t) \max} \tag{14}$$

where

$$R_{(t)} = \sqrt{R_{x(t)}^2 + R_{y(t)}^2} \tag{15}$$

To perform a numerical study, three real ground motion time histories are considered. The details of the selected earthquake records are shown in Table 1. Time history components records and the corresponding response spectra of the three selected real earthquake records considered for analysis are shown in Figs. 1 and 2.

Table 1 Details of the selected earthquakes

REC#	Name of EQ	Date	M	Focal depth [km]	Epicenter distance [km]	Comp	PGA (g)	Recording site
1	Gorkha Nepal	25/04/2015	7.9	13.40	13.60	NORT	0.157	Kirtipur
						EAST	0.253	
2	Sikkim	18/09/2011	6.7	10.00	50.30	EAST	-0.145	Gangtok
						NORT	-0.158	
3	Uttarkashi	20/10/1991	6.9	13.20	73.90	N85E	0.253	Bhatwari
						N05W	0.246	

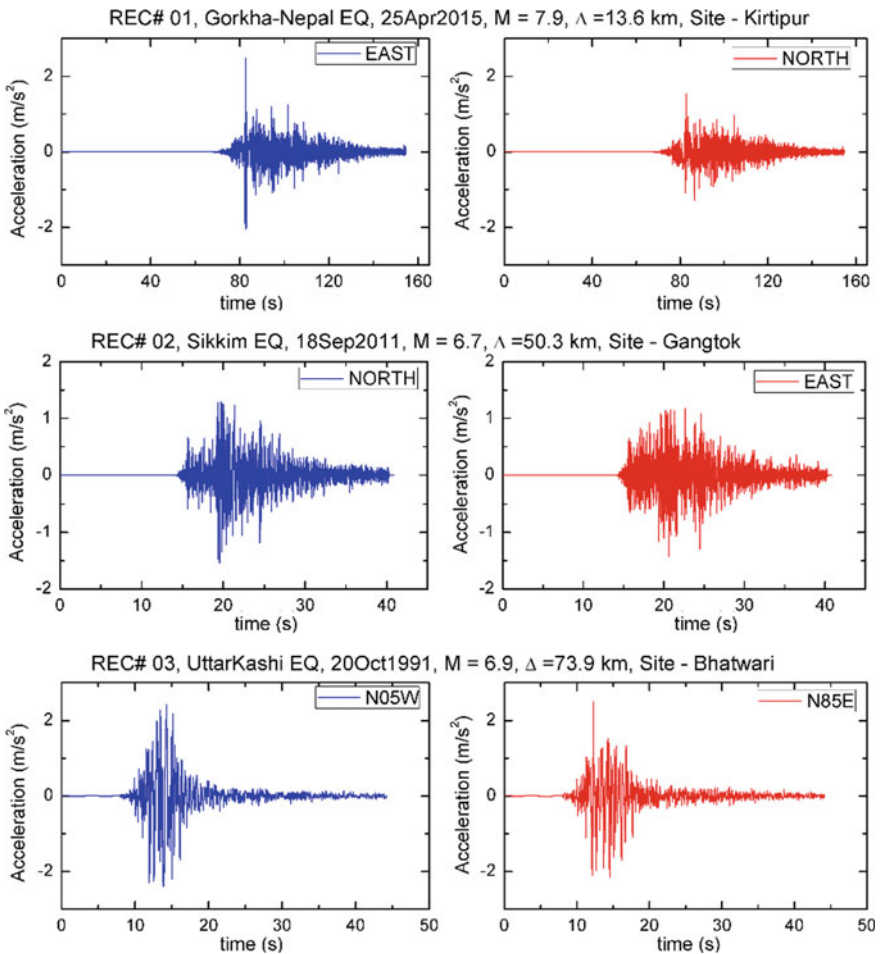


Fig. 1 Selected recorded earthquake time history

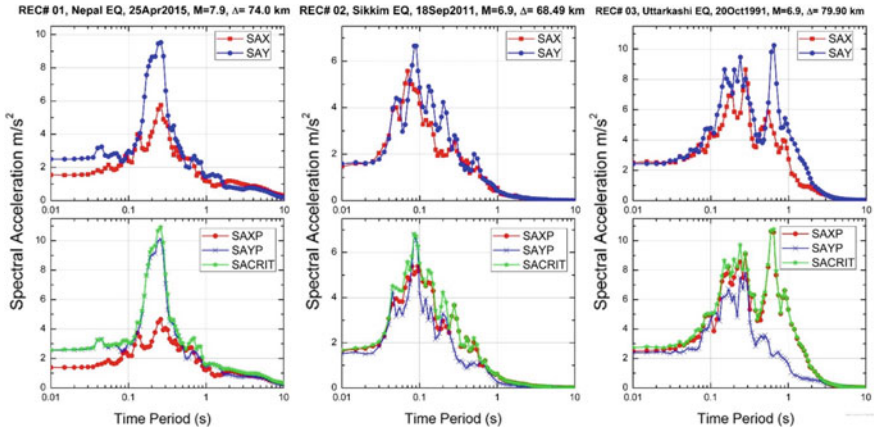


Fig. 2 Response spectra of selected earthquake records

4 Illustrative Example

4.1 A Building Considered for Analysis

A simple two-bay three-story steel building with an asymmetric plan is considered for seismic analysis. A typical floor plan building and a three-dimensional view of an example building are shown in Fig. 3. The building has Indian standard steel columns ISHB 200-1 with a 150 mm thick R.C.C. slab on each floor. The building is initially analyzed and designed for dead load intensity of 3.0 kN/m², Superimposed loads of 3.5 kN/m² acting over the intermediate floor slabs. For seismic analysis, 5% damping ratio is considered as per the provisions in IS 1893:2016. The building is assumed to

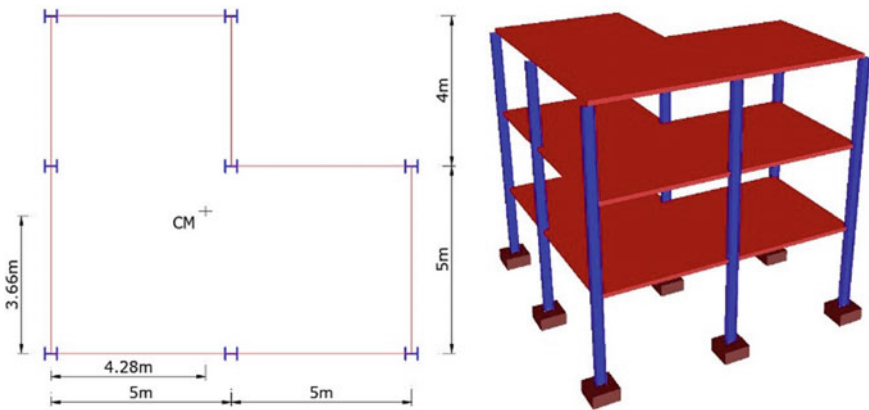


Fig. 3 Typical three-story steel building

Table 2 Natural modes and frequencies (ω_n) of example building

Mode No.	Time period [s]	Natural frequency (ω_n) [rad/s]	Cumulative mass participation (%)
1	1.34	4.70	0.87
2	0.69	9.08	80.13
3	0.63	9.91	91.87
4	0.49	12.95	91.87
5	0.37	18.22	91.87
6	0.25	25.02	98.13
7	0.23	27.30	99.04
8	0.18	35.20	99.88
9	0.16	38.41	100.00

have rigid diaphragms, mathematically modeled as 3 degrees-of-freedom ($\delta_x, \delta_y, \theta$) per floor considering lumped mass at story levels. The computed Mass and Stiffness matrix for the example building is given in Eqs. (16) and (17). The modal analysis results for time period (s) for the example building for the 9 modes of vibration are given in Table 2.

$$M = 10^3 \begin{bmatrix} 60.65 & 0.00 & 0.00 & 0.00 & 0.00 & 0.00 & 0.00 & 0.00 & 0.00 \\ 0.00 & 60.65 & 0.00 & 0.00 & 0.00 & 0.00 & 0.00 & 0.00 & 0.00 \\ 0.00 & 0.00 & 48.17 & 0.00 & 0.00 & 0.00 & 0.00 & 0.00 & 0.00 \\ 0.00 & 0.00 & 0.00 & 60.65 & 0.00 & 0.00 & 0.00 & 0.00 & 0.00 \\ 0.00 & 0.00 & 0.00 & 0.00 & 60.65 & 0.00 & 0.00 & 0.00 & 0.00 \\ 0.00 & 0.00 & 0.00 & 0.00 & 0.00 & 48.17 & 0.00 & 0.00 & 0.00 \\ 0.00 & 0.00 & 0.00 & 0.00 & 0.00 & 0.00 & 838.51 & 0.00 & 0.00 \\ 0.00 & 0.00 & 0.00 & 0.00 & 0.00 & 0.00 & 0.00 & 838.51 & 0.00 \\ 0.00 & 0.00 & 0.00 & 0.00 & 0.00 & 0.00 & 0.00 & 0.00 & 665.88 \end{bmatrix} \quad (16)$$

$$K = 10^6 \begin{bmatrix} 51.32 & -25.66 & 0.00 & 0.00 & 0.00 & 0.00 & -17.41 & 8.71 & 0.00 \\ -25.66 & 51.32 & -25.66 & 0.00 & 0.00 & 0.00 & 8.71 & -17.41 & 8.71 \\ 0.00 & -25.66 & 25.66 & 0.00 & 0.00 & 0.00 & 0.00 & 8.71 & -8.71 \\ 0.00 & 0.00 & 0.00 & 13.75 & -6.88 & 0.00 & 1.23 & -0.61 & 0.00 \\ 0.00 & 0.00 & 0.00 & -6.88 & 13.75 & -6.88 & -0.61 & 1.23 & -0.61 \\ 0.00 & 0.00 & 0.00 & 0.00 & -6.88 & 6.88 & 0.00 & -0.61 & 0.61 \\ -17.41 & 8.71 & 0.00 & 1.23 & -0.61 & 0.00 & 862.71 & -431.35 & 0.00 \\ 8.71 & -17.41 & 8.71 & -0.61 & 1.23 & -0.61 & -431.35 & 862.71 & -431.35 \\ 0.00 & 8.71 & -8.71 & 0.00 & -0.61 & 0.61 & 0.00 & -431.35 & 431.35 \end{bmatrix} \quad (17)$$

4.2 Numerical Analysis and Results

A detailed numerical analysis is carried out for the example building as shown in Fig. 3. The dynamic analysis is performed for seven different analysis cases. Details of these analysis cases are given in Table 3. In the present study, time history analysis (Case-1) is considered as the benchmark method. The response obtained by the response spectrum superposition method for Case-2 to Case-7 are compared with Case-1 time history results. In the proposed critical spectrum method, the modal response due to simultaneous action of multi-component seismic excitation is obtained based on the critical spectra as defined in Sect. 3, and the SRSS rule is used to combine the multi-component modal response. The story response quantities such as story displacements (for diaphragm), base shear force, and bending moment (for all elements in a story) are tabulated in Table 4. The normalized displacement, shear force, and bending moments plots for all seven cases are shown in Fig. 4.

To illustrate the efficacy of the proposed method over the existing methods, plots with percentage error is shown considering the time history method (Case-1) as the benchmark method as shown in Fig. 5. As shown in Fig. 5, it is evident that the simplified percentage rules viz Max + 30%, Max + 40% rules, and Sum method underestimate the response. The main reason for lower estimates of the response is due to the non-consideration of the incident angle of the earthquake in the simplified percentage rule methods. The CQC3 rule underestimates the response when compared with the time history method although the critical angle of earthquake incidence is considered while evaluating the response. However, it is seen that the proposed critical spectrum method (Case-2) provides a very good estimate of the desired response without

Table 3 Cases considered for dynamic analysis

Case#	Case details
1	Time history analysis using time history of recorded components of ground motion for the angle of incidence from 0° to 180° with an interval of 10°
2	Response spectrum analysis using SACRIT Spectra [3] and combining response using SRSS rule (Present Study)
3	Response spectrum analysis using SAXP and SAYP spectra [6] and combining response using CQC3 Rule for the critical response [4, 11]
4	Response spectrum analysis using SAX, SAY spectra (considering real components as principal components) and combining response using CQC3 Rule for the critical response
5	Response spectrum analysis using SAX, SAY spectra and combining response using [Max + 30%] rule [8]
6	Response spectrum analysis using SAX, SAY spectra, and combining response using [Max + 40%] rule [5]
7	Response spectrum analysis using SAX, SAY spectra and combining response using SUM rule

Table 4 Story response results

RE C#	Case #	Story displacement (mm)			Base shear force (kN)			Bending moment (kNm)		
		Story #			Story #			Story #		
		1	2	3	1	2	3	1	2	3
1	1	19.03	35.23	44.19	483.01	410.76	245.84	3418.83	1969.80	737.52
	2	19.43	33.41	40.72	487.55	376.08	230.21	3281.52	1818.87	690.63
	3	15.60	27.47	33.39	392.03	303.74	190.44	2658.63	1482.54	571.32
	4	15.14	25.78	31.46	379.59	292.59	188.52	2582.10	1443.33	565.56
	5	15.15	25.81	31.49	379.93	292.85	188.66	2584.32	1444.53	565.98
	6	15.16	25.81	31.50	380.04	292.94	188.71	2585.07	1444.95	566.13
	7	15.19	25.86	31.56	380.73	293.47	189.00	2589.60	1447.41	567.00
2	1	6.28	11.46	14.41	159.21	136.22	79.10	1123.59	645.96	237.30
	2	6.77	11.80	14.35	171.22	132.67	74.68	1135.71	622.05	224.04
	3	6.32	11.04	13.43	158.98	123.06	68.67	1052.13	575.19	206.01
	4	5.71	9.97	12.13	145.10	112.35	65.94	970.17	534.87	197.82
	5	5.72	9.98	12.14	145.24	112.46	66.00	971.10	535.38	198.00
	6	5.72	9.99	12.14	145.29	112.50	66.02	971.43	535.56	198.06
	7	5.73	10.01	12.17	145.57	112.72	66.15	973.32	536.61	198.45
3	1	59.14	105.20	128.13	1482.32	1153.08	573.77	9627.51	5180.55	1721.31
	2	59.54	105.49	128.14	1495.75	1160.96	583.03	9719.22	5231.97	1749.09
	3	58.23	103.22	125.39	1463.20	1135.92	568.23	9502.05	5112.45	1704.69
	4	56.52	100.13	121.63	1418.12	1100.65	553.42	9216.57	4962.21	1660.26
	5	56.55	100.17	121.69	1418.76	1101.14	553.67	9220.71	4964.43	1661.01
	6	56.56	100.19	121.71	1418.97	1101.30	553.76	9222.09	4965.18	1661.28
	7	56.61	100.27	121.81	1420.24	1102.29	554.26	9230.37	4969.65	1662.78

the need for consideration of any earthquake incident angle. The response quantities obtained by the proposed method are more consistent when compared to other methods of combining response due to multi-component seismic ground motion. The proposed method can be very easily implemented using commercial earthquake analysis programs.

5 Conclusion

The existing simplified percentage rule methods for combining the response of buildings under the simultaneous action of bi-directional seismic ground motion underestimate the desired response for all considered earthquake records. The main reason for underestimating response in percentage rule methods is due to the non-account

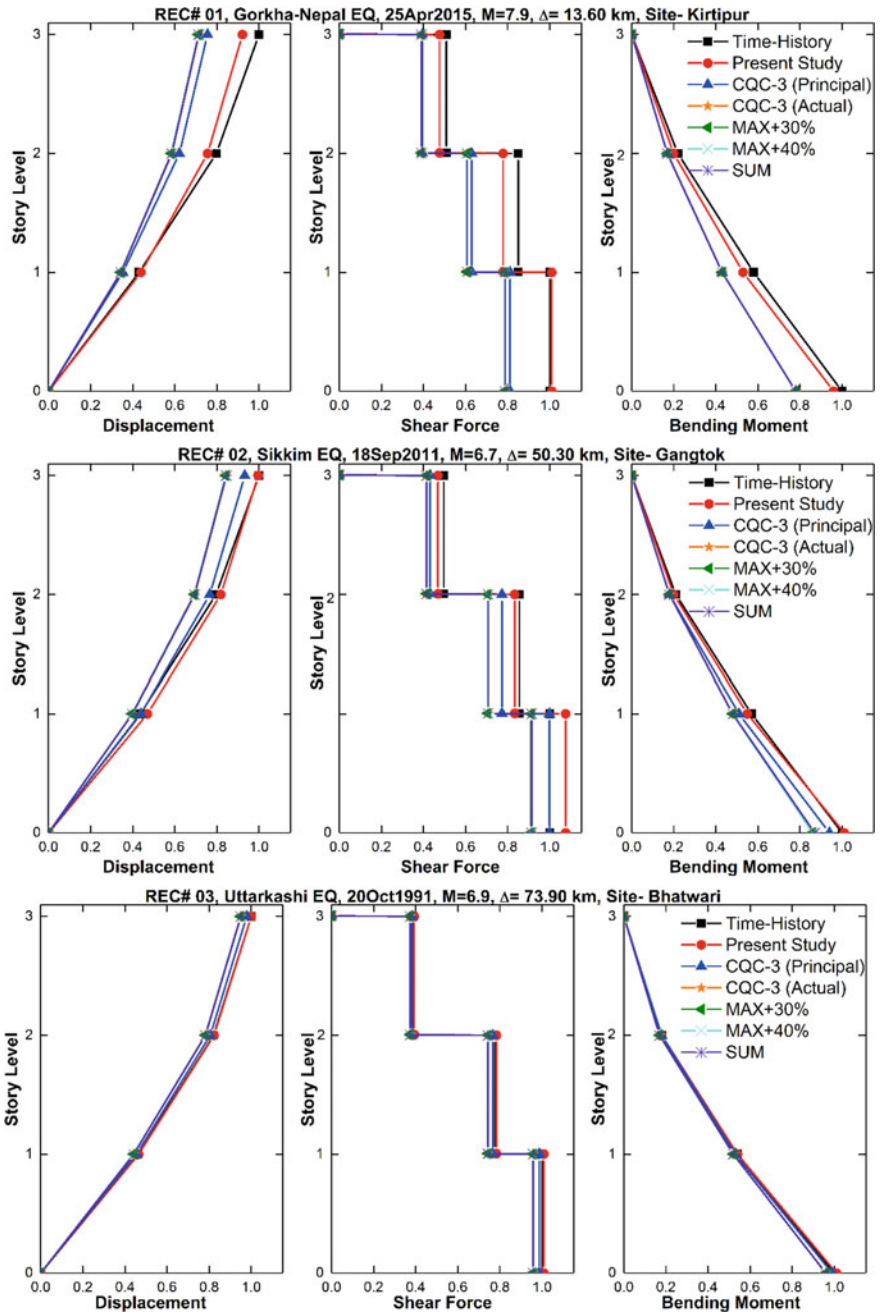


Fig. 4 Normalised response plot

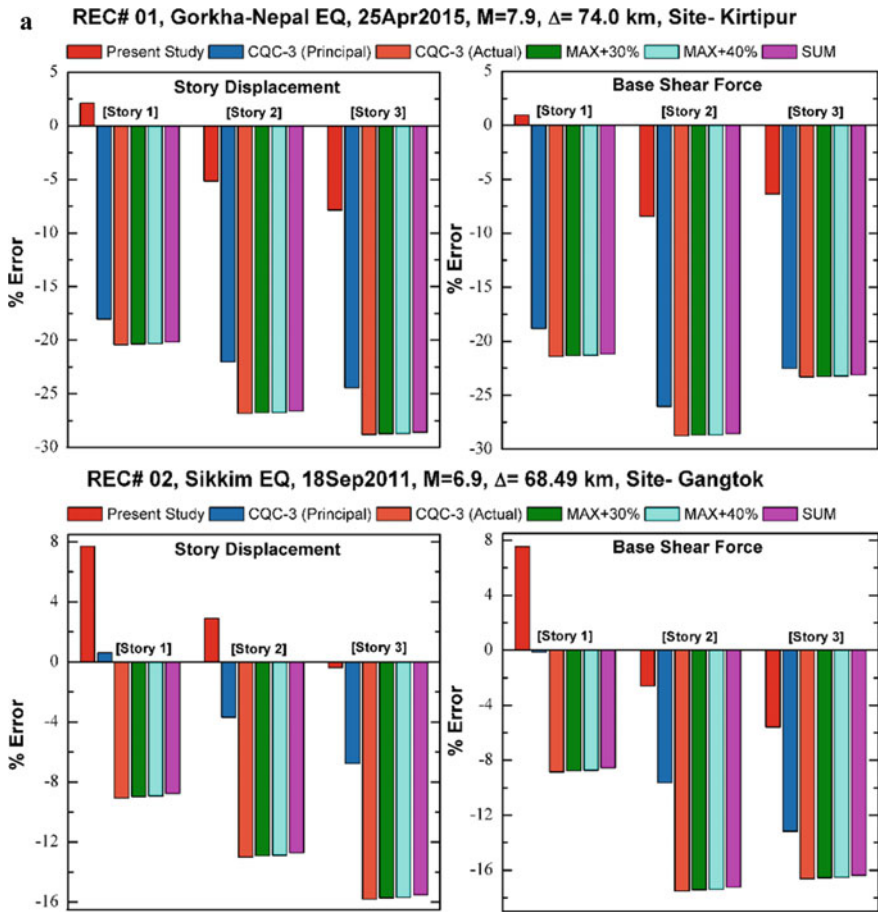


Fig. 5 % Error in story response

for the incident angle of the earthquake. The CQC-3 method considers the critical angle for a response, but in most cases, the response obtained by this method underestimates the response when compared with the exact time history solution.

From the illustrated analysis it is found that the proposed method results are consistent with the time history results and provide a very convenient approach to estimate the maximum seismic response of the buildings due to the simultaneous action of multi-component seismic ground motion without the need for computation of a critical earthquake angle. Therefore, the proposed method is computationally advantageous over the CQC-3, and thus the implementation of the proposed method for seismic analysis is easily possible using already available computer programs.

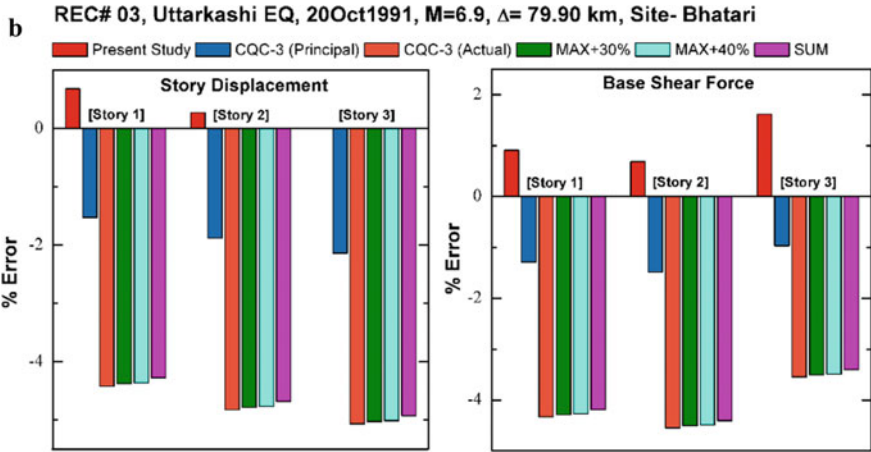


Fig. 5 (continued)

References

1. Der Kiureghian AD (1981) A response spectrum method for random vibration analysis of MDOF systems. *Earthq Eng Struct Dynam* 9(1):419–436
2. Fernández-Dávila I, Cominetti S, Cruz E (2000) Considering the bi-directional effects and the seismic angle variations in building design. In: Proceedings of 12th world conference on earthquake engineering, New Zealand
3. Kote PB, Madhekar SN, Gupta ID (2019) Investigation of 30% rule for the combination of component response with the unidirectional principal response spectrum. In: Proceedings of the 4th Indian conference on applied mechanics. Indian Society for Applied Mechanics (ISAM), IISc Bangalore, India, pp 209–212
4. Menun C, Der Kiureghian A (1998) A replacement for the 30%, 40% and SRSS rules for multi-component seismic analysis. *Earthq Spectra* 14(1):153–156
5. Newmark NM (1975) Seismic design criteria for structures and facilities, Trans-Alaska pipeline system. In: Proceedings of the U.S. national conference on earthquake engineering. Earthquake Engineering Institute, California, pp 94–103
6. Penzien J, Watabe M (1975) Characteristics of three-dimensional earthquake ground motion. *Earthq Eng Struct Dynam* 3:365–373
7. Reyes-Salazar A, Haldar A, Rivera-Salas JL, Bojórquez E (2015) Review of assumptions in simplified multi-component and codified seismic response evaluation procedures. *KSCE J Civ Eng* 19(5):1320–1335. <https://doi.org/10.1007/s12205-015-0190-x>
8. Rosenblueth E, Contreras H (1977) Approximate design for multi-component. *J Eng Mech Div ASCE* 881–893
9. Sadhu A, Gupta VK (2008) A modal combination rule for ordered peak response under multi-component ground motion. *ISET J Earthq Technol* 45(3–4):79–96
10. Salazar AR, Barraza AL, Lopez AL, Haldar A (2008) Multi-component seismic response analysis—a critical review. *J Earthq Eng* 12(1):779–799

11. Smeby W, Der Kiureghian AD (1985) Modal combination rules for multi-component earthquake excitation. *Earthq Eng Struct Dyn* 4(1):1–12
12. Wilson EL, Suharwardy I, Habibullah A (1995) A clarification of the orthogonal effects in a three-dimensional seismic analysis. *Earthq Spectra* 11(4):659–666
13. Zaghlool BS, Carr AJ, Moss PJ (2000) Inelastic behavior of three-dimensional structures under concurrent seismic excitations. In: *Proceedings of 12th world conference on earthquake engineering*, New Zealand

Finite Element Analysis of Piled Raft Foundation Using Plaxis 3D



Anupam Verma and Sunil K. Ahirwar

Abstract A piled raft foundation is a type of deep foundation capable for transferring the heavy load of superstructure into the soft soil by pile and raft support system. A numerical analysis of piled raft foundation is presented in this study. Various types of interactivity among components like pile-to-pile interactivity, raft-to-pile interactivity, pile-to-soil interactivity, and raft-to-soil interactivity are also being examined using a three-dimensional finite element software Plaxis 3D (Netherlands user manuals, [1]). The parameters taken in this study are raft thickness, pile spacing, pile cross-sectional shape, and pile length. These parameters were varied and compared with other available studies. The results obtained in the present studies are in good agreement with other research studies.

Keywords Piled raft · Soft soil · Foundation · Plaxis 3D

1 Introduction

The exponential increase in the number of high-rise structures of 150–300 m and more have presented a challenging situation among structural and geotechnical engineers in designing the foundation systems of such structures. Thus the mere application of conventional foundation design methods is insufficient for such structures; therefore, engineers are forced to follow more innovative and skillful designs. Instead of using piles and rafts alone, the concept of combination of the elements of foundations such as piles and raft can be applied to support a structure in which the role of piles is to reduce raft sinking and distinctive settlements and can also contribute to significant prudence without taking a trade-off between the safety and execution of the foundation. Such foundations can be called “piled enhanced raft” or “piled-raft foundations”. A piled raft is a compounded geotechnical formation comprising foundation elements like piles, soil, and raft. It can be distinguished from the usual

A. Verma · S. K. Ahirwar (✉)

Department of Civil Engineering and Applied Mechanics, Shri G. S. Institute of Technology and Science, Indore, Madhya Pradesh, India

e-mail: skasgsits@gmail.com; sahirwar@sgsits.ac.in

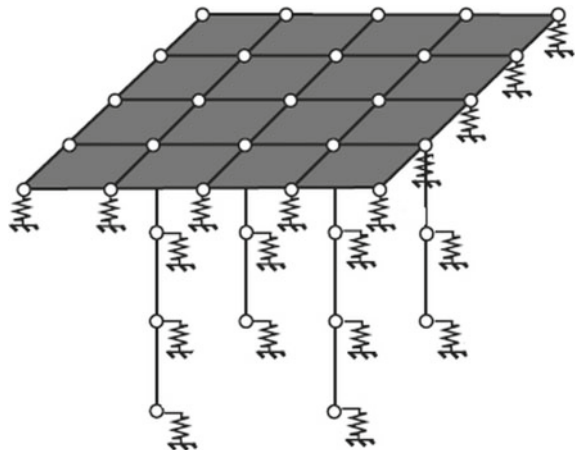
design of the foundation, where either the raft or piles transport the loads. The first to introduce the concept and design approach for piles under a raft foundation were Burland et al. [2] and called the piles “settlement reducing piles”. The Combined Piled Raft Foundation (CPRF) has been successfully implemented in various parts of the world over the last four decades to optimize foundations for structures in civil engineering. During 1994–97, one of the International Society of Soil Mechanics and Foundation Engineering’s (ISSMFE) technical committees based their efforts on piled raft foundations and provided detailed reports on collective knowledge on various design methods and case history.

First, the piled raft foundations were considered an alternative for high-rise building foundations on cohesive active settlement soils such as the Frankfurt clay, but as a result of extensive researches on its performance, pile-raft now has been preferred as a foundation for other soils too.

Clancy and Randolph [3] studied the spring model plate in which a plate element was taken in place of the raft and supported by the number of spring elements taken instead of the pile group as shown in Fig. 1 and described the interactivity between different elements. Poulos [4] conducted a similar study on the plate-spring model by performing 2D numerical analysis by examining the impact on load sharing of CPRF. The development of a numerical method carried out the study of piled raft bearing behavior by Reul [5]. The findings of variation in foundation geometry on differential and total settlements were studied by Prakoso and Kulhawy [6]. Sinha and Hanna [7] stimulated a 3D finite element analysis of a piled raft foundation and analyzed in ABAQUS software using modified Drucker-Prager Constitutive Law.

This paper compares current studies and research done by Sinha and Hanna [7] by Plaxis 3D [1] software.

Fig. 1 Plate on spring model [3]



2 Numerical Model

The development of a three-dimensional numerical model was performed for the stimulation of the combined piled raft foundation. The model consisted of a soil block, the foundation elements, zone of contact, and prescribed displacements. The software program PLAXIS 3D [1] was used in the development of the model. Figure 2 presents the structural model of the foundation bed, and the deformed mesh of CPRF is shown in Fig. 3. Because of the symmetrical conditions, only the quarter part of the foundation is modeled and analyzed.

In this study, the soil is taken as a homogenous, isotropic, and single-phase medium. Tables 1 and 2 list the soil and other component parameters.

The water table effect was not taken into consideration. A comparison of study has been made between Sinha et al. [7] and the current study by taking the similar properties in later cases and modeling the parameters in Plaxis 3D [1].

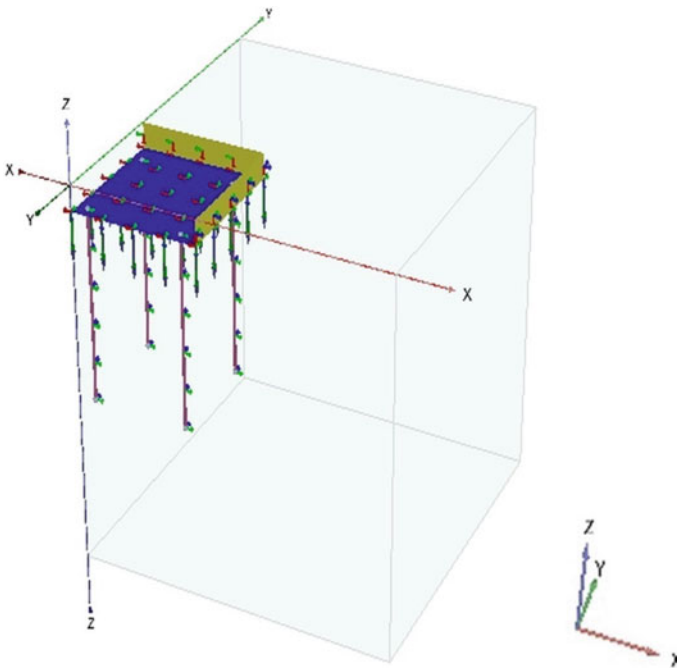


Fig. 2 Structural model of CPRF

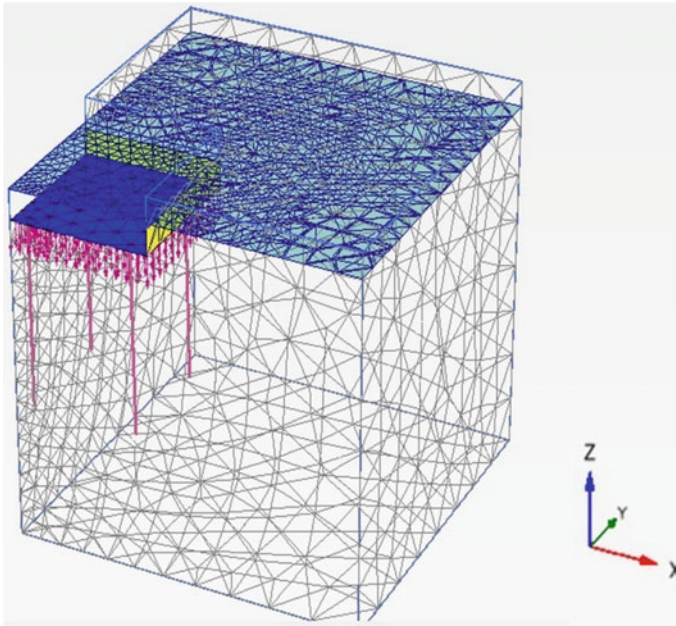


Fig. 3 Deformed finite element mesh of CPRF

Table 1 Properties of material used in the model

Parameter	Unit	Soil	Raft	Pile
Modulus of elasticity (E)	N/mm ²	30×10^3	34×10^6	25×10^6
Poisson's ratio (ν)		0.1	0.2	0.2
Dry density (γ)	N/m ³	19×10^3	25×10^3	25×10^3
Saturated density (γ')	N/m ³	20×10^3		
Internal friction angle ($^\circ$)		6		
Soil cohesion (C')	Pa	20×10^3		

Table 2 Raft size and number of piles according to pile spacing used in the model

Spacing of piles	Size of raft (m)			Pile number
	L	B	H	
2d, 3d, 4d and 6d	24	24	2	144, 64, 36 and 16
7d	28	28	2	16
8d	32	32	2	16
10d	40	40	2	16

3 Study of Parameters

The parameters studied for the load and displacement characteristics of combined piled raft foundations are examined in the corresponding section. The results of variation of structural models are compared with the previous study using different software, and the variation in results is discussed.

3.1 Variation in Raft Thickness

In this case, a 24 m square raft, 6d pile spacing, and 15 m pile length are examined. The variation in raft thickness was examined over the thickness as 0.5 m, 1 m, 1.5 m, 2 m, and 2.5 m. These variations are also compared with the behavior of an unpiled raft 0.5 m thick. The raft was subjected to the prescribed displacement of 0.5 m which was applied on the raft surface, and corresponding loads are obtained from the Load versus Settlement plot of the model. Figure 4 represents the results obtained by the analysis of the model in the form of load settlement curves. It was observed that for smaller thickness raft, the load-bearing capacity was higher as compared to thicker raft for the same pile spacing. These values were obtained for a given raft size, pile spacing and loading conditions; thus, the optimization in design can be done to obtain more economical and safe construction.

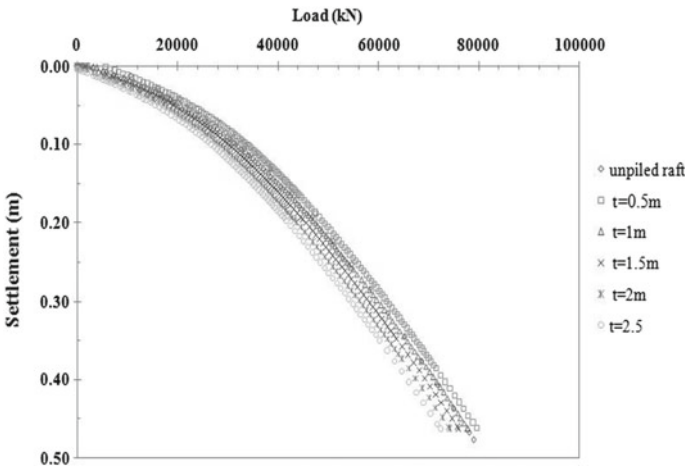


Fig. 4 Load versus settlement for variation in raft thickness

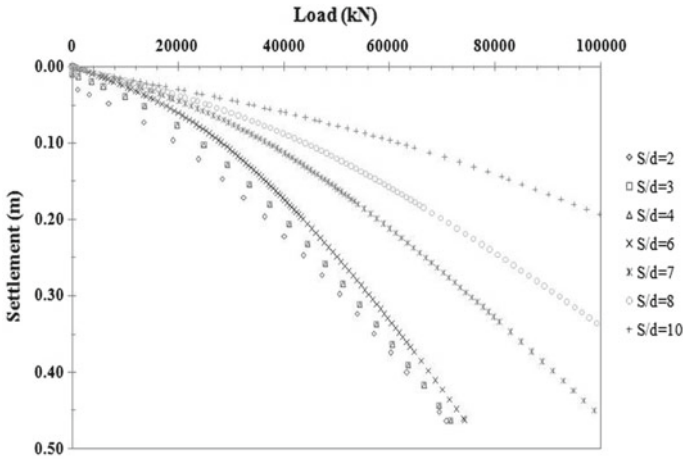


Fig. 5 Load versus settlement for variation in pile spacing

3.2 Variation in Pile Spacing

In this case, a raft of 2 m thickness and piles of 1 m diameter and 15 m length were examined. A prescribed displacement of 0.5 m was given to the raft, and analysis was performed for pile spacing varying from 2d, 3d, 4d, 6d, 7d, 8d, and 10d, where d represents the pile diameter taken into account. Figure 5 represents the load settlement relation for variation in pile spacing. The observation was recorded that the increment in load-carrying capacity of the CPRF was less up to spacing 6d, beyond that drastic increment in load carrying capacity was found for higher spacing as it can be believed that the contribution of larger size raft was more dominant, resulting in compensation for loss of capacity of the system. In addition, in the studies conducted by Sinha and Hanna [7], there was a decrease in load-carrying capacity up to 6d beyond which the authors observed a similar type of pattern. This contradicts the conventional design philosophies, which show a limit of the maximum pile spacing to 3.5d as it was an observation indicate that a decrement in pile interactions was observed beyond 3.5d, which in turn decreases the system’s capacity.

3.3 Variation in Pile Length

In this case, analysis was conducted on a pile length of 5 m, 10 m, and 15 m. The spacing adopted was 6d, and 2 m thick raft was taken into consideration. The pile diameter was kept as 1.0 m, and the size of the raft was taken as 24 m × 24 m. A prescribed displacement of 0.5 m was given in Plaxis 3D, and the corresponding load was obtained by a load-settlement curve. Since the continuum of raft and soil is symmetrical, only a quarter part has been modeled to save computation and model

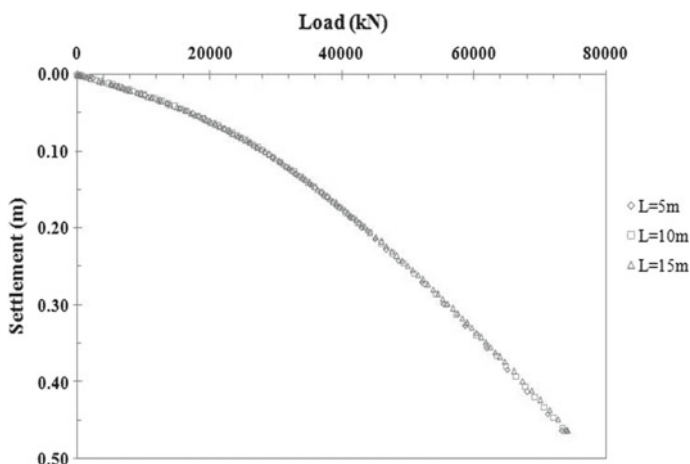


Fig. 6 Load versus settlement for variation in pile length

time. The results obtained by the analysis in the form of the load versus settlement curve are represented in Fig. 6. In the load-carrying capacity of the system, a slight increase has been observed, so there can be compensation in the design between pile length and pile spacing for the more economical design of the foundation.

3.4 Variation in Pile Cross-Section

In this case, the square cross-section was analyzed; its sides varied as 0.4 m, 0.8 m, and 1.2 m. 6d pile spacing and a 24 m and 2 m thick square raft were adopted. A prescribed displacement of 0.5 m was given in Plaxis 3D, and a corresponding load was obtained from the load settlement curve. As a symmetrical raft was adopted, so the only quarter part was modeled to save computational time. Figure 7 represents the results obtained from analysis in the form of load versus settlement curve. It was interpreted from the analysis that there was no significant effect observed by the variation in the cross-sectional size of piles. Hence it is up-to-the structural and geotechnical designers to adopt a suitable cross-section and size of the pile for the economical and safe design of the foundation.

4 Conclusions

In order to examine the effects of various parameters, FE analysis was conducted to evaluate the performance of piled raft foundations. The PLAXIS 3D [1] software program is used for successful problem stimulation. From this study, the following

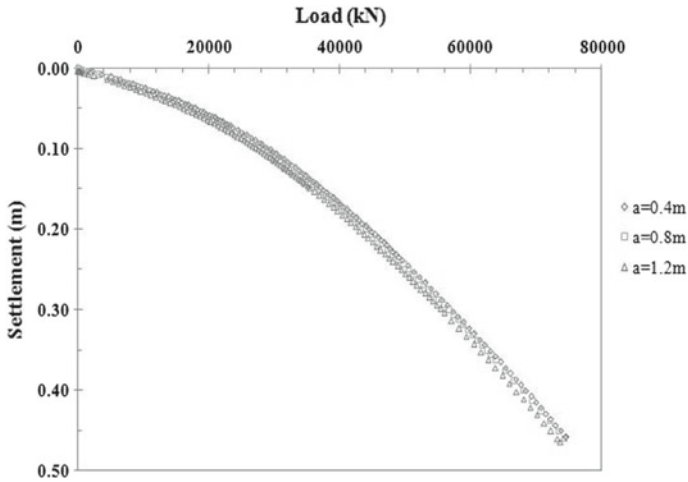


Fig. 7 Load versus settlement for variation in pile cross-section

conclusions can be made from the examination of different parameters of piled raft foundations:

1. Raft settlement increases as pile spacing increases and decreases as pile size and length increase. The system acts as a raft when the spacing between piles exceeds six times the pile diameter.
2. Increased spacing between piles diminishes the aid of increased size and length of the piles in settlement reduction. A swap between spacing, size, and length of piles should be considered to create an affordable design.
3. For the variation in raft thickness, it was noted that the system capacity increased with an increase in raft thickness of up to 1.5 m, beyond which the settlements increased due to raft self-weight, resulting in system failure and less load-carrying capacity. A thinner raft results in unequal load sharing among components of CPRF, and a thicker raft will result in excessive settlements due to more load on piles.

References

1. Plaxis BV (2013) Netherlands user manuals. Plaxis 3D
2. Burland JB, Broms BB, de Mello VFB (1977) Behaviour of foundation and structures. In: Proceedings of 9th ICSMFE, Tokyo, vol 2, pp 495–546
3. Clancy P, Randolph MF (1993) An approximate analysis procedure for piled raft foundations. *Int J Numer Anal Meth Geomech* 17:849–869
4. Poulos HG (2001) Piled raft foundations: design and applications. *Geotechnique* 51(2):95–113
5. Reul O, Randolph MF (2003) Piled rafts in over consolidated clay: comparison of in situ measurements and numerical analyses. *Géotechnique* 53(3):301–315

6. Prakoso WA, Kulhawy FH (2001) Contribution to piled raft foundation design. *J Geotech Geoenviron Eng (ASCE)* 127:1(17):17–24
7. Sinha A, Hanna AM (2017) 3D numerical model for piled raft foundation. *Int J Geomech* 17(2):040160551–040160559

FRP Strengthened Reinforced Concrete Beams Under Impact Loading: A State of Art



Swapnil B. Gorade, Deepa A. Joshi, and Radhika Menon

Abstract Reinforced Concrete structures are subjected to impact loading like collision due to vehicles, ships, and airplanes, impact due to rock-fall or debris, impact due to fall of heavy machines or object on structural member and terrorist activities such as blast or missile impact. The impact loading create severe damage to various structural members. It is not feasible to replace the structure due to high cost, hence it is desirable to repair or strengthen the members by retrofitting techniques. For retrofitting of damaged structural members under static loading the fiber reinforced polymer materials are highly preferred and used rapidly. These materials are being popular because of advantages like high strength and high fatigue resistant, higher resistant to corrosion, lighter in weight and higher stiffness, durable and easy to apply. Lot of investigation was already done on performance of retrofitted RC beams under the static loading but very limited investigation has been carried out on performance of retrofitted RC beams using FRP under impact load. The impact loading characterized by a high intensity load over a short period of time and categorized into low velocity impact or high velocity impact. Longitudinally bonded FRP sheet improve the flexural capacity where FRP bonded in transverse direction provides resistant to shear failure. It was found that the most common method used by researcher is drop weight hammer test. FEA analysis has been carried out previously to simulate the reinforced concrete beams under impact load. The aim of this paper is to review the literature on behavior of reinforced concrete beams strengthen with FRP under impact load. This paper also reviews the retrofitting materials, their properties and impact testing methods for RC beams under impact loading. It is suggested that FRP bonding to the RC beams shows improvements in strength recovery against impact loading.

S. B. Gorade (✉)

Department of Civil Engineering, Dr. D. Y. Patil Institute of Technology, Savitribai Phule Pune University, Pimpri, Pune, India
e-mail: sbgorade7@gmail.com

D. A. Joshi

Department of Civil Engineering, Dr. D. Y. Patil Institute of Technology, Pimpri, Pune, India

R. Menon

Department of Mathematics, Dr. D. Y. Patil Institute of Technology, Pimpri, Pune, India

© The Author(s), under exclusive license to Springer Nature Singapore Pte Ltd. 2023

1001

M. S. Ranadive et al. (eds.), *Recent Trends in Construction Technology*

and Management, Lecture Notes in Civil Engineering 260,

https://doi.org/10.1007/978-981-19-2145-2_74

Keywords FRP · Retrofitting · Strengthening · Impact loading · RC beams

1 Introduction

RC structures are subjected to static as well as dynamic loading. Considering the military application and recent terrorism activities to public infrastructure the study of performance of RC beams strengthened using FRP against impact loading is of great interest. Due to increased traffic density the possibility of impact of vehicle against RC structure like bridges has also increased. Many RC structures are subjected to damaging impact load due to vehicle, ship, airplane, debris, rock fall, missile impact, collapse of crane, and unregulated motions of heavy machines [1–3]. The retrofitting of existing damaged RC beams, done using conventional techniques like steel plate bonding, concrete or steel jacketing increases dead load, it is difficult to apply and tends to corrosion. However in recent years to prolong the life of damaged RC structure the most effective repairing technique is use of externally bonded FRP.

FRP material got popularity for strengthening existing RC structure because it has high strength to weight ratio, high tensile strength, non-corrosive, easy to handle and install without interruption and good resistant to chemical attack [4–11]. A considerable amount of research has been carried out to show the increase in strength, stiffness and ductility of reinforced concrete beams retrofitted with FRP under static loading. However studies on reinforced concrete beams strengthened with FRPs under impact are still limited [1, 12]. Pham and Hao [1] mentioned in their literature that under impact loading the performance of retrofitted reinforced concrete beams also includes the study of FRP-concrete bonding and energy absorption capacity of beam. In such cases size, mass and velocity of impactor are also important parameters. Design guidelines for RC beams strengthened with FRP were also developed by many codes for example guidelines given by ACI 440-2R-17 code. A review of literature was carried out in this paper on FRP retrofitted RC beams under impact loading. It was observed that research on FRC strengthen reinforced concrete beam under impact load is still limited and need more recommendations from research community.

2 FRP Materials and Strengthening Techniques for Impact

An inappropriate selection of FRP material and strengthening technique cannot solve the purpose of repair and strengthening of RC structure. To upgrade the strength requirement and increase the service life of structure, selection of proper strengthening materials and methods needed [13]. The traditional strengthening techniques may include use of concrete or steel jacketing, textile fiber sheet, wire mesh, post tension cables, metallic plate etc. need much space, and they are difficult to apply [14, 15]. For different structural members like columns, beams, slabs and walls the objectives of FRP strengthening techniques are one or more as follows: (1) to increase

the load carrying capacities under axial, flexural or shear, (2) to increase the stiffness, (3) to improve ductility, and (4) to improve durability against external environmental agents [16].

2.1 Types of FRP Materials

FRP composites are manufactured by adding two or more materials to form compound which is superior to its parent material. These composites are manufactured by embedding high strength continuous fibers in a polymer matrix also called resin. There are four FRP composites available in industry, and they are carbon (CFRP), glass (GFRP), basalt (BFRP) and aramid (AFRP) [17, 18].

Fibers are the main reinforcing elements in the polymer matrix which is act as a binder. Polymer matrices (resin) divided into two groups thermosetting (polyesters epoxies and vinyl esters) and thermoplastics (polypropylene, polyvinyl chloride, polyethylene and polyurethane). Thermoplastics are sensitive to environmental conditions, low creep and their production is costly. Thermosetting resins are most popular in construction industry due to their improved mechanical properties [19].

According to ACI 440-2R-17, the unit weight of structural steel is 7.9 g/cm^3 , unit weight of CFRP is $1.5\text{--}1.6 \text{ g/cm}^3$, unit weight of BFRP is $2.2\text{--}2.7 \text{ g/cm}^3$, unit weight of GFRP is $2\text{--}2.1 \text{ g/cm}^3$, and unit weight of AFRP $1.2\text{--}1.5 \text{ g/cm}^3$. Carbon FRP has very high tensile strength (8–10 times of steel) and possesses high strength to weight ratio. It is five times lighter than steel, and it shows very high resistant to creep and fatigue than all others materials.

Epoxy resins are used for excellent bonding between FRP composites and concrete surface. They have 0.9% elongation at break, tensile strength of 30–90 MPa, and elastic modulus of 1.1–6 GPa. CFRP shows better performance than GFRP after crack propagation till failure. When CFRP and GFRP combined together named as hybrid, FRP is the novel retrofitting material shows high ductility and deformability [4].

Figure 1 shows a relation between the stress strain curves for different FRP materials and structural steel. It clearly indicate that FRP material have high strength compare to other conventional materials.

The compressive strength of FRP composite is less than tensile strength and hence is not suitable as compression side reinforcement. BFRP is costlier than GFRP due to lack of producer but have better strength and alkalis resistant. GFRP has the lowest cost, resistant to chemical attack, good thermal insulation and heat resistant and consumed mostly for strengthening of secondary structures. AFRP has heat resistant and is good option in high alkaline environment [17].

As per ACI 440 part 6, CFRP have low specific gravity, density, and high tensile strength than structural steel and GFRP. AFRP shows good tensile strength, lower density than GFRP. FRP shows brittle character and low modulus of elasticity. Table 1 shows the mechanical properties of FRP materials and structural steel.

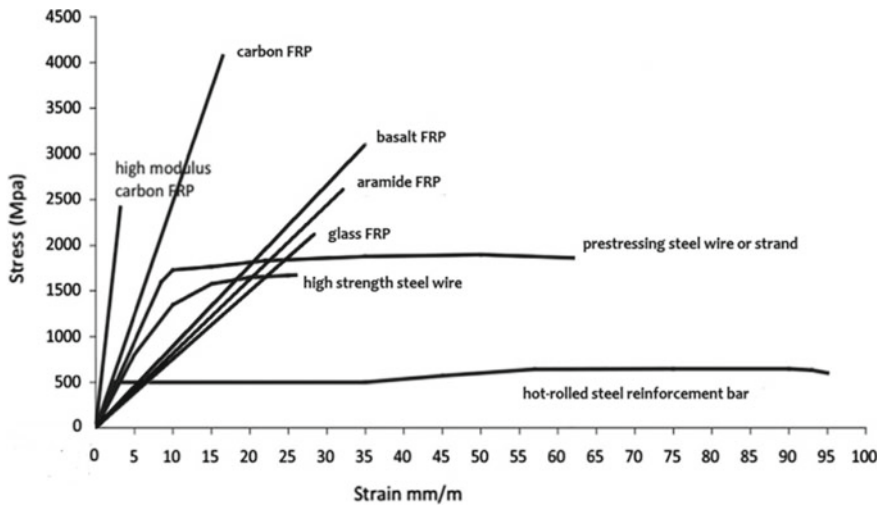


Fig. 1 Comparison of structural steel and various FRP materials [20].

Table 1 Mechanical properties of FRP materials (ACI 440 part 6)

FRP material	Specific gravity	Yield strength (MPa)	Tensile strength (MPa)	Density (g/cm ³)	Elastic modulus (GPa)	Strain at break, in %
CFRP	1.0–1.1	1755–3600	1720–3690	1.55–1.76	120–580	0.5–1.9
GFRP	1.5–2.5	600–1400	480–1600	2.11–2.70	35–51	1.2–3.1
AFRP	1.38–1.39	1700–2500	1720–2540	1.28–2.6	41–125	1.9–4.4
BFRP	2.7–2.89	1000–1600	1035–1650	2.15–2.70	45–59	1.6–3.0
Steel	7.8	500	–	7.75–8.05	200	–

CFRP shows 50–60% mass reduction but higher cost compare to structural steel. GFRP has low weight and high strength. It shows high resistant to chemical attack. Use of AFRP is restricted in construction industry up to light loaded structures due to its extreme low compressive strength. BFRP have good thermal resistivity and ductility than CFRP, and it will be used to strengthen the beams subjected to high temperature. BFRP composite shows improvement in all mechanical properties but its production is costly. While selecting the retrofitting materials, the strength requirement, availability, cost, and environmental conditions need to be considered. The alignment and orientation of fibers in FRP are also important factors and should consider while selecting the retrofitting material [4].

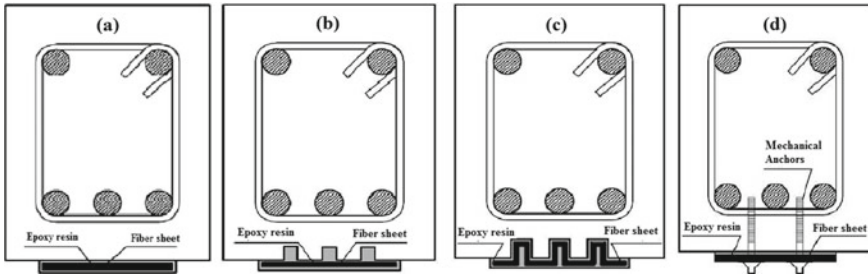


Fig. 2 Beams strengthened with EB technique, **a** using only FRP, **b** FRP on grooves, **c** FRP in grooves, **d** using mechanical anchors [21]

2.2 Strengthening System with FRP for RC Beams

The FRPs are available in the form of laminates, sheets, plates, and rods. The different strengthening systems of RC beams using FRP are as follows:

1. Externally Bonded technique (EB): with grooves, without grooves and mechanically anchored EBR
2. Near Surface Mounted (NSM) bar/strips.

2.2.1 Externally Bonded Technique (EB)

Externally bonded technique is the most common technique used to strengthen RC beam. The main deficiency of this method is possibility of failure due to early debonding of FRP laminate from the concrete surface. Surface preparation is necessary in this method, and it was done by roughening surface by sandblast technique or use of air jet and water jet which can slightly postponed the premature debonding. In this technique, number of FRP layers applied on the beam soffit with groove, without groove and using mechanical anchors as shown in Fig. 2. To strengthen the beams in shear and flexure, FRP is applied in different styles like full wrap, U wrap, side wrap, inclined U wrapping, cross wrap, etc. [1, 4, 21].

2.2.2 Near Surface Mounted (NSM) Bar/Strips

In externally bonded technique, the tensile capacity of FRP is not fully utilized due to early debonding. This deficiency is removed in NSM method. In Near surface mounted (NSM) method FRP bar or FRP strip inserted in the grooves which are provided along the bottom face of the beam (tension face) and then filling the groove completely with epoxy as shown in Fig. 3. The probability of FRP strip debonding from concrete can be reduced by providing anchors, fasteners at the end of strips. It is costly and time consuming process [1, 4, 21].

Fig. 3 RC beam strengthened with NSM, **a** inserting FRP rod in groove, **b** inserting FRP strip in groove [21]

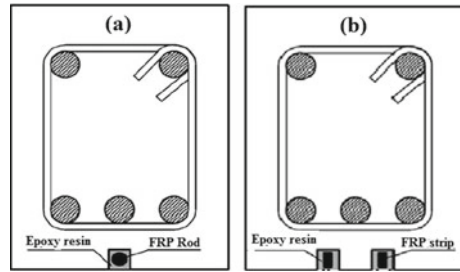


Table 2 Studies on FRP material used for strengthening of RC beams under impact

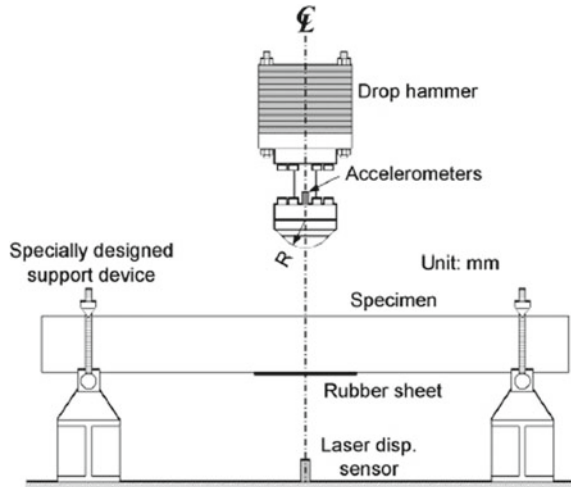
Researcher	Year	Section mm	Span in m	Samples nos	Type of FRP used
Erki and Meier	1999	400 × 300	8.15	4	CFRP laminates and steel plates
Tang and Saadatmanesh	2003	203 × 95	1.83	5	Carbon and kevlar FRP
Tang and Saadatmanesh	2005	203 × 95	1.98–2.9	27	Carbon and kevlar FRP
Soleimani et al	2007	150 × 150	0.8	10	Sprayed GFRP
Thong M. Pham et al	2016	150 × 250	1.5	13	FRP wrap
Fujikakea et al	2017	160 × 170	1.7	20	CFRP sheet and laminate
T. Liu et al	2017	200 × 400	2.4	11	CFRP wrap
A. Remennikov et al	2017	100 × 150	1.2	12	CFRP wrap
Soleimani and Roudsari	2019	150 × 150	1.0	17	Sprayed GFRP
Kishi et al	2020	200 × 250	3.0	12	AFRP and CFRP sheet

Table 2 shows the various studies on FRP material used for strengthening of RC beam under impact loading.

3 Testing Methods Under Impact Loading

Testing methods for reinforced concrete beams strengthened with FRP under impact load should be such that it will simulate the mechanism, loading conditions and failure modes likely to occur. Impact test methods divided into two types (1) impact due to large mass with low velocity and (2) impact due to small mass with high velocity. The most popular method is impact due to large mass with low velocity which includes

Fig. 4 Impact loading setup [2]



drop-weight tests, Izod and Charpy test, hydraulic test machines in which impact velocities designed upto 10 m/s [1]. Izod and Charpy pendulum test shows number of difficulties for researcher hence most common impact testing method adopted by researcher is dropping a weight on RC beam specimen from certain height. In this test the impact velocity of the hammer can be determined by accelerometer or an optical sensor or using high speed camera [1]. Generally a shape of impactor is this test is semispherical. The dynamic capacities of RC beam specimen were calculated by single drop weight test whereas fracture energy can be determined by multi drop test where specimen failed due to number of blows. Main advantage of the drop hammer test is that specimen of large range geometries can be tested. The impact loading applied on beam specimen using drop weight hammer was shown in Fig. 4.

3.1 RC Beams Under Impact Load

RC structures are subjected under impact loading during various instances like crashing vehicles, ships, airplanes, rock fall, failure of crane etc. [2]. An RC beam under impact load was described by its high amplitude in a short duration which causes inertia effects in the beams and strain rate effects in the materials. Hence compared to static loading, beams under impact load behave differently. Impact load have low loading rate of 10 s^{-1} . Impact loads are concentrated on RC beams as point loads for very short duration with higher strain rates than static loading [1, 22].

Externally bonded FRP system is decreases the crack width, decreases the deflection of RC beam and increase the impact strength. It was observed that shear deficient RC beams when retrofitted with FRP and tested under impact load, the impact strength and shear strength were increased by 15% and 96% respectively [22, 23].

Impact strength of RC beams strengthened with FRP is depends upon impact energy, material stiffness, material characteristics, loading rate and strengthening system [22].

3.2 Flexural Strengthened RC Beams Under Impact

Erki and Meier [24] experimentally studied the behavior of flexural strengthened reinforced concrete beams under impact loading. They tested four 8.15 m long beams strengthened with either CFRP laminates or steel plates. The impact loading was given by drop and lift method as lifting one end of a test beam and then dropped from height of 0.5 m, 1 m, 1.5 m and 2 m on the support. The strain rate of loading varied from an average of 0.7 s^{-1} to a maximum of 0.84 s^{-1} . The results showed that the CFRP retrofitted RC beams performed well under impact loading. Beams retrofitted with CFRP laminates could not deliver same energy absorption as the beams strengthened with steel plates. The first occurrence of rupture of FRP or deboning of FRP was not explained in the paper. However from this work is difficult to study the performance of RC beams strengthened with FRP impacted in the mid-span of beam.

Tang and Saadatmanesh [22] used five RC beams of size $203 \times 95 \times 1980 \text{ mm}$, without stirrups in their experimental work. The beams were strengthening with Carbon and Kevlar FRP laminates at top and bottom face of beam under drop weight impact hammer. A steel cylinder was used to apply impact load on top face of the beams. They observed that improvement in the strength gain depends on the type, weight, material properties and thickness of the FRP laminates. They concluded that the composite laminates increases resistant to impact load and reduce maximum deflection. Flexural cracks occurred at bottom face of beam and then propagated upward. After increase in the impact load, the transverse shear cracks were observed. These cracks were extended to the interface between FRP laminate and concrete. The stiffer laminate showed improved capacities and less deflection of the beam under impact loading. Cracks were not found between the interface of concrete and FRP because the compression strain was smaller than the tension strain. The rebound and vibrations response need to study using load cell to calculate reaction forces on both compression and tension forces.

Tang and Saadatmanesh [25] were done experimental study on twenty seven RC beams retrofitted with FRP laminates under impact loading. A steel cylinder was used as a drop weight hammer for impact loading. They observed that composite laminates perform better against impact loading. FRP laminates bonded to RC beam, increased flexural and cracking strength, stiffness of beams, reduce number of cracks. They found that FRP laminates were reduced maximum deflection of strengthen beams by 30–40% than unstrengthen beams under impact loading. During the impact loading, the maximum reaction force was three times higher than the beams under static loading. They suggested an equation for predicting the deflection of beams under impact load based on flexural wave theory. FRP delimitation was reported by same

author in their previous work [22] but it was not recorded by same author in current work. Further investigation will be needed to understand the failure mechanism and structural capacities. The negative moments caused by the structural vibrations due to impact loading was not considered in the work.

Kantar and Anil [26] experimentally investigated ten retrofitted RC beams in flexure with CFRP strips. They conducted experimental work by varying the concrete compressive strength and drop height. Five different drop heights were selected for drop hammer. They found that the dissipated energy and number of drops required for failure were increased. Yilmaz and Anil [27] experimentally tested shear deficient RC beams under impact load which are strengthened with CFRP U-wraps. CFRP strips spacing and impact velocities were the variables in this experimental work. ANSYS software was used to model the RC beams. They concluded that impact behavior of shear deficient RC beams was changes due to CFRP strips attached to beams. They found that, decrease in CFRP strip spacing reduces the acceleration, velocity and displacement.

Pham and Hao [28] experimentally investigated the performance of RC beams retrofitted with FRP under static and impact loading. They tested total thirteen RC beams out of that six RC beams in static loading where seven beams under impact loading. Beams were wrapped with U-wrap system and FRP strips in longitudinal direction. The peeling stress in the normal section of RC beams was not reduced by the tensile force in FRP. To prevent the deboning of longitudinal FRP, the cross-section of four beams soffit was modified and curved shape was given such that the confining stresses from the U-wrap FRP and the stresses in the adhesive resist the peeling stress concentration. They found that due to modification in RC beam section with the same amount of FRP material, delayed the deboning and improved the capacity of longitudinal FRP. Due to the modified RC section, the U-wrap FRP provides confinement effect on longitudinal FRP system. This also reduced the stress concentration at corners of the beam.

Kishi et al. [6] conducted experiments on reinforced concrete beams strengthen with FRP sheets on tension side. They were tested using drop weight impact test under low velocity. Total twelve specimens of 3 m length were tested. AFRP and CFRP sheets having equal axial stiffness were used. This work was carried out to study the improvements in impact resistant, its characteristics and failure pattern of AFRP, CFRP strengthen beam. Out of twelve, ten specimens of RC beams were strengthened with AFRP and CFRP sheets. These specimens were tested by dropping a 300 kg drop hammer from various heights 1, 2, 2.5 and 3 m.

3.3 Shear Strengthened RC Beams Under Impact

Huo et al. [29] investigated that the performance of bond between the concrete and CFRP under drop weight impact test from dynamic loading point of view. They also studied the result of impact loading rate on bond strength, bond length and strain distribution along CFRP strip bonded to RC beams. They found that the impact

loading rate considerably influences the bond strength. This paper focused only on impact loading effects on the bond length and strength between FRP and concrete.

Pham and Hao [28] experimentally studied the impact behavior of FRP retrofitted RC beams and contribution of CFRP to improve the shear strength. They tested thirteen beams of size $150 \times 250 \times 1500$ mm without stirrups and strengthened with CFRP U-wraps and CFRP 45° wraps to study effect of different wrapping schemes. They found that using the same amount of CFRP strips, CFRP at 45° wrapping gave better results than U-wrapping w.r.to the load carrying capacity and deflection of the beams.

Remennikov et al. [30] investigated the performance of RC beams strengthen externally with different CFRP wrapping schemes under static and impact loading. Twelve shear deficient RC beams of size $100 \text{ mm} \times 150 \text{ mm} \times 1200 \text{ mm}$ were strengthen with one or two layers of U-wraps and also one layer of CFRP was fully wrapped. To study the load-deflection, energy absorption capacity and failure modes the six beams were tested under static loading. Remaining six beams were tested under free falling drop weight impact hammer to analyze failure modes, crack patterns and mid span deflection. They concluded that the use of CFRP wrapping as an external reinforcement for shear deficient beams showed improvements in the energy absorption capacity. The failure modes of beams transformed from shear failure to flexural failure.

Fujikake [2] conducted experimental work on RC beams strengthen in shear and weaker in flexural. Twenty RC beams of cross-section 160×170 mm size and 1700 mm length were strengthened with unidirectional CFRP sheets and CFRP laminates. CFRP strengthening was applied to RC beams in four different ways. The CFRP sheets having 150 mm width and 0.222 mm thickness were bonded to the soffit of the beams. For few RC beams, CFRP sheet of width 250 mm and 0.111 mm thickness was installed at the ends of the soffit perpendicular to axis of beam. Some RC beams were bonded with 1.0 mm thick and 50 mm wide CFRP laminates to the soffit of the RC beams. A 300 kg drop hammer was dropped freely from the height of 100, 200, 400 mm to produce single impact on beams. It was observed that crack width is significantly decreased for CFRP strengthened RC beams compare to unstrengthen RC beam.

Liu and Xiao [12] done experimental work on eleven RC beams without stirrups, of cross section $200 \text{ mm} \times 400 \text{ mm}$ and length 2400 mm under static and impact loading. CFRP strips were used to retrofit RC beams and wrapped fully around it such that the strips were perpendicular to the axis of the beam. In this experimental work the effect of impact mass, impact velocity and impact energy was mainly considered. They also studied the failure modes, crack patterns, mid span deflection, strains in CFRP and dynamic behavior including time history. They concluded that for shear deficient RC beams without stirrups, full wrapping with CFRP strips found effective. To prevent local punching shear near impact area the increased width of CFRP strips was effective. The strain of CFRP strips which was far away from impact area found low. They also found that the high impact velocity under same energy decreases the reaction force and deflection but increases the impact force.

Table 3 Studies on impact technique used for FRP strengthened RC beams

Researcher	Year	Type of FRP used	Hammer weight (kg)	Drop height in m
Erki and Meier	1999	CFRP laminates and steel plates	Lift and drop	0.5 m, 1 m, 1.5 m and 2 m
Tang and Saadatmanesh	2003	Carbon and kevlar FRP	22.6	0.305, 0.61, 0.91, 1.22, 1.53, 1.83, 2.14, 2.44, 2.74 m
Tang and Saadatmanesh	2005	Carbon and kevlar FRP	22.6	0.3–1.7 m
Soleimani et al	2007	Sprayed GFRP	591	0.8 m
Thong M. Pham et al	2016	FRP wrap	230.5	2.5 m and 3 m
Fujikakea et al	2017	CFRP sheet and laminate	300	0.1, 0.2 and 0.4 m
T. Liu et al	2017	CFRP wrap	383, 513, 773	1.5 m and 3 m
A. Remennikov et al	2017	CFRP wrap	580	50 mm
Soleimani and Roudsari	2019	Sprayed GFRP	591	2.5 m
Kishi et al	2020	AFRP and CFRP sheet	300	1, 2, 2.5 and 3 m

Huo et al. [23] studied experimentally the performance of CFRP wrapping system bonded with RC beams without stirrups under impact loading and failure mechanism was observed. They also studied FRP contribution to shear strength. Total fifteen beams casted and out of that five beams for static and 10 beams for impact loading were tested. From experiments, they found that the strengthening with single 45° CFRP wraps was very effective than that of CFRP U-wraps. Test result showed that amount of CFRP, its arrangement and impact energy was played an important role. Table 3 shows the summery of studies on impact technique used for FRP strengthened RC beams.

4 Discussion and Conclusion

The proper selection of FRP material and strengthening technique achieve the objectives of strengthening such as improvements in strength, stiffness, ductility. The above literature review provides a clear understanding of the performance of reinforced concrete strengthened with FRP under impact. It is concluded that FRP bonding to the RC beams shows improvements in strength recovery and protect the RC beams against impact load. The outcome of this review listed below:

1. RC beams shows better flexural, shear resistant capacities under impact loading when wrapped externally bonded FRP.
2. The important contribution of FRP is the improvement of service life of existing RC beams.
3. The rupture and deboning mechanism of EB FRP require more investigation. If the bond strength between reinforced concrete beam and FRP improves then it gives high stiffness and resistant to impact.
4. Low velocity impact test with drop weight hammers is generally observed in most of the research work.
5. Use of end anchorage control the FRP debonding and depends on loading condition and strengthening configuration.
6. Due to change of loading from static to impact loading the failure pattern of strengthened RC beam changes from flexural to flexural shear.
7. Further investigation is needed on performance of RC beams strengthened with FRP under impact loading.

References

1. Pham TM, Hao H (2016) Review of concrete structures strengthened with FRP against impact loading. *Structures* 7:59–70
2. Fujikake K et al (2017) CFRP strengthened RC beams subjected to impact loading. *Procedia Eng* 210:173–181
3. Soleimani, Roudsari (2019) Analytical study of reinforced concrete beams tested under quasi-static and impact loading. *J Appl Sci* 9(2838):2–16
4. Siddika A et al (2019) Strengthening of reinforced concrete beams by using fiber-reinforced polymer composites: a review. *J Build Eng* 25(100798):1–12
5. Nasrin S et al (2017) Behavior of retrofitted UHPC beams using carbon fiber composites under impact loads. *J Struct Congr* 392–402
6. Kishi N et al (2020) Low-velocity impact load testing of RC beams strengthened in flexure with bonded FRP sheets. *J Compos Constr* 24(5):04020036, 1–10
7. Snehal K, Das BB (2019) Mechanical and permeability properties of hybrid fibre reinforced porous concrete. *Indian Concr J* 93(1):54–59
8. Srikumar R, Das BB, Goudar SK (2019) Durability studies of polypropylene fibre reinforced concrete. In: *Sustainable construction and building materials*. Springer, Singapore, pp 727–736
9. Yadav S, Das BB, Goudar SK (2019) Durability studies of steel fibre reinforced concrete. In: *Sustainable construction and building materials*. Springer, Singapore, pp 737–745
10. Goudar SK, Shivaprasad KN, Das BB (2019) Mechanical properties of fiber-reinforced concrete using coal-bottom ash as replacement of fine aggregate. In: *Sustainable construction and building materials*. Springer, Singapore, pp 863–872
11. George RM, Das BB, Goudar SK (2019) Durability studies on glass fiber reinforced concrete. In: *Sustainable construction and building materials*. Springer, Singapore, pp 747–756
12. Liu T, Xiao Y (2017) Impact behavior of CFRP-strip-wrapped RC beams without stirrups. *J Compos Constr* 21(5):04017035, 1–14
13. Sumukh EP, Goudar SK, Das BB (2021) Predicting the service life of reinforced concrete by incorporating the experimentally determined properties of steel–concrete interface and corrosion. In: *Recent trends in civil engineering*. Springer, Singapore, pp 399–417

14. Al-Mahaidi R, Kalfat R (2018) Methods of structural rehabilitation and strengthening. In: Rehabilitation concrete structure with fiber-reinforced polymer, chap 2. Elsevier, Amsterdam, pp 7–13
15. Siddika A et al (2019) Flexural performance of wire mesh and geotextile-strengthened reinforced concrete beam. *SN Appl Sci* 1:1324
16. Buyukozturk O, Gunes O, Karaca E (2004) Progress on understanding debonding problems in reinforced concrete and steel members strengthened using FRP composites. *Constr Build Mater* 18(1):9–19
17. Amran YHM et al (2018) Properties and applications of FRP in strengthening RC structures: a review. *Structures* 16:208–238
18. Shakir Abbood I et al (2021) Properties evaluation of fiber reinforced polymers and their constituent materials used in structures: a review. *Mater Today Proc* 43:1003–1008. <https://doi.org/10.1016/j.matpr.2020.07.636>
19. Naser MZ et al (2019) Fiber-reinforced polymer composites in strengthening reinforced concrete structures: a critical review. *Eng Struct* 198:109542
20. Rousakis T et al (2010) Retrofitting and strengthening of contemporary structures: materials used, *Encycl. Earthq. Eng., Berlin, Heidelberg: Springer Berlin Heidelberg* (eds) pp. 1–15 <https://doi.org/10.1007/978-3-642-36197-5-303-1>
21. Seyyed MB et al (2015) Reviewing the FRP strengthening systems. *Am J Civ Eng* 3(2):38–43. Special issue: research and practices of civil engineering in developing countries
22. Tang T, Saadatmanesh TH (2003) Behavior of concrete beams strengthened with fiber-reinforced polymer laminates under impact loading. *J Compos Constr* 7(3):209–218
23. Huo J et al (2018) Dynamic behavior of CFRP-strengthened reinforced concrete beams without stirrups under impact loading. *ACI Struct J* 115:775–787
24. Erki M, Meier U (1999) Impact loading of concrete beams externally strengthened with CFRP laminates. *J Compos Constr* 3(3):117–124
25. Tang T, Saadatmanesh TH (2005) Analytical and experimental studies of fiber-reinforced polymer-strengthened concrete beams under impact loading. *ACI Struct J* 102(1):139–149
26. Kantar E, Anil Ö (2012) Low velocity impact behavior of concrete beam strengthened with CFRP strip. *Steel Compos Struct* 12(3):207–230
27. Anil Ö, Yilmaz T (2015) Low velocity impact behavior of shear deficient RC beam strengthened with CFRP strips. *Steel Compos Struct* 19(2):417–439
28. Pham TM, Hao H (2016) Impact behavior of FRP-strengthened RC beams without stirrups. *J Compos Constr ASCE* 20(4):04016011, 429–440
29. Huo J et al (2016) “Experimental study on dynamic behavior of CFRP to concrete interface”, beams without stirrups under impact loading. *J Compos Constr* 20(5):1–12
30. Remennikov A et al (2017) Impact performance of concrete beams externally bonded with carbon FRP sheets. In: *Mechanics of structures and materials: advancements and challenges*, pp 1695–1699. ISBN 978-1-138-02993-4

Effect of Lateral Stiffness on Structural Framing Systems of Tall Buildings with Different Heights



A. U. Rao, Sradha Remakanth, and Aditya Karve

Abstract Even though the gravity loads are the primary loading on a building, as the building height increases, it will be exposed to the lateral loads due to wind and earthquakes. Hence, the building must be designed to have sufficient stiffness and strength in order to resist the lateral loadings. In order to limit the lateral displacement, additional structural materials will be required for tall buildings, and to achieve economy it is always desirable to use an appropriate structural system. In this paper, three-dimensional structural systems are studied and compared using six different building heights. The parameters such as lateral displacement, inter storey drifts, time period and base shear are compared between these systems with respect to the height. From the study, it has been observed that outrigger structural systems are not only proficient in controlling the top displacements but also play a substantial role in reducing the inter storey drifts.

Keywords Core walls · Lateral loads · Lateral displacement · Structural system · Tall building

1 Introduction

A building is said to be tall or high rise when it has different aspects of design, construction and use compared to those of common buildings in certain regions and periods. It is a matter of human perception and hence the definition of tall buildings cannot be universally applied. When a tall building is subjected to appreciable lateral loading, such as earthquake and high wind pressure, special structural arrangements such as moment frame, shear wall, tube structure and outrigger must be adopted to resist these forces. The selection of a structural system for a particular building

A. U. Rao (✉) · S. Remakanth
Department of Civil Engineering, Manipal Institute of Technology, Manipal Academy of Higher Education, Manipal 576104, Karnataka, India
e-mail: asha.prabhu@manipal.edu

A. Karve
Walter P Moore Engineering India Pvt. Ltd., Pune, India

© The Author(s), under exclusive license to Springer Nature Singapore Pte Ltd. 2023
M. S. Ranadive et al. (eds.), *Recent Trends in Construction Technology and Management*, Lecture Notes in Civil Engineering 260,
https://doi.org/10.1007/978-981-19-2145-2_75

1015

depends upon several factors such as architectural requirements, functionality of building, loading, occupancy and aspect ratio. Various structural systems available for tall building constructions are as follows.

1.1 Moment Frame System

It is the structural system which consists of frames, i.e. beams and columns in order to resist the gravity and lateral loading. The frames can be parallel or inclined in which the beams and columns are connected by moment-resistant joints. These structural systems are convenient due to their rectangular frame which is clear of structural forms, thereby providing an unobstructed layout. Moment frame systems are found to be efficient up to a height of 60 m, above which the sizing of the members has to be increased in order to limit the lateral displacement. The effectiveness of the building improves when the moment frame systems are adopted along with shear walls.

1.2 Structural Wall System

In this system, the walls are rigidly connected with the floor diaphragm which helps in proper load path when the building is subjected to lateral loadings. Buildings with structural walls are found to add more stiffness to the building compared with frame systems as they resist the vertical as well as lateral loading.

1.3 Moment Frame and Structural Wall System

This system is a combination of moment frame and structural wall system, where gravity loading is mainly taken by the moment frame and lateral loading is resisted by the structural wall.

1.4 Tube System

Tube system consists of a perimeter frame with closely spaced columns connected by a deep spandrel. It acts as a hollow vertical cantilever. The lateral resistance for this system is provided by the perimeter frame. A special type of tube system includes a braced tube, which allows greater spacing between the columns with diagonal bracing connected at the exterior. Another variation is the bundled tube which consists of two or more tubes tied together to form a single multi-cell tube.

1.5 Structural Wall with Outrigger System

In this system, a core wall is connected to these perimeter columns using beam elements called outriggers at discrete floor locations. It is a lateral load-resisting system where the outriggers tie the central core with the external peripheral columns. The lateral loads, due to wind and earthquake, acting on the central core will be transferred to the peripheral columns through the outriggers and hence reduce the overturning moment. Outrigger systems can be further classified into three:

1.5.1 Conventional Outrigger

In this, the outriggers are directly connected with the central core with the columns at the periphery.

1.5.2 Offset Outrigger System

Outriggers are located elsewhere than in the plane of the core wall.

1.5.3 Virtual Outrigger System

In this system, the direct load is transferred from the core to the outrigger without a direct connection. This is achieved with the help of the floor diaphragm which converts the overturning moment into a horizontal couple. Belt trusses are also added for this system.

2 Literature Review

Badami and Suresh [1] have studied the behaviour of various structural systems (moment frame system, core wall system and outrigger) subjected to lateral loading in the case of tall buildings. ETABS was used to model the buildings, wherein parameters such as lateral displacement, storey drifts, storey displacement and base shear values were checked in order to find the structural efficiency. Wind loading considered was not uniform throughout the structure, nor it was constant with time, and it varied on different sides of the building. It was observed that this creates a lot of problems for tall buildings and is the major concern of engineers. In this paper, it was concluded that outrigger systems are the most efficient in controlling top displacement as well as inter storey drifts compared to rigid frame systems which have relatively high lateral stability.

Baraskar and Kawade [2] made a comparison between the structural wall system and the conventional system for a 15-storied building using ETABS software. Wind loading and seismic loading were considered for the analysis of both structural systems. In this paper, it was concluded that the time period of the beam-column system is higher compared to the structural wall system. Also, the lateral displacement and the storey drifts of the conventional systems are found to be more than the structural wall system. The structural wall system is found to provide better performance than the conventional system. It was also concluded from the study that the structural framing of the structural wall system is cheaper than the moment frame system.

Titiksha and Gupta [3] studied various structural framing systems subjected to lateral loadings. The study was conducted for a 4-storied building with three structural systems—ordinary moment resisting frames (OMRF), special moment resisting frames (SMRF) and braced steel frames (BSF). The seismic Zone V was adopted in the analysis, and efficiencies of the building were determined by checking the storey drifts and base shear. From this study, it was concluded that the SMRF showed better results than OMRF. In BSF, lateral loading is resisted effectively and their service life is more even though they are costly. They concluded that the storey drifts are effectively resisted in BSF compared to that in OMRF and SMRF.

Jose et al. [4] have studied the effect of lateral stiffness on different structural systems (frame system, core wall system and dual system) which were subjected to lateral loadings. Staad Pro software was used for the analysis of three-dimensional models to assess all the lateral load-resisting systems under the effect of wind loads and seismic loading. It was concluded that the lateral displacement of bare frame systems is high compared to systems with external and internal infills. It was observed that there is considerable variation in the lateral displacement of the frame with core and staircase compared to that of the bare frame system.

Hemavati and Ramya [5] studied lateral load-resisting systems for high-rise buildings. They incorporated a rigid frame system, shear wall system with opening and framed tube system, and studied their behaviour by comparing the parameters such as lateral displacement, lateral drifts and base shear. They concluded that the displacement was significantly reduced by using a braced frame system than a rigid frame or frame tube system. It was observed that the stiffness parameter is achieved by the frame tube system compared to the rigid frame or braced frame system. Also, the braced frame system helped in minimizing the storey drifts.

Yadhav and Rai [6] conducted a comparison study of moment-resisting frames with regular as well as irregular structures for different seismic zones using Staad Pro software to find out their behaviour when subjected to lateral loadings. They observed that maximum bending moment, shear force and displacement occurs in irregular plaza building, whereas it is minimum in regular frame building. Thus, it was concluded that the performance of a regular frame is better than an irregular frame considering parameters such as displacement, shear force and bending moment.

Baygi and Khazae [7] investigated the optimal number of outriggers in a tall structure to reduce the top storey displacement. They considered three types of lateral loading—uniform, triangular and centralized, and also studied the effects of variation

in structural elements such as column, outriggers and core on the optimal number of outriggers. They observed that four or more outriggers did not improve the reduction in structural displacements.

Hafner et al. [8] have studied the impact of the negative and positive shear lag effect on a tall tube structure. They conducted a parametric analysis with parameters including the ratio of column spacing and column dimensions, the ratio of storey height and the height of connecting beams, the ratio of the layout dimensions of the entire building and the type (profile) of horizontal load being used. They conducted a parametric analysis with the main purpose of detecting the critical height of the tall building where the transfer from positive to negative shear lag occurs. Based on the study, they suggested the transformation from the positive to the negative shear lag is conditioned by the layout dimensions ratio in tall tube structural systems.

Sawant and Bogar [9] have studied the seismic behaviour of tall structures with outriggers and the belt truss system using linear dynamic and non-linear time history analysis along with the V and X bracing systems. They concluded that X bracing systems are better, and time history analysis gave a better response for tall buildings under earthquake loading.

Nassani and Ali [10] compared the structural response of different types of lateral load-resisting systems (moment-resisting frame system, shear wall system, dual system and framed tube system) under the effect of seismic and wind loads using ETABS. They analysed a building having 28 storeys each with an area of 625 m² (25 m × 25 m), and the storey displacements were evaluated for all lateral load-resisting systems. They found that of all the types of lateral load-resisting systems, the dual system showed a very suitable structural response for this height without exceeding the limitation.

Kavyashree et al. [11] have reviewed the outrigger structural systems from conventional outriggers as a rigid connection to damped outriggers with a passive, active, semi-active and hybrid control system. They have briefly reviewed the outriggers with respect to types, analysis of tall buildings without outriggers, formulation of equations for outrigger structure to simplify the analysis, approaches to locate optimum positioning of outriggers and the damped outrigger system. The authors particularly stressed outrigger structure with semi-active control and performance enhancement of the outrigger system with the effective devices. Based on their review, they have stressed the need for precise semi-active and hybrid control techniques which would make outrigger structural systems perform better and be economically feasible.

Based on the above brief literature review, in order to find out the effective structural systems for buildings of heights 60–250 m, it is decided to conduct a comparative study. Six different heights are considered and the lateral displacements are compared for buildings consisting of different systems such as moment frame system, structural wall system, tube system and outrigger system.

In the present paper, various lateral force-resisting structural systems such as moment frame system, structural wall system, tube system and outrigger system are compared with conventional structures for six different heights (60 m, 80 m, 120 m, 180 m, 200 m and 250 m), to conclude on an efficient system that can be adopted.

3 Modelling of Different Structures

3.1 Model Specifications

Plan dimension: 45 m \times 30 m.

Storey height: 4 m.

Seismic zone: III.

Location: Pune (Wind speed is 39 m/s).

Building type: Commercial building with LL 2.5 kN/m² and SDL 2.5 kN/m².

Grade of beam: M30.

Grade of column: M40.

The building is modelled for 4 different structural systems, such as moment frame, structural wall system, tube system and outrigger system using ETABS. Also, a comparison of these systems is done for 6 different heights such as 60 m, 80 m, 120 m, 180 m, 200 m and 250 m. Loads acting on the building are taken to be the same for all the structural systems.

3.2 Modelling of Moment Frame System

A moment frame building was modelled in ETABS with a plan dimension of 45 m \times 30 m which can be seen in Fig. 1. The beam size adopted is 300 mm \times 600 mm and the column size adopted is 800 mm \times 800 mm. The thickness of the slab provided is 175 mm. The spacing of columns is between 5 and 5.75 m.

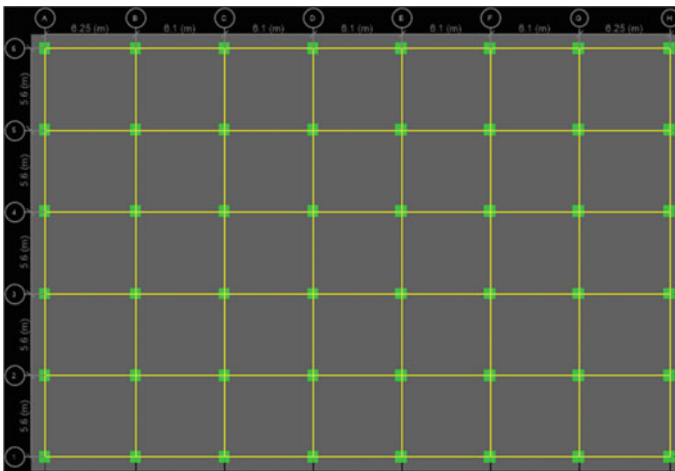


Fig. 1 Plan of moment frame building

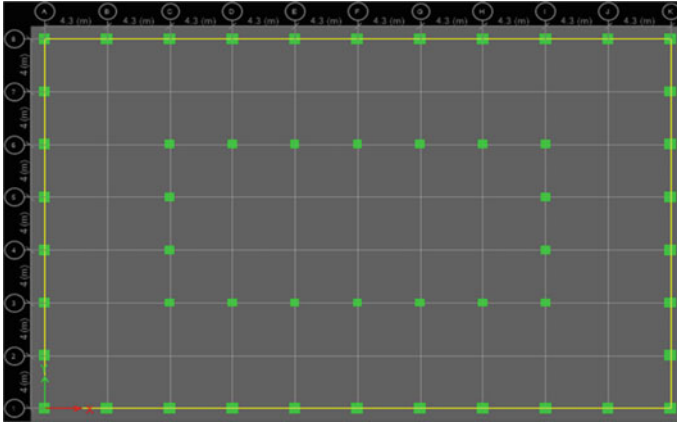


Fig. 2 Plan of tube structure

3.3 Modelling of Tube System

The columns of the tube system having sizes $800 \text{ mm} \times 800 \text{ mm}$ are spaced between 4 and 4.5 m, and are connected by deep beams of $600 \text{ mm} \times 1200 \text{ mm}$, as shown in Fig. 2. The perimeter tube frame mainly resists the lateral loads acting on the building. Interior columns of $650 \text{ mm} \times 650 \text{ mm}$ size are provided which resist mostly the gravity loading acting on the building. Loads acting on the building are taken to be the same for all the structural systems. The slab thickness provided is 275 mm and the stiffness modifier applied to them is 0.01. The diaphragm assigned is rigid, as there are no irregularities in the plan.

3.4 Modelling of Structural Wall System

In this system, the core walls are provided in the form of three I sections, and the thickness of the wall is 300 mm, as shown in Fig. 3. Perimeter beams of size $300 \text{ mm} \times 600 \text{ mm}$ and columns of dimensions $800 \text{ mm} \times 800 \text{ mm}$ are provided around the building. Perimeter beams and columns take care of the gravity loading. The slab thickness provided is 275 mm and the slab is modelled as a shell. Hence, the lateral loading acting on the building will be transferred to the wall through the meshing of the slab. The core walls take part in resisting lateral loading.

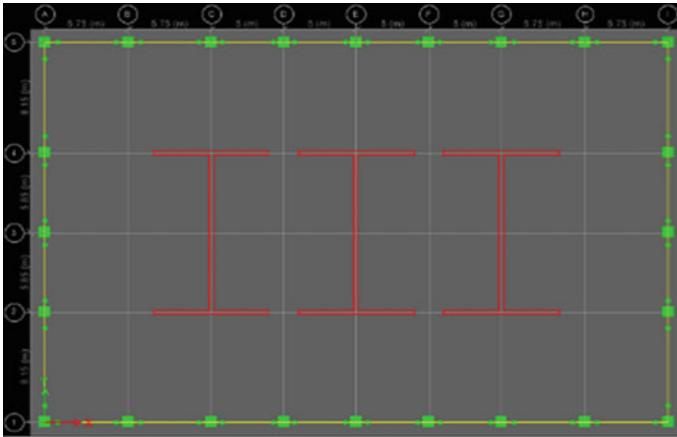


Fig. 3 Plan of structural wall system

3.5 Modelling of Outrigger System

The ETABS model is the same as that of the structural wall with a perimeter frame, where the structural core wall is connected to the exterior columns using outriggers, which are modelled as a spandrel beam having one storey height, as shown in Fig. 4. Outrigger is provided in one storey for a building with a height of 200 m, as shown in Fig. 5. The location of the outrigger is taken as mid-height of the building which is found to be more efficient.

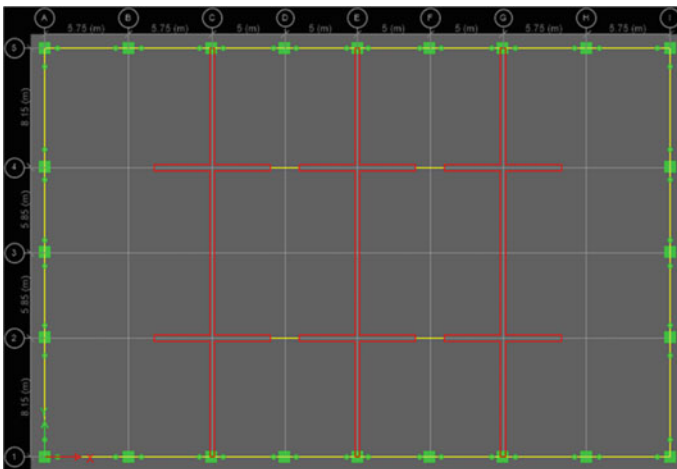
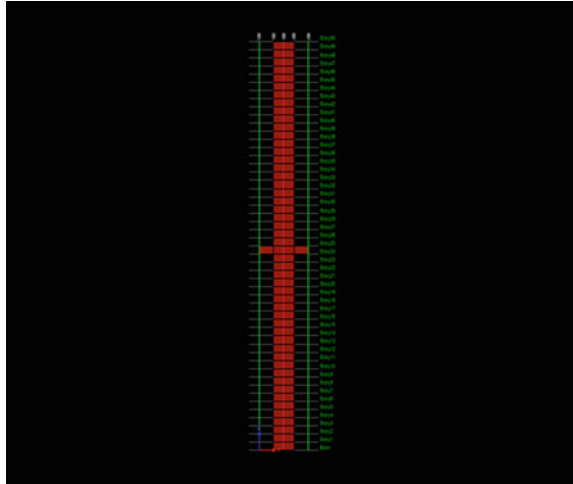


Fig. 4 Plan of outrigger system

Fig. 5 Elevation of outrigger system



4 Results and Discussions

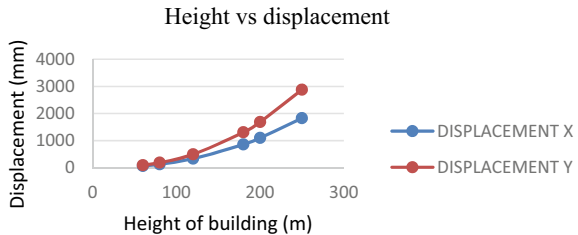
4.1 Moment Frame System

For moment frame building of 60 m, the displacement in the *X* direction and *Y* direction obtained are 64.336 mm and 93.882 mm, respectively. As the limit of displacement for a height of 60 m is 120 mm ($H/500$), the building displacements are within the limit at this particular height for a bare frame system.

When the building height is increased to 80 m, the displacement values obtained in the *X* and *Y* directions are 127.794 mm and 187.238 mm, respectively. The limit of displacement for a building height of 80 m is 160 mm, indicating that displacement in the *Y* direction is more than the limited value.

- Figure 6 shows that the displacement of the building increases with the building height. It is seen that the increase in displacement in the *Y* direction is around 40% more compared to displacement in the *X* direction.

Fig. 6 Height versus displacement plot for moment frame



- For moment frame building of 60 m, the drifts in the X direction and Y direction obtained are 0.0016 and 0.00157, respectively. The limit of inter storey drift is $H/250$ which is 0.004, which is satisfied.
- When the height is increased to 180 m, the drift values obtained are 0.00594 and 0.00581 in the X and Y directions, respectively. Hence, the building is not safe for seismic drift when it exceeds a height of 120 m (Fig. 7).
- The depth of the perimeter beam was changed from 1200 to 2000 mm and the results were checked. By increasing the depth of the spandrel beam, the displacement in the Y direction was brought down to 342 mm which is within the limit (400 mm) which can be observed in Fig. 8.
- From Fig. 9, it is observed that the drift of the building increases as the building height increases. The percentage difference of drift values in the X and Y directions is around 36%.

Fig. 7 Height versus displacement for tube structure with spandrel depth 1200 mm

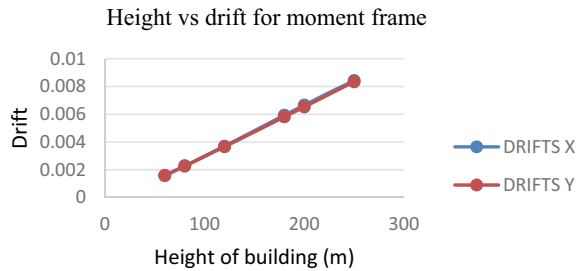


Fig. 8 Height versus displacement for tube structure with spandrel depth 2000 mm

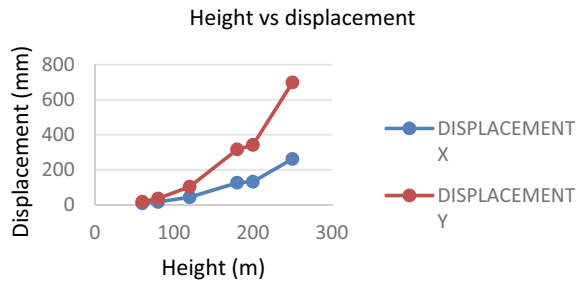
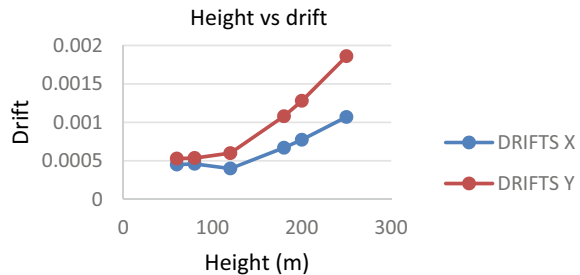


Fig. 9 Height versus drift plot for tube structure



4.2 Structural Wall with Perimeter Frame System

- From Fig. 10, it is seen that displacement is 480 mm at a height of 180 m, which exceeds the limit of $H/500$, (i.e. 400 mm).
- In order to reduce these displacements, link beams are provided to connect the structural walls, as shown in Fig. 11.
- For building height after 180 m, link beams of size 300 mm × 600 mm are used at each floor level. Coupling beams/link beams are used to connect shear wall or other elements and are used to withstand the lateral loading. Also, the horizontal wall thickness was changed from 300 to 450 mm to bring the displacements within the limit. By doing so, the displacement is found to be off the limit from a height of 200 m.

Fig. 10 Height versus displacement of building with structural wall and frame

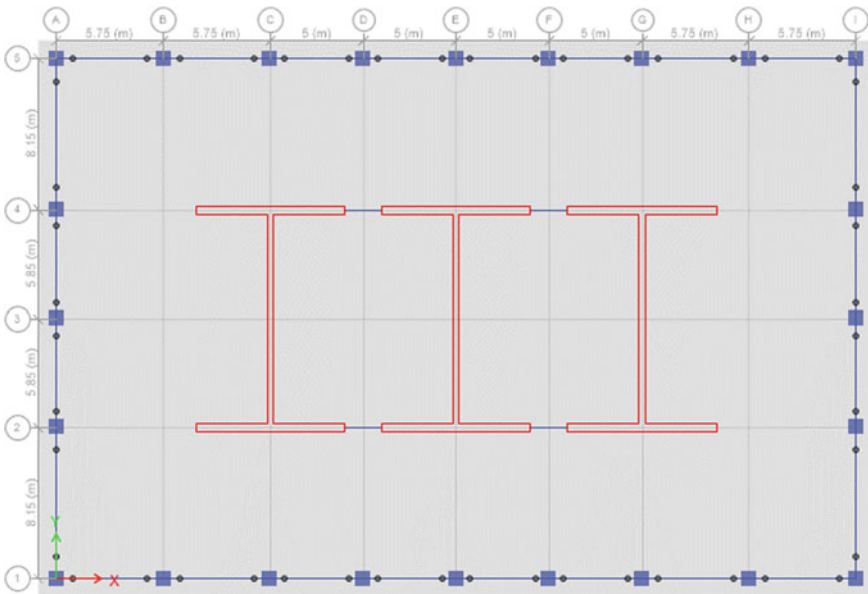
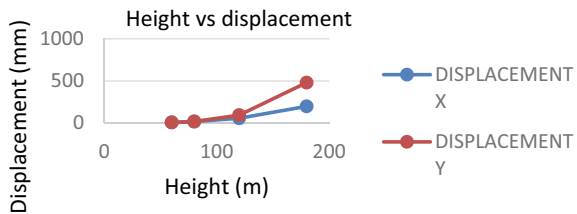


Fig. 11 Plan of structural wall system connected with link beams

Fig. 12 Height versus displacement plot of structural wall connected with link beams

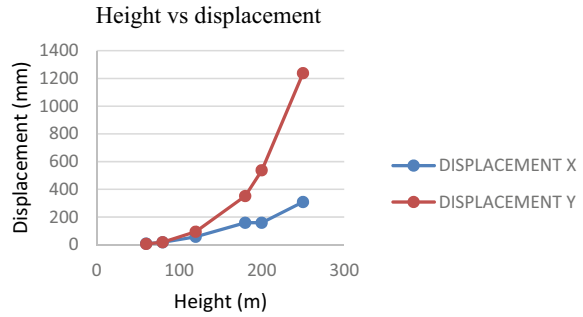
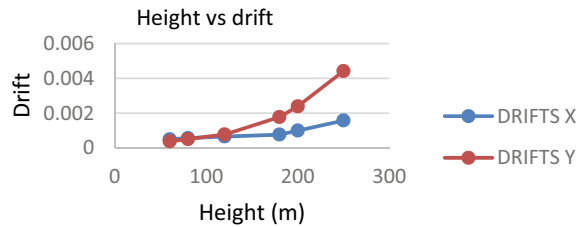


Fig. 13 Height versus drift plot for structural wall system



- Outriggers are introduced in the structural wall building which helps in resisting the lateral loading more effectively and bring the displacement values within the limit.
- From Fig. 12, it can be observed that the displacement exceeds the limiting value (400 mm) at a height of 200 m. Hence, the building is not found to be efficient from this particular height.
- It can be seen from Fig. 13 that the drift values are within the limit for the building with structural walls up to a height of 200 m. The limiting value taken is $H/250$ (0.004).

4.3 Outrigger System

- For a building with outrigger systems, it can be observed from Fig. 14 that the displacement in X and Y directions for both 200 m and 250 m is within the permissible limits. For a height of 200 m, the limit is 360 mm and for 250 m the limit is 496 mm.
- The drifts of the outrigger structure were checked for a height of 200 m and 250 m which can be seen in Fig. 15. It is observed that the drift values were within the limit (0.004).

Fig. 14 Displacement of outrigger system at 200 m and 250 m

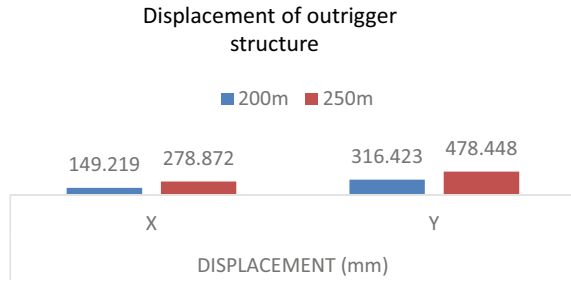
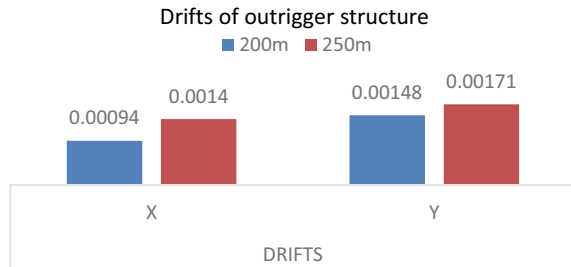


Fig. 15 Drifts in X and Y of outrigger system with heights 200 and 250 m



5 Comparison of Results

- In the present study, four different structural systems (moment frame, tube system, structural wall with perimeter frame and outrigger system) are compared for parameters such as displacement and drift, in buildings with six different heights (60 m, 80 m, 120 m, 180 m, 200 m and 250 m).
- By comparing the displacements from Figs. 16 and 17, it is seen that the outrigger is the most efficient for very tall buildings above a height of 200 m.
- The conventional moment frame system displaces highly as the height increases. This displacement can be brought down by the introduction of a structural wall system and also with tube structure.

Fig. 16 Plot of displacement values in X direction for different structural systems

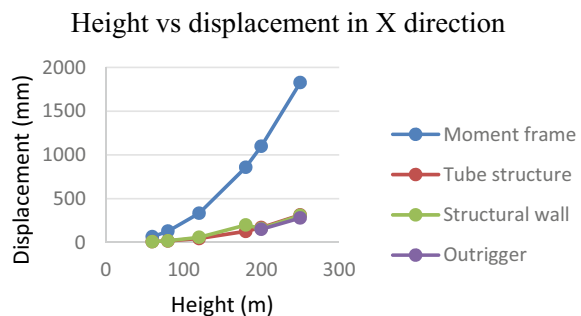
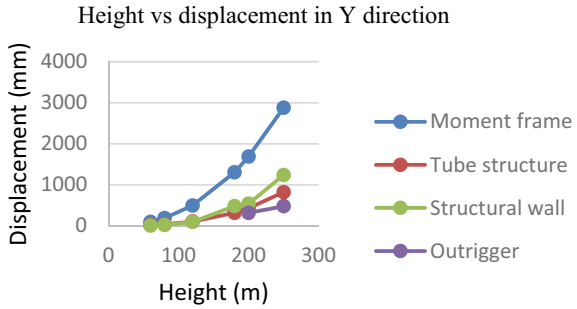


Fig. 17 Plot of displacement values in Y direction for different structural systems



- Very tall building such as with a height of 250 m is effective with the introduction of an outrigger system.
- Comparison of drift along X and Y directions for different structural systems was also plotted which can be seen in Figs. 18 and 19, respectively. Similar results as in the displacement study are obtained while checking the drift values along the X direction.

Fig. 18 Plot of drifts in X direction for different structural systems

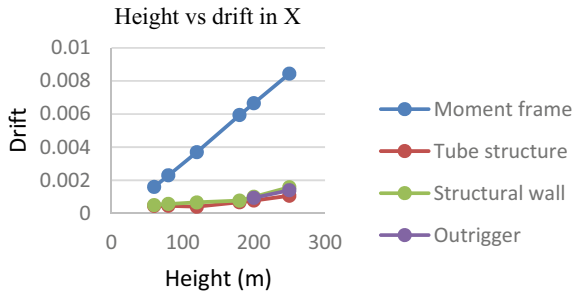
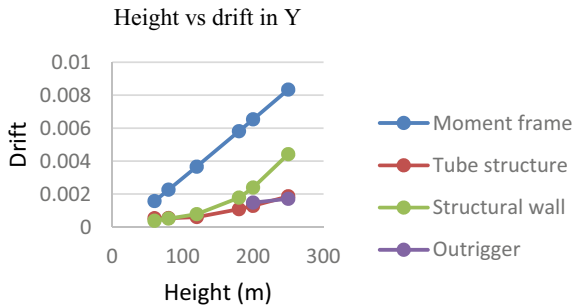


Fig. 19 Plot of drifts in Y direction for different structural systems



6 Conclusions

- From the study on the conventional system, it is observed that the lateral displacements (both X and Y) are within permissible limits for smaller heights up to 60 m. As the building height increases, the lateral displacement also increases.
- It is observed that increasing the member sizes for moment frame systems in order to control the deflection tends to be uneconomical, and hence other structural systems must be adopted.
- Structural wall systems and tube systems can be adopted for buildings from 60 to 200 m.
- In the case of the structural wall frame systems beyond 200 m, outriggers can be used to connect the core to the exterior columns so that the lateral displacements can be controlled effectively.
- For the max height for a tall building of 250 m (according to IS 16700: 2017), the outrigger system is found to be more suitable. The outrigger structural systems are not only proficient in controlling the top displacements but also play a substantial role in reducing the inter storey drifts.

Thus, from the study conducted and comparison made using six different building heights for three-dimensional structural systems with parameters such as lateral displacement, inter storey drifts, time period and base shear, it has been observed that outrigger structural systems are very efficient not only in controlling the top displacements but also reducing the inter storey drifts.

References

1. Badami S, Suresh MR (2014) A study on behavior of structural systems for tall buildings subjected to lateral loads. *Int J Eng Res Technol* 3(7):2278–3181
2. Baraskar NB, Kawade UR (2015) Structural performance of RC structural wall system over conventional beam-column system in G+15 storey building. *Int J Eng Res Gen Sci* 3(4):2091–2730
3. Titiksha A, Gupta MK (2015) A study of various structural framing systems subjected to seismic loads. *Int J Civ Eng* 2(4):2348–8352
4. Jose SM, Rao AU, Abubaker KA (2017) Comparative study on the effect of lateral stiffness on different structural framing systems subjected to lateral loads. *Int J Civ Eng Technol* 8(6):398–410
5. Hemavati S, Ramya K (2017) The structural behavior of lateral load resisting system induced in tall buildings—a comparative study. *J Chem Pharm Chem* 83:0974–2115
6. Yadav AK, Rai A (2017) A seismic comparison of RC special moment resisting frame considering regular and irregular structures. *Int J Eng Sci Res Technol* 6(2):2277–9655
7. Baygi, Khazaei (2019) The optimal number of outriggers in a structure under different lateral loadings. *J Inst Eng (India) Ser A* 100:753–761. <http://doi.org/10.1007/s40030-019-00379-7>
8. Hafner I, Vlašić A, Kišiček T, Renić T (2019) Parametric analysis of the shear lag effect in tube structural systems of tall buildings. *Appl Sci* 11:278. <https://doi.org/10.3390/app11010278>
9. Sawant VD, Bogar VM (2019) Parameters comparison of high rise RCC structure with steel outrigger and belt truss by linear and non-linear analysis. *Int J Eng Trends Technol* 67(7):15–23

10. Nassani DE, Ali K (2020) Lateral load resisting systems in high-rise reinforced concrete buildings. *Eur J Sci Technol.* <http://doi.org/10.31590/ejosat.808269>
11. Kavyashree BG, Patil S, Rao VS (2021) Evolution of outrigger structural system: a state-of-the-art review. *Arab J Sci Eng.* <https://doi.org/10.1007/s13369-021-06074-9>

Free Vibration Response of Functionally Graded Cylindrical Shells Using a Four-Node Flat Shell Element



R. B. Dahale, S. D. Kulkarni, and V. A. Dagade

Abstract In the present work, a flat shell quadrilateral element with four nodes is developed for the free vibration analysis of Functionally Graded Cylindrical Shells by modifying the ‘discrete Kirchhoff quadrilateral plate element’ based on Reddy’s third-order theory developed earlier by the second author. This four-node shell element has seven degrees of freedom (DOF) per node, namely three displacements, two rotations of mid-plane, and two transverse shear strain components. In the present work, Functionally Graded Cylindrical shell panels with simply supported and clamped boundary conditions, with various R/a ratios and with different volume fraction indices, are analysed for free vibration response. The property variation through the thickness is according to the power law. To assess the performance of the developed element, the results, of non-dimensionalised frequencies, are compared with the results presented in the literature. A comparison of results shows that the developed element yields quite accurate results with a coarser mesh, which leads to computational efficiency.

Keywords Functionally graded material · Free vibration · Cylindrical shell · Transformation matrix

1 Introduction

Functionally graded materials (FGM) are used in the aerospace industry as well as in other fields of modern technology, especially where structures are subjected to high differential temperatures. FG materials are composite material that is microscopically heterogeneous and made from metals and ceramic combination. Ceramic plays a role of a thermal barrier and the metal gives the required ductility. Unlike laminated composites, these are free from de-bonding, as the transition from one phase to another is smooth. Many researchers have tried to understand this material

R. B. Dahale (✉) · S. D. Kulkarni · V. A. Dagade
Department of Civil Engineering, College of Engineering Pune, Pune, Maharashtra 411005, India
e-mail: rajendra2299@gmail.com

© The Author(s), under exclusive license to Springer Nature Singapore Pte Ltd. 2023 1031
M. S. Ranadive et al. (eds.), *Recent Trends in Construction Technology and Management*, Lecture Notes in Civil Engineering 260,
https://doi.org/10.1007/978-981-19-2145-2_76

with different geometrical variations, supporting condition variations, material variations, and volume fraction of those material variations. The plethora of mathematical techniques of problem-solving including the 3D elasticity approach, meshless technique, 2D higher-order shear deformation theories with an analytical approach, and 2D theories with finite element solutions have been tried to get its dynamic and static study. The finite element having optimum nodes (4 nodes) and degrees of freedom (7 DOF) is the one used here with the third-order theory.

2 Material Properties of FGM

FG Material has two phases, namely the ceramic phase and the metal phase. The properties change gradually from one phase to another. The material property variation, through the thickness, is predicted by Voigt’s rule of mixtures (ROM).

$$P(z) = P_b + (P_t - P_b)(0.5 + / - z/h)^n \tag{1}$$

The material property variation profile through the thickness of the shell is characterised by power-law index n ($0 \leq n \leq \infty$). P_b is the material properties at the bottom layer, whereas P_t is for the top layer of the shell. The shell thickness is ‘ h ’. Poisson’s ratio is the same for both materials.

It is attainable to generate an infinite number of composition arrangements in the metal-ceramic phase by differing the value of ‘ n ’. The variations in the volume fraction of the ceramic phase and metal phase by non-dimensional thickness coordinate (z/h) are set out in Fig. 1 for five values of the power-law indices. ‘ n_c ’ for ‘ceramic top configured’ shell and ‘ n_m ’ for ‘metal top configured’ shell show the volume fraction index in the graphs.

It is understandable from the graphs that as volume fraction index ‘ n_c ’ increases in the ‘ceramic top configured FGM’ shell, the ceramic content drops, and metal

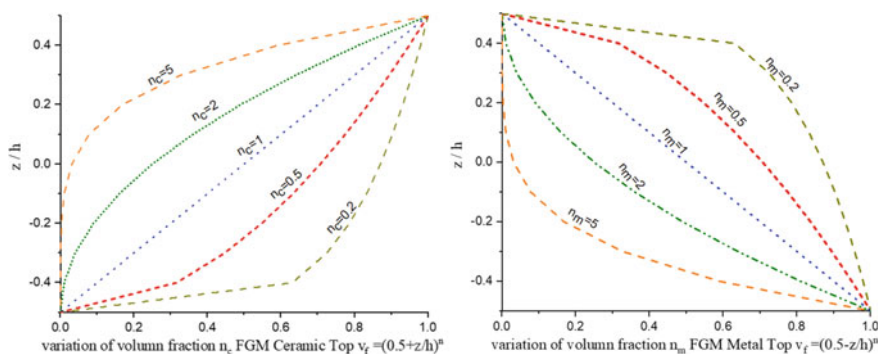


Fig. 1 Effect of variation of the volume fraction through the thickness of a shell

content increases. It means at ‘ n_c ’ = zero, the shell turns to ceramic whereas for ‘ n_c ’ = ∞ , it turns to metal and vice versa in the ‘Metal top configured’ shell.

2.1 Displacement Field Approximation

Consider a cylindrical shell (Fig. 2) with a thickness ‘ h ’ with a ceramic-layered top and metal-layered top configuration. The shell’s middle surface is known to be a reference plane where z is zero and the top surface is at $z = ‘h/2’$ and the bottom surface is at $z = ‘-h/2’$. These shells are analysed using the plate element developed by the second author and his co-workers and presented in Deshpande [1] and Deshpande [2], with necessary modifications. The plate element is based on Reddy’s Third-Order Theory.

The displacement field approximation is as follows:

$$w(x, y, z, t) = w_o(x, y, t), \tag{2}$$

$$u(x, y, z, t) = u_o(x, y, t) - z\omega_o + R(z)\psi_o(x, y, t) \tag{3}$$

where

$$u = \begin{bmatrix} u_x \\ u_y \end{bmatrix}, w_{o,d} = \begin{bmatrix} w_{o,x} \\ w_{o,y} \end{bmatrix}, u_o = \begin{bmatrix} u_{ox} \\ u_{oy} \end{bmatrix}, \psi_o = \begin{bmatrix} \psi_{ox} \\ \psi_{oy} \end{bmatrix}$$

and

$$R(z) = \left[z - \left\{ \frac{4z^2}{3h^2} \right\} \right] \tag{4}$$

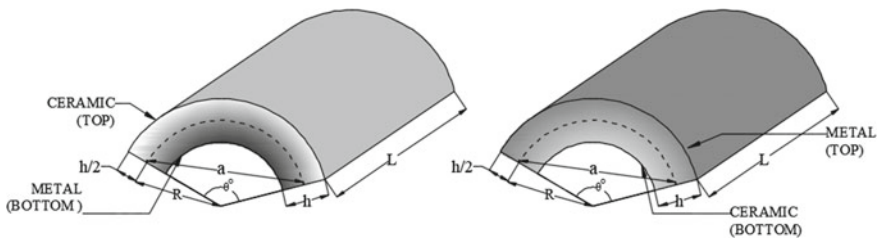


Fig. 2 Geometry of FGM ceramic top and FGM metal top configured cylindrical shells

2.2 Finite Element Formulation of Flat Shell Element

The cylindrical shell shown in Fig. 2 is discretised by using the quadrilateral elements as shown in Fig. 3. Before assembling these elements, it is required to transform the actions and displacements from local directions to global directions. The concept of two coordinate systems used for obtaining transformation matrices given by Clough [3] is extended here for the free vibration analysis of moderately a thick FG cylindrical shell. The orientations of local, global, and surface coordinate axes are shown in Fig. 3.

‘A fixed set of surface coordinates (ξ_1, ξ_2, ξ_3) in which ξ_3 is taken normal to the shell surface at every point is shown in Fig. 3. Cartesian coordinates (x, y, z) are shown in the same figure. It is assumed that rotation about the normal to the tangent plane would be negligible in the actual shell. Accordingly, rotational degrees of freedom referred to as the surface coordinates (ξ_1, ξ_2) per nodal point are only included in the base system describing the assembled structure by Clough [3]’. Thus in this approach, the local translational degrees $u_{0x}^i, u_{0y}^i, w_0^i$ are transformed to a base coordinate system with reference to global Cartesian coordinates (x, y, z) , and the rotational degrees $\theta_{0x}^i, \theta_{0y}^i, \psi_{0x}^i, \psi_{0y}^i$ are transformed to a surface coordinate system (ξ_1, ξ_2, ξ_3) , neglecting the contribution to (ξ_3) .

U_i^e is local and U_i^e is the global displacement vector for i th node shown in the following expressions.

$$U_i^e = [u_{0x}^i \ u_{0y}^i \ w_0^i \ \theta_{0x}^i \ \theta_{0y}^i \ \psi_{0x}^i \ \psi_{0y}^i]^T \tag{5}$$

$$U_i^e = [u_{0x}^i \ u_{0y}^i \ w_0^i \ \theta_{0\xi_1}^i \ \theta_{0\xi_2}^i \ \psi_{0\xi_1}^i \ \psi_{0\xi_2}^i]^T \tag{6}$$

Transformation matrix T^i for transforming the local translational DOF to global translational DOF for an i th node is given by the following expression.

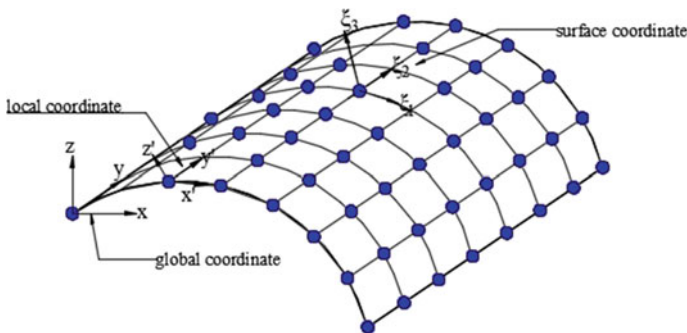


Fig. 3 Local, global, and surface coordinate systems in discretised cylindrical shell

$$\begin{bmatrix} u_{0x}^i \\ u_{0y}^i \\ w_0^i \end{bmatrix} = \begin{bmatrix} \lambda_{11} & \lambda_{12} & \lambda_{13} \\ \lambda_{21} & \lambda_{22} & \lambda_{23} \\ \lambda_{31} & \lambda_{32} & \lambda_{33} \end{bmatrix} \begin{bmatrix} u_{0x}^i \\ u_{0y}^i \\ w_0^i \end{bmatrix} \quad \text{i.e. } u_0^i = T_i u_0^i \quad (7)$$

where $\lambda_{11}, \lambda_{12}$, etc. are the direction cosines of the local (primed) axes with respect to global (unprimed) axes.

The relationship between the local rotations and global rotations for an i th node is given by the following expression.

$$\begin{bmatrix} \theta_{0x}^i \\ \theta_{0y}^i \\ \theta_{0z}^i \end{bmatrix} = \begin{bmatrix} \lambda_{22} & \lambda_{21} & \lambda_{23} \\ \lambda_{12} & \lambda_{11} & \lambda_{13} \\ \lambda_{32} & \lambda_{31} & \lambda_{33} \end{bmatrix} \begin{bmatrix} \theta_{0x}^i \\ \theta_{0y}^i \\ \theta_{0z}^i \end{bmatrix} \quad \text{i.e. } \theta_0^i = \bar{T}_i \theta_0^i \quad (8)$$

The relationship between the surface rotations $\theta_{0\xi}^i$ and θ_0^i for the i th node can be obtained as follows, For a circular cylindrical shell, the angle between the global x -axis and tangent ξ_1 can be obtained easily as this tangent is actually tangent to the circle $x^2 + z^2 = R^2$ in the x - z plane. Differentiating this expression for the circle yields $\tan\alpha = -x/z$. α is the angle between the axes ξ_1 and x . In addition, as the axis ξ_2 is along the global y -axis, the angle between them is always zero. Using this, the following relationship between $\theta_{0\xi}^i$ and θ_0^i for the i th node can be obtained as given below

$$\begin{bmatrix} \theta_{0\xi_1}^i \\ \theta_{0\xi_2}^i \\ \theta_{0\xi_3}^i \end{bmatrix} = \begin{bmatrix} 1 & 0 & 0 \\ 0 & \cos(\alpha) & \cos(\frac{\pi}{2} - \alpha) \\ 0 & \cos(\frac{\pi}{2} + \alpha) & \cos(\alpha) \end{bmatrix} \begin{bmatrix} \theta_{0x}^i \\ \theta_{0y}^i \\ \theta_{0z}^i \end{bmatrix} \quad \text{i.e. } \theta_{0\xi}^i = T_\xi^i \theta_0^i \quad (9)$$

Using Eqs. (8) and (9), relationship between the θ_0^i and $\theta_{0\xi}^i$ is given as

$$\theta_{0\xi}^i = T_\xi^i \bar{T}^T \theta_0^i = \bar{T}_i^\xi \theta_0^i \quad (10)$$

The transformation matrix T_i^ξ of size 2×2 , which relates the local rotations $\theta_{0x}^i, \theta_{0y}^i$ to tangential rotations $\theta_{0\xi_1}^i, \theta_{0\xi_2}^i$, are obtained by removing the third row and third column of the transformation matrix \bar{T}_i^T . T_i^ξ is also used for transforming ψ_{0x}^i, ψ_{0y}^i , to tangential shell directions. Finally, the element transformation matrix of size $28 \times 28 T^e$ is given as

$$T^e = \begin{bmatrix} T_1 & 0 & 0 & 0 & 0 & 0 & 0 & 0 & 0 & 0 & 0 & 0 & 0 \\ 0 & T_1^\xi & 0 & 0 & 0 & 0 & 0 & 0 & 0 & 0 & 0 & 0 & 0 \\ 0 & 0 & T_1^\xi & 0 & 0 & 0 & 0 & 0 & 0 & 0 & 0 & 0 & 0 \\ 0 & 0 & 0 & T_2 & 0 & 0 & 0 & 0 & 0 & 0 & 0 & 0 & 0 \\ 0 & 0 & 0 & 0 & T_2^\xi & 0 & 0 & 0 & 0 & 0 & 0 & 0 & 0 \\ 0 & 0 & 0 & 0 & 0 & T_2^\xi & 0 & 0 & 0 & 0 & 0 & 0 & 0 \\ 0 & 0 & 0 & 0 & 0 & 0 & T_3 & 0 & 0 & 0 & 0 & 0 & 0 \\ 0 & 0 & 0 & 0 & 0 & 0 & 0 & T_3^\xi & 0 & 0 & 0 & 0 & 0 \\ 0 & 0 & 0 & 0 & 0 & 0 & 0 & 0 & T_3^\xi & 0 & 0 & 0 & 0 \\ 0 & 0 & 0 & 0 & 0 & 0 & 0 & 0 & 0 & T_4 & 0 & 0 & 0 \\ 0 & 0 & 0 & 0 & 0 & 0 & 0 & 0 & 0 & 0 & T_4^\xi & 0 & 0 \\ 0 & 0 & 0 & 0 & 0 & 0 & 0 & 0 & 0 & 0 & 0 & T_4^\xi & 0 \end{bmatrix} \tag{11}$$

After deriving the expressions for transformation matrix T^e , local stiffness matrix $K^{e'}$, local mass matrix $M^{e'}$, and local load vector $P^{e'}$, finally the element stiffness matrix K^e of size 28×28 , element mass matrix M^e of size 28×28 , and element load vector P^e of size 28×1 with reference to global axes are given as

$$\begin{aligned} M^e &= T^{eT} M^{e'} T^e, \\ K^e &= T^{eT} K^{e'} T^e, \\ P^e &= T^{eT} P^{e'} \end{aligned} \tag{12}$$

2.3 Assembly of Element Matrices

Summing up the contributions of all elements, Hamilton’s principle yields

$$\overline{M}\ddot{U} + \overline{K}U = \overline{P} \tag{13}$$

where \overline{K} , \overline{M} , and \overline{P} are the assembled counterparts of matrices K^e , M^e , and P^e . For synchronous vibration, the \overline{P} (load vector) is set to zero. The undamped natural frequencies ω_n are obtained by solving the eigenvalue problem.

3 Numerical Results

Using the above formulation, a computer program in FORTRAN compiler 95 is developed for the free vibration analysis. The formulation is evaluated by comparing the results of non-dimensionalised natural frequencies with the results available in

the literature of Pradyumna and Bandyopadhyay [4], Aragh and Hedayati [5], and Zhu et al. [6]. In all the problems, except that presented in Table 2, the full shell ‘ceramic top’ configured panel shown in Fig. 2 is modelled with an $M \times M$ mesh of equal size elements.

The material properties considered for metal and ceramic in all the problems unless specified are:

Aluminium: Modulus of Elasticity $E_m = 70$ GPa; density $\rho_m = 2707$ kg/m³; Poisson’s ratio $\nu_m = 0.3$ and
 Zirconia: Modulus of Elasticity $E_c = 380$ GPa; density $\rho_c = 3000$ kg/m³; Poisson’s ratio $\nu_c = 0.3$.

The obtained natural frequencies are non-dimensionalised as

$$\bar{\omega} = \omega a^2 \sqrt{\rho_m h / D_m}, \quad \text{where } D_m = E_m h^3 / (12(1 - \nu_m^2))$$

3.1 Simply Supported Cylindrical Shell Panels

The non-dimensionalised fundamental frequencies of the FGM cylindrical shell with all edges simply supported are presented in Table 1. The table highlights the radius to span ratio variation from deep to shallow shell for a moderately thick ($ah = 10$) shell. When the ‘ R/a ’ ratio is 0.5, the shell is deep and when the ‘ R/a ’ is 10 it becomes a shallow shell. The results are obtained using 12×12 , 16×16 , and 24×24 mesh and are compared with those presented in Pradyumna [4] obtained using 8 node elements and 2D analytical results in Aragh [5], based on the higher-order shear deformation theories.

From Table 1, it is observed that the frequencies are inversely proportional to the ‘ R/a ’ ratio. Stiffness is higher for the deep shell, whereas it reduces in the shallow shell and so the frequencies decrease. It is also important to note that with an increase in volume fraction, the shell becomes metallic and frequencies get reduced. With the increase in volume fraction index, the mass of the shell decreases, but it has less effect on frequencies than the stiffness.

Table 2 shows the results of non-dimensionalised natural frequencies for FGM ‘ceramic top configured’ and ‘metal top configured’ rectangular cylindrical shell panels with volume fractions $n_c = 1$ and $n_m = 1$, respectively. The panels with a subtended angle of 30° and 90°, $L/R = 1$, $h/R = 0.1$, and $R = 1$ m are solved with the developed element considering various mesh sizes of $M \times M$ with unequal size elements.

The material used as metal is Aluminium and Ceramic is Zirconia, the properties of which are as follows:

Aluminium: Modulus of Elasticity $E_m = 70$ GPa; density $\rho_m = 2707$ kg/m³, Poisson’s ratio $\nu_m = 0.3$,

Table 1 Non-dimensionalised fundamental frequency parameter for (SSSS) cylindrical FG shell panels with different R/a ratios

n_c	$R/a \rightarrow$	0.5	1	5	10
0	Pradyumna [4]	68.8645	51.5216	42.2543	41.9080
	Aragh [5]	69.9700	52.1003	42.7160	42.3677
	Present (12 × 12)	70.2200	52.9231	42.0741	41.7270
	Present (16 × 16)	68.5123	50.6418	42.0952	41.7570
	Present (24 × 24)	66.7074	50.3306	42.1069	41.7570
0.2	Pradyumna [4]	64.4001	47.5968	40.1621	39.8472
	Aragh [5]	65.4304	48.1341	39.0836	38.7568
	Present (12 × 12)	67.7320	49.0650	40.3388	39.9896
	Present (16 × 16)	66.0990	48.8372	40.3596	40.0186
	Present (24 × 24)	64.3677	48.5362	40.3716	40.0390
0.5	Pradyumna [4]	59.4396	43.3019	37.2870	36.9995
	Aragh [5]	60.3574	43.7689	36.0944	35.7891
	Present (12 × 12)	61.8813	44.7951	36.2649	35.9135
	Present (16 × 16)	60.4155	44.5774	36.2844	35.9392
	Present (24 × 24)	58.8568	44.2988	36.2964	35.9577
1	Pradyumna [4]	53.9296	38.7715	33.2268	32.9585
	Aragh [5]	54.7141	39.1621	32.0401	31.7608
	Present (12 × 12)	55.6641	40.2597	32.1270	31.7834
	Present (16 × 16)	54.3597	40.0517	32.1445	31.8053
	Present (24 × 24)	52.9788	39.7949	32.1559	31.8213
2	Pradyumna [4]	47.8259	34.3338	27.4449	27.1789
	Aragh [5]	48.5250	34.6852	27.5614	27.3238
	Present (12 × 12)	49.4001	35.7563	28.5729	28.2627
	Present (16 × 16)	48.2350	35.5578	28.5886	28.2813
	Present (24 × 24)	47.8259	35.3223	28.5994	28.2952

Zirconia: Modulus of Elasticity $E_c = 151$ GPa, density $\rho_c = 3000$ kg/m³, Poisson’s ratio $\nu_c = 0.3$.

The obtained natural frequencies are non-dimensionalised as

$$\bar{\omega} = \omega L^2 / h \sqrt{\rho_c / E_c}$$

It can be perceived from the tables that the results obtained using the present element with a rectangular profile are close to the 2D analytical results of Zhu (2014). The maximum percentage difference as compared to the 2D analytical results of Zhu (2014) is less than 1.6%. The table also gives the insight that for subtended angle 30°, the frequencies are more though it is a shallow shell ($R/a = 1.92$) in comparison

Table 2 Convergence of frequencies for functionally graded all-round simply supported (SSSS) rectangular cylindrical shells

FGM config.	θ	Results	$\bar{\omega}_1$	$\bar{\omega}_2$	$\bar{\omega}_3$	$\bar{\omega}_4$	$\bar{\omega}_5$	$\bar{\omega}_6$
‘Ceramic Top’	30°	Zhu [6]	1208.65	1939.38	1982.04	3100.41	3593.17	3683.06
		Present (12 × 12)	1213.65	1968.95	1984.76	3097.74	3598.06	3689.05
		Present (16 × 16)	1211.72	1967.54	1982.92	3097.77	3597.30	3686.88
		Present (24 × 24)	1210.32	1966.07	1981.33	3097.28	3596.71	3685.71
	90°	Zhu [6]	763.86	766.02	1208.79	1228.35	1464.65	1604.52
		Present (12 × 12)	771.79	773.03	1212.47	1228.62	1464.68	1607.40
		Present (16 × 16)	769.94	770.13	1210.27	1227.93	1464.09	1605.29
		Present (24 × 24)	768.10	768.48	1208.77	1227.55	1463.53	1603.64
‘Metal Top’	30°	Zhu [6]	1227.60	1919.12	2001.33	3120.25	3649.26	3683.06
		Present (12 × 12)	1229.98	1936.20	2000.02	3113.17	3649.58	3689.14
		Present (16 × 16)	1228.77	1932.00	1999.18	3114.51	3650.24	3686.95
		Present (24 × 24)	1227.89	1928.70	1998.36	3114.97	3650.57	3685.77
	90°	Zhu [6]	767.33	774.87	1227.74	1228.35	1470.40	1615.29
		Present (12 × 12)	772.80	779.70	1230.37	1230.80	1469.95	1616.76
		Present (16 × 16)	770.44	777.21	1229.11	1229.92	1469.65	1615.19
		Present (24 × 24)	768.71	775.47	1228.22	1229.45	1469.28	1613.92

with 90° ($R/a = 0.639$) shells. With a 30° subtended angle, the shell becomes thick as ‘ alh ’ ratio is 5.29, whereas for the 90° subtended angle ‘ alh ’ ratio is 15.708, and the shell becomes very thin. The span to thickness ratio has affected the frequency values. Metal top configured cylindrical shell gives slightly higher values of the non-dimensionalised frequencies for both the subtended angles.

In Figs. 4, 5, 6 and 7, the graphs show the variations of the first six non-dimensionalised frequencies of FGM Aluminium/Zirconia all-round simply supported (SSSS) moderately thick ($alh = 10$) cylindrical shells with volume fraction index for different ‘ R/a ’ ratios. Figures 4 and 5 present the variation for deep shell $R/a = 0.5$ and 1, whereas Figs. 6 and 7 present for a shallow shell with ‘ R/a ’ = 5 and 10. The results were obtained using a mesh size of 24 × 24.

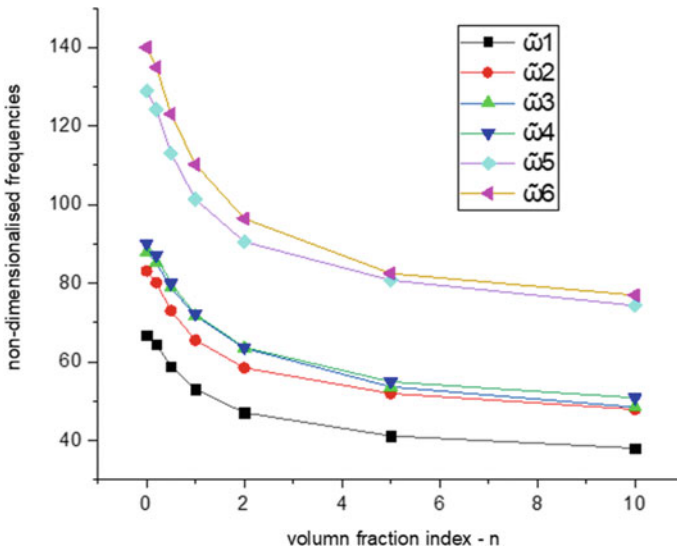


Fig. 4 Variations of the first six consecutive frequencies with volume fraction for ($R/a = 0.5$)

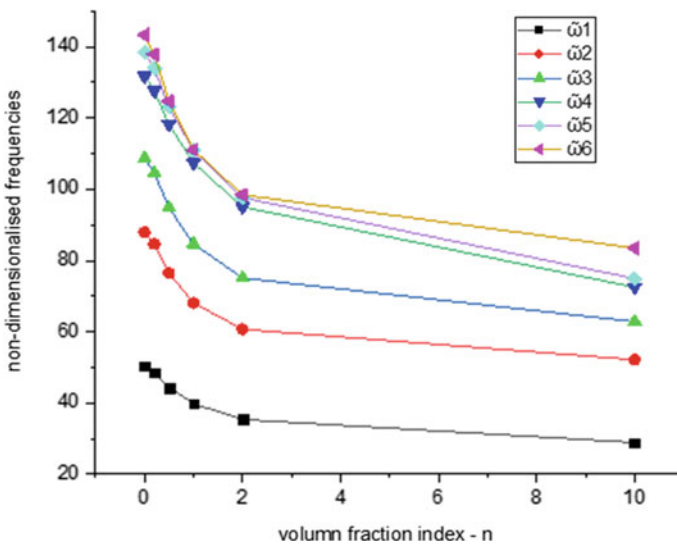


Fig. 5 Variations of the first consecutive frequencies with volume fraction for ($R/a = 1$)

With the increase in volume fraction as the shell becomes metallic, frequencies get reduced. From the graph, it is also observed that as the R/a ratio increases, the shell becomes shallow thereby resulting in reduced values of frequencies.

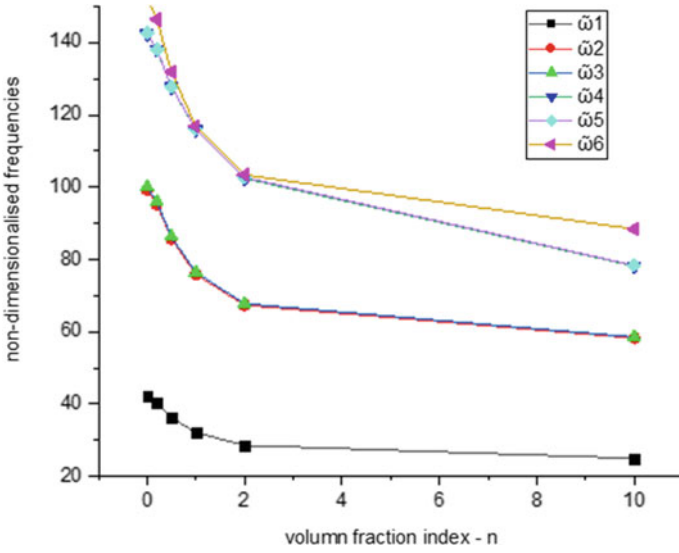


Fig. 6 Variations of the first consecutive frequencies with volume fraction for ($R/a = 5$)

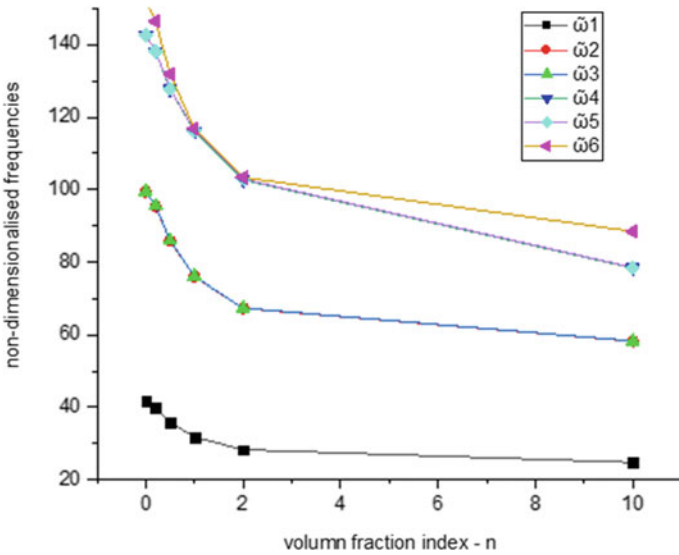


Fig. 7 Variations of the first consecutive frequencies with volume fraction for ($R/a = 10$)

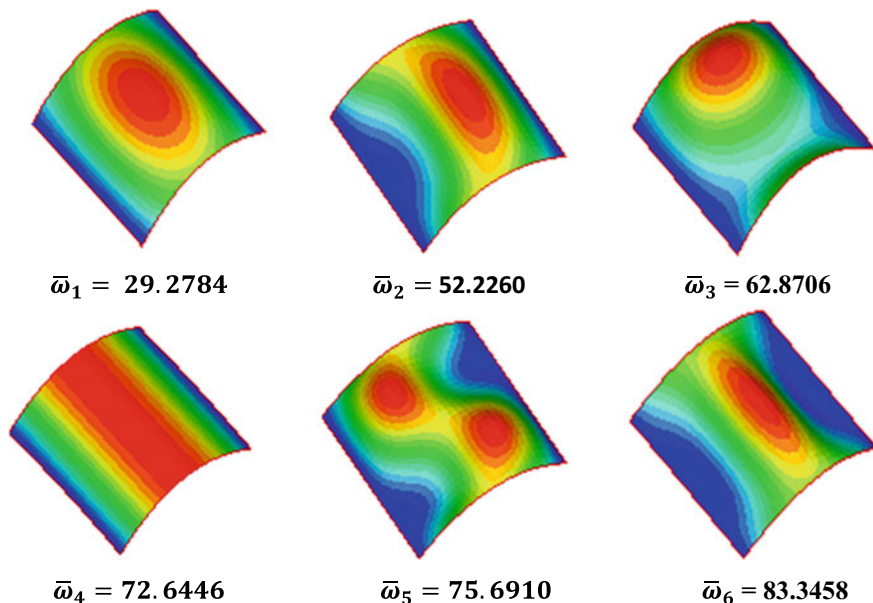


Fig. 8 First six mode shapes of all-round simply supported cylindrical shells for ($R/a = 1$ and $al/h = 10$) for volume fraction index $n = 5$

The first six mode shapes for a moderately thick simply supported deep shell with ‘ R/a ’ ratio 1 and ‘ al/h ’ ratio 10 for volume fraction index 5 are plotted in Fig. 8. It is observed that the present element is capable of capturing all the modes very precisely.

3.2 All-Round Clamped Cylindrical Shell Panel

The non-dimensionalised natural frequencies of the FGM cylindrical shell with all-round clamped panels are presented in Table 3. The results for the deep shell with radius to span ‘ R/a ’ ratio 1 and span to thickness ‘ al/h ’ ratio 10 with various volume fraction indices are presented in this table, whereas Table 4 shows the results for the shallow shell with ‘ R/a ’ ratio 5 and ‘ al/h ’ ratio 10.

From both the tables, it is clear that the frequencies converge with finer mesh. It is confirmed from the results presented in Tables 3 and 4 that an increased volume fraction index leads to reduced frequency values. With volume fraction zero, the frequencies are around 43% more than the frequencies for volume fraction 10. Comparing both the tables, considering geometry, it is confirmed that the deep shell has more stiffness and has increased frequency values.

Table 3 Convergence of frequencies for FGM ‘ceramic top configured’ (CCCC) deep cylindrical shells ($R/a = 1$)

n	Results	$\bar{\omega}_1$	$\bar{\omega}_2$	$\bar{\omega}_3$	$\bar{\omega}_4$	$\bar{\omega}_5$	$\bar{\omega}_6$
0	Pradyumna [4]	94.497	–	–	–	–	–
	Present (12×12)	93.481	129.726	150.783	191.401	216.895	240.024
	Present (16×16)	93.522	129.360	150.626	190.854	215.764	239.081
	Present (24×24)	93.525	128.977	150.413	190.250	214.704	238.169
0.2	Pradyumna [4]	87.393	–	–	–	–	–
	Present (12×12)	86.756	119.962	139.340	176.948	200.868	221.730
	Present (16×16)	86.794	119.630	139.225	176.469	199.851	220.925
	Present (24×24)	86.802	119.287	139.055	175.936	198.897	220.140
0.5	Pradyumna [4]	79.569	–	–	–	–	–
	Present (12×12)	79.267	109.000	126.560	160.686	182.804	201.222
	Present (16×16)	79.300	108.671	126.450	160.221	181.798	200.449
	Present (24×24)	79.308	108.346	126.298	159.724	180.882	199.719
1	Pradyumna [4]	71.245	–	–	–	–	–
	Present (12×12)	71.265	97.470	113.084	143.485	163.631	179.534
	Present (16×16)	71.286	97.113	112.943	142.981	162.543	178.692
	Present (24×24)	71.287	96.781	112.781	142.483	161.599	177.943
2	Pradyumna [4]	62.975	–	–	–	–	–
	Present (12×12)	63.255	86.657	100.201	127.122	145.194	158.688
	Present (16×16)	63.259	86.263	100.009	126.554	144.016	157.746
	Present (24×24)	63.250	85.912	99.817	126.025	143.026	156.944
10	Pradyumna [4]	51.380	–	–	–	–	–
	Present (12×12)	51.437	72.406	82.924	105.390	119.791	130.629
	Present (16×16)	51.427	72.055	82.711	104.847	118.815	129.798
	Present (24×24)	51.405	71.728	82.495	104.327	117.959	129.058

4 Conclusions

The present element gives sufficiently accurate results for natural frequencies for all cases of functionally graded shells including the shallow and deep shells considered in this study. The natural frequency parameters decrease for cylindrical shell panels as the radius to span ratio increases for all boundary conditions. It is observed from the table that the results obtained are converging as the mesh becomes fine, for equal as well as unequal sizes of the elements. This proves the suitability of the developed element for the functionally graded cylindrical shells.

Table 4 Convergence of frequencies for FGM ‘ceramic top configured’ (CCCC) shallow cylindrical shells ($R/a = 5$)

n	Results	$\bar{\omega}_1$	$\bar{\omega}_2$	$\bar{\omega}_3$	$\bar{\omega}_4$	$\bar{\omega}_5$	$\bar{\omega}_6$
0	Pradyumna [4]	71.8861	–	–	–	–	–
	Present (12×12)	72.7577	137.7135	138.4774	194.0111	230.3940	232.2535
	Present (16×16)	72.6719	137.3134	138.0906	193.4305	229.0914	231.0594
	Present (24×24)	72.5741	136.9046	137.6921	192.7794	227.8841	229.9528
0.2	Pradyumna [4]	68.1152	–	–	–	–	–
	Present (12×12)	69.8543	132.3580	133.0561	186.5449	221.6653	223.4163
	Present (16×16)	69.7719	131.9721	132.6844	185.9895	220.4056	222.2610
	Present (24×24)	69.6788	131.5805	132.3038	185.3694	219.2444	221.1966
0.5	Pradyumna [4]	63.1896	–	–	–	–	–
	Present (12×12)	63.0075	119.6566	120.2121	168.7720	200.8786	202.3988
	Present (16×16)	62.9234	119.2702	119.8418	168.2247	199.6302	201.2439
	Present (24×24)	62.8342	118.8949	119.4791	167.6418	198.5142	200.2145
1	Pradyumna [4]	56.5546	–	–	–	–	–
	Present (12×12)	55.9603	106.4272	106.8503	150.1176	178.9560	180.2746
	Present (16×16)	55.8637	106.0034	106.4443	149.5180	177.6236	179.0237
	Present (24×24)	55.7701	105.6174	106.0719	148.9283	176.4842	177.9598
2	Pradyumna [4]	36.2487	–	–	–	–	–
	Present (12×12)	49.6639	94.2795	94.5904	132.6947	158.1199	159.2932
	Present (16×16)	49.5510	93.8111	94.1398	132.0170	156.6989	157.9466
	Present (24×24)	49.4575	93.4250	93.7674	131.4272	155.5595	156.8827
10	Pradyumna [4]	33.6611	–	–	–	–	–
	Present (12×12)	43.0428	79.1237	79.1789	110.2672	130.1092	131.3297
	Present (16×16)	42.3387	78.9925	79.2662	110.1433	129.6637	130.7659
	Present (24×24)	42.2368	78.6148	78.8973	109.5411	128.6415	129.8151

References

1. Deshpande GA, Kulkarni SD (2016) Free vibration analysis of functionally graded sandwich plates using discrete Kirchhoff quadrilateral element based on Reddy’s third-order shear deformation theory. In: ICCMS2016, IIT Bombay, Mumbai, India, June 27–July 1, 2016
2. Deshpande GA, Kulkarni SD (2019) Free vibration analysis of functionally graded plates under uniform and linear thermal environment. *Acta Mech* 230:1347–1354
3. Clough RW, Johnson CP (1968) A finite element approximation for the analysis of thin shells. *Int J Solids Struct* 4(1):43–60
4. Pradyumna S, Bandyopadhyay JN (2008) Free vibration analysis of functionally graded panels using higher-order finite-element formulation. *J Sound Vib* 318:176–192

5. Aragh BS, Hedayati H (2012) Static response and free vibration of two-dimensional functionally graded metal/ceramic open cylindrical shells under various boundary conditions. *Acta Mech* 223:309–330
6. Zhu S, Guoyong J, Tiangui Y (2014) Free vibration analysis of moderately thick functionally graded open shells with general boundary conditions. *Compos Struct* 117:169–186

The Behaviour of Transmission Towers Subjected to Different Combinations of Loads Due to Natural Phenomenon



Devashri N. Varhade and R. R. Joshi

Abstract Many Transmission towers have collapsed during cyclones, tornadoes, thunderstorms, downbursts, lightning, ice disasters and natural hazards. These failures have been attributed mostly to wind loading. The research work to date emphasizes the consideration of rain load, lightning effect, snow load, etc. The present study is as an attempt to understand the behaviour of tower structures under strong wind and rainfall excitation taking lightning damage and snow load into consideration. The Finite element model of the tower structure was developed using STAAD-PRO Software. Then the computation of wind load for the six zones as per the provisions of IS 802-1995 was done and the rain load was also computed as per the theory proposed in previous research work. The effect of lightning was taken into account in the form of temperature-induced load. The snow load was computed as per the clause mentioned in IS 875(Part 4)-1987. Several load combinations were made which included dead, wind, rain, snow, lightning-induced loads. The finite element model of the vulnerable tower hit by the loads was analysed for different load combinations mentioned to estimate its ultimate strength and to find out the failure modes after analysis. Collapse modes of the transmission tower for various load combinations were compared. Lightning-induced load being instantaneous in nature was not included in any load combination and was applied as the only load acting on the structure and it was found to be most critical and hazardous. Out of the load combinations made, it was found that the load combination which included the combined effect of dead load, wind load and rain load was critical for all the zones, and failure was observed in the bracings from the bottom part.

Keywords Rainfall excitation · Lightning · Transmission tower · FEM analysis

D. N. Varhade (✉) · R. R. Joshi

Department of Civil Engineering (Applied Mechanics Division), College of Engineering Pune, Pune, India

e-mail: varhade.devashri@gmail.com

1 Introduction

Many transmission towers have failed during cyclones, tornadoes, thunderstorms, downbursts, lightning, ice disasters and other natural hazards. These failures have been generally attributed simply to wind loading. But the research work to date emphasizes the consideration of rain load, lightning effect, snow load, etc. and also on the structure along with wind load. The present study is an attempt to understand the behaviour of the tower structures under strong wind and rainfall excitation taking lightning damage and snow load into consideration for the transmission towers built in different zones of the Indian region.

Up till now, many researchers have focused on the structural properties of the transmission towers under stochastic winds. A few research works have given due importance to other natural loads such as rain, snow and lightning. Alipour et al. [1] deduced an analytical approach to characterize tornado-induced loads on the lattice structures. The wind risk of electric transmission power lines due to hurricane hazards was assessed by Reinoso et al. [2]. Huang et al. [3] provided the Bayesian approach for typhoon-induced fragility analysis of real overhead transmission lines. Tian et al. [4] in their study derived the velocity ratio of wind-driven rain and also studied its application on a transmission tower subjected to wind and rain loads. The failure analysis of transmission towers struck by tropical storms was carried out by Zhang et al. [5]. Fu et al. [6] studied the wind resistance of a lightning-damaged transmission tower. The impact of extreme weather on the transmission line structures was studied by Hathout et al. [7]. Yang et al. [8] studied the tower destruction mechanics of the Overhead transmission lines and prevention technologies in ice disasters. A case study of the failure of a 220 kV Double circuit transmission line tower due to lightning was presented by Nair et al. [9]. Many such research works till date present the importance of consideration of rain, snow and lightning-induced loads along with wind load acting on the transmission towers.

In the present study, the different combinations of the mentioned loads were made, and the most critical combination was found. The wind load acting on the structure was computed according to the specifications mentioned in the Indian Standard (IS) code 802-1995 for all the six zones given in the code. The rain load was computed as per the equation approach provided by Li et al. [4] in their research work. Computation of snow load acting on the conductors and cross arms was made according to the clause mentioned in IS 875-1987 (part 4). The considerations for lightning-induced loads were taken from the work of Nair et al. [9]. Different load combinations were made for the loads mentioned above taking the Indian topography, meteorology and physiography into consideration and the most critical load combination was found.

2 Overview of the Study Performed

In this study, different natural loads that are supposed to act on the transmission tower were computed as per various theories proposed, and various load combinations were made depending upon the zone in which the tower was supposed to be built taking the weather conditions and climate of that area into consideration. First of all, a finite element model of the tower was developed. The different regions of the country were categorized into six zones depending on the basic wind speeds. The wind loads were computed for all the six zones for prescribed basic wind speeds as per the equation approach taking different empirical factors such as risk factor, terrain category and topography into consideration. The equation approach proposed to compute the rain load was used which in turn was dependent on an empirical parameter called the velocity ratio. The lightning-induced load was computed and applied as temperature load. The snow load was computed for the areas where snowfall was expected; as per the IS code. Depending on the region in which the tower was located, only the expected loads in those regions were applied to the tower and corresponding combinations were made and the most critical combination for each zone was found.

3 Establishment of the Finite Element Model

The finite element (FE) model of the steel transmission tower was established in STAAD-PRO Software. The tower height was taken to be 36 m. The vertical spacing between the conductors was 4 m. The vertical spacing between the top conductor and ground wire was 7 m. Cross arm length was 4.5 m. The base width was 6.6 m and the span length was 100 m. The sections used for the tower in the first zone were Indian Standard Angle (ISA) $70 \times 70 \times 10$ mm, ISA $75 \times 75 \times 10$ mm, ISA $80 \times 80 \times 12$ mm and ISA $120 \times 120 \times 8$ mm LD (Long Leg Back-to-Back Double Angle), and they were further modified for different zones to make the tower safe against wind load. The yield stress was taken as 250 MPa (Fig. 1).

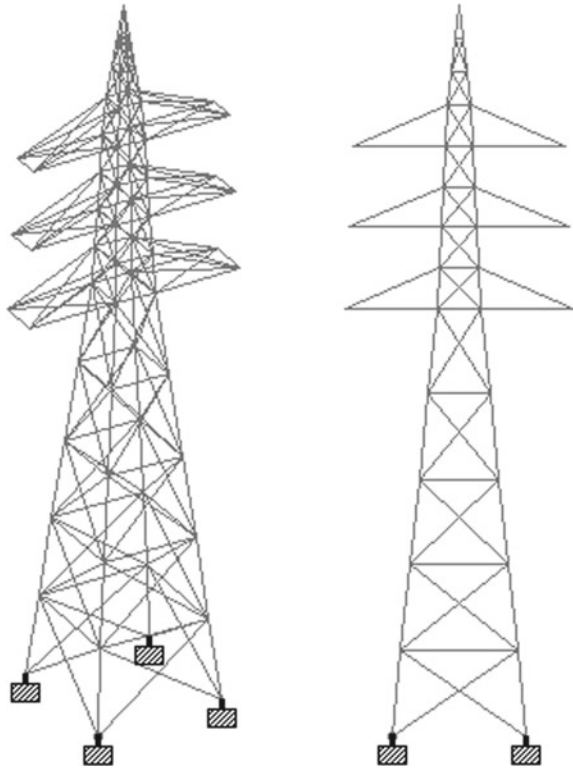
The Modulus of Elasticity of steel was taken as 200 GPa and the thermal coefficient of expansion was taken as $12 \times 10^{-6}/^{\circ}\text{C}$.

4 Computation of Loads

4.1 Wind Load

The wind load calculations were made according to the specifications mentioned in IS 802-1995. The overall region is divided into six zones. Basic wind speeds for the six wind zones are 33, 39, 44, 47, 50 and 55 m/s, respectively. The sample

Fig. 1 Finite element model of the transmission tower



calculations for Wind Load for Zone 1 are as presented below in Table 1. For the Equations for Load, computation reference could be made to IS 802-1995 (Part 1).

Table 2 shows the wind forces acting on the tower for different zones. All the forces are in kN.

4.2 Rain Load

The rain load acting on the transmission tower was computed according to the equation approach mentioned by Li et al. [4] in their research work where they have derived the velocity ratio for wind-driven rain. The rain load was computed using the expressions mentioned as follows:

$$\begin{aligned}
 V_m &= u^* \times \ln(z/z_0)/k \quad z < 30 \text{ m} \\
 V_m &= u^* \times (\ln(z/z_0) + 34.5 p z u^*)/k \quad 300 \text{ m} > z \geq 30 \text{ m}
 \end{aligned}
 \tag{1}$$

Table 1 Wind load calculations for Zone 1 (Basic wind speed = 33 m/s)

P_d	Panel	$(S.R)_x$	C_{dtx}	$(S.R)_z$	C_{dtz}	G_t	F_{wx} (kN)	F_{wz} (kN)
403	1	0.080	3.60	0.080	3.60	1.70	5.147	5.147
N/m ²	2	0.103	3.40	0.103	3.40	1.70	5.329	5.329
	3	0.114	3.35	0.114	3.35	1.74	4.930	4.930
	4	0.131	3.25	0.131	3.25	1.80	4.531	4.531
	5	0.161	3.10	0.161	3.10	1.87	4.085	4.085
	6	0.244	2.66	0.163	3.10	1.89	1.992	5.021
	7	0.258	2.66	0.258	2.66	1.92	1.941	1.941
	8	0.275	2.60	0.203	2.60	1.94	1.846	5.076
	9	0.297	2.51	0.297	2.51	1.96	1.735	1.735
	10	0.325	2.50	0.171	3.10	1.98	1.675	4.902
	11	0.410	2.20	0.410	2.20	2.00	1.230	1.230
	12	0.615	2.00	0.615	2.00	2.02	1.016	1.016
	13	1.034	2.00	1.034	2.00	2.04	0.595	0.595

$(S.R)_x, (S.R)_z$ = Solidity Ratio; C_{dtx}, C_{dtz} = Drag Coefficients; G_t = Gust Response Factor; F_{wx}, F_{wz} = Wind Forces in X and Z directions, respectively

Table 2 Wind load for different zones

Zone 2		Zone 3		Zone 4		Zone 5		Zone 6	
$P_d = 563 \text{ N/m}^2$		$P_d = 717 \text{ N/m}^2$		$P_d = 818 \text{ N/m}^2$		$P_d = 925 \text{ N/m}^2$		$P_d = 1120 \text{ N/m}^2$	
F_{wx}	F_{wz}	F_{wx}	F_{wz}	F_{wx}	F_{wz}	F_{wx}	F_{wz}	F_{wx}	F_{wz}
7.19	7.19	9.16	9.16	10.45	10.45	11.81	11.81	14.31	14.31
7.45	7.45	9.48	9.48	10.82	10.82	12.23	12.23	14.81	14.81
6.89	6.89	8.77	8.77	10.01	10.01	11.31	11.31	13.70	13.70
6.33	6.33	8.06	8.06	9.19	9.19	10.40	10.40	12.60	12.60
5.71	5.71	7.27	7.27	8.29	8.29	9.38	9.38	11.36	11.36
2.78	7.02	3.55	8.93	4.04	10.19	4.57	11.53	5.54	13.96
2.71	2.71	3.45	3.45	3.94	3.94	4.45	4.45	5.40	5.40
2.58	7.09	3.29	9.03	3.74	10.30	4.24	11.65	5.13	11.57
2.42	2.42	3.08	3.08	3.52	3.52	3.98	3.98	4.82	4.82
2.34	6.85	2.98	8.72	3.40	9.95	3.85	11.25	4.66	13.63
1.72	1.72	2.19	2.19	2.50	2.50	2.82	2.82	3.42	3.42
1.42	1.42	1.81	1.81	2.06	2.06	2.33	2.33	2.82	2.82
0.83	0.83	1.06	1.06	1.21	1.21	1.37	1.37	1.65	1.65

where V_m = mean wind speed of height z ; k = Karman constant, equalling 0.4; z_0 = surface roughness length (m); $u^* = [kV_m(z_r)/\ln(z/z_0)]$ is the friction velocity based on the mean wind velocity V_m at the reference height of z_r ; and $p = 10^{-4} \text{ s}^{-1}$ is the Coriolis parameter.

$$\begin{aligned} \gamma &= (0.5117\alpha^{2.792} \ln(d) + \beta)z^{-\alpha} + (-0.0442\alpha^{-0.2} + 0.0497)d^{1.5} \\ &\quad + (0.0493/\alpha) + 0.8928 \quad z < 30 \text{ m} \\ \gamma &= \chi(0.9492z^{-0.9} + 0.0037)(1 - 0.9541^d) + 1 \quad 150 \geq z \geq 30 \text{ m} \end{aligned} \tag{2}$$

where α , β and χ = parameters associated with the surface roughness length, γ = velocity ratio and d = raindrop diameter.

$$\gamma = V_r/V_w \tag{3}$$

$$F = (\rho\Pi^2d^3nV_r^2A)/12 \tag{4}$$

where n = total number of raindrops with average diameter in a unit volume, ρ = density of water and V_r = rain velocity. Table 3 gives the Rain Load acting on the transmission tower for different zones. All the forces in Table 3 are in kN.

Table 3 Rain load acting on the tower for different zones

Zone 1		Zone 2		Zone 3		Zone 4		Zone 5		Zone 6	
F_{wx}	F_{wz}	F_{wx}	F_{wz}	F_{wx}	F_{wz}	F_{wx}	F_{wz}	F_{wx}	F_{wz}	F_{wx}	F_{wz}
3.39	3.39	4.74	4.74	6.03	6.03	6.88	6.88	7.78	7.78	9.43	9.43
5.80	5.80	8.11	8.11	10.30	10.30	11.77	11.77	13.31	13.31	16.12	16.12
6.16	6.16	8.60	8.60	10.93	10.93	12.48	12.48	14.12	14.12	17.09	17.09
6.07	6.07	8.50	8.50	10.77	10.77	12.30	12.30	13.91	13.91	16.84	16.84
5.78	5.78	8.09	8.09	10.29	10.29	11.75	11.75	13.30	13.30	16.10	16.10
1.93	9.01	2.69	12.60	3.42	16.00	3.91	18.27	4.42	20.67	5.35	25.03
1.86	1.86	2.61	2.61	3.32	3.32	3.80	3.80	4.28	4.28	5.19	5.19
1.79	13.60	2.51	18.97	3.20	24.12	3.65	27.55	4.12	31.16	5.00	37.73
1.73	1.73	2.40	2.40	3.06	3.06	3.50	3.50	3.95	3.95	4.79	4.79
2.15	12.00	3.15	17.52	4.15	23.11	4.85	26.97	5.60	31.18	7.02	39.11
1.52	1.52	2.24	2.24	2.95	2.95	3.45	3.45	3.98	3.98	5.01	5.01
1.28	1.28	1.87	1.87	2.50	2.50	2.90	2.90	3.36	3.36	4.22	4.22
0.45	0.45	0.65	0.65	0.86	0.86	1.02	1.02	1.17	1.17	1.47	1.47

4.3 Snow Load

The snow load was calculated as per the specifications mentioned in the IS 875(part 4)-1987. The thickness of the ice deposit all around the wire was taken to be 10 mm. The mass density of ice was assumed to be equal to 0.9 g/cm². By converting the snow load into a uniformly distributed load and applying it to the conducting wire, the analysis of the conducting wire was done and the reactions in the form of the nodal load were then transferred to the nodes of the tower where they were connected to it.

The same approach was used to compute the load on the cross arms of the tower except that the load acting on the members was applied as area load which was uniformly distributed on them.

4.4 Lightning-Induced Load

The lightning-induced load was computed as per the theory proposed by Nair et al. [9]. The lightning-induced load was applied as temperature load, and hence it led to the development of thermal stresses in the members of the transmission tower and the nature of stresses was compressive. The temperature rise was taken to be 260 °C as per the results obtained by Nair et al. [9]. As the lightning struck the structure, there was a tremendous rise in the temperature which in turn induced thermal stresses in the members which were compressive in nature. The temperature load is governed by the following expression, where σ_t = thermal stress, α = coefficient of thermal expansion, Δt = rise in temperature and E = Modulus of Elasticity.

$$\sigma_t = \alpha \times \Delta t \times E \quad (5)$$

5 Load Combinations

The following load combinations were chosen to record the observations depending upon the zone in which the structure will lie. The zones were classified on the basis of physiography and topography of the country and so the load combinations were made relevant to the location of the structures in those regions. The combinations were made taking into consideration the probability of the loads acting together.

1. DL + WL
2. DL + RL
3. DL + WL + SL
4. DL + SL
5. DL + LIGHTNING.

6 Results and Conclusions

The research to date shows that rain load has a non-negligible effect on the structures and must be given due consideration. As the wind velocity was increased, the rain velocity which was based on the velocity ratio specified based on empirical considerations and based on wind velocity also increased. The maximum relative top displacements of the transmission tower due to rain load compared with the wind load for all the six zones were 13.18%, 15.50%, 17.54%, 18.80%, 20.16% and 22.31%, respectively. Figures 2 and 3 show the comparison of the top displacement of the transmission tower for the wind load and the rain load acting one at a time on the tower in *X* and *Z* directions, respectively. As the wind velocity was increased, the rain velocity also increased and the relative top displacement also increased significantly. The Transmission tower which was safe for wind load failed when it was subjected to rain load. Table 4 shows the sections that were used for the transmission tower design in the respective zone for wind load and the sections that failed when it was subjected to the rain load.

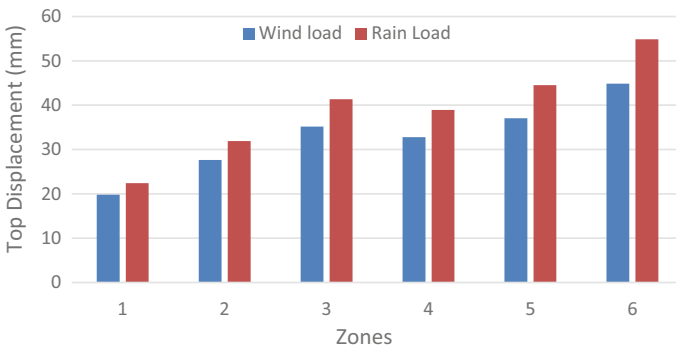


Fig. 2 Top displacement of the transmission tower for wind and rain load in *X* direction

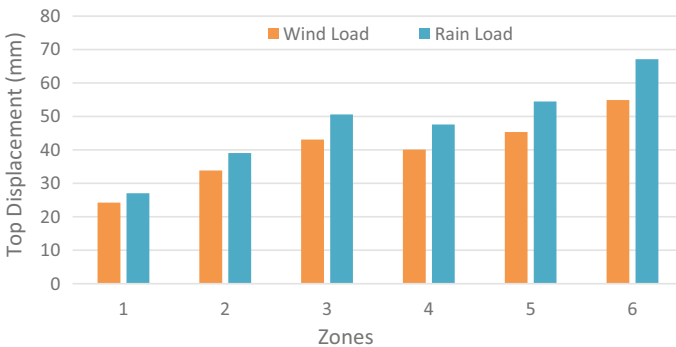


Fig. 3 Top displacement of the transmission tower for wind and rain load in *Z* direction

Table 4 Members safe for wind load but failed when subjected to rain load

Zone	Sections used in design for wind load	Failed members for rain load
1	ISA 70 × 70 × 10, ISA 75 × 75 × 10, ISA 80 × 80 × 12, ISA 120 × 120 × 8 LD	ISA 70 × 70 × 10
2	ISA 75 × 75 × 10, ISA 80 × 80 × 12, ISA 90 × 90 × 10, ISA 120 × 120 × 8 LD	ISA 75 × 75 × 10
3	ISA 80 × 80 × 10, ISA 90 × 90 × 10, ISA 90 × 90 × 12, ISA 100 × 100 × 10, ISA 120 × 120 × 8 LD	ISA 80 × 80 × 10
4	ISA 80 × 80 × 10, ISA 90 × 90 × 10, ISA 100 × 100 × 10, ISA 120 × 120 × 10 LD	ISA 80 × 80 × 10
5	ISA 90 × 90 × 10, ISA 100 × 100 × 10, ISA 120 × 120 × 10 LD	ISA 90 × 90 × 10
6	ISA 90 × 90 × 10, ISA 100 × 100 × 10, ISA 110 × 110 × 10, ISA 120 × 120 × 10 LD	ISA 100 × 100 × 10

Figure 4 shows the failure of the transmission tower when subjected to the rain load. The failure has initiated from the bottom part bracings up to the bottom cross arms. The members highlighted in red are those which will fail first in compression followed by the blue ones.

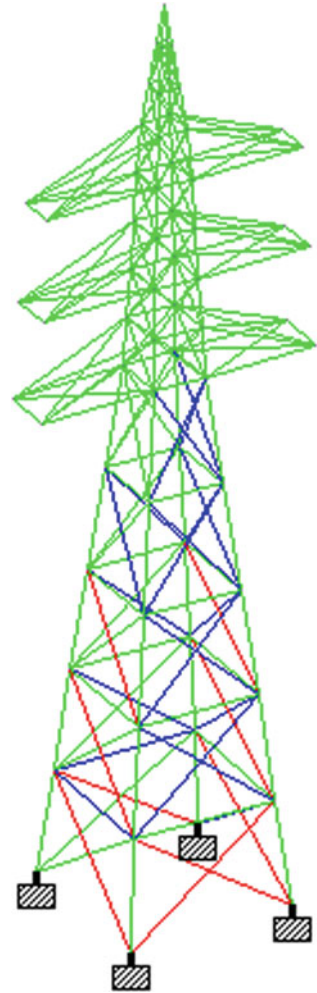
The Lightning induced load is an electrical discharge caused by imbalances between storms, clouds and the ground or within the clouds themselves. When lightning strikes a structure the, temperature rise is very high which can induce thermal stresses in the tower. According to the results obtained in the analysis, the stress developed was about 642 MPa which was much higher than the yield stress of steel members which is about 250 MPa, and the ultimate stress which is about 430 MPa. The failure of the tower members due to thermal stresses is shown in Fig. 5.

The snow load on the transmission wires was computed according to the IS code 875 (part 4) for Zone 5 as this was the zone which includes the regions of north-east and hence snowfall was expected in this region. By taking the ice density to be 0.9 g/cm², the snow load acting on the wires as well as the cross-arm members were computed. The relative top node displacement of the transmission tower for the load combination which included dead, wind, snow altogether was only 0.35% as compared to the displacement for the load combination which included dead and wind load only. Hence, in this zone as well, the most critical combination was the dead and rain loads. Figure 6 shows the failure of the transmission tower when it is subjected to the load combination that includes dead, wind and snow acting on the structure simultaneously. Figure 7 gives the maximum displacements of the tower for different load combinations for Zone 5.

The conclusions from the above study are as follows:

- The combination DL + RL was found to be the critical combination for all the six zones.

Fig. 4 Failure of the bracing due to the rain load for Zone 3



- Lightning-induced load was not included in the load combination as it was instantaneous and was not going to act continuously on the structure. As per the analysis results, the tower will fail due to lightning itself even in the absence of other prominent design loads. It led to tremendous temperature rise which in turn caused high thermal stresses in the members of the structure.
- For the snow-prone region, the top displacement of the member due to snow load was not found as significant as that for the rain load. Hence, for this region also the DL + RL load combination was the most critical one.

Fig. 5 **a** Application of temperature load, **b** failure of the transmission tower due to lightning

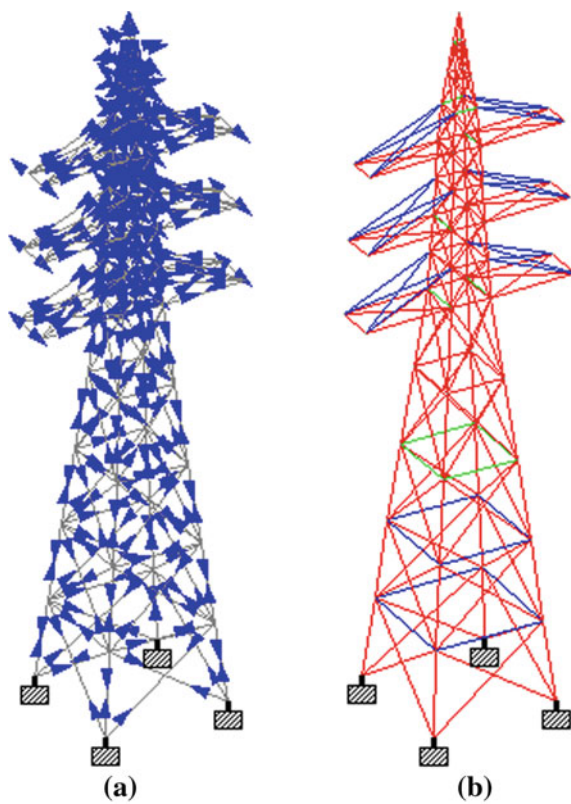
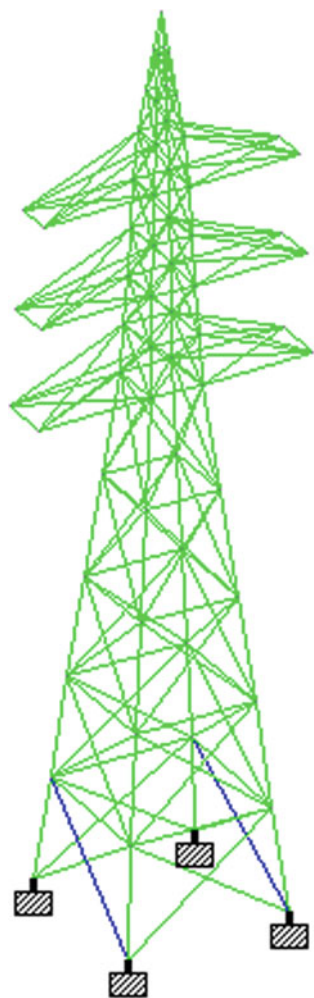


Fig. 6 Failure of the tower members due to snow load



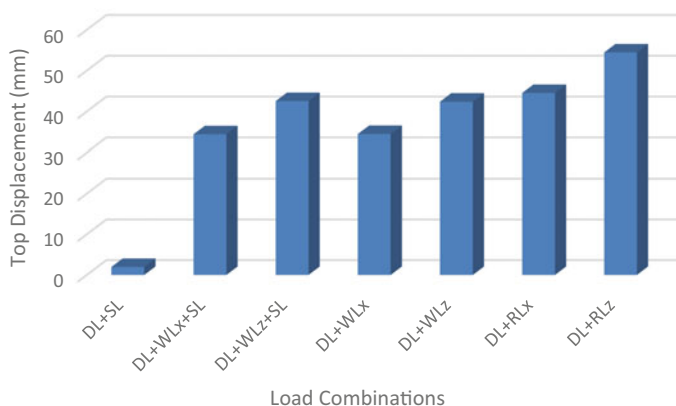


Fig. 7 Bar diagram showing top displacement of the transmission tower for Zone 5

References

1. Alipour A, Sarkar P, Dikshit S, Razavi A, Jafari M (2020) Analytical approach to characterize tornado-induced loads on lattice structures. *J Struct Eng* 146(6):04020108. [http://doi.org/10.1061/\(asce\)st.1943-541x.0002660](http://doi.org/10.1061/(asce)st.1943-541x.0002660)
2. Reinoso E, Niño M, Bery E, Inzunza I (2020) Wind risk assessment of electric power lines due to hurricane hazard. *Nat Hazards Rev* 21(2):04020010. [http://doi.org/10.1061/\(asce\)nh.1527-6996.0000363](http://doi.org/10.1061/(asce)nh.1527-6996.0000363)
- 7 Mingfeng Huang, Lieyang Wu, Qing Xu, Yifan Wang (2020) Bayesian approach for typhoon-induced fragility analysis of real overhead transmission lines. <https://ascelibrary.org/doi/abs/10.1061/%28ASCE%29EM.1943-7889.0001816>
4. Tian L, Zeng Y-J, Fu X (2018) Velocity ratio of wind-driven rain and its application on a transmission tower subjected to wind and rain loads. *J Perform Constructed Facil* 32(5):04018065. [http://doi.org/10.1061/\(asce\)cf.1943-5509.0001210](http://doi.org/10.1061/(asce)cf.1943-5509.0001210)
- 8 Jian Zhang, Qiang Xie (2018) Failure analysis on transmission tower struck by tropical storms. <https://ascelibrary.org/doi/10.1061/9780784481837.010>
6. Fu X, Li H-N, Li J-X (2018) Wind-resistance and failure analyses of a lightning-damaged transmission tower. *J Perform Constructed Facil* 32(1):04017127. [http://doi.org/10.1061/\(asce\)cf.1943-5509.0001121](http://doi.org/10.1061/(asce)cf.1943-5509.0001121)
- 9 Ibrahim Hathout, Karen Callery, M.Sc.E (2015) Impact of extreme weather on transmission line structures. <https://ascelibrary.org/doi/10.1061/9780784479414.044>
8. Yang F, Yang J, Han J, Zhang Z (2014) Tower destruction mechanics of overhead transmission lines and prevention technologies in ice disasters. In: Sustainable development of critical infrastructure—proceedings of the 2014 international conference on sustainable development of critical infrastructure, pp 355–367. <http://doi.org/10.1061/9780784413470.038>
9. Nair Z, Aparna KM, Khandagale RS, Gopalan TV (2005) Failure of 220 kV double circuit transmission line tower due to lightning. *J Perform Constructed Facil* 19(2):132–137. [http://doi.org/10.1061/\(asce\)0887-3828\(2005\)19:2\(132\)](http://doi.org/10.1061/(asce)0887-3828(2005)19:2(132))

Fragility Assessment of Mid-Rise Flat Slab Structures



B. P. Dhumal and V. B. Dawari

Abstract Flat slab structures have advantages over conventional RCC framed structures in terms of construction time as no beams are required to transfer loads from slabs to columns and thus the faster rate of construction is achieved, with less floor height demand, larger clearance of slab to floor, etc. These structures have disadvantages like higher flexibility, high punching shear at slab column junction, and poor performance under seismic loads which cannot be ignored. This study presents fragility curves for mid-rise flat slab RCC structures without masonry infill walls. A nonlinear static pushover analysis is performed to capture the nonlinear seismic response of a sample of structures while monitoring the performance limit states. The HAZUS methodology was used for developing the fragility curves given by the HAZUS technical manual. This study evaluates the losses in flat slab RCC structures due to earthquakes for specific seismic zones in India and compares them with the conventional frame structures. FEM-based software CSI ETABS 2018 has been used as a tool. The present study contributes to quantifying seismic fragility. The fragility curves are interconnected and planned to provide a logical and consistent probability treatment of damage or loss. The fragility curves are found to evaluate and interpret the results.

Keywords Fragility curves · Flat slabs · HAZUS methodology · Nonlinear static pushover analysis

1 Introduction

Prior to an earthquake, vulnerability assessments of buildings are usually made to judge the requirements for improving facilities and important buildings counter to incoming earthquakes. The best way to achieve such evaluations is the fragility curves. The significant loss to society and the economy due to various earthquakes on various steel and RCC structures has increased awareness of assessing the seismic

B. P. Dhumal (✉) · V. B. Dawari

Department of Civil Engineering, College of Engineering Pune, Shivajinagar, Pune, India
e-mail: dhumal1613@gmail.com

© The Author(s), under exclusive license to Springer Nature Singapore Pte Ltd. 2023
M. S. Ranadive et al. (eds.), *Recent Trends in Construction Technology and Management*, Lecture Notes in Civil Engineering 260,
https://doi.org/10.1007/978-981-19-2145-2_78

1061

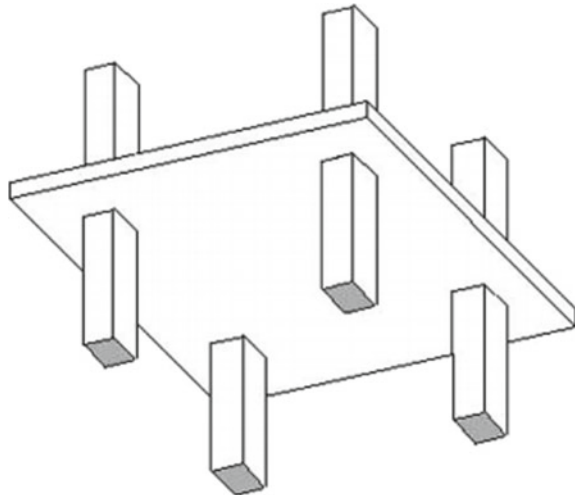
hazard analysis and vulnerability studies of existing buildings. The damage and losses in buildings caused due to earthquakes should be anticipated with an agreeable degree of confidence to mitigate the losses and post-disaster repair works. Fragility curves are a tool for assessing the likelihood of structural damage due to earthquakes as a function of ground motion indicators and otherwise design parameters.

A flat slab system is a type of reinforced concrete system that has several benefits over traditional moment-resistant frame systems. Flat slab system has a good architectural look, unobstructed space, requirement of less building height, and less construction time with easy formwork systems. However, it causes issues which demand inspection with flat slab construction systems. One of the major disadvantages of the system is large transverse displacement under seismic excitations due to the absence of beams thus resulting in lower lateral stiffness. This in turn causes damage to even non-structural members. Another issue is punching shear at slab column junctions due to the transfer of shear and destabilizing moments from slab to directly columns; these destabilizing moments generate high shear stresses under seismic excitations. A typical schematic representation of a flat slab system is shown in Fig. 1.

Therefore, flat slabs are not recommended in high seismic hazard regions such as earthquake zones 4 and 5 of the Indian seismic region. Thus, they are used only as vertical load-carrying systems combined with shear walls to carry and resist lateral loads. The design of flat slab systems is conducted in the same approach as ordinary frames. Thus, response under moderate earthquake shows extensive damage even when the codal conditions for drift limits are satisfied. This highlights the requirement to assess the susceptibility of a flat plate structure for which the fragility curves available are lower in comparison to traditional moment resistant frames.

Ahanthem et al. [1] modelled RC frames in compliance and not in compliance with strong column-weak beam (SCWB) and derived the fragility curves using the

Fig. 1 Typical flat slab system



instructions specified in the HAZUS manual and observed that frames conforming to SCWB had a lower probability of damage than frames non conforming to SCWB. Schotanus [5] applied a general method for seismic fragility analysis of systems proposed by Veneziano et al. to an RCC frame. Response surface was used to switch the capacity part in an analytical limit state function (g-function), with a categorical functional relationship which fits a second-order polynomial and is used as input for SORM analysis.

2 Methodology

There is no absolute strategy to develop fragility curves intended for a specific structure, wide uncertainty is involved in all the steps of precision; this is due to variability in analytical modelling materials defined design process ground motion characteristics and also defining limits states current study uses accepted procedures from his manual for vulnerability assessment ensuring that rational decisions are taken by deriving fragility curves for a structural system. The assumed approach used is outlined in Fig. 2.

2.1 Pushover Analysis

Pushover analysis is a nonlinear static method in which a structure is exposed to gravity loads and monotonous lateral load pattern that increases in elastic and non-elastic behaviour until an ultimate stage is attained. Pushover curve calculates the capacity of the structure and presents in the form of a capacity curve, and the performance point is calculated by intersecting the capacity and demand curve of the structure Guidelines to perform nonlinear static pushover analysis are given in FEMA 356, FEMA 273, and ATC-40. The force deformation curve for pushover analysis is shown in Fig. 3; the points marked as A, B, C, D, and E represent the force–deformation behaviour of hinges formed. The segment BC is again subdivided into Intermediate

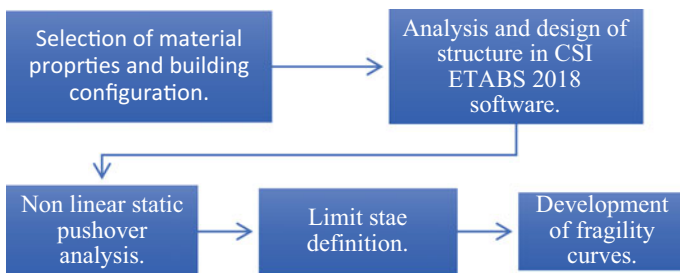
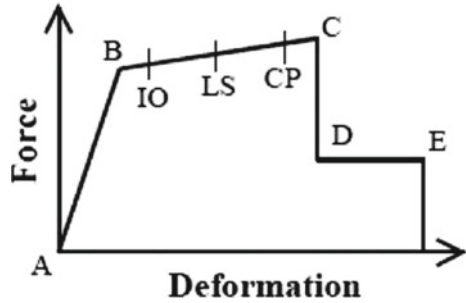


Fig. 2 Methodology used in the derivation of fragility curves

Fig. 3 Force deformation curve



Occupancy, Life Safety, and Collapse Prevention phases which are receiving criteria of hinges formed.

2.2 Capacity Spectrum Method (CSM)

The Capacity Spectrum Method is an approximate method of analysing the structure with a nonlinear static analysis (pushover), the seismic response of a structure. CSM helps to investigate the seismic response of the structure in relation to force and displacements and describes the seismic performance of structures. The concept of CSM assumes that the greatest lateral storey drifts illustrate the seismic building response and the maximum lateral storey drifts are controlled by deformations of the fundamental mode of the original flexible system. Performance point is the point where the capacity curve and demand curve meet, i.e. capacity and demand of structure equals. Figure 4 shows the performance point obtained by the capacity spectrum method.

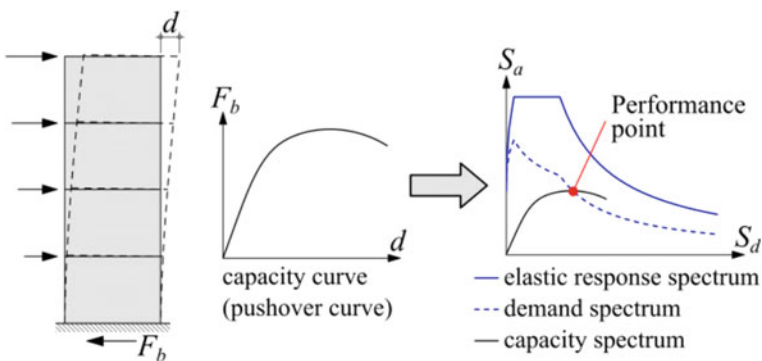


Fig. 4 Capacity spectrum method

2.3 HAZUS Methodology

2.3.1 Fragility Function

HAZUS technical manual FEMA HAZUS-MH MR4 Flood [4] gives a methodology to obtain fragility curves for several types of structures. HAZUS is a compilation of parameters that operate integrally to quote fatalities, loss of function, and financial crashes in a province owing to earthquakes. For a particular building category, various sets of curves are constructed in HAZUS separated by height as low, mid, and high rise, and level of seismic design as low, moderate, and high and seismic performance level. Figure 5 shows fragility curves given by the HAZUS manual.

HAZUS fragility curves are constructed based on damped elastic spectral displacement at the intersection of the pushover curve and the earthquake response spectrum, $S_{d(T_e)}$. Building fragility curves are log-normal functions describing the probability of reaching or exceeding structural and non-structural damage states, at certain mean estimates of the spectral response, for example, the spectral displacement. These curves consider the differences and uncertainties associated with capacity curve properties, damage states, and ground vibration.

The conditional probability (P) of being in or exceeding a given damage condition, ds , is defined given the spectral displacement, S_d , (or other seismic demand parameters) by Eq. (1)

$$P[ds/S_d] = \phi \left[\frac{\ln \left(\frac{S_d}{S_{d,ds}} \right)}{\beta_{ds}} \right] \tag{1}$$

where

S_d Spectral displacement that defines the threshold of a particular damage state.

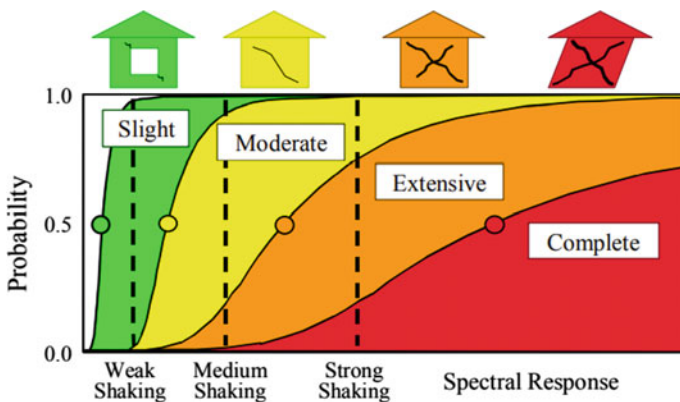


Fig. 5 HAZUS fragility curves

Table 1 Damage state model

Damage state	Spectral displacement (S_d)
Slight	$0.7 S_{dy}$
Moderate	$1.5 S_{dy}$
Extensive	$0.5(S_{dy} + S_{du})$
Complete	S_{du}

$S_{d,ds}$ Median value of spectral displacement for which the building reaches the threshold of damage states.

β_{ds} Standard deviation of the natural logarithm of spectral displacement for damage state.

ϕ Standard normal cumulative distribution function.

In this article, fragility curves are constructed based on the capacity spectrum that is achieved from pushover analysis. These capacity spectrums are utilized to get the yield spectral displacement (S_{dy}) and ultimate spectral displacement (S_{du}). Capacity spectra obtained from pushover analysis are used to construct fragility curves in this paper. Values of medians at several damage states are calculated using yield spectral displacement (S_{dy}) and ultimate spectral displacement (S_{du}). Values given by Giannini et al. (2006) for the damage state model for median values of spectral displacement ($S_{d,ds}$) are incorporated in this paper. The values are presented in Table 1.

2.3.2 Development of Damage State Variability

Overall variability of fragility curves is depicted by log-normal standard deviation (Beta). It is contributed by three primary sources, namely the variability linked with the capacity curve, β_C , the variability linked with the demand spectrum, β_D , and the variability linked with the discrete threshold of each damage state, $\beta_{T,ds}$, as described in Eq. (2). Convolution ‘‘CONV’’ process is used to combine the effect of dependence of demand and capacity spectrum in the calculation of contribution in total variability.

$$\beta_{ds} = \sqrt{\{(\text{CONV}[\beta_C, \beta_d])^2 + (\beta_{Tds})^2\}} \tag{2}$$

If there is no inconsistency of demand (response spectrum is identified precisely), then Eq. (2) would turn out to be

$$\beta_{ds} = \sqrt{[(\beta_C)^2 + (\beta_{Tds})^2]} \tag{3}$$

β_{ds} values can be imported straightforwardly from the HAZUS manual as they are already calculated considering appropriate values of kappa factors (k), β_C , and β_D values for distinct kinds of buildings. Table 2 illustrates the variability numbers

Table 2 Variability values for five-storey model

Degradation values				
Damage state	Kappa factor (k)	β_{Tds}	β_c	β_{ds}
Slight	0.9 (Minor degradation)	0.4 (Moderate)	0.3 (Moderate)	0.8
Moderate	0.5 (Major degradation)	0.4 (Moderate)	0.3 (Moderate)	0.95
Extensive	0.1 (Extreme degradation)	0.4 (Moderate)	0.3 (Moderate)	1.05
Complete	0.1 (Extreme degradation)	0.4 (Moderate)	0.3 (Moderate)	1.05

applied to the five-storied flat slab RCC model taking into account the moderate cases of degradation devoid of infill walls.

3 Structural Modelling

A hypothetical (G + 4) RCC flat slab building frame has been considered in the present study. There are two reasons for considering a mid-rise building. It might not be feasible to fulfil the drift requirements in high-rise structures because of the inherent flexibility of flat slab buildings. On the other side, low-rise buildings would be much stiffer and may not require particular attention. For simplicity, a flat slab RCC building is taken as a bare frame omitting the infill walls. The geometric specification of chosen RCC frame is shown in Table 3. The frame has the same floor plan which is displayed in Fig. 6.

Table 3 Details of geometry of flat slab RCC frame

Item	Dimensions
Plan dimension	30 m (X-Dir) \times 20 m (Y-Dir)
Beam size	300 mm \times 450 mm
Column size	550 mm \times 550 mm
Slab thickness	250 mm
Floor height	Ground storey 3.5 m and 3 m typical storey
Drop thickness and size	375 mm of 2000 mm \times 2000 mm
Live load	4 kN/m ²
Seismic zone	Zone III
Response reduction factor	3
Importance factor	1.2
Type of soil	Medium type soil
Material grades	Fe 500, Fe 415 and M30

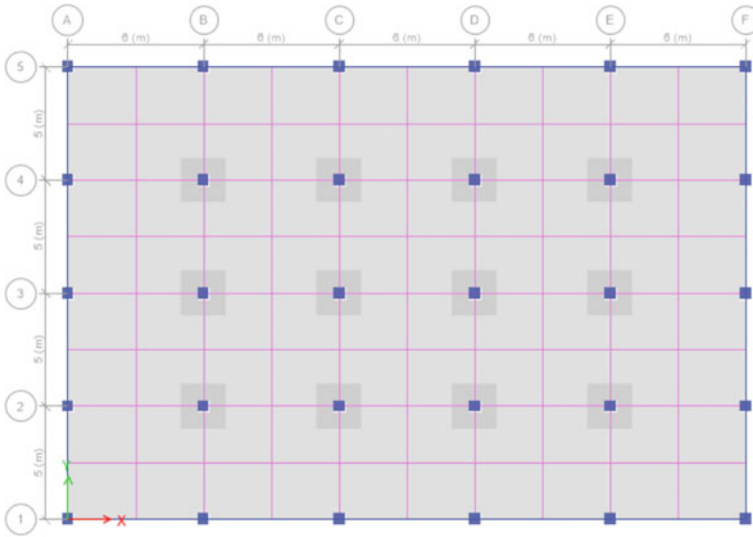


Fig. 6 Plan

3D modelling of the RCC structure conforming to the needs of IS 456:2000, IS 1893 (Part1):2016 was created in CSI ETABS 2018 software. The hinge properties provided for modelling nonlinear frame elements in ETABS 2018 are as follows. P-M2-M3 hinges for columns and M3 hinges for beams are assigned as per FEMA 356. Live load of 4 and 1 kN/m² of floor finish have been applied on each floor excluding the roof. A linear analysis was performed using the load combinations specified in IS 456:2000 and the design of RCC members was carried out for the critical load combinations. Since the most severe challenge of a flat slab system is the punching shear failure, safety measures are to be observed in the design stage to avoid this unattractive behaviour. The slab depth of 250 mm is provided which passed the punching shear check of IS 456:2000 BIS IS 456 [2].

The seismic design is carried out conforming to IS 1893:2016, IS 13920:2016. The flat slab building is supposed to be in Pune, Maharashtra, India, i.e. seismic zone 3. After the successful linear analysis and design of RC members, a nonlinear static pushover analysis was performed in ETABS 2018 software, and the required results were extracted such as pushover curve, capacity curve, and performance point.

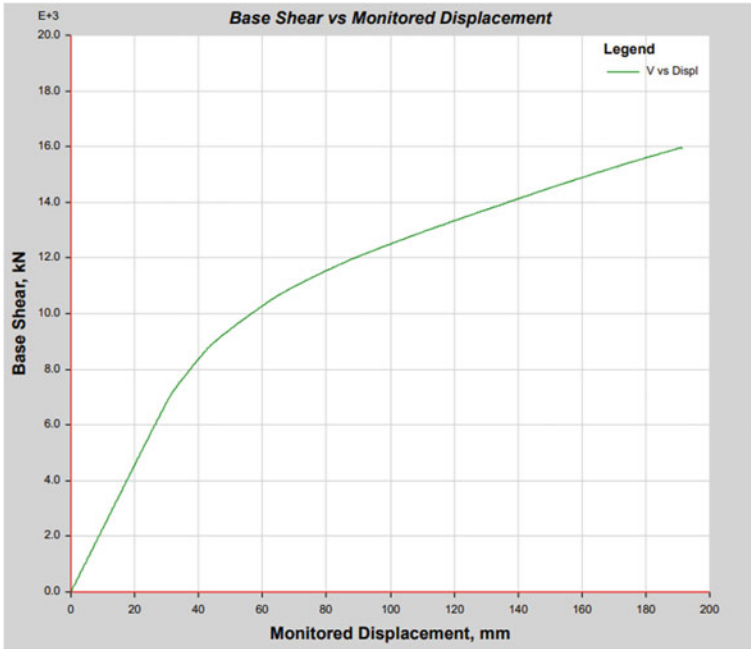


Fig. 7 Pushover curve

4 Results and Discussion

4.1 Pushover Analysis Results

To monitor the overall ductility of the structure, displacement-controlled pushover analysis was carried out. Figure 7 represents the pushover curve obtained for the flat slab structure. The structure was observed to be at the Life safety limit after the development of hinges. The plastic hinges were found to be clustered at the first three storeys, consistent with the sizeable drifts experienced by the same storeys. The performance point of the frame was found at 14,408 kN at a displacement of 147.43 mm. The performance point obtained from the Capacity Spectrum Method is shown in Fig. 8.

4.2 Fragility Curves

The hazard parameter is chosen as spectral displacement (S_d) for creating vulnerability curves. To define the damage limit states, control points were obtained from the bilinear curve obtained from pushover analysis. Table 4 shows the control points

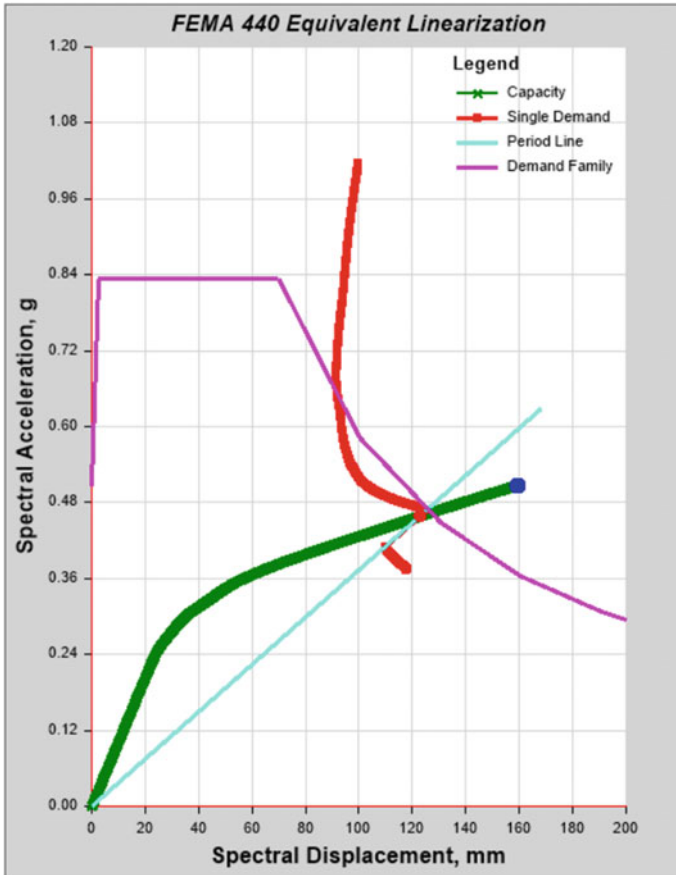


Fig. 8 Capacity spectrum

Table 4 Control points

Control points	Value
A_y	0.9
D_y	0.75
A_u	0.65
D_u	0.44

obtained and Table 5 shows the values for damage limit states in terms of spectral displacement. After calculating the probabilities of various damage states, a curve was plotted between damage hazard and probability corresponding to that damage state.

Table 5 Damage states

Damage state	Ds (mm)
Slight	28.98
Moderate	62.11
Extensive	88.43
Complete	135.45

The fragility curves for the RCC structure have also been plotted as shown in Fig. 9 as per the HAZUS methodology. Table 6 shows the probabilities of various damage states at a spectral displacement of 50 mm.

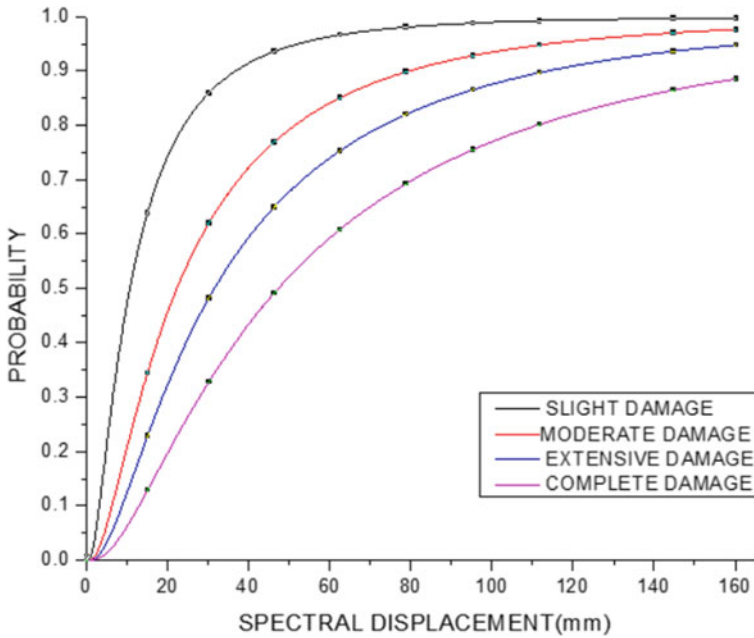


Fig. 9 Fragility curves

Table 6 Probabilities

Damage state	Probability
Slight	0.9
Moderate	0.75
Extensive	0.65
Complete	0.44

5 Conclusion

In this work, seismic fragility curves are obtained for mid-rise flat slab RCC building. It is found that the flat slab structure is more flexible than traditional moment-resisting frames owing to the absence of horizontal elements such as beams and lateral load-resisting elements like shear walls. Further, the HAZUS methodology for the development of fragility curves has been discussed for the flat slab RCC frame structure. From fragility curves, it is seen that for the same spectral displacement the probability of damage decreases as the damage level increases. The method for fragility assessment given by HAZUS technical manual is well suited for flat slab structures also to assess the damage intensities under seismic excitations. From the results obtained, it is determined that the HAZUS methodology is well suited to predict the damage level of the building corresponding to a particular value of spectral displacement.

References

1. Ahanthem N, Ningthoukhongjam SS (2021) Development of fragility curves for different types of RC frame structures. In: *Advances in structural technologies*. Springer, Singapore, pp 71–87
2. BIS IS 456 (2000) Plain and reinforced concrete code of practice, 4th revision. Bureau of Indian Standards
3. Lagomarsino S, Giovinazzi S (2006) Macroseismic and mechanical models for the vulnerability and damage assessment of current buildings. *Bull Earthq Eng* 4(4):415–443
4. Model, FEMA HAZUS-MH MR4 Flood (2009) Technical manual. Federal Emergency Management Agency, Mitigation Division, Washington, DC
5. Schotanus MI, Pinto PE (2002) Fragility analysis of reinforced concrete structures using a response surface approach. Master degree thesis, IUSS, Pavia, Italy

Seismic Response of RC Elevated Liquid Storage Tanks Using Semi-active Magneto-rheological Dampers



Manisha V. Waghmare, Suhasini N. Madhekar, and Vasant A. Matsagar

Abstract The paper presents the use of semi-active magneto-rheological (MR) dampers for the structural response reduction of the reinforced concrete (RC) elevated liquid storage tanks. The effectiveness of MR dampers is investigated based on the control strategies and the placement of the dampers in the staging. The RC elevated liquid storage tank is modeled as a multi-degree freedom system for the staging with a two-mass model for the container with liquid. Two control systems, viz., open-loop and closed-loop control systems are considered. The control algorithms employed are (1) Passive-OFF, (2) Passive-ON, (3) Clipped-Optimal Control (COC), and (4) Simple Semi-active Control (SSC). The study is also focused on the effect of change of voltage on the response quantities. For the COC algorithm, the feedback gain is obtained by considering velocity feedback. The present study proposes a SSC algorithm which is an effective way of controlling the response of RC elevated tank, which uses the ratio of the damper force and capacity of the damper. For numerical simulation, a code is developed in MATLAB. The coupled differential equations of motion for the system are solved using the state-space method. The response of the broad and slender tanks is studied by taking the ratio of the height of the liquid to the radius of the container (S) as 0.5 and 2.0, respectively. The controlled response of the tank under eight different ground motions comprising of near-field and far-field components of earthquakes is evaluated and compared with that of the uncontrolled response. Base shear, displacement, and damper force are obtained. The results showed that the structural response is effectively controlled using semi-active MR dampers with the proposed SSC strategy. The simple semi-active control algorithm proposed in this study could be considered as a proficient algorithm for the seismic response reduction of RC elevated liquid storage tanks using SAMRD.

M. V. Waghmare (✉)

Department of Civil Engineering, AISSMS College of Engineering, Pune, India
e-mail: mvwaghmare@aissmscoe.com

S. N. Madhekar

Department of Civil Engineering, College of Engineering Pune, Shivajinagar, Pune 411005, India

V. A. Matsagar

Department of Civil Engineering, Indian Institute of Technology (IIT) Delhi, Hauz Khas, New Delhi 110016, India

Keywords RC elevated liquid storage tank · Semi-active magneto-rheological damper (MR) · Semi-active control algorithms · Optimal linear control · Open-loop control · Closed-loop control

1 Introduction

Recently, a class of semi-active dampers with smart materials whose properties can be changed by the application of a magnetic field has become very popular in the field of structural control. These materials respond to the change in the magnetic field and are thus called magneto-rheological (MR) materials [2]. These materials are mainly in liquid form and are used in the devices for structural vibration control. Due to the mechanical simplicity, high dynamic range, low power requirements, large force capacity, and robustness, this device offers an attractive means of protecting civil infrastructure systems against severe earthquakes and wind loading [13].

The major objective of the present study is to study the effectiveness of semi-active MR dampers and their control algorithms in reducing the seismic response of the RC elevated liquid storage tanks subjected to different earthquakes. The detailed objectives of the present study are: (i) to investigate uncontrolled and semi-actively controlled seismic response of the RC elevated liquid storage tanks installed with MR dampers at different levels of staging and operated with Passive-OFF, Passive-ON, Clipped-Optimal Control (COC), and Simple Semi-active Control (SSC) algorithm, (ii) to examine the effect of command voltage on the efficiency of semi-active magneto-rheological dampers (SAMRDs), and (iii) to explore the effect of placement of SAMRDs on response reduction.

The focus of this paper is to investigate the effectiveness of proposed control strategies for MR dampers for installation in RC elevated liquid storage tanks. The control algorithms are evaluated for their ability to reduce the peak base shear and displacements. The controlled responses are compared with the corresponding uncontrolled responses of the RC elevated liquid storage tank.

2 Modeling of Elevated Liquid Storage Tank

In the present study, to facilitate the installation of dampers and to study the effect of placement of dampers, multi-degree freedom staging for the RC elevated liquid storage tank with a two-mass model of liquid is presented. The two-mass model for the rigid concrete container is used as per the guidelines specified by the ACI 350.3 [1] and EN 1998-4 [4]. The assumptions and formulation of the mathematical modeling RC tank are described in detail by Waghmare et al. [11, 12].

Figure 1a shows the idealized mathematical model of the RC elevated liquid storage tank considered in the study. Figure 1b, c show the placement of SAMRDs, Configuration I and Configuration II, respectively, in the staging of the RC elevated

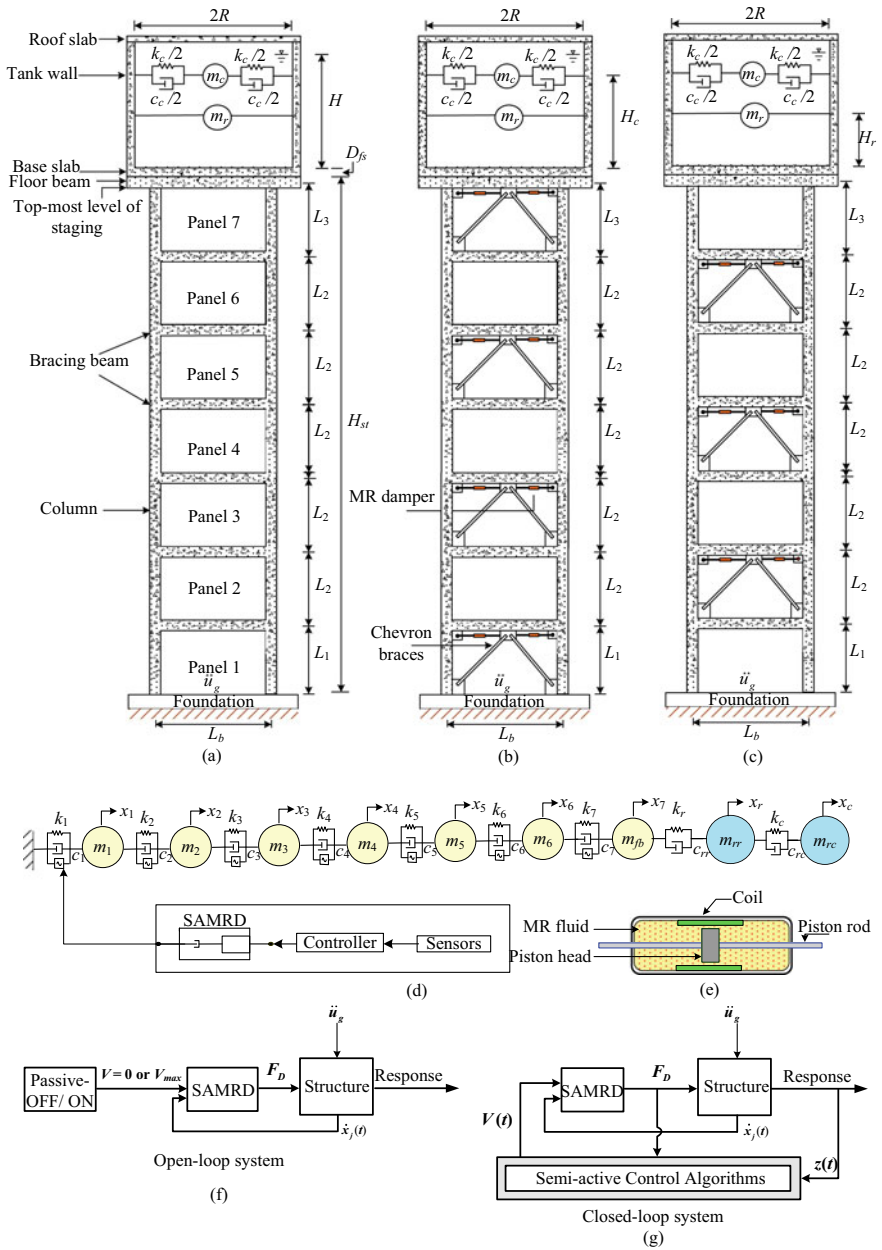


Fig. 1 Schematic diagram of the RC elevated liquid storage tank, **a** the idealized mathematical model, **b** configuration I and **c** configuration II of placement of semi-active MR dampers (SAMRDs), **d** mathematical model of RC elevated liquid storage tank with SAMRDs, **e** schematic diagram of the construction of SAMRD, **f** block diagram of open-loop control system, and **g** closed-loop control system

$$[C] = \begin{bmatrix} c_1 + c_2 & -c_2 & 0 & 0 & 0 & 0 & 0 & 0 & 0 \\ -c_2 & c_2 + c_3 & -c_3 & 0 & 0 & 0 & 0 & 0 & 0 \\ 0 & -c_3 & c_3 + c_4 & -c_4 & 0 & 0 & 0 & 0 & 0 \\ 0 & 0 & -c_4 & c_4 + c_5 & -c_5 & 0 & 0 & 0 & 0 \\ 0 & 0 & 0 & -c_5 & c_5 + c_6 & -c_6 & 0 & 0 & 0 \\ 0 & 0 & 0 & 0 & -c_6 & c_6 + c_7 & -c_7 & 0 & 0 \\ 0 & 0 & 0 & 0 & 0 & -c_7 & c_7 + c_{rr} & -c_{rr} & 0 \\ 0 & 0 & 0 & 0 & 0 & 0 & -c_{rr} & c_{rr} + c_{rc} & -c_{rc} \\ 0 & 0 & 0 & 0 & 0 & 0 & 0 & -c_{rc} & c_{rc} \end{bmatrix} \quad (6)$$

The damping associated with the column members of the staging for Panel 1, Panel 2, Panel 3, Panel 4, Panel 5, Panel 6, and Panel 7 (see Fig. 1a), denoted by c_1 , c_2 , c_3 , c_4 , c_5 , c_6 , and c_7 is given by

$$c_j = 2\xi_j \sqrt{k_j m_j} \quad (7)$$

For $j = 1$ to p , where p is the number of bracing levels, and ξ_j is the damping ratio of the staging in the elevated tank, c_{rr} is the damping associated with k_r and m_{rr} , while c_{rc} is the damping associated with m_{rc} and k_c . The stiffness associated with the Panel 1, Panel 2, Panel 3, Panel 4, Panel 5, Panel 6, and Panel 7 is denoted by k_1 , k_2 , k_3 , k_4 , k_5 , k_6 , and k_7 .

3 Equation of Motion

In this section, governing equations of motion for n degree of freedom system and their solution for time history analysis using the state-space method; for the RC elevated liquid storage tank installed with the SAMRDs is presented. The mathematical model of the RC liquid storage tank installed with SAMRDs is presented in Fig. 1d. Further, Fig. 1e shows the construction of SAMRD. Figure 1f, g show a block diagram representation of the open-loop and closed-loop control systems, respectively. The governing differential equation of motion under earthquake excitation, with semi-active dampers, is given by

$$[M]\{\ddot{X}(t)\} + [C]\{\dot{X}(t)\} + [K]\{X(t)\} = \{F_e(t)\} + [L]\{f(t)\} \quad (8)$$

where $[L]_{n \times n}$ is the control force distribution matrix.

In Eq. (8), $\{F_e(t)\} = \{F_1(t) F_2(t) \dots F_n(t)\}^T$ is a vector such that $\{F_e(t)\} = -[M]\{r\}\ddot{u}_g(t)$ where, $\{r\} = \{1 \ 1 \ \dots \ 1\}^T$ is the influence coefficient vector. Here, the degrees of freedom (n) is nine. Also, $\{f(t)\} = \{F_{D1}(t) F_{D2}(t) \dots F_{Dn}(t)\}^T$ is

a vector containing the control force exerted by the dampers corresponding to each degree of freedom, n .

The base shear, V_b , in the staging at the foundation level is expressed as

$$V_b = m_{rc}a_c + m_{rr}a_r + \cdots + m_3a_3 + m_2a_2 + m_1a_1 \quad (9)$$

3.1 State-Space Solution

In the state-space method, the response of the system is analyzed using both displacement and velocity as independent variables, called as states [6]. Vector, $z(t)$ is defined in Eq. (10) to represent both states, viz., displacement ($\dot{X}(t)$) and velocity ($\ddot{X}(t)$) of the system.

$$z(t) = \begin{Bmatrix} \dot{X}(t) \\ \ddot{X}(t) \end{Bmatrix} \quad (10)$$

Every degree of freedom is associated with two states, viz., displacement and velocity. Thus, if the degree of freedom of a structure is n , then there will be $2n$ states, first n for the displacement and the remaining n for the velocity. Equation (8) can be written in the following equivalent state-space form:

$$\begin{aligned} \dot{z}(t) = \begin{Bmatrix} \ddot{X}(t) \\ \dot{X}(t) \end{Bmatrix} &= \begin{bmatrix} \mathbf{0} & \mathbf{I} \\ -\mathbf{M}^{-1}\mathbf{K} & -\mathbf{M}^{-1}\mathbf{C} \end{bmatrix} \begin{Bmatrix} \dot{X}(t) \\ \ddot{X}(t) \end{Bmatrix} + \begin{Bmatrix} \mathbf{0} \\ \mathbf{M}^{-1}\mathbf{F}_e(t) \end{Bmatrix} \\ &+ \begin{Bmatrix} \mathbf{0} \\ \mathbf{M}^{-1}\mathbf{L}f(t) \end{Bmatrix} \end{aligned} \quad (11)$$

where $\mathbf{0}$ and \mathbf{I} are, respectively, null matrix with all zero elements and identity matrix. Time history analysis is carried out, and response quantities, viz., displacements, base shear, and damper forces are obtained.

4 Modeling of Semi-active MR Damper

The magneto-rheological (MR) fluid is a class of smart materials whose rheological properties may be controlled by the application of an external magnetic field. Further, standard electrical connectors, wires, and feed-through can be reliably used, and MR dampers can be powered directly from conventional and low voltage sources [2]. Dyke et al. [3] and Spencer et al. [10] developed a phenomenological model for MR dampers. Figure 1d shows the details of the damper.

4.1 Modified Bouc–Wen Model

The Bouc–Wen model and the modified Bouc–Wen models are computationally more tractable than the Bingham model [7]. In the present study, the modified Bouc–Wen model proposed by Spencer et al. [10] for the magneto-rheological dampers, as shown in Fig. 2a, is used. The nonlinear relationship between the damper force and velocity of the damper is shown in Fig. 2b.

The equation governing the force predicted by this model is

$$F_{Dj} = c_1 \dot{y} + k_1(u_d - x_0) \tag{12}$$

$$Z_{mr} = -\gamma |\dot{u}_d - \dot{y}| Z_{mr} |Z_{mr}|^{nmr-1} - \beta (\dot{u}_d - \dot{y}) |Z_{mr}|^{nmr} + A_{mr} (\dot{u}_d - \dot{y}) \tag{13}$$

$$\dot{y} = \frac{1}{c_0 + c_1} \{ \alpha Z_{mr} + c_0 \dot{u}_d + k_0(u_d - y) \} \tag{14}$$

where Z_{mr} is an evolutionary variable that accounts for the history dependence of the response; u_d is the damper displacement; \dot{u}_d is the velocity across the damper; y is the internal pseudo-displacement of the damper. k_1 is the accumulator stiffness; c_1 is viscous damping at lower velocity in the model to produce roll-off; c_0 is viscous damping at larger velocity; x_0 is the initial displacement in the spring and α , β , γ , nmr and A_{mr} are the characteristic parameters of the model. The model parameters α , c_0 , and c_1 depend on the input voltage to the current driver such that $\alpha = \alpha_a + \alpha_b U$, $c_0 = c_{0a} + c_{0b} U$, and $c_1 = c_{1a} + c_{1b} U$, where the dynamics involved in the MR fluid reaching rheological equilibrium and in driving the electromagnet in the MR damper are accounted through the first-order filter $U = -\eta(U - V_j)$. V_j is the voltage applied to the current driver and η is the constant.

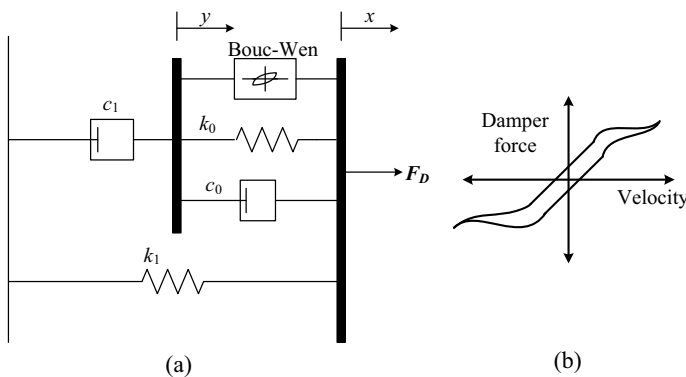


Fig. 2 **a** Mechanical model modified Bouc–Wen model [10], **b** Damper force–velocity relationship of magneto-rheological damper

5 Semi-active Control Algorithms

Figure 1f, g show the flow chart for the selection of control systems. In the present study, four types of controls using open-loop and closed-loop control are designed to achieve the desired response. These include, viz., (1) Passive-OFF, (2) Passive-ON, (3) Clipped-optimal control (COC), and (4) Simple semi-active control (SSC) as described in the following sections. The open-loop control system where the command voltage $V(t)$ is fed to the MR damper is shown in Fig. 1f for Passive-OFF and Passive-ON algorithms. In the open-loop Passive-OFF mode of SAMR damper, the command voltage is held at 0 V, while in the Passive-ON case, it is held at the maximum level V_{\max} .

5.1 Clipped-Optimal Control (COC)

The clipped-optimal control algorithm, referred to herein as a classical Linear Quadratic Regulator (LQR), is widely used for active as well as for semi-active control [9]. In this algorithm, the quadratic expression for the cost function (J) (Eq. 15) is minimized over the duration of the excitation to obtain the control force f_c .

$$J = \int_0^{t_f} [z^T(t) Q z(t) + f_c^T(t) R_r f_c(t)] dt \quad (15)$$

For the closed-loop system, minimizing the cost function in Eq. (15) results in a control force vector $f_c(t)$ controlled only by the state vector $z(t)$ [5]. The force generated by the SAMRD can be regulated by changing the command voltage, thereby changing the damping constant. Hence, the command voltage $V(t)$ is obtained by substituting the control force f_c in Eq. 16, using a clipped control algorithm based on the velocity feedback

$$V_j = V_{\max} H[(f_{cj} - F_{Dj}) F_{Dj}] \quad (16)$$

where V_j , f_{cj} , and F_{Dj} are the command voltage, control force, and the damper force required for SAMRD installed at j th panel. $H(\cdot)$ is the Heaviside step function which varies between zero for negative argument and one for positive argument. The clipped-control algorithm along with the optimal controller is called the clipped-optimal control (COC) algorithm [3].

5.2 Simple Semi-active Control (SSC)

A simple semi-active control (SSC) is proposed in the present study, which contains the force induced in the damper (F_{Dj}) and the maximum damper force (F_{Dmax}). The significant advantage of this control algorithm is that it does not require any control parameter to be decided. SSC is defined as

$$V_j = \begin{cases} \frac{V_{max}}{F_{Dmax}} |F_{Dj}| & \text{for } |F_{Dj}| \leq F_{Dmax} \\ V_{max} & \text{for } |F_{Dj}| \geq F_{Dmax} \end{cases} \quad (17)$$

6 Numerical Study

The numerical study is conducted to investigate seismic response reduction of the RC elevated liquid storage tanks installed with semi-active MR dampers. A code has been developed in MATLAB [8] for conducting time history analyses of the RC elevated liquid storage tank. The particulars of the ground motion time histories are, Imperial Valley, 1940 (PGA = 0.34 g), Tabas, 1978 (PGA = 0.93 g), Loma Prieta, 1989 (PGA = 0.57 g), Turkey, 1992 (PGA = 0.5 g), Northridge, 1994 (PGA = 0.84 g), Kobe, 1995 (PGA = 0.59 g), Chi-Chi, 1999 (PGA = 0.21 g), and Bhuj, 2001 (PGA = 0.11 g). The geometric properties of the tank considered in the numerical study are the same as in Waghmare et al. [11, 12].

The parameters of the RC tank considered for numerical simulation are presented in Table 1. The volume of the liquid is considered as 100% and 25% ($S = 2.0$ and $S = 0.5$) of the tank capacity excluding freeboard. The dynamic properties of the tank modeled herein are obtained by conducting free vibration analysis. The fundamental natural time period for Mode 1 is 5.06 s and 3.68 s; for Mode 2 is 1.12 s and 2.18 s; and for Mode 3 is 0.57 s and 0.58 s for $S = 0.5$ and $S = 2.0$, respectively.

The details of the control systems and the algorithms used in the numerical study are described in Table 2. To study the effect of voltage on open-loop and closed-

Table 1 Parameters of the RC elevated tank considered in the numerical study

Parameter	Numerical values	Parameter	Numerical values
Height of the liquid	$H = 5.05$ m	Damping ratio for convective mass	$\xi_c = 0.5\%$
Inner diameter of container	$2R = 5.06$ m	Modulus of elasticity of RC	$E = 25 \times 10^6$ kN/m ²
Aspect ratio, $S = H/R$	0.5 and 2.0	Damping ratio of RC	$\xi_t = 5.0\%$
Mass density of the contained liquid (water)	1000 kg/m ³	Number of columns	4

Table 2 Details of the control algorithms

S. No	Classification of the control system	Semi-active control algorithms	Voltage	Semi-active device/controller used for response reduction
1	Open-loop control system	Passive-OFF	$V_{\max} = 0 \text{ V}$	SAMRD
2	Open-loop control system	Passive-ON	$V_{\max} = 2.75 \text{ V}$	SAMRD
3	Closed-loop feedback control system	Clipped-optimal control (COC)	$V_{\max} = 2.75$ $V_{\max} = 10 \text{ V}$	SAMRD + controller
				$\mathbf{Q}_d = \mathbf{K}$ and $\mathbf{Q}_v = \mathbf{M}$
				$\mathbf{R}_r = 10^{-6}(\mathbf{I})_{n \times n}$ $q = 1 \times 10^5$
4	Closed-loop feedback control system	Simple semi-active control (SSC)	$V_{\max} = 2.75 \text{ V}$ $V_{\max} = 10 \text{ V}$	SAMRD + controller
				$F_{D\max} = 40 \text{ kN}$

loop systems response, the command voltage V is varied from 1 to 10 V (Passive-ON, COC, and SSC). For the Passive-OFF algorithm, the command voltage is kept constant at 0 V. In case of optimal control theory, the control force parameter, \mathbf{R}_r , and the response reduction parameter, q , are considered as 10^{-6} and 10^5 , respectively.

To study the effect of placement of dampers, three configurations of placement of dampers, viz., Configuration I (SAMRDs installed in Panel 1, Panel 3, Panel 5, and Panel 7), Configuration II (SAMRDs installed in Panel 2, Panel 4, and Panel 6); and Configuration III, where SAMRDs are installed in all the Panels in the staging of the RC elevated tank, are considered (see Fig. 1).

The seismic response quantities, viz., normalized base shear, $F_b = V_b/W$, shear at the level of lumped masses, and damper forces are obtained. Here, $W = (M_t) g$ is the total weight of the tank, where M_t is the total mass, considering bracing level masses, rigid mass, and convective mass.

The modified Bouc–Wen model is used to model nonlinear hysteretic behavior of SAMR damper. Bouc–Wen parameters used in the present study are listed in selected as $\alpha_a = 102 \text{ N/m}$, $\alpha_b = 496 \text{ N/m/V}$, $k_0 = 5000 \text{ N/m}$, $k_1 = 1200 \text{ N/m}$, $\gamma = 300/\text{m}$, $\beta = 300/\text{m}$, $x_0 = 0$, $c_{0a} = 440 \text{ N-s/m}$, $c_{0b} = 4400 \text{ N-s/m/V}$, $c_{1a} = 29,000 \text{ N-s/m}$, $c_{1b} = 500 \text{ N-s/m}$, $\eta = 50 \text{ s}^{-1}$, $A_{mr} = 1900$, $n_{mr} = 1$. The parameters selected are on the basis to suit the damper force–velocity behavior (see Fig. 2).

6.1 Effect of Voltage

The base shear response of tanks with the open-loop systems (Passive-OFF and Passive-ON) and closed-loop systems (COC and SSC) is considered when the elevated tank is installed with SAMR dampers (Configuration III). The effect of change in command voltage is studied when the command voltage, $V(t)$, is changed

from 0 to 10 V. Figure 3 shows the normalized base shear response of the tanks installed with SAMR dampers (Configuration III) for $S = 0.5$ and $S = 2.0$ for four earthquakes. Additionally Fig. 3 presents the comparison of the Passive-OFF ($V = 0$), Passive-ON, COC ($q = 10^5, R_r = 10^{-6}$), and SSC ($F_{Dmax} = 40$ kN) algorithms.

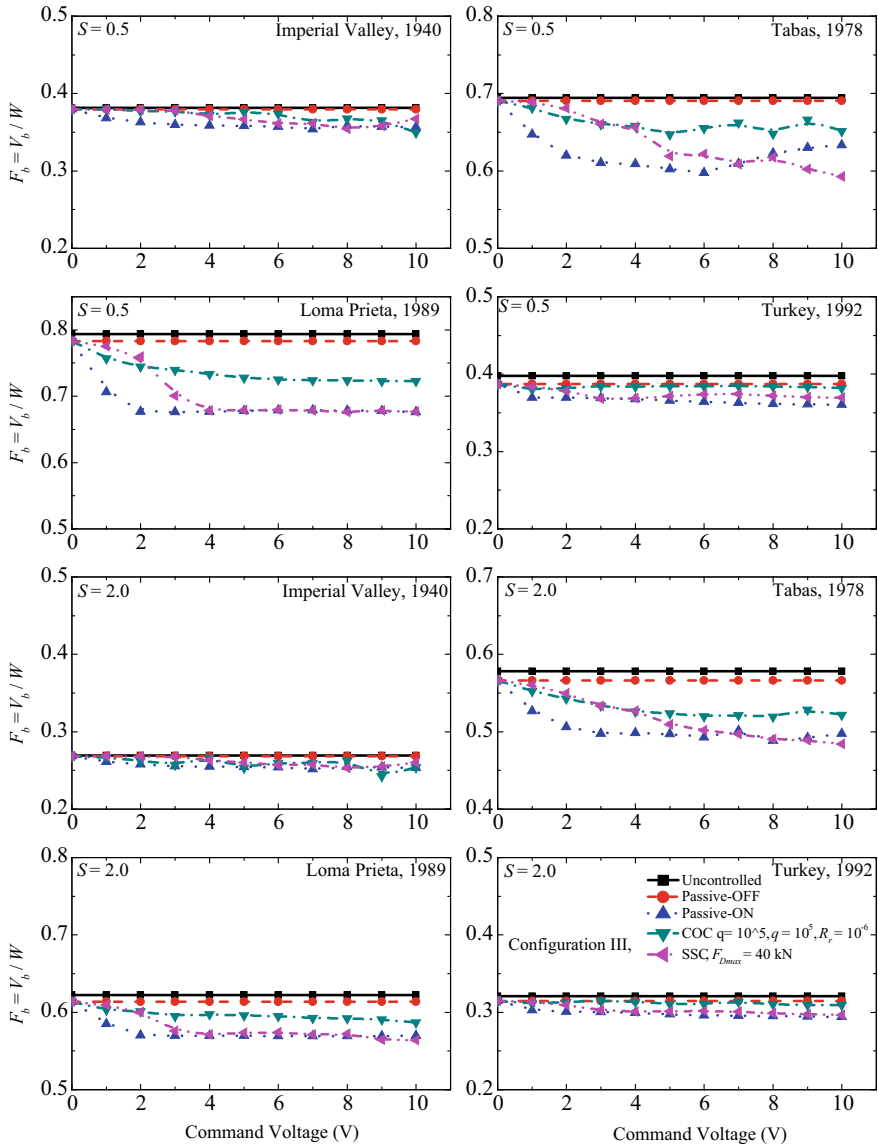


Fig. 3 Variation of base shear response with the command voltage when the RC elevated tank is installed with SAMRDs and operated with Passive-OFF, Passive-ON, COC, and SSC algorithms

From Fig. 3, it is observed that SAMR dampers reduce the base shear response of the tanks under all considered earthquakes. The increase in voltage increases the response reduction. It is the specialty of magneto-rheological dampers as the voltage is applied, the MR fluid is converted into the semisolid state, increasing the resistance motion and leading to increased response reduction. Remarkable response reduction is achieved as the voltage is increased from 0 to 3 V; however, a further increase in voltage has resulted in negligible or no additional response reduction.

Figure 4 describes the effect of voltage on the Force–displacement and Force–velocity relationship for SAMRD installed in RC tank ($S = 2.0$, Configuration III) under Loma Prieta, 1989 earthquake. The figure shows the relationship of the response quantities of the SAMRD installed in Panel 4, which portrays the peculiar nonlinear force–velocity behavior of the MR damper. The significance of the force–displacement loop is that it gives the energy dissipation characteristics of the dampers; the larger the area under the loop, the higher is the energy dissipation. It is observed from the figure that as the voltage increases from 0 to 3 V, the area under the force–displacement curve gradually increases. This highlights the fact that, as the command voltage increases, the energy dissipation increases. Further, it is also seen that the difference between the energy dissipation achieved from 0 to 1 V; and 1 to 2 V is considerably higher than the energy dissipation achieved by increasing the command voltage from 2 to 3 V.

From Figs. 3 and 4, it is seen that although Passive-ON strategy is effective in reducing the response, the saturation of the MR effect seems to have occurred after 3 V. The performance of SAMR damper can be enhanced by applying advanced control algorithms (COC and SSC) to the command voltage. It is noted from Fig. 3 that at higher command voltage SCC algorithm is the most effective strategy as far as base shear response reduction is concerned. It is observed that the effectiveness of the SAMR damper is greatly affected by the command voltage and the control algorithm employed. Moreover, it is further noted that there exists the optimum command voltage for Passive-ON algorithm. Accordingly, for further simulations, the command voltage is selected as 2.75 V for Passive-ON algorithm; and COC and SSC algorithms are further investigated for 2.75 V and 10 V.

6.2 *Effect of Control Strategies*

Figure 5 shows the variation of the acceleration, velocity, and displacement response of the tank installed with SAMRDs with Configuration I and operated with Passive-OFF, Passive-ON, COC, and SSC algorithms with designated command voltages, subjected Tabas, 1978 earthquake. It is observed that acceleration and velocity response is profoundly affected by the control strategies employed. Further, it is exciting to know that though there is a reduction in acceleration and velocity response, the response at the convective level remains unaffected. Moreover, displacement response is not much affected by the installation of the SAMRDs. It is observed from

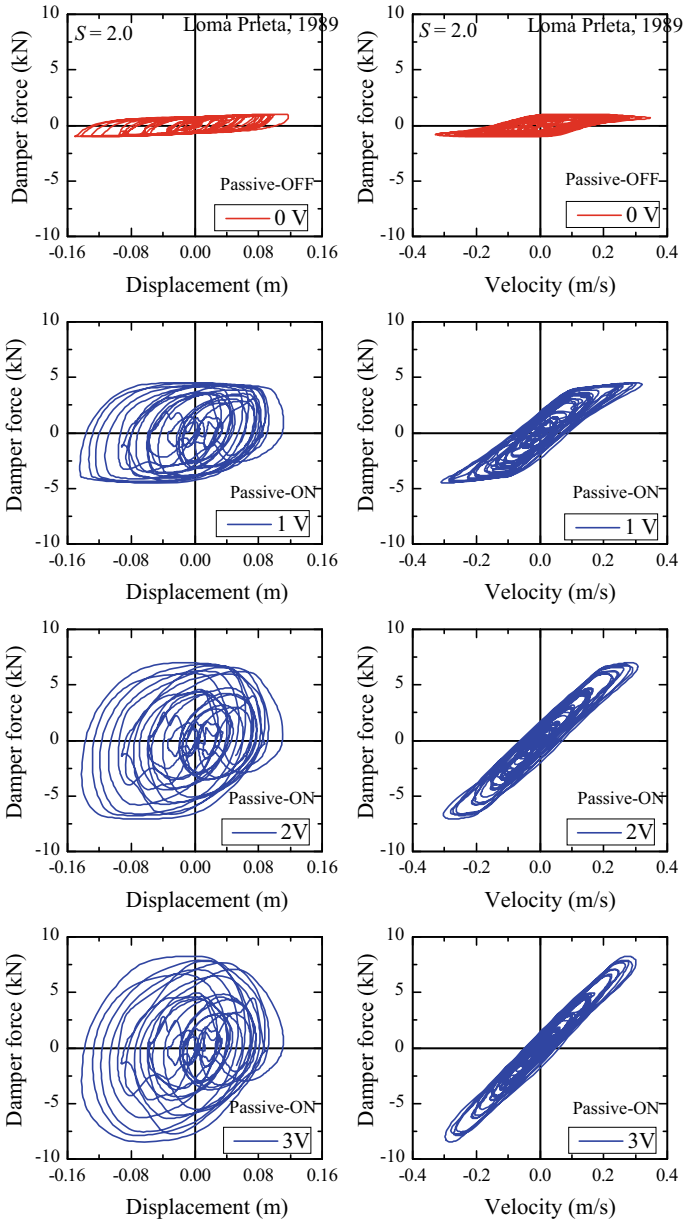


Fig. 4 Effect of voltage on the force–displacement and force–velocity relationship for SAMRDS installed at the panel 4, in RC tank ($S = 2.0$, Configuration III), under Loma Prieta, 1989 earthquake

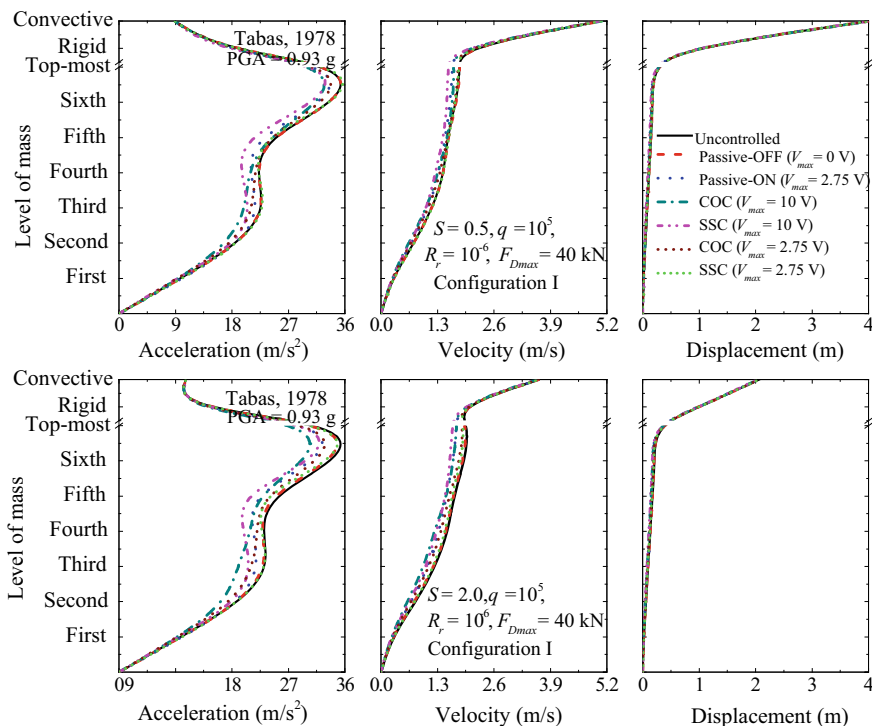


Fig. 5 Variation of the acceleration, velocity, and displacement response of the tank installed with SAMRDs operated with passive-OFF, passive-ON, COC, SSC, COC, and SSC control algorithms

the figures that the SSC ($V_{max} = 10 \text{ V}$) is superior in controlling the acceleration, velocity, and displacement response of an elevated liquid storage tank.

6.3 Effect of Placement of Dampers

In the present study, three configurations of placement of the SAMRDs are considered as discussed in Sect. 5. Figure 6 shows the time history of the base shear response of the tank installed with SAMRDs using Configuration I and employed with different control algorithms when the tank is subjected to Tabas, 1978 earthquake. It is observed from the figure that Configuration I is the suitable placement configuration of SAMRDs for Tabas, 1978 earthquake. Further, the suitability of configuration may be different for different earthquakes and different control algorithms. Though SSC ($V_{max} = 10 \text{ V}$) algorithm is found to be outstanding (30% reduction), the other algorithms such as Passive-OFF, Passive-ON, COC ($V_{max} = 10 \text{ V}$), COC ($V_{max} = 2.75 \text{ V}$) and SSC ($V_{max} = 2.75 \text{ V}$), also controlled the base

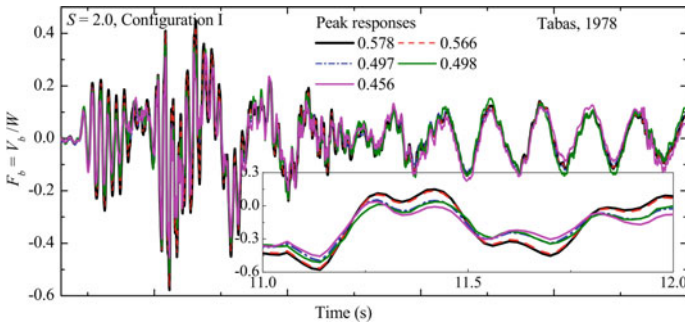


Fig. 6 Time variation of peak normalized base shear (F_b) for RC elevated liquid storage tank ($S = 2.0$), installed with SAMR dampers in configuration I, operated with passive-OFF, passive-ON, COC, and SSC algorithms and subjected to Tabas, 1978 earthquake

shear response with maximum reduction as 5%, 29%, 18%, 10%, and 16%, respectively, for broad tank; and for slender tanks it is 9%, 29%, 24%, 12%, and 12%, respectively. COC ($V_{max} = 10$ V) algorithm proved to be more capable than all the other algorithms in case of Imperial Valley, 1940, (Configuration III, $S = 0.5$ and $S = 2.0$), Tabas, 1978 (Configuration II, $S = 0.5$ and $S = 2.0$), Northridge, 1994 (Configuration I, $S = 0.5$), Kobe, 1995 (Configuration II and Configuration III, $S = 2.0$), and Bhuj, 2001 (Configuration I and Configuration III, $S = 0.5$). Whereas better results for SSC ($V_{max} = 2.75$ V) are obtained under Loma Prieta, 1989, Turkey, 1992, and Kobe, 1995 (Configuration II, $S = 0.5$ and $S = 2.0$), earthquakes. Passive-OFF and COC ($V_{max} = 2.75$ V) algorithms are not that much striking as far as base shear response reduction of the elevated liquid storage tanks is concerned.

7 Conclusions

In this paper, the effectiveness of semi-active magneto-rheological dampers (SAMRDs) for seismic response reduction of the RC elevated liquid storage tank has been demonstrated. The SAMRDS are installed in three placement configurations within the staging of the tank and are employed with four control algorithms as Passive-OFF, Passive-ON, Clipped Optimal Control (COC), and Simple Semi-active Control (SSC).

1. A simple semi-active control (SSC) is proposed in the present study which shows the outstanding performance in reducing the response of the tank. The significant advantage of this control algorithm is that it does not require any control parameter to be decided.
2. Remarkable response reduction is achieved as the voltage is increased from 0 to 3 V; however, a further increase in voltage has resulted in negligible or no additional response reduction.

3. The increase in command voltage increases the energy dissipation. Further, it is also seen that the effectiveness of the MR damper is greatly affected by the command voltage and the control algorithm employed, and there exists the optimum command voltage for Passive-ON algorithm

References

1. ACI 350.3 (2001) Seismic design of liquid containing concrete structures. American Concrete Institute, Farmington Hill, Michigan (MI), USA
2. Carlson JD, Jolly MR (2000) MR fluid, foam and elastomer devices. *Mechatronics* 10:555–569
3. Dyke SJ, Spencer BF, Sain MK, Carlson JD (1996) Modeling and control of magneto-rheological dampers for seismic response reduction. *Smart Mater Struct* 5(5):565–575
4. EN 1998-4 (2006) Euro-code 8—design of structures for earthquake resistance. Part 4: silos, tanks and pipelines. European Committee for Standardization, Brussels
5. Gluck N, Reinhorn AM, Gluck J, Levy R (1996) Design of supplemental dampers for control of structures. *J Struct Eng ASCE* 122(12):1394–1399
6. Hart GC, Wong K (2000) Structural dynamics for structural engineers. Wiley, New York
7. Jung HJ, Spencer BF Jr, Lee IW (2003) Control of seismically excited cable-stayed bridge employing magnetorheological fluid dampers. *J Struct Eng* 129(7):873–883
8. Math Works, MATLAB (2018) The language of technical computing. The Math Works Inc., USA
9. Sadek F, Mohraz B (1998) Semi-active control algorithms for structures with variable dampers. *J Eng Mech ASCE* 124(9):981–990
10. Spencer BF Jr, Dyke SJ, Sain MK, Carlson JD (1997) Phenomenological model for magneto-rheological dampers. *J Eng Mech ASCE* 123(3):230–238
11. Waghmare MV, Madhekar SN, Matsagar VA (2019) Semi-active fluid viscous dampers for seismic mitigation of RC elevated liquid storage tanks. *Int J Struct Stab Dyn* 19(03):1950020. <https://doi.org/10.1142/s0219455419500202>
12. Waghmare MV, Madhekar SN, Matsagar VA (2020) Influence of nonlinear fluid viscous dampers on seismic response of RC elevated storage tanks. *Civ Eng J* 6: 98–118 (Special issue Emerging materials in civil engineering)
13. Yang G, Spencer BF Jr, Carlson JD, Sain MK (2002) Large-scale MR fluid dampers: modeling and dynamic performance considerations. *Eng Struct* 24:309–323

Virtual Testing of Prototypes Using Test Frame Designed for Lateral Load



Suyog Nikam and I. P. Sonar

Abstract Structures such as Retaining Walls, Sheet piles, Frames, Masonry Walls, and Poles are subjected to lateral load. They are designed considering lateral load. lateral load-carrying capacity is an important factor for these structures. For verification of lateral load-carrying capacity of structures, lateral load testing of the actual prototype of such structures is needed. A vertical load testing facility is mostly available in laboratories but a lateral load testing facility is very rarely available. The lateral load testing facility is available in some of the engineering institutions in India, such as IIT Kanpur, SERC Chennai, and IIT Guwahati. During the testing of prototypes, an adequate reaction must be provided by the reaction wall specially manufactured for the lateral load test setup. The reaction wall should act as rigid lateral support and should not deflect during testing. This work includes the development and design of a reaction frame for Lateral load testing. The reaction frame is designed in such a way that prototypes of different dimensions can be tested. The designed reaction frame is used for virtual testing of the shear wall, retaining wall, and steel frame by using finite element software STAAD PRO. Obtained deflection results of the reaction frame and prototypes are analyzed. The results showed that the designed reaction frame is rigid enough to test different prototypes for lateral loading. As lateral load test setup is rarely available, it will have great demand.

Keywords Lateral load · Virtual testing · Retaining wall · Shear wall · Frame

S. Nikam (✉)
College of Engineering Pune, Pune, India
e-mail: suyognikam1765@gmail.com

I. P. Sonar
Civil Engineering Department, College of Engineering Pune, Pune, India

1 Introduction

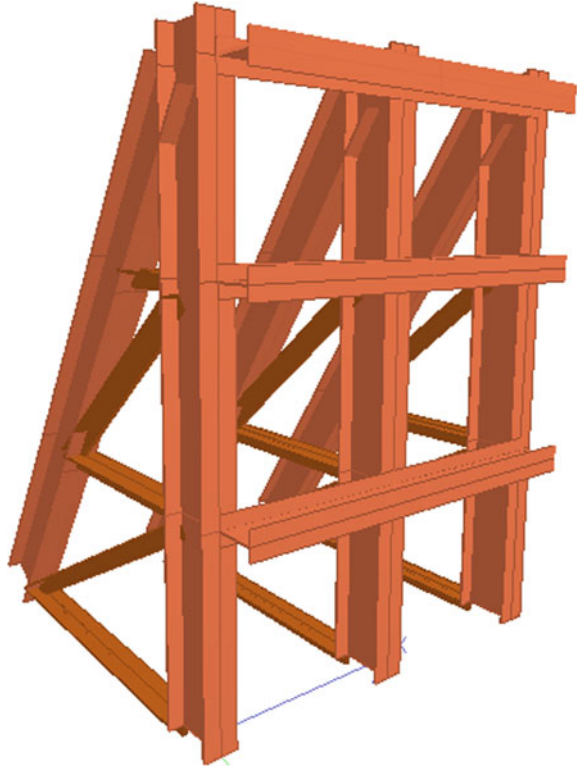
Structures like masonry walls, shear walls, and frames are subjected to lateral loading due to wind and earthquake actions. The retaining wall is under lateral loading due to soil pressure. Electric poles are under significant lateral loading due to the action of wires. These structures are designed considering lateral load. The lateral load is more critical for structures than vertical loads. Construction materials like concrete and brick are very strong in compression but very weak in tension. Lateral loading produces significant tension in these structures. Hence, lateral load-carrying capacity is an important factor for these structures. In ancient construction, resistance to lateral load is provided by using thick walls. However, in modern construction, thick wall is not preferred due to size constrain. For verification of lateral load-carrying capacity of structures, lateral load testing of the actual prototype of such structures is needed. Detail study of the behavior of structures under the application of lateral load is essential. For testing of actual prototypes, a reaction frame is required to provide adequate support during testing. As the sizes differ from specimen to specimen, it is difficult to use the same reaction frame for testing different types of test specimens [1–3]. In earlier studies, reaction frames are designed and constructed to conduct an experimental study of a single type of specimen. In this type of test, setup is very expensive and not feasible. Earlier test setups can only check the specimens of specific height and type. This test setup can check specimens of different heights and types [4]. The lateral load testing facility is available in some of the engineering institutions in India, such as IIT Kanpur, SERC Chennai, and IIT Guwahati [5]. Testing of lateral load behavior of Assam-type houses by testing full-scale frame specimens was done at IIT Guwahati. The objective of this study is to design such a reaction frame to conduct virtual testing of a different specimen such as retaining wall, shear wall, and frame using a designed reaction frame on STAAD Pro. software and also to check the performance of the reaction frame during testing.

2 Reaction Frame

2.1 Description of Reaction Frame

Lateral load testing requires a strong reaction frame while imposing lateral loads employing a hydraulic jack. For this purpose, the steel frame is designed to be built behind the test specimen. This Steel frame has a dimension of 3.6 m in height and a plan area of 2.4 m * 2.4 m. Prototypes up to height 3.4 m and 2.4 m wide can be tested using this reaction frame. Normally, the height of the shear wall, masonry wall, retaining wall, and frame is up to 3.4 m. Therefore, this height is selected for the reaction frame. For out-of-plane testing of a masonry wall and retaining wall, 2.4 m width is selected. The capacity of the test frame is 300 kN. That is frame can resist the total summation of the lateral load of 300 kN. Lateral loads can be applied by

Fig. 1 3D rendered view of reaction frame



employing horizontal members attached with jacks. The 3D shape of the test frame is shown in Fig. 1.

The Front Horizontal members are simply supported by the vertical column members. Bolted simple connection is used. These front horizontal members are movable along the vertical plane at different heights from 0.2 to 3.4 m with an interval of 0.1 m. This movement of front horizontal members is important for testing specimens with different heights. The lateral load should be applied using a hydraulic jack attached to the front horizontal members. The connection of the hydraulic jack to these members is made in such a way that hydraulic jacks are movable along the horizontal axis.

2.2 STAAD Pro. Modeling of Reaction Frame

Rolled steel sections are considered for the design of the reaction frame. Properties of steel are shown in Table 1. A Reaction frame of a steel structure presented in Fig. 3 has been analyzed using STAAD Pro. Software. Three Column Reaction frame with dimensions as given in Fig. 2. All connections are fixed connections

Table 1 Material property

Material	Elastic modulus (E) (N/mm ²)	Poisson's ratio (μ)	Density (kg/m ³)	Alpha ($^{\circ}$ C)	Yield strength (F_y) (N/mm ²)	Ultimate strength (F_u) (N/mm ²)
Steel	200,000	0.3	7833.409	0.000012	250	407.8

except the connection of the front horizontal member (M3) to the vertical column (M1). Connections have been designed and size parameters such as the thickness of the plate, diameter of bolts, gauge distance of bolts, weld size, and weld length have been evaluated from connection details using IS800-2007 provisions. Details of loading considered for frame analysis have been as follows. 300 kN of point load was applied at each point after a 0.1 m interval separately along both vertical and horizontal axis. So, during in-plane lateral load testing, an adequate reaction is provided. Then distributed load along the horizontal beam with a summation of 300 kN is applied on the same points. This type of loading will provide adequate reaction during out-of-plane lateral load testing for specimens. Finally, distributed load with a summation of 300 kN is applied along the vertical axis so that testing of the retaining wall is possible by converting soil pressure into an equivalent point load system.

Rolled Channel sections and equal angle sections are used for designing the reaction frame. Steel sections are selected and designed considering arrangements for lateral load application. Steel sections of the reaction frame are designed considering IS 800-2007 provisions. Steel sections selected for design are as shown in Fig. 2 and Table 2.

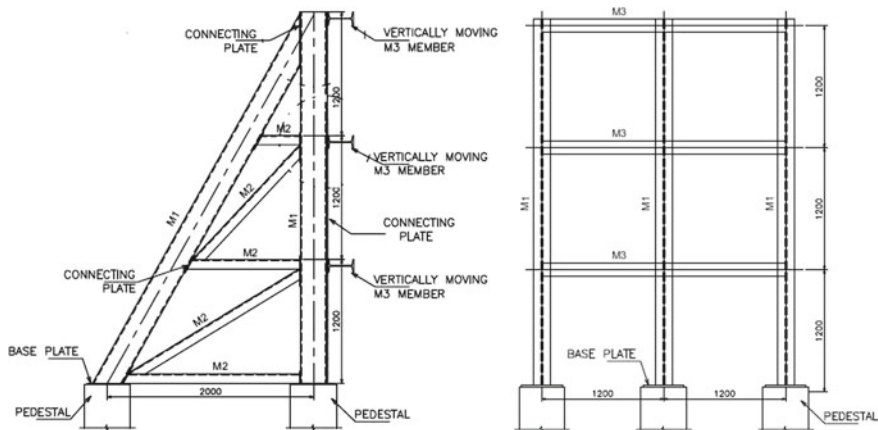


Fig. 2 A side view and front view of reaction frame

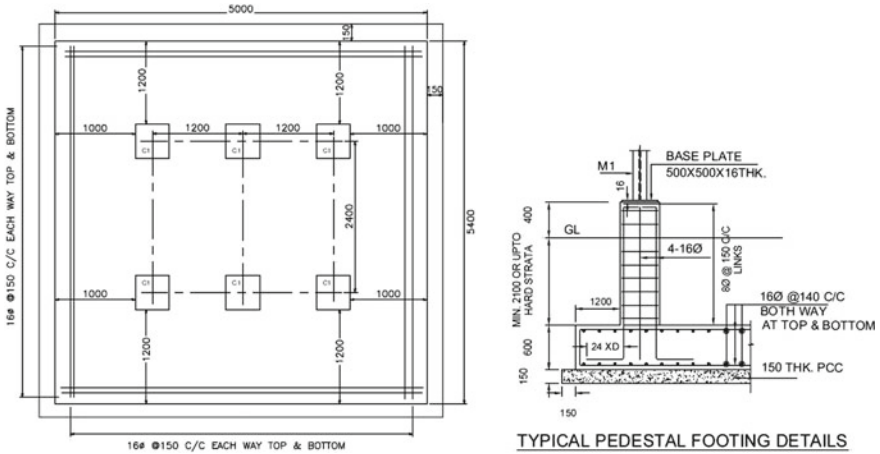


Fig. 3 Footing layout and details

Table 2 Steel sections

Member	Description	Selected section
M1	Vertical and inclined column	2ISMC 350 Back to back channel section
M2	Inclined bracing members	2 ISA 100 * 100 * 10 Back to back equal angle section
M3	Front horizontal members	2ISMC 250 Back to back channel section

2.3 Foundation Design for Reaction Frame

The foundation design of the reaction frame is critical. The reaction frame is subjected to 300 kN of lateral force. Due to the application of lateral load, the overturning and sliding effect is very significant for the reaction frame. For countering, the effect of overturning and sliding, mat footing must be provided at least at the depth of 2.1 m below the ground level. As the spacing between the columns is very less, mat footing is an appropriate option. For the design of the foundation, M30—the grade of concrete and Fe 500—grade of steel reinforcement are considered. The required depth of Mat footing is 600 mm. Details of foundation design are shown in Fig. 3. For designing the foundation, provisions of IS 456-2000 are used.

3 Virtual Testing of Prototypes Using Reaction Frame

Three different prototypes were virtually tested using the reaction frame on STAAD Pro. Software. Three different specimens are retaining wall, Shear wall, and steel frame.

3.1 Retaining Wall

Retaining walls are subjected to linearly varying soil pressure. Soil pressure is converted into an equivalent point load system. Then point loads are applied at the resultant location so that equivalent pressure is generated. Front horizontal members are adjusted to the required location. Using the designed reaction frame retaining walls up to a height of 3.4 m and a width of 2.4 m can be tested. For the different heights of the retaining walls, the locations of front horizontal members are shown in Table 3.

For virtual testing retaining wall, 3 m high retaining wall is modeled in front of designed reaction frame in STAAD Pro. An appropriate model of reaction frame is selected as per Table 3. As shown in Fig. 4, unit weight of soil is considered as 19 kN/m^3 and the angle of internal friction is taken as 30° . Concrete of grade M30 and steel of grade Fe500 are considered for designing the retaining wall. Provisions of IS 456:2000 are considered while designing the retaining wall.

Surcharge load is increased from 15 to 150 kN/m^2 . Deflection results of reaction frame and retaining wall during the virtual testing using STAAD Pro. Software, are as shown in Table 4 and Fig. 7.

Table 3 Location of horizontal members along vertical axis

Height of retaining wall (m)	Location of horizontal member 1 (m)	Location of horizontal member 2 (m)	Location of horizontal member 3 (m)
3.4	0.5	1.5	2.7
3.2	0.5	1.5	2.6
3.0	0.5	1.5	2.5
2.8	0.5	1.5	2.4
2.6	0.5	1.5	2.3
2.4	0.4	1.2	2.0
2.2	0.4	1.2	1.9
2.0	0.4	1.1	1.7
1.8	0.3	0.9	1.5
1.6	0.3	0.9	1.4

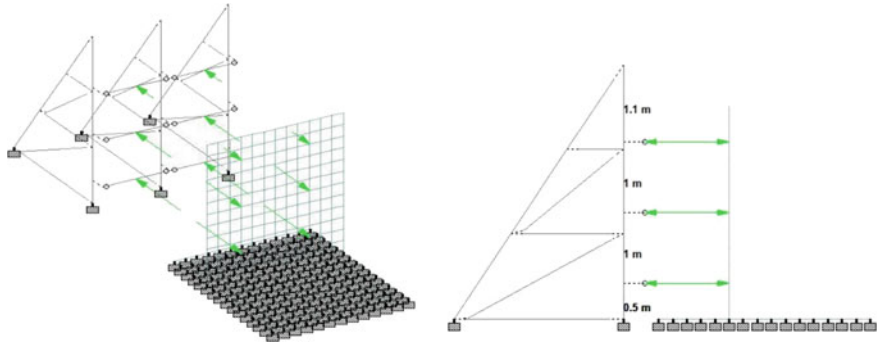


Fig. 4 3D and side view of virtual testing of retaining wall

Table 4 Test results for retaining wall

Surcharge (kN/m ²)	Deflection of retaining wall (mm)	Deflection of reaction frame (mm)
0	2.572	0.080
15	3.415	0.110
30	4.258	0.140
45	5.101	0.160
60	5.945	0.195
75	6.787	0.224
90	7.629	0.253
105	8.473	0.281
120	9.316	0.310
135	10.159	0.331
150	11.002	0.368

3.2 Shear Wall

A shear wall is a vertical element of a structural system that is designed to resist lateral forces. Virtual testing of the shear wall for out-of-plane lateral forces is performed using an earlier designed reaction frame. A shear wall of 3.0 m height and 250 mm thickness is modeled in front of an earlier designed reaction frame in STAAD Pro. As shown in Fig. 5, concrete of grade M30 is considered for designing the shear wall. Out-of-plane, lateral load from 45 to 225 kN is applied at three different locations on the shear wall.

Provisions of IS 456:2000 are considered while designing the retaining wall. Deflection Results of reaction frame and shear wall during the virtual testing using STAAD Pro. Software is shown in Table 4 and Fig. 5.

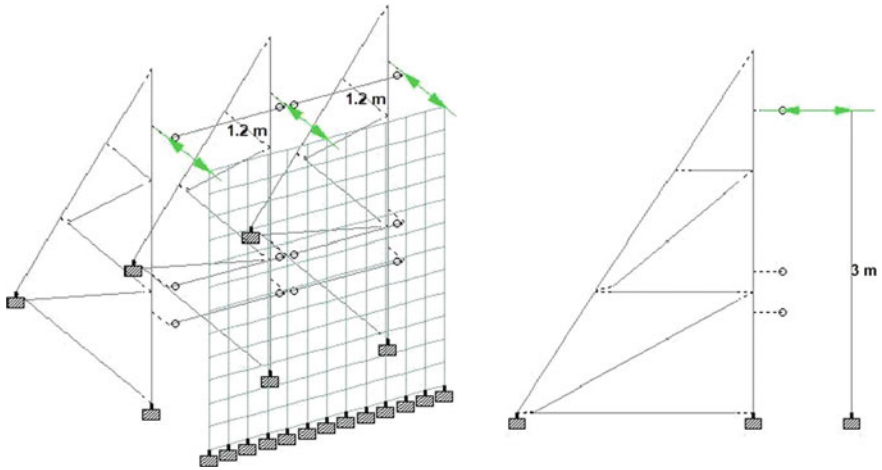


Fig. 5 3D and side view of virtual testing of shear wall

3.3 Steel Frame

The last two virtual tests are performed for out-of-plane lateral load action. This virtual test is performed for the in-plane lateral load. The steel frame of ISMB 250 and ISA 60 * 60 * 10 is modeled in front of the reaction frame and lateral point load is applied until failure (300 kN) of the steel frame prototype. The height of the steel frame prototype is 2.4 m and the length is 2.0 m (Fig. 6).

Deflection Results of reaction frame and shear wall during the virtual testing using STAAD Pro. Software is shown in Table 5 and Fig. 7.

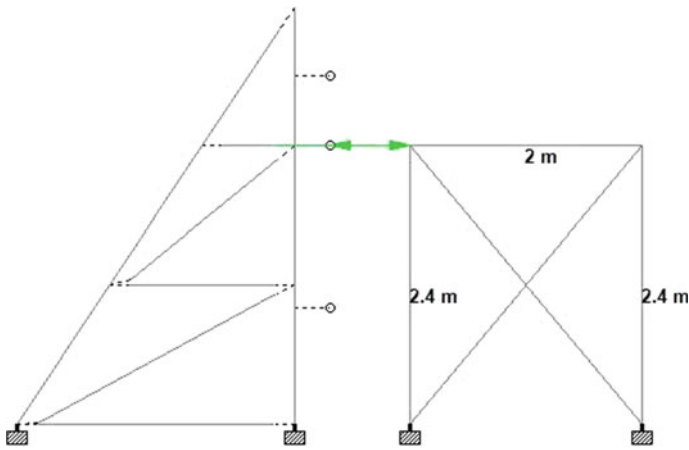


Fig. 6 3D and side view of virtual testing of the shear wall

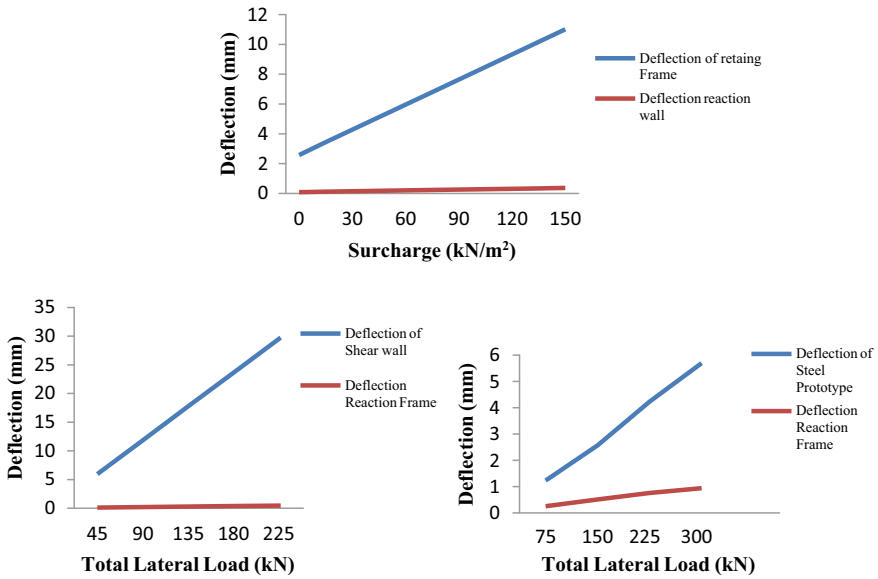


Fig. 7 Deflection of reaction wall and different prototypes

4 Results and Discussions

The results obtained from the FEM analysis using STAAD Pro. are summarized in Tables 4, 5, and 6. The comparison graph between the deflection of different prototypes and reaction frames is shown in Fig. 7. Maximum deflection on test prototypes is observed at the top end as fixed support is only assumed at the bottom of the reaction frame. The maximum deflection for retaining is 11.022 mm, for the shear wall, it is 29.741 mm, and for the steel test frame, it is 7.429 mm after members started failing. While for all prototypes, deflection of the reaction frame is very low. It shows that the reaction frame is rigid enough for testing prototypes of different dimensions up to a height of 3.4 m and a width of 2.4 m. The maximum deflection

Table 5 Test results for shear wall

Total lateral load (kN)	Deflection of shear wall (mm)	Deflection of reaction frame (mm)
45	5.948	0.086
90	11.896	0.172
135	17.844	0.259
180	23.793	0.355
225	29.741	0.444

Table 6 Test results for steel frame

Total lateral load (kN)	Deflection of steel frame (mm)	Deflection of reaction frame (mm)
75	1.225	0.254
150	2.574	0.509
225	4.227	0.763
300	5.703	0.938

of the reaction frame is 0.938 mm for a 300 kN point load. Due to Covid-19, actual construction of the reaction frame is currently postponed.

While performing an actual experiment, this deflection error should be considered. As no structure is perfectly rigid, this error is considerable.

5 Conclusions

Virtual testing using finite element (STAAD Pro. software) was performed under different lateral loading using a reaction frame specially designed for the lateral load test. Three different prototypes, namely, retaining wall, shear wall, and steel frame prototypes were tested. The performance of the reaction was checked during virtual testing and it showed good results. As the designed reaction frame is cost-efficient and compact in size, it is capable of testing various types of prototypes. Following are a few conclusions that are drawn from the study:

1. Maximum deflection of the reaction frame is 0.938 mm for 300 kN of lateral point load. This shows that the reaction frame is strong and capable testing of different prototypes.
2. Total steel requirement for assembly of the reaction frame is only 33.586 kN and the area required for the total lateral load test setup is 5.5 m by 9 m. Hence, it is cost-efficient and compact.
3. Lateral load testing of various types of prototypes with different heights from 0.2 to 3.4 m is possible using the single reaction frame.
4. Experimental setup suggested that the lateral load testing of prototypes will help for understanding the true behavior of the large specimens and this facility will create an opportunity for research work as well a revenue generation through testing of large prototypes, which is needed for the Engineering Institute.

References

1. Choudhury T et al (2020) Experimental and numerical analyses of unreinforced masonry wall components and building. *Constr Build Mater* 257. <http://doi.org/10.1016/j.conbuildmat.2020.119599>
2. Arslan ME et al (2017) Structural behavior of rammed earth walls under lateral cyclic loading: a comparative experimental study. *Constr Build Mater* 133:433–442. <http://doi.org/10.1016/j.conbuildmat.2016.12.093>
3. Graham DA et al (2010) Performance of log shear walls subjected to monotonic and reverse-cyclic loading. *J Struct Eng* 136(1):37–45. [http://doi.org/10.1061/\(asce\)st.1943-541x.0000035](http://doi.org/10.1061/(asce)st.1943-541x.0000035)
4. Morandi P et al (2014) In-plane experimental response of strong masonry infills. In: 9th international masonry conference, July 7, 8, 9, 2014, Guimarães, pp 1–12
5. Chand B et al (2019) Lateral load behavior of traditional Assam-type wooden house. *J Struct Eng* 145(8):04019072. [http://doi.org/10.1061/\(asce\)st.1943-541x.0002359](http://doi.org/10.1061/(asce)st.1943-541x.0002359)

Crack Simulation and Monitoring of Beam-Column Joint by EMI Technique Using ANSYS



Tejas Shelgaonkar and Suraj Khante

Abstract Health monitoring of structures has a great contribution to the growing interest of researchers in damage detection. The Structural Engineering Community is nowadays employing Electro-Mechanical Impedance (EMI) technique on a wide range for monitoring the health of structures. EMI technique involves the use of Piezoelectric (PZT) patches bonded to the host structure and also instruments such as Impedance analyzer/LCR meter, Wired/Wireless connections, etc. The change in conductance/impedance/susceptance signatures in comparison with the healthy signatures defines the presence of damage. The experimental arrangement in this regard resembles the impedimental system approach. So, substitutable modeling and analysis with the help of simulation are preferable. In this research, a beam-column joint has been modeled in ANSYS 19.2 software. After analysis, the joint has been monitored for baseline (healthy) results on the basis of the simulated EMI technique for health inspection. After getting the baseline conductance and susceptance signatures, the beam-column joint has been formed with a crack modeled on the joint. The fracture analyzed model was then monitored in the same way as a healthy model with the help of the PZT patch. The conductance signature so obtained was then compared with the baseline (healthy) signature, the change in which identified the presence of a crack on the joint. Root mean squared deviation (RMSD) values have been calculated for computing the change in conductance values for respective frequency ranges.

Keywords ANSYS · Damaged/cracked beam-column joint · EMI technique · SHM

T. Shelgaonkar (✉)
Structural Engineering, Government College of Engineering, Amravati, India
e-mail: shelgaonkartejas@gmail.com

S. Khante
Applied Mechanics, Government College of Engineering, Amravati, India

© The Author(s), under exclusive license to Springer Nature Singapore Pte Ltd. 2023
M. S. Ranadive et al. (eds.), *Recent Trends in Construction Technology and Management*, Lecture Notes in Civil Engineering 260,
https://doi.org/10.1007/978-981-19-2145-2_81

1101

1 Introduction

The important units of structures are expected to fulfill safety considerations all through the existence period. That is why damages and defects ranging from incipient stage to greater stage due to fatigue, overburden, and environmental impacts are necessary to be detected [1]. Around the whole world, health monitoring of structures has been continuously playing an important role in the fine development of civil, aerospace, and mechanical engineering [2]. Structural Health Monitoring (SHM) is the process of checking the present condition of structures. For reducing the repairing and maintenance cost, Non-Destructive Testing (NDT) is preferably used. Perceptible inspection is usually executed on the anticipated locations of damages by the inspectors with fine experience. Moreover, health monitoring is a work-intensive program incorporating risk factors about safety. This is the reason behind SHM works leaning toward real-time sensing systems [3]. One of the most popular methods in this regard include Electro-Mechanical Impedance Technique (EMI technique) for health monitoring [4]. Over the past years, SHM has got a prime part in improving the reliability and safety of structures, which reduces the cost of operation [5]. Structural Health Monitoring (damage detection) contains various methods according to the use, type of damage, condition of structure, etc. From all those methods, Electro-Mechanical Impedance based damage detection has gained popularity these days. Middle-sized to the greater-sized damages are easily visible, but holding the severe damages back in the incipient stage itself by detecting the damage earlier can head toward the security and well-being of the infrastructure [6]. EMI technique stands ahead in detecting the incipient level damages in the structure. It involves the use of Piezoelectric (PZT) patches. In the EMI technique, a PZT can serve as both actuator and sensor when attached to a structure. When a PZT is provided with an alternating electric field, deformation is produced in the PZT patch which then excites the parent structure to which it is glued. This excitation response is again transferred back to the piezoelectric patch as an electrical response. When any change in the response (mechanical) due to some damage is generated, the effect of that is seen there at the LCR meter (Fig. 1)/impedance analyzer in the electrical response of the piezoelectric (PZT) patch [7]. Beam-Column joint is one of the most crucial elements of a

Fig. 1 LCR meter



structure, the damage of which may lead to large-scale destruction of a structure. As soon as lateral loads act, critical problems start to arise at a joint and so in the whole structure. In the absence of an experimental setup, the simplest way of working on a system for specific results to be obtained after analysis is finite element simulation. Generation of finite element model to evaluate the performance of the system can get the required results in an efficient manner.

Divsholi et al. [8] took four differently detailed concrete structures with PZT sensors, and the impedance extracted from PZT was compared with admittance. A relation between load step and damage index was obtained. Yan and Chen [5] correlated the signature changes to properties of structures and damage detection was ensured. The thematic experimental setup is shown in Fig. 1. Baluch et al. [9] presented the finite element model of a beam-column junction with concrete having low strength, retrofitted with CFRP sheets by using 'DIANA' software. Hamzeloo et al. [10] performed the EMI technique on aluminum and steel hollow cylinders. FEM results were also compared with experimental data. The effects of the damage on damage metrics were explained. For the same, experimental and FEM results of the system were used. Lim and Soh [11] investigated fatigue crack detection and characterization by the EMI technique. Bharathi Priya et al. [7] experimentally analyzed differentially cured concrete beam embedded with PZT patches of varying thickness connected in series. Using the 2nd-day signature as baseline signature, the variation in frequency peaks was quantified using RMSD as strength index. Results show that the serial sensing method using PZT is a quick and efficient method. Venkatesan et al. [12] analyzed the seismic performance of beam-column joint with new detailing of reinforcement. Group-wise samples with various joint detailing formats along with their finite element models for un-strengthened and ferro-cement strengthened specimens were compared. Lal [13] considered beam-column joint model from a STAAD.Pro designed building. The joint was further modeled in NX-Cad and then imported to ANSYS and analyzed for corresponding shear stress and deformation. Gedam and Khante [2] performed experiments on 2 concrete beams. In the first experiment, different methods of embedment of PZT by subjecting the model to damage were implemented. In the second experiment, an embedded smart aggregate with varying orientations was implemented to get the signatures (susceptance and conductance) of various piezoelectric transducers. Khante and Chikte [14] worked for defect detection of CFST (Concrete filled steel tubes) by using the EMI technique. Four CFST columns with different properties in terms of bonding and compaction and imparted debonding were taken to detect the defect in terms of RMSD index. Na and Baek [15] reviewed studies on the EMI technique in past decades and new ideas proposed by authors were also surveyed. Zhou et al. [1] proposed a modern damage index based on EMI-based principle and a double stepped method of inspecting the damage with respect to the damage indicator. A number of piezoelectric sensors attached to the steel beam were implemented to get the output responses. Kaur et al. [16] presented damage and retrofitting monitoring in RC structures with PZT patches. They carried out both experimental and FEM analysis for checking the suitability of use of 2nd order derivative along with other derivatives with high order for mode shapes of displacement and detection of damage. It was concluded that the response

of sensors based on curvature mode shape can take out the damaged location successfully. Taha et al. [3] has taken out electromechanical responses calculated from PZT sensors for damaged and repaired concrete elements. The responses in the form of admittance signatures for damaged and repaired cases were compared and analyzed. Jayachitra and Priyadarshini [4] represented the detection of damage in concrete structures using a PZT patch. The conductance, admittance, impedance, and susceptance graphs were generated at various frequency levels. And damage index was determined by RMSD values. It was concluded that the PZT patch was found to be accurate for damage detection of structure. Su et al. [17] studied the use of 2 types of coatings with polymer on sensors as protection. The effectiveness of the polymer coated piezoelectric sensor was evaluated using an impedance analyzer. For simulation of different coating configuration sensors, finite element analysis was conducted. Kaur and Singla [6] reviewed the Electromechanical Impedance technique and its development to date for the evaluation of structures.

The review of literature gives a brief overview about the research work progressed related to the implementation of EMI technique to beam-column joints. It can be seen that simulation of finite element model for health monitoring using EMI technique is to be primarily focused yet along with the experimental works to get another choice for efficient inspection. Present work consists of finite element modeling of beam-column joint in ANSYS 19.2 software with piezoelectric patch modeled for health monitoring of the system. The conductance and susceptance signatures, which are said to be the real and imaginary parts of admittance, respectively, were expected from the responses recorded from the PZT patch model. To implement the same, a healthy beam-column joint along with a fracture analyzed (crack introduced) model were created and both the models were monitored with the help of PZT patch connected to the joint for conductance/susceptance signatures to be obtained. The change in signatures of the damaged (crack introduced) model in comparison with the healthy model was to be acquired for justification of the methodology. After this qualitative analysis of both the models on the basis of signatures, to analyze the results quantitatively, Root Mean Squared Deviation (RMSD) values were to be calculated with respect to the different values of conductance at various frequency substeps. The results in the form of an RMSD index for various frequency ranges showed the significance of variation in signatures of a healthy and damaged case.

2 Structural Health Monitoring Using EMI Technique

Structural engineering accompanying SHM forms a valued subject in the view of the economy. The performance of structures is directly linked to the strength of the economy [16]. For the safety of various types of structural systems, the development and modification of health monitoring techniques have got increasing interest in researches nowadays. Recently, piezoelectric materials, such as Lead Zirconate Titanate (PZT), have shown good performance in health monitoring [17]. Due to its

various advantages, the EMI technique which is a non-destructive evaluation technique of health monitoring; is becoming a successful health inspection strategy. The development of EMI technique was introduced initially by Liang et al. [15]. In the EMI technique, impedance/admittance can be used as an indicator of damage [8]. EMI technique is said to be a cost-effective option for SHM and non-destructive testing of engineering systems [7]. When an electric field is applied to PZT patch, the patch gets deformed [14]. Impedance/Admittance/Conductance/Susceptance curves are formed in LCR meter/impedance analyzer because of piezo sensors to detect changes in structural response, i.e., presence of structural damage. Electro-mechanical Impedance technique involves the use of piezoelectric (PZT) patches attached to the host structure which excite the host structure with provided frequency and detect the changes in electromechanical impedance curves (signatures). Getting the impedance for the damaged/defected case and comparing the same with the baseline impedance; from the observed change in impedance signature, it can be determined that the damage has taken place. In order to perform the operation with high damage sensitivity, the measurement should be taken at high frequencies. At such a high frequency, the excitation wavelength is small and it is very much sensitive for detecting the structural changes. The usage of material sensing with smart material like EMI method has provided an optional choice to the conventional techniques of health inspection, because of which, some drawbacks have overcome. The Electro-Mechanical Impedance method, with PZT as sensor/actuator is applicable with its well-known ability in the detection and characterization of damages [11].

3 Beam-Column Joint Dominance

In RC building frames, junctions can be said to be the most critical elements. Under earthquake/wind loads, flexural and shear stresses simultaneously act at the junction. As the included materials have limited capacities, joints also have limited strengths. Joints get damaged severely when forces larger than those strengths are applied to the structure during wind/earthquake action [9]. Past earthquakes have shown that failure of beam-column joint leads to the collapse of a structure partially or fully. The columns and beams that are near to the joints are most critical, and when strong waves of earthquake hit the structure, they get large shear forces and bending moments [12]. That is why; beam-column junctions are the most crucial elements of a structure, especially under the action of lateral loads. Over the past years, researches have been conducted on beam-column joints and till now, a clear picture has not been derived [13].

4 Finite Element Modeling

Finite element modeling of the system has been carried out in the software ANSYS. FE Modeling gives the numerical computation of reaction charges on each sensor node for generating the corresponding impedance/admittance/susceptance/conductance signatures [10]. A beam-column joint with steel reinforcement was modeled in ANSYS and primarily analyzed for shear stress, total deformations, etc. The dimensions and reinforcement details for beam-column joint were as shown in Table 1.

Modeling process in ANSYS involves the stepwise provision of material properties, geometry formation, model creation, and setup for meshing before analysis and result generation. In ANSYS, the analysis can be performed in both workbench and APDL tools. Some properties are in built and provided in the workbench for general analysis and some are to be given manually as per the analysis requirement. As far as reinforced concrete structure is considered, concrete and steel general material properties can be selected as they are in the workbench tool. But for modeling PZT patch, piezoelectric properties are to be given as input to the tool. In the present work, PZT patch geometry was modeled initially as steel material in the workbench tool itself. The whole model was then imported to APDL tool and properties of the PZT patch were changed to piezoelectric properties thereafter in APDL for getting solution in the form of conductance signatures. The properties of steel, concrete, and PZT materials included in the work were taken as given in Tables 2, 3, and 4, respectively.

Table 1 Dimensions, reinforcement details of beam-column joint

Beam specifications		Column specifications	
Parameter	Value (mm)	Parameter	Value (mm)
Width	150	Width	150
Depth	200	Depth	200
Span	800	Height	1000
Cover	25	Cover	25
Top steel	2#10	Longitudinal steel	4#10
Bottom steel	2#10		
Transverse steel dia	6	Transverse steel dia	6
Transverse steel spacing	120	Transverse steel spacing	150

Table 2 Steel material properties used for modeling

Density	7850	Kg/m ³
Young's modulus	2×10^{11}	Pa
Poisson's ratio	0.3	
Bulk modulus	1.67×10^{11}	Pa
Shear modulus	7.69×10^{10}	Pa
Tensile yield strength	2.5×10^8	Pa
Comp. yield strength	2.5×10^8	Pa
Tensile ultimate strength	4.6×10^8	Pa

Table 3 Properties of concrete material used for modeling

Density	2.3×10^3	Kg/m ³
Young's modulus	3×10^{10}	Pa
Poisson's ratio	1.8×10^{-1}	
Bulk modulus	1.56×10^{10}	Pa
Shear modulus	1.27×10^{10}	Pa
Tensile ultimate strength	5×10^6	Pa
Comp. ultimate strength	4.1×10^7	Pa

Table 4 Properties of PZT patch for modeling

Parameters	Symbols	Values	Unit
Density	ρ	7800	Kg/m ³
Dielectric loss factor	$\tan\delta$	0.02	
Compliance coefficients	S_{11}	15.0	10^{-12} m ² /N
	$S_{22} = S_{33}$	19.0	
	$S_{12} = S_{21}$	-4.50	
	$S_{13} = S_{31}$	-5.70	
	$S_{23} = S_{32}$	-5.70	
	$S_{44} = S_{55}$	39.0	
Electrical permittivity	ϵ_{11}^T	1.75	10^{-8} F/m
	ϵ_{22}^T	1.75	
	ϵ_{33}^T	2.12	
Piezoelectric strain coefficients	d_{31}	-2.10	10^{-10} m/V
	d_{32}	-2.10	
	d_{33}	5.0	
	d_{24}	5.80	
	d_{15}	5.80	

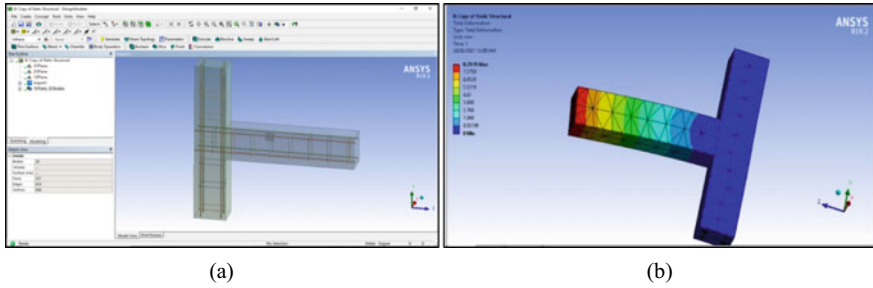


Fig. 2 **a** Geometry creation and **b** analysis results (total deformation) in ANSYS workbench

5 System Development

After selecting static structural analysis, the next step in ANSYS is there to select the engineering data (properties of materials). Then, for creating geometry, two tools, i.e., design modeler and space claim can be used. Creating geometry (Fig. 2a) is the previous step to the prime mechanical model formation (Fig. 2b), which includes meshing, defining loads, analysis, and required results generation.

5.1 Crack Introduction

For fracture analysis of the beam-column joint model, a small crack was introduced near the junction of the model (Fig. 3). The portion targeted for the development of crack was extruded along the width of the beam and the setup involved in fracture analysis was prepared. After generating the mesh, analysis similar to the healthy model along with fracture analysis for the crack was performed. Finally, whole systems of both the healthy (Fig. 4) and the damaged models were imported to APDL tool for monitoring and PZT analysis was performed in order to get the conductance/susceptance signatures.

6 Results and Discussion

As the PZT patch was initially modeled as a steel element in a mechanical workbench, after importing the whole geometry in APDL, firstly the piezoelectric element was added to the element list and after that, the specified piezoelectric properties were provided to the element by removing the earlier steel material properties. In the PZT patch, top nodes were provided with a voltage of 1 V and bottom nodes were provided with a voltage of 0 V. Both the top nodes and bottom nodes were coupled by volt degree of freedom (volt DOF). For the same frequency ranges, the conductance and

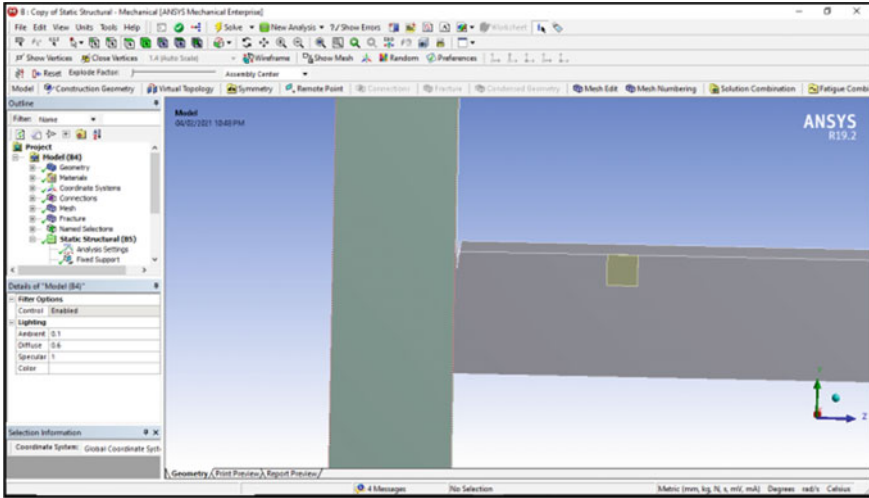


Fig. 3 Introducing crack in the model

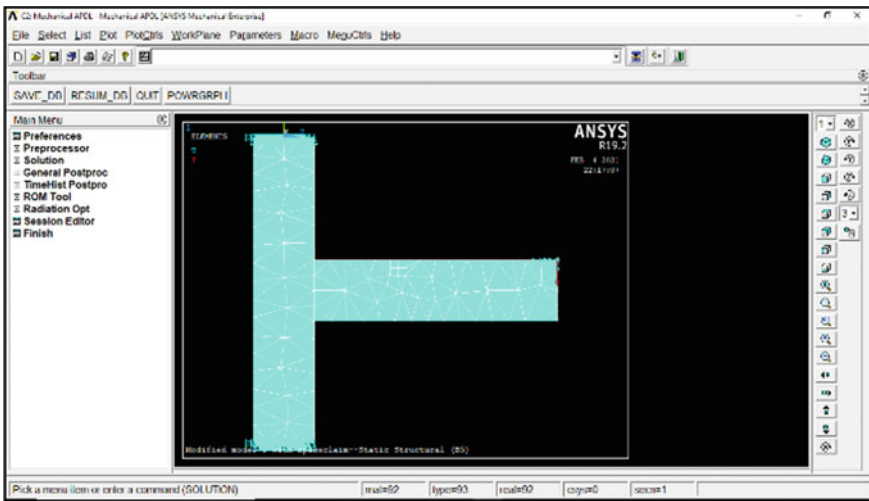


Fig. 4 Importing geometry to APDL tool for PZT patch specification

susceptance values for the healthy model and cracked model were recorded (Figs. 5 and 6).

The introduction of damage in the structural member was to be examined with the change in conductance values at the same frequency ranges. That is why the results were calculated by accounting same frequency ranges provided to the healthy and the damaged models, respectively. Consequently, the signatures (curves showing values of conductance for various frequency substeps) were observed to be varying from

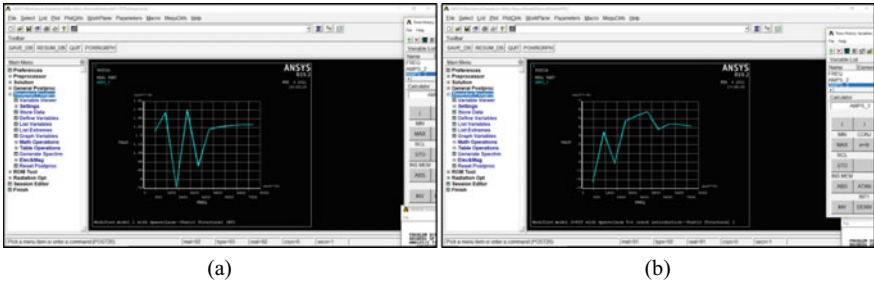


Fig. 5 Conductance signatures for healthy (a) and cracked (b) model, respectively

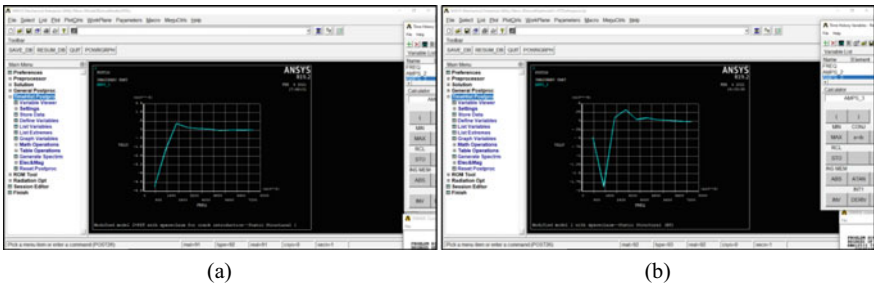


Fig. 6 Susceptance signatures for healthy (a) and cracked model (b), respectively

those of healthy signatures which justified the presence of damage in the member. The upward/downward and also the forward/backward migration of the signature in this regard can be marked to be the base of qualitative analysis for inspection of the damage. Getting the values of conductance and susceptance in a spreadsheet and generating the curve, the superimposed baseline signature and cracked model signature were obtained as shown in Figs. 7 and 8.

Root Mean Squared Deviation (RMSD) values can be determined as damage indices for various ranges. The formula for calculation of RMSD values is

$$RMSD = \sqrt{\frac{\sum_{j=1}^N (G_j^1 - G_j^0)^2}{\sum_{j=1}^N (G_j^0)^2}}$$

where

G_j^1 = Conductance at j th measurement point after damage.

G_j^0 = Conductance at j th measurement point before damage.

RMSD values were calculated for different ranges of frequencies, i.e., 75–225 kHz, 300–450 kHz, and 525–750 kHz (Fig. 9).

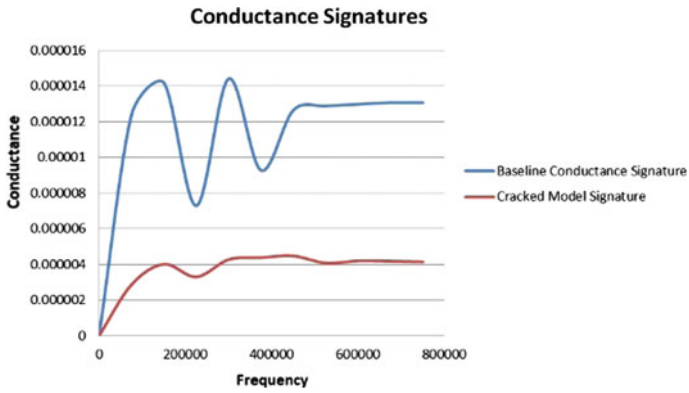


Fig. 7 Conductance signatures for healthy and cracked model combination

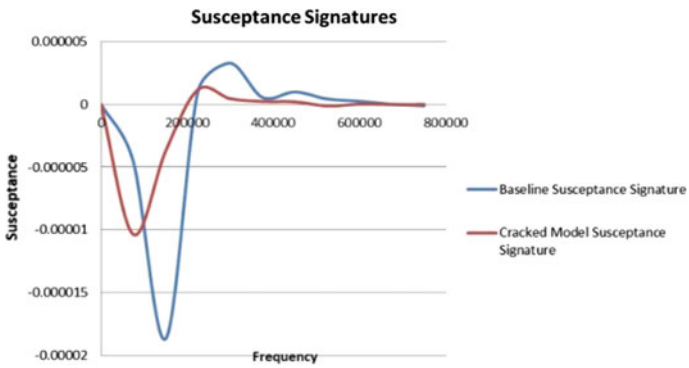


Fig. 8 Susceptance signatures for healthy and cracked model combination

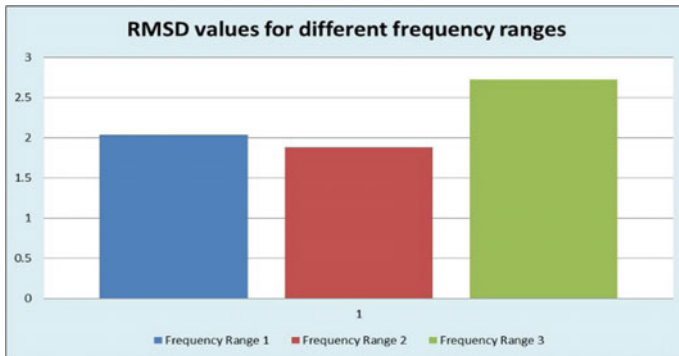


Fig. 9 RMSD values for various frequency ranges

The values of RMSD indices indicated the quantitative deviation of signature from the original (healthy) case. The equation for calculating the RMSD value corresponds to the change between conductance values for the healthy case and the damaged case at the specific frequency substeps defined.

7 Conclusion

For avoiding strength deduction of structures, non-destructive evaluation is preferred under which, the Electromechanical Impedance technique gives promising results. Under the EMI technique, further simplification of the process can be achieved by using finite element analysis of the structural element to be monitored. ANSYS tool achieves greater efficiency in modeling and analyzing structural system according to the analysis requirement. FE analysis overcomes the problems faced in the complex arrangement of the system and simplifies the implementation of the method. Results generated after the analysis showed that the conductance signature for the healthy model and cracked model differ from each other which ultimately defined the presence of damage in the member. The damage indicator, i.e., RMSD values for various frequency ranges also confirmed that the deformation/damage is monitored by the PZT patch modeled in the system by authenticating the variation in signatures. The results synthesize that PZT patch is reliable in detecting the presence of damage in a structure also with the use of a simulated system efficiently.

References

1. Zhou P, Wang D, Zhu H (2018) A novel damage indicator based on the electromechanical impedance principle for structural damage identification. *Sensors* 2199:1–17
2. Gedam SR, Khante SN (2016) Experimental investigation on sensitivity of smart aggregate embedded in reinforced concrete beam. *Open J Civil Eng* 6:653–669
3. Taha H, Ball RJ, Paine K (2019) Sensing of damage and repair of cement mortar using electromechanical impedance. *Materials* 3925(12):1–21
4. Jayachitra T, Priyadarshini R (2020) Structural health monitoring for concrete structure using impedance chip. *Int J Eng Adv Technol (IJEAT)* 9(3):1058–1060
5. Yan W, Chen WQ (2009) Structural health monitoring using high-frequency electromechanical impedance signatures. *Adv Civil Eng* 2010. Hindawi Publishing Corporation
6. Kaur H, Singla S (2020) A review of electromechanical impedance technique using piezoelectric transducers in the assessment of structures. *J Inf Technol Electr Eng (ITEE)* 9(5):24–35
7. Priya CB, Gopalakrishnan N, Rao ARM (2015) Impedance based structural health monitoring using serially connected piezoelectric sensors. *J Inst Smart Struct Syst (JISS)* 4(1):38–45
8. Divsholi BS, Yaowen Yang, Bing L (2009) Monitoring beam-column joint in concrete structures using piezo-impedance sensors. *Adv Mater Res* 79–82:59–62
9. Baluch MH, Ahmed D, Rahman MK, Ilki A (2012) Finite element simulation of low concrete strength beam-column joint strengthened with CFRP. In: *Proceedings of 15th World conference on earthquake engineering*

10. Hamzeloo SR, Shamshirsaz M, Rezaei SM (2012) Damage detection on hollow cylinders by electro-mechanical impedance method: experiments and finite element modelling. *Comptes Rendus Mecanique* 340:668–677
11. Lim YY, Soh CK (2014) Electro-mechanical impedance (EMI)-based incipient crack monitoring and critical crack identification of beam structures. *Res Nondestr Eval Am Soc Nondestr Testing* 25(2):82–98
12. Venkatesan B, Ilangovan R, Jayabalan P, Mahendran N, Sakthieswaran N (2016) Finite element analysis (FEA) for the beam-column joint subjected to cyclic loading was performed using ANSYS. *Circuits Syst* 7:1581–1597
13. Lal A (2016) Analysis of exterior beam column joint using ANSYS. *Int J Sci Res (IJSR)* 5(7):947–950
14. Khante SN, Chikte SS (2017) Defect detection of concrete filled steel tubes with PZT based technique. *Int J Innovative Res Sci Eng Technol* 6(1):673–678
15. Na WS, Baek J (2018) A review of the piezoelectric electromechanical impedance based structural health monitoring technique for engineering structures. *Sensors* 1307:1–18
16. Kaur N, Bhalla S, Maddu SCG (2019) Damage and retrofitting monitoring in reinforced concrete structures along with long-term strength and fatigue monitoring using embedded Lead Zirconate Titanate patches. *J Intell Mater Syst Struct* 30(1):100–115
17. Su Y-F, Han G, Kong Z, Nantung T, Lu N (2020) Embeddable piezoelectric sensors for strength gain monitoring of cementitious materials: the influence of coating materials. *Eng Sci* 11:66–75

The Impact of Perforation Orientation on Buckling Behaviour of Storage Rack Uprights



Kadeeja Sensy, Ashish Gupta, K. Swaminathan,
and J. Vijaya Vengadesh Kumar

Abstract Industrial storage rack uprights are the most widely used framed structures of thin-walled cold-formed steel members which are meant for the depot of palletized goods. The sensibility of uprights towards local buckling, distortional buckling, global buckling or interaction between these buckling modes in the presence of perforations results in complex behaviour of the uprights. The sustainability of the uprights in terms of the perforations, cross-section geometry, buckling and complexity might be difficult to design through the existing analytical methods alone. The test-based design being expensive leads to the necessity of an analysis-based design approach. The limited analytical methods available in the literature focus on orthogonal perforations and there is no systematic study available in terms of perforation orientation which would imply a minimum net section. This article sheds light effect of increased perforated width due to orientation which directly influences the elastic local critical buckling load calculations. The parametric analysis using finite element software is systematically done for the simple rack section with orthogonal cross-section elements having two idealized transverse web perforations of square and rectangular shape oriented at an angle other than orthogonal angles. The pre-validated FE model is used in this study, and thus the critical elastic buckling loads are procured for various perforation orientations. The CUFSM buckling analysis is done by using the reduced thickness expression recommended in the literature and compared with the FE results. The applicability of reduced thickness equations in accounting perforations in the view of perforation orientation is compared and summarized.

Keywords Elastic buckling · Perforation orientation · Storage rack uprights · CUFSM · Reduced thickness equations

K. Sensy · A. Gupta · K. Swaminathan · J. Vijaya Vengadesh Kumar (✉)
National Institute of Technology Karnataka, Surathkal, Mangalore 575025, India
e-mail: vj@nitk.edu.in

© The Author(s), under exclusive license to Springer Nature Singapore Pte Ltd. 2023
M. S. Ranadive et al. (eds.), *Recent Trends in Construction Technology and Management*, Lecture Notes in Civil Engineering 260,
https://doi.org/10.1007/978-981-19-2145-2_82

1115

1 Introduction

Storage rack uprights are the framed structure that are assimilated from cold-formed steel columns having multiple perforations along longitudinal and/or transverse directions to accommodate the beams or bracings employed for storing industrial goods. These perforations lower the load-carrying capacity of the uprights. Thus, buckling analysis is vital in the investigation and design of cold-formed members. Particularly, this article is focused on the buckling analysis aspects of industrial storage rack uprights, which is the most significant storage structure in industries and thus demands the most reliable and simple design methods. To overwhelm the failure of the racks, the research on the characteristics of industrial storage uprights with incorporating safe design is performed.

The methods for buckling analysis comprise of the Finite Element Method (FEM), the Generalized Beam Theory (GBT) [2] and the Finite Strip Method (FSM) [9]. FEM is the most flexible method adopted for the buckling analysis of complex geometries and variable load and boundary conditions using software such as ANSYS and ABAQUS. Despite that, FSM and GBT are used with the free available software CUFSM and GBTUL, respectively, as a robust tool. The design of the uprights is done using the Direct Strength Method (DSM) [11] once the buckling results are obtained [1].

Analytical-based approach through ANSYS and GBT in accordance with the European design standards for the perforated members are introduced by Davies [5] and inferred that GBT analysis has provided an adequate analytical solution for the complex problem on account of perforations and a safe design approach.

The elastic buckling analysis of cold-formed steel members having general boundary conditions by combining conventional FSM with the constrained finite strip method (cFSM) was proposed by Li and Schafer [7]. FSM solutions together with DSM were adopted in member design through a signature curve for S–S boundary conditions, while the application of DSM for other boundary conditions was not developed completely. However, the global buckling mode for other boundary conditions can be determined using the effective length factor in elastic critical buckling equations.

The determination of elastic buckling loads of rectangular perforated cold-formed storage rack columns with the help of FSM using the concept of reduced thickness expressions was demonstrated by Casafont et al. [3] and the proposed reduced thickness equations can be adopted in practical design even if it is not accurate for local buckling [4].

The determination of the critical elastic buckling loads of five cold-formed steel pallet racks upright sections, with sharp edge cross-sections and pinned-warping free boundary conditions, having web perforations was proposed by Smith and Moen [10] with a focus on the AISI's Direct Strength Method [8].

FSM and GBT are adopted for the buckling analysis of perforated members using the incorporation of reduced thickness expressions [3, 10]. Most of this literature focused on the analysis of idealized perforations oriented at orthogonal angles.

In this article, the buckling analysis of the simple rack section with orthogonal cross-section elements having two idealized transverse web perforations of square and rectangular shape oriented in an angle other than orthogonal angles are done using FE software ABAQUS. The pre-validated FE model for gross sections and idealized perforations [6] are further accounted for in this study. The CUFSM buckling analysis is done using the reduced thickness expression recommended in the literature and compared with the FE results. The aptness of reduced thickness expressions in accounting perforations in the terms of perforation orientation is compared using the analysis results and summarized.

2 Cross-Section Geometry

As a preliminary study, only one cross-section is considered in the initial phase of the investigation. The considered cross-section is finalized based on the elastic critical buckling behaviour of the cross-section in which the minimum elastic critical local and distortional modes are nearly equal. This study further limits the cross-section as sharp cornered. The dimensions of rack section are $80 \times 40 \times 20 \times 15$, in which the numeral values represent the height, flange width, rear flange width and flange stiffener length in mm (Fig. 1). The rack section of this particular dimension is referred to as R. The length of the specimen considered is three times the maximum dimension of the cross-section, i.e., 240 mm. The base metal sheet thicknesses are 1.0 mm, 1.6 mm, and 2.0 mm and the two idealized transverse web perforations of rectangular shape referred to as P, having the size of 10×20 mm, oriented in angles such as 0, 30, 45, 60, and 90 degrees are deemed (Fig. 2). The yield stress considered is 255.91 MPa. The model name R_t()_P() is used for depicting the rack section, thickness, and perforation orientation as in Table 1. The model name for 1.6 mm thickness and web perforation oriented at 30 degree is R_t1.6_P30. Thus, a total of 18 combinations, including gross sections that are unperforated sections (G), are studied.

3 FE Analysis

The software ABAQUS was used to perform the Finite Element (FE) eigenbuckling analyses to predict the perforation pattern effects on elastic local buckling load and mode shapes by the use of shell elements. The centre lines of the upright sections are modelled by means of 3D shell extrusion for the geometric modelling (Fig. 3). The material properties of the upright are considered as isotropic and homogeneous with Young's modulus, $E = 2 \times 10^5$ MPa and Poisson's ratio, $\mu = 0.30$. The elements of the end cross-section are constrained with the centroid of cross-section using Multi-Point Constraint (MPC), which is called a reference point at top and bottom end and the unit load is applied at the top end of the specimen (Fig. 4). Boundary conditions were pinned at the ends with allowing axial deformations.

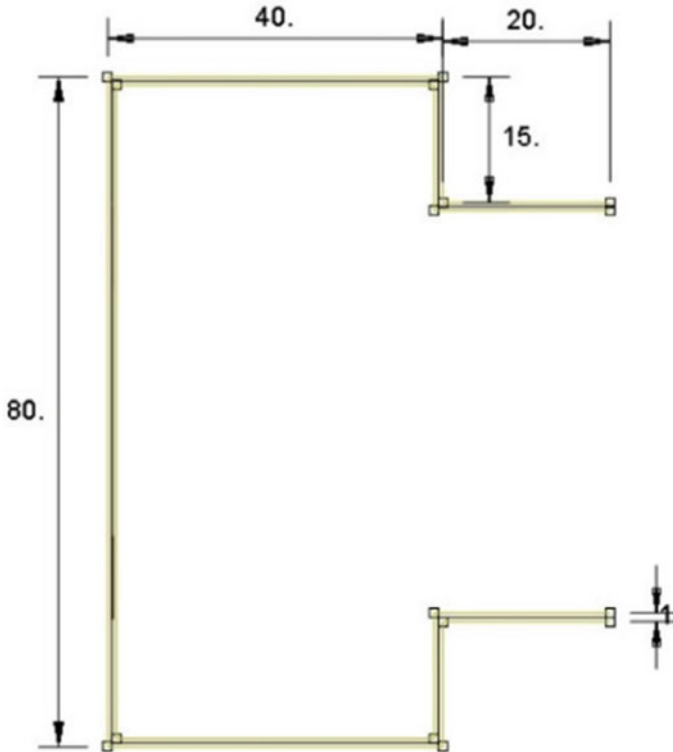


Fig. 1 Cross-section dimensions

As per the detailed convergence study done for gross sections and selected perforated sections, four-node shell elements with reduced integration are considered here to mesh the model with the mesh size equal to the thickness of the base sheet (Fig. 5). In total, the buckling analysis using FE analysis is performed for 3 gross sections and 15 perforated sections. The critical elastic local buckling loads (P_{cr1_FE}) for all the sections considered are obtained with their corresponding mode shapes directly from the Eigen value since the unit load is applied (Fig. 6).

4 FSM Analysis Using Reduced Thickness Equations

4.1 Reduced Thickness Equations

The determination of critical elastic buckling load of the perforated section can be done using both CUFSM and GBTUL software by incorporating the reduced thickness equation. The element with perforations can be divided into perforated

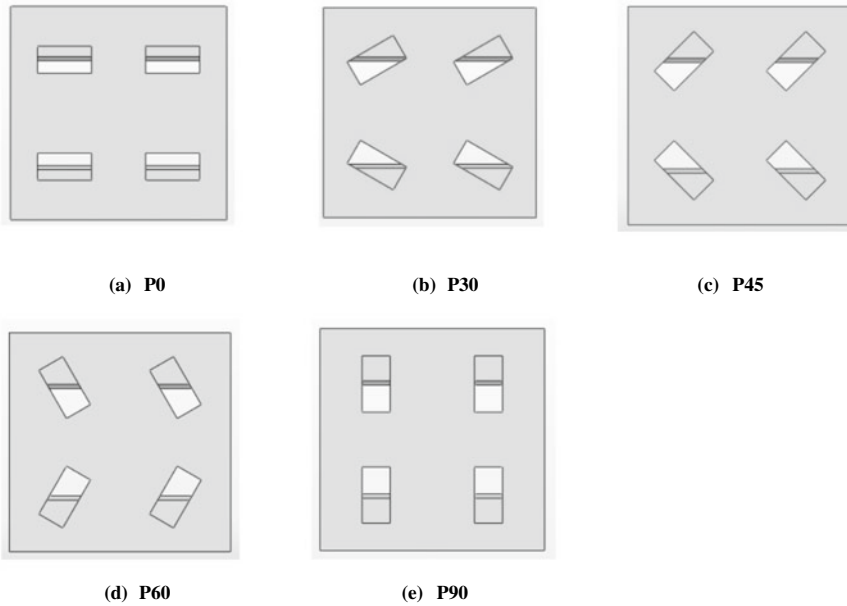


Fig. 2 Perforation orientation is one-third length of the specimen

and unperforated strips, in which the reduced thickness equation is applied for the perforated strip and the actual thickness is applied for all unperforated strips and elements. The reduced thickness expressions accounting for the thickness on the perforated strip are demonstrated in literature [3, 10].

Casafont’s reduced thickness equation for local buckling is

$$t_r = 0.61t \frac{L_{np} B_{np}}{LH} + 0.18t \frac{B_p}{L_p} + 0.11 \tag{1}$$

where

- L pitch length
- L_{np} non-perforated strip length between perforations
- B_{np} width of the non-perforated strip
- B width of the cross-section
- H height of the cross-section
- B_p width of the perforation
- L_p length of the perforation

Smith and Moen’s reduced thickness equation for local buckling is

$$t_r = t \left[1 - \frac{n_l n_t (L_h d_h + \mu d_h \alpha + \mu L_h \beta + \alpha \beta)}{Lb} \right]^{1/2} \tag{2}$$

Table 1 Upright models

S. No.	Model name	Rack section (mm)	Thickness (mm)	Perforation size (mm)	Perforation Orientation (in degrees)
1	R_t1.0_G	80 × 40 × 20 × 15	1.0	–	–
2	R_t1.0_P0	80 × 40 × 20 × 15	1.0	10 × 20	0
3	R_t1.0_P30	80 × 40 × 20 × 15	1.0	10 × 20	30
4	R_t1.0_P45	80 × 40 × 20 × 15	1.0	10 × 20	45
5	R_t1.0_P60	80 × 40 × 20 × 15	1.0	10 × 20	60
6	R_t1.0_P90	80 × 40 × 20 × 15	1.0	10 × 20	90
7	R_t1.6_G	80 × 40 × 20 × 15	1.6	–	–
8	R_t1.6_P0	80 × 40 × 20 × 15	1.6	10 × 20	0
9	R_t1.6_P30	80 × 40 × 20 × 15	1.6	10 × 20	30
10	R_t1.6_P45	80 × 40 × 20 × 15	1.6	10 × 20	45
11	R_t1.6_P60	80 × 40 × 20 × 15	1.6	10 × 20	60
12	R_t1.6_P90	80 × 40 × 20 × 15	1.6	10 × 20	90
13	R_t2.0_G	80 × 40 × 20 × 15	2.0	–	–
14	R_t2.0_P0	80 × 40 × 20 × 15	2.0	10 × 20	0
15	R_t2.0_P30	80 × 40 × 20 × 15	2.0	10 × 20	30
16	R_t2.0_P45	80 × 40 × 20 × 15	2.0	10 × 20	45
17	R_t2.0_P60	80 × 40 × 20 × 15	2.0	10 × 20	60
18	R_t2.0_P90	80 × 40 × 20 × 15	2.0	10 × 20	90

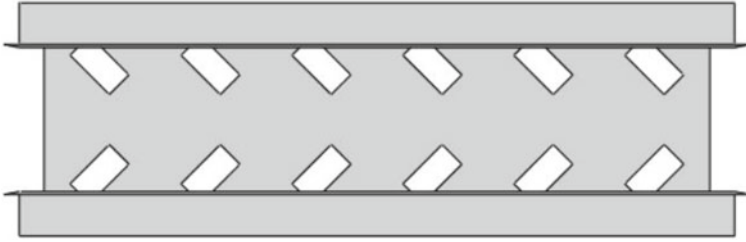


Fig. 3 Geometric modelling

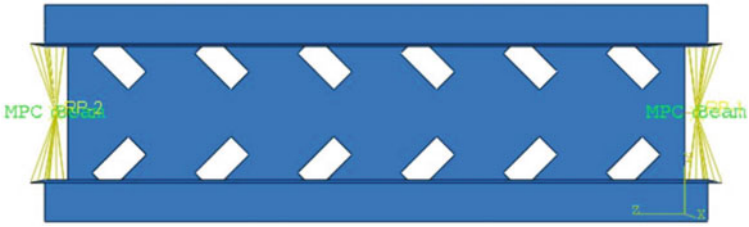


Fig. 4 MPC

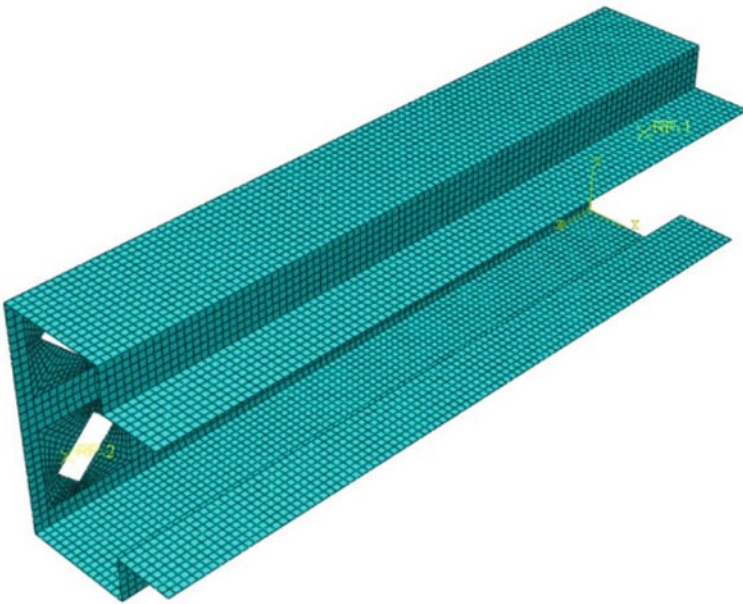


Fig. 5 Shell elements

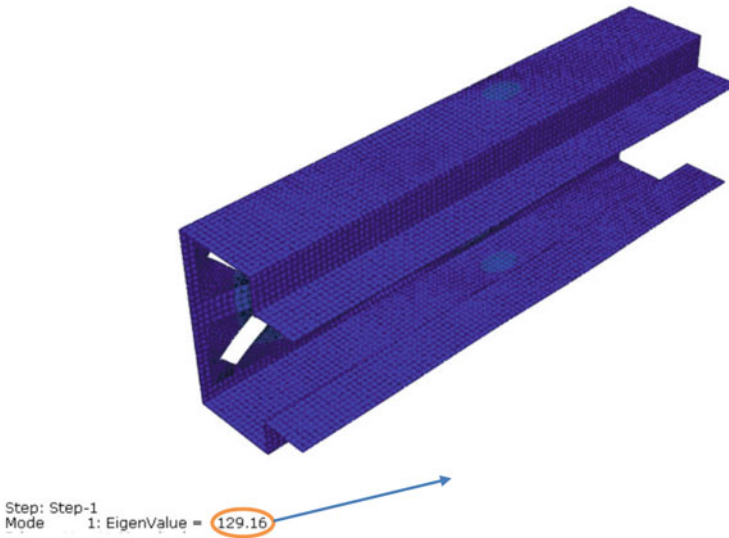


Fig. 6 Buckling load from FE analysis

$$\alpha = \frac{L}{\pi m} \sin\left(\frac{\pi L_h m}{L}\right) \tag{3}$$

$$\beta = \frac{b}{\pi n} \sin\left(\frac{\pi d_h n}{b}\right) \tag{4}$$

where

- t thickness of the base metal
- L length of the member
- B width of stiffened element
- n_l number of rows of fasteners spaced longitudinally
- n_t number of rows of fasteners spaced transversely
- L_h length of perforation
- d_h width of perforation
- μ Poisson's ratio of material
- α perforation dimension modification factor for the longitudinal direction
- β perforation dimension modification factor for the transverse direction
- m number of longitudinal half-wavelengths
- n number of transverse half-wavelengths

α and β are the modification factors which are determined from Eqs (3) and (4), by inputting $m = L/b$ and $n = 1$.

Using these reduced thickness equations, the elastic critical local buckling load can be determined using CUFSM or GBTUL.

4.2 Finite Strip Analysis

As both [3, 10] literatures are referred for the tr equations, the concerning remarks made by them should be noted. Casafont mentioned that the stress should not be applied at the perforated strip, which is not possible in GBTUL because the user has no freedom to apply the load as stress, rather it is applied as a point load at the centroid. For that reason, CUFSM analysis is chosen for the buckling analysis.

Once the reduced thickness expressions are calculated for all 15 sections, finite strip analysis was done using CUFSM to get the elastic critical local buckling stress from the signature curve. Thus, the elastic critical local buckling load (P_{cr1_trS} as the elastic critical local buckling load from Smith's tr equation and P_{cr1_trC} as the elastic critical local buckling load from Casafont's tr equation) can be obtained from the first minimum of signature curve.

5 Results and Discussion

The FE results of perforated stub columns are compared with the finite strip analysis results using reduced thickness equations proposed by Smith and Moen [10] and Casafont et al. [3] in Table 2. It should be noted that the boundary condition considered in the FE analysis is flexurally simply supported but twisting and warping are restrained. In other words, simply supported condition restraint to warping deformation is considered in FE analysis. This is to mimic the experimental behaviour to validate the FE model. By the way, in most practical cases, the warping deformations are restrained. The results from Casafont's reduced thickness equation are deviating from the FE results, however, the values are lower than FE results and hence conservative. The Moen's reduced thickness equation is relatively better than Casafont's method for local buckling. The Smith's method is best suitable for the idealized perforations, whereas it is unduly conservative for other perforation orientations which are handled as idealized perforations. The deviation of results is more pronounced for larger thickness sections with perforations oriented in angles other than 0 and 90°. Therefore, further investigation is required to improve the reduced thickness equation by including the perforation orientation in the finite strip analysis. For the slender plate elements, that is for lower thickness the perforation resulting in minimum net section (P90 orientation) exhibits a higher buckling load than other orientations in FE analysis. Although the same trend is followed in Casafont method, the Smith method leads to a different conclusion as the highest ultimate load for P0 orientation having maximum net section area. For other orientations, the buckling load is relatively in between P0 and P90 orientations and this effect is more pronounced in lower slender web elements, that is for higher thickness. As shown in Table 2, the perforation orientation significantly affects the buckling load and both analytical methods are inconsistent. Therefore, more refined research is required in terms of element slenderness as well as the perforation orientations.

Table 2 Analysis results

S. No.	Model name	P_y (kN)	$P_{\text{ent_FE}}$ (kN)	$P_{\text{ent_FE}}/P_y$	$P_{\text{ent_F,S}}$ (kN)	$P_{\text{ent_F,S}}/P_y$	$P_{\text{ent_F,C}}$ (kN)	$P_{\text{ent_F,C}}/P_y$
1	R_t1.0_G	58.35	38.85	0.67	36.36	0.62	36.36	0.62
2	R_t1.0_P0	58.35	31.84	0.55	34.19	0.59	31.54	0.54
3	R_t1.0_P30	58.35	31.59	0.54	27.09	0.46	23.11	0.40
4	R_t1.0_P45	58.35	31.80	0.55	24.53	0.42	22.80	0.39
5	R_t1.0_P60	58.35	32.19	0.55	25.08	0.43	25.72	0.44
6	R_t1.0_P90	58.35	32.86	0.56	31.91	0.55	39.27	0.67
7	R_t1.6_G	92.86	159.14	1.71	149.94	1.61	149.94	1.61
8	R_t1.6_P0	92.86	129.33	1.39	140.86	1.52	124.88	1.34
9	R_t1.6_P30	92.86	128.34	1.38	110.99	1.20	84.90	0.91
10	R_t1.6_P45	92.86	129.16	1.39	100.16	1.08	82.98	0.89
11	R_t1.6_P60	92.86	130.83	1.41	102.58	1.10	93.24	1.00
12	R_t1.6_P90	92.86	133.76	1.44	131.34	1.41	151.90	1.64
13	R_t2.0_G	115.67	310.16	2.68	293.93	2.44	281.92	2.44
14	R_t2.0_P0	115.67	251.01	2.17	275.89	2.39	237.06	2.05
15	R_t2.0_P30	115.67	248.89	2.15	216.65	1.87	156.49	1.35
16	R_t2.0_P45	115.67	250.51	2.17	195.11	1.69	153.45	1.33
17	R_t2.0_P60	115.67	253.86	2.19	199.98	1.73	174.32	1.51
18	R_t2.0_P90	115.67	259.79	2.25	257.11	2.22	230.02	1.99

6 Conclusions

In this study, the impact of perforation orientation in the elastic critical local buckling behaviour of storage rack upright is focused. Numerical analysis results were generated using FE analysis. The minimum elastic critical buckling load was determined using Smith's reduced thickness approach and Casafont's reduced thickness approach for local buckling. Comparing the results, the perforation orientation significantly influences the elastic critical local buckling load compared to FE results. Although most of the results fall on the conservative side, few results are showing unconservative behaviour for the same perforations but oriented in angles. This nature is significant for the larger thickness sections. Therefore, the reduced thickness equations currently available in the literature for local buckling can be further improved by including the element slenderness and perforation orientation as one of the key parameters to determine the reduced thickness for perforated strip in the cross-section. Detailed research in this domain is under process.

Acknowledgements The authors highly acknowledge and appreciate Prof. S Arul Jayachandran's (IIT Madras) help in various stages of this current research, in particular the numerical analysis.

References

1. American Iron And Steel Institute (2016) AISI S100: North American specification for the design of cold-formed steel structural members. p 505
2. Bebiano R, Silvestre N, Camotim D (2008). GBTUL—a code for the buckling analysis of cold-formed steel members. In: 19th International specialty conference on recent research and developments in cold-formed steel design and construction, pp 61–79
3. Casafont M, Pastor M, Bonada J, Roure F, Peköz T (2012) Linear buckling analysis of perforated steel storage rack columns with the finite strip method. *Thin-Walled Struct* 61:71–85. <https://doi.org/10.1016/j.tws.2012.07.010>
4. Casafont M, Pastor MM, Roure F, Bonada J, Peköz T (2013) Design of steel storage rack columns via the direct strength method. *J Struct Eng (United States)* 139(5):669–679. [https://doi.org/10.1061/\(ASCE\)ST.1943-541X.0000620](https://doi.org/10.1061/(ASCE)ST.1943-541X.0000620)
5. Davies JM, Leach P, Taylor A (1997) The design of perforated cold-formed steel sections subject to axial load and bending. *Thin-Walled Struct* 29(1–4):141–157. [https://doi.org/10.1016/s0263-8231\(97\)00024-4](https://doi.org/10.1016/s0263-8231(97)00024-4)
6. Harisanth KS (2019) Buckling behaviour of cold-formed steel storage racks. MTech Thesis, Indian institute of technology madras
7. Li Z, Schafer BW (2010) Buckling analysis of cold-formed steel members with general boundary conditions using CUFSM: conventional and constrained finite strip methods. In: 20th International specialty conference on cold-formed steel structures—recent research and developments in cold-formed steel design and construction, pp 17–31
8. Moen CD, Schafer BW (2011) Direct strength method for design of cold-formed steel columns with holes. *J Struct Eng* 137(5):559–570. [https://doi.org/10.1061/\(ASCE\)ST.1943-541X.0000310](https://doi.org/10.1061/(ASCE)ST.1943-541X.0000310)
9. Schafer B, Adany S (2006) Buckling analysis of cold-formed steel members using CUFSM. In: 18th International specialty conference on cold-formed steel structures

10. Smith FH, Moen CD (2014) Finite strip elastic buckling solutions for thin-walled metal columns with perforation patterns. *Thin-Walled Struct* 79:187–201. <https://doi.org/10.1016/j.tws.2014.02.009>
11. Yu W, Laboube RA, Wiley J (2010) *Cold-Formed steel design*

Modelling Interfacial Behaviour of Cement Stabilized Rammed Earth Using Cohesive Contact Approach



T. Pavan Kumar Reddy and G. S. Pavan

Abstract A monolithic construction formed by compacting processed soil in progressive layers in a formwork is called a rammed earth wall. A lot of applications of using rammed earth walls for both load bearing and non-load bearing can be seen across the world and carbon content is low in this building material. The construction of rammed earth structures involves layered compaction, thus forming an interface between two layers. Modelling of interface plays an important role in the strength and durability of these structures. The interface is modelled using a cohesive contact approach and the response of the rammed earth triplet is obtained. The slope of load vs displacement curve of the rammed earth triplet is 81% accurate with the experimental slope and the peak load of the triplet is 82% accurate with the experimental peak load. Thus, the comparison of load versus displacement obtained from the finite element method with experimental data of load versus displacement yields almost similar results.

Keywords Rammed earth · Interface · Cohesive contact · Triplet

1 Introduction

A monolithic construction formed by compacting processed soil in progressive layers in a formwork is called a rammed earth wall. A lot of applications of using rammed earth walls for both load bearing and non-load bearing can be seen across the world. Rammed earth constructions can be classified into two categories: stabilized rammed earth and unstabilized rammed earth. A mixture of soil, sand and gravel can be defined as unstabilized rammed earth. There are no additional stabilizers that are

T. Pavan Kumar Reddy
NITK Surathkal, Mangaluru, India

G. S. Pavan (✉)
Department of Civil Engineering, NITK Surathkal, Mangaluru, India
e-mail: pavan.gs@nitk.edu.in

added to this. In addition to the materials used in unstabilized rammed earth, stabilizers (cement, lime, etc.) are added for rammed earth to improve the strength and durability of the structure and this is called stabilized rammed earth. An interface is defined as a common layer or a surface that is present between two bodies. The construction of rammed earth structures involves layered compaction, thus forming an interface between two layers. This interface plays an important role in the stability and durability of these structures. During earthquakes, there will be in-plane shear forces which makes the behaviour of the interface important. Also, when there is an uneven settlement of foundations, in-plane shear forces play a major role in the behaviour of the interface. Hence, it is important to model the interface such that it resists the loads due to structural loads or an earthquake, etc. making it more durable. This presentation shows how an interface of a rammed earth triplet is modelled using a cohesive contact approach. The main objectives of our present study are to model the interface of the rammed earth triplet using the cohesive contact approach present in commercial approaches, to obtain the values of applied loads and corresponding displacements till the failure of the rammed earth triplet and to plot load vs displacement curve and compare with the curve obtained from experimental values. Reddy and Kumar [1] conducted an experimental study on the physical properties and compaction characteristics of compacted cement stabilized rammed earth (CSRE) and cement stabilized soil mixtures. Standard Proctor test is conducted to determine the values of OMC and MDD of the samples tested. Results show that the addition of ordinary Portland cement (OPC) does not show any effect on OMC and MDD values of soil. Also, as the clay fraction of the cement mixed soil increases, MDD decreases and OMC increases. As the time lag increases, OMC increases and MDD decreases irrespective of soil type and cement content. Reddy and Kumar [2] explained the elastic properties of CSRE and stress–strain relationships considering the effects of density and moisture. Compressive strength tests both wet and dry are conducted on the rammed earth specimens. Results show that the optimum clay fraction required is about 16% for yielding maximum compressive strength for CSRE. Strength is directly proportional to the density, i.e., there is an increase in strength as the density increases and the relationships are linear. There is a significant increase in the strength as the density is changed from 1600 to 2000 kg/m³. An increase in 20% of density resulted in increasing the strength by 300–500%. Lepakshi and Reddy [3] explained that the objective of this paper is to establish shear strength parameters and Mohr–Coulomb failure envelopes for CSRE. Tri-axial shear tests are conducted to determine the shear strength parameters. The results show that the shear strength of the specimen in wet condition is almost half of the shear strength of the specimen in dry condition. Irrespective of the confining pressure and the testing condition, the shear strength and cohesion of CSRE were greatly influenced by cement content. The tri-axial compressive strength and the shear strength increase as the confining pressure increases. Pavan et al. [4] explained enhancing the interface shear strength of CSRE and the overall shear behaviour of CSRE by bonding techniques. Three bonding techniques: (i) using dents, (ii) applying a coating of cement slurry and (iii) a combination of dents and cement slurry are formed in between the interfaces of rammed earth specimens and are tested under loading. A 90% increase in shear bond

strength of CSRE specimens with bonding techniques is observed when compared to triplets without any bonding technique, under dry condition. Also, CSRE specimens with cement slurry as a bonding technique exhibits higher strength when compared to CSRE specimens with bonding techniques of dents or a combination of both dents and cement slurry. Some of the other studies focused on rammed earth have been conducted by Lepakshi and Reddy [5], Shrestha et al. [6], El-Nabouch et al. [7] and Hiroyuki et al. [8] (Figs. 1 and 2).

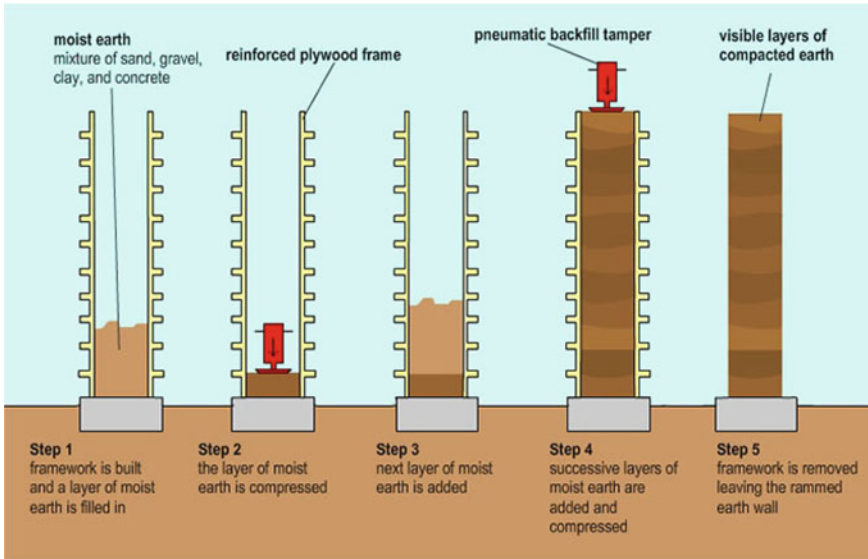


Fig. 1 Steps involved in rammed earth construction [2]

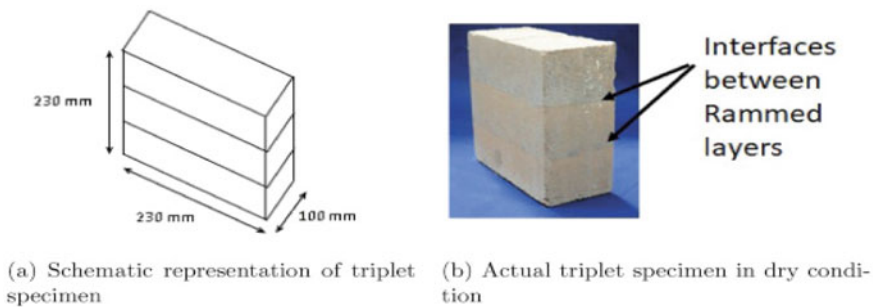


Fig. 2 Rammed earth triplet showing the interface [3]

2 Methodology

Modelling is done by using Abaqus 6.14, Finite Element Method (FEM) based software. This section shows step by step procedure showing the modelling of the rammed earth triplet adopted in the software package. In the parts section, three rammed earth blocks of dimensions 230 mm × 230 mm × 100 mm are developed. In the materials section, the blocks are defined with material properties and are named as elastic. The density of the material is defined as $\rho = 1800 \text{ kg/m}^3$. Young's modulus and Poisson's ratio of the rammed earth block are also defined.

$$E = 1500 \text{ MPa} \quad (1)$$

$$\mu = 0.15 \quad (2)$$

A solid homogenous section with elastic material property is created and assigned to the three blocks. In the assembly section, an instance is created by selecting the 3 parts and the interaction properties of the interior surfaces are defined. The interaction property of the surfaces in contact is defined as **cohesive behaviour**. The values of the stiffness coefficients for the above-defined interaction property are

$$K_{nn} = 1.9565 * 10^{10} \text{ N/m} \quad (3)$$

$$K_{tt} = 6,521,739,130 \text{ N/m} \quad (4)$$

$$K_{ss} = 6,521,739,130 \text{ N/m} \quad (5)$$

The max nominal stress of damage initiation criteria in normal mode is 7 MPa and in shear 1 and shear 2 is 0.4 MPa. In damage evolution, the maximum displacement at failure is 0.35 mm. To apply load on the member, we need to create a step named apply load which comes next to the initial step. The load is applied on the middle member of the assembly as a pressure force which is gradually increased and corresponding values of stresses and displacements are noted. The values of load taken are 20 N, 200 N, 2 kN, 3 kN, 4 kN, and so on up to 20 kN. The boundary conditions are applied at the bottom of the exterior members and it is a fixed boundary condition (ENCASTRE $U1 = U2 = U3 = UR1 = UR2 = UR3 = 0$). Meshing the member is an important step in modelling and analysis of the member. The approximate global size of the seed is taken as 0.0115 mm. The elements of the mesh are defined as an 8-node linear brick element (C3D8R). By selecting the mesh part instance, the members are meshed with a seed size of 0.0115 mm and an element type of C3D8R. A job is created by giving a name to the file and model as the source. The job created is submitted and the results are observed from the visualization section.

3 Results and Discussion

The rammed earth triplet is loaded and for each load, corresponding stresses and displacements are calculated. At a peak load of 16.25 kN, the contour plot of shear stresses (τ_{xy}) is shown in Fig. 3. It can be observed that the shear stresses are symmetric about both the interfaces. The values of the shear stress also attain peak value at the interface and gradually reduce as we move away from the interface towards the ends.

Further, Fig. 4 shows the vertical displacement contour plot of the triplet corresponding to a load of 16.5 kN. We can observe the sliding behaviour of the middle layer of the triplet relative to the outer layers of the rammed earth triplet. The middle layer was displaced to a vertical displacement of about 0.26 mm. The results obtained from the numerical simulation compare well with the results obtained from experiments conducted in the study by Pavan et al. [4].

Upon reaching a load of 16.5 kN, the simulation failed to converge and was unable to simulate the post-peak deformation behaviour of the triplet.

A graph is plotted between the numerical values of loads and displacements obtained from the numerical model and experimental values of loads and displacements and is shown in Fig. 5.

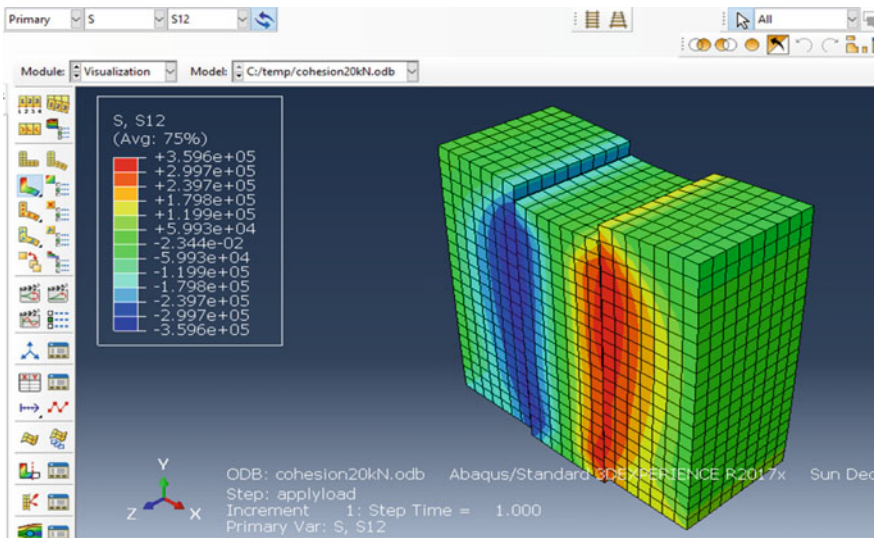


Fig. 3 Stress contour plot of rammed earth triplet

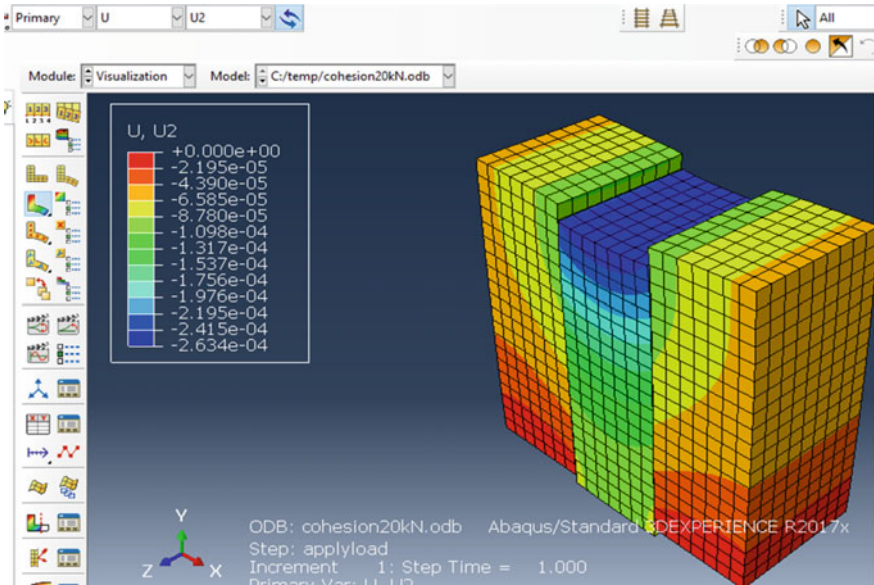


Fig. 4 Displacement contour plot of rammed earth triplet

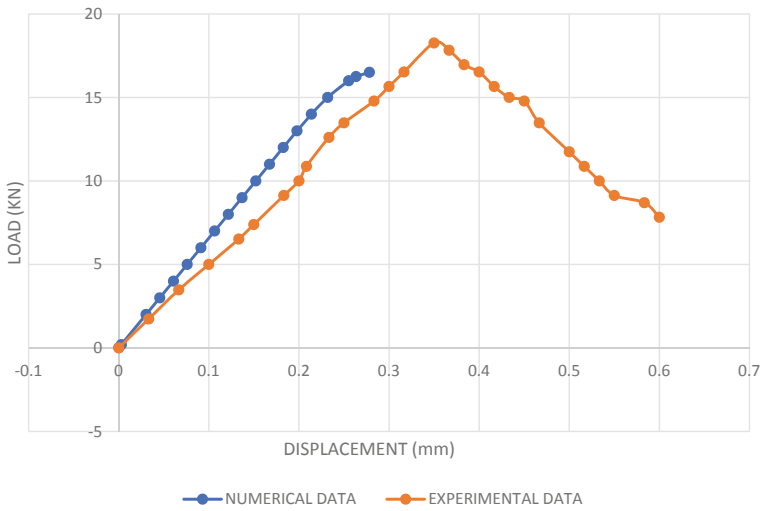


Fig. 5 graph of numerical and experimental data [4]

4 Conclusion

From the numerical modelling done above, we can conclude that the simulation was successful in producing the sliding action between successive layers of rammed earth triplet when it is subjected to in-plane shear loading. The slope of the load–displacement diagram as per the numerical simulation was found to be equal to 59.6 kN/mm and was found to be 81% accurate in comparison to experimental values. The peak load as captured by numerical simulation was found to be 16.5 kN and is 82% accurate in comparison to the peak load witnessed during experiments available in the literature. The elastic response of the triplet, along with a part of the inelastic response of the rammed earth triplet under in-plane shear loading was captured by the numerical model in this study. Further studies can adopt advanced contact modelling strategies to capture the entire inelastic response of the rammed earth triplet under in-plane shear loading.

References

1. Venkatarama Reddy BV, Prasanna Kumar P (2010) Cement stabilised rammed earth. Part A: compaction characteristics and physical properties of compacted cement stabilised soils. *Mater Struct (RILEM)*. <https://doi.org/10.1617/s11527-010-9658-9>
2. Venkatarama Reddy BV, Prasanna Kumar P (2010) Cement stabilised rammed earth. Part B: compressive strength and stress–strain characteristics. *Mater Struct (RILEM)*. <https://doi.org/10.1617/s11527-010-9659-8>
3. Lepakshi R, Venkatarama Reddy BV (2020) Shear strength parameters and Mohr-Coulomb failure envelopes for cement stabilised rammed earth. *Constr Build Mater* 249:118708
4. Pavan GS, Ullas SN, Nanjunda Rao KS (2020) Shear behavior of cement stabilized rammed earth assemblages. *J Build Eng* 27(2020):100966
5. Lepakshi Raju BV, Reddy V (2018) Influence of layer thickness and plasticizers on the characteristics of cement-stabilized rammed earth. *Am Soc Civil Eng*. [https://doi.org/10.1061/\(ASCE\)MT.1943-5533.0002539](https://doi.org/10.1061/(ASCE)MT.1943-5533.0002539)
6. Shrestha KC, Aoki T, Miyamoto M, Wangmo P (2020) In-Plane shear resistance between the rammed earth blocks with simple interventions: experimentation and finite element study. *Buildings* 10(3):57
7. El-Nabouch R, Bui QB, Perrotin P, Plé O (2018) Shear parameters of rammed earth material: results from different approaches. *Adv Mater Sci Eng* 2018. <https://doi.org/10.1155/2018/8214604>
8. Arakia H, Kosekia J, Satob T (2015) Tensile strength of compacted rammed earth materials. *Jpn Geotech Soc* 56:189–204

Four Node Flat Shell Quadrilateral Finite Element for Analysis of Composite Cylindrical Shells



V. A. Dagade and S. D. Kulkarni

Abstract This work presents the free vibration and static analysis of laminated composite cylindrical shells with a 2D computationally efficient facet-shell finite element that is formed by combining the plate bending and membrane element. The element is based on zigzag theory and is augmented using the discrete Kirchhoff quadrilateral element developed earlier by the second author for the analysis of composite and sandwich plates. It is vital to convert the actions and displacements from local to global direction using a transformation matrix. DKZigTS is developed by adding two fictitious degrees of freedom and has nine local and global degrees of freedom per node. It does not face the problem of the ill-conditioned stiffness matrix. The performance of the developed element is assessed for its exactitude by comparing the results obtained with analytical 2D, 3D and finite element solutions available in the literature. Various boundary conditions, geometrical shapes and material properties are used in this study. The element exhibits a very satisfactory performance for moderately thick and thick shell panels.

Keywords Finite element · Cylindrical shell · Composite · Free vibration · Static

1 Introduction

Composite laminated shell characteristics can be modified, by tailoring the orientation of fiber and stacking sequence of the layer, which results in the use of laminated shells in high-performance and weight-sensitive engineering applications. It is showing good performance in the medical field applications such as bone fixation plates, bone grafts and hip joint replacement by virtue of its dimensional stability, high specific strength, thermal stability and tribological properties. Shell is a much stronger structural form than others have; hence understanding the static and dynamic response of shell structure with composite material is essential. Deflections, stresses,

V. A. Dagade (✉) · S. D. Kulkarni
College of Engineering Pune, Pune, Maharashtra 411005, India
e-mail: dagadeva14.civil@coep.ac.in

© The Author(s), under exclusive license to Springer Nature Singapore Pte Ltd. 2023
M. S. Ranadive et al. (eds.), *Recent Trends in Construction Technology and Management*, Lecture Notes in Civil Engineering 260,
https://doi.org/10.1007/978-981-19-2145-2_84

1135

natural frequencies and their associated mode shapes are studied in this work for the symmetric and anti-symmetric composite cylindrical shell.

2 Displacement Field Approximation

Consider composite material cylindrical shell of thickness h and radius R_x at mid-plane as shown in Fig. 1. The mid-plane of the shell is chosen as the reference plane $z = \text{zero}$. The top surface is at $z = \frac{h}{2}$, and bottom surface is at $z = -\frac{h}{2}$.

“The zigzag theory being 2D layer-wise theory has approximations, which are listed here:

1. Vertical Deflection ‘ w ’ is Independent of ‘ z ’.

$$w(x, y, z, t) = w_0(x, y, t). \tag{1}$$

2. The in-plane displacements ‘ u_x ’ and ‘ u_y ’ are a combination of global third-order variation in ‘ z ’ across the thickness and layer-wise piecewise linear variation, i.e. with discontinuity in slopes $u_{x,z}, u_{y,z}$ at the layer interfaces. Accordingly, u_x, u_y for the k th layer can be expressed as

$$u(x, y, z, t) = u_0(x, y, t) - zw_{0d}(x, y, t) + R^k(z)\psi_0(x, y, t)$$

$$u = \begin{bmatrix} u_x \\ u_y \end{bmatrix}, w_{0d} = \begin{bmatrix} w_{0,x} \\ w_{0,y} \end{bmatrix}, u_o = \begin{bmatrix} u_{ox} \\ u_{oy} \end{bmatrix}, \psi_o = \begin{bmatrix} \psi_{ox} \\ \psi_{oy} \end{bmatrix} \tag{2}$$

$R^k(z)$ is a 2×2 matrix of layer-wise functions of z of the form

$$R^k(z) = \hat{R}_1^k + z\hat{R}_2^k + z^2\hat{R}_3 + z^3\hat{R}_4 \tag{3}$$

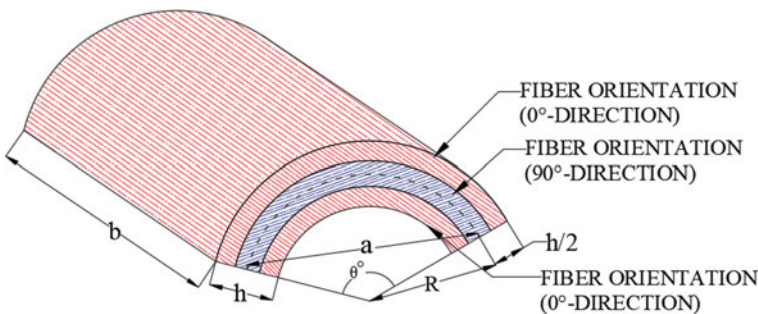


Fig. 1 Geometry of composite (0°/90°/0° stacking sequence configured) cylindrical shell

where $\widehat{R}_1^k, \widehat{R}_2^k, \widehat{R}_3$ and \widehat{R}_4 coefficient matrices depend on the material properties and lay-ups. Expressions for these matrices are given in the Kapuria and Kulkarni.” [1].

2.1 Finite Element Formulation

Figure 2 shows the four-node quadrilateral element. x, y, z are the global and x', y', z' are the local axes.

The plate element initially developed by Kapuria and Kulkarni [1] has seven local DOF per node but to transform it globally, two additional fictitious degrees of freedom need to be added per node as mentioned in Zienkiewicz et al. [2]. After the considerations of these two additional fictitious DOF, namely, $\theta'_{oz}{}^i$ and $\psi'_{oz}{}^i, U_i^{e'}$ and U_i^e which are the local and the global nodal displacement vectors for the i th node are given in the following expressions.

$$U^{e'} = \left[u_{0x}^i \ u_{0y}^i \ w_0^i \ \theta_{0x}^i \ \theta_{0y}^i \ \theta_{0z}^i \ \psi_{0x}^i \ \psi_{0y}^i \ \psi_{0z}^i \right]^T$$

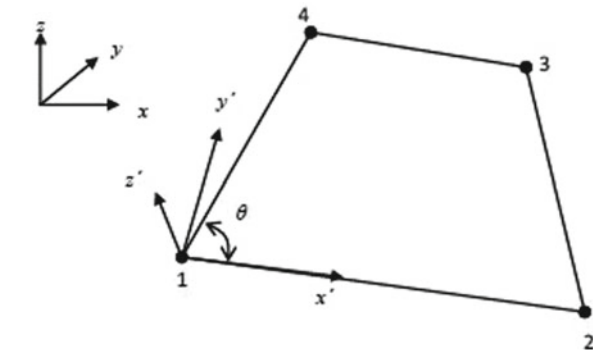
$$U^e = \left[u_{0x}^i \ u_{0y}^i \ w_0^i \ \theta_{0x}^i \ \theta_{0y}^i \ \theta_{0z}^i \ \psi_{0x}^i \ \psi_{0y}^i \ \psi_{0z}^i \right]^T. \tag{4}$$

It is crucial to transform actions and displacements from local to global directions, to use plate elements for analysing cylindrical shells. The transformation is achieved using the following expression.

$$U_i^{e'} = T_i^e U_i^e; \quad i = 1, 2, 3, 4$$

T_i^e = the transformation matrix for i th node given as

Fig. 2 Geometry of the element



$$T_i = \begin{bmatrix} \lambda_{11} & \lambda_{12} & \lambda_{13} & 0 & 0 & 0 & 0 & 0 & 0 \\ \lambda_{21} & \lambda_{22} & \lambda_{23} & 0 & 0 & 0 & 0 & 0 & 0 \\ \lambda_{31} & \lambda_{32} & \lambda_{33} & 0 & 0 & 0 & 0 & 0 & 0 \\ 0 & 0 & 0 & \lambda_{22} & \lambda_{21} & \lambda_{23} & 0 & 0 & 0 \\ 0 & 0 & 0 & \lambda_{12} & \lambda_{11} & \lambda_{13} & 0 & 0 & 0 \\ 0 & 0 & 0 & \lambda_{32} & \lambda_{31} & \lambda_{33} & 0 & 0 & 0 \\ 0 & 0 & 0 & 0 & 0 & 0 & \lambda_{22} & \lambda_{21} & \lambda_{23} \\ 0 & 0 & 0 & 0 & 0 & 0 & \lambda_{12} & \lambda_{11} & \lambda_{13} \\ 0 & 0 & 0 & 0 & 0 & 0 & \lambda_{32} & \lambda_{31} & \lambda_{33} \end{bmatrix} \tag{5}$$

where $\lambda_{11}, \lambda_{12}$, etc. are the direction cosines of the local axes with respect to the global axes.

Stiffness matrix becomes singular, due to zero stiffness corresponding to θ_{0z}^i and ψ_{0z}^i . This problem of singularity is overcome by placing a small stiffness coefficient corresponding to the degrees of freedom $\theta'_{0z}{}^i$ and $\psi'_{0z}{}^i$ equal to an arbitrary number in the local stiffness matrix of size 36×36 , where the arbitrary number can be taken equal to the minimum value of stiffness coefficient in the diagonal of local stiffness matrix $\times 10^{-2}$. The same treatment is given to the mass matrix.

The global element mass matrix M^e of size 36×36 , global element stiffness matrix K^e of size 36×36 , and global element load vector P^e of size 36×1 are given in Eq. (6).

$$M^e = T^{eT} M^{e'} T^e, \quad K^e = T^{eT} K^{e'} T^e, \quad P^e = T^{eT} P^{e'} \tag{6}$$

where

T transformation matrix of size 36×36 ,

$M^{e'}$ element local mass matrix of size 36×36 ,

$K^{e'}$ element local stiffness matrix of size 36×36 ,

$P^{e'}$ element local load vector of size 36×1

$$T^e = \begin{bmatrix} T_1 & 0 & 0 & 0 \\ 0 & T_2 & 0 & 0 \\ 0 & 0 & T_3 & 0 \\ 0 & 0 & 0 & T_4 \end{bmatrix}. \tag{7}$$

Summing up the contributions of all elements, we get

$$\bar{M}\ddot{U} + \bar{K}U = \bar{P} \tag{8}$$

where \bar{K} , \bar{M} and \bar{P} are the assembled counterparts of matrices K^e , M^e and P^e , respectively. For free vibration, analysis right-hand side is set to zero and natural frequencies are obtained using subspace iteration technique. For static analysis, \bar{M} is set to null matrix.

3 Numerical Results

The formulation of the four node flat shell element (DKZigTS) and the computer program developed are assessed by comparing the results of non-dimensionalised frequencies, deflection and stresses. The composite cylindrical shells of different configurations are modeled with $M \times N$ mesh of equal size elements in all the problems considered in this study. In the static analysis, shells are subjected to the transverse load acting on the top surface of the shell.

Uniformly distributed load of intensity q_0 and Sinusoidal load $q(x, y) = q_0 \sin(\frac{x\pi}{a}) \sin(\frac{y\pi}{b})$ are considered in this study.

The results are non-dimensionalised as follows:

- Natural frequencies

$$\bar{\omega} = \omega \times \frac{a^2}{h} \times \sqrt{\frac{\rho}{E_2}}; \tag{9}$$

- In-plane displacement and vertical deflection:

$$\begin{aligned} \bar{u}_x(0, \frac{b}{2}, \frac{z}{h}) &= u_x \times E_2 \times \frac{h^2}{a^3 \times q_0}; \\ \bar{w}(\frac{a}{2}, \frac{b}{2}, \frac{z}{h}) &= 100 \times w \times E_2 \times \frac{h^3}{a^4 \times q_0}; \end{aligned} \tag{10}$$

- In-plane stresses:

$$\bar{\sigma}_x, \bar{\sigma}_y(\frac{a}{2}, \frac{b}{2}, \frac{z}{h}) = \sigma_x, \sigma_y \times \frac{h^2}{a^2 \times q_0};$$

- Transverse stresses:

$$\begin{aligned} \bar{\tau}_{xy}(0, 0, \frac{z}{h}) &= \tau_{xy} \times \frac{h^2}{a^2 \times q_0}; \quad \bar{\tau}_{yz}(\frac{a}{2}, 0, \frac{z}{h}) \\ &= \tau_{yz} \times \frac{h}{a \times q_0}; \quad \bar{\tau}_{zx}(0, \frac{b}{2}, \frac{z}{h}) = \tau_{zx} \times \frac{h}{a \times q_0}; \end{aligned} \tag{11}$$

The material properties used for analysis is:

$$E_1 = 172.5 \text{ GPa}, E_2 = E_3 = 6.9 \text{ GPa};$$

$$G_{12} = G_{31} = 3.45 \text{ GPa}, G_{23} = 1.38 \text{ GPa};$$

$$\mu_{12} = \mu_{13} = \mu_{23} = 0.25, \rho = 1580 \text{ kg/m}^3.$$

3.1 Free Vibration Response

3.1.1 Symmetric Cross-Ply Composite Shell

In Table 1, the natural frequencies for the first seven modes obtained using the developed elements with the mesh sizes 12×12 , 16×16 and 24×24 are presented. The results are compared for all-round simply supported ($0^\circ/90^\circ/0^\circ$) configured, shallow shell panels of square planform with the results of 2 D higher-order shear deformation theories given by various researchers and 3D FE results of [3] for the various radius to span ratios ranging from ‘R/a’ = 5 to ‘R/a’ = 20. The ‘h/a’ ratio considered is 0.1. 3D FE results of (ANSYS 2019) are using mesh size of ($24 \times 24 \times 6$).

It is observed for the moderately thick shells, that the results of present elements are quite close to the 3D finite element results obtained with 20 node brick elements

Table 1 Non-dimensionalised seven consecutive frequencies for (SSSS) composite cylindrical shell panels ($0^\circ/90^\circ/0^\circ$) with varying ‘R/a’ ratios

R/a	Theory	$\bar{\omega}_1$	$\bar{\omega}_2$	$\bar{\omega}_3$	$\bar{\omega}_4$	$\bar{\omega}_5$	$\bar{\omega}_6$	$\bar{\omega}_7$
	3D FE [3]	11.545	18.242	22.211	22.180	28.170	30.656	31.886
	HSDT [4]	11.850	–	–	–	–	–	–
5	HSDT [5]	11.746	–	–	–	–	–	–
	HSDT [6]	11.851	–	–	–	–	–	–
	HSDT [7]	11.846	18.489	–	–	29.399	30.856	32.961
	DKZigTS (12×12)	11.424	18.418	22.249	22.309	28.236	31.488	31.838
	DKZigTS (16×16)	11.429	18.438	22.222	22.283	28.245	31.506	31.909
	DKZigTS (24×24)	11.433	18.457	22.202	22.263	28.254	31.531	31.968
	3D FE [3]	11.434	18.225	22.200	22.205	28.088	30.598	31.822
10	DKZigTS (12×12)	11.413	18.311	22.277	22.285	28.294	31.363	31.861
	DKZigTS (16×16)	11.419	18.332	22.249	22.257	28.305	31.380	31.934
	DKZigTS (24×24)	11.425	18.350	22.230	22.238	28.314	31.402	31.992
	3D FE [3]	11.452	18.222	22.132	22.216	28.157	30.586	31.574
20	DKZigTS (12×12)	11.444	18.342	22.28	22.285	28.342	31.38	31.948
	DKZigTS (16×16)	11.453	18.368	22.253	22.257	28.354	31.401	32.027
	DKZigTS (24×24)	11.460	18.389	22.233	22.237	28.365	31.427	32.089

of [3], even for higher modes with maximum percentage difference is less than 2.85. The present element has captured the third and fourth shear modes perfectly, which are not reported by Fiorenzo et al. [7], as their results are based on 2D analytical theory. The fundamental frequencies for the case ‘R/a’ = 5 and ‘h/a’ = 0.1 are presented by Mantari et al. [5], Ferreira et.al. [6] and Reddy [4] using 2D shear deformation theories are also presented in the table.

Table 2 shows the comparison of non-dimensionalised fundamental frequencies obtained by the present element DKZigTS and 3D FE results of [3] for composite cylindrical shell with (0°/90°/90°/0°) stacking sequence. The radius to span ratios varying from 1 to 10 is studied in this table for thickness to span ratio ‘h/a’ = 0.1 and ‘h/a’ = 0.25. The 2D results are obtained by solving closed-form formulations by Garg et al. [8], and 2D higher-order shear deformation theories results of [4] are also presented in the table.

From the table, it can be easily understood that the augmentation of the radius span ratio leads to the decrease of frequencies in the case of the moderately thick shell, whereas it is reversed in the case of the thick shell. It is seen that results of DKZigTS are close to 3D FE results of [3] obtained using 20 node brick element with mesh size of (24 × 24 × 8), for the deep and shallow shell as well as for the moderately thick and thick shell. The maximum percentage difference is less than 2.10 for moderately thick shell and 2.14 for thick shell.

Figure 3 shows the first 5 mode shapes obtained using present elements of mesh size (12 × 12) for a cylindrical shell panel (0°/90°/0°) of square planform, with one curved edges clamped and all other three edges free. The mode shapes obtained using 3D FE 20 node elements of ANSYS [3] with a mesh size of (24 × 24 × 6) are also

Table 2 Dimensionless natural frequencies for (0°/90°/90°/0°) cylindrical shell (SSSS) panel with varying ‘R/a’ ratio and ‘h/a’ ratio

‘R/a’	‘h/a’	3D FE [3]	HSDT [4]	HOST [8]	DKZigTS (12 × 12)	DKZigTS (16 × 16)	DKZigTS (24 × 24)
1	0.1	11.991	–	12.698	12.096	12.041	11.963
	0.25	6.805	–	7.057	6.966	6.902	6.833
2	0.1	11.513	–	11.999	11.641	11.634	11.625
	0.25	6.905	–	7.150	7.068	7.062	7.053
3	0.1	11.463	–	11.856	11.586	11.610	11.610
	0.25	7.052	–	7.171	7.099	7.100	7.100
4	0.1	11.383	–	11.805	11.584	11.592	11.596
	0.25	7.053	–	7.178	7.130	7.133	7.135
5	0.1	11.367	11.830	11.781	11.578	11.584	11.589
	0.25	7.072	–	7.182	7.140	7.144	7.148
10	0.1	11.346	11.790	11.749	11.571	11.579	11.585
	0.25	7.152	–	7.187	7.157	7.157	7.157

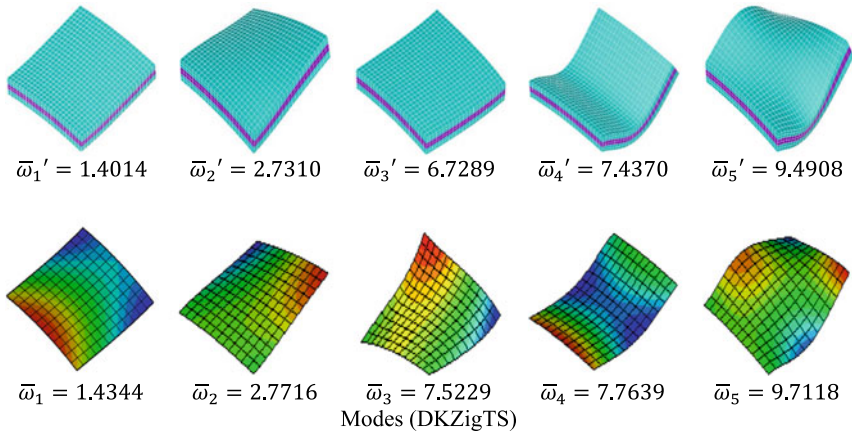


Fig. 3 Comparison of first five mode shapes for cantilever composite cylindrical shell with staking sequence (0°/90°/0°), ‘R/a’ = 5 and ‘h/a’ = 0.15

shown for comparison. The present element has correctly depicted all the five modes indicating the effectiveness of the present element based on zigzag theory.

3.1.2 Anti-Symmetric Cross-Ply Composite Shell

Table 3 shows the developed DKZigTS element is assessed for moderately thick (‘h/a’ = 0.1) and thick (‘h/a’ = 0.15) anti-symmetric cross-ply composite shell panel with (0°/90°) stacking sequence and all-round simply supported boundary conditions. The results are compared with the 3D elasticity results of Bhimaraddi [9], Ye and Soldatos

Table 3 Dimensionless natural frequencies for (0°/90°) cylindrical shell (SSSS) panel with varying ‘R/a’ ratio and ‘h/a’ ratio

‘R/a’	‘h/a’	3D Elast. [9]	3D Elast. [10]	HSZT [11]	DKZigTS (12 × 12)	DKZigTS (16 × 16)	DKZigTS (24 × 24)
1	0.1	10.408	10.697	10.655	10.482	10.388	10.258
	0.15	8.606	8.969	8.911	8.704	8.585	8.453
2	0.1	9.362	9.495	9.489	9.270	9.258	9.241
	0.15	8.358	8.507	8.513	8.343	8.328	8.304
4	0.1	9.061	9.116	9.137	9.036	9.031	9.026
	0.15	8.273	8.331	8.378	8.337	8.333	8.328
5	0.1	9.020	9.062	9.089	9.017	9.013	9.010
	0.15	8.256	8.257	8.357	8.347	8.343	8.341
10	0.1	8.956	8.978	9.018	8.981	8.980	8.979
	0.15	8.225	8.247	8.319	8.353	8.351	8.351

[10] and Higher-order zigzag theory (HSZT) results of Garg [11]. Garg et al. [11] used nine node finite elements having seven degrees of freedom per node with 18×18 mesh size resulting in 9583 degrees of freedom. It is seen that the present results with 24×24 mesh size and 5625 degrees of freedom, even for deep shell panels are closer to 3D elasticity results of Alavandi (1992), than the 2D HSZT results of Garg [11]. It is clear from the comparison that the results of present elements are in good agreement with 3D elasticity results with a maximum percentage difference is less than 1.44 for moderately thick shells and 1.77 for a thick shell.

3.2 Static Response

Table 4 working is for computation of deflection and stresses of all-round simply supported ($0^\circ/90^\circ/0^\circ$) configured composite cylindrical shells under sinusoidal distributed load. The shell has rectangular planform with ‘b/a’ = 3 and radius to span ratio ‘R/a’ = 4. The results for thick ‘h/a’ = 0.2 and moderately thick ‘h/a’ = 0.1 shells are presented in the table. The results obtained using present formulation are compared with result published by Exact 3D of Huang et al. [12]. Equivalent single layer theory results using finite element solution of Dau et al. [13] having triangular element with 6 nodes with 18 DOF at a corner node and 9 DOF at a mid-side node based on sinus model SIN-C are also presented in the Table. The mesh of size (4 × 4) with 32 triangular element, which gives total 954 DOF on full shell, is used by Dau et al. [13] for analysing the results. The results of the present element with mesh size (24 × 72) give 16,425 DOF, but give results that are more accurate, with the maximum percentage difference for the transverse deflection is 1.16, for normal stresses it is 3.99.

Table 4 Deflection and stresses of ($0^\circ/90^\circ/0^\circ$) configured rectangular cylindrical shells

‘h/a’	Theory	\bar{w}	$\bar{\sigma}_x$	$\bar{\sigma}_y$	$\bar{\tau}_{xy}$	$\bar{\tau}_{zx}$	$\bar{\tau}_{yz}$
0.2	Exact 3D [12]	2.1180	1.0220	1.1161	0.2588	0.3867	0.2729
	ESL FE [13]	1.9371	0.9230	1.0240	0.2358	0.2930	0.2858
	DKZigTS (12 × 36)	2.3504	1.0501	1.1345	0.2321	0.4152	0.2507
	DKZigTS (16 × 48)	2.2596	1.0289	1.1295	0.2332	0.404	0.2591
	DKZigTS (24 × 72)	2.1425	1.0177	1.1245	0.2532	0.3928	0.2631
	(% Diff.)	1.16	0.42	0.75	2.16	1.58	3.59
0.1	Exact 3D [12]	0.9396	0.7463	0.6468	0.151	0.4271	0.1555
	ESL FE [13]	0.8763	0.7026	0.6076	0.1412	0.3029	0.1734
	DKZigTS (12 × 36)	0.9515	0.7095	0.6402	0.1252	0.4041	0.1558
	DKZigTS (16 × 48)	0.9308	0.7207	0.6614	0.1464	0.4053	0.1670
	DKZigTS (24 × 72)	0.9305	0.7319	0.6726	0.1576	0.4064	0.1682
	(% Diff.)	0.97	1.93	3.99	4.37	4.85	8.17

Table 5 Deflection and stresses of (0°/90°/0°) and (0°/90°) configured cylindrical shells

Type	'R/a'	Mesh Size	\bar{u}_x	\bar{w}	$\bar{\sigma}_x$	$\bar{\sigma}_y$	$\bar{\tau}_{xy}$	$\bar{\tau}_{zx}$	$\bar{\tau}_{yz}$
0°/90°/0°	5	(12 × 12)	0.0193	1.1529	0.8696	0.0531	0.0469	0.4920	0.6355
		(16 × 16)	0.0193	1.1534	0.8696	0.0531	0.0479	0.5029	0.6353
		(24 × 24)	0.0193	1.1537	0.8695	0.0531	0.0490	0.5086	0.6346
	10	(12 × 12)	0.0157	1.1565	0.8753	0.0526	0.0526	0.4960	0.6427
		(16 × 16)	0.0157	1.1568	0.8752	0.0526	0.0530	0.5061	0.6424
		(24 × 24)	0.0156	1.1570	0.8751	0.0525	0.0534	0.5115	0.6417
	20	(12 × 12)	0.0139	1.1574	0.8757	0.0523	0.0559	0.4969	0.6445
		(16 × 16)	0.0139	1.1577	0.8756	0.0523	0.0561	0.5069	0.6442
		(24 × 24)	0.0139	1.1578	0.8755	0.0523	0.0563	0.5123	0.6440
0°/90°	5	(12 × 12)	0.0527	1.8634	1.1015	0.1260	0.0466	0.1902	0.3471
		(16 × 16)	0.0527	1.8653	1.1019	0.1261	0.0506	0.1900	0.3487
		(24 × 24)	0.0527	1.8665	1.1022	0.1261	0.0530	0.1898	0.3494
	10	(12 × 12)	0.0476	1.8634	1.1147	0.1261	0.0460	0.1898	0.3598
		(16 × 16)	0.0476	1.8653	1.1149	0.1262	0.0485	0.1896	0.3613
		(24 × 24)	0.0476	1.8665	1.1150	0.1262	0.0508	0.1893	0.3620
	20	(12 × 12)	0.0449	1.8874	1.1150	0.1257	0.0466	0.1888	0.3651
		(16 × 16)	0.0449	1.8883	1.1152	0.1258	0.0477	0.1885	0.3666
		(24 × 24)	0.0448	1.8888	1.1153	0.1258	0.0488	0.1883	0.3672

Table 5 presents computation of normal and transverse stresses along with vertical and in-plane deflections of all-round simply supported, symmetrical (0°/90°/0°) and anti-symmetrical (0°/90°) layered composite cylindrical shells under uniformly distributed load. The results for the moderately thick (h/a = 0.1) having square plan-form shell panels with 'R/a' = 5, 10 and 20 are presented in this table. From the table, it can be concluded that deflection is proportional, whereas in-plane displacement is inversely proportional to the 'R/a' ratio.

From Figs. 4, 5, 6 and 7 the through thickness distribution of in-plane normal stresses $\bar{\sigma}_x$, $\bar{\sigma}_y$, and transverse shear stress $\bar{\tau}_{zx}$, $\bar{\tau}_{yz}$ are plotted, respectively, for (0°/90°/0°) laminated composite shell Panel, with all-round simply supported boundary conditions and subjected to uniformly distributed load. All the figures are plotted for two 'R/a' ratios, namely, 5 and 10 with 'h/a' ratio is equal to 0.1. Full shell is discretised with a mesh size of (24 × 24) of present element.

From Figs. 4 and 5, it is clear that there is discontinuity at layer interface of 0° and 90°. In Figs. 6 and 7, it is clear that the transverse shear stresses are zero at top and maximum value at 'z/h' = 0 at bottom.

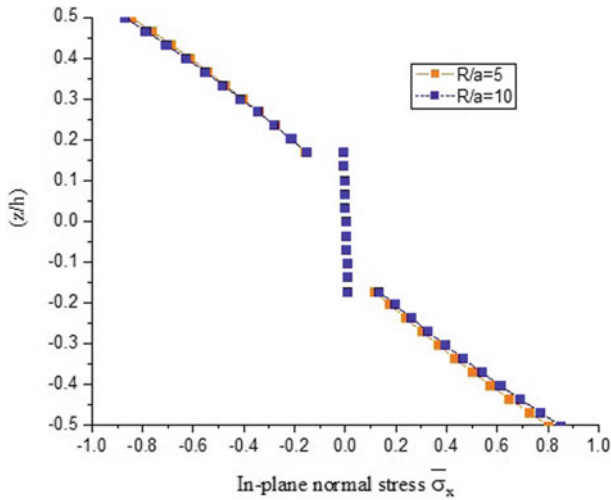


Fig. 4 In-plane normal stress $\bar{\sigma}_x$ variation for $(0^\circ/90^\circ/0^\circ)$ configured shell

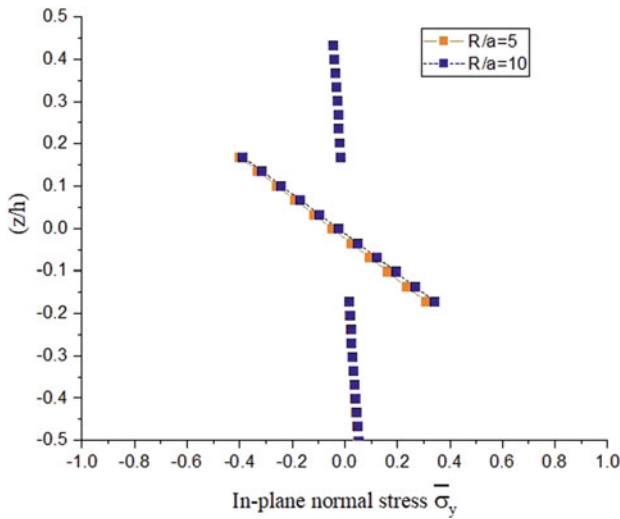


Fig. 5 In-plane normal stress $\bar{\sigma}_y$ variation for $(0^\circ/90^\circ/0^\circ)$ configured shell

4 Conclusions

The developed DKZigTS element gives sufficiently accurate results for static and free vibration analysis of composite cylindrical shell panels for moderately thick as well as thick shells considered in the study. The element results are very close to 3D exact results from literature for moderately thick and thick shells. The present

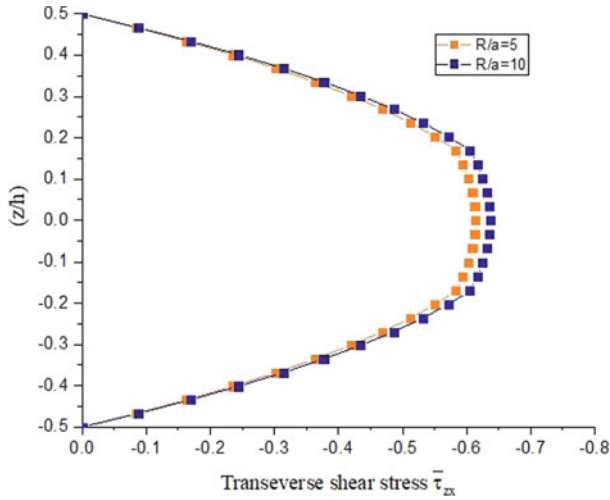


Fig. 6 The transverse shear stress $\bar{\tau}_{zx}$ variation for $(0^\circ/90^\circ/0^\circ)$ configured shell

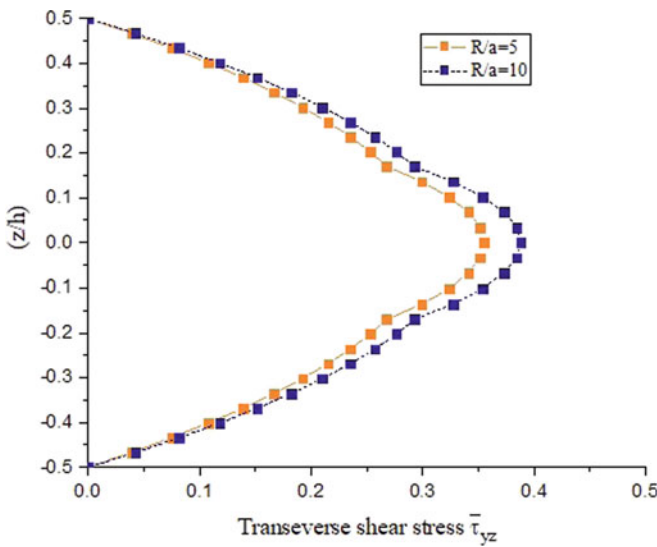


Fig. 7 The transverse shear stress $\bar{\tau}_{yz}$ variation for $(0^\circ/90^\circ/0^\circ)$ configured shell

element results are in close agreement with the results reported in the literature when tested for symmetric as well as anti-symmetric laminates. The present formulation is quite capable of depicting the mode shapes and in depicting the through thickness variation of transverse shear stresses. The formulation is suitable for general-purpose finite element programming as it is unpretentious. The novelty of this element is in its potential to analyse any curved pattern shell, without any modification.

Referencess

1. Kapuria S, Kulkarni SD (2007) An improved discrete Kirchhoff quadrilateral element based on third-order zigzag theory for static analysis of composite and sandwich plates. *Int J Numer Meth Eng* 69:1948–1981
2. Zienkiewicz OC, Taylor RL (2000) *The finite element method: solid mechanics*, vol 2. Butterworth-Heinemann, Oxford
3. ANSYS Mechanical APDL (2019) ANSYS User Manual
4. Reddy JN, Liu CF (1985) A higher-order shear deformation theory of laminated elastic shells. *Int J Eng Sci* 23(3):319–330
5. Mantari JL, Oktem AS, Soares CG (2011) Static and dynamic analysis of laminated composite and sandwich plates and shells by using a new higher-order shear deformation theory. *Compos Struct* 94:37–49
6. Ferreira AJM, Castro LM, Bertoluzza S (2011) A wavelet collocation approach for the analysis of laminated shells. *Compos B* 42:99–104
7. Fiorenzo AF (2014) A refined dynamic stiffness element for free vibration analysis of cross-ply laminated composite cylindrical and spherical shallow shells. *Compos B* 62:143–158
8. Garg AK, Khare RK, Kant T (2006) Higher-order closed-form solutions for free vibration of laminated composite and sandwich shells. *J Sandwich Struct Mater* 8(3):205–235
9. Bhimaraddi A (1991) Free vibration analysis of doubly curved shallow shells on rectangular plane-form using three-dimensional elasticity theory. *Int J Solids Struct* 27:897–913
10. Ye J, Soldatos KP (1994) Three-dimensional vibration of laminated cylinders and cylindrical panels with symmetric or antisymmetric cross-ply lay-up. *Compos Eng* 4:429–444
11. Garg AK, Chakrabarti A, Bhargava P (2013) Vibration of laminated composites and sandwich shells based on higher order zigzag theory. *Eng Struct* 56:880–888
12. Huang NN (1994) Influence of shear correction factors in the higher order shear deformation laminated shell theory. *Int J Solids Struct* 31:1263–1277
13. Dau F, Polit O, Touratier M (2004) An efficient C1 finite element with continuity requirements for multi-layered/sandwich shell structures. *Comput Struct* 82:1889–1899

Exact Elasticity Analysis of Sandwich Beam with Orthotropic Core



Ganesh B. Irkar and Y. T. LomtePatil

Abstract Sandwich beam consists of three layers such that two face sheets at top and bottom are separated by a comparatively soft core between them. Due to its specific advantages over a conventional structure, it is been widely used in areas like aerospace, automobiles, and many more. As the use of Sandwich structure is increasing nowadays, it becomes necessary to explore this area in more depth and provide new solution technique for the analysis of such structures. In this study, the sandwich beam with orthotropic core is analyzed as plane stress problem. With the help of elasticity equations, governing differential equations (GDEs) are developed in terms of displacements. Series expansion approach is used to solve GDEs and unknown stresses and displacements within the sandwich laminate are evaluated. Obtained results concur with available analytical solution ensuring correctness of adopted methodology.

Keywords Displacement based formulation · Exact elasticity analysis · Sandwich structure · Series expansion approach

1 Introduction

Sandwich is type of composite structure. As sandwich structure outplays conventional structure in terms of structural advantages, it is used in many industries such as aerospace, marine, and automobiles. Structures are constructed to serve certain purpose throughout their life span. Safety is the most important parameter in structural engineering field. When stress induced inside the structural element due to external loads exceeds strength of that element then that member fails. This kind of local failure can result in complete collapse of structure which is not acceptable by safety point of view. So, it is necessary to study the distribution of stresses inside the structural element when subjected to external loading in the same sense as actual loading in working life. After analyzing distribution of stresses and considering the

G. B. Irkar · Y. T. LomtePatil (✉)
Civil Engineering Department, College of Engineering Pune, Pune 411005, India
e-mail: lomteyt@gmail.com

© The Author(s), under exclusive license to Springer Nature Singapore Pte Ltd. 2023
M. S. Ranadive et al. (eds.), *Recent Trends in Construction Technology and Management*, Lecture Notes in Civil Engineering 260,
https://doi.org/10.1007/978-981-19-2145-2_85

1149

material strength, safety can be ensured by keeping lemniscates in appropriate direction. There are several methods using which analysis of sandwich structure can be done. The literatures which provided elasticity solution to sandwich beam has been discussed in the next paragraph.

Saint–Venant [1] considered cantilever beam with rectangular cross section having anisotropy of special form and obtained the exact elasticity solution. Silverman [2], Hashin [3], Gerstner [4], Rao and Ghosh [5], and Cheng et al. [6] used Airy’s stress functions and provided exact solution to shear deformable laminated composite beam. Holt and Webber [7] presented exact solution for honeycomb sandwich beams. Pagano [8, 10] analyzed laminated composite plate under cylindrical bending and obtained exact elasticity solution. Srinivas et al. [9] developed 3D linear, small deformation theory of elasticity for the free vibration of simply supported homogeneous isotropic thick rectangular plate. Venkataraman [12] considered simply supported sandwich beam for analysis. In this study, the face sheets of sandwich beam are modeled as Euler–Bernoulli beam theory. Displacement-based formulation is used for obtaining the GDEs for core and then solved using Pagano’s approach. This methodology to analyze sandwich beam is explained in Sankar [11]. Kant et al. [13] provided the semi-analytical elasticity solution to simply supported sandwich beam. The GDEs developed using mixed formulation are solved using numerical integration technique. The exact elasticity solution is always used as a basis to check the accuracy of any refined shear deformation theory.

In this study, exact 2D elasticity solution to sandwich beam with orthotropic core is provided. To achieve this displacement-based formulation is employed and the governing differential equations are expressed in terms displacements. The solution to these equations is obtained using series expansion approach. Series expansion approach is adopted because it gives the solution to differential equations with constant coefficients as well as with variable coefficients without making any modification in the formulations. MATLAB R2019a software is used for programming. The results obtained by this solution technique are thoroughly compared with available literature. The through thickness variation of displacements and stresses is also provided in the tabular and graphical form for better understanding.

2 Theoretical Formulation

Simply (diaphragm) supported sandwich beam having span L along x -axis and total depth H along z -axis subjected to sinusoidal loading is considered as plane stress problem (Fig. 1). The loading is applied on top surface in positive z -direction, whereas bottom surface is free from any traction. The x -axis is along the mid-depth of the beam. The depth of each face sheet is $H_f = 0.1H$ and that of core is $2H_c$. For the simplicity of analysis, the sandwich beam is divided into four layers. Layer no. 1 corresponds to bottom face sheet, whereas layer nos. 2 and 3 indicate the lower half and upper half part of the core, respectively, and layer 4 represent the top face sheet.

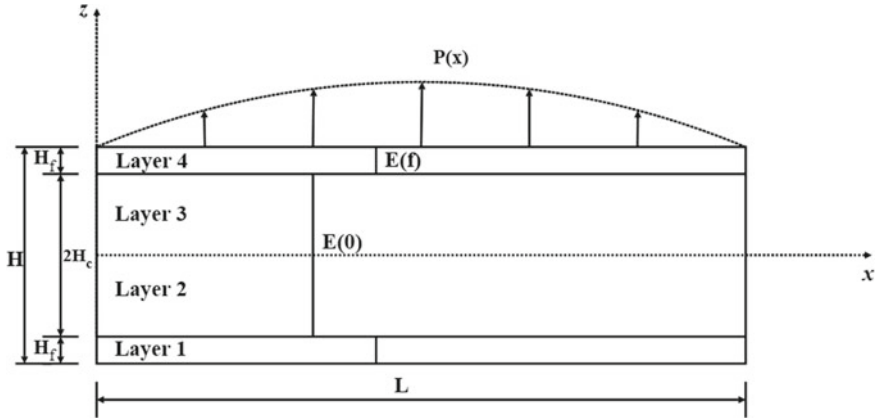


Fig. 1 Sandwich beam

If the properties of face sheets and core are matched, the same formulation can be adopted for homogeneous isotropic/orthotropic beam.

The sandwich beam shown in Fig. 1 $E(0)$ represents the modulus of elasticity for the core, whereas $E(f)$ represents the modulus of elasticity for face sheet. From this, it can be seen that the material properties for the sandwich beam change abruptly at the interface which may lead to the delamination between core and face sheets.

The loading acting on the beam is expressed in terms of Fourier series as given by Eq. (1) so that any kind of loading can be handled. In this case, only sinusoidal load is considered so only one term in the series is sufficient.

$$P(x) = \sum_{m=1,3}^{\infty} P_0 \sin(px) \tag{1}$$

where $p = \frac{m\pi}{L}$.

The simple support condition yields boundary conditions (BCs) at ends of the beam as given by Eq. (2),

At $x = 0$ and $x = L$

$$\sigma_x = w = 0 \tag{2a}$$

At $x = \frac{L}{2}$

$$u = 0 \tag{2b}$$

Also the BCs at top and bottom of the beam are

$$\begin{aligned}
 \sigma_z(x, \frac{H}{2}) &= P_0 \sin(px) \\
 \tau_{zx}(x, \frac{H}{2}) &= 0 \\
 \sigma_z(x, -\frac{H}{2}) &= 0 \\
 \tau_{zx}(x, -\frac{H}{2}) &= 0.
 \end{aligned}
 \tag{2c}$$

2.1 Equations of Elasticity

In this case as the material for both core as well as face sheets is homogeneous orthotropic hence the governing equations are derived for only one layer which is equally applicable to the remaining layers. Only we need to match the displacements and transverse stresses at the interface to maintain the continuity at the interface.

2.1.1 Differential Equations of Equilibrium

In the absence of body force, differential equation of equilibrium becomes

$$\begin{aligned}
 \frac{\partial \sigma_x}{\partial x} + \frac{\partial \tau_{zx}}{\partial z} &= 0 \\
 \frac{\partial \sigma_z}{\partial z} + \frac{\partial \tau_{xz}}{\partial x} &= 0
 \end{aligned}
 \tag{3}$$

where $\tau_{zx} = \tau_{xz}$

2.1.2 Material Constitutive Relationship

For 2D elasticity plane stress problem material constitutive relationship can be represented as

$$\begin{Bmatrix} \sigma_x \\ \sigma_z \\ \tau_{xz} \end{Bmatrix} = \begin{bmatrix} C_{11} & C_{12} & 0 \\ C_{21} & C_{22} & 0 \\ 0 & 0 & C_{33} \end{bmatrix} \begin{Bmatrix} \varepsilon_x \\ \varepsilon_z \\ \gamma_{xz} \end{Bmatrix}
 \tag{4}$$

2.1.3 Strain–displacement Relation

Strain can be written in terms of displacement as

$$\begin{Bmatrix} \varepsilon_x \\ \varepsilon_z \\ \gamma_{xz} \end{Bmatrix} = \begin{Bmatrix} \frac{\partial u}{\partial x} \\ \frac{\partial w}{\partial z} \\ \frac{\partial u}{\partial z} + \frac{\partial w}{\partial x} \end{Bmatrix} \tag{5}$$

2.2 Displacement Based Formulation

In displacement-based formulation, elastic displacements are considered as primary variables and differential equations of equilibrium are written in terms of displacements using material constitutive relation (Eq. 4) and strain–displacement relationships (Eq. 5). This gives a set of two coupled partial differential equations (PDEs) (Eq. 6).

Substituting strain–displacement relations Eq. (5) and constitutive relations Eq. (4) in Equilibrium equations Eq. (3) set of equation is obtained

$$\begin{aligned} C_{11} \frac{\partial^2 u}{\partial x^2} + C_{33} \frac{\partial^2 u}{\partial z^2} + (C_{12} + C_{33}) \frac{\partial^2 w}{\partial x \cdot \partial z} &= 0 \\ (C_{21} + C_{33}) \frac{\partial^2 u}{\partial x \cdot \partial z} + C_{33} \frac{\partial^2 w}{\partial x^2} + C_{22} \frac{\partial^2 w}{\partial z^2} &= 0. \end{aligned} \tag{6}$$

PDEs are quite difficult to tackle as it contains more than one variable. To convert PDEs into a set of ordinary differential equations (ODEs), Fourier series expansion technique is used. Primary variables are expressed in the following manner such that it satisfies end boundary conditions (2a) and (2b) exactly.

$$\begin{aligned} u(x, z) &= U(z) \cos(px) \\ w(x, z) &= W(z) \sin(px). \end{aligned} \tag{7}$$

Substituting Eq. (7) in Eq. (6) and applying orthogonality condition following set of ODEs is obtained

$$\begin{aligned} C_{33}U''(z) - p^2C_{11}U(z) + p(C_{12} + C_{33})W'(z) &= 0 \\ - p(C_{12} + C_{33})U'(z) + C_{22}W''(z) - p^2C_{33}W(z) &= 0 \end{aligned} \tag{8}$$

where $(\prime) = \frac{d}{dz}$

2.2.1 Solution Technique

Series expansion approach is solution technique for displacement-based formulation. In this technique, the solution obtained ODEs Eq. (8) is assumed in the form of power

series in transverse direction of the beam.

$$\begin{aligned}
 U(z) &= \sum_{r=0}^{\infty} A_r z^r \\
 W(z) &= \sum_{r=0}^{\infty} B_r z^r
 \end{aligned}
 \tag{9}$$

where A_r and B_r are the coefficients in the power series.

The differentiation of two displacement components after simple algebraic manipulation is

$$\begin{aligned}
 U'(z) &= \sum_{r=0}^{\infty} A_{r+1}(r+1)z^r, \\
 U''(z) &= \sum_{r=0}^{\infty} A_{r+2}(r+2)(r+1)z^r, \\
 W'(z) &= \sum_{r=0}^{\infty} B_{r+1}(r+1)z^r, \\
 W''(z) &= \sum_{r=0}^{\infty} B_{r+2}(r+2)(r+1)z^r.
 \end{aligned}
 \tag{10}$$

Substituting Eq. (9) and Eq. (10) in Eq. (8),

$$\begin{aligned}
 &\left\{ \begin{aligned} &C_{33}A_{r+2}(r+2)(r+1) - p^2C_{11}A_r \\ &+ p(C_{12} + C_{33})B_{r+1}(r+1) \end{aligned} \right\} \sum_{r=0}^{\infty} z^r = 0 \\
 &\left\{ \begin{aligned} &-p(C_{21} + C_{33})A_{r+1}(r+1) \\ &+ C_{22}B_{r+2}(r+2)(r+1) - p^2C_{33}B_r \end{aligned} \right\} \sum_{r=0}^{\infty} z^r = 0
 \end{aligned}
 \tag{11}$$

Equation (11) is obtained. For solution to be nontrivial, the term inside curly bracket must be zero. Thus, recurrence relationship occurring in power series is obtained.

$$\begin{aligned}
 A_{r+2}(r+2)(r+1) &= I_1 A_r + I_2 B_{r+1}(r+1) \\
 B_{r+2}(r+2)(r+1) &= I_3 A_{r+1}(r+1) + I_4 B_r
 \end{aligned}
 \tag{12}$$

where

$$I_1 = \frac{p^2 C_{11}}{C_{33}}, \quad I_2 = \frac{-p(C_{12} + C_{33})}{C_{33}},$$

$$I_3 = \frac{p(C_{12} + C_{33})}{C_{22}}, I_4 = \frac{p^2 C_{33}}{C_{22}}.$$

The successive evaluation of Eq. (12) for $r = 0, 1, 2 \dots$ gives the coefficients $A_2, B_2, A_3, B_3, \dots$ of the two power series in terms of only four independent coefficients A_0, B_0, A_1, B_1 . Hence the primary variables $U(z)$ and $W(z)$ can also be expressed in terms of the same four coefficients. These unknown coefficients are determined using the BCs given by Eq. (2c). Once four unknown coefficients of the power series are obtained the complete solution for the primary variables $u(x, z)$ and $w(x, z)$ are also known and hence the stresses at any point in the beams can be evaluated in a straightforward manner.

3 Results

3.1 Validation

To check the accuracy of the present approach, the results obtained by series expansion approach are compared with Kant et al. [13]. For validation purpose, same material properties (Table 1) and normalization (Eq. 13) as used by the author are followed.

Table 2 shows the convergence study for the aspect ratio ($\eta = 1/4$) from which it can be seen that the results are converging for 9 terms of series.

$$\eta = \frac{H}{L}$$

Table 3 gives the comparison of results for homogeneous isotropic beam on the

Table 1 Material properties

Sr. No.	Material	Property	Source
1	Homogeneous Isotropic	$E = 1.0 \text{ GPa}, \nu = 0.3, G = 0.3846 \text{ GPa}$	–
2	Homogeneous Orthotropic	$E_x = 172.4 \text{ GPa}; E_z = 6.89 \text{ GPa}$ $\nu_{xz} = 0.25 G_{xz} = 3.45 \text{ GPa}$	Pagano [14]
3	Face sheets- Homogeneous orthotropic	<i>For face sheet</i> $E_x = 172.4 \text{ GPa}; E_z = 6.89 \text{ GPa}$ $\nu_{xz} = 0.25 G_{xz} = 3.45 \text{ GPa}$	Pagano [14]
	Core- Homogeneous orthotropic	<i>For core</i> $E_z = 3.450 \text{ GPa}; E_x = 0.276 \text{ GPa}$ $\nu_{xz} = 0.25 G_{xz} = 0.414 \text{ GPa}$	

Table 2 Convergence study for Homogeneous Isotropic beam ($\eta = \frac{1}{4}$)

No of terms retained in series (r)	\bar{u}		\bar{w}	$\bar{\sigma}_x$		$\bar{\tau}_{xz}$
	$x = 0$	$x = 0$	$x = L/2$	$x = L/2$	$x = L/2$	$x = 0$
	$z = H/2$	$z = -H/2$	$z = 0$	$z = H/2$	$z = -H/2$	$z = 0$
3	-0.4157	0.4337	7.6666	0.3452	-0.3406	0.2524
4	-0.7838	0.8036	14.3489	0.6344	-0.6312	0.4756
5	-0.7591	0.7790	13.9368	0.6150	-0.6118	0.4692
6	-0.7686	0.7884	14.1085	0.6224	-0.6192	0.4750
7	-0.7684	0.7883	14.1058	0.6223	-0.6191	0.4749
8	-0.7685	0.7883	14.1067	0.6223	-0.6192	0.4750
9	0.7685	0.7883	14.1067	0.6223	-0.6192	0.4750

Table 3 Validation of results for Homogeneous Isotropic beam

Aspect ratio (η)	Source	$\bar{\sigma}_x$		$\bar{\tau}_{xz}$	\bar{w}
		$x = L/2$	$x = L/2$	$x = 0$	$x = L/2$
		$z = H/2$	$z = -H/2$	$z = 0$	$z = 0$
1/4	Present work	0.6223	-0.6192	0.4750	14.1067
	Kant et. al. [12]	0.6223	-0.6192	0.4750	14.1076
1/10	Present work	0.6100	-0.6099	0.4771	12.6075
	Kant et. al. [12]	0.6100	-0.6099	0.4771	12.6086
1/20	Present work	0.6084	-0.6084	0.4774	12.3913
	Kant et. al. [12]	0.6084	-0.6084	0.4774	12.3925
1/30	Present work	0.6081	-0.6081	0.4774	12.3513
	Kant et. al. [12]	0.6082	-0.6082	0.4774	12.3524
1/40	Present work	0.6081	-0.6081	0.4774	12.3372
	Kant et. al. [12]	0.6081	-0.6081	0.4774	12.3383
1/50	Present work	0.6080	-0.6080	0.4774	12.3307
	Kant et. al. [12]	0.6080	-0.6080	0.4774	12.3318

contrary Tables 4 and 5 presents the results for homogeneous orthotropic and sandwich beam with orthotropic core, respectively. From these results, it can be concluded that the results obtained by the present formulation are in well agreement with the considered literature.

$$\bar{w} = \frac{100E_z\eta^3 w(L/2, 0)}{p_0L}, \bar{\sigma}_x = \frac{\eta^2\sigma_x(L/2, 0)}{p_0}, \bar{\tau}_{xz} = \frac{\eta\tau_{xz}(0, z)}{p_0}. \quad (13)$$

Table 4 Validation of results for Homogeneous Orthotropic beam

Aspect ratio (η)	Source	$\bar{\sigma}_x$		$\bar{\tau}_{xz}$	\bar{w}
		$x = L/2$	$x = L/2$	$x = 0$	$x = L/2$
		$z = H/2$	$z = -H/2$	$z = 0$	$z = 0$
1/4	Present work	0.9026	-0.8468	0.4328	1.9483
	Kant et. al. [12]	0.9028	-0.8469	0.4328	1.9509
1/10	Present work	0.6570	-0.6551	0.4683	0.7325
	Kant et. al. [12]	0.6570	-0.6551	0.4683	0.7333
1/20	Present work	0.6203	-0.6201	0.4751	0.5527
	Kant et. al. [12]	0.6203	-0.6201	0.4751	0.5532
1/30	Present work	0.6134	-0.6134	0.4764	0.5192
	Kant et. al. [12]	0.6134	-0.6134	0.4764	0.5197
1/40	Present work	0.6110	-0.6110	0.4769	0.5075
	Kant et. al. [12]	0.6110	-0.6110	0.4769	0.5079
1/50	Present work	0.6099	-0.6099	0.4771	0.5020
	Kant et. al. [12]	0.6099	-0.6099	0.4771	0.5024

Table 5 Validation of results for sandwich beam

Aspect ratio (η)	Source	$\bar{\sigma}_x$		$\bar{\tau}_{xz}$	\bar{w}
		$x = L/2$	$x = L/2$	$x = 0$	$x = L/2$
		$z = H/2$	$z = -H/2$	$z = 0$	$z = 0$
1/4	Present work	2.3319	-2.3775	0.3408	11.0675
	Kant et. al. [12]	2.3839	-2.3470	0.3396	11.0600
1/10	Present work	1.4252	-1.4347	0.3506	2.6658
	Kant et. al. [12]	1.4317	-1.4314	0.3504	2.6688
1/20	Present work	1.2893	-1.2918	0.3521	1.4237
	Kant et. al. [12]	1.2910	-1.2910	0.3521	1.4252
1/30	Present work	1.2640	-1.2651	0.3524	1.1925
	Kant et. al. [12]	1.2647	-1.2647	0.3524	1.1936
1/40	Present work	1.2551	-1.2557	0.3525	1.1114
	Kant et. al. [12]	1.2555	-1.2555	0.3525	1.1125
1/50	Present work	1.2510	-1.2514	0.3526	1.0739
	Kant et. al. [12]	1.2512	-1.2512	0.3525	1.0750

3.2 Results and Discussion for the Present Work

In the present work, an attempt has been made to check the applicability of the assumptions made in Euler–Bernoulli beam theory, for this the variation of displacements and stresses for various aspect ratios through the depth of the beam are plotted

which will also help to give the demarcation between thick and thin beam. Also the properties of face sheets and core are varied in the ratio (β) of 1/1, 1/25, 1/50, 1/75, and 1/100 to study the effect of core softening on the behavior of sandwich beam. Equation (14) represents the non-dimensional form used. The properties of the face sheets used for the present work are same as used by Pagano [14] and mentioned in Table 1 sr. no. 3.

$$\begin{aligned} \bar{u} &= \frac{E_z \sqrt{\eta^5} u(0, z)}{p_0 H}, \bar{w} = \frac{100 E_z \eta^3 w(L/2, 0)}{p_0 L}, \\ \bar{\sigma}_x &= \frac{\sqrt{\eta^5} \sigma_x(L/2, 0)}{p_0}, \bar{\tau}_{xz} = \frac{\eta^2 \tau_{xz}(0, z)}{p_0}, \bar{z} = \frac{z}{H}. \end{aligned} \tag{14}$$

Table 6 gives results for homogeneous isotropic beam with various aspect ratios, whereas the through thickness variation of displacements and stresses for aspect ratio 1/4, 1/10, 1/20, and 1/50 are given in Tables 7, 8, 9, and 10, respectively. The same results are shown graphically in Fig. 2. Similarly, Tables 11, 12, 13, 14 and 15, and Fig. 3 correspond to homogeneous orthotropic material.

Table 6 Results of homogeneous isotropic beam for various aspect ratios

Aspect ratio (η)	\bar{u}		\bar{w}		$\bar{\sigma}_x$		$\bar{\tau}_{xz}$
	$x = 0$ $z = H/2$	$x = 0$ $z = -H/2$	$x = L/2$ $z = H/2$	$x = L/2$ $z = -H/2$	$x = L/2$ $z = H/2$	$x = L/2$ $z = -H/2$	$x = 0$ $z = 0$
1/4	-0.3842	0.3942	13.9818	13.7865	0.3112	-0.3096	0.1187
1/10	-0.6110	0.6139	12.5660	12.5610	0.1929	-0.1929	0.0477
1/20	-0.8650	0.8661	12.3802	12.3799	0.1360	-0.1360	0.0239
1/50	-1.3682	1.3685	12.3289	12.3289	0.0860	-0.0860	0.0095

Table 7 Variation of displacements and stresses through the depth of homogeneous isotropic beam for $\eta = 1/4$

\bar{z}	$\bar{u}(x = 0)$	$\bar{w}(x = L/2)$	$\bar{\sigma}_x(x = L/2)$	$\bar{\tau}_{xz}(x = 0)$
-0.5	0.3942	13.7865	-0.3096	0
-0.4	0.3101	13.8905	-0.2433	0.0434
-0.3	0.2305	13.9722	-0.1801	0.0766
-0.2	0.1541	14.0344	-0.1190	0.1001
-0.1	0.0798	14.0789	-0.0594	0.1141
0	0.0065	14.1067	-0.0004	0.1187
0.1	-0.0670	14.1182	0.0587	0.1142
0.2	-0.1416	14.1130	0.1186	0.1003
0.3	-0.2186	14.0899	0.1801	0.0768
0.4	-0.2991	14.0471	0.2440	0.0436
0.5	-0.3842	13.9818	0.3112	0

Table 8 Variation of displacements and stresses through the depth of homogeneous isotropic beam for $\eta = 1/10$

\bar{z}	$\bar{u}(x = 0)$	$\bar{w}(x = L/2)$	$\bar{\sigma}_x(x = L/2)$	$\bar{\tau}_{xz}(x = 0)$
-0.5	0.6139	12.5610	-0.1929	0
-0.4	0.4898	12.5775	-0.1538	0.0172
-0.3	0.3667	12.5903	-0.1151	0.0306
-0.2	0.2445	12.5995	-0.0766	0.0401
-0.1	0.1229	12.6053	-0.0383	0.0458
0	0.0015	12.6075	0.0000	0.0477
0.1	-0.1198	12.6063	0.0383	0.0458
0.2	-0.2415	12.6015	0.0766	0.0401
0.3	-0.3637	12.5933	0.1151	0.0306
0.4	-0.4868	12.5815	0.1539	0.0172
0.5	-0.6110	12.5660	0.1929	0

Table 9 Variation of displacements and stresses through the depth of homogeneous isotropic beam for $\eta = 1/20$

\bar{z}	$\bar{u}(x = 0)$	$\bar{w}(x = L/2)$	$\bar{\sigma}_x(x = L/2)$	$\bar{\tau}_{xz}(x = 0)$
-0.5	0.8661	12.3799	-0.1360	0
-0.4	0.6924	12.3840	-0.1088	0.0086
-0.3	0.5191	12.3872	-0.0815	0.0153
-0.2	0.3461	12.3895	-0.0543	0.0201
-0.1	0.1733	12.3909	-0.0272	0.0229
0	0.0005	12.3913	0.0000	0.0239
0.1	-0.1722	12.3909	0.0272	0.0229
0.2	-0.3450	12.3896	0.0543	0.0201
0.3	-0.5180	12.3874	0.0815	0.0153
0.4	-0.6913	12.3842	0.1088	0.0086
0.5	-0.8650	12.3802	0.1360	0

From these tables and figures, it can be clearly seen that for higher aspect ratios greater than 1/10 significant warping of section is observed hence plane section remains plane this assumption is not applicable and the transverse displacement w is also not constant which means that thickness of the beam does not remain constant. It is observed that for thicker beam the distribution of the transverse shear stress is not symmetric. This may be because the load is applied on the top surface of the beam which is nonsymmetric. The in-plane normal stress σ_x distribution is also non-linear.

For laminated sandwich beam with orthotropic core, the results are presented for the material property used for validation purpose because in that problem very soft core and stiff face sheets are considered. Table 16 presents summarized results of

Table 10 Variation of displacements and stresses through the depth of homogeneous isotropic beam for $\eta = 1/50$

\bar{z}	$\bar{u}(x = 0)$	$\bar{w}(x = L/2)$	$\bar{\sigma}_x(x = L/2)$	$\bar{\tau}_{xz}(x = 0)$
-0.5	1.3685	12.3289	-0.0860	0
-0.4	1.0947	12.3296	-0.0688	0.0034
-0.3	0.8210	12.3301	-0.0516	0.0061
-0.2	0.5473	12.3304	-0.0344	0.0080
-0.1	0.2737	12.3307	-0.0172	0.0092
0	0.0001	12.3307	0.0000	0.0095
0.1	-0.2734	12.3307	0.0172	0.0092
0.2	-0.5470	12.3304	0.0344	0.0080
0.3	-0.8207	12.3301	0.0516	0.0061
0.4	-1.0944	12.3296	0.0688	0.0034
0.5	-1.3682	12.3289	0.0860	0

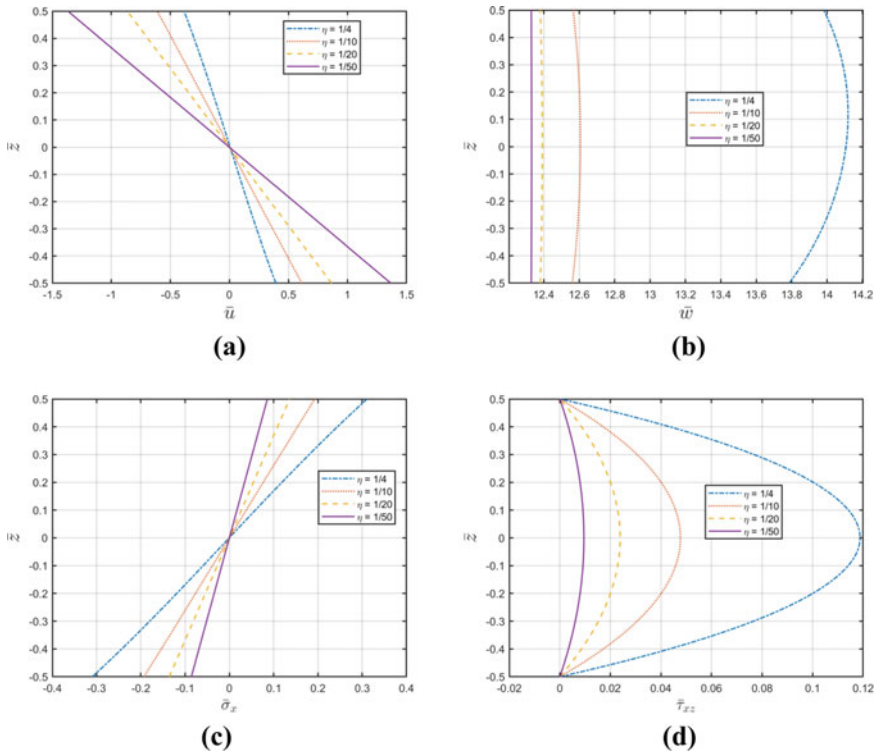


Fig. 2 Variation of normalized (a) in-plane displacement \bar{u} (b) transverse displacement \bar{w} (c) in-plane normal stress $\bar{\sigma}_x$ (d) transverse shear stress $\bar{\tau}_{xz}$ through the thickness of a homogeneous isotropic beam

Table 11 Results of homogeneous orthotropic beam for various aspect ratios

Aspect ratio (η)	\bar{u}		\bar{w}		$\bar{\sigma}_x$		$\bar{\tau}_{xz}$
	$x = 0$	$x = 0$	$x = L/2$	$x = L/2$	$x = L/2$	$x = L/2$	$x = 0$
	$z = H/2$	$z = -H/2$	$z = H/2$	$z = -H/2$	$z = H/2$	$z = -H/2$	$z = 0$
1/4	-0.0226	0.0215	2.0953	1.9015	0.4513	-0.4234	0.1082
1/10	-0.0263	0.0264	0.7351	0.7301	0.2078	-0.2072	0.0468
1/20	-0.0353	0.0353	0.5526	0.5523	0.1387	-0.1387	0.0238
1/50	-0.0549	0.0549	0.5020	0.5019	0.0862	-0.0862	0.0095

Table 12 Variation of displacements and stresses through the depth of homogeneous orthotropic beam for $\eta = 1/4$

\bar{z}	$\bar{u}(x = 0)$	$\bar{w}(x = L/2)$	$\bar{\sigma}_x(x = L/2)$	$\bar{\tau}_{xz}(x = 0)$
-0.5	0.0215	1.9015	-0.4234	0
-0.4	0.0124	1.9060	-0.2427	0.0510
-0.3	0.0071	1.9112	-0.1378	0.0802
-0.2	0.0039	1.9193	-0.0755	0.0965
-0.1	0.0020	1.9315	-0.0356	0.1051
0	0.0005	1.9483	-0.0051	0.1082
0.1	-0.0011	1.9701	0.0263	0.1066
0.2	-0.0032	1.9967	0.0690	0.0993
0.3	-0.0066	2.0274	0.1371	0.0836
0.4	-0.0125	2.0610	0.2523	0.0538
0.5	-0.0226	2.0953	0.4513	0

Table 13 Variation of displacements and stresses through the depth of homogeneous orthotropic beam for $\eta = 1/10$

\bar{z}	$\bar{u}(x = 0)$	$\bar{w}(x = L/2)$	$\bar{\sigma}_x(x = L/2)$	$\bar{\tau}_{xz}(x = 0)$
-0.5	0.0264	0.7301	-0.2071	0
-0.4	0.0197	0.7307	-0.1547	0.0179
-0.3	0.0140	0.7312	-0.1099	0.0310
-0.2	0.0090	0.7316	-0.0705	0.0399
-0.1	0.0044	0.7321	-0.0345	0.0451
0	0.0001	0.7325	-0.0001	0.0468
0.1	-0.0043	0.7331	0.0342	0.0451
0.2	-0.0089	0.7336	0.0703	0.0400
0.3	-0.0139	0.7342	0.1099	0.0311
0.4	-0.0196	0.7347	0.1550	0.0179
0.5	-0.0263	0.7351	0.2078	0

Table 14 Variation of displacements and stresses through the depth of homogeneous orthotropic beam for $\eta = 1/20$

\bar{z}	$\bar{u}(x = 0)$	$\bar{w}(x = L/2)$	$\bar{\sigma}_x(x = L/2)$	$\bar{\tau}_{xz}(x = 0)$
-0.5	0.0353	0.5523	-0.1387	0
-0.4	0.0277	0.5524	-0.1090	0.0087
-0.3	0.0205	0.5525	-0.0806	0.0153
-0.2	0.0135	0.5526	-0.0532	0.0200
-0.1	0.0067	0.5527	-0.0264	0.0228
0	0.0000	0.5527	0.0000	0.0238
0.1	-0.0067	0.5527	0.0264	0.0228
0.2	-0.0135	0.5527	0.0532	0.0200
0.3	-0.0205	0.5527	0.0806	0.0153
0.4	-0.0277	0.5527	0.1090	0.0087
0.5	-0.0353	0.5526	0.1387	0

Table 15 Variation of displacements and stresses through the depth of homogeneous orthotropic beam for $\eta = 1/50$

\bar{z}	$\bar{u}(x = 0)$	$\bar{w}(x = L/2)$	$\bar{\sigma}_x(x = L/2)$	$\bar{\tau}_{xz}(x = 0)$
-0.5	0.0549	0.5019	-0.0863	0
-0.4	0.0438	0.5020	-0.0688	0.0034
-0.3	0.0327	0.5020	-0.0515	0.0061
-0.2	0.0218	0.5020	-0.0343	0.0080
-0.1	0.0109	0.5020	-0.0171	0.0092
0	0.0000	0.5020	0.0000	0.0095
0.1	-0.0109	0.5020	0.0171	0.0092
0.2	-0.0218	0.5020	0.0343	0.0080
0.3	-0.0327	0.5020	0.0515	0.0061
0.4	-0.0438	0.5020	0.0688	0.0034
0.5	-0.0549	0.5020	0.0863	0

displacements and stresses for various aspect ratios on the other hand the detailed through thickness variation of these quantities is shown in Tables 17, 18, 19, and 20 for aspect ratio 1/4, 1/10, 1/20, and 1/50, respectively, and the graphical representation is given in Fig. 4. For aspect ratios greater than 1/10, the variation of in plane displacement u is different for face sheets and core but its value is same at the interface, whereas for aspect ratios lower than 1/10 relatively smooth variation is observed. On the other hand for transverse displacement w , no significant change is observed. In this case as the core is very soft, the in-plane normal stress σ_x (bending stress in case of beam) is completely resisted by the face sheets. Besides this a sudden change is observed in σ_x at the interface of face sheets and core. In case of transverse

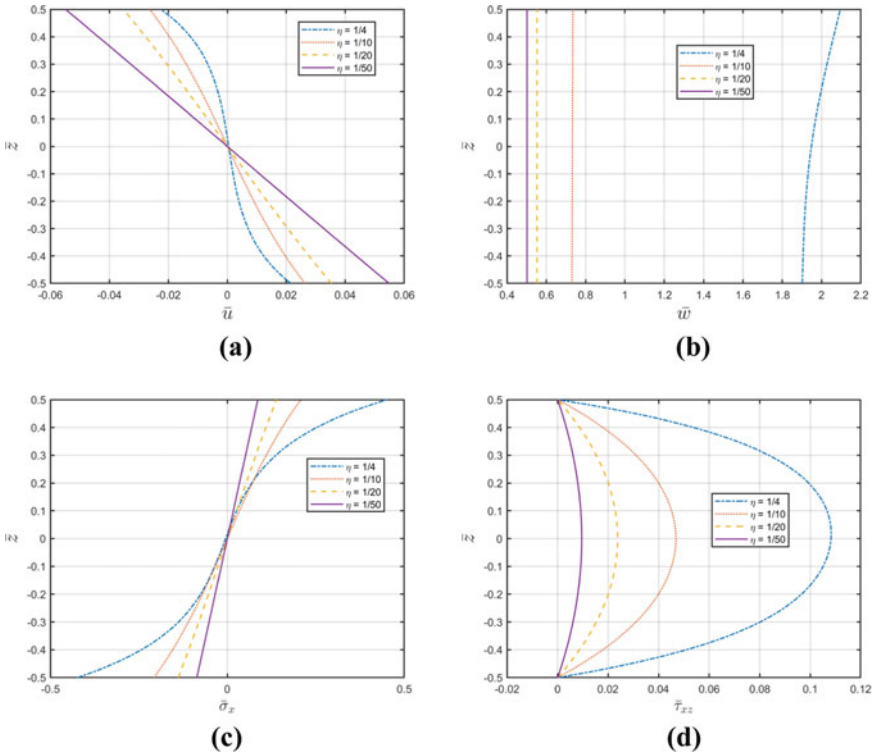


Fig. 3 Variation of normalized (a) in-plane displacement \bar{u} (b) transverse displacement \bar{w} (c) in-plane normal stress $\bar{\sigma}_x$ (d) transverse shear stress $\bar{\tau}_{xz}$ through the thickness of a homogeneous orthotropic beam

Table 16 Results of sandwich beam for various aspect ratios

Aspect ratio (η)	\bar{u}		\bar{w}		$\bar{\sigma}_x$		$\bar{\tau}_{xz}$
	$x = 0$ $z = H/2$	$x = 0$ $z = -H/2$	$x = L/2$ $z = H/2$	$x = L/2$ $z = -H/2$	$x = L/2$ $z = H/2$	$x = L/2$ $z = -H/2$	$x = 0$ $z = 0$
1/4	-0.0589	0.0605	11.1545	11.0378	1.1660	-1.1888	0.0852
1/10	-0.0572	0.0577	2.6654	2.6626	0.4507	-0.4537	0.0351
1/20	-0.0733	0.0735	1.4231	1.4229	0.2883	-0.2889	0.0176
1/50	-0.1125	0.1126	1.0738	1.0738	0.1769	-0.1770	0.0071

shear stress, a non-symmetric variation is observed for higher aspect ratio and also a significant change is observed in the distribution for face sheets and core but the values are matching at the interface.

Table 17 Variation of displacements and stresses through the depth of sandwich beam with orthotropic core for $\eta = 1/4$

\bar{z}	$\bar{u}(x = 0)$	$\bar{w}(x = L/2)$	$\bar{\sigma}_x(x = L/2)$	$\bar{\tau}_{xz}(x = 0)$
-0.5	0.0605	11.0378	-1.1888	0
-0.4667	0.0383	11.0419	-0.7521	0.0507
-0.4333	0.0174	11.0445	-0.3410	0.0792
-0.4	-0.0029	11.0458	0.0585	0.0866
-0.3667	-0.0021	11.0461	0.0009	0.0865
-0.3333	-0.0012	11.0467	0.0012	0.0865
-0.3	-0.0004	11.0476	0.0014	0.0864
-0.2667	0.0005	11.0487	0.0017	0.0863
-0.2333	0.0012	11.0502	0.0020	0.0862
-0.2	0.0020	11.0519	0.0022	0.0861
-0.1667	0.0027	11.0538	0.0025	0.0860
-0.1333	0.0034	11.0560	0.0027	0.0859
-0.1	0.0041	11.0585	0.0030	0.0857
-0.0667	0.0046	11.0612	0.0033	0.0856
-0.0333	0.0052	11.0642	0.0035	0.0854
0	0.0057	11.0675	0.0038	0.0852
0.0333	0.0061	11.0709	0.0041	0.0850
0.0667	0.0064	11.0746	0.0043	0.0848
0.1	0.0067	11.0786	0.0046	0.0845
0.1333	0.0069	11.0827	0.0049	0.0843
0.1667	0.0070	11.0871	0.0051	0.0840
0.2	0.0071	11.0916	0.0054	0.0837
0.2333	0.0070	11.0964	0.0057	0.0835
0.2667	0.0069	11.1014	0.0060	0.0832
0.3	0.0067	11.1065	0.0062	0.0828
0.3333	0.0063	11.1119	0.0065	0.0825
0.3667	0.0059	11.1173	0.0068	0.0822
0.4	0.0053	11.1230	0.0071	0.0818
0.4333	-0.0153	11.1348	0.3079	0.0763
0.4667	-0.0365	11.1454	0.7244	0.0494
0.5	-0.0589	11.1545	1.1660	0

4 Conclusions

Exact elasticity analysis of sandwich beam with orthotropic core is presented using series expansion approach. As this approach is exact analytical approach, it can be used for thick as well as thin beams. In case of series expansion approach, same

Table 18 Variation of displacements and stresses through the depth of sandwich beam with orthotropic core for $\eta = 1/10$

\bar{z}	$\bar{u}(x = 0)$	$\bar{w}(x = L/2)$	$\bar{\sigma}_x(x = L/2)$	$\bar{\tau}_{xz}(x = 0)$
-0.5	0.0577	2.6626	-0.4537	0.0000
-0.4667	0.0490	2.6630	-0.3855	0.0139
-0.4333	0.0406	2.6634	-0.3195	0.0256
-0.4	0.0325	2.6637	-0.2552	0.0351
-0.3667	0.0298	2.6640	-0.0003	0.0351
-0.3333	0.0271	2.6642	-0.0002	0.0351
-0.3	0.0245	2.6645	-0.0002	0.0351
-0.2667	0.0218	2.6647	-0.0001	0.0351
-0.2333	0.0191	2.6649	0.0000	0.0351
-0.2	0.0165	2.6651	0.0000	0.0351
-0.1667	0.0138	2.6652	0.0001	0.0351
-0.1333	0.0111	2.6654	0.0001	0.0351
-0.1	0.0085	2.6655	0.0002	0.0351
-0.0667	0.0058	2.6656	0.0003	0.0351
-0.0333	0.0031	2.6657	0.0003	0.0351
0	0.0004	2.6658	0.0004	0.0351
0.0333	-0.0022	2.6659	0.0005	0.0350
0.0667	-0.0049	2.6659	0.0005	0.0350
0.1	-0.0076	2.6660	0.0006	0.0350
0.1333	-0.0103	2.6660	0.0006	0.0350
0.1667	-0.0130	2.6660	0.0007	0.0350
0.2	-0.0157	2.6660	0.0008	0.0349
0.2333	-0.0184	2.6659	0.0008	0.0349
0.2667	-0.0211	2.6659	0.0009	0.0349
0.3	-0.0238	2.6658	0.0010	0.0349
0.3333	-0.0265	2.6657	0.0010	0.0348
0.3667	-0.0292	2.6656	0.0011	0.0348
0.4	-0.0320	2.6655	0.0011	0.0348
0.4333	-0.0401	2.6655	0.3163	0.0254
0.4667	-0.0486	2.6655	0.3825	0.0138
0.5	-0.0572	2.6654	0.4507	0.0000

formulation can be adopted for differential equations with constant coefficients as well as variable coefficients. The through thickness variation of displacements as well as stresses presented here can work as benchmark for other beam theories and finite element solution. Typical design guideline of aspect ratio being less than 1/20 can be considered appropriate for thin beam designs as shown by the present analysis.

Table 19 Variation of displacements and stresses through the depth of sandwich beam with orthotropic core for $\eta = 1/20$

\bar{z}	$\bar{u}(x = 0)$	$\bar{w}(x = L/2)$	$\bar{\sigma}_x(x = L/2)$	$\bar{\tau}_{xz}(x = 0)$
-0.5	0.0735	1.4229	-0.2889	0.0000
-0.4667	0.0669	1.4230	-0.2628	0.0065
-0.4333	0.0604	1.4231	-0.2372	0.0123
-0.4	0.0539	1.4232	-0.2119	0.0176
-0.3667	0.0494	1.4233	-0.0003	0.0176
-0.3333	0.0449	1.4233	-0.0003	0.0176
-0.3	0.0405	1.4234	-0.0002	0.0176
-0.2667	0.0360	1.4235	-0.0002	0.0176
-0.2333	0.0315	1.4235	-0.0002	0.0176
-0.2	0.0270	1.4236	-0.0001	0.0176
-0.1667	0.0225	1.4236	-0.0001	0.0176
-0.1333	0.0180	1.4236	-0.0001	0.0176
-0.1	0.0136	1.4237	0.0000	0.0176
-0.0667	0.0091	1.4237	0.0000	0.0176
-0.0333	0.0046	1.4237	0.0000	0.0176
0	0.0001	1.4237	0.0001	0.0176
0.0333	-0.0044	1.4237	0.0001	0.0176
0.0667	-0.0089	1.4237	0.0001	0.0176
0.1	-0.0133	1.4237	0.0002	0.0176
0.1333	-0.0178	1.4237	0.0002	0.0176
0.1667	-0.0223	1.4237	0.0002	0.0176
0.2	-0.0268	1.4236	0.0003	0.0176
0.2333	-0.0313	1.4236	0.0003	0.0176
0.2667	-0.0358	1.4235	0.0003	0.0176
0.3	-0.0403	1.4235	0.0004	0.0176
0.3333	-0.0448	1.4234	0.0004	0.0176
0.3667	-0.0492	1.4234	0.0004	0.0175
0.4	-0.0537	1.4233	0.0005	0.0175
0.4333	-0.0602	1.4232	0.2366	0.0123
0.4667	-0.0667	1.4232	0.2623	0.0064
0.5	-0.0733	1.4231	0.2883	0.0000

Table 20 Variation of displacements and stresses through the depth of sandwich beam with orthotropic core for $\eta = 1/50$

\bar{z}	$\bar{u}(x = 0)$	$\bar{w}(x = L/2)$	$\bar{\sigma}_x(x = L/2)$	$\bar{\tau}_{xz}(x = 0)$
-0.5	0.1126	1.0738	-0.1770	0.0000
-0.4667	0.1046	1.0738	-0.1645	0.0025
-0.4333	0.0967	1.0738	-0.1520	0.0049
-0.4	0.0888	1.0738	-0.1396	0.0070
-0.3667	0.0814	1.0739	-0.0002	0.0070
-0.3333	0.0740	1.0739	-0.0002	0.0070
-0.3	0.0666	1.0739	-0.0002	0.0070
-0.2667	0.0592	1.0739	-0.0001	0.0070
-0.2333	0.0518	1.0739	-0.0001	0.0070
-0.2	0.0444	1.0739	-0.0001	0.0070
-0.1667	0.0370	1.0739	-0.0001	0.0070
-0.1333	0.0296	1.0739	-0.0001	0.0070
-0.1	0.0222	1.0739	-0.0001	0.0071
-0.0667	0.0148	1.0739	0.0000	0.0071
-0.0333	0.0074	1.0739	0.0000	0.0071
0	0.0000	1.0739	0.0000	0.0071
0.0333	-0.0074	1.0739	0.0000	0.0071
0.0667	-0.0148	1.0739	0.0000	0.0071
0.1	-0.0222	1.0739	0.0001	0.0070
0.1333	-0.0296	1.0739	0.0001	0.0070
0.1667	-0.0370	1.0739	0.0001	0.0070
0.2	-0.0444	1.0739	0.0001	0.0070
0.2333	-0.0518	1.0739	0.0001	0.0070
0.2667	-0.0592	1.0739	0.0002	0.0070
0.3	-0.0666	1.0739	0.0002	0.0070
0.3333	-0.0740	1.0739	0.0002	0.0070
0.3667	-0.0814	1.0739	0.0002	0.0070
0.4	-0.0888	1.0738	0.0002	0.0070
0.4333	-0.0967	1.0738	0.1520	0.0049
0.4667	-0.1046	1.0738	0.1644	0.0025
0.5	-0.1125	1.0738	0.1769	0.0000

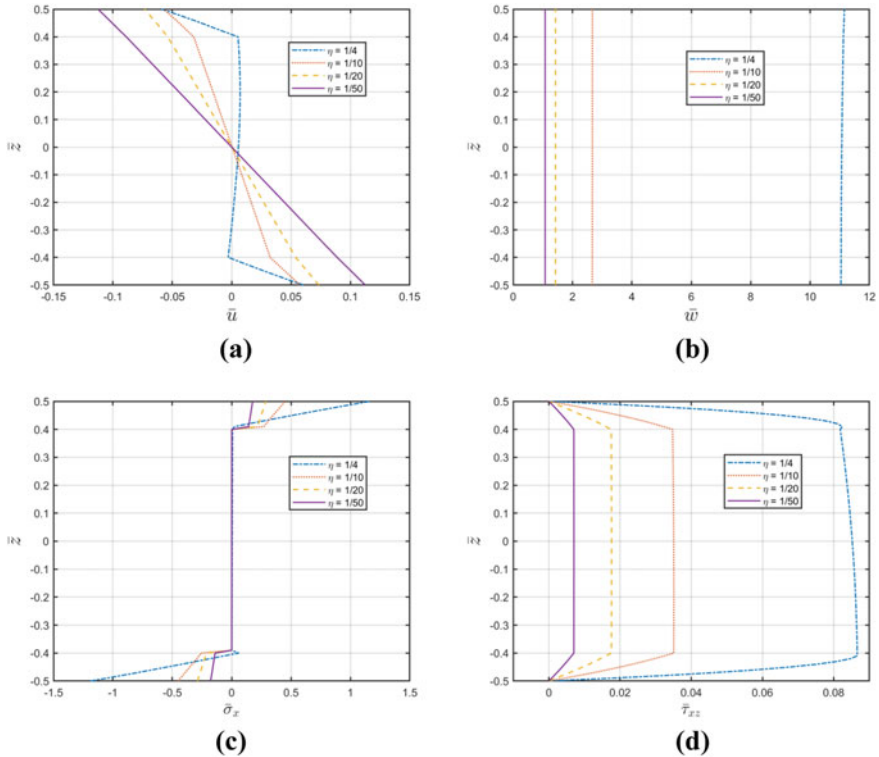


Fig. 4 Variation of normalized (a) in-plane displacement \bar{u} (b) transverse displacement \bar{w} (c) in-plane normal stress $\bar{\sigma}_x$ (d) transverse shear stress $\bar{\tau}_{xz}$ through the thickness of a sandwich beam

References

1. Saint Venant A and Barre de (1856) Memoire sur la flexion des prismes. *J De Math Pures et appl* 2:89–189
2. Silverman IK (1964) Orthotropic beams under polynomial loads. *ASCE J Eng Mech* 90:293–319
3. Hashin Z (1967) Plane an isotropic beam. *ASME J Appl Mech* 34:257–262
4. Gerstner RW (1968) Stresses in composite cantilever. *J Compos Mater* 2:498–501
5. Rao KM, Ghosh BG (1979) Exact analysis of unsymmetric laminated beam. *ASCE J structural* 105:2313–2325
6. Cheng S, Wei X, Jiang T (1989) Stress distribution and deformation of adhesive- bonded laminated composite beams. *ASCE J Eng Mech* 115:1150–1162
7. Holt PJ, Weber JBH (1982) Exact solution to some honeycomb sandwich beam, plate and shell problem. *J Strain Anal Eng* 17:1–8
8. Pagano NJ (1969) Exact solution for composite laminates in cylindrical bending. *J Compos Mater* 3:398–411
9. Srinivas S, Rao G, Rao AK (1970) An exact analysis for vibration of simply-supported homogeneous and laminated thick rectangular plates. *J Sound Vib* 12:187–199
10. Pagano NJ (1970) Influence of shear coupling in cylindrical bending of anisotropic laminates. *J Compos Mater* 4:330–343

11. Sankar BV (2001) An elasticity solution for functionally graded beams. *Compos Sci Technol* 61:689–696
12. Venkataraman S, Sankar BV (2003) Elasticity solution for stresses in sandwich beam with functionally graded core. *AIAA J* 41:2501–2505
13. Kant T, Pendhari SS, Desai YM (2007) On accurate stress analysis of composite and narrow sandwich beams. *Int J Comput Methods Eng Sci Mech* 8:165–177
14. Pagano NJ (1970) Exact solution for rectangular bidirectional composites and sandwich plates. *J Compos Mater* 4:20–34

Flexural Fatigue Analysis of Cross Ply and Angle Ply Laminates



Sammed Patil and Y. T. LomtePatil

Abstract Composite materials are believed to be materials of future with potential application in high performance structure. Composites being light weight and having higher strength to weight ratio proves very efficient and economical. The static strength of laminated composite materials can be calculated easily but it's analysis under cyclic loading is a quite complicated phenomenon. Continuous degradation of material occurs under cyclic loading which causes redistribution of the stresses within the laminate hence failure of single lamina does not indicate failure of entire laminate which in turn increases the complexity of the analysis. Also laminated composite materials being nonhomogeneous and anisotropic its fatigue analysis involves a lot of calculations; this can be reduced with the help of finite element-based software. Plenty of work has been carried out for fatigue analysis of laminated composite materials subjected to axial loading but the flexural fatigue analysis needs some attention. Here, the attempt has been made to perform the flexural fatigue analysis of laminated composite material using finite element-based software ANSYS. The results are presented for cross ply and angle ply laminates with two material combinations, namely, E-Glass epoxy and Carbon epoxy for different aspect ratios.

Keywords Laminated composite · Flexural fatigue analysis · ANSYS · E-glass epoxy

1 Introduction

Flexural fatigue analysis of a cantilever laminated composite beam (formed by stacking different plies together) is subjected to a point load at the free end is carried out. For this purpose, unidirectional, cross ply, and angle ply laminates with different span to depth ratios and stacking sequences are considered. The S–N curves from the literatures are given as an input data while performing fatigue analysis. Constant amplitude fully reversible cyclic loading is applied and stress life-based approach

S. Patil · Y. T. LomtePatil (✉)

Department of Civil Engineering, College of Engineering Pune, Pune, 411005, India
e-mail: lomteyt@gmail.com

© The Author(s), under exclusive license to Springer Nature Singapore Pte Ltd. 2023
M. S. Ranadive et al. (eds.), *Recent Trends in Construction Technology and Management*, Lecture Notes in Civil Engineering 260,
https://doi.org/10.1007/978-981-19-2145-2_86

1171

is used to predict the fatigue life of laminated composite material. These results are obtained for material, namely, E-Glass epoxy. Results are tabulated for each stacking sequence by defining maximum stress in beam and corresponding fatigue life and fatigue life contour plots are shown. Graphs are plotted by varying parameters to understand the behavior under the fatigue for different cases.

Laminated composite materials are believed to be materials of future with potential application in high-performance structures. Laminated composite materials being lightweight and having high directional stiffness as well as high strength to weight ratio are gaining more attention. Fatigue loads for many composite structures are unavoidable so recent designs of composite materials without fatigue analysis are not possible. The heterogeneous and anisotropic nature of laminated composites leads to the formation of different stress levels within the material, which may cause damage modes such as matrix cracking, fiber breakage, delamination, debonding, and ply failure. Laminated composite material under fatigue loading is subjected to continuous degradation of material properties which are responsible for redistribution of the stresses within the laminate so failure of single lamina does not mean failure of entire laminate. This involves a lot of calculation work to make the calculation simple finite element-based softwares helpful. Under fatigue action failure of the material occurs way before the load reaching its ultimate value. So, the fatigue strength of material should be taken into consideration while designing any member subjected to cyclic loading.

The work done by various researchers in the field of fatigue analysis of laminated composite materials is discussed here [1]. The damage mechanism of laminated composite materials has been thoroughly explained by taking different sets of examples and entire idea of fatigue failure is explained [2]. Here, authors have studied flexural fatigue behavior of glass and Kevlar fiber using cross ply laminate. They have also considered the effect of reduction in stiffness for 5% and 10% reduction and studied the effect of the stacking sequence and the reinforcement type on the behavior of cross ply laminates in cyclic loading [3]. In this paper, 3D fatigue progressive damage models are developed for damage accumulation and life of CFRP laminate is studied. Fatigue failure analysis was performed by using a set of Hasin's failure criteria and Ye delamination criteria [4]. In this paper, author prepared FEA model to evaluate damage in composite laminate and predicted fatigue life of laminates with different layup sequence based on fatigue characteristics of longitudinal, transverse, and in plane shear direction [5]. Here authors discussed fatigue life estimation for multidirectional laminates and proposed mathematical models for the improvement of fatigue life of multidirectional laminates. But it is important to note that those models have not considered progressive damage and stiffness degradation occurring throughout the life of the laminate [6]. In this work, the axial fatigue analysis has been done by considering reduction in stiffness after every cycle of loading, and Tsai-Hill failure criteria are used to predict fatigue life of cross and angle ply laminates [7]. This paper discusses the prediction of fatigue response of composites using an empirical strength and stiffness degradation scheme coupled to a cumulative damage accumulation approach. The fatigue analysis was performed using ABAQUS™ finite

element software using a user-defined material subroutine UMAT developed for the material response.

From the literature, it can be seen that most of the work is done on axial fatigue analysis, whereas flexural fatigue analysis needs more attention. Hence in the present paper flexural fatigue analysis of laminated composite material is performed using finite element-based software ANSYS. The cantilever beam of 1 m span and different stacking sequences, subjected to a point load at the free end is considered. The results are presented for the aspect ratios ranging from 5 to 25. A comprehensive comparison of results for unidirectional, cross ply and angle ply laminates with E-Glass epoxy and carbon epoxy material combination is done.

2 Theoretical Formulation

In the present paper, flexural fatigue analysis of the laminated composite member having different stacking sequences and aspect ratio (span to depth ratio) is presented. One end of the flexural member is assumed to be fixed and other is completely free. A point load is applied at the free end of the member. The span and width of the member is held constant, whereas its depth is varied to get the aspect ratios ranging from 5 to 25. The details are given in Fig. 1. The flexural member is assumed to be made up of two materials, namely, E-glass epoxy and carbon epoxy with various laminate arrangements like unidirectional laminate, symmetric cross ply laminate, and angle ply laminate. The details are mentioned in Table 1. A constant amplitude fully reversible cyclic loading is applied to know the flexural fatigue life of the member (as shown in Fig. 2).

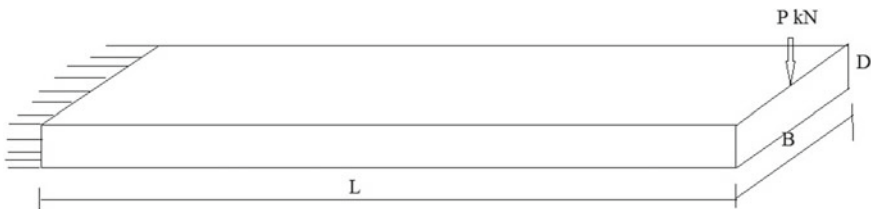


Fig. 1 Flexural member with point load at free end

Table 1 Details of stacking sequence and aspect ratios

Sr. No.	Stacking sequence	Aspect ratio	Actual depth (mm)
1	[0] _s	5	200
2	[90] _s	10	100
3	[0/90/90/0] _s	15	66
4	[+45/-45] _s	20	50
5	[0/30/60/90]	25	40

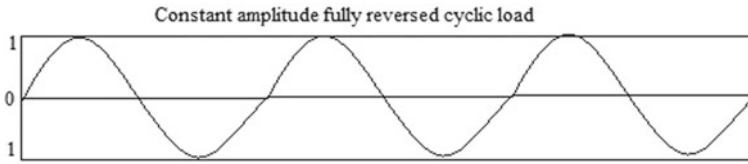


Fig. 2 Type of cyclic loading applied

Table 2 Material properties of E-Glass epoxy

Parameter	Property	Parameter	property
E_{xx}	1.21E + 11 Pa	G_{xy}	4.7E + 09 Pa
E_{yy}	8.6E + 9 Pa	G_{yz}	3.1E + 09 Pa
E_{zz}	8.6E + 9 Pa	G_{xz}	4.7E + 09 Pa
ν_{xy}	0.27	X_T	2.31E + 09 Pa
ν_{yz}	0.4	Y_T/Z_T	2.9E + 07
ν_{xz}	0.27	X_C	-1.08E + 09
		Y_C/Z_C	-1E + 08

Here, the S–N curve-based approach is used to find out flexural fatigue life of laminated composite material under out of plane loading. The S–N curves for laminated composite materials are given as input in the ANSYS software, and flexural fatigue life is determined. The material properties for E-glass epoxy and carbon epoxy are given in Tables 2 and 3, respectively.

Table 3 Material properties of carbon epoxy

Parameter	Property	Parameter	Property
E_{xx}	4.5 E + 10 Pa	G_{xy}	5E + 09 Pa
E_{yy}	1E + 10 Pa	G_{yz}	3.84E + 09 Pa
E_{zz}	1E + 10 Pa	G_{xz}	5E + 09 Pa
ν_{xy}	0.3	X_T	1.11E + 09 Pa
ν_{yz}	0.4	Y_T, Z_T	35E + 07 Pa
ν_{xz}	0.3	X_C	-6.75E + 08 Pa
		Y_C, Z_C	-1.2E + 08 Pa

3 Results

3.1 Validation of Results

In the reference [8], fatigue analysis of E-glass epoxy material is carried out experimentally and the results are presented for different stacking sequences such as [90] 4 s, [0/90/90/0]s, [45/0/0/-45]s, [45/90/-45/0], [0/45/-45/90], and [0/45/90/-45]s. The material properties used by the author are mentioned in Table 2. For this purpose, an axially loaded member having dimensions 500 × 127 × 8 mm and subjected to a tensile load of 70 kN (Fig. 3) is considered. The same problem is analyzed for the validation purpose using ANSYS software and for modeling 8 noded 3D solid 46 element with 3D.O.F is used. Table 4 shows the comparison of results from which it can be seen that the results obtained by ANSYS are in good agreement with the literature.

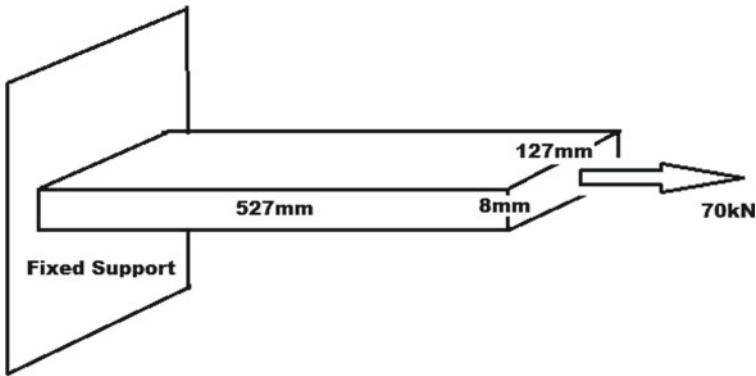


Fig. 3 Fixed at one end and axially loaded

Table 4 Validation of results with results

Sr. No.	Stacking sequence	No. of cycles (N) By reference [8]	ANSYS results (N)	Percentage error
1	[90]4 s	1.2944E + 6	1.1949E + 6	-7.68
2	[0/90/90/0]s	1.936E + 6	1.998E + 6	3.2
3	[45/0/0/-45]s	7.6674E + 5	7.8449E + 5	2.41
4	[45/90/-45/0]	9.4883E + 5	9.1883E + 5	-3.161
5	[0/45/-45/90]	2.1943E + 6	2.1089E + 6	-3.71
6	[0/45/90/-45]s	1.275E + 6	1.2068E + 6	-5.34

3.2 Present Work Results and Discussion

In the present work, the results are presented for E-glass epoxy and carbon epoxy material with the aspect ratio ranging from 5 to 25 with an increment of 5. The results are given in the form of maximum stress developed in the laminate and fatigue life in terms of number of cycles. Table 5 presents the results for unidirectional laminate where all the fibers are oriented along longitudinal direction $[0]_s$, whereas Table 6 shows the results for unidirectional laminate with fibers oriented along transverse direction $[90]_s$.

Table 7 gives the results for cross ply laminate $[0/90]_s$. Tables 8 and 9 present the results for angle ply laminates with symmetric $[45/-45]_s$ and asymmetric $[0/30/60/90]$ stacking sequences, respectively.

From the results obtained it can be seen that the fatigue life for the laminate where fibers are oriented along longitudinal direction is maximum compared to all other stacking sequences, as the fibers are oriented along the longitudinal direction they help in resisting flexural action in a better manner. Contrarily for laminate with fibers oriented in a transverse direction least fatigue life is obtained.

Table 5 Fatigue life of $[0]_s$ laminate

Stacking sequence	Span to depth ratio	E-glass Epoxy	Carbon epoxy		
		Max stress (MPa)	Fatigue life in No. of cycles (N)	Max stress (MPa)	Fatigue life in No. of cycles (N)
$[0]_{200s}$	5	30.54	1E + 10	48.79	1E + 10
$[0]_{100s}$	10	46.04	4.91E + 09	74.24	7.09E + 09
$[0]_{66s}$	15	76.11	6.887E + 7	100.72	5.71E + 8
$[0]_{50s}$	20	130.67	8.57E + 5	166.71	3.84E + 5
$[0]_{40s}$	25	205.58	43,336	275.02	47,463

Table 6 Fatigue life of $[90]_s$ laminate

Stacking sequence	Span to depth ratio	E-glass Epoxy		Carbon epoxy	
		Max stress (MPa)	Fatigue life in No. of cycles (N)	Max stress (MPa)	Fatigue life in No. of cycles (N)
$[90]_{200s}$	5	38.82	1E + 10	56.79	1E + 10
$[90]_{100s}$	10	56.51	8.64E + 8	87.42	5.94E + 8
$[90]_{66s}$	15	86.04	1.495E + 6	115.67	1.675E + 7
$[90]_{50s}$	20	142.88	2.39E + 5	183.44	9.22E + 4
$[90]_{40s}$	25	218.63	30,099	296.27	30,274

Table 7 Fatigue life of [0/90]_s

Stacking sequence	Span to depth ratio	E-glass Epoxy		Carbon epoxy	
		Max stress (MPa)	Fatigue life in No. of cycles (N)	Max stress (MPa)	Fatigue life in No. of cycles (N)
[0/90] _{100s}	5	36.73	1E + 10	53.44	1E + 10
[0/90] _{50s}	10	52.19	1.221E + 9	83.58	9.06E + 8
[0/90] _{33s}	15	83.47	6.96E + 6	111.94	3.19E + 7
[0/90] _{25s}	20	140.51	3.9737E + 5	179.09	1.33E + 5
[0/90] _{20s}	25	215.72	35,889	291.78	34,704

Table 8 Fatigue life of [+45/-45]_s

Stacking sequence	Span to depth ratio	E-glass Epoxy		Carbon epoxy	
		Max stress (MPa)	Fatigue life in No. of cycles (N)	Max stress (MPa)	Fatigue life in No. of cycles (N)
[45/-45] _{100s}	5	32.67	1E + 10	52.79	1E + 10
[45/-45] _{50s}	10	49.93	2.617E + 9	79.21	1.05E + 9
[45/-45] _{33s}	15	80.37	1.4774E + 7	107.38	6.65E + 7
[45/-45] _{25s}	20	136.21	5.778E + 5	174.23	4.18E + 5
[45/-45] _{20s}	25	210.96	41,230	286.93	39,044

Table 9 Fatigue life of [0/30/60/90]_s

Stacking sequence	Span to depth ratio	E-glass Epoxy		Carbon epoxy	
		Max stress (MPa)	Fatigue life in No. of cycles (N)	Max stress (MPa)	Fatigue life in No. of cycles (N)
[0/30/60/90]	5	31.82	1E + 10	53.44	1E + 10
	10	47.24	4.04E + 9	76.27	4.55E + 9
	15	78.18	2.6732E + 7	103.37	9.67E + 7
	20	133.23	7.389E + 5	170.24	8.47E + 5
	25	207.37	42,085	280.96	43,296

The cross ply laminate will have less fatigue life than that of angle ply laminate as it contains alternate ply's oriented along transverse direction that makes the cross ply laminate susceptible to the fiber matrix debonding. Among the angle ply laminate, the laminate with gradual introduction of angle leads to better fatigue resistance compared to laminate where sudden change in angle is provided. In all stacking sequences, it is observed that as the span to depth ratio increases fatigue life of the flexural member decreases which is quite obvious.

In Figs. 4 and 5, numbers 1, 2, 3, 4, 5 indicate stacking sequences [0]s, [90]s, [0/90]s, [45/-45]s, [0/30/60/90], respectively.

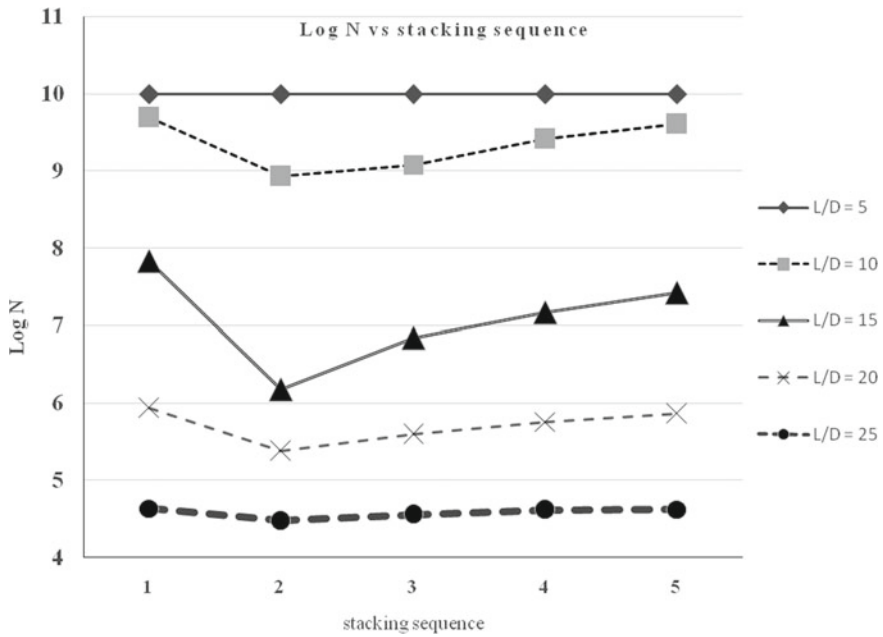


Fig. 4 Log N versus stacking sequence for different Span to depth ratio for E-glass epoxy material

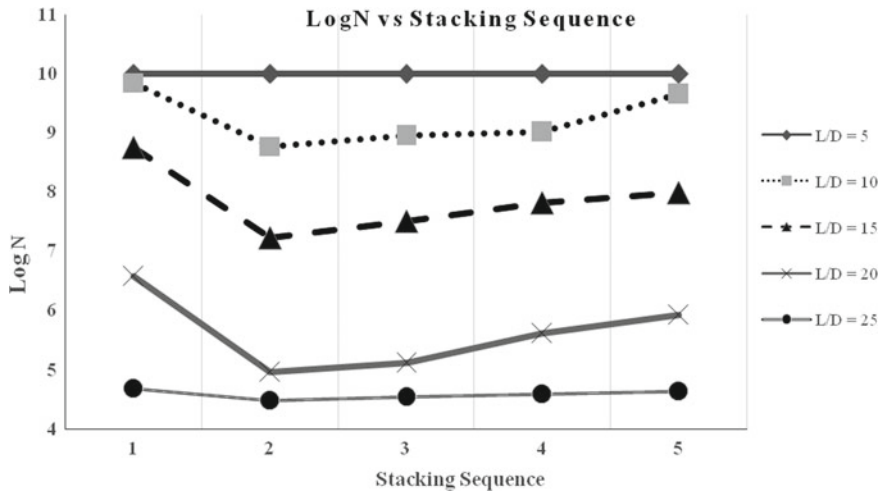


Fig. 5 Log N versus stacking sequence for different Span to depth ratio for carbon epoxy material

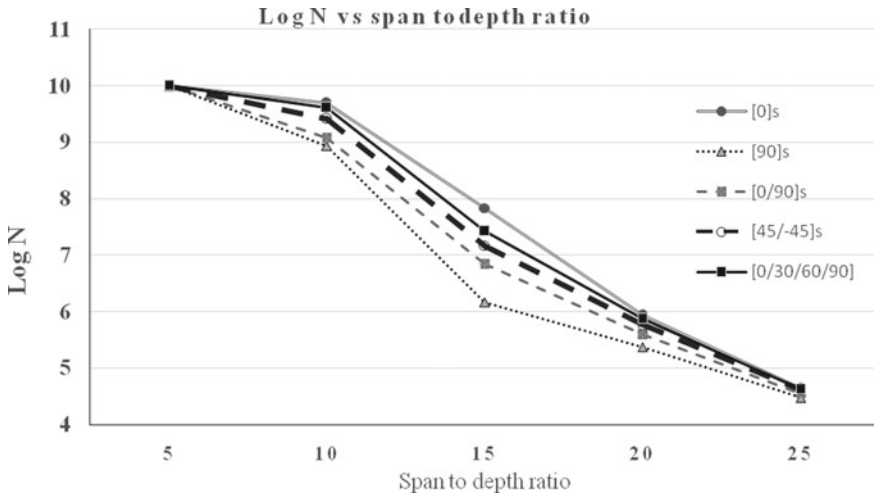


Fig. 6 Log N versus Span to depth ratio for different stacking sequence for E-glass epoxy material

Above results are also expressed in the graphical form for better understanding. Figure 4 shows the variation of fatigue life with different stacking sequences for various aspect ratios for E-glass epoxy material, whereas Fig. 5 gives these results for carbon epoxy material.

From the graph, it can be clearly seen that for aspect ratio 25 there is no significant difference between the fatigue life for all stacking sequences. From this, it can be concluded that for thin flexural members fatigue life is not affected by stacking sequences. Figures 6 and 7 show the variation of fatigue life with different span to depth ratio.

4 Conclusion

Flexural fatigue life is obtained for 5 different stacking sequence and 5 different span to depth ratios for two materials, namely, E-glass epoxy and carbon epoxy. The Laminated composite beam with point load at free end is modeled in ANSYS software and results for fatigue life are obtained. The following conclusions are drawn from the above study.

1. Unidirectional laminate with fiber orientation along longitudinal direction has the highest fatigue life among all stacking sequences. On the other hand, unidirectional laminate with fiber orientation in the transverse direction has the lowest fatigue life. So when the fibers are oriented along the longitudinal direction which is also the direction along which fiber bends, they help to resist the flexural action in a better manner.

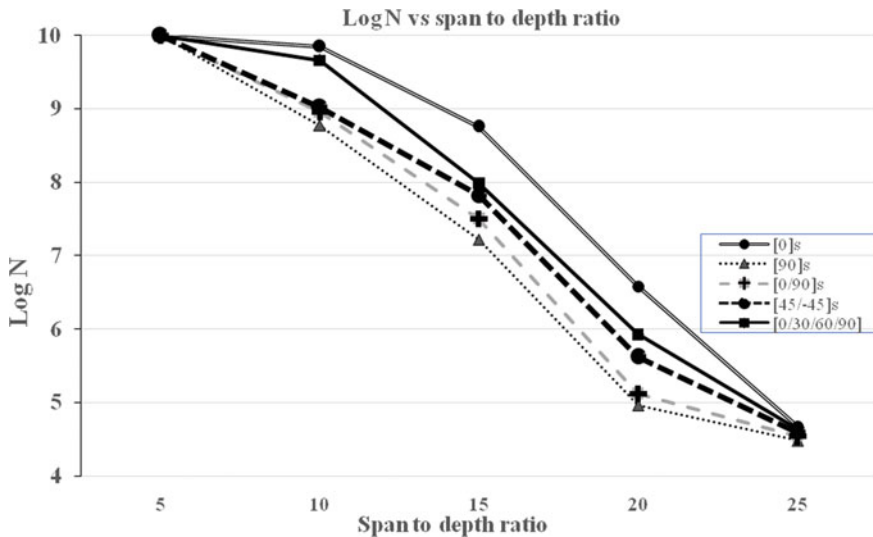


Fig. 7 Log N versus Span to depth ratio for different stacking sequence for carbon epoxy material

2. Among the angle ply and cross ply laminate the [0/30/60/90] configuration will have better fatigue strength than that of [45/-45]s and [0/90]s laminate because of the gradual introduction of angle.
3. In all stacking sequences, it is observed that as the span to depth ratio increases fatigue life of the flexural member decreases which is quite obvious.

References

1. Talreja R (1981) Fatigue of composite material: damage mechanism and fatigue life diagram. *Pro Royal Soc London A* 378:461–47
2. Bezazi AR, El Mahi A, Berthelot JM, Bezzazic B (2003) Flexural fatigue behavior of cross ply laminate an experimental approach. *Strength Mater* 35(2)
3. Toumi RB, Renard J et al (2013) Fatigue damage modelling of continuous E-glass fibre/epoxy composite. *Procedia Eng* 66:723–736
4. Lian W, Yao W (2010) Fatigue life prediction of composite laminates by FEA simulation method. *Int J Fatigue* 32:123–133
5. Arda Deveci H, Secil Artem H (2018) On the estimation and optimization capabilities of the fatigue life prediction models in composite laminates. *J Reinf Plast Compos* 0(0):1–18
6. Alireza AA, Sayid A (2011) Experimental and finite element analysis approach for fatigue of unidirectional fibrous composites. *Mech Mater* 87:106–112

7. Vasantha Kumar K, Ram Reddy P (2014) Flexural fatigue analysis of carbon/Epoxy angle Ply laminates. *Int J Eng Res Dev* 10(7):52–62
8. Plumtree H, Cheng GX (1999) Fatigue parameter for off-axis unidirectional fiber reinforced composites. *Int J Fatigue* 21:844–856

Recent Trends in Transportation and Traffic Engineering

Review on Mechanisms of Bitumen Modification: Process and Variables



N. T. Bhagat and M. S. Ranadive

Abstract The use of bitumen in road construction has been done since over a century, and the modification of bitumen has started in the 1950s. Bitumen plays a very substantial role in various aspects of road construction quality such as adhesion, friction, durability, ageing resistance and strength of pavement. It has been the subject of research to modify the bitumen for increasing these benefits and decreasing the damages in pavements like rutting, loss of strength, cracking, etc. Many modifiers like polymers, plastics, nano materials, organic wastes, oils and other waste materials have been used to modify bitumen over the years. However, the mechanisms of bitumen modification include certain processing conditions and variables like mixing temperature, mixing time, shear rate, etc. that affects the quality and performance of resulting modified bitumen. This paper presents an overview of the processes used and the processing conditions that are adopted for bitumen modification. It also reviews the effects on the performance of the resulting modified bitumen caused due to variations in the processing conditions and factors.

Keywords Bitumen · Modification process · Modifiers · Processing conditions

1 Introduction

Bitumen is the oldest engineering material known to be used as sealant, adhesive, preservative, waterproofing agent, and paving material for road construction. Earlier natural bitumen was used directly as obtained from the Earth's surface. Later on, the use of refined bitumen started in early 1900s in USA that was obtained from the refinement of crude oil [25]. After that, world utilization of bitumen increased rapidly over the years, especially as a binder in pavement construction. Bitumen binders have

N. T. Bhagat (✉) · M. S. Ranadive
Department of Civil Engineering, College of Engineering Pune, Pune 411005, India
e-mail: bhagat.nikita14@gmail.com

M. S. Ranadive
e-mail: msr.civil@coep.ac.in

a varying range of thermal and mechanical demands for road construction. Defects in pavements like rutting due to high temperatures, fatigue, and propagation of cracks due to low temperatures are the results of the thermal susceptibility of bitumen in addition to repeated traffic loading [11]. In order to reduce these defects and increase the performance characteristics of pavement such as strength, durability, moisture resistance and resistance to rutting and fatigue cracking, the enhancement of binder and bituminous mixtures has become a necessity in this era of changing weather conditions and increased traffic on roads. Also, addition of modifiers in the form of municipal solid wastes, plastic wastes, organic wastes, fibres and rubber wastes in bituminous binders and mixtures helps to reduce the solid waste pollution from the environment and proves to be an effective way of waste management [12]. Ranadive et al. [18] proposed the use of fibres extracted from refrigerator door panels and waste plastic in the stone mastic asphalt and asphaltic concrete mixtures. They found the Marshall stability and indirect tensile strength of the mixtures increased by addition of fibres from the refrigerator door panels. Similarly, lot of research is being done to improve the properties of bitumen by modifying it with various modifying agents such as polymers, recycled oils, organic waste, nanomaterials, etc. to improve the moisture damage resistance, adhesion, rutting resistance, fatigue resistance and strength of binders. Kulkarni and Ranadive [11], modified VG10 cutback bitumen using pyrolytic oil obtained from low density polyethylene (LDPE) to improve the shear strength of the conventional cutback.

The pristine characteristics of bitumen depend majorly on the production and processing mechanisms as well as the crude oil characteristics [2, 17]. Similarly, the improved performance characteristics of the modified bitumen is dependent on the compatibility between modifier and base bitumen, which majorly depends on the circumstances of their polarity, particle size, morphology, surface energy, interfacial stability, etc. Nowadays, the factors such as procedure of modification, preparation temperature, shear rates of mixing, etc. are found to be responsible for the improved or enhanced characteristics of the modified bitumen as well [3]. This paper focuses on the review of the bitumen modification process and factors of modification procedures that are responsible for the behaviour of the resulting modified bitumen.

2 Process

The susceptibility to temperature changes is a virtue of bitumen on which its performance depends, and the performance characteristics of bitumen are affected by the rate of the temperature changes and its range. Indian road applications need a range of 0–50 °C for material of pavement, whereas a 60–150 °C range of temperature is necessary for mixing, compaction, pumping and other intermediate operations. Hence, the characteristics of bitumen that help to withstand the deformation occurring because of the thermal shocks during the process of applying and operations, determine its performance. Bitumen can be qualified as high-performance grade bitumen depending on the rheological behaviour with respect to temperature changes

[21]. Chemical composition of bitumen consists an intricate linking of majorly polar and non-polar compounds. The feasibility of producing high-performance modified bituminous binder, having correctly balance chemical composition and physical characteristics, depends on the proper selection of crude source and processing conditions.

For stable formulation and obtaining desirable mechanical properties of the bitumen, the chemical compatibility and processing conditions like time, shear and temperature are necessary. The binder composition and mechanical performance of the modified bitumen may alter due to effect of processing variables and in turn may sometimes lead to undesirable in service properties [5]. It is not new to blend, mix or alloy two or more materials to get a new material product with different and enhanced physical and mechanical properties that those of the constituent materials. According to McNally [14], the heat and entropy of mixing are the major driving factors for homogeneity of resulting mixtures. He states that when the components in the mixture are polymers, the entropy change is very small and the heat of mixing alone will be responsible for the homogeneity of the mixture.

Bitumen also contains polymeric compounds that require proper range of temperature for mixing with any type of modifier. Many researchers have used similar procedure of mixing modifier in bitumen using a shear mixer at a temperature range for a specific time. McNally [14], explained why high shear and high processing temperatures were necessary for polymer modification of bitumen. According to the author the polymer modifiers that are most frequent in use for modification such as styrene-butadiene-styrene (SBS), styrene-butadiene rubber (SBR), crumb tire rubber (CR), ethylene vinyl acetate (EVA), low as well as high density polyethylene (LDPE, HDPE), and some other waste polymers, may have a significant effect of the mixing conditions on the resulting blend as well as the cost of production. Hence, high processing temperatures (170–180 °C) and high shear rates are required for reducing the difference of viscosity between polymers and bitumen, and for obtaining suitable polymer dispersions withing the bitumen matrix. He also showed that, the addition of reactive polymers such as isocyanate based reactive polymers require gentle processing conditions as they are in liquid form and they react with the functional groups of bitumen to form chemical bonds. The blends of these reactive polymers with bitumen are prepared using a low shear stirring device at temperatures between 60 and 180 °C.

Guilani et al. [4] used a high shear mixer to blend the bitumen and polyvinyl acetate at 180 °C at a shear mixing rate of 4000 revolutions per minute for quarter of an hour. The bitumen was pre heated to 180 °C before adding the modifier. Rossi et al. [19] prepared organosilicon based surfactant modified bitumen using a shear mixing homogeniser (high speed shear mixer). Bitumen was heated to 150 °C until it was fully flowing and then the modifier was added at a mixing speed of 800–1000 rpm for the next 10 min. Naskar et al. [16] followed the similar procedure of preparing polymer modified bitumen blends, by mixing at a high shear rate of 3500 rpm for 45 min at a temperature of 180 °C with a laboratory mechanical stirrer. They state that the mixing heat energy should not exceed 185 °C and there should be enough mixing time for homogeneous distribution of plastic molecules in the bitumen. Munera and

Ossa [15] prepared SBS polymer, crumb rubber, and polyethylene wax modified bitumen blends by using a conventional mechanical mixer. The binder mixes were mixed at a shear rate of 1200 ± 10 rpm for two hours in case of SBS and CR, while for PW 45 min of shearing time was required. The mixing temperature was kept between 180 and 190 °C for all the blends. Yu et al. [24] prepared asphalt rubber (AR) binder by mixing the crumb rubber with the base binder with the help of a high shear mixer at a shear rate of 4000 rpm at 176 °C for one hour. There is another method of adding polymeric modifiers in the bitumen, which is done by using the oil obtained from the pyrolysis of waste polymers as modifiers. Hadole and Ranadive [7] prepared HDPE pyrolytic oil modified bitumen at a rate of 3000 rpm at 160 °C for 2 h. Al-Sabaei et al. [1] used the tyre pyrolysis oil (TPO) for modifying the conventional 60/70 penetration Grade bitumen. TPO was mixed in the binder using a multi-mix high shear mixer in laboratory. First the binder was heated to 160 °C in oven to achieve sufficient fluidity, then the tyre pyrolysis oil was added and blend was mixed manually for two minutes followed by mixing at 100 rpm for one hour to obtain a homogenous blend of TPO and bitumen. Hadole et al. [6] prepared pyro-oil modified VG30 bitumen at a temperature of 150 °C at 5000 rpm for first 15 min and then at 3000 rpm for the next 5 min to ensure proper mixing of the oil in bitumen. You et al. [23] fabricated asphalt nanocomposite binder, by adding nano clay in base asphalt using a high shear mixer. The base binder was first heated to 160 °C till it was liquid, then the nano clay was blended in it at a rate of 2500 rpm for 3 h so that the inserted montmorillonite (MMT) nano clay is dispersed properly. Saltan et al. [20] used high shear mixer to prepare ZnO nano particles modified bitumen at a rate of 4000 rpm for 2 h at 160 °C. Kavussi and Barghabany [9] used organo-montmorillonite nano clay to prepare modified bitumen at high shear rate of 5200 rpm, for 30 min at a temperature of 155 °C. Khapne et al. [10] used a high shear mixer for blending HDPE pyro-oil into base bitumen VG30 at a shear rate of 3000 rpm at 160 °C for 15 min.

3 Processing Variables

The important processing variables that determine the properties and behaviour of the modified binder are as follows.

3.1 *Mixing Temperature*

Shaffie et al. [22] examined the effect of varying processing variables on the physical properties of modified bituminous binder. The authors used an 80/100 penetration grade bitumen and modified it with natural rubber latex at two different processing temperatures of 140 and 160 °C. The resulting blend was tested for physical properties such as softening point, penetration and penetration index. Both softening point

and penetration index values (PI) have found to be increased with increase in mixing temperature. The higher PI value indicates more resistance to temperature susceptibility. Hence the higher temperature of 160 °C was found more suitable for the modification process. Martin-Alfonso et al. [13] studied the effect of temperature at the time of mixing on the reactive polymer modified bitumen. They recorded rheokinetics curves at different processing temperatures for the blending of bitumen and polymer. A varying temperature range of 60–180 °C was adopted for preparation of modified bitumen. The results showed, that low processing temperature led to normalized torque increase, while higher processing temperature led to a low increase in the torque and faster modification process. When the mixing temperature is low, larger asphaltene particles will react with other higher molecules, resulting an increase in the viscosity and torque of mixing. While with high processing temperature (180 °C), the rate of reaction increases and the viscosity lowers, with a low increase in torque. Hence high processing temperature is recommended. Gonzales et al. [5] investigated the effect of processing variables on the rubber and PMB. They found that increase in temperature reduces the amount of insoluble material in the binder and also allows more rubber and polymer digestion. However, no effect was observed on the softening point and penetration of the binder due to increased process temperature, signifying very little influence over ageing. They observed that processing temperature increase between 180 and 200 °C didn't modify linear viscoelastic behaviour of the modified binder and a significant lowering in the viscosity had been observed up to 200 °C corresponding to the amount of polymer digestion increase. There is an increase in viscosity and viscoelastic behaviour due to ageing phenomenon, whereas the digestion of rubber/polymer have a reverse effect of decreasing the same, which in turn means that the effect of ageing in these conditions is less significant than that of digestion. However, further increase in processing temperature up to 210 °C causes the modified binder to have an increased viscosity as the effect of ageing dominates. It was observed that the highest amount of polymer digestion reached up to 200 °C, and any further increase in processing temperatures will not improve the binder.

3.2 Mixing Time

The effects of two different mixing times 30 min and 60 min, keeping the mixing speed constant, on the physical properties of modified bitumen were observed [22]. They found that for longer mixing time from 30 to 60 min, the softening point and penetration value increased. This was due to better dispersion of natural rubber latex modifier within the bitumen for longer mixing time. They found that the bitumen showed improved physical properties at higher temperature of 160 °C for more processing time of 60 min. Gonzales et al. [5] examined the results of using different mixing times ranging from 15 to 120 min on the characteristics of polymer and rubber blended bitumen. It was observed that at low temperatures, the viscosity value remains practically similar for low mixing time. However, more than 30 min processing times, show an increase in the viscosity exponentially, which is less

marked at 135 °C, than at 60 °C. In other words, viscosity remains unchanged for a minimum processing time of 45 min, whereas it increases with an increase in a further mixing time, at low temperatures. Whereas, for higher temperatures (180 °C), viscosity does not show a much higher increase for processing times up to 45 min. But high mixing temperature may cause the binder to undergo primary ageing.

3.3 *Shear Rate/Speed*

Shaffie et al. [22] observed the effect of four different mixing shear rates of 500, 1000, 1500, and 2000 rpm on the physical properties of the modified bitumen. They found that mixing speeds have considerable effect on the properties. Softening point value increased significantly after a specified mixing speed, whereas the shear rate of blending did not show any considerable effect on the penetration value which showed up and down trend during the test. They determined the optimum shear rate of mixing using the penetration index values from softening point and penetration values, and found the optimum mixing shear rate to be 1270 rpm. Jamal and Giustozzi [8] studied the effect of two different shear rates of 700 rpm and 3500 rpm on the rheological performance of the crumb rubber modified binder. It was found that there was almost no effect on the complex shear modulus when the binder was mixed at low shear rate of 700 rpm. However, the complex shear modulus was found to be similar to that of neat binder when the higher shear rate of 3500 rpm was used for mixing. The ageing analysis of different shear rates indicated that higher shear rate enhances the ageing. They concluded that shear rate/ mixing speed have a significant influence on the performance of the binder, and the complex shear modulus of the modified binder increases along with ageing, and the phase angle decreases at higher mixing rates.

4 **Summary and Conclusions**

This study was mainly focussed on the common methods or processes adopted for the modification of standard base bitumen with different modifiers, and the processing conditions that are necessary for the preparation of modified bitumen. We reached at following conclusions;

- The mixing temperature, mixing time, and shear rate of mixing are the major processing conditions that are significant for the process or mechanism of modification.
- The first and foremost important thing to know about these three processing conditions is that the performance of the resulting modified bitumen, physical and rheological, is dependent on the interdependence of the variations in mixing time, temperature and shear rate.

- Different types of modifiers require different mixing temperatures, mixing time, and mixing speeds depending upon the chemical reaction, dispersion and reactivity of the modifier with the base bitumen.
- High mixing temperatures ensure proper modifier digestion in the bitumen resulting in lowering of viscosity and making the blend more resistant to temperature susceptibility.
- More mixing time increases the viscosity at low processing temperatures, whereas more mixing time up to 45 min does not have a considerable effect on viscosity with high processing temperatures.
- Shear rate imparts a considerable influence on the properties of modified bitumen. Higher shear rate mixing gives a similar complex modulus as that of base bitumen. Ageing of the bitumen increases at higher shear rates along with the rutting characteristics.
- High mixing temperatures and high shearing rates are usually required for decreasing the difference in viscosities of the bitumen and modifiers with optimum processing time for proper dispersion and reaction of the modifier within the bitumen matrix.

References

1. Al-Sabaei AM, Napiah MB, Sutanto MH, Alaloul WS, Yusoff NIM, Khairuddin FH, Memon AM (2021) Evaluation of the high-temperature rheological performance of tire pyrolysis oil-modified bio-asphalt. *Int Jof Pavem Eng* 1–16
2. Carrera V, Partal P, García-Morales M, Gallegos C, Pérez-Lepe A (2010) Effect of processing on the rheological properties of poly-urethane/urea bituminous products. *Fuel Process Technol* 91(9):1139–1145
3. Fang C, Liu P, Yu R, Liu X (2014) Preparation process to affect stability in waste polyethylene-modified bitumen. *Constr Build Mater* 54:320–325
4. Giuliani F, Merusi F, Filippi S, Biondi D, Finocchiaro ML, Polacco G (2009) Effects of polymer modification on the fuel resistance of asphalt binders. *Fuel* 88(9):1539–1546
5. González V, Martínez-Boza FJ, Gallegos C, Pérez-Lepe A, Páez A (2012) A study into the processing of bitumen modified with tire crumb rubber and polymeric additives. *Fuel Process Technol* 95:137–143
6. Hadole HP, Suryawanshi SD, Khapne VA, Ranadive MS (2021) Moisture damage resistance of short-term aged pyro-oil–modified bitumen using rolling thin film oven by surface free energy approach. *J Mater Civ Eng* 33(10):04021268
7. Hadole HP, Ranadive MS (2019), Analysis of ageing mechanism of HDPE pyro-oil modified bitumen compared to VG30 based on fourier transform infrared spectrum. In: 5th national conference of transportation research group India. CTRG, Bhopal
8. Jamal M, Giustozzi F (2020) Low-content crumb rubber modified bitumen for improving Australian local roads condition. *J Clean Prod* 271:122484
9. Kavussi A, Barghabany P (2016) Investigating fatigue behavior of nanoclay and nano hydrated lime modified bitumen using LAS test. *J Mater Civ Eng* 28(3):04015136
10. Khapne V, Hadole H, Ranadive M (2020) Assessment of anti-stripping property of pyro-oil modified bituminous mixes using surface free energy approach. In: International conference on transportation and development 2020, pp 127–137. American Society of Civil Engineers, Reston, VA

11. Kulkarni SB, Ranadive MS (2020) Modified cutback as tack coat by application of pyro-oil obtained from municipal plastic waste: experimental approach. *J Mater Civ Eng* 32(5):04020100
12. Kulkarni SB, Ranadive MS (2021) A feasibility study towards the application of municipal waste pyrolysis oil in bituminous pavement. In: *Civil infrastructures confronting severe weathers and climate changes conference*, pp 130–147. Springer, Cham
13. Martín-Alfonso MJ, Partal P, Navarro FJ, García-Morales M, Bordado JCM, Diogo AC (2009) Effect of processing temperature on the bitumen/MDI-PEG reactivity. *Fuel Process Technol* 90(4):525–530
14. McNally T (ed) (2011) *Polymer modified bitumen: properties and characterisation*. Elsevier
15. Munera JC, Ossa EA (2014) Polymer modified bitumen: optimization and selection. *Mater Des* 1980–2015(62):91–97
16. Naskar M, Chaki TK, Reddy KS (2010) Effect of waste plastic as modifier on thermal stability and degradation kinetics of bitumen/waste plastics blend. *Thermochim Acta* 509(1–2):128–134
17. Porto M, Caputo P, Loise V, Eskandarsefat S, Teltayev B, Oliviero Rossi C (2019) Bitumen and bitumen modification: A review on latest advances. *Appl Sci* 9(4):742
18. Ranadive MS, Hadole HP, Padamwar SV (2018) Performance of stone matrix asphalt and asphaltic concrete using modifiers. *J Mater Civ Eng* 30(1):04017250
19. Rossi CO, Caputo P, Baldino N, Szerb EI, Teltayev B (2017) Quantitative evaluation of organosilane-based adhesion promoter effect on bitumen-aggregate bond by contact angle test. *Int J Adhes Adhes* 72:117–122
20. Saltan M, Terzi S, Karahancer S (2019) Mechanical behavior of bitumen and hot-mix asphalt modified with zinc oxide nanoparticle. *J Mater Civ Eng* 31(3):04018399
21. Selvavathi V, Sekar VA, Sriram V, Sairam B (2002) Modifications of bitumen by elastomer and reactive polymer—a comparative study. *Pet Sci Technol* 20(5–6):535–547
22. Shaffie E, Arshad AK, Alisibramulisi A, Ahmad J, Hashim W, Abd Rahman Z, Jaya RP (2018) Effect of mixing variables on physical properties of modified bitumen using natural rubber latex. *Int J Civil Eng Technol* 9(7):1812–1821
23. You Z, Mills-Beale J, Foley JM, Roy S, Odegard GM, Dai Q, Goh SW (2011) Nanoclay-modified asphalt materials: preparation and characterization. *Constr Build Mater* 25(2):1072–1078
24. Yu H, Leng Z, Zhou Z, Shih K, Xiao F, Gao Z (2017) Optimization of preparation procedure of liquid warm mix additive modified asphalt rubber. *J Clean Prod* 141:336–345
25. Zhu J, Birgisson B, Kringos N (2014) Polymer modification of bitumen: advances and challenges. *Eur Polymer J* 54:18–38

Alkali Activated Black Cotton Soil with Partial Replacement of Class F Fly Ash and Areca Nut Fiber Reinforcement



B. A. Chethan, A. U. Ravi Shankar, Raghuram K. Chinnabhandar, and Doma Hemanth Kumar

Abstract Alkali activation has received great attention for improving the soil properties with suitable precursor materials. Industrial byproduct class F fly ash was suitably utilized to improve Black Cotton (BC) soil properties along with ordinary Portland cement by various researchers. However, the CO₂ emission associated with cement production has enforced the evaluation of alternative binders. Laboratory investigations were conducted on BC soil by admixing various fly ash dosages (0–50%) and reinforcing the mix with 0.5% areca nut fiber. Alkali activator solution prepared using 8 molar sodium hydroxide solution (SH) and sodium silicate solution (SS) at 1.5 SS/SH ratio showed significant improvement in Unconfined Compressive Strength (UCS) of stabilized BC soil on 7 and 28 days curing. The reinforcement was effective in improving the flexural strength of stabilized mixes. Exorbitant unsoaked California Bearing Ratio (CBR) values were observed on 28 days of curing. However, the samples could retain low soaked CBR values despite reinforcement. Scanning Electron Microscope (SEM) images showed the reduction of shrinkage cracks and strong bonding of fibers in the stabilized mix. X-Ray Diffraction (XRD) patterns evidenced the formation of various hydration products due to the alkali reaction, which resulted in the high strength gain of mixes at ambient temperature curing. The leaching of mineral constituents from the set mix lead to the failure of durability samples. Due to nondurability, the alkali activation with a selected precursor cannot suit pavement materials requirements.

Keywords Alkali solution · Black cotton soil · Strength · Durability · SEM · XRD

1 Introduction

The stable and durable foundation soils are essential for the construction of any civil engineering structure. Soil stabilization is widely used to improve desirable properties of soil with various cementitious and marginal materials. In the recent

B. A. Chethan (✉) · A. U. R. Shankar · R. K. Chinnabhandar · D. H. Kumar
Department of Civil Engineering, NITK, Surathkal, India
e-mail: chethanba@gmail.com

© The Author(s), under exclusive license to Springer Nature Singapore Pte Ltd. 2023
M. S. Ranadive et al. (eds.), *Recent Trends in Construction Technology and Management*, Lecture Notes in Civil Engineering 260,
https://doi.org/10.1007/978-981-19-2145-2_88

1193

era, alkali-activated industrial byproduct fly ash is considered as one of the green construction materials. Portland cement utilization can be minimized by the use of fly ash along with a suitable alkali additive. The proper utilization of fly ash can reduce environmental problems due to its reduced disposal [6]. Alkali-activated precursor materials are clinker-free binders, which can greatly reduce CO₂ emissions by 70–90% resulting from cement production [4]. Alkali-activated composites can provide high early-age strength [9]. A low-ordered crystalline structure of sodium aluminum silicate hydrate (NASH) gel is a common product resulting from the alkali activation process [17]. The use of fly ash in the black cotton soil can control its swelling [5]. BC soil's inherent volume change behavior due to moisture content variations reduces its workability, strength, and suitability for construction, which can be suitably improved with fly ash geopolymer [11]. The use of 7.5 molar NaOH solution for alkali-activated cement using fly ash for improvement of silty sand was considered to give better strength at a lesser cost [12]. An optimum SS/SH ratio of 1.5 was suitable for a fly ash geopolymer [11]. When the fly ash was admixed to BC soil, the rise in stiffness and reduction in the free swell index were observed due to reduced water affinity by particle flocculation [13].

As a ground improvement technique, natural coir fibers are effectively utilized with different cementitious compounds due to their low cost and abundant availability [14]. Cellulose percentage governs natural fiber's tensile strength, and lignin percentage governs biodegradation resistance [7]. The fiber reinforcement can greatly reduce bare soil's crack propagation potential [8]. Along with improved strength, stabilized soil's brittleness can be decreased by using natural coir fiber reinforcement [2]. The use of fibers is an economical and eco-friendly means of soil improvement. The formation of the spatial thread bridge network enhances the particle holding capacity around the fiber surface and results in strength improvement of alkali-activated BC soil with class F fly ash and slag mixes [15]. Areca nut fiber reinforcement effectively improved the strength, durability, and fatigue life of cement-treated lateritic soil due to enhanced bonding of the mix [10]. Linseed oil treatment was found to increase the interface friction and tensile strength of the treated fibers, which can further contribute to improvement in the strength of stabilized soil [16].

Numerous studies stated the benefit of various fibers for soil reinforcement along with different binders. However, limited studies were reported on areca fiber reinforcement's suitability with fly ash geopolymer to improve BC soils strength and durability. Hence comprehensive research was conducted to evaluate the strength, durability, and fatigue performance of stabilized BC soil. The bonding effect of alkali-activated soil with fiber was studied using flexure, CBR, and durability tests.

2 Materials and Methods

Expansive BC soil was procured from Chikmagalur District, Karnataka. A representative disturbed soil sample was obtained at 0.3 m depth below the ground surface.

Class F fly ash was procured from M/s Udupi thermal power plant, a rich aluminosilicate material suitable for alkali activation. Coarser areca fibers were extracted from mature areca nut shells. Preliminary investigations showed that 0.5% of coarser areca fibers with 25 mm length give a better reinforcing effect. Areca fiber has a density of 1.09 g/cc, an average diameter of 0.35 mm, and tensile strength of 2.2 kN/m². These fibers consist of 35–64.8% hemicellulose and 13–14.8% lignin content [10]. Areca fibers were coated with linseed oil and dried in the oven at 120 °C to obtain rougher morphology. Alkali solution was prepared by using commercially available sodium hydroxide pellets and sodium silicate solution. NaOH pellets were dissolved in a calculated quantity of potable water to prepare 8 molar solution. NaOH pellets reaction with water is exothermic, liberating enormous heat; therefore, it is allowed to cool down. After that, the NaOH solution and Na₂SiO₃ solutions were mixed to obtain a SS/SH ratio of 1.5. Alkali solution prepared was used for stabilization after 24 h. The dry ingredients, namely, BC soil, class F fly ash, and areca fibers, were thoroughly mixed. To this dry mixture, a calculated quantity of alkali solution was added, and mixing is continued. The prepared homogeneous mixture was immediately used for the preparation of specimens without any delay. Compacted samples were cured at ambient room temperature. Stabilized specimens after 3, 7, and 28 days of curing were tested for UCS. The flexural strength of beam specimens was determined after 3, 7, and 28 days of curing by a two-point loading method. Evaluation of CBR was done on 28 days cured specimens. Durability of specimens cured for 7 days was evaluated by conducting wetting–drying and freezing–thawing tests. Fatigue behavior of 28 days cured UCS samples was evaluated using a repeated load testing machine. Changes in the morphology of the stabilized sample were studied using Scanning Electron Microscope (SEM) images. The end products responsible for strength improvement were identified using X-Ray Diffraction (XRD) micrograms (Tables 1 and 2).

3 Experimental Outcomes

3.1 Compaction

Modified Proctor compaction characteristics of BC soil replaced with 0–50% of fly ash along with 0.5% areca fiber reinforcement compacted using water are depicted in Fig. 1. The use of water for compaction instead of alkali solution resulted in insignificant changes in compaction characteristics. The compact packing of the mix at 10% fly ash replacement resulted in the highest density of 18.5 kN/m³. The addition of a higher dosage of fly ash reduced the mix density due to low specific gravity fly ash particles. BC soil with areca fibers has achieved the MDD of 18.1 kN/m³ at the OMC of 16.8%. The OMC of the mix has reduced to 15.3% at 15% fly ash replacement. Further addition of fly ash resulted in an increase in OMC due to the

Table 1 Index properties of BC soil

Test properties	Unit	Test method	Average value
Specific gravity, G _s	–	IS 2720 (Part 3), 1980	2.56
γ _d	kN/m ³	IS 2720 (Part 7), 1980	16.1
OMC	%	IS 2720 (Part 7), 1980	22.2
Liquid limit (LL)	%	IS 2720 (Part 5), 1985	60
Plastic limit (PL)	%	IS 2720 (Part 5), 1985	33
Plasticity index (PI)	%	IS 2720 (Part 5), 1985	27
Shrinkage limit (SL)	%	IS 2720 (Part 6), 1972	23
Gravel (%)	%	IS 2720 (Part 4), 1987	2
Sand (%)	%	IS 2720 (Part 4), 1987	26
Silt (%)	%	IS 2720 (Part 4), 1987	68
Clay	%	IS 2720 (Part 4), 1987	4
Free swell index (FSI)	%	IS 2720 (Part 40), 1977	58
Organic content	%	IS 1498 (1970)	2.25
Indian standard soil classification system	–	IS 1498 (1970)	MH

Table 2 Chemical properties of BC soil and class F fly ash

Test properties	Unit	BC soil	Class F fly ash
pH	–	8.24	10.7
SiO ₂	%	75.4	70.5
Al ₂ O ₃	%	7.06	10.98
Fe ₂ O ₃	%	2.64	1.84
CaO	%	0.007	0.003
SO ₃	%	0.16	0.15
LOI	%	2.30	1.70

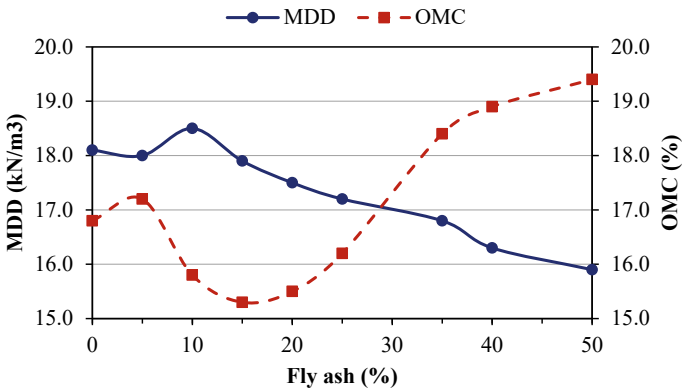


Fig. 1 Variation of modified proctor compaction characteristics of fly ash admixed BC soil

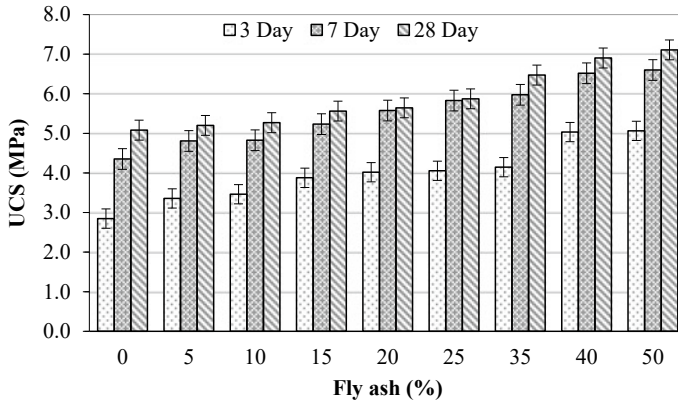


Fig. 2 Variation of UCS of stabilized BC soil

higher demand for water required for particle coating. The higher specific surface area of fly ash particles has contributed to a rise in the OMC.

3.2 UCS

It is revealed that the alkali activation of fiber-reinforced BC soil with fly ash precursor significantly influenced UCS strength gain. On a low curing period of 3 days, the dissolution of aluminosilicate precursor and subsequent geopolymerization was not enough; therefore, low UCS improvements were observed. The use of alkali solution significantly increased the UCS of stabilized samples on 7 days of curing. On further curing, a slight improvement in UCS values was observed for most of the mixes. Higher UCS values were observed at the maximum fly ash replacement level due to the availability of a high quantity of precursor material. On 28 days of curing, the alkali-activated BC soil constituting 50% fly ash along with 0.5% areca fiber reinforcement has achieved a maximum UCS of 7.1 MPa. The reinforcement has made the specimens more ductile when compared to unreinforced ones (Fig. 2).

3.3 CBR

Based on the UCS test results, it was observed that 28 days of curing promotes the UCS of stabilized soil significantly. Hence, CBR samples were prepared and cured for 28 days. The samples became very hard; therefore, excellent plunger penetration resistance was observed for the unsoaked test. Samples with more than 15% fly ash exhibited unsoaked CBR values of more than 100%. Areca fibers can take tensile load; hence the reinforcement formed a strong matrix, due to which resistance to

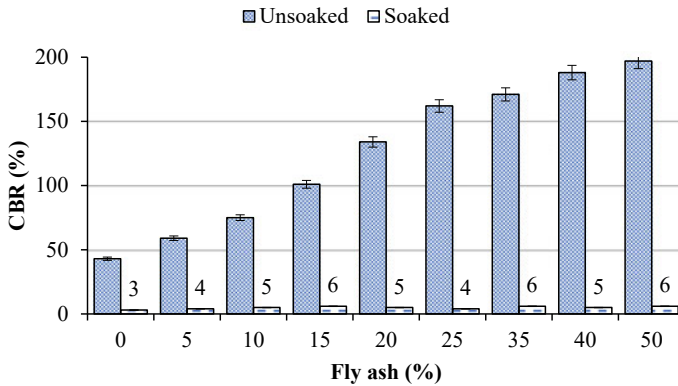


Fig. 3 Variation of CBR of stabilized BC soil

the plunger penetration was increased. When immersed in water, due to the delectation of structure by minerals leaching from the set mix, the samples lost most of their strength. The soaked samples exhibited low resistance to plunger penetration. However, a small improvement in the soaked CBR of the mix was observed when compared to untreated soil (Fig. 3).

3.4 Flexural Strength

Beam specimens of size 76 by 290 mm [1] cured for 3, 7, and 28 days showed significant flexural strength improvement. A high fly ash dosage of 50% has resulted in maximum flexural strength of 1.47 MPa on 28 days of curing. Marginal improvement in flexural strength was noticed after 7 days of curing for all the mixes. BC soil at modified Proctor density exhibited a low flexural strength of <0.02 MPa. The presence of fiber reinforcement along with improvement in flexural strength also reduced the development of shrinkage cracks on curing. Fibers strongly bonded to the stabilized soil and resisted failure during flexural load applications due to their high tensile capacity. Interfacial friction between fibers and bonded soil restricted the pullout of fibers from the set soil. Frictional resistance to the shrinkage was offered due to soil fiber interaction and interlocking mechanism [3] (Fig. 4).

3.5 Fatigue

The fatigue life is defined as the number of repetitions a stabilized material can withstand at the specified load stress. The 28 days cured samples were tested using a fatigue testing machine to evaluate the resistance under repeated load application.

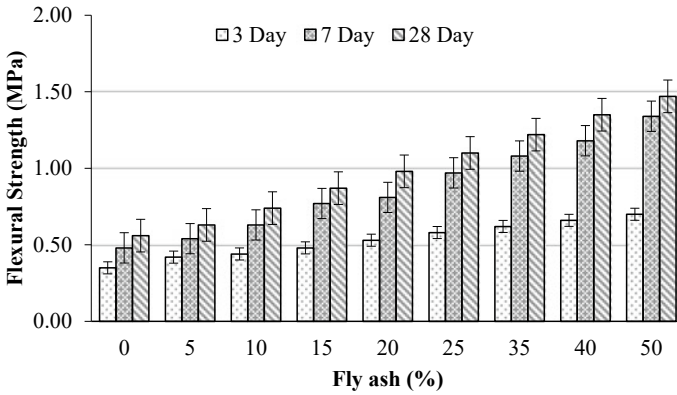


Fig. 4 Variation of flexural strength of stabilized BC soil

A frequency of 1 Hz and a rest period of 0.1 s was selected for testing. The samples were subjected to fatigue tests under different loads, which is considered as a certain percentage of UCS load. A fraction of load stress, which is equivalent to 0.35, 0.5, and 0.65 times that of UCS of each specimen, was applied, and the number of repetitions to failure was recorded. At applied stress of 0.35, the specimens failed after taking >47,000 repetitions, as shown in Fig. 5. All the samples at an applied stress of 0.2 times UCS have sustained >2 lakh fatigue repetitions, and the test was not continued further.

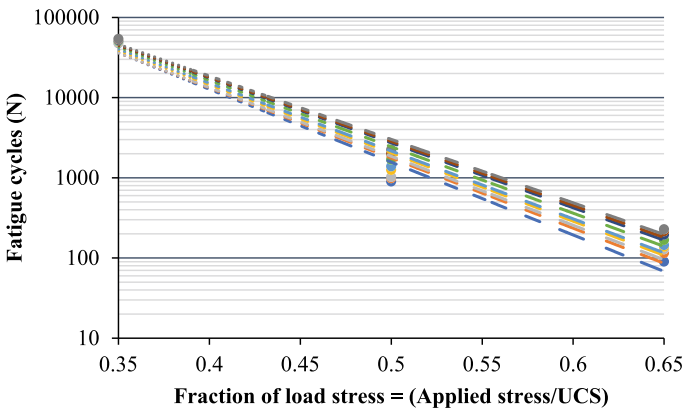


Fig. 5 Fatigue cycles to failure at different applied stress values

3.6 Durability

Samples cured for 7 days were tested for durability in order to check their retention under cyclic seasonal changes. In the wetting–drying test, all the stabilized samples, when immersed in water, were failed with sudden softening of the mix. During the freezing cycle in the freezing–thawing test, the samples slightly expanded by absorbing water from felt pads. In the succeeding thawing cycle, the samples completely failed by absorption of water and subsequent softening. The failure of the specimens is due to the leaching of metals such as Na, Al, Si, Ca, Fe present in the raw material and alkaline content that is capable of forming (N–A–S–H) gel and (C–(N)–A–S–H) gel. Hence, the stabilized mixes exhibited no resistance to the durability tests.

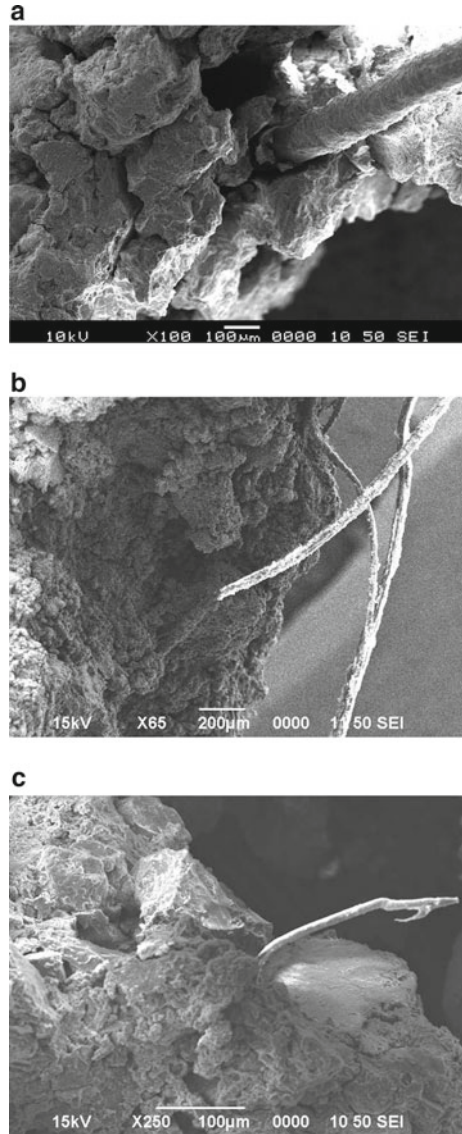
3.7 SEM Analysis

The effect on the morphology of the stabilized mix using fly ash precursor for improving BC properties using alkali solution is depicted in Fig. 6. Figure 6a depicts the discontinues and loose structure of the BC soil with more pores. The shrinkage cracks developed due to dehydration of soil are clearly visible. Due to shrinkage, the debonding of areca fibers with soil was observed. Due to polymerization compound formations by alkali-activated fly ash precursor, the pore spaces were sealed; thus, no cracks and discontinuities are observed, as depicted in Fig. 6b. Dense packing of soil particles due to continuous geopolymer matrix sealed the void spaces. Also, the polymerization compounds deposited on the rougher fiber surface exhibited excellent bonding of the set mix. Hence, the set soil interlocked by the fibers is responsible for improving the flexural strength and plunger penetration resistance during the CBR test. Figure 6c depicts the change in morphology of stabilized soil due to geopolymer product formations.

3.8 XRD Analysis

The change in crystalline phases of alkali-activated BC soil with precursor fly ash was identified using XRD analysis. XRD patterns justified the strength improvement by the formation of many hydration products. Peaks observed at different 2θ angle revealed the involvement of dissolvable alumina and silica in the formation of varying hydration products. XRD microgram depicted below shows the formation of these hydration products at the highest intensity. However, the mentioned hydration products were spread over multiple 2θ angles. Gismondine ($\text{CaAl}_2\text{Si}_2\text{O}_8 \cdot 4\text{H}_2\text{O}$), Liottite ($(\text{Ca}, \text{Na})_4 (\text{Si}, \text{Al})_6 \text{O}_{12} (\text{SO}_4, \text{OH}, \text{Cl}, \text{CO}_3)_2 \cdot x\text{H}_2\text{O}$), Millosevichite ($\text{Al}_2 (\text{SO}_4)_3$), Foshagite ($\text{Ca}_4 (\text{SiO}_3)_3 (\text{OH})_2$), Nordstrandite ($\text{Al} (\text{OH})_3$), Xonotlite ($\text{Ca}_6\text{Si}_6\text{O}_{17}$

Fig. 6 **a** Black cotton soil exhibiting shrinkage cracks along with debonded areca fiber, **b** areca nut fibers bonded in alkali-activated mix, **c** mix showing geopolymer compounds



(OH)₂), Calcium Sulfate Hydrate (CaSO₄·0.15H₂O), and Sodium Hydrogen Sulfate (NaHSO₄) are the common phases observed in the set stabilized mix. Along with this, Quartz low (SiO₂) and Pigeonite ((Ca, Mg, Fe) (Mg, Fe) Si₂O₆), which is a mineral of the clinopyroxene subgroup of the pyroxene group, were also found in the stabilized mix (Fig. 7).

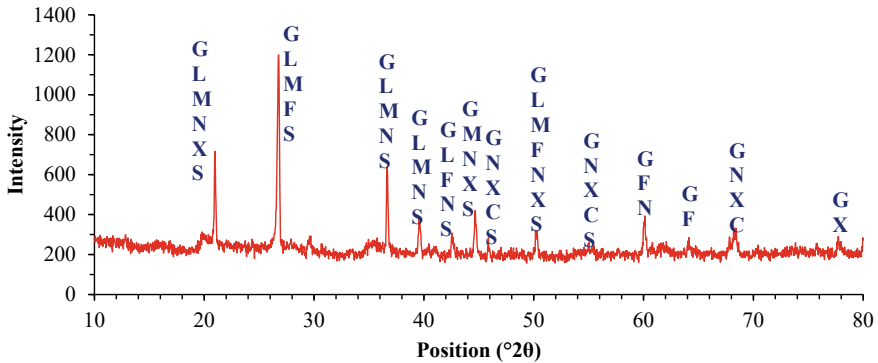


Fig. 7 XRD peaks showing the hydration products

4 Conclusions

Effect of using alkali-activated class F fly ash binder with areca nut fiber as reinforcement was reported in this investigation. The effect of stabilization was studied in terms of strength development, durability, and microstructural changes. The following outcomes are highlighted.

- (1) Regardless of fly ash dosage, all alkali-activated specimens attained maximum strength on 7 days of curing, and on further curing slight increase in strength was noticed.
- (2) The use of areca fiber reinforcement has made the specimens more ductile and reduced the density of mixes. However, the reinforcement has a significant influence on improving flexural strength and the crack propagation resistance of specimens.
- (3) Under the dry condition, the specimens showed a noticeable improvement in plunger penetration resistance. The stabilized mixes exhibited excellent performance under the fatigue load repetitions.
- (4) The alkali-activated BC soil with fly ash and areca fibers reinforcement was highly susceptible to weathering due to seasonal changes associated with wetting, drying, and frost actions like freezing and thawing. The leaching of minerals from the set mix weakens the soil.

The tested mix combinations are performing better at low moisture content conditions. The weakness of mixes lies in softening whenever they come in contact with water. As the pavement layers are seasonally subjected to moisture changes, the damages may be foreseen due to mix softening and the entire pavement deformation. Hence, these stabilized mix combinations cannot be used for pavements.

References

1. ASTM (2000) Standard test method for flexural strength of soil-cement using simple beam with third-point loading. D1635
2. Bai Y, Liu J, Song Z, Chen Z, Jiang C, Lan X, ... Kanungo DP (2019) Unconfined compressive properties of composite sand stabilized with organic polymers and natural fibers. *Polymers* 11(10):1576
3. Dang LC, Fatahi B, Khabbaz H (2016) Behaviour of expansive soils stabilized with hydrated lime and bagasse fibres. *Procedia Eng*
4. Davidovits J (1993) Geopolymer cements to minimize carbon dioxide greenhouse warming. *Ceram Trans* 37:165–182
5. Gajghate V, Patil P (n.d.) Experimental study of use of flyash as retarding agent in black cotton soil. In: *Advances in civil engineering and infrastructural development*, pp 655–664. Springer
6. Gupta S, GuhaRay A, Kar A, Komaravolu VP (2018) Performance of alkali-activated binder-treated jute geotextile as reinforcement for subgrade stabilization. *Int J Geotech Eng* 1–15
7. Hearle JWS, Morton WE (2008) *Physical properties of textile fibres*. Elsevier
8. Hussain R, Bordoloi S, Gadi VK, Garg A, Ravi K, Sreedeeep S (2020) Effect of filament type and biochemical composition of lignocellulose fiber in vegetation growth in early plant establishment period. In: *Problematic soils and geoenvironmental concerns*, pp 201–213. Springer
9. Kong DLY, Sanjayan JG (2010) Effect of elevated temperatures on geopolymer paste, mortar and concrete. *Cem Concr Res* 40(2):334–339
10. Lekha BM, Goutham S, Shankar AUR (2015) Evaluation of lateritic soil stabilized with Arecanut coir for low volume pavements. *Trans Geotech* 2:20–29. <https://doi.org/10.1016/j.trgeo.2014.09.001>
11. Murmu AL, Patel A (2020) Studies on the properties of fly ash-rice husk ash-based geopolymer for use in black cotton soils. *Int J Geosynth Ground Eng* 6(3):1–14
12. Rios S, Ramos C, Viana da Fonseca A, Cruz N, Rodrigues C (2019) Mechanical and durability properties of a soil stabilised with an alkali-activated cement. *Eur J Environ Civ Eng* 23(2):245–267
13. Saride S, Dutta TT (2016) Effect of fly-ash stabilization on stiffness modulus degradation of expansive clays. *J Mater Civ Eng* 28(12):4016166
14. Shenal Jayawardane V, Anggraini V, Emmanuel E, Yong LL, Mirzababaei M (2020) Expansive and compressibility behavior of lime stabilized fiber-reinforced marine clay. *J Mater Civ Eng* 32(11):4020328
15. Syed M, GuhaRay A (2020) Effect of fiber reinforcement on mechanical behavior of alkali-activated binder-treated expansive soil: reliability-based approach. *Int J Geomech* 20(12):04020225. [https://doi.org/10.1061/\(asce\)gm.1943-5622.0001871](https://doi.org/10.1061/(asce)gm.1943-5622.0001871)
16. Tan T, Huat BBK, Anggraini V, Shukla SK, Nahazanan H (2019) Strength behavior of fly ash-stabilized soil reinforced with coir fibers in Alkaline environment. *J Nat Fibers* 1–14
17. Zhang Y, Zhang J, Jiang J, Hou D, Zhang J (2018) The effect of water molecules on the structure, dynamics, and mechanical properties of sodium aluminosilicate hydrate (NASH) gel: a molecular dynamics study. *Constr Build Mater* 193:491–500

Development of Road Safety Models by Using Linear and Logistic Regression Modeling Techniques



Krantikumar V. Mhetre and Aruna D. Thube

Abstract Road accidents are caused by many factors like alcohol consumption, uncontrolled vehicle speed, poor road surface conditions, bad weather, inadequate traffic signs, and vehicle defects. A single solution cannot address these factors. Therefore, various engineering departments are engaged in road accident studies and their minimization. One of the solutions to study road accidents is to make use of accident prediction models. Regression is one of the essential techniques of predictive analytics in which a lot of prediction problems are modeled. Regression is a kind of supervised learning algorithms since a regression model requires both the dependent as well as the independent variables in the data set. Four simple linear regression models are developed, and two of them are best fitted. The fitted models are logarithmic-linear. The model's output is to find the number of fatalities based on the total number of accidents. The special cases considered here are accidents on a T-junction and accidents due to the intake of alcohol. A binary logistic regression model is developed for the accidents from the year 2014–2019, and the prediction of causing fatality is computed by using a cut-off probability value of 0.33. The overall model is accepted.

Keywords Road accidents · Road safety · Road safety modeling · Accident prediction modeling · Regression

1 Introduction

The third global road safety conference on was held in February 2020 at Stockholm, Sweden. In this conference, all the countries promised to reduce the deaths due to road accidents by 50% for 2030. China ranks 2nd, USA ranks 3rd, whereas India ranks 1st in deaths due to road accidents among the 199 countries involved in the World Road Statistics, 2018. World Health Organization's global report on road safety 2018 says India has a contribution of 11% in the world's accident-related deaths. In 2019,

K. V. Mhetre (✉) · A. D. Thube
Department of Civil Engineering, College of Engineering Pune, Pune, Maharashtra, India
e-mail: kvm18.civil@coep.ac.in

© The Author(s), under exclusive license to Springer Nature Singapore Pte Ltd. 2023
M. S. Ranadive et al. (eds.), *Recent Trends in Construction Technology and Management*, Lecture Notes in Civil Engineering 260,
https://doi.org/10.1007/978-981-19-2145-2_89

1205

4,49,002 road accidents were recorded by India, out of which 1,51,113 are deaths and 4,51,361 are injuries. Savolainen and Mannering [17] developed models for motorcycle injuries in single as well as multiple vehicle crashes for Indiana, USA, using multinomial and nested logit modeling techniques. The authors concluded that motorcyclist age was one of the critical parameters causing severe injuries. Candappa et al. [3] proved the importance of developing the accident prediction models and the data required for road safety analysis. The data related to road geometry, accidents, traffic volume, and road users are useful for developing accident prediction models. Tay et al. [19] studied the factors contributing to hit and run cases in California, USA, by developing a logistic regression model. The parameters like traffic control devices, speed limit, and road profile are associated with “hit and run” cases for fatal crashes. Chen and Chen [5] collected ten years of accident data for a rural highway and developed accident prediction models using a mixed logit-modeling technique and studied the severity of injury in case of truck accidents.

Hu and Donnell [9] collected 5-years of crash data and developed injury-severity models for rural divided highways in Pennsylvania for crossover and rollover crash types. They considered influential factors related to vehicle, driver, median, and roadway in developing models. Altwaijri et al. [1] used mixed logit and multinomial logit-modeling techniques to perform statistical analysis on the crash data of Riyadh city in Saudi Arabia. The authors concluded that single-vehicle crashes were more severe than multiple vehicle crashes. The involvement of non-Saudi and illiterate people was found significant with the severity of crashes. Theofilatos et al. [20] developed separate models for urban areas of Greece to determine factors responsible for severity of accident. They have used the binary logistic regression technique to compute the probability of fatality/severe injury versus slight injury. Landge and Sharma [10] conducted a study to identify the accident-prone locations on NH-58 in India, connecting New Delhi to Mana. They have used 3 years of accident data to develop accident prediction models by using multiple regression techniques. Martensen and Dupont [11] concluded about the single and multi-vehicle accidents by using logistic multiple regression techniques. They have used the crash data from six countries of Europe and identified the variables like traffic flow, junction, and the median are critical. Yannis and Dragomanovits [23] prepared a questionnaire to understand the use of accident prediction models worldwide. They conclude that the accident prediction models are essential for reducing accidents and must be used by all organizations. The study reports that many organizations worldwide are not using accident prediction modeling in achieving road safety.

Atipathi et al. [2] developed an accident prediction model for a national highway in India using linear regression analysis. The authors have used four years of accident data from the year 2009–2012 and studied the impact of crashes on the Indian economy. Naqvi et al. [15] developed accident prediction models for three national highways in India using the binomial logistic regression modeling technique and identified the factors responsible for fatal motorcycle crashes. The influential variables were type of collision, number of lanes, and vehicles. Authors recommended that riders should use properly fastened helmets along with the reflective tapes.

Wegman [22] stated that most accidents in the world happened in low and middle-income countries and observed road safety implementation in high-income countries. The author concludes that road accidents will stay an alarming issue in the future if road safety is not improved. Sing [18] analyzed the Indian road accidents at a micro-level and commented on the variation of road accidents. The interpretation depends upon the date and time of accidents, age and sex of the road user. The author predicts that the fatalities will be around 2,50,000 for the year 2025. Chandra and Mohan [4] studied the behavior of drivers on roads from the USA and India. The authors made a comparison and concluded that driver's fault is the primary reason responsible for accidents in India. Goel [7] established a model by considering the modal split as the explanatory variable and the number of accidents as the response variable. The author concludes that 2-wheelers, cars, and heavy vehicles have a higher risk of fatalities, whereas walking, bicycle and public transport use has a lower risk of fatalities.

Haghighattalab et al. [8] concluded about the importance of implementing engineering ethics, which can prevent the accidents resulting from the decisions of engineers. Valen et al. [21] examined associations of accidents due to intake of alcohol or drugs with the risk factors of driver, which significantly contribute to fatal road traffic crashes. The important factors like absence of driving licence, over speeding, no use of helmets or seat-belts were responsible for fatal injury cases. Fountas et al. [6] studied the combined result of atmospheric and lighting conditions on the severity of injury for accidents involving single-vehicles in Scotland, United Kingdom, using injury-severity data of the years 2016 and 2017. The model shows that all the conditions have the variable impacts on the severity of injury.

Qureshi et al. [16] studied the impact of mandated societal lockdown on the road accidents. Authors have found a significant minimization in road accidents leading to minor injuries. For accidents connected with fatal or severe injuries after mandated societal lockdown.

Road accidents occur by many factors like improper geometric design of roads, defects in the vehicle, driver behavior, and vehicle's speed. There is a need to reduce the number of accidents since it produces fatalities, which we cannot ignore. No doubt, as the road accidents are uncertain and cannot be zero, the minimization of road accidents can be achieved and must be studied to reduce road accidents. The use of road safety models is one of the essential tools for achieving road safety worldwide.

2 Case Study

Two case studies have the consideration for developing simple linear regression and binomial logistic regression models. For simple linear regression models, the data is taken from the report "road accidents in India-2016" which is published by the 'ministry of road transport and highways [13], government of India. This information is available for entire India, consisting of 36 states for the year 2016. The accident data selected for developing models from the report is as shown in Table 1.

Table 1 Accident data for developing models 1–4

Sr. No.	Location	Type of classification	Categorization	Actual records
1	36 States of India	Type of junctions	T-junction	Total number of accidents
2		Responsibility of driver	Intake of alcohol	Total number of fatalities Total number of injuries

For developing a binomial logistic regression model, the accident data is collected from the local police stations of Pune city, Maharashtra, India, over a stretch of 19 km.

The accident data from the year 2014–2019 is collected, which has classified accidents like date and time, age of complainer, number of accidents, and number of fatalities. The complainer's age is the dependent variable, and the model predicts the likelihood of fatality.

3 Methodology

Regression is one of the essential techniques of predictive analytics in which a lot of prediction problems are modeled. Regression is a kind of supervised learning algorithms since a regression model requires both the dependent as well as the independent variables in the data set [12].

3.1 Simple Linear Regression

Regression is used to find the relationship a tool for finding an association relationship between a response variable (Y) and one or more explanatory variables ($X_1, X_2 \dots X_n$) of the study. The relationship can be linear or non-linear. The Eq. (1) is not exact; due to the error term ε .

$$Y = \beta_0 + \beta_1 X + \varepsilon \quad (1)$$

where Y = response variable, X = explanatory variable, β_0 = Y -intercept, and β_1 = slope of the line.

The intercept is the mean value of the dependent variable when the independent variable is 0. The slope is the change in the dependent variable's value for a unit change in the independent variable.

3.1.1 Assumptions in Linear Regression Models

- The error term is normally distributed.
- For various values of explanatory variable, the variance of the error remains same.
- There is no auto-correlation between the two error values.

3.1.2 Coefficient of Determination (R-square)

R-square measures the fitness of the regression line with the data. Its estimate ranges from 0 to 1, and it explains the percentage of variation of the regression model. R-square is equal to the ratio of the sum of squares due to regression to the total sum of squares.

3.1.3 Standard Error and T-test

Standard error estimates the regression errors' standard deviation, which measures the observed values' variability or scatters around the regression line. A smaller standard error of the estimate indicates a better fit. If the standard error is zero, then there is a perfect fit. If the significance value for the T-test is less than 0.05, the model is accepted.

3.2 Logistic Regression

Logistic regression estimates the conditional probability of an event. It evaluates how the likelihood of an event gets affected by explanatory variables. The logistic function is as shown in Eq. (2).

$$P(Y = 1) = \pi = e^z / (1 + e^z) \quad (2)$$

3.2.1 Binomial Logistic Regression

In this method, the response variable is binary. The response variable can have only two values. The logistic function (sigmoidal function) is as shown in Eq. (3).

$$\pi(z) = e^z / (1 + e^z) \quad (3)$$

where, $z = \beta_0 + \beta_1x_1 + \dots + \beta_nx_n$.

3.2.2 Interpretation of Logistic Regression Coefficients

Wald's test checks the importance of explanatory variables, which is identical to the t-test in simple linear regression. When the p -value is below 0.05, then the explanatory variable is significant.

The omnibus test checks the significance of the model coefficients. When the p -value is less than 0.05, then the explanatory variable is significant. Hosmer–Lemeshow goodness of fit test checks the model's overall fitness for a binary logistic regression. When the p -value is greater than 0.05, then there is no difference between the predicted and observed frequencies; that is, the model is accepted.

3.2.3 Classification Table

It is the table, which classifies all the probabilities into outcomes depending on the cut-off value used.

$$\text{Sensitivity} = [P/(P + Q)] \quad (4)$$

$$\text{Specificity} = [R/(R + S)] \quad (5)$$

where P = true positive; Q = false negative; R = true negative; S = false positive.

3.2.4 Receiver Operating Characteristic (ROC) Curve

It plots the graph of false-positive ratio and the true positive ratio. The higher the area covered under the ROC curve, the better the prediction ability of the model.

4 Results and Discussion

The results with discussion for all developed models are as follows, showing separate computations for both the case studies considered here.

4.1 Prediction of Fatal Accidents Based on the Total Number of Accidents on T-junction

SLR predicts the total number of fatalities with the help of a total number of accidents as the explanatory variable, as shown in Table 2. The r-square value is 0.826,

Table 2 Model-1 summary and coefficients

ANOVA					
<i>Model-1</i>	<i>Sum of squares</i>	<i>Df</i>	<i>Mean square</i>	<i>F</i>	<i>Significance</i>
Regression	20,411,348.17	1	20,411,348.17	160.993	0.000
Residual	4,310,669.827	34	126,784.407		
Total	24,722,018.00	35			
<i>Model summary</i>					
<i>Model-1</i>	<i>R</i>	<i>R-square</i>	<i>Adjusted R-square</i>	<i>Standard error</i>	
	0.909	0.826	0.821	356.0680	
<i>Coefficients</i>					
<i>Model-1</i>	<i>Unstandardized coefficients</i>		<i>Standardized coefficients</i>	<i>t</i>	<i>significance</i>
	<i>B</i>	<i>Standard error</i>	<i>Beta</i>		
(constant)	75.945	70.224		1.081	0.287
Total number of accidents	0.271	0.021	0.909	12.688	0.000

which means the developed model explains 82.6% of the variation. The SLR model developed is given by Eq. (6).

$$Y = 75.945 + 0.271 * X \quad (6)$$

where Y = Total number of fatalities, X = Total number of accidents.

The independent variable's significance value is less than 0.05; the model is accepted. The significance value for F-test is less than 0.05, which implies that the model is accepted. The histogram with the residuals' distribution in Fig. 1 shows the curve's approximate normal distribution. The p-p plot of the dependent variable indicating the expected and observed cumulative probabilities, as shown in Fig. 2, ensures the model's fitting. This p-p plot can be more close concerning the diagonal line, which implies developing a more accurate model than the model-1.

Model-2 has a better fit as shown in Table 3. The dependent variable is the log natural of the total number of fatalities, and the independent variable is the total number of accidents. The r-square value is 0.455, which implies that the model explains 45.5% of the variation, and the standard error is 0.7583, which is significantly less than model-1.

The SLR model developed is given by Eq. (7).

$$\text{Log}(Y) = 1.645 + 0.0003 * X \quad (7)$$

where Y = Total number of fatalities, X = Total number of accidents.

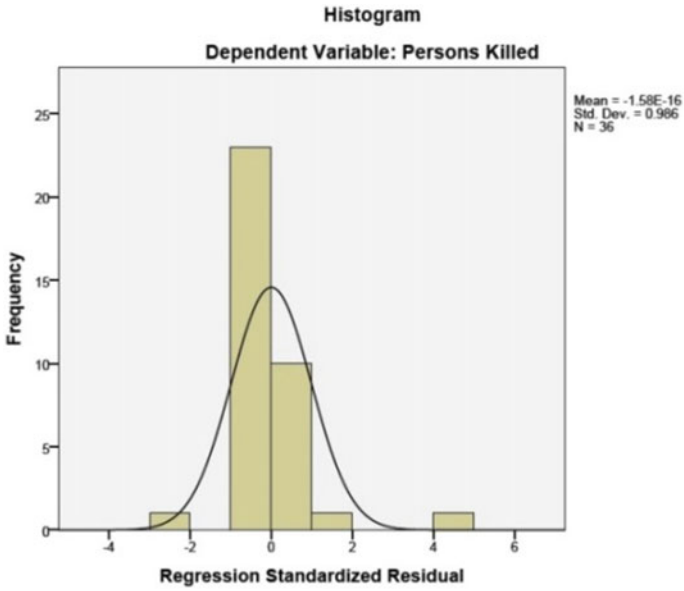


Fig. 1 Histogram, model-1

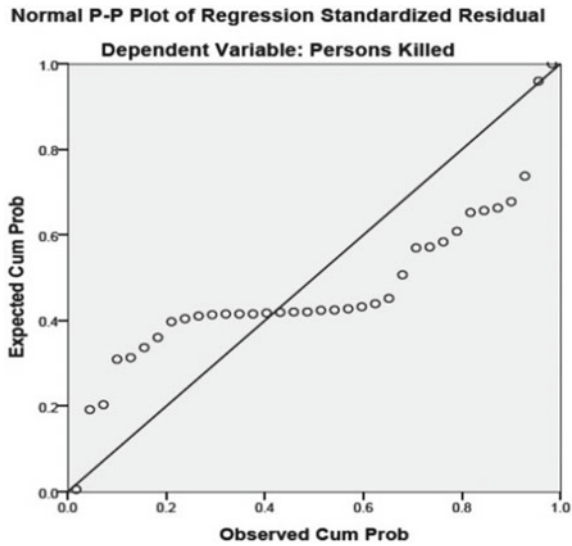


Fig. 2 p-p plot, model-1

Table 3 Model-2 summary and coefficients

ANOVA					
Model-1	Sum of squares	Df	Mean square	F	Significance
Regression	15.357	1	15.357	26.700	0.000
Residual	18.405	32	0.575		
Total	33.762	33			
Model summary					
Model-1	R	R-square	Adjusted R-square	Standard error	
	0.674	0.455	0.438	0.758397	
Coefficients					
Model-1	Unstandardized coefficients		Standardized coefficients	t	Significance
	B	Standard error	Beta		
(constant)	1.645	0.156		10.560	0.000
Total number of accidents	0.0003	0.000	0.674	5.167	0.000

The significance value is also less than 0.05; therefore, the model is accepted.

The histogram with the residuals' distribution in Fig. 3 shows the normal distribution of the curve.

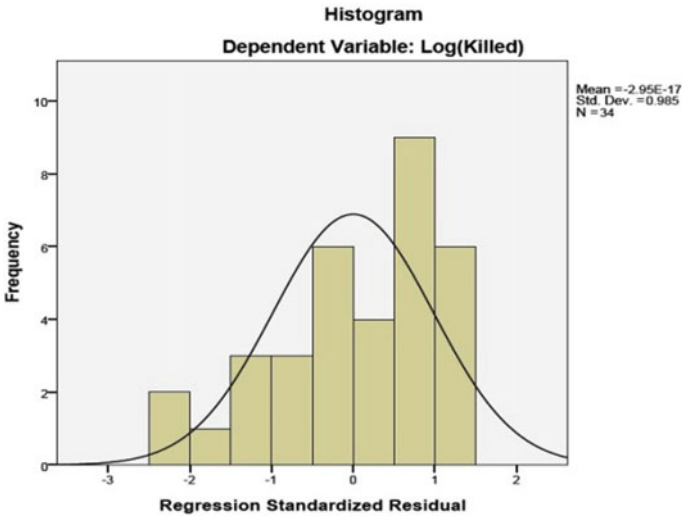


Fig. 3 Histogram, Model-2

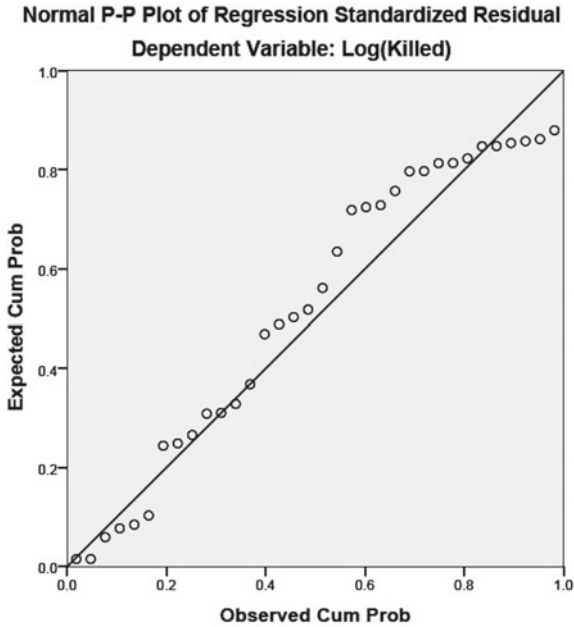


Fig. 4 p-p plot, Model-2

The dependent variable’s p-p plot shows the expected and observed cumulative probabilities given in Fig. 4, which ensures the model’s fitting. This p-p plot is more close concerning the diagonal line, and hence model-2 is more accurate than model-1.

4.2 Prediction of the Total Number of Fatalities from the Total Number of Accidents Due to Intake of Alcohol

SLR predicts the total number of fatalities with a total number of accidents as the explanatory variable.

The r-square value is 0.8142, which means that the model explains 81.42% of the variation. The SLR model developed is given by Eq. (8).

$$Y = -22.6062 + 0.4599 * X \tag{8}$$

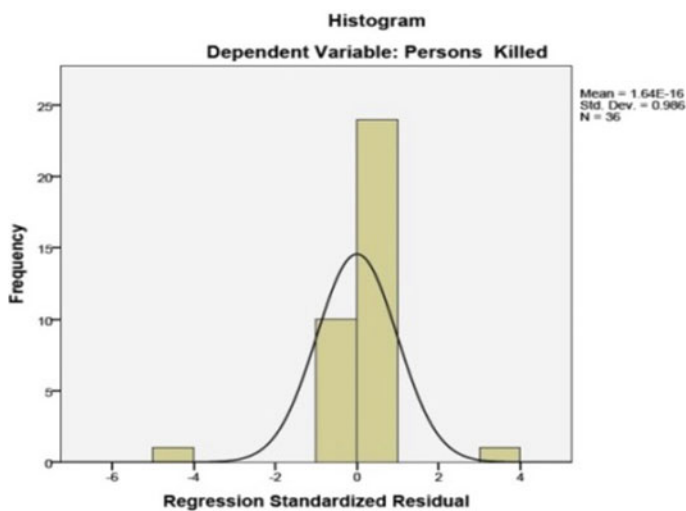
where Y = Total number of fatalities, X = Total number of accidents

The independent variable’s significance value is less than 0.05; the model is accepted, as shown in Table 4. Also, the F-value’s significance is less than 0.05, which implies that the model is accepted. The histogram showing the residuals’

Table 4 Model-3 summary and coefficients

Summary Output					
<i>Regression statistics</i>					
Multiple R	0.902377083				
R-square	0.8142844				
Adjusted R-square	0.807880414				
Standard error	215.3632453				
Observations	31				
<i>ANOVA</i>					
	<i>df</i>	<i>SS</i>	<i>MS</i>	<i>F</i>	<i>Significance F</i>
Regression	1	5,897,512.924	5,897,512.924	127.1527412	4.04361E-12
Residual	29	1,345,058.495	46,381.32743		
Total	30	7,242,571.419			
	<i>Coefficients</i>	<i>Standard error</i>	<i>t</i>	<i>P-value</i>	
Intercept	-22.60615674	43.3374	-0.52163	0.605888	
X Variable 1	0.459898409	0.04078	11.27620	4.043E-12	

distribution in Fig. 5 indicates the curve's approximate normal distribution. The dependent variable's p-p plot shows the expected and observed cumulative probabilities are shown in Fig. 6, ensuring the model's fitting. This p-p plot can be more

**Fig. 5** Histogram, Model-3

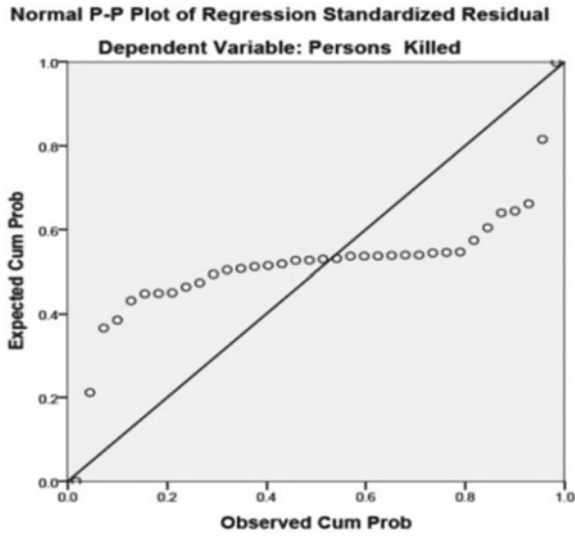


Fig. 6 p-p plot, Model-3

close concerning the diagonal line, which implies developing a more accurate model than model-3.

Table 5 Model-4 summary and coefficients

Summary output					
<i>Regression statistics</i>					
Multiple R	0.66298024				
R-square	0.439542799				
Adjusted R-square	0.420216689				
Standard error	0.618332834				
Observations	31				
<i>ANOVA</i>					
	<i>df</i>	<i>SS</i>	<i>MS</i>	<i>F</i>	<i>Significance F</i>
Regression	1	8.695635594	8.695635594	22.74346936	4.81901E-05
Residual	29	11.08772933	0.38233549		
Total	30	19.78336492			
	<i>Coefficients</i>	<i>Standard error</i>	<i>t</i>	<i>P-value</i>	
Intercept	1.36179556	0.124426813	10.9445828	8.19322E-12	
X Variable 1	0.000558442	0.000117098	4.769011361	4.81901E-05	

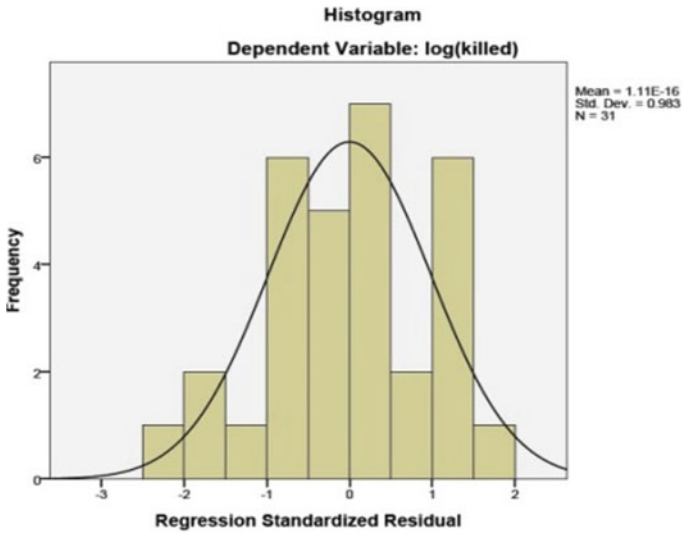


Fig. 7 Histogram, Model-4

Model-4 has a better fit, shown in Table 5. The dependent variable is the log natural of the total number of fatalities, and the independent variable is the total number of accidents. The r-square value is 0.4395, which implies that the model explains 43.95% of the variation, and the standard error is 0.6183, which is significantly less than the model-3.

The SLR model developed is given by Eq. (9).

$$\text{Log}(Y) = 1.3618 + 0.00056 * X \tag{9}$$

where Y = Total number of fatalities, X = Total number of accidents.

The histogram and p-p plot of the logarithmic model is as shown in Figs. 7 and 8. The fitting of the logarithmic model-4 is perfect as compared to the original model-3.

4.3 Binomial Logistic Regression

This model helps to predict whether the occurrence of an individual accident results in fatal or non-fatal injury. The fatality has an output of 1, and the non-fatality has an output of 0. The explanatory variable is the age of the complainer. The model output is as shown in Table 6. The total observations are 118, and the data for all 118 observations have consideration in the model building.

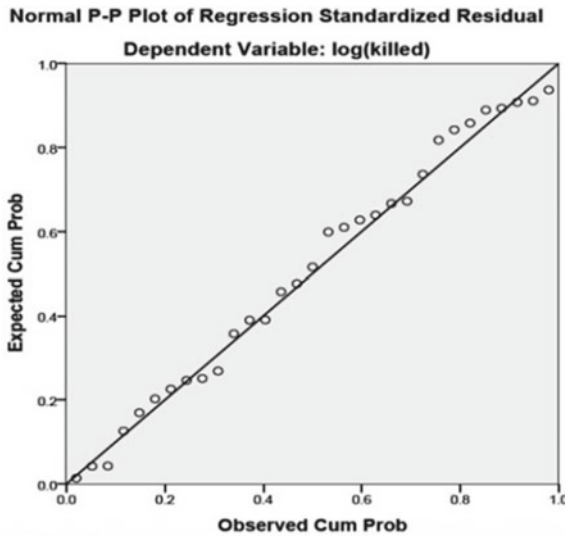


Fig. 8 p-p plot, Model-4

The omnibus test result shows that the significance values are less than 0.05; therefore, the model is accepted. Similarly, the Hosmer–Lemeshow test’s output reveals a significance value greater than 0.05; therefore, the model is accepted.

The classification table automatically uses a cut-off value of 0.5, which means that if the probability of the outcome is less than 0.5, it takes the value 0 as an output. If the outcome’s likelihood is higher than 0.5, it has 1 as an output value. Here, as shown in Table 6, all cases are classified correctly out of eighty-five numbers of 0-cases. The specificity value is 100%. Similarly, Out of thirty-three numbers of 1-cases, all are classified incorrectly. The sensitivity value is 0%, and the overall percentage is 72%. This value implies that the cut-off should be clearly defined to increase the sensitivity of the model.

The variables in the equation are as shown in Table 6, and the model built is as given in Eq. (10).

$$\pi(z) = e^z / (1 + e^z) \tag{10}$$

where $z = 0.627 - 0.048 * \text{age of complainer}$.

The explanatory variable’s significance value is less than 0.05, and the confidence interval does not contain the value of 1; therefore, the model is accepted. Now, changing the cut-off value to 0.33, the results are as shown in Table 6. The omnibus test result shows that the significance values are less than 0.05; therefore, the model is accepted. Similarly, the Hosmer–Lemeshow test’s output shows a significance value greater than 0.05; therefore, the model is accepted. The cut-off value of 0.33 means that if the probability of the outcome is less than 0.33, it takes the value 0

Table 6 (continued)

Summary									
								Lower	Upper
Age of complainer	- 0.048	0.019	6.080	1	0.014	0.953	0.917	0.990	
Constant	0.627	0.638	0.968	1	0.325	1.873			
<i>Classification Table with cut-off value 0.33</i>									
Step	Observed	Predicted							
		Fatal/Non-fatal							
		0	1						
1	Fatal/Non-fatal	0	26		69.4				
		1	20		60.6				
	Overall %				66.9				

as an output. If the outcome’s likelihood is greater than 0.33, it takes the value 1 as an output. Here, as shown in Table 6; Out of eighty-five numbers of 0-cases, fifty-nine cases are classified correctly, and twenty-six instances have been classified incorrectly. The specificity value is 69.40%. Similarly, Out of thirty-three numbers of 1-cases, twenty cases are classified correctly, and thirteen cases are classified incorrectly.

The sensitivity value is 60.60%, and the overall percentage is 66.90%. Now, these computations look good as compared to the cut-off value of 0.5.

Finally, the ROC curve explains the model’s overall effect, as shown in Table 7 and Fig. 9.

The area covered under the ROC curve is 0.678, which means that with 67.8% accuracy, the model quantifies the output as 1. Therefore, the model is acceptable and can predict fatality or non-fatality when a particular accident occurs, depending upon the complainer’s age.

Table 7 Area under the ROC curve

ROC summary (model-5)				
Area	Standard error	Asymptotic significance	Asymptotic 95% confidence interval	
			Lower bound	Upper bound
0.678	0.056	0.003	0.567	0.788

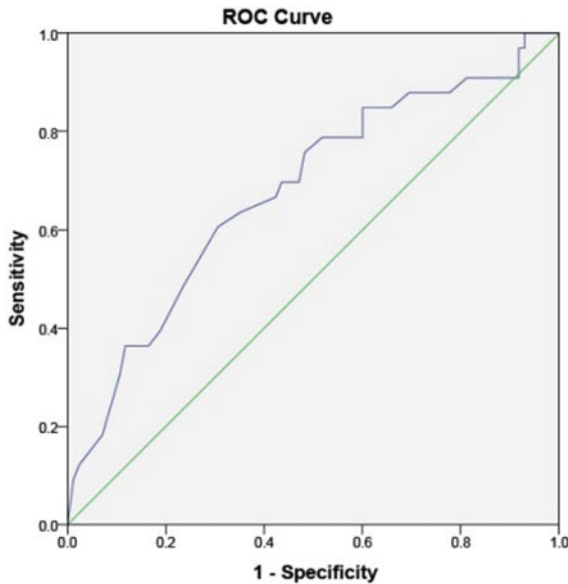


Fig. 9 ROC curve

5 Conclusions

The four simple linear regression models predict the number of fatalities with the total number of accidents that happened in various conditions.

5.1 Prediction of Fatalities Based on the Number of Accidents on T-junction

Out of Models 1 and 2, model-2 is the best-fitted model as the standard error value is significantly less than model-1, as shown in Table 8. Also, the comparison of the p-p plot between model-1 and model-2, as shown in Fig. 10, suggests using model-2 for predicting the number of fatalities.

Since the variables in model-1 are number of accidents and number of fatalities, they have a perfect correlation and hence the r-square value is high. In model-2, the correlation between the number of accidents and log of the number of fatalities is not as perfect as model-1 and hence the r-square for model-2 is less than model-1.

Table 8 Model 1 and 2 summary

Model number	Model	R-square	Standard error
1	$Y = 75.945 + 0.271 * X$	0.826	356.06
2	$\text{Log}(Y) = 1.645 + 0.0003 * X$	0.455	0.7584

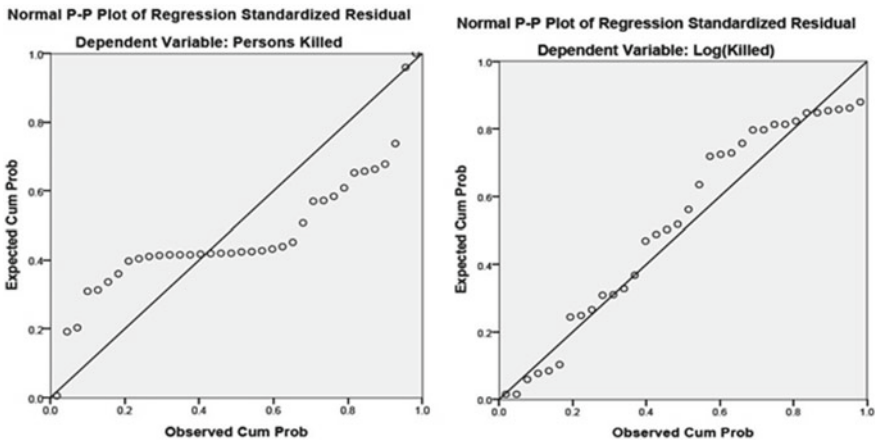


Fig. 10 Comparison of the p-p plot between model-1 and model-2

Table 9 Model 3 and 4 summary

Model number	Model	R-square	Standard error
3	$Y = -22.6062 + 0.4599 * X$	0.8143	215.36
4	$\text{Log}(Y) = 1.3618 + 0.00056 * X$	0.4395	0.6183

5.2 Prediction of Fatalities Based on the Total Number of Accidents Due to Intake of Alcohol

Out of models 3 and 4, model-4 is the best-fitted model as the standard error value is significantly less than model-3, as shown in Table 9.

Also, the comparison of the p-p plot between model-3 and model-4, as shown in Fig. 11, suggests using model-4 for predicting the number of fatalities.

Four simple linear regression models are developed, and two of them are the best fit. The fitted models are logarithmic-linear models. The model’s output is to find the number of fatalities based on the total number of accidents. The special cases considered here are accidents on a T-junction and accidents due to intake of alcohol. The binary logistic regression model is developed for 118 number accidents from the year 2014 to 2019, and the prediction of causing fatality is computed by using a cut-off probability value of 0.33. The overall model is accepted. The developed models are valid.

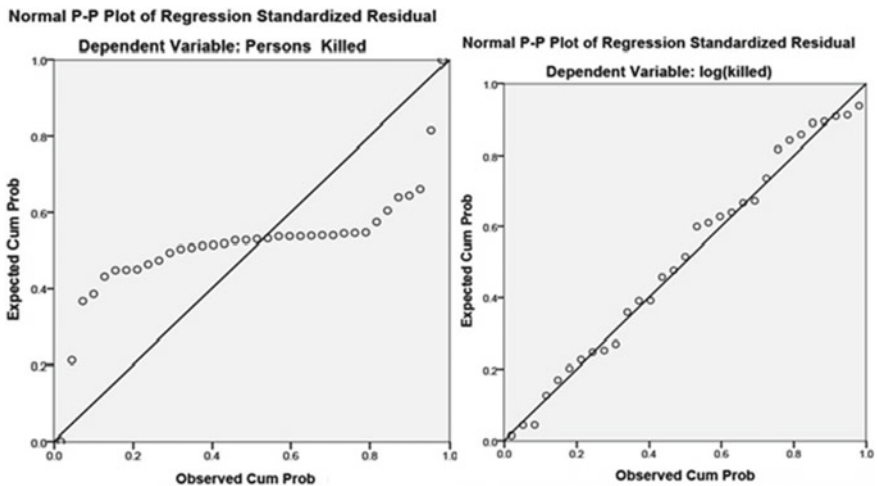


Fig. 11 Comparison of the p-p plot between model-3 and model-4

Acknowledgements The authors wish to thank the Civil Engineering Department, College of Engineering Pune, for giving the opportunity to do research. Also, extremely grateful to Local Police stations Pune City, Ministry of Road Transport and Highways for providing data used in this study.

References

1. Altwaijri S, Quddus M, Bristow A (2012) Analysing the severity and frequency of traffic crashes in Riyadh city using statistical models. *Int J Trans Sci Technol* 01(04):351–364
2. Athipathi G, Nagan S, Baskaran T (2017) Accident prediction on national highways in India. *Int J Theor Appl Mech* 12(01):153–165
3. Candappa NL, Schermers G et al (2014) Data requirements for road network inventory studies and road safety evaluations- guidelines and specifications. *Road Infracst Saf Manage Evaluat Tools* 03:1–87
4. Chandra S, Mohan M (2018) Analysis of driver behavior at unsignalized intersections. *J Indian Road Congress* 79(02):05–10
5. Chen F, Chen S (2011) Injury severities of truck drivers in single and multi-vehicle accidents on rural highways. *J Accid Analy Prevent* 43(05):1677–1688
6. Fountas G, Fonzone A et al (2020) The joint effect of weather and lighting conditions on injury severities of single-vehicle accidents. *J Accid Analyt Methods Accid Res* 27:1–19
7. Goel R (2018) Modeling of road traffic fatalities in India. *J Accid Analy Prevention* 112:105–115
8. Haghghattalab S, Chen A, Fan Y, Mohammadi R (2019) Engineering ethics within accident analysis models. *J Accide Analy Prevention* 129:119–125
9. Hu W, Donnell ET (2011) Severity models of cross-Median and rollover crashes on rural divided highways in Pennsylvania. *J Safety Res* 42(05):375–382
10. Landge VS, Sharma AK (2013) Identifying accident prone spots on rural highways—a case study of national highway No. 58. *Int J Chem Environ Biol Sci* 01(02):296–299
11. Martensen H, Dupont E (2013) Comparing single vehicle and multi-vehicle fatal road crashes: a joint analysis of road conditions, time variables, and other driver characteristics. *J Accid Analy Prevention* 60:466–471
12. Mendenhall W, Sincich T (2012) *A second course in statistics: regression analysis*, 7th edn. USA: Pearson Education, Print
13. Ministry of Road Transport & Highways (2016) Road accidents in India-2019. Government of India, pp 77–99
14. Ministry of Road Transport & Highways (2019) Road accidents in India-2019. Government of India, pp 15–25
15. Naqvi HM, Tiwari G (2017) Factors contributing to motorcycle fatal crashes on national highways in India. *Procedia Trans Res* 25:2084–2097
16. Qureshi AI, Huang W et al (2020) Mandated societal lockdown and road traffic accidents. *J Accid Analy Prevention* 146:1–4
17. Savolainen PT, Mannering F (2007) Probabilistic models of motorcyclists injury severities in single and multi-vehicle crashes. *J Accid Analy Prevention* 39(05):955–963
18. Singh SK (2017) Road traffic accidents in India: issues and challenges. *Trans Res Procedia* 25:4708–4719
19. Tay R, Barua U, Kattan L (2009) Factors contributing to hit and run in fatal crashes. *J Accid Analy Prevention* 41(02):227–233
20. Theofilatos A, Graham D, Yannis G (2012) Factors affecting accident severity inside and outside urban areas in Greece. *J Traffic Injury Prevention* 13(05):458–467

21. Valen A, Bogstrand ST, Vindenes V, Frost J, Larsson M, Holtan A, and Gjerde H (2019) Driver-related risk factors of fatal road traffic crashes associated with alcohol or drug impairment. *J Accid Anal Prev* 131:191–199
22. Wegman F (2017) The future of road safety: a worldwide perspective. *J IATSS Res* 40:66–71
23. Yannis G, Dragomanovits A et al (2016) Use of accident prediction models in road safety management: an international inquiry. *Trans Res Procedia* 14:4257–4266

Finite Element Analysis for Parametric Study of Mega Tunnels



Shilpa Kulkarni and M. S. Ranadive

Abstract The development of any country has a positive relation to the infrastructural development, and the tunnels are a very much important part of it. The increased need for tunnel infrastructure in urban areas demands tunnel excavation using Tunnel Boring Machine (TBM) to avoid surface traffic disturbance during the project execution period. The construction of Mega Tunnels provides a successful and profitable solution for urban development. Mega Tunnel is a large-diameter tunnel in which the diameter is greater than 10 m. The construction of Mega Tunnels involves more cost of construction for the station, as we must go deeper for stability purposes. Face Stability of such types of tunnels has been a hot topic for researchers, as this issue gets more critical with the increase in tunnel diameter. The collapse pressure plays an important role in the face stability of tunnels with increased overburden. Therefore, with the advantage of mega tunnel construction, ground-induced settlement and deformation should be taken into account. This paper focuses on the ground-induced settlement at various cover to diameter (C/D) ratios. The parametric study had been done by three-dimensional finite element analysis using Midas Gtx Nx software with different C/D ratios and pressure parameters for soft soil. The diameter of the tunnel is considered as 15 m. The analysis showed that the application of requisite pressures plays a significant role in the face stability of mega tunnels. Conclusions were drawn based upon analysis, and approximate preliminary lining thickness was suggested for different C/D ratios, which will be beneficial to ascertain preliminary tunnel design in actual practice.

Keywords Finite element analysis · Mega tunnel · TBM · Face stability · Collapse pressure

S. Kulkarni (✉)
College of Engineering Pune, Pune, India
e-mail: shilpakul10@gmail.com

M. S. Ranadive
Department of Civil Engineering, College of Engineering Pune, Pune, India
e-mail: msr.civil@coep.ac.in

1 Introduction

Urban infrastructure development is a key to progress in the livelihood of any country. It saves time as well as the per capita cost of transport. Due to urbanization, the city population growth rate increased rapidly in the last few decades. It minimizes the usable surface area required for public utility purposes. Therefore, as the need for urbanization increases, the importance of tunnel construction for infrastructure development also rises. The single-bore, large-diameter tunnels are a feasible solution for time and cost-saving in the construction of tunnel infrastructure projects in urban areas. It proves beneficiary as it can be facilitated with a multi-operating transport system.

Tunnel excavation using TBM gives various major benefits for such projects, as it gives more structural stability and safety at the face and working area which has more prime concern while tunneling work. It also gives more speedy construction due to continuous operations. Though some challenges are intercrop while accessing the face stability, Wang et al. [1] proposed DEM model to study the face stability, and impact of depth and friction angle was clarified. Khezri et al. [2] assessed the stability of tunnel face in layered soil by using an upper bound theorem of limit analysis. A numerical approach to study tunnel face stability with the experimental and analytical approach presented and found in good agreement using Midas was developed by many researchers [3]. Mollon et al. [4] presented a probabilistic approach to determine the range of pressures that can be applied to tunnel face to avoid face collapse or blow-out. Authors have also suggested that the failure probability is very high due to the application of insufficient pressures. Pan and Dias [5, 6] present the need for consideration of pore water pressure in face stability analysis of circular tunnel and conclude that water table exerts significant unfavorable impact on it.

The face stability of the tunnel was affected by two main aspects such as geotechnical parameters of surrounded ground strata and the application of various pressures in the excavation and construction stages. Previous research showed the impact of one of the above aspects with consideration of only one pressure parameter. The objective of this study is to analyze the face stability of the mega tunnels by analyzing the effect of various pressures such as earth pressure, Jack thrust, and skin friction between ground strata and TBM. The effect of pore water pressure and tunnel lining thickness on face stability was also analyzed. This integrated approach of study benefited to tunnel industry for preliminary tunnel design.

2 Literature Review

As per Mollon et al. [7], the determination of minimal pressure and ground deformation to prevent the collapse of tunnel face was very important for the determination of tunnel face stability issue. The C/D ratio has more importance in the failure mechanism. Mollon et al. [8] suggests that the soil mass verging, the tunnel face can

collapse into the tunnel if the applied face pressure drops below a critical value. It also states that if $C > D$, the collapse mechanism never offshoots. Chen et al. [9] studied the face instability of shield tunnels in the sand by proposing an experimental model at various C/D ratios. Soil arching during failure was monitored. Souza et al. [10] gives various critical pressure parameters to be considered for EPB TBM while tunnel advancing and its effect on structural stability. It also gives required calculation models for various pressures like thrust pressure and grout pressure. Zeng et al. [11] concludes that the face pressure is an important parameter to avoid face collapse. This also confirmed that the reliability of tunnel face stability increases significantly as face support increases or tunnel diameter decreases. Zhang et al. [12] concluded that the face stability had become a more challenging issue with increment in the tunnel diameter. Hernandez et al. [13] analyzed the face stability by numerical method at higher tunnel depth and suggest more pressure needed to support excavation face in soil. Shiau and Al-Asadi [14] describes the combined effect of surcharge load, self-weight, and internal supporting pressure and studies stability numbers for the circular tunnel in cohesive soil.

3 Data Collection

Data were collected for various geotechnical and pressure parameters required for tunnel modeling for soft computing analysis, as shown in Tables 1 and 2.

Table 1 Geotechnical parameter

No.	Design parameter	Soil	Segment	Steel	Grout
1	Modulus of elasticity (E) (MPa)	1.3e ⁶	2.1e ⁷	2.5e ⁸	1e ⁷
2	Poisson's ration	0.3	0.3	0.2	...
3	Unit weight (kN/m ³)	19	24(saturated)	78	22.5
4	Cohesion (Mpa)	15
5	Friction angel (°)	30
6	K ₀	0.5	1

Table 2 Pressure parameters (set 1)

No.	Type of pressure	Pressure QTY (kN/m ²)
		Pressure set 1
1	Drilling/Horizontal/Face pressure	200
2	Jack thrust	-4500
3	Pressure due to contraction over the body of the shield TBM	50
4	Pressure due to gap between shield TBM and the segment diameter	1000

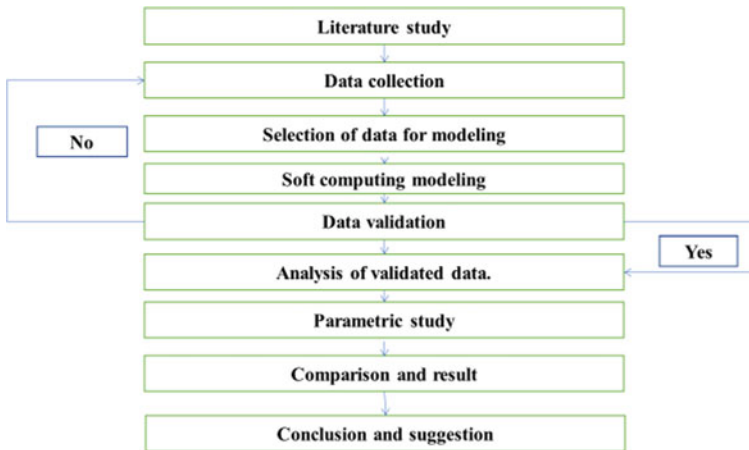


Fig. 1 Research methodology flow chart

4 Problem Statement

To perform a face stability analysis of a large single-bore tunnel of 15 m. diameter in soft soil.

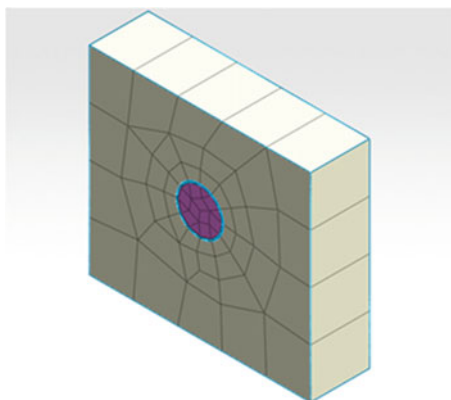
5 Research Methodology

The adopted research methodology is given in the flow chart. At first, the geotechnical data and primary set of pressure parameter to be applied to the tunnel model was collected from various literature. These data were analyzed by the soft computing method for validation purposes. It was observed that collected pressure parameters were inadequate for the face stability of large-diameter tunnels. Hence, again data were collected. Once it validates, a parametric study had been done for drawing conclusions, and suggestions were made according to it (Fig. 1 flow chart).

6 Data Analysis

The three-dimensional models were prepared for analysis at different C/D ratios by keeping longitudinal margin and vertical side margin below tunnel invert. Cover depth (C) variate from $C = 1D$ to $C = 12D$. Geotechnical data of soft soil and pressure parameters (shown in Tables 1 and 2) were taken from the collected data. Mohr's coulomb model was used. Five main cases were considered for study as follows and they are discussed in detail in the next section.

Fig. 2 Typical modeling and meshing for analysis



- Effect of adequate pressure on tunnel face.
- Effect of surcharge load on tunnel face.
- Effect of surcharge load with 10 m water table on tunnel face.
- Effect of surcharge load with 10 m submerged water level on tunnel face.
- Effect of lining thickness on tunnel face.

Figure 2 shows the typical tunnel modeling used for analysis. 13 sets of analysis, for each main case, were performed for observation purposes

Initially, to validate the collected data, models were prepared for $C/D = 1$, $C/D = 2$, $C/D = 4$, and $C/D = 6$, respectively, and the displacement profile was observed for the tunnel face at key locations, i.e., at the crown, at the invert, and at the right and left vertical side walls. The analysis and obtained profile showed that the applied pressure parameters were inadequate. Hence, required face pressure was calculated from modeling, i.e., by numerical method. From empirical formulas which were based upon the relation of jack thrust, TBM contraction pressure, and TBM gap pressure with respect to pipe diameter of TBM, the weight of pipe, length of pipe, the weight of Shield, and segment thickness were calculated by considering 2% volume loss. Meshing was done at the closed interval for accuracy. EPB TBM was considered, and construction stages for simulation were given according to it. The parametric study was done at the crown, at the invert, and at the right and left vertical walls of the tunnel for each model.

Maximum displacement and Total translation due to three directional loads at four key locations were observed. Self-weight was considered for analysis. After the application of calculated pressures, get an acceptable displacement profile. To observe it closely, again analysis was done by modeling at $C/D = 1$ to $C/D = 4$ at every 0.5 m interval, $C/D = 4$ to $C/D = 8$ at every 1 m. interval, and $C/D = 10$ and $C/D = 12$ at 2 m. interval. Analysis result was observed for all cases. From observed results, conclusions were drawn for tunnel face stability at the preferred C/D ratio on structural stability and on economical basis.

The design thickness for preliminary lining purposes was suggested for three different C/D ratios. M30 grade of concrete was considered. Minimum and maximum lining thickness were considered as 200 mm and 450 mm, respectively.

7 Observations

7.1 Case 1. Effect of Adequate Pressure on Various Parameters of Mega Tunnel

Application of pressure set 1 (Table 2) on TBM while tunnel advancing gives the minimum displacement of the crown and the invert, comparatively with both vertical walls. Vertical walls displace more because of inadequate face pressure and jack thrust. Figure 3 shows the displacement profile. It refers that while advancing of mega tunnels adequate application of pressure plays an important role.

Mollon et al. [8] suggested the collapse pressure should be based on the work equation, to avoid tunnel face collapse into the tunnel which are dependent on the following:

- The weight of soil.
- The collapse face pressure.
- A possible surcharge loading on the ground.

After calculating the adequate pressure parameter (Table 3), maximum displacement of the crown and the invert of the tunnel was observed, and comparatively less displacement of both vertical walls was found, as shown by the graph in Fig. 4.

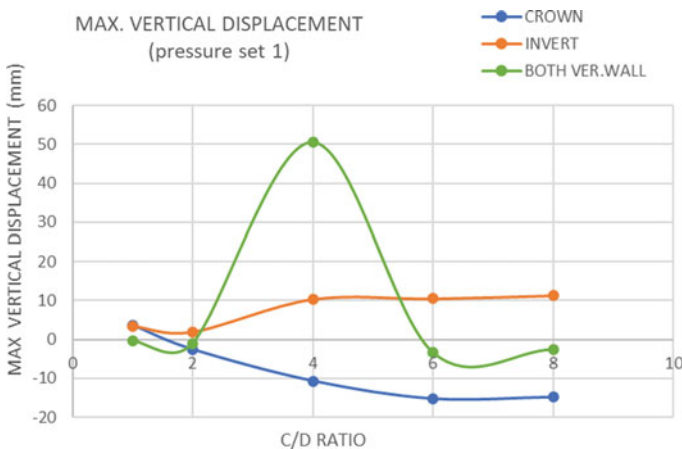


Fig. 3 Graph showing vertical displacement profile due to application of pressure set 1

Table 3 Pressure parameter (set 2)

No.	Type of pressure	Pressure QTY (kN/m ²)
		Pressure set 2
1	Drilling/Horizontal/Face pressure	232.5
2	Jack thrust	-75670
3	Pressure due to contraction over the body of the shield TBM	2120
4	Pressure due to gap between shield TBM and the segment diameter	5510

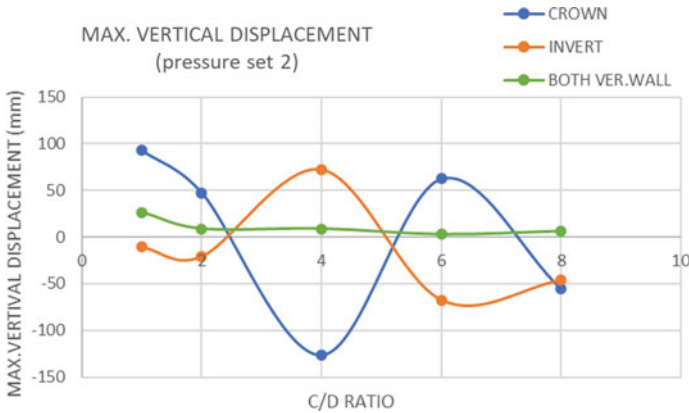


Fig. 4 Graph showing vertical displacement profile due to application of pressure set 2

7.2 Case 2. Effect of Surcharge Load on Various Parameters of Mega Tunnel

The arching effect was observed at $C/D = 1$ and $C/D = 1.5$ because of unequal distribution of stresses due to sufficiently lesser critical cover respective to the tunnel diameter. After $C/D = 2$, the displacement of nodes starts to change, and the crown of the tunnel starts to accept a particular trend of displacement till $C/D = 4$. The tunnel showed stabilized behavior in $C/D = 4$ to $C/D = 8$. The tunnel crown gives stable displacement but the invert showed a considerable rise in displacement in this region.

Due to the application of uniformly distributed pressure and static load, both side walls, i.e., right and left vertical walls give equal displacement. But it is negligible as compared to the crown and the invert (Fig. 6 for displacement profile) (Fig. 5).

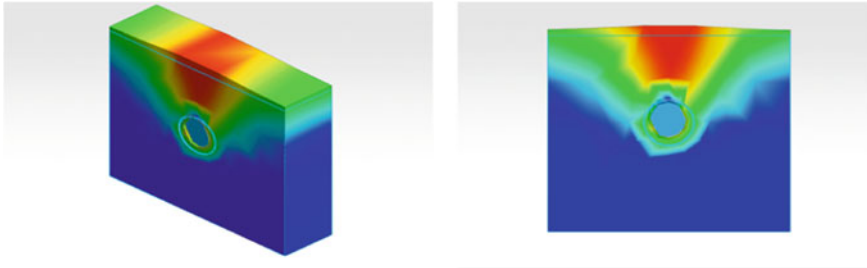


Fig. 5 Figure showing front and 3D view of the arching effect of the ground

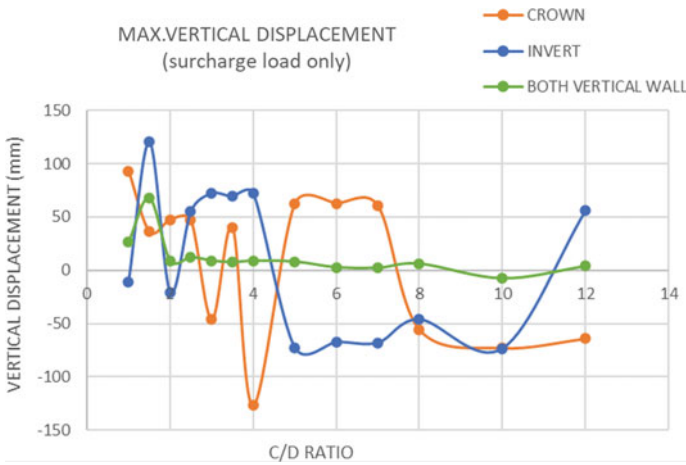


Fig. 6 Graph showing vertical displacement profile for the effect of surcharge load on tunnel key locations

7.3 Case 3: Effect of Surcharge Load with 10 m. Groundwater Table on Various Parameters of Mega Tunnel

The crown and the invert show the same displacement profile at $C/D = 1$ to $C/D = 2$, as that of the previous case in the application of only surcharge load. But, from $C/D = 3$, the downward displacement will be decreased up to $C/D = 4$. The displacement of the crown increases from $C/D = 5$ and $C/D = 7$ and shows a slight decrement at $C/D = 6$. The displacement of the crown at $C/D = 8$ decreased considerably. As stated above, the crown displacement decreased rapidly but from $C/D = 8$ to $C/D = 12$, it goes on increasing continuously. The invert also showed the same displacement as that of the previous case. From $C/D = 3$ to $C/D = 12$, the only change was the direction.

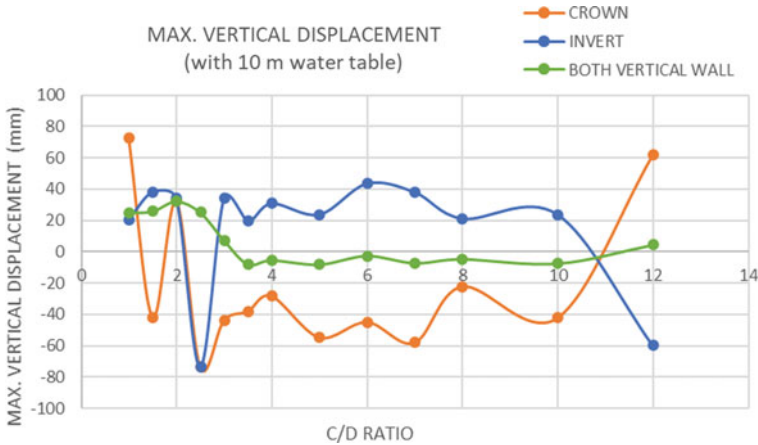


Fig. 7 Graph showing vertical displacement profile for the effect of surcharge load with 10 m groundwater table on tunnel key location

In this case, each vertical wall shows the same displacement profile as that of the invert and the crown though it was negligible in its comparison (Fig. 7 for displacement profile).

7.4 Case 4: Effect of Surcharge Load with 10 m. Submerged Water Level on Various Parameters of Mega Tunnel

The crown was displacing considerably in the downward direction from $C/D = 1-2$, but at $C/D = 2$, the crown displaced in the upward direction. The displacement gets increased slightly up to $C/D = 3$ followed by the change in the profile after it. At $C/D = 3.5$, the sudden change was observed in the displacement profile of the crown and the invert in opposite direction followed by a sudden change at $C/D = 4$.

The crown gets displaced in the downward direction up to $C/D = 6$. After it continued to be displaced in the upward direction up to $C/D = 8$. The invert showed the same displacement profile as that on the crown but in the opposite direction. Vertical displacement profile starts to be stable from $C/D = 8$, and it showed a stable profile till $C/D = 12$. The important behavior shown by the crown and the invert, in this case, is that the amount of displacement from $C/D = 3.5$ to $C/D = 12$ was the same but in the opposite direction.

In this case, each vertical wall shows a negligible displacement as compared to the crown and the invert (Fig. 8 for displacement profile).

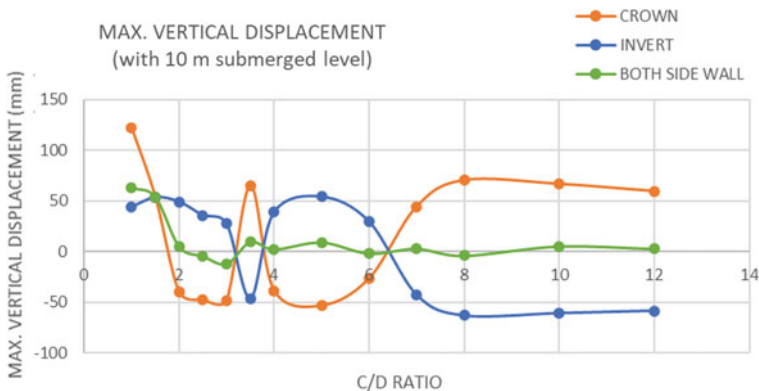


Fig. 8 Graph showing vertical displacement profile for the effect of surcharge load with 10 m water table on tunnel key locations

7.5 Total Translation of Mega Tunnel

Total translation of the tunnel is the resultant displacement that occurs of the node due to the application of the pressures on that node in three directions. For tunnel face stability purposes, the total translation of the tunnel due to pressure in all three direction is important to observed, with maximum displacement of the crown, the invert, and the vertical walls. From analysis, it was seen that between $C/D = 2$ and $C/D = 4$, case 2 (with only surcharge load) and case 4 (surcharge with 10 m submerged level) show the nearly equal translation. Case 3 (surcharge load with 10 m water table) had a maximum total translation than the other two cases. Case 2 and case 4 show consequently low total translation.

At $C/D = 3.5$, $C/D = 7$ and $C/D = 8$ give a nearly equal total translation of tunnel. At $C/D = 5$, case 2 and case 4 show the equal total translation (Fig. 9).

8 Discussion on Cases

From all above-observed parameters, a comparison was made based on maximum vertical displacement and total translation of all four nodes, i.e., the crown, the invert, and both vertical walls.

It was seen that the displacement and the translation of mega tunnel were more due to the effect of surcharge load with respect to surcharge load with the water table and submerge level. The total translation of the tunnel was the same in all cases at $C/D = 3.5$, $C/D = 7$ from $C/D = 8$. Though the effect of the water table and water level was more on vertical displacement, the translation was minimum due to forces in the X- and Y-directions.

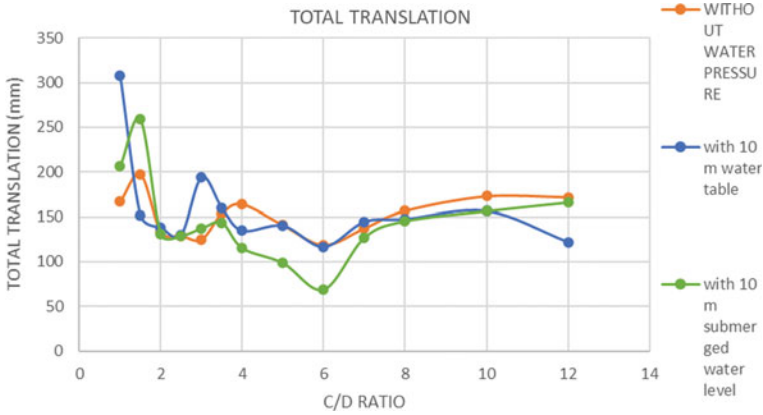


Fig. 9 Graph showing the total translation of mega tunnel

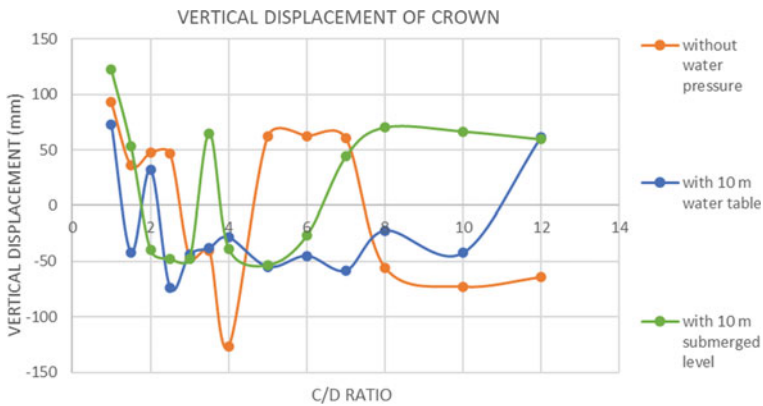


Fig. 10 Graph showing the comparison of vertical displacement profile of the crown

Previous research concludes that pore water pressure due to the presence of water table is affected more on face stability of tunnel [5, 6], but this study proposes the overburden or earth pressure above tunnel possesses more impact on tunnel face stability in soft soil (Figs. 10, 11 and 12).

9 Effect of Lining Thickness

From the above parametric study, it was observed that the tunnel starts to stabilize from $C/D = 3.5$, and it will show equal displacement and the total translation of the crown, the invert, and both vertical walls up to $C/D = 7$. Therefore, for observing the effect of lining thickness, $C/D = 3.5$, $C/D = 5$, and $C/D = 7$ were selected

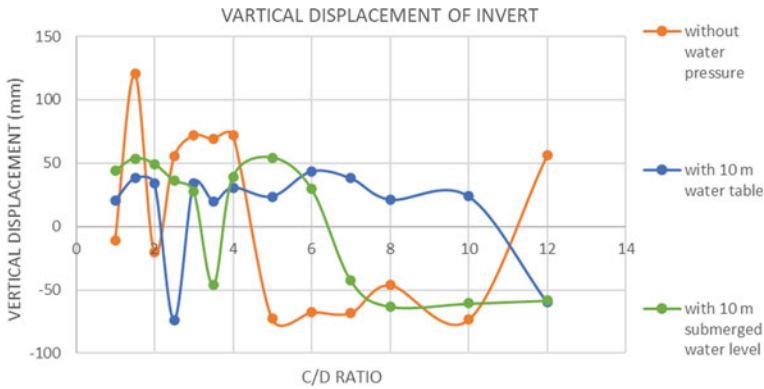


Fig. 11 Graph showing the comparison of vertical displacement profile of the invert

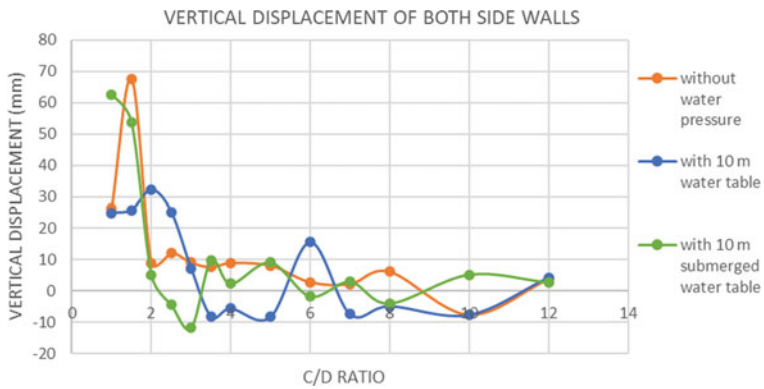


Fig. 12 Graph showing the comparison of vertical displacement profile of the vertical walls

for observation from a case surcharge with a 10 m submerged level. M30 grade of in-situ lining was considered. Maximum displacement and maximum solid stresses were observed at the crown and at the invert only. From the above study, it was observed that the displacement and translation at both vertical walls were negligible; hence, it was omitted. The range of lining thickness is in which the displacement of the node and the invert changes were observed (Figs. 13, 14, 15, 16, 17, and 18). Similarly, solid stresses were also observed. Lining thickness for preliminary design was selected. In the selected range, 50 mm thickness was added for safety purposes. The graph was plotted for the required C/D ratio vs lining thickness (Fig. 19).

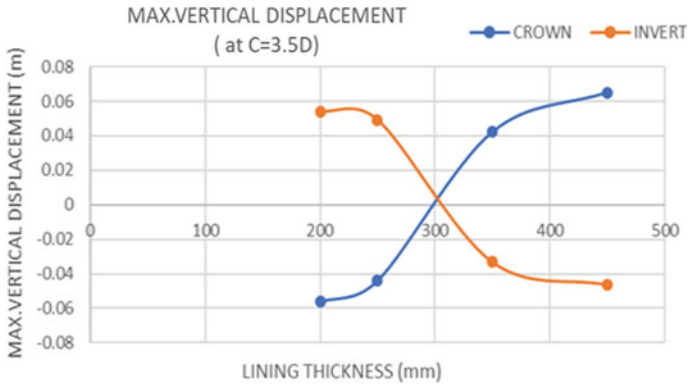


Fig. 13 Graph showing the effect of lining thickness on vertical displacement profile at C = 3.5D

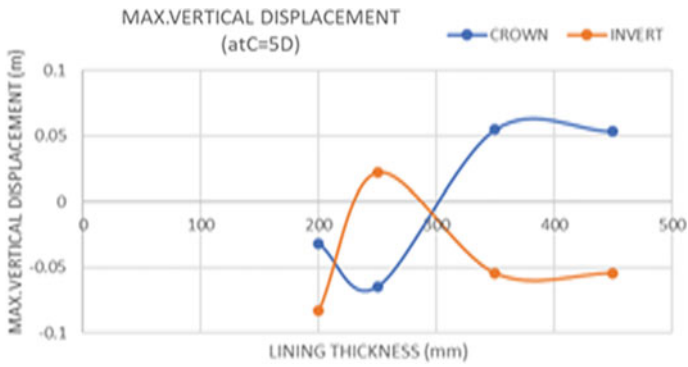


Fig. 14 Graph showing maximum solid stresses at C = 3.5D

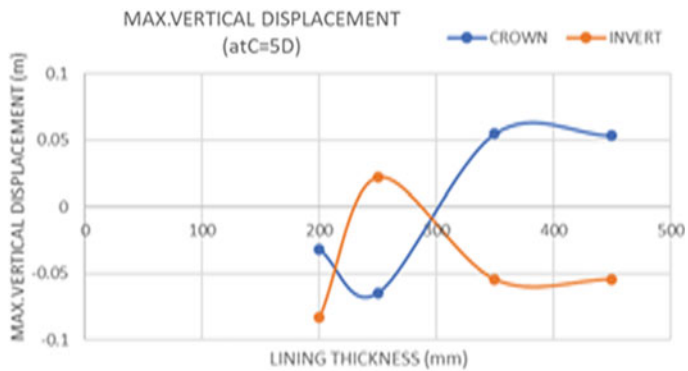


Fig. 15 Graph showing the effect of lining thickness on vertical displacement at C = 5D

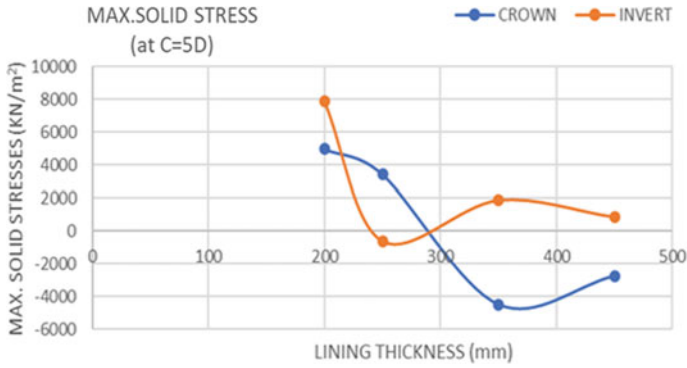


Fig. 16 Graph showing maximum solid stresses at C = 5D

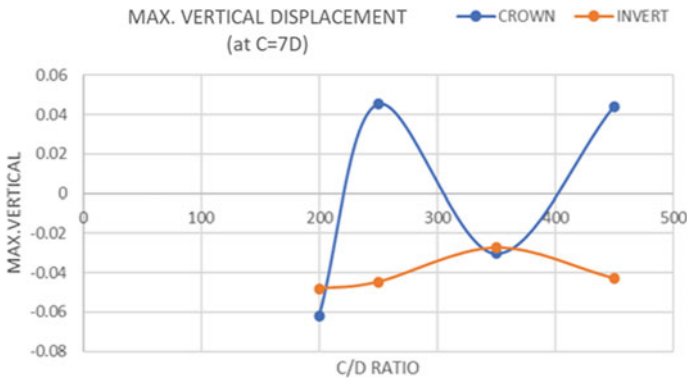


Fig. 17 Graph showing the effect of lining thickness on vertical displacement at C = 7D

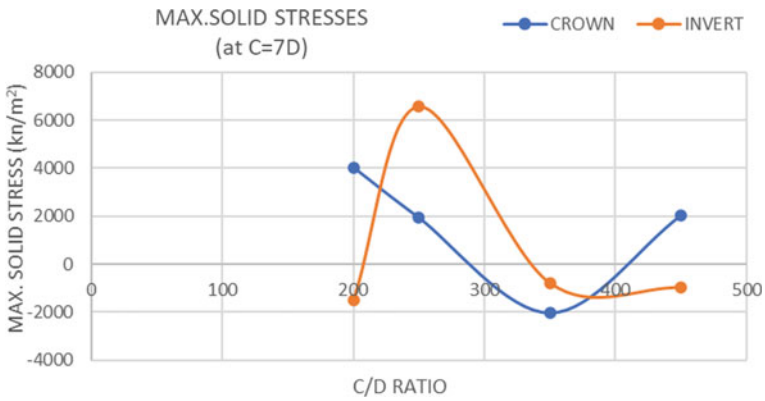


Fig. 18 Graph showing maximum solid stresses at C = 7D

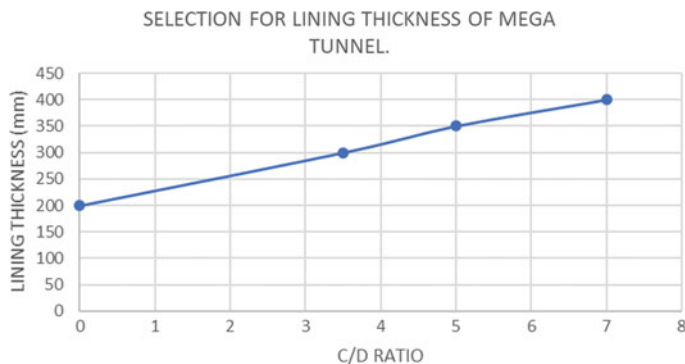


Fig. 19 Graph showing suggested preliminary lining thickness for required C/D ratio of mega tunnels

10 Suggestions

As per the above study, it can be concluded that the tunnel face can be stable at $C/D = 3.5$, $C/D = 5$, $C/D = 7$, and $C/D = 8$. From an economic point of view, preference will be given to $C/D = 3.5$. The required preliminary lining for the required C/D ratio is suggested and can be selected by referred graphical representation (Fig. 19).

11 Conclusions

Large-diameter tunnels more than 10 m in diameter are known as Mega Tunnel. It is beneficial to the society as it can facilitate a multi-transport system; hence, it is a profitable solution for urban infrastructure.

Face stability of Tunnel concerns with two aspects such as geotechnical strata and an adequate amount of pressure application while tunnel excavation. The elastic Modulus of strata is an important factor to decide the application of horizontal thrust. Earth pressure above the crown shows agreed behavior with horizontal thrust when adequately investigated.

The jack thrust application also varies with soil strength parameters such as unit weight and cohesion. TBM specification is one more prime concern while calculating jack thrust. It was observed that significant application of jack thrust is necessary to support excavating strata. The verge of collapse of ground is more in the initial three excavation stages.

Earth pressure or overburden is critical pressure for tunnel face stability in the case of Mega Tunnel rather than water pressure; hence, face stability may be analyzed by considering it. Hence, it can be concluded that a significant amount of applied pressure plays an important role in tunnel face stability; at this pressure, the tunnel

face can be stable at $C/D = 3.5$ in soft soil and ground deformation behavior will be nullified and can be neglected from $C/D = 7$.

The requirement of preliminary lining thickness in the mega tunnel is depending upon the C/D ratio. The required preliminary lining thickness is directly proportional to the given C/D ratio in soft soil.

References

1. Wang J et al (2019) Face stability analysis of EPB shield tunnels in dry granular soils considering dynamic excavation process. *J Geotech Eng, ASCE*
2. Khezri N, Mohamad H et al (2016) Stability assessment of tunnel face in a layered soil using upper bound theorem of limit analysis. *Geomech Eng*
3. Ibrahim E, Soubra AH et al (2015) Three—dimensional face stability analysis of pressurized tunnel driven in multilayered purely frictional medium. Elsevier, *Tunneling and Underground Space Technology*
4. Mollon G, Dias D et al (2017) Range of the safe retaining pressures of a pressurized tunnel face by probabilistic approach. *J Geotech Geoenviron Eng, ASCE*
5. Pan Q, Dias D (2016) The effect of pore water pressure on tunnel face stability. *Int J Numer Anal Methods Geomech*
6. Pan Q, Dias D (2017) Three-dimensional face stability of tunnel in weak rock masses subjected to seepage forces. Elsevier, *Tunnelling and Underground Space Technology incorporating to Trenchless technology*
7. Mollon G, Dias D, Soubra A-H (2010) Face stability analysis of circular tunnels driven by a pressurized shield. *J Geotech Geoenviron Eng* [https://doi.org/10.1061/\(ASCE\)GT.1943-5606.0000194](https://doi.org/10.1061/(ASCE)GT.1943-5606.0000194)
8. Mollon G, Phoon KK, Dias D, Soubra A-H (2011) Validation of a new 2D failure mechanism for the stability analysis of a pressurized tunnel face in spatially varying sand. *J Eng Mech* 10.1061/(ASCE)EM.1943-7889.0000196
9. Chen R-P et al (2013) Experimental study on face instability of shield tunnel in sand. Elsevier, *Tunnelling and Underground Space Technology*
10. Souza TG et al (2015) TBM pressure models—observations. *Theory and Practice, Geotechnical Synergy in Buenos Aires*
11. Zeng P et al (2014) Reliability analysis of circular tunnel face stability obeying Hoek-Brown failure criterion considering different distribution types and correlation structure *ASCE*
12. Zhang ZX, Liu C, Huang X (2017) Numerical analysis of volume loss caused by tunnel face stability in soft soil. *Springer*
13. Hernandez YZ et al (2019) Three-dimensional analysis of excavation face stability of shallow tunnels. Elsevier, *Tunnelling and Underground Space Technology*
14. Shiau J, Al-Asadi F (2020) Three-dimensional analysis of circular tunnel heading using broms and bennermark's original stability number. *Int J Geomech* 20(7):06020015, *ASCE*
15. Broere W (1998) Face stability calculation for a slurry shield in heterogeneous soft soil. *Tunnels Metropol* 215–218
16. Kawadas MJ (2005) Monitoring ground deformation in tunnelling: current practices in transportation tunnels. Elsevier, *Engineering Geology*
17. Kim S-H et al (2006), Evaluation of shield tunnel face stability in soft ground. In: *International symposium on underground excavation and tunneling*
18. Kirsch A (2010) Experimental investigation of the face stability of shallow tunnel in sand. *Springer*
19. Senent S, Mollon G et al (2013) Tunnel face stability in heavily fractured rock masses that follows the Hoek-Brown failure criterion. *Int J Rock Mech Min Sci* 60:440–451

20. Zeng P, Senent S, Jimenez R (2014) Reliability analysis of circular tunnel face stability obeying Hoek-Brown failure criterion considering different distribution types and correlation structures, (ASCE) [https://doi.org/10.1061/\(ASCE\)CP.1943-5487.0000464](https://doi.org/10.1061/(ASCE)CP.1943-5487.0000464)
21. Elarabi H, Mustafa A (2014) Comparison of numerical and analytical method of analysis of tunnel. In: Conference paper
22. Vu MN et al (2015) The impact of shallow cover on stability when tunnelling in soft soils. Elsevier, Tunnelling and Underground Space Technology incorporating to Trenchless technology
23. Xizang CL (2016) Three dimensional FEA on ground responses during twin tunnel construction using the URUP method. Elsevier, Tunneling and Underground Space Technology
24. Shiau J et al (2017) Stability charts for unsupported plane strain tunnel heading in homogeneous undrained clay. Int J GEOMATE
25. Dias D (2018) Three-dimensional face stability analysis of circular tunnels by numerical simulation, ASCE
26. Liu C, Peng Z et al (2020) Influence of TBM advance on adjacent tunnel during URUP tunneling: a case study and numerical investigation. Appl Sci
27. Neuner M et al (2020) On discrepancies between time—dependent nonlinear 3D and 2D finite element simulation of deep tunnel advance: a numerical study on Brenner Base tunnel. Comput Geotech 119:103355

Development of Financial Model for Hybrid Annuity Model Road Project



Pratiksha B. Gilbile and Gayatri S. Vyas

Abstract Public-Private-Partnership (PPP) models are in demand for infrastructure development all over the world. Road transport is an important infrastructure for the economic development of the country. Commonly adopted PPP models by the National Highways Authority of India in road projects are Build-Operate-Transfer (BOT) toll, BOT—annuity, Hybrid Annuity Model (HAM), toll-operate-transfer, operate—maintain—transfer, Engineering Procurement Construction (EPC). HAM is a combination of the traditional EPC and BOT—annuity model. HAM considers the involvement of both the parties that is the public and private sector. Mixed initial investment and different risk allocations make HAM distinct from other PPP models. PPP models are often long-term in nature, which makes both the parties check project's financial viability. This study aims to develop a financial risk model using Net Present Worth (NPW)-at-risk method. From the literature, financial key risk parameters are identified. A case study is selected and cash flows from the public's perspective are prepared. Probability distributions are allocated to risk parameters and Monte Carlo simulation is carried out using @Risk tool. The study also compares central and state policies of HAM. The findings from the developed financial model show variation of NPW as well as critical risk parameters. This financial model can be used as a decision tool for public authority and certain mitigation techniques can be applied to optimize project characteristics for the identified critical risk parameter.

Keywords Financial risk model · Hybrid annuity model · Net present worth-at-risk · Public-private-partnership

P. B. Gilbile (✉)

Construction Management, College of Engineering Pune, Pune, India
e-mail: gilbilepb19.civil@coep.ac.in

G. S. Vyas

Department of Civil Engineering, College of Engineering Pune, Pune, India
e-mail: gsv.civil@coep.ac.in

1 Introduction

Road transport is a critical infrastructure for the country's economic growth. India has the world's second-largest road network of around 58.98 lakh kilometers [1]. Road networks in India comprise expressways, national highways, state highways, major district roads, village roads. Historically, the government has been making investments in the transport sector. The Engineering, Procurement, and Construction (EPC) contracting method was in practice before the introduction of Public-Private Participation (PPP) in the early 1990s. However, to encourage private sector participation, the ministry has laid down comprehensive policy guidelines for private sector participation in the development of National Highways. In the last two decades, PPP models have been used in road infrastructure. Build-Operate-Transfer (BOT) is the most popular used PPP model. Variants of PPP are evolved to encourage the private sector's participation. Hybrid Annuity Model (HAM) is one of the variants of PPP introduced by the National Highways Authority of India (NHAI) in 2016. This introduced model is a combination of traditional EPC and BOT. One of the main risks associated with infrastructure projects is financial risk. HAM involves initial investment by both the sectors—public and private. So risk associated with the finance is altered in this model as it incorporated the concept of the time value of money and life cycle cost by introducing new bidding parameter-lowest project life cycle cost [2].

In this study, a financial risk model is developed by using Net Present Worth (NPW) @Risk concept. For developing a financial model following objectives are defined (i) To identify financial risk parameters, (ii) to define cash flows, (iii) to perform MCS in @Risk tool, (iv) to compare between state and government policies of HAM model. A case study is taken for comparison between state and government policies about HAM. Financial risk parameters affecting the Bid Project Cost (BPC) are identified and risks associated with those parameters are assigned. Monte Carlo Simulation (MCS) is done in @Risk tool to obtain the results. This developed model gives variable NPW thus helping the public sector to understand variations in financial statements. It also gives an idea about the critical risk parameter involved in cash flows.

2 Literature Review

2.1 Overview of PPP in India

The contracting method used earlier for the road network is EPC. The Government of India (GoI) has initiated economic liberalization and globalization since 1991. Inadequacies in the national road network, both in terms of magnitude and quality, have been identified as one of the hurdles to economic growth [3]. This necessitates the introduction of PPP models in India. Various PPP models used by NHAI

Table 1 Risk allocations of EPC, BOT, and HAM

Risks	EPC	BOT	HAM
Financing risk	Public sector	Private sector	Public sector
Demand risk	Public sector	Private sector	Public sector
O and M risk	Public sector	Private sector	Private sector
Construction risk	Public sector	Private sector	Private sector

are Build-Operate-Transfer (BOT) toll, BOT—annuity, HAM, toll-operate-transfer, operate—maintain—transfer. Among PPP models, BOT is one of the most popular models in roads [4]. In a typical BOT highway project, a private sector is authorized to construct and operate a transportation infrastructure facility and in return, is allowed to collect tolls for a specified period to recover all the costs and earn a reasonable profit. The contractor has financial risk in a project under the BOT model. So government authority introduced HAM which is with different risk allocations. Table 1 summarizes financing, demand, O and M, construction risk in EPC, BOT, and HAM.

2.2 Key Features of HAM

HAM is one of the PPP models in which initial investment is done by both the sectors—public and private. Following are the key features of HAM [1, 2].

- The public sector contributes to 40% of the BPC which is to be given in equal installments according to project milestones.
- 60% of BPC initially invested by the private sector, which designs, construct and maintain the project for 15 years.
- These investment ratios can be different for state and central government policies.
- Public Sector returns this (60% of project cost) in biannual annuity payments (inflation-indexed) over 15 years. Along with annual payments, interest shall be paid on reducing the balance of the cost.
- Bid parameter in HAM is the life cycle cost that is NPW of the BPC and first-year NPW of Operation and Maintenance (O and M) should be quoted. Equation 1 represents project life cycle cost.

$$\text{Lowest Project Life cycle cost} = \sum_{k=1}^n (\text{NPW of BPC} + \text{NPW of 1st O and M}) \tag{1}$$

- For the calculation of NPW, discounting rate is taken as bank rate + 3% are used.
- The private sector will be responsible for O and M throughout the concession period.
- Toll collection will be the responsibility of the public sector.

2.3 *Financial Risk Parameters*

The following 4 financial risk parameters are considered as uncertain parameters while developing a financial model:

- **BPC**

BPC is the most uncertain parameter as it involves construction cost. The minimum cost is favorable. For the analysis, a lognormal probability distribution is taken with Coefficient of Variation (CoV) 0.1 [4–6].

- **O and M cost**

O and M cost is the cost for all the expenditures during the concession period. It is the responsibility of the private sector. For this project, a normal probability distribution is considered with CoV 0.1 [6].

- **Inflation rate**

The inflation rate may vary during the project life and it can majorly affect project cash flows. It is taken as normal probability distribution with CoV 0.1 [4, 5].

- **Discounting rate**

For the calculation of NPW, discounting rate is taken as bank rate + 3%. A probability distribution is taken as a normal distribution with CoV 0.1 [4, 5].

2.4 *Financial Risk and Evaluation Methods*

Various risks are associated with infrastructure projects like construction risk, O and M risk, financial risk, demand risk, etc. Projects for road networks are mostly long-term in nature and require large initial expenditure. Financial management becomes necessary to determine the feasibility of the project. Various researchers have focused on different evaluation methods. These methods can be categorized into discounted cash flows and non-discounted cash flows [5]. These two methods can be differentiated based on the Time Value of Money (TVM) concept. TVM is nothing but the value of money changes with time. Discounted cash flows determine the present value of the future cash flows by considering the time value of money. Methods used in discounted cash flows are—NPW, Internal Rate of Return (IRR). Methods that are used in non-discounted cash flows do not consider the time value of money. For example—payback period, accounting rate of return. However, all these methods are based on assumption that cash flows are certain but the project's cash flows may differ from forecasted cash flows. Tiong [6] has developed an NPW @Risk method that incorporates NPW and MCS to account for uncertainty in the cash flow diagram. MCS is used to generate the possible distribution of NPW. Kumar et al.

[5] applied the NPW @Risk concept to 30 real-world BOT projects and developed a financial model. This NPW @Risk method considers probability associated with risk parameters and calculates variable NPW.

3 Research Methodology

From the literature review, financial risk parameters affecting project life cycle cost are identified. Various financial methods are studied from the literature survey and the NPW @Risk method is selected for this study. For the development of the financial risk model, a case study of “improvement of Belhe-Satara road, Maharashtra, India” is selected. Differences in-between state and central policies for HAM are studied and their effect on cash flows is comparatively analyzed. For that cash flows are developed for both cases. MCS is performed using the @Risk tool on both case studies. Comparative analysis of central and state policies is done. Figure 1 shows the research methodology of the study.

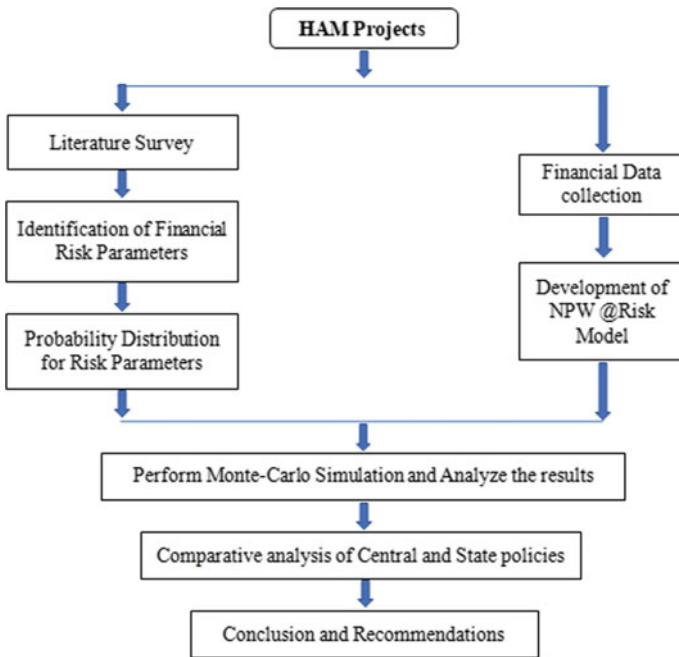


Fig. 1 Research methodology

4 Development of Financial Risk Model

A case study of improvement of Belhe–Satara road, Maharashtra India is selected. The BPC for the case study is 211 crore having a construction period of 2 years. First-year O and M quoted is 1.2 crore. Bank rate is assumed as 6.25%. For calculation of NPW, it is taken as bank Rate + 3% that is 9.25%. The inflation rate is taken as 5%. Bid due date is 23-04-2018.

Details for calculating NPW of BPC and first NPW of O and M payment are as follows:

- BPC—This is the cost of construction of the project which is payable by the public sector to the private sector. Initial Investment (60% of the BPC) given by the public sector is given in 5 equal installments during the construction period. Table 2 shows details of payments during the construction period.
- Adjusted BPC—It is the revised BPC accounted for variation in price index multiple. Revised values are calculated for NPW calculation. Table 3 shows details of adjusted BPC for the price index multiple confirming to respective physical progress. In Table 3, 10% of the BPC is adjusted for the price index multiple confirming to 10% physical progress.

Case 1: Cash flows as per state policies (60% initial investment from public sector + 40% Initial investment from the private sector).

Table 2 Details for payments during the construction period

Milestone details	Payment stages
First payment milestone	On achievement of 10% physical progress
Second payment milestone	On achievement of 30% physical progress
Third payment milestone	On achievement of 50% physical progress
Fourth payment milestone	On achievement of 75% physical progress
Fifth payment milestone	On achievement of 90% physical progress

Table 3 Adjusted BPC details

BPC details	Physical progress
10% of the BPC	10%
20% of the BPC	30%
20% of the BPC	50%
25% of the BPC	70%
15% of the BPC	90%
10% of the BPC	On completion

Table 4 Calculation of construction support and adjusted BPC for case 1 and case 2

Date	Construction support for case 1	Construction support for case 2	Adjusted BPC for case 1 and case 2
23-04-2018	–	–	–
05-06-2019	26.74	17.82	22.28
28-01-2020	27.56	18.37	45.93
24-06-2020	28.07	18.71	46.78
27-10-2020	28.50	19.00	59.38
13-01-2021	28.77	19.18	35.97
05-03-2021	–	–	24.13

All values are in crore

Case 2: Cash flows as per central policies (40% initial investment from public sector + 60% Initial investment from the private sector).

- Construction support is calculated as 20% of each payment (inflation-indexed). Table 4 shows the calculation of construction support and adjusted BPC for case 1 and case 2. On a date 05-06-2019, first payment should be released which is 20% of the BPC subjected to inflation on achievement of 10% physical progress is 26.74 crore. Similarly for case 2 17.82 crore is calculated. In both the cases, adjusted BPC is calculated as 10% of the BPC on achievement of 10% physical progress.

The completion cost to be paid out in O and M period is 94.83 crore in case 1 and 141.38 crore in case 2.

O and M (inflation-indexed) calculations as per concession draft agreement are calculated in Table 5. The amount to be quoted for O and M for each annuity payment is stated in detail. For 1st annuity payment, 33.33% of quoted O and M amount should be given that is 33.33% of 1.2 crore. Calculated O and M (inflation-indexed) value is 0.47 crore.

The lowest project life cycle cost as per Eq. (1) is calculated. For case 1, static NPW is 197.95 crore and static NPW of case 2 is 195.28 crore.

5 Results and Discussion

Results were obtained in @Risk tool is to determine variable NPW. On a developed model of both cases, 1000 iterations were carried out. The calculated static NPW for case 1 is 197.95 crore. NPW of BPC of case 1 has 90% probability that value lies between 166.9 crore and 231.5 crore (Refer Fig. 2). Tornado chart gives a ranking of the risk parameters according to their effect on cash flows. BPC is the critical influencing parameter for case 1 (Refer Fig. 3). It also shows variation from the mean. NPW of BPC of case 2 has 90% probability that value lies between 165.5

Table 5 O and M calculations

Annuity	Percentage of amount quotes toward O and M (%)	Calculated O and M (in crore)
1st Annuity	33.33	0.47
2nd Annuity	33.33	0.48
3rd Annuity	33.33	0.49
4th Annuity	33.33	0.50
5th Annuity	33.33	0.51
6th Annuity	33.33	0.52
7th Annuity	50.00	0.79
8th Annuity	50.00	0.80
9th Annuity	50.00	0.82
10th Annuity	50.00	0.83
11th Annuity	50.00	0.85
12th Annuity	50.00	0.86
13th Annuity	50.00	0.88
14th Annuity	50.00	0.89
15th Annuity	66.67	1.21
16th Annuity	66.67	1.23
17th Annuity	66.67	1.25
18th Annuity	66.67	1.27
19th Annuity	66.67	1.29
20th Annuity	66.67	1.31

All values are in crore

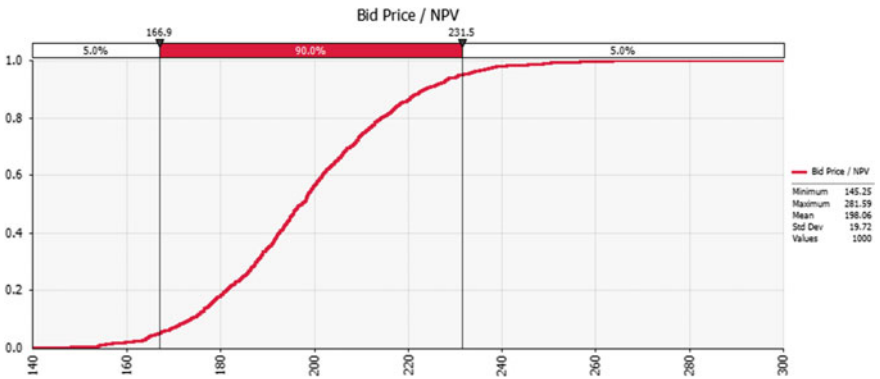


Fig. 2 NPV variation for case 1

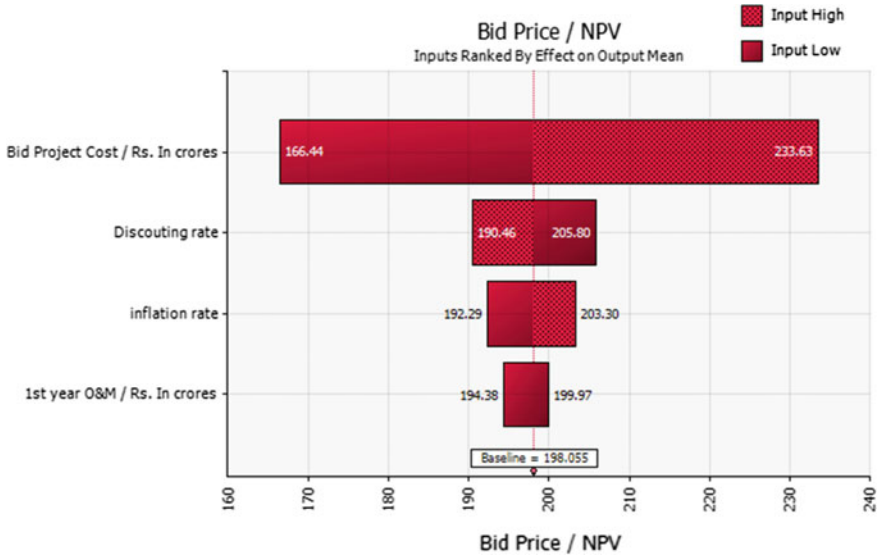


Fig. 3 Tornado chart for case 1

crore and 228.4 crore (Refer Fig. 4). Critical influencing parameter for case 2 is also coming as BPC (Refer Fig. 5).

From the results obtained through analysis, it was observed that there is not much difference between state and central policies. Table 6 summarizes comparative results between state and central policy.

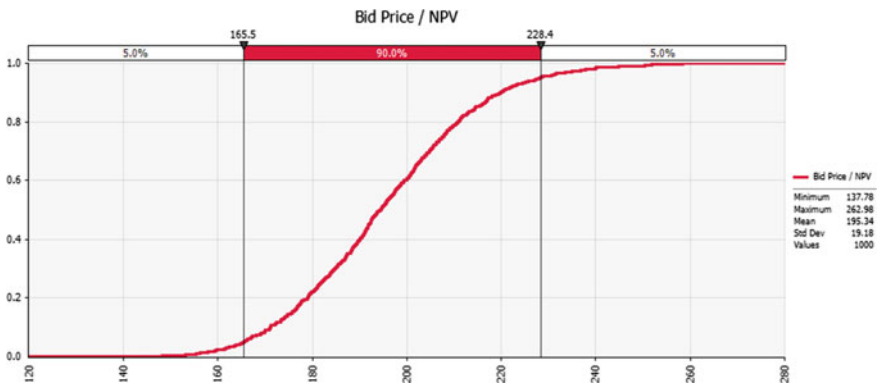


Fig. 4 NPW for case 2

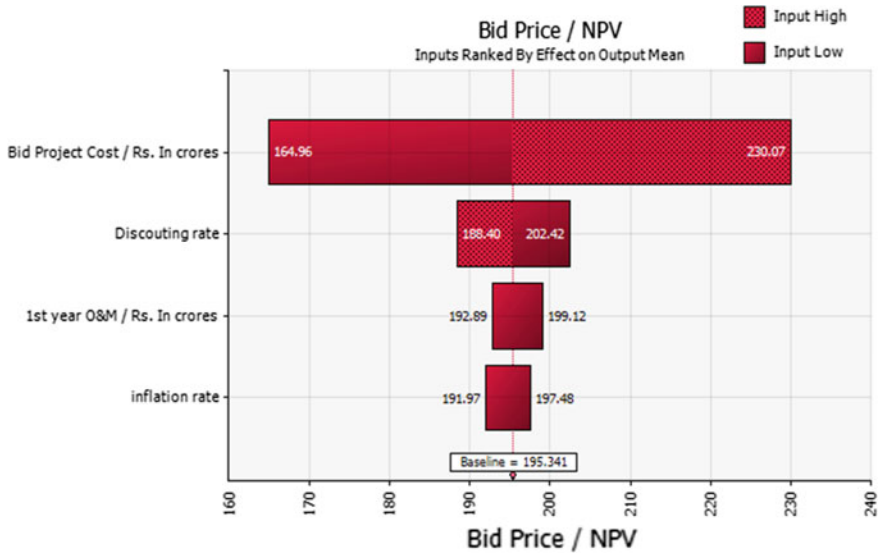


Fig. 5 Tornado chart for case 2

Table 6 Comparative results between state and central policy

	Case 1 (as per state policy)	Case 2 (as per central policy)
Static NPW	197.95	195.28
Variable NPW (Maximum value)	231.5	228.4
Variable NPW (Minimum value)	166.9	165.5
Critical influencing parameter (1st parameter)	BPC	BPC
Critical influencing parameter (2nd parameter)	Discounting rate	Discounting rate

All values are in crore

6 Conclusion

In this study, a financial risk model is developed using NPW @Risk concept for HAM project. This model gives variable NPW having maximum of 231.5 crore and minimum of 166.9 crore for case 1 (Refer Fig. 2) and for case 2 maximum value is 228.4 crore and minimum value is 165.5 crore (Refer Fig. 4). This gives an idea about the uncertainty associated with risk parameters. The Tornado chart gives a critical influencing parameter. BPC is the critical influencing parameter in both cases. Mitigation techniques can be applied to reduce the effect of critical influencing parameters and maximize profit. The study also compares the NPW @Risk model between the state and central policies. The findings obtained for both

cases are similar (Refer Table 6). It implies that risks associated are nearly equal irrespective of policy. It will help public sector to understand financial risk. This study can be applied to other PPP models too. Further additional risk parameters may be considered incorporating additional uncertainties which may increase the accuracy of the outcome.

References

1. GOI (2019–20) Report of Ministry of Road Transport and Highways, Government of India
2. Garg S, Mahapatra D (2019) Hybrid annuity model: hamming risk allocations in Indian highway public-private partnerships. *J Public Aff* 19(1):e1890
3. Singh LB, Kalidindi SN (2006) Traffic revenue risk management through annuity model of PPP road projects in India. *Int J Project Manag* 24(7):605–613
4. Kagne RK, Vyas GS (2020) Investigation and modeling of financial risks associated with PPP road projects in India. In: International conference on transportation and development 2020. American Society of Civil Engineers, Reston, VA
5. Kumar L, Jindal A, Velaga NR (2018) Financial risk assessment and modelling of PPP based Indian highway infrastructure projects. *Transp Policy* 62:2–11
6. Ye S, Tiong RLK (2000) NPV-at-risk method in infrastructure project investment evaluation. *J Constr Eng Manag* 126(3):227–233

Analysis of Perpetual Pavement Design Considering Subgrade CBR, Life-Cycle Cost, and CO₂ Emissions



Saurabh Kulkarni and M. S. Ranadive

Abstract The current study aims to evaluate the possibility of perpetual pavement design for the proposed ring road to the City of Pune. Perpetual Pavement concept is relatively new for Indian scenario. In India, national highways are still designed for 15–20 years of service life where as perpetual pavements can provide better service period. The Indian Road Congress guideline (IRC 37:2018) mentions various combinations of pavement design. A comparative study was carried out between proposed pavement design by Pune Metropolitan Region Development Authority and five categories of flexible pavement mentioned in IRC guidelines designed with perpetual pavement concept. The comparison is carried out on the grounds of checking the effect of raising California Bearing Ratio of subgrade soil from 10 to 15% with respect to life cycle cost assessment and carbon dioxide emissions. The study analyses whether the improvement in CBR of subgrade has any substantial change in design, cost and CO₂ emission of all five combinations of perpetual pavement. IITPAVE software was used to design perpetual pavements. KENPAVE and WESLEA software were used to validate the design. It is observed that the flexible perpetual pavement can be a better alternative considering the factors like expected service period, life-time cost, and environmental concerns. The study also concludes that positive impact of improved subgrade CBR in terms of overall thickness, life cycle cost, and CO₂ emission depends on type of pavement combination used for perpetual pavement design.

Keywords Perpetual pavement · Life cycle cost assessment · Carbon dioxide emissions

1 Introduction

Pune is one of the largest cities and an important industrial hub in the state of Maharashtra. The traffic in and around Pune city is increasing due to increased

S. Kulkarni (✉) · M. S. Ranadive
Department of Civil Engineering, College of Engineering, Pune, India
e-mail: ssk15.civil@coepp.ac.in

© The Author(s), under exclusive license to Springer Nature Singapore Pte Ltd. 2023
M. S. Ranadive et al. (eds.), *Recent Trends in Construction Technology and Management*, Lecture Notes in Civil Engineering 260,
https://doi.org/10.1007/978-981-19-2145-2_92

1257

population and industrial growth. The bypass roads constructed for the city have now become internal part of the city limits, because of this traffic coming from outside the city and destined to another location is passing through the Pune city. This has resulted in overburden on the intra city road networks and creating traffic congestion throughout the city. The bypass roads are also experiencing heavier traffic than expected, resulting in deterioration of those roads. Therefore, to address this issue Maharashtra State Road Development Corporation (MSRDC) has decided to build circumferential 4 lane and 14 m-wide road of connecting all major highways to each other.

Government of Maharashtra has formed the Pune Metropolitan Region Development Authority (PMRDA) as the executive authority for the project [1]. The Proposed ring road Connects Pune-Mumbai, Pune-Solapur, Pune-Nagar, and Pune-Satara highway to each other bypassing the city. The service period of perpetual pavement (PP) is about 50 years. It does not require major structural repair work and to face distresses restricted to the top of the pavement, periodic maintenance with regard to surface renewal is required. India did not have any official code for the design of PP. However, with the latest publication by the IRC [2], the mechanistic method for the design of pavement to serve longer service periods can be adopted.

1.1 Objectives and Scope

- Design PP using IRC 37:2018 guidelines.
- Perform LCCA comparison between proposed pavement for ring road and five different combinations of PP.
- Determine and compare total CO₂ emissions caused by proposed pavement and different combinations of PP.
- Finding out the best suited option among five combinations of PP.
- Examine the effect of improvement in CBR of subgrade of all the five PP design combinations with respect to overall pavement thickness, total lifetime cost, and CO₂ emission.

2 Design Criteria

The compressive strain acting in the vertical direction at the top of subgrade and tensile strain acting in the horizontal direction at the bottom of asphalt layer is considered as the critical strains. The key point in PP design is to keep these strains in some particular limits. Strain level below which there is no cumulative damage over an infinite number of cycles is called as Endurance Limit (EL). The EL for horizontal tensile strain in the bituminous layer and vertical compressive strain at the top of subgrade is 70 μ and 200 μ , respectively, as per tests conducted in laboratories at Asphalt Institute at 20 °C in United States. In major part of India, the average annual

pavement temperature generally is close to 35 °C. IRC 37 has proposed that for such conditions, corresponding limiting strains for the fatigue and rutting endurance limit may be considered as 80 μ and 200 μ micro strains, respectively.

2.1 Design Traffic

The proposed road is going to have two lanes on both side with a width of 3.75 m for each lane. For the preliminary planning purpose, the project road is divided into 19 sections. The data from the traffic survey done for the proposed ring road is used for design purpose in this paper. Almost 5976 commercial Vehicles per day are expected to be served in this project according to ring road summary report. As per IRC 37, the cumulative number of standard axles to be allowed during the design life is given by Eq. 1.

$$N = \frac{365 \times [(1 + r)^n - 1] \times D \times A \times F}{r} \quad (1)$$

where

- N Cumulative number of standard axles in terms of million standard axle (msa)
- r Growth rate according to IRC (SP: 84-2009) is considered as 5%
- n Design life assumed for proposed pavement is 15 years as per PMRDA report
- D Lane distribution factor (0.75)
- A Commercial vehicles per day
- F Vehicle damage factor (6.0).

All the values are considered from IRC 37:2018 and summary report of Pune Ring Road.

According to the calculation, pavement should be designed for approximately 212 msa.

3 Information About Soil Characteristics Observed in the Region of the Proposed Project

The soils occurring in the region are mostly black soil which are classified in the four categories namely reddish-brown soil, lateritic black soil, medium light brownish black soil, and coarse shallow reddish black soil. The California Bearing Ratio (CBR) of the subgrade soil, for the design of the proposed pavement was determined as per IS:2720 Part-16. The design CBR is taken as 10%. There are many methods to improve subgrade CBR. For the design purpose, the effective resilient modulus is limited to a maximum value of 100 MPa as per the IRC guidelines. Hence, present

study explores the effect of improvement in CBR from 10 to 15% in the analysis. The study also investigated whether improvement in CBR cause any beneficiary difference in pavement design, life cycle cost, and CO₂ emissions.

3.1 Resilient Modulus

For the present study, the relationship suggested in IRC 37 between resilient modulus and CBR as shown in Eq. 2 is considered.

$$M_{RS} = 17.6 * (CBR)^{0.64} \quad (2)$$

where M_{RS} = Resilient modulus of subgrade soil (MPa).

Equation 3 is used here as per IRC guidelines for estimation of modulus of the granular layer.

$$M_{R \text{ Granular}} = 0.2(h)^{0.45} M_{RS} \quad (3)$$

where h = Thickness of granular layer in mm.

4 Pavement Combination

The possible combinations proposed are

1. Bituminous surface course (BC) with granular sub-base (GSB) and base (Combination A).
2. BC with Cement Treated Base (CTB), Cement Treated sub-base (CTSB) and granular crack relief layer (CRL) (Combination B).
3. BC with CTSB, CTB and Stress absorbing membrane interlayer (SAMI) at the interface of base and the bituminous layer (Combination C).
4. BC with GSB, CTB and CRL (Combination D).
5. BC with CTSB and GSB (Combination E).

The SAMI is not considered as a part of structural layer for the pavement analysis. As per IS SP53:2010, SAMI may consist of elastomeric modified binder like Styrene-Butadiene Rubber (SBR) applied at the rate of minimum 1 kg/m², complying with Ministry of Road Transport and Highways (MoRT&H) clause number 521. As per the IRC guidelines, for protection against rutting, Viscosity Grade 40 (VG 40) bitumen shall be used for surface course and for the dense bituminous macadam (DBM). The modulus of different pavement layers as mentioned in Table 1 are considered for analysis here. Poisson's ratio for CTSB as well as for CTB is considered as 0.25 and for remaining layer types, it is considered as 0.35 as per the IRC guidelines.

Table 1 Structural layers properties as per IRC guidelines

Layer	Elastic/resilient modulus (MPa)
Subgrade	$17.6 * (CBR)^{0.64}$
Unbound granular layers	$0.2(h)^{0.45} M_{RS}$
Granular base over CTSB sub-base	350 for crushed aggregates
CTB	5000
CRL	450
CTSB	600
Bituminous layer	3000

4.1 Fatigue Criteria

For the analysis purpose, the fatigue equation suggested in the IRC 37 guidelines was adopted.

$$N_f = 0.561 \times C \times 10^{-4} \times \left(\frac{1}{\epsilon_t}\right)^{3.89} \times \left(\frac{1}{M_{Rm}}\right)^{0.854} \tag{4}$$

where

$$C = 10^M, \text{ and } M = 4.84 \times \left[\frac{V_{be}}{V_a + V_{be}} - 0.69\right]$$

V_a = Percent volume of air void in the mix,

V_{be} = Percent volume of effective bitumen,

N_f = Fatigue life of bituminous layer,

ϵ_t = Maximum horizontal tensile strain at the bottom of the DBM,

M_{Rm} = Resilient modulus (MPa) of the bituminous mix,

C = Adjustment factor to consider the effect of effective binder volume and air void content on the fatigue life.

For the present study, the V_a , V_{be} values considered are 3.5% and 11.5%, respectively, as recommended in IRC guidelines. So, Eq. 4 becomes

$$N_f = 0.000132 \times \left(\frac{1}{\epsilon_t}\right)^{3.89} \times \left(\frac{1}{M_{Rm}}\right)^{0.854} \tag{5}$$

4.2 Rutting Criteria

The equivalent number of standard axle load (80 KN) repetitions that can be served by the pavement for 90% reliability levels as per the IRC guidelines is given by Eq. 6.

$$N_R = 1.41 \times 10^{-8} \times \left(\frac{1}{\varepsilon_v} \right)^{4.5337} \quad (6)$$

where N_R = subgrade rutting life, ε_v = vertical compressive strain at the top of the subgrade.

EL provides a thickness limit for the pavement and helps to avoid extra expenditure as well as overdesign. Therefore, as shown in Tables 2 and 3, the design of pavement is carried out by trial and error with till endurance limit of the strain values closest to 80 and 200 μ , whichever first are obtained [3, 4]. For the analysis purpose, a single axle dual wheel assembly with the standard axle load of 80 KN was considered. The contact radius and tire pressure are considered as 15.5 cm and 0.56 MPa, respectively, as per the IRC guidelines.

In this study, minimum thickness permissible for CRL, sub-base and base layer is considered for all the trial sections and bituminous pavement layers are kept as variable ones for PP design. It was done so to provide sufficient stiffness in the upper pavement layers as per the concept of PP [5]. From Table 2 and putting strain values in Eqs. 5 and 6, it can be said that perpetual design provides better service period for far larger amount of traffic. The top layer acts as a protective barrier, as the distresses are restricted to the wearing course. From Table 3 and as shown in Fig. 1, it is evident that only combination A would be having greater thickness that proposed conventional pavement by PMRDA. Table 3 shows that compared to proposed conventional pavement, PP design with combination A shall have more overall thickness, which shows increase of 5.64–2.36% as subgrade CBR is improved from 10 to 15%. In case of combination B, pavement thickness is reduced by 4.83% but no change is observed even if subgrade CBR is improved from 10 to 15%. In case of combination C, pavement thickness is reduced by 22.58, 23.38, 24.1, 25, 26.61, and 27.41% as subgrade CBR is increased from 10 to 15% successively. In case of combination D, pavement thickness is reduced by 3.22%, irrespective of improvement in subgrade CBR from 10 to 15%, no change is observed in pavement thickness. In case of combination E, overall thickness is reduced by 1.61–2.41% if subgrade CBR is improved as mentioned above.

5 Life-Cycle Cost Analysis

The cost comparison for a 1 km long and 14 m wide section of Pune Ring Road for five mentioned combinations of PP was done using the standard rates in Indian rupees as per the state of Maharashtra government's schedule of rates [6]. Material

Table 2 Modulus of materials (in MPa) and corresponding strain values for pavement combinations

Trial combination	Subgrade	Sub-base	Base	Crack relief interlayer	BC + DBM	Horizontal tensile strain (μ)	Vertical compressive strain (μ)
Proposed by PMRDA	76.82	–	240.13	–	3000	151.4	245.4
<i>Perpetual with CBR 10%</i>							
A	76.82	–	214.45	–	3000	79.64	161.8
B	76.82	600	5000	450	3000	80	172.9
C	76.82	600	5000	–	3000	13.31	198.80
D	76.82	166.71	5000	450	3000	80	171.4
E	76.82	600	350	–	3000	78.53	171.9
<i>Perpetual with CBR 11%</i>							
A	81.66	–	227.96	–	3000	79.70	159.40
B	81.66	600	5000	450	3000	80	168.9
C	81.66	600	5000	–	3000	13.00	198.20
D	81.66	177.21	5000	450	3000	80	167.10
E	81.66	600	350	–	3000	78.21	167.40
<i>Perpetual with CBR 12%</i>							
A	86.33	–	241	–	3000	79.88	157.40
B	86.33	600	5000	450	3000	80	162
C	86.33	600	5000	–	3000	12.67	198
D	86.33	187.35	5000	450	3000	79.84	163.20
E	86.33	600	350	–	3000	79.67	166.7
<i>Perpetual with CBR 13%</i>							
A	90.87	–	253.67	–	3000	80.00	155.8
B	90.87	600	5000	450	3000	80	161.8
C	90.87	600	5000	–	3000	12.31	198.10
D	90.87	197.20	5000	450	3000	79.68	159.6
E	90.87	600	350	–	3000	79.49	162.9
<i>Perpetual with CBR 14%</i>							
A	95.29	–	266.0	–	3000	78.66	151.4
B	95.29	600	5000	450	3000	80	158.7
C	95.29	600	5000	–	3000	11.91	198.5
D	95.29	206.79	5000	450	3000	79.54	156.4
E	95.29	600	350	–	3000	79.24	159.40
<i>Perpetual with CBR 15%</i>							
A	99.59	–	278.0	–	3000	79.08	150.4
B	99.59	600	5000	450	3000	80	155.8

(continued)

Table 2 (continued)

Trial combination	Subgrade	Sub-base	Base	Crack relief interlayer	BC + DBM	Horizontal tensile strain (μ)	Vertical compressive strain (μ)
C	99.59	600	5000	–	3000	11.47	199.20
D	99.59	216.12	5000	450	3000	79.40	153.4
E	99.59	600	350	–	3000	79.01	156.10

Table 3 Thickness of trial combinations

Trial combination with CBR value	Sub-base (mm)	Base (mm)	CRL/SAMI (mm)	DBM (mm)	BC (mm)	Total thickness (mm)
Proposed by PMRDA (Conventional) 10%CBR	200 (GSB)	250 (WMM)	–	120	50	620
<i>Combination A</i>						
	GSB	WMM		DBM	BC	
10–11%	200	150		255	50	655
12%	200	150		250	50	650
13–14%	200	150		240	50	640
15%	200	150		235	50	635
<i>Combination B</i>						
	CTSB	CTB	CRL	DBM	BC	
10–15%	200	100	100	140	50	590
<i>Combination C</i>						
	CTSB	CTB	SAMI	DBM	BC	
10%	200	100		130	50	480
11%	200	100		125	50	475
12%	200	100		120	50	470
13%	200	100		115	50	465
14%	200	100		110	50	460
15%	200	100		105	50	455
<i>Combination D</i>						
	GSB	CTB	CRL	DBM	BC	
10–15%	200	100	100	150	50	600
<i>Combination E</i>						
	CTSB	Granular base course		DBM	BC	
10–11%	200	150		210	50	610
12–15%	200	150		205	50	605

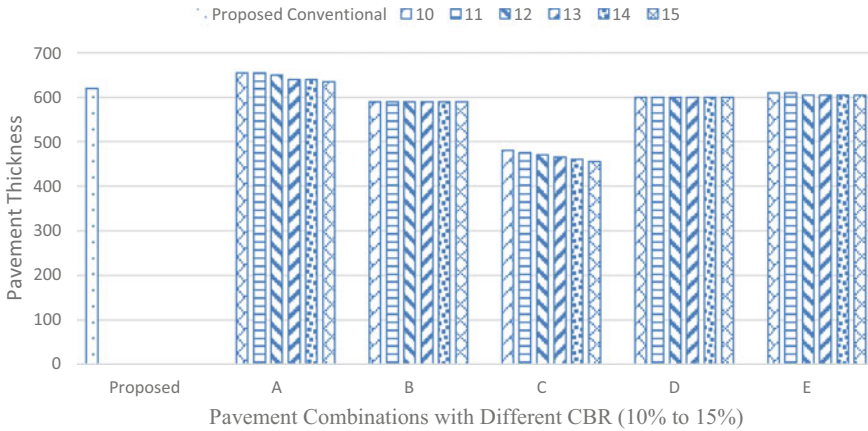


Fig. 1 Comparison of pavement thickness

Table 4 Schedule of rates

Layer	MoRT&H Clause	Rate (INR)	Unit
GSB	401	1598	m ³
WMM	406	1657	m ³
CTSB	404	1827	m ³
CTB	404	1902	m ³
CRL	401	1657	m ³
BC	509	7272	m ³
DBM	507	6742	m ³
SAMI	517	100	m ²

Specification and work requirements are considered as per MORT&H Clause [7] as shown in Table 4. In the present study, the long-term cost analysis using the Net Present Value (NPV) method has been discussed. The discount rate and an inflation rate has been adopted as 10%, and 5% respectively. MORT&H guidelines suggest that a layer of 25 mm BC should be provided once every five years. As the proposed pavement is designed for 15 years, it needs to be rebuilt after the 15th, 30th, and 45th years of service.

The present study considers limited number of parameters like cost due to initial construction, periodic maintenance, and life cycle cost for a span of 50 years. Depending on these points, cost of laying an overlay for proposed conventional pavement and five combinations of PP have been shown in Tables 5 and 6. Calculations for pavement reconstruction for proposed pavement and PP are shown in Tables 7 and 8, respectively. LCCA is carried out for 50 years to compare the lifetime cost linked with construction of one-kilometer length of PP and the proposed conventional pavement. Based on information from people related with road construction and available literature, it was found that while estimating the future cost of road

Table 5 Maintenance cost (millions INR) calculation for proposed conventional pavement

Year	Maintenance for proposed pavement (mm)	Cost per km	Inflation	NPV
5th	Overlay of 25	2.54	3.24	2.01
10th	Overlay of 25	2.54	4.14	1.60
15th	Major repair work			
20th	Overlay of 25	2.54	6.74	1.00
25th	Overlay of 25	2.54	8.60	0.79
30th	Major repair work			
35th	Overlay of 25	2.54	14.01	0.50
40th	Overlay of 25	2.54	17.88	0.40
45th	Major repair work			
50th	Overlay of 25	2.54	29.13	0.25
Total				6.55

Table 6 Maintenance cost (millions INR) for PP

Year	Maintenance for PP	Cost per km	Inflation	NPV
5th	Overlay of 25 mm	2.54	3.24	2.01
10th		2.54	4.14	1.60
15th		2.54	5.28	1.26
20th		2.54	6.74	1.00
25th		2.54	8.60	0.79
30th		2.54	10.98	0.63
35th		2.54	14.01	0.50
40th		2.54	17.88	0.40
45th		2.54	22.82	0.31
50th		Reconstruction work in 50th year		
Total				8.50

Table 7 Cost (millions INR) of pavement reconstruction for proposed conventional pavement

Year	Full pavement reconstruction	Initial construction cost per km	Inflation	NPV
15th	Proposed Conventional Pavement	26.69	38.48	18.82
30th		26.69	55.48	13.28
45th		26.69	80.00	9.37
Total				40.97

Table 8 Cost (millions INR) of pavement reconstruction (after 50 years) for proposed PP

CBR value	Initial construction cost	5.0% Inflation per annum (millions)	NPV
<i>PP combination A</i>			
10–11	37.11	125.67	11.60
12	36.64	124.08	11.45
13–14	35.70	120.89	11.16
15	35.23	119.30	11.01
<i>PP combination B</i>			
10–15	28.40	96.17	8.88
<i>PP combination C</i>			
10	25.16	85.20	7.86
11	24.67	83.54	7.71
12	24.20	81.95	7.56
13	23.72	80.32	7.41
14	23.25	78.73	7.27
15	22.78	77.14	7.12
<i>PP combination D</i>			
10–15	28.71	97.22	8.97
<i>PP combination E</i>			
10–11	33.38	113.04	10.43
12–15	32.91	111.44	10.29

construction, it is considered that the inflation in price happen only during 50% of the tenure of design period. The design period for the PP is 50 years. Hence, to provide an equivalent platform for comparison, LCCA is carried out for total life of 50 years as shown in Table 9. It can be observed that savings in range of 22.91–48.26% can be achieved in case of PP depending upon combination considered. Table 9 shows that any combination of PP is better option than conventional pavement even though initial construction cost is less in case of proposed pavement except compared to combination C. But if we consider life cycle cost for a span of 50 years then considerable amount of saving can be achieved by adopting any kind of PP combination as shown in Fig. 2.

6 Emission of CO₂

Embodied carbon means all the CO₂ emitted in producing and disposing materials at the end of its lifetime. The data from inventory of carbon and energy [8] as well as from the study of Auroville Earth Institute [9] was used for the calculations of embodied CO₂ as shown in Table 10. A generalized proportioning of various

Table 9 Life-cycle cost analysis for proposed conventional pavement and five combinations of PP

NPV (in millions INR)					
Pavement type and CBR	Initial construction	Overlay	Reconstruction	Total	Saving in case of PP (%)
Proposed by PMRDA	26.69	6.55	40.97	74.21	
<i>PP combination A</i>					
10 and 11	37.11	8.50	11.60	57.21	22.91
12	36.64	8.50	11.45	56.59	23.74
13 and 14	35.70	8.50	11.16	55.36	25.41
15	35.23	8.50	11.01	54.74	26.24
<i>PP combination B</i>					
10–15	28.40	8.50	8.88	45.78	38.31
<i>PP combination C</i>					
10	25.16	8.50	7.86	41.52	44.05
11	24.67	8.50	7.71	40.88	44.92
12	24.20	8.50	7.56	40.26	45.75
13	23.72	8.50	7.41	39.64	46.59
14	23.25	8.50	7.27	39.02	47.42
15	22.78	8.50	7.12	38.40	48.26
<i>PP combination D</i>					
10–15	28.71	8.50	8.97	46.18	37.77
<i>PP combination E</i>					
10–11	33.38	8.50	10.43	52.32	29.50
12–15	32.91	8.50	10.29	51.70	30.34

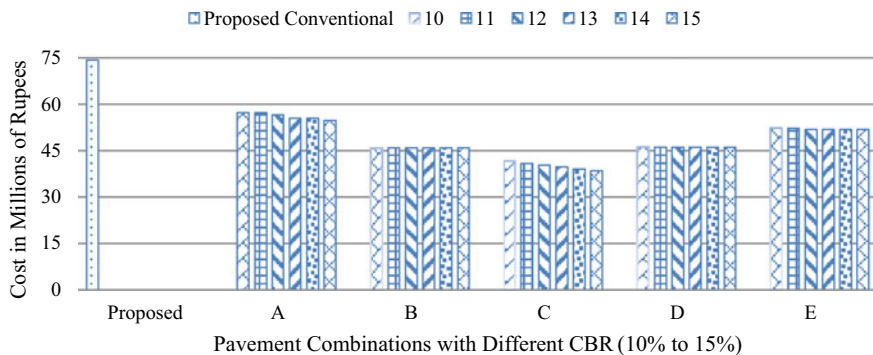


Fig. 2 Comparison of total life-cycle cost for 50 years for different pavement combination

Table 10 Embodied CO₂ (kg/kg material) of different materials

Material	Embodied CO ₂
Cement	0.83
Bitumen	0.48
Coarse aggregate	0.0216
Fine aggregate	0.002

materials used in different layers of the pavement is shown in Table 11 which is based on the MoRT&H specifications, IRC SP:49 [10], IRC SP:53 [11], and IRC SP:89 [12].

Embodied CO₂ for different pavement layers is shown in Table 12. Initial total CO₂ Emission for Proposed and PP Combinations have been reported in Table 13 whereas overall CO₂ emission for span of 50 years is reported in Table 14. In case of Combination C, from the available literature, Embodied CO₂ value for SBR is considered as 2.76 kg/Kg. So, Embodied CO₂ for SAMI Layer per KM is 38.64 tons/m³. Table 13 shows that initial total CO₂ emission of conventional pavement is less by almost 13–37%, but if we consider lifetime emissions, PP is superior option as shown in Table 14. It shows that in comparison with proposed conventional pavement for whole lifespan, combination A causes 53.16–54.42% less CO₂ emission as subgrade CBR is increased from 10 to 15% successively. Similarly, Combination B and D show a reduction of 50.30% and 55.57%, respectively. Combination E shows reduction of 49.56–49.87% as subgrade CBR is improved whereas combination C would cause reduction in CO₂ emission by 50.28–51.86% as subgrade CBR is increased from 10 to 15% successively.

Table 11 Generalized properties for various materials of flexible pavements

Properties of the mix	Pavement layers						
	CTB	CTSB	CRL	WMM	GSB	BC	DBM
Bitumen by mass (%)	–	–	–	–	–	5.5	4.5
Cement by mass (%)	2	2	–	–	–	–	–
Aggregates by mass (%)	98	98	100	100	100	94.5	95.5
Coarse fraction of total aggregates (%)	65	80	70	70	80	55	60
Fine fraction of total aggregates (%)	35	20	30	30	20	45	40
Density (kg/m ³)	2300	2300	2300	2300	2300	2400	2300

Table 12 Embodied CO₂ (in Kg) for flexible pavement layers of various combinations

Pavement layer	WMM	GSB	CTSB	CTB	BC	DBM
Embodied CO ₂ for 1/m ³	36.15	40.66	78.03	71.40	92.34	79.90

Table 13 Initial total CO₂ emission for proposed conventional pavement and five combinations of PP

Proposed by PMRDA/Proposed conventional					
Total embodied CO ₂ (ton)	439.24				
Total embodied CO ₂ (ton)					
Combination trial	A	B	C	D	E
PP (10% CBR)	539.64	590.30	567.14	496.85	603.41
PP (11% CBR)	539.64	590.30	561.55	496.85	603.41
PP (12% CBR)	534.05	590.30	555.95	496.85	597.82
PP (13% CBR)	522.87	590.30	550.36	496.85	597.82
PP (14% CBR)	522.87	590.30	544.77	496.85	597.82
PP (15% CBR)	517.27	590.30	539.18	496.85	597.82

Table 14 Total CO₂ emission for proposed conventional pavement and five combinations of PP for 50 years span considering overlays and reconstruction

Proposed by PMRDA/Proposed conventional					
Total embodied CO ₂ (ton)	1773.12				
Total embodied CO ₂ (ton)					
Combination trial	A	B	C	D	E
PP (10% CBR)	830.52	881.17	858.01	787.72	894.29
PP (11% CBR)	830.52	881.17	852.42	787.72	894.29
PP (12% CBR)	824.92	881.17	846.82	787.72	888.69
PP (13% CBR)	813.74	881.17	841.23	787.72	888.69
PP (14% CBR)	813.74	881.17	835.64	787.72	888.69
PP (15% CBR)	808.14	881.17	830.05	787.72	888.69

7 Conclusion

The study led us to conclude that combination C is the most cost friendly option in addition to have least design thickness among various Combinations of PP. This also shows that strong base and sub-base layers with higher modulus can provide cost effective and strong pavement structure. Though the pavement thicknesses proposed in this study are not absolute, they give a fair idea about comparison between conventional and perpetual pavements. The concept of perpetual pavement suggests having thicker bituminous layers to keep the strain levels under limit but the study shows that providing a stable foundation, use of treated subgrade and use of high stiffness base materials are important considering the huge expenditure in road construction and maintenance. This can be related to the rising price of crude oil and therefore increased cost of bitumen in the developing country like India. Further investigation about CO₂ emissions reveals that combination D among all the five combinations is

the most preferred option considering environmental aspect. The comparison among isolated perpetual pavement combination reveals that improvement in subgrade CBR combinations results in no change in overall pavement thickness, total lifetime cost, and CO₂ emission in case of combination B and D. If one considers expenditure as a major factor then the sequence of preference among the five combinations would be C, B, D, E, and A. But with respect to environmental issue the sequence of preference would be D, A, C, B, and E. India is still a developing country and signatory of Kyoto Protocol, so there can be a dilemma in choosing between least costly and most eco-friendly option. Overall, it can be said that PP should be advocated for the construction of highways in India.

References

1. Executive summary report of Pune ring road
2. Indian Road Congress IRC 37 (2012) Guidelines for design of flexible pavement
3. Ranadive M, Kulkarni S (2016) Perpetual pavement for rural roads: a concept. In: A national conference on fifteen years of PMGSY. Transportation Engineering Group, Civil Engineering Department, Indian Institute of Technology Roorkee, India
4. Kulkarni S, Ranadive M (2021) Effect of change in the resilient modulus of bituminous mix on the design of flexible perpetual pavement. In: Proceedings of the 3rd international conference on advanced technologies for societal applications, vol 1, chapter 83. Springer Nature, Switzerland AG
5. Walubita LF, Scullion T (2010) Texas perpetual pavements—new design guidelines. Report No: 0-4822-P6, Texas Department of Transportation and the Federal Highway Administration
6. Government of Maharashtra (2019–20) PWD schedule of rates
7. Ministry of Road Transport and Highways Government of India (2013) Specification for road and bridge works
8. Hammond G, Jones C (2008) Inventory of carbon & energy: ICE. Sustainable Energy Research Team, Department of Mechanical Engineering, University of Bath, UK
9. Maini S, Thautam V (2009) Embodied energy of various materials and technologies. Auroville Earth Institute (AEI), Tamil Nadu, India
10. Indian Road Congress IRC SP:49 (2010) Guidelines for the use of dry lean concrete as sub-base for rigid pavement
11. IRC SP:53 (2010) Guidelines on use of modified bitumen in road construction. Second revision, Indian Road Congress, New Delhi
12. IRC SP:89 (2010) Guidelines for soil and granular material stabilization using cement lime and fly ash. Indian Road Congress, New Delhi

Laboratory Investigation of Lateritic Soil Stabilized with Arecanut Coir Along with Cement and Its Suitability as a Modified Subgrade



B. A. Chethan, B. M. Lekha, and A. U. Ravi Shankar

Abstract If a pavement is constructed on weak soil, its lifespan drastically reduces due to the low strength induced by moisture-induced distresses. Such soils may undergo considerable changes in volume. In order to modify these properties, soil stabilization can be done. By stabilizing the soil along with the improvement in strength, its durability can be increased. Stabilization may be of chemical or mechanical type. In this investigation, lateritic soil was stabilized using 0.2–1% arecanut coir, and its compaction characteristics were evaluated. The lateritic soil is found to be nondurable. The reinforcement alone could not improve the strength and durability effectively. Therefore, 3% binding agent ordinary Portland cement (43 grade) was added to the mix. Due to cement stabilization, UCS and CBR values were improved, and the optimum values were observed at 0.6% arecanut coir dosage. The addition of cement has resulted in a change in silica, alumina, and calcium oxide contents, thereby contributing to the formation of hydration products. The samples with 1% coir and cement have completed 12 wet–dry cycles, but the weight loss observed was >14%. All the specimens showed low soil loss under freeze–thaw cycles. The performance of cured specimens under fatigue loading was satisfactory. Since the specimens could not pass wet–dry durability criteria, they can be considered for modified subgrade.

Keywords Lateritic soil · Stabilization · UCS · CBR · Durability · Fatigue

1 Introduction

In Malabar, India, laterites were used for building construction [1]. This term was cited in the eighteenth century. The lateralization process occurs due to alternate

B. A. Chethan (✉) · A. U. Ravi Shankar
Civil Engineering Department, NITK Surathkal, Mangaluru, India
e-mail: chethanba@gmail.com

B. M. Lekha
Department of Civil Engineering, KVG College of Engineering, Sullia, D.K. Dist, Karnataka, India

© The Author(s), under exclusive license to Springer Nature Singapore Pte Ltd. 2023
M. S. Ranadive et al. (eds.), *Recent Trends in Construction Technology and Management*, Lecture Notes in Civil Engineering 260,
https://doi.org/10.1007/978-981-19-2145-2_93

1273

wet–dry seasons, where heavy rainfall, humidity, and elevated temperatures exist. India includes 60–80% red, yellowish-red laterite soils, extending from 0.1 to 0.5 m in depth. Due to their high weathering resistance, they are used as building stones. A substantial amount of aluminum (Al) and iron (Fe) is present in these soils. They are originated from igneous rocks. Leather in 1898 and Voelcker in 1893 investigated these soils [15] and stated that these soils are common in coastal areas. Weak lateritic soils can lead to pavement distresses. Therefore, the necessity of stabilization comes into the picture. Ordinary Portland cement and lime are commonly used stabilizers from the olden days. Stabilization can change the microstructure of soil due to the formation of hydration products. The lateritic soils are locally available; hence, in situ stabilization can be done at a lower cost instead of borrowing a good material. This soil is weathered naturally, where the iron, aluminum hydroxides were formed due to the chemical process [6], and may exhibit low plasticity. These hydrated oxides govern the characteristics of the deposit. If a high amount of clay is present in this soil, it may cause severe structural distress due to its low bearing capacity. The lowered plasticity may be due to sesquioxides dehydration, stronger bond formation between the particles, resisting water penetration [2].

Stabilization with a low dosage of cement is the economical and easiest way to upgrade granular soils [4, 5, 8, 22]. If the fines are <40%, cement stabilization can suit better for the granular soils. In order to improve aggregate bases, cement is found to be a suitable additive, where a linear relationship was found between cement dosage and UCS values [16]. At a cement dosage of 1 or 2%, the granular base materials performed better than recycled cement concrete materials [7]. But a higher dosage of cement may cause increased stiffness and brittle failures. An increase in compaction effort and curing period results in significant improvement of strength, and cement content reduction causes a decrease in strength [13].

India is considered to be one of the major contributors to arecanut production in the world. Karnataka and Kerala produce 72% of arecanut (482,000 tons in the cultivation area of 388,000 ha) [3]. These fibers are cheaper, naturally, abundantly available, and can be effective as reinforcing material. The hard, fibrous husk is about 30–45% of areca fruit. These fibers have rich hemicellulose content. The use of reinforcement in soil [21] may increase shear strength. Reinforced weak soil has exhibited an increase in OMC, CBR, whereas the MDD was reduced due to low fiber density [11]. The polypropylene fibers with cement showed improvement in UCS, shear strength of clayey soil. The specimens failed at higher strains due to higher ductility [20]. The fly ash and polypropylene fiber amended soil was found to be suitable for base and sub-bases [10]. The coir fiber was found to be an efficient reinforcement for improving the CBR of rural road clayey subgrade soil [14]. The fiber and sand inclusion improved the plunger penetration resistance in lithomargic clay, and resulted in higher UCS [19] values. As the arecanut coir is biodegradable, the loss of strength of reinforced soil can be expected with time. But, if a stabilizer is used along with fiber, it can compensate for strength loss, thereby not hampering the structural condition [17]. The CBR of fiber-reinforced soil with fly ash was found to be suitable for low-volume roads [9]. Similar results were observed when the soil

specimens were reinforced with palm fibers [18]. Even the fiber reinforcement was found to improve CBR of black cotton soil [12].

2 Materials and Methodology

2.1 Lateritic Soil

All basic test properties of lateritic soil are determined as per relevant IS codes, a summary of which is presented in Table 1. This soil has a red color. A major fraction of the soil passes through 4.75 mm and retains over 75 micron IS sieve. Also, 32% clay portion is present in this soil; hence, this soil is classified as clayey sand (SC) as per IS code.

Laboratory chemical analysis was conducted to determine the compositions of uncemented and cemented soil. Table 2 shows that SiO_2 , Al_2O_3 , and CaO percentages were increased after stabilizing with cement. It indicates that silica, alumina, and CaO significantly contributed to enhance the strength of set soil.

Table 1 Basic properties of lateritic soil

Test property and values		
Specific gravity		2.45
Grain size distribution (%)	a) Gravel	9
	b) Sand	44
	c) Silt	15
	d) Clay	32
Consistency limits (%)	Liquid limit (LL)	56
	Plastic limit (PL)	29
	Plasticity index (PI)	27
IS soil classification		SC
At	IS standard Proctor compaction	IS modified Proctor compaction
MDD (g/cc)	1.68	1.91
OMC (%)	19.2	14.0
Unsoaked CBR (%)	8	13
Soaked CBR (%)	2	3
UCS (kPa)	138	206
Co-efficient of permeability (cm/s)	0.35×10^{-7}	0.20×10^{-7}

Table 2 Chemical composition of untreated and treated soil

Oxides (%)	SiO ₂	Fe ₂ O ₃	Al ₂ O ₃	S	CaO	MgO	pH	EC (μS/cm)
Lateritic soil	55.36	6.24	4.98	0.042	0.019	0.003	5.91	1.27
Stabilized lateritic soil	58.26	5.06	7.21	0.19	2.45	2.94	8.1	4.28

Table 3 Physical properties of arecanut coir

Diameter (mm)	Length (mm)	Density (g/cc)	Young modulus (kN/mm ²)	Tensile strength (kN/m ²)
0.35	28	1.09	27	2.2

Table 4 Chemical composition of arecanut coir

Cellulose (%)	Hemicellulose (%)	Lignin (%)	Ash (%)	Pectin (%)	Wax (%)
Nil	35–64.8	13–24.8	4.4	Nil	Nil

2.2 *Arecanut Coir*

Arecanut coir was collected from Puttur Taluk, Karnataka. Dried arecanut shells have a brown color. These shells were soaked in water for a week, and coir was manually extracted. The physical and chemical properties of the arecanut coir are tabulated in Tables 3 and 4. These fibers have an aspect ratio of 80 and a specific gravity of 0.67.

The dosage of coir can have significant effects on the strength improvement of reinforced soil. A low coir dosage may be insufficient to bind the soil and may lead to low strength. A high coir dosage may be ineffective due to excess fiber concentration, which hampers strength development. Therefore, the optimum dosage was estimated based on experimental results by varying dosages from 0.2 to 1%. All strength tests, durability, and fatigue tests were performed to justify the effectiveness of fiber dosage.

2.3 *Cement*

Based on the literature, 3% of ordinary Portland cement of 43 grade was used as a stabilizer for this investigation. Cement is a substance, a binder that sets and hardens on curing. The free carbon dioxide from the air reacts with cement to bind mixed materials together. In cement manufacture, basic raw materials used are limestone or chalk, containing calcium carbonate, and clay or shale, containing silica, alumina, and iron oxide. Its basic properties are tabulated in Table 5.

Table 5 Physical properties of cement

Test conducted	Results	Requirements as per IS 8112-1989
Specific gravity	3.16	–
Normal consistency (%)	32	–
Setting time (minutes)	Initial 60	Not >30 min
	Final 225	Not >600 min
Fineness (m ² /kg)	330	Not <300 m ² /kg
Soundness (mm)—Le Chatelier test	2.50 (Expansion)	Not >10 mm

2.4 Stabilization Using Arecanut Coir with 3% Cement

The reinforced soil was not cured, as there is no chemical reaction taking place in order to improve the strength. Hence, uncemented, but fiber-reinforced specimens were tested immediately after casting. IRC SP: 72, 2015 suggests the use of a minimum of 2–3% cement for the stabilization of soils, which are to be used for modified subgrades. As the soil blended with coir can not develop any bonding at the soil-coir interface, this cement addition was found to be essential. The UCS strength was measured till 365 days of curing. At the same time, the CBR improvements were evaluated till 60 days of curing.

2.5 Sample Preparation

Sample preparations were done as per relevant Indian Standard code procedures. To the dry soil, coir was added initially and mixed using 0.5 times the OMC quantity of water. The mix is further blended with the remaining water until a homogeneous mixture is obtained. For the cemented mix preparation, same procedure was followed, but care was taken to mold the specimens within the initial setting time of cement. For conducting durability tests, ASTM codes were followed. All specimens were cured to the specified curing period, and to maintain the moisture content, samples were covered in plastic raps or kept covered in the desiccator. The samples used for soaked CBR were immersed in potable water for 4 days before testing.

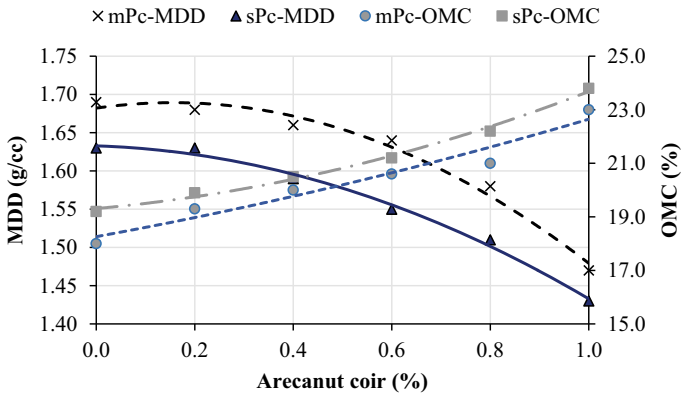


Fig. 1 Compaction properties for lateritic soil reinforced with different percentages of arecanut coir

3 Experimental Outcomes

3.1 Compaction

The arecanut coir-reinforced soil was tested to evaluate the standard and modified compaction parameters. Various dosages of fibers were tried, and the test results are depicted in Fig. 1. The increased low-density fiber dosage has resulted in a density dropdown of the mix, whereas water affinity of coir was higher, leading to an increase in the OMC of the mixes with increased dosages. Higher compaction effort has led to improved density and lowered OMC values. The same compaction characteristics were considered for 3% cement-treated lateritic soil with different arecanut coir dosages. As the dosage of cement is very low, it does not change the compaction characteristics of treated soil.

3.2 UCS

The lateritic soil, when reinforced with different percentages of arecanut coir, showed improvement in UCS to 0.6% fiber dosage (Fig. 2). A further increase in fiber dosage leads to a slight dropdown in UCS due to excess fiber concentration at certain portions of the specimen. When reinforced soils were compacted to standard Proctor density along with 3% cement, the improvement in UCS values was magnified due to the bonding effect (Fig. 3). The soil and fiber bonding was enhanced with the addition of cement due to the formation of hydration products. The higher compaction effort could improve the UCS values of mixes slightly. The observed slight improvement in UCS was due to the compact packing of mixes with lowered voids resulting in higher

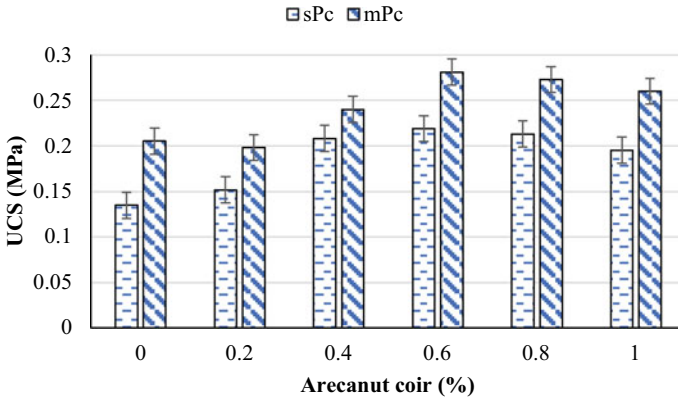


Fig. 2 UCS variation for arecanut coir-reinforced soil

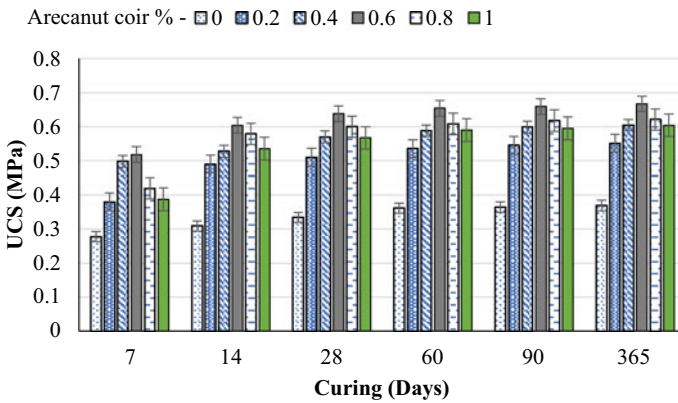


Fig. 3 UCS variation for cement and arecanut coir-treated soil under standard Proctor compaction

densities (Fig. 4). Therefore, CBR, durability, and fatigue tests were conducted on the specimens prepared at modified Proctor density.

3.3 CBR

When the soil is reinforced with coir alone, without the addition of cement, the CBR values were enhanced in comparison to unreinforced soil (Fig. 5). The addition of tensile reinforcement can improve the shear resistance of the mix, leading to a CBR hike. Further improvement in CBR strength can be expected if the soil and fibers were bonded with a cementing agent.

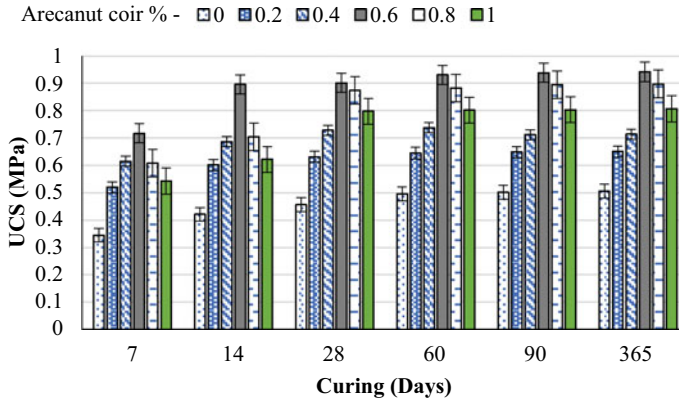


Fig. 4 UCS variation for cement and arecanut coir-treated soil under modified Proctor compaction

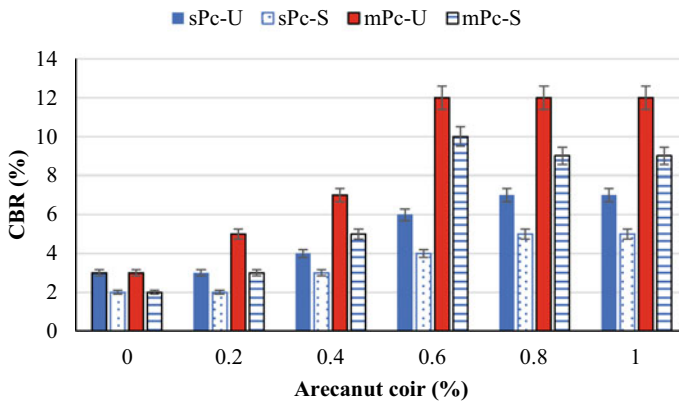


Fig. 5 CBR values for arecanut coir-treated soil

The samples cured for various days exhibited significant improvement in CBR values. Even when soaked in water, the samples could retain considerable CBR values. Unreinforced but cement-treated soil also exhibited CBR improvement. The higher CBR values were observed for mixes with 0.6% coir reinforcement (Fig. 6). This may be due to the proper distribution of reinforcement in the mix, thus improving plunger penetration resistance. Further increase in dosage could not improve CBR strength. The higher fiber dosages may cause the excess concentration of fibers, thus hampering strength improvement.

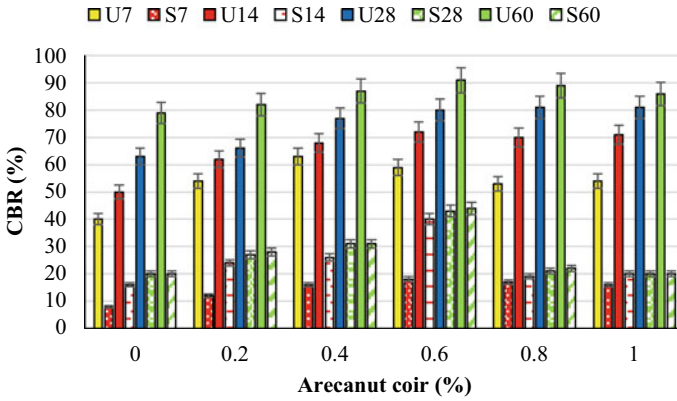


Fig. 6 Variation of CBR with curing period for 3% cement-stabilized lateritic soil at various dosages of arecanut coir reinforcement under modified Proctor compaction

3.4 Durability

The field performance of a pavement structure depends on the wheel loads to which it is subjected, along with variations in the climatic conditions. The changes in weather lead to changes in the temperature and moisture content of the pavement layers. These variations will affect the structural integrity and performance of the pavement. In order to evaluate the influence of weather changes, durability tests were conducted on the stabilized material. To simulate the weather changes in high rainfall areas wet–dry test was conducted as per ASTM D 559. And to resemble cold region effects, freeze–thaw tests were conducted as per ASTM D 560. The 7 days stabilized samples of UCS will be subjected to 12 cycles of durability test, which lasts for 24 days. During each cycle, the integrity of the material will be tested in terms of soil loss. A material is said to pass the durability test if it sustains 12 cycles with a weight loss not exceeding 14%.

3.4.1 Wet–Dry

The unstabilized, unreinforced lateritic soil could not pass first wet–dry cycle. The cemented samples with lower coir percentage failed with a fewer number of cycles due to insufficient reinforcement. The cement hydration resulted in the setting of the mix. As the coir dosage increased, the set soil improved the integrity due to a hike in the tensile capacity of the mix. At the highest dosage of coir, the samples could complete 12 wet–dry cycles, but with weight loss exceeding 14%. Few negative values were observed due to the weight gain of mixes during the wetting cycle. Therefore, these mixes are not suitable for base or sub-base courses of pavement. However, these mixes can be suitably used as the modified subgrade due to improvement in strength values (Table 6).

Table 6 Weight loss of stabilized soil under wet–dry test

Cement (%)	3									
Areca nut coir (%)	0.2		0.4		0.6		0.8		1	
Cycles	W	D	W	D	W	D	W	D	W	D
1	−2.0	9.0	−1.8	9.9	−1.2	10.2	−1.9	7.7	−2.4	8.9
2	Failed		0.7	12.9	0.6	11.6	−2.1	9.0	−3.3	9.2
3			Failed		0.9	14.3	1.3	10.2	−2.5	10.7
4					5.6	12.4	0.5	13.3		
5					7.6	14.6	1.1	14.7		
6					9.9	16.6	1.9	15.2		
7					Failed		2.7	17.2		
8					3.6	20.0				
9					9.7	20.1				
10					10.3	21.5				
11					11.2	22.0				
12					12.7	22.2				

W Wet; D Dry

3.4.2 Freeze–Thaw

Improvement in the resistance to the weight loss was observed for the cement-treated soil with the increase in coir dosage under freeze–thaw test. All the specimens sustained 12 freeze–thaw cycles with weight loss within 14%. The freezing and thawing are not considered to damage the set soil. The good structural integrity of the mixes was observed after the test. Therefore, the mixes are considered durable under freeze–thaw weather conditions (Table 7).

3.5 Fatigue

Fatigue is a common phenomenon that the pavement layers undergo during their lifespan. As a result of this distress mechanism, the structural stability of the pavement will be lost. Due to repeated wheel loads, the stabilized layers may develop micro-cracks, which further continue to macrocracks. These cracks will further develop in size, where the width of the crack increases and propagates through the pavement depth. Under the repeated wheel load on cracked pavement, a sudden failure can be observed, and the integrity of the pavement is disturbed. Therefore, it becomes necessary to test the modified materials used in the pavement for their fatigue load-receiving capacity, which will be measured in terms of the number of fatigue cycles to failure under the specified loading conditions. The stabilized soil materials used

Table 7 Weight loss of stabilized soil under freeze–thaw test

Cement (%)	3									
Arecanut coir (%)	0.2		0.4		0.6		0.8		1	
Cycles	F	T	F	T	F	T	F	T	F	T
1	3.4	3.5	3.2	2.6	3.5	3.1	2.0	2.4	0.2	0.2
2	3.6	4.0	3.0	3.5	3.0	3.4	2.4	2.6	0.6	0.4
3	4.2	4.3	3.0	3.1	3.8	3.8	2.7	2.8	1.0	0.6
4	4.5	4.6	3.2	3.3	3.1	4.0	2.7	2.9	0.9	0.7
5	4.9	5.0	2.9	3.4	4.1	4.3	2.9	3.0	1.1	0.8
6	5.1	5.4	3.4	3.5	4.3	4.6	3.0	3.2	1.2	1.0
7	5.9	6.0	3.5	3.9	4.5	5.0	3.2	3.4	1.4	1.2
8	6.3	6.5	4.0	4.2	4.8	5.3	3.4	3.5	1.5	1.6
9	6.7	7.0	4.3	4.8	5.3	5.3	3.6	3.7	1.8	1.5
10	6.9	7.2	4.2	5.0	5.4	5.4	3.7	3.8	1.9	1.6
11	7.2	7.4	5.4	5.5	5.8	5.8	3.8	3.8	2.0	1.6
12	7.8	7.9	5.5	5.7	5.9	5.9	3.9	4.3	2.1	2.3

F Freeze; *T* Thaw

in this study cured for 7 days were subjected to the repeated loads of 0.33, 0.5, and 0.6 times their corresponding UCS values.

The specimen was placed in position on the loading frame. LVDTs were used to record the deformation levels. Loading is done with the help of a load cell. The data acquisition system records the load, fatigue cycles, deformation values, etc., during the experiment. Both loading and data acquisition systems work together, and testing will be stopped when the specimen fails. The failure pattern of the specimen was also noted down. At a frequency of 1 Hz, a rest period of 0.1 s selected load was applied repeatedly, which resembles a sinusoidal waveform. The fatigue life was varied depending on the effectiveness of cementation and the dosage of coir reinforcement. Untreated lateritic soil failed only after a few cycles due to lack of bonding, whereas the cemented soil, along with reinforcement, exhibited improvement in fatigue resistance with the higher fiber dosages (Fig. 7). The low stress applied was unable to cause the distress quickly; hence, the specimens could withstand more fatigue load repetitions. Therefore, reinforcement along with cementation of soil is helpful in improving the capacity to withstand repeated loads.

4 Conclusions

Based on the laboratory tests conducted, the following findings were observed.

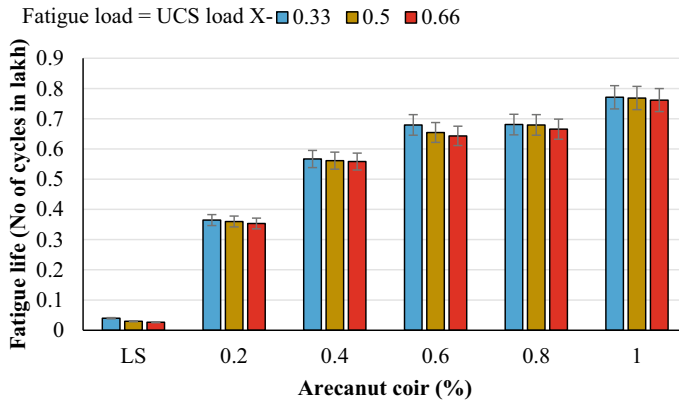


Fig. 7 Fatigue test results for lateritic soil and cement-fiber-treated lateritic soil

1. Arcanaut coir tensile reinforcement alone was found to considerably improve the strength properties due to the holding of soil clods due to improved capacity. The dosage of 0.6% coir was found to be optimum for strength improvement.
2. Considerable UCS improvements resulted as the soil is treated with 3% cement and coir reinforcement due to the bonding of soil and fibers.
3. With the increase in cement, fiber dosage, and curing days, CBR values were improved. The maximum CBR improvements were observed at 3% cement along with 0.6% coir reinforcement. At further increased coir dosages, a marginal decrease in CBR was found.
4. The durability test indicates these samples can not be used as sub-base or base course layers since weight loss is more than 14%.
5. The improvement in fatigue life was observed for stabilized soil. The samples sustained >75,000 fatigue cycles at 1% coir dosage and 3% cement.

References

1. Buchanan F (1807) A journey from Madras through the countries of Mysore, Canara, and Malabar,...: for the express purpose of investigating the state of agriculture, arts, and commerce; the religion, manners, and customs; the history natural and civil, and antiquities, in the dominions of the rajah of Mysore, and the countries acquired by the honourable East India company, in the late and former wars, from Tippoo Sultan vol 2. T. Cadell and W. Davies; and Black, Parry, and Kingsbury; W. Bulmer and Company
2. Bwalya M (2006) Utilization and improvement of lateritic gravels in road bases. International Institute for Aerospace Survey and Earth Sciences (ITC), Section Engineering Geology, Delft, The Netherlands
3. Campco Arcanaut|| <http://www.campco.org/index.php/arecanut>. Accessed 26 Sep 2015
4. Chavva PK, Vanapalli SK, Puppala AJ, Hoyos L (2005) Evaluation of strength, resilient moduli, swell, and shrinkage characteristics of four chemically treated sulfate soils from north Texas. In: Innovations in grouting and soil improvement, pp 1–10

5. Das BM (2015) Principles of foundation engineering. Cengage Learning
6. Gidigasu MD (1971) A contribution to the study of the physico-chemical implications of tropical weathering and laterisation. Geotech Eng Bangkok 2:131–149
7. Haichert R, Kelln R, Wandzura C, Berthelot C, Guenther D (2012) Cement stabilization of conventional granular base and recycled crushed Portland cement concrete. Transp Res Rec 2310(1):121–126
8. Hicks RG (2002) Alaska soil stabilization design guide
9. Kar RK, Pradhan PK (2012) Laboratory tests of reinforced fly ash mix for use as sub-base in low volume rural roads. Indian Highways 40(1)
10. Kumar P, Singh SP (2008) Fiber-reinforced fly ash subbases in rural roads. J Transp Eng 134(4):171–180
11. Lekha KR, Sreedevi BG (2006) Coir fibre for the stabilisation of weak subgrade soils. Highway Engineering Lab, NATPAC, Thiruvananthapuram
12. Maheshwari K, Desai AK, Solanki CH (2012) Analytical modeling of flexile pavement resting on fiber reinforced clayey soil. In: Proceedings of Indian geotechnical conference, pp 1173–1176
13. Mohammad LN, Raghavandra A, Huang B (2000) Laboratory performance evaluation of cement-stabilized soil base mixtures. Transp Res Rec 1721(1):19–28
14. Mohanty B, Chauhan MS, Mittal S (2011) California bearing ratio of randomly oriented fiber reinforced clayey subgrade for rural roads. In: Proceedings of Indian geotechnical conference, Kochi, (Paper No. J-354), pp 611–614
15. Murthy RS, Pandey S (1983) Soil map of India. Natl Bur Soil
16. Peng Y, He Y (2009) Structural characteristics of cement-stabilized soil bases with 3D finite element method. Front Architect Civil Eng China 3(4):428
17. Ramaswamy SD, Aziz MA (1989) Jute geotextiles for roads. In: Proceedings of international workshop on geotextile, Bangalore pp 259–270
18. Sarbaz H, Ghiassian H, Heshmati AA (2014) CBR strength of reinforced soil with natural fibres and considering environmental conditions. Int J Pavement Eng 15(7):577–583
19. Shankar AU, Chandrasekhar A, Bhat HP (2012) Experimental investigations on lithomargic clay stabilized with sand and coir. Indian Highways 40(2)
20. Tang C, Shi B, Gao W, Chen F, Cai Y (2007) Strength and mechanical behavior of short polypropylene fiber reinforced and cement stabilized clayey soil. Geotext Geomembr 25(3):194–202
21. Vidal H (1969) The principle of reinforced earth. Highw Res Rec 282
22. Zhang Z, Tao M (2008) Durability of cement stabilized low plasticity soils. J Geotech Geoenvironmental Eng 134(2):203–213

Pavement Analysis and Measurement of Distress on Concrete and Bituminous Roads Using Mobile LiDAR Technology



Prashant S. Alatgi and Sunil S. Pimplikar

Abstract Good quality of roads play a major role in depicting the development of any country. Pavement analysis and measurement of distress on roads play an important role in deciding the optimal budget allocation for the maintenance of the roads. Since the deterioration of the roads is a continuous process, the measurement of distress has to be carried out frequently on all the roads, ideally twice or thrice a year. The technology used should be fast enough to take care of the above demand and frequent inspection of the roads. Hence, automated instruments and technology, like Mobile LiDAR, have to be adopted for pavement analysis and measurement of distress (viz., cracks, potholes, International Roughness Index (IRI), etc.) on the roads. A test road of 2.8 km was selected in Pune and data was captured using “Leica Pegasus Two” mobile LiDAR instrument with pavement camera. The data processing and analysis were done using the Leica software. It was found that the measurement of distress on concrete and bituminous roads using Mobile LiDAR “Leica Pegasus Two” along with pavement cameras and required Leica softwares could be carried out with an automated process with positional accuracy better than 5 cm and quite efficiently even with the ongoing traffic conditions. Due to the in-built high precise GNSS (Global Navigation Satellite System) and IMU (Inertial Measurement Unit) system of “Leica Pegasus Two”, and trajectory processing using the GPS base station data, the accurate location/position of the distress (cracks, potholes, etc.) on the field; could be precisely located and marked on the GIS maps. This will help the road maintenance engineers to locate these pavement distresses easily and efficiently using appropriate GPS enabled devices for carrying out the maintenance works efficiently and effectively.

Keywords Mobile LiDAR · 3D point cloud · International roughness index (IRI) · Inertial measurement unit (IMU) · Global navigation satellite system (GNSS)

P. S. Alatgi (✉) · S. S. Pimplikar
Dr. Vishwanath Karad MIT World Peace University, Kothrud, Pune 411038, India
e-mail: prashantalatgi@gmail.com

1 Introduction

Automated methods of pavement distress measurements have more scope than the manual methods which are very slow, have poor repeatability/reproducibility, and the traffic safety risk for the surveyor [1, 2]. Some previous authors have even used crude automated methods like video data acquired by the car's parking camera [3]. Attempt for integration of geographic information system (GIS), global positioning system (GPS), and computer vision system (CVS) was also made [4]. Whereas some have experimented with the video cameras, laser and image processing techniques [5, 6] but have not done the GPS/GNSS integration for getting the high-precise position or location of the cracks in the pavements. The paper published by Radopoulou [3] clearly states in "the further scope" to integrate GPS device to assist Road inspectors to provide the exact location of the detected defects. Some work has been previously done to determine roughness index (RI) using Bump Integrator method at the standard speed of 32 km/h [7], but have not used the Laser-based LiDAR technology for the same.

2 Objective and Improvements Planned

The objective of the present work is to perform "Pavement analysis and measurement of distress on concrete and bituminous roads using Mobile LiDAR Technology."

The improvements in the field planned w.r.t. the current status of the technology are as follows:

It is planned to give preference to the accurate location/position of the distress (cracks, potholes, etc.) on the field with better than 5 cm so that the maintenance staff can locate these easily and efficiently using appropriate GPS enabled devices for carrying out the maintenance works effectively.

Emphasis has been laid to automatically capture the pavement distress on field without disturbance to the existing traffic on road and with great speed and accuracy.

Efforts have been taken to mark the position of the cracks and potholes on GIS-enabled map automatically and compare them with the actual photographs at those positions to draw appropriate inferences.

3 Method

3.1 Work Planning: Stage I

The appropriate and available LiDAR Instrument was identified for the project to capture data on site. Reconnaissance studies were done for selection of site feasible for data capture with different types of pavements; concrete, bituminous, paver



Fig. 1 Data capture on site by mobile LiDAR, “Leica Pegasus Two” for 2.8 km road in Pune

blocks, etc., with moving traffic. Estimation of resources was done (manpower, machines and material) required for the task of this project along with the time lines and the budget (cost) required to be made available.

3.2 Data Capture on Site: Stage II

Data capture was done on site using Leica Pegasus Two Mobile LiDAR system, with high-resolution pavement camera for pavement analysis and measurement of distress (cracking, potholes, etc.) on the selected road of 2.8 km near Ganga Dham Chowk in Pune city. Installation of two numbers of GPS/GNSS base stations was carried out on wooden tripod using Leica GS14 dual-frequency survey grade GNSS receivers, before start of actual data capture by the Mobile LiDAR instruments. Dense 3D point cloud data was captured by the Laser scanner Z+F 9012 and the high-definition photographs were captured in all directions. Pavement data was captured with the additional pavement camera attached to the Pegasus system. The trajectory and GNSS data was captured with the two high-precise dual-frequency GNSS receivers kept as base stations in static mode on ground along with the alignment and by the on board GNSS receiver (rover) of the “Leica Pegasus Two” system (Figs. 1 and 2).

3.3 Data Processing and Analysis: Stage III

The data captured by Mobile LiDAR: “Leica Pegasus Two” was downloaded in external hard disk of 1 Terabyte. The DGPS base station points observations in



Fig. 2 Enlarged view of the pavement camera attached to the mobile LiDAR, “Leica Pegasus Two”

static mode were recorded on site and downloaded in the RAW/REINEX format. The 3D point cloud data, camera data and the DGPS raw data thus captured by the Leica Pegasus LiDAR system were then processed and analyzed on Workstations with standard workflow using licensed Leica softwares and Road Assessment tools (Figs. 3, 4, 5 and 6).

Along with the visual condition of the road, cracks and the surface distress of the roads, the IRI values in m/Km were calculated from the data captured along the 2.8 km road using the “Leica Pegasus Two” Mobile LiDAR system and compared with the maximum permissible IRI values as specified by the IRC: SP: 16–2019. It was found that all the values of IRI were found within the permissible limits under the “Good” category for cemented roads (Fig. 7) (Table 1).

4 Inferences

After the above automatic pavement distress outputs were generated, the data was compared to the actual photographs captured at that particular locations by the Leica Pegasus LiDAR instrument and suitable inferences were drawn. The accuracy of the entire data was checked by making random checks at three locations using the DGPS in RTK (Real-Time Kinematic) mode on the bases of DGPS base station coordinates. It was observed that at all the 3 locations, the positional accuracy of the data captured and pavement distress depicted (cracks, potholes), was well within 5 cm, which is sufficient for future maintenance works. The values of IRI in m/Km were found within the permissible limits under the “Good” category for cemented roads as specified by the IRC: SP: 16–2019.

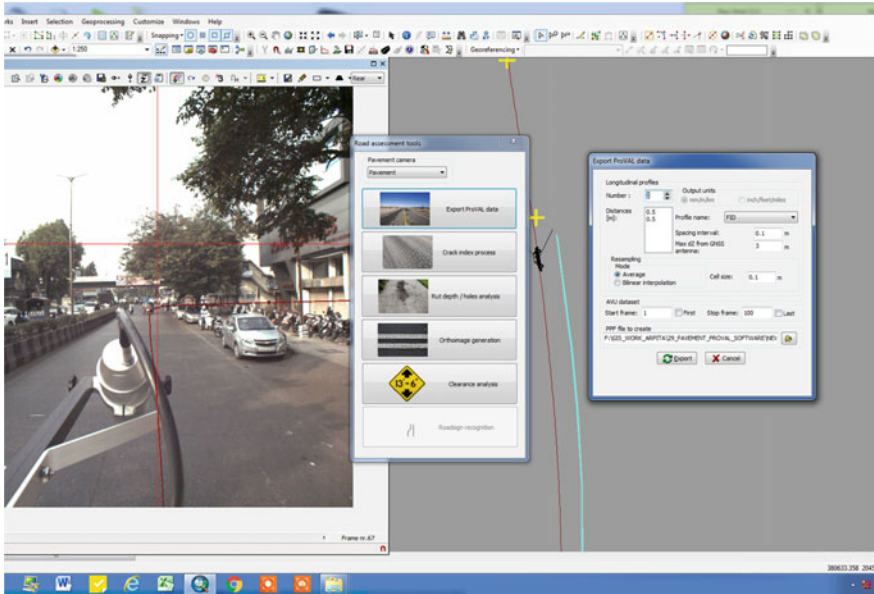


Fig. 3 Screen shot of the automatic pavement analyses using “Road assessment tools” in “Leica Map Factory”



Fig. 4 Screen shot of the “Crack Index” in red circles, with the topographic features of the road

5 Conclusion

The measurement of distress on concrete and bituminous roads using Mobile LiDAR “Leica Pegasus Two” along with pavement cameras and required Leica softwares

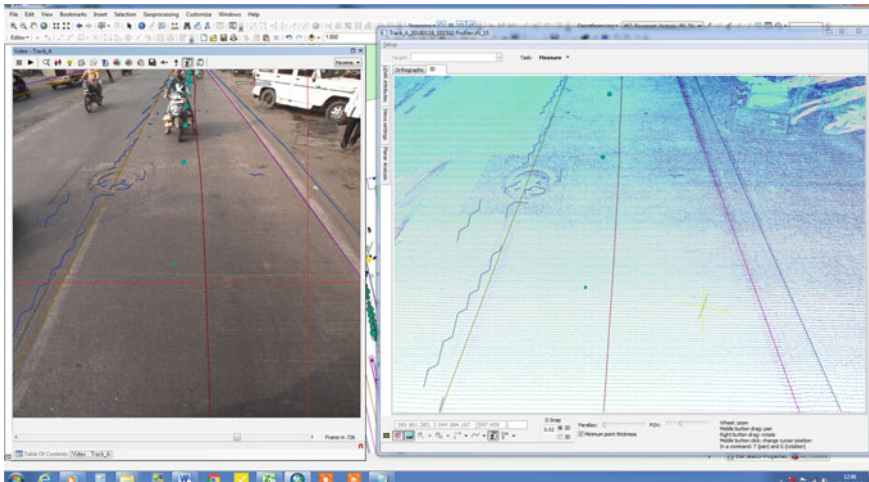


Fig. 5 Screen shot of the automatic detection of the “Longitudinal Cracks” and the “pot hole” in camera and 3D point cloud data



Fig. 6 Leica GS14 dual frequency DGPS receiver kept as a base station on ground for GPS observations in static mode

could be carried out with automated process quite efficiently and accurately even with the ongoing traffic conditions.

Due to the in-built high-precise GNSS & IMU (Inertial Measurement Unit) system of “Leica Pegasus Two”, and trajectory processing using the GPS base station data, the accurate location/position of the distress (cracks, potholes, etc.) on the field; could be precisely located and marked on the GIS maps.

	C	D	E	F	G	H	I	J	K	L	M	N	O	P	Q
	Start Chainage/End Chainage	Direction	Lane Number	Length	Right/Left	Lane/ft	Speed	Survey Date	Latitude	Longitude					
2	0+000.00	2+100.00	Increasing	L1	2.59	2.48	2.54	30	10/04/2021	19.456510	75.722170				
3	0+100.00	2+200.00	Increasing	L1	2.43	2.54	2.49	30	10/04/2021	19.457270	75.722690				
4	0+200.00	2+300.00	Increasing	L1	2.80	2.13	2.47	30	10/04/2021	19.458060	75.723130				
5	0+300.00	2+400.00	Increasing	L1	2.00	2.34	2.17	30	10/04/2021	19.458900	75.723490				
6	0+400.00	2+500.00	Increasing	L1	2.70	2.36	2.53	30	10/04/2021	19.459740	75.723840				
7	0+500.00	2+600.00	Increasing	L1	2.11	2.48	2.30	30	10/04/2021	19.460580	75.724180				
8	0+600.00	2+700.00	Increasing	L1	2.80	2.54	2.67	30	10/04/2021	19.461410	75.724560				
9	0+700.00	2+800.00	Increasing	L1	2.33	2.13	2.23	30	10/04/2021	19.462210	75.725010				
10	0+800.00	2+900.00	Increasing	L1	2.33	2.28	2.31	30	10/04/2021	19.463010	75.725470				
11	0+900.00	3+000.00	Increasing	L1	2.09	2.34	2.22	30	10/04/2021	19.463800	75.725920				
12	1+000.00	3+100.00	Increasing	L1	2.27	2.36	2.32	30	10/04/2021	19.464590	75.726380				
13	1+100.00	3+200.00	Increasing	L1	2.45	2.39	2.42	30	10/04/2021	19.465380	75.726840				
14	1+200.00	3+300.00	Increasing	L1	2.79	2.38	2.59	30	10/04/2021	19.466180	75.727290				
15	1+300.00	3+400.00	Increasing	L1	2.41	2.36	2.39	30	10/04/2021	19.466970	75.727750				
16	1+400.00	3+500.00	Increasing	L1	2.78	2.39	2.59	30	10/04/2021	19.467770	75.728200				
17	1+500.00	3+600.00	Increasing	L1	2.77	2.38	2.58	30	10/04/2021	19.468560	75.728660				
18	1+600.00	3+700.00	Increasing	L1	2.29	2.36	2.33	30	10/04/2021	19.469350	75.729120				
19	1+700.00	3+800.00	Increasing	L1	2.79	2.39	2.59	30	10/04/2021	19.470150	75.729570				
20	1+800.00	3+900.00	Increasing	L1	2.77	2.38	2.58	30	10/04/2021	19.470940	75.730020				
21	1+900.00	4+000.00	Increasing	L1	2.44	2.36	2.40	30	10/04/2021	19.471740	75.730470				
22	1+000.00	4+100.00	Increasing	L1	2.63	2.39	2.51	30	10/04/2021	19.472550	75.730900				
23	1+100.00	4+200.00	Increasing	L1	2.33	2.38	2.36	30	10/04/2021	19.473360	75.731320				
24	1+200.00	4+300.00	Increasing	L1	2.35	2.45	2.40	30	10/04/2021	19.474150	75.731780				
25	1+300.00	4+400.00	Increasing	L1	2.47	2.55	2.51	30	10/04/2021	19.474940	75.732230				

Fig. 7 International roughness index (IRI) values obtained in m/Km

Table 1 Maximum permissible values of roughness (RI and IRI) for SH, NH and expressways as per IRC: SP: 16–2019

S. no.	Type of surface	Condition of road surface					
		Good		Fair		Poor	
		RI	IRI	RI	IRI	RI	IRI
1	Bituminous (BC, SMA, SDBC)	<1800	<2.55	1800–2400	2.55–3.30	>2400	>3.30
2	Cemented	<2000	<2.81	2000–2400	2.81–3.30	>2400	>3.30

This will help the road maintenance engineers to locate these pavement distresses (cracks and potholes) easily and efficiently using appropriate GPS-enabled devices for carrying out the maintenance works efficiently and effectively.

Using the Leica softwares and crack detection algorithm, under “Road assessment tools” the cracks and potholes could be automatically extracted (vector form) from the captured data and marked on the GIS-enabled high-precise maps.

The values of IRI in m/Km were found within the permissible limits under the “Good” category for cemented roads as specified by the IRC: SP: 16–2019.

After analysis of the results and comparison with the actual photographs taken by the Leica Pegasus Two LiDAR system, it was found that the automatic crack detection software could detect the cracks, potholes, on concrete, bituminous roads, and even road patches with paver blocks to a great extent with high precision.

This process will save a lot of time, manpower and money, since the entire process from data capture to the output generation is automated.

6 Future Scope

Though the process is automated, human expertise is required for inspecting the end results by comparing with the actual site photographs taken by the Pegasus LiDAR system. It is required to verify and validate the actual presence of cracks detected by the automatic crack detection software. In the present study, the rumble strips/speed breakers present on ground were picked up by the software as a set of transverse cracks since the automatic crack detection algorithm may not be designed for the same. The future scope for improvement will be to fine tune and update the automatic crack detection algorithm to the area and country specific road conditions.

Acknowledgements I hereby acknowledge the leading Land Surveying and Mapping company of India “Prashant Surveys”, Pune, for providing the “Leica Pegasus Two” Mobile LiDAR instrument along with the pavement camera, Leica GS14 DGPS receivers for GPS base station observations and sufficient manpower with Leica software for capturing, processing, and analysis of all the captured data for my selected 2.8 km road length in Pune.

References

1. Petra Offrell ASCE 0733-947X (2005) Repeatability in crack data collection on flexible pavements. 131(7):552
2. PENG Bo (2015) Review on automatic pavement crack image recognition algorithms. J Highw Transp Res Dev (English Ed.) 9(2):13–20
3. Radopoulou SC (2015) Patch detection for pavement assessment. Autom Constr 53:95–104
4. Obaidat MT (2006) Integration of geographic information systems and computer vision systems for pavement distress classification. Constr Build Mater 20:657–672
5. Fukuhara T (1990) Automatic pavement-distress-survey system. J Transp Eng 116(3):280–286
6. Serigos PA (ASCE) (2016) Evaluation of 3D automated systems for the measurement of pavement surface cracking. J Transp Eng 142(6):05016003
7. Pal M (2014) Pavement roughness prediction systems: a bump integrator approach. Int J Civ Environ Eng 8(12)

Laboratory Study on New Type of Self-consolidating Concrete Using Fly Ash as a Pavement Material



Bhupati Kannur and Hemant Chore

Abstract India is witnessing tremendous development in the transportation sector, especially in the construction of new expressways, upgrading the existing national and state highways to the superior standards. Road development in the rural area assumed significance in the last two decades and Pradhanmantri Gram Sadak Yojana (PMGSY), playing an important role in the development of the rural roads, is advocating the use of waste materials in the pavement construction. Such huge development in the highway sector would necessitate large amount of conventional construction materials. Therefore, there is a need to explore the possibility of utilisation of the alternative materials in the construction of the pavements. The semi-flowable self-consolidating concrete (SF-SCC) is environment friendly, efficient and economical alternative. This type of concrete is innovatively used in pavement construction replacing the conventional pavement quality concrete (PQC). This paper presents the preliminary laboratory experimental results of fresh and early strength properties of SFSCC using industrial wastes such as fly ash as the cement replacing material in the level of 20, 30 and 40%. The flow, slump, compaction factor and green strength of fresh concrete are tested. The cores extracted from the slab casted using a Mini-paver model are used to test the compressive, tensile strength and further, the beam specimen casted for flexural strength are tested. The results from the laboratory tests show that confirms the efficacy of the SFSCC so developed as the material for construction of rigid pavement as compressive strength of the SFSCC with fly ash up to 30% is more than 40 MPa and with that with 40% fly ash is more than 30 MPa. Flexural strength of all the four mixes is more than 4.5 MPa. Thus, SFSCC with fly ash up to 30% satisfies the requirement of concrete for urban road construction and the SFSCC with 40% fly ash as the material for rural rigid pavement construction.

Keywords Semiflowable self-consolidating concrete · Fly ash · Rigid pavement · Industrial waste

B. Kannur (✉) · H. Chore

Department of Civil Engineering, Dr B R Ambedkar National Institute of Technology Jalandhar, Jalandhar, India

e-mail: bhupatik.ce.19@nitj.ac.in

1 Introduction

There are mainly two problems due to increased population and globalisation. One is the requirement for the creation of infrastructure, which mainly depends on the concrete. Concrete is a composite material of cement, sand and aggregates, which demands the use of a huge amount of natural resources. Secondly, the production of industrial wastes in such a quantity that for the disposal of which requires acres of open lands for dumping and creates environmental pollution like land contamination, water pollution etc., posing health consequences. The solution for these two aspects lies in exploring the possibilities of using the industrial wastes in production of the concrete.

In India, 72% of electric power is being generated by the power stations using the coal/lignite and is of the opinion that this trend will be same during the near future. The Indian coal is a low grade with high ash content of about 30–45%. Managing such a huge amount of fly being generated in coal/lignite-based power plants is a big challenge. It is becoming tough to acquire lands for disposal of the ash thus generated. If not managed properly the fly ash may cause water and air pollution. The utilisation level of fly ash in different construction activities as reported during the year 1996–97 was less than 10% (6.64 metric ton). In year 2019–20, the fly ash utilisation has been tremendously increased to 83% (187.81 metric ton) due to many initiatives and policies by Government of India to increase the fly ash utilisation in construction industry like fly ash-based building materials, fly ash-based cement, roads/flyovers, low area reclamation, in construction of dams by roller compacted concrete etc. Even though a lot more fly ash is yet left unutilised and needs further attention to search for the viability to use the same. Table 1 summarises the generation and utilisation levels of fly ash in India during the Year 2019–20 [1].

Figure 1 visualises the areas of fly ash utilisation during the year 2019–20. It can be observed that the maximum fly ash is been used in manufacturing of cement (26%). Construction of roads and flyovers is also an area of substantially high amount of fly ash utilisation (9%). 17% of fly ash still unutilised.

Figure 2 explains the year wise fly ash generated and being utilised from 1996–97 to 2019–20. One can observe that the production as well as utilisation of fly ash is sharply increased. The fly ash utilisation is tremendously increased in the recent years. However, 100% fly ash generated is not being utilised. Hence, as in Fig. 2,

Table 1 Fly ash production and utilisation during 2019–20 [1]

Particulars	Year 2019–20
Number of thermal power stations considered	197
Capacity (MW)	200,691.50
Coal consumption (million tons)	678.68
Fly ash generated (million tons)	226.13
Fly ash utilised (million tons)	187.81
Utilisation (%)	83.05

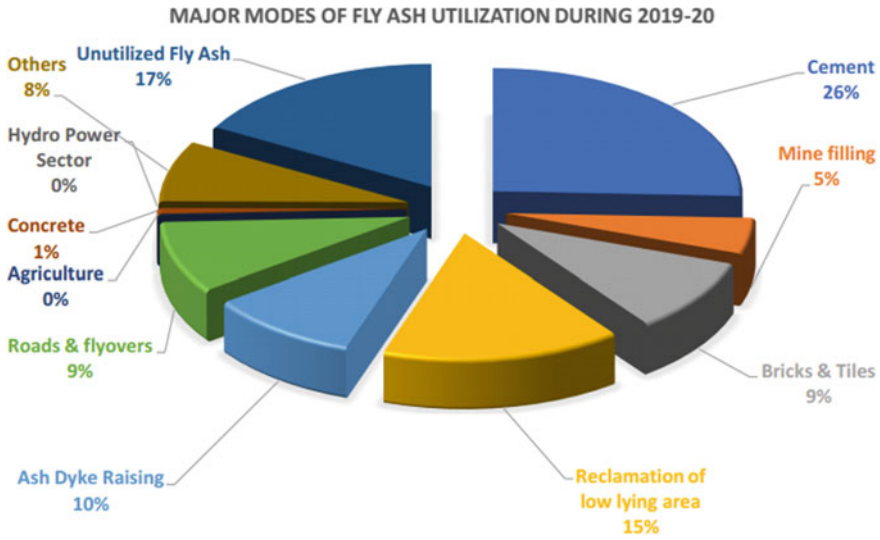


Fig. 1 Areas of fly ash utilisation during 2019–20 [1]

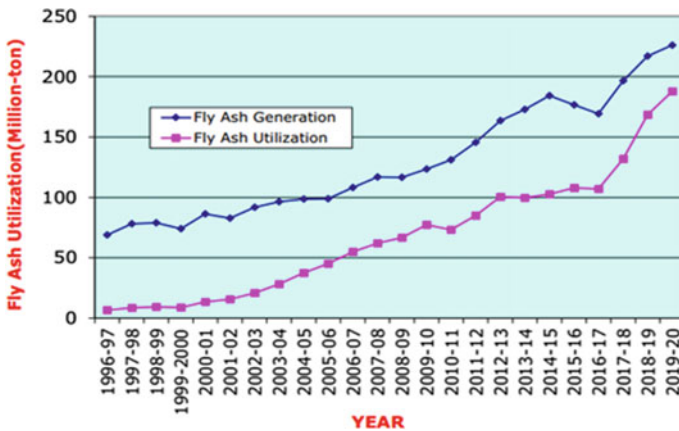


Fig. 2 Fly ash generation and utilisation from 1996–97 to 2019–20 [1]

the gap between both the generation and utilisation lines is still considerable. An expert committee formed to advise the thermal power plants to increase the fly ash utilisation recommends that plants should provide incentives through the R&D to various entities that come up with products using minimum 75% fly ash [1]. Fly ash is the best mineral admixture, which can be added easily and proves to be low-cost admixture [2]. SEM analysis of the concrete with fly ash as mineral admixture by Jindal and Ransinchung RN [3] shows the increasing amounts of calcium silicate

hydrate (CSH) and calcium hydroxide (CH) in fly ash. Thus, incorporation of fly ash in concrete mix increases the hydration products by increased hydration process.

As per the Mohod and Kadam [4] rigid pavements are becoming popular compared to the flexible pavements. Rigid pavements have got the advantage of durability and resistance to failure against detrimental environment conditions. Concrete pavements are preferred over bituminous pavements in India due to substantial rise in cost of the bituminous pavements, less life span and requirement for frequent maintenance.

In India, pavement quality concrete (PQC) is being extensively used for the construction of rigid pavements. But the problem with PQC is that it is of zero or low slump and during the construction it needs high degree of compaction either by vibratory rollers or by slip form technique with internal needle vibrators. The compaction by rollers results in over consolidation or under consolidation of concrete; on the other hand, the slip form technique with needle vibrators leaves trails [5]. The solution for these problems is to develop a novel concrete mix, which needs no internal vibration during construction of concrete pavements by the slip-form paving technique. This is possible only when the concrete by slip-form paver exhibits higher flowability along with sufficient green strength to hold its shape. Sufficient green strength, the ability of the concrete to stand up and hold its shape without any edge support soon after the forward movement of slip form paver, is critical [6].

The concrete with such properties is called as semi-flowable self-consolidating concrete (SFSCC), which has non-rodde slump varying from 152 to 203 mm, flow diameter of 279–330 mm, green strength of 1.3–2.5 kPa, and compaction factor not less than 0.98. SFSCC can be used advantageously for slip-form construction. Conventional slip-form concrete is very stiff and demands heavy vibration. SFSCC needs no vibration and thus, reduces energy for consolidation and noise during construction [7]. High amount of cement required (458–525 kg/m³) for the production of SFSCC as compared to that of conventional pavement concrete (355 kg/m³) makes it costly and induces the cracking due to shrinkage [8]. Thus, there is a need to explore the possibilities of reducing the cement content by adding other cementitious materials.

Thus, in this study, the fresh and hardened properties of SFSCC with fly ash as a cement replacing material at 20, 30 and 40% are reported. In the present study, the fresh properties and early strength properties of the SFSCC thus produced using the supplementary cementitious material fly ash are investigated for its suitability in the construction of the rigid pavements using the slip form technology.

2 Materials

2.1 Cement

Ordinary Portland cement (OPC) of grade 43 conforming to IS 8112: 2013 [9] is used for the production of the SFSCC. Table 2 represents the physical properties of the cement used.

Table 2 Physical properties of cement

Grade	OPC 43	Requirements (IS 8112: 2013)
Sp. gravity	3.13	
Fineness modulus (retained on 90 micron sieve)	6.1%	10% maximum
Standard consistency	33%	
Initial setting time	70 min	60 min minimum
Final setting time	450 min	600 min maximum
Compressive strength		
3 days	25 MPa	23 minimum
7 days	34 MPa	33 minimum
28 days	44.8 MPa	43 minimum

Table 3 Properties of coarse aggregate

Sp. gravity	2.69	IS 2386 Part III [11]
Water absorption	0.7%	IS 2386 Part III
Impact value	12.82%	IS 2386 Part IV [12]
Crushing value	11.87%	IS 2386 Part IV

2.2 Aggregates

Fine aggregates used are the natural river sand confirming to Zone II and coarse aggregate of natural stone are procured from the local material supplier. The fineness modulus of the sand from the laboratory test result is found to be 2.77. Specific gravity of the sand is found to be 2.62.

Coarse aggregates of nominal size 20 and 10 mm are used and proportioned as per IRC 44: 2017 [10] keeping maximum size as 12.5 mm. Physical and mechanical properties of the aggregates used are tested in the laboratory, and the results of the same are in the Table 3.

2.3 Mineral Admixture

Fly ash of type c is used in the study as cement replacing material is obtained from the Thermal power plant Ropar. The specific gravity of the fly ash is found to be 1.87. Potable water is used for mixing and curing (Fig. 3).

The X-ray diffraction analysis of the fly ash is shown in Fig. 4. The sharp peak between the angles 20–30° 2 θ is of Quartz (SiO₂). This implies that the fly ash contains high amount of silica and thus induces the pozzolanic activity.

Table 4 Physical properties of admixtures used in mix

Product	TamCem 53SP(HRWR)	TamCem SBR(Bonding)
Relative density	1.09	1.02
Dry material content	–	39 ± 5%
pH	>6	–
Chloride ion content	<0.2%	–

3 Concrete Mix Design

Performance-based mix design method is used in the present study [13]. The mix proportion should aimed at achieving required slump, flow, compaction factor, green strength and other hardened properties. The mix proportion is arrived in three steps.

1. Design of Mortar:

This step involves the determination of the w/b ratio and fine aggregate proportion. w/b ratio can be selected based on the concrete strength and the exposer condition. If no data available the w/b can be referred by ACI 211.1 and ACI 318. To determine the fine aggregate proportion, the modified flow test as per the AASHTO (ASTM C230). The acceptance criteria for the mortar design are to achieve the initial flow at 0th drop should be 10% (110 mm) and final flow at 16–18th drop to be 138% (238±5 mm).

2. Determination of Coarse Aggregate Proportion:

After the successful design of the mortar, the next step is to determine the coarse aggregate content. The coarse aggregate amount should be selected by trial and error method using the modified slump cone test (ASTM C1611) and compaction factor test (AASHTO T126/AASHTO T23) on the unrodded concrete. The concrete thus produced should satisfy the unrodded slump of 150–200 mm, flow diameter of 275–325 mm and a regular cone shape in the fresh state. The compaction factor, ratio of unrodded to rodded density, should be minimum 0.98.

3. Mix Verification by Minipaver Test:

A minipaver system as shown in Fig. 5 is used for the performance verification of the fresh slab extruded. For the final verification of the mix design of SFSCC, a slab extruded from the minipaver system is inspected. The performance of the fresh slab in terms of shape, surface quality, strength and durability is studied. The freshly extruded slab should be rectangular in shape with edge slump maximum of 8% of the thickness and surface quality with less than 15% surface area defects. There should be no honeycombing or segregation is found in the cross-section of the slab. The performance in terms of the strength and durability is also to be verified.

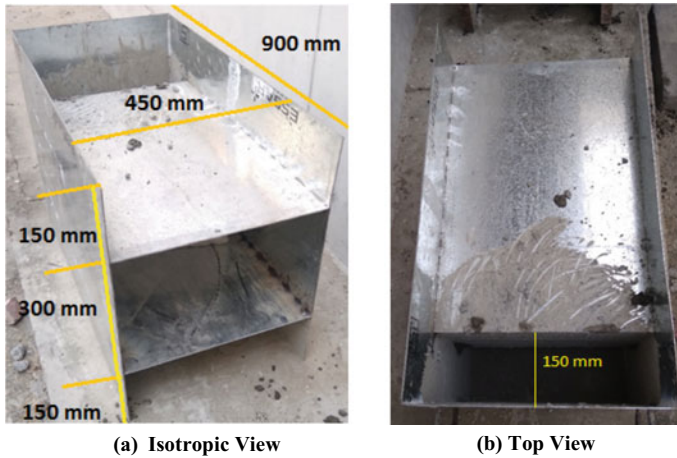


Fig. 5 Minipaver system

The mix design has been finalised for all the mixes in the study after initial trials to achieve all the stated properties of the above-mentioned mix design method stages. Figure 6 shows the steps involved in the laboratory production of SFSCC mix.

The ratio of CA: FA to satisfy the requirements of SFSCC is found to be 45:55. The finalised mix proportions are presented in the table. Figure 6 shows the different stages of the mix design process. The target compressive strength for the concrete design was kept at 40 MPa as it is aimed to use the SFSCC thus produced for the rigid pavement construction. Also to facilitate the required flexural strength of the concrete at 4.5 MPa, a bonding agent has been used in the mix.

Total 4 mixes are produced. The mix with 100% ordinary Portland cement is Control SFSCC, and the mixes with 20, 30, and 40% Fly ash as cement replacing material are indicated as SFSCCF20, SFSCCF30, and SFSCCF40 (Tables 5 and 6).

4 Results and Discussions

4.1 Fresh Properties of SFSCC

4.1.1 Slump and Flow

The freshly produced concrete is filled into the slump cone from a height of 300 mm from the top of the slump cone. No tamping is done by the tamping rod, the excessive concrete is struck off and levelled using the hand scoop. The slump cone is lifted vertically up without any disturbance or vibrations to the concrete filled. The slump and flow diameter of the concrete are measured. All the mixes are proportioned to



Fig. 6 Steps involved in laboratory production of the SFSCC

Table 5 Mix proportion (kg/m³)

Mix	OPC	Fly ash	w/b	CA		FA	SBR	SP	%VMA
				20 mm	10 mm				
Control SFSCC	420	0	0.39	304	517	975	0	0.40	0.20
SFSCCF20	336	84	0.39	305	519	979	1%	0.30	0.20
SFSCCF30	308	132	0.39	296	503	950	1%	0.20	0.20
SFSCCF40	276	184	0.39	285	484	914	1%	0.20	0.20

Table 6 Fresh properties of SFSCC

Mix	Slump (mm)	Flow (mm)	Green strength (kPa)	Compaction factor
Control SFSCC	163	292	1.67	1.000
SFSCCF20	160	288	1.75	0.986
SFSCCF30	157	276	1.47	0.981
SFSCCF40	155	269	1.31	0.980
<i>SFSCC Acceptance criteria [7, 13]</i>	<i>150 to 200 mm and regular cone shape</i>	<i>250 to 300 mm</i>	<i>1.3–2.5</i>	<i>0.98 (Minimum)</i>

achieve the required slump and flow. It can be observed from the mix proportions that the addition of fly ash reduces the dosage of superplasticiser at the constant w/b ratio to achieve the required slump and flow. The reduction in the superplasticiser dosage indicates that fly ash addition increases the workability of the concrete.

4.1.2 Compaction Factor

All the mixes produced are checked for the target compaction factor of minimum 0.98. Compaction factor is determined by the ratio of non-rodded density to the rodded density. To determine the unrodded density, the container is filled with the concrete by pouring from a height of 300 mm above the top of the container.

4.1.3 Green Strength

The green strength is defined as the ratio of the load taken by the cylinder of the fresh concrete to the cross-sectional area of the concrete cylinder. Cylindrical mould of diameter 100 mm and height of 100 mm is filled with the concrete by pouring from a height of 300 mm above the top of the cylindrical mould. To maintain the height of fall, an inverted slump cone is placed over the mould.

4.1.4 Properties of Slab Extruded from the Minipaver System

Figure 7 shows the SFSCC slab extruded from the minipaver in fresh state. The shape of the slab is found to be perfect rectangular with negligible edge slump of about 0.6 cm (4%) out of the total thickness of 15 cm. The surface quality of the slab is satisfactorily good with level, no segregation and honeycombing on the top of the slab.

Fig. 7 Shape stability and surface quality of the fresh SFSCC slab extruded from the minipaver system



4.2 *Hardened Properties of SFSCC*

To test the SFSCC thus produced for its strength properties such as compressive strength and tensile strength, the cores are taken out of the slab as shown in Fig. 8 after curing for the required period using gunny bags (Table 7).

4.2.1 *Compressive Strength*

It is observed that the compressive strength of the concrete mixes, as in Fig. 9, is decreased with the incorporation of the fly ash compared to that of the control mix. Even though, the 28 days compressive strength of the mixes up to fly ash content of 30% was found to be more than 40 MPa. The compressive strength of the mix with 40% fly is also found to be more than 30 MPa. The decrease in the strength may due to the fact that at the early age fly ash is slow in pozzolanic action. The long-term strength is to be studied to study the fly ash effectiveness as supplementary cementitious material.

Fig. 8 Drilling cores from the slab



Table 7 Mechanical properties of SFSCC

Mix	Compressive strength (MPa)		Split tensile strength (MPa)		Flexural strength (MPa)	
	7 day	28 day	7 day	28 day	7 day	28 day
Control SFSCC	30.89	45.19	2.22	3.13	3.88	4.94
SFSCCF20	29.27	43.12	2.51	2.93	3.72	5.16
SFSCCF30	24.89	40.62	2.33	2.82	3.80	5.09
SFSCCF40	22.73	36.26	2.22	2.56	3.10	4.53

4.2.2 Split Tensile Strength

The split tensile strength results also follow the same trend as that found in case of compressive strength. With the addition of the fly ash, the tensile strength is found to decrease. The split tensile strength is very important as the resistance to cracking of the pavement is a desirable criterion (Fig. 10).

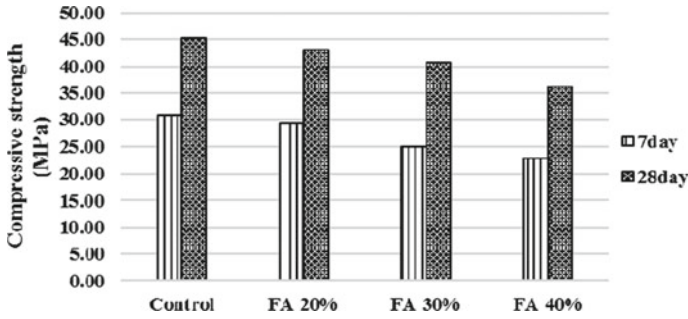


Fig. 9 Compressive strength of SFSCC mixes

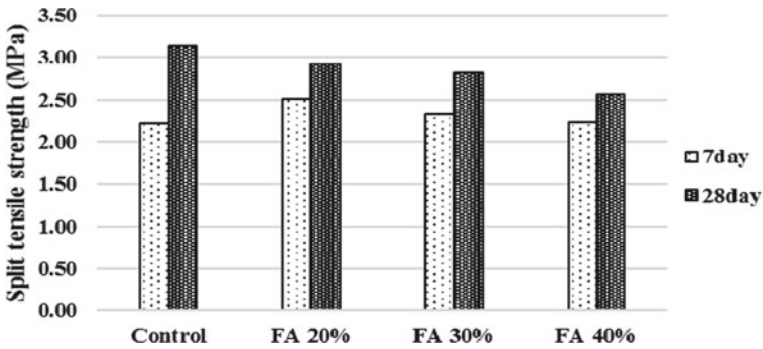


Fig. 10 Split tensile strength of SFSCC mixes

4.2.3 Flexural Strength

To test the flexural strength of the SFSCC beam, specimens of 100 mm × 100 mm × 500 mm are casted. While casting the beam specimens, the concrete is poured into the moulds from a height of 300 mm from the top of the mould to ensure same consolidation effect as that achieved in the slab extruded from the minipaver system. From Fig. 11, it can be observed that the flexural strength of all the mixes is more than 4.5 MPa satisfying the requirement for the SFSCC as material for pavement construction. But the variation in the flexural strength of all the mixes is found to be negligibly small and the trend of the flexural strength due to the incremental addition of the fly ash is not same as in the case of compressive strength and split tensile strength this phenomenon may be attributed to the effect of bonding agent used in the study and for deep understanding further study is to be done. The mix with 40% fly ash is having the lowest flexural strength of 4.53 MPa.

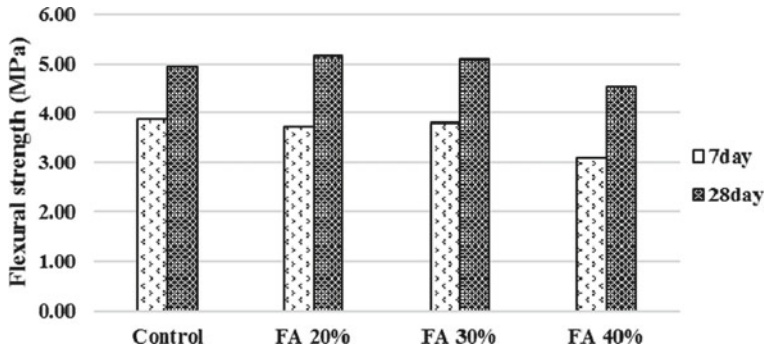


Fig. 11 Flexural strength of SFSCC mixes

5 Conclusion

SFSCC is a new type of concrete that has many advantages over the conventional pavement concrete. The production of SFSCC using the fly ash as cement replacing material and its laboratory investigation are presented in this study. From the experimental investigation on the fresh and hardened properties of the SFSCC mixes thus produced the following conclusions are drawn.

1. The production of SFSCC enables to utilise the fly ash being produced in huge quantities disposal of which is a challenging task for the thermal power plants.
2. The concrete produced using the fly ash as replacement to cement in the present study satisfies all the requirements as semi-flowable self-consolidating concrete (SFSCC).
3. Slump, flow, compaction factor and green strength of all the mixes are in line with the specifications as SFSCC for the construction of the rigid pavement using slip form technique.
4. The addition of fly ash in 20, 30 and 40% by weight of cement in the SFSCC production resulted in reduction of the compressive and split tensile strength. Even though mixes with fly ash up to 30% satisfies the compressive strength requirement as pavement quality concrete for urban roads which is M40 as per IRC 44-2008. The mix SFSCC40% can be utilised in the construction of the rigid pavement in rural roads for which the required grade is limited to M30.
5. The results of flexural strength of all the mixes fulfil the requirement for the concrete road construction as IRC 44-2008 specifies 4.5 MPa as the minimum flexural strength for concrete to be used in road construction.

SFSCC is a type of concrete that has flowability between conventionally vibrated concrete and self-consolidating concrete. As it has the semi-flowability, it also offers the shape stability in the fresh state, which enables the speeder construction using slip form technology. It also enables the use of waste materials in its production. Thus SFSCC along with industrial waste fly ash can be used in the construction of the rigid pavements by slip form paving technique.

References

1. Report on fly ash generation at coal/lignite based thermal power stations and its utilization in the country for the year 2019–20. Government of India, Ministry of Power. Central Electricity Authority, Thermal Civil Design Division, New Delhi, Nov 2020
2. Priya CC, Rao MVS, Reddy VS, Shrihari S (2020) High volume fly ash self compacting concrete with lime and silica fume as additives. In: E3S web of conferences, vol 184. ICMED 2020, p 01109. <https://doi.org/10.1051/e3sconf/202018401109>
3. Jindal A, Ransinchung RNGD (2018) Behavioural study of pavement quality concrete containing construction, industrial and agricultural wastes. *Int J Pavement Res Technol* 11(5):488–501. <https://doi.org/10.1016/j.ijprt.2018.03.007>
4. Mohod MV, Dr. Kadam KN (2016) A comparative study on rigid and flexible pavement: a review. *IOSR J Mech Civ Eng (IOSR-JMCE)* 13(3):84–88. <https://doi.org/10.9790/1684-1303078488>
5. Girish MG, Shetty KK, Raja AR (2018) Self-consolidating paving grade geopolymer concrete. *IOP Conf. Ser Mater Sci Eng* 431:092006. <https://doi.org/10.1088/1757-899X/431/9/092006>
6. Voigt T, Mbele J-J, Wang K, Shah SP (2010) Using fly ash, clay, and fibers for simultaneous improvement of concrete green strength and consolidatability for slip-form pavement. *J Mater Civ Eng* 22(2):196–206. <https://doi.org/10.1061/ASCE0899-1561201022:2196>
7. Lomboy GR, Wang K (2015) Semi-flowable self-consolidating concrete and its application. *Int J Mater Struct Integrity* 9(1/2/3):61–71. <https://doi.org/10.1504/IJMSI.2015.071110>
8. Wang K, Shah SP, Grove J, Taylor P, Wiegand P, Steffes R, Lomboy GR, Quanji Z, Gang L, Tregger N (2011) Self-consolidating concrete—applications for slip-form paving: phase II, Report No. DTFH61–06-H-00011 Work Plan 6, Pooled Fund Program Study TPF–5(098), National Concrete Pavement Technology Center, Iowa State University
9. IS 8112: 2013 Indian Standard, ordinary portland cement, 43 grade—specification, Second Revision
10. IRC: 44-2008 Indian Road Congress, guidelines for cement concrete mix design for pavements, Second Revision
11. IS 2386 Part III–1963, (Reaffirmed 1990) Indian Standard, methods of test for aggregates for concrete part III specific gravity, density, voids, absorption and bulking. Eighth Reprint Mar 1997
12. IS 2386 Part IV–1963, (Reaffirmed 1990) Indian Standard, methods of test for aggregates for concrete Part IV mechanical properties. Tenth Reprint Mar 1997
13. Lomboy GR, Wang K, Taylor P, Shah SP (2012) Guidelines for design, testing, production and construction of semi-flowable SCC for slip-form paving. *Int J Pavement Eng* 13(3):216–225. <https://doi.org/10.1080/10298436.2011.610797>

FTIR Analysis for Ageing of HDPE Pyro-oil Modified Bitumen



H. P. Hadole and M. S. Ranadive

Abstract All over the world, the production of plastic is increasing over the years due to its various applications in different sectors. As the demand for plastic is increasing day by day, it consequently results in accumulation of plastic waste. Till the time various elastomer, plastomer, and rubber are used to modify binder. Here an attempt was made to modify bitumen with plastic oil also known as pyro-oil and to check ageing properties of the same. The rheological and chemical behavior of bitumen and modified bitumen is complex due to its unpredictable nature. In this investigation, bitumen was modified with pyro-oil from High-Density Polyethylene (HDPE). Pyro-oil was obtained by pyrolysis of HDPE at about 750 °C. Pyro-oil modified bitumen (PRMB) was prepared by addition of 5, 10, and 15% of HDPE pyro-oil by total weight of bitumen binder mixed at 3000 rpm for about 120 min. The oxidation process of PRMB was studied by using Fourier transform infrared spectroscopy (FTIR). The effect of short-term ageing for VG30, PRMB was studied by SuperPave test protocol and normal oven ageing. The effect of long-term ageing was studied by normal oven ageing. The FTIR results of SuperPave and normal oven aged samples were compared and change in functional group was recorded. Bitumen binders (VG30, PRMB) subjected to ageing and changes in chemical composition were analyzed using FTIR spectroscopy. FTIR results were used to validate chemical bond like C=O and S=O which leads to changes in viscosity and stiffness of binder. It was observed that ageing influences the bitumen chemistry.

Keywords Pyro-oil · FTIR · VG30 · PRMB · HDPE

H. P. Hadole (✉) · M. S. Ranadive
Department of Civil Engineering, College of Engineering, Pune, Maharashtra 411005, India
e-mail: hadole50@gmail.com

M. S. Ranadive
e-mail: msr.civil@coep.ac.in

1 Introduction

In present scenario, road infrastructure development is growing in all parts of India. In addition to this, majority of road projects has bituminous layer at top. In pavement industries, bitumen is widely used due to its viscoelastic properties. In current trend, bitumen is widely obtained from crude petroleum as byproduct. Currently, IS 15462 and IS [14] are used to check quality of supplied bitumen by different agencies of India. However, petroleum is one of the non-renewable resources, and recoverable amount of which is about to decrease in near future. As per Yao et al. [31], 90–95% by weight of bitumen contains hydrogen, carbon, heteroatoms, and metals. Heteroatoms contain nitrogen, oxygen, and sulfur which replace carbon by heat and contribute to physical and chemical behavior of bitumen. Metal atoms mainly include vanadium, nickel, and iron. Oxidation of bitumen is nothing but change in its properties due to change in temperature when it comes in contact with oxygen and oxidation of bitumen is also known as ageing of bitumen. Author continues that the important reason for such failures lies in insufficient performance-based binder specification for its selection. In performance grading, ageing analysis plays vital role. Jahromi and Khodaii [19] stated that oxidation leads to stiffer and brittle bitumen which results in rutting and fatigue cracking. This is the main reason that low- and high-temperature performance of bitumen should be improved and for the same many researchers are modifying the bitumen in different ways. Generally styrene butadiene styrene (SBS), fibers, styrene butadiene rubber crumb rubber, etc. were used for improving the properties of bitumen. Al-Hadidy and Tan [1] explained that SBS improves low-temperature performance of bitumen. On the other hand, Thodesen et al. [29] and Bischoff and Toepel [3] explained that crumb rubber could improve rheological, rutting, viscosity, and thermal cracking of bitumen. Recently for modification of bitumen lime was also used as the additive and Cheng et al. [5] studied its moisture susceptibility. Ageing of bitumen is of two types, short-term and long-term ageing. As per Hofko et al. [10], short-term ageing deals with chemical changes during mixing at elevated temperature of about 140–200 °C based upon type of asphalt. Rolling thin film oven (RTFO) is used for short-term ageing effect and pressure ageing vessel (PAV) for long-term ageing. But as explained by Behera et al. [2] normal oven can also be used to access short- and long-term effect of binder with proper temperature for particular duration concerned to specific type of binder. But as per Nivitha et al. [22], the mechanism of ageing for modified bitumen supposed to be different when compared with short- and long-term ageing as production temperature for it is above 150 °C.

As all know, world is facing major problem regarding disposal of plastic waste. Researchers from all over the world are trying to reuse plastic waste in various fields of engineering. In the same way, many researches have been done for use of plastic in flexible pavement. Researchers found out various polymers to modify the bitumen binder and checked physical, chemical, and rheological properties of the same. Here an attempt is made to use pyro-oil for modification of binder. To conclude, HDPE pyro-oil is used to modify the base bitumen to form PRMB. This modifier reacts with

bitumen in chemical as well as in physical way. Such interaction leads to change in physical as well as chemical properties of base bitumen. Here some general properties such as penetration, ductility, viscosity, etc. were discussed before and after ageing. Along with this to analyze chemical properties FTIR spectroscopy was used and results are discussed in detail. Primarily, functional groups associated with oxidation are focused in the present research.

2 Literature Review

As explained by Hofko et al. [10] and Eberhardsteiner et al. [6], ageing of bitumen takes place due to oxidation of bitumen and continued that oxidative ageing is categorized into two main types, short-term and long-term ageing. Oxidation of binder during production process, in which aggregate and binder are mixed at temperature of about 150–200 °C. When bituminous mix is in service over time then corresponding oxidation of bitumen is known as long-term ageing. For materials like bitumen having very high absorption coefficient, there is problem of very low transmission which leads to unacceptable low signal-to-noise ratio. Before finding out chemical properties of modified bitumen with different modifiers it is necessary to firstly understand chemical structure of bitumen in aged and unaged condition. As per Chen et al. [4], bitumen binder consists of four fractions including saturates, asphaltenes, resins, and aromatics. Petersen [23], Harnsberger et al. [9], Nivitha et al. [22] mainly focus on the FTIR spectroscopy results to track the changes in chemical compounds after ageing for unmodified and modified bitumen.

In present scenario, ageing is the main problem pavement engineers are facing. Different researches have been coming up to decrease the ageing of bitumen and still it is always hot topic for research. Hofko et al. [10] and Eberhardsteiner et al. [6] explain about chemical sensitivity of bitumen. Shen et al. [27] concluded that ageing leads to decrease in penetration and ductility. On the other hand, viscosity, softening point, complex modulus, and creep stiffness increase. Further, author explains that this effect leads to elastic recovery, resistance to thermal cracking, and thermal fatigue becomes poor which leads to decrease in life of pavement. In the same manner, Petersen [23] stated that the ketone functional group is formed primarily from the oxidation of benzyl carbon. The ketones are formed by oxidation and asphaltenes are primarily responsible for increase in viscosity on ageing. The ageing of bitumen is caused by the processes of oxidation, steric hardening and volatilization.

Khapne et al. [20] studied HDPE pyro-oil modified bitumen (PRMB) with respect to the surface energy of the base bitumen and the modified PRMB. They prepared PRMB by adding HDPE pyro-oil in 2, 3, and 5% by weight of bitumen in the base bitumen VG30, using homogenizer to mix the pyro-oil with bitumen at a rate of 3000 rpm for 20 min. They studied the suitability of adding anti-stripping agents, hydrated lime, and fly ash, in the PRMB to enhance the resistance to moisture damage of PRMB.

Ranadive et al. [25] analyzed the effect of modifiers on the stone matrix asphalt (SMA) and bituminous concrete (BC) mixtures. Author analyzed the effects on the properties of SMA and BC modified with fibers extracted from refrigerator door panels (FERD), and of BC mixture modified with waste plastic in granular form. The optimization was done for the length of FERD in SMA and BC and for the percentage of waste plastic in AC mixtures. The lengths of fiber used were 2, 4, 6, and 8 mm, with a dosage rate of 0.3% by weight of aggregates. The granular plastic used for modification of AC mixture was 3–5 mm in size. Test such as Schellenberg drain down test, indirect tensile, and Marshall stability test were done to compare the strength and stability of the modified mixtures. The results showed an increase in both the Marshall stability and tensile strength at an optimum dose of 0.3% with a length of 6 mm of fiber, for both the SMA and BC mixtures as compared to conventional mixes.

3 Objective

The principal objective of this research is to analyze oxidative result of base binder VG30 and PRMB for different ageing conditions using FTIR spectrographs. The study of physical properties of VG30 and PRMB, chemical changes in oxidation groups due to ageing phenomenon, and compare the results of FTIR test for both short-term ageing and long-term ageing for normal oven condition. Further the analyses of results with respect to FTIR are to be studied.

4 Experimental Materials

4.1 Materials

The study was carried out with base bitumen VG30 for research work. The base bitumen was modified using HDPE pyro-oil. Pyrolysis of HDPE was done using pilot pyrolysis plant developed in TRE lab, College of Engineering, Pune, Maharashtra at about 700 °C. For the process of pyrolysis, HDPE waste was selected of about 3 kg and 68.3% by weight of pyro-oil was produced at reactor temperature of about 730–750 °C. The physical and chemical properties of HDPE pyro-oil was explained by the same author in other works [8].

Modified bitumen was prepared at temperature of about 160 °C at about 3500 rpm for 2 h. Due to this blending composition of virgin bitumen undergoes chemical changes and these chemical changes were analyzed by FTIR. 5%, 10%, and 15% HDPE pyro-oil by weight of bitumen were used for modification of base bitumen and abbreviated as PRMB5, PRMB10, and PRMB15, respectively.

The modification procedure of base bitumen with pyro-oil was explained by Hadole et al. [8], Khapne et al. [20], Suryawanshi et al. [28], and Kulkarni and Ranadive [21] in detail with other physical properties of modified bitumen.

4.2 Bitumen Ageing

The short-term ageing occurs during construction of bituminous material and long-term ageing deals with chemical changes in bitumen after 15–20 years of life and both are associated with oxidation of bitumen which leads to stiffer bituminous binder. As per SuperPave guidelines, RTFO is used for short-term ageing effect. Along with this, short-term ageing of bitumen was also conducted by normal oven method as explained by Reddy [26]. Long-term ageing of base and modified bitumen was conducted using normal oven method.

Each sample was aged for short-term ageing using Rolling Thin Film Oven Test (ASTM D2872) at 163 °C for 75 min to get short-term aged sample and denoted by AB5%, AB10%, and AB15%. The same percentage modified samples were aged by normal oven technique. For that, 10 g binder is spread in circular plate of 140 mm diameter with 650 µm of average thickness uniformly as explained by Behera et al. [2]. After preparation of sample, it is kept in preconditioned oven for 16 h at 163 °C and ageing duration is about 5 h so that result of RTFO ageing can be comparable for VG30.

For long-term ageing of base and modified bitumen, normal oven technique was used. Long-term ageing of different samples was checked after 3 days and 5 days, heated at 85 °C with allowable deviation of 2 °C. The change in chemical characterization and variation in different functional groups due to this ageing were studied using FTIR spectra.

4.3 FTIR

Fourier transform infrared spectrum plays a vital role in research work. FTIR test was used for chemical analysis. FTIR spectral data was obtained for various wavelengths. In this study, FTIR conducted using Bruker FTIR.

4.4 Test Methods

VG30 and modified bitumen samples were checked for physical properties and results were tabulated in Table 1. Habal and Singh [7] analyzed different samples which are checked for FTIR spectra using IR. Spectra were recorded from 4000 to 500 cm⁻¹. The test was conducted on base bitumen, modified bitumen, short- and long-term

Table 1 Physical properties of bitumen

Experiment	Standard	VG30	B5	B10	B15
Penetration at 25 °C (1/10 mm)	IS [13]	58	78	89	107
Softening point (°C)	IS [12]	66	52	46	38
Ductility (cm)	IS [11]	80	86	96	108
Viscosity at 60 °C (poise)	IS [16]	2850	–	–	–
Kinematic viscosity at 135 °C (cSt)	IS [17]	480	–	–	–
Viscosity at 150 °C (poise)	IS [15]	–	630	460	290
<i>Results after rolling thin film oven test</i>					
Loss in mass (%)	IS [18]	<1	<1	<1	<1
Softening point (°C)	IS 1205/ ASTM D36	72	63	53	44

aged bitumen, and HDPE pyro-oil. It is just to understand morphological changes when pyro-oil is used for modification of base bitumen.

5 Methodology

Complete laboratory test procedure is explained in Fig. 1.

6 Results and Discussion

6.1 Physical Properties of Bitumen and Pyro-oil

Physical properties of base and modified bitumen are explained in Table 1. It reflects penetration value increase with increase in percentage of pyro-oil which implies PRMB has less consistency than base bitumen. High-temperature performance of bitumen is observed using softening point. Softening point decreases which implies high-temperature performance of PRMB decreases. Evaluating low-temperature tensile deformation and flexibility of bitumen based on results of ductility. Higher ductility means better low-temperature performance. Increase in ductility of PRMB shows that PRMB don't harm low-temperature performance of bitumen application. But it is also important to note that, from these results, we cannot arrive at a conclusion that the PRMB has no application for high-temperature region until and unless conducting detailed study of rheological properties of PRMB. Loss of mass during short-term ageing is reported here, and it focuses on lightweight volatile compounds. Increase in loss of weight associated with increasing the average molecular weight leads to increase in bitumen viscosity. Loss of mass also has effect on indication of

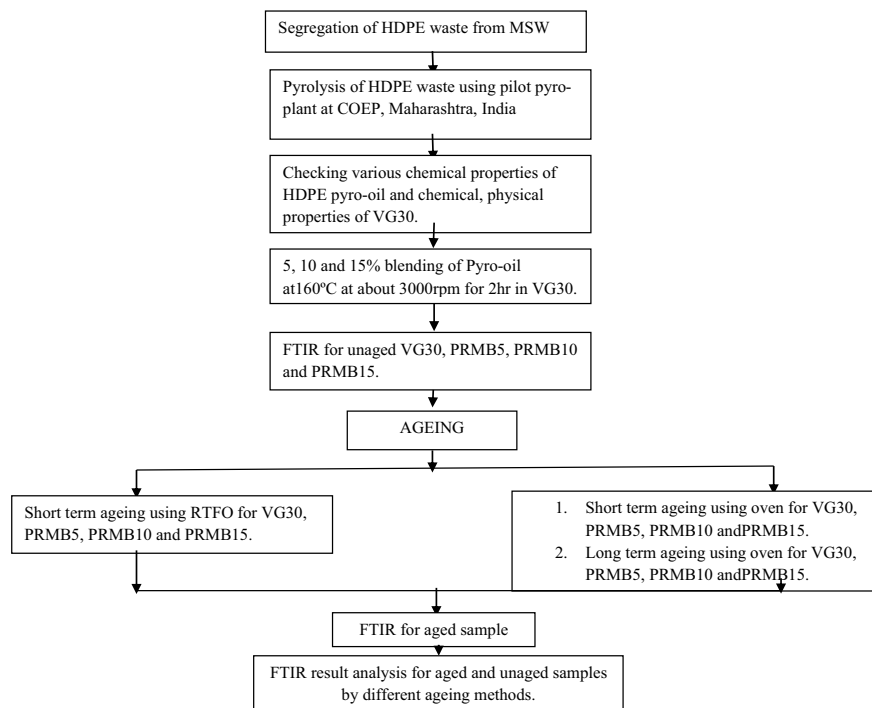


Fig. 1 Flowchart for methodology

potential bitumen binder emission during construction. The loss in mass for base bitumen and PRMB is less than 1%, which indicates that there was not much higher amount of light volatiles in pyro-oil. But lightweight fractions are more than base bitumen which might be due to pyrolysis process. It can be further concluded that there are some lightweight compounds in modified bitumen whose boiling point is lower than temperature in RTFO test.

6.2 FTIR Analysis of Base Bitumen and HDPE Pyro-oil Modified Bitumen

6.2.1 Short-Term Aged Sample by RTFO

Figures 2, 3, 4 and 5 show FTIR spectra. In the figures, horizontal axis is wave number (cm^{-1}) and vertical axis is transmission rate. From the graph, it is observed that the eminent peaks indicated for VG30 are crystal clear for bitumen. For the analysis of FTIR spectra, different groups of molecular bonds are categorized at different and specified wavelength of absorbance spectra. The four peaks in FTIR

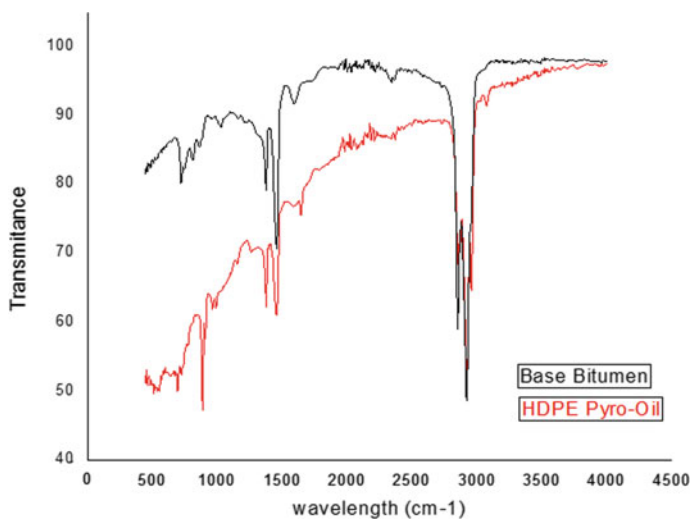


Fig. 2 FTIR spectra of VG30 and HDPE pyro-oil at room temperature

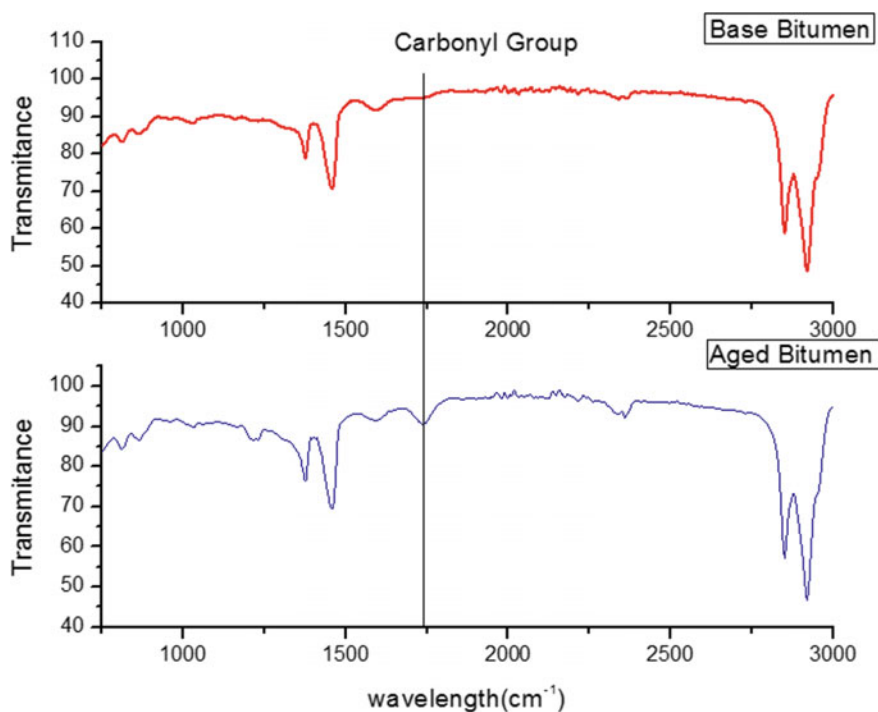


Fig. 3 FTIR spectra of VG30 (base bitumen) and short-term aged base bitumen at room temperature

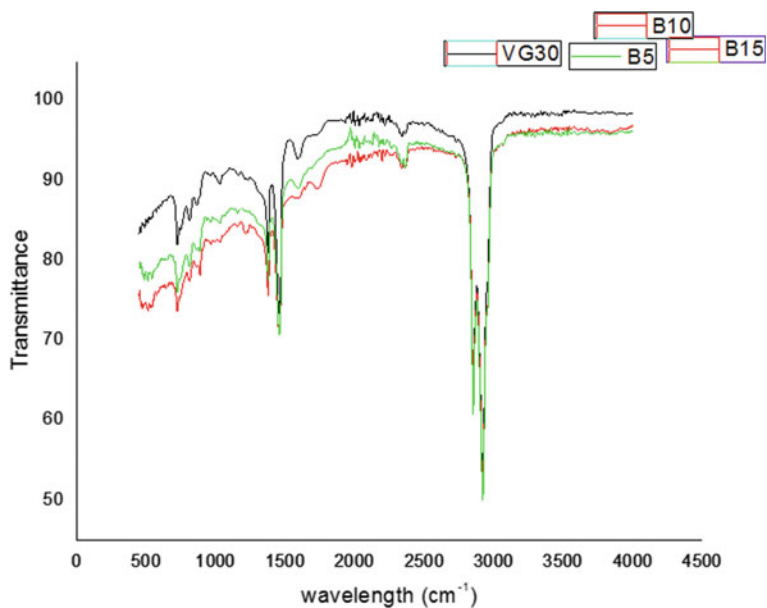


Fig. 4 FTIR spectra of VG30 (base bitumen), B5, B10 and B15 modified bitumen at room temperature

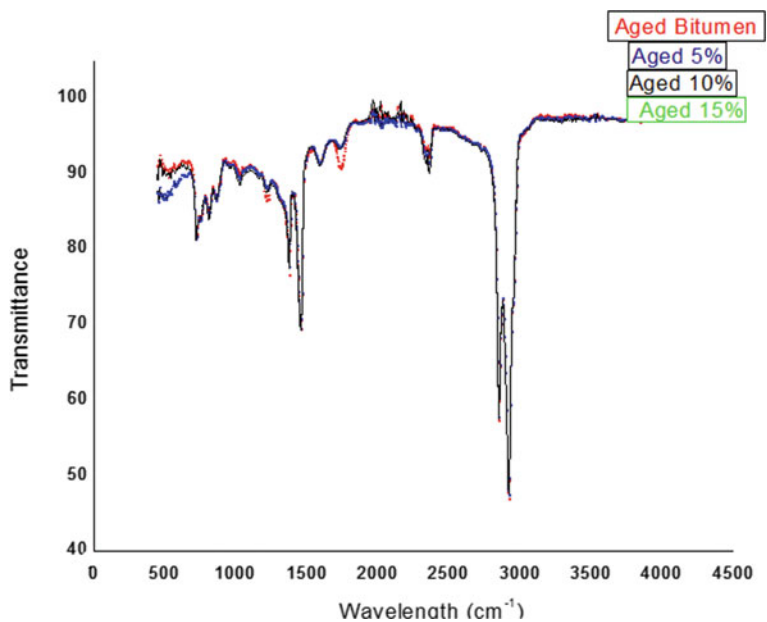


Fig. 5 FTIR spectra of short-term aged base bitumen, B5, B10 and B15 modified bitumen at room temperature

spectra for VG30 were observed in the range $2800\text{--}3000\text{ cm}^{-1}$, which region mainly corresponds to asymmetric and symmetric stretches of C–H in CH_2 and CH_3 . The major band at 2877 cm^{-1} typically represents hydrocarbon stretching vibrations and peak at 1458 cm^{-1} implies that C–H bond deformation vibrations. The other peak at 1600 cm^{-1} corresponds to C=C bond in benzene ring also known as vibration in aromatics whereas same bond in non-benzene ring appears for peak 960 cm^{-1} . Along with these prominent peaks, there are some other peaks like S=O, C=O which occurs at 1032 cm^{-1} and 1700 cm^{-1} , respectively, and as discussed by Petersen [24], S=O and C=O are generally used to characterize ageing in bitumen. The strong bond 1030 and 1280 cm^{-1} indicates C–O stretching vibration, implies presence of ether, alcohols, and phenols. The weak peaks at absorbance of about $1370\text{--}1380\text{ cm}^{-1}$ described regarding C–H deformation vibration, and this bonding is also present in PRMB. Figure 2 represents the variation in spectra for base bitumen VG30 and HDPE pyro-oil. One can observe the actual variation in spectra. Characteristics peak can observe and identify the existence of pyro-oil by comparing the spectra. For modification of base bitumen, HDPE pyro-oil was added and FTIR spectra for modified binder is observed and structural changes in base bitumen depend on the way in which modifier reacts with bitumen. Figure 3 gives spectra for base bitumen and PRMB and it is observed that both samples have nearly same peaks, which shows presence of same functional group, only intensity of some peaks vary obviously. From the same figure, this is also be verified that oxidation peaks for carbonyl and sulphoxides group change and for all other peaks remain unaltered/no prominent changes were observed. In general, it was noticed that this is common phenomenon for all types of modified bitumen.

6.2.2 Short-Term Aged Sample by Normal Oven Method

With the same modification to base bitumen, all samples were again tested for short-term ageing with the help of normal oven method as explained earlier. Figures 6, 7 and 8 show variation in FTIR spectra for both RTFO and normal oven aged base and modified bitumen. From these graphs, it is concluded that the formation of functional group during different ageing techniques shows formation of same functional group. Figure 9 shows the variation in FTIR spectra for short-term aged base and modified bitumen by normal oven method. Modified bitumen is formed by addition of 5, 10, and 15% of HDPE pyro-oil and denoted by SOPRMB5, SOPRMB10, and SOPRMB15. Whereas RTFO ageing of base and modified bitumen by addition of 5, 10, and 15% of HDPE pyro-oil and is denoted by SRVG30, SRPRMB5, SRPRMB10, and SRPRMB15, respectively. From Fig. 6, it is observed that ageing spectra is near about same for both RTFO and normal oven ageing technique which implies that we can use normal oven ageing for VG30 to simulate RTFO ageing effect as already explained by Behera et al. [2]. Figure 9 shows that as HDPE pyro-oil percentage increases sulphoxides also increases. But for relative comparison in between all these modified bitumen, one should go for calculation of different indexes using area under absorption curve. Whereas it is noted that sulphoxides group gets formed

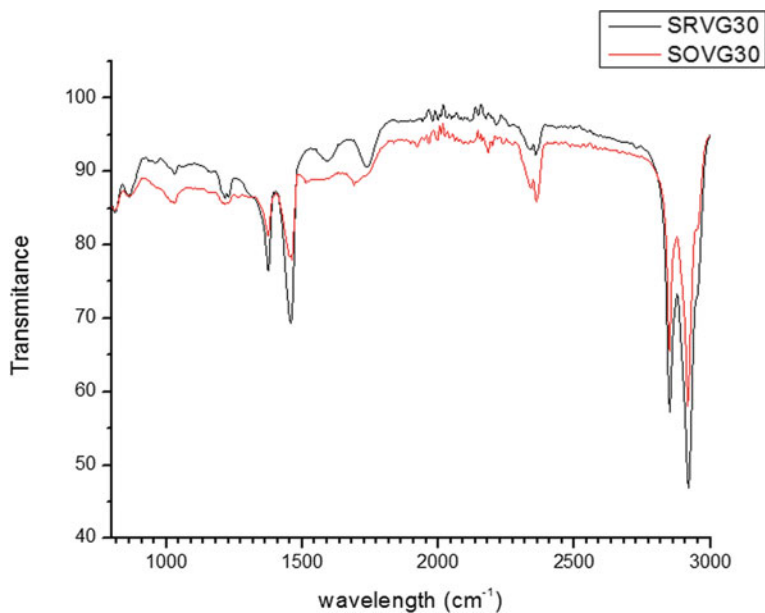


Fig. 6 FTIR spectra of short-term aged base bitumen modified bitumen by RTFO and normal oven method

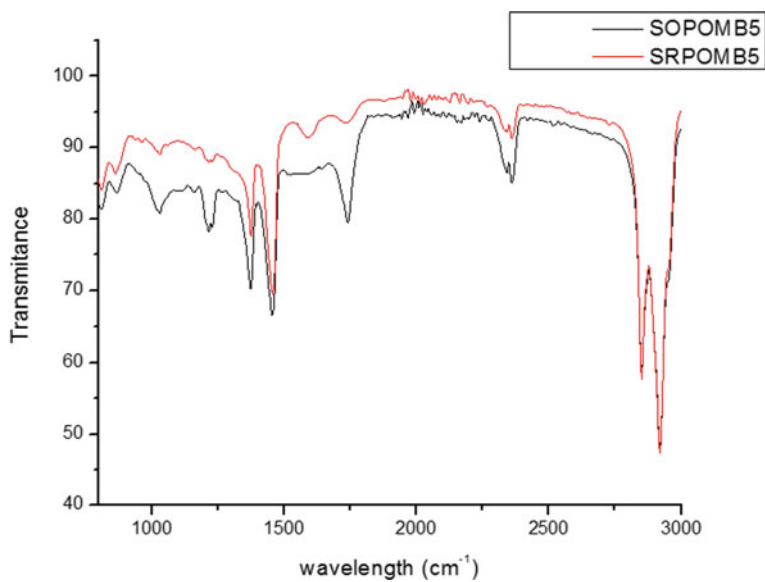


Fig. 7 FTIR spectra of short-term aged PRMB5 by RTFO and normal oven method

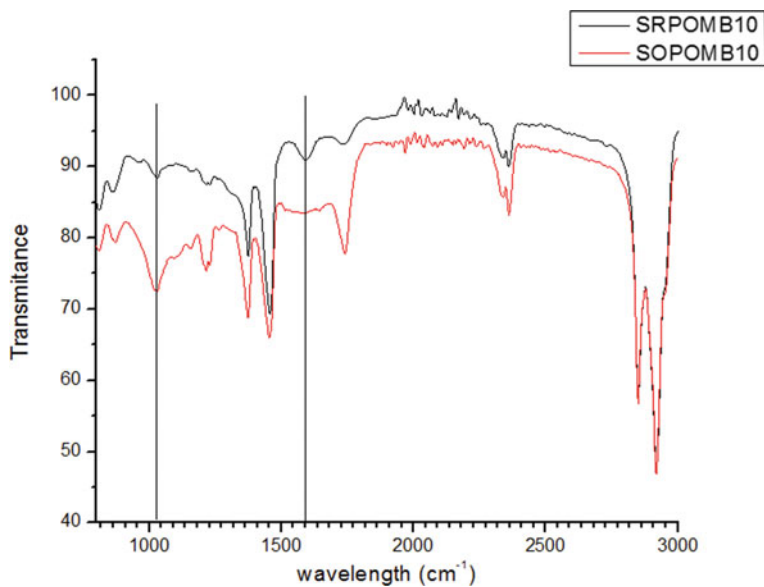


Fig. 8 FTIR spectra of short-term aged PRMB10 by RTFO and normal oven method

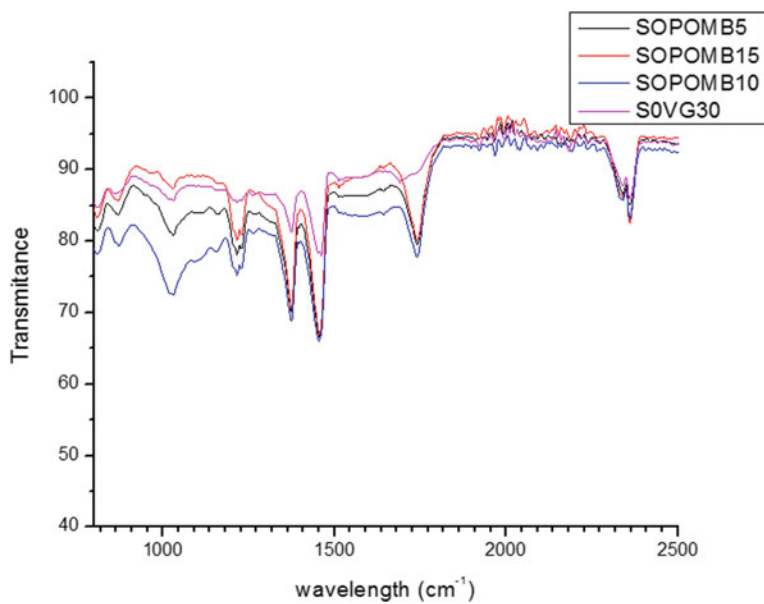


Fig. 9 FTIR spectra of short-term aged VG30, PRMB5, PRMB10, and PRMB15 normal oven method

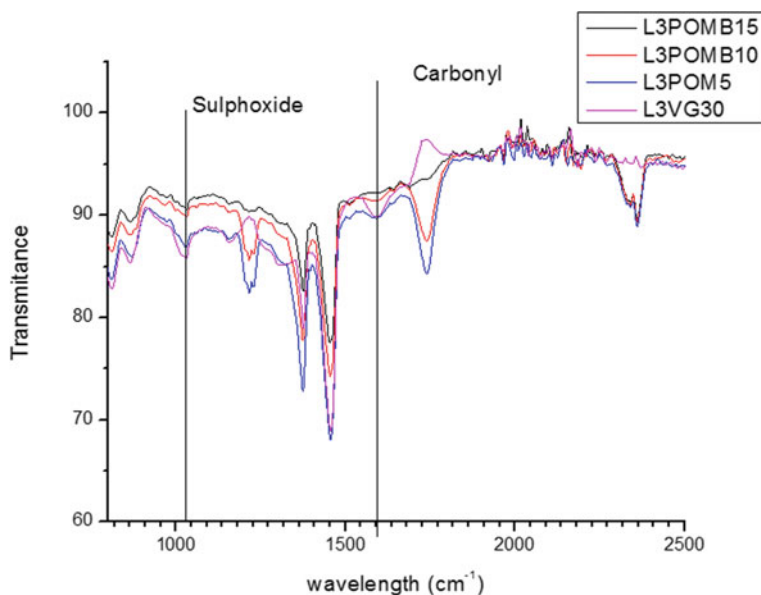


Fig. 10 FTIR spectra of 3-day long-term aged VG30, PRMB5, PRMB10, and PRMB15 by normal oven method

during short-term ageing which implies sulfur has more affinity toward oxygen than carbon.

6.2.3 Long-Term Aged Sample by Normal Oven Method

Figures 10, 11, 12 and 13 show the FTIR spectra for VG30, PRMB5, PRMB10, and PRMB15 of long-term ageing by normal oven method for 3 and 5 days at about 85 °C and denoted by L3VG30, L3PRMB5, L3PRMB10, L3PRMB15, L5VG30, L5PRMB5, L5PRMB10, and L5PRMB15, respectively. Due to the addition of HDPE pyro-oil, the variation in functional group during ageing also takes place. It is observed that with increase in ageing from 3 to 5 days carbonyl index increases. Again, to analyze further one should go for calculation of carbonyl and sulphoxides index in detail.

6.2.4 Quantification of Ageing on Unmodified and Modified Bitumen

As stated by Yang et al. [30], the ageing of bitumen during construction phase is mainly from two dimensions, the loss of volatile, and oxidation effect. The loss in volatile is calculated with the help of RTFO and already tabulated in Table 1. Along with this, oxidation of bitumen was also determined by chemical bondage

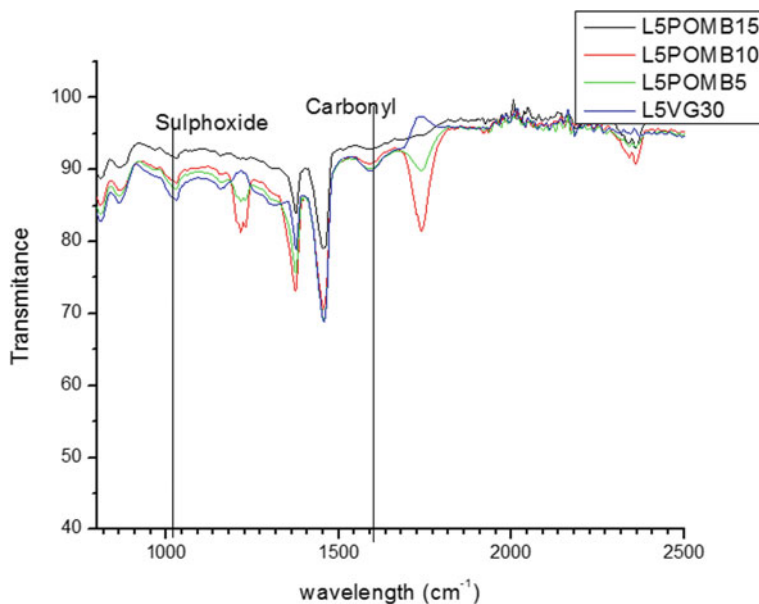


Fig. 11 FTIR spectra of 5-day long-term aged VG30, PRMB5, PRMB10, and PRMB15 by normal oven method

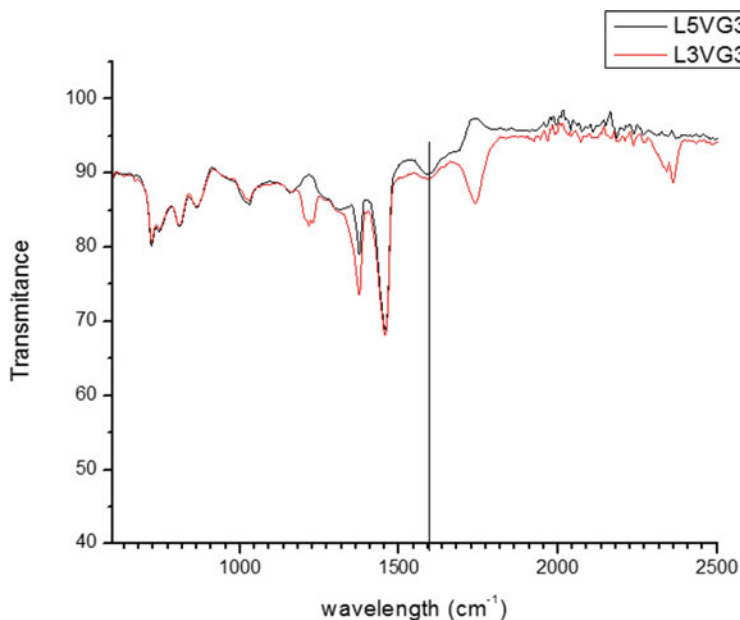


Fig. 12 FTIR spectra of 3-day long-term aged VG30, PRMB5, PRMB10, and PRMB15 by normal oven method

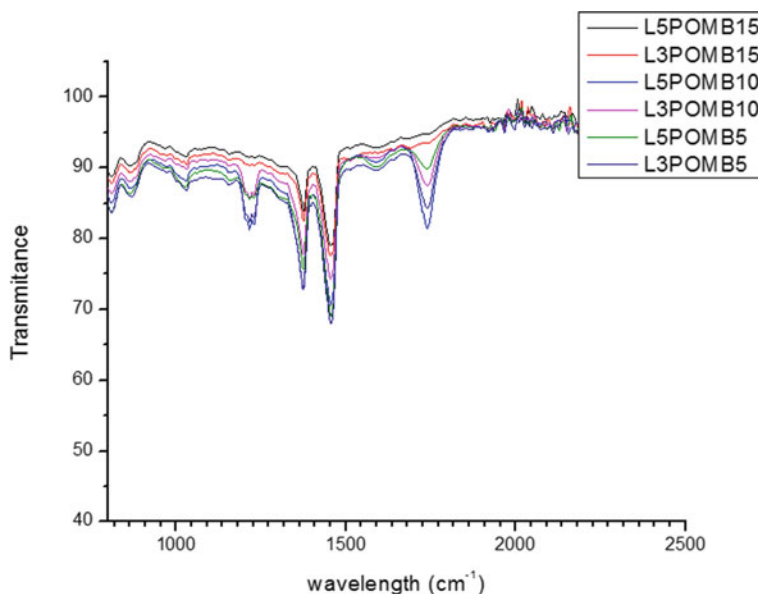


Fig. 13 FTIR spectra of 3-day long-term aged VG30, PRMB5, PRMB10, and PRMB15 by normal oven method

such as C=O and S=O in FTIR test. As explained by Nivitha et al. [22], ageing effect is monitored by peaks corresponding to carbonyl, sulphoxides, aliphaticity, and aromaticity. For the study of ageing, chemical modifications in base and modified bitumen was observed by analyzing FTIR spectra. As stated earlier, carbonyl (C=O) and sulphoxides (S=O) peaks change during oxidation of bitumen and same was observed from Fig. 3. As bitumen during modification subjected to temperature of about 160 °C for 2 h, oxidation takes place which leads to considerable amount of hydroperoxide formation. So to decrease in per hydromatic ring during the oxidation is the reason for absence of spurt during short-term ageing in modified binders. The results of FTIR graphs form Fig. 4 show that oxidation reaction lead to the formation of unsaturated bonds which may be due to addition of HDPE pyro-oil. In order to analyze the variation in functional group during ageing process, absorption peaks are recorded. These all transmission spectra converted into absorption peaks area of carbonyl, sulphoxides to calculate indices. Formation of C=O bond in carboxyl signifies the absorption of oxygen and S=O bond is formed due to the absorption of oxygen in sulfur content. But, the generation of sulphoxides mainly occurred in short-term ageing. So, it is concluded that sulfur atom has a stronger ability to absorb oxygen than carbon. C=C index decreases which implies that C=C gets affected or ruptured during ageing. The functional carbonyl groups in modified bitumen are less than those of base bitumen when ageing occurs. This indicates that this modification leads to less affinity toward oxygen. Table 2 shows important functional groups containing carbonyl in bitumen binder. It is found from the study of spectra that six

Table 2 Functional groups containing in bitumen binder

Functional group	Wavenumber (cm ⁻¹)
<i>Carboxylic</i>	
C=O	1700–1725
O–H	2500–3300
C–O	1210–1320
<i>Aldehyde</i>	
C=O	1720–1740
=C–H	2820–2850
<i>Amid</i>	
C=O	1640–1690
N–H	3100–3500 (stretching vibration)
N–H	1550–1640 (bending vibration)
<i>Anhydride</i>	
C=O	1800–1830
<i>Ester</i>	
C=O	1735–1750
C–O	1000–1300

functional group, namely, carboxylic acid, aldehyde, amide, anhydride, ester, and ketone contain carbonyl group in bitumen. This also proved and explained by different researchers. As per SuperPave report, bitumen contains around 1% of nitrogen and due to the same reason the peak of nitrogen and hydrogen bond (amide group) in bitumen not so strong but detectable. As explained by Yao et al. [31], due to the coverage of strong bands, the peaks around anhydrides are not easily observed but evidences are found to support that anhydrides are present in bitumen. From spectra, it is found that, ester formed during ageing of bitumen and carbonyl group in the ester is observed at range of 1735–1750 cm⁻¹.

7 Conclusions

In this study, HDPE pyro-oil was added to base bitumen (VG30) to investigate the effect of ageing. The base bitumen and modified bitumen were tested by FTIR to study the different functional groups under short-term and long-term ageing conditions. Based on the results of FTIR for different bitumen samples following results are summarized.

From physical properties, it was found that pyro-oil modified bitumen has better application in low-temperature region compared to hotter climate but this should be supported with rheological results. Short-term ageing by both RTFO and normal oven method gives same FTIR spectra. FTIR spectra show carbonyl area increases from

unaged sample to RTFO/oven aged and thereafter maximum area under band for long-term ageing for 3 days and 5 days. It is found that pyro-oil modified bitumen has loss in mass less than 1% of base bitumen, which is as per SuperPave specifications provided for RTFO mass loss. Six functional groups amide, anhydride, aldehydes, carboxylic acid, ketone, and esters contain carbonyl group. Upper and lower wavenumber for different base and modified bitumen found to be in the range of 1600–1750 cm^{-1} for carbonyl group, 920–1060 cm^{-1} for sulphoxides. Base binder and HDPE pyro-oil exhibit physical as well as chemical interaction as peaks of some functional groups change and shift in position of peaks was recorded. Modified bitumen undergoes less ageing compared with base bitumen as carbonyl functional group is less than base bitumen.

References

1. Al-Hadidy AI, Tan YQ (2010) The effect of SBS on asphalt and SMA mixture properties. *J Mater Civ Eng* 1(1):156
2. Behera PK, Singh AK, Amaranatha Reddy M (2013) An alternative method for short-and long-term ageing for bitumen binders. *Road Mater Pavement Des* 14(2):445–457
3. Bischoff D, Toepel A (2004) Tire rubber in hot mix asphalt pavements. Wisconsin Department of Transportation, Division of Transportation Infrastructure Development, Bureau of Highway Construction, Technology Advancement Unit
4. Chen M, Leng B, Wu S, Sang Y (2014) Physical, chemical and rheological properties of waste edible vegetable oil rejuvenated asphalt binders. *Constr Build Mater* 66:286–298
5. Cheng J, Shen J, Xiao F (2011) Moisture susceptibility of warm-mix asphalt mixtures containing nanosized hydrated lime. *J Mater Civ Eng* 23(11):1552–1559
6. Eberhardsteiner L, Füssl J, Hofko B, Handle F, Hospodka M, Blab R, Grothe H (2015) Towards a microstructural model of bitumen ageing behaviour. *Int J Pavement Eng* 16(10):939–949
7. Habal A, Singh D (2018) Influence of recycled asphalt pavement on interfacial energy and bond strength of asphalt binder for different types of aggregates. *Transp Res Rec* 2672(28):154–166
8. Hadole HP, Suryawanshi SD, Khapne VA, Ranadive MS (2021) Moisture damage resistance of short-term aged pyro-oil–modified bitumen using rolling thin film oven by surface free energy approach. *J Mater Civ Eng* 33(10):04021268
9. Harnsberger PM et al (1993) Comparison of oxidation of SHRP asphalts by two different methods. *Fuel Sci Technol Int* 11(1):89–121
10. Hofko B, Handle F, Eberhardsteiner L, Hospodka M, Blab R, Füssl J, Grothe H (2015) Alternative approach toward the aging of asphalt binder. *Transp Res Rec J Transp Res Board* 2505(2505):24–31
11. IS 1208 Methods for testing tar and bituminous materials. Bureau of Indian Standards, New Delhi
12. IS 1205 Methods for testing tar and bituminous materials: determination of softening point. Bureau of Indian Standards, New Delhi
13. IS 1203 Methods of testing tar and-bituminous materials: determination of penetration
14. IS 73 (2013) Indian standard for paving bitumen-specification (fourth revision). Bureau of Indian Standards, New Delhi
15. IS 1206-Part1. Methods for testing tar and bituminous materials: determination of viscosity
16. IS 1206-Part2. Methods of testing tar and bituminous materials: determination of absolute viscosity
17. IS 1206-Part3. Methods of testing tar and bituminous materials: determination of kinematic viscosity

18. IS 9382: Methods for testing tar and bituminous materials: determination of effect of heat and air by thin film oven tests. Bureau of Indian Standards, New Delhi
19. Jahromi SG, Khodaii A (2009) Effects of nanoclay on rheological properties of bitumen binder. *Constr Build Mater* 23(8):2894–2904
20. Khapne V, Hadole H, Ranadive M (2020) Assessment of anti-stripping property of pyro-oil modified bituminous mixes using surface free energy approach. In: International conference on transportation and development 2020, American Society of Civil Engineers, Reston, VA, pp 127–137
21. Kulkarni SB, Ranadive MS (2020) Modified cutback as tack coat by application of pyro-oil obtained from municipal plastic waste: experimental approach. *J Mater Civ Eng* 32(5):04020100
22. Nivitha MR, Prasad E, Krishnan JM (2016) Ageing in modified bitumen using FTIR spectroscopy. *Int J Pavement Eng* 17(7):565–577
23. Petersen JC (1975) Quantitative method using differential infrared spectrometry for the determination of compound types absorbing in the carbonyl region in asphalts. *Anal Chem* 47(1):112–117
24. Petersen JC (2009) A review of the fundamentals of asphalt oxidation: chemical, physicochemical, physical property, and durability relationships. *Transp Res Circular E-C140*
25. Ranadive MS, Hadole HP, Padamwar SV (2017) Performance of stone matrix asphalt and asphaltic concrete using modifiers. *J Mater Civ Eng* 30(1):04017250
26. Reddy KS (2007) Investigation of rutting failure in some section of national highways-2. between KM 317 and KM 65. Transportation Engineering Section, Department of Civil Engineering, IIT Kharagpur, India
27. Shen J, Amirkhaniyan S, Xiao F, Tang B (2009) Influence of surface area and size of crumb rubber on high temperature properties of crumb rubber modified binders. *Constr Build Mater* 23(1):304–310
28. Suryawanshi SD, Hadole HP, Ranadive MS (2021) Evaluation of moisture susceptibility of pyro-oil modified bitumen by surface free energy approach. In: Ground improvement techniques: select proceedings of 7th ICRAGEE 2020, vol 118. p 363
29. Thodesen C, Shatanawi K, Amirkhaniyan S (2009) Effect of crumb rubber characteristics on crumb rubber modified (CRM) binder viscosity. *Constr Build Mater* 23(1):295–303
30. Yang X, Mills-Beale J, You Z (2017) Chemical characterization and oxidative aging of bio-asphalt and its compatibility with petroleum asphalt. *J Clean Prod* 142:1837–1847
31. Yao H, Dai Q, You Z (2015) Fourier transform infrared spectroscopy characterization of aging-related properties of original and nano-modified asphalt binders. *Constr Build Mater* 101:1078–1087

Utilization of Aluminium Refinery Residue (ARR), GGBS and Alkali Solution Mixes in Road Construction



Nityanand S. Kudachimath, Raviraj H. Mulangi, and Bhibuti Bhusan Das

Abstract Manufacturing and the construction industries are on the boom with the growing economy of the world. Aluminium and steel are produced in very large quantities compared to other metals. These industries also produce by-products that are either partially utilized or unutilized. Aluminium refinery residue (ARR) with its colour known as Redmud, produced from bauxite by Bayer process, because of its high pH demands huge storage land. In road construction, a large quantity of material is required at the lower layers. In the present work wastes from both industries are tried for reuse. Ground-granulated blast furnace slog (GGBS) from the iron and steel industry makes complex compounds with sodium silicate and sodium hydroxide to increase the strength properties of aluminium refinery residue (ARR) and is verified with basic laboratory experiments for strength and durability tests on stabilized aluminium refinery residue (ARR). Ground-granulated blast furnace slog (GGBS) of 20–30% is used to stabilize ARR, and cured for up to 28 days, and the result of the various mix has shown an increase in strength with curing periods. The highest UCS test result of 4.01 MPa was observed for 28 days cured sample. For durability tests, the treated specimens are passed through wet/dry cycle and freeze/thaw conditions for various curing periods.

Keywords Aluminium refinery residue (ARR) · Ground-granulated blast furnace slag (GGBS) · Sodium silicate (Na_2SiO_3) · Sodium hydroxide (NaOH) · Alkaline solution

N. S. Kudachimath (✉) · R. H. Mulangi · B. B. Das
Department of Civil Engineering, National Institute of Technology Karnataka, Surathkal,
Mangaluru, India
e-mail: nskudachimath@gmail.com

R. H. Mulangi
e-mail: ravirajhm@nitk.edu.in

B. B. Das
e-mail: bdas@nitk.edu.in

N. S. Kudachimath
Department of Civil Engineering, Jain College of Engineering, Belagavi, Karnataka, India

Notations Used

ARR	Aluminium refinery residue
GGBS	Ground-granulated blast furnace slag
MDD	Maximum dry density
OMC	Optimum moisture content
UCS	Unconfined compressive strength

1 Introduction

1.1 About ARR

A huge quantity of waste materials is generated due to infrastructure development and industrialization. These wastes require dumping areas (land) to reduce environmental pollution. Redmud, also called bauxite residue/aluminium refinery residue (ARR), is one of the waste materials. Nearly about 1 ton of ARR is generated on extraction per ton of aluminium [1]. The extraction of ARR is followed by Bayer's process (Fig. 1). ARR is alkaline in nature and pH is about 11–13 [2]. This waste combined with alkalinity and heavy metals indirectly leads to difficulties when disposed of. Redmud consists of fine particles which consolidate slowly and contaminate the surroundings, and hence it becomes the need of the hour to reuse for other works or construction works [3].

1.2 About GGBS

GGBS is a by-product of the production of iron. The gradation of GGBS is dependent upon slag chemical composition. Hence it acts as a binding/cementitious material that leads to the formation of C–A–H and C–S–H gel [4].

Many researchers worked on soil stabilization by mixing red mud and other available industrial wastes. In 2012, Satayanarayana et al. [5] noticed that 10% of lime with red mud gave better stabilized results. Walid et al. [6] used metakaolin with sodium silicate solution, prepared new material, and named geopolymer. From experimental results, they concluded that the prepared new material behaves as an alkali activator and gives higher compressive strength results.

The present study deals with the stabilization of soil properties with the application of ARR and GGBS with activator solutions. Here, the selected activators are NaOH and Na_2SiO_3 because of their non-side effects on soil. The best proportion of ARR and GGBS is made by conducting several trials. The mechanical properties of the prepared sample are studied and explained the same.

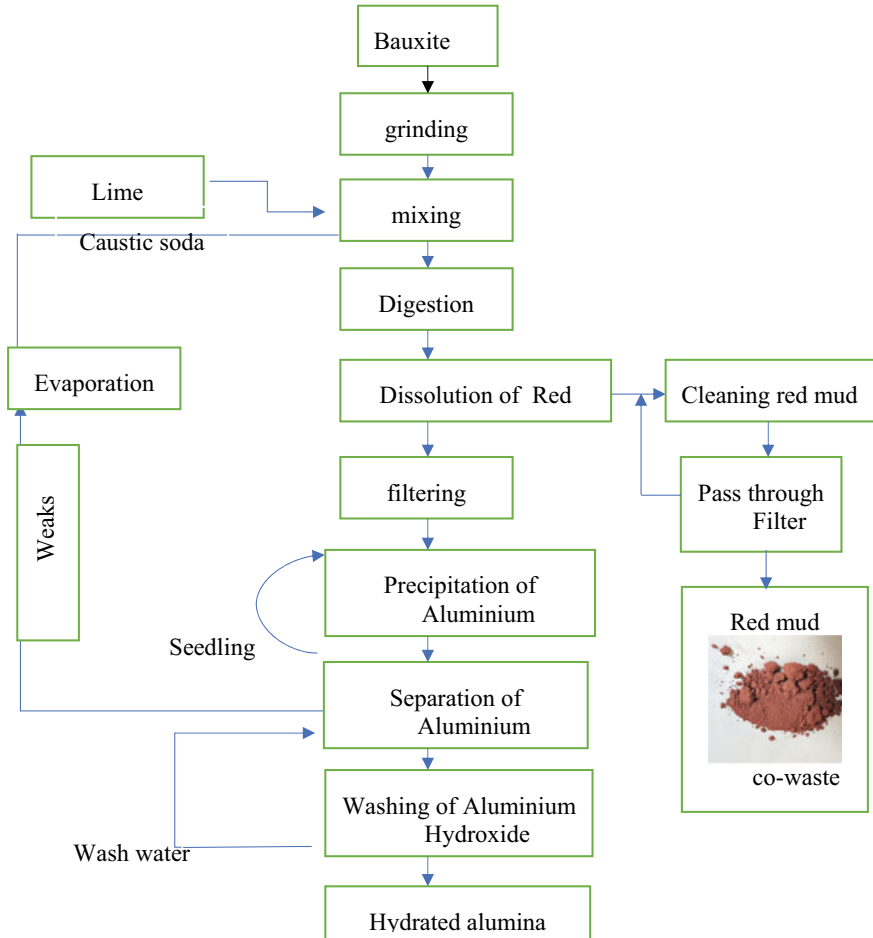


Fig.1 Bayer's process

2 Materials and Methodology

Experimentations were done by collecting AAR from HINDALCO Industries Ltd. Located in Belagavi and GGBS from JSW Ltd Bellary. Collected samples were having moisture content. To remove this, the collected sample is dried in an oven from 105 to 110 °C. The activator Na_2SiO_3 was purchased from Shanti Chemicals located in Belagavi, and dilution of NaOH is prepared 24 h prior to conducting experiments.

To examine the basic properties of the collected sample, some tests were conducted as per IS codes and the obtained results are discussed in Tables 1, 2 and 3.

Table 1 Chemical composition of ARR

Composition	Na ₂ O	TiO ₂	Fe ₂ O ₃	LOI	SiO ₂	CaO	Al ₂ O ₃
Percentage (%)	7.3	9.2	36.3	10.4	12.1	1.2	22.1

Table 2 Chemical composition of GGBS

Composition	TiO ₂	Na ₂ O	Al ₂ O ₃	FeO	CaO	SiO ₂	K ₂ O	MgO
Percentage (%)	14.28	4.56	17.23	29.92	20.52	12.96	0.61	0.98

Table 3 Other properties of ARR and GGBS

Properties	ARR	GGBS
Specific gravity	3.2	2.9
Plastic limit	32	–
Liquid limit	37	33
Plastic index	3	–

Table 4 OMC and MDD results

Particulars	Modified proctor test	
	OMC in percentage	MDD in g/cc
20-4-1	28	1.93
25-4-1	24	1.98
30-4-1	22	1.89

3 Results and Discussions

3.1 OMC and MDD

The OMC and MDD were examined for the modified proctor test. Experimental results are listed in Table 4 for different mixes altering the GGBS from 20, 25 and 30% of the required total soil sample. From experimentation it is noticed that MDD obtained for 25% of GGBS is the highest, and a further increase in GGBS content caused reduction in strength and it is concluded that (25-4-1) 25% of GGBS, 4% of Na₂O content with 1 silica modulus gave a result of 1.98 g/cc.

3.2 UCS Test

UCS test was conducted for different proportions of GGBS and ARR by altering silica modulus from 0.5 to 1.5 and GGBS is altered from 20 to 30% by weight of the required soil sample. From experimental results, the below discussions are made (Fig. 2 and Table 5).

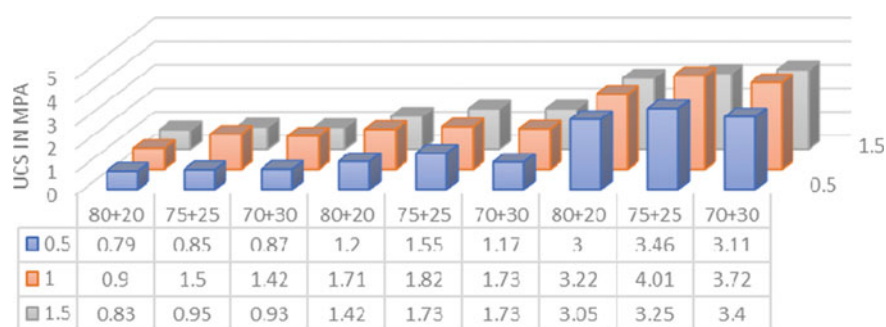


Fig. 2 UCS results for various mix proportions

Table 5 UCS test results

Proportion (ARR+GGBS) out of total required sample (in %)	Curing period (in days)	Silica modulus		
		0.5	1	1.5
80 + 20	0	0.79	0.9	0.83
	7	1.2	1.71	1.42
	28	3	3.22	3.05
75 + 25	0	0.85	1.5	0.95
	7	1.55	1.82	1.73
	28	3.46	4.01	3.25
70 + 30	0	0.87	1.42	0.93
	7	1.17	1.73	1.73
	28	3.11	3.72	3.4

From the above-obtained results, it is concluded that stabilized ARR for a combination of GGBS:Na₂O:silica modulus of 25-4-1 for curing periods of 0, 7 and 28 days gave a positive effect on the UCS test. The strength increased due to the formation of alumina silicate gel. The obtained results are compared with stabilized ARR (25-4-1, 25% GGBS, 4% Na₂O and 1% silica modulus) to find the best result among the selected mix, and it is concluded that there is an increase in strength by 66, 6 and 24.5% for 0, 7 and 28 days of curing (comparison of 20 and 25% GGBS mix). And for further increase in the amount of GGBS content, the strength is reduced by 5.3, 4.9 and 7.2% when compared with 25-4-1 (comparison of 25 and 30% GGBS mix). The best-obtained results are 1.5, 1.82 and 4.01 MPa for 0, 7 and 28 days of curing for a combination of 75% of ARR and 25% of GGBS (Table 5).

4 Durability Test

The test has been conducted over the prepared sample, during wet and dry processes. From test results shown in Table 6, it is noticed that the prepared sample cured for 0 day failed at the initial stage/cycle and the sample cured for 3 days failed at 6

Table 6 Durability test results

Number of cycles	Percentage reduced weight (%)															
	W&D test						F&T test									
	W		D		W		D		W		D					
	Curing period (days)															
	0		3		7		28		0		3		7		28	
1	W	D	W	D	W	D	W	D	F	T	F	T	F	T	F	T
	Failed		-10.4	8.5	-12.5	4.9	-15.4	-3.6	6	6.5	2.4	3.1	0.2	0.8	0.3	0.3
2			-9.3	9.4	-12.3	5.2	-15.3	-1.4	9.1	8.2	2.4	3.1	0.2	0.8	0.3	0.4
3			-6.5	10.2	-12.3	5.2	-14.5	2.2	9.1	9.2	2.6	3.4	0.3	0.8	0.4	0.4
4			-5.3	11	-12.1	5.4	-14.6	2.5	9.3	9.2	2.8	3.4	0.3	1.3	0.4	0.5
5			-4.7	11.5	-12.1	5.6	-14.4	2.8	9.3	9.2	3.1	3.4	0.3	1.5	0.5	0.5
6			Failed		-11.5	5.7	-13.9	3.5	9.4	9.3	3.1	4	0.4	1.5	0.5	0.6
7					-11.7	5.7	-13.5	3.9	9.5	9.3	3.6	4	0.4	1.6	0.5	0.6
8					-11.2	6.2	-12.7	4.3	9.5	9.5	3.6	4	0.5	1.6	0.6	0.6
9					-11	6.2	-11.4	4.7	9.6	9.5	3.7	4	0.7	1.8	0.7	0.7
10					-10.5	6.3	-11.4	5.5	9.6	9.7	3.8	4.2	0.8	1.8	0.8	0.7
11					-10.5	6.4	-10	5.9	9.7	9.9	4.1	4.2	0.8	1.8	0.9	0.8
12					-10.5	6.5	-10.3	6.7	10	9.9	4.2	4.2	1.2	1.8	1	1

cycles. While the sample was cured for 7 and 28 days it passed all 12 cycles of dry and wet with a ratio weight gain of 10.5 and 10.3%, respectively. However, in the freeze–thaw test, the prepared sample passed all cycles for 0, 3, 7 and 28 days of curing with percentage weight loss of 9.9, 4.2, 1.8 and 1 correspondingly. With consideration of all the results, the stabilized ARR sample for 7 and 28 days of curing passed the dry and wet tests and hence, the considered dosage can be used for construction activities.

5 Conclusions

- Highest MDD is obtained for 25% of GGBS and 75% of ARR, and a further increase in GGBS content caused a reduction in density.
- Stabilized ARR for a combination of GGBS:Na₂O:silica modulus of 25-4-1 for curing periods of 7 and 28 days gave a positive effect on UCS.
- It is noticed that increase in strength by 66, 6 and 24.5% for 0, 7 and 28 days of curing (comparison of 20 and 25% GGBS mix). And on further increase in the amount of GGBS content, the strength is reduced by 5.3, 4.9 and 7.2% when compared with 25-4-1 (comparison of 25 and 30% of GGBS).
- The best-obtained results are 1.5, 1.82 and 4.01 MPa for 0, 7 and 28 days of curing for a combination of 75% of ARR and 25% of GGBS.
- A durability test was conducted and the prepared sample cured for the same days failed in the initial stage/cycle and the sample cured for 3 days failed at 6 cycles.
- The sample cured for 7 and 28 days passed all 12 cycles of dry and wet with a ratio weight gain of 10.5 and 10.3%, respectively.
- In the freeze and thaw test, the prepared sample passed all cycles for 0, 3, 7 and 28 days of curing with weight loss of 10, 4.2, 1.8 and 1% correspondingly.
- The stabilized ARR sample for 7 and 28 days of curing passed the dry and wet tests and hence, the considered dosage can be used for construction activities.

References

1. Samal S, Ray AK (2013) Utilization and process of redmud in India. *Int J Miner Process* 118:43–55
2. Newton T (2006) Effect of structure on geotechnical properties of bauxite residue. *J Geotech Geoenvironmental Eng* 132(2):143–151
3. Kudachimath N, Raviraj HM, Das BB (2021) Effect of Ggbs on strength of aluminium refinery residue stabilized by alkali solution. In: *Recent trends in civil engineering*. Springer, Singapore, pp 331–339
4. Davidovitz J (1991) Inorganic polymeric new materials. *J Therm Anal* 37:1633–1656

5. Satyanarayana PVV, Adishesa, Ganpati Naidu (2012) Characterization of lime stabilised redmud mixfor feasibility in road construction. *Int J Eng Res Dev* 3(7):20–26
6. Walid H, Andreej Kovic, Alshaer M (2013) Composition and technological properties of GP based metakaolin and redmud. *52:648–654*